

Lecture Notes in Mechanical Engineering

Sendhil Kumar Natarajan  
Rajiv Prakash  
K. Sankaranarayananasamy *Editors*

# Recent Advances in Manufacturing, Automation, Design and Energy Technologies

Proceedings from ICoFT 2020

 Springer


# Lecture Notes in Mechanical Engineering

## Series Editors

Francisco Cavas-Martínez, Departamento de Estructuras, Universidad Politécnica de Cartagena, Cartagena, Murcia, Spain

Fakher Chaari, National School of Engineers, University of Sfax, Sfax, Tunisia

Francesca di Mare, Institute of Energy Technology, Ruhr-Universität Bochum, Bochum, Nordrhein-Westfalen, Germany

Francesco Gherardini , Dipartimento di Ingegneria, Università di Modena e Reggio Emilia, Modena, Italy

Mohamed Haddar, National School of Engineers of Sfax (ENIS), Sfax, Tunisia

Vitalii Ivanov, Department of Manufacturing Engineering, Machines and Tools, Sumy State University, Sumy, Ukraine

Young W. Kwon, Department of Manufacturing Engineering and Aerospace Engineering, Graduate School of Engineering and Applied Science, Monterey, CA, USA

Justyna Trojanowska, Poznan University of Technology, Poznan, Poland



**Lecture Notes in Mechanical Engineering (LNME)** publishes the latest developments in Mechanical Engineering—quickly, informally and with high quality. Original research reported in proceedings and post-proceedings represents the core of LNME. Volumes published in LNME embrace all aspects, subfields and new challenges of mechanical engineering. Topics in the series include:

- Engineering Design
- Machinery and Machine Elements
- Mechanical Structures and Stress Analysis
- Automotive Engineering
- Engine Technology
- Aerospace Technology and Astronautics
- Nanotechnology and Microengineering
- Control, Robotics, Mechatronics
- MEMS
- Theoretical and Applied Mechanics
- Dynamical Systems, Control
- Fluid Mechanics
- Engineering Thermodynamics, Heat and Mass Transfer
- Manufacturing
- Precision Engineering, Instrumentation, Measurement
- Materials Engineering
- Tribology and Surface Technology

To submit a proposal or request further information, please contact the Springer Editor of your location:

**China:** Ms. Ella Zhang at [ella.zhang@springer.com](mailto:ella.zhang@springer.com)

**India:** Priya Vyas at [priya.vyas@springer.com](mailto:priya.vyas@springer.com)

**Rest of Asia, Australia, New Zealand:** Swati Meherishi at [swati.meherishi@springer.com](mailto:swati.meherishi@springer.com)

**All other countries:** Dr. Leontina Di Cecco at [Leontina.dicecco@springer.com](mailto:Leontina.dicecco@springer.com)

To submit a proposal for a monograph, please check our Springer Tracts in Mechanical Engineering at <http://www.springer.com/series/11693> or contact [Leontina.dicecco@springer.com](mailto:Leontina.dicecco@springer.com)

**Indexed by SCOPUS. All books published in the series are submitted for consideration in Web of Science.**

More information about this series at <http://www.springer.com/series/11236>

Sendhil Kumar Natarajan · Rajiv Prakash ·  
K. Sankaranarayananamy  
Editors

# Recent Advances in Manufacturing, Automation, Design and Energy Technologies

Proceedings from ICoFT 2020

 Springer

*Editors*

Sendhil Kumar Natarajan  
Department of Mechanical Engineering  
National Institute of Technology  
Puducherry  
Karaikal, Puducherry, India

Rajiv Prakash  
School of Materials Science  
and Technology  
Indian Institute of Technology (Banaras  
Hindu University)  
Varanasi, India

K. Sankaranarayanan  
Department of Mechanical Engineering  
National Institute of Technology  
Puducherry  
Puducherry, India

ISSN 2195-4356

ISSN 2195-4364 (electronic)

Lecture Notes in Mechanical Engineering

ISBN 978-981-16-4221-0

ISBN 978-981-16-4222-7 (eBook)

<https://doi.org/10.1007/978-981-16-4222-7>

© The Editor(s) (if applicable) and The Author(s), under exclusive license to Springer Nature Singapore Pte Ltd. 2022

This work is subject to copyright. All rights are solely and exclusively licensed by the Publisher, whether the whole or part of the material is concerned, specifically the rights of translation, reprinting, reuse of illustrations, recitation, broadcasting, reproduction on microfilms or in any other physical way, and transmission or information storage and retrieval, electronic adaptation, computer software, or by similar or dissimilar methodology now known or hereafter developed.

The use of general descriptive names, registered names, trademarks, service marks, etc. in this publication does not imply, even in the absence of a specific statement, that such names are exempt from the relevant protective laws and regulations and therefore free for general use.

The publisher, the authors and the editors are safe to assume that the advice and information in this book are believed to be true and accurate at the date of publication. Neither the publisher nor the authors or the editors give a warranty, expressed or implied, with respect to the material contained herein or for any errors or omissions that may have been made. The publisher remains neutral with regard to jurisdictional claims in published maps and institutional affiliations.

This Springer imprint is published by the registered company Springer Nature Singapore Pte Ltd. The registered company address is: 152 Beach Road, #21-01/04 Gateway East, Singapore 189721, Singapore

# Preface

We are pleased to publish the selected and recommended manuscripts presented in the Three days Virtual Mode “International Conference on Future Technologies 2020 (ICoFT 2020) in Manufacturing, Automation, Design and Energy” (MADE) held at National Institute of Technology Puducherry, Karaikal, U.T. of Puducherry, India, from 28 to 30 December 2020.

In this book, around 107 quality papers in the area of manufacturing, automation, design and energy are included for publication in Springer—*Lecture Notes in Mechanical Engineering*. We assured that all the chapters presented in the book entitled *Recent Advances in Manufacturing, Automation, Design and Energy Technologies* will be helpful for the research community to know the latest trends in the above-mentioned areas.

We are thankful to various reviewers in the domain of mechanical engineering and allied areas for their valuable suggestions for improving the quality of the chapters. We are also thankful to the session chairs, Organizing Committee, sponsors (M/s. Swelect Energy Systems Ltd., Chennai, India, and Renewable Energy Agency Puducherry, U.T. of Puducherry, India) and host institute (National Institute of Technology Puducherry, Karaikal, U.T. of Puducherry, India) for their support.

Karaikal, U.T. of Puducherry, India  
Varanasi, India

Dr. Sendhil Kumar Natarajan  
Prof. Rajiv Prakash

# Contents

## Manufacturing

<b>Smart Materials for 4D Printing: A Review on Developments, Challenges and Applications</b> .....	3
Sreenivasulu Reddy	
<b>Examining the Build Properties of PolyJet Printed Multi-material Parts in Additive Manufacturing</b> .....	11
Arivazhagan Pugalendhi and Rajesh Ranganathan	
<b>Design of Workplace in Assembly Unit Using Ergonomic Principles</b> ....	19
V. Manivelmuralidaran, M. Balaji, and V. Arun	
<b>Experimental Investigation on Electrochemical Discharge Machining of Zirconia</b> .....	27
Vijay Manoharan, Sekar Tamilperuvalathan, Elango Natarajan, and Prasanth Ponnusamy	
<b>Risk Management for e-Commerce Supply Chain Network Using Robust Optimization Approach: A Case Study</b> .....	35
Shubhender Singh, Pradeep Kumar, Manish Bhandari, and Gunjan Soni	
<b>Calculation of Filling Characteristic of Cast Al–Si Alloy</b> .....	47
Samavedam Santhi, U. S. Jyothi, and K. Srinivasa Vadayar	
<b>Review on Materials and Method Used to Develop Antimicrobial Coatings in Medical and Food Processing Industry</b> .....	57
Vinod Babu Chintada, Sasidhar Gurugubelli, and Sudhakar Uppada	
<b>Influence of Drilling Operation Variables on Surface Roughness and Thrust Force of Aluminium Reinforced with 10% Al<sub>2</sub>O<sub>3</sub> Functionally Graded Metal Matrix Composite</b> .....	65
S. Prathap Singh, T. Prabburam, D. Elilraja, and J. Immanuel Durairaj	

<b>Effect of Laser Scan Speed on Microstructure and Microhardness on Titanium Clad Magnesium</b> .....	75
Kannan Ganesa Balamurugan and Muthukannan Duraiselvam	
<b>Detonation Gun Spray Coatings on Martensitic Stainless Steels</b> .....	85
J. Jhansi, S. Santhi, P. V. S. Lakshmi Narayana, and Bhomik Ketari Deogade	
<b>Joining of Dissimilar Aluminum Alloys AA2024 and AA7075 by Friction Stir Welding: A Review</b> .....	95
Ajay Kaushal, Sachindra Shankar, and Somnath Chattopadhyaya	
<b>Observational Exposition of Metal Matrix Composite Aluminum 6069 (Al) Fraction Variance Strengthened with Molybdenum (Mo) and Coconut Shell Ash (CSA)</b> .....	105
Fathimunnisa Begum, Sasidhar Gurugubelli, and N. Ravi Kumar	
<b>Recent Advances in Machining of Composites and Super Alloys by Using Wire-EDM. A Review</b> .....	115
Tariq Ahmad, Noor Zaman Khan, Babar Ahmad, and Annayath Maqbool	
<b>Effect of Buffer Layer on Crack Susceptibility, Mechanical and Microstructural Properties of Ni Hard Coatings</b> .....	125
Nikhil Thawari, Nikhil Chaubey, Aayush Chandak, and T. V. K. Gupta	
<b>Experimental Investigation on Properties of Acetic Acid-Treated Banana Fiber Polymer Composites</b> .....	135
J. Ronald Aseer, S. Renold Elsen, and K. Sankaranarayananamy	
<b>Laser Beam Welding of Advanced High-Strength Steels (Dual Phase Steels)</b> .....	141
P. V. S. Lakshminarayana, Jai Prakash Gautam, P. Mastanaiah, G. Madhusudan Reddy, and K. Bhanu Sankara Rao	
<b>Plasma Cladding of Copper on Cylindrical SS 316L Surface</b> .....	149
C. Aditya, C. Gagan, R. Poojith Raj, V. Balaji, V. Srinivasa Chari, and Suyog Jhavar	
<b>Effect of Curvilinear Weld Profile Shapes on Weld Line Movement in the Stamping of Tailor Welded Blanks</b> .....	157
Suresh Arjula, V. V. N. Satya Suresh, and S. P. Regalla	
<b>The Effect of HSS and Carbide Tools on the Mechanism of Chip Formation During Turning of Medium Carbon Steel (AISI1030)</b> .....	165
Sumit Mahajan and Kalyan Chakraborty	

**General Regression Neural Network-Based Frame Work for the Evaluation of Ultimate Tensile Strength of Vibratory-Assisted Welded Joints** ..... 173  
 M. Vykunta Rao, M. V. A. Raju Bahubalendruni, and Vinod Babu Chintada

**Experimental Studies on Material Removal Rate of Die Steel in Electrochemical Micromachining Process Using Taguchi Method** .... 181  
 K. Vijayakumar, T. Sekar, and M. Vijay

**Microstructural Characterization and Microhardness Investigations on Friction Stir Additive Manufactured Commercially Pure Aluminium Alloy** ..... 189  
 R. Dinesh Kumar, Baskaran Balaji, and Kannan Ganesa Balamurugan

**Finite Element Modeling to Predict the Defect Formation in Friction Stir Welds of AA6061** ..... 195  
 Sumit Kumar Purswani, Vikas Upadhyay, A. Karapagray, and L. R. Shobin

**Effect of Turning Parameters on Surface Roughness of EN-9 Steel Using Taguchi Robust design—An Analysis** ..... 203  
 Shahid Khurshid, Mehjooba Zainab, Yasir Farooq, Faizan Yousuf, Tamjeed Ayoub, Fayaz Ahmad Mir, and Junaid Hassan Masoodi

**Study and Analysis of Milk-Run Model for Minimum Cost Under Upstream Supply Chain of a Dairy Plant** ..... 213  
 Sanjay Kumar, Asim Gopal Barman, and Vishal Kumar

**Effect of Micro-milling Parameters on Surface Roughness of Soft Metal Cutting and Their Regression Models** ..... 221  
 S. Bhattacharyya, H. Chelladurai, and M. Z. Ansari

**Application of Taguchi Procedure to Decide Optimum Variable Levels for Powder Blended EDM** ..... 229  
 K. Santarao, Ch. Suresh, and C. L. V. R. S. V. Prasad

**Numerical and Experimental Studies on Pressure Drop in Milling Parameter Optimized Aluminium Heat Sink Channel** ..... 237  
 S. Bhattacharyya, J. Pandey, H. Chelladurai, A. Husain, and M. Z. Ansari

**Microstructural Analysis of Friction Stir Processed Al5083 Alloy** ..... 245  
 D. Hari, N. Narmada Devi, R. Prabhakaran, M. Sutharsan, and Kannan Ganesa Balamurugan

**Performance Evaluation Through Audit of 519 Organizations** ..... 253  
 Karri Naveen, Chithirai Pon Selvan, and Amiya Bahumik

<b>Effect of Varying Tool Parameters on Chip Formation and Reaction Force</b> .....	259
Raunika Anand, Jeet Desai, and G. Rajyalakshmi	
<b>Wood-Plastic Composite Processing and Mechanical Characteristics—A Brief Literature Review</b> .....	269
Sachin S. Raj	
<b>Effect of Filler Content on the Performance of Epoxy/Haritaki Powder Composite</b> .....	277
N. Narmadadevi, V. Velmurugan, R. Prabhakaran, and R. Venkatakrishnan	
<b>Surface Alteration and Effect of Fiber Amount on the Optimization of Palmyra and Moringa Oleifera Fibrils Fortified Composites</b> .....	285
Gowdagiri Venkatesha Prasanna, Rapolu Srilekha, Achyutuni Venkata Naga Sri Harsha, and Vemula Sunil Kumar	
<b>Optimization of Specific Cutting Energy in Turning of AISI 304 Stainless Steel Using Taguchi Method</b> .....	295
S. Annamalai, B. Guruprasad, and N. Vaithianathan	
<b>Influence of Squeeze Time on Fracture Mode of SS304 Spot Weldments</b> .....	305
Bikash Kumar, Binaya Ranjan Maharana, Ajit Kumar Sahu, Swagat Dwibedi, Arijeet Jena, Subham Das, and Suraj Prasad	
<b>Finite Element Modeling of Temperature Evolution During Selective Laser Melting</b> .....	315
Nithya Srimurugan, Rishi Dwivedi, Vineesh Vishnu, Basil Kuriachen, and K. P. Vineesh	
<b>Effects on Mechanical Properties of High-Density Polyethylene (HDPE) Reinforced with Walnut Shell Powder</b> .....	323
Adnan Ali Khan, Uzair Ali Khan, and Rafid Hassan	
<b>Grey-Fuzzy Modelling and Analysis of Optimizing Turning Process Parameters for Stainless Steel Material</b> .....	331
V. Jegan Prasath, R. Karthick Kannan, R. Shanmuga Mugesh, N. Sugeesh, S. R. Sundara Bharathi, and A. Arul Marcel Moshi	
<b>The Study of Kenaf/E-Glass Fibre Content on Mechanical Properties of Biopolymer Cashew Nut Shell Liquid/Epoxy Matrix Blended Composites</b> .....	339
R. Prabhakaran, R. Venkatakrishnan, and N. Narmada Devi	
<b>Study on Mechanical Behaviours of Newly Formulated Aluminium Alloy (6082) Reinforced with Boron Carbide and Rice Husk Ash</b> .....	347
V. Thirumaran, M. Ganesh, K. Ganesha Balamurugan, and M. Sutharsan	



**Automation**

**Attractor Plot as an Emerging Tool in ECG Signal Processing for Improved Health Informatics** ..... 359  
 Varun Gupta, Yatender Chaturvedi, Parvin Kumar, Abhas Kanungo, and Pankaj Kumar

**Quanser QUBE Twinning** ..... 369  
 Burada Phanindra, Paruchuri Srinivas, and Korupu Vijaya Lakshmi

**Finite Element Analysis of Lightweight Robot Fingers Actuated by Pneumatic Pressure** ..... 379  
 M. Appadurai and E. Fantin Irudaya Raj

**Design and Development of Home Automation System** ..... 387  
 R. Boopathi Rani, N. Bavithran, and S. Prasannakumar

**Design and Development of Automatic System to Protect Crop from Animals and Birds** ..... 397  
 R. Boopathi Rani, A. Preetha, and S. Gnanavalli

**Spectrogram as an Emerging Tool in ECG Signal Processing** ..... 407  
 Varun Gupta, Monika Mittal, Vikas Mittal, and Nitin Kumar Saxena

**Automation to Find Adulteration in Downstream Petroleum Monitoring Using Machine Learning: An Overview** ..... 415  
 S. Hemachandiran, G. Aghila, and R. Siddharth

**Smart Dispensing of Ingredients Using VL53LOX and Piezoelectric Polymer Sensor** ..... 425  
 K. R. Prakash, V. Guruprasad, and K. S. Nithin

**Implementation of Industrial IoT Laboratory for Sensors** ..... 435  
 K. R. Prakash, Pratiksha Narake, and M. V. Ramya

**A Mechatronic System to Distribute Tennis Balls Using Pneumatics** .... 445  
 Pradnya Avinash Patil

**Weld Microstructural Image Segmentation for Detection of Intermetallic Compounds Using Support Vector Machine Classification** ..... 455  
 Nalajam Pavan Kumar, Ramesh Varadarajan, K. N. Mohandas, and Muni Kumar Gundu

**Navigation of Mobile Robot Through Mapping Using Orbbec Astra Camera and ROS in an Indoor Environment** ..... 465  
 M. Basavanna, M. Shivakumar, and K. R. Prakash

**Automation in Retail ‘Follow-Me-Auto Shopping Cart’:  
A Self-propelled Computer Vision-Based Shopper Following Cart  
with Auto-billing Feature Using IIoT** ..... 475  
Ayaskanta Mishra, Aditya Mohan, Abhranil Mandal,  
Anamika Mohanty, and Akashdeep Chowdhury

**An Intelligent and Robust Fault Diagnostics  
for an Electromechanical System Using Vibration and Current  
Signals** ..... 485  
Purushottam Gangsar, Zeeshan Ali, Manoj Chouksey, and Anand Parey

**Analysis of Cache Memory Architecture Design Using Low-Power  
Reduction Techniques for Microprocessors** ..... 495  
Reeya Agrawal

**Low-Power SRAM Memory Architecture for IoT Systems** ..... 505  
Reeya Agrawal

**Design**

**Design and Structural Analysis of Nano-satellite** ..... 515  
R. Balaji, Estheru Rani Talasila, L. Oblisamy, V. S. Ajith,  
and A. Basithrahman

**Unbalance Identification and Balancing Using Model  
Sensitivity-Based Approach** ..... 523  
Dinesh Kumar Pasi, Manoj Chouksey, and Ashesh Tiwari

**8-Bit Electromechanical Processor Design for Education in Digital  
Computation** ..... 533  
Shashwath Sundar and Vijay Kumar Tayal

**Effect of Nonlinearly Varying Loads and Position of Stiffener  
on Buckling Behaviour of Stiffened Composite Panels** ..... 543  
K. S. Subash Chandra, T. Rajanna, and K. Venkata Rao

**Determination of Exact Optimal Tuning of Dynamic Vibration  
Absorbers to Control Vibration Due to Rotating Mass Unbalance** ..... 553  
Anant J. Sheth and Utkarsh A. Patel

**Finite Element Analysis for Material Optimization of a Spur Gear  
by Radial Holes** ..... 561  
Sanjay Sutar, G. C. Mohan Kumar, and Mrityunjay R. Doddamani

**Inhibiting COVID-19 Transmission in India Through Design  
of Automated Contactless Face Mask Vending Cum Disposal  
Machine with Self-Sterilization Unit** ..... 573  
Aniruddha Ghosh, Rajendran Dinesh Kumar, and Varthini Rajagopal

**Investigation on Mechanical Behaviour of Kenaf Fabric/Bio-Epoxy/Egg-Shell Powder Reinforced Composites for Medical Applications** ..... 581  
 M. Nalla Mohamed and G. VR. Sakthivel

**Effect of Wall Thickness Variation on the Energy Absorption Efficiency of Cylindrical Tubes Under Axial Loading** ..... 589  
 M. Nalla Mohamed

**Low – Cost Portable Smart Ventilator** ..... 599  
 Sourabh Dogra, Lokendra Singh, and Arpan Gupta

**Investigation on the Effect of Patterned Holes on Energy Absorption Characteristics of Aluminium Square Tubes** ..... 607  
 M. Nalla Mohamed and R. Sivaprasad

**Ansys Fluent Analysis of a Thermo-Hydrodynamically Lubricated Journal Bearing** ..... 615  
 N. Vaithianathan and S. Annamalai

**Investigation on Deflection Characteristics of Auxetic Beam Structures Using FEM** ..... 621  
 Hrishikesh G. Menon, Shammo Dutta, M. P. Hariprasad, and Balakrishnan Shankar

**Interdependence of Eccentric Force and Torque on Joint Angle and Angular Velocity During Human Multi-joint Leg Extension** ..... 629  
 Rajesh Kumar Bhushan and Ashutosh Swain

**Design and Analysis of 3D Printable Prosthetic Foot** ..... 637  
 T. Prakash, N. Jayakumar, V. Monish Kumar, P. Karthick, A. Mutharasu, and A. Naveen Kumar

**Experimental Investigation on Adhesive Bonded Fold Tubes Under Quasi-Static Loading** ..... 657  
 M. Nalla Mohamed and R. Sivaprasad

**Numerical Crashworthiness Investigation of Multi-Section Tubes** ..... 667  
 M. Nalla Mohamed and R. Sivaprasad

**Design of Tabletop Automated Plane Polariscopes for Digital Photoelastic Measurements** ..... 675  
 M. Gagan Keerthi, Ananthesh D. Shenoy, B. Devanarayanan, V. S. Sharath, and M. P. Hariprasad

**Structural and Vibration Analysis of Barge Ship Hull** ..... 683  
 S. Ramana Babu and Baswani Harikrishna Raju

<b>Investigation of Failure in L-shaped Woven Carbon Fiber-reinforced Polymer Composite Under Pull-out and 4-Point Bending</b> .....	693
Bipin Kumar Chaurasia, Deepak Kumar, and Vasvani Ashish Maheshbhai	
<b>Vibrations Characteristics Analysis of Rotor-Bearings System Due to Surface Defects Based in CNC Machines</b> .....	705
R. G. Desavale, Jitendra Kumar Katiyar, and T. Jagadeesha	
<b>The Diagnostic Analysis of the Rolling Element Bearings for the Machine Tool Applications Using Dimension Theory</b> .....	711
R. G. Desavale, Jitendra Kumar Katiyar, and T. Jagadeesha	
<b>Topology Optimization of Bench Problems—Stress and Deformation Perspective</b> .....	719
Dara Ashok, M. V. A. Raju Bahubalendruni, and Johnney Mertens	
<b>Internal Logistics Optimization in the Assembly Line Using Lean Techniques</b> .....	731
P. Jeyaraman, R. Jeeva, T. Niruban Projoth, and R. Rohith Renish	
<b>Energy</b>	
<b>Control Strategies for Transient Stability of Power Grid for Large Sudden Change in Electrical Load</b> .....	743
Subash Chandra Parida, V. K. Tayal, and S. K. Sinha	
<b>Improved Control Design for AGC of Two Area Thermal-Thermal Power System Using Hybrid Fuzzy-PID Control</b> .....	753
Subash Chandra Parida, V. K. Tayal, and S. K. Sinha	
<b>Experimental Investigation of a Line Focus Solar Collector Using Flat and Parabolic Reflector</b> .....	763
Gunjan Kumar and Hemant Gupta	
<b>Design and Implementation of a 3 Level Battery Management System (BMS) for an Electric Vehicle</b> .....	773
Bhumica Dutta, Sharestha Jaiswal, Vinay Phatarpekar, Vijay Kumar Tayal, and H. P. Singh	
<b>Effect of Flow Velocity on the Performance of the Savonius Hydrokinetic Turbine</b> .....	785
Vimal Patel and Kushal Shah	
<b>Review on Pragmatic Refrigerants Deployed in Refrigeration and Air Conditioning System</b> .....	795
Shaik Abdulla and T. S. Ravikummar	

**Optimization of Nanofluid Parameters for Double Pipe Heat Exchanger** ..... 803  
 K. Manjunath

**CFD Analysis of a Mixed Convection Heat Transfer Square Cavity with Hybrid Nanofluids** ..... 815  
 Chinta Rajeev Durga Sai, Satish Pujari, B. Sreenivasulu, and Ajit Burra

**Impact of Graphene Nanoparticles Addition to Jatropha Biodiesel Blend on the Performance and Emission Characteristics of a Diesel Engine** ..... 825  
 D. Mallikarjuna Rao, Venkata SomiReddy Janga, V. Dhana Raju, and Syed Arifa

**Numerical Investigation on the Thermal Management of 18650 Battery Module Using Phase Change Material** ..... 835  
 Priya Chaudhary and Abhik Majumder

**MPC-Based Power Quality Solution Using Energy Storage Technology for PV Based Islanded Microgrids** ..... 843  
 M. Jayachandran and G. Ravi

**Biogeography-Based Centralized PID Controller for ALFC in Presence of Wind Farms** ..... 853  
 E. Sri Lalitha, A. M. S. V. Sushma, G. Pavan Kumar, and Ch. Durga Prasad

**CFD Analysis of Heat Transfer Through Natural Convection Inside Square Cavity Using Various Nano Fluids** ..... 859  
 Hari Kishan Veeranki, Sreenivasulu Bondala, and Ajit Burra

**Working Fluids for Ejector Refrigeration Systems: A Comprehensive Review** ..... 869  
 C. Manimaran, A. Sathiamourthy, and A. Selvaraju

**Experimental Study on Heat and Mass Exchanger of a Dew Point Indirect Evaporative Cooler** ..... 877  
 C. Deepak, Rudra Naik, and H. K. Prashanth

**Effect of Nozzle Inclination Angle on the Performance of Hybrid Jet Impingement Microchannel Heat Sink** ..... 887  
 Jyoti Pandey, Mohd. Zahid Ansari, and Afzal Husain

**Numerical Investigation of Swirl Flow on Heat Transfer Enhancement in a Stepped Pipe** ..... 897  
 B. Prince Abraham, F. Michael Thomas Rex, P. Samuel Ponraj, R. Jayavenkatesh, and A. Andrews

<b>An Integrated Approach by Using Various Approaches for a Green Supplier Selection Problem</b> .....	909
A. V. A. R. Durga Rao, A. K. Chaitanya, T. Sessaiah, P. Bridjesh, and Sivakrishna	
<b>Testing the Engine Performance with Cotton Seed Oil Biodiesel</b> .....	921
G. Senthilkumar, S. Lakshmi Sankar, and M. Purusothaman	
<b>A Study on the Combustion Characteristics of Dieseline Blend in HCCI Engines</b> .....	927
P. S. Srivathsan, Praveen Ramanujam, K. Prasanth, and S. Soma Sundaram	
<b>Comparative Analysis of Transformer Less Bi-directional DC–DC Converter and Conventional Converter for Battery Charging-Discharging Applications</b> .....	935
Radhika Swarnkar and R. HariKrishnan	
<b>Comparative Enviro-Economic Analysis of Transparent Water Heating Systems and Conventional Systems</b> .....	945
Kirti Tewari and Rahul Dev	
<b>Harvesting Electric Energy from Waste Vibrations of an Electric Motor Using the Piezoelectric Principle</b> .....	955
Nitin Yadav and Rajesh Kumar	
<b>Thermal Decomposition Kinetics of Medical Non-woven Fabrics Wastes: Model-Fitting Method</b> .....	965
Uthayakumar Azhagu and Anand Ramanathan	
<b>Exergy Analysis of R1234yf and R1234ze as an Alternative to R134a in a Domestic Refrigeration System</b> .....	975
Guna Muthuvairavan, S. Soma Sundaram, and P. K. Palani	
<b>Enhancement of Natural Convection Heat Transfer in Cylindrical Enclosure with Internal Heat Source</b> .....	983
Sarthak Gautam, Mohd Juned Khan, Areeb Khan, Vivek Sharma, Fahad Farid, and Anil Kumar Sharma	

## About the Editors

**Dr. Sendhil Kumar Natarajan** is currently an Assistant Professor and Head in the Department of Mechanical Engineering, Associate Dean—Faculty Welfare, National Institute of Technology (NIT) Puducherry. He pursued his B.Tech. in Mechanical Engineering and M.Tech. in Energy Technology from Pondicherry Engineering College in 2001 and 2003, respectively, followed by Ph.D. in solar energy from Indian Institute of Technology (IIT) Madras in 2008. After his Ph.D., he joined as Senior R&D Engineer, at CSEM-UAE, Ras Al Khaimah, UAE. Later, he joined as a Post Doctoral Research Fellowship at Heriot-Watt University, Edinburgh, United Kingdom under European Union Project. He got young faculty award and outstanding researcher award in the field of Solar Thermal. He has published papers in 30 international journals and 40 national and international conferences in the area of energy. Based on his research work, he has filed four patents in the area of solar energy. He has three funded projects from DST-SERB as a PI for Concentrating Solar Systems, DST-UKIERI as a Co-PI for fuel cell research, and BRICS as a Co-PI for Solar Based Biomass Conversion. His research area lies in solar thermal system and CSP system, CPV, integration of high temperature solar thermal systems, heat transfer, fluid flow, and fuel cells.

**Dr. Rajiv Prakash** received his M.Tech. in Materials Technology from Institute of Technology Banaras Hindu University (IIT-BHU), India and completed his Ph.D. from Tata Institute of Fundamental Research, Bombay. Currently, he is a Professor of Materials Science and Technology, and Dean (Research and Development) of IIT-BHU. He has worked with the CSIR lab in Lucknow as a Scientist for over 7 years. He has been the recipient of Young Scientist Award (Council of Science and Technology), Young Engineer Awards (Indian National Academy of Engineering) of India and Materials Society Medal Award of India. His current research interests include architecture and design of functional polymers and nanocomposites for their applications in organic electronic devices and sensors/biosensors. He is participating as PI/Coordinator in various National Mission projects like Technology Innovation Hub, IMPRINT, SPARC and Energy Mission projects of the Department of Science

and Technology, Government of India. He has published over 200 publications in international journals of repute and has 20 patents in his credit.

**Dr. K. Sankaranarayanan** is serving currently as Director of NIT Pondicherry, formerly a professor of Mechanical Engineering at National Institute of Technology Tiruchirappalli, received his B.E. Mechanical Engineering (Hons) in 1981 from PSG College of Technology, India. He received his M.Tech. Production Engineering in 1983 and Ph.D. in 1989 from Indian Institute of Technology Madras, India. His research targets finite elements simulation of welding Process. Ergonomics study and Gear Design. He has authored more than 75 papers in international and national journals and has attended conferences in Slovak Republic, China, America and Austria. To his credit, he has completed several sponsored projects (total worth of Rs. 60 lakhs) funded by BHEL, Trichy, NLC Neyveli and DST. He served in administrative responsibilities such as Head of the Department, Dean and Director of NIT.



# **Manufacturing**

# Smart Materials for 4D Printing: A Review on Developments, Challenges and Applications



Sreenivasulu Reddy 

## 1 Introduction

Manufacturing is an intricate action by consuming materials in raw condition or semi processed parts and power to create useful products to the society by sales with some profits. This is achieved by involving human resources with typical skills and wide range of disciplines, and broad variety of machine tools and tooling [1]. All these actions must be responsive to the component or a product client as per demand. Current manufacturing techniques involve utilization of computers to control machines that process and assemble the parts. To control the movement of all resources like human workers, materials in all processing stages and machines with required tooling along the shop floor and distribution to the points of sale are completely controlled by automation with computer integrated manufacturing (CIM) environment [2]. This is done by allowing designers, technocrats and marketers to take decision on how new components looks, works and how it may be manufactured quickly than earlier. Due to rapid evolution and development in the areas of contemporary manufacturing technologies like rapid prototyping reduces the time for manufacturing and cost incurred to complete the product, finally it causes to reduce the lead time [3]. Technology is a significant means of transportation for factory floor to transform into knowledge-based (includes AI, ML and Cloud Computing) with minimum value added factory operations [4]. This is only possible if the modern manufacturing industry equips itself with necessary managerial information systems to coordinate all the resources successfully. It is expected that manufacturing sector will change in the next 10 years as current manufacturing practices are abandoned in favor of cleaner, flexible, more efficient manufacturing [5]. Advanced connectivity technologies play a vital role in helping entrepreneurs connect millions of assets and devices globally. 5G technology can help to promote greater flexibility, visibility,

---

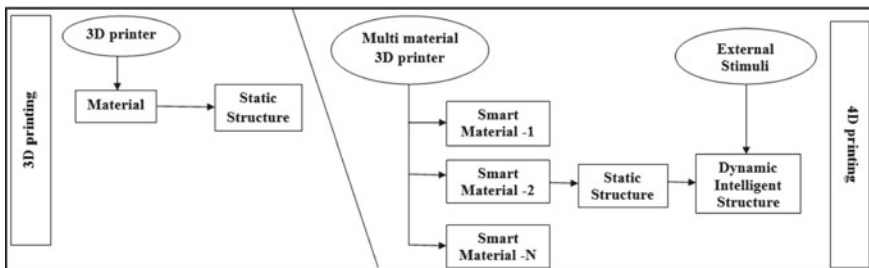
S. Reddy (✉)

R. V. R & J. C. College of Engineering (Autonomous), Guntur, Andhra Pradesh 522019, India

versatility, usability and efficiency of goods across the globe and also promotes real-time updates on market conditions. Recognizing the importance of manufacturing of goods to their industrial future, various countries have started its inaugural programs to create new startup companies by young minds to support the deployment of these technologies to their domestic manufacturers [6].

## 2 4D Printing—New Era of RP Technology

By introducing the fourth-dimensional parameter, three-dimensional (3D) printed parts/components acquire the talent to alter its contour forms by its own over the effect of peripheral replication like thermal effects, optical effects, electrical effects, magnetic effects, etc. this is often possible by adding the dimension of your time. Three-dimensional printing is one in all the foremost disruptive innovations within the field of contemporary manufacturing. It permits the producers and innovators to produce intricate shapes. These are not possible with existing traditional methods [7]. Three-dimensional printing has been observed incessant progression over the past years. Even though its capability to design and fabricate complex shapes like bio-inspired, multi-material designs, three-dimensional printing so far capable to approved in the industrial sector. Increasing day-to-day customer requirements and demand in the market toward flexible manufacturing systems (FMS) needs to instantaneous designs by reprogramming. These include self-folding packaging, adaptive wind turbines and bio-implanting, etc., and have been fulfill the urgent need of innovation of 4D printing technologies. At present, young minds in this field searching for replacement of materials in conventional 3D printing such as building of components layer by layer from one material to meta-material to be created by combining those to give superimposed structural 3D objects. The young incubators who are established startups advised that expanding these structural alterations to innovate intricate objects, viz. lockers, lifters, micro-tubes, soft robots, toys etc. The capability to do remodeling of 3D objects with respect to time using the behavior (responsiveness either with change of temperature or loading conditions) of materials termed as fourth-dimensional (4D) printing [8]. Figure 1 shown in below describes



**Fig. 1** Differences between three-dimensional and fourth-dimensional printing technologies

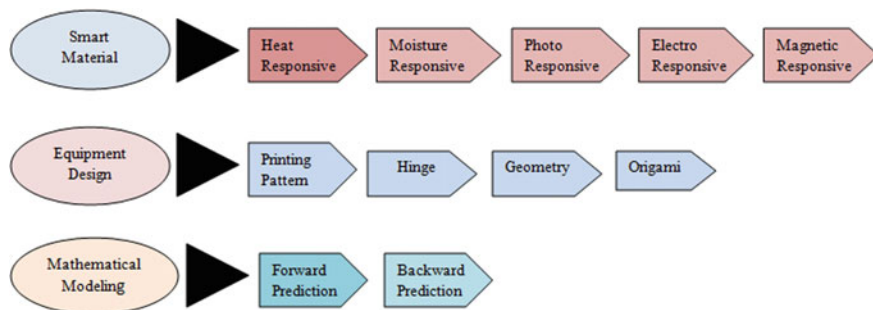
**Table 1** Major differences in the usage of parameters 3D versus 4D Printing processes

Parameter	Three-dimensional printing methodology	Fourth-dimensional printing technique
Transient change while formation of part or component	–	Alter the color, shape, function with respect to time
Raw materials or substances used	Inorganic materials	Self-healing smart materials
	Nonferrous metals and their alloying elements	–
	Bio-inspired fluidic materials (MR fluids) and hydrogels	–
	Nanoparticle composites and fluids	–
Printable amenities or services	3D Printer—working with a principle of Stereo lithography	–
	Fused deposition modeling	Multi-material 3D printer operating with time as a fourth parameter
	Selective laser sintering methods	–

clearly to understand the main gaps among the three-dimensional printing (3D) and fourth-dimensional (4D) printing (Table 1).

### 2.1 *Fourth-Dimensional (4D) Printing Materials and Technologies*

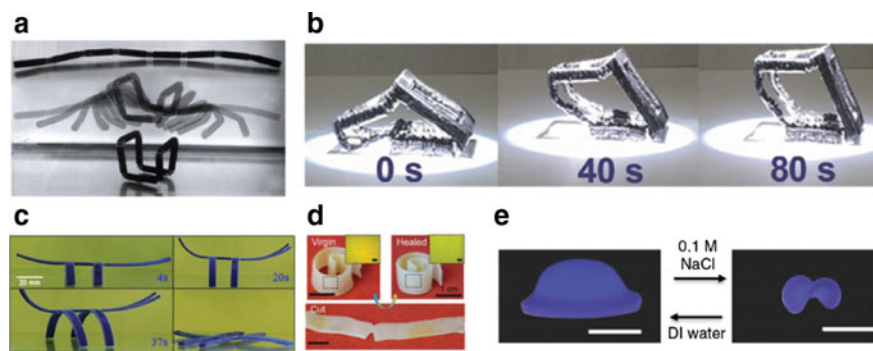
As discussed in the previous sections, the fourth-dimensional (4D) printing process carried to be in its starting stage, so there is no recent development in the area of self-healing material technologies till date. However, the researchers expected to convey the possibilities in advances in 3D printing by assistance of programmable automation. The basic level of investigations in these areas, at this instant of time is in focal point regarding to fourth-dimensional (4D) printing. These are summarized in Fig. 2. Self-healing substances either solid or liquid state is one the well-focused innovative ideas to be considered by budding entrepreneurs to inaugurate innovation & incubation center’s under the regime of digital making India schemes. Presently, industrial engineers who were worked in printing technologies used inkjet cure for direct printing in the they are applying fused deposition modeling technique to build the component in 3D shape and apply the existing available material especially polymers in SLP approach. Laser assisted bio-printing and selective laser melting techniques required for fourth-dimensional, i.e., variant time factor in 4D printing.



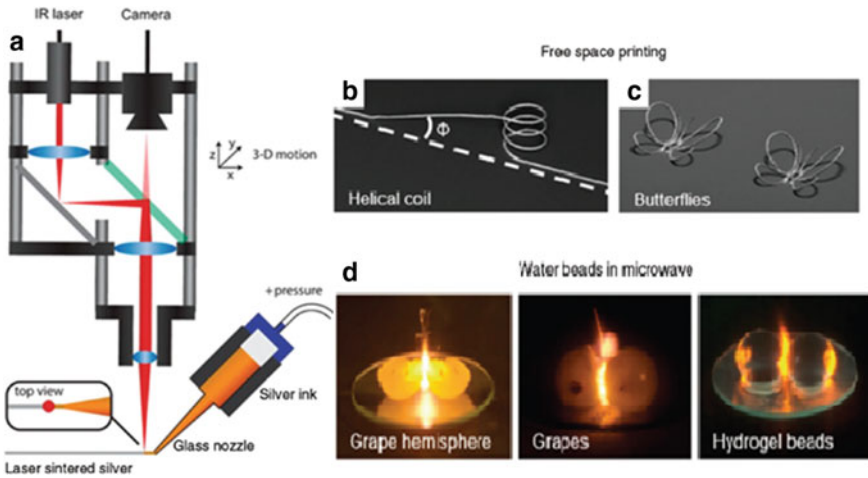
**Fig. 2** Primary levels of different areas of research work under 4D printing processes

## 2.2 Smart Materials for Fourth-Dimensional (4D) Printing

3D printing of smart materials that are conscious of external stimuli (such as heat, moisture, electric/magnetic fields, and pH) is termed 4D printing (the dimension is time). During this case, 3D-printed structures aren't any longer static; rather, their shapes or functionalities can transform over time. More information regarding general 4D printing research is found in recent reviews [1–5]. In this section illustrated about particulars on responsive of stimuli of smart materials that are extensively used in the studies of fourth-dimensional (4D) printing such as smart material polymers, hydrogels and liquid elastomers shown in Figs. 3 and 4. The 4D printing of



**Fig. 3** Fourth-dimensional (4D) printing with self-healing materials. Top of form. **a** Fourth-dimensional (4D) printed object that alters its dimension from a one-dimensional line to three-dimensional cube [1]. **b** The form memory process of the cubic frame manufactured from lamp-black doped polyurethane under light illumination of  $87 \text{ mW/cm}^2$  [3]. **c** 3D-printed structure that's mimicking the insect. The deformation behavior of the structure in very  $30^\circ\text{C}$  water is shown over time. The image on the lower right corner is that the fully recovered structure within the  $60^\circ\text{C}$  water [2]. **d** Photographs of the form memory assisted self-healing effect. Inserted pictures are the optical microscope images with a scale bar of 1 mm [4]. **e** Hydrogel-based 4D-printed structure (scale bar: 1 cm) [5]



**Fig. 4** Perspectives in near future. **a** Diagram for metal—link three-dimensional printing with infrared laser sintering. **b** Helical coils with free standing type (diameter: 500 μm). **c** Butterflies with free standing wings printed [8]. **d** Two grape (or hydrogel) beads separated by plasma [7]

SMPs involves 3D printing of an imaginative shape, followed by thermomechanical programming by writing a code.

### 3 Prospective Applications

- (a) **Repair—without human intervention:** The plumbing pipe line is a lively shifting their size in response to the discharge and demand of supply of water. So, if the pipes can be possible to heal themselves without human intervention. If they crack or break because of their ability to alter in response to environmental change could be a smart material which is used to manufacture the piping systems.
- (b) **Self assembled systems:** Since three-dimensional printing equipment's are in limited scale arrangement in the printing machine, fourth-dimensional printing can permit a printing on a plane board which will bend into a chair (required complex shape for example) by just adding water or light into it apart from the material. Fourth-dimensional printing is helpful especially in large scale projects and more profitable. In space applications, presently three-dimensional printing of building causes certain problems economically, efficiency and power consumption. So, rather than using three-dimensional printed materials, fourth-dimensional (4D) printed materials may be comfortable to take more benefits on their convertible object shapes as they might buildup themselves or repair themselves just in the case of variable climatic conditions. Another application of fourth-dimensional (4D) printing is in the bio-medical field to

design and implant stents in human bodies and travel through the vein and once they reach their destination, they might open up by self-healing.

- (c) **Fancy or fashion Technology:** One of the ideas of 4D printing is that clothing could change per the climate or activity of the one who wear that cloth or dress made thereupon cloth. For example, shoes could damage their shape after we start running, so to produce well design with better comfort shoes then customers feel happy and satisfied more. All these potential applications give very inspiring and promising for the long run indeed. 4D printing still requires more research and development.

### 4 Material Selection

The materials used in the case of fourth-dimensional (4D) printing are categorized based on environmental conditions and exterior stimuli when they react with climatic changes depicted in Fig. 5. These are classified into two categories:

- (a) **Subjected to temperature (thermal response):** Material, which mainly works on the mechanism of the shape memory effect called as temperature or thermal responsive materials. Again these are classified into shape memory alloys, shape memory polymers, shape memory hybrids, shape memory ceramics and shape memory gels. Authors, in this particular area generally preferred shape memory polymers because of easy to print on these materials. These substances formed in one shape and deformed into another shape when they undergo temperature region or heat energy is applied on a stimulus then they react with water or moisture under this category. These materials are extensively preferable by the innovators in this field. The hydrogel is one of the smart self-healing material reacts vigorously with water and increase its size up to 2 times of its original volumetric size when it comes contact with water.

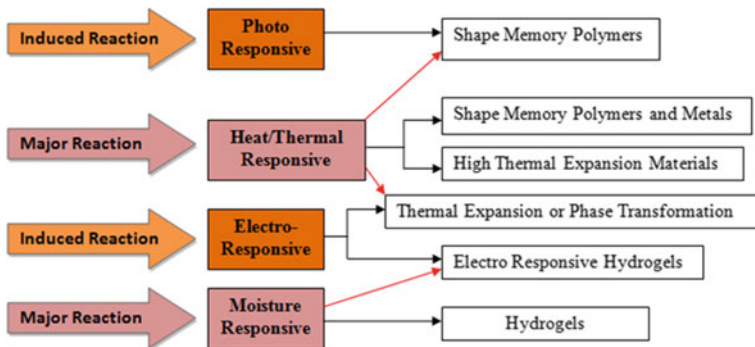


Fig. 5 Fast sensing of materials w.r.t various criteria of reactions

**Table 2** Potential product development of 4D printing

Item	Company	Primary Predicted Products	Secondary Predicted Products	Full time Predicted Products
1	Electrical & Electronics	Fast response sensors	Adjustable or flexible sensors	Nanotechnology
2	Hospitals & Pharmaceutical	Manmade soft tissues	Biomedical objects like stents	Manmade biological supporting limbs
3	Industrial Machinery	Building and Pipes	Heave & Earth moving machinery and equipment	–
4	Automotive and Aerospace	–	Space Vehicles	Automobile body parts
5	End user appliances	Fashion and Lifestyle	Domestic devices	–

- (b) **Fast Response by reacting with Light/Current/Magnetic fields:** These substances respond with light, electric current and electromagnetic fields. As an example, at particular locations polymer gels fused with photo responsive chromophores, they become bulge by absorbing light when exposed to source of light. Similarly, ethanol contaminated objects undergoes electric current then they are evaporate and increase the volume. Magnetized nanoparticles are inserted into the 3D printed object to realize magnetic control of the device.

## 5 Potential Product Development of 4D Printing

Healthcare industry comprises goals on drug delivery, preparation of stunts for negligible surgical assault, growth of shape shifting splints, etc. The growth in the innovations on soft robotics, hydraulic and pneumatic actuator systems involves more number of applications in the present automated industry. Nowadays in advanced countries following the design and construction of roads with self-healing materials and also fabrication and erection of bridges could be potential applications in the Roads and Building departments [9] (Table 2).

## 6 Conclusions

The main aim of this review on this novel and imaginative fourth-dimensional printing was to inculcate the budding engineers to gain basic information regarding materials, challenges and recent advancements. Also this literature study has been provided an outline of fourth-dimensional (4D) printing, covering the smart substance, technological and style needed by customers has been considered while constructing



components with this technique. Research and development projects especially in 4D printing techniques are ongoing in the present industries such as healthcare, electronics, automotive, aerospace and defense, consumer appliances (fashion and consumer durables), textile, construction and industrial machinery. In spite of being an imaginative technology, probable chances offered by fourth-dimensional (4D) printing are vast and are renowned by numerous professionals in the field of rapid prototyping. At present, printing with fourth-dimensional technology market is more in demand and would be inaugurated in near future. In coming days, customers can avail the products online and whatever they like on the spot itself. However, this is a novel technology in its infancy phase and it depends on the market growth which is varied among experts.

## References

1. Tibbits, S.: 4D printing multi-material shape change, architectural design. *Archit. Des.* **84**(1), 116–121 (2014)
2. Wu, J., Yuan, C., Ding, Z.: Multi shape active composites by 3D printing of digital shape memory polymers. *Sci. Rep.* **6**, 24224 (2016)
3. Yang, H., Leow, W.R., Wang, T.: 3D printed photo responsive devices based on shape memory composites. *Adv. Mater.* **29**(33), 1701627 (2017)
4. Kuang, X., Chen, K., Dunn, C.K., Wu, J., Li, V.C.F., Qi, H.J.: 3D printing of highly stretchable, shape memory and self healing elastomers toward novel 4D printing. *ACS Appl. Mater. Interfaces* **10**(8), 7381–7388 (2018)
5. Huang, L., Jiang, R., Wu, J.: Ultrafast digital printing toward 4D shape changing materials. *Adv. Mater.* **29**(7), 1605390 (2017)
6. Pei, E., Loh, G.H.: Technological considerations for 4D printing: an overview. *Prog. Addit. Manuf.* **3**, 95–107 (2018)
7. Khattak, H.K., Bianucci, P., Slepков, A.D.: Linking plasma formation in grapes to microwave resonances of aqueous dimmers. *Proc. Nat. Acad. Sci. U. S. A. (PNAS)* **116**(10), 4000–4005 (2019)
8. Javaid, M., Haleem, A.: 4D printing applications in medical field: a brief review. *Clin. Epidemiol. Global Health* **7**, 317–321 (2019)
9. Zhang, Z., Demir, K.G., Gu, G.X.: Developments in 4D-printing: a review on current smart materials, technologies, and applications. *Int. J. Smart Nano Mater.* **10**(3), 205–224 (2019)

# Examining the Build Properties of PolyJet Printed Multi-material Parts in Additive Manufacturing



Arivazhagan Pugalendhi and Rajesh Ranganathan

## 1 Introduction

PolyJet technology is an influential Additive Manufacturing (AM) method that can create complex multi-material parts in various colors with superior finish and accuracy [1]. PolyJet 3D printers selectively sprinkle the droplets of photopolymer resins through multiple nozzles onto the build tray which are immediately cured by ultraviolet light [2]. Applications of this unique technology is utilized in many fields such as bio-medical, aerospace, automobile, education and consumer products [3]. Capabilities of material jetting are used to produce functionally graded materials with different mechanical/chemical properties by mixing the soft and rigid materials [4].

Total cost of the PolyJet printed part is based on printing time, consumption of materials and energy [5]. Additionally, the quality of PolyJet printed part is determined by the dimensional accuracy, surface finish and mechanical property that are controlled by process parameters as well as material [6]. Mechanical properties and dimensional accuracy of multi-material parts depends on the polymerization speed, concentration and distribution of the base materials [7, 8]. Leakage or relaxation of deposited resin is determined by time in between the deposition and solidification periods [9]. Properties of the PolyJet printed parts are significantly affected by the process parameters of finish/built style and orientation [10].

In this regard, many researchers studied the effects of PolyJet process parameters on the mechanical properties and the material consumption as well as printing time [11–15]. Kim and Oh [11] investigated the mechanical properties, accuracy, roughness, speed, and material cost. The authors exposed that the building direction strongly affects the mechanical properties and part accuracy which is dependent on the geometry and dimension of the part. Tee et al. [12] investigated the mechanical

---

A. Pugalendhi (✉) · R. Ranganathan  
Department of Mechanical Engineering, Coimbatore Institute of Technology, Coimbatore, Tamil Nadu 641014, India

and fractographic analysis of PolyJet printed polymer composites. They reported that the micro-composites having the size small as  $62.5 \mu$  also feasible in PolyJet printing. Stiffness of the composite is influenced by orientations and geometries of reinforced particles while subjected to compression. Compared to other samples, ultimate tensile strength and elongation at break is minimized in a  $45^\circ$  part orientation. In another study, PolyJet process parameters (part orientation, type of finish, printing mode, support material style and layer thickness) and different materials (Digital ABS Ivory, VeroGray, RGD720 and Rigur) have been examined using design of experiments. This study found, glossy surface finish, high speed printing mode and a  $90^\circ$  part orientation gives the enhanced properties of surface quality, surface hardness, bending strength, tensile strength, tensile modulus and elongation at break [13].

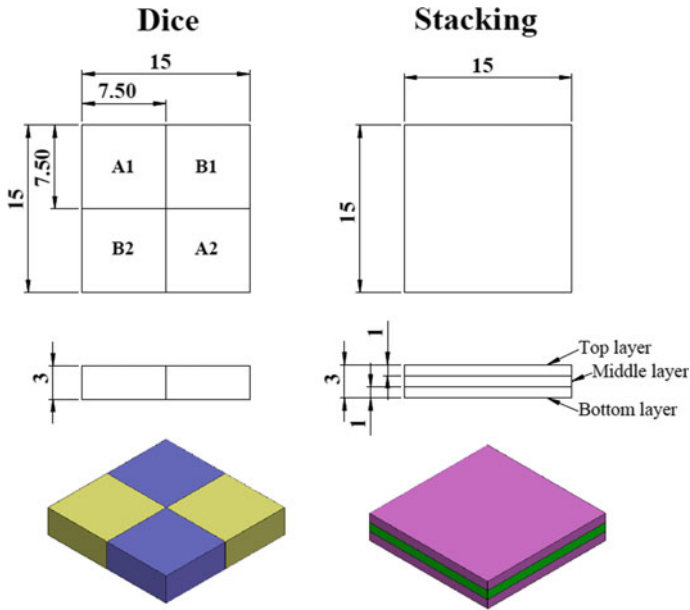
Kechagias et al. [16] reported the effects of process parameters such as layer thickness, build style and scale on accuracy of the PolyJet printed specimens by using the Taguchi's  $L_4 (2^3)$  orthogonal array. The results infer that the dimensional accuracy is significantly affected by the layer thickness and built style. In another study, influences of dimensional accuracy of PolyJet printed parts are investigated by the same process parameters utilizing the gray Taguchi method [17]. The aim of this study is to offer a better understanding about the build properties of PolyJet printed multi-material parts by investigating the effects of process parameters using a statistical method of Taguchi orthogonal array. An investigation of build properties on PolyJet printed digital parts with the mixed part approach has not been reported yet.

## 2 Methodology

### 2.1 Machine, Materials and Specimen Design

Stratasys Objet260 Connex 3D printer was used to print the samples in mixed part approach of digital material printing mode having  $30 \mu$  layer thickness. The mixed part approach can build the single product that contains different model materials in different regions, which is very useful for self-assembled parts that to be eliminated through secondary operations. This machine offers both the matte (M) and glossy (G) finish. In finish "M", printed part is fully covered by support material which offers a uniform surface finish. But in "G" finished part, support material covers the overhanging features, while the top surface of the printed part is free from support material [18]. Communication to AM machine and preprocessing like material assignment, orientation, selection of finish type and layer thickness was performed by Objet Studio software. 3D samples which differ in design not in overall dimensions are selected for this investigation and named as dice and stacking as shown in Fig. 1.

The rigid build materials of VeroWhite (W), VeroClear (C) and rubber like Tango-Plus (T) is chosen for this study. Mechanical properties of selected materials are



**Fig. 1** Two-dimensional drawing of samples

populated in Table 1. The selected build materials are categorized for three different combinations namely; VeroWhite-TangoPlus (WT), VeroClear-VeroWhite (CW) and VeroClear-TangoPlus (CT). Primary and secondary material is defined by order of material combination. In case WT, “W” referred as a primary material and “T” referred as a secondary material. In dice sample, portion A1 and A2 are filled by primary material, portion B1 and B2 are filled by secondary material and it is denoted by D0. Top layer and bottom layer of the stacking sample is filled by primary material and middle layer is filled by secondary material which is named as stacking-1 and

**Table 1** Mechanical properties of selected PolyJet materials

Properties	VeroWhite	VeroClear	TangoPlus	VeroWhite and TangoPlus	VeroClear and TangoPlus
Tensile strength (MPa)	50–65	50–65	0.8–1.5	40–60	35–45
Elongation at break (%)	10–25	10–25	170–220	15–25	20–30
Flexural strength (MPa)	75–110	75–110	–	55–75	45–60
Flexural modulus (MPa)	2200–3200	2200–3200	–	1500–2500	1400–1800
Shore hardness	83–86 D	83–86 D	26–28 A	81.1–85.5 D	79.5–83.5 D

**Table 2** Selected control factors and their levels

Control factor	Level 1	Level 2	Level 3
Finish type	M	G	–
Material	WT	CW	CT
Design	D0	S1	S2

the same is denoted by S1. Similarly, material assignment of S2 sample is a vice versa of S1 sample, which is named as stacking-2.

## 2.2 Design of Experiments

In this study, Minitab software is used to determine the number of experiments through the statistical method of Taguchi orthogonal array. Finish type, material combination and design of sample are referred as selected control factors. Levels of selected control factors are displayed in Table 2. Taguchi's  $L_{18}$  ( $2^1, 3^2$ ) orthogonal array was used to examine the effect of selected control factors. Printing time, number of layers and height of the printed specimen are referred as responses. Faster production can be achieved by lesser value of all responses. Average response values are recorded and each experiment from  $L_{18}$  orthogonal array was conducted three times randomly.

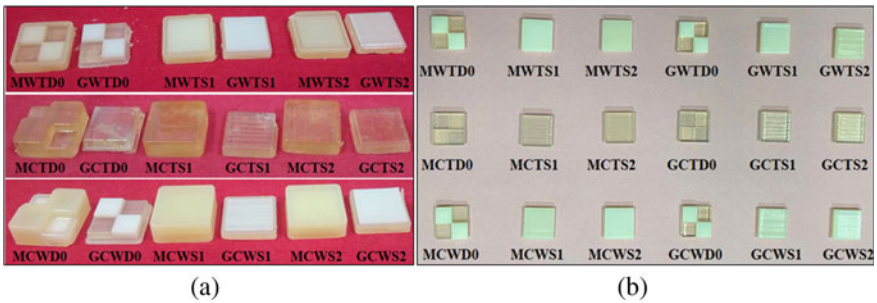
## 3 Results and Discussion

Details of each experiment and its printing details are populated in Table 3. Description column of the table determines the combination of each parameter. For example, experiment number 1 "MWTD0" refers matte finish, primary material of "W" and secondary material of "T" is selected for printing a sample D0. Material consumptions and printing time is obtained from job manager window of Objet Studio software. Similarly, 3D printed specimen height and number of layer values are acquired from machine window. PolyJet printed samples with support material and without support materials are shown in Fig. 2a and b respectively. Values of Table 3 reveals that, printing time of glossy finished samples are lesser when compared to matte finished samples. Because, support material deposition on top surface of the glossy finished sample is neglected. Noticeably, material consumption, printing time, specimen height and number of layers of all the glossy finished samples are equal. Specimen height and number of layers of matte finished WT samples are 6.88 and 7.35% higher, when compared to glossy finished samples and the same was takes one minute additional printing time.

On other hand, except "MCTS2" and "MCWS2" sample, all other matte finished samples (4 no's) of "CT" and "CW" shows uniform reading. Compared to glossy

**Table 3** Results of printing details for eighteen printed parts

Experiment number	Description	Primary material (g)	Secondary material (g)	Support material (g)	Printing time (min)	Specimen height (mm)	Number of layers
1	MWTD0	2	2	3	18	4.36	146
2	MWTS1	2	2	4	18	4.36	146
3	MWTS2	2	2	4	18	4.36	146
4	GWTD0	2	2	3	17	4.06	136
5	GWTS1	2	2	3	17	4.06	136
6	GWTS2	2	2	3	17	4.06	136
7	MCTD0	2	2	4	27	7.06	236
8	MCTS1	2	2	5	27	7.06	236
9	MCTS2	2	2	4	23	7.06	236
10	GCTD0	2	2	3	17	4.06	136
11	GCTS1	2	2	3	17	4.06	136
12	GCTS2	2	2	3	17	4.06	136
13	MCWD0	2	2	4	27	7.06	236
14	MCWS1	2	2	5	27	7.06	236
15	MCWS2	2	2	4	23	6.05	202
16	GCWD0	2	2	3	17	4.06	136
17	GCWS1	2	2	3	17	4.06	136
18	GCWS2	2	2	3	17	4.06	136



**Fig. 2** PolyJet printed samples **a** with support materials, **b** without support materials

finished samples, specimen height of the above mentioned four samples are increasing 73.89%, the number of layers increases 73.52% and it consumes an extra printing time of 10 minutes. Printing time, specimen height and number layers of the sample MCTD0, MCTS1, MCWD0 and MCWS1 are higher when compared to matte finished WT samples and the percentage of increasing value are 50%, 61.92% and

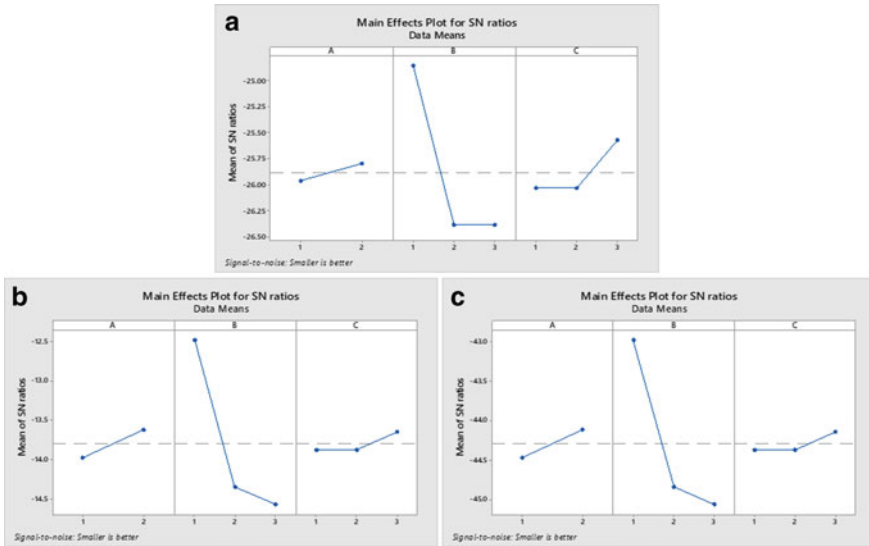
**Table 4** S/N response table for all the responses

Response	Control factors	Level 1	Level 2	Level 3	Rank
Printing time	Finish type	-25.96	-25.79	-	3
	Material	-24.86	-26.39	-26.39	1
	Design	-26.03	-26.03	-25.57	2
Specimen height	Finish type	-13.98	-13.62	-	2
	Material	-12.48	-14.35	-14.57	1
	Design	-13.88	-13.88	-13.65	3
Number of layers	Finish type	-44.47	-44.12	-	2
	Material	-42.98	-44.84	-45.06	1
	Design	-44.37	-44.37	-44.14	3

61.64% respectively. However, both the “CT” and “CW” experiments show higher values than “WT” experiments.

Significance of each control factor over the selected responses was determined by signal-to-noise (S/N) ratio. Table 4 displays the S/N response table for all the responses. From this result, material selection is an important control factor to optimize all the responses of PolyJet printed parts followed by design of the sample and selection of finish type. Ranking order of the specimen height and number of layers reveals the same results. Here, second and third rank is secured by finish type and sample design respectively. However, glossy finished stacking-2 sample printed by WT material combination (GWTS2) shows the optimum selection. Main effects plot for S/N ratios of all the response is shown in Fig. 3.

From this research, it is observed that printing time is significantly influenced by the selection of model material. Outcome of all the responses is equal in glossy finished samples. In matte finish, printing time and support material consumption of material “C” is more when compared to material “W” and “T”. Printing time and support material consumption is based on material property, bonding strength and curing temperature. Owing to neglecting the support material deposition at the top surface of the part, glossy finished samples require shorter printing time when compared to matte finished samples. Noticeably, responses of printing time, height of the 3D printed specimen and number of layers are directly proportion to other responses. This research paper offers an understanding of optimum selection of process parameters of the PolyJet machine. The obtained results are very useful for investigating the material properties of PolyJet materials in different combinations and fabrication of multi-material products.



**Fig. 3** Main effects plot for S/N ratio for all the responses **a** printing time, **b** specimen height and **c** number of layers

## 4 Conclusion

This study investigated the build properties of PolyJet printed multi-material parts. Eighteen samples were built according to the  $L_{18}$  Taguchi orthogonal array that had been selected as the experimental design. The effects of build properties on process parameters such as finish type, material combination and design of the samples were studied. Findings of this investigation reveal that build properties are significantly affected by material combination. Printing time and support material consumption of VeroClear is higher than other materials discussed. Glossy finish, VeroWhite-TangoPlus material combination and sample stacking-2 is identified as an optimal selection. Compared to matte finish, build properties are better in glossy finish. Matte finished CT and CW samples require additional 50% of printing time when compared to matte finished WT samples.

**Acknowledgements** We hereby acknowledge the facilities and technical assistance of the Centre of Excellence in Manufacturing Sciences (CoEMS) at Coimbatore Institute of Technology.



## References

1. Krujatz, F., Lode, A., Seidel, J., Bley, T., Gelinsky, M., Steingroewer, J.: Additive biotech—chances, challenges, and recent applications of additive manufacturing technologies in biotechnology. *New Biotechnol.* **39**, 222–231 (2017)
2. Cazón, A., Morer, P., Matey, L.: PolyJet technology for product prototyping: tensile strength and surface roughness properties. *Proc. Inst. Mech. Eng. Part B J. Eng. Manuf.* **228**(12), 1664–1675 (2014)
3. Rivera, F.J.M., Arciniegas, A.J.R.: Additive manufacturing methods: techniques, materials, and closed-loop control applications. *Int. J. Adv. Manuf. Technol.* **109**(1), 17–31 (2020)
4. Ituarte, I.F., Boddeti, N., Hassani, V., Dunn, M.L., Rosen, D.W.: Design and additive manufacture of functionally graded structures based on digital materials. *Addit. Manuf.* **30**, 100839 (2019)
5. Di Angelo, L., Di Stefano, P.: A neural network-based build time estimator for layer manufactured objects. *Int. J. Adv. Manuf. Technol.* **57**(1–4), 215–224 (2011)
6. Kęsy, A., Kotliński, J.: Mechanical properties of parts produced by using polymer jetting technology. *Arch. Civ. Mech. Eng.* **10**(3), 37–50 (2010)
7. Meisel, N.A., Dillard, D.A., Williams, C.B.: Impact of material concentration and distribution on composite parts manufactured via multi-material jetting. *Rapid Prototyping J.* **24**, 872–879 (2018)
8. Mueller, J., Courty, D., Spielhofer, M., Spolenak, R., Shea, K.: Mechanical properties of interfaces in inkjet 3D printed single-and multi-material parts. *3D Print. Addit. Manuf.* **4**(4), 193–199 (2017)
9. Kent, N.J., Jolivet, L., O'Neill, P., Brabazon, D.: An evaluation of components manufactured from a range of materials, fabricated using PolyJet technology. *Adv. Mater. Process. Technol.* **3**(3), 318–329 (2017)
10. Moore, J.P., Williams, C.B.: Fatigue properties of parts printed by PolyJet material jetting. *Rapid Prototyping J.* **21**, 675–685 (2015)
11. Kim, G.D., Oh, Y.T.: A benchmark study on rapid prototyping processes and machines: quantitative comparisons of mechanical properties, accuracy, roughness, speed, and material cost. *Proc. Inst. Mech. Eng. Part B J. Eng. Manuf.* **222**(2), 201–215 (2008)
12. Tee, Y.L., Tran, P., Leary, M., Pille, P., Brandt, M.: 3D printing of polymer composites with material jetting: mechanical and fractographic analysis. *Addit. Manuf.* **36**, 101558 (2020)
13. Kampker, A., Kreisköther, K., Reinders, C.: Material and parameter analysis of the PolyJet process for mold making using design of experiments. *Int. J. Mater. Metall. Eng.* **11**(3), 242–249 (2017)
14. Gay, P., Blanco Fernández, D., Fernández Fernández, P., Noriega González, Á., Fernández Álvarez, P.: Analysis of factors influencing the mechanical properties of flat PolyJet manufactured parts. *Procedia Eng.* **132**, 70–77 (2015)
15. Kumar, K., Kumar, G.S.: An experimental and theoretical investigation of surface roughness of poly-jet printed parts: this paper explains how local surface orientation affects surface roughness in a poly-jet process. *Virtual Phys. Prototyping* **10**(1), 23–34 (2015)
16. Kechagias, J.P., Stavropoulos, P., Koutsomichalis, A., Ntintakis, I., Vaxevanidis, N.: Dimensional accuracy optimization of prototypes produced by PolyJet direct 3D printing technology. *Adv. Eng. Mech. Mater.* 61–65 (2014)
17. Aslani, K.E., Korlos, A., Kechagias, J.D., Salonitis, K.: Impact of process parameters on dimensional accuracy of PolyJet 3D printed parts using grey Taguchi method. In: *MATEC Web of Conferences*, vol. 318, pp. 01015. EDP Sciences (2020)
18. Meisel, N., Williams, C.: An investigation of key design for additive manufacturing constraints in multimaterial three-dimensional printing. *J. Mech. Des.* **137**(11), 1–9 (2015)

# Design of Workplace in Assembly Unit Using Ergonomic Principles



V. Manivelmuralidaran , M. Balaji, and V. Arun

## 1 Introduction

Ergonomics is commonly used to decrease occupational injuries by finding the tasks and postures that creates continuous musculoskeletal stresses. K. H. F. Morrel at 1949 coined the concept of ergonomics, who derived it from Greek word ‘ergo’ which means work and ‘nomos’ which means law. According to International Ergonomics Association (IEA), the term ergonomics is concerned with the understanding of human interactions and the profession that applies theory, principles, data and methods to design in order to optimize human well-being and overall system performance [1].

Productivity improvement by worker is one of the important objectives of industries, particularly involved in assembly workstations. Assembly workstations are characterized by repetitive works. These works in these workstations are considered to be fatigue and tiresome. This in turn tends to reduce the worker productivity and larger rate of absenteeism [2]. Manufacturers of varying industries found that along with investing huge amount of money on man, machine, material and methods, incorporating ergonomics principles in design of workplace is cost saving [3, 4].

This study is conducted on assembly and collection workstation which has suffering from high cycle time. Fixed workstation involves three set of sub-assemblies, collection of fasteners and a final main assembly for the completion of single process. The objective of this research article is to avoid the long reaches and in providing the adjustable workstation with individual seating which will enable to work in sitting or standing position, thereby the time taken for operation is also reduced.

---

V. Manivelmuralidaran (✉) · M. Balaji · V. Arun  
Kumaraguru College of Technology, Coimbatore, India  
e-mail: [manivelmuralidaran.v.mec@kct.ac.in](mailto:manivelmuralidaran.v.mec@kct.ac.in)

© The Author(s), under exclusive license to Springer Nature Singapore Pte Ltd. 2022  
S. K. Natarajan et al. (eds.), *Recent Advances in Manufacturing, Automation, Design and Energy Technologies*, Lecture Notes in Mechanical Engineering,  
[https://doi.org/10.1007/978-981-16-4222-7\\_3](https://doi.org/10.1007/978-981-16-4222-7_3)

## 2 Literature Review

Workplace with good design reduces injuries and make the workers to work effectively and efficiently to manufacture the good quality products [5]. Workstation with efficient design is essential to for mass production and flexibility in an effective way, thus allows the organization to increase their quality level and production indicators [6]. Improper planning in the design of workstation makes the workers to accommodate into working conditions that were not designed for them [7]. Handling heavy loads, repetitiveness of work, awkward and static postures are the factors that allows the assembly line workers to risks of musculoskeletal disorders [8]. Researchers pointed out that working at shop floor is a complex task with high level of responsibility, working for a prolonged period of time results in higher risk of musculoskeletal disorders [9]. Thus, the poor performance is given by the workers suffered from the high risk because of inappropriate match between the workstation and the anthropometry. During the time of assembly works and repetitive manual handling tasks, workers are susceptible to the risk of injuries. A workplace should be designed by incorporating ergonomic principles will yield high productivity and worker efficiency [10].

Ergonomics is traditionally used to decline the number of occupational injuries by finding the tasks and postures that develops the musculoskeletal stresses, and thus, good ergonomic design is used to enhance the organization productivity [11, 12]. One of the basic principles of ergonomics, fit the machine to the man or else fit the man to the machine [13]. Success for major industries depends on how quickly the products are delivered to the customers. The industries must implement new technologies and concepts to achieve success [14].

Optimizing the safety, health and comfort of the human in the working system is the main aim of the ergonomics; thus, it is necessary to implement safety and health policy to protect the workers [15, 16]. Fixed workstations of the assembly line have restrictions on anthropometric dimensions of the operators who are involved in assembly operations. Further, it affects the stress on musculoskeletal system of the operators [17]. The normal time required to do a specific task by a qualified and well-trained person is determined by the method of time study [18, 19].

The innovation in taking up this work is to incorporate the ergonomic principles in workplace design, and this modification has not been attempted in the organization. Hence, the design changes of the workplace has been suggested, and it is evident that the modification brings increase in production of the products that has been presented.

### 3 Methodology

#### 3.1 Objectives

The objectives of the present research study are to design workplace with ergonomic consideration. This is needed to improve the working performance of the workers to increase the production. The second objective of taking up this research is to reduce the operator fatigue. There are number of workers facing occupational health problems due to prolonged working in the standing position. It is essential to redesign the workstation to reduce the occupational health problems. The third objective is to ensure a good workflow which facilitates the improvement in production.

By incorporating the ergonomic principles in workstation design, this objective can be achieved, and it is evident from the literature [20, 21]. This project initiated with the study on existing workstation with five workers, by identifying the major problems faced by the workers during their normal working time. The problems were analyzed, and then a better solution is implemented. Decision analysis process starts with the study on current process and identify the major problems. Then, the analysis of the problem will be done to find the better solution, and the data collected for the process. Layout design will be done, and it will be validated and implemented. The implemented solution reduces the fatigue problems faced by the workers, and the result shows the improvement in productivity.

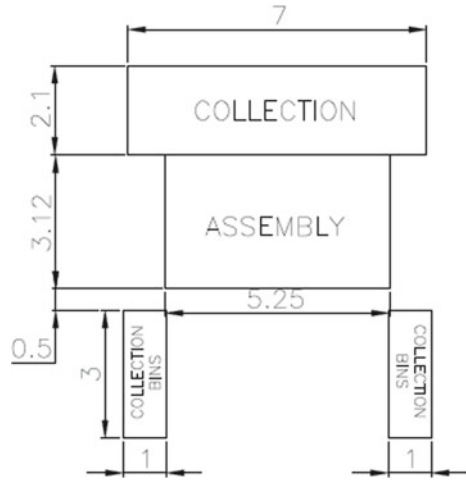
### 4 Existing Workstation

An assembly and collection workstation which are used to assemble fasteners was selected for the study. Through the measurements of the existing workstation, it was decided that the workstation was not designed by considering the ergonomic principles, and hence, the workers were not using the proper working posture during the time of work.

The task was performed in standing position for about 9 h abandoning the lunch and break time. Due to this reason itself, some of the workers cannot expose their effort properly after completing their half day work. The assembly table height was fixed as 3.37 ft with the inadequate table surface area ( $5.25 \times 3.12$  ft). The footrest was not designed to provide a proper support to the workers, it looked like an attached bar along the front bottom of the table. The collection table height was fixed as 3.1 ft with the surface of ( $7 \times 2.1$  ft). The shoulder stress and back pain are caused when the worker is working under such conditions for a prolonged period of time [21, 22].

The bins (B25) containing fasteners were located at the farther right end corner and superimposed by ( $2 \times 3$  ft) in straight line on the assembly table. A pneumatic press of 21 kg is located at the front right end of the assembly table and the screw driver is hinged at a distance of 1.7 ft from the front of the assembly table with locating the fixture straight to it on the table. Thus, the workers will have to move

**Fig. 1** Layout of the existing workstation



their arm by providing some force to pick the fasteners during the time of assembly and some operators took certain volume of fasteners and kept it within their easy reach, which are to be used in next operation. So, it stands as a little disturbance to the worker during their arm motions.

Here, the limit to hold the screw driver by the worker was exceeded. Figure 1 shows the layout of the existing workstation, the collection of fasteners was done on the bins (B15) located at the left and right of the assembly table, and it was transferred to the collection table for the next stage of inspection. All the dimensions mentioned in this article are given in ft. Since, it has been measured from the workstations and recorded.

## 5 Design and Development of Multiple New Workstation

The redesigned workstation was proposed by taking into account of the ergonomic factors while designing. It is proposed to develop the new workstation that could be used by an individual irrespective of their height and working in the desired posture. For designing the new workstation, anthropometric data of five workers were taken to identify the range of movements which is essential to have worker comfort. Table 1 gives the anthropometric data of the workers. Anthropometric data of workers such as standing height (SH), vertical grip reach (VGR), forward grip reach (FGR), foot length (FL) and sitting height (SH) are collected. In order to do the work without any kind of unnecessary movements and fatigue, the fully adjustable ergonomically designed chair and working table were suggested.

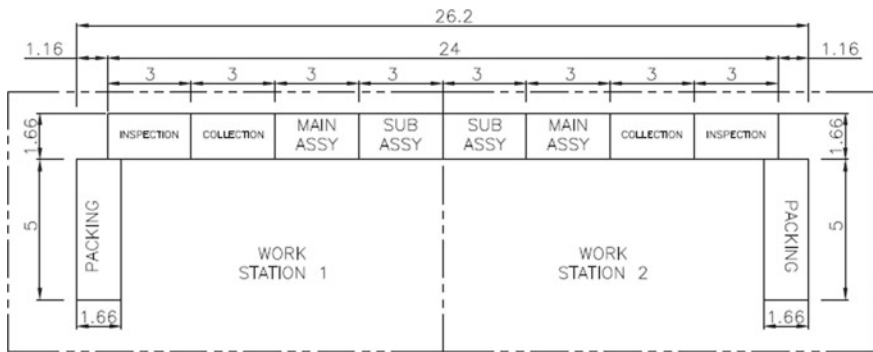
By taking into account of the ergonomic principles and the anthropometric data of the workers, new advanced tables were designed with adjustable vertical movement

**Table 1** Anthropometry data of workers

	Worker 1	Worker 2	Worker 3	Worker 4	Worker 5
SH	5.53	5.39	5.27	5.59	5.25
VGR	6.73	6.57	6.28	6.84	6.19
FGR	2.42	2.38	2.34	2.45	2.31
FL	0.77	0.75	0.73	0.8	0.72
SH	2.87	2.66	2.59	2.92	2.56

**Table 2** Dimensions of storage bins

Storage bins	Length (ft)	Breadth (ft)	Height (ft)
B15	0.66	0.46	0.33
B25	0.75	0.5	0.416
B45	1.1	0.68	0.65



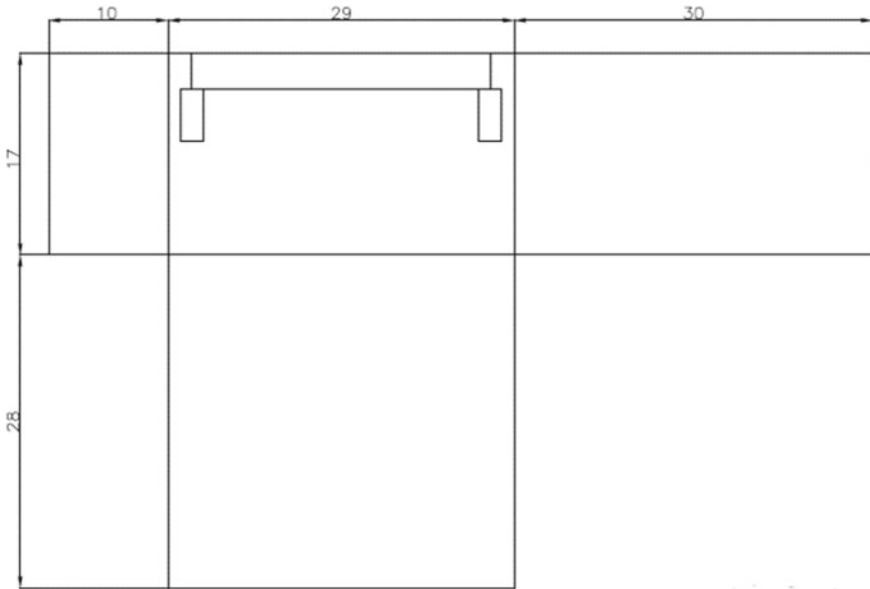
**Fig. 2** Layout of the new workstation

[23–25]. The total gap between the vertical heights of each bins was maintained at 0.15ft. Table 2 gives the dimensions of the individual storage bins.

Finally two packing tables were designed with breadth and height of the previous table with varying length of 5-ft. A lamp with 750 lx was used in the individual worktable at distance of 4.10-ft from workplace [26, 27]. Figure 2 shows the layout of new workstation designed with considering ergonomic principles.

## 6 Results and Discussions

A test was conducted on both the workstations to estimate the new workstations in terms of productivity. The assembly of mounting kit consists of four assembly work and three non-assembly work (collection, inspection and packing) and the assembly



**Fig. 3** Layout of assembly unit after implementing the ergonomic principles

performed on the workstations that are not designed by taking into consideration of ergonomic principles. Also, the workflow in the existing workstation was not followed properly. Workers completed the assembly work in certain periodic time, and the remaining non assembly work in an individual time. The experiment was conducted in two ways: (1) assembling mounting kits on the existing workstation method and (2) assembling the mounting kits on the new workstation that incorporated ergonomic principles. The output of these two scenarios are compared and suggested to the organization. The layout of assembly unit after implementing the new workstation with extended area is shown in Fig. 3.

The time study for each and every work classified by the elements is noted for both the existing and new workstation. The comparison of time study shows that the new workstation was higher in comparison to the mean time of the existing workstation. The number of products produced per day by single new workstation increases to 117, compared with the existing workstation with output quantity around 99. This increase is achieved through the reduction of time in collection of fasteners of about 75 to 50 s by modifying the workstation. Thus, by incorporating the flexibility and ergonomic principles with proper work flow provides higher worker performance [9–11]. The workplace has been designed in such a way that it suits the workmanship which increases the number of products that is evident from the results. Major changes incorporated in the new workstation were: (1) appropriate table surface area with the height adjustments, (2) fully ergonomically designed chair with suitable back rest and height adjustment, (3) locating the bins in the assembly and collection table using bin rails. Since the workstation was fully adjustable, a flexible posture in the

task performance is possible by the workers. Hence, the workers can easily adjust the new workstation depending upon their level of use. The ergonomics and the proper work flow incorporated to the workstation made the worker comfortable, less fatiguing and more efficient [21–23]. The results obtained in this research work are in consistent with the earlier research which improves the productivity by incorporating the ergonomic principles [25].

## 7 Conclusion

A new workstation was developed, and it is fully adjustable by the workers for comfort and could be used in sitting and standing posture. Hence, the job rotation is also easily achieved by adjusting the worktable height depending on the workers' comfort. So, the new workstation designed ergonomically had a positive effect on increasing the worker efficiency. The collection of fasteners of about 75 s was reduced to 50 s by modifying the workstation. The output product of the multiple new workstation is around 234, while the existing workstation had output of 99 products per day. Thus, the efficiency result proposes that the new workstation was comfortable to the workers. In other words, justification was done on a good workstation with consideration of ergonomic principles could ensure workers' health and safety and also improves the productivity. Future scope of this research work includes implementation of indication light system to each bins, and bar code is used in place of bill of materials during collection. By the scanning of bar code, the corresponding bins will illuminate which enables the operator to pick the fasteners from bins quickly.

## References

1. Shikdar, A., Garbie, I., Khan Khadem, Md.M.R.: Development of a smart workstation for an assembly task. In: International Conference on Industrial Engineering and Operations Management, pp. 826–831 (2011)
2. Shinde, G.V., Jadhav, V.S.: Ergonomic analysis of an assembly workstation to identify time consuming and fatigue causing factors using application of motion study. *Int. J. Eng. Technol.* **4**, 220–227 (2012)
3. Mali, S.C., Vyahare, R.T.: An ergonomic evaluation of an industrial workstation: a review. *Int. J. Curr. Eng. Technol.* **5**(3), 1820–1826 (2015)
4. Muhundhan, M.: Improved work station design for improved productivity. *Int J. Sci. Eng. Technol.* **2**, 225–227 (2013)
5. Gonçalves, M.T., Salonitis, K.: Lean assessment tool for workstation design of assembly lines. *Procedia CIRP* **60**, 386–391 (2007)
6. Hernandez-Arellano, L., Serratos-Perez, J.N., de la Torre, A.: Design proposal of an adjustable workstation for very short and very tall people. *Int. Conf. Appl. Human Factors Ergon.* **3**, 5699–5706 (2015)
7. Helander, M.: *A Guide to Human Factors and Ergonomics*, 2nd edn. Taylor and Francis Group (2006)



8. Vaidya, R.D., Sontakke, K.G., Ansari, N.A.: Ergonomics evaluation of body posture of worker in SSI. *J. Emerg. Technol. Innov. Res.* **1**, 430–434 (2014)
9. Mossa, G., Boenzi, F., Digiesi, S., Mummolo, G., Romano, V.A.: Productivity and ergonomic risks in human based production systems: a job-rotation scheduling model. *Int. J. Prod. Ergon.* **171**, 471–477 (2016)
10. Bagnara, S., et al. (eds.): *6Ws in Ergonomics Workplace Design*, IEA 2018, AISC 824, pp. 1282–1286 (2019)
11. Leskova, A.: Designing of manual workstation structure with emphasis on ergonomics. *Bull. Eng.* **7**, 41–46 (2014)
12. Smellie, S.: The limitations of a standard workstation for its user population. *Clin. Chiropractic* **6**, 101–108 (2003)
13. Vijaya Rammatha, B., Suresh Kumar, C., Riyaz Mohamed, G.: Analysis of occupational safety and health of workers by implementing ergonomic based kitting assembly system. *Procedia Eng.* **97**, 1788–1797 (2014)
14. Mali, S.C., Vyavahare, R.T.: An ergonomic evaluation of an industrial workstation: a review. *Int. J. Curr. Eng. Technol.* **5**, 1820–1826 (2015)
15. Chan, A.H.S., Hoffmann, E.R., Chung, C.M.W.: Subjective estimates of times for assembly work. *Int. J. Ind. Ergon.* **61**, 149–155 (2017)
16. Permata, L., Hartanti, S.: Work measurement approach to determine standard time in assembly line. *Int. J. Manage. Appl. Sci.* **2**, 192–195 (2016)
17. Barnes, R.M.: *Motion and Time Study Design and Measurement of Work*. Wiley (1980)
18. Halim, I., Omar, A.R.: Health effects associated with prolonged standing in the industrial workplaces. *Int. J. Res. Rev. Appl. Sci.* **8**, 14–21 (2011)
19. Grandjean, E.: *Fitting the Task to Man: An Ergonomic Approach*, vol. 2, pp. 231–239. Taylor and Francis, London (2016)
20. Deros, B.M., Khamis, N.K., Ismail, A.R., Jamaluddin, H., Adam, A.M.: An ergonomics study on assembly line workstation design. *Am. J. Appl. Sci.* **8**, 1195–1201 (2011)
21. Otto, A., Scholl, A.: Incorporating ergonomic risks into assembly line balancing. *Eur. J. Oper. Res.* **212**, 277–286 (2011)
22. Boenzi, F., Digiesi, S., Facchini, F., Mummolo, G.: Ergonomic improvement through job rotations in repetitive manual tasks in case of limited specialization and different ergonomic requirements. *IFAC Paper Online* **49**, 1667–2167 (2016)
23. Kaya, Ö.: Design of work place and ergonomics in garment enterprises. *Procedia Manuf.* **3**, 6437–6443 (2015)
24. Chiasson, M.-E., Major, J.: Influence of musculoskeletal pain on workers' ergonomic risk-factor assessments. *Appl. Ergon.* **49**, 1–7 (2015)
25. Widana, I., Sumetri, N.W., Sutapa, K.: Ergonomic work station design to improve workload quality and productivity of the craftsmen. *IOP Conf. Ser.: J. Phys.: Conf. Ser.* **953** (2018)
26. Telsang, M.: *Industrial Engineering and Production Management*. S Chand Publishers (2016)
27. Singh, L.P.: *Work Study and Ergonomics*, 1st edn. Cambridge University Press (2018)

# Experimental Investigation on Electrochemical Discharge Machining of Zirconia



Vijay Manoharan, Sekar Tamilperuvalathan, Elango Natarajan,  
and Prasanth Ponnusamy

## 1 Introduction

Nowadays, the manufacturing industries adopt non-traditional machining processes. It reduces the tool cost and also effectively machining high-strength materials without any thermal defects [1]. Electrochemical discharge machining (ECDM) is a non-traditional machining process that combined electrochemical machining (ECM) and electrical discharge machining (EDM) [2]. ECDM process uses NaOH as an electrolyte with voltage to machining the ceramics [3]. In this research work, the ECDM process uses various levels of NaOH electrolyte concentrates and voltage. High-strength and corrosive resistance materials are used to produce dental and medical instruments. Zirconia ( $ZrO_2$ ) is widely used for the production of medical and dental instruments due to its high resistance to corrosion and high strength [4]. This experimental work uses zirconia as a working material, and ECDM is the process of machining the zirconia [5].

In ECDM, the parameters used to machine zirconia are electrolyte concentrate, electrolyte flow type or stagnate type, applied voltage, duty cycle and tool, inter-electrode gap (IEG), critical depth, etc. This work involves parameters such as electrolyte concentrations, applied voltage, and duty cycles in three levels and also uses the design of experiments [6] with response surface methodology for this work;

---

V. Manoharan (✉) · S. Tamilperuvalathan  
Department of Mechanical Engineering, Government College of Technology, Coimbatore, Tamil Nadu, India

E. Natarajan  
Department of Mechanical and Mechatronic Engineering, UCSI University, UCSI Heights, Jalan Menara Gading, Kuala Lumpur, Malaysia

P. Ponnusamy  
Department of Mechanical Engineering, Tagore Institute of Engineering and Technology, Attur, Salem, Tamil Nadu, India

ECM [7, 8] and EDM [9] processes also studied to achieve optimization of material removal rate (MRR) in ECDM having three process parameters such as electrolyte concentration, duty cycle, and applied voltage; [10] in this work, various process parameters are studied and predict that the electrolyte concentration is reducing the tool wear and increasing the MRR. In this research work, the electrolyte concentration is used to three levels to achieve maximum material removal rate; [11] in this work, they used the various design of experiments such as the Taguchi design and GA algorithm to optimize. In this work, we used response surface methodology for the design of experiments; [12] in this experimental work, they used to machine glass workpiece in ECDM with four parameters such as voltage, duty factor, electrolyte concentration, and temperature. They used response surface methodology to design experiments to conduct experiments, and they revealed that MRR increased in voltage and temperature. The electrolyte used in this work NaOH is kept stagnate instead of circulation which is one of the important machine setups in this process; [13] in this experiment, they prove that the better MRR is achieved where the electrolyte is stagnating position, so in our experiment, we kept the electrolyte stagnate [14] while machining.

## 2 Design of Experiment

The stainless steel tool is used to remove the material to make a hole in the zirconia plate. The tool is stationary and electrolytes kept stagnate condition. The material removal rate is observed under the impact of three distinguished parameters, such as applied voltage, duty cycle, and electrolytic concentration.

### 2.1 *The Process Parameters*

The process parameters ranges for the experiments are given below:

Electrode	Stainless Steel
Workpiece	Zirconia
Workpiece thickness	1 mm
Electrolyte	NaOH (with various concentrations)

### 2.2 *Selection of Machining Parameters*

For the machining of hard materials like ceramics, the following machining parameters voltage, electrolyte concentration, and duty cycle are the most influencing machining parameters in the ECDM and selected the above-mentioned parameters based on the literature work.

**Table 1** Levels of process parameter

Name	Units	Low	High
Electrolyte concentration	%wt	15	25
Voltage	V	80	100
Duty cycle	%	50	70

### 2.3 Box–Behnken Design

To conduct the experiments, Box–Behnkan design from response surface methodology is selected.

Table 1 depicts the process parameters and the level of their value on experiments.

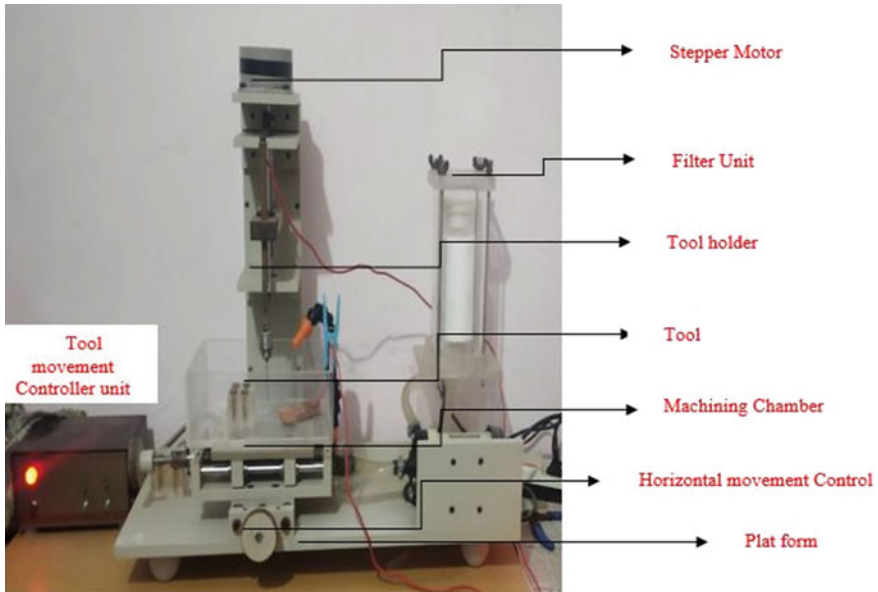
## 3 Experimental Work

### 3.1 Material for Workpiece

Zirconia ( $ZrO_2$ ) is one of the strongest material as well as highly corrosive resistant. Table 1 depicts the mechanical properties of Zirconia ( $ZrO_2$ ), and they studied zirconia is a material having tremendous properties such as high resist to indentation strength, high resist to wear, great thermal hardness, and more chemical durability, and also noted the zirconia material is strongly recommended to produce dental crowns and wear-resistant coating. Further, they observed from experiments that MRR is increasing due to increasing applied voltage and also noticed that overcut issues were also raised [15]. The objective of this research work is to maximize the MRR.

### 3.2 Electrochemical Discharge Machining (ECDM) Processing

The non-traditional machining processes are used to machining the hard and brittle material such as zirconia [16]. They used the ultrasonic machining process in their experimental work and revealed that higher voltage causes to tool wear [17] which utilize the ultrasonic machining process to machine the zirconia composite material and revealed the slurry with abrasives which are causes to damage the workpiece surface. In this work, the ECDM is used to avoid surface damage due to abrasive slurry. Figure 1 shows the experimental arrangement for the ECDM. This setup consists of a stepper motor, filter unit, tool holder, machining chamber, tool horizontal movement control handwheel, and programmed tool movement controller.



**Fig. 1** ECDM machining setup

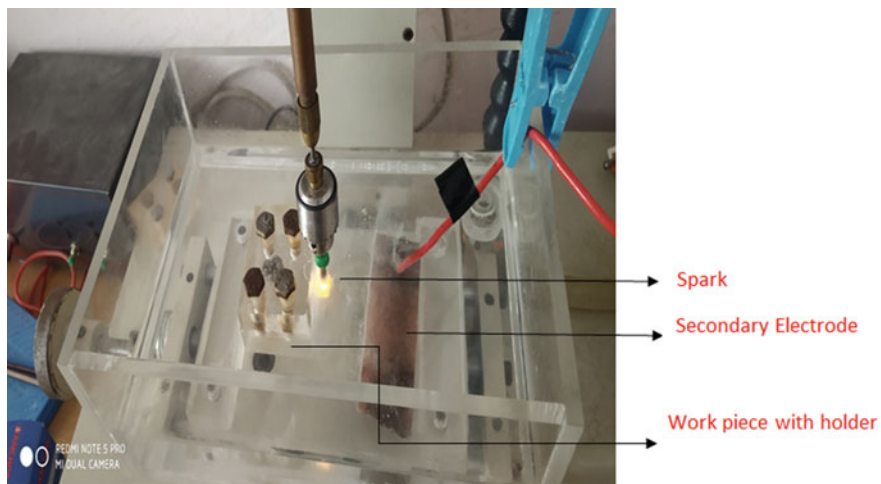
The workpiece is kept in the machining chamber, and beforehand, the machining chamber is filled with NaOH electrolyte up to cover the workpiece surface. The stainless steel tool is mounted with a tool holder. The workpiece is moving with the help of a handwheel in X- and Y-direction to drill the zirconia material.

Beforehand, the design of experiments (DOE) is used to conducting experiments. Response surface methodology is select to DOE in Box–Behnken model design using design-expert software.

## 4 Results and Discussion

Figure 2 shows the machining of the workpiece material into the machining chamber. The spark is produced between the workpiece and electrolyte. The Electrochemical Discharge Machining process beginning, electrolyte enclosed the tool gets debase by the reaction, produces gas bubbles, as a result, the bubbles release the pressure energy causes to material removal. The electrode gets wear and contaminates due to spark. Therefore, for each experiment, a new electrode is used with a fresh electrolytic concentration solution.

Table 2 shows the material removal rate of the machining of zirconia. The work-piece has been observed before and after machining to calculate the material removal rate.



**Fig. 2** Machining of workpiece

**Table 2** Material removal rate (MRR)

Run	Electrolyte concentration (A)	Voltage (B)	Duty cycle (C)	MRR ( $\mu\text{g}/\text{min}$ )
1	20	90	60	238
2	20	90	60	237
3	20	90	60	238
4	15	90	50	210
5	25	80	60	249
6	20	100	70	245
7	25	90	70	263
8	15	100	60	234
9	20	90	60	236
10	20	80	70	239
11	15	80	60	214
12	25	100	60	276
13	20	80	50	227
14	15	90	70	226
15	20	90	60	237
16	20	100	50	242
17	25	90	50	247

### 4.1 Observations During Experimentation (MRR)

Time duration 30 min, (Each Cycle)  
Tool Stainless Steel  
Tool diameter 1 mm

Regression equations obtained for the material removal rate is given below. This equation helps in the prediction and optimization of output variables concerning input variables.

$$\text{MRR} = 237.2 + 18.875 A + 8.5 B + 5.875 C + 1.75 AB + 5.55958 e - 16AC + -2.25 BC + 2.15 A^2 + 3.9 B^2 + -2.85 C^2 \tag{1}$$

where A is electrolyte concentration, B is voltage, and C is duty cycle.

Table 2 shows the result of the material removal rate of zirconia in g/min. These table values are clearly indicating that zirconia is machined using ECDM with NaOH.

From the above table values, we clearly infer that experimental run no: 12 achieved more MRR than others, and in the 12th run, we used the parameters that are electrolyte concentration is 25% wt., the applied voltage is 100 V, and the duty cycle is 60%.

Figure 3 shows the parameter relations regarding the material removal rate. The graph shows that voltage gives a most influencing effect on material removal rate. Increases in voltage lead to increase in the rate of spark generation in the sparking area.

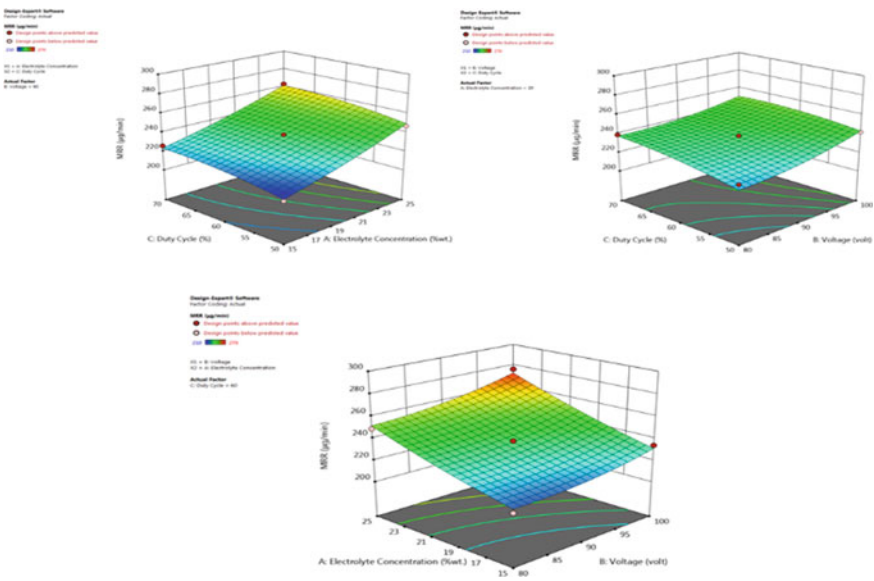


Fig. 3 Response surface plots for MRR

## 5 Conclusion

1. The electrochemical discharge machining (ECDM) technique is able to machine non-conductive materials like ceramics, glass, polymers, etc., in an effective manner. Based on experimental studies by the machining of zirconia, the following conclusions are drawn out:
2. From this experimental work, hard and brittle material like zirconia can be effectively machined without any fracture or thermal defects to the workpiece.
3. In this work, voltage plays a major role then followed by electrolyte concentration in the material removal rate of zirconia.
4. It was found that the maximum MRR is achieved when the voltage is and the electrolyte concentration in the peak, and the duty cycle was in the nominal stage.
5. In the future study can be carried out for radial overcut, roughness of machined area, and tool wear rate.

**Acknowledgements** The author's acknowledge research work is supported by Technical Education Quality Improvement Program (TEQIP) - III (R&D) Proceedings No. 1096/TEQIP-III/R & D/2020, Government College of Technology, Coimbatore, Tamil Nadu, India. The authors gratefully acknowledge the support provided by the Principal, the TEQIP coordinator, and the Head of the Department, Department of Mechanical Engineering (P.G), for the successful completion of this research work.

## References

1. Basak, I., Ghosh, A.: Mechanism of spark generation during electrochemical discharge machining: a theoretical model and experimental verification. *J. Mater. Process. Technol.* **62**(1–3), 46–53 (1996)
2. Zhu, Z., Dhokia, V.G., Nassehi, A., Newman, S.T.: A review of hybrid manufacturing processes—state of the art and future perspectives. *Int. J. Comput. Integr. Manuf.* **26**(7), 596–615 (2013)
3. Bhattacharyya, B., Doloi, B.N., Sorkhel, S.K.: Experimental investigations into electrochemical discharge machining (ECDM) of non-conductive ceramic materials. *J. Mater. Process. Technol.* **95**(1–3), 145–154 (1999)
4. Grech, J., Antunes, E.: Zirconia in dental prosthetics: a literature review. *J. Mater. Res. Technol.* **8**(5), 4956–4964 (2019)
5. Kumar, M., Vaishya, R.O., Suri, N.M.: Machinability study of Zirconia material by micro-ECDM. In: *Manufacturing Engineering*, pp. 195–209. Springer, Singapore (2020)
6. Kumar, A.S., Arularasu, M., Sekar, T., Suresh, P.: Investigation on the effects of silver nitrate solution mixed electrolyte in electrochemical machining of AISI 202. *Asian J. Res. Soc. Sci. Hum.* **6**(8), 2019–2026
7. Sekar, T., Marappan, R.: Experimental investigations into the influencing parameters of electrochemical machining of AISI 202. *J. Adv. Manuf. Syst.* **7**(02) (2008)
8. Sekar, T., Arularasu, M., Sathiyamoorthy, V.: Investigations on the effects of nano-fluid in ECM of die steel. *Measurement* **83**, 38–43 (2016)



9. Abbas, N.M., Solomon, D.G., Bahari, M.F.: A review on current research trends in electrical discharge machining (EDM). *Int. J. Mach. Tools Manuf.* **47**(7–8) (2007)
10. Gupta, P.K., Dvivedi, A., Kumar, P.: Developments on electrochemical discharge machining: a review of experimental investigations on tool electrode process parameters. *Proc. Inst. Mech. Eng. Part B: J. Eng. Manuf.* **229**(6), 910–920 (2014)
11. Stru, O.P., Hibridnega, E., Aluminija, M.N.O.: Optimization of machining parameters in turning of hybrid aluminium-matrix (LM24–SiCp–coconut shell ash) composite. *Mater. Technol.* **53**(2), 263–268 (2019)
12. Paul, L., Hiremath, S.S.: Characterization of micro channels in electrochemical discharge machining process. *Appl. Mec. Mater.* **490**, 238–242 (2014)
13. Cheng, C.P., Wu, K.L., Mai, C.C., Hsu, Y.S., Yan, B.H.: Magnetic field-assisted electrochemical discharge machining. *J. Micromech. Microeng.* **20**(7) (2010)
14. Dhanvijay, M.R., Ahuja, B.B.: Micromachining of ceramics by electrochemical discharge process considering stagnant and electrolyte flow method. *Procedia Technol.* **14**, 165–172 (2014)
15. Shimizu, K., Oka, M., Kumar, P., Kotoura, Y., Yamamuro, T., Makinouchi, K., Nakamura, T.: Time-dependent changes in the mechanical properties of zirconia ceramic. *J. Biomed. Mater. Res.* **27**(6), 729–734 (1993)
16. Kumar, M., Vaishya, R.O., Suri, N.M.: Machinability study of Zirconia material by Micro-ECDM. In: *Manufacturing engineering*, pp. 195–209. Springer, Singapore (2020)
17. Hocheng, H., Kuo, K.L., Lin, J.T.: Machinability of zirconia ceramics in ultrasonic drilling. *Mater Manuf. Process.* **14**(5) (1999)

# Risk Management for e-Commerce Supply Chain Network Using Robust Optimization Approach: A Case Study



Shubhender Singh, Pradeep Kumar, Manish Bhandari, and Gunjan Soni

## 1 Introduction

Supply chain (SC) encompasses all events involved in the transformation of goods from the raw material stage to the final stage, i.e., when the goods and services reach the end client. A supply chain comprises of flow of materials, information, funds, and services from suppliers, factories, distribution centers to the end clients. Income growth and urbanization along with high use of communication technologies are expected to cause a significant increase in demand for products purchased through e-shopping. Presently, maintaining a web based market place and providing the facility of online shopping is extremely important to all leading manufactures or retail firms. There are a number of vast applications of E-supply chain in e-business model, examples are Amazon, Dell, Alibaba, Flipkart, e-bay, Snapdeal, etc. In today's business world, complex supply chain had become a fact of life for firms. Very first step in supply chain risk analysis is risk identification which is basically mapping all possible causes of risk in the supply chain to recognize factors responsible for disruption in operations. A measure of risk combines a measure of the probability of occurrence of each primary event with a measure of the consequences of that event. Quantitatively, risk can be calculated as the product of the probability of an event and the business impact (or severity) of that event [1]. Supply chain risk management (SCRM) is defined as collaborating with partners to deal with risks and uncertainties caused by, or impacting on, logistics-related activities or resources [2]. Mitigation approach is based on the analysis of the processes with the aim of reducing the likelihood

---

S. Singh

Central Electricity Authority, Ministry of Power, Government of India, New Delhi 110066, India

P. Kumar (✉) · M. Bhandari

MBM Engineering College, J.N.V University, Jodhpur 342003, India

G. Soni

Department of Mechanical Engineering, MNIT, Jaipur 302017, India

of occurrence [3, 4]. The introduction of operational buffers along the supply chain (e.g., excess inventory or productive capacity, backup sourcing, multiple sourcing) is another approach to manage risks [5]. Much attention has been given to closed-loop supply chain which includes forward and reverse supply chains. The forward flow and reverse flow are considered together in this model allowing simultaneous optimality of network [6, 7]. A stochastic model is proposed for network design problems [8]. An optimization model is exhibited for reverse logistic network design [9]. The insights of application of CLSC network is also presented [10]. Demand uncertainty is the uncertainty in the customer demand for a product. Therefore considering demand side uncertainty seem necessary in the supply chain network design. Majority of existing reverse and closed-loop logistics network design models neglect the uncertain nature of various input parameters in a strategic planning horizon. Forward and reverse logistics network design under demand is proposed and return as uncertainty parameters [11]. A model is proposed for a supply chain network design (SCND) under uncertainty. Risk averseness of retailers is applied to the model under uncertain demand. Model is made robust by using Conditional Value at Risk (CVaR) [12]. Efficient risk and uncertainty management tools are vital to obtain optimal and robust decisions in supply chain network design, e.g., Conditional value at risk (CVaR) and robust stochastic programming approaches [13]. Effective environmental and social life-cycle evaluations are provided to assess the associated effects of the model on society, environment, and energy consumption [14].

Based on the insight gained from the literature about supply chain, e-commerce supply chain, risk factors, risk management, etc. gaps are observed in the literature but there is a visible research gap of studies dealing with the interrelationships of supply chain risks and selection of appropriate mitigation strategies. Also, an information sharing strategy will foster close collaboration among member enterprises that can make them more capable to mitigate operational risks and disruption risks. In e-supply chain model, direct shipping and shipping through distribution center take place. If the customer sites are nearby the factory location, then direct shipping of product takes place from factory to the customer sites. The current work is an effort to provide the firms with the models so as to help the managers to take strategic level decisions under uncertainty. A close loop supply chain (CLSC) network design that consists of forward and reverse flow is carried out. The robust optimization (RO) based modeling with both direct shipping of the products and shipping through distribution center under demand uncertainty is proposed and analyzed. The results are presented for supply chain planning strategies for an e-supply chain of case company (furniture manufacturing firm).

## 2 Robust Optimization Approach

Robust optimization involves two types of robustness: “solution robustness” (the solution is nearly optimal in all scenarios) and “model robustness” (the solution is nearly feasible in all scenarios). The definition of “nearly” is left up to the modeler;

their objective function has general penalty function for both model and solution robustness, weighted by a parameter intended to capture the modeler's preference between the two. The robust optimization method extends stochastic programming through replacing traditionally expected cost minimization objectives with one that explicitly addresses cost variability [15].

## 2.1 Deterministic Model for Robust Optimization

The demand is considered as uncertain parameter which is assumed to vary in a specified closed bounded box [16]. In the Stochastic programming approach, some parameters are regarded as random variables with known probability distributions. In real world, it is not possible to have a known probability distribution. In comparison, the Robust optimization approach represents uncertainty through setting up different scenarios which demonstrate realizations of uncertain parameters. The aim of this approach is to find a robust solution which ensures that all specified scenarios are "close" to the optimum in response to changing input data. In this study robust optimization approach is used as it has advantages over other approaches. Robust optimization approach based on theory of Ben-Tal is chosen for further study. Based on, the related uncertain linear optimization problem that consists of a collection of linear optimization problems can be defined as follows:

$$\begin{aligned} & \text{Min } cx + d \\ & \text{s.t. } Ax \leq b \\ & c, d, A, b \in U \end{aligned} \tag{1}$$

The above model has the parameters  $c, d, A, b$  belongs to uncertainty set  $U$  and vary in that set. The elements of matrix  $A$  are subject to uncertainty. Each entry of matrix  $A$  can be modeled as an independent, symmetric, and bounded parameter, which can take values in with in box. There has to be a nominal value and a maximum deviation from the nominal value. A parameter is introduced called the budget of uncertainty, for every constraint. When budget of uncertainty is 0, it means that there is no protection against uncertainty, and in other cases when budget of uncertainty is 1; it means there is complete protection against uncertainty.

## 3 Mathematical Modeling for E-Supply Chain Network

### 3.1 E-Supply Chain Network

The study focuses on capturing the practical aspect of e-commerce supply chain. A generic model with closed-loop forward and reverse supply chain network is

proposed. It consists of a Plant cum recovery center (PCR), distribution center (DC), disposal center (DIC), and customer sites. The PCR are hybrid facilities which can ship the product to customers directly or through DC and also able to handle the return coming from the customers.

## 3.2 Model Formulation

### 3.2.1 Objective Function

CLSC network design problem, the objective function is to minimize the total cost of CLSC network, which consist of fixed opening cost, production cost, distribution cost, transportation cost (TR), recovery cost, collection cost, disposal cost, and penalty cost for non-satisfied demand.

$$\begin{aligned} \text{Min } Z = & \text{Fixed cost} + \text{Production cost} + \text{Distribution cost} + \text{Transportation cost} \\ & + \text{Recovery cost} + \text{Collection cost} + \text{Disposal cost} \\ & + \text{Penalty cost of non - satisfied demand} \end{aligned}$$

The fixed cost include cost of opening PCR, DC, and DIC.

### Constraints

There are two types of constraints: (a) Restrictions related to capacity. (b) Restriction related to binary and non-negativity decision variables.

The various constraints involved are as follows:

- The quantity recovered at PCR should balance the recovered quantity shipped from PCR to DC and recovered quantity shipped from PCR to the customer site.
- The quantity produced at PCR should balance the sum of the quantity of new product shipped from PCR to DC and quantity of new product shipped from PCR to customer site.
- The quantity shipped to the customer sites should be greater than the demand.
- The returned products from customer site to PCR.
- Flow constraint is for DC to customer site.
- Balance of the quantity of return product.

The above modeling is for a closed-loop e-supply chain network design which is our third objective.

### Robust Optimization

The above deterministic model is reformulated to accommodate the right hand side uncertainty in the model. In general form, the deterministic linear optimization model can be written as in Eq. (1). On the above lines, to develop the robust counterpart of the proposed e-supply chain model, the demand is considered as uncertain parameter

which is assumed to vary in a specified closed bounded box. This is the robust counterpart of the e-supply chain model. The above formulation is a robust counterpart of closed-loop e-supply chain network structure which is our fourth objective. To assess the performance proposed e-supply chain model of DS and SDC under uncertainty, several numerical experiments are performed using RO counterpart and the related results are reported in next section.

## 4 Numerical Example

### 4.1 Data Generation and Problem Tests

To take the insight of varying problem size and uncertain parameters in closed-loop e-supply chain DS and SDC network design four instances of the problem with four different problem sizes are designed. Nominal data for test problem are randomly generated using the random distributions and is given in Table 1.

The following notations and indices are used in the formulation of model.

$i$ : Potential number of plants cum recovery centers (PRC)  $i = 1, \dots, I$

$j$ : Potential number of distribution center (DC)  $j = 1, \dots, J$

$k$ : Potential number of customer sites  $k = 1, \dots, K$

$l$ : Potential number of disposal center (DIC)  $l = 1, \dots, L$ .

The test problem consists of four different problem sizes and is denoted by network 1, network 2, network 3, and network 4 respectively. In order to analyze the performance of selected networks four uncertainty levels ( $\rho = 0.2, 0.4, 0.6, 0.8$ ) for each problem size is computed. The robust and deterministic models are solved under nominal data for all four network sizes. The deterministic and robust models are programmed in AIMMS 4.2 environment and solved by CPLEX 12.6.

### 4.2 Behavior of Proposed Model Under Different Levels of Uncertainty and Network Sizes

First, deterministic models are solved under nominal data. These models are solved again under uncertainty of the demand parameter for robust optimization. Four uncertainty levels ( $\rho = 0.2, 0.4, 0.6, 0.8$ ) are considered to evaluate the role of the uncertainty level and results are given in Table 2. Objective function values for deterministic and a RO model is considered as the main comparison criterion. Table 2 presents the summary of all network sizes and corresponding objective function values for all uncertainties levels. At higher uncertainty levels robust optimization approach performs better as evident from Table 2. The model shows that while designing the e-supply chain network firm can incorporate level of uncertainty from 0.4 to 0.6 with

**Table 1** The source of random generation of nominal data

Parameters	Data (uniform)	Parameters	Data
Demand of customer site $k$ ( $d_k$ )	(400, 500)	Distribution cost per unit of product at DC $j$ ( $n_j$ )	(10, 20)
Return rate of used product from customer site $k$ ( $rr_k$ )	(0.05, 0.1)	Transportation cost per unit of product from PCR $i$ to DC $j$ ( $a_{ij}$ )	(40, 60)
Production capacity of PCR $i$ in forward flow ( $pc_i$ )	(2500, 4000)	Transportation cost per unit of product from DC $j$ to customer site $k$ ( $b_{jk}$ )	(60, 80)
Distribution capacity of $j$ th DC in forward flow ( $dc_j$ )	(700, 1200)	Transportation cost per unit of product from PCR $i$ to customer site $k$ ( $e_{ik}$ )	(50, 1500)
Collection capacity of PCR $i$ in reverse flow ( $cc_i$ )	(300, 500)	Collection cost per unit of product at PCR $i$ ( $c_i$ )	(20, 50)
Disposal capacity of disposal center $l$ ( $sc_l$ )	(100, 300)	Disposal cost per unit of scrap product at DIC $l$ ( $s_l$ )	(20, 50)
Average disposal fraction ( $df$ )	(0.1, 0.2)	Recovery cost per unit of product at PCR $i$ ( $r_i$ )	(20, 50)
Fixed cost for opening PCR $i$ ( $f_i$ )	(500,000, 700,000)	Transportation cost per unit of returned product from customer site $k$ to PCR $i$ ( $p_{ki}$ )	(50, 70)
Fixed cost for opening DC centers $j$ ( $g_j$ )	(50,000, 70,000)	Transportation cost per unit of scrap product from PCR $i$ to DIC $l$ ( $q_{il}$ )	(50, 70)
Fixed cost for opening DIC $l$ ( $h_l$ )	(10,000, 20,000)	Penalty cost per unit of non-satisfied demand of customer site $k$ ( $\mu_k$ )	(2200, 3000)
Production cost per unit of product at PCR $i$ ( $m_i$ )	(1500, 2000)		

a moderate costs factor. However, the decision maker has to decide up to which level of uncertainty, the firm should target and its capability to bear the cost of robustness. The test result shows that objective function value of robust model increases with increase in network size and level of uncertainty in demand. It is so because to incorporate high level of uncertainty, the cost of robustness must be high. Figure 1 shows these trends for all network sizes.

Test result shows that firms can aim to design their network to accommodate uncertainty of  $\rho = 0.2$  with about 24% increase in cost. A common trend in Table 2 is that when uncertainty level increases, the cost of robustness drastically increases because model considered the worst cases realization of demands uncertainty.

**Table 2** Network size and corresponding objective function values, for different sets of uncertainties

Network Size	Levels of uncertainties ( $\rho$ )	Objective function values		Solution time (RO Model)		No. of constraints	No. of variables	No. of iterations	Gap (%)
		Robust	Deterministic	(Sec)					
				Model	(Sec)				
Network-1 3*5*7*2	0.2	7,372,311	5,952,414	0.45		77	176	310	0.00
	0.4	9,014,747	5,952,414	0.55*		77	176	1778*	0.00
	0.6	10,224,383	5,952,414	0.05		77	176	158	0.01
	0.8	11,498,209	5,952,414	0.02		77	72	272	0.00
Network-2 4*8*14*2	0.2	14,165,797	11,677,263	30.12		131	421	4106	0.00
	0.4	17,097,589	11,677,263	55.52*		131	421	11,036*	0.00
	0.6	19,755,537	11,677,263	31.23		131	421	5383	0.00
	0.8	23,087,306	11,677,263	31.98		131	421	7278	0.00
Network-3 6*14*22*2	0.2	22,445,176	18,055,167	726.2*		203	989	967,725*	0.03
	0.4	26,675,143	18,055,167	89.83		203	989	6274	0.00
	0.6	31,014,787	18,055,167	92.12		203	989	7514	0.00
	0.8	35,869,587	18,055,167	688.4*		203	989	1,090,654*	0.02
Network-4 8*20*28*3	0.2	29,085,690	23,412,801	58.25		264	1712	30,954	0.08
	0.4	34,727,810	23,412,801	57.77		264	1712	34,046	0.03
	0.6	40,370,735	23,412,801	69.73		264	1712	59,247	0.03
	0.8	46,377,225	23,412,801	57.97		264	1712	53,090	0.02

*Note* The gap is the relative difference between best LP Bound and Best Solution in AIMMS. The values marked with \* are exceptionally high because solver is allowed to minimize the gap and keep it < 0.10



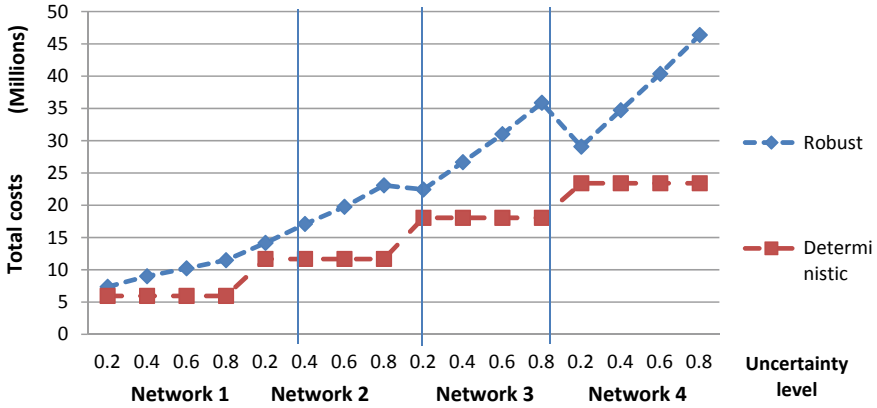


Fig. 1 Total costs for robust and deterministic model for different sets of network

## 5 Case Study

### 5.1 Supply Chain of Case Company Profile

Case company is India’s leading furniture and home products e-commerce marketplace headquartered in South-west part of India offers more than 45,000 products across categories like Furniture, Home Décor, and Housekeeping, etc. The firm has more than 1200 suppliers across India. The firm manages the entire e-commerce process for the suppliers. The company has warehouse operations in Mumbai, Delhi, Bengaluru, Jodhpur, and Kolkata while 11 fulfillment centers in various cities of India.

### 5.2 Modeling of Supply Chain of Case Company and Computations

This study efforts to develop a robust optimization based methodology to address uncertainty in CLSC network design. Optimizing the network design under uncertainty has managerial implications and improves the firm responsiveness, efficiency, and capabilities. This can be achieved more efficiently by solving a real world problem and can help practitioners in applying theoretical developments in real world cases and problems. Nominal data for test problem are randomly generated using the random distributions and is given in Table 3. Parameters are defined in column ‘P’.

**Table 3** Parameters of case study (amounts are in INR)

S. No.	$P$	Case data (uniform)	S. No.	$P$	Case data (uniform)	S. No.	$P$	Case data (uniform)
1	$d_k$	(1500, 2000)	8	$f_i$	(700,000, 900,000)	15	$e_{ik}$	(100, 1000)
2	$rr_k$	(0.1, 0.2)	9	$g_j$	(20,000, 50,000)	16	$c_i$	(40, 60)
3	$pc_i$	(10,000, 15,000)	10	$h_l$	(100,000, 200,000)	17	$s_l$	(40, 60)
4	$dc_j$	(8000, 12,000)	11	$m_i$	(2500, 6000)	18	$r_i$	(40, 60)
5	$cc_i$	(2000, 5000)	12	$n_j$	(50, 80)	19	$p_{ki}$	(150, 200)
6	$sc_l$	(500, 1000)	13	$a_{ij}$	(80, 150)	20	$q_{il}$	(150, 200)
7	$df$	(0.1, 0.2)	14	$b_{jk}$	(120, 200)	21	$\mu_k$	(4200, 6200)

### 5.3 Result and Discussion

To solve the case, 4 instances are made by keeping demand as uncertain parameters. The problem is formulated with the procedure as discussed in Sect. 3 in AIMMS 4.2 and solved by CPLEX 12.6 solver. The solution reports that the case problem has 347 constraints, 2808 variables, and 11,049 integers it. Table 4 presents the results of the case study analysis. It is visible that for the case study, demand uncertainty  $\rho = 0.2, 0.4, 0.6$  and  $0.8$  is taken into consideration. The objective function value for robust model increases for increase in uncertainty level. This increase in the objective function value for robust model is because of meeting the customer’s demand in worst case.

It can be seen from the Table that as the demand uncertainty increases, the number of MF at strategic sites for robust model increases, e.g., for demand uncertainty = 0.6 manufacturing facilities opened are P1, P2, P3, P4, P6, P7, P8 and P9 which are more in number than MF at demand uncertainty = 0.2. These strategic facilities meet the customer’s demand for worst case. As discussed above, this MF is serving two purposes, (1) major role as plant where goods are produced and (2) MF can also act as DC, which sends product to the customer sites after an order is placed by the customers by working with ES. It is depicted in the Table 4 that as the demand uncertainty increases, the number of DC’s location for robust model decreases, e.g., for demand uncertainty = 0.2, DC’s opened are DC3, DC7, DC15, DC19, and DC 21 which are more in number than DC’s at demand uncertainty = 0.8. This is because that the MF is serving purpose of DCs, thus shows a sign of decrease in number. Thus, for the case company it was observed that for uncertain parameters (demand = 0.8), opening of total 9 MF and 4 DC can accommodate the worst case of network

**Table 4** Results of the case study analysis (in INR)

S. No.	Network size	Uncertainty level	Objective function values		Time (s)	Iterations	MF open		DC open	
			Robust	Det			Det	Robust	Det	Robust
1	10*25*38*4	0.2	283,636,042	223,959,951	60.01	34,597	1,2,6,7,8	1,2,3,6,7,8	7,15,19,21	3,7,15,19,21
2		0.4	347,173,119	223,959,951	41.95	9194	1,2,6,7,8	1,2,3,6,7,8,9	7,15,19,21	3,15,19,21,22
3		0.6	414,436,799	223,959,951	60.01	40,274	1,2,6,7,8	1,2,3,4,6,7,8,9	7,15,19,21	3,19,21,22
4		0.8	489,761,638	223,959,951	43.14	8074	1,2,6,7,8	1,2,3,4,6,7,8,9	7,15,19,21	3,5,22

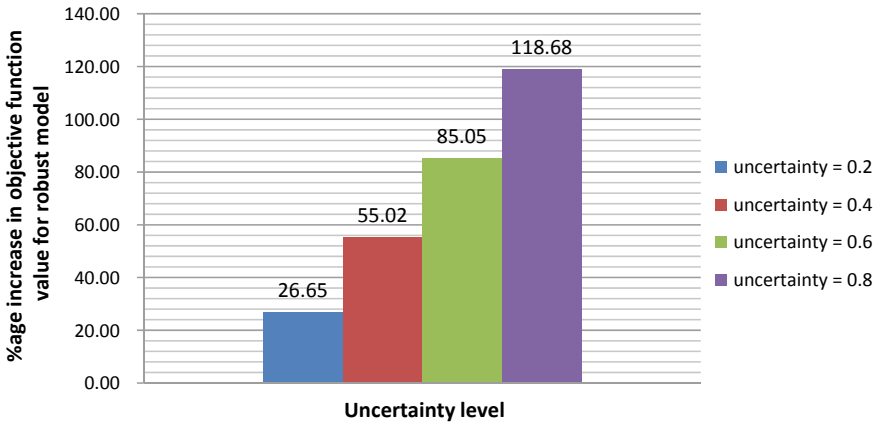


Fig. 2 % age increase in objective function value for robust model for different levels of uncertainty

design. It can be depicted from Fig. 2 that as the demand uncertainty increases, there is increase in the percentage of objective function value for robust model.

## 6 Conclusion

A close loop supply chain (CLSC) network design which consists of forward and reverse flow is carried out. The robust optimization (RO) based modeling with both direct shipping of the products and shipping through distribution center under demand uncertainty is proposed and analyzed. The proposed RO model is validated by applying it in a real-life case study. A closed-loop e-supply chain network design under uncertain demand parameters is proposed for an e-retailing (e-commerce) firm. A robust counterpart of the proposed e-supply chain closed-loop network design problem is developed. The results are presented for supply chain planning strategies for an e-supply chain of case company (furniture manufacturing firm). The proposed model can be useful for supply chain managers to decide on their supply chain design and determining the level of risk the firm can tolerate. The computational results indicate that robust model is better than the deterministic one for uncertain parameters.

In the present study, single product and single period is taken. This study can be extended to multi product, multi period, etc. The input data used for the study is for a furniture company. The study can be extended by taking data and performing modeling for other industries. Other parameters can be taken as uncertain, such as return rate, transportation cost, etc.

## References

1. DeLoach, J.W.: *Enterprise-Wide Risk Management: Strategies for Linking Risk and Opportunity*. Financial Times Prentice Hall, London (2000)
2. Norrman, A., Lindroth, R.: Categorization of supply chain risk and risk management. *Supply Chain Risk* **2**(1), 14–27 (2004)
3. Sheffi, Y., Jr, J.R.: A supply chain view of the resilient enterprise. *MIT Sloan Manage. Rev.* **47**(1), (2005)
4. Chen, J., Sohal, A.S., Prajogo, D.I.: Supply chain operational risk mitigation: a collaborative approach. *Int. J. Prod. Res.* **51**(7), 2186–2199 (2013)
5. Chopra, S., Sodhi, M.: Managing risk to avoid supply-chain breakdown. *MIT Sloan Manage. Rev.* (2012)
6. Fleischmann, M., Beullens, P., Bloemhof-Ruwaard, J.M., Wassenhove, L.N.: The impact of product recovery on logistics network design. *Prod. Oper. Manage.* **10**(2), 156–173 (2001)
7. Özceylan, E., Paksoy, T., Bektaş, T.: Modeling and optimizing the integrated problem of closed-loop supply chain network design and disassembly line balancing. *Transp. Res. Part E Logist. Transp. Rev.* **61**, 142–164 (2014)
8. Listeş, O.: A generic stochastic model for supply-and-return network design. *Comput. Oper. Res.* **34**(2), 417–442 (2007)
9. Pishvae, M.S., Jolai, F., Razmi, J.: A stochastic optimization model for integrated forward/reverse logistics network design. *J. Manuf. Syst.* **28**(4), 107–114 (2009)
10. Ramezani, M., Kimiagari, A.M., Karimi, B.: Closed-loop supply chain network design: a financial approach. *Appl. Math. Model.* **38**(15), 4099–4119 (2014)
11. Pishvae, M.S., Rabbani, M., Torabi, S.A.: A robust optimization approach to closed-loop supply chain network design under uncertainty. *Appl. Math. Model.* **35**(2), 637–649 (2011)
12. Golpîra, H.: Supply chain network design optimization with risk-averse retailer. *Int. J. Inf. Syst. Supply Chain Manage.* **10**(1), 16–28 (2017). <https://doi.org/10.4018/IJISSCM.2017010102>
13. Babazadeh, R., Sabbaghnia, A.: Optimisation of supply chain networks under uncertainty: conditional value at risk approach. *Int. J. Manag. Decis. Mak.* **17**(4), 488 (2018). <https://doi.org/10.1504/IJMDM.2018.095736>
14. Lotfi, R., Mehrjerdi, Y.Z.: A robust optimization model for sustainable and resilient closed-loop supply chain network design considering conditional value at risk. *Resilience and sustainable closed-loop supply chain*. *Numerical Algebra* (2020). <https://doi.org/10.3934/naco.2020023>
15. Mulvey, J., Vanderbei, R., Zenios, S.: Robust optimization of large-scale systems. *Oper. Res.* **43**(2), 264–281 (1995)
16. Ben-Tal, A., Nemirovski, A.: Robust solutions of linear programming problems contaminated with uncertain data. *Math. Program.* **88**(3), 411–424 (2000)

# Calculation of Filling Characteristic of Cast Al–Si Alloy



Samavedam Santhi, U. S. Jyothi, and K. Srinivasa Vadayar

## 1 Introduction

Aluminium silicon casting alloys contain strengthening and sufficient amounts of eutectic-forming elements for adequate fluidity making the metal flow through the cavities [1]. Cast Al–Si alloys have good wear resistance, and applications are pistons, ring gears and engine blocks. Foundries using casting simulation and computer-aided design technique show lower lead time and rejection rates, thereby reaching the desired internal quality of the castings [2, 3]. By appropriate combination of simulation techniques with solid modelling, the good quality and less amount of defects in the casting can be achieved.

The filling is influenced by metallostatic equilibrium among the established metal pressure and surface tension of molten alloy. Faster filling guides to turbulence are followed by mould erosion, air aspiration and inclusions. In case of slow filling leads to cold shuts and misruns, the control provided by low-pressure filling makes sure of the melt rates necessary for maintaining low turbulence resulting in quality castings [4–6]. Engler and Ellerbrok have designed a pin test piece for the determination of filling [7]. The key variables influencing filling are alloy composition, casting design, heat transfer, pouring and gating issues [8, 9].

---

S. Santhi (✉)

Department of Metallurgical and Materials Engineering, Mahatma Gandhi Institute of Technology, Hyderabad, India

U. S. Jyothi

Gokaraju Rangaraju Institute of Engineering and Technology, Hyderabad, India

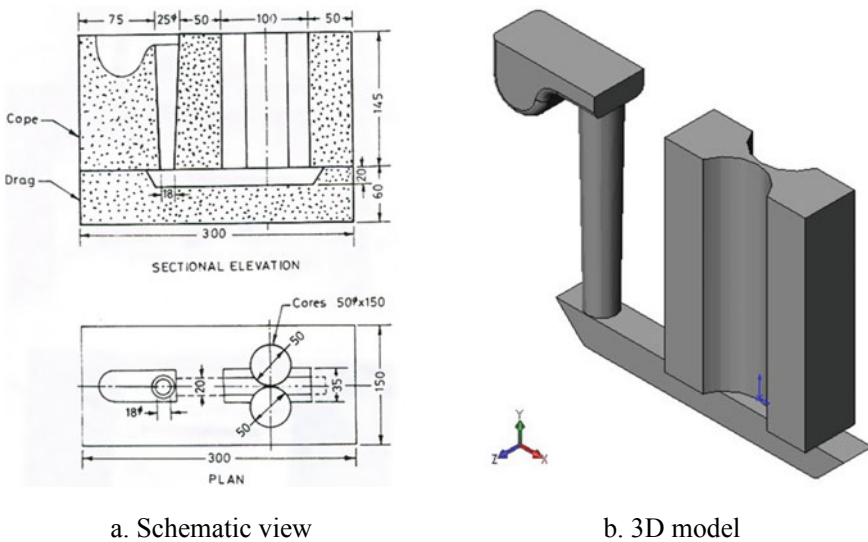
K. Srinivasa Vadayar

Jawaharlal Nehru Technological University College of Engineering Hyderabad, Hyderabad, India

## 2 Experimental Plan

US 413 (11Si–0.65Fe–0.15Cu–0.55Mn–0.1 Mg–0.1Ni–0.15Zn–0.1Pb–0.2Ti–Remainder Al) cast aluminium-silicon eutectic alloy is considered for the present study. Supplementary temperature of pouring increases the fluid life of the liquid metal [1, 6, 9]; hence, superheat temperature with 20 °C of superheat temperature is considered. The schematic view and solid model for the present study as developed by Engler and Ellerbrok are given in Fig. 1. Fineness of the sand improves surface finish and strength of the casting, so American Foundry Society (AFS) sand fineness numbers 25 and 48 are considered. Total 4 experiments are conducted for casting simulation as given in Table 1.

Casting simulations are conducted using virtual casting software module 1 [10], which is using FDM. 3D solid model, physical properties and boundary conditions are considered as input data for the simulation studies. The physical properties and heat transfer coefficient (HTC) between mould and metal are given in Table 2. For mould, the initial temperature considered is room temperature. Fraction of solid and



**Fig. 1** Filling characteristic

**Table 1** List of experiments for characterization of filling ability of US 413 alloy

Exp. No.	AFS number	Superheat temperature (°C)
1	25	T + 20
2	25	T
3	40	T + 20
4	40	T

**Table 2** Physical properties of US 413 and silica sand for simulation studies [11, 12]

S. No.	Parameter	US 413	Silica Sand
1	Thermal conductivity (W/mm K)	0.121338	$90.27 \times 10^{-5}$
2	Specific heat (J/kg K)	1170	1076.076
3	Density (kg/m <sup>3</sup> )	2650	1520
4	Liquidus temperature (K)	847.15	–
5	Freezing range (K)	303.15	–
6	Latent heat of fusion (J/kg)	389.112	–
7	HTC (W/m <sup>2</sup> K)	0.0025	–

cooling rate of the alloy is the results of the simulation studies. The exit solid fraction is the total volume per cent of solid at which the solver exits and exit solid fraction is 1 for the US 413 alloy (short freezing range alloy). Schematic diagram and 3D solid model of the filling characteristic are given in Fig. 1a and b.

### 3 Results and Discussion

The value of filling is measured at every 5 mm elevation of molten alloy column above the filling point and is calculated as the diameter of meniscus of molten alloy straight away at the time of solidification in the casting. The hot alloy entered into the sprue raises in the mould cavity and fills it between the two cylindrical cores having a line contact at the centre, but solidifies before filling up the complete casting as shown in Fig. 2. The value of the filling is calculated from the opposite of the diameter of curvature of the border tip of the fin.

The diameter at the tip of the fin gives the meniscus diameter of the molten alloy at the time of solidification as represented in Fig. 3 for one particular pressure head.

Equation (1) uses for calculating the diameter of the tip of the border which is given below.

As per Fig. 3:

$$R^2 + (r + x)^2 = (r + R)^2 \tag{1}$$

so  $1/d = (R - x)/x^2$ .

$R$  = core radius, mm,  $r$  = meniscus radius ( $2r = d$ ), mm.

$2x$  = distance connecting borders, mm,  $1/d$  = filling, 1/mm.

Post-processing shows the distance connecting two fins at different locations of the test piece in 2D which is difficult to measure as shown in Fig. 2. So, 3D model of the images is generated using Solidworks as shown in Fig. 4.

The large tolerance level of 0.1 mm which is characteristic in foundry process [13] is considered for the present study as shown in Fig. 4, which shows the distance between two fins ( $2x$ ) and  $2 \times$  for 4 experiments are given in Table 3.



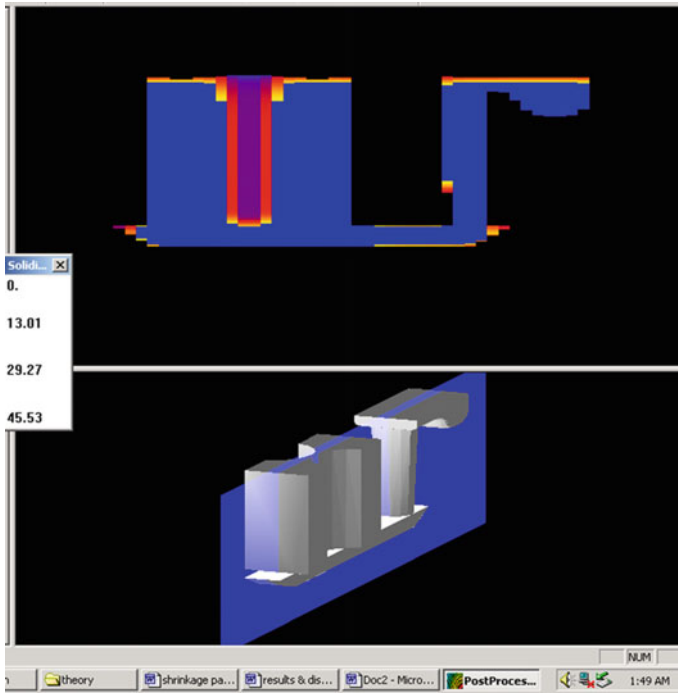


Fig. 2 Test casting obtained for simulation

The filling values are found for every 5 mm augmentation using Eq. (1) and are given in Table 3.

Higher the metallostatic pressure, higher is the velocity of the liquid metal and so higher filling ability.

### 3.1 Influence of Pressure Head

Figure 5 shows the influence of pressure head on filling of present alloy for simulation studies. The metallostatic force of molten alloy has been raised with rise in pressure head, results in smooth filling of finer contours among the cylindrical cores and hence reduces the fin borders and increases the filling values.

Filling characteristic in solidifying region is controlled by pressure head, whereas the density and surface tension are ignored and  $180^\circ$  angle of contact is assumed. Superior pressure head gives in higher filling ability because the metal has to be in contact with larger area in order to penetrate into cavity which promotes faster solidification [6, 13].

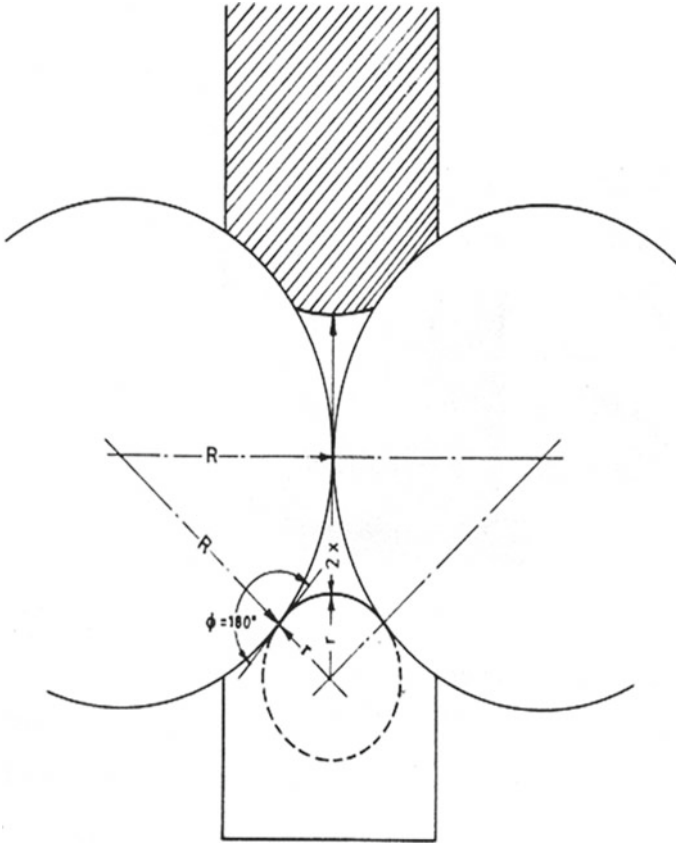
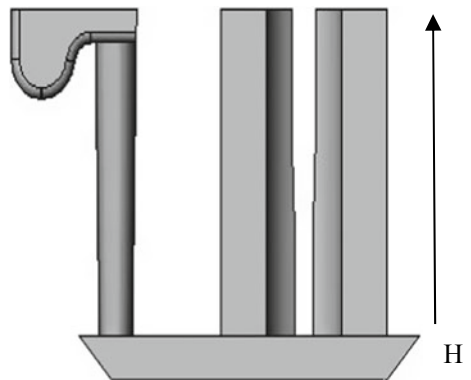


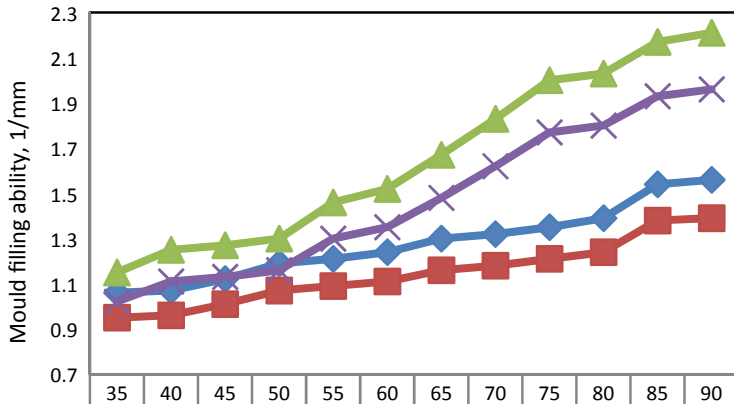
Fig. 3 Measurement of filling value

Fig. 4 Exp no. 3



**Table 3** Distance between the fin borders (2x) and filling value for US 413

H (mm)	Distance between the fin borders, 2x (mm)				Filling value, 1/mm			
	1	2	3	4	1	2	3	4
35	9.32	8.88	9.64	9.16	1.06	0.95	1.15	1.02
40	9.35	8.90	10.01	9.51	1.07	0.96	1.25	1.11
45	9.54	9.08	10.10	9.59	1.12	1.01	1.27	1.13
50	9.79	9.32	10.19	9.68	1.19	1.07	1.30	1.16
55	9.88	9.42	10.73	10.2	1.21	1.09	1.46	1.30
60	9.98	9.51	10.92	10.37	1.24	1.11	1.52	1.35
65	10.17	9.69	11.37	10.81	1.30	1.16	1.67	1.48
70	10.27	9.78	11.83	11.23	1.32	1.18	1.83	1.62
75	10.36	9.87	12.28	11.67	1.35	1.21	2.00	1.77
80	10.49	9.99	12.37	11.75	1.39	1.24	2.03	1.80
85	10.98	10.46	12.74	12.10	1.54	1.38	2.17	1.93
90	11.03	10.51	12.83	12.18	1.56	1.39	2.21	1.96

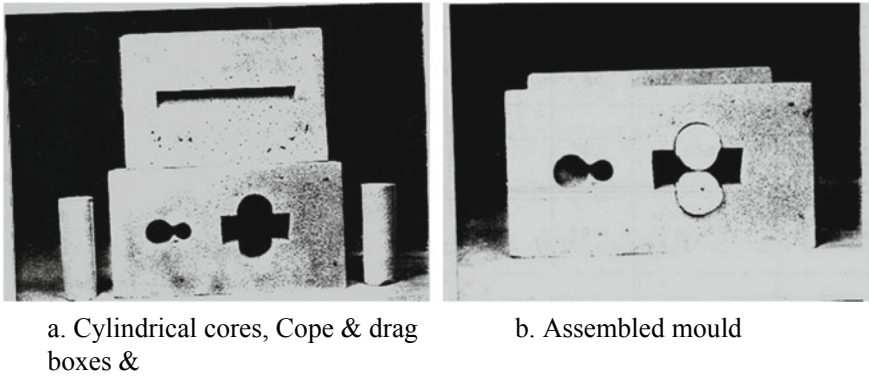


	35	40	45	50	55	60	65	70	75	80	85	90
US413T+2025	1.06	1.07	1.12	1.19	1.21	1.24	1.3	1.32	1.35	1.39	1.54	1.56
US413T25	0.95	0.96	1.01	1.07	1.09	1.11	1.16	1.18	1.21	1.24	1.38	1.39
US413T+2040	1.15	1.25	1.27	1.3	1.46	1.52	1.67	1.83	2	2.03	2.17	2.21
US413T40	1.02	1.11	1.13	1.16	1.3	1.35	1.48	1.62	1.77	1.8	1.93	1.96

**Fig. 5** Influence of pressure head on filling characteristic

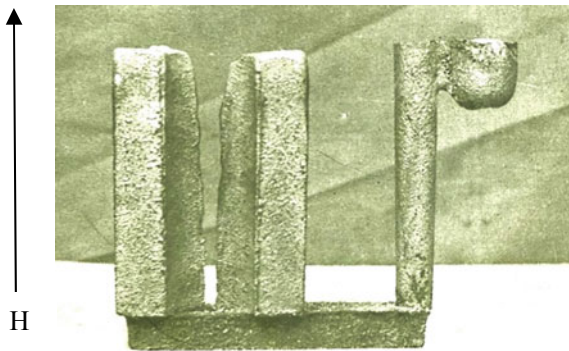
### 4 Validation Experiments

The validation experiments are carried out to authenticate the simulation results, and the experiments are 1 and 3 of Table 1. Tooling and assembled mould for the



**Fig. 6** Tooling and assembled mould for the experiments

**Fig. 7** Solidified casting for validation studies



experiments are in Fig. 6. Bentonite and water considered to prepare green sand mould are 6% and 7% of silica sand weight, respectively. The mould hardness is in the range of 76 on B scale for green sand. 20 kg electric resistance furnace with mild steel crucible is used for melting of alloy. With the help of thermocouple, the temperature is monitored and the molten alloy is tapped into a ladle. The pouring height is maintained to follow laminar flow. The solidified mould filling ability is shown in Fig. 7.

### 4.1 Results

Same methodology as that of simulation has been taken up in calculating the values (Fig. 3 and Eq. 1). With the help of height gauge, the height at every 5 mm interval (pressure head) is marked on the solidified castings. Vernier micrometre is used to measure the distance between the fin borders  $2 \times$  and is given in Table 4.

**Table 4** Distance between the fin edges ( $2x$ ) and filling ability for US 413 for validation studies

H (mm)	Distance between the fin edges for sim run order, $2x$ (mm)		Mould filling ability, 1/mm	
	1	2	1	2
35	9.75	10.6	1.18	1.42
40	9.79	11	1.19	1.55
45	9.98	11.1	1.24	1.58
50	10.25	11.2	1.32	1.61
55	10.35	11.8	1.35	1.82
60	10.45	12	1.38	1.89
65	10.65	12.5	1.44	2.08
70	10.75	13	1.47	2.28
75	10.85	13.5	1.50	2.49
80	10.98	13.6	1.54	2.54
85	11.5	14	1.71	2.72
90	11.55	14.1	1.73	2.76

Using Eq. (1), the filling characteristic is calculated for every 5 mm pressure head which is given in Table 4.

## 5 Association of Simulation and Experimental Studies

The results of simulation for filling ability value are in agreement with validation experiments (shown in Fig. 8), though minor variation is observed. Throughout solidification the cavity of mould always varies the properties of liquid and solid phases due to interactions between metal-mould, metal-ambient and mould-ambient. Accurately predicting the change in properties during solidification is very difficult in virtual environment (casting simulations). Precise simulation outcomes need all physical properties to be set carefully as of the real casting material and process conditions. The development of an air gap and the corresponding decrease in heat transfer is difficult to simulate and limits the accuracy. Interfacial heat transfer, which can vary remarkably with air gap formation, is important in sand moulds.

## 6 Conclusions

Quantification of filling characteristic obtained from simulation is realized with the help of 3D CAD. The parameters providing optimum filling ability increase in pressure head, sand fineness number 40 and superheat  $T + 20$  °C (for both simulation

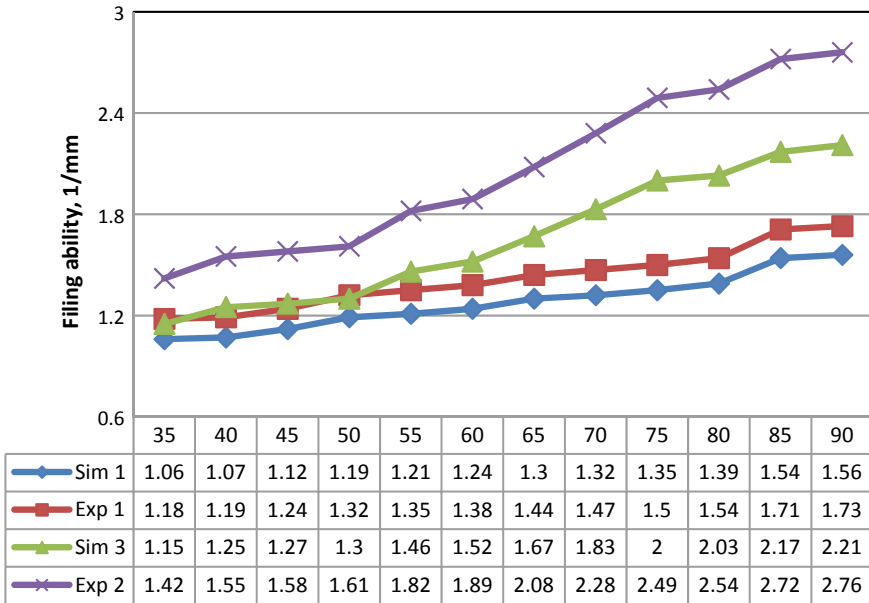


Fig. 8 Simulation results are in agreement with validation experiments

and validation experiments). The simulation results are in agreement with validation experiments with minor variations.

**Funding/Acknowledgements** The authors thank JNTUH TEQIP-III for supporting this R&D work.

## References

- Campbell, J., Harding, R.A.: TALAT Lecture 3206, The Feeding of Castings, IRC in Materials. The University of Birmingham, EAA—European Aluminium Association (1994)
- Joshi, D., Ravi, B.: 10 year survey of computer applications in Indian foundry industry. *Indian Foundry J.* **56**(1), 23–30 (2010)
- Lee, J.Y., Jeong, W.J., Yim, Y.H., Lee, J.H.: Application of computer simulation on large size steam turbine casing. *Indian Foundry J.* **56**(1), 31–34 (2010)
- Rasmussen, N.W.: New filling/feeding process produces vertically-parted aluminum green sand castings. *Modern Casting* (April 2000)
- Cantor, B.: Solidification and casting. Department of Materials, University of Oxford. UK, MJ Goringe, School of Mechanical and Materials, Engineering, University of Surrey, UK (2011)
- Sundarrajan, S., Roshan, H.Md.: Studies on mould filling ability characteristics of Mg–Al Alloys, pp. 607–616. *Transactions of American Foundrymen Society* (1989)
- Engler, S., Ellerbok, R.: Ueber des form full engsvermoegen, p. 49. *Giess, Forsch* (1974)
- Cooksey, C.J., Kondic, V., Wilcock, J.: The casting fluidity of some foundry alloys. *Br. Foundryman* **52**, 381 (1959)

9. Campbell, J., Harding, R.A.: TALAT Lecture 3205, The Fluidity of Molten Metals, prepared by IRC in Materials, The University of Birmingham (1994)
10. User manual Virtual casting developed by Regional Research Laboratory, Thrivandrum (2006)
11. Trovant, M.: A Boundary Condition Coupling Strategy for the Modeling of Metal Casting Processes. National Library of Canada, Acquisitions and Bibliographic Services (1998)
12. Cellini, G.S., Tomesani, L.: Metal head-dependent HTC in sand casting simulation of Aluminium alloys. *J. Achievements Mater. Manuf. Eng.* **29**(1), 47–52 (2008)
13. Santhi, S.: Modeling and simulation of flow and fill characteristics of non-ferrous alloys. Ph.D. Thesis submitted to JNTUH, Hyderabad (August 2012)

# Review on Materials and Method Used to Develop Antimicrobial Coatings in Medical and Food Processing Industry



Vinod Babu Chintada, Sasidhar Gurugubelli, and Sudhakar Uppada

## 1 Introduction

Many diseases spread due to the bacteria and virus infections and which causes a lot of personal loss. Yearly, throughout the world influenza virus causes hundreds of thousands of deaths. Contact with microbes contaminated surface was the main reason to catch infections. Epidemiological studies confirm that hand contact with contaminated surfaces is the most common route for the transmission of infection [1, 2]. Pathogenic virus can survive on surfaces for many hours and days. Therefore, surface disinfection is important to prevent the spreading of infectious diseases. Antimicrobial coatings play a crucial role to prevent the spreading of diseases and infections in public area. Surface coating technique is extensively used nowadays to provide antimicrobial surface [3–5]. To enhance the antimicrobial properties of the various surfaces of medical devices such as wound dressings, personal protective equipments, separation membranes, and food packages, different types of surface coating methods and materials are available [6, 7]. Metals like copper, silver, zinc, and gold are having good antibacterial properties for long time. In these metals, copper and silver most effectively inactivate the MRAS and influenza virus like swine flu [8, 9]. Most of the researches are focused on influence of copper and silver coatings on antimicrobial properties of the surfaces. Few researches also focused on anti-viral properties of the copper powder and silver nanoparticles. Various deposition methods like PVD, CVD, electroless deposition, electrodeposition, and thermal spraying are used to depositing all the above metals to improve the antimicrobial surface properties. Therefore, the present literature summary provides information about various coating materials and methods with good antimicrobial properties, which can inactivate the various types of bacteria and viruses in a short period of time.

---

V. B. Chintada (✉) · S. Gurugubelli · S. Uppada  
Department of Mechanical Engineering, GMRIT, Rajam, Andhra Pradesh 532127, India



## 2 Results and Discussions

### 2.1 Antimicrobial Coating Materials and Methods

Copper and silver are used as coating materials for contact killing of virus on touch surface due to the good antimicrobial properties [10, 11]. Nano-sized Cu particles show high antimicrobial resistance against gram-positive *Staphylococcus aureus* (*S. aureus*) and gram-negative *Escherichia coli* (*E. coli*). Interaction of cell membrane with synthesized Cu nanoparticles is high due to its larger surface area, which results in bacteria death [12]. Compared to conventional copper coating, nano-copper coating is more efficient to contact killing of influenza A virus. Higher crystallinity in nano-copper coating increases the volume of the grain boundaries, which leads to discharge of more copper ions from loosely bonded atoms in the crystal-lite boundary [13]. Augustin et al. [14] tried electrodeposited copper coating on aluminum surface and evaluated the antibacterial properties of the deposit against *Escherichia coli* bacteria. Antimicrobial ability of the coating was proven by the reduction of 94% of *E. coli* cells on copper-coated surface after 6 h of contact. Compared with bulk copper, increase in electrodeposited coating surface area due to increase in crystallinity of the deposit results in better anti-bacterial properties [15]. Negatively charged copper nanoparticles offer good antibacterial resistance against gram-positive bacteria. Therefore, polyelectrolyte–copper nanocomposite coatings effectively reduce the *staphylococcus aureus* bacteria [16]. Reinforcement of titanium dioxide particles into the copper composite coating effectively reduces the *S. aureus* and *E. coli* bacteria strain during 24 h of period [17]. The presence of Cu ions in electrodeposited Cu and Cu-SiC coatings damages the bacterial cell membrane, which result in better antimicrobial resistance against *Escherichia coli* and *Bacillus subtilis* pathogens [18]. Influences of various surface coating on antimicrobial properties of the different substrates are presented in Table 1.

Reinforcement of silver nanoparticles into hybrid polymer coatings inhibits the *staphylococcus aureus* bacteria activity around 99%. [14] Investigated the antiviral behavior of the hybrid coating contains silver, zinc, and copper. Results confirm that the hybrid coating reduces the 98–100% HIV-1 titers after 120 min exposure. After 240 min of exposure to dengue, herpes simplex and influenza virus titers are reduced by 97%, 100%, and 77%, respectively. On textile fabric copper, silver, and gold and its mixture of coatings developed by photochemical method effectively inhibition the *Escherichia coli* and *staphylococcus aureus* bacteria activity. Deposited coatings anti-bacteria activity ability decrease in the following order: silver, copper + silver, copper + silver + gold, copper + gold, gold + silver, copper, gold [19]. PDMS coating developed by solution blow spraying method offers good antimicrobial resistance against *S. aureus* and *E. coli* bacteria. Reinforcement of silver nano-powder at the outer surface of the PDMS coating enhances its antimicrobial resistance nearly 22 times [20].

Pradhaban et al. [21] found that electrodeposited  $ZrO_2$ -Ag coating offers good anti-bacterial properties as compared to  $ZrO_2$  coating. Silver ions released from

**Table 1** Antimicrobial coatings on various substrate materials

Surface	Microbe	Coating	Coating results	Reference
Stainless steel	E. coli and S. aureus	Cu-TiO <sub>2</sub> composite coatings	80 and 40% E. coli and S. aureus bacteria reduction is observed	[17]
Stainless steel	E. coli and S. aureus	ZrO <sub>2</sub> and ZrO <sub>2</sub> -Ag coating	Antibacterial ability of the ZrO <sub>2</sub> -Ag coating is higher than ZrO <sub>2</sub> coating	[21]
Stainless steel	P. fluorescens, Cobetia and Vibrio	Electroless Ni-P-TiO <sub>2</sub> coating	Reduces the bacterial adhesion up to 75%	[22]
Stainless steel	E. coli	Electroless Ag-PTFE coating	Reduces the E. coli adhesion 94–98%	[23]
Stainless steel	E. coli	Electroless Ni-B coating	Less E. coli adhesion to the coating surface compared with the bare substrate	[24]
Al surface	Influenza A virus	Conventional and nano-copper coating	99.3 and 97.7% virus reduction observed in both the coatings	[13]
Al surface	E. coli	Copper coating	Reduces the E. coli bacteria by 94%	[14]
Ti substrate	E. coli and S. aureus	ZrO <sub>2</sub> -Ag coatings	Shows good antibacterial effect	[7]
Mg alloy	E. coli and S. aureus	Silver coating	87.3 and 74.6% E. coli and S. aureus bacteria reduction is observed	[25]
Textile material	E. coli and S. aureus	Silver, Copper, and Gold coating	Antibacterial ability of the coating follows the following order silver > Copper > gold coating	[19]
Blended fabric	E. coli and S. aureus	Cu Coating	Coating having excellent antibacterial properties against both the bacteria	[26]
Silk fabric	E. coli and S. aureus	Electroless Ag coating	99.98 and 99.83% anti-bacterial efficiency is observed	[27]

the coating surface bind with bacterial cell surface proteins and create imbalanced membrane diffusion in bacteria, which kills the bacteria. Copper-coated fabrics offer good antibacterial properties against E. coli and S. aureus bacteria [26]. Silver nanoparticles inhibit the Klebsiella pneumonia, Staphylococcus aureus, Pseudomonas aeruginosa, and Escherichia coli bacterial growth. Compared to zinc oxide quantum dots, the addition of acetic acid to silver nano-powder is increased the

release of Ag<sup>+</sup> ions rate, which results in increase in anti-bacterial properties of the Ag nano-powder [28]. Silver nanoparticles reinforced hybrid polymer coatings offer staphylococcus aureus bacteria inhibition capacity which is around 99%. In the presence of moisture, nano-sized silver releases the silver ions, which kills the bacteria [29]. Ag coating offers good anti-bacterial property against *S. aureus* with good adhesion strength. The number of viable bacterial on substrate reduces from  $2.44 \times 10^6$  to 10 cfu/mL after coating, which confirms that the electroless Ag coating offers good anti-bacterial properties [30]. Synergistic actions of both titania and ZnO results in good antimicrobial properties of the nano-ZnO reinforced titania coating [31].

Bacteria adhesion to the touch surface can be effectively minimized by electroless Ni–P coating. Bacteria adhesion rate of the Ni–P coatings further effectively reduced by the co-deposition of TiO<sub>2</sub> and ZnO nanoparticles into the nickel matrix. Increase in electron donor surface energy of the coating by the co-deposition of nanoparticles decreases the number of bacteria adhered to the surface [22, 32]. Antibacterial resistance of the equipments used in medical field is enhanced by hybrid nanocomposite ZnO coating developed by using sputtering technique. Composite coating antimicrobial resistance against *Pseudomonas aeruginosa* and *Staphylococcus aureus* bacteria effectively enhances by the reinforcement of carbon and copper into the coating matrix. Antimicrobial resistance of the carbon co-deposited coating is nearly equal to copper-doped hybrid ZnO coating [33]. *Staphylococcus aureus* bacteria are reduced to 99.5% by using electrospayed ZnO coating [34]. Additionally, TiNi nanoparticles into the electroless Ni–P coating on steel surface reduce the cell viability of *E. coli* bacteria by 73%. Higher surface area of the TiNi nanoparticles efficiently penetrated into the cell walls of the bacteria causes cellular components alteration, which results in cell death [35]. Co-deposition of PTFE and TiO<sub>2</sub> particles into the electroless Ag coating reduces the adhesion of *E. coli* bacteria to 94% and 54%, respectively, [27, 36]. 99.98 and 99.83% anti-bacterial efficiency observed for the electroless Ag-coated silk fabrics against *E. coli* and *S. aureus* bacteria [27]. Reduction in active colony ratio of *E. coli* and *S. aureus* bacteria are 87.3% and 74.6%, respectively, which prove that the silver coating enhances the anti-bacterial properties of the Mg alloy [25].

Formation of superoxide radicals by selenium (Se) ions in selenium coatings effectively reduces the bacterial growth on the touch surface. Selenium ions released from the selenium coatings causing death to the staphylococcus aureus bacteria by disrupting the cell walls and damaging the structure. Multilayer Cu/Ni coatings having higher bacterial inhibition capacity as compared to bilayer Cu/Ni coatings. Higher surface area of Cu particles in multilayer coating effectively reduces the number of bacteria on the surface [37]. Bülbül et al. [38] Developed anti-bacterial electroless Ni–B coatings on AISI 316L stainless steel. Less bacterial adhesion of the Ni–B coating as compared to the substrate surface confirms its anti-bacterial properties.

Nowadays challenging task in food industry is reducing the microbial pathogens from the food contact surface. Antimicrobial coatings on food contact surface can increase the self-life of the food products and reduce the food wastage [24].

Food safety and preservation field's antimicrobial polymer coating offers good self-sanitization resistance [39]. Edible coating formed from the micro-emulsion appreciably diminishes the risk of food-borne diseases. Edible coating reduces the population of *Escherichia coli* and *Salmonella* pathogens considerably in the food industry [40].

### 3 Conclusions

Variety of surface coating methods and materials are used to improve the antimicrobial properties of the touch surfaces which are explained in detail in the present study, and the following conclusions are drawn based on the literature.

- Copper and silver are extensively used as antimicrobial coating materials due to their higher germ-killing ability in short period of time
- Virus inactivating potential of copper composite coating enhanced by the co-deposition of nano-sized ZnO, Ag, TiO<sub>2</sub> particles into the copper matrix.
- In the medical field developed Cu and Ag composite coating can be deposited on equipments fabricated by using fabrics, plastics, and metals to reduce the adhesion of the virus
- Food processing industry development of antimicrobial coating can reduce the wastage of food and increase the self-life of the food by killing the food spoiling pathogens.

### References

1. Guo, L., Yuan, W., Lu, Z., Li, C.M.: Polymer/nanosilver composite coatings for antibacterial applications. *Colloids Surf., A* **439**, 69–83 (2013)
2. Nakamura, S., Sato, M., Sato, Y., Ando, N., Takayama, T., Fujita, M., Ishihara, M.: Synthesis and application of silver nanoparticles (Ag NPs) for the prevention of infection in healthcare workers. *Int. J. Mol. Sci.* **20**(15), 3620 (2019)
3. Chouirfa, H., Bouloussa, H., Migonney, V., Falentin-Daudré, C.: Review of titanium surface modification techniques and coatings for antibacterial applications. *Acta Biomater.* **83**, 37–54 (2019)
4. Raghupathy, Y., Natarajan, K.A., Srivastava, C.: Microstructure, electrochemical behaviour and bio-fouling of electrodeposited nickel matrix-silver nanoparticles composite coatings on copper. *Surf. Coat. Technol.* **328**, 266–275 (2017)
5. Terzioglu, F., Grethe, T., Both, C., Joßen, A., Mahltig, B., Rabe, M.: State of the art and future prospects for textile finishing. *Handb. Antimicrob. Coat.* 123 (2017)
6. Suryaprabha, T., Sethuraman, M.G.: Fabrication of copper-based superhydrophobic self-cleaning antibacterial coating over cotton fabric. *Cellulose* **24**(1), 395–407 (2017)
7. Alagarsamy, K., Vishwakarma, V., Kaliaraj, G.S., Vasantha, N.C., Samuel, S.J.R.: Biological adhesion and electrochemical behavior of Ag-ZrO<sub>2</sub> bioceramic coatings for biomedical applications. *J. Adhes. Sci. Technol.* **34**(4), 349–368 (2020)

8. Mei, L., Wang, J., Wang, X., Yang, C: Antimicrobial activity of Ag surfaces sputtered by magnetron sputtering. *Mater. Res. Innov.* **18**(S4), 875 (2014)
9. Shivananda, C.S., Madhu Kumar, R., Narayana, B., Byrappa, K., Renu, P., Wang, Y., Sangappa, Y.: Preparation and characterisation of silk fibroin–silver nanoparticles (SF–AgNPs) composite films. *Mater. Res. Innov.* **21**(4), 210–214 (2017)
10. Li, Y., Pi, Q.M., You, H.H., Li, J.Q., Wang, P.C., Yang, X., Wu, Y.: A smart multi-functional coating based on anti-pathogen micelles tethered with copper nanoparticles via a biosynthesis method using l-vitamin C. *RSC Adv.* **8**(33), 18272–18283 (2018)
11. Feng, Q.L., Cui, F.Z., Kim, T.N., Kim, J.W.: Ag-substituted hydroxyapatite coatings with both antimicrobial effects and biocompatibility. *J. Mater. Sci. Lett.* **18**(7), 559–561 (1999)
12. Balela, M.D.L., Amores, K.L.S.: Electroless deposition of copper nanoparticle for antimicrobial coating. *Mater. Chem. Phys.* **225**, 393–398 (2019)
13. Sundberg, K., Champagne, V., McNally, B., Helfritsch, D., Sisson, R.: Effectiveness of nanomaterial copper cold spray surfaces on inactivation of influenza A virus. *J. Biotechnol. Biomater.* **5**(4), 1 (2015)
14. Hodek, J., Zajícová, V., Lovětinská-Šlamborová, I., Stibor, I., Müllerová, J., Weber, J.: Protective hybrid coating containing silver, copper and zinc cations effective against human immunodeficiency virus and other enveloped viruses. *BMC Microbiol.* **16**(1), 1–12 (2016)
15. Augustin, A., Huilgol, P., Udupa, K.R., Bhat, U.: Effect of current density during electrodeposition on microstructure and hardness of textured Cu coating in the application of antimicrobial Al touch surface. *J. Mech. Behav. Biomed. Mater.* **63**, 352–360 (2016)
16. Kruk, T., Gołda-Cępa, M., Szczepanowicz, K., Szyk-Warszyńska, L., Brzychczy-Włoch, M., Kotarba, A., Warszyński, P.: Nanocomposite multifunctional polyelectrolyte thin films with copper nanoparticles as the antimicrobial coatings. *Colloids Surf., B* **181**, 112–118 (2019)
17. Wrona, A., Bilewska, K., Lis, M., Kamińska, M., Olszewski, T., Pajzderski, P., Kamysz, W.: Antimicrobial properties of protective coatings produced by plasma spraying technique. *Surf. Coat. Technol.* **318**, 332–340 (2017)
18. Banthia, S., Hazra, C., Sen, R., Das, S., Das, K.: Electrodeposited functionally graded coating inhibits Gram-positive and Gram-negative bacteria by a lipid peroxidation mediated membrane damage mechanism. *Mater. Sci. Eng. C* **102**, 623–633 (2019)
19. Abdurazova, P.A., Nazarbek, U.B., Bolysbek, A.A., Sarypbekova, N.K., Kenzhibayeva, G.S., Kambarova, G.A., Prokopovich, P.: Preparation of photochemical coatings of metal films (copper, silver and gold) on dielectric surfaces and studying their antimicrobial properties. *Colloids Surf., A* **532**, 63–69 (2017)
20. Ferreira, T.P., Nepomuceno, N.C., Medeiros, E.L., Medeiros, E.S., Sampaio, F.C., Oliveira, J.E., Santos, A.: S: Antimicrobial coatings based on poly (dimethyl siloxane) and silver nanoparticles by solution blow spraying. *Prog. Org. Coat.* **133**, 19–26 (2019)
21. Pradhban, G., Kaliaraj, G.S., Vishwakarma, V.: Antibacterial effects of silver–zirconia composite coatings using pulsed laser deposition onto 316L SS for bio implants. *Prog. Biomater.* **3**(2–4), 123–130 (2014)
22. Zhao, Q., Liu, C., Su, X., Zhang, S., Song, W., Wang, S., Gong, W.: Antibacterial characteristics of electroless plating Ni–P–TiO<sub>2</sub> coatings. *Appl. Surf. Sci.* **274**, 101–104 (2013)
23. Zhao, Q., Liu, Y., Wang, C.: Development and evaluation of electroless Ag-PTFE composite coatings with anti-microbial and anti-corrosion properties. *Appl. Surf. Sci.* **252**(5), 1620–1627 (2005)
24. Manfredi, M., Fantin, V., Vignali, G., Gavara, R.: Environmental assessment of antimicrobial coatings for packaged fresh milk. *J. Cleaner Prod.* **95**, 291–300 (2015)
25. Aktug, S.L., Durdu, S., Aktas, S., Yalcin, E., Usta, M.: Surface and in vitro properties of Ag-deposited antibacterial and bioactive coatings on AZ31 Mg alloy. *Surf. Coat. Technol.* **375**, 46–53 (2019)
26. Rani, K.V., Sarma, B., Sarma, A.: Plasma sputtering process of copper on polyester/silk blended fabrics for preparation of multifunctional properties. *Vacuum* **146**, 206–215 (2017)
27. Yu, D., Kang, G., Tian, W., Lin, L., Wang, W.: Preparation of conductive silk fabric with antibacterial properties by electroless silver plating. *Appl. Surf. Sci.* **357**, 1157–1162 (2015)

28. Sedira, S., Ayachi, A.A., Lakehal, S., Fateh, M., Achour, S.: Silver nanoparticles in combination with acetic acid and zinc oxide quantum dots for antibacterial activities improvement—A comparative study. *Appl. Surf. Sci.* **311**, 659–665 (2014)
29. Guran, C., Pica, A., Ficai, D., Ficai, A., Comanescu, C.: Antimicrobial coatings-obtaining and characterization. *Bull. Mater. Sci.* **36**(2), 183–188 (2013)
30. Li, W., Chen, Y., Wu, S., Zhang, J., Wang, H., Zeng, D., Xie, C.: Preparing high-adhesion silver coating on APTMS modified polyethylene with excellent anti-bacterial performance. *Appl. Surf. Sci.* **436**, 117–124 (2018)
31. Shibli, S.M.A., Remya, R., Chinchu, K.S.: Nano-ZnO incorporated titania composite coating for orthodontic applications. *Mater. Res. Innov.* **16**(3), 186–197.
32. Sharifalhosseini, Z., Entezari, M.H., Jalal, R.: Evaluation of antibacterial activity of anticorrosive electroless Ni–P coating against *Escherichia coli* and its enhancement by deposition of sonosynthesized ZnO nanoparticles. *Surf. Coat. Technol.* **266**, 160–166 (2015)
33. Piedade, A.P., Pinho, A.C., Branco, R., Morais, P.V.: Evaluation of antimicrobial activity of ZnO based nanocomposites for the coating of non-critical equipment in medical-care facilities. *Appl. Surf. Sci.* **513**, 145818 (2020)
34. Valenzuela, L., Iglesias, A., Faraldos, M., Bahamonde, A., Rosal, R.: Antimicrobial surfaces with self-cleaning properties functionalized by photocatalytic ZnO electro sprayed coatings. *J. Hazard. Mater.* **369**, 665–673 (2019)
35. Fayyad, E.M., Hassan, M.K., Rasool, K., Mahmoud, K.A., Mohamed, A.M., Jarjoura, G., Abdullah, A.: M: Novel electroless deposited corrosion—resistant and anti-bacterial NiP–TiNi nanocomposite coatings. *Surf. Coat. Technol.* **369**, 323–333 (2019)
36. Liu, C., Geng, L., Yu, Y., Zhang, Y., Zhao, B., Zhao, Q.: Mechanisms of the enhanced antibacterial effect of Ag-TiO<sub>2</sub> coatings. *Biofouling* **34**(2), 190–199 (2018)
37. Saranya, K., Kalaiyaran, M., Rajendran, N.: Selenium conversion coating on AZ31 Mg alloy: a solution for improved corrosion rate and enhanced bio-adaptability. *Surf. Coat. Technol.* **378**, 124902 (2019)
38. Bülbül, F., Bülbül, L.E.: Fabrication of antibacterial and hydrophilic electroless Ni–B coating on 316L stainless steel. *Appl. Phys. A* **122**(1), 25 (2016)
39. Hung, Y.T., McLandsborough, L.A., Goddard, J.M., Bastarrachea, L.J.: Antimicrobial polymer coatings with efficacy against pathogenic and spoilage microorganisms. *LWT* **97**, 546–554 (2018)
40. Guo, M., Yadav, M.P., Jin, T.Z.: Antimicrobial edible coatings and films from micro-emulsions and their food applications. *Int. J. Food Microbiol.* **263**, 9–16 (2017)

# Influence of Drilling Operation Variables on Surface Roughness and Thrust Force of Aluminium Reinforced with 10% Al<sub>2</sub>O<sub>3</sub> Functionally Graded Metal Matrix Composite



S. Prathap Singh, T. Prabhuram, D. Elilraja, and J. Immanuel Durairaj

## 1 Introduction

Functionally Graded Materials (FGMs) are establishing latest element replacing homogenous composites by satisfying the requirement of modern industrial applications. These FGMs possess continuously varying composition and microstructure along the radial direction. Therefore it is feasible to reinforce selectively on the particular location of the component where the better properties are required [1, 2]. Gradient distribution of ceramic particles is the challenging objective in functionally graded materials. Centrifugal casting is the separation of the inexpensive method utilized to fabricate FGMs with gradient distributed ceramic particles [3, 4]. In centrifugal casting, centrifugal force was created due to the continuous constant rotation of the circular die. As an outcome of centrifugal force, the lesser density elements travel towards the axis of rotation whereas the higher density elements travel towards the outer circumference. This is the cause for the formation of different microstructures within a single specimen [5]. Aluminium Functionally Graded Metal Matrix Composites are widely attracted for industrial applications such as brake disc, internal combustion engine pistons and engine blocks due to its superior properties such as higher hardness, good wear opposition and low coefficient of heat expansion [6]. Huang et al. [7] manufactured aluminium alloy piston emphasized with SiC particles by centrifugal technique. They investigated the influence of different variables such as slurry temperature, mould temperature and rotation speed on particle segregation. The result revealed that the better segregation of SiC particles was achieved by increasing the slurry pouring and the mould temperature. Currently, manufacturing industries are facing difficulties in machining newly developed composites. These advanced materials are good enough to replace the component because of its properties like huge strength even at heavier temperatures and wear resisting

---

S. Prathap Singh (✉) · T. Prabhuram · D. Elilraja · J. Immanuel Durairaj  
Department of Mechanical Engineering, St. Joseph's Institute of Technology, Chennai, India

ability. So machining is required for these components to get the necessary dimension and surface finish [8]. Drilling is the frequently used secondary machining operation among various machining operations for ceramic composites. But the drilling process is very hard due to the existence of harder ceramic elements in the softer composite [9]. Ramulu et al. [10] conducted the drilling study on aluminium reinforced with 10 and 20 vol% alumina metal matrix composite with different drills. They studied the effect of polycrystalline diamond, high-speed steel and carbide-tipped drills on chip formation, drilling force, drilled-hole quality and tool wear. They concluded that the polycrystalline diamond drills were produced holes with minimum drilling forces. Many researches have been implemented to examine the influence of operation variables on the workpiece and tool materials. For higher productivity, it is mandatory to choose proper machining conditions and tool material. So many researchers used optimization techniques to figure out the responses of various drilling process variables in machining [11]. Sarbjit Singh [12] optimized the drilling operation variables such as feed, reinforcement size, cutting speed and drill bit geometry in the aluminium using Taguchi technique. The result revealed that the output feedback such as torque, surface roughness and thrust force is highly affected by cutting force. Paulo Davim et al. [13] performed drilling study on aluminium reinforced with 20% SiC composite using polycrystalline diamond drills. They studied the impact of operation variables such as cutting velocity, feed rate and cutting time on surface roughness, tool wear and specific cutting pressure using Taguchi technique. They halted that feed rate is the important process variable in the drilling operation. Shakeel Ahmed et al. conducted a drilling study on titanium alloy with varied levels of machining environments, feed rate and cutting speed using various cooling conditions. They optimized cutting temperature, torque, thrust force, circularity, cylindricity and surface roughness using TOPSIS technique. They concluded that TOPSIS is one of the most significant techniques for multiresponse optimization [14, 15].

The motive of the present experimentation is to optimize the drilling operation variables such as speed, feed, point angle and zone distance to get better output responses such as surface roughness and thrust force in the fabricated FGMMC using multi criteria decision making techniques called TOPSIS.

## 2 Materials and Methods

In this investigation, Aluminium A356 alloy is selected as the matrix alloy. The contents of as cast aluminium matrix composites are 7.0% Si, 0.35% Mg, 0.20% Fe, 0.20% Cu, 0.10% Zn, balance 90.15% Al. The  $Al_2O_3$  of 25  $\mu m$  moderate grain size was utilized as reinforcement. The density of selected aluminium alloy is  $2.68 \text{ g/cm}^3$  and the SiC particle is  $3.95 \text{ g/cm}^3$ . To fabricate FGMMC, Stir casting was done and subsequently, the centrifugal casting was done. Initially, aluminium alloy was grabbed in a clay graphite crucible and melted using electric resistance furnace. Preheating was done on the reinforcement particles to about  $600 \text{ }^\circ\text{C}$  to remove the



moisture content and impurities. Small amount of Mg was added to the melt at temperature of 730 °C to compensate for the Mg loss in the aluminium alloy due to oxidation. Then the preheated  $\text{Al}_2\text{O}_3$  particle was mixed to the molten aluminium alloy manually. Degassing was done to eliminate the hydrogen formation in the melt. This was achieved by passing nitrogen gas along with sulphuric acid for about 20 min till the melt reaches a temperature of 760 °C. Nitrogen gas will remove the hydrogen from the melt and sulphuric acid will act as purifier. After that, mechanical stirring was carried out using electric motor driven impeller with a controlled rotational speed of 350 rpm for 15 min. The composite made by the liquid metal stir casting method was poured into the rotating centrifugal casting mould to get the functionally graded centrifugally cast component. The horizontal centrifugal facility was utilized for the manufacturing of FGM components. Normally, the mould was made to rotate at a speed of 1400 rpm. Constant pouring speed and metal flow were maintained during the centrifugal casting. Then the molten metal was poured into the mould via pouring cup at a temperature of 760 °C. During centrifugal casting,  $\text{Al}_2\text{O}_3$  ceramic particles are made to move towards outer edge to form a gradient structure from outer edge to inner edge due to the centrifugal force. Variation of density in the selected elements is the cause for the formation of gradient dissemination. Finally, a hollow circular FGMMC with a dimension of 90 mm outer diameter and 150 mm length was manufactured and is presented in Fig. 1.

Microstructural analysis was done to examine the gradient dissemination of  $\text{Al}_2\text{O}_3$  particles from inner surface to outer surface on the fabricated FGMMC specimen. The drilling operation was carried on the Hartford CNC vertical drilling centre with Kistler piezoelectric dynamometer. A typical 5 mm diameter twist drill with titanium aluminium nitride coating was utilized for the machining study. The drill tool is made to adjust in three different angles such as 90°, 120°, 140°. The drilling operations were done under dry conditions.

In the present study, four operation variables such as speed, feed, point angle and zone distance from the exterior edge were used to conduct the drilling experiment and three levels were taken for each parameter. L9 orthogonal array table is utilized to carry out the experiments. Table 1 shows the operation parameters to be evaluated

**Fig. 1** Al-10%  $\text{Al}_2\text{O}_3$  FGMMC specimen



**Table 1** Selected operation parameters and their levels for machining

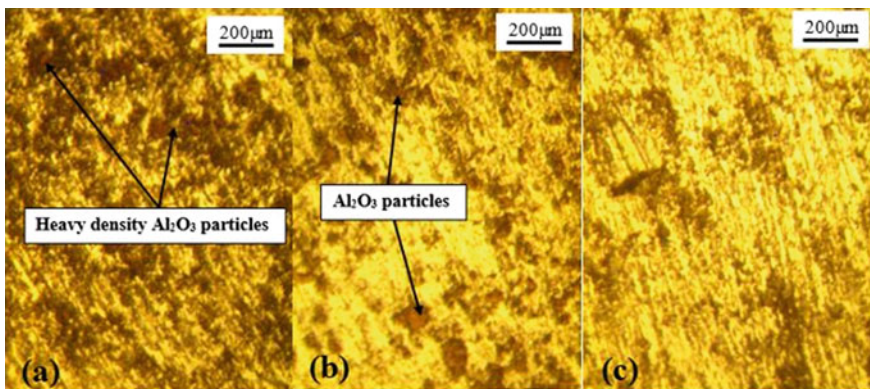
S. No.	Factors	Level-1	Level-2	Level-3
1	Speed (rpm)	1000	2000	3000
2	Feed (mm/rev)	0.05	0.15	0.25
3	Point Angle (deg)	90	120	140
4	Zone distance from the outer edge (mm)	5	10	15

in the FGMMC machining and their corresponding levels. The output response such as surface roughness and thrust force was measured for every set of operation parameters. The surface roughness was evaluated using Mitutoyo-Surfest SJ-201 surface roughness measuring device at three different positions and the averages of three values are considered. Thrust force was measured using the dynamometer facility fitted in the CNC vertical drilling machine.

### 3 Results and Discussions

#### 3.1 Microstructural Appraisal

Figure 2 illustrates the microstructures on the aluminium alloy reinforced with  $Al_2O_3$  FGMCC at various zones from the outer edge to inner edge. Figure 2a shows the microstructure of region measured 5 mm from the outer edge and this zone shows higher intensity of  $Al_2O_3$  particle. Due to the centrifugal force, ceramic particles are made to travel towards the outer edge during centrifugal casting. This region is named as ceramic wealthy zone. Figure 2b illustrates the microstructure discovered



**Fig. 2** Microstructure of **a** ceramic wealthy zone, **b** ceramic moderate zone, **c** ceramic depletion zone

**Table 2** L9 orthogonal array table and their experimental responses

Run	Speed (rpm)	Feed (mm/rev)	Point angle (°)	Zone distance (mm)	Surface roughness (µm)	Thrust force (N)
1	1000	0.05	90	15	5.236	32.6
2	1000	0.15	120	45	7.473	37
3	1000	0.25	140	75	9.216	60.5
4	2000	0.05	120	75	7.045	20.8
5	2000	0.15	140	15	6.38	13.5
6	2000	0.25	90	45	8.946	90
7	3000	0.05	140	45	7.13	16.3
8	3000	0.15	90	75	9.41	57
9	3000	0.25	120	15	6.536	61

between 6 and 10 mm regions. This zone shows a moderate amount of Al<sub>2</sub>O<sub>3</sub> particle distribution and this region is called ceramic moderate zone. Figure 2c shows the microstructure of region between 11 and 15 mm from the outer edge. This region is closer to the inner edge of the FGMMC. This region is named as ceramic depletion zone because of the absence of Al<sub>2</sub>O<sub>3</sub> particles.

Drilling operation was performed on the FGMMC based on L9 orthogonal array table and values of the surface roughness and thrust force was measured after drilling of FGMMC. Table 2 gives the L9 orthogonal array table and their responses such as surface roughness and thrust force.

### 3.2 TOPSIS

The multi criteria decision making techniques are highly recommended by previous researchers in machining operations to select optimal process parameters which are affecting the machining operation from a larger number of alternatives. TOPSIS is separate multi criteria decision making technique used to prefer a suitable alternative from a limited count of alternatives. The main intention of the current examination is to find the relationship between nine alternatives (experimental runs) and two attributes (output response) such as surface roughness and thrust force to the drilled FGMMC. TOPSIS is practised to describe the positive ideal solution and negative ideal solution. The optimum process parameters are closest to the positive ideal solution and isolated from the negative ideal solution [16]. The following steps are utilized to calculate the optimum process parameters that affect the drilling operation.

**Step 1:** Calculation of normalised matrix ( $N_{ij}$ ) by identifying the substitutes that terminate the units of all the responses since it is a ranking order technique. So the experimentally found attributes are converted to normalised matrix through Eq. (1).

$$N_{ij} = \frac{a_{ij}}{\sqrt{\sum_{i=1}^m a_{ij}^2}} \quad i = 1, 2, 3, \dots, 9; j = 1, 2 \quad (1)$$

where  $a_{ij}$  denotes experimental output values of  $i$ th alternative on  $j$ th attribute.

**Step 2:** Calculation of the weighted normalized matrix ( $W_{ij}$ ). This matrix was calculated by multiplying every normalized value with the weight of each response ( $W_j$ ). Equal weight was considered for each response in the present drilling study. Because surface roughness and thrust force are important responses at the time of drilling operation. The weighted normalized matrix was calculated using Eq. (2).

$$W_{ij} = N_{ij} \times W_j \quad i = 1, 2, 3, \dots, 9; j = 1, 2 \quad (2)$$

**Step 3:** Establishment of positive ideal solution ( $P^+$ ) and negative ideal solution ( $P^-$ ).  $P^+$  and  $P^-$  are calculated using Eqs. (3) and (4).

$$P^+ = \{(\max(W_{ij})|j \in J), (\min(W_{ij})|j \in J')\} \quad (3)$$

$$P^- = \{(\min(W_{ij})|j \in J), (\max(W_{ij})|j \in J')\} \quad (4)$$

where  $J = 1, 2$  and  $j$  is related to the benefit norms. Whereas  $J' = 1, 2$  and  $j$  is related to the cost norms. The positive ideal solution and negative ideal solution for surface roughness and thrust force are

$$P^+ = \{\text{Surface Roughness, Thrust Force}\} = \{0.114, 0.046\}$$

$$P^- = \{\text{Surface Roughness, Thrust Force}\} = \{0.205, 0.304\}$$

**Step 4:** Determination of better alternative distance ( $S_i^+$ ) from  $P^+$  values and worst alternative distance ( $S_i^-$ ) from  $P^-$  values. This alternative distance was calculated through Eqs. (5) and (6).

$$\text{Better alternative distance, } S_i^+ = \sqrt{\sum (W_{ij} - A_j^+)^2} \quad i = 1, 2, 3, \dots, 9; j = 1, 2 \quad (5)$$

$$\text{Worst alternative distance, } S_i^- = \sqrt{\sum (W_{ij} - A_j^-)^2} \quad i = 1, 2, 3, \dots, 9; j = 1, 2 \quad (6)$$

**Step 5:** Calculation of closeness coefficient ( $C_i$ ) for each alternative using Eq. (7) and rank the closeness coefficient values from higher to lower value. The first rank was given to the closeness coefficient with a higher value. The values associated with the higher closeness coefficient will give the optimum process parameters.

**Table 3** Consolidated values of output responses

Run	Normalised values		Weighted normalization matrix values		Better and worst alternative distance values		Closeness coefficient	Rank
	Surface roughness	Thrust force	Surface roughness	Thrust force	$S_i^+$	$S_i^-$		
1	0.228	0.220	0.228	0.220	0.253	0.534	0.679	4
2	0.32	0.250	0.325	0.250	0.357	0.471	0.569	5
3	0.40	0.409	0.401	0.409	0.495	0.323	0.395	8
4	0.30	0.141	0.306	0.141	0.252	0.534	0.680	3
5	0.27	0.091	0.277	0.091	0.156	0.570	0.785	1
6	0.38	0.608	0.389	0.608	0.582	0.102	0.150	9
7	0.31	0.110	0.310	0.110	0.224	0.547	0.710	2
8	0.40	0.385	0.409	0.385	0.487	0.334	0.407	7
9	0.284	0.412	0.284	0.412	0.434	0.401	0.480	6

$$\text{Closeness coefficient, } C_i = \frac{S_i^-}{(S_i^+ - S_i^-)} \quad i = 1, 2, 3, \dots, 9 \quad (7)$$

Table 3 shows the consolidated values of output responses.

Experiment number 5 displayed the huge closeness coefficient measurement. So the process parameters associated with experiment number 5 are taken as optimum drilling parameters to get minimum surface roughness and thrust force. Therefore the optimum operation parameters setting maintained during the drilling machining are speed of 2000 rpm (A2), feed of 0.15 mm/rev (B1), point angle of 140° (C3) and zone distance from outer edge of 15 mm (D1).

### 3.3 Verification Experiment

After the calculation of optimal drilling operation parameters, a verification experiment was done to certify the optimized outcomes. Equation (8) is used for estimating the optimum surface roughness and thrust force.

$$\hat{\alpha} = \alpha_m + \sum_{i=1}^q (\hat{\alpha}_i - \alpha_m) \quad (8)$$

where  $\alpha_m$  is the average closeness coefficient,  $\alpha_i$  is the mean closeness coefficient at the optimal height and  $q$  is the quantity of the drilling variables that attack the closeness coefficient significantly. Based on TOPSIS method, optimum operation parameters to get the least surface roughness and thrust force are A2, B1, C3 and D1. Table 4 gives the values of verification evaluation and it shows the successful optimization.

**Table 4** Results of confirmation evaluation

	First drilling process variables	Optimal drilling variables	
		Predicted	Experimental
Level	A1B1C1D1	A2B1C3D1	A2B1C3D1
Surface Roughness	5.236	–	5.147
Thrust Force	32.6	–	1. 201
Closeness coefficient value	0.679	0.785	0.894

## 4 Conclusions

In the present work, Aluminium reinforced with  $Al_2O_3$  FGMMC was invented through stir casting approach progressed by horizontal centrifugal casting approach. Drilling process was done on the fabricated FGMMC using CNC machining centre with four operation parameters with three varying levels and the output response such as surface roughness and thrust force were evaluated. TOPSIS methodology was utilized to evaluate the optimal drilling operation parameters to bring the least measure of surface roughness and thrust force. Following are the conclusions made based on the examination:

The microstructural examination confirmed the gradient dissemination of  $Al_2O_3$  particles on the fabricated specimen.

Experiment number 5 given the highest closeness coefficient value for multiresponse optimization and their corresponding operation parameters yield the optimum values. Therefore the optimum operation parameters are 2000 rpm of speed, 0.15 mm/rev of feed,  $140^\circ$  of point angle and 15 mm of zone distance from the outer edge.

Verification experiment showed the improvement in the closeness coefficient value from 0.679 to 0.894. So this methodology is worth the elimination of manufacturing time and costs in the drilling process of FGMMC.

## References

1. Saleh, B., Jiang, J., Ma, A., Song, D., Yang, D.: Effect of main parameters on the mechanical and wear behaviour of functionally graded materials by centrifugal casting: a review. *Metals Mater. Int.* <https://doi.org/10.1007/s12540-019-00273-8>
2. Prathap Singh, S., Prabhuram, T., Vinoth Babu, K., Elilraja, D., Uthayakumar, M., Rajan, T.P.D.: Solid particle erosion studies on SiC reinforced functionally graded aluminium matrix composites. *IOP Conf. Ser. Mater. Sci. Eng.* <https://doi.org/10.1088/1757-899X/764/1/012005>
3. Adelakin, T.K., Suárez, O.M.: Study of Boride-reinforced aluminum matrix composites produced via centrifugal casting. *Mater. Manuf. Process.* <https://doi.org/10.1080/10426910903124829>

4. Katamreddy, S.C., Punnath, N., Radhika, N.: Multi-response optimisation of machining parameters in electrical discharge machining of Al LM25/AIB<sub>2</sub> functionally graded composite using grey relation analysis. *Int. J. Mach. Mach. Mater.* <https://doi.org/10.1504/IJMMM.2018.093529>
5. Prathap Singh, S., Arun Vasantha Geethan, K., Elilraja, D., Prabhuram, T., Immanuel Durairaj, J.: Optimization of dry sliding wear performance of functionally graded Al6061/20% SiC metal matrix composite using Taguchi method. *Mater. Today Proc.* <https://doi.org/10.1016/j.matpr.2020.03.414>
6. Lin, X., Liu, C., Xiao, H.: Fabrication of Al-Si-Mg functionally graded materials tube reinforced with in situ Si/Mg<sub>2</sub>Si particles by centrifugal casting. *Compos. Part B.* <https://doi.org/10.1016/j.compositesb.2012.09.001>
7. Huang, X., Liu, C., Lv, X., Liu, G., Li, F.: Aluminum alloy pistons reinforced with SiC fabricated by centrifugal casting. *J. Mater. Process. Technol.* <https://doi.org/10.1016/j.jmatprotec.2011.04.006>
8. Gururaja, S., Ramulu, M., Pedersen, W.: Machining of MMCs—a review. *Mach. Sci. Technol.* <https://doi.org/10.1080/10910344.2012.747897>
9. Rayat, M.S., Gill, S.S., Singh, R., Sharmad, L.: Fabrication and machining of ceramic composites—a review on current scenario. *Mach. Sci. Technol.* <https://doi.org/10.1080/10426914.2017.1279301>
10. Ramulua, M., Raob, P.N., Kao, H.: Drilling of (Al<sub>2</sub>O<sub>3</sub>)p/6061 metal matrix composites. *J. Mater. Process. Technol.* **124**, 244–254 (2002)
11. Rajmohan, T., Palanikumar, K.: Optimization of machining parameters for surface roughness and Burr height in drilling hybrid composites. *Mater. Manuf. Process.* <https://doi.org/10.1080/10426914.2011.585491>
12. Singh, S.: Study the drilling behaviour of aluminium 6061 metal matrix composites using Taguchi's methodology. *Int. J. Mach. Mach. Mater.* <https://doi.org/10.1504/IJMMM.2016.077707>
13. Paulo Davim, J.: Study of drilling metal-matrix composites based on the Taguchi techniques. *J. Mater. Process. Technol.* [https://doi.org/10.1016/S0924-0136\(02\)00935-4](https://doi.org/10.1016/S0924-0136(02)00935-4)
14. Senthilkumar, C.: Optimisation of EDC parameters using TOPSIS approach. *Int. J. Mach. Mach. Mater.* **22**(5/6), 480–492 (2019)
15. Shakeel Ahmed, L., Pradeep Kumar, M.: Multiresponse optimization of cryogenic drilling on Ti-6Al-4V alloy using TOPSIS method. *J. Mech. Sci. Technol.* **30**(4), 1835–1841 (2016)
16. Yuvaraj, N., Pradeep Kumar, M.: Optimisation of abrasive water jet cutting process parameters for AA5083-H32 aluminium alloy using fuzzy TOPSIS method. *Int. J. Mach. Mach. Mater.* **20**(2), 118–140 (2018)

# Effect of Laser Scan Speed on Microstructure and Microhardness on Titanium Clad Magnesium



Kannan Ganesa Balamurugan and Muthukannan Duraiselvam

## 1 Introduction

Magnesium alloys are influencing various sectors due to their low density and better manufacturing characteristics [1]. The magnesium and its alloys have extensive usage in orthopedic applications due to their biocompatibility and similar modulus of elasticity with the natural bone [2]. Their inferior corrosion resistance of the magnesium limits their end usage [3]. Numerous surface modification techniques are utilized to retard the corrosion rates of the magnesium alloys, like laser treatment, ion implementation, friction stir processing and thermal spraying [4]. Additionally, the protective coating can be applied to the magnesium surfaces through thermal spraying and laser cladding routes. In recent years, laser cladding gains more attraction to apply the protective coatings on the metallic materials. The laser cladding significantly improves the tribological properties of the metallic materials [5]. Various researchers have been attempting laser cladding technique to enhance the tribological properties of the magnesium alloys. Zeqin et al. [6] investigated a composite coatings on AZ31B magnesium alloy by laser cladding. The results revealed that the coating had enhanced the tribological properties of the AZ31B magnesium alloy substrates. Huang et al. [7] fabricated zirconium-based coating on AZ91D magnesium by laser cladding. The corrosion resistance and wear resistance of the AZ91D magnesium alloy had been enhanced by the presence of zirconium oxide and zirconium aluminide in the coating. Gao et al. [8] laser clad Aluminum–Silicon on AZ91HP magnesium alloy. The results showed that the formation of multiple intermetallic particles like  $Mg_2Si$ ,  $Mg_{17}Al_{12}$ , and  $Mg_2Al_3$  showed higher hardness, improved the tribological properties. However, the hardness of the coated magnesium alloys was higher than their

---

K. G. Balamurugan (✉)

IFET College of Engineering, Villupuram, Tamil Nadu 605108, India

M. Duraiselvam

National Institute of Technology Tiruchirappalli, Tiruchirappalli, Tamil Nadu 620015, India



uncoated counterparts. Even though the corrosion resistance of the coated magnesium alloys showed improvement than un-coated magnesium alloys; the results were not up to the expected level. There is a lack of literature regarding the Ti6Al4V cladding on pure magnesium. Therefore, the present work attempts the laser clad Ti6Al4V powder on pure magnesium substrate and aims to study its compatibility with the pure magnesium substrates by investigating through macrostructures and microstructures.

## 2 Experimental

Commercially pure magnesium with a dimension of  $30 \times 60 \times 10$  mm was used. The surfaces were polished with metallographic sandpapers and washed with alcohol. The Ti6Al4V powders with the average particle size of 60 microns were used as the coating material. The laser cladding on the magnesium substrate was carried out using the YB:YAG disk laser (solid-state laser), 4 kW capacity. The laser power of 600 watts and powder feed rate of 5 g/min were kept constant, and the laser scan speed was varied from 100 mm/min to 600 mm/min with the increment of 100 mm/min. The Ti6Al4V powders were coaxially fed into the molten pool of the substrate material, and the Argon was supplied at the rate of 10 L/min to protect the molten pool. Metallographic characterizations were carried out by cross-sectioned the laser clad specimens and polished to the silver finish. The Kroll's etchant was applied on the Ti6Al4V coating and Picral. Microhardness measurements were taken on the coating, interface and the substrate with the test load of 0.5 kg. The XRD analysis was performed at the cross-section of the clad substrates to identify the secondary phase particles formed due to laser cladding.

## 3 Results and Discussion

### 3.1 Ti6Al4V Clad Morphology with Magnesium Substrate

Figure 1 indicates the cross-section of the sample coated in 100 mm/min scan speed. Figure 1a reveals that coating has a large void present in the magnesium substrate near the interface. Microcracks were visible (Fig. 1a). Figure 1b shows the interface of the coating and the substrate. The interface indicated that the coating and the substrate were a metallurgically bonded. Formation of the oxide layer at the interface was evident from Fig. 1b. The micro-dimples were observed near the interface in the magnesium. Figure 2a shows the cross-section of the sample coated in 200 mm/min scan speed. Presence of microcracks was observed in the coating (Fig. 2b), and the metallurgical bonding was created between the substrate and the coating. Formation of the oxide layers was evident at the interface, and micro-dimples were also formed in the magnesium side near the interface (Fig. 2b). Figure 3a shows the cross-section

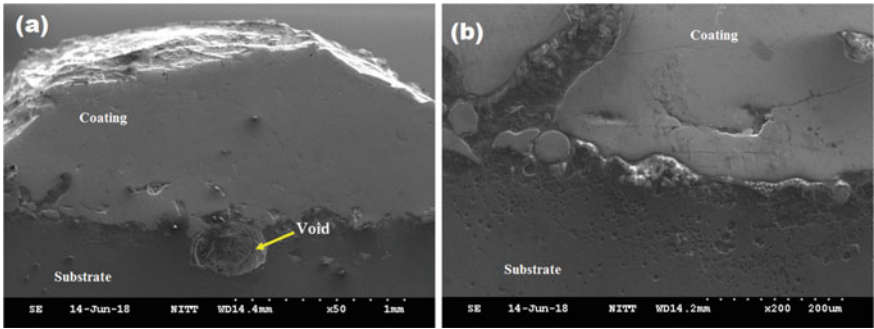


Fig. 1 SEM images of sample coated in 100 mm/min scan speed, a overall cross-section, b interface

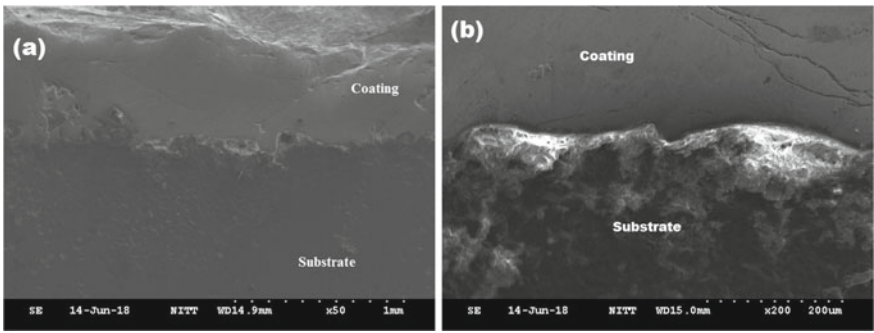


Fig. 2 SEM images of sample coated in 200 mm/min scan speed, a overall cross-section, b interface

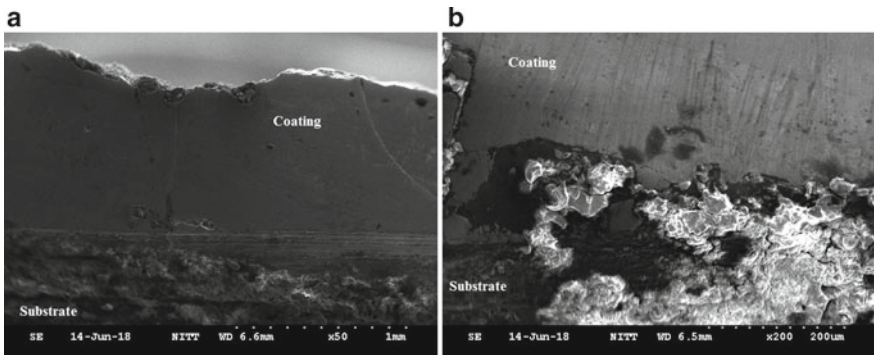
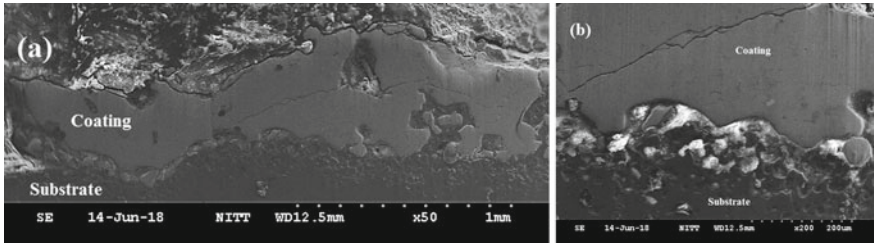
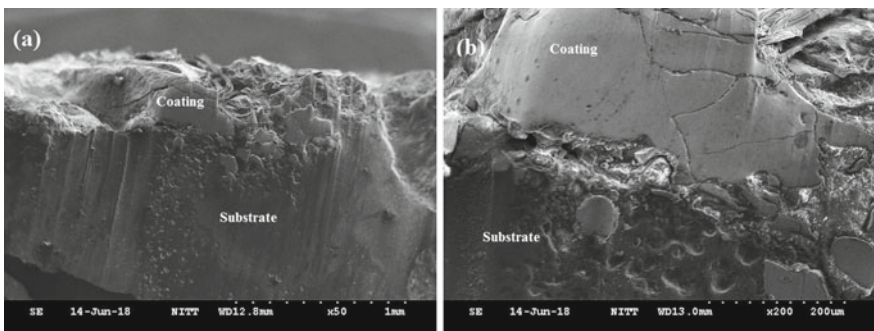


Fig. 3 SEM images of sample coated in 300 mm/min scan speed, a overall cross-section, b interface

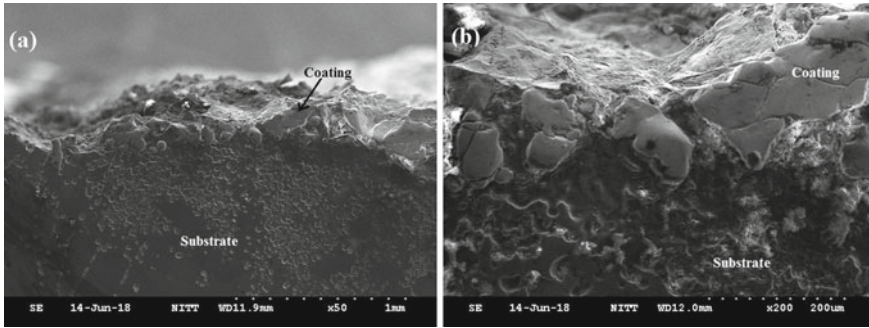


**Fig. 4** SEM images of sample coated in 400 mm/min scan speed, **a** overall cross-section, **b** interface

of the sample coated in 300 mm/min scan speed. Figure 3a reveals that the formations of microcracks were minimum and the interface revealed a metallurgical bonding existed. Formation of oxide layer was also evident at the interface (Fig. 3b). Figure 4a shows the cross-section of the sample clad at 400 mm/min scan speed. Figure 4a indicates that the coating was not uniformly deposited and the presence of large cavities was observed. Figure 4b shows the formation of cracks in the coating. Like other samples, oxide layers were formed at the interface as evident from Fig. 4b. Insufficient coating formed at 500 and 600 mm/min scan speeds, as evident from the Figs. 5 and 6 Laser scan speed significantly affects the coating deposition on the magnesium substrate. Figures 1, 2, 3, 4, 5 and 6 indicate the deposition nature of the different scan speeds. The observations from the figures clarified that increased scan speed has resulted in unsatisfactory coating deposition. Especially in higher scan speeds like 500 and 600 mm/min, poor deposition has been resulted. The coating material was coaxially fed along with laser source and argon gas. The laser source melts the coating materials and forms the plume. The plume was focused on the surface of the magnesium substrate. When the high energy plume hits the substrate surface, it loses the energy and got solidified. This mechanism continues along the desired length on the substrate. The scan speed affects interacting period of the plume with the substrate. At lower scan speed, the plume has sufficient interaction time for the deposition and solidification. However, at the higher scan speed, the plume has



**Fig. 5** Sample coated in 500 mm/min scan speed, **a** overall cross-section, **b** interface

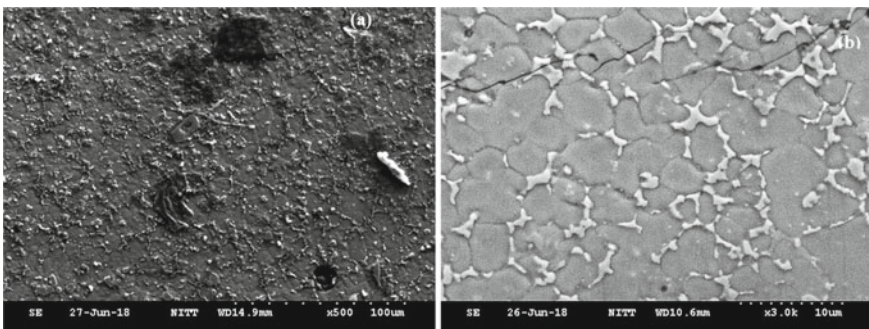


**Fig. 6** Sample coated in 600 mm/min scan speed, **a** overall cross-section, **b** interface

lower interaction time with the substrate which resulted in insufficient deposition and solidification. The substrate magnesium material was subjected to high irradiation in lower scan speed like 100 mm/min due to intense laser energy interaction which forms voids at the interface and cracks in the coating material (Fig. 1a).

### 3.2 *Microstructure of the Ti6Al4V Clad Magnesium Substrates*

Figure 7 shows the microstructures of the Ti6Al4V coating. Distinct grains were formed (Fig. 7a) and secondary phase particles were precipitated in their grain boundaries (Fig. 7b). During laser melting, the Ti6Al4V alloy powder attained beta transus temperature and rapidly solidified while hitting the surface of magnesium substrate. This rapid solidification yields various sizes of the grains and allows the some phases precipitated at grain boundaries. These precipitates form a dendritic structure at the



**Fig. 7** Microstructure of the Ti6Al4V coating, **a** lower magnification SEM image, **b** magnified SEM image

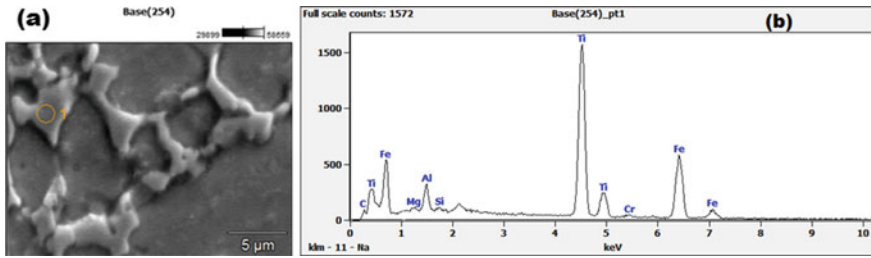


Fig. 8 a SEM image of the precipitate, b EDS result of the precipitate

grain boundaries. This phase contains  $\alpha + \beta$  platelet structure. This is the commonly forming phase in Ti6Al4V alloy [9]. Figure 8 shows the magnified image of the precipitate and the corresponding EDS result. The EDS result indicates that the precipitate contains the major elements of titanium, iron and aluminum and small traces of magnesium (Fig. 8b). During laser cladding process, considerable amount of magnesium substrate materials diffused in the titanium alloy matrix. The elemental mapping for cladding material proves the diffusion of magnesium substrate is significant (Fig. 9). Interface indicates the formation of oxide (Fig. 10a). EDS results ensure that the magnesium oxide is the constituent of this oxide layer (Fig. 10b). Elemental level diffusion occurred between Ti6Al4V coating and the magnesium substrate. However, substrate material shows higher diffusion in coating side than

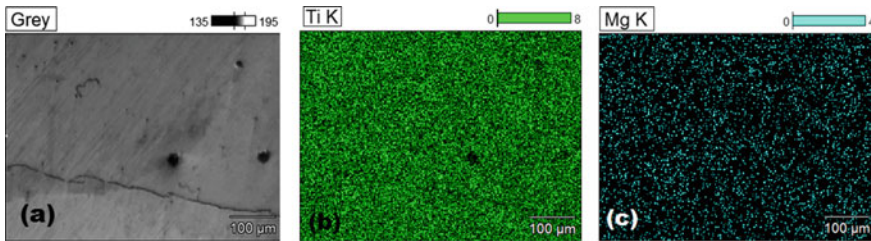


Fig. 9 Elemental mapping of Ti6Al4V coating, a SEM image of Ti6AlV4 coating, b Titanium elements in the coating, c Magnesium elements in the coating

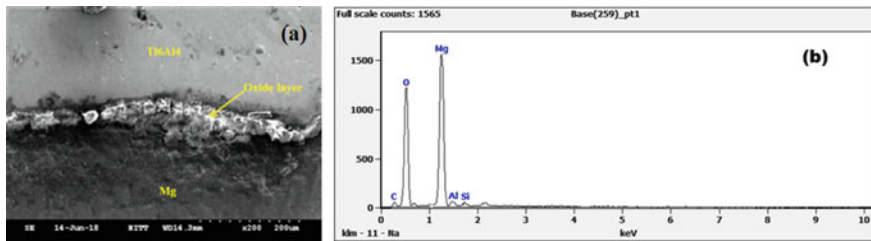
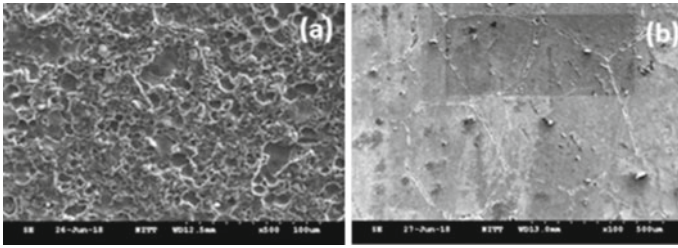


Fig. 10 a SEM image of the interface oxide layer, b EDS result of the oxide layer

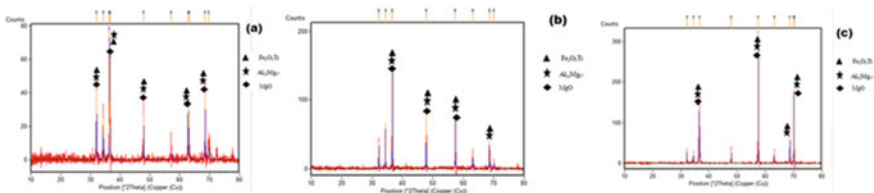




**Fig. 11** a SEM image of heat affected zone of Ti6Al4V clad substrate, b Magnesium substrate microstructure

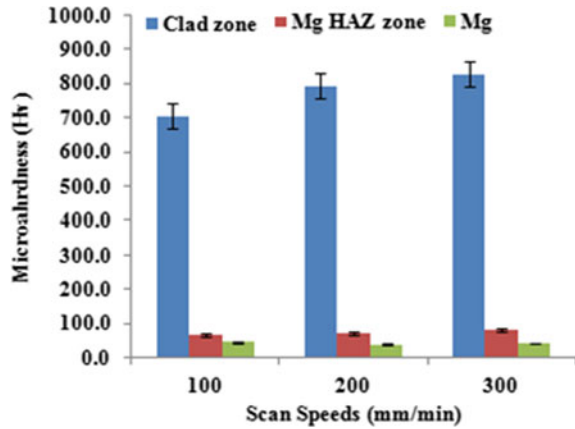
coating material into the substrate side as evident from the line scan. The magnesium substrate attained the melting temperature during the laser irradiation and diffused into the solidifying Ti6Al4V plume. The rate of solidification of Ti6Al4V plume was high compared to the magnesium substrate, thus the quantity of diffusion of magnesium into the coating material was high. Figure 11a shows the heat affected zone of Ti6Al4V clad magnesium substrate.

The heat affected zone of the magnesium contains network dendrites usually forms during laser treatment [10]. Figure 11b shows SEM image of magnesium substrate microstructure taken below the heat affected zone and the parent metal primary phase with large grains. The effect of heat input during laser cladding has no effect in this region. The laser scan speeds have less influence on the grain sizes and orientation of the coating and heat affected substrate. However, the scan speeds affect the intensities of intermetallic particles in the coating and heat affected substrate material. The intensities of the intermetallics vary with the scan speed. Figure 12 shows the XRD results of the laser clad specimens processed in various scan speeds. The XRD results revealed that the dominating intermetallic particles in the clad zones are  $Al_{12}Mg_{17}$ ,  $Fe_2O_3Ti$  and  $MgO$ . The  $Fe_2O_3Ti$  has been precipitated in the clad material and  $MgO$  has been precipitated in the interface (Fig. 10a). However,  $Al_{12}Mg_{17}$  has been resulted from the diffusion of substrate and coating materials on either side. Especially, due to the diffusion of magnesium into the coating side. The intensities of these intermetallic particles increasing while increasing the scanning speed (Fig. 12). At the higher scan speed, rapid heating and cooling of the coating and substrate material restricts the dissolution of the precipitated intermetallics into



**Fig. 12** XRD results of Ti6Al4V clad samples at a 100 mm/min, b 200 mm/min, c 300 mm/min

**Fig. 13** Microhardness of the Ti6Al4V clad magnesium substrates at various scan speeds



their matrix. However, in case of lower scan speed, sufficient dissolution time was persisted.

### 3.3 Microhardness of Ti6Al4V Clad Magnesium Substrate

Figure 13 shows the microhardness of the Ti6Al4V clad magnesium substrates at various scan speeds. The microhardness result revealed that the clad zone has attained higher hardness than other zones like heat affected and non-heat affected magnesium substrate. Cladding zone shows ~95% higher microhardness than other zones. Similarly, heat affected zone shows ~44% increase than non-heat affected magnesium substrate. The intensities of the intermetallics present in the clad, HAZ zones influence the microhardness of the clad samples. Figure 13 indicates that the sample clad at 300 mm/min scan speed shows comparatively higher clad microhardness with higher intensity of intermetallics. The intermetallics are hard particles and offer resistance to indentation. Therefore, their increase in intensities increases the hardness of the clad specimens.

## 4 Conclusion

In this work, Ti6Al4V alloy was clad on pure magnesium substrate by laser cladding. The influence of laser scan speed on cladding morphology, microstructure and microhardness were investigated. Following conclusions were derived from this investigation.

- The optimum scan speed is identified as 300 mm/min. Increasing the laser scan speed above 300 mm/min resulted in inadequate coating deposition. However, at lower scan speeds, cracks and voids formed due to high interaction time of intense laser energy.
- The influence of laser scan speed on the grain size and their orientation was minimal in the clad and heat affected zones. However, it influences the intensities of intermetallic particles formed. The intensity of the intermetallics increase with increase in scan speed due to rapid solidification. The lower scan speed let the intermetallic particles to dissolve again into the matrix.
- Cladding zone shows ~95% higher microhardness than other zones and heat affected zone shows ~44% increase than non-heat affected magnesium substrate. Intensities of intermetallics affect the microhardness of the clad specimens. Higher intensity of intermetallics offered high resistance to indentation which resulted in increase in microhardness.

**Acknowledgements** This project is funded by the Science and Engineering Research Board (SERB), a statutory body of Department of Science and Technology (DST), Government of India under National Post-Doctoral Fellowship scheme (File No: PDF/2017/000412). The authors gratefully acknowledge the financial support by the DST-SERB, Government of India for this research work.

## References

1. Riquelme, A., Rodrigo, P., Escalera-Rodríguez, M.D., Rams, J.: Analysis and optimization of process parameters in Al–SiCp laser cladding. *Opt. Lasers Eng.* **78**, 165–173 (2016)
2. Kunjukunju, S., Roy, A., Ramanathan, M., Lee, B., Candiello, J.E., Kumta, P.N.: A layer-by-layer approach to natural polymer-derived bioactive coatings on magnesium alloys. *Acta Biomater.* **9**(10), 8690–8703 (2013)
3. Kirkland, N.T.: Magnesium biomaterials: past, present and future. *Corros. Eng. Sci. Technol.* **47**, 322–328 (2012)
4. Khalajabadi, S.Z., Bin Haji Abua, A., Ahmad, N., Azizi Mat Yajid, M., BtHjRedzuan, N., Nasiric, R., Haiderd, W., Noshadie, I.: Bio-corrosion behavior and mechanical characteristics of magnesium titania-hydroxyapatite nanocomposites coated by magnesium-oxide flakes and silicon for use as resorbable bone fixation material. *J. Mech. Behav. Biomed. Mater.* **77**, 360–374 (2018)
5. Liu, B., Zhang, X., Xiao, G.Y., Lu, Y.P.: Phosphate chemical conversion coatings on metallic substrates for biomedical application: a review. *Mater. Sci. Eng. C* **47**, 97–104 (2015)
6. Cui, Z., Yang, H., Wang, W., Wu, H., Xu, B.: Laser cladding Al-Si/Al<sub>2</sub>O<sub>3</sub>-TiO<sub>2</sub> composite coatings on AZ31B magnesium alloy. *J. Wuhan Univ. Technol. Mater. Sci. Ed.* **27**, 1042–1104 (2012)
7. Huang, K., Lin, X., Xie, C., Yue, T.M.: Laser cladding of Zr-based coating on AZ91D magnesium alloy for improvement of wear and corrosion resistance. *Bull. Mater. Sci.* **36**(1), 99–105 (2013)
8. Gao, Y., Wang, C., Lin, Q., Liu, H., Yao, M.: Broad-beam laser cladding of Al–Si alloy coating on AZ91HP magnesium alloy. *Surf. Coat. Technol.* **201**, 2701–2706 (2006)



9. Murr, L.E., Quinones, S.A., Gaytan, S.M., Lopez, M.I., Rodela, A., Martinez, E.Y., Hernandez, D.H., Martinez, E., Medina, F., Wicker, R.B.: Microstructure and mechanical behavior of Ti-6Al-4V produced by rapid-layer manufacturing, for biomedical applications. *J. Mech. Behav. Biomed. Mater.* **2**, 20–32 (2009)
10. Liu, S.Y., Hu, J.D., Yang, Y., Guo, Z.X., Wang, H.Y.: Microstructure analysis of magnesium alloy melted by laser irradiation. *Appl. Surf. Sci.* **252**, 1723–1731 (2005)

# Detonation Gun Spray Coatings on Martensitic Stainless Steels



J. Jhansi, S. Santhi, P. V. S. Lakshmi Narayana, and Bhomik Ketari Deogade

## 1 Introduction

Erosive wear is the removal of material from a surface due to mechanical interaction between the surface and a fluid, or impinging liquid or solid particles or liquid + solid particles [1]. Even though erosion wear is a surface phenomenon, it leads to structural failures directly or as a part of combined effects (erosive wear with corrosion or fatigue etc.). Erosion is prominent in subsea gate valves, power station boiler valves, and turbine blades used in the steam generation of thermal power plants [2]. The presence of erosive environments recommends the relevance of harder and wear-resistant coatings that protects the base material [3]. For hydro-turbines, cavitation erosion advances formation of cavities and pits at the surface and modifies the hydraulic profile of the components [4].

The application of harder and wear-resistant coatings improves the performance of substrate material under erosive environments [5]. Martensitic stainless steels as substrate material are commonly adopted for automotive industry [6], nuclear reactors [7], and power plants [8]. Cermet coatings (carbide-type coatings, WC-Co-Cr, and  $\text{Cr}_3\text{C}_2\text{-NiCr}$ ) have been opted because of good hardness against wear. These coatings are composed of carbides reinforcing a metal matrix, with good amount of hardness, toughness, and ductility. WC coatings are used in  $<500^\circ\text{C}$  temperatures and

---

J. Jhansi (✉) · S. Santhi · P. V. S. Lakshmi Narayana · B. K. Deogade  
Mahatma Gandhi Institute of Technology, Hyderabad, Telangana 500075, India  
e-mail: [jjhansibai\\_mme@mgit.ac.in](mailto:jjhansibai_mme@mgit.ac.in)

S. Santhi  
e-mail: [ssanthi\\_mme@mgit.ac.in](mailto:ssanthi_mme@mgit.ac.in)

P. V. S. Lakshmi Narayana  
e-mail: [pvsln\\_mme@mgit.ac.in](mailto:pvsln_mme@mgit.ac.in)

B. K. Deogade  
e-mail: [dbhomikketary\\_mme@mgit.ac.in](mailto:dbhomikketary_mme@mgit.ac.in)

also in non-corrosive environments. The  $\text{Cr}_3\text{C}_2$ -NiCr coating materials are employed at high temperature  $\leq 900$  °C. This type of coating is produced using thermal spray processes like detonation and plasma-coating techniques. These methods are now widely used to spray coatings against wear, erosion, and corrosion and thermal barrier coatings for practical purposes [9]. Coating properties are determined by the type of coating material, the deposition process, and the set of parameters used [10]. The aim of this present work is to study the erosion resistant coatings behavior on martensitic stainless steel using DG process. The thickness of coating materials (WC-Co-Cr and  $\text{Cr}_3\text{C}_2$ -NiCr) obtained is 200 to 400  $\mu\text{m}$ . Application of above materials for surface coatings on martensitic stainless steel substrate, results in complex microstructure consists of carbides, metallic phases, and oxides.

## 2 Materials and Processes

### 2.1 Materials

The chemical composition of the substrate (martensitic stainless steel) is determined by spectroscopic analysis and is given in Table 1, and the lathe martensitic structure of the substrate is shown in Fig. 1.

**Table 1** Chemical composition of the substrate

Constituent	C	Si	Mn	P	S
wt%	0.075	0.79	0.67	0.009	0.012
Constituent	Cr	Ni	B	Cu	Mo
wt%	13.95	3.79	0.00012	0.156	0.42

\*Fe is the balance

**Fig. 1** Optical microstructure of substrate material at 100X magnification



### 2.1.1 Coating Materials

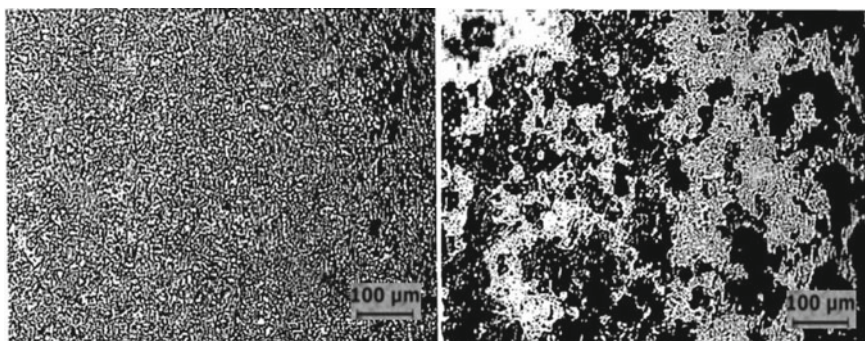
WC–Co–Cr and  $\text{Cr}_3\text{C}_2$ -NiCr are the coating materials considered, and the details are given in Table 2. The microstructures of the coatings are characterized using the metallurgical microscope and are shown in Fig. 2. The microstructure of WC–Co–Cr coating consists of WC grains revealing straight edges and sharp angles embedded in a cobalt matrix.

The white area in the images (Fig. 2a) consists of W, C, and  $\text{W}_2\text{C}$  and pure beta cobalt (Co–Cr) binder as the dark gray area [11]. The microstructure of  $\text{Cr}_3\text{C}_2$ -NiCr coating (Fig. 2b) shows a dense skeletal network of fine  $\text{Cr}_3\text{C}_2$  and  $\text{Cr}_2\text{O}_3$  bound within the ductile matrix [12]. The white phases are of metallic bonding matrix, and dark phases and gray phases are of oxides and carbides of rounded and flattened aspect, respectively.

Spectroscopic analysis is carried out to find the chemical composition of coatings along with substrate and is given in Table 3.

**Table 2** Coating powder characteristics

<i>Powder characteristics</i>	
Particle size	4.5 $\mu\text{m}$
Particle shape	Spherical



**Fig. 2** Optical microstructures at 100X magnification of **a** 86WC-10Co-4Cr coating and **b** 75 $\text{Cr}_3\text{C}_2$ -25NiCr coating

**Table 3** Chemical composition of coating materials

Coating	Chemical composition
WC–Co–Cr	86WC-10Co-4Cr
$\text{Cr}_3\text{C}_2$ -NiCr	75 $\text{Cr}_3\text{C}_2$ -25NiCr

## 2.2 Coating Processes

Detonation gun coating process was employed on martensitic stainless steel substrate and coating materials are 86WC-10Co-4Cr and 75Cr<sub>3</sub>C<sub>2</sub>-25NiCr.

### 2.2.1 Detonation Gun Spray Process

Before coating process the martensitic stainless steel samples are grit blasted with Al<sub>2</sub>O<sub>3</sub> grits of size 150 mm at a pressure of 3–3.5 bars at room temperature. In DG process, the reaction gases (C<sub>2</sub>H<sub>6</sub> and oxygen), a carrier gas, and powdered coating material as given in Table 3 are allowed into the combustion chamber. This powdered coating mixture is mixed and ignited by a spark from a spark plug. The coating material is heated by detonation energy release, resulting in high-pressure ultra-sonic wave, thereby propagating hot gas stream and accelerating the powder particles up to 900 m/s and hits the surface of the substrate. After each detonation process leads to combustion process and are about 4–8 detonations cycles per second. The flushing gas like argon and nitrogen cleans the combustion chamber before each new cycle. There, the collision of hot powder particles with high velocity on the surface of the sample resulting in a very dense and strong thermal barrier coating [13, 14]. Table 4 is showing the spraying conditions adopted in this work.

## 3 Characterization Techniques

Tribological behavior of DG spray coatings depends on composition, microstructure and distribution of the phases, porosity and hardness. In the present study, micro-hardness and porosity techniques are performed to evaluate the erosion resistance of the coatings on the substrate.

**Table 4** Spraying parameters adopted for DG process

Parameters	Values
Spraying atmosphere	Air
Spray Spot diameter	25 mm
Spraying distance	200 mm
– (Al <sub>2</sub> O <sub>3</sub> )	165 mm
– (Carbides)	
Thickness per shot	5–6 μm
Shots per sec	3 shots

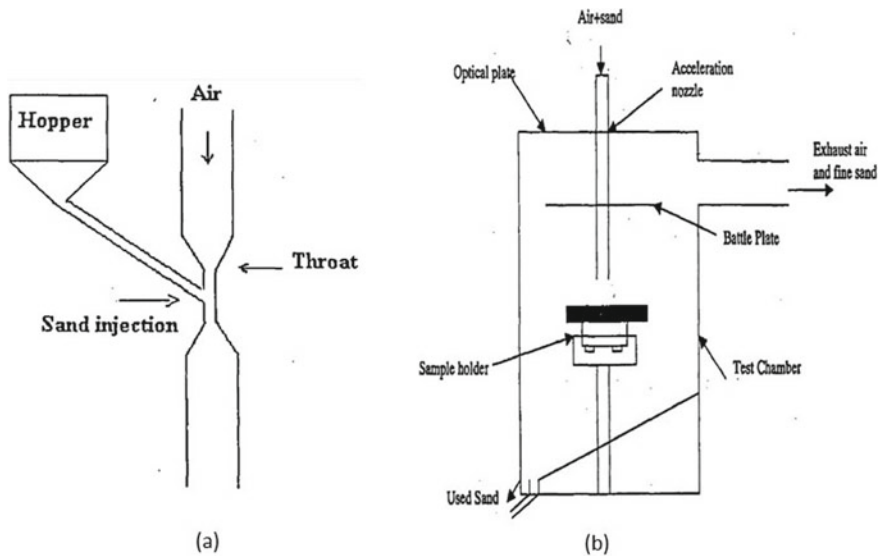
### 3.1 Hardness and Porosity

The microhardness of coatings was taken at 300 gm load for 10 s and macrohardness of the substrate is evaluated at a load of 30 kgf for 10 s. Porosity of coated substances was carried out, with the help of optical microscope with image analyzer, on the sectioned and mirror finished surface of coatings.

### 3.2 Erosion Test

An air jet erosion tester (Fig. 3) is used for testing the coated and uncoated samples. Solid particle erosion test was done as per ASTM G76-95 standard [15]. The erodent ( $\text{SiO}_2$ ) is fed by particle feeder in a controlled rate by maintaining constant flow rate of air with particles by connecting the compressor to the mixing chamber. The  $\text{SiO}_2$  particles further accelerated with help of air stream during a stainless steel congregating nozzle and hitting the specimen placed at sample holder. A total of 10 cm distance is kept between the sample and nozzle, where nozzle outlet diameter is 10 mm and the feed rate is maintained at 45 g/min. The erosion test is carried out as in the steps given below.

The coated samples are dirt freed in acetone, dried, and weighed with an electron balance where an accuracy level of 0.01 mg is maintained. Sample is fixed to the



**Fig. 3** Schematic diagram of air jet erosion test, **a** sand injection system, **b** details of erosion chamber

**Table 5** Erosion test conditions

Erosion conditions	
Erodent material	Silica
Particle velocity (m/s)	60
Silica-feed rate (g/min)	45.33
Angle of impact (°)	90
Particle shape	Round and Angular
Nozzle distance (mm)	10
Particle Size (μm)	250–350

sample holder and eroded for 10 min with SiO<sub>2</sub> particles, at a fixed particle feed rate, impact velocity, and impact angle.

The sample is then removed and again cleaned in acetone, dried, and determined the loss in weight. Erosion rate is measured by weight loss to that of mass of erodent. The time allowed for each sample to erode is two hours in this present work. The erosion test conditions are presented in Table 5.

## 4 Results and Discussion

### 4.1 Hardness and Porosity

The macrohardness obtained for the substrate is 315 HV30kg, and the microhardness of coating materials are given in Table 6. The coated sample's porosity values are found out using microprobe analyzer fitted to optical microscope, which are given in Table 6. It is observed that the porosity is low (<1%) for 86WC-10Co-4Cr and Cr<sub>3</sub>C<sub>2</sub>-NiCr coated samples. The porosity of DG-sprayed coatings is low because the kinetic energy of the powder particles is high enough, to get deformed and fills the pores between them.

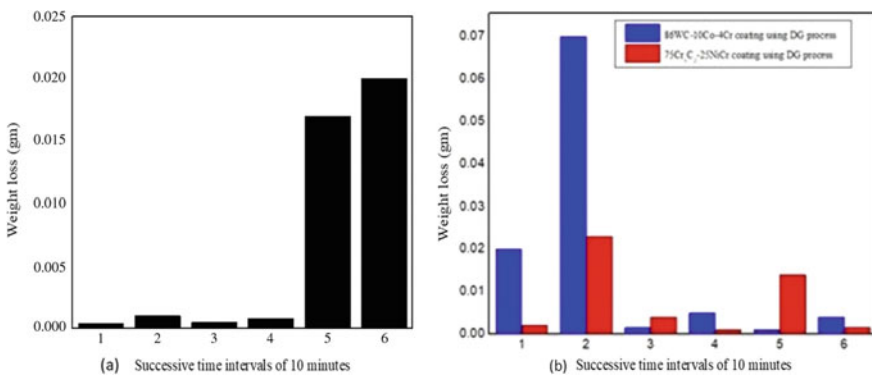
**Table 6** Hardness of coatings

Coating material	Microhardness [HV0.3 kg]	Porosity (%)
86WC-10Co-4Cr	1075	0.41
75Cr <sub>3</sub> C <sub>2</sub> -25NiCr	961	0.46

## 4.2 Erosion Test

### 4.2.1 Step-Wise Erosion

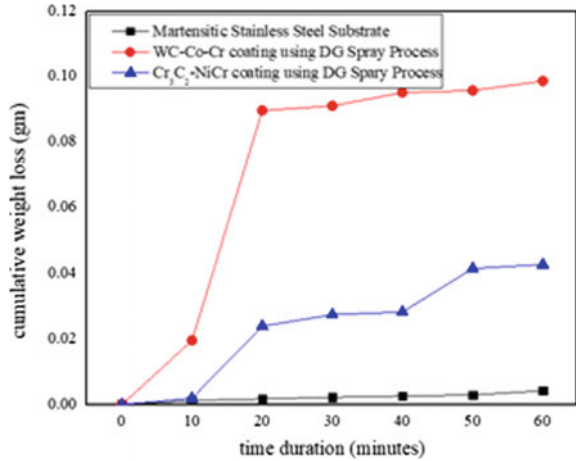
Air–sand erosion testing has been conducted as discussed in Sect. 4.2, and the test conditions employed are as per Table 6. It was observed that in Fig. 4(a), in first four intervals, the weight loss for martensitic stainless steel is very less and almost uniform. This is due to low carbon and toughness of steel which delayed the crack initiation and propagation. Stepwise increment of weight loss is observed in the next two intervals. Drastic increase in the weight loss is observed in the last interval, where crack propagation is faster and material removal takes place by development of a lip or platelet and its consequent fracture. On the whole, erosion efficiency of metallic materials is low when compared to cermet coatings and ceramics materials [16]. The comparison of 86WC-10Co-4Cr and 75Cr<sub>3</sub>C<sub>2</sub>-25NiCr coatings on martensitic stainless Steel using DG process is shown in Fig. 4(b). It is observed that there is a drastic raise in erosion from first interval to second interval, owing to the prevailing nature of brittle erosion. It is due to fast initiation and crack propagation, and the WC particles were pulled out from Co-Cr binder phase where the bonding between the splats is weak. The repeated impact of erodent particles leads to crack initiation and propagation near splat boundaries which leads to more weight loss [17]. Then, it is observed that erosion increases drastically in the second interval for 75Cr<sub>3</sub>C<sub>2</sub>-25NiCr coating, due to dominant brittle erosion by fracturing of metal carbide particles or pulling of the coating from the distorted binder. At third and fourth intervals, the erosion decreases, due to ductile erosion of Ni–Cr binder phase. The abrupt raise in the erosion at the fifth interval is because of pullout of particles and voids formation. Then, there is trivial raise in the erosion at sixth interval which is due to better adhesion between the splats [14].



**Fig. 4** **a** Erosion of martensitic stainless steel substrate. **b** Comparison of erosion of 86WC-10Co-4Cr and 75Cr<sub>3</sub>C<sub>2</sub>-25NiCr coatings



**Fig. 5** Cumulative weight loss of coating materials



### 4.2.2 Cumulative Weight Loss

The cumulative weight loss of uncoated substrate and two coated substrates with time (one hour) is shown in Fig. 5. The erosion behavior of WC–Co–Cr and Cr<sub>3</sub>C<sub>2</sub>-NiCr coatings on martensitic stainless steel is shown in the Fig. 5. It is observed that erosion rate is more for brittle coating material (86WC-10Co-4Cr) and less for comparatively ductile coating material (75Cr<sub>3</sub>C<sub>2</sub>-25NiCr) because the effect of impact angle at 90° is different for ductile and brittle materials [18]. At this impact angle, erosion is highest for brittle materials and lowest for ductile materials and is shown in Fig. 5. It is observed, from the graph, that there is almost sudden increase at second and third interval of WC–Co–Cr graph, and coating material is brittle in nature. With minimum amount of plastic deformation, brittle fracture occurs in metals. So the crack is ‘unstable’ once the crack nucleates and the propagation keeps on impulsively without any change/increment in the value of the applied stress [17].

## 5 Conclusions

In this work, detonation gun spray process is employed for coating 86WC-10Co-4Cr and 75Cr<sub>3</sub>C<sub>2</sub>-25NiCr on martensitic stainless steel. Based on cumulative weight loss, it is observed that 75Cr<sub>3</sub>C<sub>2</sub>-25NiCr coating on martensitic steel substrate has exhibited improved erosion resistance compared to 86WC-10Co-4Cr coating.

## References

1. Friction, Lubrication, Wear Technology, ASM Handbook, vol. 18 (1992)
2. Basu, P., Kefa, C., Jestin, L.: Erosion prevention in boilers in mechanical engineering series, Boilers and Burners, Springer, New York, NY (2000)
3. Thermal spray coating processes, ASM Handbook, vol. 5, Surface Engineering (1994)
4. Fauchais, P., Vardelle, A.: Thermal sprayed coatings used against corrosion and corrosive wear. (2012). <https://doi.org/10.5772/34448>
5. Santaa, J.F., Blanco, J.A., Giraldo, J.E., Toroa, A.: Cavitation erosion of martensitic and austenitic stainless steel welded coatings. *Wear* **271**, 1445–1453 (2011)
6. Fagoaga, I., Viviente, J.L., Gavin, P., Bronte, J.M., Garcia, J., Tagle, J.A.: Multilayer coatings by continuous detonation system spray technique. *Thin Solid Films* **317**, 259–265 (1998)
7. Mohrbacher, H.: Martensitic automotive steel sheet-fundamentals and metallurgical optimization strategies. *Adv. Mater. Res.* **1063**, 130–142 (2015)
8. Klueh, R., Nelson, A.T.: Ferritic/martensitic steels for next-generation reactors. *J. Nucl. Mater.* **371**, 37–52 (2007)
9. Abe, F.: Precipitate design for creep strengthening of 9% Cr tempered martensitic steel for ultra-supercritical power plants. *Sci. Technol. Adv. Mater.* **9**, 013002 (2008)
10. Psyllaki, P.P., Jeandin, M., Pantelis, D.I.: Microstructure and wear mechanism of thermal sprayed alumina coatings. *Mater. Lett.* **47**, 77–82 (2001)
11. Kamal, S., Jayaganthan, R., Prakash, S.: High temperature oxidation studies of detonation-gun-sprayed Cr<sub>3</sub>C<sub>2</sub>-NiCr coating on Fe- and Ni-based superalloys in air under cyclic condition at 900 °C. *J. Alloys Compd.* **472**(1–2), 378–389 (2009). ISSN 0925-8388
12. Grewal, H.S., Bhandari, S., Singh, H.: Parametric study of slurry-erosion of hydroturbine steels with and without detonation gun spray coatings using Taguchi technique. *Metall. Mater. Trans. A* **43**, 3387–3401 (2012)
13. Fauchais, P., Vardelle, A.: Thermal sprayed coatings used against corrosion and corrosive wear, SPCTS, UMR 7315, University of Limoges, France (2012)
14. Rointan., Bunshah, F.: Deposition technologies, properties and applications, pp. 77–81 and 92–102, Noyes Publications (2001)
15. ASTM G76–95: Standard test method for conducting erosion tests by solid particle impingement using gas jets (2000)
16. Harsha, A.P., Bhaskar, D.K.: Solid particle erosion behaviour of ferrous and non-ferrous materials and correlation of erosion data with erosion models. *Mater. Des.* **29**, 1745–1754 (2008)
17. Wood, R.J.K.: Tribology of thermal sprayed WC-Co coatings. *Int. J. Refract. Metals Hard Mater.* **28**, 82–94 (2010)
18. Hutchings, I.M.: Tribology: friction and wear of engineering materials. Edward Arnold, London (1992)

# Joining of Dissimilar Aluminum Alloys AA2024 and AA7075 by Friction Stir Welding: A Review



Ajay Kaushal, Sachindra Shankar, and Somnath Chattopadhyaya

## 1 Introduction

Aluminum 2024 alloy has high ratio of strength to weight but the major problem with 2024 is that it has poor corrosive resistance and on this ground it is sometime clad with more zinc containing aluminum alloys, i.e., 7 series alloys. As these alloys contain high strength to weight ratio, aerospace industries have always looked for better welding technique for 2XXX alloys. There are various techniques available for joining dissimilar aluminum alloys as shown in Fig. 1.

Vijay et al. [1] performed TIG welding of Al2024 and Al6063 by changing three types of input parameters such as gas flow rate, current and root gap. It was reported that with the increase in root gap, gas flow rate and current the TS of the joint increases. Nasser [2] performed MIG welding for aluminum alloys 2024-T351 and 6061-T651 using argon as shielded gas and ER-4043(AlSi5) as a filler metal. Maximum ultimate tensile strength and tensile strength of about 323 and 295 MPa was achieved respectively. Third homogenous method used for welding of dissimilar aluminum alloy is laser welding. Zang et al. [3] performed CO<sub>2</sub> laser welding of aluminum alloys 2024 and 7075 using different filler materials. Tensile strength of 339.5 and 308.6 MPa was reported when 2319 and 4043 were used as filler materials. Homogenous joining process used for joining dissimilar aluminum alloys of 2XXX and 7XXX series does not give sufficient strength because of higher susceptibility to hot cracking. For this reason solid-state welding processes are used for welding 2XXX and 7XXX series. Vaporizing foil actuated welding is quite similar to explosive welding with the difference in the driving force for weld formation. In this process, very fast electrical vaporization of thin foil takes place which results in the formation of very high pressure pulse that moves away thin flyer sheets to very high speed [4]. Highest ultimate tensile force was observed when the standoff distance was halved [5]. Second

---

A. Kaushal (✉) · S. Shankar · S. Chattopadhyaya  
Department of Mechanical Engineering, IIT (ISM) Dhanbad, Dhanbad, Jharkhand, India

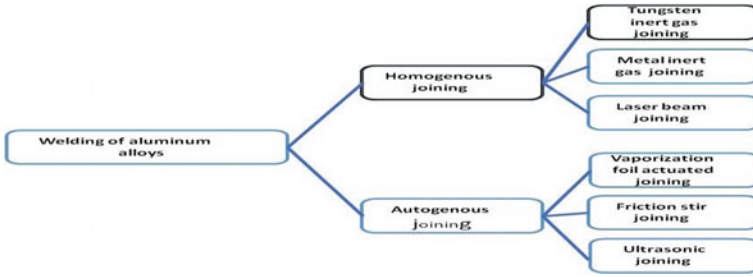


Fig. 1 Different processes used for joining of dissimilar aluminum alloys

solid-state welding process used is ultrasonic welding process wherein the plates to be welded are kept one over the other and the ultrasonic vibration were given to the top plate and due to friction between plates heat energy is produced and after obtaining sufficient heat the vibration are stopped and pressure is applied to form the weld [6]. FSW is the highly used process for welding AA2024 and AA7075 dissimilar alloys together. AA2024 and AA7075 alloys mainly finds its application in aerospace industries where it is required to have high strength at lower weight [7, 8]. FSW process is mainly used in welding of aluminum alloys as all the earlier process used are performed at high temperature leading to high susceptibility to hot cracking.

## 2 Process of FSW

FSW process can be subdivided into 4 phases which are shown in Fig. 2: plunging, dwelling, welding, dwelling and pulling out.

The last two phases, i.e., dwelling and pulling out are non productive process but they are only there to finalize the weld joint and hence cannot be avoided. In the

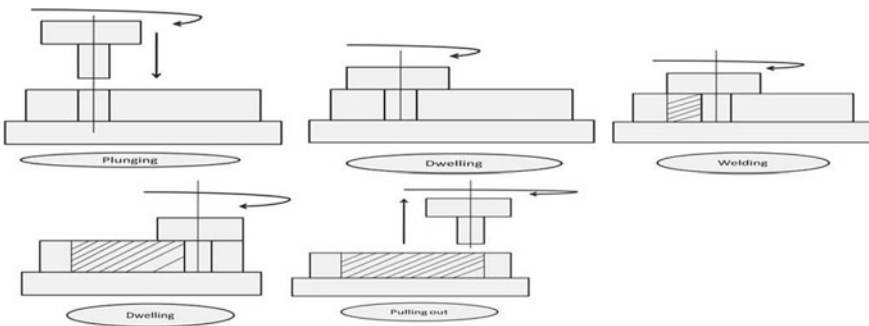
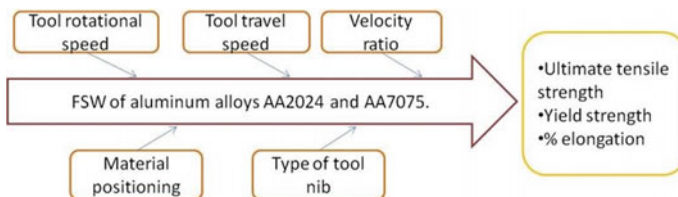


Fig. 2 Different phases of FSW

first phase, the tool is plunged into the workpiece and in order to reduce the vertical force in the  $z$ -direction a pre-technological hole can be made. After the rotating tool has been plunged into the workpieces it stays there for some time and this phase is called dwelling phase. During dwelling phase, there is velocity difference between stationary work pieces and rotating tool heat gets produced by the frictional forces. After producing sufficient heat between the tool and the workpiece third phase, i.e., welding phase starts wherein the tool is traveled along the weld center producing a joint between the base metals [9].

### 3 Parameters Effecting the Welded Joint

Figure 3 shows the parameter effecting FSW process. Heat generated in the course of FSW process is the main factor which controls the mechanical properties of the welded joint formed. Heat generated depends mainly upon the downward pressure or downward normal force acts on the tool and the rotational speed of shoulder and pin. Traveling velocity of the tool determine the rate of heat input and material flow around the tool nib. As the linear velocity ( $v$ ) of the tool increases the heat rate reduces and at a particular location tool spends less time now which gives rise to smaller Stir Zone (SZ) [10]. The positioning of the material also influences the properties of the joint formed. To achieve better results (weld quality) in FSW process of dissimilar metals mainly harder material is put on the advancing side and softer material is put on the retreating side but in case of AA2024 and AA7075 the reverse shows better results [11, 12]. Khodir et al. [10] reported that maximum T.S of the welded joint was obtained when AA2024 (AA7075 is more hard when compared to AA2024) was put on the advancing side. The ratio (velocity ratio) of tool spinning speed and tool traveling speed also influences the welded joint. Devaraju et al. [13] reported that when the velocity ratio increase then microhardness also increases this happens because of more heat input causing softening of the material leading to more intense stirring of the soften metal in the WZ and this results in the grain refinement, ultimate tensile strength and yield strength also improves because of this grain refinement. Tool nib design used also effect the mechanical properties of the joint produced [13].



**Fig. 3** Fish bone diagram representing the cause and its effect on the welded joint

### 4 Macrostructure

Figure 4 shows the macrostructure of the FSW welded dissimilar aluminum alloys AA2024 and AA7075 at different material positioning and linear speed. The 3 zone which are observed under optical microscope are (1) SZ or NZ, (2) TMAZ and (3) HAZ. Stir zone or nugget zone is the area surrounding the weld line where actually stirring of the base material occurs and due to this stirring or mixing the when the weld zone gets solidified onion ring like structure can be observed [10]. It is clear from Fig. 5 that on increasing the welding speed size of the stir zone decreases this happens because on increasing the linear velocity the heat concentration at a particular point will decrease leading to less softening of material which results in reduced stirring of the weld material in the nugget zone. TMAZ is around the NZ on both sides and this TMAZ is surrounded by HAZ. Outside the HAZ there is BM which is the unaffected region. The defects like kissing bond and tunnel defects were reported by Khodir et al. [10] when FSW was performed at high linear velocity keeping AA7075 on AS of the joint. Kissing bond is the descriptive term for two surfaces which are very close to each other but not so close that the majority of the surface irregularities gets deformed sufficiently and form metallic bonds. Depending upon the location and extent of the kissing bond defect the load bearing capacity and fatigue life of the component gets effected [14]. The tunneling defect occurs mainly due to lack of material flow and insufficient heat input [15].

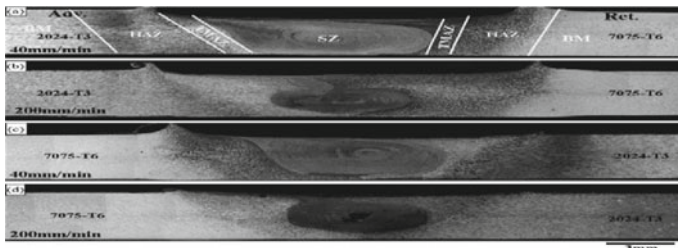


Fig. 4 Macrostructure of FSW dissimilar aluminum alloys AA2024 and AA7075 at different welding position and linear velocity [10]

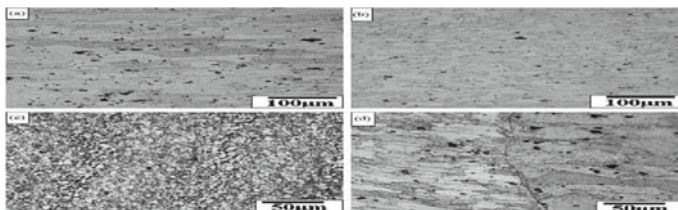


Fig. 5 Microstructure in base metal and stir zone, a base metal AA2024, b base metal AA7075, c onion rings, d kissing bond defect [10]

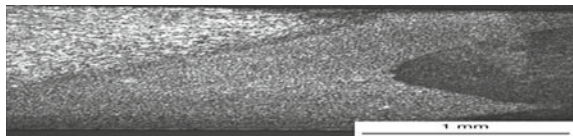
## 5 Microstructure

Figure 5a and b represents microstructure of the BM of AA2024 and AA7075 respectively. The micro-structural grains can be seen elongated in the direction of rolling along with the random distribution of the constituent particles. These random distributed particles are represented by black color in the microstructure and from figure it is also clear that the concentration of the constituent particles are more in the AA2024 side than on the AA7075 side.

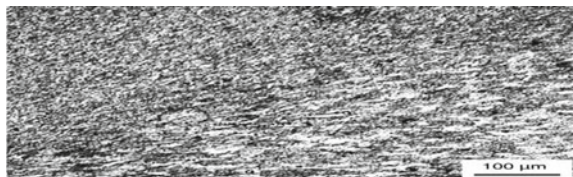
Figure 5c represents microstructure of the onion rings in the stir zone when welding was performed keeping AA2024 on advancing side and at 1.2 mm/s [10]. In the microstructure bands of course and fine grains can be observed and the average sizes of these grains are 5.8 and 4.1  $\mu\text{m}$  [10]. Figure 5d shows the kissing defect when the welding was performed keeping AA2024 on the retreating side, i.e., on the right side kissing crack and at tool travel speed of 3.3 mm/s. The kissing cracks are formed due to inadequate metal flow of the BM or improper acumen of tool nib at the weld root due to insufficient heat generation during the process.

Figure 6 shows the different zone observed in the optical microscope. Due to severe plastic deformation and higher temperature in the SZ at a space of 2 mm from the center of the weld on the AA2024 side fine equiaxed grains formed. In the stir zone of AA7075 side the grains become bigger in dimension and less equiaxed character was observed. In the TMAZ zone due to less heating (low temperature) no recrystallization occurs and so the deformed grains were observed in this region (Fig. 7). At an interval of 4 mm from the center of weld more parent metal grains are observed and this region coincides to HAZ wherein low micro-hardness was observed when compared to that of base metal [17]. Zhang et al. [18] performed FSW of similar and dissimilar AA2024 and AA7075 aluminum alloys of 5 mm thickness at varying speed of 600, 950, 1300, 1650 rpm. It was observed that the size of TMAZ is greater on RS side as compared AS and on increasing the tool rotational speed TMAZ size increases on both sides. Zhang et al. [19] performed quantitative analysis of the FSW AA2024 and AA7075 and it was observed that when the welding speed was reduced from 240 mm/min to 60 mm/min then the average grain size increases from  $2.54 \pm$

**Fig. 6** Microstructure showing SZ, TMAZ and base metal [16]



**Fig. 7** Microstructure showing deformed grains in the TMAZ zone [16]



1.2  $\mu\text{m}$  to  $3.34 \pm 1.8 \mu\text{m}$  this happens because the low tool traverse speed produces high thermal cycle in the NZ.

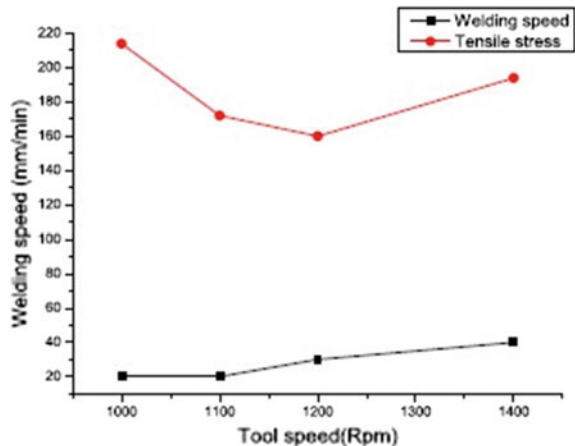
## 6 Mechanical Properties

### 6.1 Tensile Strength

Gowthaman et al. [11] performed the FSW of AA2024 and AA7075 using varying rotational speed and linear speed. The tool spinning speed was diverse in between 1000 to 1400 rpm and similarly the tool traverse speed was diverse in between 20 mm/min to 40 mm/min (Fig. 8). When tool was rotating at speed was 1000 rpm with travel speed was 20 mm/min the maximum tensile and Y.S of about 214.2 MPa and 191.8 MPa were observed. When the graph was plotted then a decrease in tensile strength was observed from 1000 rpm and  $v = 20$  mm/min to 1200 rpm and  $v = 30$  mm/min this is due to the development of fine strengthening precipitates and uniform equiaxed grains in the weld zone [11].

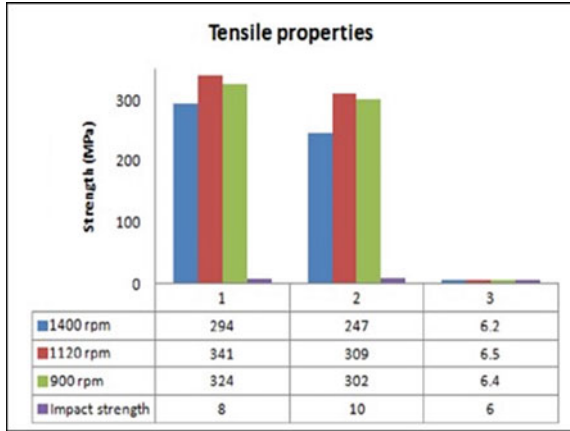
Srinivas et al. [20] reported that on increasing the velocity ratio, i.e., the ration of rotational speed of tool to its travel speed the U.T.S, Y.S and % Elongation increases (Fig. 9) because of increase in the heat generated which is entered into the weld but after a limit as this velocity ratio is increased then the strength of the weld decreases due to matrix softening wherein when the heat generation become more than a particular value then there is dissolution and/or coarsening of the strength giving precipitates in the aluminum matrix [20].

**Fig. 8** Graph showing the variation in tensile strength with linear and rotational velocity [11]



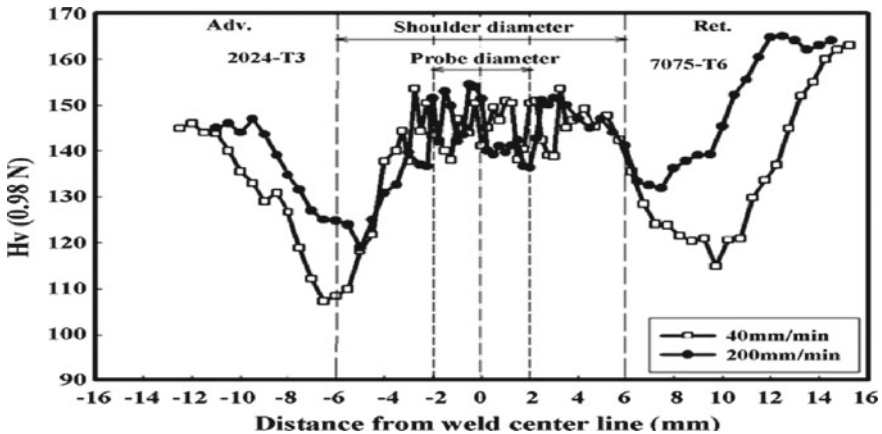


**Fig. 9** Tensile property of the samples of dissimilar welded aluminum alloys at various velocity ratio [20]



### 6.2 Micro-Hardness

Figure 10 represents micro-hardness distribution of AA2024 and AA7075 at 40 and 200 mm/min. The rock bottom value of micro-hardness was noted in the HAZ on the AA2024 side this happens because in HAZ coarsening of precipitates lead to loss in the consistency with the matrix due to changing temperature [10]. On increasing the welding speed, the heat affected zone starts shifting toward the weld center, and this happens because of less heat interaction in the welding zone. The randomness of the hardness value in the stir zone is due to onion ring formation wherein bands of AA2024 (lower hardness) and AA7075 (higher hardness) are formed. Slightly decreased value of the hardness as compared to stir zone is noted in the TMAZ [10].



**Fig. 10** Micro-hardness dissemination on the transversal section of the FSW joint at various tool travel speed [10]

## 7 Conclusion

From the FSW of AA2024 and AA7075 following conclusions can be drawn:

- The location of fracture of all either similar or dissimilar joint coincides with the minimum hardness value in the particular joint.
- The hardness value of both similar or dissimilar joint first increases and then decreases when moved along the weld thickness from top to bottom.
- Under the effect of high strain rate and quasistatic loading yield stress of both AA2024 and AA7075 decreases [21].

## References

1. Vijay, S., Rajanarayanan, S., Ganeshan, G.N.: Analysis on mechanical properties of gas tungsten arc welded dissimilar aluminium alloy (Al2024 & Al6063). *Mater. Today Proc.* **21**, 384–391 (2020). <https://doi.org/10.1016/j.matpr.2019.06.136>
2. Al-Ramahi, N.J.N.: Mechanical properties of MIG joints for dissimilar aluminum alloys (2024–T351 and 6061–T651). *Al-Khwarizmi Eng. J.* **12**, 121–128 (2016)
3. Zhang, D., Zhao, Z., Gao, S., Zhao, H.: Research on CO<sub>2</sub> laser welding with filler wire of dissimilar high strength aluminum alloy 2024 and 7075. In: 2012 Symposium on Photonics Optoelectronics, SOPO 2012, p. 3 (2012). <https://doi.org/10.1109/SOPO.2012.6270445>
4. Hahn, M., Weddeling, C., Taber, G., Vivek, A., Daehn, G.S., Tekkaya, A.E.: Vaporizing foil actuator welding as a competing technology to magnetic pulse welding. *J. Mater. Process. Technol.* **230**, 8–20 (2016). <https://doi.org/10.1016/j.jmatprotec.2015.11.010>
5. Meng, Z., Wang, X., Guo, W., Hu, Z., Vivek, A., Hua, L., Daehn, G.S.: Joining performance and microstructure of the 2024/7075 aluminium alloys welded joints by vaporizing foil actuator welding. *J. Wuhan Univ. Technol. Mater. Sci. Ed.* **34**, 368–372 (2019). <https://doi.org/10.1007/s11595-019-2061-7>
6. Kumar, S., Wu, C.S., Padhy, G.K., Ding, W.: Application of ultrasonic vibrations in welding and metal processing: a status review. *J. Manuf. Process.* **26**, 295–322 (2017). <https://doi.org/10.1016/j.jmapro.2017.02.027>
7. Mishra, R.S., Ma, Z.Y.: Friction stir welding and processing. *Mater. Sci. Eng. R Reports.* **50**, 1–78 (2005). <https://doi.org/10.1016/j.mser.2005.07.001>
8. Meng, X., Huang, Y., Cao, J., Shen, J., dos Santos, J.F.: Recent progress on control strategies for inherent issues in friction stir welding. *Prog. Mater. Sci.* **115**, 100706 (2021). <https://doi.org/10.1016/j.pmatsci.2020.100706>
9. Durdanović, M.B., Mijajlović, M.M., Milčić, D.S., Stamenković, D.S.: Heat generation during friction stir welding process. *Tribol. Ind.* **31**, 8–14 (2009)
10. Khodir, S.A., Shibayanagi, T.: Friction stir welding of dissimilar AA2024 and AA7075 aluminum alloys, *Mater. Sci. Eng. B Solid-State Mater. Adv. Technol.* **148**, 82–87 (2008). <https://doi.org/10.1016/j.mseb.2007.09.024>
11. Gowthaman, P.S., Saravanan, B.A.: Determination of weldability study on mechanical properties of dissimilar Al-alloys using friction stir welding process. *Mater. Today Proc.* (2020). <https://doi.org/10.1016/j.matpr.2020.08.599>
12. Guo, J.F., Chen, H.C., Sun, C.N., Bi, G., Sun, Z., Wei, J.: Friction stir welding of dissimilar materials between AA6061 and AA7075 Al alloys effects of process parameters. *Mater. Des.* **56**, 185–192 (2014). <https://doi.org/10.1016/j.matdes.2013.10.082>
13. Devaraju, M., Manichandra, B., Jeshrun Shalem, M., Manzoor Hussain, M.: Impact on mechanical properties & metallographic of solid state welded 2024 & 7075 Al alloys dissimilar joint

- by varying its parameters. *Mater. Today Proc.* **24**, 937–941 (2020). <https://doi.org/10.1016/j.matpr.2020.04.405>
14. Oosterkamp, A., Oosterkamp, L.D., Nordeide, A.: “Kissing bond” phenomena in solid-state welds of aluminum alloys. *Weld. J. (Miami, Fla)* **83**, 225-S (2004)
  15. Al-Moussawi, M., Smith, A.J.: Defects in friction stir welding of steel. *Metallogr. Microstruct. Anal.* **7**, 194–202 (2018). <https://doi.org/10.1007/s13632-018-0438-1>
  16. Cavaliere, P., Nobile, R., Panella, F.W., Squillace, A.: Mechanical and microstructural behaviour of 2024–7075 aluminium alloy sheets joined by friction stir welding. *Int. J. Mach. Tools Manuf.* **46**, 588–594 (2006). <https://doi.org/10.1016/j.ijmactools.2005.07.010>
  17. Muruganandam, D., Ravikumar, S., Das, S.L.: Mechanical and micro structural behavior of 2024–7075 aluminium alloy plates joined by friction stir welding. In: *Proceedings of International Conference on Frontiers in Automobile and Mechanical Engineering-2010, FAME-2010*, pp. 247–251 (2010). <https://doi.org/10.1109/FAME.2010.5714835>
  18. Zhang, C., Huang, G., Cao, Y., Zhu, Y., Liu, Q.: On the microstructure and mechanical properties of similar and dissimilar AA7075 and AA2024 friction stir welding joints: effect of rotational speed. *J. Manuf. Process.* **37**, 470–487 (2019). <https://doi.org/10.1016/j.jmapro.2018.12.014>
  19. Zhang, C., Huang, G., Liu, Q.: Quantitative analysis of grain structure and texture evolution of dissimilar AA2024/7075 joints manufactured by friction stir welding. *Mater. Today Commun.* **26**, 101920 (2020). <https://doi.org/10.1016/j.mtcomm.2020.101920>
  20. Srinivas, B., Devaraju, A.: Investigation of velocity ratios on mechanical and microstructural characterization of friction stir welded dissimilar 2024 and 7075 aluminium alloy. *Mater. Today Proc.* **5**, 19250–19254 (2018). <https://doi.org/10.1016/j.matpr.2018.06.282>
  21. Chao, Y.J., Wang, Y., Miller, K.W.: Effect of friction stir welding on dynamic properties of AA2024-T3 and AA7075-T7351. *Weld. J. (Miami, Fla)* **80**, 196–200 (2001)

# Observational Exposition of Metal Matrix Composite Aluminum 6069 (Al) Fraction Variance Strengthened with Molybdenum (Mo) and Coconut Shell Ash (CSA)



Fathimunnisa Begum, Sasidhar Gurugubelli , and N. Ravi Kumar

## 1 Introduction

A composite is a material made up of components generated by physically combining pre-existing elements in order to create a new material with unique qualities that differ from those of a monolithic material. This description distinguishes a composite from other multi-phase materials formed by bulk processes where one or more phases are the products of phase transformation. The word matrix and reinforcement are also used. Composites are classified by (a) phase matrix (b) reinforcement.

Various studies have been published on the use of natural fillers in composites such as coconut shell ash, jute, cotton, and rice husk wood as composite reinforcements. Sasidhar et al. [1] experimented with new aluminum 6069 alloy metal matrix composites (MMCs) fortified amid molybdenum and coconut shells for use in automobiles and found that the strength of the tensile was improved by adding molybdenum and coconut ash grains to the aluminum 6069 alloys. Shireesha Y. et. al., studied the mechanical properties of natural fibre reinforced composites and the factors that affect the mechanical properties of natural fiber composites [2, 3]. A new 6069 aluminum alloy for hot and cold extrusion and forging and observed desirable formability, and carried out systematic tensile and impact tests and measurements of hardness on hot forged aluminum metal matrix composites in order to understand the effect of the alloy material and the shaping process on its mechanical properties [4, 5]. Metal matrix composite (MMC) was successfully manufactured using the

---

F. Begum

Department of Mechanical, BABA Institute of Technology, Visakhapatnam, India

S. Gurugubelli (✉)

Department of Mechanical, GMR Institute of Technology, Rajam, India

e-mail: [sasidhar.g@gmrit.edu.in](mailto:sasidhar.g@gmrit.edu.in)

N. Ravi Kumar

Department of Mechanical, MVGR College of Engineering, Vizianagaram, India

aluminum plate and molybdenum powder amid friction Stir process (FSP) to create a surface MMC layer on the Al plate in order to increase the mechanical properties of the Al plate being obtained. Also produced aluminum metal matrix hybrid composite reinforced aluminum 7075 alloy beside silicon carbide (SiC) and aluminum oxide (aluminum) by mixing a casting process is less costly and very effective [6, 7]. Sunil et al. [8] provided a detailed overview of the state of the art in the manufacture of magnesium-based composites by friction stir processing and also discussed the effect of the secondary phase particles and grain refining produced by friction stir processing on the properties of these composites. Zaid et al. [9] examined the impact, by pressing the ECAP process at room temperature, of the addition of molybdenum either solo or in the presence of titanium in commercially pure aluminum. Rebba et al. [10] have reported results of an experimental analysis of the mechanical properties in composite samples of aluminum alloy (Al-2024) reinforced with molybdenum disulfide ( $\text{MOS}_2$ ) powders compared to base alloys. Sapuan et al. [11] investigated the tensile and flexural strengths attributed to epoxy composites based on coconut shell filler particles. Many studies have abided toward the use of other innate fillers in composites in the former, and the coconut shell filler is a possible contender for the production of contemporary composites due to their immense strength and modulus properties. On the basis of these considerations, this research has shown that a new composite is effectively prepared with Al-Mo and coconut shell ash by a stir-casting process, and an analysis of mechanical properties just as hardness and compression strength has been carried out.

## 2 Properties of Materials Used

### 2.1 Aluminum 6069

Aluminum 6069 is considered to be one of the lightest and strongest alloys in the world. It is cheaper and commonly used in automotive engineering today. The alloy has favorable fatigue, stress-corrosion; moreover, Table 1 shows long-term load-cracking properties by cause of a mixture of structure, high strength, thermal and mechanical treating.

**Table 1** Properties of aluminum 6069

Physical properties	Mechanical properties
High strength and less weight	Tensile strength—400 Mpa
Easily machined and recycled	Compression strength—495 N/mm <sup>2</sup>
Excellent corrosion property	Density—2.72 g/cm <sup>3</sup>
Good thermal and electrical conductivity	Melting point—660 °C

**Table 2** Properties of molybdenum

Physical properties	Mechanical properties
Highest melting temperature	Tensile strength—324 Mpa
More resistant to corrosion	Compression strength—400 N/mm <sup>2</sup>
Low thermal expansion	Density—10.22 g/cm <sup>3</sup>
Good thermal and electrical conductivity	Melting point—2623 °C

## 2.2 Molybdenum

Molybdenum can only be found in different oxidation states in materials. Molybdenum is a silver-gray metal in its pure form. It is the 42nd largest element in the universe. Most high-resistance steel alloys comprise molybdenum from 0.28 to 8%. The following Table 2 contains a list of all molybdenum attributes.

## 2.3 Coconut Shell Ash

Coconut shell ash is agricultural waste and is commonly available in tropical countries around the world, such as India. This waste utilization would not only be economical but may also result in environmental pollution control. In black smithy, coconut shell can be used as fuel material in their casting and forging operations. In this work, coconut shell ash having a density of 1.6 g/cm<sup>3</sup> is used, and it is having some good properties like good tensile strength and hardness.

# 3 Fabrication of Aluminum 6069 with Molybdenum and Coconut Shell Ash Reinforced

Several steps in aluminum 6069 fabrication have been discussed below.

## 3.1 Stir Casting

Casting is the mechanism by that molten metal is transferred to a mold and can solidify into an object. The resulting entity is also called a casting, see Fig. 1.

Keep the aluminum 6069 alloy in the crucible and heat up to its melting point 650 °C. Add coconut shell and molybdenum reinforcement material to the alloy based on the composition and stir well for uniform distribution of element in the furnace.

**Fig. 1** Image of the stir casting process



### **3.2 Melting and Streaming**

Melting is the preparedness and transition from a solid to a liquid state of the metal into a furnace. In a ladle, it is then forced into the mold region of the foundry and then poured into the molds shown in Fig. 2.

The molds are vibrated after the metal is solidified, which is called a shakeout process where sand is removed from the casting. By stir casting method, the aluminum metal matrix composite has been prepared. We used 4000 gm of commercially available aluminum alloy for this. In the resistance furnace, the commercially pure aluminum 6069 alloy was melted. It increased the temperature of the melt to 700 °C. At an impeller speed of 200 rpm, the stirring was sustained about 5 and 7 min. During the addition of reinforcement materials, the melt temperature was held at 700 °C. The melt was poured into the sand molds prepared earlier with reinforced particulates.

## **4 Methodology**

The main intent of the present work is toward strengthening the aluminum fusion particles by adding molybdenum and coconut shell ash to the liquid base metal. In the first part of the work, an attempt is made to prepare the composites and to classify

**Fig. 2** Melting and streaming process for compression test





**Fig. 3** Shows **a** specimens before compression test, **b** specimens after compression test

them by identifying the different compounds that have been produced in the matrix. The physical and mechanical properties of the composites are stated in the Sect. 2.

#### ***4.1 Experiment on Compression Test***

The compression test shall assess the characteristics of the materials under crushing loads. The most widely used compression test is one of all mechanical tests. As per ASTM E-9, the ends of the specimen are fixed to the grips attached to the straining device and to the load measuring device in this test. If the applied load is small enough the compression of any solid body is completely reduced and the solid can return to its original state as soon as the load is removed. However, if the load is too high, the material may be permanently compressed. Specimens before and after compression test were shown in the Fig. 3a and b.

#### ***4.2 Experiment on Hardness Test***

This test method involves determining the hardness of Brinell metallic materials using the Brinell indentation hardness theory. The Brinell method applies a predetermined test charge to a fixed diameter carbide ball that is retained and removed for a predetermined period of time. The resulting impression is generally measured in at least two diameters at the right angles, and the results are summed. The indent size (see Fig. 4) is optically determined by the calculation of two diagonals of the circular indent with a compact, or integrated, microscope.



**Fig. 4** Ball indentations of Brinell hardness test on Al composite specimen



## 5 Results and Discussions

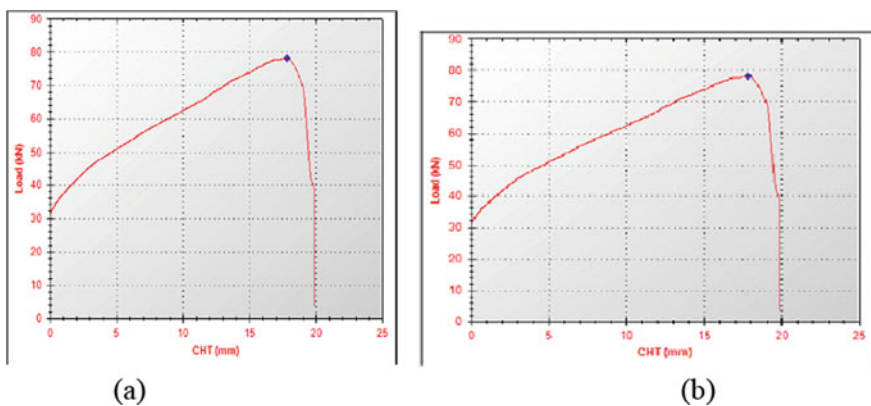
### 5.1 Compression Test Results

The following tabular and graphical results will show the effect of coconut shell ash on compression strength of aluminum composite.

The graphs shown in Fig. 5 and Tables 3 and 4 show that as coconut shell ash increases, compression strength also increases gradually while 1% of molybdenum kept constant. Higher compression strength of 994.274 N/mm<sup>2</sup> was observed at composition 95% Al, 1% Mo, 4% CSA compared to other compositions.

The following tabular and photographs will also try to show the effect of molybdenum on the compression strength of aluminum composites.

The graphs shown in Fig. 6 and Tables 3 and 5 show that as molybdenum content increases, compression strength also increases gradually while 1% of coconut shell



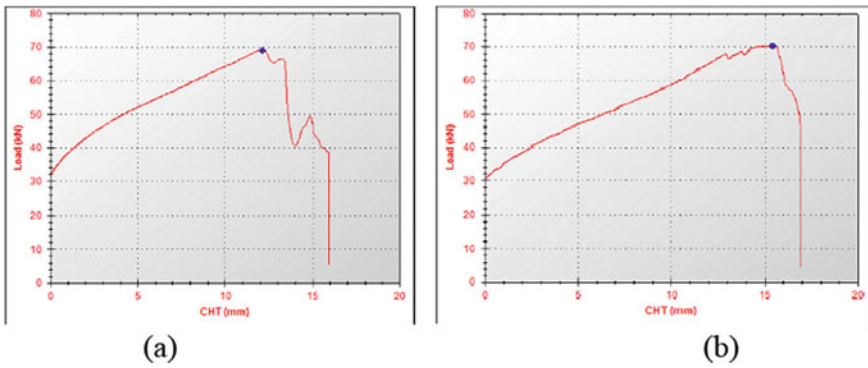
**Fig. 5** Graph of load versus elongation **a** at composition (97% Al, 1% Mo, 2% CSA) and **b** at composition (95% Al, 1% Mo, 4% CSA)

**Table 3** Input data for Compression test of the different compositions of Al, Mo, and CSA

Input data	
Specimen shape	Solid round
Specimen type	Aluminum
Specimen diameter	13 mm
Initial guage length for % elongation	62.5 mm
Specimen cross section area	132.73 mm <sup>2</sup>
Final specimen diameter	11 mm
Final guage length	70 mm
Final area	95.03 mm <sup>2</sup>

**Table 4** Shows at 1% Mo the compression strength of different compositions of Al versus CSA

Observations	Composition	
	97% Al, 1% Mo, 2% CSA	95% Al, 1% Mo, 4% CSA
Load at peak (kN)	69.420	78.090
Compression strength (N/mm <sup>2</sup> )	883.884	994.274



**Fig. 6** Graph of load versus elongation, **a** at composition (95% Al, 4% Mo, 1% CSA) and **b** at composition (93% Al, 6% Mo, 1% CSA)

**Table 5** Shows at 1% CSA the compression strength of different compositions of Al versus Mo

Observations	Composition		
	97% Al, 2% Mo, 1% CSA	95% Al, 4% Mo, 1% CSA	93% Al, 6% Mo, 1% CSA
Load at peak (kN)	56.910	68.940	70.230
Compression strength (N/mm <sup>2</sup> )	724.601	877.772	894.197

**Table 6** Shows hardness test results for different compositions and loads

Composite samples	Hardness (BHNs) at 400 kgf Load	Hardness (BHNs) at 600 kgf Load	Hardness (BHNs) at 800 Kgf Load
97% Al + 1% Mo + 2% CSA	23.80	28.51	30.89
95% Al + 1% Mo + 4% CSA	30.5	35.3	38.01
95% Al + 4% Mo + 1% CSA	30.5	28.51	30.89
93% Al + 6% Mo + 1% CSA	27.53	28.51	30.89

ash kept constant. Higher compression strength of 894.197 N/mm<sup>2</sup> was observed at composition 93% Al, 6% Mo, 1% CSA composition compared to other compositions.

## 5.2 Hardness Test Results

The Brinell hardness test machine was used to calculate the hardness. The load applied on Brinell hardness test were 400, 600, and 800 kgf at dwell time 15 s for each sample.

The result of Brinell hardness test for alloy without reinforcement (aluminum 6069) and the wt% variation of reinforcements such as molybdenum and coconut shell ash of various compositions are given in Table 6.

## 6 Conclusions

MMCs strengthened by molybdenum powder and coconut shell ash particles derived from aluminum 6069 were successfully prepared using the method of stir casting to examine compression strength. The hardness of various composition of aluminum composites specimen were tested and observed that the hardness increases with coconut shell ash content increased. Also, the compression strength of the specimen increased by increasing coconut shell ash and molybdenum percentage to the aluminum alloy. High compression strength is obtained at composition 95% Al, 4% CSA, 1% Mo. The results show that the composite metal matrix with a composition of 95% Al, 1% Mo, 4% CSA is best suited in the automotive industry as the use of aluminum is higher.

## References

1. Gurugubelli, S., Begum, F., Prasad, L.S.V.: Experimental tensile strength characterization of metal matrix composite aluminum-6069 percentage variation reinforced with molybdenum and coconut shell ash. *Int. J. Sci. Technol. Res.* **9**(2), 803–808 (2020)
2. Rambabu, P., Eswara Prasad, N., Kutumba Rao, V.V., Wanhill, R.J.H.: Aluminium alloys for aerospace applications. In: *Aerospace Materials and Material Technologies*, Indian Institute of Metals Series, pp. 29–52. Springer, Singapore (2017).
3. Shireesha, Y., Nandipati, G., Chandaka, K.: Properties of hybrid composites and its applications—a brief review. *Int. J. Sci. Technol. Res.* **8**(8), 335–341 (2019)
4. Bergsma, S.C., Kassner, M.E., Li, X., Wall, M.A.: Strengthening in the new aluminum alloy AA 6069. *Mater. Sci. Eng. A* **254**(1–2), 112–118 (1998)
5. Narayan, S., Rajeshkannan, A.: Hardness, tensile and impact behaviour of hot forged aluminium metal matrix composites. *J. Mater. Res. Technol.* **6**(3), 213–219 (2017)
6. Arora, Astarita, A., Boccarussob, L., Mahesh, V.P.: Experimental characterization of metal matrix composite with aluminium matrix and molybdenum powders as reinforcement. *Procedia Eng.* **167**, 245–251 (2016)
7. Rajesh, A.M., Kaleemulla, M.: Experimental investigations on mechanical behavior of aluminium metal matrix composites. In: *IOP Conference Series: Materials Science and Engineering*, p. 149. IOP Publishing, Bangalore, India (2016)
8. Ratna Sunil, B., Pradeep Kumar Reddy, G., Patle, H., Dumpala, R.: Magnesium based surface metal matrix composites by friction stir processing. *J. Magnes. Alloys* **4**(1), 52–61 (2016).
9. Zaid, A.I.O., Atieh, A.M.: Effect of molybdenum addition on aluminium grain refined by titanium on its metallurgical and mechanical characteristics in the as cast condition and after pressing by the equal angular channel process. In: *IOP Conference Series: Materials Science and Engineering*, vol. 60, pp. 23–27. IOP Publishing, Pakistan (2013)
10. Rebba, B., Ramanaiah, N.: Evaluation of mechanical properties of aluminium alloy (Al-2024) reinforced with molybdenum disulphide ( $\text{MOS}_2$ ) metal matrix composites. *Procedia Mater. Sci.* **6**, 1161–1169 (2014)
11. Sapuan, S.M., Harimi, M.: Mechanical properties of epoxy/coconut shell filler particle composites. *Arab. J. Sci. Eng.* **8**(2), 171–181 (2003)

# Recent Advances in Machining of Composites and Super Alloys by Using Wire-EDM. A Review



Tariq Ahmad , Noor Zaman Khan, Babar Ahmad, and Annayath Maqbool

## 1 Introduction

### 1.1 Composites

Aluminum-based composites possess low density and high strength which makes them suitable for wide range of industrial applications [1, 2]. Metal matrix composites (MMC) must have at least two constituent parts, i.e., one constituent is metal and other can be metal or non-metal. Matrix is usually a lighter metal like aluminum, which exhibits capability to support reinforcement. Further, particles or fiber could also be as reinforcement. MMC's are being widely used in many industrial sectors due to various desirable properties such as better tribological and corrosion behavior, high strength, wear resistance, low thermal coefficient, good mechanical properties at elevated temperature but they possess poor machinability [3–5]. The composite materials are suitable for nuclear power plants as well [6]. The classification of composites materials is shown in Fig. 1 [7].

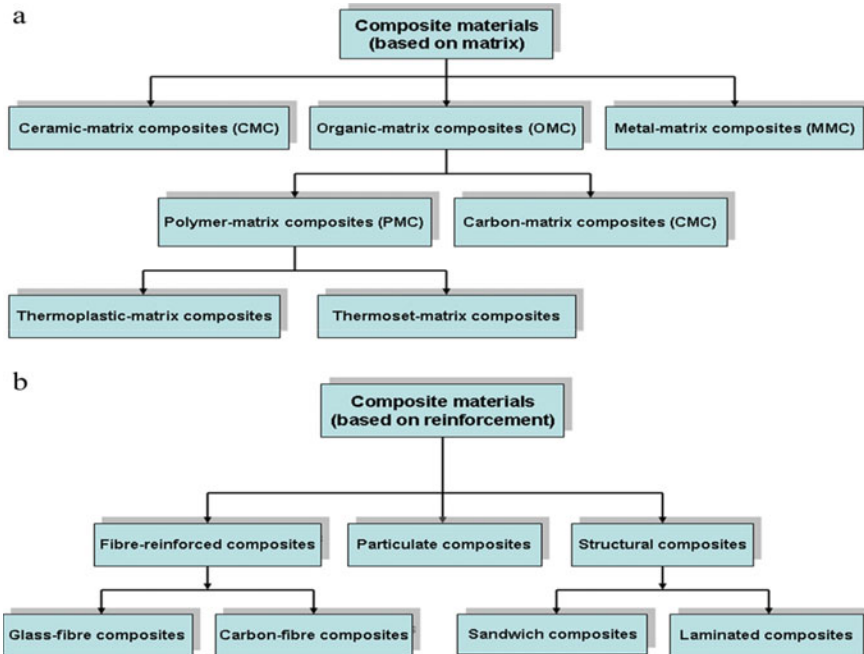
The reason of poor machinability of composite materials is the presence of hard reinforcement particle which cause hindrances while machining which in turn increases tool wear. Machining of MMCs is very difficult by using conventional machining processes. [4, 8]. To fulfill this gap non-conventional machining technique got more importance, among them wire electrical discharge machining (WEDM) is best suited for giving better machining profiles in composite materials [8]. WEDM is non-contact machining process and can machine any conducting material regardless of hardness and strength of the material being machined [9]. In order to achieve better machining performance, various mathematical models and statistical models

---

T. Ahmad (✉) · N. Z. Khan · B. Ahmad · A. Maqbool

Department of Mechanical Engineering, National Institute of Technology, Srinagar, Jammu and Kashmir, India

e-mail: [tariq\\_31phd19@nitsri.net](mailto:tariq_31phd19@nitsri.net)



**Fig. 1** Classification of composites, **a** based on matrix **b** based on reinforcement [7]

are used by researchers to establish the relation between process parameters and response variables [10].

## 1.2 Super Alloys

One of the best materials used in last few decades for high temperature application is super alloy. Super alloys show better performance in high temperature applications like jet and rocket engines where the temperature reaches around 12,000 °C to 14,000 °C [11]. Nimonic super alloys possess high specific strength and thereby used in various aero engine components [12]. The chemical composition of Nimonic super alloys is 38–76% nickel, 27% chromium and 20% cobalt, and some more components are needed such as tungsten (W), tantalum (Ta) and Molybdenum (Mo) to enhance its properties [13]. Super alloys are classified as in Fig. 2 [14]. Inconel 718 is age-hardened nickel–chromium-based super alloy having better mechanical and tribological properties and retains its mechanical properties in the range of  $-423$  °F to 1300 °F. It also exhibits good weldability to resist with post-weld cracks. Inconel 718 is difficult to be machined by conventional processes. To efficiently machine such alloys, non-conventional machining process needs to be adopted, and WEDM is generally preferred to machine high strength super alloys [15].

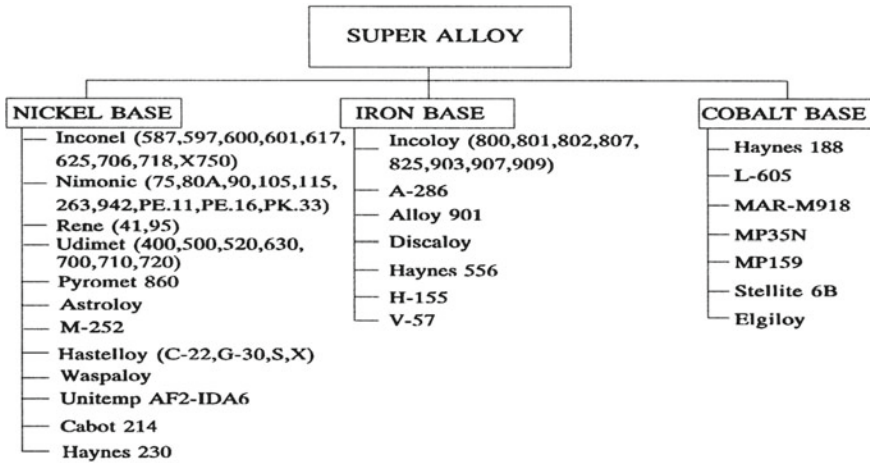


Fig. 2 Classification of super alloys [14]

Titanium-based alloys exhibit good mechanical properties like creep resistance, fatigue strength, wear resistance, functional and structural strength at elevated temperature and are thereby used in multiple applications like aerospace, ballistics, machine components, automobiles. Due to its cost, it should be handled with great effort and processing like fabrication, machining operations must be chosen carefully. WEDM is an easy and economical machining process to machine any grade of super alloys and titanium alloys [16].

## 2 Literature Survey

See Table 1.

## 3 Latest Techniques for Machining Composites and Super Alloys Using WEDM

WEDM comprises number of response variables and among them material removal rate (MRR) and surface roughness (Ra) are important that affect the productivity and surface texture of manufacturing components. From the literature survey, it is clear that most of the research has been done on MRR and Ra. The MRR refers to the amount of material removal which depends upon polarity of wire electrode as well. Higher MRR is attained by the negative polarity of wire electrode and positive polarity of work piece.

**Table 1** Recent studies on composites and super alloys, using WEDM

Investigator	Work material, machining process and method used	Process/input parameters	Response/output variables	Research finding
Kumar et al. [17]	Al-SiC-B <sub>4</sub> C composites, WEDM	Current (12Ae20A), pulse on time (100mse120 ms), wire feed (6 mm/m and 10 mm/m) and composition of B <sub>4</sub> C w%	(RSM), kerf width & cutting speed	RSM method was used which gives current = 20 A, POT = 108.6 ms, B <sub>4</sub> C = 5.65% & wire feed rate = 10 mm/min as significant parameters. Also, gives kerf = 0.271 mm & max cutting speed = 4.76 mm/min
Manikandan et al. [18]	Incoloy 825, 603XL,600, Monel K400 super alloy, WEDM, SEM	POT, voltage, PFT, wire feed and mean current	Perpendicularity, straightness and Ra	Monel K400 produced better significance over other super alloys
Vellingiri et al. [19]	LM13 and LM13/SiC alloys, WEDM	POT, PFT and Current	MRR and Ra	Better hardness and tensile strength, POT (30–40 ms), PFT (4–10 ms) and current (I <sub>p</sub> , 1–3 A) for better MRR and Ra
Sing et al. [20]	AA7075/SiC, WEDM, Fuzzy logic modeling	POT, PFT and Peak Current	MRR and Ra	Influencing parameters for AA7075 + 5wt%SiC, POT for Ra. PFT for MRR. And Influencing parameters for AA7075, PFT for Ra and peak current for MRR
Kavimani et al. [21]	AZ31 + (0.2–0.4) %r-GO@ (10–30) % SiC, WEDM	POT, PFT, Wire Feed Rate	MRR and Ra	POT increases Ra, Hybrid technique can be used

(continued)



**Table 1** (continued)

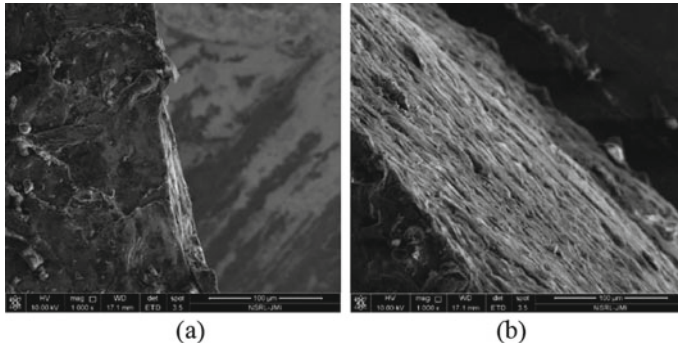
Investigator	Work material, machining process and method used	Process/input parameters	Response/output variables	Research finding
He et al. [22]	2D C/SiC Composite, WEDM	POT, PFT and No. of tubes	Mach. speed (Cs) and Ra	Fibber orientation has got more significant effect on the Ra than machining speed
Ishfaq et al. [23]	SS316 and mild steel, WEDM	WP orientation, hight of one layer, voltage of servo, PON, wire dia, wire feed and pressure ratio	Spark gap	Wire dia. and pressure ratio contribute 71% and 16%, respectively, to the spark gap
Sing et al. [24]	MWCNT alumina composites, WEDM, SEM	POT, Peak current, Wire speed	Ra and MRR	MRR increases with POT, current. Wire speed also influences
Sing et al. [24]	MWCNT alumina composites	POT, Peak current, Wire speed	Allowance	Multi-pass WEDM shows steep decrease in surface roughness
Nain et al. [25]	Aeronautics super alloy, WEDM, Fuzzy logic and BP-ANN	POT, PFT, IP, SV, WT and WF	Ra and waviness	The variable POT, interaction between POT and PFT, wire tension and spark gap voltage have influenced Ra. The waviness is influenced greatly by POT and PFT and spark gap voltage
Goyal Ashish [26]	Inconel 625 super alloy, WEDM, SEM, TAGUCHI & ANOVA	Tool electrode, current intensity, POT, PFT, wire feed and tension	Ra and MRR	POT, electrode and current are the input parameters affecting Ra and MRR
Yusoff et al. [27]	Ti-48Al intermetallic alloys, WEDM, ANN & multi-GA	POT, PFT, feed rate, peak current and servo voltage	MRR, Ra, Vc and Dk	The approach, OrthoANN, reduced ANN experimentation time and optimization by integrated with multi-GA

(continued)

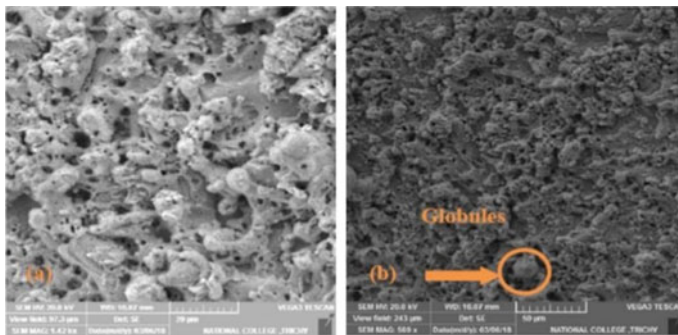
**Table 1** (continued)

Investigator	Work material, machining process and method used	Process/input parameters	Response/output variables	Research finding
Mandal et al. [28]	Nimonic C 263, WEDM	R- cut, F- cut, Grinding & post Grinding	Ra, Rz, Rt and Rsk	The average Ra is as minimum as 0.024 $\mu\text{m}$ after recast layer, and new surface is generated along with compressive residual stress 500 MPa
Garg et al. [29]	Nickel-based super alloys, WEDM & RSM	POT, PFT, spark gap voltage & wire feed	Cutting speed, gap current and Ra	Significant parameters are POT and PFT, with minimum spark gap voltage, and wire feed is insignificant
Nain et al. [30]	Udimet-L605 super alloy, WEDM, Taguchi, GRA	POT, PFT, Peak current, Spark gap voltage, Wire tension and feed	MRR and Ra	Spark- gap voltage, POT, interaction POT x PFT and wire tension are optimum variable for Ra while POT, spark gap voltage and PFT are optimum variables for MRR

To increase MRR, the discharge current should be increased. Surface roughness (Ra) is one of the parameters of surface integrity and it depends on the type of contact friction, deformation and accuracy. The machined component should have good surface quality for mainstream applications. Figure 3a and b shows the SEM image of machined composite material by WEDM and illustrates the 3D-Topography of machined surfaces. Figure 4 shows SEM images of the WEDMed surfaces of super alloy Monel K400 [14]. Among various unconventional machining techniques, WEDM is most preferred one and plays the vital role in machining of complex shape, precision shape components, intricate shapes, making dies, micromachining, etc. The major challenge for researchers now a days is the efficient machining of high temperature composite materials and super alloys. Various researchers concluded that the WEDM process parameters which significantly affect the machining performance during machining of super alloys and composites materials are (POT), (PFT), servo voltage and peak current. For better machining performance, these process parameters need to be optimized to obtain desired surface integrity, MRR and kerf.



**Fig. 3** a SEM image of WEDM machined edge. b SEM image of WEDM machined surface



**Fig. 4** SEM image of WEDMed surface of Monel K400 [18]

## 4 Conclusions and Future Scope

The machining of composites materials and super alloys is difficult by using conventional methods and this arises the need of non-conventional machining methods. One of the most convenient machining processes for precise machining of composite materials and super alloys is Wire electric discharge machining. WEDM is an efficient process for precise and micro level machining of composites and super alloys. Literature reveals that the WEDM process parameters significantly affect the surface integrity/roughness, MRR and kerf during machining of super alloys and composites materials. The process parameters which significantly affect the machining performance are (POT), (PFT), servo voltage and peak current. As per this study these process parameters need to be optimized to obtain desired productivity and quality of the machined component.

In future machining of insulating composites and ceramics can be done on WEDM. Furthermore, surface quality can be enhanced along with high temperature machining performance.

## References

1. Zhou, W., Xu, Z.M.: Casting of SiC reinforced metal matrix composites. *J. Mater. Process. Technol.* **63**, 358–363 (1997)
2. Ahamed, A.R., Asokan, P., Aravindan, S., Prakash, M.K.: Drilling of hybrid Al-5%SiCp-5%B4Cp metal matrix composites. *Int. J. Adv. Manuf. Technol.* **49**, 871–877 (2010). <https://doi.org/10.1007/s00170-009-2453-5>
3. Gore, A.S., Patil, N.G.: Wire electro discharge machining of metal matrix composites: a review. *Procedia Manuf.* **20**, 41–52 (2018)
4. Rahul, Datta, S., Biswal, B.B., Mahapatra, S.S.: Machinability analysis of Inconel 601, 625, 718 and 825 during electro-discharge machining: on evaluation of optimal parameters setting. *Meas. J. Int. Meas. Confed.* **137**, 382–400 (2019)
5. Azimi, A., Shokuhfar, A., Nejadseyfi, O.: Mechanically alloyed Al7075-TiC nanocomposite: powder processing, consolidation and mechanical strength. *Mater. Des.* **66**, 137–141 (2015). <https://doi.org/10.1016/j.matdes.2014.10.046>
6. Kalaiselvan, K., Murugan, N., Parameswaran, S.: Production and characterization of AA6061-B4C stir cast composite. *Mater. Des.* **32**, 4004–4009 (2011)
7. Yang, Y., Boom, R., Irion, B., van Heerden, D.J., Kuiper, P., de Wit, H.: Recycling of composite materials. *Chem. Eng. Process. Process Intensif.* **51**, 53–68 (2012)
8. Kumar, R., Sahoo, A.K., Mishra, P.C., Das, R.K.: Measurement and machinability study under environmentally conscious spray impingement cooling assisted machining. *Meas. J. Int. Meas. Confed.* **135**, 913–927 (2019)
9. Saini, V.K., Khan, Z.A., Siddiquee, A.N.: Optimization of wire electric discharge machining of composite material (Al6061/SiCp) using Taguchi Method. *Int. J. Mech. Prod. Eng.* **2**, 2315–4489 (2013)
10. Sivaiah, P., Chakradhar, D.: Performance improvement of cryogenic turning process during machining of 17–4 PH stainless steel using multi objective optimization techniques. *Meas. J. Int. Meas. Confed.* **136**, 326–336 (2019)
11. Koli, D.K., Agnihotri, G., Purohit, R.: Advanced aluminium matrix composites: the critical need of automotive and aerospace engineering fields. *Mater. Today Proc.* 3032–3041 (2015). <https://doi.org/10.1016/j.matpr.2015.07.290>
12. Ezugwu, E.O.: Key improvements in the machining of difficult-to-cut aerospace superalloys. *Int. J. Mach. Tools Manuf.* **45**, 1353–1367 (2005)
13. Shinde, M.Y., Raut, T.G.: A review on optimization of machining parameters in EDM. *Int. J. Innov. Res. Sci. Eng. Technol.* **04**, 893–896 (2015)
14. Choudhury, I.A., El-Baradie, M.A.: Machinability of nickel-base super alloys: a general review. *J. Mater. Process. Technol.* **77**, 278–284 (1998)
15. Rahul, Srivastava, A., Kumar Mishra, D., Chatterjee, S., Datta, S., Bhusan Biswal, B., Sankar Mahapatra, S.: Multi-response optimization during electro-discharge machining of super alloy Inconel 718: application of PCA-TOPSIS. *Mater. Today Proc.* 4269–4276 (2018)
16. Maurya, R., Porwal, R.K., Singh, R.: Concerning drifts to optimization techniques of wire-EDM process for titanium based super alloys: a review. *Mater. Today Proc.* **18**, 4509–4514 (2019). <https://doi.org/10.1016/j.matpr.2019.07.421>
17. Kumar, S.S., Erdemir, F., Varol, T., Kumaran, S.T., Uthayakumar, M., Canakci, A.: Investigation of WEDM process parameters of Al–SiC–B4C composites using response surface methodology. *Int. J. Light. Mater. Manuf.* **3**, 127–135 (2020)
18. Manikandan, K., Ranjith Kumar, P., Raj Kumar, D., Palanikumar, K.: Machinability evaluation and comparison of Incoloy 825, Inconel 603 XL, Monel K400 and Inconel 600 super alloys in wire electrical discharge machining. *J. Mater. Res. Technol.* **9**, 12260–12272 (2020)
19. Vellingiri, S., Soundararajan, R., Mohankumar, N., Nithyananthakumar, K., Muthuselvam, K.: Exploration on WEDM process parameters effect on LM13 alloy and LM13/SiC composites using Taguchi method. *Mater. Today Proc.* (2020)
20. Singh, A.K., Roy, K., Das, S., Das, S.: WEDM investigation and fuzzy logic modelling of AA7075/SiC metal matrix composites. *Mater. Today Proc.* **26**, 1988–1994 (2019)

21. Kavimani, V., Soorya Prakash, K., Thankachan, T.: Multi-objective optimization in WEDM process of graphene—SiC-magnesium composite through hybrid techniques. *Meas. J. Int. Meas. Confed.* **145**, 335–349 (2019)
22. He, W., He, S., Du, J., Ming, W., Ma, J., Cao, Y., Li, X.: Fiber orientations effect on process performance for wire cut electrical discharge machining (WEDM) of 2D C/SiC composite. *Int. J. Adv. Manuf. Technol.* **102**, 507–518 (2019)
23. Ishfaq, K., Ahmed, N., Mufti, N.A., Pervaiz, S.: Exploring the contribution of unconventional parameters on spark gap formation and its minimization during WEDM of layered composite. *Int. J. Adv. Manuf. Technol.* **102**, 1659–1669 (2019)
24. Singh, M.A., Sarma, D.K., Hanzel, O., Sedláček, J., Šajgalík, P.: Surface characteristics enhancement of MWCNT alumina composites using multi-pass WEDM process. *J. Eur. Ceram. Soc.* **38**, 4035–4042 (2018)
25. Nain, S.S., Sihag, P., Luthra, S.: Performance evaluation of fuzzy-logic and BP-ANN methods for WEDM of aeronautics super alloy. *MethodsX.* **5**, 890–908 (2018)
26. Goyal, A.: Investigation of material removal rate and surface roughness during wire electrical discharge machining (WEDM) of Inconel 625 super alloy by cryogenic treated tool electrode. *J. King Saud Univ. Sci.* **29**, 528–535 (2017)
27. Yusoff, Y., Zain, A.M., Amrin, A., Sharif, S., Haron, H., Sallehuddin, R.: Orthogonal based ANN and multiGA for optimization on WEDM of Ti–48Al intermetallic alloys. *Artif. Intell. Rev.* **52**, 671–706 (2019)
28. Mandal, A., Dixit, A.R., Chattopadhyaya, S., Paramanik, A., Hloch, S., Królczyk, G.: Improvement of surface integrity of Nimonic C 263 super alloy produced by WEDM through various post-processing techniques. *Int. J. Adv. Manuf. Technol.* **93**, 433–443 (2017)
29. Garg, M.P., Kumar, A., Sahu, C.K.: Mathematical modeling and analysis of WEDM machining parameters of nickel-based super alloy using response surface methodology. *Sadhana Acad. Proc. Eng. Sci.* **42**, 981–1005 (2017)
30. Nain, S.S., Garg, D., Kumar, S.: Modeling and optimization of process variables of wire-cut electric discharge machining of super alloy Udimet-L605. *Eng. Sci. Technol. Int. J.* **20**, 247–264 (2017)

# Effect of Buffer Layer on Crack Susceptibility, Mechanical and Microstructural Properties of Ni Hard Coatings



Nikhil Thawari, Nikhil Chaubey, Aayush Chandak, and T. V. K. Gupta

## 1 Introduction

Laser cladding process is a hard coating technique being widely used due to its potential in material processing such as high-value component repair, metallic coating, small volume production and prototyping [1]. The process uses laser as a heat source which creates a melt pool over the substrate producing a hard-coated/deposited layer [2] as shown in Fig. 1. There are two ways of powder feeding in this process, i.e. pre-placed and co-axial, where co-axial feeding is commonly used that can provide uniform flow to the laser source creating a uniform deposition. Some of the advantages of laser cladding are less dilution, minimum distortion and heat-affected zone (HAZ), low heat input to the substrate, higher accuracy, etc. [3, 4]. The process is primarily used for refurbishment and rebuilding of worn-out parts and make them sustainable to work in harsh environments and perform their function at a satisfactory level to enhance the component service life [5–7]. Nickel-based alloys are widely deposited with laser cladding to produce high heat resistant coatings. N480 and N9062 are specialized Ni-based alloys, where N480 possesses medium hardness (500HV), good abrasion and corrosion resistance with a reasonable impact resistance, and N9062 has higher hardness (750HV), excellent abrasion resistance, low ductility which provides low impact resistance. Both the coatings are better for wear and corrosion resistance applications. Whereas, the deposition of these hard coatings by laser cladding generates cracks, dilution and residual stresses because of which extensive research is in progress to minimize these problems [8–11].

---

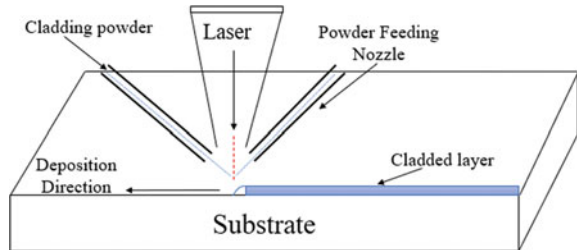
N. Thawari · N. Chaubey · T. V. K. Gupta (✉)

Mechanical Engineering, Visvesvaraya National Institute of Technology, Nagpur 440010, India  
e-mail: [tvkgupta@mec.vnit.ac.in](mailto:tvkgupta@mec.vnit.ac.in)

A. Chandak

Shreenath Engineering Industries, MIDC-Higna, Nagpur 440016, India  
e-mail: [aayush.chandak@shreenath-industries.com](mailto:aayush.chandak@shreenath-industries.com)

**Fig. 1** Laser cladding process



Stanciu et al. [12] deposited a dual coating of NiCrBSi with Inconel718 as buffer layer using laser cladding and reported that crack susceptibility of the top layer is reduced since the compressive stresses are reduced with uniform heat distribution. Also, a significant increase in hardness with 7% increase in wear resistance and 20% in corrosion resistance are claimed. Another study on crack behaviour of composite coating of Ni-based WC by Zhou et al. [13] revealed dissolution of cladded particles is minimized at high scanning speeds and the increased preheating reduced the temperature gradients to obtain crack-free cladding. Wang et al. [14] investigated the crack susceptibility and microstructural behaviour of  $V_2O_5$ /NiCrBSi alloys and observed that the thermal stresses govern the crack occurrence. Also, Doliveira et al. [15] found that buffer layer addition in multilayer cladding reduces the tensile residual stresses which may lead to early failure of the component. Thawari et al. [16] added Inconel 625 as buffer layer while cladding Stellite 6 and observed higher hardness and wear resistance as compared to direct Stellite 6 deposition. Also, cladding on Fe-based substrate, dilution of Fe elements increases the rise of crack formation and also deteriorates the mechanical and microstructural properties of the coating [17, 18].

The literature proposed different methods to minimize the crack susceptibility of hard coatings where the substrate was pre-heated to reduce the crack formation [19–21], while this method can only be recommended if the coefficient of thermal expansion of the cladding material and substrate is not vastly different. Reports also revealed that addition of buffer layer reduces the crack formation, also enhances the mechanical and microstructural properties of different hard coatings, showing improved results than the direct deposition. Despite this research reported, no study was available on buffer layer addition in cladding of Ni-based hard alloys. To fill this gap and investigate the role of buffer layer addition, an attempt was made by cladding Inconel 625 between the substrate and Ni-based alloys to reduce the crack susceptibility, dilution and enhance the properties of N480 and N960 coatings. It was found that buffer layer plays a vital role in reducing the possibility of crack formation and reduced substrate element diffusion into the hard-deposited layers.

**Table 1** Chemical composition (% by weight)

Material	Ni	Cr	B	Si	C	Fe	Mo	Cu	W	Co	Nb	Others
Inconel 625	58.0	20–23	–	–	–	5.0	8–10	–	–	1	3.15	2–5
N480	39.8	13.0	2.5	3.4	0.45	4.5	5.9	1.36	29.0	–	–	–
N9062	72.4	15.5	2.9	4.3	0.7	4.2	–	–	–	–	–	–
SS410	–	11.5–13.5	–	1.0	0.15	84–86	–	–	–	–	–	–

## 2 Experimental Set-Up

### 2.1 Cladding and Substrate Material

In the present work, N480 and N9062 (Ni alloys) were used as hard coatings with Inconel 625 as buffer layer (particle size 30–100  $\mu\text{m}$ ) for experimentation. The substrate is a hollow cylindrical sleeve made of AISI SS410 martensitic stainless steel with 115 mm length, 34 mm and 50 mm inner and outer dia., respectively. Table 1 gives the chemical composition of Inconel 625, N480, N9062 and SS410.

### 2.2 Experimental Procedure

All the experiments are performed with a fibre-coupled diode laser (Model Laserline LDF 4000–100) having max. output power of 4 kW. The laser beam is focused perpendicular to the substrate surface at a distance of 20 mm with clad materials being fed (M/s Suzlor Metco) through a co-axial nozzle into the processing region. The devices, i.e. optics and nozzles, are integrated with a 6 DOF KUKA KR16 robotic arm controlled by a central computer. Argon is used as a carrier and shielding gas to deliver the powders and also to protect the cladding zone from oxidation. During the experimentation, the optimum process parameters are used, i.e. laser power—2.8 KW, powder feed rate—46 g/min and scanning speed—20 mm/sec for cladding buffer, N480 and N9062 layers.

Initially, Inconel 625 powder as the buffer layer was cladded on two different samples and further allowed to cool to room temperature. Then, N480 and N9062 powders were deposited over the Inconel 625 creating a hard layer. The samples were pre-heated to 180–200 °C before cladding, and the cladded samples are shown in Fig. 2.





**Fig. 2** Laser cladded samples

**Table 2** Micro-hardness of N9062 and N480 along the depth direction

Distance from top surface (mm)	0	0.25	0.5	0.75	1.0	1.25	1.5
N9062 Micro-hardness (HV)	797	808	843	848	831	814	716
N480 Micro-hardness (HV)	608	616	635	598	522	–	–

### 2.3 Characterization and Micro-hardness Measurement

The samples are transversely cut with electric discharge machine (EDM) for microstructural characterization. The specimens are mirror polished using various grades (from 120 to 2500) of abrasive/sandpapers followed by velvet cloth polishing. Before performing the microstructural characterization through SEM, the samples are etched with a mixture of HF and HNO<sub>3</sub> in the ratio of 3:7 for about 5–8 s. The micro-hardness along the clad thickness (radial direction) is measured using TUKON 2100 Wolpert, INSTRON Vickers micro-hardness tester at a load of 300 g for 15 s, and the results obtained are given in Table 2.

## 3 Results and Discussion

### 3.1 Micro-hardness

In this study, before measuring the micro-hardness of cladded buffer layer, N480 and N9062, SEM micrograph at different locations using multiple point dimension were taken, whereas no tracks are observed from the optical images as shown in Fig. 5a, d. From the results, an average clad height of 1.3, 1.01 and 1.50 mm are obtained for buffer layer, N480 and N9062, respectively. The graph plotted in Fig. 3 shows the specimen micro-hardness variation along the depth direction. Each reading represents an average of three readings. The maximum hardness was found to be just below the coating surface and reduced near the interface (hard coating and buffer layer). This

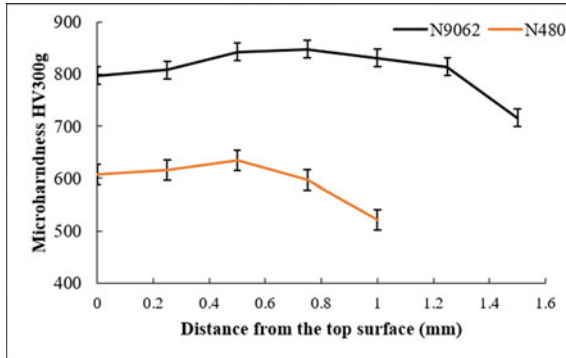


Fig. 3 Micro-hardness variation along the radial direction in N9062 and N480 coating

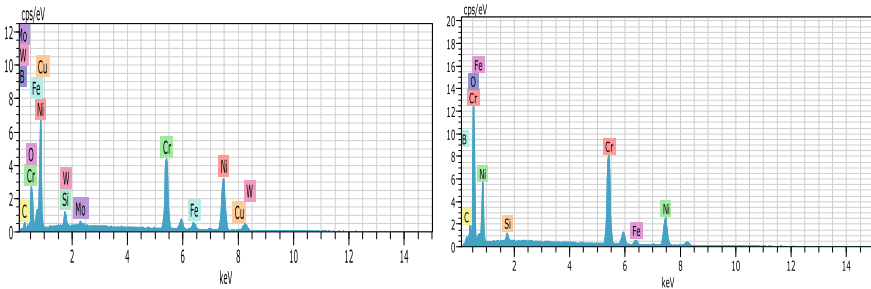
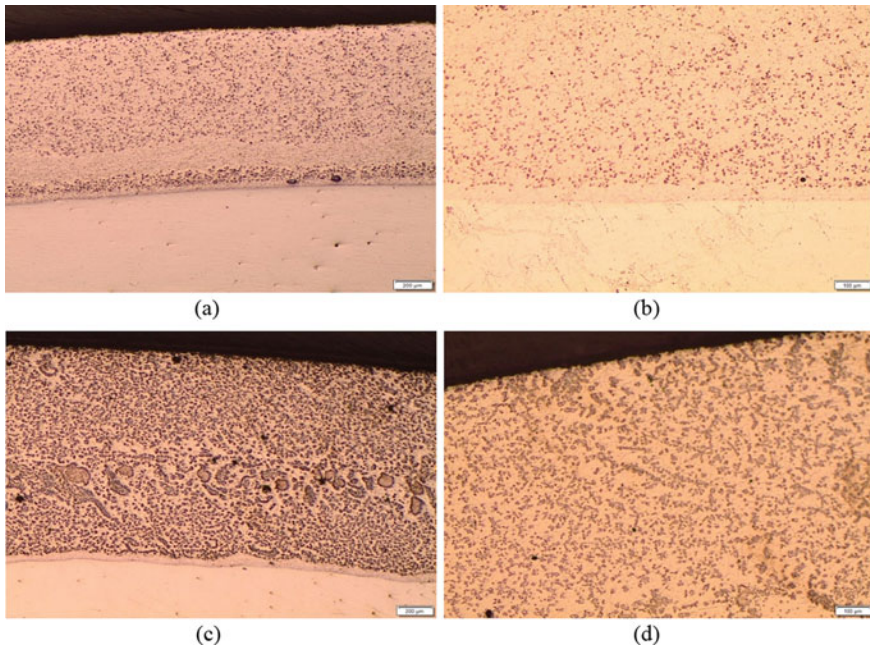


Fig. 4 EDS of N480 and N9062 hard coating layers at the middle of cladding

is due to the diffusion of some elements from the buffer layer. It is predicted that the high heat resistance property of Inconel 625 (buffer layer) resulted in smaller penetration depth of hard coatings over Inconel 625. Hence, the diffusion of Inconel 625 elements into the hard coatings was reduced as compared to the substrate material which decreases the dilution and maintains a good chemical composition as observed in EDS (Fig. 4). A 5–7% increase in hardness is obtained after cladding as compared to the original one. The higher hardness in the coating is due to the formation of hard carbides during cladding, which is also observed in SEM characterization.

### 3.2 Crack Formation

Most of the cracks in laser cladded components are because of the difference in thermal expansion coefficients of the substrate and coated materials. A buffer layer having an intermediate expansion coefficient reduces the thermal gradient during the cooling process in cladding. The heat transfers from the top layer to buffer layer at a different rate than the heat transfer between the buffer and substrate, due to different

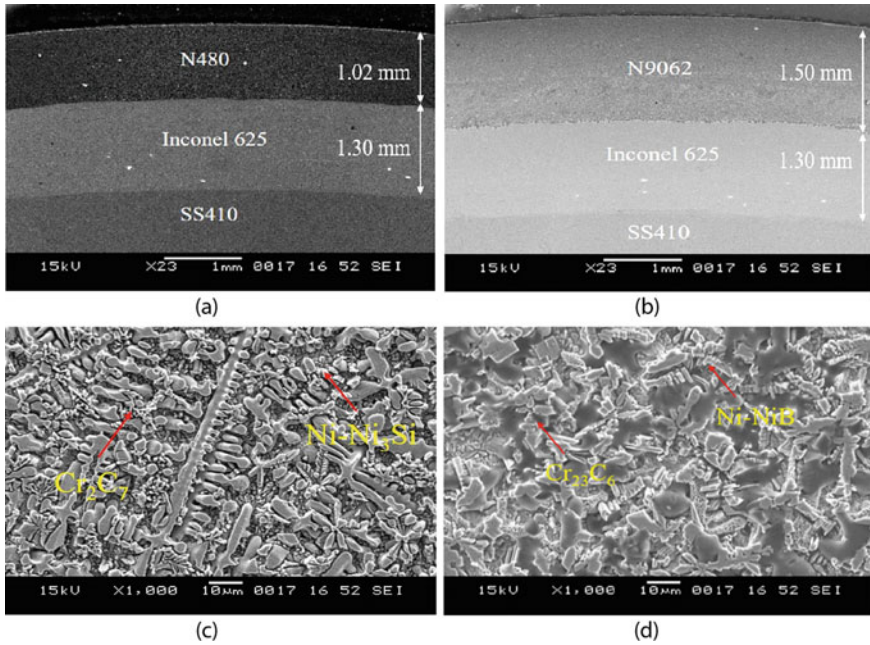


**Fig. 5** Optical images. **a** N480 coating with buffer layer and substrate. **b** No crack initiation in hard coating. **c** N9062 coating with buffer layer and substrate. **d** No crack initiation in hard coating

thermal conductivities and heat resistivity of coated and the substrate materials. As a result, the buffer layer acts as a heat sink ensuring more uniform cooling as compared to direct deposition [12]. This induces compressive thermal stresses within the layer which decreases the chances of crack formation in the clad. Figure 5 also confirms hard-coated layer with no cracks in the optical measurements. Also, the crack formation is eliminated because the substrate is pre-heated to 180–200 °C prior cladding to reduce the solidification rate. At higher solidification rates, some amount of powder will not able to melt and mix properly with other elements in the melt pool which also results in cracks and other defects. The dispersion of hard (refractory) phases in N480 and N9062 coatings is more homogenous when a buffer layer is present than in direct cladding.

### 3.3 Microstructural Characterization

The SEM micrographs of the clad region with buffer layer for both the coatings are placed in Fig. 6. The image shows that the cladding is mainly composed of fine equi-axial dendritic structures. The presence of  $\text{Cr}_{23}\text{C}_6$  and  $\text{Cr}_2\text{C}_7$  carbides in Ni-rich dendrite matrix is responsible for higher hardness. These are found at the outer side



**Fig. 6** **a** N480 coating with buffer layer and substrate. **b** N9062 coating with buffer layer and substrate. **c** Microstructural image of N480 hard coating. **d** Microstructural image of N9062 hard coating

of the grain boundaries. Inter dendritic eutectics of Ni-NiB is formed in N9062 layer while Ni-Ni<sub>3</sub>Si in N480 as the quantity of Ni is higher in N9062 as compared to N480. The microstructure shows that near to the diffusion zone, columnar and free precipitation dendrites are present. The coarse needle-like structure of CrB precipitates near the overlapping zone is seen, due to the dilution by buffer layer elements. These precipitates have a pessimistic effect on hardness and crack susceptibility of the metal matrix. The buffer layer acts as a heat sink between the hard coating and substrate, thus reducing the thermal gradient which gave a fine grain structure.

The EDS analysis along the thickness was performed to know the effect of dilution on major alloying elements mainly Cr, Si, B, Mo on N480 and N9062. The EDS data shows that the weight % of the alloying element is reduced from top to near interface region as amount of buffer layer element; i.e. Ni is increased in the clad due to dilution. As a result, less carbides are formed and hence sudden fall in micro-hardness is observed near the interface which is still lower as compared to direct deposition.

## 4 Conclusions

Laser cladding of N480 and N9062 alloys with Inconel 625 as buffer layer on SS410 substrate was performed successfully. The following conclusions can be made based on the experiments and microstructural analysis:

- The buffer layer addition increases the micro-hardness of the hard coating depositions.
- Buffer layer also reduces the diffusion and dilution of the substrate elements into hard coating which increases wear and corrosion resistance of substrate.
- Uniform thermal gradients are observed in the hard coating with buffer layer, thus reducing the chances of crack formation.

**Acknowledgements** The authors acknowledge DST, Government of India for the financial support and testing equipment under Project No. DST/ECR/2016/001403.

## References

1. Toyserkani, E., Khajepour, A., Corbin, S.F.: Laser Cladding. CRC (2004)
2. Kumar, V., Rakshit, R., Das, A.K.: Mechanical and tribological performance of fiber laser clad h-BN+ SS316 composite on SS316 surface. *J. Mater. Process. Technol.* **278**, 116509 (2020)
3. Jendrzewski, R., Navas, C., Conde, A., de Damborenea, J.J., Sliwinski, G.: Properties of laser-clad stellite coatings prepared on preheated chromium steel. *Mater. Des.* **29**(1), 187–192 (2008)
4. Feng, K., Chen, Y., Deng, P., Li, Y., Zhao, H., Lu, F., Li, Z.: Improved high-temperature hardness and wear resistance of Inconel 625 coatings fabricated by laser cladding. *J. Mater. Process. Technol.* **243**, 82–91 (2017)
5. Song, L., Zeng, G., Xiao, H., Xiao, X., Li, S.: Repair of 304 stainless steel by laser cladding with 316L stainless steel powders followed by laser surface alloying with WC powders. *J. Manuf. Process.* **24**, 116–124 (2016)
6. Liu, H., Hu, Z., Qin, X., Wang, Y., Zhang, J., Huang, S.: Repair of 304 stainless steel by laser cladding with 316L stainless steel powders followed by laser surface alloying with WC powders. *Int. J. Adv. Manuf. Tech.* **91**(9–12), 3967–3975 (2017)
7. So, H., Chen, C.T., Chen, Y.A.: Wear behaviours of laser-clad stellite alloy 6. *Wear* **192**(1–2), 78–84 (1996)
8. Aubry, P., Blanc, C., Demirci, I., Dal, M., Malot, T., Maskrot, H.: Laser cladding and wear testing of nickel base hard facing materials: Influence of process parameters. *J. Laser Appl.* **29**(2), 022504 (2017)
9. Näkki, J., Tuominen, J., Vuoristo, P.: Effect of minor elements on solidification cracking and dilution of alloy 625 powders in laser cladding. *J. Laser Appl.* **29**(1), 012014 (2017)
10. Vostrak, M., Houdková, Š., Hruška, M.: Comparison of WC and (TiW) C in nickel-based alloy coatings prepared by laser cladding. *Int. IOP Conf. Ser. Mater. Sci. Eng.* **461**, 012092 (2019)
11. Korsmik, R.S., Turichin, G.A., Klimova-Korsmik, O.G., Alekseeva, E.V., Novikov, R.S.: Development of laser powder cladding technology for restoration of heat-resistant nickel alloys turbine blades. *J. Phys. Conf. Ser.* **1109**, 12–23 (2018)

12. Stanciu, E.M., Pascu, A., Țierean, M.H., Voiculescu, I., Roată, I.C., Croitoru, C., Hulka, I.: Dual coating laser cladding of NiCrBSi and Inconel 718. *Mater. Manuf. Process.* **31**(12), 1556–1564 (2016)
13. Zhou, S., Zeng, X., Hu, Q., Huang, Y.: Analysis of crack behavior for Ni-based WC composite coatings by laser cladding and crack-free realization. *Appl. Surf. Sci.* **255**(5), 1646–1653 (2008)
14. Wang, D.S., Liang, E.J., Chao, M.J., Yuan, B.: Investigation on the microstructure and cracking susceptibility of laser-clad V<sub>2</sub>O<sub>5</sub>/NiCrBSiC alloy coatings. *Surf. Coat. Technol.* **202**(8), 1371–1378 (2008)
15. Huang, Y., Zeng, X.: Investigation on cracking behavior of Ni-based coating by laser-induction hybrid cladding. *Appl. Surf. Sci.* **256**(20), 5985–5992 (2010)
16. Thawari, N., Gullipalli, C., Katiyar, J.K., Gupta, T.V.K.: Influence of buffer layer on surface and tribomechanical properties of laser clad stellite 6. *Mat. Sci. Eng. B.* **263**, 114799 (2021)
17. Sun, S., Durandet, Y., Brandt, M.: Parametric investigation of pulsed Nd: YAG laser cladding of stellite 6 on stainless steel. *Surf. Coat. Technol.* **194**(2–3), 225–231 (2005)
18. Lin, W.C., Chen, C.: Characteristics of thin surface layers of cobalt-based alloys deposited by laser cladding. *Surf. Coat. Technol.* **200**(14–15), 4557–4563 (2006)
19. Luo, X., Li, J., Li, G.J.: Effect of NiCrBSi content on microstructural evolution, cracking susceptibility and wear behaviors of laser cladding WC/Ni–NiCrBSi composite coatings. *J. Alloys Compd.* **626**, 102–111 (2015)
20. D'Oliveira, A.S.C., da Silva, P.S.C., Vilar, R.M.: Microstructural features of consecutive layers of stellite 6 deposited by laser cladding. *Surf. Coat. Technol.* **153**(2–3), 203–209 (2002)
21. Fallah, V., Alimardani, M., Corbin, S.F., Khajepour, A.: Impact of localized surface preheating on the microstructure and crack formation in laser direct deposition of stellite 1 on AISI 4340 steel. *Appl. Surf. Sci.* **257**(5), 1716–1723 (2010)

# Experimental Investigation on Properties of Acetic Acid-Treated Banana Fiber Polymer Composites



J. Ronald Aseer, S. Renold Elsen, and K. Sankaranarayananasamy

## 1 Introduction

Today, manufacturing industries need lightweight composite panels for making household components which will be beneficial for society. In India, natural plants such as banana, coir, and sisal are discarded in the land after cultivation [1–4]. Nowadays, environmental protection rules and regulations lead the industries to look viable solution for the utilization of naturally available resources. Some researchers shifted their attention toward the effective usage of natural resources in the field of composite manufacturing industries. In general, natural fibers are good alternate for synthetic fiber due to their optimum properties like no environmental pollution, biologically degradable, no economical cost, lightweight, no tooling hazardous, and chip formation handling issues which all industries faced by using synthetic fibers [5, 6]. The mechanical properties of banana fiber composites using polyester have shown optimum mechanical properties when it is added with chemically treated fibers [7]. The morphological, microstructural properties of sansevieria fibers are analyzed, and their properties have shown it can be used as a replacement for other synthetic fibers. The mechanical properties of 40% volume fraction of fiber concentration have shown better values [8]. The sisal fiber treated with alkaline content has shown better structural values as compared to the neat epoxy resin. The water absorption properties have also shown that this fiber can be used for making panels for cottage industries [9]. Banana fiber cultivation is higher in tropical regions. India, especially, southern region it contributes sizable economy. After cultivation of banana fruit, plant is usually used as manure for other growing other plants. Fiber is extracted

---

J. Ronald Aseer (✉) · K. Sankaranarayananasamy  
Department of Mechanical Engineering, National Institute of Technology Puducherry, Karaikal,  
India

S. Renold Elsen  
School of Mechanical Engineering, VIT University, Vellore, India



**Fig. 1** Plant fiber extraction, **a** raw fiber, **b** chemically treated fiber

from the bast of the banana plant using scrapping by knife. These fibers are used for making commercial products such as fiber mats, and bags. So, using banana fiber as reinforcement in thermosetting resin for making good composite panel is the need hour in the composite industries. Aseer et al. [10] investigated the mechanical and surface properties of NaClO treated banana fiber reinforced with urea-formaldehyde resin which shows good results can be used for composite panel application.

In this work, banana fiber is reinforced with epoxy resin using hand layup technique and pressed with hydraulic press. The raw fibers are treated with chemicals to improve the interfacial strength between matrix and fiber. Also, the mechanical properties such as tensile, bending, and impact strength of composites are analyzed.

## 2 Materials Used

Banana fiber is collected from Kanyakumari District, Tamil Nadu, India, from the local farms. Epoxy resin and hardeners were supplied by SS polymers, Chennai, India. The banana fiber is pretreated with NaOH solution and chemically treated with sodium hypochlorite along with aqua solution with 50:50 chemical proportion followed by acetic acid [10, 11]. Initially, fiber obtained from the local farm is cleaned with water. After cleaning, the cleaned fiber is kept in the sodium hypochlorite/aqua solution. After chemical treatment, treated fiber is cleaned with water for few times to remove all the unwanted content from the surface of the fiber. After cleaning, treated fiber is dried by hot oven at 100 °C. The raw and treated fibers are shown in Fig. 1a and b. Chemical treatment of fibers are shown in Fig. 2.

## 3 Fabrication Methods

Silicon gel was pasted on the inner surface of metallic mold using brush, and the mixed banana fibers were manually placed in the mold. It was loaded with 70 kN and





**Fig. 2** Chemical treatment of fibers

maintained to cure at 29 °C for six hours. After curing, the fiber mat was trimmed as per the suitable size. The composite was prepared using hydraulic press. The epoxy resin matrix and hardener were mixed in the ratio of 1:1, and the mold was coated with silicon gel on the mold surface. The mixed with epoxy resin was applied into the mold, and the banana fiber was kept in the mold by layer-by-layer. Banana fiber mats used for making composites were pressed with handroller for proper wetting of the fiber mats with the matrix. The mold was then placed in a hydraulic press under a load of 70 kN. After 24 h, the composite (Fig. 3a) sample was removed manually and cut as per the ASTM standards (Fig. 3b).



**Fig. 3** a Composite panel, b composite for testing

## 4 Results and Discussion

### 4.1 Influence of Fiber Addition on Properties of Composites

When the epoxy resin is subjected to tensile loading using universal testing machine, tensile, and bending strength of neat epoxy resin is low due to its brittle properties. Composite with various concentrations from 10 to 40% volume fraction of fiber is shown in Fig. 3b.

Composite with 10% volume fraction of fiber has shown increase of tensile and bending strength. When the fiber addition increases, properties are increased until 40% volume fraction of fiber. This is mainly by the fiber and resin interface strength [12]. The internal bonding strength of fiber increase the adherence ability of resin in the composites. The composites with 40% of fiber shown higher tensile and bending strength. This is mainly by the fiber breakage in the composites (Fig. 4). When the fiber concentration increases beyond 50% in the composites, fiber agglomeration leads to the failure of the composites. Mechanical properties are given in Table 1. When the composite is subjected to sudden loads using impact testing machine, impact properties are increased up to 40% volume fraction of fiber. Composite with 40% fiber concentration has shown better values compared to other composites. Usually, fiber breakage increases the load absorbing ability of the composites [13]. Fiber and resin create the thick region when composite is subjected to impact loading. Composite with less fiber concentration such as 10 and 20% fiber does not take the shocking load due to the fiber pullout which leads to failure [14].

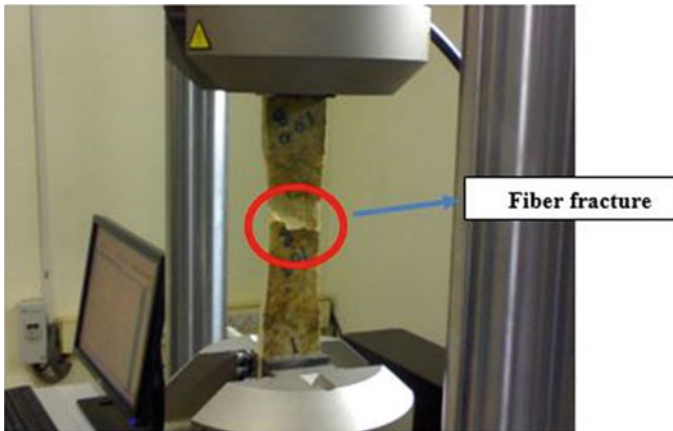


Fig. 4 Composites after fracture

**Table 1** Tensile, bending, and impact strength of the chemically treated composites

Fiber volume fraction (%V <sub>f</sub> )	Tensile strength (MPa)	Tensile modulus (GPa)	Bending strength (MPa)	Bending modulus (GPa)	Impact strength (J/cm <sup>2</sup> )
Neat resin	47 ± 1.2	4.4 ± 1.2	74 ± 1.1	2.4 ± 0.6	0.4 ± 0.1
10	58 ± 2.2	5.3 ± 2.2	83 ± 3.3	3.1 ± 1.1	6 ± 1.1
20	69 ± 1.1	6.3 ± 2.1	93 ± 2.2	4.1 ± 1.3	11 ± 2.2
30	77 ± 1.3	7.4 ± 2.1	99 ± 2.1	5.3 ± 3.2	17 ± 1.4
40	89 ± 1.2	8.3 ± 1.2	110 ± 2.3	6.2 ± 4.2	26 ± 3.2
50	72 ± 2.1	7.2 ± 1.1	103 ± 3.1	5.4 ± 3.2	19 ± 1.1

## 5 Conclusion

Mechanical analysis of banana fiber-reinforced epoxy composite was conducted. The experimental values indicated that the suitability of banana fiber for the replacement of other synthetic fiber in various commercial and construction industries. Composite with 40% has shown better mechanical values which shows the superior qualities of lignocellulose fibers. Impact values of composites also showing optimum results. So, the making of composite panels is a viable solution for waste management of lignocellulosic fibers and also using the panels for commercial and household components with superior properties.

## References

1. Sumaila, M., Ibhadode, A.O.A.: Technical properties of some plant fibres compared with glass. *Int. J. Eng. Res. Africa* **11**, 11–26 (2014)
2. Rajak, D.K., Wagh, P.H., Menezes, P.L., Chaudhary, A., Kumar, R.: Critical overview of coatings technology for metal matrix composites. *J. Bio- Tribo-Corrosion* **6**(1), 12 (2020)
3. Darwish, M.A., Trukhanov, A.V., Senatov, O.S., Morchenko, A.T., Saafan, S.A., Astapovich, K.A., Trukhanov, S.V., Trukhanova, E.L., Pilyushkin, A.A., Sombra, A.S.B., Zhou, D., Jotania, R.B., Singh, C.: Investigation of AC-measurements of epoxy/ferrite composites. *Nanomaterials* **10**(3), 492 (2020)
4. Kumar, U., Rathi, R., Sharma, S.: Carbon nano-tube reinforced nylon 6,6 composites: a molecular dynamics approach. *Eng. Solid Mech.* **8**(4), 389–396 (2020)
5. Weick, B.L.: Characteristics of each bonded layer of a polymer-based magnetic tape using rule-of-mixtures and dynamic mechanical analysis. *Int. J. Polym. Anal. Charact.* **19**(8), 669–681 (2014)
6. Joseph, S., Sreekala, M.S., Oommen, Z., Koshy, P., Thomas, S.: A comparison of the mechanical properties of phenol formaldehyde composites reinforced with banana fibres and glass fibres. *Compos. Sci. Technol.* **62**, 1857–1868 (2002)
7. Saba, N., Jawaid, M., Alothman, O.Y., Paridah, M.T.: A review on dynamic mechanical properties of natural fibre reinforced polymer composites. *Constr. Build. Mater.* **106**, 149–159 (2016)

8. Sreenivasan, V.S., Rajini, N., Alavudeen, A., Arumugaprabu, V.: Dynamic mechanical and thermo-gravimetric analysis of *Sansevieria cylindrica*/polyester composite: effect of fibre length, fibre loading and chemical treatment. *Compos. B Eng.* **69**(7), 6–86 (2015)
9. Mishra, S., Mohanty, A.K., Drzal, L.T., Misra, M., Parija, S., Nayak, S.K.: Studies on mechanical performance of biofibre/glass reinforced polyester hybrid composites. *Compos. Sci. Technol.* **63**, 1377–1385 (2003)
10. Ronald Aseer, J., Sankaranarayanan, K., Jayabalan, P., Natarajan, R., Priya Dasan, K.: Morphological, physical, and thermal properties of chemically treated banana fiber. *J. Nat. Fibers* **10**(4), 365–380 (2013)
11. Sreekala, M.S., Kumaran, M.G., Thomas, S.: Water sorption in oil palm fiber reinforced phenol formaldehyde composites. *Compos. A Appl. Sci. Manuf.* **33**(6), 763–777 (2002)
12. Ornaghi, H.L., Jr., Silva, H.S.P., Zattera, A.J., Amico, S.C.: Hybridization effect on the mechanical and dynamic mechanical properties of curaua composites. *Mater. Sci. Eng. A* **528**, 7285–7289 (2011)
13. Gregorova, A., Hrabalova, M., Kovalcik, R., Wimmer, R.: Surface modification of spruce wood flour and effects on the dynamic fragility of PLA/wood composites. *Polym. Eng. Sci.* **51**, 143–150 (2011)
14. Velmurugan, R., Manikandan, V.: Mechanical properties of palmyra/glass fiber hybrid composites. *Compos. Part A Appl. Sci.* **38**, 2216–2226 (2007)

# Laser Beam Welding of Advanced High-Strength Steels (Dual Phase Steels)



P. V. S. Lakshminarayana, Jai Prakash Gautam, P. Mastanaiah,  
G. Madhusudan Reddy, and K. Bhanu Sankara Rao

## 1 Introduction

The Global Legislators have given new set regulations on the emission of greenhouse gases by automobiles and on passenger safety. As per these regulations, without affecting the passenger safety the CO<sub>2</sub> emissions per kilometer must be decreased over the next decade. Different countries have different targets based on the present emission levels [1, 2]. Tail pipe emissions can be reduced by decreasing the weight of the vehicle which can be achieved either by the application of Lightweight materials or thinner sections. But for passenger safety, stronger materials or heavier sections are to be used. Steel researchers are focusing on the development new class of steels which meet these complex requirements [3]. Advanced High-Strength Steels (AHSS) are an alternate to the existing steels. DP steels, the first generation of AHSS, are most widely applied steel in automobiles to replace conventional structural steels [4]. Dual Phase steels possess composite microstructure with hard Martensitic phase and soft Ferritic phase. These steels show high strength and improved formability over conventional steels, high strain hardening rate, lower yield strength to higher ultimate tensile strength ratio. These special properties have attained because of its

---

P. V. S. Lakshminarayana (✉)

Department of Metallurgical and Materials Engineering, Mahatma Gandhi Institute of Technology, Gandipet, Hyderabad 500075, India

J. P. Gautam

SEST, University of Hyderabad, Hyderabad, India

P. Mastanaiah

DRDL, Hyderabad, India

G. Madhusudan Reddy

Defence Metallurgical Research Laboratory, Hyderabad, India

K. Bhanu Sankara Rao

Pratt & Whitney Chair Professor, SEST, UOH, Hyderabad, India

microstructure [5, 6]. Addition of Nb, V, and Ti, as microalloying elements, to the base chemistry of DP steel enhances strength further and facilitates the usage of thinner sections [7, 8]. Welding is the primary manufacturing process in automobile production. Among the available welding processes applicable to the welding of DP steels, Laser Beam Welding has gained industrial importance due to its rapid production rates, flexibility in welding the intricate areas, ability to produce weld beads with minimum distortion and narrower weld zone dimensions [9, 10]. CO<sub>2</sub>, Nd: YAG, diodes are the commercially available laser sources. Laser Beam Power (LBP), Welding Speed (WS), and Focal Length (FL) are the key variables of Laser Beam Welding [11, 12].

In the present paper, the influence of Heat Input (HI) on weld geometry and weld bead dimensions was studied by producing weld beads on DP 780 of 2.2 mm thickness using Nd: YAG fiber laser welding. Also, studied the correlation between the microhardness variation and microstructural changes across the fusion zone.

## 2 Experimental Details

Dual Phase 780 grade steel plate of 90 mm × 90 mm × 2.2 mm was taken in the present study. Chemical composition of the Base Material (BM) is given in Table 1.

Yield Strength of DP 780 steel is 550 ± 10 MPa, and Ultimate Tensile Strength is measured as 800 ± 10 MPa with an elongation of 16%. Beads on Plate were produced using Nd: YAG fiber lasers (ARNOLD MAKE). Before welding, the plate was cleaned by buffing followed by acetone cleaning to avoid the foreign particle interaction with the liquid pool during welding. Beads were produced at the beam power of from 2.5, 3.0, and 3.5 kW and at the Welding Speed (WS) of 4 m/min keeping the constant focal length of 300 mm. Weld beads were produced perpendicular to the rolling direction. The details of welding parameters are listed in Table 2.

**Table 1** Chemical composition of base material of DP 780

Element	C	Si	Mn	Al	V	Ti	Nb	Fe
Wt%	0.095	0.33	2.2	0.044	0.03	0.055	0.012	Balance

**Table 2** Details of laser welding parameters

S. No.	Parameter	Specification
1	Laser beam power	2.5, 3.0, 3.5 kW
2	Welding speed	4 m/min
3	Focal length	300 mm
4	Diameter of fiber core	0.02 mm
5	Laser head angle	90°
6	Shielding gas	Argon

Transverse section of BM and weld joints was cut by EDM wire cutting machine and prepared these samples as per the standard Metallographic procedure. 2% Nital solution was used to etch the specimens. Macrostructure of weld beads, Microstructure of BM and weld joints were observed by Olympus BX51M. Field Emission Scanning Electron Microscopic (FE-SEM) studies were carried out using FIE-NovananoSEM-450 in secondary electron mode at an accelerating voltage of 15–20 kV. Hardness profile of the weld beads and the Base Material hardness was measured by using Microhardness tester (MATSUZAWA MMT X7) at a load of 500 g with dwell time of 15 s.

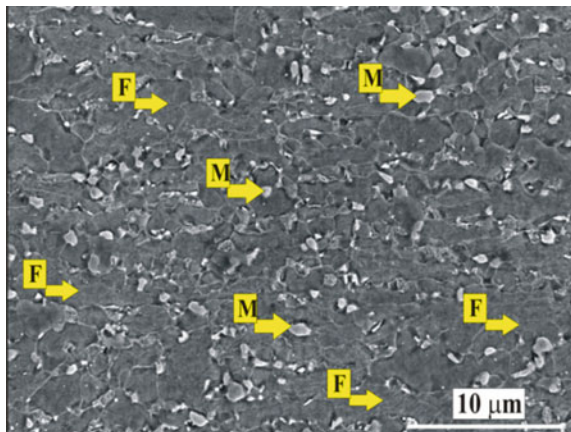
### 3 Results and Discussion

#### 3.1 Base Material Characterization

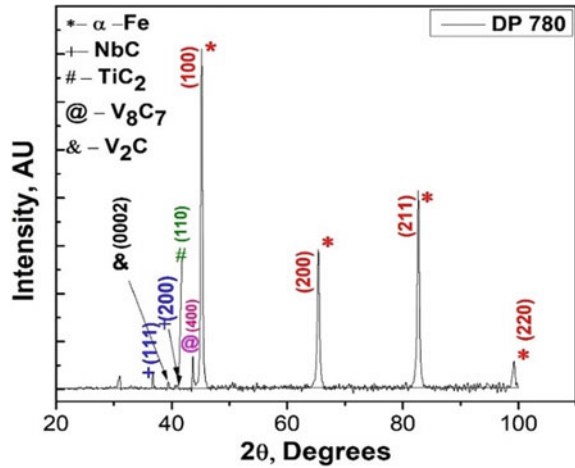
Figure 1 shows FE-SEM micrograph of the Base Material of DP 780. It was observed from this micrograph that the martensite was uniformly distributed along the grain boundaries of Ferrite in a neckless fashion. During the cooling from intercritical temperature, the austenite available at the grain boundaries transformed to the martensite.

The average grain size of ferrite was 5–6  $\mu\text{m}$ , and the martensite volume fraction was 20–22%. The average microhardness of the base material is  $270 \pm 10 \text{ HV}0.5$ . X-Ray Diffraction results of BM is shown in Fig. 2. From this diagram, it was observed that there is no evidence of Retained Austenite (RA) in the BM. Also, it was confirmed from XRD analysis that the carbides of Nb, Ti, and V were present.

**Fig. 1** FE-SEM micrograph of base material of DP 780 (F—ferrite; M—martensite)



**Fig. 2** XRD graph of DP 780 base material

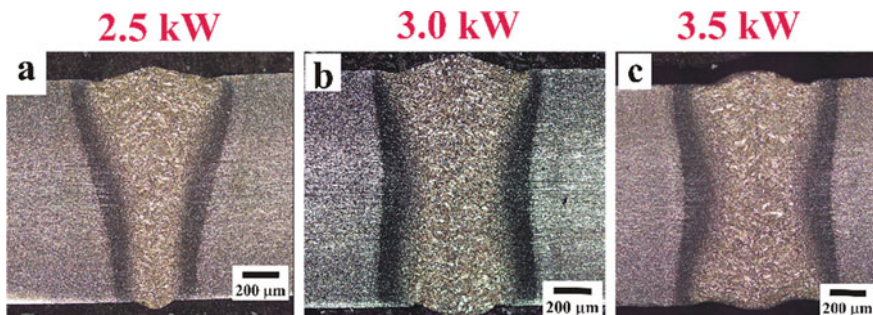


### 3.2 Influence of Heat Input on Weld Structures

Macrostructures of the weld beads produced at the LBP of 2.5, 3.0, and 3.5 kW and at the WS of 4 m/min are shown in Fig. 3.

The ratio of laser beam power to the product of welding speed is known as heat input and is normalized with thickness. Laser beam power provides the necessary heat energy required to melt the base material under focus. With increasing the laser beam power, the amount of heat energy supplied will increase. Welding Speed controls the rate of solidification and is directly related. Figure 3a–c shows the macrostructure of heat inputs of  $17 \text{ J/mm}^2$ ,  $20 \text{ J/mm}^2$ , and  $24 \text{ J/mm}^2$ , respectively.

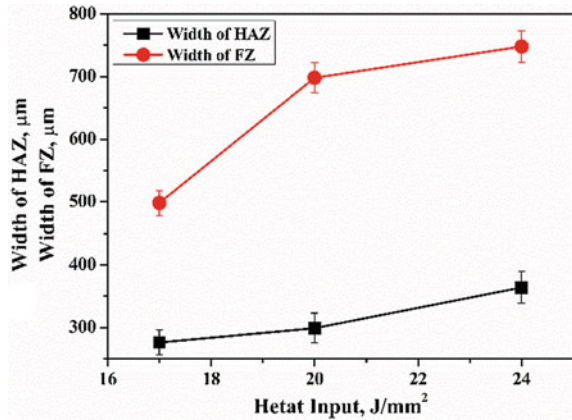
From this figure, it was observed that complete Depth of Penetration was achieved at all heat inputs without any weld defects. As the welding speed was maintained constant, i.e., 4 m/min, the molten pool was solidified at a constant rate. From the columnar dendritic structure of the Fusion Zone (FZ), it was understood that the



**Fig. 3** Macrostructures of weld beads of DP 780. a–c shows the macrostructures at laser beam power of 2.5, 3.0, and 3.5 kW at the constant welding speed of 4 m/min



**Fig. 4** Variation of widths of heat affected zone and fusion zone with heat input



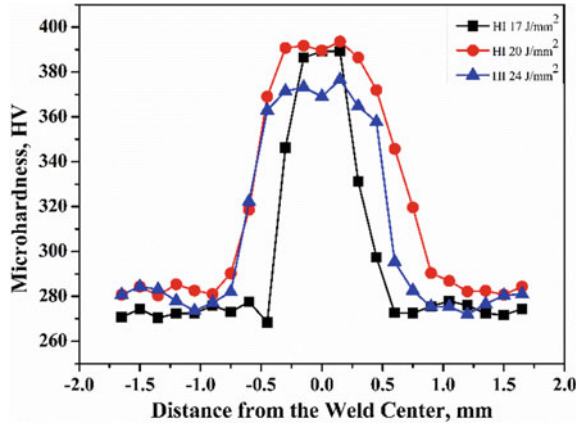
solidification initiated at the solid boundary at both ends and proceeded to the center of the weld pool. During solidification, latent heat of fusion dissipated to the surrounding material by conduction. Due to this, the material adjacent to the Fusion Zone (FZ) was heated above  $A_{c1}$  and  $A_{c3}$  and associated rapid cooling caused phase transformation and the corresponding zone is known as Heat Affected Zone (HAZ). The influence of heat input on width of HAZ and FZ is shown in Fig. 4.

It was observed from Fig. 4 that the width of FZ and HAZ has increased with increase in the heat input. As the HI increased, more quantity of liquid metal produced and upon solidification the width of FZ increased. As the latent heat of fusion increased with heat input due to which the width of the adjacent metal which got heated up also increased. So, the width of HAZ increased with increasing the heat input.

With increasing the heat input, the weld bead shape was changed from wine glass profile to X profile. For the given thickness of 2.2 mm, complete penetration was achieved with the heat input of 17 J/mm<sup>2</sup>, but the heat input was not enough to give the uniform FZ throughout. Similarly, Fig. 3c was corresponding to the heat input of 24 J/mm<sup>2</sup> and a wider fusion zone was observed at the bottom which was an indication that the heat input was excess and with this heat input complete penetration can be achieved for more thicker sheets. In Fig. 3b, weld bead was produced with the heat input of 20 J/mm<sup>2</sup> and observed a uniform FZ throughout the thickness.

From the above discussion, it was observed that the weld bead produced with the heat input of 20 J/mm<sup>2</sup> showed uniform penetration of FZ and HAZ throughout the thickness with optimum weld zone dimensions.

**Fig. 5** Microhardness profile of weld joints produced with three heat inputs



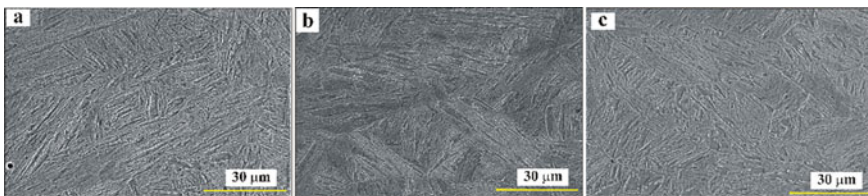
### 3.3 Microstructural and Mechanical Property Correlation

Microhardness profile of weld beads of all heat inputs is shown in Fig. 5. The average hardness of fusion zone for the heat inputs of 17 J/mm<sup>2</sup> and 20 J/mm<sup>2</sup> was  $390 \pm 10$  HV0.5 and that of heat input of 24 J/mm<sup>2</sup> the Hardness was  $370 \pm 10$  HV0.5.

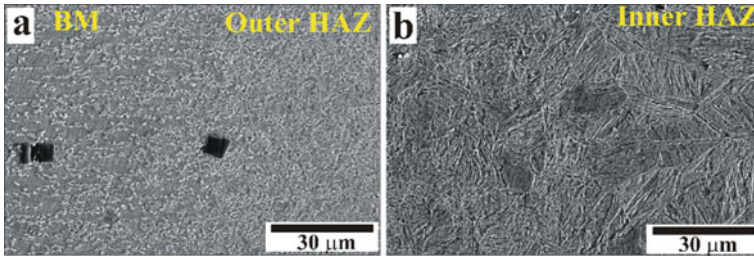
J E Gould et al. have reported that the cooling rates of Laser Beam Welding vary from 200 to 5000 °C/s, depending on process parameters [13]. As the rapid solidification rates were associated with the FZ, liquid, metal has transformed to lath martensite, shown in Fig. 6.

This phase transformation was responsible to increase in the hardness in the FZ. Microstructural investigation, shown in Fig. 6, of the FZ of these weld beads confirmed the presence of martensite phase predominantly from Ferrite and Martensite Dual phase. From these phase transformations, it was confirmed that with the set of welding parameters taken, the cooling rates of the fusion zone are much above critical cooling rates of martensitic transformation.

With increasing the distance from the weld center increased, the hardness was decreased. As the heat energy conducted from fusion zone, to adjacent materials,



**Fig. 6** FE-SEM micrographs of fusion zone showing lath martensite in prior austenitic grains a heat input 17 J/mm<sup>2</sup>, b 20 J/mm<sup>2</sup>, c 24 J/mm<sup>2</sup>



**Fig. 7** FE-SEM images shows base material, outer HAZ and inner HAZ

this zone experienced the temperature above the Austenitic transformation temperature and because of rapid cooling from that temperature austenite transformed into martensite within the prior austenitic grains.

With increase in the distance from the weld center toward base material, the peak temperature to which the material was heated up decreased. Upon cooling, through solid phase transformation austenite transformed into martensite and ferrite. The proportion of martensite and ferrite was depending on the peak temperature. So, the hardness decreased in proportion to the volume fraction of martensite. The zone adjacent to the fusion zone is known as inner HAZ, and the zone adjacent to the base material is known as outer HAZ, shown in Fig. 7.

## 4 Conclusions

Beads on plate were produced using Nd: YAG fiber Laser source on Dual Phase Steel of 780 grade by varying Laser Beam Power at 2.5, 3.0, and 3.5 kW at a constant Welding Speed of 4 m/min. The following are the conclusions drawn from the work.

- Macrostructural studies of transverse section of weld joints have confirmed the Complete Depth of Penetration without any weld defects.
- Increase in the heat input from 17 to 24 J/mm<sup>2</sup> weld bead dimensions (FZ and HAZ) was increased. Also, with increasing the heat input the profile of the weld Zone varied from wine glass profile to X shape.
- Microhardness of the fusion zone was 1.5 times to the Base Material. As the distance from the weld center increased, a decrease in the hardness was observed.
- The cooling rate of the fusion zone was above the critical cooling rates of martensitic transformation. So, upon solidification lath martensite was resulted in fusion zone. The volume fraction of martensite decreased with the distance from weld center and the hardness also decreased accordingly.

## References

1. Hannappel, R.: The impact of global warming on the automotive industry. In: AIP Conference Proceedings. vol. 1871. No. 1. AIP Publishing LLC, 2017
2. Bouaziz, O., Zurob, H., Huang, M.: Driving force and logic of development of advanced high strength steels for automotive applications. *Steel Res. Int.* **84**(10), 937–947 (2013)
3. Evin, E., Tomas, M., Katalinic, B., Wessely, E., Kmec, J.: Design of dual phase high strength steel sheets for autobody. *DAAAM Int. Sci. Book.* **1**, 767–786 (2013)
4. Kuziak, R., Kawalla, R., Waengler, S.: Advanced high strength steels for automotive industry. *Arch. Civ. Mech. Eng.* **8**(2), 103–117 (2008)
5. Speich, G.R., Demarest, V.A., Miller, R.L.: Formation of austenite during intercritical annealing of dual-phase steels. *Metall. and Mater. Trans. A.* **12**(8), 1419–1428 (1981)
6. Rashid, M.S.: Dual phase steels. *Annu. Rev. Mater. Sci.* **11**(1), 245–266 (1981)
7. Bhattacharya, D.: Micro-alloyed steels for the automotive industry. *Tecnol. Metal. Mater. Miner., São Paulo* **11**(4), 371–383 (2014)
8. Bleck, W., Frehn, A., Ohlert, J.: Niobium in dual phase and trip steels. In: *Niobium—Science & Technology. Proceedings. Niobium 727–752* (2001)
9. Mazumder, J.: Laser-beam welding. *ASM Handbook: welding, Brazing, and soldering.* *ASM Int.* **6**, 755–767 (1993)
10. Walsh, C.A.: Laser welding—literature review. *Mater. Sci. Metall. Dept., Univ. Cambridge, Cambridge, U.K., Tech. Rep.* (2002)
11. Nayak, S.S., Biro, E., Zhou, Y.: Laser welding of advanced high-strength steels (AHSS). In: *Welding and Joining of Advanced High Strength Steels (AHSS)*, pp. 71–92. Woodland Publishing (2015)
12. Biro, E., Lee, A.: Welded properties of various DP600 chemistries. In: *Proceedings of Sheet Metal Welding Conference XI, May, 2004.* 11–14, Sterling Heights, MI
13. Gould, J.E., Khurana, S.P., Li, T.: Predictions of microstructures when welding automotive advanced high-strength steels. *Weld. J.-New York* **85**(5), 111 (2006)

# Plasma Cladding of Copper on Cylindrical SS 316L Surface



C. Aditya, C. Gagan, R. Poojith Raj, V. Balaji, V. Srinivasa Chari, and Suyog Jhavar

## 1 Introduction

Cladding is a progressive technology for depositing material with the desired properties on a metal substrate. The main objective of this process is to improve the characteristics like hardness, wear resistance, corrosion resistance, conductivity, etc., or refurbishing of worn out parts. Cladding can be performed using various processes that perform overlay welding such as shield metal arc welding (SMAW), gas metal arc welding (GMAW), gas tungsten arc welding (GTAW), flux cored arc welding (FCAW), cold spray method, plasma arc welding (PAW), laser beam welding (LBW) and electron beam welding (EBW) [1, 2]. Each process has its advantages and limitations when it comes to the characteristics of cladding. There are various problems associated with cladding reported in the literature including: (i) porosity due to atmospheric gases, (ii) inclusions of foreign particles, (iii) cracks due to thermal stresses induced during heating and cooling, and (iv) high dilution due to excessive heating [3]. Therefore, based on the application of the deposited clad a particular welding process is selected.

Copper is an interesting metal largely used for its properties of electrical and thermal conductivity, excellent corrosion resistance and management of heat [4]. It can help in diffusing the heat from local points to larger areas and recommended for fusion reactors, petroleum industries, crystallizers, etc. [5] However, it has poor strength, low hardness, and poor wear resistance at high temperature. Stainless steel offers its own unique properties such as high creep, stress to rupture and tensile strength at elevated temperatures. Stainless steel 316L is usually considered as the marine grade stainless steel, but it is not corrosive resistant to seawater. This combination of materials has many applications in fusion reactors and marine applications. In the present study, SS316L is considered as substrate material for providing high

---

C. Aditya · C. Gagan · R. Poojith Raj · V. Balaji · V. Srinivasa Chari · S. Jhavar (✉)  
Atria Institute of Technology, Anand Nagar, HA Farm, Bangalore 560024, India

strength and copper as clad material to provide required thermal, electrical and corrosion resistant properties. However, coating of copper on stainless steel 316L is highly challenging as there is a distinct difference in the material properties of these two materials, including melting point, thermal conductivity, and thermal expansion.

For performing such cladding, there are two major categories of processes reported in the literature as fusion-based processes and cold coatings [6]. In conventional fusion-based cladding process, one of the metals is used as electrode, which directly absorbs the arc heat and melts to participate in cladding. This often results in excessive melting of the substrate and accumulation of Cu at the interface. Here, large amount of stresses will be developed at the interface due to difference in the coefficient of thermal expansion of both the metals. It causes the Cu to penetrate in SS and induce liquid embrittlement in stainless steel [7]. Laser and electron beam cladding are relatively new technologies having better control over the heat involved during deposition; however, it is challenging to process copper using these techniques due to its inherent property of being a reflective material. Theoretically, the absorptivity of copper for laser in the literature is about 25% which is quite different experimentally. For a wavelength of around 1  $\mu\text{m}$ , the absorptivity reported about 3% at room temperature and 8 and 13% at elevated temperatures [8–11]. Reports present the successful deposition of copper on SS316L surface using cold spray method; however, it is limited to thin layer deposition where deposition of thick coating without porosity is still a challenge. Referring to the past literature, cladding of copper on cylindrical SS 316L surface is very limited and no efforts have been made to study it using plasma welding as a source. This fact motivated the authors for the work presented in this article.

In the present study, plasma welding source is used to confine the welding energy in a confined area. Plasma transferred arc is an effective method [12] for hard facing or cladding between arc welding processes with advantages such as very high-quality deposition, high energy concentration, narrow heat affected zone (HAZ), less weld distortion and some drawbacks, such as low deposition rates, overspray and high cost of equipment if compared with other conventional welding processes. The elevated plasma arc temperature enables the use of metallic wires to melt and deposit over the substrate. All most 100% wire can be deposited in the process which is about 70–80% in case of powder deposition [13].

## 2 Materials and Method

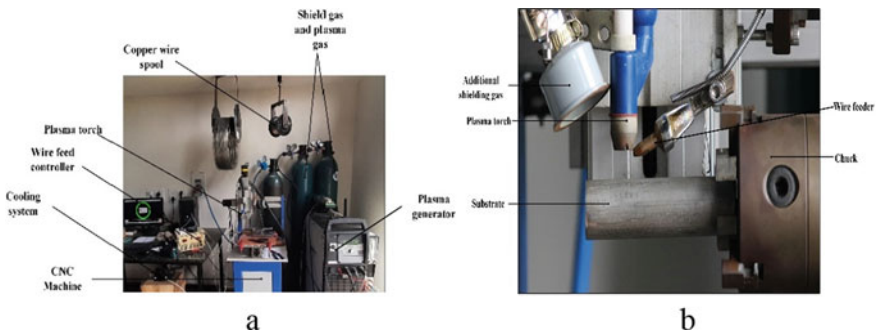
A substrate in the form of hollow pipe of stainless steel 316L having outer diameter 25 mm, length 130 mm and thickness 2 mm was used for all the experiments. The substrate was cleaned with acetone and polished with *A120* flap disks, later *600* grit sandpaper was used for a smooth finish and to do away with any foreign particles prior to deposition. Commercially available copper wire of 500  $\mu\text{m}$  diameter was used as a feedstock material for deposition. The chemical composition of the deposition material and substrate is given in Table 1.

**Table 1** Chemical compositions of the wire and substrate

	C	Si	Mn	P	Cr	Ni	Mo	Fe
Substrate (SS316L)	0.08	0.25	0.81	0.014	16.68	10.08	2.06	Bal
	Cu	Bi	Sb	Fe	As	Pb		
Clad material (Copper)	99.9	0.001	0.002	0.005	0.002	0.001		

### 2.1 Experimental Setup

A plasma welding source (make: EWM, Germany) was used as the energy source for the deposition. The welding torch was attached to a 3-axis CNC machine having a travel accuracy of 0.01 mm in all the directions. An indigenously developed wire feeder was attached to the plasma welding torch to supply the required feed of deposition material. This wire feeder has a wire feeding range of 800–3200 mm/min. with an accuracy of  $\pm 3$  mm. The angle for feeding the clad material was kept constant at  $45^\circ$  as referred from the previous literature [14]. The CNC machine, wire feeder and plasma parameters have been controlled by an integrated software through the computer. Two separate cylinders of argon gas were used. One of the argon cylinders was used for generating plasma and the other to provide a shielding atmosphere for the deposition. For shielding purpose, the gas flow rate was kept constant as 5 l/min throughout the experiments, and a gas flow rate of 0.4 l/min was used to generate plasma. An additional rotational axis attachment was mounted on the bed of CNC machine to hold and rotate the substrate pipe. The rotation of the additional axis was kept constant as one rotation per minute during the experiments. An additional argon cylinder is used to protect the deposited clad from further oxidation while solidification of the clad. Figure 1a shows the actual photographs of the arrangement prepared for experiments, and Fig. 1b presents the detailed view of the experimental setup. Clads were then deposited on the hollow pipe of stainless steel 316L substrate in an open atmosphere.



**Fig. 1** a Plasma welding setup used for experimentations; b detailed view of arrangements

**Table 2** Range of process parameters used for clad deposition

Parameter	Unit	Value
Plasma power ( $P$ )	Watt	625–875
Wire feed rate ( $W$ )	mm/min	3200–800
Travel speed ( $V$ )	mm/min	4–8

## 2.2 Experimental Details

Different combinations of processing parameters were used for preliminary experiments, post which main experiments were designed using the  $L_9$  orthogonal array method. Table 2 presents the range of process parameters used for clad deposition. Argon gas was used for generating plasma as well as for shielding purpose to resist oxidation of copper clad and steel substrate during plasma cladding at elevated temperatures. The single track and multi-track were achieved by varying the process parameters, i.e., travel speed, wire feed rate and the power. The cross section of the cladding was investigated, and factors such as height of the clad, width of the clad, heat affected zone, geometric dilution and geometric shape were examined using AutoCAD software for geometrical investigations. Selected tracks were selected for further investigations for microscopy and micro-hardness measurement.

## 2.3 Clad Characterization

Cylindrical clad sample was sectioned into  $5 \times 5$  mm and cut using wire EDM for high precision and low surface roughness. Utmost care was taken to maintain the standard metallurgical procedure. Analysis of clad geometry was done by visual observations, and the cross-section features were measured using a Zeiss inverted microscope. The samples were polished and etched with standard metallurgical procedure. The images were then processed on AutoCAD software for measurement of clad height and width. SEM analysis was carried out using TESCAN Vega 3. Micro-hardness was also measured at the load of 200 g for 10 s using Leica UHL VMHT micro-hardness tester. All the observations are discussed in the later section of this manuscript.

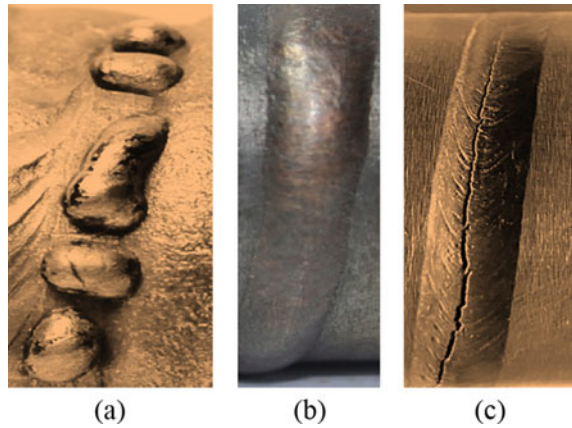
# 3 Results and Discussion

## 3.1 Geometrical Observations

Figure 2a–c presents the variety of clads deposited as a result of different combinations of processing parameters. The results are mainly due to the combinations of plasma power and wire feed rate which directly affects the welding heat input in the



**Fig. 2** A variety of clads deposited at different combination of processing parameters **a** discontinuous clad; **b** smooth clad; **c** clad with liquid embrittlement

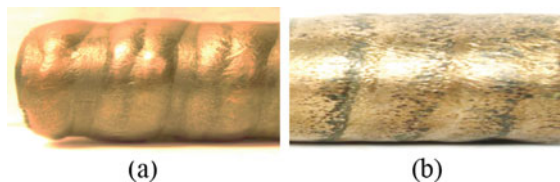


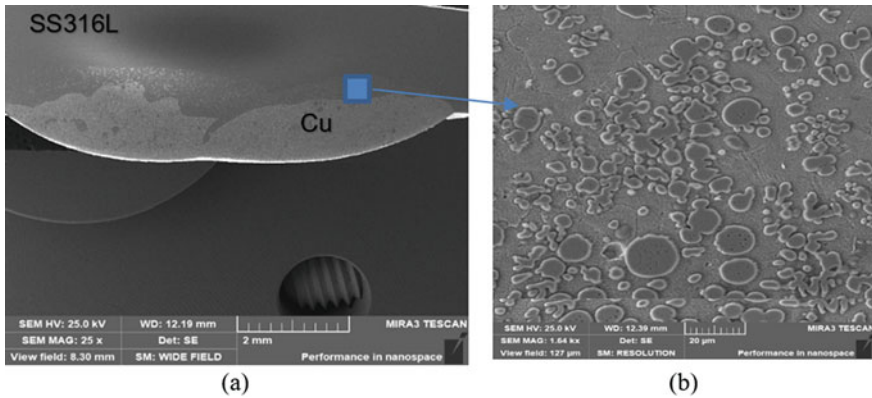
substrate. The rotational speed of the pipe is kept constant for all the combinations at varying travel speed which helps in controlling the overlap distance to form multi-clad and form a smooth surface. Figure 2a shows poor combination of the plasma power and wire feed rate (P:625, W:800) producing discontinuous clad, whereas the combination of high plasma power and lower wire feed rate (P:875, W:800) resulted clad effect with liquid metal embrittlement shown in Fig. 2c. Figure 2b represents a good-quality smooth clad as a result of optimal parameters (P:750, W:800) measures clad width of 5.2 mm and clad height of 1.3 mm. This results in an aspect ratio of 4 (ratio of clad width to height). It has been reported in the previous literature that an aspect ratio above 4 is preferable for smooth and regular deposition [14]. The optimum combination of parameter was further used for multi-clad deposition to form a surface.

### 3.2 Effect of Overlapping Distance

The overlapping distance is the effect of travel speed which is governing the lead distance from the start point. The trials were made at various combinations of input variables. Figure 3a represents the clad formation of two successive layers at a travel speed of 8 mm/min. Figure 3b demonstrates the actual picture of smooth deposition with a combination of optimum parameters with a travel speed of 4 mm/min. This

**Fig. 3** Clad at various overlapping distances **a** double clads; **b** continuous clads





**Fig. 4** SEM observation of Cu clad on SS316L **a** double-clad representation; **b** micrograph at interface

clad was used for further examination using scanning electron microscopy to understand the bonding characteristics mechanism and the different phases present at the interface.

### 3.3 *Microstructural Observations*

Figure 4 reveals the SEM micrograph of selected clad which determines the joint strength between the two materials. The dilution between the two materials is optimum which provides enough strength to the joint, and the interfacial zone is thinner and cleaner. The interfacial zone is explained in Fig. 4b, where the mixing of Fe and Cu can be easily seen. Here, stainless steel is partially melted and is mixed with copper. This interfacial region depicts interesting phenomena for further studies. This clearly shows the possibility of using plasma welding equipment for the application of preparing Fe-Cu surface clads.

### 3.4 *Micro-hardness Observations*

For copper claddings, the cross-sectional micro-hardness versus distance from the cladding-substrate interface plots is shown in Fig. 5. The average of three values was taken for each value for better accuracy. It can be observed from the plot that in the substrate regions, the variation in micro-hardness is negligible beyond a distance of  $-0.3$  mm from the interface. In the heat affected region, relatively higher micro-hardness values were measured for the sample. Lower hardness values were measured in the area between HAZ and unaffected substrate due to diffusion region to the HAZ.

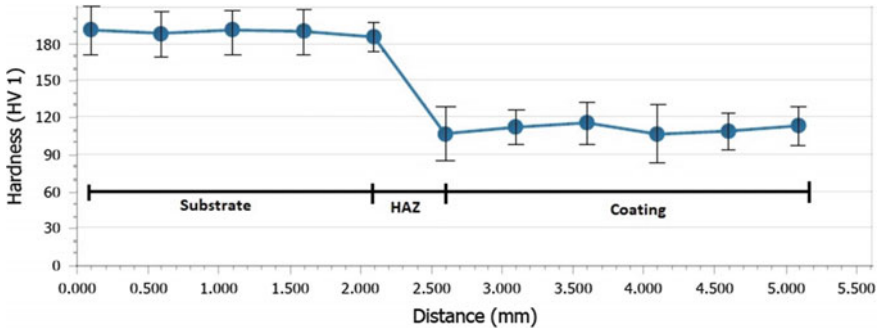


Fig. 5 Micro-hardness of surface layers of Cu-cladded SS316L pipe

The mean micro-hardness of the SS316L part was 198 HV, while the mean micro-hardness of the copper cladding part was 106 HV. The change in micro-hardness values shows the variation between substrate, HAZ and the coating region. There is a smooth transition in the hardness values from the substrate to the clad. The values of micro-hardness confirm the microstructure shown in Fig. 4, where clear separation between stainless steel and copper region is visible. However, a thin mixed Fe-Cu interfacial zone is visible at the interface which has no significant hard faces present in it.

### 4 Conclusions

In the present work, plasma welding is used for thick Cu cladding on stainless steel 316L pipe. The cylindrical cladding was prepared through autogenous setup presented in this study. The following conclusion can be drawn post-deposition:

1. Plasma overlay clads were successfully developed between Cu and stainless steel 316L pipe.
2. The parameters were optimized for single clad, and the optimized value was used for multi-clad deposition. A smooth and regular deposition was achieved as a result of the above work.
3. SEM images verdict sound deposition at optimum combination of parameters without much porosity even in the interface region.
4. Fe is precipitated and fused with Cu in the interfacial region. There is an accumulation of iron-rich phase present in copper.
5. The strong bonding of Cu and SS316L is evident through micro-hardness test. The mean micro-hardness of the SS316L part was 198 HV, while the mean micro-hardness of the copper part cladding was 106 HV.

## References

1. Lee, J.W., Nishio, M., Katoh, T., Yamaguchi, K., Mishima, F.: The performance of wear resistance cladding layer on a mild steel plate by electric resistance welding. *Weld. World* **49**(9/10), 94–101 (2005)
2. Chen, H., Chen, P.N., Hua, P.H., Chen, M.C., Chang, Y.Y., Wu, W.: Microstructure and abrasive wear properties of Fe-Cr-C hardfacing alloy cladding manufactured by gas tungsten arc welding (GTAW). *J. Metal Mater. Int.* **19**(1), 93–98 (2005)
3. Sexton, C.L.: *Rapid Alloy Scanning by Laser Cladding*. Shaker, Aachen (1995)
4. Magnabosco, I., Ferro, P.S., Bonollo, T., Arnberg, F.: An investigation of fusion zone microstructures in electron beam welding of copper-stainless steel. *Mater. Sci. Eng. A* **424**, 163–173 (2006)
5. Surinder Singh, F., Manoj Kumar, S., Gurvinder Pal Singh Sodhi, T., Ramesh Kumar Buddu, F., Harpreet Singh, F.: Development of thick copper claddings on SS316L steel for In-vessel components of fusion reactors and copper-cast iron canisters. *Fusion Eng. Des.* **128**, 126–137 (2018)
6. Loki, K., Barabash, C., Bachmann, P., Chappuis, C.H., Choi, J.-J., Cordier, B., Giraud, Y., Gribov, P., Heitzenroeder, N., Her, G., Johnson, L., Jones, C., Jun, B.C., Kim, E., Kuzmin, D., Loesser, A., Martin, M., Merola, H., Pathak, P., Readman, M., Sugihara, A., Terasawa, Y., Utin, X., Wang, S., Wu, J. Yu.: Design finalization and material qualification towards procurement of the iter vacuum vessel. *J. Nucl. Mater.* **417**, 860–865 (2011)
7. Heiple, C., Bennett, W., Rising, T.: Embrittlement of several stainless steels by liquid copper and liquid braze alloys. *Mater. Sci. Eng.* **52**, 277–289 (1982)
8. Palik, E.D. (Ed.): *Handbook of Optical Constants of Solids*. Academic Press, Orlando (1985)
9. Engler, S., Ramsayer, R., Poprawe, R.T.: Process studies on laser welding of copper with brilliant green and infrared lasers. *Phys. Procedia* **12**, 339–346 (2011) <https://doi.org/10.1016/j.phpro.2011.03.142>
10. Blom, A., Dunias, P., van Engen, P., Hoving, W., Kramer, J.D.: Photon processing in microelectronics and photonics II 2003. *SPIE* **4977**, 493–507 (2003)
11. Ujihara, K.: Reflectivity of metals at high temperatures. *J. Appl. Phys.* **43**(5), 2376–2383 (1972), <https://doi.org/10.1063/1.1661506>
12. Jhavar, S., Paul, Jain, N.K.: Micro-Plasma transferred arc additive manufacturing for die and mold surface remanufacturing. *J. Manuf.* **68**, 1801–1809 (2016). <https://doi.org/10.1007/s11837-016-1932-z>
13. Jhavar, S., Jain, N.K.: *Daaam International Scientific Book*. DAAAM International, Vienna, Austria (2014)
14. Jhavar, S., Jain, N.K., Paul, C.P.: Enhancement of deposition quality in micro-plasma transferred arc deposition process, *Mater. Manuf. Process.* **29**, 1017–1023 (2014). <https://doi.org/10.1080/10426914.2014.892984>

# Effect of Curvilinear Weld Profile Shapes on Weld Line Movement in the Stamping of Tailor Welded Blanks



Suresh Arjula, V. V. N. Satya Suresh , and S. P. Regalla

## 1 Introduction

Nowadays, there is a growing concern of environmental pollution due to automotive emissions. To improve fuel efficiency, there is a greater need to optimize the weight of the automobile than before. Thus, TWBs have come into existence in automobile industries about two decades back to manufacture light weight vehicles which also lead to cost reduction; without compromising on structural integrity and crash worthiness.

Weld line movement is considered to be an important parameter in the stamping of TWBs because of two reasons: Firstly, when two automobile components are assembled, there would be a mismatch between them because the weld line shifts from its current location after forming. Secondly, WLM which is typically toward the stronger material causes necking and fracture in the weaker material. Such WLM contributes to tearing, distortion, wrinkling, die wear and parts with varying dimensions as compared to conventional single-sheet material.

WLM is significantly not high with soft steel combinations (<400 MPa tensile strength), but it becomes critical when high-strength steels such as dual phase/stainless steels are joined with soft forming steels viz. interstitial free steels/mild steels. Due to substantial difference in flow stress, based on thickness and strength ratio, the stronger material deforms much less compared to the softer material which leads to the movement of the weld line.

---

S. Arjula  
JNTUH College of Engineering, Jagtial, Telangana, India

V. V. N. Satya Suresh (✉)  
Mahatma Gandhi Institute of Technology, CBIT Post, Gandipet, Hyderabad, India  
e-mail: [vnvsatyasuresh\\_mct@mgit.ac.in](mailto:vnvsatyasuresh_mct@mgit.ac.in)

S. P. Regalla  
BITS-Pilani Hyderabad Campus, Hyderabad, India

## 2 Literature Review

In order to arrest the movement of weld line, researchers involved with TWBs identified several factors responsible for WLM occurring during forming viz. weld line location, thickness ratio, lubrication, parent materials strength, etc. They applied variable blank holder force (BHF) used draw beads of different sizes and also made changes in tooling. But, these techniques escalated manufacturing costs. Wherever thickness is one of the variable factors, newer designs are needed which increases the product cost.

Few authors suggested using preform design and made recommendations to use non-linear welded joint such as multiple welds in a TWB to overcome the problem of WLM. They have studied the effects of geometry and the position of weld line based on WLM and considered curvilinear welds as suitable alternative in their works. Hu et al. [1] and Panda et al. [2] studied the formability aspects involved in TWBs with respect to circular shaped weld line with variation in blank holder force (BHF). They observed an improvement in the dome height using the curved weld line. Li et al. [3] studied the dependence of formability parameters such as thickness ratio, strength ratio, etc., on the weld line shape by conducting experiments on laser welded TWBs. They have proposed a circular shaped weld profile and studied its effect on the formability of TWB by placing the weld at an offset distance with respect to the center of the blank. They could able to optimize the shape of the TWB component which led to manufacture a better component. Hossein et al. [4] also studied on the performance of TWBs with respect to formability under the influence of curved line using BHF strategy to achieve force equilibrium. Non-linear weld was prepared instead of a straight linear weld to overcome the movement of weld line. Kinsey [5] designed a special die setup in which adaptive controllers were used to maintain pressure on the TWB so that WLM could be reduced. Their work could be adopted in situations wherein there is no change in thickness ratio. Heo et al. [6] used different shapes and sizes of draw beads to control WLM. The shapes included are viz. square, triangle, semicircle, etc., to arrest the WLM. Riahi, et al. [7] conducted experiments by varying the location of weld line and thickness ratio. They concluded that the effect of thickness ratio on the WLM is far greater compared to the weld line location (WLL).

Tian et al. [8] worked on curved welds and studied its effect on the forming height. By increasing the curve radius, they found an increase in forming height especially at thickness ratios greater than 1.5. They also found that by increasing the radius, and a large variation in forming height took place during biaxial stretch forming thus concluded that the shape of the profile has an adverse effect on the formability. Very few authors [9–11] worked on multiple straight welds with inclinations. They concluded that greater the cup depth, minimum weld line movement could be achieved by considering optimum value in the inclination of weld. Since there is a gap in the literature with respect to the study of different curvilinear welds on the WLM, therefore, it is necessary to consider at least few of them.

**Table 1** Material properties of the base materials and weld seam

Material	UTS (MPa)	YS (MPa)	E (GPa)	% elong	<i>K</i> (MPa)
ASS 304 (SS)	693	431	208	69.47	1483
IS 513 (MS)	337	202	210	44.02	677
Weld bead	479.4	293.6	209	15.6	1000

### 3 Numerical Simulation

Preparation of a comprehensive finite element simulation model for stamping of TWB of a combination of industrially relevant materials using finite element analysis (FEA) has been undertaken in LS-Dyna software. Validation of the FEA model was carried out by conducting experiments for certain parameters for which assumptions were made in the simulation model. The model has been redefined based on the experimental results. Later, studies related to the weld line movement using different weld profiles were undertaken.

Adaptive meshing which is an automatic meshing option given in LS-Dyna software was applied on the model to generate elements and nodes by considering four node quadrilateral elements developed by Belytschko-Tsay. At the interface between the parent material and the weld, nodes were merged thus producing a single-TWB sheet. Material properties as shown in Table 1 related to the parent materials and weld have been assigned to each material in the model. All the surfaces of the tools, viz., punch; die and blank holder were modeled using rigid shell elements. A coupled structural-dynamic analysis using fully integrated shell elements has been performed with a friction factor of 0.1.

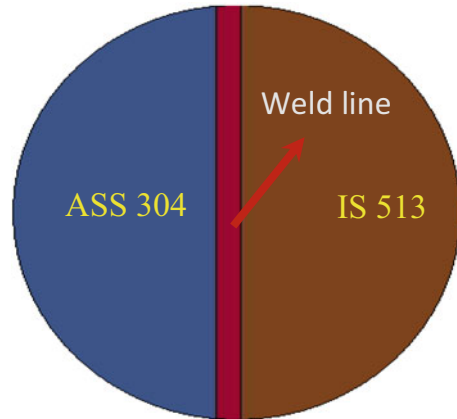
The most common method, of rule of mixture as per Eq. (1), has been used to correlate the material properties of the weld seam given as

$$X_w = X_{ASS}(0.4) + X_{IS}(0.6) \quad (1)$$

where suffixes ASS, *w* and IS stand for austenitic stainless steel, weld and mild steel materials, respectively. Table 1 gives the properties of the respective materials from the tests conducted on a universal testing machine.

### 4 Experimental Work

Most of the TWB sheets are joined by welding processes. TIG welding has been carried out with the following parameters: Welding current of 80–100 amps, welding speed of 3.2 mm/s, rated output voltage as 25 V and heat input of 2.18 kJ/min. Argon gas with flow rate of 12 l/min was used to shield the material from oxidation. Radiographic tests have been performed to check the quality of weld in terms of

**Fig. 1** Tailored weld blank

porosity and air gaps. TWB specimens were prepared by welding the two parent materials, and stamping operations were carried on an electronically operated 40 Ton hydraulic press for straight welds to validate the of simulation studies. Later, the simulation model was used with a change in profile shapes to study its effect on weld line movement.

As a case study, TWB preparation is made by considering semi-circular shaped blanks with base materials viz. IS 513 and ASS 304 each of 1-mm thickness as shown in Fig. 1. The materials were modeled for a diameter of 75 mm with a weld seam of 3-mm width in between them because the weld bead obtained from TIG welding was about 3-mm wide.

#### ***4.1 Weld Profile Shape***

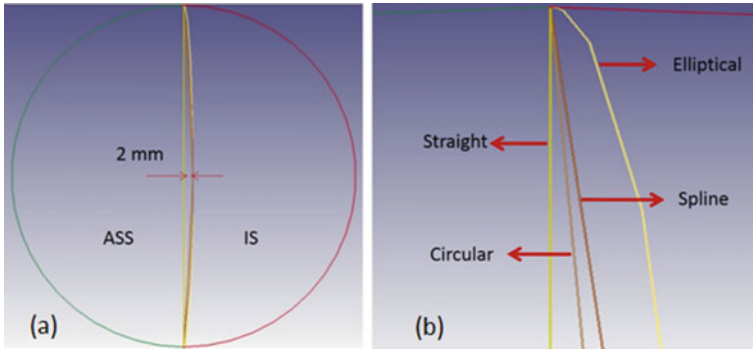
In this work, analytical curves viz. straight, circular, elliptical shapes and a synthetic curve, i.e., B-Spline as shown in Fig. 2 have been considered to model the weld seam with an offset distance of 2 mm placed toward the weaker material, since the maximum WLM obtained from experiments for a straight weld is 2 mm.

## **5 Results and Discussion**

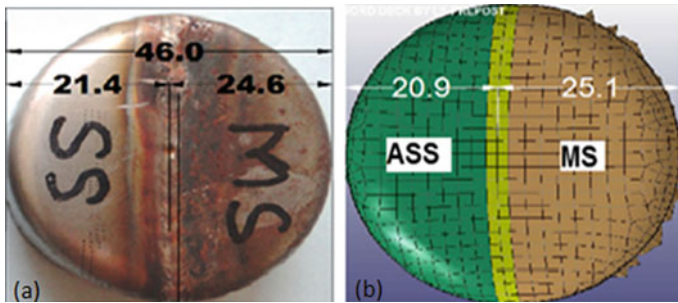
### ***5.1 Weld Profile Shape***

The effect of curvilinear welds on the weld line movement is a promising research work which has not been addressed so far. The requirement of curvilinear welds is





**Fig. 2** a Curvilinear weld profiles in a TWB b enlarged view of the profile shape



**Fig. 3** The weld seam shape at the bottom of the cup a experimental b simulation

mostly in the design of car inner doors since it consists of multiple straight line welds which give rise to inflection points leading to fracture of weld during forming.

The weld seam in the cup bottom took the shape of a curvilinear which can be observed from both the simulation and laboratory experiments as shown in Fig. 3 [12]. Due to unequal plastic deformation, the stronger material among the two materials viz. ASS 304 pulled the weld toward itself.

The simulation model was further analyzed for other profile shapes viz. elliptical, spline and circular shapes. The finite element simulation carried out with these profiles gave contrasting results. The WLM in the case of spline curve gave better results as compared to the results obtained through analytical manner [13]. But, the reduction in sheet thickness was greater in the case of spline curve compared with the other curves. The deviation of WLM in the TWB cups with straight weld was 2.1 mm which reduced to nearly 1 mm in the case of circular and elliptical curves and about 0.7 mm in the case of spline curve as shown in Figs. 4 and 5, respectively. Thus, spline curve exhibited a reduction of 30% in WLM compared with the other two curves.

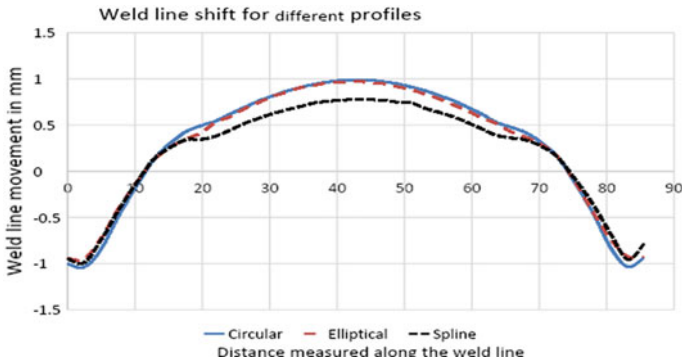


Fig. 4 Weld line shift for different profiles

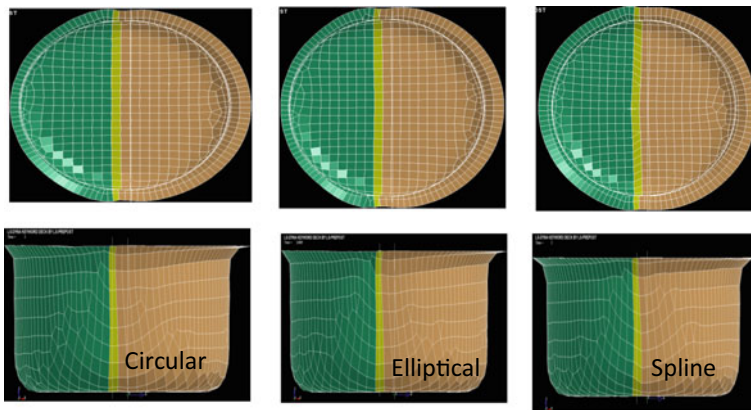


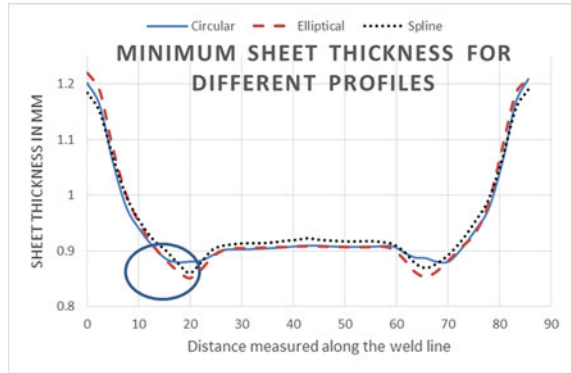
Fig. 5 Weld line movement of different profiles

### 5.2 Sheet Thickness Distribution Measured Across the Weld Section

Reduction in thickness after forming is an indication to predict for the fracture of the component. When the allowable thinning is less than 80% of the sheet thickness, failure/fracture is assumed to occur. In this study, it was noticed that all weld profiles have passed the test of fracture as shown in Fig. 6, since the thickness of sheet material after forming especially at the punch corner is above 80% with respect to the original dimension of 1 mm. The area under the elliptical curve is not evenly distributed, i.e., it is flat at the middle and bulged at the ends, which led to greater thinning at the punch corner as compared to the other curves.

The performance of B-spline in arresting the weld line movement is good due to its properties of localized control by using a special set of blending functions that provide local influence within the convex hull of the polygon. They also provide the

**Fig. 6** Sheet thickness at punch corner



ability to add control points without increasing the degree of the curve. B-spline has C2 continuity which facilitates common tangent and center of curvature at the joints. In fact, the spline curve can be easily controlled with its parametric representation by shifting the control points. There is a possibility of greater control of spline curves in comparison with elliptical/ circular curves which are close bounded and come under the category of analytic curves, in which control is not possible. Moreover, the order of the curves in parametric form is only 1 in both circular and elliptical curves, whereas spline curve has higher order degree. Perhaps, this might be the reason for the spline curve to exhibit good formability.

## 6 Conclusions

1. In this work, the effect of different shapes of weld profiles viz. circular, elliptical and spline shapes on the weld line movement have been studied.
2. Simulation results showed that the shape of weld seam has a considerable effect on weld line movement as well as formability.
3. Weld line movement is less in case of spline profile at the cup bottom. It is more or less the same in case of circular and elliptical profiles.
4. In the cup wall, with respect to the pole, the weld line movement is maximum for the elliptical profile, followed by circular and spline profiles.
5. Maximum thinning occurred for the elliptical profile compared to the other profile shapes.

## 7 Future Work

A parametric representation of the weld profile (spline curve) can be established to minimize the weld line movement. Non-linear weld profiles viz. parabolic, hyperbolic, NURBS, etc., can also be attempted in future work to solve the problem of

WLM. A correlation between the WLM and the weld profile can be established. Further, a mathematical relation involving thickness ratio and strength ratio can also be derived.

**Acknowledgements** The authors express gratitude to JNTU Hyderabad, Telangana, India for arranging funds under collaborative research scheme to carry out this research work with Project No. JNTUH/TEQIP-III/CRS/2019/MECH/06 under TEQIP-III project in the year 2019.

## References

1. Hu, X., Zhao, H., Xing, Z.: Numerical simulation on formability of tailor welded blanks with curved line under different blank holder force. *J. Comput. Theor. Nano Sci.* **9**(9), 1236–1241 (2012). <https://doi.org/10.1166/jctn.2012.2178>
2. Panda, S.K., Kuntz, M.L., Zhou, Y.: Finite element analysis of effects of soft zones on formability of laser welded advanced high strength steels. *Sci. Technol. Weld. Join.* **14**, 52–61 (2009). <https://doi.org/10.1179/136217108X343920>
3. Li, J., Nayak, S.S., Biro, E., Panda, S.K., Goodwin, F., Zhou, Y.: Effects of weld line position and geometry on the formability of laser welded high strength low alloy and dual-phase steel blanks. *Mater. Des.* **52**, 757–766 (2013). <https://doi.org/10.1016/j.matdes.2013.06.021>
4. Hossein, M., Ardakani, A., Morovvati, M.R., Mimia, M.J., Dariani, B.M.: Theoretical and experimental investigation of deep drawing of tailor-welded IF steel blanks with non-uniform blank holder forces. *Proc. Inst. Mech. Eng., Part B: J. Eng. Manuf.* **231**(2), 286–300 (2015). <https://doi.org/10.1177/0954405415577559>
5. Kinsey, L.B., Wu, X.: *Tailor Welded Blanks for Advanced Manufacturing*. Woodhead Publishing Series, Cambridge, UK (2011)
6. Heo, Y.M., Wang, S.H., Kim, H.Y., Seo, D.G.: The effect of the drawbead dimensions on the weld-line movements in the deep drawing of tailor-welded blanks. *J. Mater. Process. Technol.* **113**(1–3), 686–691 (2001). [https://doi.org/10.1016/S0924-0136\(01\)00672-0](https://doi.org/10.1016/S0924-0136(01)00672-0)
7. Riahi, M., Amini, A., Sabbaghzadeh, J., Torkamany, M.J.: Analysis of weld location effect and thickness ratio on formability of tailor welded blank. *Sci. Technol. Weld. Join.* **17**, 282–294 (2012). <https://doi.org/10.1179/1362171812Y.0000000005>
8. Tian, H., Liu, X., Lin, J., Smith, L.M.: Investigation on the formability of tailor welded blanks with curved seams. *Adv. Mater. Res.* **83–86**, 1160–1164 (2010). <https://doi.org/10.4028/www.scientific.net/AMR.83-86.1160>
9. Kochan, A.: Laser welding adapts to non-linear tailor welded blanks. *Assem. Autom.* **21**(1), 48–51 (2001). <https://doi.org/10.1108/01445150110381727>
10. Jiang: Numerical simulation and experimental study on weld line movement of tailor welded blanks, *Adv. Mater. Res.* 97–101, 357–360 (2010). <https://doi.org/10.4028/www.scientific.net/AMR.97-101>
11. Satya Suresh, V.V.N., Regalla, S.P.: Approximation of initial shape of the weld line in the stamping of tailor welded blanks. *IOP Publishing: Mater. Sci. Eng.* **455**, 012136, (2018). <https://doi.org/10.1088/1757-899X/455/1/012136>
12. Satya Suresh, V.V.N., Regalla, S.P., Gupta, A.K.: Combined effect of thickness ratio and selective heating on weldline movement in stamped TWBs. *J. Mater. Manuf. Processes* **32**, 1363–1367 (2016). <https://doi.org/10.1080/10426914.2016.1257128>
13. Abbasi, M., Hamzeloo, S.R., Ketabchi, M., et al.: Analytical method for prediction of weld line movement during stretch forming of tailor-welded blanks. *Int. J. Adv. Manuf. Technol.* **73**, 999–1009 (2014). <https://doi.org/10.1007/s00170-014-5850-3>

# The Effect of HSS and Carbide Tools on the Mechanism of Chip Formation During Turning of Medium Carbon Steel (AISI1030)



Sumit Mahajan and Kalyan Chakraborty

## 1 Introduction

The machining chip formation process is strictly based on plastic deformation. Machining chip is actually defined as a plastically (permanently) deformed part of the work material. Formed chip thickness is a measure of the extent of plastic deformation during machining. The entire machining study should therefore be performed from the point of view of plasticity transition of the work material. Formed chip thickness is therefore an important machining response parameter. Flow stress is defined as instantaneous yield shear stress of the material. Such stress is enhanced by high strain hardening and higher strain rate hardening during machining. Therefore, machining study should be performed from the point of view of the formed shear flow stress in the transitional flow region. Built up von Mises stress (VMS) is directly relating to the plastically deformed material. It is therefore justified to employ the von Mises stress factor during machining analysis. The von Mises stress during machining depends upon the chip thickness and work material properties, mainly strain hardening index ( $n$ ) and strength coefficient ( $K$ ). Present study incorporates the effect of chip thickness, “ $n$ ” and “ $K$ ” to explain the mechanism of chip formation during machining.

## 2 Literature Review

The influence of cutting parameters and tool damage on surface quality of the heat-treated steel was examined [1]. The steel was machined without coolant. They concluded that machined surface was strongly affected. The type of the surface

---

S. Mahajan · K. Chakraborty (✉)

M. E. Department, NIT Silchar, Silchar, Assam 788010, India

depended much on parameter conditions. Temperature and friction at the tool work interface are the important factors to influence the surface quality. At smaller speed, formed surface was having several geometrical errors. Such error was caused due to formed discontinuous chip and speed variation. Microstructural changes occurred on the surface at higher speed. Surface damage occurred because of developed heat and seizure between chip tool interface. Chinchankar et al. [2] evaluated the extent of developed heat during machining of hardened steel under changing parameters. Various types of coated tools were used for machining study. Selected cutting parameters affected the interface temperature. Gupta and Sood [3] experimentally examined the effect of process parameters and cooling methods on cutting forces, tool life and surface quality. They concluded that cryogenic cooling provided better results than dry and wet cooling with tungsten carbide insert. They found that optimal velocity and feed rate for cryogenic cooling were 51 m/min and 0.179 mm/rev. ANOVA analysis showed that cooling is the important parameter for best results.

### 3 Experimental Conditions and Theory

#### 3.1 Experimental Conditions

Tables 1 and 2 show the values of considered experimental parameters.

Chip thicknesses were measured for different experimental conditions, and subsequently chip reduction coefficients ( $\zeta$ ), shear angles and von Mises stresses were determined. Chip surfaces were examined under scanning electron microscope.

**Table 1** Experimental conditions with HSS tool

Expt. No.	RPM	Velocity (m/min.)	Feed (mm/rev.)	DOC (mm)
1	48	7.358	0.138	1
2	76	11.26		
3	116	16.50		

**Table 2** Experimental conditions with carbide tool

Expt. No.	RPM	Velocity (m/min.)	Feed (mm/rev.)	DOC (mm)
1	421	51.052	0.138	1
2	646	75.49		
3	1000	114.66		

### 3.2 Theory

Chip Thickness,  $t_2$ , is given by Eq. (1).

$$t_2 = W/(\rho \cdot w \cdot l) \tag{1}$$

where,  $t_2$  = Chip thickness,  $W$  = Weight of chip in grams.  $\rho$  = Density of the chip in  $g/cm^3$  (work material density is assumed to be remaining unchanged during machining),  $w$  = Width of chip in centimeter and  $l$  = Average length of chip in centimeter. Von Mises stress,  $\sigma_v$ , is given by Eq. (2) [4].

$$\sigma_v = 1.74K (\ln C)^n \tag{2}$$

## 4 Results of Mechanical Test

Using the engineering stress strain graph, corresponding true stress ( $\sigma$ )–true strain ( $\epsilon$ ) graph was obtained in the log–log graph paper. Finally, from the log–log graph of true stress versus true strain, values of  $n$  and  $K$  were found to be 0.55 and 5250. So, the power law equation of the form  $\sigma = K \epsilon^n$  is established from the true stress versus true strain graph and is given by Eq. (3).

$$\sigma = 5250 \epsilon^{0.55} \tag{3}$$

## 5 Results and Discussions on Machining

### 5.1 HSS Tool

Figure 1a shows that the chip thickness decreases with increase in speed VMS also decreases with increase in speed (see Fig. 1b). However, the shear angle increases

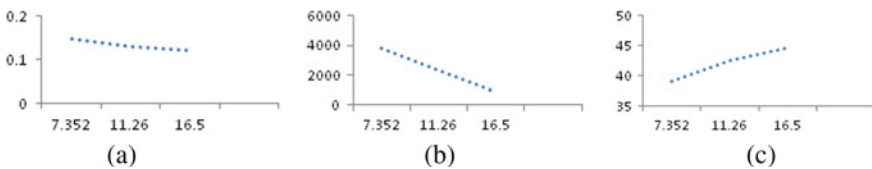


Fig. 1 a Chip thickness versus velocity, b VMS versus velocity and c shear angle versus velocity

**Fig. 2** Type of chip at lowest velocity

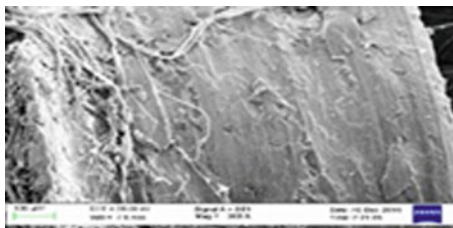


with increase in speed (see Fig. 1c). The trend in variation of chip thickness, VMS and shear angle are in good agreement (Fig. 1a, b and c). Figure 2 shows that at lower speed, formed chips are of shorter tubular type. Higher von Mises stress at this cutting condition is indicative to the work hardening of the material and this leads to the formation of smaller chips. Shorter sized formed chips at lower speed (7.358m/min) shows the effect of strain - hardening of the material at this cutting condition. Such hardening causes tool edge chipping /fracturing leading to the formation of the chip with the maximum side flow. Higher strain hardening index (0.55) (equation 3) of the work material further confirms the higher hardening of this type of material. It is seen that this work hardening effect operates strongly to cause the tool damaging at the cutting edge forming higher amount of side flow of the work material. Such extra side flowing chips get adhered with the chip under the surface which is seen in the SEM image of the chip at lower cutting speed (see Fig. 3 and see Fig. 4).

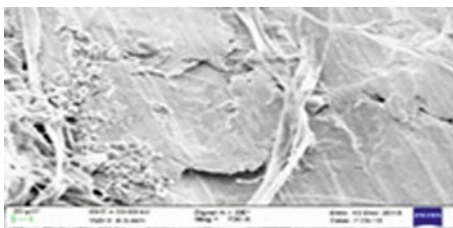
The von Mises stress is lower at higher cutting speed which is indicative to the thermal softening effect. This causes a continuous type of chip formation at this cutting condition (Fig. 5). However, at higher cutting speed (16.50 m/min), the mode of the chip formation process was improved. The top surface of the chip indicated a shear lamellar flow of the material (see Fig. 6a, b).

Higher temperature generation at higher cutting speed promoted material transition to the semi-viscous state at the under surface of the chip. The layer wise material flow at the under surface of the chip is clearly seen in the SEM image (see Fig. 7).

**Fig. 3** Chip undersurface X100

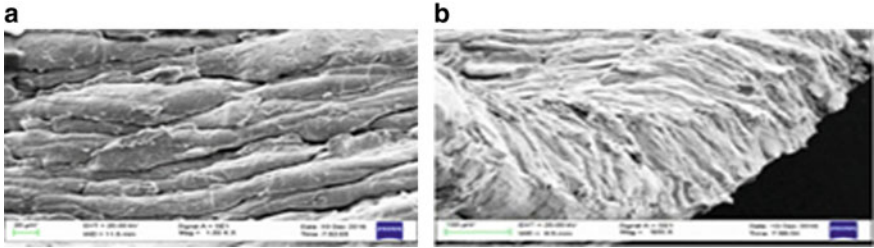
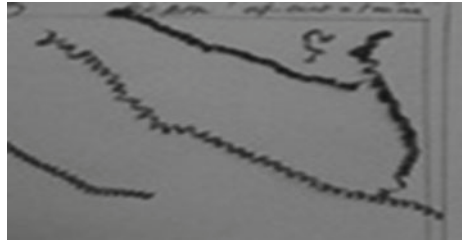


**Fig. 4** Chip undersurface X700



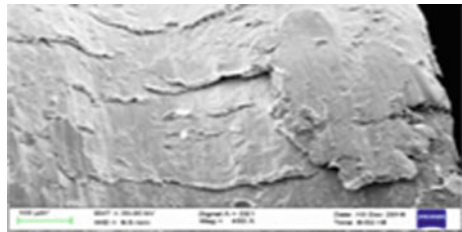


**Fig. 5** Type of chip at maximum speed



**Fig. 6** **a** Chip top surface X1000, **b** chip top surface X500

**Fig. 7** Chip undersurface X400



This confirms the predominating thermal softening effect over strain hardening effect at this cutting condition. HSS tool material however, releases its fracture toughness and finally tool tip fracturing occurs at this cutting condition.

## 5.2 Carbide Tool

Figure 8a shows decrease in chip thickness with increase in speed. VMS also decreased with increase in speed (see Fig. 8b). However, the shear angle increases with increase in speed (see Fig. 9). The variations in chip thickness, VMS and shear angle showed that these are in conformity with reasonable trends.

Chip under surface (see Fig. 10) at lower speed (51.052 m/min) showed better chip formation mode. No side flow of the work material was observed. Top surface

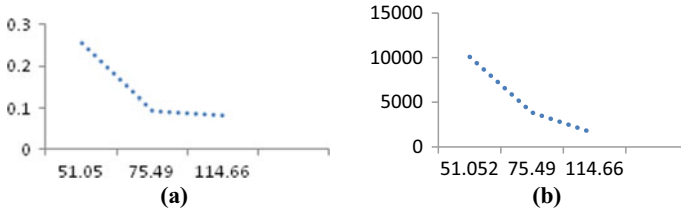


Fig. 8 a Chip thickness versus velocity, b VMS versus velocity

Fig. 9 Shear angle versus velocity

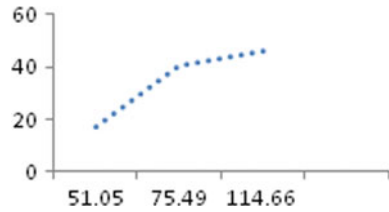
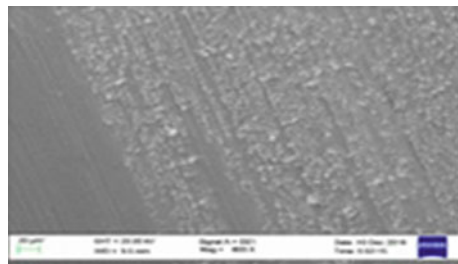


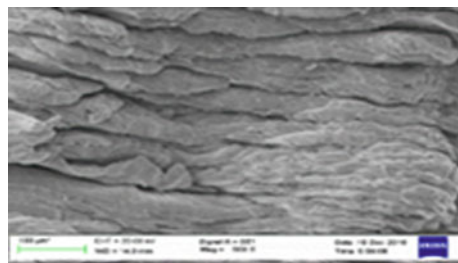
Fig. 10 Chip undersurface X800



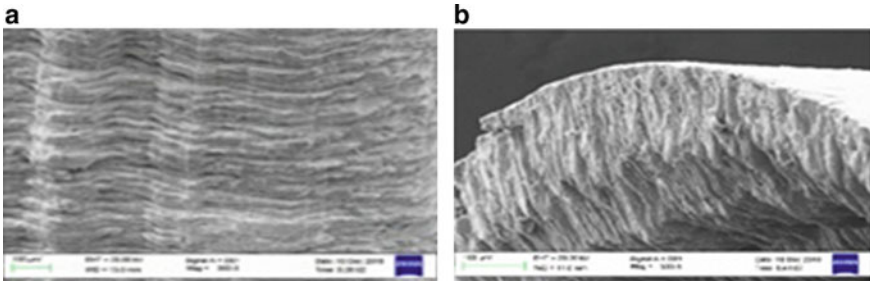
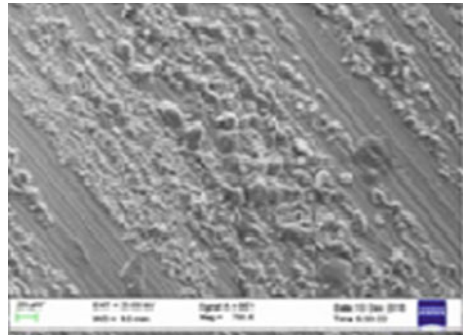
of the chip also showed better chip formation mode by shear lamellar flow during chip formation (see Fig. 11).

At high speed (114.66 m/min), chip under surface showed significant improvement in the process of chip formation. Some worn tool particles are seen to be adhering to the chip under surface (see Fig. 12). Top surface of chip indicated shear lamellar flow during the process of chip formation (see Fig. 13a and see Fig. 13b).

Fig. 11 Chip top surface X800



**Fig. 12** Chip undersurface  
X700



**Fig. 13** **a** Chip top surface X300, **b** chip top surface. X500

## 6 Conclusion

Mode of the chip formation process was seen to be somewhat improved with HSS at higher cutting speed (16.50 m/min). But, improved mode of the chip formation process was observed at all speed conditions in case of machining with carbide tool. Effect of work hardening of the work material at lower speed has been found to be very effective in tool damaging during machining with HSS tool. Use of HSS tool is not at all preferable at lower speed so far as chip formation mode is concerned. But, such role of strain hardening in tool damaging is not observed in case of machining with carbide tool. This is due to retention of material properties by the carbide tool at elevated temperature. Such property retention effect contributes to the formation of chip in better mode. In case of machining with carbide tool, VMS magnitude was relatively higher, indicating much temperature generation and subsequent thermal softening. Plasticity transition of the work material is evidenced by higher values of VMS which is attributed to the thermal softening effect.

**Acknowledgements** The authors sincerely and gratefully acknowledge the assistance with necessary permission provided by IIT Kanpur while using SEM lab and material testing lab of IIT Kanpur.

## References

1. Bailey George, A., Jeelani, S., Becker, S.E.: Surface integrity in machining AISI 4340 steel. *J. Eng. Ind.* 999–1006 (1976)
2. Chinamania, S., Choudhury S.K.: Evaluation of chip-tool interface temperature, effect of tool coating and cutting parameters during turning hardened AISI 4340 Steel. *Procedia Mater. Sci.* **6**, 996–1005 (2014)
3. Gupta, M.K., Stood, P.K.: Optimization of machining parameters for turning AISI4340 steel using Taguchi based grey relational analysis. *Indian J. Eng. Mater. Sci.* **22**, 679–685 (2015)
4. Astakhov, V.P.: *Tribology of Metal Cutting*, Tribology and Interface Engineering Series, Elsevier

# General Regression Neural Network-Based Frame Work for the Evaluation of Ultimate Tensile Strength of Vibratory-Assisted Welded Joints



M. Vykunta Rao, M. V. A. Raju Bahubalendruni, and Vinod Babu Chintada

## 1 Introduction

Tungsten inert gas welding is a widely used method to join magnesium and aluminum alloys. In TIG welding, inert gas is used to protect the weld pool from the atmospheric contaminants. TIG welding is the replacement for manual metal arc welding (MMAW). Quality welded joints are prepared by using TIG welding compared to MMAW. During the welding process, the formation of residual stresses is a common phenomenon. Residual stresses cause plastic deformation in the material, which leads to fatigue failure or distortion. Reduction of residual stresses is achieved through vibration-assisted welding. In vibration-assisted welding, the specimens vibrated in two different modes. Vibrating the specimen with its natural frequency is the first one and another one is vibrating the specimen with unknown frequency (random vibration). Imparting mechanical vibrations during welding reduces the residual stresses or improves the weldments mechanical properties [1, 2].

GRNN comes under the category of the probabilistic neural network model. GRNN is a memory-based algorithm which predicts the continuous variables in one-pass. GRNN needs a certain portion of data to train the network. In this, the output is predicted by the weighted average of the outputs of trained data. Weights are calculated by the Euclidean distance between the test and trained data. If the Euclidean distance is less than the required, it will add some more weight on output data and if the distance is more reduces the weight. Prediction in GRNN depends on the

---

M. Vykunta Rao (✉) · V. B. Chintada

Department of Mechanical Engineering, GMR Institute of Technology, Rajam, Andhra Pradesh, India

e-mail: [vykuntarao.m@gmrit.edu.in](mailto:vykuntarao.m@gmrit.edu.in)

M. V. A. Raju Bahubalendruni

Department of Mechanical Engineering, National Institute of Technology Puducherry, Karaikal, India

smoothing factor ( $s$ ), larger the smoothing factor provides more smoothing. Lower values of the smoothing factor provide close approximation with a dwell [3]. GRNN is implemented to predict the engine performance, i.e., specific fuel consumption, brake thermal efficiency, Nox, hydrocarbons, CO%, and CO<sub>2</sub>%. For the given diesel fuel, biodiesel blends with and without ZnO, different load conditions [4, 5].

Majumder, H., and Maity, K. P. proposed a multiple regression and general regression neural network model to predict the various wire electrical discharging machining machinability aspects, i.e., surface roughness, average kerf width, and material removal rate for the input of pulse-off time, pulse-on time, wire tension, and wire feed [6]. Rao, P. G. et al. developed a tool to estimate the impact strength of vibratory welded joints for the input of vibration parameters. The prepared GRNN model predicts the impact strength at an accuracy of 99.2% for unused experimental data [7–9]. Rooki, R. observed that measurement of pressure loss in an oil well is costlier and time-consuming. GRNN is modeled to predict the non-Newtonian fluids loss of pressure. The author proposed a GRNN modeled to predict the loss of pressure for a given input of a fluid rate ( $Q$ ), diameter ratio ( $D_i/D_o$ ), and consistency index, flow behavior index; yield stress, the eccentricity of annulus [10].

Panda, B. N. et al. formulated GRNN model to predict the weld joint strength for a given resistance spot welding parameters (electrode force, electrode force, sheet thickness, welding time, and welding current). Differential evaluation algorithm was also applied to identify the optimum combination of input parameters at which weld joint strength maximum. Authors built a part using fused deposition modeling (additive manner) with the ABS material. The part prepared at various input parameters, i.e., raster angle, layer thickness and orientation. Effect of these input parameters on the compressive strength was studied. Experimental data are used to develop GRNN and multigene genetic programming model to predict the compressive strength of ABS material [11, 12]. Wei, W., et al. established the relationship between vehicles mass center sideslip angle, yaw speed, and acceleration. Authors proposed GRNN estimation for vehicle sideslip angle. Proposed GRNN method has a high-precision fast response to predict the vehicle sideslip angle for the input yaw speed and acceleration [13].

From the literature, it is clear that vibratory-assisted welding is a proven method to improve weld joint mechanical properties. The relations between vibratory TIG welding parameters to weld joint mechanical properties have not yet established. Hence, in this paper, an attempt is made to establish the relationship between vibratory TIG parameters to the tensile strength of the weld joint.

## 2 Experimentation

Figure 1 represents the experimental setup. The setup consists of a vibration platform and unbalanced vibromotor. Vibrations imparted to the specimen through eccentric circulating vibromotor, surface plate, and springs on which the surface plate is mounted. Specimens are vibrated at different frequencies and amplitudes by

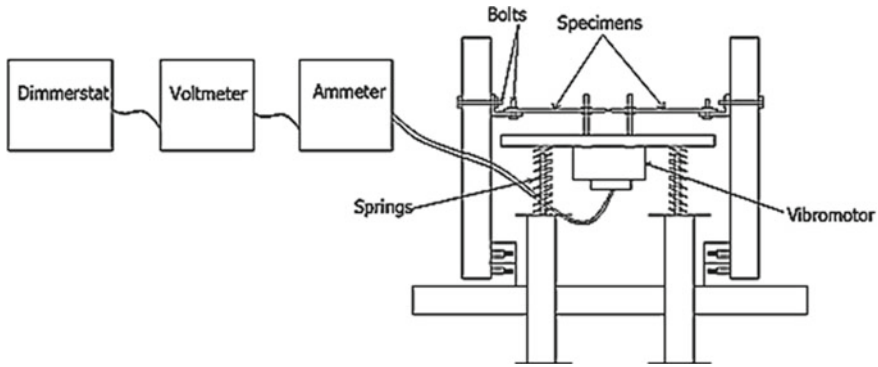


Fig. 1 Experimental setup line diagram [14]

regulating the voltage of vibromotor. Imparting the vibration to the specimen will vibrate the molten weld pool and result in the formation of smaller dendrites. The experimental details are discussed by Rao et al. [14–16].

This paper is mainly concentrated on the development of general regression neural network tool to predict the output parameters (ultimate tensile strength) for the given input parameters (voltage of vibromotor and vibration time).

### 3 General Regression Neural Network Model

GRNN comes under the category of the probabilistic neural network model. This neural network model is a non-iterative process that needs certain portion of the training data. The prime advantage of GRNN is that the network learns in iteration from the data. GRNN is an efficient network than backpropagation. The neural network requires training data. Experimental data are used to train the GRNN model. Training data contain input–output mapping. The network predicts the output from the training dataset. In the case of GRNN, the output is predicted by the weighted average of the outputs of trained data. Weights are calculated by the Euclidean distance between the test and trained data. In GRNN, weights are calculated based on the Euclidean distance of training and testing data. In order to balance, if the Euclidian distance is less it will add more weight and if the Euclidian distance is more which will reduces the weight.

GRNN network consists of four layers. The first layer consists of an input layer, which feeds the input to the second layer that is the pattern layer. In the pattern layer, distance of Euclidian and functions of activations are calculated. The third one is the summation layer, which consists of two subparts. The first one is the numerator part, which contains the summation of the product of activation function and training output data. The second subpart is the denominator, which is the sum of activation functions. Summation layer feeds this to the decision layer. The output layer contains

one neuron; in the decision layer, output is calculated by the ratio of the summation of the numerator part to the denominator part.

In GRNN, output parameter  $Y(X)$  can be estimated by Eq. (1)

$$Y(X) = \frac{\sum_{i=1}^n Y_i \exp\left(-\frac{D_i^2}{2\sigma^2}\right)}{\sum_{i=1}^n \exp\left(-\frac{D_i^2}{2\sigma^2}\right)} \quad (1)$$

where

$$D_i^2 = (X - X_i)^T (X - X_i) \quad (2)$$

$Y(X)$ —estimated GRNN output;  $(X_i, Y_i)$  is a sample observations of  $(X, Y)$ ;  $\sigma$ —smoothing factor.

### 3.1 GRNN Model Preparation

In the present work, GRNN has been modeled to obtain the relationship between input parameters to the out parameters. The vibromotor voltage input and time at which the specimen is vibrated (time of vibration) are considered as input parameters  $(X_1, X_2)$ , and ultimate tensile strength (UTS) is the output parameter.

GRNN requires two types of data: one is the training data and the other one is testing data. From the 54 available experimental datasets, random 47 datasets are taken for training the GRNN model, and remaining 7 datasets are considered for testing or validation. Tables 1 and 2 show the training and testing datasets, respectively. In the GRNN model, the standard deviation values of input parameters are calculated. From the standard deviation values, the scaling factors are calculated. These values are shown in Table 3.

Error percentage is estimated for the training data and testing data or validation dataset. The deviations in the output values obtained by the GRNN for the training and testing data are graphically represented in Figs. 2 and 3, respectively. During the training procedure, the smoothing constant is chosen based on the minimum mean squared error. To achieve the optimum smoothness parameter, the iterative process has been carried out until the deviations are of minimum. Smoothness factor considered for training the network is 4, which is giving minimum deviations.

## 4 Conclusions

In this study, the GRNN prediction tool has been modeled for measuring weld joint ultimate tensile strength. The experimental data obtained from the past literature are



**Table 1** Training dataset for tensile strength

S. No.	$X_1$	$X_2$	$Y_1$	S. No.	$X_1$	$X_2$	$Y_1$
1	50	80	199.27	26	170	90	225.32
2	70	80	204.77	27	180	90	223.67
3	80	80	207.36	28	190	90	219.64
4	90	80	209.27	29	210	90	213.33
5	110	80	214.61	30	220	90	202.33
6	120	80	217.13	31	50	100	200.92
7	130	80	219.67	32	60	100	202.77
8	140	80	221.98	33	70	100	206.83
9	160	80	226.81	34	80	100	208.61
10	170	80	224.96	35	90	100	210.43
11	180	80	222.36	36	100	100	213.33
12	190	80	218.98	37	110	100	216.41
13	200	80	214.41	38	130	100	220.73
14	210	80	209.38	39	140	100	222.38
15	220	80	200.77	40	150	100	225.26
16	60	90	202.86	41	160	100	227.33
17	70	90	205.78	42	170	100	225.28
18	80	90	208.33	43	180	100	223.66
19	90	90	210.22	44	190	100	219.26
20	100	90	212.7	45	200	100	215.26
21	110	90	215.13	46	210	100	213.71
22	120	90	218.66	47	220	100	208.74
23	130	90	220.36				
24	140	90	222.29				
25	150	90	224.43				

$X_1$ : voltage input (volts);  $X_2$ : time of vibration (s);  $Y_1$ : ultimate tensile strength (MPa)

**Table 2** Validation dataset for ultimate tensile strength

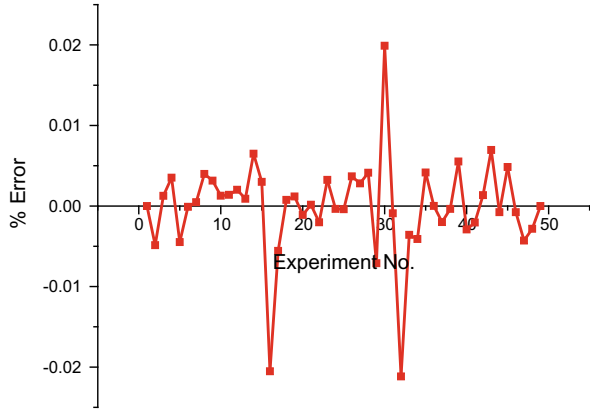
S. No.	$X_1$	$X_2$	$Y_1$	$G(P)$	$E$
1	60	80	201.14	202.02	-0.43762
2	100	80	211.78	211.94	-0.07556
3	150	80	223.77	224.39	-0.27923
4	50	90	200.73	202.86	-1.06125
5	160	90	227.28	224.87	1.058237
6	200	90	215.14	216.48	-0.62504
7	120	100	218.91	218.57	0.155343

$X_1$ : voltage input (volts);  $X_2$ : time of vibration (s);  $E$ : % error  
 $Y_1$ : ultimate tensile strength (MPa);  $G(P)$ : GRNN predicted value

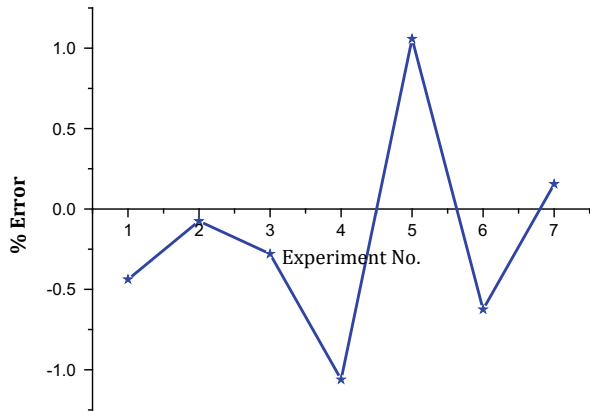
**Table 3** Scaling factors and standard deviation values

	$X_1$	$X_2$
Standard deviation	52.28	8.33
Scaling factor	1	6.276

**Fig.2** Error percentage of training dataset



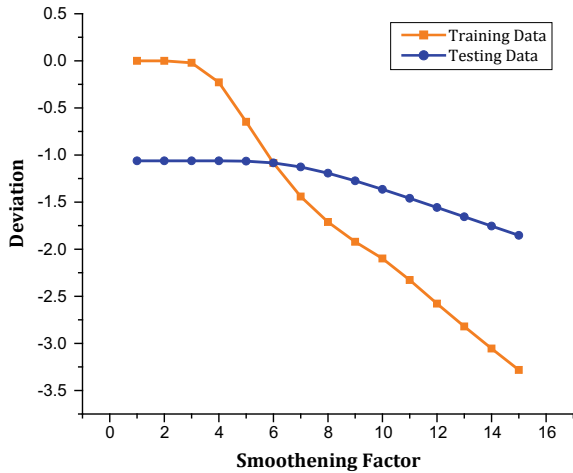
**Fig. 3** Error percentage of testing dataset



used to develop the GRNN model. The prepared GRNN model values are compared with experimental values. The developed prediction model can predict the ultimate tensile strength of welded joints for a given input of vibratory TIG welding process parameters at an accuracy of 98.94%.

Figure 4 shows the deviations of the GRNN model for the different smoothening factor values. The smoothening factor varied from 0 to 15 in order to validate the developed prediction model for its accuracy. Training and testing data deviations with the smoothening factor are shown in Fig. 4. Training data deviations vary from 0 to 3.28%, and testing data vary from 1.06 to 1.85%. The developed model can predict the ultimate tensile strength of welded joints without fabricating and testing.

**Fig.4** Deviations of ultimate tensile strength of welded joint



## References

1. Rao, P.G., Rao, P.S., Krishna, A.G.: Mechanical properties improvement of weldments using vibratory welding system. Proceedings of the Institution of Mechanical Engineers, Part B: Journal of Engineering Manufacture **229**(5), 776–784 (2015)
2. Bade, V.S., Srinivasa Rao, P., Govinda Rao, P.: The effect of vibratory conditioning on tensile strength and microstructure of 1018 mild steel. World J. Eng. **17**(6), 837–844 (2020)
3. Specht, D.F.: A general regression neural network. IEEE Trans. Neural Netw. **2**(6), 568–576 (1991)
4. Seela, C.R., Ravisankar, B., Raju, B.M.V.A.: A GRNN based frame work to test the influence of nano zinc additive biodiesel blends on CI engine performance and emissions. Egypt. J. Pet. **27**(4), 641–647 (2018)
5. Bendu, H., Deepak, B.B.V.L., Murugan, S.: Application of GRNN for the prediction of performance and exhaust emissions in HCCI engine using ethanol. Energy Convers. Manage. **122**, 165–173 (2016)
6. Majumder, H., Maity, K.P.: Predictive analysis on responses in WEDM of titanium grade 6 using general regression neural network (GRNN) and multiple regression analysis (MRA). SILICON **10**(4), 1763–1776 (2018)
7. Rao, P.G., Rao, P.S., Gopala Krishna, A.: A smart prediction tool for estimating the impact strength of welded joints prepared by vibratory welding process. Proc. Inst. Mech. Eng., Part E: J. Process Mech. Eng. **231**(2), 343–346 (2017)
8. Rao, P.G., Rao, P.S., Krishna, A.G.: Evaluation of bending strength of the vibratory welded joint using regression technique. Int. J. Offshore Polar Eng. **25**(03), 227–230 (2015)
9. Kalpana, J., Ramana, S.V., Rao, P.G., ChittiBabu, V., Santa Rao, K.: Implementation of generalized regression neural network to establish a relation between vibration parameters and time of vibration for welded joints. IOSR J. Mech. Civ. Eng. **6**(4), 36–42 (2013)
10. Rooki, R.: Application of general regression neural network (GRNN) for indirect measuring pressure loss of Herschel-Bulkley drilling fluids in oil drilling. Measurement **85**, 184–191 (2016)
11. Panda, B.N., Bahubalendruni, M.R., Biswal, B.B.: A general regression neural network approach for the evaluation of compressive strength of FDM prototypes. Neural Comput. Appl. **26**(5), 1129–1136 (2015)

12. Panda, B.N., Bahubalendruni, M.R., Biswal, B.B.: Optimization of resistance spot welding parameters using differential evolution algorithm and GRNN. In: 2014 IEEE 8th International Conference on Intelligent Systems and Control (ISCO), pp. 50–55 (2014)
13. Wei, W., Shaoyi, B., Lanchun, Z., Kai, Z., Yongzhi, W., Weixing, H.: Vehicle sideslip angle estimation based on general regression neural network. *Math. Prob. Eng.* (2016)
14. Vykunta Rao, M., Srinivasa Rao, P., Surendra Babu, B.: Vibratory weld conditioning during gas tungsten arc welding of al 5052 alloy on the mechanical and micro-structural behavior. *World J. Eng.* **17**(6), 831–836 (2020)
15. Rao, M.V., Rao, P.S., Babu, B.S.: Effect of vibratory tungsten inert gas welding on tensile strength of aluminum 5052–H32 alloy weldments. *Mater. Focus* **6**(3), 325–330 (2017)
16. Rao, M.V., Rao, P.S., Babu, B.S.: Vibration effect on the impact strength of Al 5052–H32 weldments. *J. Mech. Eng. Res. Dev.* **40**(1), 134–139 (2017)

# Experimental Studies on Material Removal Rate of Die Steel in Electrochemical Micromachining Process Using Taguchi Method



K. Vijayakumar, T. Sekar, and M. Vijay

## 1 Introduction

Electrochemical machining is commonly used unconventional machining processes to machine the complicated shapes in electrically conducting hard and highly resistant to machine materials [1]. The merits of ECM are over the conventional machining practices which can process hard materials with negligible tool wear, the good surface finish of the workpieces, and it can develop workpieces with higher precision and intricate geometry without cracks [2–4]. Machining of difficult to machine materials in traditional machining process leads to more surface distortion, larger heat-affected zone, and high thermal stress. Creating microholes is the basic machining operation, and it is required in machine parts [5]. Microholes and microchannels are the common features made by micromachining, and they are applied in many areas such as microdies and nozzles, when produced in large numbers using conventional machining processes, usually present problems such as high tool wear, high heat generation, and change in materials properties [6, 7]. With minimal tool wear, microelectrochemical machining ( $\mu$ ECM) is a suitable material removal process for machining conductive materials in microdomain.  $\mu$ ECM has wider applications in high-precision equipment's manufacturing [8, 9]. When the anode (workpiece) and a cathode (electrode) are dipped in the electrolyte solution and DC is supplied through it, the material is ruptured and forced away from the anode surface. As per Faraday's law, the amount of material removed on the surface of workpiece depends upon applied current and machining distance between tool and workpiece [10]. It

---

K. Vijayakumar (✉)

Department of Mechanical Engineering, TPEVR Government Polytechnic College, Vellore, Tamil Nadu, India

T. Sekar · M. Vijay

Department of Mechanical Engineering, Government College of Technology, Coimbatore, Tamil Nadu, India

is more reliable to machine hard materials such as HCHCr die tool steel, AISI 202 Austenitic stainless steel, and superalloys [11]. It explores the machining of die steel in electrochemical machining process [12] from the above studies; this research work attempts the machining of hardened die steel by electrochemical micromachining using Taguchi method.

## 2 Planning of Experimentation

An L9 orthogonal array is chosen to reduce the experimental run and get the better results based on Taguchi the experiment. Taguchi's design is to identify the impact of machining parameter settings over the output parameters with unavoidable variations in external noise. The software Minitab version 2019 is used for the design of the experiments. As per the design problem, different S/N ratios are applicable, including larger is better and smaller is better [13].

### 2.1 The Process Parameters

The process parameters range for the experiments are given below:

- Electrode—Tungsten carbide.
- Workpiece—Hardened die steel.
- Workpiece thickness—0.5 mm.
- Electrolyte—NaCl (with various concentrations).

## 3 Experimentation

### 3.1 Selection of Machining Parameters

Table 1 depicts the process parameters and the level of their value on experiments, and the feasible range of machining parameters for the material hardened die steel is recommended as follows.

**Table 1** Machining parameters and their levels

Name	Units	Level 1	Level 2	Level 3
Voltage	V	10	15	20
Electrolyte Concentration	g/l	100	150	200
Duty cycle	%	60	70	80

### 3.2 The ECMM Process

The principle of Electrochemical Micro Machining is the anodic dissolution that takes place between the workpiece (anode) which is positively charged and the tool (cathode) which is negatively charged. Electrolytes used in the ECMM are to initiate the chemical action on the surface of the workpiece; it leads to material removal in the workpiece. Electrolytes play the role to dissipate the heat reaction over the areas of tool and workpiece and to carry machined material generated out of the gap to avoid hitting the particles snarled machining process on the results.

The ECMM setup consists of a tool movement arrangement, electrolyte control, filter unit, and DC supply unit as shown in Fig. 1 Die steel workpiece of 0.5 mm thickness is accessed for the experimentation. Die steel is utilized in this work because it is having applications such as die manufacturing and refractory industry. Tungsten carbide tool electrode of  $\Phi = 150\mu\text{m}$  is acted as a cathode. NaCl is used as electrolyte liquid in concentrations of 100, 150, 200g/l. The experiment is conducted at room temperature. Pulsed DC supply with the varying voltage at 10, 15, 20 V and duty cycle of 60, 70, 80% is used for conducting the experiments. The time taken for the through-hole machining is noted, and the weight is measured in the weight scale having three-digit accuracy for the calculation of material removal rate.

## 4 Results and Discussion

Figure 2 shows the SEM image that shows the drilled hole by the ECMM process. The hydrogen bubbles are generated between the tool and workpiece due to the passing of the electric supply. The material removal is taking place due to the atomic dissolution of the workpiece. Electrochemical dissolution is worked on the basis of Faraday's

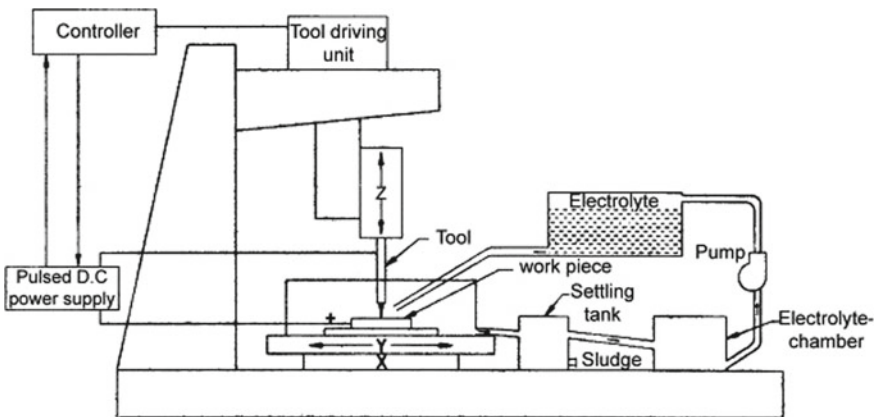
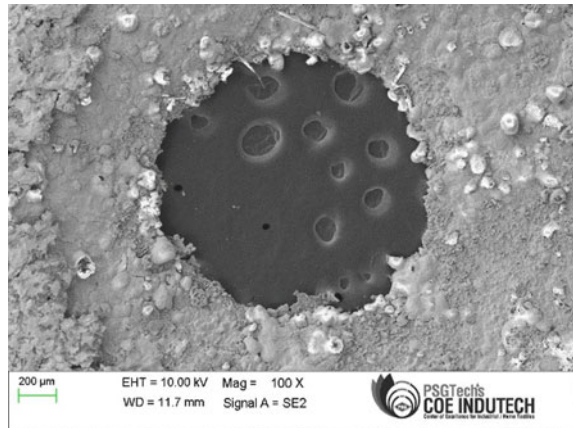


Fig. 1 Schematic diagram of ECCM

**Fig. 2** SEM image of the machined workpiece



**Table 2** Material removal rate (MRR)

Exp. No.	Voltage	Electrolyte concentration	Duty cycle	MRR mm <sup>3</sup> /min	SNRA1
1	10	100	60	0.0412	-27.7021
2	10	150	70	0.0319	-29.9242
3	10	200	80	0.0351	-29.0939
4	15	100	70	0.0582	-24.7015
5	15	150	80	0.0312	-30.1169
6	15	200	60	0.0816	-21.7662
7	20	100	80	0.0669	-23.4915
8	20	150	60	0.1483	-16.5772
9	20	200	70	0.0395	-28.0681

law of electrolysis [14]. It is also termed as a reversed electroplating process. The tool was maintained a minimal distance with the workpiece called interelectrode gap (IEG). The IEG is maintained constantly during the tool feed also.

Table 2 shows the material removal rate of the machining hardened die steel using ECMM. Each workpiece was weighed using a weight scale having three-digit accuracy before machining and after machining to calculate the material removal rate.

#### **4.1 Observations During Experimentation (MRR)**

Time duration = 15 min, (each cycle).

Tool = Tungsten carbide.

Tool diameter = 150 μm.



The material removal rate is calculated by the difference between the initial and final weight of the workpiece, per unit time. The weight of the workpiece is measured with a three-digit accuracy weight scale.

Regression equations obtained for the material removal rate are given below. This equation helps in the prediction and optimization of output variables concerning input variables.

$$MRR = 0.152 + 0.00488 \text{ voltage} - 0.000034 \text{ Electrolyte Concentration} + 0.00230 \text{ Duty Cycle} \tag{1}$$

This research aims to find the value of the optimal response for the material removal rate (MRR) relatively the factors involved, and Taguchi method is selected for the design of experiments because it offers minimal experiments and gives optimal results with comparing to another approach, the sequence of the run, MRR, and signal-to-noise ratio as shown in Table 2.

Figure 2 shows that the machining area is enlarged due to electrochemical erosion. It can be controlled by proper insulation in the tool piece.

Figure 3 shows that the best obtained MRR indicates that the highest achievable MRR is 0.1483 mm<sup>3</sup>/min found as A3B3C2 when a voltage is at a higher level 20 volts, electrolyte concentration is also at a higher level 150 g/l, and the duty cycle at middle level 70%. The higher-level voltage leads to a higher MRR level and the same also reflects in electrolyte concentration. For the duty cycle, the middle value leads to higher MRR. According to Faraday’s first law of electrolysis, the amount of electrochemical dissolution is proportional to the amount of charge passed through the electrochemical cell.

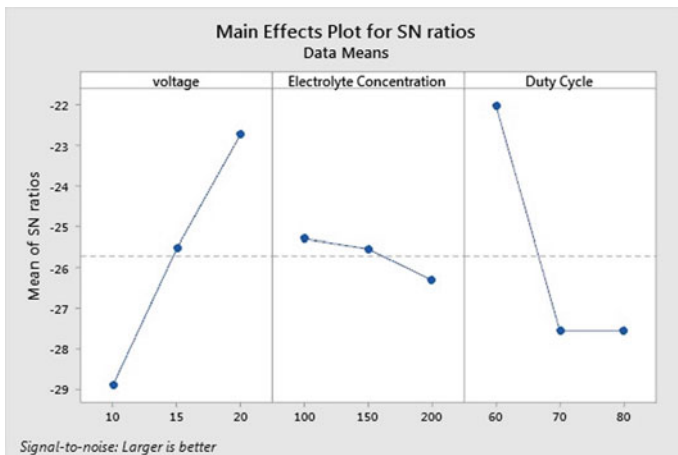


Fig. 3 Main effect plot for SN ratio for MRR

## 5 Conclusion

The electrochemical micromachining (ECMM) technique is used to machine die steel in this work, based on experimental investigation on machining of hardened die steel. From this experimental work, the conclusions can be summarized as follows.

1. Hard and brittle material like hardened die steel can be effectively drilled into the microhole with negligible fracture and thermal defects to the workpiece.
2. In this work, voltage is the most influencing parameter then the electrolyte concentration contributes in second place and the duty cycle is in the least impact on the material removal rate of die steel.
3. The optimal values for maximum MRR were found in the combination A3B3C2 when a voltage is at a higher level 20 V, electrolyte concentration is also at a higher level 150 g/l, and the duty cycle at middle level 70%.

## References

1. Chandrakar, D., Venugopal, A.: Multi-objective optimization of electrochemical machining of EN31 steel by grey relational analysis. *Int. J. Model. Optimiz.* **1**(2) (2011)
2. Mathew, R., Sundaram, M.M.: Modeling and fabrication of micro tools by pulsed electrochemical machining. *J. Mater. Process. Technol.*, **212**(7), 1567–1572 (2012)
3. Deconinck, D., Van Damme, S., Albu, C., Hotoiu, L., Deconinck, J.: Study of the effects of heat removal on the copying accuracy of the electrochemical machining process. *Electrochim. Acta* **56**(16), 5642–5649 (2011)
4. Rajurkar, K.P., Hadidi, H., Pariti, J., Reddy, G.C.: Review of sustainability issues in non-traditional machining processes. *Procedia Manuf.* **7**, 714–720 (2017)
5. Muthuramalingam, T., Mohan, B.: A review on influence of electrical process parameters in EDM process. *Arch. Civ. Mech. Eng.* **15**, 87–94 (2015)
6. Choi, S.H., Kim, B.H., Chu, C.N.: Micro electrochemical machining of tungsten carbide. *J. Kor. Soc. Prec. Eng.* **23**, 111–116 (2006)
7. Kim, B.H., Na, C.W., Lee, Y.S., Choi, D.K., Chu, C.N.: Micro electrochemical machining of 3-D microstructure using dilute sulfuric acid. *CIRP Ann—Manuf Technol* **54**(1):191–194.
8. Kim, B.H., Ryu, S.H., Choi, D.K., et al.: Micro electrochemical milling. *J. Micromech. MicroEng.* **15**, 124 (2004)
8. Hen, W., Kunieda, M.: A novel method to switch machining mode between micro-ECM and micro-EDM using oxide film on surface of tungsten electrode. *Precis. Eng.* **56**, 455–465 (2016)
9. Bhattacharyya, B., Malapati, M.: Munda, J: Influence of tool vibration on machining performance in electrochemical micro machining of copper. *Int. J. Mach. Tool. Manuf.* **47**, 335–342 (2007)
10. Sekar, T., Marappan, R.: Experimental investigations into the influencing parameters of electrochemical machining of AISI 202. *J. Adv. Manuf. Syst.* **7**(2), 337–343 (2008)
11. Sekar, T., Arularasu, M., & Sathiyamoorthy, V: Investigations on the effects of nano-fluid in ECM of die steel. *Measurement* **83**, 38–43 (2016)
12. Soepangkat, B O.P., Pramujati, B., Lusi, N.: Optimization of multiple performance characteristics in the wire EDM process of AISI D2 tool steel using Taguchi and fuzzy logic **789** (2013)

13. Lin, T., Guo, Y.-F.: Experimental study of special purpose stainless steel on electrochemical machining of electrolyte composition. *Mater. Manuf. Process.* **28**, 457–462 (2013)
14. Kalra, C.S., Kumar, V., Manna, A.: Analysis of electrochemical behavior on micro-drilling of cast hybrid Al/(Al<sub>2</sub>O<sub>3</sub>pSiCpCp)-MMC using micro-ECM process. *J. Mater. Des. Appl.* 1–13 (2016)

# Microstructural Characterization and Microhardness Investigations on Friction Stir Additive Manufactured Commercially Pure Aluminium Alloy



R. Dinesh Kumar, Baskaran Balaji, and Kannan Ganesa Balamurugan

## 1 Introduction

Aluminium alloys have wide application in automobile, aerospace and marine sectors due to its lower density and strength ratio. However, joining of aluminium alloys are always challenging by fusion welding processes. To overcome this, friction stir welding was introduced by TWI in UK [1–4]. The friction stir welding technique has been identified and utilized as unique surface modification tool which is popularly identified as friction stir processing [5–7]. In the recent scenario, both FSW and FSP techniques are grouped under the common name of friction stir processing (FSP). The contribution of friction stir processing on various manufacturing methods is ever expanding. One of its prominent contributions is in the additive manufacturing method. The additive manufacturing is a near net shape fabrication process by adding materials by layer by layer [8–10]. FSAM opens a martial window in supporting the aluminium stack welds which are mostly used in automobiles and aerospace. Near net-shaped components with refined equiaxed grain was obtained which drastically improves the joint strength [11]; volume fraction and number of passes might initiate particle fragmentation, continuous dynamic recrystallization, and deforming the initial matrix grain results in improved property gradients [12]; recrystallization led to ultra-fine grain size, when refined grain structure is linked with precipitations which induces higher mechanical properties [13]. The friction stir additive manufacturing is suitable technique to attain higher performances in lightweight alloys categories [14]. The present work aims to fabricate aluminium layers by friction stir additive manufacturing technique and to investigate the effect of process parameters on the microstructural and hardness of the FAM fabricated layers.

---

R. Dinesh Kumar  
National Institute of Technology Srinagar, Srinagar, India

B. Balaji · K. G. Balamurugan (✉)  
IFET College of Engineering (Autonomous), Villupuram, Tamil Nadu, India

## 2 Experimental Work

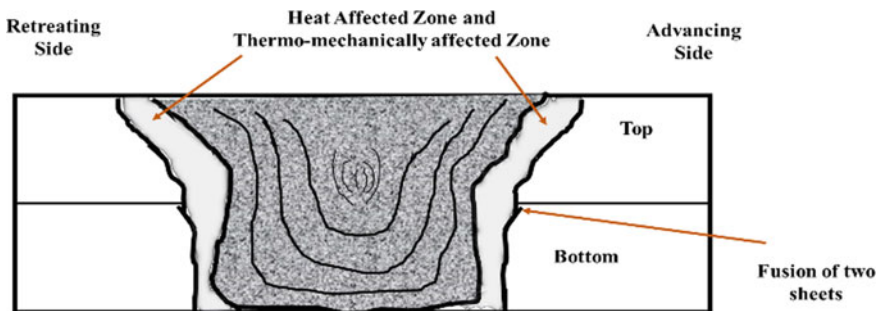
Commercially pure Al1100 aluminium grade was selected for the friction stir additive process (FSAP). The composition of Al1100 is given in Table 1. The FSAP tool was made out of high-speed steel with the dimensions of 18 mm shoulder diameter, 6 mm pin diameter and 5 mm pin diameter. The plates were firmly mounted on the machine table using proper clamping. The required process parameter values were programmed in the controller of the machine and activated. The process parameters values are shown in Table 2. After activation of the program, the FSAP tool started rotating and plunged into the plates. After a pass, the tool got offset of half of the diameter of the shoulder (9 mm) and performed a second pass. After completion of entire passes, the tool retrieved to its original position. The processed samples were subjected to metallographic and mechanical testing. For metallographic analysis, samples were cross-sectioned and mounted in the bakelite moulds. The schematic representation of a cross section of FAM sample is shown in Fig. 1. Then, samples were polished to silver finish and etched with Keller's reagent. Both optical and scanning electron microscopy were utilized for metallographic studies. Microhardness

**Table 1** Chemical composition of Al1100 aluminium

Elements	Al	Cu	Fe	Mn	Si	Zn	Residuals
Composition %	99.0–99.5	0.05–0.20	0.95	0.05	0.95	0.1	0.15

**Table 2** Process parameters values

Sample No.	Tool rotation speed (RPM)	Tool travel speed (mm/min)
01	700	15
02	700	30
03	1000	15
04	1000	30



**Fig. 1** Schematic of the cross section of the FAM specimen

surveys were carried out on cross-sectioned samples with 0.5 g of the load for 10 s dwell time.

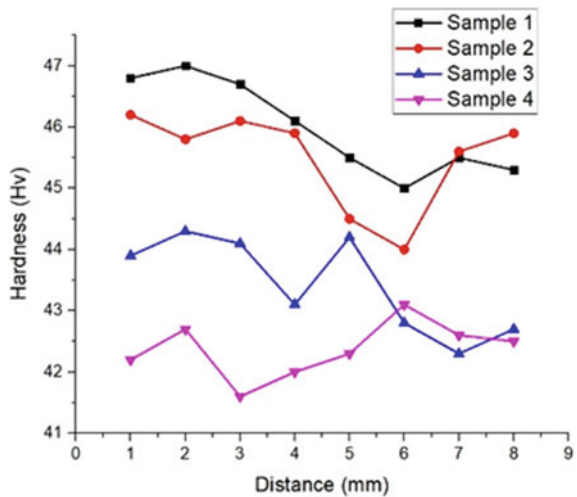
### 3 Results and Discussion

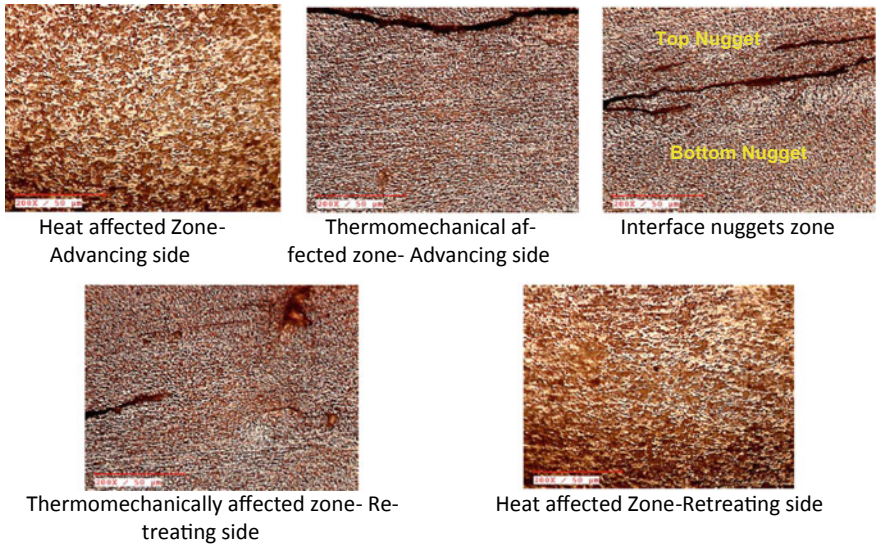
The experimental results are plotted in the form of graph. Figure 2 shows the hardness profile of FAM samples processed at specified process parametric conditions. The hardness decreases as from advancing side to retreating side in the sample-1. The similar pattern was observed in sample-2; however, a marginal increase in hardness was noticed at retreating side. In sample-3, a slight drop in hardness was observed at nugget zone with a sudden steep increase in TMT zone and a gradual reduction of hardness was noticed towards the retreating side.

In the sample-4, the hardness dropped near advancing side. TMT zone and gradually increase from nugget zone to retreating side HAZ. Near the end of retreating side HAZ, decreasing trend occurred. The microhardness of FAM samples decreases from sample-1 to sample-4. Sample-1 shows higher microhardness among other samples. Likewise, sample-4 shows the lower microhardness. The processed zones grain size and microstructural patterns affect the microhardness variations. Figure 3 shows the microstructures of processed zones of FAM-1 sample. The heat-affected zones of advancing have equiaxed grains, and the retreating side has slightly elongated grains. Therefore, the hardness at advancing side heat-affected zone is higher than the retreating side. The top and bottom nugget zones have very refined grains.

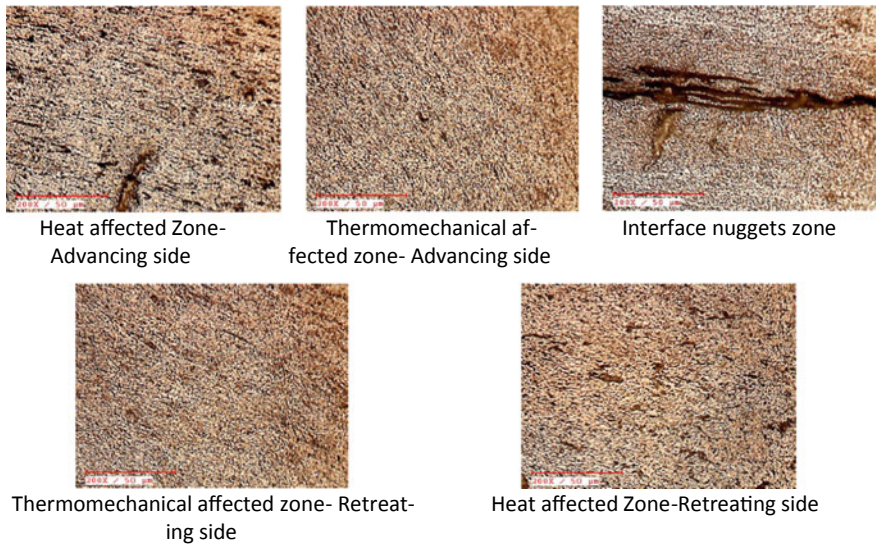
Due to the extreme refining of grains, materials softening occurred in the nugget zones which leads to a reduction of hardness in this zone. Figure 4 shows the microstructures of processed zones of FAM-4 sample. The heat-affected zones of

Fig. 2 Microhardness profiles of FAM specimens





**Fig. 3** Microstructures of processed zones of FAM sample-1



**Fig. 4** Microstructures of processed zones of FAM sample-4

advancing have elongated grains, and the retreating side has compressed grains. Therefore, the hardness at advancing side heat-affected zone is lower than the retreating side. The nugget zones have refined grains and inclusions. The considerable grain refinement leads to a slight increase in hardness. Apart from the grain refinements and orientations, the presence of secondary particles like intermetallics will affect the microhardness of the processed samples. At lower rotational speed and travel speed, the precipitated intermetallic particles survived due to low heat input. However, at higher rotational speed and higher travel speed, the precipitated intermetallic particles dissolved again into the matrix material due to the high heat input. Therefore, higher hardness resulted in lower rotational and lower travel speed combinations like sample-1 process parameter. Likewise, lower hardness resulted in higher rotational and higher travel speed combinations like sample-4.

## 4 Conclusion

The following are the conclusion drawn from the experimental study on friction stir additive manufactured commercial pure aluminium alloy:

- The low tool rotational speed and travel speed form the equiaxial and refined grains in the stirred zones. Due to low heat input at this processing condition, the intermetallic particles have survived. Therefore, the samples processed in this processing conditions show higher hardness.
- The high tool rotational speed and travel speed form the elongated and refined grains in the stirred zones. Due to high heat input at this processing condition, the dissolution of intermetallic particles occurred in the matrix material. Therefore, the samples processed in this processing conditions show lower hardness.

## References

1. Chandran, R., Ramaian, S., Shanbhag, A.G., Senthil Kumar, V.S.: Optimization of welding parameters for friction stir lap welding of AA6061-T6 alloy. *Mod. Mech. Eng.* **8**, 31–41 (2018)
2. Venukumar, S., Baby, B., Muthukumaran, S., Kailas, S.V.: Microstructural and mechanical properties of walking friction stir spot welded AA 6061-T6 sheets. *Procedia Mater. Sci.* **6**, 656–665 (2014)
3. Yong, P., Changbin, S., Yadong, Z., Ying, C.: Comparison of electrochemical behaviors between FSW and MIG joints for 6082 aluminum alloy. *Rare Metal Mater. Eng.* **46**, 344–348 (2017)
4. Bodukuri, A.K., Eswaraiyah, K. Rajendar, K., Siddartha, A.: Comparison of aluminum alloy 5083 properties on TIGW and FSW processes. *Mater. Today. Proce.* **4**, 10197–1020 (2017)
5. Ganesa Balamurugan, K., Mahadevan, K.: Investigation on the effects of process parameters on the mechanical and corrosion behaviour of friction stir-clad AZ31B magnesium alloy. *Arab. J. Sci. Eng.* **40**, 1647–1655 (2015)
6. Węglowski, M.S.: Friction stir processing—state of the art. *Arch. Civ. Mech. Eng.* **18**, 114–129 (2018)



7. Mishra, R.S., Ma, Z.Y.: Friction stir welding and processing. *Mater. Sci. Eng. R. Rep.* **50**, 1–78 (2005)
8. Farsadi, M.; Bagheri, S., Ismail, N.A.: Nanocomposite of functionalized graphene and molybdenum disulfide as friction modifier additive for lubricant. *J. Mol. Liq.* **244**, 304–308 (2017)
9. Kannan, G.B., Rajendran, D.K.: A review on status of research in metal additive manufacturing. In: Wimpenny, D.I. Pandey, P.M. Kumar, L.J. (eds.) *Advances in 3D Printing & Additive Manufacturing Technologie*, pp. 95–100. Springer: Singapore (2017)
10. Padhy, G.K., Wu, C.S., Gao, S.: Friction stir based welding and processing technologies—processes, parameters, microstructures and applications: a review. *J. Mater. Sci. Technol.* (2017)
11. Riveraa, O.G., Allisona, P.G., Jordona, J.B., Rodrigueza, O.L., Brewerb, L.N., McClellandc, Z., Whittingtond, W.R., Francisd, D., Sue, J., Martensf, R.L., Hardwicke, N.: Microstructures and mechanical behavior of Inconel 625 fabricated by solid-state additive manufacturing. *Mater. Sci. Eng., A* **694**, 1–9 (2017)
12. Sharmaa, A., Vijendraa, B., Ito, K., Kohamab, K., Ramjia, M. Himasekhar Sai, B.V.: A new process for design and manufacture of tailor-made functionally graded composites through friction stir additive manufacturing. *J. Manuf. Process.* **26**, 122–130 (2017)
13. Palanivel, S., Nelaturu, P., Glass, B., Mishra, R.S.: Friction stir additive manufacturing for high structural performance through microstructural control in an Mg based WE43 alloy. *Mater. Des.* **65**, 934–952 (2015)
14. Palanivel, S., Nelaturu, P., Glass, B., Mishra, R.S.: 2 Friction stir additive manufacturing: route to high structural performance. *The Miner., Metals & Mater. Soc.* **67** (2015)

# Finite Element Modeling to Predict the Defect Formation in Friction Stir Welds of AA6061



Sumit Kumar Purswani , Vikas Upadhyay , A. Karapagraj ,  
and L. R. Shobin 

## 1 Introduction

At present decade, reduction of deadweight of automotive components resulted in increased use of lightweight alloys and development of advanced welding methods. Friction stir welding (FSW) is relatively a newer technique specifically used for joining thin sheets of aluminum, steel and dissimilar materials. FSW is the best choice solid-state welding process with less defects formation for the above-mentioned materials. Because defects like porosity and hot cracking were not generated during fusion welding [1]. Determination of viable range of operating parameters is crucial for the formation of defect-free welds.

Literature review and preliminary information are generally used to determine the initial range of welding parameters. Later, actual experiments were carried out with these parameters to find the optimum value of operating parameters. This process is a lengthy and time consuming one. FSW is costly process due to intensive characterization and process requirements. Simulation of FSW process is an effective and viable alternative for these problems [2].

Nandan et al., 2006 numerically modeled FSW by considering the 3D viscoplastic flow and temperature field [3]. In this model, non-Newtonian viscosity was correlated with temperature-dependent material properties and temperature. It was concluded that temperature fields, cooling rates and the geometry of the thermo-mechanically affected zone were in agreement with experimental work. Buffa et al., 2011 carried out thermal stresses prediction from the finite element model [4]. It was reported that the material behavior model has significant role in controlling the simulation/computational time. Trimble et al., 2012 investigated the tool force for

---

S. K. Purswani · V. Upadhyay · A. Karapagraj (✉)  
Mechanical Engineering Department, National Institute of Technology Patna, Patna, India

L. R. Shobin  
Department of Education, Central University of Tamil Nadu, Thiruvavur, India

different joint configurations using FSW process [5]. Dynamometer was used to determine the tool force experimentally, and it was compared with the finite element analysis results. The predictions showed good agreement of finite element model with the experimental work. This shows the ability of the finite element model on the force predictions using finite element modeling. Dialami et al., 2017 studied the pin profile effect on the material flow, forces and thermal behavior of FSW [6]. Various profiles like circular, triflute, trivex and triangular profiles were taken for the study. Additionally, slip and stick limiting friction cases between pin and work piece were also engaged along with the finite element study. It was concluded that types of pin and flutes were contributing a lot with temperature generation. Assidi et al., 2010 formulated a simulation for FSW with circular profile [7]. It was found that the effect of friction on the temperature distribution was affected by the pin profile. It was reported that coulomb's law of friction (coefficient of friction = 0.3) gives better result of temperature distribution in the vicinity of the tool. Chen et al., 2018 studied the effect of tool pin on the material flow and temperature distribution [8]. It was pointed out that pin thread can also be able to disturb the trapping of materials while moving at high velocity.

It is evident that a number of studies on simulation and finite element modeling of FSW process have been carried out. But to the best of author's knowledge, there are very few studies on defect prediction in FSW process. Hence, an attempt was made in this research to address the defect formation.

## 2 Materials and Methods

### 2.1 Material

Precipitation hardening Al–Mg–Si alloy AA6061 was selected as base metal for this work. AA6061 is available in various forms as rolled plate and sheet, extrusions, forgings and tubing and piping and used in general for high-strength heavy-duty structures requiring good corrosion resistance such as vehicles, rolling stock, marine applications and architectural applications [9]. AA6061 in T6 temper condition having strips size of 70 mm × 70 mm × 5 mm was used in welding simulation. Mechanical and thermal properties are taken for current research materials as referred with the existing literature [10]. With respect to the temperature interval (25–482 °C), Young's modulus ( $E$  (GPa)), specific heat capacity  $C_p$  ( $\text{Jkg}^{-1} \text{ } ^\circ\text{C}^{-1}$ ), density  $\rho$  ( $\text{kgm}^{-3}$ ) and thermal expansion  $\alpha$  ( $\mu\text{mm}^{-1} \text{ } ^\circ\text{C}^{-1}$ ) are taken and implemented for conducting the simulation. A cylindrical tool of H13 steel of 2.66 mm and 8 mm pin and shoulder diameter, respectively, was used. Rotational speed and traverse speed were kept fixed at 900 rpm and 60 mm/min, respectively, whereas shoulder plunge depth of 0.1 mm, 0.3 mm and 0.5 mm has been taken for the analysis.

## 2.2 Simulation Details

In this work, a finite element analysis (FEA)-based simulation of FSW process has been carried out using Abaqus /Explicit software. Eulerian explicit analysis is used while performing the analysis of FSW. The complete domain is divided into small elements, and interactions (mechanical and thermal) of these small elements produces the overall output of the process. Explicit dynamic mechanical interaction between various elements takes place by following equations for force and displacement [11]

$$F/D = X\ddot{a} + Y\dot{a} + Za \quad (1)$$

Here  $F$  and  $D$  denotes any displacement or force on any element, while the term on the right side  $X\ddot{a}$  denotes sum of any inertial factor associated with element,  $Y\dot{a}$  denotes sum of all energy damped in element,  $Za$  denotes total stiffness of the element. Coefficient  $X$ ,  $Y$  and  $Z$  are mass, damping coefficient, stiffness coefficient of the body, respectively, while terms  $a$ ,  $\dot{a}$  and  $\ddot{a}$  denote the displacement, velocity and acceleration in the element, respectively.

The major equation for heat transfer is as following [12]

$$\frac{\partial}{\partial x} \left( k_x \frac{\partial T}{\partial x} \right) + \frac{\partial}{\partial y} \left( k_y \frac{\partial T}{\partial y} \right) + \frac{\partial}{\partial z} \left( k_z \frac{\partial T}{\partial z} \right) + Q = \rho C \frac{\partial T}{\partial t} \quad (2)$$

where  $\rho$  is density of the material;  $C$  is specific heat;  $T$  is temperature;  $t$  is time;  $K_x$ ,  $K_y$  and  $K_z$  are thermal conductivity in  $X$ ,  $Y$  and  $Z$  direction, respectively;  $Q$  is heat generated within the body. Corresponding counterpart of heat transfer in Abaqus /Explicit is as follows [11],

$$K(t) + C(t)\dot{T} = H(t) \quad (3)$$

where  $K(t)$  is time-dependent thermal conductivity matrix;  $C(t)$  is capacitance matrix dependent on time;  $\dot{T}$  is derivative of temperature with respect to the time;  $H(t)$  is time dependent hat matrix. Also the material model used in Abaqus/Explicit to simulate the FSW process is based on Johnson–Cook formula. In this model, flow stress in a material is given as [10, 13],

$$\sigma_{fs} = \left( A + B\bar{\varepsilon}_{pl}^n \right) \left( 1 + C \ln \frac{\dot{\varepsilon}_{pl}}{\varepsilon_0} \right) \left( 1 - \left( \frac{T - T_{ref}}{T_{melt} - T_{ref}} \right)^m \right) \quad (4)$$

where  $\bar{\varepsilon}_{pl}$  is equivalent strain,  $\dot{\varepsilon}_{pl}$  is equivalent plastic strain rate,  $\varepsilon_0$  is normalizing strain rate,  $n$  denotes strain hardening,  $m$  models high temperature softening effect,  $C$  (0.002) represents strain rate sensitivity,  $A$  (324 MPa) and  $B$  (114 MPa) are material constants. Johnson–Cook (JC) constants for AA6061-T6 have been used for the

simulation work [10]. Where  $A, B, C, m$  and  $n$  are material constants;  $T_{\text{room}}$  (24 °C) is temperature where value of  $A, B, m$  (1.34) and  $n$  (0.42) are calculated;  $T_{\text{melt}}$  (583 °C) is solidus temperature. Where,  $\sigma_y$  is flow stress;  $A, B, C$  are material constants;  $\varepsilon$  is effective plastic strain;  $\varepsilon_p$  is strain rate;  $\varepsilon_o$  is reference strain rate;  $m$  is constant for thermal softening. In this formula, it is assumed that flow stress in an element is individually affected by thermal softening, strain rate sensitivity and strain hardening (refer Formula 4) [10, 12].

For modeling of FSW process, thermo-mechanical interaction is adopted for contact between tool and work piece. To establish these interactions, two surfaces are created, i.e., master and slave. In these surfaces, the work piece surface is interacted with tool during the FSW process. It has been selected as master, while the surface of pin and shoulder in tool which interact during process has been selected as slave surface. Further, the normal pressure between tool and work piece has been converted into frictional stress by adopting simple coulomb law in modeling. Frictional stress will be responsible for frictional heating which is a major factor for heating in welding zone in FSW. For movement of the work piece along the pin, basic coulomb law is adopted in the modeling. According to this law, sticking of master–slave surface will take place if shear stress is less than the critical shear stress.

$$\tau = \mu P \quad (5)$$

where  $\tau$  is critical shear stress;  $\mu$  is coefficient of friction and  $P$  is normal pressure between master and slave surface. To analyze the defect formed during FSW process in Abaqus, we study the Eulerian volume fraction (EVF) in the work piece. At the location of defect, there will be absence of material in that particular portion, so for corresponding location, EVF will be one and at the point of defect-free region EVF, will be zero.

Though simulation was close to real-time environment of FSW process, it has several assumptions:

1. Tool has been considered as rigid body. The other parameters like tool speed and pressure are uniform during the welding operation.
2. Simple coulomb law has been used to analyze the tangential interaction of tool and work piece. Material sticking and its flow take place according to simple coulomb law.
3. Model does not consider microstructural change in the work piece. Temperature-dependent material properties were used.
4. Heat transfer to the surrounding was considered only due to convection mode. Radiation losses are neglected.
5. Tool is moving and work piece is stationary.
6. Initial temperature of the work piece and tool are 24 °C.
7. Tool was assumed rigid whereas work piece was taken as deformable material (Eulerian).

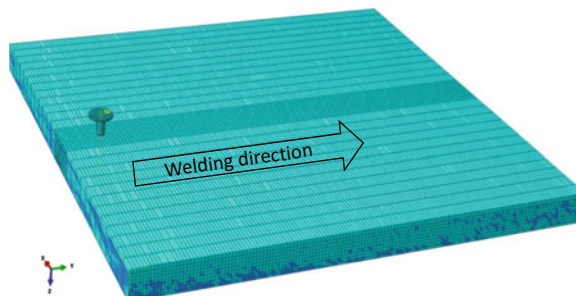
### 3 Results and Discussion

In this work, an attempt has been made to predict the defects in FSW process through simulation. For this purpose, defect-generating operating parameters have been used with an optimal pin to shoulder diameter ratio. Arrangement used in FSW simulation has been modeled in Abaqus as shown in Fig. 1. The specimen with mesh arrangement is shown in Fig. 1. Fine mesh is placed at the weld center, and the coarse mesh is placed for other than weld center. This will help to reduce the computational time and generates accurate result at the analysis domain. Plunge depth has been varied as 0.1 mm, 0.3 mm and 0.5 mm to analyze the corresponding effect on the resulting weld. Simulation results indicates the effect of plunge depth on defect formation and it is displayed in Fig. 2.

It is evident from Fig. 2 that with increase in plunge depth, defect formation in the vicinity at the bottom of tool pin decreases. This effect occurs because most of the heat in FSW is obtained from frictional contact between shoulder and work piece. With increase in plunge depth, contact area (lateral surface of the shoulder) between tool and work piece also increases and the distance between bottom of the work piece and shoulder decreases which allows sufficient heat at the bottom of the work piece. These two factors allow sufficient heat to reach at the bottom zone and optimum softening takes place. So, with increase in plunge depth, proper softening at the bottom of the work piece allows desired flow of material and results in the formation of a defect-free joint [14].

Effect of varying the plunge depth of tool shoulder was investigated by Muhayat et al., 2014 experimentally in FSW of 4 mm sheet welded by 3.8 mm long tool pin [15]. It was found that increasing the plunge depth of 0.5 mm make tunnel defect formed at the advancing side of the tool bottom. On the other hand, at the depth of 0.1 mm, defect formation is reduced to void with the depth of 0.15 mm; there is small shaped defect on advancing side of the joint. But there is limitation on increase of plunge depth as increase in plunge depth leads to depression at the top of the work piece. This in turn reduces the work piece thickness at the joint-line resulting in weak joint, so generally plunge depth was kept between 0.1 mm and 0.4 mm for efficient joint [15]. As the defect cannot be eliminated by increasing the plunge depth up to

**Fig. 1** Tool, welding plates and direction of welding



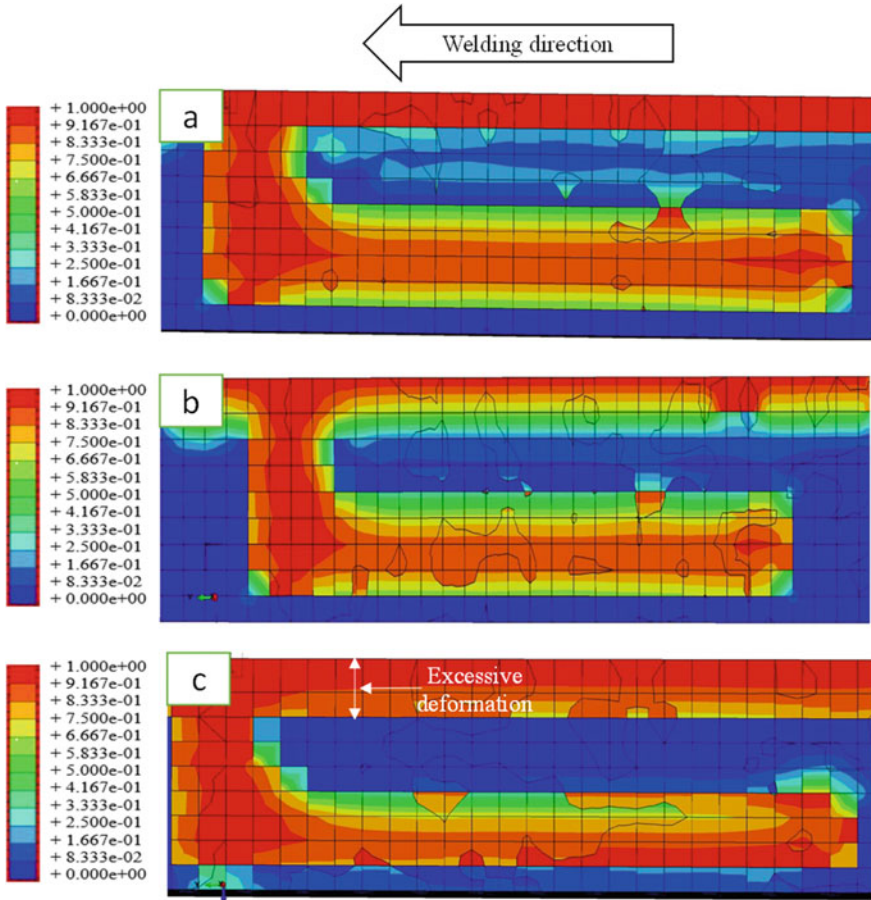


Fig. 2 Defect formation at plunge depth of a 0.1 mm, b 0.3 mm, c 0.5 mm

the permissible limit. So it indicates that there are other parameters responsible for defect formation and thus needs further investigation.

### 4 Conclusion

The following important points have been concluded from this work. CEL method of analysis is suitable for study of defect as it permits the flow of the material in the processing zone. In this investigation, plunge depth has been varied between the ranges of 0.1–0.5 mm. The defect formed at the root is minimum at 0.5 mm depth. Increase in plunge depth of the shoulder decreases the defect formation at the root of the welded joints. But there is limitation on plunge depth value as higher depth

may lead to depression on the surface of developed joint. It is possible to use the numerical tools to predict the defects produced during the FSW process. This work can help the researchers to develop better joints. Future work may cover various tool profiles in connection with defect formation.

## References

1. Arbegast, W.J.: Modeling friction stir joining as a metalworking process. Hot deformation of aluminum alloys III, 313 (2003)
2. He, X.: Numerical studies on friction stir welding of lightweight materials. *Adv. Mater. Res.* **743**, 118–122 (2013)
3. Nandan, R., Roy, G.G., Debroy, T.: Numerical simulation of three-dimensional heat transfer and plastic flow during friction stir welding. *Metall. Mater. Trans. A.* **37**(4), 1247–1259 (2006)
4. Buffa, G., Ducato, A., Fratini, L.: Numerical procedure for residual stresses prediction in friction stir welding. *Finite Elem. Anal. Des.* **47**(4), 470–476 (2011)
5. Trimble, D., Monaghan, J., O'donnell, G.E.: Force generation during friction stir welding of AA2024-T3. *CIRP Ann.* **61**(1), 9–12 (2012)
6. Dialami, N., Cervera, M., Chiumenti, M., de Saracibar, C.A.: A fast and accurate two-stage strategy to evaluate the effect of the pin tool profile on metal flow, torque and forces in friction stir welding. *Int. J. Mech. Sci.* **122**, 215–227 (2017)
7. Assidi, M., Fourment, L., Guerdoux, S., Nelson, T.: Friction model for friction stir welding process simulation: calibrations from welding experiments. *Int. J. Mach. Tools Manuf.* **50**(2), 143–155 (2010)
8. Chen, G., Li, H., Wang, G., Guo, Z., Zhang, S., Dai, Q., Shi, Q.: Effects of pin thread on the in-process material flow behavior during friction stir welding: a computational fluid dynamics study. *Int. J. Mach. Tools Manuf.* **124**, 12–21 (2018)
9. Kumar, R., Ghost, A., Chattopadhyaya: Emerging friction stir welding for aluminium and its applications. *J. Manuf. Ind. Eng.* **14**(1–2), 1–5 (2014)
10. Al-Badour, F., Merah, N., Shuaib, A., Bazoune, A.: Coupled Eulerian Lagrangian finite element modeling of friction stir welding processes. *J. Mater. Process. Technol.* **213**(8), 1433–1439 (2013)
11. Ahmad, B., Galloway, A., Toumpis, A.: Advanced numerical modelling of friction stir welded low alloy steel. *J. Manuf. Process.* **34**, 625–636 (2018)
12. Karpagaraj, A., Shanmugam, N. S., Sankaranarayananasamy, K.: Experimental investigations and numerical prediction on the effect of shielding area and post flow time in the GTAW of CP Ti sheets. *Int. J. Adv. Manuf. Technol.* **101**(9–12), 2933–2945 (2019)
13. Zhu, Z., Wang, M., Zhang, H., Zhang, X., Yu, T., Wu, Z.: A finite element model to simulate defect formation during friction stir welding. *Metals* **7**(7), 256 (2017)
14. Chauhan, P., Jain, R., Pal, S.K., Singh, S.B.: Modeling of defects in friction stir welding using coupled Eulerian and Lagrangian method. *J. Manuf. Process.* **34**, 158–166 (2018)
15. Muhayat, N., Zubaydi, A., Yuliadi, M.Z.: Effect of tool tilt angle and tool plunge depth on mechanical properties of friction stir welded AA 5083 joints. *Appl. Mech. Mater., Trans. Tech. Publ. Ltd.* **493**, 709–714 (2014)



# Effect of Turning Parameters on Surface Roughness of EN-9 Steel Using Taguchi Robust design—An Analysis



Shahid Khurshid, Mehjooaba Zainab, Yasir Farooq, Faizan Yousuf, Tamjeed Ayoub, Fayaz Ahmad Mir, and Junaid Hassan Masoodi

## 1 Introduction

Machining plays a crucial part in today's manufacturing world. The commonly known machining processes include turning, milling, drilling, boring, threading, etc. Turning is a machining process, where diameter is reduced from a cylindrical job using cutting tool [1]. In turning, work piece is held firmly in revolving chuck, while feed and depth of cut are given to single point cutting tool. Lathe machine, also known as mother of all machines, is used to produce cylindrical parts by the help of turning process. To produce desired surfaces, material removal takes place. In turning, input parameters like feed rate, spindle speed, depth of cut and tool material plays significant character on performance characteristics [2]. Surface roughness has a vital contribution in execution of mechanical components; thus, it is considered an important parameter in manufacturing engineering [3]. Thus, it is very important to select the input parameters in such a way to get the desired output, which can be achieved by setting of these parameters in systematic manner, so to achieve highest performance characteristics. To achieve this requirement, there is a need of optimization of performance parameters. Various optimization techniques were used by various researchers to optimize various input parameters to achieve good surface quality. Taguchi method is considered one of the most favorable optimization techniques, which helps to achieve optimized results by identifying noise sources, which have the greatest effects on product variability. Many researchers in the past

---

S. Khurshid (✉) · M. Zainab · Y. Farooq · F. Yousuf · T. Ayoub · J. H. Masoodi  
Department of Mechanical Engineering, Institute of Technology, Zakura Campus - University of Kashmir, Srinagar 190006, India

F. A. Mir  
Department of Mechanical Engineering, National Institute of Technology Srinagar, Srinagar 190006, India

also have successfully used Taguchi method to obtain optimized process parameters [4–6]. Kolluru et al. found that depth of cut has a greater impact on surface followed by feed rate and spindle speed [7]. Ravuri et al. used Taguchi technique and found optimal values of speed, DOC, feed and nose radius at 1400 rpm, 0.1 mm, 0.05 mm/rev and 0.4, respectively [8]. Dutta et al. during their investigation on optimization of surface roughness and cutting force found that feed rate alone significantly effects the surface roughness, while as effect feed rate and depth of cut were found significant on cutting force [9]. The objective of this work is to achieve desired surface roughness by optimizing the process parameters using Taguchi robust technique. For the present study, three input parameters (SS, FR and DOC) have been selected to examine their consequences on surface roughness of EN 9 steel. By the help of analysis of mean, the optimal combination was generated [10]. The results were further investigated on SYSTAT software, a statistical tool. ANOVA was also used to check the significance and percentage distribution of each parameter.

In the future, further studies may be conducted on other factors like cutting angle, cutting tool material, different coating materials, lubricants, etc.

## **2 Material and Experimental Details**

### **2.1 Work Piece Material**

Steel is an alloy of iron and carbon with the carbon content up to about 2% wt. Material used in this study is EN-9 Steel (grade-1020), which is a well-known grade of steel alloy. With high degree of hardness, strength and wear resistance properties, this steel grade is mostly used in axles, sprockets, gears, cams bolts and shafts [11]. The chemical composition of this steel alloy is given in Table 1.

### **2.2 Cutting Tool**

The trials were conducted using CVD-coated carbide tool. The property of such tool is given in Table 2.

### **2.3 Turning Experiments**

Nine turning tests were conducted using centerless lathe machine as shown in Fig. 1.

**Table 1** Chemical composition of EN-9 steel (grade-1020)

Element	C	Si	Mn	S	P	Cr	Ni	Cu
(wt%)	0.170-0.240	0.170-0.370	0.700-1.000	≤0.035	≤0.060	≤0.250	≤0.250	≤0.250

**Table 2** Cutting tool properties

Coating method	Material	Thickness	Grade	Hv
CVD	TiAlN	4	C20 (GC1020)	1600

**Fig. 1** Experimental setup for turning tests**Table 3** Process parameters at level three each

Symbol	Parameter	Unit	L <sub>I</sub>	L <sub>II</sub>	L <sub>III</sub>
A	Spindle speed (SS)	rpm	350	550	750
B	Feed rate (FR)	mm/min	15	20	25
C	Depth of cut (DOC)	mm	0.40	0.80	1.20

## 2.4 Experimental Design

Three parameters (Spindle speed, Feed rate, Depth of cut) each at level three, as given in Table 3, are used to study their effect on surface roughness of EN 9 steel.

## 2.5 $L_9$ Orthogonal Array

On the basis,  $L_9$  orthogonal array, nine experiments were designed as shown in Table 4. The 1's, 2's and 3's in the matrix represents the low, medium and higher level, respectively, of the process parameters. For, three factors, each at level three

**Table 4** L<sub>9</sub>-orthogonal array

Trail	A	B	C
T <sub>1</sub>	1	1	1
T <sub>2</sub>	1	2	2
T <sub>3</sub>	1	3	3
T <sub>4</sub>	2	1	3
T <sub>5</sub>	2	2	1
T <sub>6</sub>	2	3	2
T <sub>7</sub>	3	1	2
T <sub>8</sub>	3	2	3
T <sub>9</sub>	3	3	1

(33), twenty-seven experiments were needed under full factorial design. Using L<sub>9</sub>-Taguchimatrix helps to design the experimental plan in a more systematic way, thus helps in minimizing total number of experimental runs [12].

### 3 Results and Discussion

#### 3.1 Analysis of Surface Roughness

Taguchi robust design is widely used for experimental analysis. This method uses standard orthogonal arrays, which helps to conduct the experiments in a more systematic manner and results in minimizing the total number of experiments. Surface roughness was measured by surface roughness measuring tester (MITUTOYO-SURFTEST SV-2100). Taguchi philosophy is based on robust design, according to which, quality should be designed in a product/process rather than inspect it. S/N ratio plays an important role in a robust design, where “S” defines signal controllable variables and “N” gives the noise value. For better surface finish, the S/N ratio should always be maximum. In the present study, lower the better approach was used to calculate S/N ratio as given below:

$$\eta = -10 \log \left[ 1/n \sum_{i=1}^n y_i^2 \right] \tag{1}$$

where  $y_i$  is observed Ra at  $i$ th experimental trial, and  $n$  represents the total experimental trials.

As per L<sub>9</sub> orthogonal array, nine experiments were conducted on nine work samples (cylindrical) without replication as shown in Fig. 2, and results of response Ra (μm) and S/N ratio for each trail are shown in Table 5



**Fig. 2** Machined work piece

**Table 5** Ra and S/N ratio

Exp. No.	A	B	C	Ra( $\mu\text{m}$ )	S/N ratio
1	350	15	0.4	3.826	-11.655
2	350	20	0.8	0.915	0.772
3	350	25	1.2	4.315	-12.699
4	550	15	1.2	1.563	-3.823
5	550	20	0.4	3.978	-11.993
6	550	25	0.8	8.584	-18.673
7	750	15	0.8	1.509	-3.573
8	750	20	1.2	4.570	-13.198
9	750	25	0.4	10.721	-20.604

### 3.2 Analysis of Mean S/N Ratio

The results are given in Table 6. ANOM is used to identify the optimal combination. It is calculated by taking the mean average of S/N ratio at each level.

For better response, it is always recommended that the S/N ratio should be as maximum as possible, thus from analysis of mean S/N ratio response, the optimal combination so generated is A1B2C2.

**Table 6** S/N ratio response table

Symbol	L <sub>I</sub>	L <sub>II</sub>	L <sub>III</sub>	Range ( $\Delta$ )	Rank
A	-7.860	-11.490	-12.450	4.590	3
B	-8.139	-6.350	17.325	10.975	1
C	-14.750	-7.158	-9.906	7.592	2

**Table 7** Analysis of variance

SOV	SS	D.O. F	M.S	F-value	% cont	P-value
A	10.523	2	5.261	10.914	12.138	0.174
B	60.570	2	30.285	62.831	69.87	0.018
C	14.631	2	7.3155	15.177	16.87	0.154
Error	0.964	2	0.482	1	1.11	
Total	86.688	8	75.649			

where  $V_1 =$  D.O.F of Parameters,  $V_2 =$  D.O.F of Error

### 3.3 Analysis of Variance

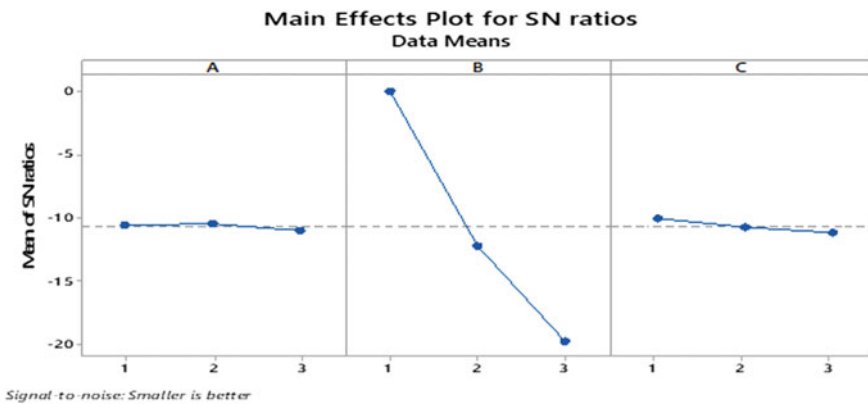
ANOVA is used to check the significance of each parameter on the response, results of which are given in Table 7.

Now, at 5% significance level, using  $F$ -table, we have:

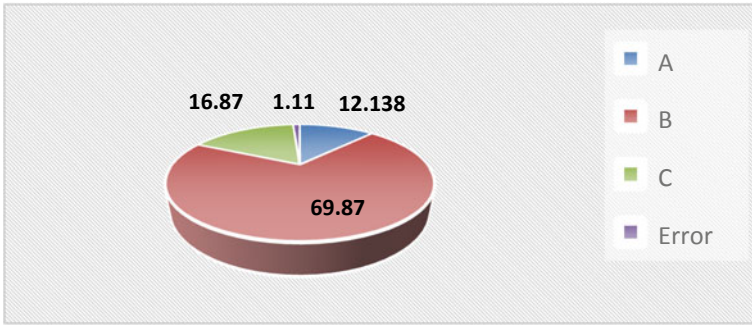
$$F_{\text{Critical}} = F_{0.05,2,2} = 19 \tag{2}$$

On comparing,  $F$ -calculated with  $F$ -critical, we have  $F$ -calculated greater than  $F$ -critical only for feed rate. Thus, it is concluded that only feed rate significantly affects the response, which is surface roughness in present study. Also, the  $P$ -value for spindle speed and depth of cut are higher than the significant level (0.05), hence, null hypothesis cannot be rejected, reveals their insignificant effect on surface roughness ( $\mu\text{m}$ ). Also,  $p$ -value for feed rate is lower than 0.05, thus null hypothesis can be rejected.

The main effect plot and percentage contribution of parameters and error are shown in Figs. 3 and 4, respectively.



**Fig. 3** Main effects plot



**Fig. 4** Percentage contribution of parameters and error

## 4 Conclusions

In the present study, Taguchi robust design was successfully applied to generate efficient setting of process parameters in turning of EN-9 steel with CVD-coated tool.

- The optimum levels of process parameters generated is  $A_1B_2C_2$ , i.e., spindle speed (SS) = 350 rpm, feed rate (FR) = 20 mm/min, depth of cut (DOC) = 0.8 mm, Therefore, they are advisable levels for controllable variables of the turning process to reduce surface roughness of EN9 steel.
- ANOVA analysis revealed that FR significantly affects the surface roughness. The contribution of FR was 69.87%, whereas SS and DOC were found insignificant. Also, the percentage contribution of SS and DOC are 12.138% and 16.87%, respectively.
- The order of importance for the parameters of the present response (Ra) is FR followed by DOC and SS. Thus, FR is the most overtop factor for turning process in the present study.

## References

1. Bhattacharya, A., Das, S., Majumder, P., Batish, A.: Estimating the effect of cutting parameters on surface finish and power consumption during high-speed machining of AISI 1045 steel using Taguchi design and ANOVA. *Prod. Eng.* **3**, 31–40 (2009). <https://doi.org/10.1007/s11740-008-0132-2>
2. Asiltürk, İ., Akkuş, H.: Determining the effect of cutting parameters on surface roughness in hard turning using the Taguchi method. *Measurement* **44**, 1697–1704 (2011). <https://doi.org/10.1016/j.measurement.2011.07.003>
3. Hwang, Y.K., Lee, C.M.: Surface roughness and cutting force prediction in MQL and wet turning process of AISI 1045 using design of experiments. *J. Mech. Sci. Technol.* **24**, 1669–1677 (2010)



4. Ahmad Mir, F., Khan, Z.A., Noor Siddiquee, A., Shihab, S.K.: Investigations on the effect of radius milling process parameters on surface roughness (2017)
5. Rai, A., Yadav, S., Sachan, V.: application of Taguchi method in the optimization of boring (2013)
6. Abbas, A.T., Ragab, A.E., Benyahia, F., Soliman, M.S.: Taguchi robust design for optimizing surface roughness of turned AISI 1045 steel considering the tool nose radius and coolant as noise factors (2018)
7. Kolluru, U.K., Kumar, S., Narala, R., Dutta, S.: Materials today: proceedings optimization of cutting forces and surface roughness in dry turning of AM magnesium alloy using Taguchi method. *Mater. Today Proc.* (2020). <https://doi.org/10.1016/j.matpr.2020.08.774>
8. Ravuri, M., Kumar, Y.S., Vardhan, D.H.: Materials today: proceedings parametric optimization of face turning parameters for surface roughness on EN 31 material using RSM and Taguchi method. *Mater. Today Proc.* **31** (2020). <https://doi.org/10.1016/j.matpr.2020.05.816>
9. Dutta, S., Kumar, S., Narala, R.: Optimizing turning parameters in the machining of AM alloy using Taguchi methodology. *Measurement* **169**, 108340 (2021). <https://doi.org/10.1016/j.measurement.2020.108340>
10. Use of Analysis of Means (ANOM) for statistical evaluation of production data—PRRS.com. <https://www.prrs.com/en/publications/abstracts/use-analysis-means-anom-for-statistical-evaluation-production-data/>, last accessed 2020/11/17
11. Khalkho, J.U., Davis, R., Alfred, J., Ekka, J., Lakra, A.K., Kandir, S.: An experimental analysis of surface roughness of EN9 steel under the influence of pressurized steam jet **2**, 191–195 (2015)
12. Nadagouda, M.N., Sillanpää, M., Asiri, A.M., Agarwal, S.: Taguchi L<sub>9</sub> (3<sup>4</sup>) orthogonal array study based on methylene blue removal by single-walled carbon nanotubes-amine: adsorption optimization using the experimental design method, kinetics, equilibrium and thermodynamics. *J. Mol. Liq.* **9**, 112001 (2019). <https://doi.org/10.1016/j.molliq.2019.112001>

# Study and Analysis of Milk-Run Model for Minimum Cost Under Upstream Supply Chain of a Dairy Plant



Sanjay Kumar, Asim Gopal Barman, and Vishal Kumar

## 1 Introduction

Collection of raw milk from multiple milk farms is an essential activity of upstream supply chain for a dairy plant. In this paper, milk-run model of the upstream supply chain is considered to focus on the vehicle routing problems (VRP) in order to minimize transportation cost. The milk-run model is a distinct transportation model from perspective of logistics and supply chain. In the manufacturing industry, material handling accounts for 25% of workers, 87% of production time, and 55% of all factory space. The aim of vehicle routing problem model is to reduce transportation expenses. The idea of VRP method was put forward by Dantzig and Ramser [1]. The VRP model focused on routing of a fleet of gasoline delivery trucks between a bulk terminal to many small service stations.

### 1.1 The Milk-Run Concept

A milk run is an effective logistic system, which is round trip that facilitates delivery and/or pick-up of the goods. In the milk-run model, the milkman uses his dray to deliver milk-containing bottles to his customers and take back empty bottles from the doors of customers' in the specified route. Jeon et al. [2] presented a milk-run model for a particular case of VRP problem. Milk runs have been considered as round trips to the material supply system, either goods collected from multiple suppliers for single customer or goods collected from single supplier for multiple customers

---

S. Kumar · A. G. Barman (✉) · V. Kumar  
Department of Mechanical Engineering, National Institute of Technology Patna, Patna 800005,  
India

© The Author(s), under exclusive license to Springer Nature Singapore Pte Ltd. 2022  
S. K. Natarajan et al. (eds.), *Recent Advances in Manufacturing, Automation, Design  
and Energy Technologies*, Lecture Notes in Mechanical Engineering,  
[https://doi.org/10.1007/978-981-16-4222-7\\_25](https://doi.org/10.1007/978-981-16-4222-7_25)

213

moved in a pre-defined path. The various advantages of milk-run model enlisted as follows:

- The material and parts inflow get smoothened for the production line.
- Supply chains and logistics perform better because of their ability to effectively utilize the spaces of transport vehicles, control transportation fees, in order to reduce levels of parts inventory and their maintenance costs.
- It minimizes the factory's warehouse space.
- It shortens lack of confidence at time of delivery.
- It induces flexibility in supplying system of parts.
- The capital expenditures, operating expenses, and maintenance/repair costs are less due to the reduction in total number of required palates during supply chain.

### **Problem identification and research objectives**

To address the problem of having route development for milk-run supply system, an effective mathematical model and a heuristic approach need to be developed that construct routes and determine the number of vehicles, scheduling and service minimize total transportation cost. The critical issues noted in supply industries are:

- The transportation system has a vital effect on total transportation costs.
- As traffic congestion is a major issue in urban areas and highway. Supplier has to make sure that product delivery takes place in shortest time and distance along with low cost by determining effective route.
- Inappropriate utilization of the vehicle can enhance the number of vehicles in the supply network.

Hence, the primary **objectives** of the current study may be summarized as follows:

- To minimize total transportation cost.
- To find an optimal route that has the minimum transportation cost.

## **2 Literature Review**

The term milk-run logistics originates from the dairy industry. It is a conception of transportation network, where one vehicle covered all output and input demands of materials into numerous stations and circulated every station according to a pre-defined schedule [3]. During review of milk-run supply chain management, papers of two interrelated topics were studied: internal and external milk-run material supply system. The various optimization techniques and mathematical methods were reviewed and analyzed to understand the effect and limitations of computer modeling in solving vehicle routing problems. You and Jiao [4] proposed an application based on saving algorithm to develop and apply of milk-run distribution system in the express industry. The milk-run distribution system is considered to express logistics through feasibility analysis of application of cyclic goods taking schema in

the express industry. Sadjadi et al. [5] applied a milk-run method to manage supply chain problem and compare obtained results with optimal solutions. Robust linear optimization is used to solve problems like binary variables in our model, so it will be unable to solve large problems results. Eksioglu et al. [6] studied a VRP model for defining and integrating the domain of the extensive VRP literature and define all facts of VRP model in an ungenerous and discriminative manner by presenting a taxonomic framework. Kilic et al. [7] studied the milk-run distribution system which relates to the applications of manufacturing area. It also explains the handling process beneath lean manufacturing conditions such as pull-based and repetitive manufacturing. Jafari-Eskandari et al. [8] presented an approach of the robust optimization to solve milk-run system with inventory uncertainty. It satisfies all the bounded uncertainty sets of inventories to minimize the transportation cost by approaching the yield routes. Novaes et al. [9] analyzed a dynamic OEM picking-up (milk-run) routing problem in over-congested traffic conditions. If the time limit is exceeded in a route which is allocated to alternative vehicles due to highly congestion in traffic. Kluska and Pawlewski et al. [10] developed a model that is intended for simulation of milk-run intralogistics systems. This methodology is basically designed and implemented in several stages.

## **2.1 Research Gap**

The literature review demonstrated that various heuristic approaches have been attempted by the researchers so far, such as robust optimization approach, genetic algorithm, mixed integer programming method, modified saving algorithm, simulated annealing, greedy algorithm, dynamic programming, and Tabu search. However, there is often conflict for selection of an appropriate heuristic model, as it has an impact on optimality of the solution. Thus, there is a considerable number of studies required for optimization of milk-run supply system. Therefore, in this study, contribution is noteworthy to both industry and literature.

## **3 Milk-Run Model—Case of a Real Dairy Plant of India**

The paper focuses on upstream milk-run model of a real Indian dairy plant located on the eastern side of India in order to minimize transportation cost. The upstream milk-run model of transportation is shown in Fig. 1. Milk farmers deposited milks to the Dairy Cooperative Societies (DCS) located at multiple geographical positions. Afterwards, raw milks are transported from DCSs to dairy plant. A suitable mathematical model is adopted [5] and modified for the current case to minimize the transportation cost.

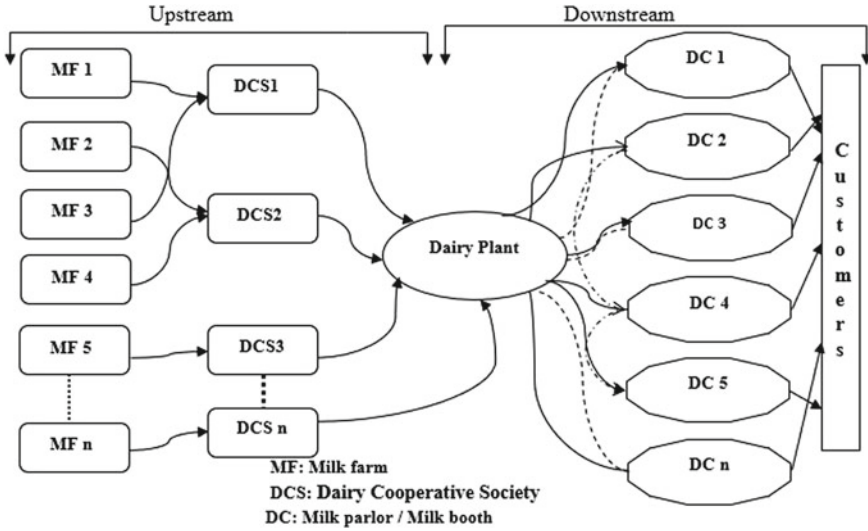


Fig. 1 Milk-run model for the supply chain of the dairy plant

### 3.1 Decision Variables and Parameters

$C_{nij}$  = Cost of the truck 'n' moving from supplier i to supplier j,

$\bar{C}$  = Fixed cost of waiting a vehicle at each supplier,

$V_n$  = Maximum volume of truck 'n',

$V_c^{cL}$  = Maximum milk capacity in a Can,

$U_{tc}$  = Average consumption of milk in time 't',

$x_{tncj}$  = The number of shipping Can of milk transported with vehicle 'n' from supplier j with due date of time 't',

$\gamma_{cj}$  = The percentage of part 'c' allocated to supplier j,

$$y_{tnij} = \begin{cases} 1 & \text{if } x_{tncj} > 1 \\ 0 & \text{if } x_{tncj} = 0 \end{cases}$$

#### Objective functions

The aim of the objective functions is to minimize transportation costs and also shorten level of inventory at warehouse (DCS) by implementing a milk-run system with time windows. The following objective function is considered:

$$\text{minimise } \sum_t \sum_n \sum_i \sum_j [C_{nij} + \bar{C}] y_{tnij} \tag{1}$$

subject to:

$$\sum_n \sum_j x_{tmij} \times V_c^{cL} \leq V_n \quad \forall(t, n) \quad (2)$$

$$\sum_n \sum_j x_{tncj} = \gamma_{cj} \quad \forall(n, j) \quad (3)$$

$$\sum_n \sum_j y_{tmij} \leq 1 \quad \forall_i \geq 2, \forall_t \quad (4)$$

$$\sum_n \sum_i y_{tmij} \leq 1 \quad \forall_j \geq 2, \forall_t \quad (5)$$

$$\sum_j y_{tn1j} \leq 1 \quad \forall(t, n) \quad (6)$$

$$\sum_i y_{mi1} \leq 1 \quad \forall(t, n) \quad (7)$$

$$\sum_i y_{miq} = \sum_i y_{mqj} \quad \forall(t, n), \forall q > 1 \quad (8)$$

$$\sum_{i \in s} \sum_{j \in s} y_{tmij} \leq |s| - 1 \quad s \subseteq \{2, 3, \dots, NT\} \quad \forall(t, n) \quad (9)$$

where  $NT$  = total number of suppliers.

Equation (1) minimizes the total transportation costs (TTC). It tells that if any transporting vehicle travels from one supplier to another one, then fixed cost of loading and transportation cost with vehicle must be considered.

Constraint (2) ensures that number of pallets (milk can) collected from supplier (milk farmers) for transportation to distribution center (DC) from a proper volume of parts for aggregation and transporting to DC would not exceed number of transporting vehicles. Constraint (3) tells that each supplier is allowed to transfer volume of parts committed in agreement. Constraints (4) and (5) state that the constraints of vehicle transport for given time schedule 't'. For this model, it assumed not to use two or more vehicle simultaneously. The DC of the company is represented with 'i = 1' number. Constraints (6) and (7) are alike to the constraints (4) and (5), but difference is that these constraints are exclusively related to the distribution center of manufacturing firms (dairy plant). Constraint (8) ensures that designed for sequencing the route of the vehicle if they get to a knot, then exit from it. It avoids stoppage of the vehicle in place of one supplier and each transporting vehicle, entering and exiting same place. Constraint (9) states that the starting point of each transporting vehicle is supplier's warehouse and the same warehouse is final destination.

## 4 Computational Results

In this study, the TTC is minimized by selecting the best route for vehicle moving from supplier 'i' to supplier 'j' because cost is varied according to different geographical locations of the suppliers. Existing vehicle routes are studied and analyzed in a detailed study separately. The routes covering the shortest possible distances are only considered for minimizing the transportation cost using GA and MIP in this current study. So, the milk-run model in the upstream part of the dairy supply chain is based on the shortest vehicle routes. It is observed that the number of suppliers and routes are increased then TTC is increased almost exponentially. There are several binary variables in the presented method, so it is difficult to run resulted model for large-scale problems. Therefore, a meta-heuristic procedure is used to solve problem. Genetic algorithm (GA) and mixed integer programming (MIP) are coded in MATLAB and executed using real data of dairy plants. The computational results are shown in Table 1.

From the optimization techniques, it is observed that the total cost of transportation decreases  $1.2352e+05$  in MIP while in the case of GA the total transportation cost decreases up to  $1.3072e+05$ , which is shown in Fig. 2. MIP and GA both produce optimal solutions those are very close to each other. As the number of suppliers increases, the gap between the cost through MIP and GA increases. So, it concludes that GA is more effective when the number of suppliers is less.

### 4.1 General Implications

There are several implications of the current study on a dairy processor's unit. The GA and MIP are used to optimize the milk-run model with real input data of dairy plant. This study is focused on shortening the distance and minimizing the transportation cost by using GA and MIP. The relationships between the farmers and dairy processors should be transparent regarding the milk quality. The outcomes of the current study are found to be in good agreement with the concerned unit and can

**Table 1** Computational results of MIP and GA

S. No.	Route	Milk quantity (kg)/day	TTC (MIP) (rupee)	TTC (GA) (rupee)
1	5	25,098.71	2.2490e+04	2.2990e+04
2	10	159,440.4	3.1256e+04	3.2256e+04
3	15	235,210.9	3.8269e+04	3.9769e+04
4	20	310,752.3	6.0542e+04	6.2542e+04
5	25	328,494.8	7.7459e+04	7.9959e+04
6	30	355,305.3	9.9005e+04	1.2000e+05
7	36	397,815.6	1.2352e+05	1.3072e+05

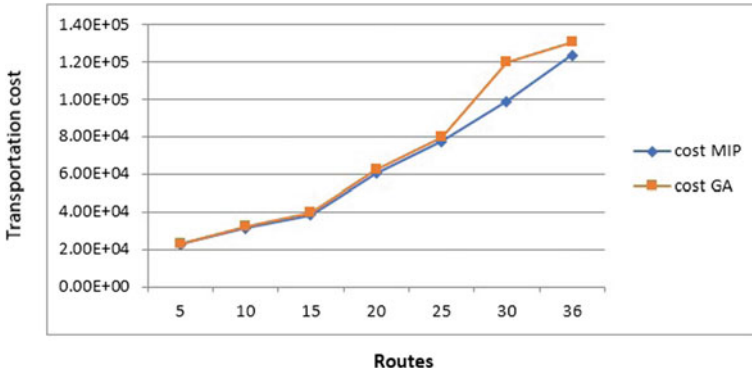


Fig. 2 MIP versus GA cost graph

be implemented with minor modifications. The results further motivate various dairy plants located in several other geographical regions to review their existing milk-run models for further improvements. Also, start-up companies can get insights of this study prior to design their own transportation model.

### 5 Conclusions

This paper adopted and modified a mathematical model to solve milk-run problem in order to minimize transportation cost. In this paper, the proposed approach is different from the other existing models. The problem is considered as a VRP model, and the model is optimized by GA and MIP using real input data of dairy plant.

In this study, routes are constructed for transportation, and obtained computational results conform the reality. The overall transportation cost has been minimized considering milk-run model in transportation network rather than direct shipment. It is observed from the results that the overall transportation cost is reduced by 35.14% in a day by MIP, which is Rs 64,013 less than that of direct shipment in a day. On the other hand, GA reduces the total transportation cost by 30.29% in a day, which is Rs 56,813 less per day as compared to direct shipment.

Few limitations are associated with the current study. The current study only deals with the upstream supply chain. The overall logistics cost can be minimized by optimizing both the upstream and downstream processes.



## References

1. Dantzig, G.B., Ramser, J.H.: The truck dispatching problem. *Manage. Sci.* **6**(1), 80–91 (1959)
2. Jeon, G., Leep, H.R., Shim, J.Y.: A vehicle routing problem solved by using a hybrid genetic algorithm. *Comput. Ind. Eng.* **53**(4), 680–692 (2007)
3. Baudin M.: *Lean logistics: the nuts and bolts of delivering materials and goods*. Productivity Press (2005)
4. You Z., Jiao Y.: Development and application of milk-run distribution systems in the express industry based on saving algorithm. *Math. Prob. Eng.* 6 p (2014)
5. Sadjadi, S.J., Jafari, M., Amini, T.: A new mathematical modeling and a genetic algorithm search for milk run problem (an auto industry supply chain case study). *The International Journal of Advanced Manufacturing Technology* **44**(1–2), 194 (2009)
6. Eksioglu, B., Vural, A.V., Reisman, A.: The vehicle routing problem: A taxonomic review. *Comput. Ind. Eng.* **57**(4), 1472–1483 (2009)
7. Kilic, H.S., Durmusoglu, M.B., Baskak, M.: Classification and modeling for in-plant milk-run distribution systems. *The International Journal of Advanced Manufacturing Technology* **62**(9–12), 1135–1146 (2012)
8. Jafari-Eskandari, M., Aliahmadi, A.R., Khaleghi, G.H.H.: A robust optimisation approach for the milk run problem with time windows with inventory uncertainty: an auto industry supply chain case study. *International Journal of Rapid Manufacturing* **1**(3), 334–347 (2010)
9. Novaes, A.G., Bez, E.T., Burin, P.J., Aragão, D.P., Jr.: Dynamic milk-run OEM operations in over-congested traffic conditions. *Comput. Ind. Eng.* **88**, 326–340 (2015)
10. Kluska, K., Pawlewski, P.: The use of simulation in the design of Milk-Run intralogistics systems. *IFAC-PapersOnLine* **51**(11), 1428–1433 (2018)

# Effect of Micro-milling Parameters on Surface Roughness of Soft Metal Cutting and Their Regression Models



S. Bhattacharyya, H. Chelladurai, and M. Z. Ansari 

## 1 Introduction

With the advancements of technologies, there is an increasing demand for micro-components in many fields like electronics, telecommunication, optics, aerospace, biotechnology. Most micro-manufacturing methods employ advanced fabrication methods like laser beam machining, electric discharge machining and focussed ion beam machining. Considering the very low material removal rate (MRR) encountered in these advanced techniques, micro-mechanical machining has become one of the more promising methods for producing micro-parts not only for its higher MRR, but also for its flexible in producing complex features with 3-D shapes [1]. Among these processes, micro-milling is the most common and versatile one. Similar to a conventional milling process, micro-milling process uses a micro-milling cutter that is rotated by spindle and removes material [2, 3]. The scaling down of macro-milling process to micro-scale, however, results in several complications. As the tool diameter is reduced in micro-milling, small feed rates are used to avoid excessive tool bending and sudden breakage of the tool. Compared to uncut chip thickness, the edge radius of the tool in micro-milling is considerably larger than that in conventional milling. This large edge radius of tool causes the minimum chip thickness effect dominant in micro-milling [4–6]. It is observed that the chip formation occurs only when the uncut chip thickness is greater than a minimum chip thickness. Therefore, for uncut chip thickness values less than the minimum chip thickness, no material removal occurs and the material is rather elastically or plastically deformed. This phenomenon is known as ploughing. Under this condition, the cutting forces and

---

S. Bhattacharyya (✉) · H. Chelladurai · M. Z. Ansari  
Mechanical Engineering Discipline, PDPM Indian Institute of Information Technology, Design and Manufacturing, Airport Road, Jabalpur, MP 482005, India  
e-mail: [1813308@iiitdmj.ac.in](mailto:1813308@iiitdmj.ac.in)

© The Author(s), under exclusive license to Springer Nature Singapore Pte Ltd. 2022  
S. K. Natarajan et al. (eds.), *Recent Advances in Manufacturing, Automation, Design and Energy Technologies*, Lecture Notes in Mechanical Engineering,  
[https://doi.org/10.1007/978-981-16-4222-7\\_26](https://doi.org/10.1007/978-981-16-4222-7_26)

221

cutting tool vibration effects are increased. Therefore, it is a difficult task to maintain the surface quality of a micropart for obtaining the desired functional performance.

Surface finish plays an important role in the context of quality for a micropart produced. The finish of the part depends on various factors like cutting parameters, tool wear, temperature, cutting forces, surface characteristics, vibration effects, tool and workpiece material properties. Wang et al. [7] analysed the effect of machining parameters on surface roughness in micro-end milling of brass by a miniature machine tool. Thepsonthi and Ozel [8] conducted micro-milling experiments in Ti–6Al–4V titanium alloy and performed multi-objective particle swarm optimization to find out optimum process parameters to minimize surface roughness and burr formation. Aslantas et al. [9] also investigated the effect of cutting parameters on surface roughness and burr formation in Ti–6Al–4V titanium alloy and carried out optimization using Taguchi-based grey relational analysis. Kuram and Ozcelik [10] investigated the influence of cutting parameters on tool wear, surface roughness and cutting forces during micro-end milling of Al 7075 material and performed optimization for the output responses using Taguchi-based grey relational analysis. Kiswanto et al. [11] performed an analysis to find out the behaviour of cutting parameters and machining time towards surface roughness and burr formation during micro-milling of aluminium alloy 1100. Xu et al. [12] developed a Ti(C<sub>7</sub>N<sub>3</sub>) based cermet micro-mill tool and studied the cutting characteristics and tool performance during micro-milling of aluminium alloy 2024. Kumar [13] carried out optimization using genetic algorithm for minimizing surface roughness and machining time in micro-milling of C360 copper alloy material.

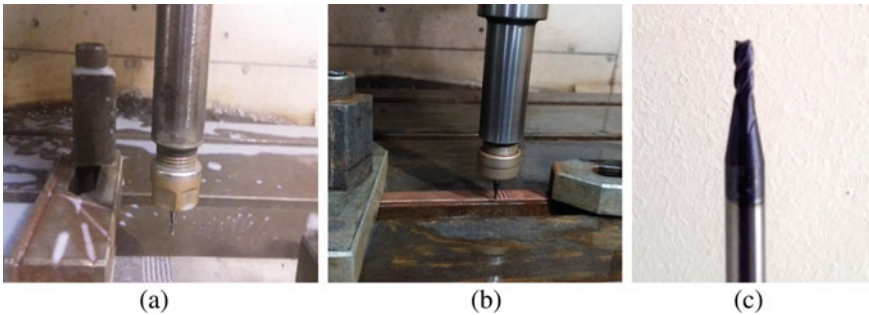
In this current study, micro-milling experiments on high purity aluminium and copper were conducted to analyse the characteristics and influence of cutting parameters with respect to surface roughness. Statistical analysis techniques like analysis of variance (ANOVA) and Taguchi array design were used to find the dependence of surface roughness to cutting speed, feed and depth of cut. *S/N* quality characteristic and mains effect plots were obtained and were later used for analysis. Finally, a regression curve is proposed for micro-milling of aluminium and copper.

## 2 Materials and Methods

About four-millimetre thick high purity (>99 wt%) aluminium and copper plates were procured from local market and were cut into strip form. Typical mechanical properties of the two soft metals used are listed in Table 1. A tungsten carbide (WC) square end-mill cutter of 2 mm diameter (NPlus, PRC) was used to cut rectangular cross-section channels in the samples. The tool had four flutes and the flute angle was 50°. Hardness of the tool was HRC 50. A precise three-axis CNC vertical milling machine (Okuma, Japan) was used to provide precise controls of milling parameters with micrometre scale control over depth of cut. The microchannels were cut for a length of 20 mm. Cutting was carried out under wet condition with the use of

**Table 1** Typical mechanical properties of aluminium and copper samples

Property	Aluminium	Copper
Density (kg/m <sup>3</sup> )	2700	8960
Elastic modulus (GPa)	69	110
Yield strength (MPa)	100	210
Poisson's ratio	0.33	0.34
BHN	37	60



**Fig. 1** Channel cutting arrangement in **a** aluminium and **b** copper samples using **c** WC square end-mill cutter

fat-sulphur-chlorine emulsion cutting fluid in 1: 20 composition with water. Figure 1 shows the experimental arrangement.

For experimental design to vary the cutting conditions, Taguchi *L*<sub>9</sub> orthogonal array design was selected, as shown in Table 2. This orthogonal array design reduces the number of experiments in order to find out how the output response gets affected by the control factors. The cutting parameters selected as control factors are spindle speed, feed rate and depth of cut (μm). The cutting parameters and their levels are shown in Tables 2 and 3 for aluminium and copper, respectively. Lower values of feed rate have been used for copper as hardness of copper is higher than aluminium.

The most commonly used roughness parameter for defining a surface is the average surface roughness given as  $R_a = \frac{1}{n} \sum_{i=1}^n y_i$  where *n* is the number of sample points

**Table 2** Control factors and their levels selected for end-mill channel cutting

Notation	Control factors	Aluminium			Copper		
		Level 1	Level 2	Level 3	Level 1	Level 2	Level 3
A	Spindle speed (rpm)	5000	6000	7000	4000	5000	6000
B	feed rate (mm/min)	30	40	50	15	20	25
C	depth of cut (μm)	10	20	30	10	25	40

**Table 3** Measured values of average surface roughness for aluminium

Expt. No.	Spindle speed (rpm)	Feed (mm/min)	Depth of cut ( $\mu\text{m}$ )	$R_a$ ( $\mu\text{m}$ )
1	5000	30	10	0.3114
2	5000	40	20	0.5607
3	5000	50	30	0.5015
4	6000	30	20	0.5776
5	6000	40	30	0.4628
6	6000	50	10	0.4058
7	7000	30	30	0.4531
8	7000	40	10	0.3790
9	7000	50	20	0.4869

**Fig. 2** Surface roughness tester and measurement arrangement

considered and  $y_i$  is the absolute values of deviation of the points evaluated from the mean line. Accordingly,  $R_a$  was measured in this work as the output variable. A contact type roughness tester (Mitutoyo SJ-500, Japan) was used to measure  $R_a$  values of the bottom surface of the channels cut. The cut-off length was kept as 0.8 mm, as per standard ISO 4287, in steps of five divisions. Thus, total measuring length was 4 mm. Two replications made for each measurement along the different length of microchannel, and their mean value was taken for further analysis (Fig. 2).

### 3 Results and Discussion

Tables 3 and 4 show results of surface roughness measurements for aluminium and copper at different milling parameters obtained using Taguchi  $L_9$  orthogonal array design. It can be seen in the tables that compared to aluminium roughness values for copper vary little with the control parameters selected. To investigate further, signal-to-noise ( $S/N$ ) analysis was conducted by taking average roughness as response variable. The term signal denotes desired effect of output response and noise stands for undesirable output characteristics.  $S/N$  ratio measures the deviation of quality

**Table 4** Measured values of average surface roughness for copper

Expt. No.	Spindle speed (rpm)	Feed (mm/min)	Depth of cut (μm)	R <sub>a</sub> (μm)
1	4000	15	10	0.0901
2	4000	20	25	0.1004
3	4000	25	40	0.1140
4	5000	15	25	0.1148
5	5000	20	40	0.1134
6	5000	25	10	0.1231
7	6000	15	40	0.1381
8	6000	20	10	0.1123
9	6000	25	25	0.1091

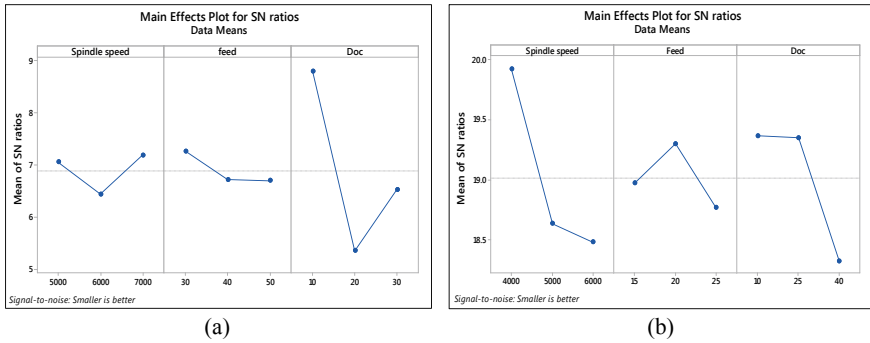
characteristics from the desired values. Higher values of *S/N* ratio for a parameter represent its optimum level. However, since lower surface roughness was desirable, the smaller-the-better *S/N* quality characteristic was used in this study.

*S/N* quality characteristic of the smaller-the-better is calculated as  $S/N = -\log_{10}[\frac{1}{n}(\sum_{i=1}^n y_i^2)]$ , where  $y_i$  is the  $i$ th experimental measured results in a run and  $n$  is the number of measurements in each test trial. In this analysis,  $y$  takes the value of average roughness. Table 5 shows the *S/N* values for aluminium and copper, respectively.

The main effects are plotted in Fig. 3 by taking mean of *S/N* ratios for each level of parameter. The level of a parameter that has the highest *S/N* ratio represents the optimum level. It is clear in the figure that *A3B1C1* is the optimum process parameter combination for aluminium and *A1B2C1* for copper. These combinations represent speed, feed and depth of cut as 4000 rpm, 20 mm/min and 10 μm for aluminium and 4000 rpm, 20 mm/min and 10 μm for copper, respectively. It can also be concluded from the main effects plot that the parameter with the highest slope

**Table 5** *S/N* values for R<sub>a</sub> in aluminium and copper. Smaller *S/N* values are better

Expt. No.	Factors	Aluminium		Copper	
		Mean R <sub>a</sub> (μm)	<i>S/N</i> value	Mean R <sub>a</sub> (μm)	<i>S/N</i> value
1	<i>A1B1C1</i>	0.3114	10.1336	0.0900	20.9151
2	<i>A1B2C2</i>	0.5607	5.0254	0.1000	20.0000
3	<i>A1B3C3</i>	0.5015	5.9946	0.1140	18.8619
4	<i>A2B1C2</i>	0.5775	4.7690	0.1148	18.8012
5	<i>A2B2C3</i>	0.4627	6.6940	0.1134	18.9077
6	<i>A2B3C1</i>	0.4058	7.8338	0.1231	18.1948
7	<i>A3B1C3</i>	0.4531	6.8761	0.1381	17.1961
8	<i>A3B2C1</i>	0.3790	8.4272	0.1123	18.9924
9	<i>A3B3C2</i>	0.4868	6.2530	0.1091	19.2435



**Fig. 3** Main effects plot for  $S/N$  ratio for **a** aluminium and **b** copper

of  $S/N$  ratio is the most significant factor for response  $R_a$ . Since depth of cut has the highest slope in case of aluminium, and depth of cut is the most influential factor in determining its surface roughness in milling. Similarly, the spindle speed becomes the most influential parameter in case of copper.

Analysis of variance (ANOVA) was performed to determine the significant factors affecting the surface roughness and to determine the contributions of each process parameter towards output response. ANOVA results are given in Tables 6 and 7 for aluminium and copper, respectively. It is observed in Table 6 that depth of cut has the highest  $F$ -value and therefore it has the most significant effect on average surface roughness for aluminium with an overall contribution of 81.56% towards it. This observation is consistent with  $S/N$  ratio analysis result presented above. Spindle

**Table 6** Analysis of variance for  $R_a$  in aluminium

Source	DOF	Sum of square, SS	Mean square, MS	$F$ -value	Contribution (%)
Speed	2	0.002710	0.001355	0.37	4.65
Feed	2	0.000715	0.000357	0.10	1.24
Doc	2	0.047319	0.023660	6.50	81.56
Error	2	0.007279	0.003639		12.55
Total	8	0.058023			100

**Table 7** Analysis of variance for  $R_a$  in copper

Source	DOF	Sum of square, SS	Mean square, MS	$F$ -value	Contribution (%)
Speed	2	0.000598	0.000299	1.5	41.27
Feed	2	0.000081	0.000040	0.2	5.59
Doc	2	0.000371	0.000186	0.93	25.60
Error	2	0.000399	0.000200		27.54
Total	8	0.001449			100

speed and feed rate influenced the surface roughness values by 4.65% and 1.24%, respectively. Similarly, it can be concluded from Table 7 that spindle speed has the highest  $F$ -value and therefore it influences the surface roughness most by 41.27% in copper. Apart from that depth of cut and feed rate have contributions of 25.60% and 5.59%, respectively. This result is also consistent with its  $S/N$  ratio analysis result.

Response surface methodology (RSM) is a statistical technique useful for modelling and analysing problems with several process variables. It was utilized here for establishing a correlation model among the three milling parameters for aluminium and copper milling operations. The relations can be given as:

$$R_{a,al}(\mu m) = -0.865 + 0.000078 A + 0.00844 B + 0.1094 C \\ - 0.001227 C^2 - 0.000006 AC - 0.000521 BC, \\ R^2 = 98.58\% , R^2(\text{adj}) = 94.32\%$$

$$R_{a,cu}(\mu m) = -0.3686 + 0.00127 A + 0.01725 B - 0.002739 C \\ - 0.000003 AB - 0.000001 AC, \\ R^2 = 98.93\% , R^2(\text{adj}) = 95.73\%$$

Here,  $A$  is spindle speed in rpm,  $B$  is feed in mm/min,  $C$  is depth of cut in  $\mu\text{m}$ .  $R$ -square and adjacent  $R$ -square values obtained for these relations are showing high degree of confidence in predicting surface roughness values for the two metals in terms of their milling parameters. Thus, we can conclude that these regression models can be used effectively to predict the surface roughness values expected for given milling parameters.

## 4 Conclusions

In this work, an attempt has been made to experimentally investigate the effects of spindle speed, feed rate and depth of cut on surface roughness during micro-milling of aluminium and copper. Taguchi  $L_9$  method has been employed for experimental design. The experimental values were analysed by Taguchi signal-to-noise ratio analysis for finding optimum parameters combination. ANOVA was carried out to find out the significant factors and their contributions towards surface roughness. Experimental results for aluminium show that average surface roughness of  $0.3314 \mu\text{m}$  was achieved for cutting parameters combination of spindle speed 5000 rpm, feed rate 30 mm/min and depth of cut  $10 \mu\text{m}$ . Similarly, for copper, results show that surface quality of  $0.0901 \mu\text{m}$  has been achieved for spindle speed of 4000 rpm, feed rate 15 mm/min and depth of cut of  $10 \mu\text{m}$ . The main effects plot and analysis of variance show that depth of cut has significant effect on  $R_a$  value of aluminium and spindle speed has significant influence on copper. The  $S/N$  ratio analysis for aluminium



produces an optimum parameters combination of spindle speed 7000 rpm, feed rate of 30 mm/min and depth of cut 10  $\mu\text{m}$ , which should minimize surface roughness most. In case of copper, *S/N* ratio analysis produces an optimum parameters combination of spindle speed 4000 rpm, feed rate 20 mm/min and depth of cut 10  $\mu\text{m}$ .

**Acknowledgements** This study was supported by IIITDM Jabalpur.

## References

1. Asad, A.B.M.A., Masaki, T., Rahman, M., Lim, H.S., Wong, Y.S.: Tool-based micromachining. *J. Mater. Process. Technol.* **192**, 204–211 (2007)
2. Filiz, S., Conley, C.M., Wasserman, M.B., Ozdoganlar, O.B.: An experimental investigation of micro-machinability of copper 101 using tungsten carbide micro-endmills. *I. J. Mach. Tool. Manuf.* **47**, 1088–1100 (2007)
3. Vázquez, E., Rodríguez, C.A., Elías-Zúñiga, A., Ciurana, J.: An experimental analysis of process parameter to manufacture metallic micro-channels by micro-milling. *Int J Adv Manuf. Technol.* **51**, 945–955 (2010)
4. Dhanorker, A., Özel, T.: Meso/micro scale milling for micromanufacturing. *Int. J. Mechatron. Manuf. Syst.* **1**, 23–43 (2008)
5. Kang, I.S., Kim, J.S., Kim, J.H., Kang, M.C., Seo, Y.W.: A mechanistic model of cutting force in the micro end milling process. *J. Mater Process. Technol.* **187**, 250–255 (2007)
6. Ikawa, N., Shimada, S., Tanaka, H.: Minimum thickness of cut in micromachining. *Nanotechnology* **3**, 6–9 (1992)
7. Wang, W., Kweon, S.H., Yang, S.H.: A study on roughness of the micro-end-milled surface produced by a miniaturized machine tool. *J. Mater. Process. Technol.* **162**, 702–708 (2005)
8. Thepsonthi, T., Özel, T.: Multi-objective process optimization for micro-end milling of Ti-6Al-4V titanium alloy. *I. J. Adv. Manuf. Technol.* **63**, 903–914 (2012)
9. Aslantasa, K., Ekicib, E., Çiçekc, A.: Optimization of process parameters for micro milling of Ti-6Al-4V alloy using Taguchi-based gray relational analysis. *Measurement* **128**, 419–427 (2018)
10. Kuram, E., Ozcelik, B.: Multi-objective optimization using Taguchi based grey relational analysis for micro-milling of Al 7075 material with ball nose end mill. *Measurement* **46**, 1849–1864 (2013)
11. Kiswantoa, G., Zariatina, D.L., Koba, T.J.: The effect of spindle speed, feed-rate and machining time to the surface roughness and burr formation of Aluminium Alloy 1100 in micro-milling operation. *J. Manuf. Process.* **16**, 435–450 (2014)
12. Xu, K., Zou, B., Wang, Y., Guo, P., Huang, C., Wang, J.: An experimental investigation of micro-machinability of aluminium alloy 2024 using Ti(C7N3)-based cermet micro end-mill tools. *J. Mater. Process. Technol.* **235**, 13–27 (2016)
13. Kumar, S.P.L.: Experimental investigations and empirical modelling for optimization of surface roughness and machining time parameters in micro end milling using genetic algorithm. *Measurement* **124**, 386–394 (2018)

# Application of Taguchi Procedure to Decide Optimum Variable Levels for Powder Blended EDM



K. Santarao , Ch. Suresh , and C. L. V. R. S. V. Prasad 

## 1 Introduction

In recent years, among available non-traditional machining techniques, electric discharge machining (EDM) received attention due to its efficacy in machining: micro-size and precision products [1], difficult-to-cut tool, die and mould materials [2], tools and components that require special micro-features [3], very complex shapes without consideration of material hardness [4]. This process is based on organized thermal attrition of electrically conductive material sunk in dielectric with initiation of quick, recurring sparks between the workpiece (anode) and the tool electrode (usually cathode) in the absence of physical contact between them. Powder mixed/suspended dielectric fluid (PMEDM or PSEDM); vibration, applied either to the tool electrode or the workpiece; mandrel or tool rotation are common methods that have been employed to improve machining efficiency in EDM. Among all methods mentioned, PMEDM augments the quality of machined surfaces that can extend their service life. In this method, a specific material in powder form is blended to the EDM dielectric. Through holes were drilled on stainless mould steel using a 300- $\mu\text{m}$  tungsten rod tool electrode at various energy settings after blending SiC (40–47 nm) and  $\text{Al}_2\text{O}_3$  (45–55 nm) into Idemistu Daphene cut HL25-S oil. Added powders reduced the average surface roughness by 14–24% compared to that with a pure dielectric [5]. Through micro-holes were fabricated on titanium plate (500  $\mu\text{m}$  thick) using 300- $\mu\text{m}$  tungsten tool electrode when vibrating the workpiece using PZT actuator and reported the effects of addition of graphite (55 nm) into kerosene. It was reported that surface microstructures produced are well characterized and uniformly sized [6].

---

K. Santarao (✉) · C. L. V. R. S. V. Prasad  
GMR Institute of Technology, Rajam, India  
e-mail: [santarao.k@gmrit.edu.in](mailto:santarao.k@gmrit.edu.in)

Ch. Suresh  
Vignan's Institute of Engineering for Women, Visakhapatnam, India

The influence of the addition of SiC powder (45–55 nm) into synthetic electric spark oil at concentrations (0–0.5 g/L), tool electrode speed (1000 rpm, 3000 rpm), pulse on time duration (166, 362, 60 ns), discharge energy setting (5.0, 11.7, 21.0  $\mu$ J) on subsurface characteristic, i.e. recast layer thickness, was elucidated. It was argued that recast layer thickness reduced by 15–35% at a powder concentration of 0.1 g/L and pulse on time between 166 and 606 ns. It was also observed that low (1000 rpm) tool electrode rotation speeds generate thicker recast layers. Further, it was observed that use of  $\leq 0.5$  g/L SiC nanopowder along with discharge energies and microjoule to sub-microsecond pulse on time is favourable for PMD micro-EDM [7]. Surface topography of workpiece was assessed by varying CNTs concentration, peak current (3, 6, 12 A) and pulse duration (50, 100, 150  $\mu$ s). A 40% enhanced machining rate along with 67% reduced surface roughness was reported at 4 g/L CNTs [8]. 70–80-nm particles generated the best surface finish when the effect of 70–80 nm, 10–15  $\mu$ m and 100  $\mu$ m powders was experimented on the SKD-11 surface [9]. Blind holes were drilled on INCONEL718 using  $\phi 300$ - $\mu$ m tungsten electrode and suspending MoS<sub>2</sub> powder (10 nm, 50 nm and 2  $\mu$ m) in kerosene. Powder concentration is also varied with three levels, i.e. 0, 5, 10 g/l. It was argued that the optimum powder size to obtain maximum material removal rate is 50 nm [10]. The effect of Gr powder (55 nm) mixed in Total FINA ELF EDM3 oil dielectric fluid was investigated. Fine finishing was performed on cemented TUNGSTEN CARBIDE using tungsten electrode of 500  $\mu$ m diameter. It was found that lower surface roughness (Ra and Rmax values) and moderately higher MRR were achieved at 0.2–0.6 g/L [11]. It was mentioned that the average surface roughness reduced by 22% after investigating the combined effect of suspending nanographite (55 nm) into kerosene and its vibration [12]. The addition of Ti nanopowder (40–60 nm) to hydrocarbon oil considering pulse on time (120, 210 and 340  $\mu$ s), peak current (6, 12 and 20 A) and powder concentration (0, 2 g/L) on EDM performance considering material removal rate and surface roughness was investigated. Machining was performed on die steel (D2) using  $\phi 10$ -mm copper electrode at 70 V and duty factor 60%. It was found that suspending Ti nanopowder to the dielectric resulted in an enhancement of ~69 and ~35% in both material removal rate and average surface roughness, respectively. It was also observed that surface micro-defects were diminished due to the creation of low-height ridges and shallower craters [13]. The effect of mixing nano-TiC in kerosene when machining Inconel718 using brass electrode was investigated. Quality of process is assessed by altering TiC nanopowder in to dielectric fluid, pulse on time, pulse off time and current. It is reported that enhanced MRR along with reduced TWR is observed [14].

After a thorough study of literature mentioned above, it has been found that there is no study detailed on the use of boric acid nanopowder suspended into EDM dielectric when machining AISI D3 steel using electric discharge machining. In order to fill this gap observed from the literature, machining has been done with a combination of AISI D3 steel as a workpiece material and copper as an electrode. Furthermore, this research aims to study the surface roughness of AISI D3 steel and optimize the same.

## 2 Experimental Set-Up and Method

### 2.1 Machine

Electrical discharge machine model S-50 ZNC available in the Machine Tools laboratory at the first author's institute is utilized to perform experiment with some modifications. Many variables, for instance, polarity, pulse on time, flushing method, discharge voltage, % Duty factor and peak current, can be varied in this EDM.

This machine is equipped with a machining tank of dimensions 800 mm × 500 mm × 350 mm requiring 140L of dielectric fluid. In order to reduce the amount of dielectric used and to avoid the damage of present filtering system due to clogging of nanopowder in filters, a new experimental set-up is designed for nanopowder blended EDM (NPBEDM). The new fabricated set-up presented in Fig. 1 consists of a small tank occupying a volume of 10L accompanied with a motorized stirrer and dielectric recirculation pump, dielectric supply tank accommodated with filters and monoblock pump in chronological order.

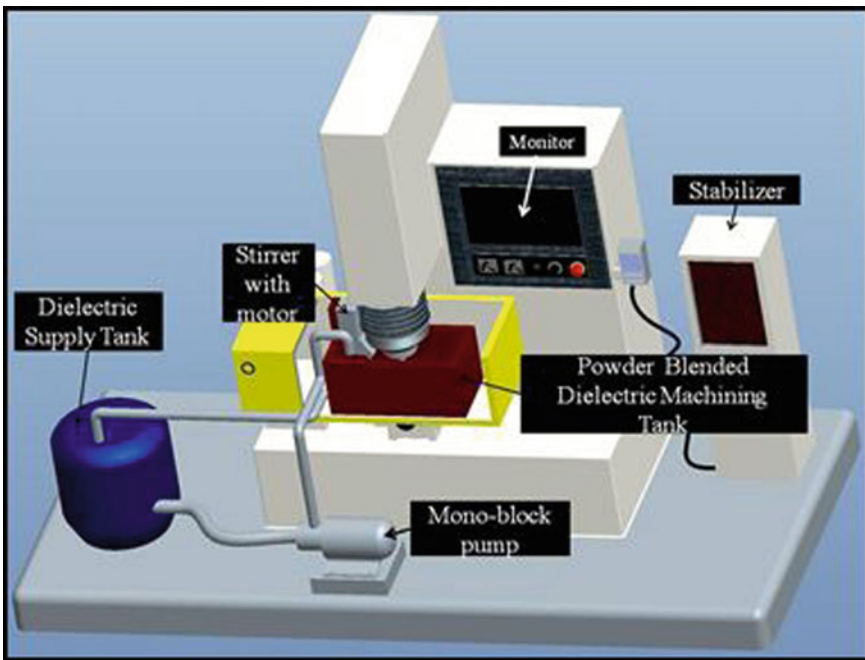


Fig. 1 PMEDM set-up

**Fig. 2** Mitutoyo surface roughness tester



## 2.2 Measuring Equipment

Surface roughness tester, Mitutoyo make, is utilized to check the surface roughness [15]. It is presented in Fig. 2. Powered via an AC adapter, it operates in the range of  $-200 \mu\text{m}$  to  $+150 \mu\text{m}$ .

## 2.3 Work Piece, Electrode and Powder Material

AISI D3 die steel of size  $4.5 \text{ cm} \times 3.25 \text{ cm} \times 1.2 \text{ cm}$  and  $1.5 \text{ cm} \times \text{Ø}0.95 \text{ cm}$  copper rod is confirmed as workpiece and tool, respectively. A tool with the circular cross-sectional area is best suited for machining in EDM [16]. 50 nm boric acid powder opted for present investigation is procured from Sisco Research Laboratories Pvt. Ltd. (SRL)—India.

## 3 Experiment Plan

A total of eighty-one ( $3^4$ ) experiments can be needed to optimize the variables by completing the full factorial design [17]. The Taguchi method uses orthogonal arrays that allow the entire parameter space to be examined and its effect on response with only a small number of experiment sets [18, 19]. The present investigation is performed with four quantitative process type parameters, peak current, gap voltage, pulse on time and powder concentration. Surface roughness (SR) is treated as response. Taguchi recommends L9 orthogonal array, where 9 experiments are sufficient to optimize the selected process variables [20]. Process variables and their levels taken into account for the experimentation are shown in Table 1. Throughout the experimentation, positive polarity, machining time: 30 min, % duty factor: 10, arc sensitivity: 3 are kept fixed. Standard L9 orthogonal array and experiment design using orthogonal array are shown in Table 2. Process variables levels are finalized after preliminary tests with one variable at a time technique. Surface roughness in  $\mu\text{m}$  is measured along horizontal (MHD) and vertical diameters (MVD).

**Table 1** Process variables codes and levels

Process variable	Code	Levels		
		1st level ( $l_1$ )	2nd level ( $l_2$ )	3rd level ( $l_3$ )
Peak current, $I_p$ , (A)	A	5	6	7
Pulse on time, TON, ( $\mu$ s)	B	50	100	150
Gap voltage, $V_g$ , (V)	C	50	60	70
Powder concentration, PC, (g/L)	D	0	0.5	1

**Table 2** Experimental design using orthogonal array

Experiment trail	Levels				Surface roughness			
	A	B	C	D	MHD	MVD	Mean	S/N ratio
1	5	50	50	0	5.71	6.16	5.935	-15.4684
2	5	100	60	0.5	4.76	5.12	4.940	-13.8745
3	5	150	70	1	4.82	5.32	5.070	-14.1002
4	6	50	60	1	5.05	5.88	5.465	-14.7518
5	6	100	70	0	5.22	4.74	4.980	-13.9446
6	6	150	50	0.5	6.19	5.85	6.020	-15.5919
7	7	50	70	0.5	5.66	5.29	5.475	-14.7677
8	7	100	50	1	5.57	5.98	5.775	-15.2310
9	7	150	60	0	5.99	6.98	6.485	-16.2382

### 4 Analysis and Discussion

Influence of each process variable at various levels on surface roughness (SR) can be extracted as the experiment strategy is orthogonal. The Taguchi design employs S/N (signal-to-noise ratio) to compute variation in data [21]. In the existing work, S/N ratio formula represented in (1) is used [22, 23].

Lower is best:

$$\frac{S}{N} \text{ratio} = -10 \log_{10} \left[ \frac{1}{r} \sum_{i=1}^r y_i^2 \right] \tag{1}$$

Data collected through experiments for all trails (1–9) are transformed into their respective S/N ratio by means of MINITAB software and presented in Table 2. Tables 3 and 4 represent the averaged SR raw data and that of S/N ratios for each and every parameter level. The contribution of each variable on SR and S/N ratio for SR is calculated and summarized in the last column of respective tables. A careful observation of these columns reveals that gap voltage (C) is the dominant variable in comparison with others. It is also substantiated by the relative contribution of gap voltage towards mean SR (37.02%) and S/N ratio for SR (38.15%).

**Table 3** Averaged SR raw data at various levels

Process variable representation	Averaged values			Main effects		% Contribution
	$l_1$	$l_2$	$l_3$	$l_2-l_1$	$l_3-l_2$	
A	<b>5.315</b>	5.488	5.912	0.173	0.424	25.35
B	5.625	<b>5.232</b>	5.858	-0.393	0.626	26.99
C	5.91	5.63	<b>5.175</b>	-0.28	-0.455	37.02
D	5.8	5.478	<b>5.437</b>	-0.322	-0.041	10.64

**Table 4** Averaged SR S/N data at various levels

Process variable representation	Averaged values			Main effects		% Contribution
	$l_1$	$l_2$	$l_3$	$l_2-l_1$	$l_3-l_2$	
A	<b>-14.48</b>	-14.76	-15.41	-0.28	-0.65	25.61
B	-15.00	<b>-14.35</b>	-15.31	0.65	-0.96	26.90
C	-15.43	-14.95	<b>-14.27</b>	0.48	0.68	38.15
D	-15.22	-14.74	<b>-14.69</b>	0.48	0.05	9.34

### 4.1 Methodology for the Determination of Suitable Input Variables Settings for Best SR

The procedure adopted from reference [21] is used to figure out the best input variables levels for finest SR. Steps contained within the method are:

1. Choose the lowest average SR value variable level from “Table of Average values of raw data” as quality characteristic of SR is lower the best type.
2. Choose the maximum S/N variable level from “Table of Average values of S/N data”.
3. Compare the variable level values in steps 1 and 2.
4. If the levels are unique, then the best response to the variable is achieved.
5. If they are not unique, compare the process variable %contribution towards mean & S/N ratio and then pick the level matching to a higher contribution.

Tables 3 and 4 hold the variables levels with the least SR and the maximum S/N ratio for SR in bold based on steps 1 and 2 of summarized method. It is clear that the A1, B2, C3 and D3 variables levels have the best surface roughness (SR) settings as they are unique to Step4.

## 5 Conclusions

In this work, boric acid of 50 nm in powder form is blended into EDM dielectric. Its impact on the surface roughness of blind holes created on AISI D3 steel is studied

together with three other process variables. Inferences drawn after implementing Taguchi technique to optimize the parameter levels are as follows:

Gap voltage is the most significant variable that affects the surface roughness of the blind hole.

The other major variables influencing surface property are the peak current and pulse on time in chronological order.

Surface roughness is less affected by powder concentration.

Variables levels for improved surface roughness are peak current—5Amp, gap voltage—70 V, powder concentration—1 g/L, and pulse on time—100  $\mu$ s.

## References

1. Bhaumik, M., Maity, K.: Effect of machining parameter on the surface roughness of AISI 304 in silicon carbide powder mixed EDM. *Decis. Sci. Lett.* **57**(2), 261–268 (2017)
2. Jatti, V.S., Bagane, S.: Thermo-electric modelling, simulation and experimental validation of powder mixed electric discharge machining (PMEDM) of BeCu alloys. *Alex. Eng. J.* **57**(2), 643–653 (2018)
3. Umar Farooq, M., Pervez Mughal, M., Ahmed, N., Ahmad Mufti, N., Al-Ahmari, A.M., He, Y.: On the investigation of surface integrity of Ti6Al4V ELI using Si-mixed electric discharge machining. *Materials* **13**(7), 1549 (2020)
4. Nguyen, T.D., Nguyen, P.H., Banh, L.T.: Die steel surface layer quality improvement in titanium  $\mu$ -powder mixed die sinking electrical discharge machining. *Int. J. Adv. Manuf. Technol.* **100**(9), 2637–2651 (2019)
5. Tan, P.C., Yeo, S.H., Tan, Y.V.: Effects of nanopowder additives in microelectrical discharge machining. *Int. J. Precis. Eng. Manuf.* **9**(3), 22–26 (2008)
6. Prihandana, G.S., Mahardika, M., Sambo, S.A.R., Hamdi, M., Wong, Y. S., Mitsui, K.: Work-piece vibration aided nano-graphite powder suspended dielectric fluid in micro-electrical discharge machining ( $\mu$ -EDM) processes. In: 5th International Conference Proceedings on Leading Edge Manufacturing in 21st Century, pp. 3–8. The Japan Society of Mechanical Engineers, Tokyo (2009)
7. Tan, P.C., Yeo, S.H.: Investigation of recast layers generated by a powder-mixed dielectric micro electrical discharge machining process. *Proc. Inst. Mech. Eng., Part B: J. Eng. Manuf.* **225**(7), 1051–1062 (2011)
8. Kumar, H.: Development of mirror like surface characteristics using nano powder mixed electric discharge machining (NPMEDM). *Int. J. Adv. Manuf. Technol.* **76**(1–4), 105–113 (2014)
9. Yih-Fong, T., Fu-Chen, C.: Investigation into some surface characteristics of electrical discharge machined SKD-11 using powder-suspension dielectric oil. *J. Mater. Process. Technol.* **170**(1–2), 385–391 (2005)
10. Prihandana, G.S., Sriani, T., Mahardika, M., Hamdi, M., Miki, N., Wong, Y.S., Mitsui, K.: Application of powder suspended in dielectric fluid for fine finish micro-EDM of Inconel 718. *Int. J. Adv. Manuf. Technol.* **75**(1–4), 599–613 (2014)
11. Jahan, M.P., Rahman, M., Wong, Y.S.: Study on the nano-powder-mixed sinking and milling micro-EDM of WC-Co. *Int. J. Adv. Manuf. Technol.* **53**(1–4), 167–180 (2011)
12. Prihandana, G.S., Mahardika, M., Hamdi, M., Wong, Y.S., Mitsui, K.: Accuracy improvement in nanographite powder-suspended dielectric fluid for micro-electrical discharge machining processes. *Int. J. Adv. Manuf. Technol.* **56**(1–4), 143–149 (2011)
13. Marashi, H., Sarhan, A.A.D., Hamdi, M.: Employing Ti nano-powder dielectric to enhance surface characteristics in electrical discharge machining of AISI D2 steel. *Appl. Surf. Sci.* **357**, 892–907 (2015)



14. Boopati, R., Sundaram, S.: Influence of process parameters for electrical discharge machine Using nano particle and brass electrode. *Int. J. Res. Advent Technol.* **2**(11), 45–49 (2014)
15. Pavani, P.N.L., Pola Rao, R., Santa Rao, K.: Performance assessment and mathematical modeling of process parameters in electrical discharge machining of EN-31 tool steel material using taguchi DOE. *Eng. J.* **21**(2), 227–236 (2017)
16. Uday kumar, J.S., Prasad, L.V.R.S.V.C., Santarao, K.: Simulation studies of impact of electrode geometry on thermal profiles in micro EDM by using CFX tools. *Int. J. Mech. Eng. Technol.* **7**(4), 196–204 (2016)
17. Thiagarajan, C., Sivaramkrishnan, R., Somasundaram, S.: Modeling and optimization of cylindrical grinding of Al/SiC composites using genetic algorithms. *J. Braz. Soc. Mech. Sci.* **34**(1), 32–40 (2012)
18. Phillip, J.R.: *Taguchi Techniques for Quality Engineering*. 2nd edn. Tata McGraw-Hill, India (2005)
19. Ranjit, K.R.: *A Primer on the Taguchi Method* 2nd edn. Society of Manufacturing Engineers, Michigan (2010)
20. Paul G.M.: *Design of Experiments with MINITAB*. 1st edn. ASQ Quality Press, Wisconsin (2004).
21. Kansal, H.K., Singh, S., Kumar, P.: Application of Taguchi method for optimisation of powder mixed electrical discharge machining. *Int. J. Manuf. Technol. Manage.* **7**(2–4), 329–341 (2005)
22. Al-Refaie, A., Wu, T.-H., Li, M.-H.: An effective approach for solving the multi-response problem in Taguchi method. *Jordan J. Mech. Indust. Eng.* **4**(2), 314–323 (2010)
23. Vannan, S.E., Vizhian, S.P.: Statistical investigation on effect of electroless coating parameters on coating morphology of short Basalt Fiber. *Jordan J. Mech. Indust. Eng.* **8**(3), 153–160 (2014)

# Numerical and Experimental Studies on Pressure Drop in Milling Parameter Optimized Aluminium Heat Sink Channel



S. Bhattacharyya, J. Pandey, H. Chelladurai, A. Husain, and M. Z. Ansari

## 1 Introduction

Miniaturization and portability have become the most sought after features in modern equipment device for application in various fields such as electronics, biomedical, telecommunications and aerospace. Ever-increasing power density and miniaturization of the electronic circuits and components have raised the concern of thermal management. It becomes necessity to maintain the device temperature below critical limit to avoid early failure. Because of the generation of such high heat flux, conventional air cooling technique gets inadequate with the time. Liquid cooled mini-/microchannel heat sink proved to be a suitable technique to be applied for the cooling purpose. Such heat sinks are already employed in several applications such as automobiles, refrigeration and air conditioning, aerospace, cooling of gas turbine blades, cooling of nuclear reactor components, gas processing, fuel cells, solar system cooling and liquid rocket engines.

The use of microchannel heat sink as an effective cooling scheme was first proposed by Tuckerman and Pease [1]. Since then, numerous research studies have been performed by researchers to improve performance in terms of high heat flux dissipation at low pumping power [2–7]. The main advantages of such channel heat sinks are robust design, compactness and high surface-to-volume ratio. Basically, higher surface area density of microchannels increases the convection heat transfer rate due to reduction of thermal resistance. When hydraulic diameter of the

---

S. Bhattacharyya (✉) · J. Pandey · H. Chelladurai · M. Z. Ansari  
Mechanical Engineering Discipline, PDPM Indian Institute of Information Technology, Design and Manufacturing, Airport Road, Jabalpur, MP 482005, India  
e-mail: [1813308@iiitdmj.ac.in](mailto:1813308@iiitdmj.ac.in)

A. Husain  
Department of Mechanical and Industrial Engineering, Sultan Qaboos University, Muscat  
PC-123, Oman

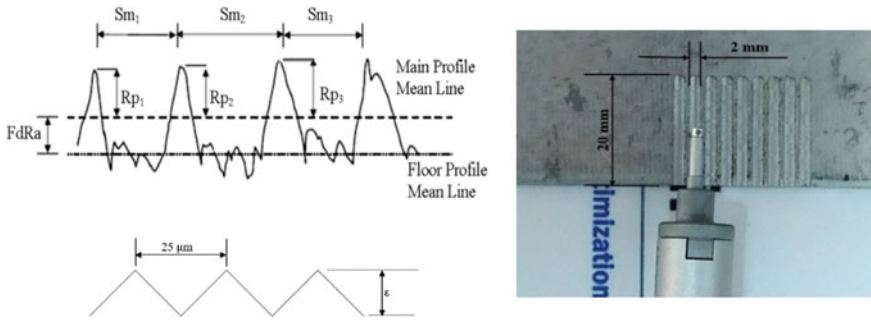
microchannel is considerably reduced, the number of channels increases which in turn enhances the heat transfer rate. Wu and Cheng [8] conducted experimental study for smooth trapezoidal silicon microchannel for different aspect ratios. It was found that Navier–Stokes equation remains valid for laminar flow of water within smooth microchannel having smaller hydraulic diameter. Duryodhan et al. [9] investigated the flow characteristic in converging microchannel and compared with the diverging microchannel. Pressure drop within the converging channel followed inverse relation with the convergence angle. Anbumeenakshi and Thansekhar [10] presented the experimental study for flow maldistribution within microchannel heat sink due to different header shape and flow inlet direction. It was observed that small maldistribution at low flow rate can be obtained in case of trapezoidal and triangular header shape while in rectangular header, it can only be obtained at high flow rate.

Microchannels can be fabricated using advanced manufacturing techniques like Laser Beam Machining, EDM and Focused Ion Beam Machining. In recent years traditional micro-milling machining has become one of the most promising methods for producing microparts because the process is flexible for producing complex features. This technique also has a higher material removal rate and therefore high part production rate. However, surface roughness of such products is still a concern. Since pressure drop is one of the most critical features of a microchannel heat sink, present study investigated experimentally as well as numerically the effect of channel surface roughness on coolant flow pressure drop and flow characteristics in aluminium heat sink. The channel was micro-milled using square-end mill cutter with optimized milling parameters to achieve best surface finish.

## 2 Theory, Experimental and Numerical Analysis

Pressure drop is an important criterion to be considered for fluid flow design in microchannel heat sinks. High pressure drop increases high pumping power requirement of the coolant system. In case of steady, fully developed, laminar flow, the value of surface friction factor can be calculated from the value of Poiseuille number given as  $P_o = f \times Re$ , where  $f$  is Darcy friction factor and  $Re$  is Reynolds number. According to this theory, the pressure drop or friction factor is not affected by the surface roughness of channels. However, at mini- and micro-scale surface roughness considerably affects the flow properties.

Average surface roughness ( $R_a$ ) is among the most commonly used roughness parameter to define roughness. But it does not give accurate results to represent surface roughness for fluid flow. To replace the use of average roughness value, Kandlikar et al. [11] suggested a new set of parameters for representing roughness in micro-scale in terms of roughness height,  $\varepsilon = R_p + FdR_a$  where  $R_p$  is defined as the maximum peak height of the roughness profile from the mean line and  $FdR_a$  is the average distance of the floor profile ( $F_p$ ) from the average mean line ( $Z_m$ ).  $S_m$  represents the mean of the profile peaks and also corresponds to the pitch of roughness profile.  $Z_m$  is calculated by taking the arithmetic average of all data points of profile



**Fig. 1** Schematic of roughness parameters and their measurement setup

evaluated from channel wall or datum level. Thus,  $\epsilon$  can be used as replacement of average roughness. Figure 1 shows the schematic of these roughness parameters and their measurement arrangement.

End-milling is one of the most flexible machining processes for fabrication of channels with complex shape and curvature. Hence, in experiments, a channel of  $2 \times 2 \text{ mm}^2$  cross section and 20 mm length is made on aluminium plate using WC square-end mill cutter. The hydraulic diameter ( $D_h$ ) of the channel is 2 mm, and it can be classified as mini-channel [11]. The optimum values of milling parameters are determined experimentally from Taguchi  $L_9$  orthogonal array design as 5000 rpm spindle speed, 30 mm/min feed and 10  $\mu\text{m}$  depth of cut [12]. From experimental design, the minimum surface roughness values obtained were  $R_a = 0.3314 \mu\text{m}$  with a maximum peak height,  $R_p = 2.195 \mu\text{m}$ . The maximum roughness profile achieved was  $R_a = 0.5607 \mu\text{m}$  and  $R_p = 3.3038 \mu\text{m}$ . To calculate the roughness height ( $\epsilon$ ) of these profiles, the floor profile to mean line distance ( $fdR_a$ ) has been approximated to the nearest value of  $R_a$ . Therefore, for  $R_a = 0.3314 \mu\text{m}$ ,  $fdR_a \approx 0.3 \mu\text{m}$  and for  $R_a = 0.5607 \mu\text{m}$ ,  $fdR_a \approx 0.55 \mu\text{m}$ . Therefore, the minimum roughness height is 2.5  $\mu\text{m}$ , and the maximum is 3.85  $\mu\text{m}$ . Now, with these two roughness heights, two rough channels were designed separately with triangular roughness elements, as shown in Fig. 1. The roughness elements have been modelled on the top and bottom walls of the channels using geometric modelling software, SolidWorks.

Figure 2 shows the minichannel heat sink fabricated with optimum parameters level as mentioned earlier and its pressure-drop measurement arrangement. The channel was sealed with transparent acrylic top plate cover and four ports were provided for fluid flow and measurements.  $P_1$  and  $P_2$  were used as differential pressure reading ports across the channel. Water inlet and outlet is also indicated.

Numerical simulation was carried out for the smooth channel and two different rough channels with different surface roughness values. Comparative study has been made between experimental and numerical results to determine the characteristic of laminar fluid flow for various Reynolds numbers. Water flow in the aluminium channel is simulated using CFD-based commercial software ANSYS FLUENT. In this analysis, continuity and momentum equations were solved for single-phase

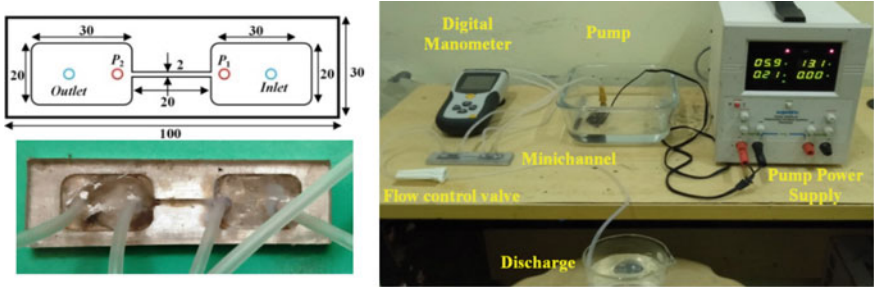


Fig. 2 Fabricated heat sink and its pressure drop measurement setup

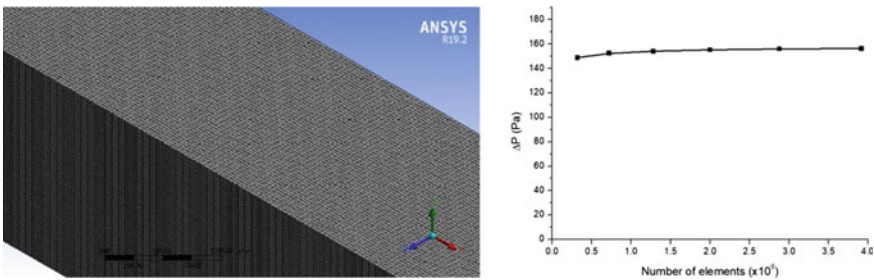


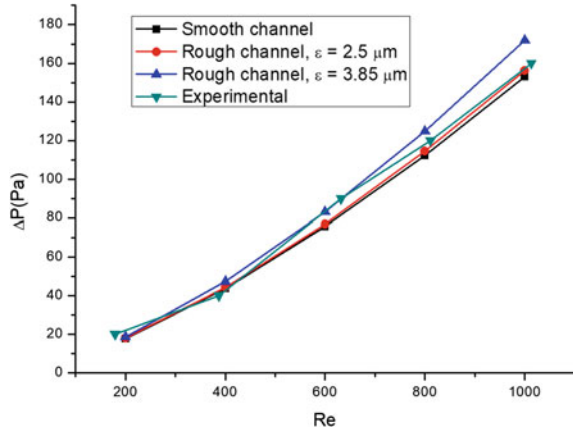
Fig. 3 Meshed channel model and its mesh convergence test

laminar fluid flow under steady and incompressible flow. The density and viscosity of water was taken as  $\rho = 997 \text{ kg/m}^3$  and  $\mu = 0.0089 \text{ kg/m}\cdot\text{s}$ . The geometries have been meshed with hexagonal linear elements as illustrated in Fig. 3. As the channel cross section is same in axial direction, sweep method has been used for meshing. Number of elements used for meshing are 2,880,000. Mesh convergence analysis has been performed, also shown in Fig. 3. The graph indicates that the solution is almost accurate and refined mesh elements have been used for simulations.

### 3 Results and Discussion

Figure 4 shows the comparison between experimental and numerical results for pressure drop across the channel at different Reynolds numbers. The drop is ranging from a minimum of 20 Pa at  $Re = 200$  to a maximum of about 170 Pa at  $Re = 1000$ . The variation is almost linear. Maximum pressure drop is occurring in case of channel with maximum roughness, i.e.,  $\epsilon_{max} = 3.85 \mu\text{m}$ , and is about 12% higher than in smooth channel. The results for  $\epsilon_{min} = 2.5 \mu\text{m}$  are lying in-between these. The experimental results are closely following this rough channel, indicating the relatively low pressure drop expected from a channel with low roughness height.

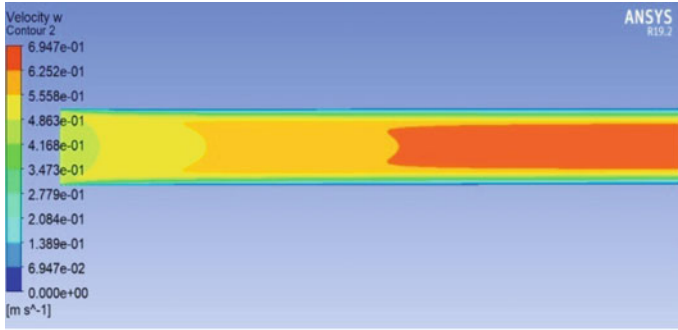
**Fig. 4** Effect of surface roughness on pressure drop in channel



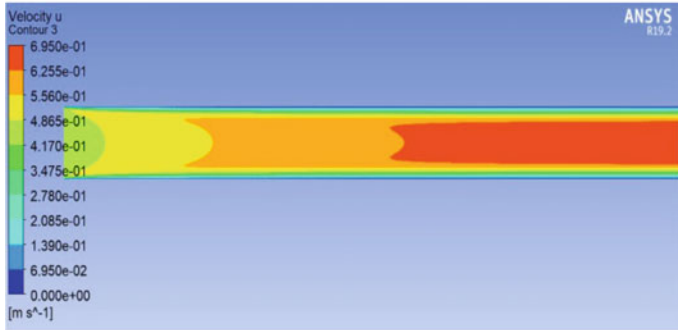
Thus, the experimental results are attesting to the fact that the fabricated channel can be considered to be practically a smooth channel. Thus, based on the results shown in figure, we can conclude that a channel fabricated with our optimum end-milling parameters and tool-workpiece combination can be predicted to have very low surface roughness and can be assumed to be a smooth channel.

Figure 5 shows the numerical analysis results for fluid velocity distribution inside the channel for the three surface conditions at  $Re = 1000$ . The velocities are varying from 0.45 m/s at channel inlet to a maximum of about 0.7 m/s at channel outlet. The maximum outlet velocities increase slightly with surface roughness. It can be noted in the figure that the velocity profile has not fully developed. The minimum entrance length required for a laminar pipe flow to fully develop into the parabolic profile can be given as,  $L_{en} = 0.06 D_h \times Re$  [13], which comes to be 120 mm in this case. Since the length of our channel is 20 mm, which is well short of the required minimum length. Therefore, the velocity profile is not fully developed. In case of fully developed flow, shear forces and pressure gradient balance each other and the flow continues with a constant velocity profile.

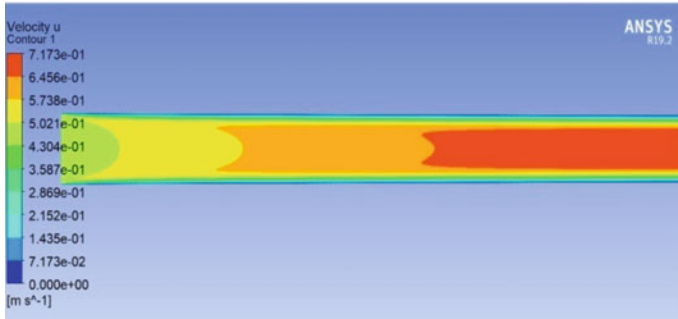
Figure 6 shows the results for pressure distribution along the channel length for the three surface conditions at  $Re = 1000$ . The pressure is increasing from 210 to 270 Pa as the surface conditions change from smooth to rough. Since the flow is not fully developed in our case, inertial forces also come into the picture and a balance between inertial, viscous force due to shear and the pressure force is achieved in this entrance region. Since in the entrance region the fluid is decelerating, the pressure gradient is not constant. In addition, larger frictional resistance offered by the rough surface to the fluid flow also adds to pressure drop. Thus, it is essential to focus on the surface roughness to reduce the pumping power cost required in a heat sink.



(a) Smooth channel



(b) Rough channel,  $\epsilon = 2.5 \mu\text{m}$

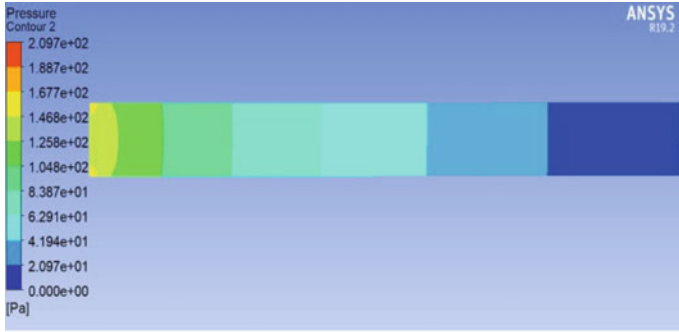


(c) Rough channel,  $\epsilon = 3.85 \mu\text{m}$

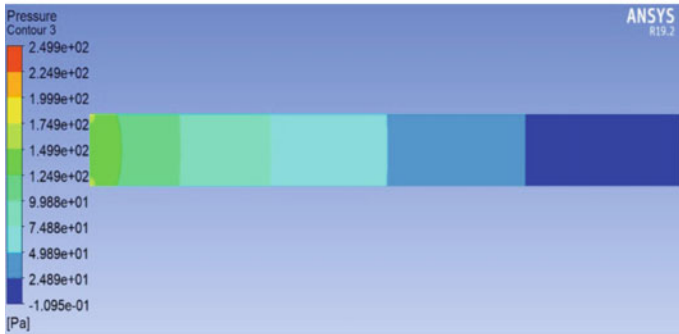
Fig. 5 Effect of surface roughness on velocity distribution along the channel length

## 4 Conclusions

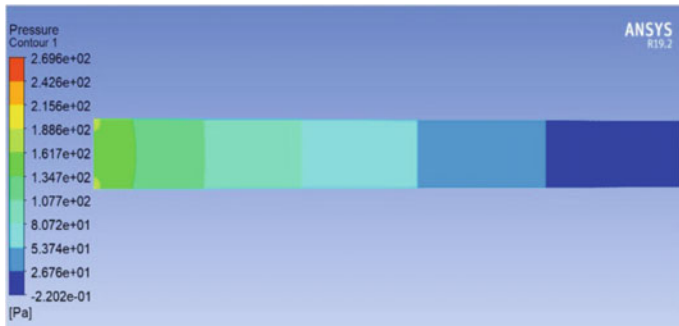
Numerical simulations have been made for smooth and rough channel geometries for various Reynolds numbers to quantitatively evaluate the effects of roughness height on pressure drop characteristics of single-phase laminar fluid flow in minichannel. Properties of liquid water have been used as single-phase fluid in simulations. For



(a) Smooth channel



(b) Rough channel,  $\epsilon = 2.5 \mu\text{m}$



(c) Rough channel,  $\epsilon = 3.85 \mu\text{m}$

**Fig. 6** Effect of surface roughness on pressure distribution along the channel length

modelling the rough wall, surface roughness values obtained from Taguchi  $L_9$  orthogonal array experimental design in aluminium have been used. The flows have been simulated using ANSYS FLUENT software. The main effects plot and analysis of variance for Taguchi  $L_9$  experimental design show that depth of cut has significant effect on  $R_a$  value during micro-end milling of aluminium material. The simulation results show that pressure drop characteristics of smooth channel are almost same



with that of rough channel modelled with minimum surface roughness level achieved in aluminium.

**Acknowledgements** This study was supported by IIITDM.

## References

1. Tuckerman, D.B., Pease, R.F.W.: High-Performance Heat Sinking for VLSI. *IEEE Electron Device Lett.* **2**(5), 126–129 (1981)
2. Li, S.N., et al.: Numerical study on the heat transfer performance of non-Newtonian fluid flow in a manifold microchannel heat sink. *Appl. Therm. Eng.* **115**, 1213–1225 (2017)
3. Qu, W., Mudawar, I.: Experimental and numerical study of pressure drop and heat transfer in a single-phase micro-channel heat sink. *Int. J. Heat Mass Transf.* **45**(12), 2549–2565 (2002)
4. Tiwari, R., Andhare, R.S., Shooshtari, A., Ohadi, M.: Development of an additive manufacturing-enabled compact manifold microchannel heat exchanger. *Appl. Therm. Eng.* **147**, 781–788 (2019)
5. Jing, D., He, L.: Numerical studies on the hydraulic and thermal performances of microchannels with different cross-sectional shapes. *Int. J. Heat Mass Transf.* **143**, p. 118604 (2019).
6. Pandey, J., Ansari, M. Z., Husain, A., Ansari, M. A.: Comparative study of flow characteristics in uniformly varying microchannel for DI water and nanofluid. *AIP Conf. Proc.* **2105** (2019).
7. Husain, A., Ariz, M., Al-Rawahi, N.Z.H., Ansari, M.Z.: Thermal performance analysis of a hybrid micro-channel, -pillar and -jet impingement heat sink. *Appl. Therm. Eng.* **102**, 989–1000 (2016)
8. Wu, H.Y., Cheng, P.: Friction factors in smooth trapezoidal silicon microchannels with different aspect ratios. *Int. J. Heat Mass Transf.* **46**(14), 2519–2525 (2003)
9. Duryodhan, V. S., Singh, S. G., Agrawal, A.: Liquid flow through converging micro-channels and a comparison with diverging microchannels. *J. Micromechanics Micro-engineering* **24** (12), p. 125002 (2014).
10. Anbumeenakshi, C., Thansekhar, M.R.: Experimental investigation of header shape and inlet configuration on flow maldistribution in microchannel. *Exp. Therm. Fluid Sci.* **75**, 156–161 (2016)
11. Kandlikar, S., Schmitt, D., Carrano, A., Taylor, J.: Characterization of surface roughness effects on pressure drop in single-phase flow in minichannels. *Physics of Fluids* **17**, p. 100606 (2005).
12. S. Bhattacharyya, H. Chelladurai and M. Z. Ansari, “Effect of micro-milling parameters on surface roughness of soft metal cutting and its regression mod-el,” 1st International Conference on Future Technologies in Manufacturing, Automation, Design & Energy (ICoFT 2020), 28–30 Dec 2020, NIT Puducherry, India (accepted)
13. Incropera, F.P.: *Fundamentals of Heat and Mass Transfer*, 7th edn. John Wiley & Sons, New York (2006)

# Microstructural Analysis of Friction Stir Processed Al5083 Alloy



D. Hari, N. Narmada Devi, R. Prabhakaran, M. Sutharsan,  
and Kannan Ganesa Balamurugan

## 1 Introduction

Aluminium and its alloys find prominent applications in variety of engineering fields due to their low density and appreciable mechanical properties [1]. Aluminium alloys possess wide application in both wrought and cast forms. In general, microstructures of the metallic materials govern their mechanical properties. Modification of the microstructure can improve their mechanical properties. The microstructures of the metals can be altered by the solidification, heat treatment and solid-state methods. Friction stir processing (FSP) is a solid-state materials joining and surface modification technique [2]. FSP has a unique tool that contains a shoulder and a pin part. The pin plunges into the material's surface and deforms its subsurface by stirring action. The shoulder part confines the deformed particles inside its space and sealed the cavity or groove created along the path of movement of the tool. Different kinds of research have been conducted on the various aluminium alloy grades. Suri et al. [3] have attempted FSP on Al 2024 alloy with the process parameters of tool feed rate of 25 mm/min and tool rotational speeds of 1200 and 1800 rpm. Effect of these parameters on the microhardness, tensile and impact strength was evaluated. FSP has significantly improved the microhardness by 1.5 times the unprocessed aluminium alloy. Moreover, tensile strength had been increased to 20%. Likewise, the impact strength also increased 2.5 times the unprocessed alloy. N. Nadammal et al. [4] have used a bottom-up approach to optimize the process parameters of the FSP in Al 2024-T3 plate. The optimized process parameters improved the tensile strength 93% of base metal. Compared with other grades of aluminium alloys, 5xxx series alloys show higher corrosion resistance alloys with excellent mechanical properties. Most of the FSP-related studies related to these alloy grades are focussed on preparation of

---

D. Hari (✉) · N. N. Devi · R. Prabhakaran · M. Sutharsan · K. G. Balamurugan  
Department of Mechanical Engineering, IFET College of Engineering (Autonomous),  
Villupuram, Tamil Nadu, India

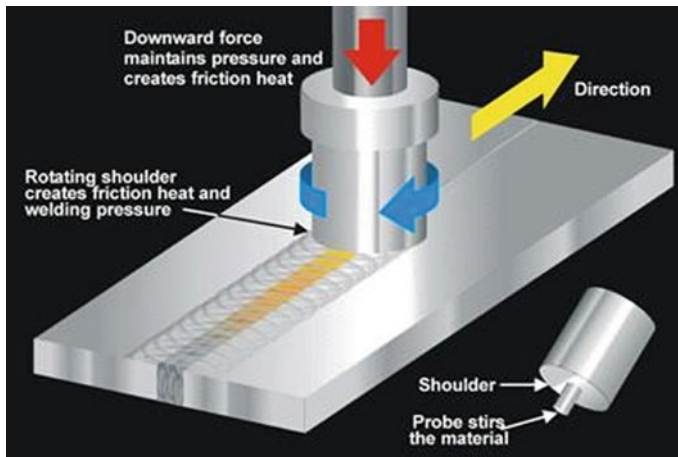
© The Author(s), under exclusive license to Springer Nature Singapore Pte Ltd. 2022  
S. K. Natarajan et al. (eds.), *Recent Advances in Manufacturing, Automation, Design  
and Energy Technologies*, Lecture Notes in Mechanical Engineering,  
[https://doi.org/10.1007/978-981-16-4222-7\\_29](https://doi.org/10.1007/978-981-16-4222-7_29)

245

surface composites. Availability of studies on the FSP studies on 5xxx series alloys is very scarce; especially in 5083 grade alloys. Therefore, the present work concerns to study about the effect of process parameters on the microstructure of the Al5083 alloy.

## 2 Experimental

The commercially available 5083 aluminium alloy was used for the FSP investigations. The sample dimension was  $50 \times 100 \times 5$  mm. An HcHcr steel tool with 18-mm shoulder diameter and 6-mm pin diameter with 4-mm pin length was used for the processing. The process parameters are tool rotational speed and tool feed rate. The tool rotational speeds were 700 rpm and 1000 rpm. Likewise, the tool feed rates were 20 mm/min and 40 mm/min. The Al5083 plate was fixed to the FSP machine table firmly using appropriate fixtures. The FSP tool was fixed to spindle and tightened. Required process parameter values were programmed into the FSP machine and activated. The rotating tool was plunged into the material at one end and performed FSP on its surface and retrieved back at another end. Single pass only performed. The process was repeated for other process parameter sets. The schematic representation of the FSP is shown in Fig. 1. The microstructures of the FSP samples were investigated through optical microscopy (OM). Cross section of the processed samples was sectioned and mounted in a Bakelite mould. Moulded samples were grinded in different grade sheets and finally polished in a soft cloth with alumina paste. Polished samples were etched with Keller's reagent. The microhardness testing was carried out in a Vicker's microhardness tester with a load of 0.5 kg and 10 s dwell time.



**Fig. 1** Schematic representation of FSP

### 3 Results and Discussion

The common FSP zones are shown in Fig. 2. It contains parent zone, heat-affected zone (HAZ), thermomechanically affected zone (TMAZ) and nugget zone. The nugget zone is the complete FSP zone that mostly contains the ultrarefined grains. Formation of this zone is due to combined plastic deformational effects of pin and frictional heat. The thermomechanically affected zone forms due to the combined effects of plastic deformation by the shoulder and frictional heat. The material flow patterns are commonly observed in this region with refined grains. The heat-affected zone forms due to frictional heat dissipation from the nugget and TMAZ. Usually, coarse grains are observed in this region. The parent zone is the unaffected region, otherwise called as parent material. Figures 3, 4, 5 and 6 show the microstructure of FSP Al5083 alloy processed at different processing conditions. Microstructures of processed samples indicate that there is no distinct variation in grain structures between the parent and HAZ. Therefore, the microstructure of parent zone has been presented. Figure 3a, b shows the TMAZ of samples processed in 700 rpm-20 mm/min and 700 rpm-40 mm/min, respectively. The microstructures indicate the distinct flow patterns that occurred during the FSP by the shoulder. In 700 rpm-40 mm/min sample, these flow patterns are very distinct than 20 mm/min sample. This is due to severe plastic deformation by the shoulder due to rapid movement of the tool. However, in case of 1000 rpm processing condition, the flow patterns are disappeared into the matrix due to higher frictional heat input. The frictional heat input at 1000 rpm processing condition is higher than 700 rpm condition due to increased frictional forces occurred between the tool shoulder and substrate. Similarly, formation interface boundary between the TMAZ and nugget zones is disappeared in lower feed rate condition in all tool rotational speed processing (20 mm/min) (Ref. Figures 3c and 5c). This disappearance of the boundary is attributed to the increased heat input and higher plastic deformation during the lower feed rate. The nugget zone in all processing conditions contains the ultrarefined grains (Figs. 3d, 4d, 5d, 6d).

Figure 7 shows the microhardness of the FSP samples at various processing conditions. Figure.a compares the microhardness of the samples processed at 700 rpm in

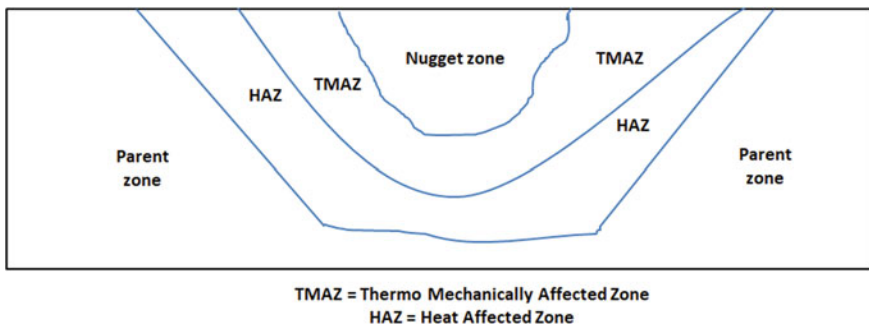
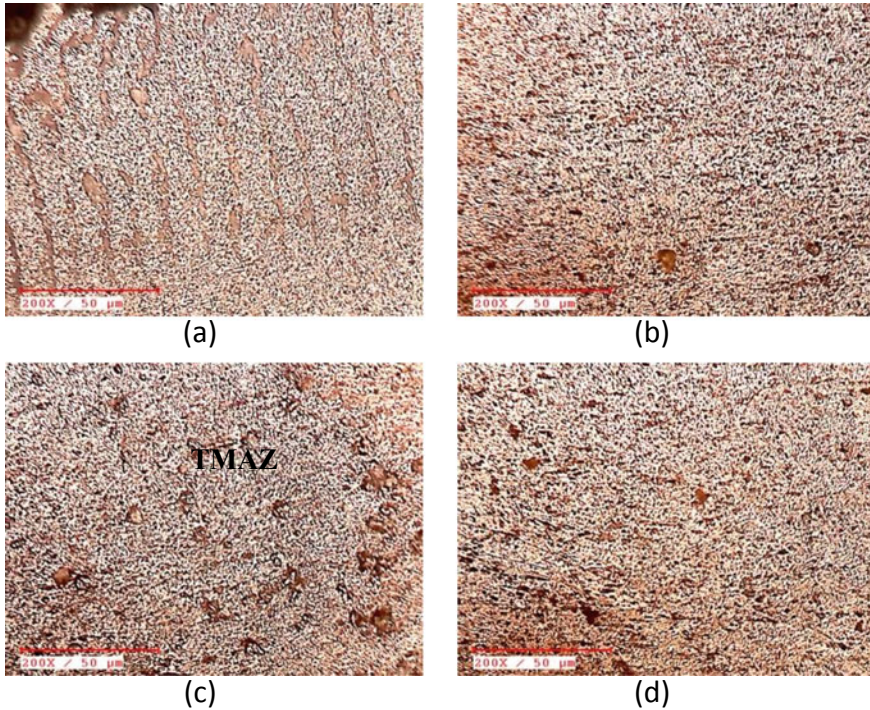


Fig. 2 Schematic representation of different zones of FSP



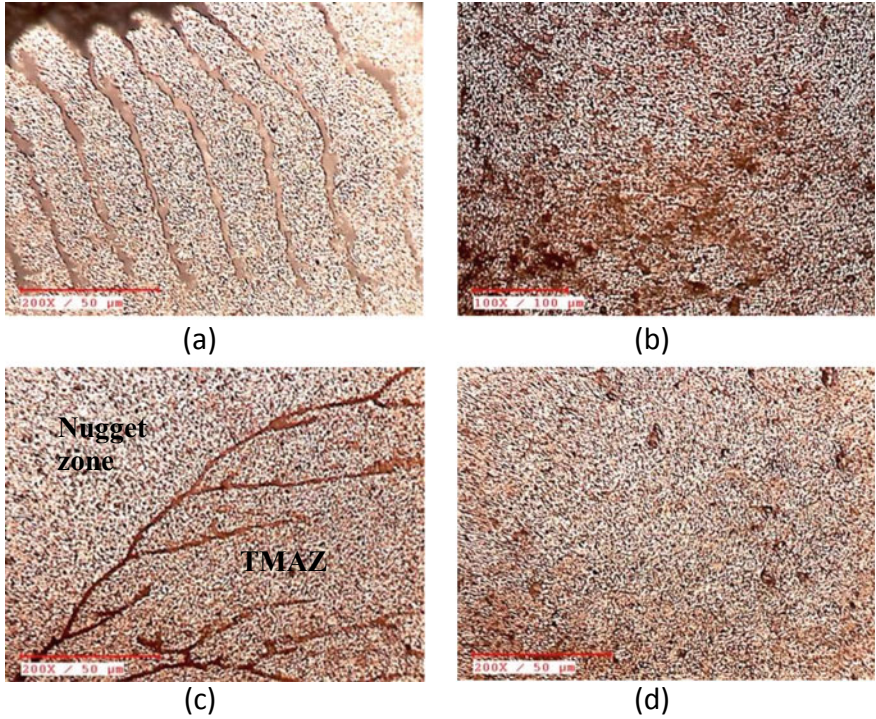
**Fig. 3** Microstructure of sample processed at 700 rpm-20 mm/min **a** TMA zone, **b** parent zone, **c** TMAZ–nugget interface zone, **d** nugget zone

different feed rates. Similarly, Figure.b compares the microhardness of the samples processed at 1000 rpm. In case of 700 rpm-20 mm/min, microhardness increases from one side of the parent material to nugget zone and again reduced at another side of the parent material zone. The lower feed rate imparts higher processing time which leads to higher heat input. Higher heat input and plastic deformation facilitated the ultragrain refinement. Grain refinement improves the microhardness in the HAZ and nugget zones. Similar trend has been observed on the samples processed at 1000 rpm (Fig. 7b). The higher heat input and subsequent rapid solidification resulted in the grain refinement. Therefore, samples processed at 1000 rpm yield higher microhardness by supplementing higher heat input.

## 4 Conclusion

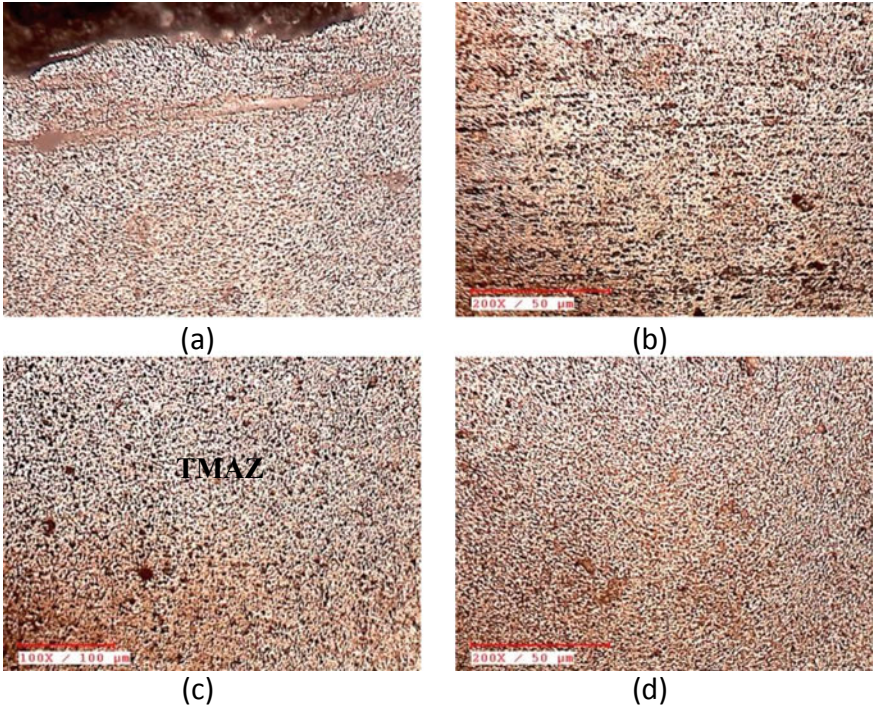
In this present work, friction stir processing was carried out on the Al5083 aluminium alloy. The present investigation revealed that grain refinement occurred in the





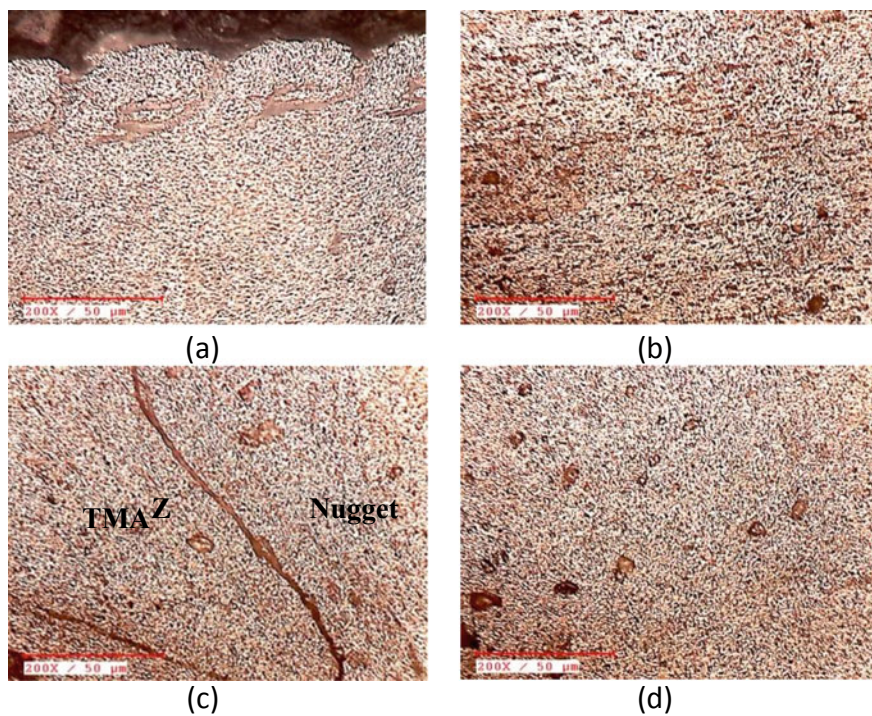
**Fig. 4** Microstructure of sample processed at 700 rpm-40 mm/min **a** TMA zone, **b** parent zone, **c** TMAZ–nugget interface zone, **d** nugget zone

different zones of the FSP specimens. Higher heat input and subsequent rapid solidification enhance the grain refinement in the FSP zones. Lower feed rate and higher rotational speed supplement the higher heat input by extreme frictional forces. Therefore, even at the 700 rpm condition, 20 mm/min of feed rate supplement higher heat input due to higher interaction time. Microhardness increases with the grain refinement. The grain refinement starts from the HAZ, and the ultrarefined grains were observed in nugget zones. Hence, the microhardness shows higher value in the nugget zones.



**Fig. 5** Microstructure of sample processed at 1000 rpm-20 mm/min **a** TMA zone, **b** parent zone, **c** TMAZ–nugget interface zone, **d** nugget zone





**Fig. 6** Microstructure of sample processed at 1000 rpm-40 mm/min **a** TMA zone, **b** parent zone, **c** TMAZ–nugget interface zone, **d** nugget zone



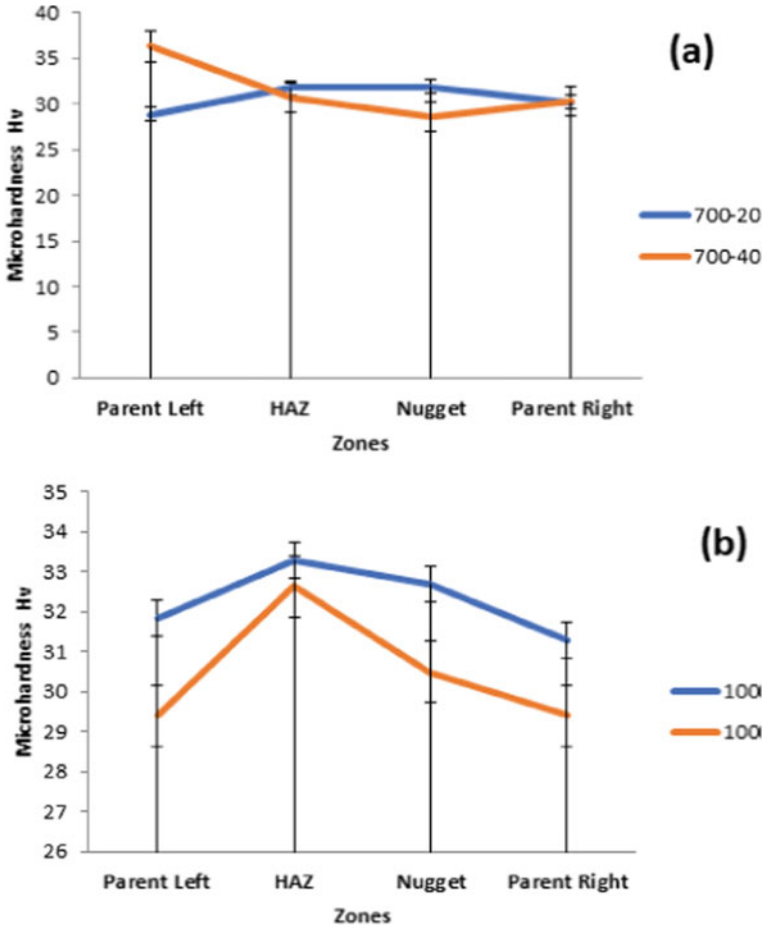


Fig. 7 Microhardness of FSP samples

### References

1. Mavhungu, S.T., Akinlabi, E.T., Onitiri, M.A., Varachia, F.M.: Aluminum matrix composites for industrial use: advances and trends. *Procedia Manuf.* **7**, 178–182 (2017)
2. Chainarong, S., Muangjunburee, P., Suthummanon, S.: Friction stir processing of SSM356 aluminium alloy. *Procedia Eng.* **97**, 732–740 (2014).
3. Suri, A., Sahai, A., Hans Raj, K., Gupta, N.K.: Impact and tensile testing of Al2024 alloy processed by friction stir processing. *Procedia Eng.* **173**, 679–685 (2017)
4. Nadammal, N., Kailas, S.V., Suwas, S.: A bottom-up approach for optimization of friction stir processing parameters; a study on aluminium 2024-T3 alloy. *Mater.Des.* **65**, 127–138 (2015)

# Performance Evaluation Through Audit of 519 Organizations



Karri Naveen , Chithirai Pon Selvan, and Amiya Bahumik

## 1 Introduction

The prime interest of the stakeholders would be in their organization's performance evaluation. ISO 9001 provides a framework for performance evaluation through monitoring, measurement, analysis, evaluation, internal audit and management review. Internal factors governing the organization's performance are determined in the quality management system. ISO conducts annual survey of management systems certifications [1]. 883 521 ISO 9001 certificates were issued all over the world in year 2019. The highest number of certificates issued were in the "Basic Metal & Fabricated Products" industry. There are many tools and techniques adopted by the mechanical engineering organizations conventionally used for evaluating performance.

## 2 Literature Review

Mehmet et al. [2] conducted a survey on a sample size of 225 small and medium organizations in Turkey to study the performance of certified and non-certified organizations. Mehmet has concluded that there is no sufficient evidence to determine

---

K. Naveen (✉)

Department of Mechanical Engineering, Lincoln University College, Petaling Jaya, Selangor, Darul Ehsan, Malaysia

e-mail: [phdstudent.naveen@lioncoln.edu.my](mailto:phdstudent.naveen@lioncoln.edu.my)

C. P. Selvan

Head of School—Science and Engineering, Curtin University, Dubai, UAE

A. Bahumik

Lincoln University College, Petaling Jaya, Selangor Darul Ehsan, Malaysia

the correlation between performance and ISO 9001 certification. Mihalj et al. [3] have carried out the literature review on a sample size of 24 articles to establish a correlation between certified organizations and non-certified organizations on business performance. Jordi et al. [4] conducted a research study on a sample size of 90 wind turbine organization by performing second party audits. Jordi concludes the area for improvement in certain criteria of the ISO 9001 standard. Behnam et al. [5] conducted the literature review on 68 research articles to determine correlation between organizations performance and ISO 9001. Anttila et al. [6] conducted a research study to determine interpreting factors for the application of the requirements of ISO 9001 standard. Luc [7] concluded that lack of sufficient data to establish correlation between ISO 9001 certified organizations has significant impact on the perception of e-service quality. Saleh [8] conducted a survey on consumer satisfaction on a sample size of 340 organizations in industries of Damascus Governorate, and he concluded that more research in marketing is essential to determine the cause of customer dissatisfaction and retention. Waqar [9] conducted a survey through questionnaire on a sample size of 300 ISO certified organizations in Pakistan to analyse the impact of transitions on organizational performance. Waqar concluded that there is a positive correlation between organizational performance and effective implementation of the requirements of the standard. Luís [10] conducted a survey with IRCA registered management system auditors on a sample size of 393 respondents, and he concluded based on the analyses of the data gathered through survey is there is a positive correlation between ISO 9001 certification and organizational performance. Ifroh et al. [11] conducted a survey on a sample size of 37 participants from an education and training centre as a case study to determine correlation between employee performance and the quality management system. Evangelos et al. [12] conducted a survey on a sample size of 100 ISO certified service organizations to determine the effectiveness of the ISO 9001. Evangelos established correlation between organizational operational performance, financial performance in context of the market volatility.

Majority of the research studies were carried out through survey and secondary data on impact, benefits and motivational factors of ISO 9001; very less evidence-based research and analysis has been done on performance evaluation from an Auditor's perspective.

### 3 Research Gap

Cross country research studies on performance evaluation of organizations in accordance with ISO 9001 are very meagre, and hence, this research study is undertaken to fulfil this gap.

## 4 Research Methodology

An objective evidence-based onsite audit was conducted in 519 organizations, and the primary data was collected by spending 879 mandays onsite. Conformance to ISO 9001 criteria were determined by using a five point Likert scale. A simple random sample of 519 organizations were selected in New Zealand, India, UAE, Bahrain, Qatar, Oman, Kingdom of Saudi Arabia, Kuwait, Malaysia, Australia, Malaysia.

## 5 Reliability Analysis

Consistent and reliable questionnaire was determined by Cronbach’s alpha arriving at  $\alpha = 0.948$ . The questionnaire is prepared in accordance with ISO 19011 the guidelines for auditing techniques.

## 6 Results

Jamovi software is used for analysing the research data. Table 1 indicates the descriptive statistics of conformity assessment variable on monitoring, measurement, analysis and evaluation (average: 3.63; Median: 4; standard deviation: 0.554). The results indicate that 40.7% of the sample was non-conforming to the requirements of the conformity assessment variable. Only 19 organizations out of sample size of 519 organizations were found to complying with conformity assessment variable to their fullest extent. 289 organizations contributing to 55.7% of the sample size were just fulfilling the minimum requirements of the conformity assessment variable.

Table 2 indicates the conformance to the criteria of internal audit. Point-5 of Likert scale represents the least by 0.2%, and point-4 represents 61.8% the highest degree of conformance to internal audit criteria. The Mean value observed was 3.62,

**Table 1** Descriptive statistics

	Monitoring, measurement, analysis and evaluation
N	519
Missing	0
Mean	3.63
Median	4
Standard Deviation	0.554
Minimum	3
Maximum	5

**Table 2** Frequency of internal audit

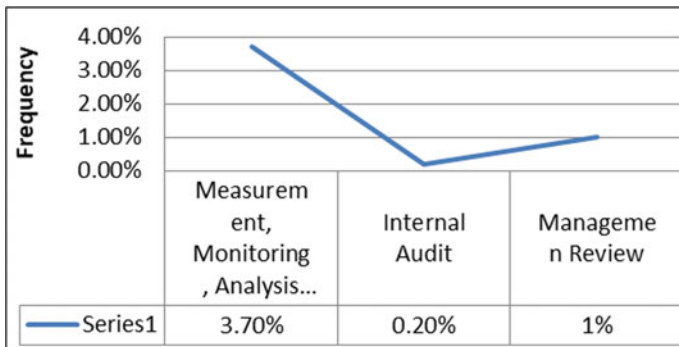
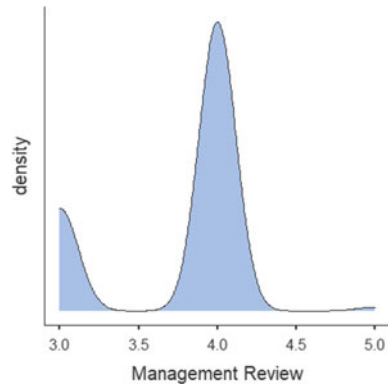
Levels	Counts	% of total
3	197	38.0
4	321	61.8
5	1	0.2

whereas the Median value is 4. Point-3 of Likert scale indicates 38% of the sample not complying with the requirements of the conformity assessment variable.

Figure 1 indicates the density distribution of the requirements of management review criteria where the Mean is 3.75, Median is 4 and standard deviation is 0.455. 135 organizations out of sample size of 519 organizations were contributing 38% who were not fulfilling the requirement of the conformity assessment variable.

The potential to gain enhanced benefits from the effective implementation of ISO 9001 is not fully explored. Figure 2 indicates the research study results where the point-5 of Likert Scale distribution is found to be very low. Conformance to the

**Fig. 1** Density of management review



**Fig. 2** Consolidated results of research study

measuring, monitoring, analysis and evaluation is 3.70%, and management review is 1% and the least being internal audit about 0.20%.

## 7 Conclusion

- a. Organizations shall make arrangements to evaluate the organizational performance at defined frequency.
- b. Organizations should review the arrangements made for customer satisfactions to be effective.
- c. Organization should conduct internal audit on continual basis by a competent person.
- d. Organization should review to confirm adequacy and effectiveness of the quality management system.

The following aspects could be considered as scope for future research study:

- a. A universal sample across the world could be undertaken for research study to endorse this research results.
- b. Internal audits could be outsourced to avail expert service for better outcome of the exercise.
- c. Industry specific factors could be determined for under performance of internal audit exercise.
- d. Adequacy of the documented information could be studied to determine the monitoring, measurement, evaluation and analysis.

## References

1. International Organization for Standardization Homepage: <http://www.iso.org>, last accessed 2020/09/13.
2. İlkay, M.S., Aslan, E.: The effect of the ISO 9001 quality management system on the performance of SMEs. *Int. J. Qual. Reliab. Manag.* **7**, 753–778 (2012)
3. Bakator, M., Čočkaló, D.: Improving business performance with ISO 9001: a review of literature and business practice. *The Eur. J. Appl. Econ.* (2018)
4. Dalmau, J.C., Gimenez, G., De Castro, R.: ISO 9001 aspects related to performance and their level of implementation. *J. Ind. Eng. Manag.* (2016)
5. Neyestani, B., Berlin J., Juanzon, P.: ISO 9001 Standard and Organization's performance: a literature review. *Int. J. Adv. Multidiscip. Res.* **4**, (2017)
6. Anttila, J., Jussila, K.: ISO 9001:2015-a questionable reform. What should the implementing organisations understand and do? *Total Qual. Manag. Bus. Excellence* **28**, (2017)
7. Yaya, L.H.P., Marimon, F., Casadesus, M.: *Industrial Management & Data Systems*. Emerald Group Publishing Limited **111**, 1194–1213 (2011)
8. Ali Hussein, S., Ali Al-shami, S., Fam, S.-F., Al Derej, S.: Impact of ISO 9001 certification on consumer satisfaction. *J. Adv. Res. Dyn. Control Syst.* **10**, (2018)

9. Ahmed, W.: ISO 9001 transition and its impact on the organizational performance: evidence from service industries of Pakistan. *Int. J. Res. Bus. Stud. Manag.* **4**, 39–54 (2017)
10. Fonseca, L., Domingues, J.P.: ISO 9001:2015 edition-management, quality and value. *Int. J. Qual. Res.* **11**(1), 149–158 (2016)
11. Dalimunthe, I. Nazaruddin, S.S.: The effect analysis of quality management system application on improving employees' performance through quality culture. *Int. J. Res. Rev.* (2019)
12. Psomas, E.L., Pantouvakis, A., Kafetzopoulos, D.P.: The impact of ISO 9001 effectiveness on the performance of service companies. *Manag. Serv. Qual.* **23**, (2013)

# Effect of Varying Tool Parameters on Chip Formation and Reaction Force



Raunika Anand, Jeet Desai, and G. Rajyalakshmi

## 1 Introduction

One of the highly used manufacturing processes that involve removal of material is machining process [1]. Machining is one amongst the oldest industrial processes, and it is the foremost oftentimes employed in the manufacturing of commercial workpieces. It is calculable that about 15% of the worth of all mechanical elements manufactured within the world comes from a machining operation. In spite of its economic and technical importance, metal cutting remains one amongst the lesser understood processes thanks to the inefficient prognostic capability of the models [2]. It encompasses of varied forms of material removal processes. Though machining is not thought of to be economical, material wastage is virtually greater than the other material removal production methods. However, it is evidenced to be a superior alternative as a secondary production method wherever material removal needed is comparatively less. Moreover, machining offers the best surface finish and high tolerance; thence, its popularity as a material removal method is clear.

The machining method involves material removal as chips. The chips are removed by an intricate method of deformation and fracture directly before the cutting edge [3]. The cutting parameters' correct choice and tool geometric angles' adoption can have an effect on the material removal method in terms of chip formation and machined surface formation processes [4]. Throughout the machining of titanium alloys, chip

---

R. Anand · J. Desai (✉) · G. Rajyalakshmi  
Vellore Institute of Technology, Vellore, Tamil Nadu 632014, India  
e-mail: [jeetketan.desai2017@vitstudent.ac.in](mailto:jeetketan.desai2017@vitstudent.ac.in)

R. Anand  
e-mail: [raunika.anand2017@vitstudent.ac.in](mailto:raunika.anand2017@vitstudent.ac.in)

G. Rajyalakshmi  
e-mail: [rajyalakshmi@vit.ac.in](mailto:rajyalakshmi@vit.ac.in)



morphology and segmentation play a major role in defining machinability and tool wear.

The chip is commonly discontinuous at lower cutting speeds, whereas when the cutting speeds are higher, the chip becomes serrate [5].

Through the speedy development of superior computing technologies, computational methods are widely adopted to research on the mechanics and dynamics of metal cutting processes [6]. Enhancements in production technologies need higher modelling and simulation of metal cutting processes. Theoretical and experimental investigations of machining are extensively distributed exploring varied techniques [7]. The shape and property of the chip are anticipated to be projected in automatic production as a result of the handling of chip which could be a key for effective performance. The property of the finished surface is additionally a vital issue for effective machining. If the properties of chip and surface may be analysed by the theoretical ways, the analysis is going to be of commercial importance. To predict these properties for varied mixtures of metals to be cut and also the operating conditions, ways for modelling of metal cutting are necessary [8].

Materials selected for this explicit study are Ti6Al4V and Inconel 718. Titanium alloys are engaging materials for aerospace thanks to their glorious combination of high specific strength, fracture-resistant characteristics and general corrosion resistance. They are additionally being employed more and more in chemical process and biomedical, automotive and nuclear industries [9]. Nickel-based superalloys are mostly utilized within the aerospace industry, especially within the hot sections of turbine engines; this is mainly because of their extreme temperature strength and high corrosion resistance [10].

Finite element analysis (FEA) is employed as a tool to further provide a prediction of chip formation, and the data obtained from the simulation will be helpful in understanding and envisaging the process of formation of different types of chips due to varying cutting parameters. Chip morphology is studied in detail to have a better understanding of chip formation. The stresses, such as von Mises stress and strains, such as equivalent plastic strain (PEEQ), generated in the workpiece material also play an important role in studying chip formation. The reaction force on the tool material is vital data obtained from the FEA simulation and is used for further study in the process of chip formation in orthogonal cutting.

## 2 Methodology

### 2.1 Workpiece and Tool Material

The simulation is conducted on two different materials, namely Ti6Al4V and Inconel 718. The detailed properties of Ti6Al4V are provided in the literature [11]. The detailed properties of Inconel 718 are provided in the literature [12]. The tool material

use is high-speed steel (HSS), which is very commonly used by manufacturers in machining processes.

The outstanding properties of titanium and its alloys such as high strength, low weight and extraordinary corrosion resistance are responsible for their usage in a wide range of applications. These applications include medical industry, aerospace, automotive, oil and gas, power generation and other key industries, where highly reliable performance is required. In most of these industries and other engineering fields, titanium and its alloys have replaced the heftier, less functional or less economic materials.

Nickel-iron-based superalloys are predominantly used for high-temperature applications where creep, corrosion and thermal shock resistances are desired. Inconel is widely used throughout the world, and it is known as a refractory superalloy due to the reason that its applications are at a temperature of 1400 °C and above. The value of Young’s modulus of Inconel 718 is almost double to that of Ti6Al4V. Inconel 718 is used in aerospace and aviation industries. Material properties for both Ti6Al4V and Inconel 718 are mentioned in Table 1.

Johnson–Cook material model and failure parameters have been implemented here. The Johnson–Cook material model expression is as follows:

$$\sigma = (A + B\varepsilon^n) \left( 1 + C \ln \frac{\dot{\varepsilon}}{\dot{\varepsilon}_0} \right) \left[ 1 - \left( \frac{T - T_r}{T_m - T_r} \right)^m \right]$$

where flow stress is denoted by  $\sigma$ , equivalent plastic strain is denoted by  $\varepsilon$ , dimensionless plastic strain rate is denoted by  $\frac{\dot{\varepsilon}}{\dot{\varepsilon}_0}$ , reference strain rate is denoted by  $\dot{\varepsilon}_0$ , strain hardening rate index is denoted by  $n$ , initial yield stress is denoted by  $A$ , hardening coefficient is denoted by  $B$ , strain rate sensitivity coefficient is denoted by  $C$ , temperature softening index is denoted by  $m$ , lowest experimental temperature is denoted by  $T_r$  and material melting temperature is denoted by  $T_m$ . Johnson–Cook material model data are compiled in Table 2.

The Johnson–Cook failure model expression is as follows:

**Table 1** Material properties

Properties	Ti6Al4V	Inconel 718
Density (g/cm3)	4.428	8.192
Young’s modulus (Gpa)	113.8	199.25
Poisson’s ratio	0.342	0.295
Elastic limit (Mpa)	848	725
Tensile strength (Mpa)	1031	1100

**Table 2** Johnson–Cook material model data

Parameters	Ti6Al4V	Inconel 718
A (Mpa)	862	1290
B (Mpa)	331	895
<i>n</i>	0.34	0.526
<i>m</i>	0.8	1.55
<i>C</i>	0.012	0.0134

**Table 3** Johnson–Cook failure model data

Parameters	Ti6Al4V	Inconel 718
D1	-0.09	0.04
D2	0.25	0.75
D3	0.5	-1.45
D4	0.014	0.04
D5	3.87	0.89

$$\bar{\epsilon}_f = \left[ D_1 + D_2 \exp\left( D_3 \frac{P}{\sigma} \right) \right] \left[ 1 + D_4 \ln \frac{\dot{\epsilon}}{\epsilon_0} \right] \left[ 1 + D_5 \frac{T - T_r}{T_m - T_r} \right]$$

where  $\bar{\epsilon}_f$  is the equivalent strain, average of the three principal stresses is denoted by P and equivalent stress is denoted by  $\sigma$ . D1, D2, D3, D4 and D5 are the failure parameters. The material melting temperature is denoted by  $T_m$ . Johnson–Cook failure model data are compiled in Table 3.

## 2.2 Simulation Set-Up

The simulation of orthogonal cutting of the workpiece has been carried out using ABAQUS finite element software. The chip formation and chip morphology for different materials at different rake angles and multiple cutting speeds are studied using simulation model. Using the simulation of orthogonal cutting stresses and strains in different materials with a change in cutting speed and change in rake angle of the tool is studied.

This particular study of orthogonal cutting process, which includes the simulation of chips while changing different cutting parameters, would further provide a theoretical aid to manufacturers in the field of titanium alloy, nickel alloy and steel processing.

**Modelling.** Two different 3D CAD models are generated in Abaqus software’s inbuilt CAD modelling feature. The workpiece material has the shape of a bar with dimensions 200 mm × 40 mm × 20 mm as length, width and depth, respectively. Such shape and dimensions are chosen to assist and enable orthogonal cutting. The

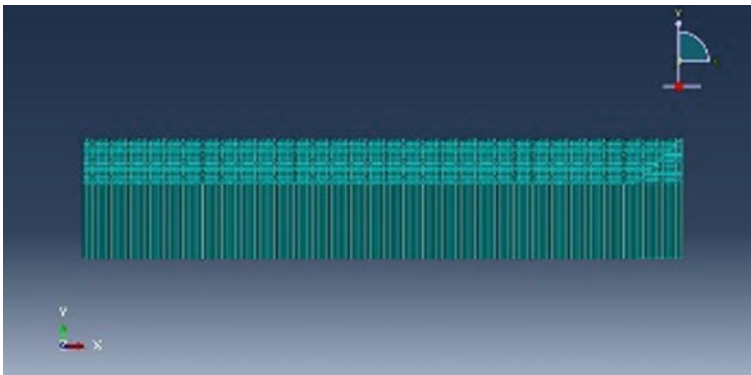
tool's size is of the order  $40\text{ mm} \times 40\text{ mm} \times 40\text{ mm}$ . Furthermore, three CAD models were modelled to achieve the change in rake angle.

The workpiece has been divided into two sections. This has been done to enable us to assign different properties to the two different sections of the workpiece. The material removal and thus chip formation will take place in the upper section.

**Meshing.** Meshing is one of the most crucial parts of finite element analysis. Meshing divides a complex structure or a plane into small elements. The element chosen in this particular study for both workpiece and tool is hexahedron (HEX8). A hexahedral mesh is best suited in situations where the geometry is simple. A hexahedral mesh has also been proven to take lesser computational time. Furthermore, it is comparatively easy to modify the geometry with hexahedral meshing.

An overall approximate mesh size of the workpiece is set as 2 mm. After setting up the global seeds of the workpiece, individual edges are selected and local seeds are applied. These local seeds are applied only to the upper section of the workpiece. This is done because the upper section would be the area of study as the chip formation will take place there. By setting up local seeds to the upper section, the number of elements is increased so as to provide a better result of the simulation analysis of material removal via chip formation. Also, as in the lower section only global seeds are applied, the number of elements would be less, hence saving precious computational power as no major analysis is taking place there. Workpiece mesh is shown in Fig. 1.

**Interaction properties and Boundary conditions.** Abaqus/Explicit is used for interaction between the tool and the workpiece. Abaqus/Explicit works suitably well for simulations of brief transient dynamic events. It performs appropriate analysis of events of nonlinear behaviour such as contact. Abaqus/Explicit is usually applied to those portions of the analysis where high-speed, nonlinear, transient response plays a major role in the solution.

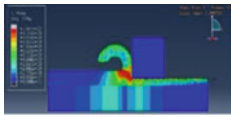

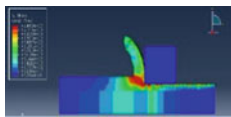


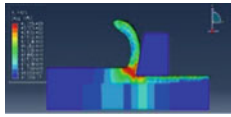





**Fig. 1** Workpiece mesh










### 3 Results

The chip formation and chip morphology results of the analysis are given in the following tables. Also, the reaction force acted on the tool by the workpiece has been presented in graphs of force vs time. S Mises stress, PEEQ and force vs time results for Ti6Al4V are given in Tables 4, 5 and 6, respectively. S Mises stress, PEEQ and force vs time results for Inconel 718 are given in Tables 7, 8 and 9, respectively.

**Table 4** S Mises stress on Ti6Al4V

Rake angle	Cutting speed		
	100 m/min	140 m/min	180 m/min
0°			
15°			
30°			

**Table 5** PEEQ on Ti6Al4V

Rake angle	Cutting speed		
	100 m/min	140 m/min	180 m/min
0°			
15°			
30°			

**Table 6** Force vs time graphs of Ti6Al4V

Rake angle	Cutting speed		
	100 m/min	140 m/min	180 m/min
0°			
15°			
30°			










**Table 7** S Mises stress on Inconel 718

Rake angle	Cutting speed		
	100 m/min	140 m/min	180 m/min
0°			
15°			
30°			

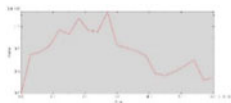
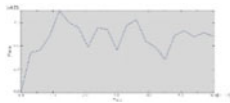
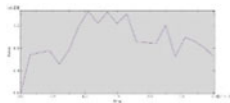
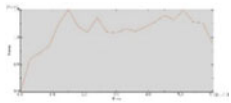
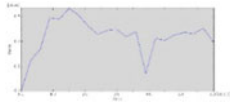
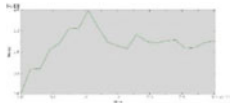


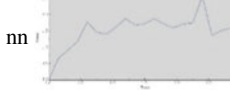
## 4 Conclusion

A general trend that was observed is that with an increase in the rake angle, the chip flow was getting smoother, shear banding decreased (in case of Ti6Al4V only), the stress generated in the primary shear zones increased, the surface finish increased (exception in Inconel 718), chip curl radius decreased and chip length increased, while width decreased. Meanwhile, another observation made is that with an increase in cutting speed, the stress in the primary shear zone increased with a decrease in the

**Table 8** PEEQ on Inconel 718

Rake angle	Cutting speed		
	100 m/min	140 m/min	180 m/min
0°			
15°			
30°			

**Table 9** Force vs time graphs of Inconel 718

Rake angle	Cutting speed		
	100 m/min	140 m/min	180 m/min
0°			
15°			
30°			

shear zone area, surface finish increased and uniform stress distribution in the chip comparatively.

In almost all cases, generally, the value of the reaction force jumps to the highest value and then slowly decreases to a lower value, and this event marks the initialization of the contact between the tool and the workpiece. The reaction force fluctuates quite a lot within a small range until the reaction force suddenly drops nearing zero, indicating that the contact between the tool and the workpiece is about to terminate.

These observations collected through the means of computational simulation analysis with variation in rake angle and cutting speed of the tool would prove to be

helpful in the commercial and industrial orthogonal cutting process where Ti6Al4V and Inconel 718 are used extensively.

## References

1. Ducobu, F., Rivière-Lorphève, E., Galindo-Fernandez, M., Ayvar-Soberanis, S., Arrazola, P.-J., Ghadbeigi, H.: Coupled Eulerian-Lagrangian (CEL) simulation for modelling of chip formation in AA2024-T3. In: 17th CIRP Conference on Modelling of Machining Operations. ISSN: 2212-8271(82), 142-147 (2019).
2. Calamaz, M., Coupard, D., Girod, F.: A new material model for 2D numerical simulation of serrated chip formation when machining titanium alloy Ti-6Al-4V. *Int. J. Machine Tools & Manuf.* **48**, 275-288 (2007)
3. Syed Adnan, A., Subbiah, S.: Experimental investigation of transverse vibration-assisted orthogonal cutting of AL-2024. *Int. J. Machine Tools & Manuf.* **50**, 294-302 (2009)
4. Li, A., Zang, J., Zhao, J.: Effect of cutting parameters and tool rake angle on the chip formation and adiabatic shear characteristics in machining Ti-6Al-4V titanium alloy. *Int. J. Adv. Manuf. Tech.* (2020)
5. Hua, J., Shivpuri, R.: Prediction of chip morphology and segmentation during the machining of titanium alloys. *J. Mat. Process. Tech.* **150**(1-2) (2004)
6. Gao, Y., Ko, J. H., Lee, H. P.: 3D coupled Eulerian-Lagrangian finite element analysis of end milling. *Int. J. Adv. Manuf. Tech.* **98**, 849-857 (2018)
7. Xie, J. Q., Bayoumi, A. E., Zbi, H. M.: FEA modeling and simulation of shear localized chip formation in metal cutting. *Int. J. Machine Tools Manuf.* **38**, 1067-1087 (1998)
8. Iwata, K., Osakada, K., Terasaka, Y.: Process Modeling of orthogonal cutting by the rigid-plastic finite element method. *ASME. J. Eng. Mater. Technol.* **106**(2), 132-138 (1984)
9. Sun, J., Guo, Y.B.: A new multi-view approach to characterize 3D chip morphology and properties in end milling titanium Ti-6Al-4V. **48**, 12-13 (2008)
10. Devillez, A., Le Coz, G., Dominiak, S., Dudzinski, D.: Dry machining of Inconel 718, workpiece surface integrity. *J. Materials Processing Tech.* **211**, 1590-1598 (2011)
11. Lesuer, D. R.: Experimental investigations of material models for Ti-6AL-4V titanium and 2024-T3 aluminum. US Department of Transportation Federal Aviation Administration (2000)
12. Baufeld, B.: Mechanical properties of INCONEL 718 parts manufactured by shaped metal deposition (SMD). *J Mater. Eng. Perform.* (2012)



# Wood-Plastic Composite Processing and Mechanical Characteristics—A Brief Literature Review



Sachin S. Raj 

## 1 Introduction

Natural fibre reinforcements into polymers are known to provide enhanced mechanical strength to the base matrix material [1]. Natural fibres are reinforced into polymers as long fibres, short fibres, laminated sheets or in particle forms. Wood-plastic composite (WPC) or plastic wood is a material developed by the impregnation of natural wood fibres in powdered form into a polymer matrix [2]. The earliest WPC was first processed using wood flour with phenol–formaldehyde which found its application in automobile gear shift knobs [3]. WPCs were commercially developed in the USA, as a substitute for plain wood components and are widely used for flooring, roofing, fencing, door and window frames, park benches and other interior infrastructure [2, 4]. WPCs are normally resistant to rot, decay and erosion and possess low water absorption character when compared with conventional wood planks and plywood [5]. Pecas et al. (2018) performed a detailed review of natural fibre-reinforced biocomposites and their versatile applications. The authors state that there would be an economic revolution for bio-based wood-plastic composites. Industries like the construction field, the automobile sector and other commercial Bio-WPC products developed through thermoforming, injection moulding and extrusion methods would face a high demand for their production from the year 2020 onwards [6]. The new era has now begun, and the demand for bio-WPCs and biocomposites using wood fibre reinforcements is getting to newer heights day by day in all industrial sectors. Petroleum-based polymers that are commonly used to fabricate wood-plastic composites are polypropylene (PP) [7], PE [8], PS [9] and polyvinylchloride (PVC) [10]. The most widely used biopolymer to fabricate WPCs in the recent times is polylactic acid [11], due to its competitive mechanical characteristics. Wood-plastic composites are processed under additive manufacturing. Polymer materials that are

---

S. S. Raj (✉)

Gnanamani College of Technology, Namakkal, Tamil Nadu 637018, India

used for the fabrication of WPCs are commonly available in granular form and hence require a heat treatment process to melt and blend the polymer with the filler material [11].

## 2 Processing of Wood-Plastic Composites

The most widely used methods for processing WPCs are:

- Extrusion moulding [12].
- Compression moulding [13].
- Injection moulding [3].

Injection moulding technique is used for fabricating complex shapes [7], and extrusion technique is used for pelletizing and designing test specimens and compression moulding technique to fabricate simple shapes [4]. In the case of both compression moulding and injection moulding, a dual-stage of processing is followed. The blending of the raw materials is initially carried out in an extruder or heat mixer which melts and mixes the polymer and wood flour into pellets. These pellets are then used as input in the compression moulding and injection moulding methods to fabricate composites of desired shapes [14–17]. Biopolymers like PLA have low glass transition temperature and can turn brittle due to its integral property and hence dual thermal processing methods tend to deteriorate the properties of the final composite [18]. In industries, a single screw extruder is commonly used to process composite pellets while a twin-screw extruder provides enough processing profile to run the molten WPC directly through dies to form desired shapes [19]. The best processing method for fabricating wood-plastic composites is by extrusion technique [20].

Ferreira et al. (2015) [21] studied the properties of plasticized starch-added PLA with organic clay-reinforced hybrid composite. The PLA and starch were maintained at 70:30 weight ratios, and the quantity of organic clay content was varied during the study. The author had processed the hybrid composites using the extrusion method, compression moulding method and injection moulding technique. The extrusion- and compression-moulded composites showed improved properties with increasing organic clay content. In the injection moulded samples, the properties changed with respect to the dispersion of the organic clay into the matrix material. The extrusion method ended up producing the best dispersion due to the excellent blending procedure that was used to combine the base polymer and the reinforcement material. Vandi et al. (2019) [22] used the extrusion technique to process pinewood fibre-reinforced polymer composite with PHBV as the matrix material. The study elaborated on the extrusion process by varying the wood fibre content between 10 and 40 wt%, varying the processing temperature between 170 °C up to 210 °C and varying the screw speed at 50, 100, 150 and 200 rpm. The analysis was also carried out using the ANOVA plotting method which resulted in the following settings as the optimum parameters for the extrusion of polymer/wood fibre composites. Processing temperature—190 °C, screw speed—100 rpm, feed rate—40 cm<sup>3</sup>/min and L/D ratio—40:1.

In comparison with a composite processed at 190 °C, the composite processed at 180 °C had reduced tensile modulus and the composite was processed at 210 °C had reduced tensile strength. The processing speed at 50 rpm, 150 rpm and 200 rpm had lowered the tensile properties of the composite in comparison with the composite processed at 100 rpm. PLA processed through compression moulding methods also used a processing temperature of 190 °C [23]. In a previous study, attempts have also been made to process wood-plastic composites using stir casting methods at temperatures up to 210 °C. However, the properties of the composites manufactured through stir casting were found to be lower than other regular methods [24].

### 3 Mechanical Characteristics of Wood-Plastic Composites

Ichazo et al. [7] added different hardwoods into PP to fabricate WPCs. The fibres were chemically treated with NaOH with a concentration of 18% for half an hour. Composites were first pelletized using a twin-screw extruder at 110 rpm with a temperature of 165 °C and then injection-moulded at 190 °C with a pressure of 800 psi. The specimens were tested to ASTM standards. The tensile strength of the composite had increased by 40% and elongation had decreased by 80%. The impact strength of the composite had also reduced by 50%. Alkali treatment had improved the fibre dispersion into the matrix but did not affect the mechanical properties of the composite. Kamdem et al. [25] characterized the tensile and impact properties of pinewood flour-reinforced high-density polyethylene (HDPE) composite. The wood fibres were sieved through a #100 mesh size to obtain a wood flour size of 0.15 mm, and the filler was combined with HDPE through the compression moulding method. A processing temperature of 200 °C at 800 psi compressive pressure was adapted. The composite had been fabricated with an equal weight ratio of polymer and wood flour. The tensile strength of the composite was 35% greater than that of the plain polymer. The impact strength of the polymer had also increased by 11% with the addition of pinewood flour. This research had also studied the density of the specimens, where the polymer had a density of 1018 kg/m<sup>3</sup> and the pinewood flour filled composite had a density of 1000 kg/m<sup>3</sup>. This shows that reinforcement of wood flour into a polymer leads to a lighter weighing composite material. Tisserat et al. (2013) [26] had used various sized paulownia wood flour as reinforcements that were obtained through different sieve/mesh sizes. The different sized wood flours were reinforced into PLA at a constant 25 wt% ratio using the extrusion method. A processing temperature of 170 °C was implemented. Tensile strength was analysed to ASTM standard which showed an increasing pattern with decreasing size of reinforcement. The addition of paulownia wood flour in common reduced the tensile strength of PLA but increased the modulus value drastically. This increase in the tensile modulus was due to the high stiffness of the composite when compared with plain PLA. In this literature, paulownia is also referred to have very high lignin content of 20% which may be the reason for the high stiffness of the wood as well as the composite. The size of wood particles used in various studies is plotted out in Fig. 1, and the maximum

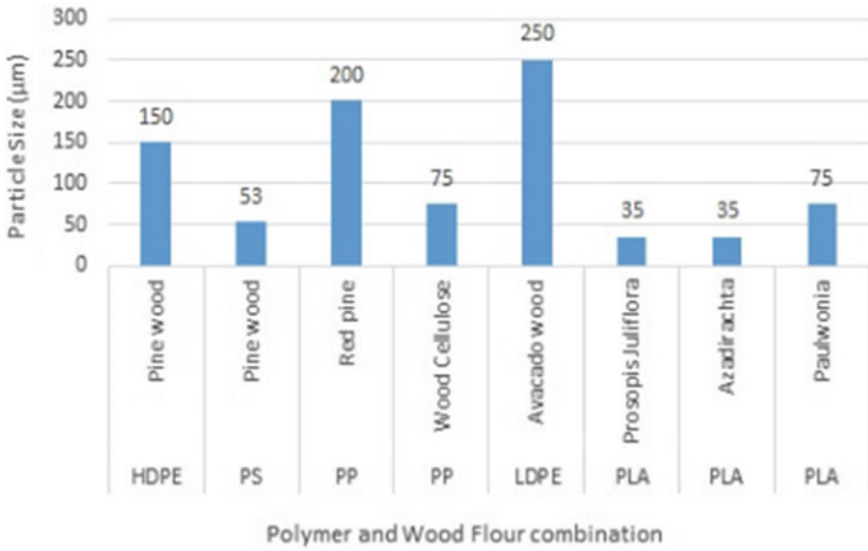


Fig. 1 Reinforced wood particle size in various studies

amount of wood flour reinforcements made into polymer matrices in various studies is represented in Fig. 2.

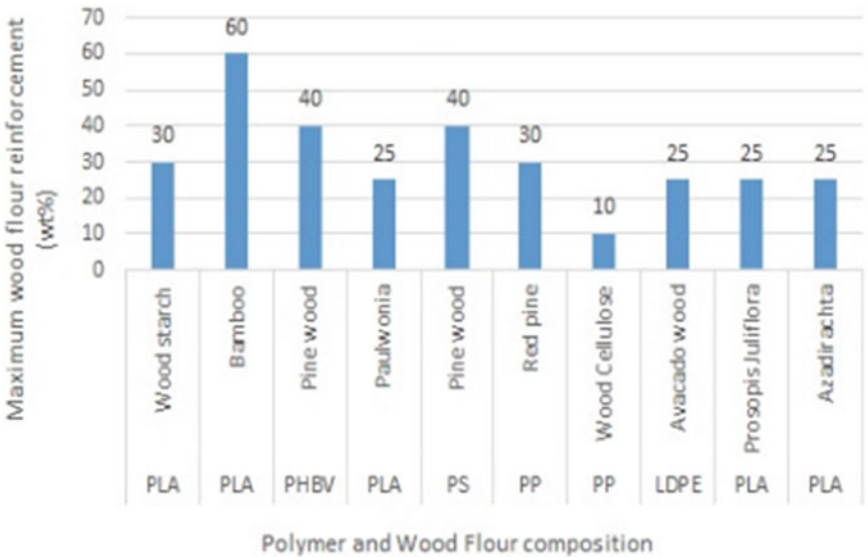


Fig. 2 Maximum amount of wood flour reinforced into polymers in various studies

Poletto et al. [9] processed pinewood flour-reinforced PS by using injection moulding method at 180 °C. Composite specimens had been fabricated at 10, 20, 30 and 40 wt% ratios of wood flour reinforcement. The size of the wood flour was 53 µm. ASTM standards were followed for analysing the mechanical characteristics by using 5 mm/min crosshead speed for the tensile test, 1.5 mm/min crosshead speed for the flexural test and 25 J impact force on the un-notched composite specimens. The tensile strength of the polymer was 37 MPa, and the addition of pinewood flour at 10 wt% reduced the tensile strength to 33 MPa. The composite with 20 wt% reinforcement showed an increase in the tensile strength to 35 MPa. Further increase in wood flour content showed reduced tensile character. Modulus values increased with increasing fibre content. Flexural strength of the plain PS was 46 MPa, and the addition of pinewood flour at 10 wt% increased the flexural strength to 54 MPa. Increasing the fibre content beyond 10 wt% showed a reducing pattern of flexural strength. Impact strength reduced with the addition of pinewood flour and with further increase in the filler content. Perez et al. [4] studied the tensile behaviour of red pinewood flour-reinforced polypropylene. The composite was processed by mixing pinewood flour in weight ratios of 10, 20 and 30% with PP using the compression moulding method under a pressure of 50 bar at 190 °C. The size of the wood flour was 200 µm. The addition of pinewood showed an increase in the young's modulus. PP had a young's modulus of 1965 MPa, and the 30 wt% reinforced composite had a modulus of 2760 MPa. The elongation and the tensile strength of the composite had reduced with increasing fibre content. PP had a tensile strength of 34.6 MPa, and the 30 wt% reinforced composite had a reduced tensile strength of 20.54 MPa. Haque et al. [27] performed detailed studies on the fatiguing nature of PP-reinforced cellulose nano-fibres at a ratio of 10 wt%. The particle size was 75 µm, and the composite was processed by the extrusion method. The maximum processing temperature was set at 200 °C, and the screw speed at 85 rpm. The tensile strength of the polymer had increased by 75% with the addition of wood flour content. The literature further deals with the inclusion of a couple of additives, namely maleic anhydride and peroxide. The composites that were prepared with the addition of these additives showed reduced tensile strength when compared to the plain wood flour-reinforced composite. The tensile strength of PP was 33 MPa, plain wood flour/PP composite was 46.9 MPa, and the additive included composite was 44.2 MPa. This study concluded that some factors like the addition of plasticizers, variation in the processing temperature and the processing time did not play any major role in the mechanical properties of the final composite material. Government et al. [8] optimized the mechanical properties of avocado wood flour-reinforced low-density polyethylene (LDPE) composite. The wood fibre was treated with 6% NaOH and 4% acetic acid and combined with LDPE at different ratios of 5, 10, 15, 20 and 25 wt%. The injection moulding technique was used to blend the materials. Tensile strength, elongation at break, hardness and impact strength values of the composite were greater than those of the plain polymer. Flexural strength and modulus values of the polymer had reduced with the addition of the wood flour. In an earlier study, bio-based WPCs were developed using *Prosopis Juliflora* wood flour and *Azadirachta Indica* wood flour reinforcements in micro- and nano-forms into polylactic acid

**Table 1** Comparison table depicting the mechanical properties of PLA reinforced with various flour reinforcements

Matrix	Filler	% of filler that provided the best results	Maximum % variation in the mechanical properties of PLA due to different wood flour reinforcements			References
			Tensile strength	Flexural strength	Impact strength	
PLA	Rubber wood	30	138	122	300% lower than PLA	[14]
PLA	Maple wood	20	5	20	8% lower than PLA	[16]
PLA	Poplar wood	20	15	34	–	[17]
PLA	Bamboo wood	10	43% lower than PLA	20% lower than PLA	–	[23]
PLA	Paulownia wood	25	18% lower than PLA	–	–	[26]
PLA	Prosopis Juliflora wood	20	146	228	142	[28]
PLA	Azadirachta Indica wood	20	148	164	73	[29]
PLA	Almond shell	30	313% lower than PLA	–	128% lower than PLA	[30]
PLA	Pinewood	20	No change	-	130% lower than PLA	[31]

biopolymer. Both the reinforcements proved in increment in the mechanical properties of the plain polymer. The nano-wood particle-reinforced WPCs showed better mechanical character when compared with the micro-sized reinforcements in the researches [28, 29]. Bio-wood-plastic composites, especially using polylactic acid as the matrix material, have been gaining more attention in recent years which provide a vast scope for young researchers to explore. The variation in the mechanical properties of PLA by addition of different wood flour reinforcements is given in Table 1.

## 4 Conclusion

Wood-plastic composites are focused to substitute structural-based applications which mainly provide good flexural and impact properties along with low water absorption tendency, high thermal stability and lightweight. WPC can be used as a substitute in the constructional field for interior furniture in buildings, decorative false ceiling applications and as tables and benches in institutions, schools and

offices. In the automotive sector, it can be used for automotive interior components, train roofing and chairs, aircraft interiors and as a base board for electrical and electronic components. The advantages of the WPCs over conventional plywood and wood-based constructional materials are that it is resistant to termite, bacterial and fungal attack and has higher thermal stability, low water absorption tendency and higher mechanical strength.

## References

1. Raj, S.S., Kannan, T.K., Babu, M., Vairavel, M.: Processing and testing parameters of PLA reinforced with natural plant fiber composite materials – A brief review. *Int. J. Mech. Prod. Eng. Res. Dev.* **9**(2), 933–940 (2019)
2. Clemons, C.: Wood Plastic Composites in the United States -The interfacing of two industries. *For. Prod. J.* **52**(6), 10–18 (2002)
3. Gardner, D.J., Han, Y., Wang, L.: Wood-plastic composite technology. *Curr. For. Rep.* **1**(3), 139–150 (2015)
4. Perez, E., Fama, L., Pardo, S.G., Abad, M.J., Bernal, C.: Tensile and fracture behavior of PP/wood flour composites. *Compos.: Part B* **43**(1), 2795–2800 (2012)
5. Stark, N.: Influence of moisture absorption on mechanical properties of wood flour-Polypropylene composites. *J. Thermoplast. Compos. Mater.* **14**(1), 421–432 (2001)
6. Pecas, P., Carvalho, H., Salman, H., Leite, M.: Natural fiber composites and their applications: A review. *J. Compos. Sci.* **2**(66), 1–20 (2019)
7. Ichazo, M.N., Albano, C., Gonzalez, J., Perera, R., Candal, M.V.: Polypropylene/wood flour composites: treatments and properties. *Compos. Struct.* **54**(1), 207–214 (2001)
8. Government, R.M., Onukwuli, O.D., Azeez, T.O.: Optimization and characterization of the properties of treated avocado wood flour-linear low density polyethylene composites. *Alex. Eng. J.* **58**(3), 891–899 (2019)
9. Poletto, M., Dettenborn, J., Zeni, M., Zattera, A.J.: Characterization of composites based on expanded polystyrene wastes and wood flour. *Waste Manag.* **31**(1), 779–784 (2011)
10. Praprudivongs, C., Sombatsompop, N.: Roles and evidence of wood flour as an antibacterial promoter for triclosan-filled poly (lactic acid). *Compos.: Part B* **43**(1), 2730–2737 (2012)
11. Wood Plastic Composites. [https://en.wikipedia.org/wiki/Wood-plastic\\_composite](https://en.wikipedia.org/wiki/Wood-plastic_composite)
12. Fowler, P.A., Hughes, J.M., Elias, R.M.: Review Biocomposites: technology, environmental credentials and market forces. *J. Sci. Food Agric.* **86**(1), 1781–1789 (2006)
13. Tabarsa, T., Khanjanzadeh, H., Pirayesh, H.: Manufacturing of wood-plastic composite from completely recycled materials. *Key Eng. Mater.* **471–472**, 62–66 (2011)
14. Petchwattana, N., Covavisaruch, S.: Mechanical and morphological properties of wood plastic biocomposites prepared from toughened Poly(lactic acid) and rubber wood sawdust (*Hevea brasiliensis*). *J. Bionic Eng.* **11**(1), 630–637 (2014)
15. Wan, L., Li, C., Sun, C., Zhou, S., Zhang, Y.: Conceiving a feasible degradation model of poly-lactic acid-based composites through hydrolysis study to polylactic acid/wood flour/polymethyl methacrylate. *Compos. Sci. Technol.* **181**(1), 107675–107685 (2019)
16. Huda, M.S., Drzal, L.T., Misra, M., Mohanty, A.K.: Wood-fiber-reinforced Poly(lactic acid) Composites: Evaluation of the physicomechanical and morphological properties. *J. Appl. Polym. Sci.* **102**(1), 4856–4869 (2006)
17. Lee, S. H., Wang, S.: Biodegradable polymers/bamboo fiber bio composite with bio-based coupling agent. *Compos.: Part A* **37**(1), 80–91 (2006)
18. Nampoothiri, K.M., Nair, N.R., John, R.P.: An overview of the recent developments in polylactide (PLA) research. *Biores. Technol.* **101**(1), 8493–8501 (2010)

19. Mapleston, P.: Processing Technology: A wealth of options exist. *Mod. Plast.* **78**(5), 56–60 (2001)
20. Youngquist, J.A.: Unlikely partners? The marriage of wood and nonwood materials. *For. Prod. J.* **45**(10), 25–30 (1995)
21. Ferreira, W.H., Carmo, M.M.I.B., Silva, A.L.N., Andrade, C.T.: Effect of structure and viscosity of the components on some properties of starch-rich hybrid blends. *Carbohydr. Polym.* **117**(1), 988–995 (2015)
22. Vandi, L.J., Chan, C.M., Werker, A., Richardson, D., Laycock, B., Pratt, S.: Extrusion of wood fibre reinforced poly(hydroxybutyrate-co-hydroxyvalerate) (PHBV) biocomposites: Statistical analysis of the effect of processing conditions on mechanical performance. *Polym. Degrad. Stab.* **159**(1), 1–14 (2019)
23. Wang, Y.N., Weng, Y.X., Wang, L.: Characterization of interfacial compatibility of polylactic acid and bamboo flour (PLA/BF) in biocomposites. *Polym. Testing* **36**(1), 119–125 (2014)
24. Sachin, S.R., Kannan, T.K., Kathiresan, M., Balachandar, K., Krishnakumar, S.: Why not stir casting for polymer composites? Investigations on poly lactic acid based wood plastic composite. *Materials Today: Proceedings* (2020). <https://doi.org/10.1016/j.matpr.2020.02.926>.
25. Kamdem, D.P., Jiang, H., Cui, W., Freed, J., Matuana, L.M.: Properties of wood plastic composites made of recycled HDPE and wood flour from CCA-treated wood removed from service. *Compos.: Part A* **35**(1), 347–355 (2004)
26. Tisserat, B., Joshee, N., Mahapatra, A.K., Selling, G.W., Finkenstadt, V.L.: Physical and mechanical properties of extruded poly(lactic acid)-based Paulownia elongate biocomposites. *Ind. Crops Prod.* **44**(1), 88–96 (2013)
27. Haque, M.M.U., Goda, K., Ogoe, S., Sunaga, Y.: Fatigue analysis and fatigue reliability of polypropylene/wood flour composites. *Adv. Ind. Eng. Polym. Res.* **2**(1), 136–142 (2019)
28. Raj, S.S., Kannan, T.K., Rajasekar, R.: Influence of *Prosopis Juliflora* wood flour in Poly Lactic Acid– Developing a novel Bio-Wood Plastic Composite. *Polímeros: Ciência e Tecnologia* **30**(1), e2020012 (2020)
29. Sachin, S.R., Kannan, T.K., Rajasekar, R.: Effect of wood particulate size on the mechanical properties of PLA biocomposite. *Pigm. Resin Technol.* **49**(6), 465–472 (2020)
30. Carrillo, L.Q., Montanes, N., Sammon, C., Balart, R., Giner, S.T.: Compatibilization of highly sustainable polylactide/almond shell flour composites by reactive extrusion with maleinized linseed oil. *Ind. Crops Prod.* **111**(1), 878–888 (2018)
31. Pilla, S., Gong, S., O'Neill, E., Rowell, R.M., Krzysik, A.M.: Polylactide-Pine wood flour composites. *Polym. Eng. Sci.* **48**(3), 578–587 (2008)

**Dr. Sachin S. Raj** is currently working as an Assistant Professor in the Department of Mechanical Engineering at Gnanamani college of Technology, Namakkal, Tamilnadu, India since 2016. He completed his Bachelor of Engineering under Mechanical Engineering specialization in the year 2014 with a first class and a CGPA of 8.3 from Gnanamani College of Technology affiliated to Anna University Chennai. He completed his Master of Engineering under the Manufacturing Engineering specialization in the year 2016 with a University Gold medal and Distinction under Vinayaka Mission's University, Salem, Tamilnadu, India. He completed his Ph.D under Anna University Chennai in 2020, working as a part time research scholar in the specialization of materials science. His research work involves Bio polymer composites developed with natural fiber reinforcements for structural applications.



# Effect of Filler Content on the Performance of Epoxy/Haritaki Powder Composite



N. Narmadadevi, V. Velmurugan, R. Prabhakaran, and R. Venkatakrisnan

## 1 Introduction of Composites

The addition of filler materials into epoxy resin matrix materials greatly influences and improves composite material properties provided that filler particles are bonded to polymer matrix [1]. The advantages of filler material content change material's property of tensile property such as thermal resistance, toughness, color appearance, etc., and the filler material is widely used in manufacturing of polymer composite materials. It saves the raw material cost of the polymer matrix materials. Epoxy resin is a one of the main synthetic thermosetting polymer resin which is used to produce small- or large-scale polymer composite materials [2]. Epoxy resin materials are used in a broad range of structure of building material composites, automobile industries [3]. The matrix material of epoxy resin is one of the mainly used polymer matrices in the composite industry, due to its proper adhesion bonding to many fiber reinforcements [4]. Kadukkai powder could even be a naturally available herbal material which was used as an additive for creating delicious food. From the studies administered on Kadukkai it has been observed that Kadukkai has powerful binding property and desirable hardening properties for creating construction material and concrete [5]. Kadukkai was extracted from Kadukkai tree as a naturally available fruit then it had been dried in sunlight. The dried Kadukkai was made into powder form for effective mixing with binders like cement, lime [6]. The aim of the paper is to report the research works on the results of filler materials of haritaki fine powder mixing with epoxy resin reinforced by E-glass fiber composites.

---

N. Narmadadevi (✉) · V. Velmurugan · R. Prabhakaran · R. Venkatakrisnan  
Department of Mechanical Engineering, IFET College of Engineering (Autonomous),  
Villupuram, Tamil Nadu, India

© The Author(s), under exclusive license to Springer Nature Singapore Pte Ltd. 2022  
S. K. Natarajan et al. (eds.), *Recent Advances in Manufacturing, Automation, Design and Energy Technologies*, Lecture Notes in Mechanical Engineering,  
[https://doi.org/10.1007/978-981-16-4222-7\\_33](https://doi.org/10.1007/978-981-16-4222-7_33)

## **2 Raw Materials and Its Method**

### ***2.1 Sources of Raw Materials***

The E-glass fibers are easily available resources in the market. Glass fibers are stretching in the way of woven mat. The orientations of fibers are perpendicular stands of fiber mats. The matrix materials of Epoxy resin along with Hardener were bought from a private manufacturing company. The filler materials of haritaki powder are brought from organic medical shops.

### ***2.2 Kadukkai Filler Powder (Haritaki Powder)***

Kadukkai extract is added in several concentrations of 0%, 5%, 10%, 15% and 20% to the lime and dirt mortar and its effects on workability, compressive strength and porosity are studied. The test results showed that Kadukkai filler materials are improving properties of epoxy resin characteristics to the composite materials. The filler materials of haritaki powder are evenly distributed through the special attachment of the roller spindle by electric motors.

### ***2.3 Hardener and Epoxy Resin Blending Ratio***

The matrix material of epoxy resin is blended with hardener in proper mixing in the ratio of 10:1. The 10 ml of resin material is mixed with 1 ml of hardener which induces the curing process of the polymer chains [7].

### ***2.4 Methods of Preparation of Composite Materials***

Table 1 shows the E-glass fiber composite materials which are fabricated as per prepared percentage of sample composition. Mostly matrix materials have higher percentage when compared to fiber reinforcement, because of the good wettability of the composites. From Table 1 as shown, 30% of fiber (90 g) and 70% of resin (200 g) are taken. Further filler content of haritaki fine powder is added to resin materials along the ratio of 0, 5, 10, 15, and 20% of Epoxy resin. The mixing ratio of resin with hardener is 10:1 ratio for curing of liquid form to solid form of resin materials. These are primary preparations of composite materials. And next preparation is mold preparation as given required size of samples. The size of the mold is 300 mm of length, 300 mm of breadth and 10 mm of thickness to fabricate rectangular plate of composite materials. Before applying resin, polyvinyl acetate or spray wax are

**Table 1** Classification of sample preparation

Samples (%)	Haritaki powder (gms)	E-glass fibers in gms (six laminas)	Epoxy resin + hardener in gms
0	0	90	200
5	14.5	90	185.5
10	29	90	171
15	43.5	90	156.5
20	58	90	142

**Fig. 1** a Laminas of E-glass fiber, b applied Haritaki Epoxy mixing resin, c finished fabrication of laminated composites

coated in the outer surface of the mold for easy removal of fabricated composite after curing. After coating of wax, initially the first layer of resin was applied to wettability of fibers. These composites consist of six layers of lamina of Kenaf/E-glass woven mat fibers. Layer by layer resin and fiber are compressed by dead weight above the film sheets of mold. After curing of composite materials, it's removed from mold surface without cracking/damaging fibers. Figure 1 shows the final product of laminated composites.

## 2.5 Various Testing of Composites

The experimental testing of haritaki filler powder effect in E-glass fiber composite materials involves a wide range of testing types and tests in a variety of different environments. The main objective of the mechanical testing of composite materials is the examination of mechanical parameters such as strength, stiffness and other physical properties. Elasticity, flexural strength and impact strength were resolved in a Universal Testing Machine (UTM), while Universal Pendulum Impact System for Charpy tests. Five specimen samples were tried for every creation and normal outcomes were utilized. Rigidity, flexural strength and impact strength esteems were resolved for different examples and appeared.

### 3 Results and Conversation

#### 3.1 Longitudinal of Tensile Strength

Longitudinal of tensile strength is the amount of load or stress that can be withstood by a composite material before it stretches and cracks. The longitudinal tensile strength of composite materials is determined mostly by the strength and volume content of the fiber reinforcement. For tensile strength, specimens are prepared as per the ASTM standard of ASTM D3039. Figure 2 shows before and after test of tensile test samples. The results are obtained after carrying out specimen test; the data are plotted in graph as shown in Fig. 3. From these plotted graph data, the obtained results include haritaki filler materials added to the epoxy matrix which can increase the tensile property of epoxy resin matrix composites. The values of tensile strength gradually increase from 0 to 20% of specimen samples of composite materials. The better results values are in 15% and 20% of haritaki filler powder content epoxy matrix composite materials. Haritaki filler materials improve the tensile property of epoxy resin.

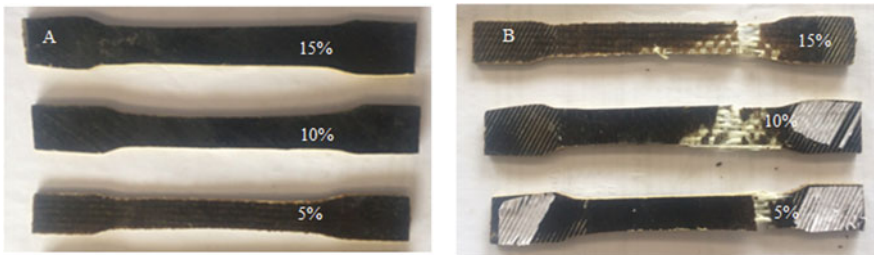
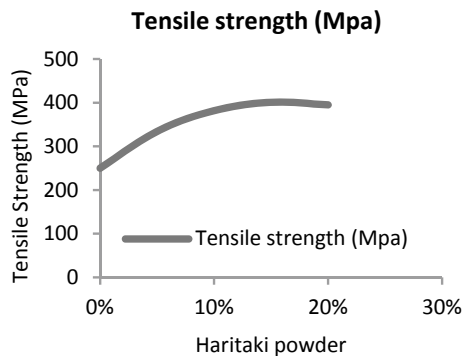


Fig. 2 a Three different samples of before tensile test, b three different samples of after tensile test

Fig. 3 Different filler content of haritaki/epoxy composite on tensile strength



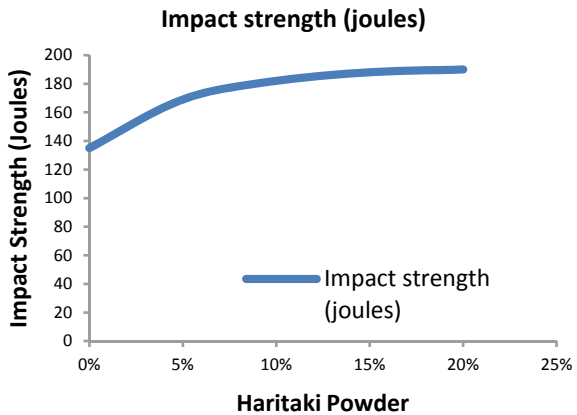
### 3.2 Drop Weight Impact Test

The impact resistance of composite materials can be performed with a swinging or a dropping known weight. For impact strength, specimens are prepared as per the ASTM standard of ASTM D7136. Figure 4 shows the impact test samples after load applied. The results are obtained after carrying out an impact specimen test; the values are plotted in graph as shown in Figure 5. From these plotted graph data, the obtained results haritaki filler powder is added to epoxy matrix material which can increase impact strength property of epoxy resin matrix composites. The values of impact strength gradually increase from 0 to 20% of specimen samples of composite materials. The better results values are in 15% and 20% of haritaki filler powder content epoxy matrix composite materials. Haritaki filler materials improve the impact property of epoxy resin because of improving the hardness of epoxy resin materials.

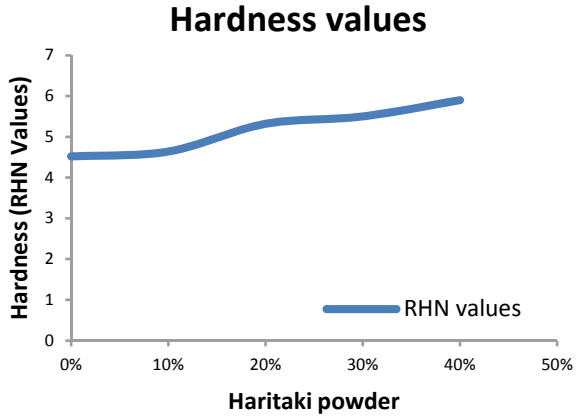
Fig. 4 Sample shows that breakage of after impact test



Fig. 5 Different filler content of haritaki/epoxy composite on impact strength



**Fig. 6** Different filler content of haritaki/epoxy composite on hardness strength



### 3.3 Experiment of Hardness Test

The hardness strength of composite materials which can be valued is measured based on the net increase in depth of impression by applied load to specimens. For hardness strength, specimens are prepared as per the ASTM standard of ASTM D785. The specimens were prepared for Rockwell-B hardness test; the preparation of specimen samples is of 25 mm diameter and a length of 20 mm. The results are obtained after hardness specimen test is carried out; the values are plotted in graph as shown in Figure 6. From these plotted graph data, the obtained results of haritaki filler powder are added to epoxy matrix material which can increase hardness strengthen property of epoxy resin matrix composites. The values of impact strength gradually increase from 0 to 20% of specimen samples of composite materials. The better results values are in 15% and 20% of haritaki filler powder content epoxy matrix composite materials. Haritaki filler materials improve the hardness strength of epoxy resin because of improving the toughness and brittle properties of the epoxy resin materials.

## 4 Conclusion

The haritaki fine powder filler content on the E-glass fiber reinforcement with Epoxy matrix composite has been fabricated. Testing results of various strengths of tensile, flexural and impact strength of natural composite can be examined. From the results, the elongation of tensile property of 20% of filler content of haritaki/epoxy matrix composite is higher than the other filler content of composite materials. The filler material of haritaki powder which increases highly resists impact load on materials due to brittle property of the matrix materials.

## References

1. Venkatakrishnan, R., Senthilvelan, T., Vijayakumar, T.: Fabrication and mechanical properties of hybrid natural composite. *Appl. Mech. Mater.* **813**, 57–61 (2015)
2. Gopinath, T., Senthilvelan, T., Venkatakrishnan, R.: Characterization of hybrid matrix natural fibre composite. *ARPJ. Eng. Appl. Sci.* **11**(12), 7921–7926 (2006)
3. Venkatakrishnan, R., Pabhakaran, R., NarmadaDevi, N.: The effect of e-waste particle on mechanical behavior of particulate reinforced epoxy matrix composite. In: *IOP Conference Series: Earth and Environmental Science* 573(1), (2020)
4. Naveenkumaret, T.S.: Axial load behavior of mud block layered composite column with steel core. *Int. J. Civ. Eng. Technol.* **9**(4), 1724–1736 (2018)
5. Venkatakrishnan, R., Narmada Devi, N., Prabhakaran, R.: Characterization of natural fibers reinforced CNSL matrix composite. *Int. J. Eng. Sci. Comput.* **7**(4), (2017)
6. Njoku, R.E., Ofili, I., Agbiogwu, D.O., Agu, C.V.: Effect of alkali treatment and fiber content variation on the tensile properties of coir fiber reinforced cashew nut shell liquid (CNSL) composite. *Niger. J. Technol.* **31**(2), 108–110 (2012)
7. Ofem, M.I., Abam, F.I., Ugot, I.U.: Mechanical properties of hybrid periwinkle and rice husk filled CNSL composite. *Int. J. Nano Mater. Sci.* **1**(2), 74–80 (2012)

# Surface Alteration and Effect of Fiber Amount on the Optimization of Palmyra and Moringa Oleifera Fibrils Fortified Composites



Gowdagiri Venkatesha Prasanna, Rapolu Srilekha,  
Achyutuni Venkata Naga Sri Harsha, and Vemula Sunil Kumar

## 1 Introduction

For the most part counterfeit fibrils like aramid, carbon, glass are broadly used due to their low density, high strength and stiffness properties in polymer-based composites. Aside from the points of interest of utilizing synthetic fibrils in various purposes, these artificial fibrils have serious hindrance such as their vitality utilization, biodegradability, machine scraped spot, recyclability, initial handling cost, health hazards. So, to conquer this crisis, the need for natural composites is high. Bio-fibrils were used for fortification for polymer composite materials and as an elective material to synthetic fibrils. The usage of fibrils as potential reinforcement in the manufacture of composites is limited by the wet incorporation property of fibrils. Table 1 reveals the information of the chemical composition of the natural fibers. The nature of polymer framework is hydrophobic. This may root fibrils and network contrasting between the fibrils and the resin mix. The main purpose of this surface modification was to reduce the wet retention property of the natural fibrils and also to enhance the resemblance with polymer matrix. The polymer mix has abundant favorable circumstances in terms of the items for explicit end use applications and improving resins successful properties, usage and execution [1–3]

Epoxy is widely used component for various applications, for example, equipment segments, propelled composites and rocket types of gear on account of its mechanical, dielectric properties and great holding capacity. Epoxy polymers have broadly utilized on account of their prevalent thermo-mechanical properties and magnificent process ability. The substandard attributes can be reduced by using mixing strategy. By the miscible polymer, a new improvised material from less unrivaled single segment is produced [4–6]. In the same way, the result will be the mixing with

---

G. Venkatesha Prasanna (✉) · R. Srilekha · A. V. N. Sri Harsha · V. Sunil Kumar  
Department of Mechanical Engineering, CVR College of Engineering, Vastunagar, Mangalpalli,  
Telangana 501510, India



**Table 1** Composition of natural fibers

S. no	Fiber	Cellulose (%)	Hemicellulose (%)	Lignin (%)
1	Palmyra fiber	53.4	28.51	18.54
2	Moringa Oleifera fiber	44.8	17.28	7.86

toughening agent due to the usage of epoxies [7–9]. Alongside epoxy materials, vinyl ester can be utilized. It is used as mixing agent due to the versatile nature in the structure of epoxy. The hardness is expanded because of mixing the epoxy with elastomers and polymers [3, 6, 8, 10]. Subsequently, an appropriate polymer was expected to upgrade the efficient opposition by holding solidness stress–strain properties, warm soundness of the epoxy resin and glass change temperature. Due to their expanded mechanical properties advancement, a cross-connected polymer system is obtained. The generally utilized thermosetting material is the vinyl ester on account of their low cost and high blend of properties such as warm, mechanical and compound opposition properties [11–13]. The hydroxyl bunches upgrade the extremity of vinyl ester and boosts bond, mechanical and thermal properties. The extremity of vinyl ester is improved by hydroxyl bunches and encourages shade wetting properties and bond, resulting in the fiber wetting. For this objective, a blend of vinyl ester/epoxy (90/10% w/w) polymers was prepared. The specimens of composites with the 50, 40, 30, 20 and 10% wt. content of untreated, alkali  $[C_6H_5N_2]Cl$ -treated Palmyra-Drumstick Fruit Fibrils were reinforced with blend of vinyl ester/epoxy were made-up.

## 2 Experimentation

### 2.1 Material Used

We considered two resins, they are vinyl ester and Epoxy Araldite LY556, Hardener HY951 and two fibers namely Palmyra Fiber as shown in Fig. 1 and Drumstick Fruit fiber (Moringa Oleifera) as shown in Fig. 2.

**Fig. 1** Palmyra fiber

**Fig. 2** Drumstick fruit fiber  
(*Moringa Oleifera*)



## ***2.2 Surface Modification of Natural Fibrils***

Because of the closeness in hydrophilic hydroxyl groups of natural fibril, hardly, several issues occur along the interface in the fortification of natural fibrils into the resin mix. Hydrophilic nature in natural fibers hampers successful holding of strands with resins mix. Apart from these, oil, pectin, grease and waxy substance spread sympathetic functional congregation in fibrils and going as boundary for the interlock with resins blend. To enhance adequacy of inter facial cement holding, surfaces of fiber need to be adjusted with various chemical reactions.

## ***2.3 Chemical Treatments***

To enhance the efficiency in interfacial adhesiveness connections, fiber surface need to be changed with various chemical treatments, coupling agents and receptive supplements. Surface handling gives superfluous reflex parts on the fibrils surface which gives capable union in the matrix. Surface alteration with fibrils after alkaline treatments in diverse percentages 10 and 5 wt% sodium hydroxide is carried out, and effect of concentration of chemicals on performance with the composites is noticed at the work.

## ***2.4 Preparation of $[C_6H_5N_2]Cl$***

8 cm<sup>3</sup> intense hydrochloric acids is inserted into bubbling cylinder consisting 3 cm<sup>3</sup> of PHENYL AMINE (aniline) and 10 cm<sup>3</sup> water. Blend is vibrated until amine get fragmented, and afterward, this arrangement is chilled to 5 °C by cooling it in ice shower. Afterward, an answer of NaNO<sub>2</sub> [3 g in 8 cm<sup>3</sup> H<sub>2</sub>O] precooled at 5 °C is also included. Temperature of mixture is conserved under 10 °C over the expansion in NaNO<sub>2</sub> [3, 6].

## 2.5 $[C_6H_5N_2]Cl$ Treatment of Palmyra and Drumstick Fiber

Palmyra-Drumstick Fruit Fibril is slashed in a length of 10 mm, cleaned with filtered water and is preserved in out with heater in 70 °C about 24 h. Dried fibrils are soaked in 6% NaOH arranged in 2.0 L measuring glass up to 10 min approximately at 5 °C. The arranged diazo was subsequently emptied into the above mix with steady mixing. Fibrils are then removed, cleaned with cleanser arrangement followed by filtered water, lastly preserved outside for about 48 h [1, 2, 4].

## 2.6 Fabrication of Blended Hybrid Bio-Composites

Mold cavity is covered with a small thickness of solid wax for clear discharge and withdraw of composites specimen as shown in Fig. 3. Directly after the wax is reestablished, lean alcohol POLY VINYL ALCOHOL (PVA) was applied. Bio-fibrils crossover composite is assembled using the hand layup system. At that point of crossbreed, bio-strands of the treated and untreated palmyra-moringa oleifera fibers are reinforced with matrix mix to get required bio-composite for the examination of performance and mechanical specifications. Afterward, air bubbles are removed carefully using rollers of delicate rotating. For the purpose of complete cure, composite samples are post-cured in the temperature 80 °C for about two hours by placing the specimen in hot oven. After complete curing, raw and processed bio-composite specimen samples are tested using digital universal testing machine as shown in Fig. 4.

**Fig. 3** Fabrication





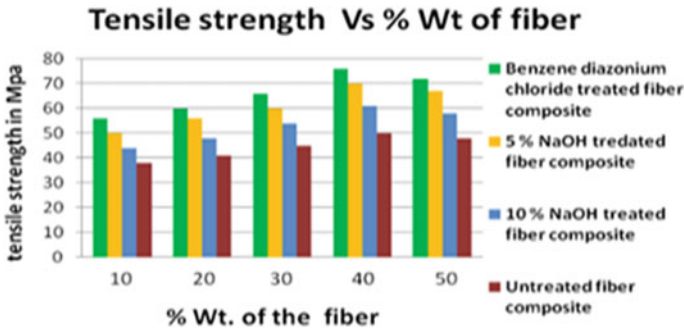
Fig. 4 Digital universal testing machine

### 3 Discussion & Result

#### 3.1 Tensile Strength Properties

Specimens of the composites were prepared considering measurement of tensile property, including dimensions  $150 \times 15 \times 3 \text{ mm}^3$  were evaluated as indicated by ASTM D 3039 models. Tensile power for these samples was dictated through utilizing universal testing machine for a crosshead pace about 50 mm/min. The untreated fiber composites reveal poorer tensile strength properties because of the repellency and poor compatibility between hydrophobic resins mix and hydrophilic bio-fibers unfavorably impact on the interfacial holding amid fibril exterior path and matrix blend and that take about diminishing the fastness and results in deficient and improper stress transfer from these resins blends into fibers [2, 6, 8]. The effect of fiber stacking and fibers exterior alteration by the chemical modification in these tensile properties of bio-fiber composite is demonstrated in Fig. 5. Typically, synthetically modified bio-fibers-protected composite displays greater tensile strength over these uncompleted fiber fortified composites.

The evaluation noticeably reveals that 40% fibril amount of  $[\text{C}_6\text{H}_5\text{N}_2]\text{Cl}$ -treated composite exposes superior and optimum values than 5% sodium hydroxide treated, 10% sodium hydroxide treated and 20, 30 and 50% fibril quantity chemically processed and raw bio-composites. Through these fiber distribution in matrix, blend materials are formed, which upgraded their interfacial bonding and morphological properties [1, 4, 10]. Apart from that with benzene diazonium treatment, the fibril surface improves uniformly because of end in small-scale void and subsequently stress transfer capacity increases. In any case, apparent high tensile strength was observed in alkali-treated Palmyra-Drumstick Fruit Fibrils composites and critical



**Fig.5** Tensile strength of untreated, alkali treated and  $[C_6H_5N_2]Cl$  composites

increment was seen for the  $[C_6H_5N_2]Cl$ -treated Palmyra-Drumstick Fruit Fibrils composite. Examination plainly recommends that chemical reactions formed solid interface with fibril cell walls and pairing response happens between  $[C_6H_5N_2]Cl$  and cellulose of fibril brings about development in diazo cellulose compounds, which are represented to watch critical increment of the tensile property of composites.

Surface treatment by method for both  $[C_6H_5N_2]Cl$ , sodium hydroxide gives us route for expulsion of unwanted materials with improvement in these fibril distribution in matrix blends [3, 10].  $[C_6H_5N_2]Cl$  treatment advances progressively compelling zone of the fibrils surfaces needs wetting with the polymers contrasted with soluble base treatments to have hard holding [3, 4, 7] and results in upgraded mechanical property.

### 3.2 Flexural Properties

Specimen of dimensions  $150\text{ mm} \times 15\text{ mm} \times 3\text{ mm}$  was made and tested to know the flexural property according ASTM D 5943–96 specification. Disparity in estimations of flexural quality as bio-fibrils composite of fibril quantity, without and with chemical treatments, is shown in Fig. 6. It was observed after evaluation that flexural properties of 40% fibril amounts,  $[C_6H_5N_2]Cl$ -treated bio-fibrils composites revealed superior and predominant quality compared to 40% fibril amounts, 5% sodium hydroxide treated, 10% sodium hydroxide treated, 10, 30, 20 & 50% fibril amounts treated and untreated composite [1, 6, 10]. Due to high alkali usage (10% sodium hydroxide) compared to (5% sodium hydroxide), great quantity delignification of the fibril occurs, which leads to debilitating, harming of the fibril surface that leads to reduced flexural qualities indicated in Fig. 6 [8, 10]. Superior fibril-matrix compatibility, good fiber matrix collaboration and handling were seen at 5% sodium hydroxide treated bio-fibers composites than 10% sodium hydroxide-treated bio-fibrils composites [4, 7, 8]. Greater and noteworthy development of fibril dissemination matrix, stress and aspect ratio transfer capacity was seen in  $[C_6H_5N_2]Cl$ -treated

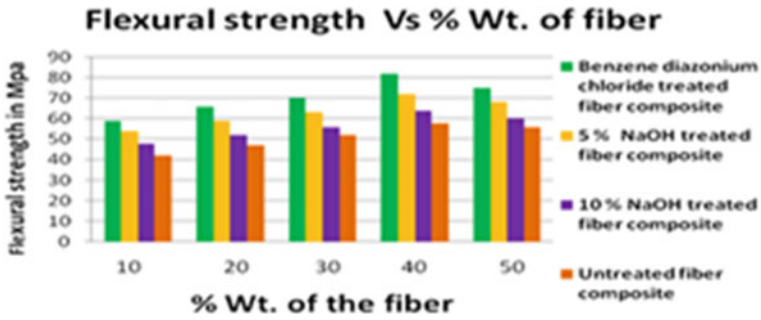


Fig.6 Flexural properties of untreated, alkali treated and [C<sub>6</sub>H<sub>5</sub>N<sub>2</sub>]Cl composites

bio-fibrils composite compared to alkali-treated bio-fibrils composites and untreated bio-fibrils composites.

### 3.3 Compressive Strength

Composites samples are readied and evaluated to know the compressive strength property as per ASTM D695–15, stipulations. Adjustment in estimations for compressive quality properties for fibril amounts without and with surface alteration is seen in Fig. 7. Likewise, observed that [C<sub>6</sub>H<sub>5</sub>N<sub>2</sub>]Cl-tested bio-fibrils composites show high and ideal conditions for compressive properties than alkali tested and raw bio-composites [3, 4, 9]. Ideal and superior conditions are due to ideal fibril stacking and chemical treatment that advanced good interfacial holding between filaments framework mix brought about sufficient stress transfer and execution [3, 4, 10]. Previous works uncover that fibril surfaces change by chemical treatment which increases surfaces roughness [6, 8, 9]. The less decrease in compressive properties

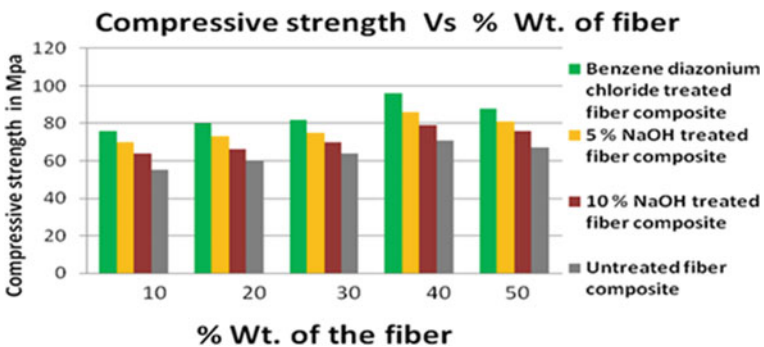


Fig. 7 Compressive strength of untreated, [C<sub>6</sub>H<sub>5</sub>N<sub>2</sub>]Cl treated and alkali-treated composites

of composites is shown at 50% fibril magnitude. At 50% fibril contents treated and untreated composite (higher fibril loads), the decrease in compressive properties indicates low fibril-grid interfacial gripping & small scales breakage developments at interface prompt insufficient stresses transfers. Most noteworthy compressive strength was shown in 40% fibril stackings. However,  $[C_6H_5N_2]Cl$  treatment occupies voids space of fibril and adjusted lopsided fibril, as looked at alkali-treated composites [2, 9].

### 3.4 Moisture Content Test

Fig. 8 shows rate ingestion in dampness amounts by untreated fibril composites, alkali-treated and  $[C_6H_5N_2]Cl$ -treated composite fabricated as per ASTM D 543–87. The bio-fibrils composites manufactured from hydrophilic nature of fibril display hydrophilic properties [8, 9]. In any case, the alkali-responsive hydroxyl groups present among molecules are busted down, which at points react with the water molecules (OH-H) and shift from these fibril structures. Because of this, hydrophilic hydroxyl groups were declined by alkali and  $[C_6H_5N_2]Cl$  treatment and outside the fibril tailored and increase dampness obstruction properties. [1, 4, 12]. The percentage absorption of moisture quantities by unprocessed fibril composites is high when compared to alkali treated and  $[C_6H_5N_2]Cl$ -treated composites [12, 13].

$$\% \text{ water absorption} = 100 \times (W_f - W_i) / W_i$$

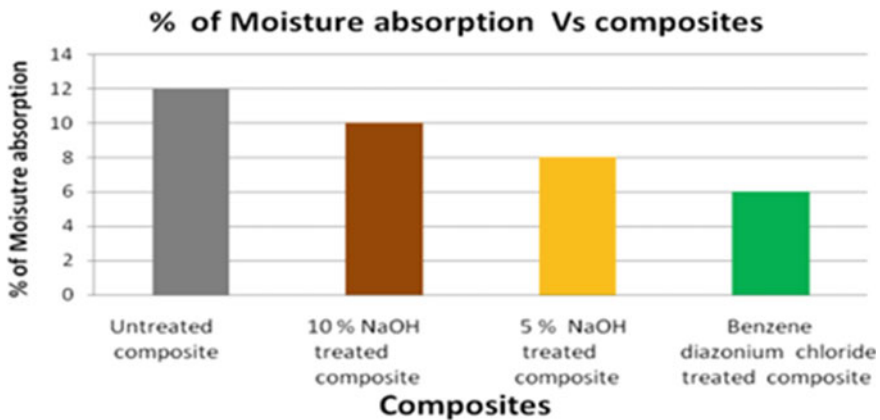


Fig. 8 Absorption of moisture for alkali-treated and  $[C_6H_5N_2]Cl$ -treated composites

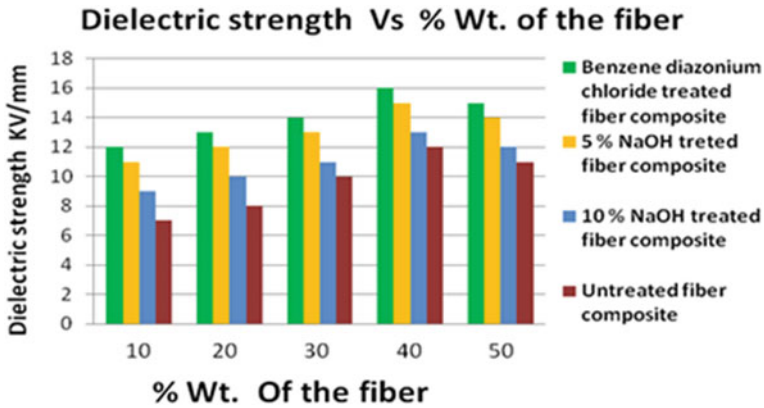


Fig. 9 The dielectric strengths of untreated and chemically treated composites

### 3.5 Dielectric Strength

To Contemplate Dielectric qualities of raw, alkali-treated and  $[C_6H_5N_2]Cl$ -treated composite, these composites samples were made with ASTM-D-149 measures. Composite possessing dimensions 120 mm x 120 mm x 3 mm are reinforced with strand a single way with 120 mm length. Dielectric separating voltage is found for five of the specimens and mean value is used in investigations. Test is undergone at 50 Hz recurrence and room temperature. Digital micrometer 0.001 mm least count was used to find thickness of composite at individual points. Additionally calculable to see that the dielectric quality of crossover fiber composites increments with increment in amount of fibril from 10% to 40% wt of fibril, however, reduces at 50% fibril magnitude composites [6, 8, 9]. At 50% fibril magnitude composites, decline in dielectric qualities was due to lack of interfacial holding in between strands and resins blend [1, 2] (Fig. 9).

## 4 Conclusion

The work shows that ideal chemical action on fibrils extensively enhances fibril qualities, fibril–resins blended bonds and henceforth displaying the characteristics of fibril composite. Results indicate that compressive, flexural, tensile and dielectric strengths of composite are increased for  $[C_6H_5N_2]Cl$ , as well as alkali treatments fibril composites, and are maximum at 40%, but below or above 40%, it shows decrease in these strength properties. Generally, surplus measures fibril rests into each other against being blends with resin blend at 50% fibril load, which additionally prompt decreased stress transfer ability. After surface modification or chemical treatment of fibrils, it was identified that increase in composites properties with the



removal of undesired elements like dampness, hemicelluloses, lignin, wax and oils from surfaces of fibrils generates unpleasant surface geology, aspect ratio. Also, fiber matrix interfacial bonding improves which leads to greater stress transfer and hence improvement of properties in composites.

## References

1. Venkatesha Prasanna, G., Sunil Kumar, V., Srilekha, R., Sri Harsha, A.V.N., Sai Abhi Chandan, V.: Hybridization and influence of chemical treatment on the Morphology and Optimization of composites, Elsevier, Materials today proceedings (2020)
2. Venkatesha Prasanna, G., Sri Harsha, A.V.N., Srilekha, R., Sunil Kumar, V., Sai Abhi Chandan, V.: Modification of exterior fibril dimensions and performance. In: Materials Today Proceedings (2020)
3. Morrison, R.T., Boyd, R.N.: Organic chemistry. Prentice-Hall, London (1989)
4. Venkatesha Prasanna, G., Nikhil, M., Sai Kiran, A.: Hybridization & influence of chemical treatment on the morphology and optimization of composites. Materials Today (2020)
5. Venkatesha Prasanna, G., VenkataSubbaiah, K.: Modification, flexural, impact, compressive properties and chemical Resistance of natural fibers reinforced blend Composites. Malays. Polym. J. **8**(1), 38–44 (2013)
6. Venkatesha Prasanna, G., Venkata Subbaiah, K., VaradaRajulu, A: Chemical resistance, impact, flexural, compressive properties and optimization of fibers of natural fibers reinforced blend composites. Sch. J. Eng. Res. **1**(6), 85–89 (2012)
7. Alamgi, M.K., Monimul, M.H., Islam, R.M., Bledzki, A.K.: BioResources **5**, 1618–1625 (2010)
8. Venkatesha Prasanna, G., Jha, N.K.: Optimisation & mechanical Testing of hybrid bio composites. Materials Today, 1395–1404 (2019)
9. VaradaRajulu, A., Devi, G., Babu Rao, G.: Miscibility studies of epoxy/unsaturated polyester resin blend in chloroform by viscosity, ultrasonic velocity and refractive index methods. J. App. Polymer Sci. **89**, 2970–2972 (2003)
10. Sreekal, M.S., Thomas, S.: Effect of fibre surface modification on water-sorption characteristics of oil palm fibres. Compos. Sci. Technol. **63**, 861–869 (2003)
11. Venkatesha Prasanna, G. Jayadeep, T., Poornabhodha, N.: Chemical treatment, influence of fiber content and optimization of hybrid natural fibers reinforced composites. The Smart Innovation, Systems & Technologies (SIST). ISSN: 2190-3018 (2019)
12. Prasanna, G.V.: Surface modification, characterization & optimization of hybrid bio composites. Springer (2020)
13. Venkatesha Prasanna, G., Venkata Subbaiah, K.: Hardness, tensile properties and morphology of blend hybrid biocomposites. Sch. J. Eng. Res. **2**(1), 21–29 (2013)
14. Prasanna Venkatesha, G.A., Kiran, S., Nikhil, M.: Surface modification and Effect of fiber content on the Optimization of Natural fibers reinforced Composites. Materials Today (2020)

# Optimization of Specific Cutting Energy in Turning of AISI 304 Stainless Steel Using Taguchi Method



S. Annamalai, B. Guruprasad, and N. Vaithianathan

## 1 Introduction

In the last two decades, the need for electricity has risen. There is a need to find ways to reduce energy usage during the machining process. [1]. Turning is an eventual industrial process, so this approach has been used by all metal cutting industries to extract the excess material in chip form. In turning operations, the analysis of cutting force is important because cutting forces are closely associated with cutting efficiency, surface roughness, tool wear, tool breakage, cutting temperature, cutting energy, self and excited vibrations, etc. [2]. There are many factors affecting efficiency in turning, such as tool parameters, workpiece parameters and cutting parameters, where tool parameters include material of tool and geometry of the tool (back rake angle, end relief angle) and workpiece parameters include material mechanical (hardness), chemical and physical (density, melting point) properties. In addition, cutting requirements include cutting speed, feed rate and cutting depth. In the present research, the energy requirement for the machining process and cutting energy may be treated as a significant parameter [3]. King and hann note that it is possible to understand that cutting energy would be a combination of cutting power and the rate of material removal. The SCE is strictly proportional to the results of the machining process. The high SCE value produces increased temperature and increased internal stresses in the machined workpiece that will contribute low veracity of the body [4]. The SCE found a strong material machinability index which made it easy to grasp the whole cutting process [5]. The high-performance cutting processes can be adapted to reduce the energy consumption by selecting tool design, tool material and cooling strategies like MQL, dry cutting and cryogenic machining [6]. The selection

---

S. Annamalai (✉) · N. Vaithianathan  
IFET College of Engineering, Villupuram, Tamil Nadu 605108, India

B. Guruprasad  
AC Government College of Engineering and Technology, Karaikudi, Tamil Nadu 630003, India

of inserts also plays an important role reduce the SCE by retaining the sharp edges due to high hardness and low coefficient of friction [7]. Three groups were classified for the calculation of specific energy dependent on machine instruments, material characteristics and process variables, namely numerical, theoretical and mechanistic methodology [8, 9]. The precise cutting energy [13] was also affected by the diameter of blank [10], angle of tool cutting edge and tool geometry angle of chip breaker [11, 12]. With the special properties such as oxidation resistance, retaining high strength at high temperature and resistance to corrosion, AISI 304 stainless steels have found their applications in many fields. It is therefore also used in the areas of ships, pressure vessels, cryogenic applications, gas turbines, high-temperature steam boilers, warheads and generating units of nuclear power. AISI 304's performance in machining is largely based on resolving some of the alloy's intrinsic characteristics or properties. The work hardening characteristics of AISI 304 steel increase the cutting force and makes it very dynamic in nature. The increase in cutting force leads to deflection, vibration, tool failure and deterioration of surface quality [14]. During the machining process, AISI 304 continues to stick to the tool material, thereby resulting in build-up edge forming and premature failure of the tool. In addition, its poor thermal conductivity increases the temperature at the sliding surface of tool and workpiece, adversely affecting tool life. Hence, AISI 304 Stainless steel classified as "Difficult to Machine material." The purpose of this research is therefore to understand and use the Taguchi approach for the optimization of the machining conditions, especially turning of AISI 304 Steel [15].

## 2 Materials and Methods

### 2.1 Work Materials

The-25 mm-diameter austenitic stainless steel bar was selected as a workpiece. The alloying element composition in SS 304 is shown in Table 1, and the physical properties are listed in Table 2.

**Table 1** Alloying element composition of SS 304

Type	C	Mn	Si	Cr	Ni	P	S
AISI 304	0.08	2.00	1.00	18.0–20.0	8.0–10.5	0.045	0.03

**Table 2** Properties of AISI 304 steel

Density	8.06 g/cc
Thermal conductivity	15 W/mK
Melting point	1450 °C
UTS (MPa)	515a

## 2.2 Methods

The cutting experiments were carried out on the Mysore Kirloskar made ENTERPRISE 1550 model All geared head lathe (shown in Fig. 1) using uncoated carbide and TiN-coated inserts with the grade of P-20 for the turning of 304 SS bars. Model of tool holder: DCLNR2020K12. TiN-coated inserts CNMG432 are used as the cutting tool material. The experiments were conducted under dry conditions. The cutting force was measured using lathe tool dynamometer. Each test is performed three times, and the average value is listed in the table. The machined workpiece is shown in Fig. 2.



**Fig. 1** All geared head lathe

**Fig. 2** Machined workpiece



### 2.3 Design of Experiments

The design of the experiment is a valuable method for evaluating the effect on some particular variables of the process variables. The collection of the variables that control the output measurements is the key step in the Taguchi process. Parameters chosen and their ranges were presented in Table 3. The orthogonal sequence L18 has been selected to minimize the number of tests because it blends a maximum of two levels with one factor and three levels with three parameters. To research the influence of process variables, analysis of variance (ANOVA) was carried out. The cutting force plays a significant role in material machinability assessment. To obtain the increased tool life, high surface smoothness, lower deflection and lower energy utilization, we have to maintain lower cutting force.

The calculation is obtained by the signal-to-noise (S/N) ratio, which reflects the relation among the signal and the noise. Optimization tool Taguchi found numerous representations of S/N ratio: Best is smaller, better is nominal, and better is larger. For our analysis, smaller is better has been chosen since cutting energy is the response component. Equation (1) reflects the lower is better relationship, where  $n$  is experiment count,  $y_i$  is the calculation of the objective variable in  $i$ th test and  $y_i$  is the particular cutting energy in this analysis

$$\frac{S}{N} = -\log \left( \frac{1}{n} \sum_{i=1}^n y_i^2 \right) \quad (1)$$

In order to find the noteworthy parameters and relations in the S/N ratio in a confident interval of 95%, an analysis of variance (ANOVA) was carried out.

## 3 Results and Discussion

In order to establish a consistent finding of the levels linked with all parameter in all step, in Table 3 machining conditions and the ranges of levels were tabulated. Experimental data are listed in Table 4. The findings below demonstrate the importance of the particular cutting strength.

Trial findings in Table 4 have been analyzed using analysis of variance (ANOVA), which is used in Table 5 to classify the variables that greatly influence the particular

**Table 3** Factors and levels of the experiments

Machining conditions	Level 1	Level 2	Level 3
Insert type	Uncoated WC	TiN-coated	–
Cutting speed	90	150	224
Feed	0.35	0.4	0.45
Depth of cut	0.1	0.2	0.4

**Table 4** Experimental data

No. of test	Machining parameters with levels				Specific cutting energy (J/mm <sup>3</sup> )
	Tool material	Cutting speed (rpm)	Feed (mm/rev)	Depth of cut (mm)	
1	Uncoated	90	0.35	0.1	37.62
2	Uncoated	90	0.40	0.2	17.77
3	Uncoated	90	0.45	0.4	8.13
4	Uncoated	150	0.35	0.1	29.23
5	Uncoated	150	0.40	0.2	12.11
6	Uncoated	150	0.45	0.4	10.71
7	Uncoated	224	0.35	0.2	22.70
8	Uncoated	224	0.40	0.4	14.95
9	Uncoated	224	0.45	0.1	44.82
10	TiN-coated	90	0.35	0.4	6.50
11	TiN-coated	90	0.40	0.1	28.24
12	TiN-coated	90	0.45	0.2	12.74
13	TiN-coated	150	0.35	0.2	16.36
14	TiN-coated	150	0.40	0.4	9.03
15	TiN-coated	150	0.45	0.1	36.89
16	TiN-coated	224	0.35	0.4	10.09
17	TiN-coated	224	0.40	0.1	24.76
18	TiN-coated	224	0.45	0.2	12.54

**Table 5** ANOVA for the specific cutting energy

Source	DF	Adj SS	Adj MS	F Value	P-value	C (%)
Tool material	1	0.23585	0.23585	4.25	0.067	4.20
Speed	2	0.14894	0.07447	1.33	0.306	2.65
Feed	2	0.00639	0.00320	0.06	0.945	0.11
Depth of cut	2	4.66252	2.33126	41.78	0.000	83.08
Error	10	0.55794	0.05579			9.94
Total	17	5.61165				100

cutting energy response variable. For  $\alpha = 0.5$  level of significance, i.e., 95 percent level of confidence, this study was carried out. A statistically meaningful contribution to success measurements is known to be from sources with a P-value of less than 0.1. Percentage contribution rate of each parameter has been illustrated in the last column.

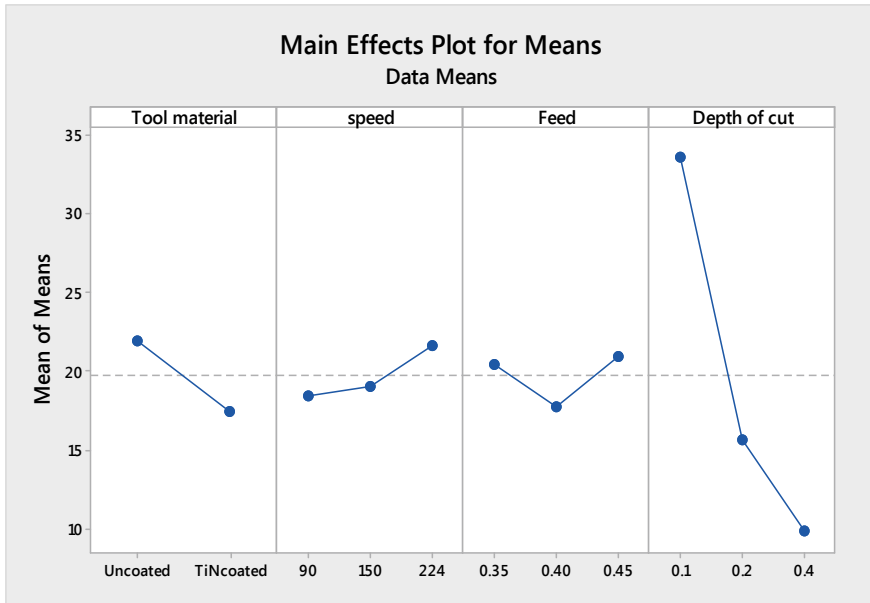


Fig. 3 Main effects plot for specific cutting energy

### 3.1 ANOVA for Specific Cutting Energy

From Table 5, the most critical element in the cutting energy is the cutting depth, which accounts for around 83.08% of the overall variability. The next element impacting the basic cutting energy with a 4.20% input is instrument material. There is no effect on real cutting energy of the pace and feed. In Fig. 3, the main result plot for the cutting energy reveals that with the use of TiN-coated carbide inserts, the SCE decreases. The cutting speed and feed have positive relation with the specific cutting energy and have negative correlation with depth of cut.

### 3.2 Influence of Tool Material on Specific Cutting Energy (SCE)

Cutting energy generated during machining depends on cutting force. Sharpness of the carbide insert keeps the cutting force as constant. Figure 3 shows that TiN-coated insert has minimum specific cutting energy compared to uncoated cemented carbide insert. The reason for the consumption of minimum SCE is retaining the sharp edge of TiN-coated carbide insert. The TiN coating provides low friction, high hardness, higher refractoriness and good adhesion to the substrate.

### 3.3 *Influence of Cutting Speed on Specific Cutting Energy (SCE)*

Cutting speed has positive correlation with cutting energy as shown in Fig. 3. Although the working material is hard to machine, the SCE often increases as the speed increases. This finding shows that with minimum energy consumption, an optimal cutting speed can be chosen.

### 3.4 *Influence of Feed on Specific Cutting Energy (SCE)*

From Fig. 3, relation between the cutting energy and feed rate of tool was established. The cutting strength decreases with increasing the tool traversing. It can be inferred hereby that with increased feed, the overall specific energy has a decreasing trend. Thus, the SCE reduces if the substance removal rate rises. From the formula, it is noted

$$U = \frac{F_c V}{t w V} = \frac{\text{Power}}{\text{MRR}} \quad (2)$$

where

$U$ —specific cutting energy.

$F_c$ —cutting Force.

$V$ —cutting velocity.

$t$ —thickness of the material.

$w$ —width of the work material.

### 3.5 *Influence of Depth of Cut on Specific Cutting Energy (SCE)*

It was also observed that with increasing cutting depth as shown in Fig. 3, the real cutting energy decreases. The volume of material removed is directly proportional to the tool advancement, i.e., depth of cut. From Eq. (2), we know that MRR is inversely proportional to the SCE. Table 5 shows that specific cutting energy was greatly influenced by cutting depth.



## 4 Conclusion

In this work, we have measured and refined the machining parameters for the machining of 304 stainless steel using coated and uncoated carbide tool inserts. As per the machining parameters and levels, the Taguchi's L18 orthogonal array was selected and experiments were performed according to the experiment design in order to obtain quality characteristics. To figure out the importance of each cutting parameter, analysis of variance was used. The conclusions of the present work are given below.

- The cutting depth revealed that the basic cutting energy accompanied by the insert type had more impact on it.
- The highest specific cutting energy  $44 \text{ J/mm}^3$  was observed at speed 224 rpm, high feed rate 0.45 mm/rev and minimum depth of cut 0.1 mm with uncoated carbide tool.
- The minimum specific cutting energy  $6.50 \text{ J/mm}^3$  was observed at 90 rpm, 0.35 mm/rev feed rate and 0.4 mm cut depth, with TiN-coated carbide insert.
- Minimum speed at 90 rpm, feed at 0.40 mm/rev, maximum cutting depth 0.4 mm and tool-type TiN-coated carbide insert were observed to have minimal specific cutting energy and are the ideal cutting parameters.

## References

1. Saikia, P., Hazarika, M.: An experimental study on green machining. In: Proceedings of 5th International & 26th All India Manufacturing Technology, Design and Research Conference, pp.125-1–125-5, IIT Guwahati, Assam, India, (2014)
2. Amit Akash, K., Patel, J., Kumar Dey, A.: Cutting parameters effects on cutting force and Surface Roughness in Hard Turning of AISI 52100 Steel with CBN Tool. *IJRASET* **3**(3), 364–371 (2015)
3. King, R.I., Hahn, R.S.: Handbook of modern grinding technology. Chapman and Hall, USA (1986)
4. Erosy, A., Atici, U.: Performance characteristics of circular diamond saws in cutting of Different types of rocks. *Diam. Relat. Mater.* **13**(1), 22–37 (2004)
5. Polini, W., Turchetta S.: Force and specific energy in stone cutting by Diamond Mill. *Int. J. Mach. Tools Manuf.* **44**(1), 1189–1196 (2004)
6. Neugebauer, R., Drossel, W.: Resource and energy efficiency in machining using high performance and hybrid processes. In: 5th CIRP Conference on High-Performance Cutting, pp 3–16 *Procedia CIRP* **1**, (2012)
7. Domingo, R., Maria Marin, M.: Selection of cutting inserts in dry machining for reducing energy consumption and CO<sub>2</sub> emissions. *Energies* **8**, 13081–13095 (2015)
8. Gutowski, T., Dahmus, J., Thiriez, A.: Electrical Energy Requirements for manufacturing processes. In: Proceedings of 13th CIRP International Conference on Life Cycle Eng, pp. 625, Leuven (2006)
9. Li, W., Kara, S.: An Empirical model for predicting energy consumption of manufacturing processes: a case of turning process. *Proc. Inst. Mech. Eng. Part B-J. Eng. Manuf.* **225**(B9), 1636–1646 (2011)

10. Guo, Y., Loenders, J., Duflou, J., Lauwers, B.: Optimization of energy consumption and surface quality in finish turning. *Procedia CIRP* **1**, 512–517 (2012)
11. Lucca, D., Seo, Y., Komanduri, R.: Effect of tool edge geometry on energy dissipation in ultraprecision machining. *CIRP Ann. Manuf. Technol.* **42**(1), 83–86 (1993)
12. Rodrigues, A.R., Coelho, R.T.: Influence of the tool edge geometry on specific cutting energy at high-speed cutting. *J. Braz. Soc. Mech. Sci. Eng.* **29**(3), 279–283 (2007)
13. Balogun, V.A., Gu, H., Mativenga, P.T.: Improving the integrity of specific cutting energy coefficients for energy demand modeling. *Proc. Inst. Mech. Eng., Part B: J. Eng. Manuf.* **229**(12), 2109–2117 (2014)
14. Sredanović, B., Čiča, Đ., Tešić, S., Kramar, D.: Optimization of cutting parameters for minimizing specific Cutting energy and maximizing productivity in turning of AISI 1045 steel. *Int. Sci. J. Machines Technologies. Mater.* **13**(11), 491–494 (2019)
15. Su, Y., Zhao, G., Zhao, Y., Meng, J., Li, C.: Multi-objective optimization of cutting parameters in turning AISI 304 austenitic stainless steel. *Metals* **10**(2), 217 (2020)

# Influence of Squeeze Time on Fracture Mode of SS304 Spot Weldments



**Bikash Kumar** , **Binaya Ranjan Maharana** , **Ajit Kumar Sahu** ,  
**Swagat Dwibedi** , **Arijeet Jena** , **Subham Das** , and **Suraj Prasad** 

## 1 Introduction

In accordance with ongoing researches on resistance spot welding (RSW), it is expressed as the principal method to join sheet metal for automotive-based structural components such as transportation vehicles, commercially used spare parts, beverage containers, household utensils. This process is extensively used and categorized as an essential tool in automotive body construction owing to economic in nature, minimal skill need, and robustness to structure tolerance variation [1]. The electric resistance spot welding renders interplay between time, pressure, and heat simultaneously. In this process, mechanical assemblies are readily accomplished by squeezing the base metals in lap configuration to a particular pressure for a certain period using a copper electrode and followed by high current flow at localized areas [2]. The application of RSW has numerous advantages i.e., highest throughput, high-speed production,

---

B. Kumar · A. K. Sahu · S. Dwibedi (✉)

Department of Mechanical Engineering, Indian Institute of Technology Guwahati, Guwahati, Assam 781039, India

e-mail: [swagatsudhadwibedi@iitg.ac.in](mailto:swagatsudhadwibedi@iitg.ac.in); [swagatsudhadwibedi@yahoo.com](mailto:swagatsudhadwibedi@yahoo.com)

B. Kumar

e-mail: [bikash.kumar@iitg.ac.in](mailto:bikash.kumar@iitg.ac.in)

A. K. Sahu

e-mail: [ajit.sahu@iitg.ac.in](mailto:ajit.sahu@iitg.ac.in)

B. R. Maharana · S. Dwibedi · A. Jena · S. Das

Department of Mechanical Engineering, Veer Surendra Sai University of Technology, Burla, Odisha 768018, India

S. Prasad

Department of Mechanical Engineering, Silicon Institute of Technology, Sambalpur, Odisha 768200, India

e-mail: [prasadsrkl67@gmail.com](mailto:prasadsrkl67@gmail.com)

and adaptability for automation, to join especially low carbon and austenitic stainless steel sheets [3]. Austenitic stainless steels of 300 series are preferential candidate for structural application especially in the structural framework and body parts of railway coaches and buses and house-based commercial components. Stainless steel is a superior choice in terms of weight saving, increasing crashworthiness, corrosion resistance, and recyclability. This group of steel exhibits an anomalous attribute of mechanical toughness and fire resistance properties along with excellent manufacturability, among the other steels [4, 5].

Weldability of stainless steel is one of the essential components that determine its implementation in several industries. The nucleation of a certain phase with a particular phase fraction leads to the deterioration in mechanical and functional properties of welded joints [6, 7]. This issue can be resolved either by the appropriate selection of process or controlling process parameters. Several conventional and high energy beam welding techniques are already explored to obtain excellent and sophisticated welded joints. However, in the RSW process, no filler is required during welding, and the optimum amount of heat input implies the least risk of fluctuation of dimension in post-weld condition. Hence, this process is adopted for the present investigation. Besides, weld quality and performance of electric spot welds remarkably affect the safety design and durability of the structure. The failure mode of spot weld subjects dramatic impact on the performance of welded structure, therefore, it can be stated that failure mode is a qualitative measurement of mechanical properties [8].

Several researchers have given eminent effort to analyze the performance and behavior of resistance spot welded structure and influence of various parameters on the mechanical characteristics of final weldments. Principally it is revealed that welding current, weld time, and electrode force are fundamental parameters that decide the weld nugget size [9]. The geometrical dimension of the welded area is characterized as a micro-indentation produced by an electrode during welding and perceived that indentation size increases with process variables. Furthermore, Charade, N. [3] studied the effect of welding current and electrode force on nugget size and bond strength of thin SS304 spot welded structure. It is conveyed that both i.e., diameter of weld nugget and strength (tensile-shear condition) of spot weld increases with welding current, however, nugget size decreases with increasing electrode pressing force. Hence, it can be concluded that less amount of electrode force is required for the failure of spot weldments. It is also perceived that the hardness value of the weld zone is somewhat higher than the HAZ and base metal [3]. It might be due to the presence of retained  $\delta$ -ferrite by virtue of partial transformation of  $\delta \rightarrow \gamma$  phase in the fusion zone [3]. On the contrary, for Ti-alloy, it was stated that the increasing current time and electrode force improves tensile shear strength, and the joint obtained under the argon atmosphere gave better strength [10]. Moreover, hardness distribution showed a similar pattern as predicted by Charade et al. [3]. Bouyousfi et al. [11] investigated the influence of arc intensity, welding duration, and applied load on the mechanical characteristics of welded joints of SS304 and described that applied load seems to be the dominating control factor for mechanical characterization rather than welding duration and the current intensity. Further, it is also confirmed that there is no significant interrelation between nugget size and

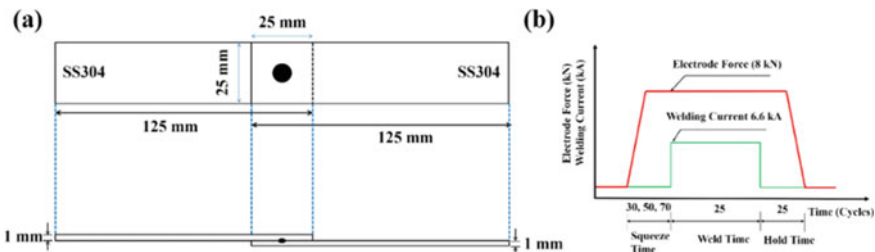
hardness distribution. Recently, Dwibedi et al. [12] illustrated the impact of welding time on weld strength, size of nugget, mode of failure of resistance spot welded structure and revealed that the nugget size widens upon increasing weld time as well as the strength of welded metal increases with enhancing weld time up to an optimized level.

From the above discussion, it is noticeable that diversification in mechanical strength of spot-welded joint is possible by controlling weld input variables. Estimation of optimized input parameters is a difficult task for the manufacturer to own the desired strength. Hence, establish an interrelation between the input variable and associated joint strength is of great interest in the present investigation. There is a lack of literature available that focuses on squeeze time (which is a prevalent stage during electric spot welding) on mechanical strength for thin stainless steel (SS304) joint. In the present investigation, interrelation between squeeze time and mechanical strength is analyzed. Furthermore, EDX testing is performed to investigate the change in metallurgical characteristics within FZ and HAZ. Nevertheless, the significance of the mode of failure attained at different input parameters is extensively explored.

## 2 Experimental Procedure

### 2.1 Materials and Methodology

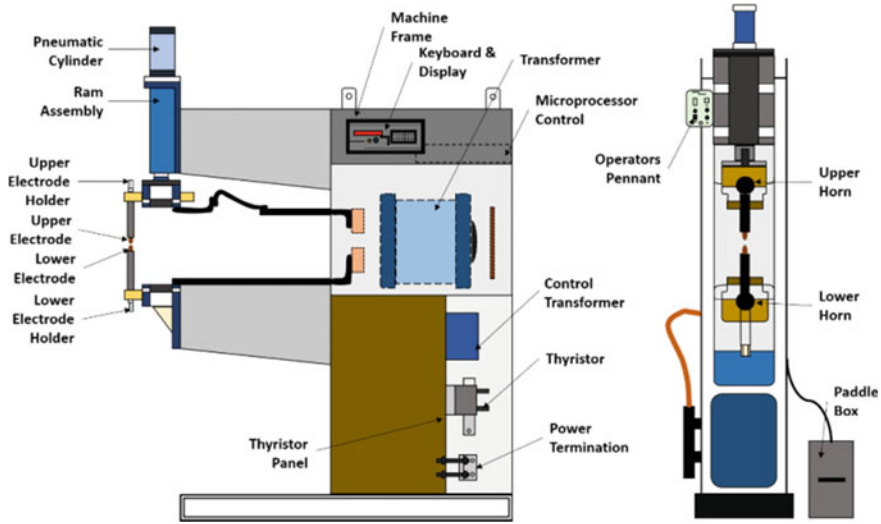
Thin sheets of austenitic stainless steel (SS304) of cross Section  $125 \text{ mm} \times 25 \text{ mm} \times 1 \text{ mm}$  are employed to form electric spot weld in lap framework, as presented in Fig. 1. Prior-weld edge processing of weldment is done by a conventional method to avoid extra unwanted contaminated layer before welding. Prior weld coupons of dimension  $125 \times 25 \text{ mm}^2$  are overlapped in such a way that the overlap dimension is observed to be 25 mm. The elemental composition of the employed SS304 extracted from EDX analysis, is documented in Table 1. The geometrical dimension of weldments



**Fig. 1** a Layout of RSW weldment in lap configuration and b demonstration of welding parameters applied during RSW process

**Table 1** Chemical composition of SS304 (wt.%)

Cr	Ni	Mo	Si	P	Al	C	Mn	Fe
18.4	8.9	8.42	0.34	0.03	0.164	0.08	1.06	Balance



**Fig. 2** Overall experimental resistance spot welding setup used for the experimentation

and the sets of parameters applied during weld fabrication W1, W2, and W3 are illustrated in Fig. 1a and b, respectively.

### 2.2 Experimental Setup

The electric spot welding setup used to perform the welding action is illustrated in Fig. 2. The welding system comprises five major parts, i.e., electronic control, paddle, pressure gage, electrode, and compressor. The air compressor, coupled with a water motor pump is used for cooling the entire welding setup. The fascinating feature of RSW process is generating an enormous amount of energy for a significantly less time span, that assist joining of metal within 10–100 ms for the part to be welded.

### 2.3 Welding Process Parameters

In order to scrutinize the influence of squeezing time during RSW of SS304 thin sheets, weld joints are fabricated at three different squeezing time (cycles) i.e., 30,

**Table 2** Process variables employed for RSW of SS304

Case	P (kg/cm <sup>2</sup> )	I (kA)	T <sub>s</sub> (cycles)	T <sub>w</sub> (cycles)	T <sub>h</sub> (cycles)	T <sub>o</sub> (cycles)
W1	5.0	6.6	30	25	25	20
W2	5.0	6.6	50	25	25	20
W3	5.0	6.6	70	25	25	20

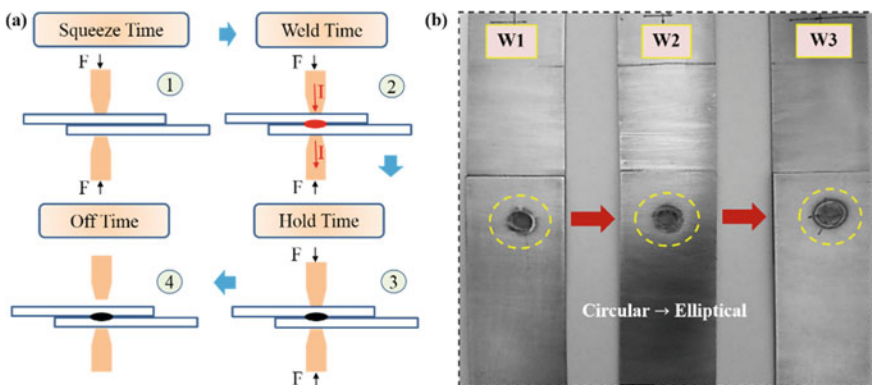
P: Pressure, I: Current, T<sub>s</sub>: Squeeze time, T<sub>w</sub>: Weld time, T<sub>h</sub>: Hold time, T<sub>o</sub>: Off time

50 and 70 cycles by keeping other parameters i.e., electrode force, welding current, hold time, and weld time constant as illustrated in Table 2. A suitable combination of welding parameters is required to produce stable and defect-free weld. Therefore, several trials are done to optimize the three constant parameters after that fourth variable i.e., squeezing time varied for weld fabrication. During the post welding stage, the tensile-shear strength test is performed on the welded samples by using the Universal Testing Machine to track the fracture mode/failure mode attained by the SS304 weldments. All the tests are conducted with a cross-head speed of 2 mm/min.

### 3 Results and Discussion

#### 3.1 Stage Performance of Spot Weld and Nugget Analysis

The entire RSW process is carried out in four different stages: T<sub>s</sub> → T<sub>w</sub> → T<sub>h</sub> → T<sub>o</sub>, also demonstrated in Fig. 3a. The former two stages are significantly important that decide the mechanical behavior of the final structure. Initially, the time span up to which electrode applied pressure upon weld coupon



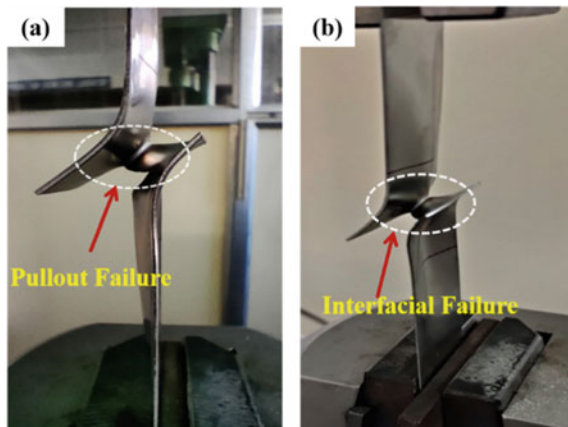
**Fig. 3** a Interpretation of RSW process and b resistance spot welded samples under varied weld condition

prior to current flow is categorized as squeeze time. Squeezing operation impinges on the lap configured weld-coupon by the electrode. The subsection of adequate electrode force for an optimal time to subject squeezing action is the fundamental prerequisite of weld fabrication. It should be noted that variation in squeezing time can dramatically alter the mode of failure, which leads to the diversification in metallurgical and resulting mechanical properties [13]. As squeezing time (W1~30; W2~50; W3~70 cycles) gets over, welding time begins. Both heat and current are simultaneously applied to the weld coupon that has to be weld. Highly localized current is subjected so that spot melts the coupon, as a result, welded joint formed. Furthermore, holding time as well as off time is subsequently applied for the proper stability of welded joint up to ambient temperature. Figure 3b depicts the weld nugget size evolved for different welded samples W1, W2 and, W3. The geometry of the weld nugget shifted from circular to elliptical upon increasing squeeze time. Owing to higher squeezing time, local heating takes place at a localized area which softens the metal volume and, upon impingement of current heat, easily travels along rolling direction rather than transverse direction. Hence, nugget geometry changes from circular to elliptical, and the size of the weld nugget increases as well at the micro scale but not significantly.

### 3.2 Mode of Failure Analysis

Figure 4 illustrates the mode of failure attained by the welded samples at two different process conditions. It is observed that specimen W1 accomplished at lowest squeeze time i.e., 30 cycles render pullout failure (PF), whereas specimen W3 (70 cycles) exhibited interfacial failure (IF) mode. During PF mode, the weld nugget withdrew from the one weldment sheet. A fracture may initiate from any region, which depends upon the geometrical and metallurgical characteristics of the weld zone and subjected

**Fig. 4** Illustrates mode of failure attained at different weld condition **a** W1 (30 cycles) and **b** W3 (70 cycles)

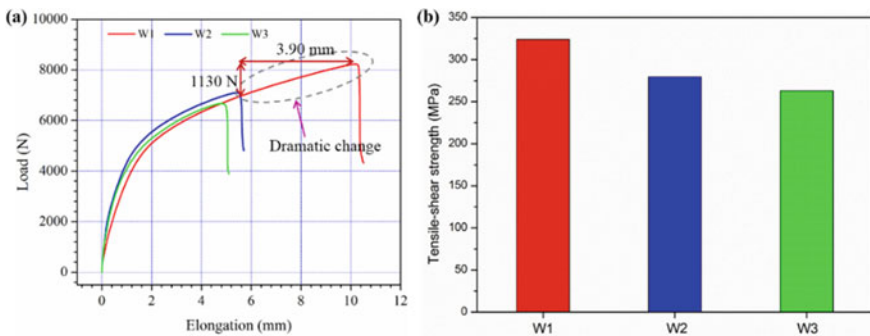




loading condition. Nevertheless, it is conveyed in the literature that the PF mode is the most desirable failure mode and can render excellent mechanical properties. On the contrary, the IF is an undesirable mode since failure propagates from the fusion zone (FZ). Hence, it can be concluded that the specimens which are fabricated at low squeeze time can exhibit good mechanical and metallurgical characteristics rather than at high squeeze time.

### 3.3 Tensile-Shear Test Analysis

Mode of failure attained during the tensile shear test is the most prominent deciding factor of mechanical performance. Figure 4 demonstrates the PF mode during the tensile test for weld coupon W1 at lowest squeezing time i.e., 30 cycles. However, IF mode is exhibited for W2, W3 weld metal fabricated at squeezing time of 50 and 70 cycles, respectively. The fracture initiation and propagation occur through the FZ in an IF mode. Nevertheless, fracture initiates from base metal or HAZ or HAZ-FZ boundary based on metallurgical and dimensional characteristics of FZ and subjected load condition. Figure 5 shows the load-bearing capacity w.r.t elongation prior to shear failure at different weld conditions. Maximum load-bearing capacity of 8.32 kN and tensile strength of 324.04 MPa are perceived for weld metal W1 at PF mode, whereas 7.10 kN and tensile strength of 279.4 MPa are found for W2 at an IF mode. Another possible reason for the increase in load-bearing capacity for W1 weld conditions is the presence of dimples in the fracture surface, leading to a ductile mode of fracture [14]. Additionally, 6.67 kN and tensile-shear strength of 262.7 MPa is found for W3. Weld nugget W1 (squeeze time ~ 30 cycles) implies relatively higher plastic deformation and enriched energy absorption during the pullout mechanism. On the contrary, IF mode has an adverse impact on the crashworthiness of welded structures. During weld nugget formation, the molten metal is squashed to transfigure into spatter through the application of relatively high squeezing time.



**Fig. 5** a Illustration of load bearing capacity and associated elongation at different weld condition and b tensile-shear strength at various weld condition

Hence, the deterioration of load-bearing capacity and associated tensile properties with increasing squeeze time are indicated.

## 4 Conclusions

The present study conveys that failure mode is a sign of load-bearing ability and energy absorption capacity. Additionally, the geometrical interpretation of the weld nugget is carefully explored. The interrelation between squeezing time, mode of failure and mechanical strength is established in the present study as well. Some inferences drawn on the basis of present work are as follows:

- a .Squeezing time is observed to be a crucial process parameter that influences the weld nugget characteristics. Weld nugget geometry transformed to elliptical from circular profile upon increasing squeezing time owing to metal softening and local heating. Variation in size of weld nugget also noticed at the micro level.
- b .Specimen fabricated at lowest squeezing time i.e., 30 cycles, exhibited pullout failure that can access better mechanical properties, whereas specimen welded at highest i.e., 70 cycles rendered interfacial failure, which is an indication of detrimental performance.
- c .Maximum load-bearing capacity of 8.32 kN and tensile strength of 324.04 MPa are perceived for weld metal W1 (30 cycles) at pullout failure mode, whereas 6.67 kN and tensile strength of 262.7 MPa are found for W3 (70 cycles) at an interfacial mode of failure.

## References

1. Ozsarac, U.: Investigation of mechanical properties of galvanized automotive sheets joined by resistance spot welding. *J. Mater. Eng. Perform.* **21**, 748–755 (2012)
2. Moshayedi, H., Sattari-Far, I.: Resistance spot welding and the effects of welding time and current on residual stresses. *J. Mater. Process. Technol.* **214**, 2545–2552 (2014)
3. Charde, N.: Effects of electrode deformation of resistance spot welding on 304 austenitic stainless steel weld geometry. *J. Mech. Eng. Sci.* **3**, 261–270 (2012)
4. Dwibedi, S., Jain, N.K., Pathak, S.: Investigations on joining of stainless steel tailored blanks by  $\mu$ -PTA process. *Mater. Manuf. Processes* **33**, 1851–1863 (2018)
5. Dwibedi, S., Bag, S., Lodhi, D.K., Kalita, A.: Joining of different thickness dissimilar materials SS 316L/SS 310 by  $\mu$ -PAW process. In: Shunmugam, M., Kanthababu, M. (eds) *Advances in additive manufacturing and joining. Lecture Notes on Multidisciplinary Industrial Engineering*, pp 569–578. Springer, Singapore (2020)
6. Dwibedi, S., Jain, N.K.: Investigation on autogenous joining of stainless steel sheets of different thickness using micro Plasma Transferred Arc ( $\mu$ -PTA) process (2016). <http://dspace.iiti.ac.in:8080/xmlui/handle/123456789/329>
7. Kumar, B., Bag, S.: Phase transformation effect in distortion and residual stress of thin-sheet laser welded Ti-alloy. *Opt. Lasers Eng.* **122**, 209–224 (2019)

8. Pouranvari, M.: Prediction of failure mode in AISI 304 resistance spot welds. *Assoc. Metallurgical Engineers of Serbia*, **17**, 23–29 (2011)
9. Aravinthan, A., Nachimani, C.: Analysis of spot weld growth on mild and stainless steel. *Weld. J.* **90**, 143–147 (2011)
10. Kahraman, N.: The influence of welding parameters on the joint strength of resistance spot-welded titanium sheets. *Mater. Des.* **28**, 420–427 (2007)
11. Bouyousfi, B., Sahraoui, T., Guessasma, S., Chaouch, K.T.: Effect of process parameters on the physical characteristics of spot weld joints. *Mater. Des.* **28**, 414–419 (2007)
12. Dwibedi, S., Kumar, B., Bhoi, S.R., Tripathy, S.R., Pattanaik, S., Prasad, S., Behera, R.: To investigate the influence of weld time on joint characteristics of Hastelloy X weldments fabricated by RSW process. *Materials Today: Proceedings* **26**, 2763–2769 (2020)
13. Sadasue, T., Igi, S., Taniguchi, K., Ikeda, R., Oi, K.: Fracture behaviour and numerical study of resistance spot welded joints in high-strength steel sheet. *Weld. Int.* **30**, 602–613 (2016)
14. Dwibedi, S., Bag, S.: Assessment by destructive and non-destructive approach to characterize 90/10 cupronickel weldments. *Materials Today: Proceedings* **33**, 5014–5018 (2020)

# Finite Element Modeling of Temperature Evolution During Selective Laser Melting



Nithya Srimurugan, Rishi Dwivedi, Vineesh Vishnu, Basil Kuriachen, and K. P. Vineesh

## 1 Introduction

Additive manufacturing is a direct production process in which the components are made from a 3D model using layer by layer deposition. Additive manufacturing has emerged as a widely accepted technique in aerospace, automotive, medical, and food industries owing to its capabilities of making net-shaped complex geometries, better properties, no wastage of material, and less production time compared to the conventional manufacturing methods. Powder bed fusion is a promising metal additive manufacturing method that utilizes various printing techniques such as Selective Laser Melting (SLM), Electron Beam Melting (EBM), Direct Metal Laser Sintering (DMLS), and Selective Laser Sintering (SLS). The SLM technique uses a high-power density laser with a large thermal gradient to melt and fuse the metallic powders and a rapid cooling cycle to solidify the part in an inert atmosphere. Despite many advantages, SLM parts also suffer some defects include porosity, lack of fusion, and tensile residual stresses. The defects finally cause the formation of cracks in the printed parts and change in the part dimension and shape. The balling effect, tensile residual stresses, and deteriorated surface finish, and localized thermal stresses are detrimental to the acceptability of the parts for heavy-duty applications [1, 2]. Various researchers focused their studies on residual stresses and part deformation during the SLM process [3, 4]. Experimental techniques employed to measure the temperature field and the residual stresses are very expensive and time-consuming [5]. Accurate prediction of residual stress depends on the temperature field distribution during the melting operation. To study the evolution of temperature in the SLM process, an effective modeling is required.

---

N. Srimurugan (✉) · R. Dwivedi · V. Vishnu · B. Kuriachen · K. P. Vineesh  
Department of Mechanical Engineering, National Institute of Technology Calicut, Calicut  
673601, India

© The Author(s), under exclusive license to Springer Nature Singapore Pte Ltd. 2022  
S. K. Natarajan et al. (eds.), *Recent Advances in Manufacturing, Automation, Design  
and Energy Technologies*, Lecture Notes in Mechanical Engineering,  
[https://doi.org/10.1007/978-981-16-4222-7\\_37](https://doi.org/10.1007/978-981-16-4222-7_37)

315

Roberts et al. [6] developed a 3D finite element model without radiation heat transfer loss and predicted the temperature field during the SLM of Ti6Al4V alloy. In another study, Li et al. [7] predicted the optimum process parameters needed for a sound metallurgical bonding for AlSi10Mg alloy with the help of a 3D FEM model. Khan et al. [8] performed heat transfer analysis during SLM of AlSi10Mg alloy using adaptive remeshing technique to bring down the computational time and storage size. Fu et al. [2] examined the effects of process parameters on the melt pool geometry using FE model and validated the simulation results with experiments. Numerous models were developed to study the temperature profile but are limited to predict the temperature behavior with consideration of convective heat transfer inside the molten pool.

In the present work, the transient temperature field is predicted using a finite element model that is developed in the ABAQUS software. The model takes into account of all the heat losses by conduction, convection, radiation and also by convection inside the melt pool.

## 2 Methodology

### 2.1 Governing Equations for Heat Transfer Problem

The governing differential equation for a 3D heat transfer problem is given as

$$\rho c \frac{\partial T}{\partial t} = \frac{\partial}{\partial x} \left( k \frac{\partial T}{\partial x} \right) + \frac{\partial}{\partial y} \left( k \frac{\partial T}{\partial y} \right) + \frac{\partial}{\partial z} \left( k \frac{\partial T}{\partial z} \right) + Q \quad (1)$$

where  $\rho$ ,  $c$  and  $k$  are the density, specific heat, and thermal conductivity of the material and  $Q$  is the internal heat generation. The boundary conditions are the convection and radiation heat transfer from the exposed surfaces which are given by the Eqs. (2) and (3)

$$Q_C = h(T - T_0) \quad (2)$$

$$Q_R = \sigma \varepsilon (T^4 - T_0^4) \quad (3)$$

To avoid the nonlinearity in the radiation term, an equivalent convective heat transfer coefficient is defined as  $0.0024 \varepsilon T^{1.61}$  with  $\varepsilon = 0.35$ . The related loss in accuracy is predicted to be less than 5% on using this term [9]. The initial temperature of the powder layer and the build platform is taken as 293 K.

## 2.2 Laser Energy Modeling

The laser energy is modeled by assuming it as a Gaussian surface heat flux which is symmetrical across the beam in terms of its irradiance [6]. The Gaussian heat flux for the fundamental mode (TEM<sub>00</sub>) is given by

$$q(r) = \frac{2\alpha P}{\pi R^2} e^{-\frac{2r^2}{R^2}} \quad (4)$$

where  $P$  denotes laser power,  $R$  denotes radius of laser beam and  $\alpha$  denotes absorptance of material which is taken as 0.1 [10]. The Gaussian heat flux is implemented using the DFLUX subroutine in ABAQUS [11].

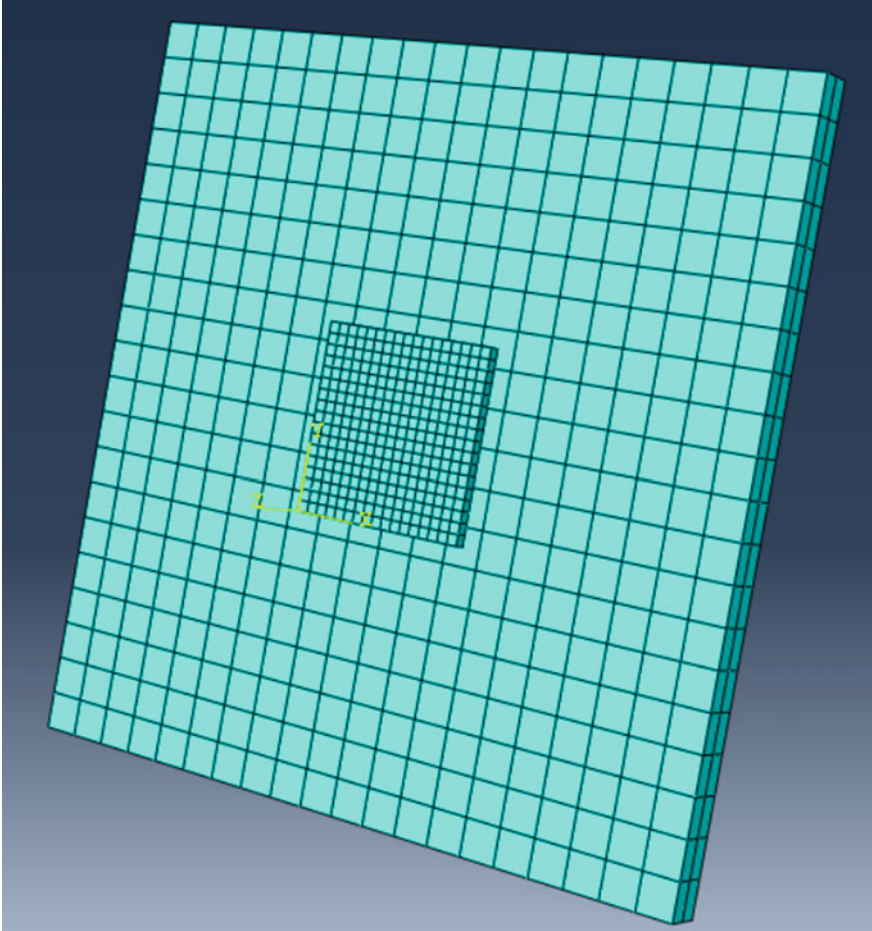
## 2.3 Finite Element Modeling

The Finite element model consists of a single layer of powder and build platform as depicted in Fig. 1. The dimensions of the powder layer are 0.5 mm × 0.5 mm × 0.03 mm and are made of Ti6Al4V alloy. The dimensions of the build platform are 2 mm × 2 mm × 0.1 mm and are made of AISI steel. The geometry of the FE model is taken to be very small in size to reduce the computational time.

The powder layer is given as a fine mesh, whereas a coarser mesh is used for the build platform. An 8-noded hexahedral element (DC3D8) is used for the heat transfer analysis. Since latent heat effects are involved, a linear order element is used [12]. The thermal properties are given as a function of temperature and field variables for the powder layer [10]. The liquid's thermal conductivity is artificially enhanced to account for the convective heat transfer within the melt pool [9]. Field variable value 0 indicates powder state and field variable value 1 indicates solid/liquid state. By using the USDFLD subroutine [11], the field variable value is changed to 1 from 0 when the temperature at the integration point reaches above the melting point (i.e. 1923 K). The simulation is performed for a single line laser scan track. The processing parameters used in the simulation process are given in Table 1. A tie constraint is used between the regions having dissimilar meshes [13]. The incrementation time is controlled by setting a value to the maximum allowable temperature change per increment.

## 3 Results and Discussion

The nodal temperatures obtained at the end of the simulation are shown in Fig. 2. The temperature distribution is analogous to the ones mentioned in the literature [7, 10]. The temperature is very high at the front end of the laser than at the rear end. This is due to the liquid's higher thermal conductivity than the powder, allowing improved heat transfer.



**Fig. 1** Finite element model used in the simulation

**Table 1** Process parameters for SLM of Ti6Al4V

Process parameters	Value
Powder layer thickness	0.03 mm
Laser power	140 W
Hatch spacing	0.1 mm
Scan speed	1.2 m/s
Laser spot size	0.1 mm

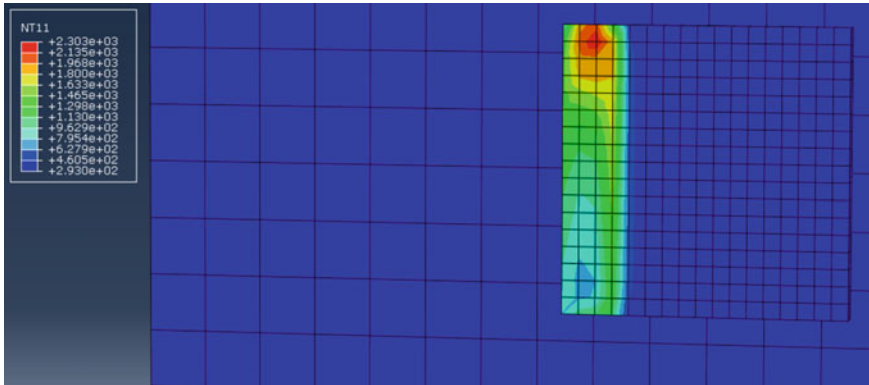


Fig. 2 Nodal temperatures obtained at the end of the simulation

The temperature–time history for a point on the surface of the powder layer is shown in Fig. 3. Once the laser beam approaches the point mentioned above, the temperature increases above the melting point to a value of around 2000 K. When the laser beam shifts forward, the temperature drops rapidly to around 750 K in a span of few milliseconds. Thus, it can be concluded that the temperature changes occur rapidly during the SLM process.

The variation of field variable with time is shown in Fig. 4, for the same point which was discussed earlier. The field variable becomes 1 when the temperature increases beyond 1923 K and this happens around 0.054 ms. After that, the field variable value remains 1 up to the end of the simulation indicating a solid/liquid state.

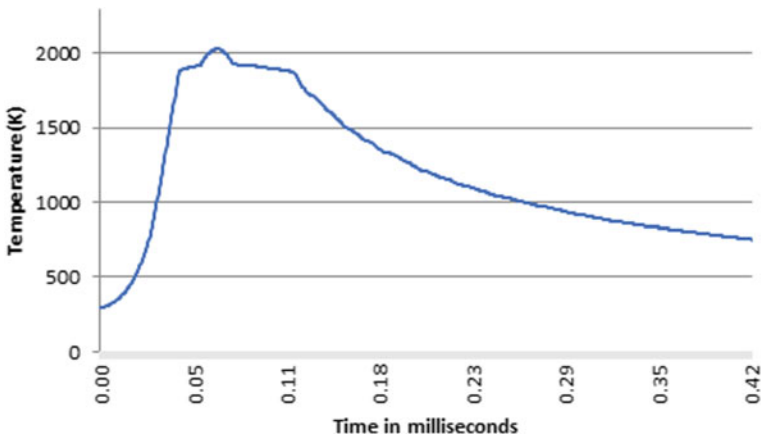


Fig. 3 Temperature–time history at a point on the powder layer surface



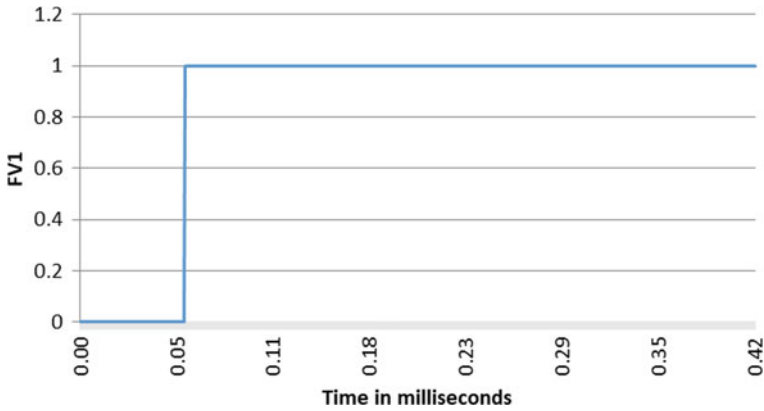


Fig. 4 Variation of field variable with time at a point

The field variables obtained at the end of the simulation are shown in Fig. 5. The red-colored region indicates the transformation of powder to solid-state, i.e., the solidified part and the unmelted regions shown in other colors. The unmelted regions can lead to part porosity. This defect could be avoided by either decreasing the scanning speed or increasing the laser power. Also, finer mesh could have reduced the region of unmelted powder.

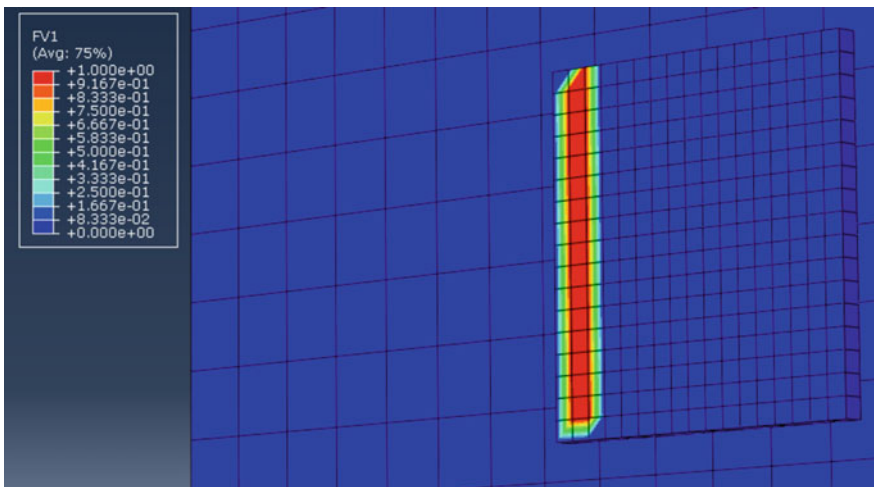


Fig. 5 Field variables representing the melted regions

## 4 Conclusion

A finite element model in 3D was developed in ABAQUS to obtain the temperature field for a single line laser scan track by considering the physical characteristics of the SLM process such as powder-liquid-solid phase transformation, temperature-dependent thermal properties, and accounting for all the heat transfer losses. The major findings are summarized below.

- (1) The convection heat transfer which is taking place inside the melt pool is taken into account and the temperature field obtained is analogous to those mentioned in the literature.
- (2) The developed model captured the rapid heating and cooling cycles involved in the SLM process which is solely culpable for the formation of residual stresses in the built part.
- (3) The liquid's thermal conductivity had a great impact on the cooling rate of the melted portions of the powder layer
- (4) The temperature near the front end of the laser is very high when compared to the region near the rear end of the laser.
- (5) To estimate the residual stresses, the temperature field obtained using the heat transfer analysis can be used as a predefined field in the stress analysis.

## References

1. Zaeh, M., Branner, G.: Investigations on residual stresses and deformations in selective laser melting. German Academic Society for Production Engineering (WGP) (2009)
2. Fu, C.H., Guo, Y.B.: Three-dimensional temperature gradient mechanism in selective laser melting of Ti-6Al-4V. *J. Manuf. Sci. Eng.*, **136**(6), 061004 (2014)
3. Jamison, L., Bartlett, Li, X.: An overview of residual stresses in metal powder bed fusion. *Additive Manuf.* **27**, 131–149 (2019)
4. Kruth, J.P., Froyen, L., Van Vaerenbergh, J., Mercelis, P., Rombouts, M., Lauwers, B.: Selective laser melting of iron-based powders. *J. Material Processing Tech.* **149**, 616–622 (2004)
5. Bandyopadhyay, A., Traxel, K.D.: Metal-additive manufacturing—Modeling strategies for application-optimized designs. *Addit. Manuf.* **22**, 758–774 (2018)
6. Roberts, I.A., Wang, C.J., Esterlein, R., Stanford, M., Mynors, D.J.: A three-dimensional finite element analysis of the temperature field during laser melting of metal powders in additive layer manufacturing. *Int. J. Mach. Tools Manuf* **49**(12–13), 916–923 (2009)
7. Li, Y., Dongdong, Gu.: Parametric analysis of thermal behavior during selective laser melting additive manufacturing of aluminum alloy powder. *Mater. Des.* **63**, 856–867 (2014)
8. Khan, K., De, A.: Modelling of selective laser melting process with adaptive remeshing. *Sci. Technol. Weld. Joining* **24**, 391–400 (2019)
9. Liu, H.: Numerical analysis of thermal stress and deformation in the multi-layer laser metal deposition process. Masters Theses, 7242, (2014)
10. Sani: Selective Laser Melting process simulation: advancements towards a cost-effective model. Ph.D. thesis (2016)
11. Abaqus user subroutines reference manual (6.12), Dassault systems
12. Abaqus theory manual (6.12), Dassault systems
13. Abaqus Analysis user's manual (6.12), Dassault systems

# Effects on Mechanical Properties of High-Density Polyethylene (HDPE) Reinforced with Walnut Shell Powder



Adnan Ali Khan, Uzair Ali Khan, and Rafid Hassan

## 1 Introduction

A series of repeating monomers that may be either non-biodegradable or biodegradable with technical properties for a good range of applications are called polymers. Non-biodegradable materials are replaced by New and Eco-friendly materials developed by the industries driven by the present scenario to achieve a clean and green environment Polymer. Composites are Two or more combined constituents are present at the macroscopic level and are not soluble with one another. For composites' development based on non-biodegradable polymers and natural filler, remarkable research work has been done. In several applications, polymers have replaced many traditional metals/materials in the last few decades. The reason behind this is the benefits offered by polymers over conventional materials. The convenience of processing, construction, and productivity is the foremost vital advantages of using polymers. Polymers properties are modified using fibers and fillers in most of these applications, to match the high modulus or high strength requirements. When specific properties are compared, over other conventional materials, fiber-reinforced polymers give advantages. Applications of these composites are in various fields from space crafts to appliances [1].

Apart from the base polymers, the plastic industry's subsequent materials in terms of volume are fillers. In plastic industries, natural fillers and mineral fillers are the most frequently used fillers. Nowadays, for reducing the dependence on petroleum-based resources due to the fast depletion rate of natural resources and improving

---

A. A. Khan

Department of Community College (Production Technology), Aligarh Muslim University, Aligarh 202002, India

U. A. Khan · R. Hassan (✉)

Department of Mechanical Engineering, Aligarh Muslim University, Aligarh 202002, India

the plastic properties, conventional mineral fillers are replaced by natural fillers in plastic compounding [2].

Also, to overcome the other limitation related to the utilization of mineral fillers (mainly talc, silica, glass fiber, asbestos, mica) in the plastic industry, which includes; non-biodegradable, high cost, abrading of processing equipment, loss of energy during processing, and increase in density of composite systems, a non-renewable and abundant resource and its hazardous effect to the environment [3]. However, the natural filler's drawbacks are summarized as follows, poor surface adhesion to hydrophobic polymers, degradation by moisture, non-uniform filler sizes, not suitable for the high-temperature application, susceptibility to fungal, insect attack, etc., [4]. Polyethylene offers an outstanding combination of thermal, mechanical, chemical, physical, and electrical properties that are not present in other thermoplastics. When compared to polypropylene, it has a high impact strength.

## 2 Materials and Material Methods

In the agro-industry, the walnut particle residue was generated in high proportion by the walnut shell's grinding. The walnut shells are underutilized, renewable agricultural material, and generally, its color varies from light brown to dark brown. The powder is purchased from a nearby local market. Manufacturer: HERBS AND CROPS, particle size up to 60–100 mesh.

HDPE is manufactured from the natural gas ethane at low pressures and temperatures, using Ziegler–Natta and Phillips catalyst(activated chromium oxide) or metallocene catalysts.

### 2.1 *Method of Preparation of Filler Reinforced Polymer Composites*

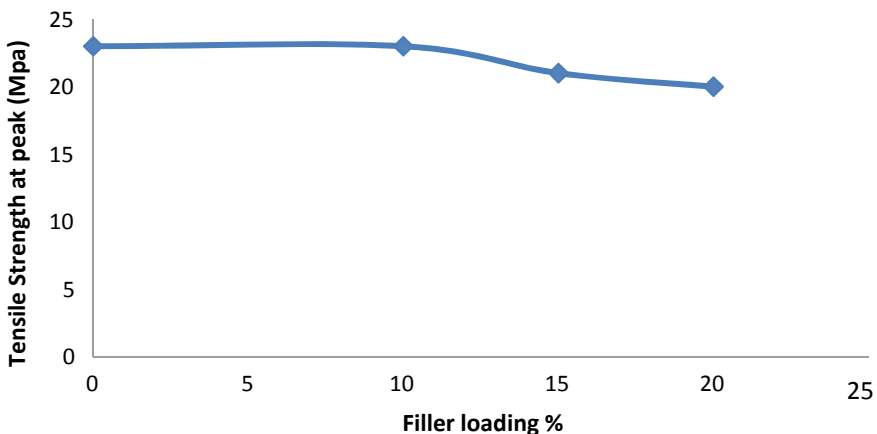
Compounding to obtain required composites was done on mold cylinder in injection machines. The pre-blend mixture was fed to the injection molding machine tube through a hopper. The piston pushes material as the material entered the first zone of the injection molding machine, the heated coil, and barrel melt or soften the thermoplastic. The molten material was then forced through a nozzle to make a continuous profile of the desired. Extrude strands were cooled at room temperature and pelletized with the help of the cutter. The resulting pellets were kept in poly bags, and they were dried for 2 h in sunlight. The dried pellets were put into the hopper before being injection molded into the American Society for Testing, and the standard test specimens were made following the ASTM standard. All the specimens were molded using a manual injection molding machine. The melt temperature was kept below 150 °C to prevent the thermal degradation of fillers.

Three samples of each filler loading percentage (0%,10%,15%,20%) were prepared to calculate the mean value of each filler loading percentage specimens, i.e., tensile strength test specimen, wear test specimen, flame propagation rate test, and water absorption test specimen on injection molding machine by using dies according to ASTM standards, for studying the samples under tensile loading with D638 ASTM standards, for studying the samples underwater absorption with D570 ASTM standards, for studying the samples under the flame propagation rate (burning test) with D635 ASTM standards, for studying the samples under Wear test with G99 ASTM standards.

### 3 Results and Discussions

#### 3.1 Tensile Strength at Peak (Yield Stress)

When the percentage of filler is increased, stress at peak (yield) decreases, as shown in Fig. 1. Virgin HDPE shows maximum stress at yield, i.e., 23.7 MPa. At 10%, 15% and 20% tensile strength at the peak is 22.9 MPa, 20 MPa, 19 MPa, respectively. This shows the filler's inability to assist the transmission of the stress to filler particles from the matrix throughout deformation. The attributed behavior is due to the accumulation of the filler particles and poor interfacial adhesion between the filler and the matrix. This is because the interfacial area increases with an increase in filler content, which abridges interfacial bonding between matrix polymer (hydrophobic) and filler particle (hydrophilic) and thus the tensile strength at peak is decreased.



**Fig. 1** Tensile strength at the peak of walnut shell powder and HDPE composite tensile strength at break

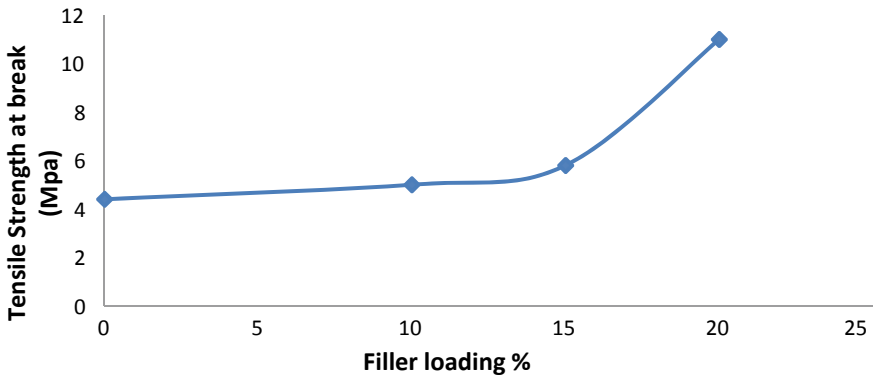


Fig. 2 Tensile strength at break of walnut shell powder and HDPE composite

The stress at break (tensile strength at break) of HDPE composites increases with an increase in filler percentage from 0 to 20%, which is 4.7–12.8 MPa as shown in Fig. 2. This behavior could be because of the toughness of natural filler property, which reduces the elongation character of high-density polyethylene and increases the tensile strength at break.

### 4 Elongation at Break

The change in the elongation property of filled HDPE due to filler loading is shown in Fig. 3. The figure also shows a decrease in the elongation at break of the HDPE composites on increasing the filler content of any particle size and leads to poor interfacial bonding. Increased brittleness and decreased elongation at the break are

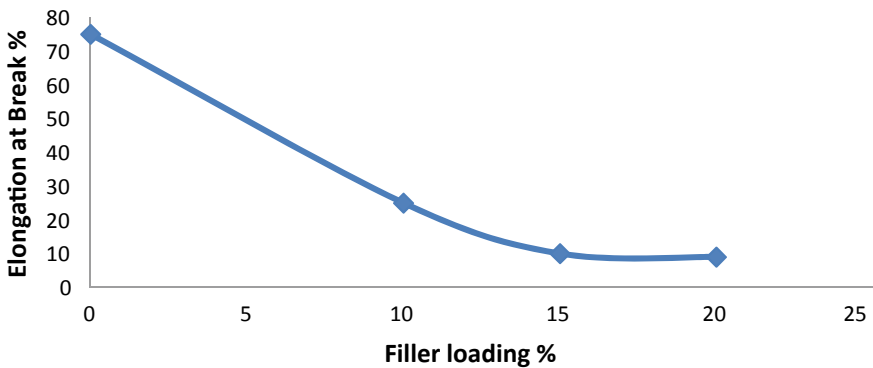
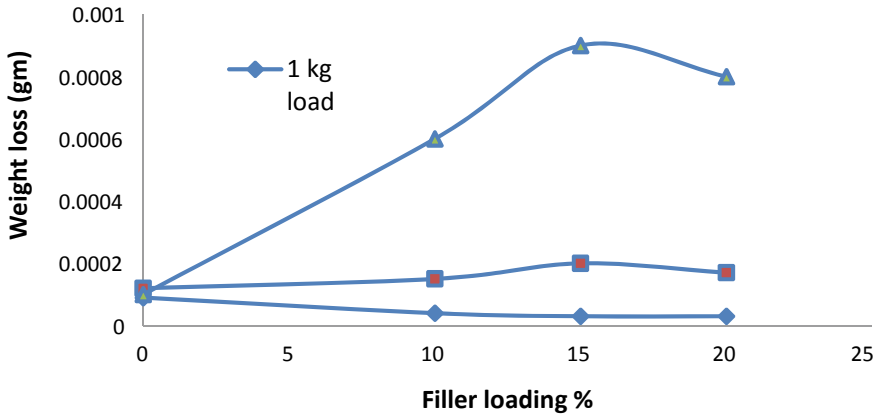


Fig. 3 Elongation at break of walnut shell powder and HDPE composite



**Fig. 4** Weight loss (gm) versus filler loading at different loads

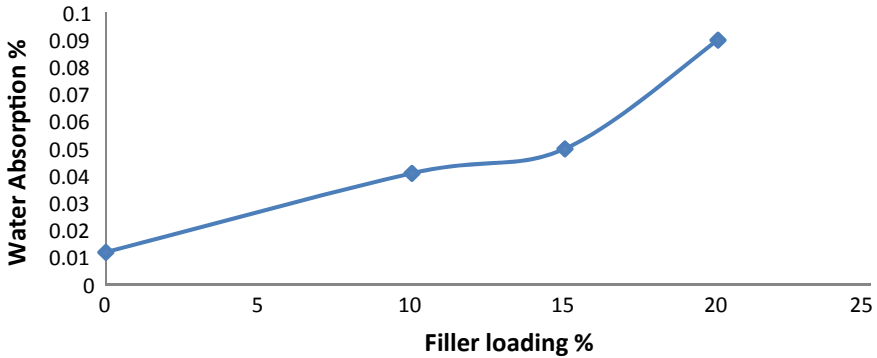
induced by partial separation of interfacial spaces between the polymer matrix and filler to obstruct stress propagation when tensile stress is loaded. Hence, the ductility of the material is measured by the elongation at the break.

#### 4.1 Wear Test

In Fig. 4, the load applied to the specimen is varied. When load applied is 1 kg, weight loss decreases with an increase in filler content. When the load applied on specimens is 2 kg, weight loss increases with an increase in filler loading. Similarly, weight loss increases at 3 kg of load. It may be due to the presence of micro spaces between the polymer matrix and natural filler particles. Generally, abrasion resistance is affected by the heat dissipation characteristics of the polymer. The type and amount of fillers added influence abrasion resistance. The bonding between the matrix and filler at the interfacial regions gets weakened due to the frictional heating at the contacting area and the normal load exerted by the abrasives over the composite. When the matrix failed to support the fibers, serious fiber removal could occur and thus wear rate increases rapidly. High wear and large wear particles formation is due to the fracture of polymer at higher sliding velocity.

#### 4.2 Water Absorption

The above figure shows the influence on polyethylene composites' water absorption behavior at different walnut shell powder filler content. A similar pattern of water absorption is observed by all the HDPE composites as shown in Fig. 5, i.e., As the filler



**Fig. 5** Water absorption% versus filler loading

content increases, the water absorption uptake also increases for all examined particle sizes of the walnut shell powdered filler. An increase in water absorption uptake of the polymer composite is also observed on increasing the particle size of the walnut shell powdered filler. The strong hydrophilic nature of the walnut shell with many hydroxyl groups within the fiber structure has been attributed to the behavior of a walnut shell as a natural fiber. The water absorption of the lignocellulosic materials is due to the hydrophilic nature of the walnut shells and leads in the emergence of hydrogen bonds between water molecules on the filler's cell wall and fillers.

### **4.3 Flame Propagation Rate**

It is being analyzed that the walnut shell powder is expeditious as filler, and with the reduction of the rate of burning of composite of HDPE and superior portion of walnut shell powder will bolster the combustion and thus enhanced the filler loading to make the environment by which the flame spread of composite decreases.

Proper dispersal of walnut shell powder filler inside the polymer matrix could result from the above behavior. It is also being observed that the energy required to commence burning in the composite system decreases due to the impotence of filler (Fig. 6).

## **5 Conclusion**

- The composite of the polymer, prepared using walnut shell powder and HDPE matrix, is synthesized successfully.
- Characteristic changes have been observed in tensile strength, wear rate, water absorption, and flame propagation rate of a composite.



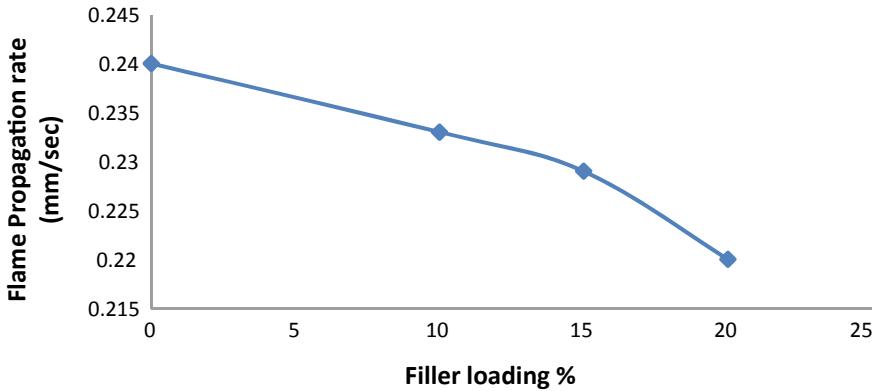


Fig. 6 Flame propagation rate(mm/sec) versus Filler loading

- Tensile strength at break increases at 20% filler, and tensile at peak decreases when filler percentage increases.
- In composite, when filler percentage increases, the Elongation percentage decrease.
- Wear and abrasion properties show the best result at 1 kg load.
- It is found that, as filler, walnut shell powder is inefficient in decreasing the burning rate of HDPE composite, and the flame spread of the composite increases at a good percentage of walnut shell fiber content.
- In case of water absorption, it is observed that the water absorption uptake of the polymer composite increases with an increase in the particle size of the walnut shell powdered filler.
- It is also concluded that walnut shell powder and HDPE composite are competent for lightweight application.
- Additionally, it is being analyzed that the applications in which the critical factor is a heavy load, the composite is not worthy. Moreover, it is also seen that as the tensile strength reduces, the adhesive forces among HDPE matrix and walnut shell powder become deficient or of low order.
- Twin co-rotating extruders for compounding should be used to ameliorate the fiber matrix interfacial bondings and enhance the composites' mechanical properties.

## 6 Validation of Results

A systematic and similar study of surface treatments' effect on the properties of PP/walnut shell fiber has been carried out by Ahmed J. Mohammed et al. [5], Tensile properties at peak decrease as an increase in the percentage of filler. A similar trend is observed by Ismail et al. [6] in lignocellulose filled composites. Furthermore, a

decrease in tensile strength shows a poor or low order adhesion between the polyethylene matrix and walnut shell powder. Increased brittleness is induced when tensile stress is loaded and partially separated micro spaces are created between the polymer matrix and the filler due to this poor interfacial bonding obstructing stress propagation. It is suggested that the composite's tensile strength can be enhanced with a coupling agent's assist. Significant work on polymer composites abrasive wear behavior has been done by Khan et al. [7]; they performed the abrasive wear study of natural fiber-filled epoxy composites. The wear/abrasion rate decreases when the load applied is 1 kg but gradually increases when the specimen's load is 2 kg and 3 kg.

The walnut shell's hydrophilic nature causes the water absorption of the HDPE/walnut shell composite materials. It results in hydrogen bonds forming between filler and water molecules on the filler's cell wall. Husseinsyah et al. [8] have reported a similar observation in filling polyester systems using coconut shells, i.e., an increase in filler content percentage; there is an increase in water absorption percentage. M.U Obidiegwu et al. [9] observed different results with polypropylene/walnut composite compared to this research, i.e., when increasing percentages, flame propagation rate increases. Furthermore, HDPE/ walnut shell powder composite shows a decrease in flame propagation rate when the percentage is increased. This is because the walnut shell powdered filler's inability decreases the energy required to start burning in the composite system, demonstrating that increasing the proportion of the walnut shells powder has a negative impact on the flame resistance and heat spread through the matrix polymer.

## References

1. Hassan, A.A., et al.: Mechanical and physical properties of PP and HDPE. *Engineering Sci.* **4**(2), 34–42 (2019)
2. Sapuan, S.M., Harimiand, M., Maleque, M.: Mechanical properties of epoxy/coconut shell filler particle composites. *Arab. J. Sci. Eng.* **28**(2), 171–182 (2003)
3. Nor Khairusshima, M.K. et al.: Tool wear and surface roughness on milling carbon fiber-reinforced plastic using chilled air. *J. Asian Scientific Res.* **2**(11), 593 (2012)
4. Raj, R.G., Kokta, B.V., Daneault, C.: Wood flour as a low-cost reinforcing filler for polyethylene: studies on mechanical properties. *J. Mater. Sci.* **25**(3), 1851–1855 (1990)
5. Mohammed, A.J.: Study the effect of adding powder Walnut shells on the Mechanical Properties and the flame resistance for Low Density Polyethylene (LDPE). *Int. J. Sci. Tech.* **3**(1), 18–22 (2014)
6. Ismail, H., Nizam, J.M., Abdul Khalil, H.P.S.: Material properties the effect of a compatibilizer on the mechanical properties and mass swell of white rice husk ash filled natural rubber/linear low density polyethylene blends. *Polym Test* **20**, 125–133 (2001)
7. Khan, A., Ahmad, M.A., Joshi, S., Al Said, S.A.F.: Abrasive Wear Behavior of Chemically Treated Coir Fibre Filled Epoxy Polymer Composites. *American J. Mech. Eng. Automation* **1**(2), 1–5 (2014)
8. Husseinsyah, S., Mostapha, M.: The effect of filler Content on properties of coconut shell filled polyester composites. *Malaysian Polymer J.* **6**(1), 87–97 (2011)
9. Obidiegwu, M.U., et al.: The effect of walnut shell powder on the properties of polypropylene filled composite. *Int. Asian Res. J.* **2**(1), 22–29 (2014)

# Grey-Fuzzy Modelling and Analysis of Optimizing Turning Process Parameters for Stainless Steel Material



V. Jegan Prasath, R. Karthick Kannan, R. Shanmuga Mugesh, N. Sugeesh, S. R. Sundara Bharathi, and A. Arul Marcel Moshi

## 1 Introduction

All types of Stainless steel materials are used in the chemical, pharmaceutical, health, textile, food production, nuclear and biomedical industries for varieties of applications. They have excellent mechanical characteristics even under high-temperature conditions; and also have better oxidation and corrosion resistance properties [1]. Austenitic stainless steel is one of the important type of stainless steel class materials, which is most commonly employed in the production facilities. Generally, austenitic stainless steel has a better mechanical properties as well as superior corrosion resistance [2]. Austenitic stainless steel is the majorly utilized steel material in the production industries, nearly 70% over the other steel grades [3]. Austenitic stainless steels find application in cutlery, tubing industries as well as in the production of mechanical components like springs, screws, nuts and bolts because of their high strength and corrosion resistance [4]. While performing turning process on any material, it is very important to correctly consider the cutting parameters so that one can achieve superior cutting performance. The mechanism behind the generation of surface roughness is a complicated one and which is process dependent [5]. The optimal selection of turning process parameters is always a leading phenomenon to produce efficient products. In this research field, surface roughness and material removal rate are normally considered as the significant output responses [6]. Fuzzy logic modelling is followed by the researchers to obtain an effective way of interpreting the unclear data. Modern researchers had hybridized grey relational analysis with the fuzzy logic modelling to create a great and flexible platform to improve the production processes [7]. Multi-response optimization tools such as grey relational analysis and grey-fuzzy reasoning grade analysis are employed to identify the

---

V. J. Prasath · R. K. Kannan · R. S. Mugesh · N. Sugeesh · S. R. S. Bharathi (✉) · A. A. M. Moshi  
Department of Mechanical Engineering, National Engineering College, Kovilpatti 628503, Tamil Nadu, India

**Table 1** Independent parameters considered at three levels

Parameters	Level 1	Level 2	Level 3
Spindle speed (m/min)	200	400	600
Feed rate (mm/rev)	0.1	0.125	0.15
Depth of cut (mm)	0.1	0.2	0.3

better input parameter setting that simultaneously optimize the surface roughness and material removal rate [8].

From the literature study, the significant usage of SS303 material in industries was understood. Also, the importance of optimizing the CNC turning process parameters was understood. With this motivation, a multi-objective optimization study was planned to perform on speed, feed and depth of cut using grey-fuzzy modelling technique.

## 2 Materials and Methods

In the current study, spindle speed, feed rate and depth of cut are chosen as the primary independent factors at three distinct levels, which are represented in Table 1. The mechanical properties and chemical composition of SS303 were referred from literature [9]. Physical vapour deposited carbide inserts were used for the machining work. The experimental analysis was performed based on Taguchi's  $L_9$  orthogonal array design. The output responses considered for optimizing the input parameters are MRR and SR.

## 3 Optimization Analysis

### 3.1 Grey Relational Analysis

Generally, a system containing few known and few unknown information is termed as grey system. For obtaining the optimal results for more than one output responses simultaneously with a common input parameter combination, grey relational analysis is followed [10–12]. The ultimate objectives of the present study are (i) minimization of SR and (ii) maximization of MRR on the finished product machined by CNC turning process [8, 13]. Thus, the responses SR and MRR are simultaneously considered for the optimization analysis, for which grey relational analysis is followed.

### 3.2 Grey-Fuzzy Logic

In fuzzy logic modelling, raw information about a process is correlated by mimicking the way of human reasoning. In fuzzy modelling, the input data and arrived experimental results are fed as normalized values, i.e. between ‘0’ and ‘1’. This technique is used to predict the output values for various input factor settings within the range inspite of not performing the actual experimentation. It is an efficient mathematical model in which, the fuzzifier uses various membership functions to fuzzify the input factors. For the present study, grey relational coefficient values are considered as the input parameters for the grey-fuzzy reasoning grade analysis. The normalized values of the input and output data are correlated with the help of fuzzy inference engine. At the end of the process, the defuzzifier helps to convert the fuzzy value into a grey-fuzzy reasoning grade.

## 4 Results and Discussion

Experimentation was performed based on the  $L_9$  orthogonal array design, and the results for SR and MRR are obtained and represented in Table 2. Since the considered output response values are with different units, each set of responses are normalized between ‘0’ and ‘1’ using the formula referred from literature [14, 15]. In the next step of GRA, the deviation sequence values are predicted for normalized output response values by quantifying the variation between each value and their maximum response value [9]. The normalized values and deviation sequence corresponding to the output responses for the nine experimental set are represented in Table 2.

**Table 2** Output responses and grey relational analysis results

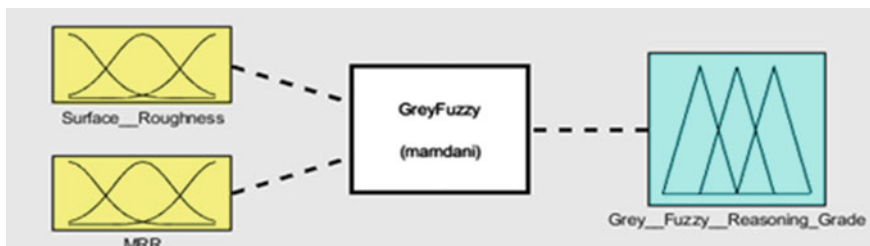
Output responses		1	2	3	4	5	6	7	8	9
SR	Exp	0.240	0.250	0.280	0.210	0.380	0.370	0.230	0.290	0.220
	Nor	0.824	0.765	0.588	1.000	0.000	0.059	0.882	0.529	0.941
	Devi	0.176	0.235	0.412	0.000	1.000	0.941	0.118	0.471	0.059
	GRC	0.739	0.680	0.548	1.000	0.333	0.347	0.810	0.515	0.895
MRR	Exp	2.000	5.000	9.000	8.000	15.00	6.000	18.00	8.000	18.00
	Nor	0.000	0.188	0.438	0.375	0.813	0.250	1.000	0.375	1.000
	Devi	1.000	0.813	0.563	0.625	0.188	0.750	0.000	0.625	0.000
	GRC	0.333	0.381	0.471	0.444	0.727	0.400	1.000	0.444	1.000
GRG	0.536	0.530	0.509	0.722	0.530	0.373	0.905	0.480	0.947	
Rank	4	5	7	3	6	9	2	8	1	

In the third step, grey relational coefficient values are calculated using the regular procedure mentioned in the literature [16, 17]. Then, grey relational grades are calculated just by taking the average of the grey relational coefficients of the output responses for each set [18]. The calculated values are represented in Table 2. Based on the GRG values, the results are ranked from '1' to '9'. Rank '1' refers to the most optimal input factor combination.

GRC values predicted from the grey relational analysis are fed as the input factors for developing the grey-fuzzy model. The corresponding grey relational grades for the corresponding nine experimental set are fed as the output responses. The developed grey-fuzzy Mamdani model is as shown in Fig. 1. All the input and output values are not directly fed; instead of that, they are included through the fuzzy rules. For that, the inputs are considered at five different fuzzy levels such as (a) Very Small—VS, (b) Small—S, (c) Medium—M, (d) Large—L and (e) Very Large—VL. The output responses are considered at nine different fuzzy levels such as (i) Tiny—T, (ii) Very Small—VS, (iii) Small—S, (iv) Small Medium—SM, (v) Medium—M, (vi) Medium Large—ML, (vii) Large—L, (viii) Very Large—VL and (ix) Huge—H. The developed grey-fuzzy rules are simply represented in Table 3.

The GRG can be predicted using the generated fuzzy logic analysis. The defuzzifier converts the fuzzified value into non-fuzzified value. The converted non-fuzzified value is termed as grey-fuzzy reasoning grade. Trapezoidal type of membership function is used as the membership function in the current study. Figure 2 represents the developed MF of grey-fuzzy reasoning grade.

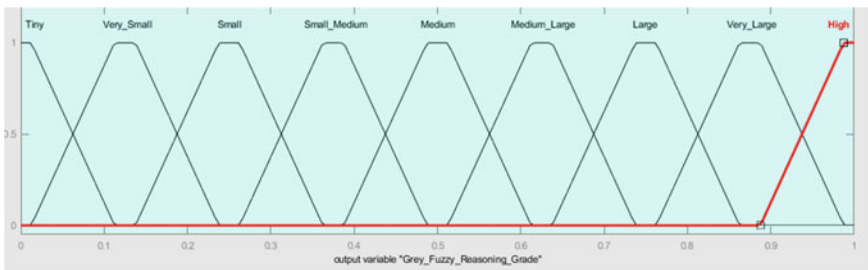
Figure 3 represents the graphical representation of grey-fuzzy reasoning procedure for the Exp. No. 1, in which the generated grey-fuzzy rules are represented in rows, and the columns represent the inputs and grey-fuzzy reasoning grade. The locations of trapezoidal zones represent the predicted fuzzy logic sets for each set of input and the corresponding output value. The height of the trapezoidal zone represents the fuzzy membership value corresponding to the fuzzy set. For the Ex. No. 1, the input values of grey relational coefficient of surface roughness and MRR are 0.739 and 0.333, respectively; the grey-fuzzy reasoning grade value obtained for Ex. No. 1 was obtained from the generated model as 0.54.



**Fig. 1** Developed Fuzzy logic model for the machining responses

**Table 3** Fuzzy rule for Grey-fuzzy reasoning grade

S. no	MF for GRC of SR	MF for GRC of MRR	Grey-fuzzy reasoning grade	S. no	MF for GRC of SR	MF for GRC of MRR	Grey-fuzzy reasoning grade
1	VS	VS	T	14	M	L	ML
2	VS	S	VS	15	M	VL	L
3	VS	M	S	16	L	VS	SM
4	VS	L	SM	17	L	S	M
5	VS	VL	M	18	L	M	ML
6	S	VS	VS	19	L	L	L
7	S	S	S	20	L	VL	VL
8	S	M	SM	21	VL	VS	M
9	S	L	M	22	VL	S	ML
10	S	VL	ML	23	VL	M	L
11	M	VS	S	24	VL	L	VL
12	M	S	SM	25	VL	VL	H
13	M	M	M				



**Fig. 2** MF for grey-fuzzy reasoning grade

After the successful generation of grey-fuzzy model, the available set of grey relational coefficient values are fed and checked for the entire experimental combinations. The grey-fuzzy reasoning grades obtained from the developed model are represented in Table 8. The deviation of the grey-fuzzy reasoning grade values from the actual grey relational grade values are computed and represented in Table 4, which is found to be very minimal or negligible.

Table 4 shows that Ex. No. 9 indicates the best combination of process parameters for machining with best quality in short time. For considering the effect of uncontrollable factors in the experimental results, signal-to-noise ratio values for the predicted grey-fuzzy reasoning grade values are calculated using Minitab software and the main effect plot for the S/N ratio values of the grey-fuzzy reasoning grades is arrived as shown in Fig. 4.

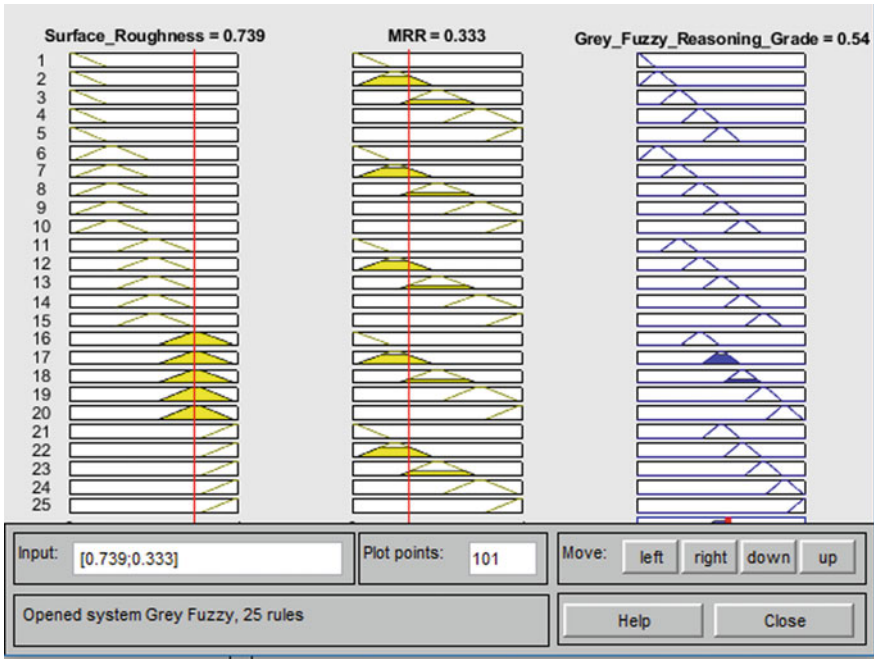


Fig. 3 Fuzzy logic rules checker for the model exp. no. 1

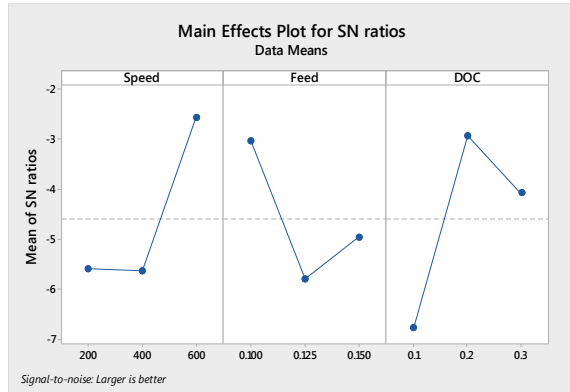
Table 4 Grey-fuzzy reasoning grades and their ranks

Ex. no	Grey-fuzzy reasoning grade	Rank	Actual grey relational grade	% of deviation from actual GRG
1	0.540	4	0.536	0.75
2	0.529	6	0.530	0.19
3	0.515	7	0.509	1.80
4	0.727	3	0.722	0.69
5	0.539	5	0.530	1.70
6	0.374	9	0.373	0.27
7	0.879	2	0.905	2.87
8	0.477	8	0.480	0.63
9	0.904	1	0.947	4.54

From the main effect plot drawn for the grey-fuzzy reasoning grade values, the optimal parameter combination has been found to be (A3-B1-C2) [19]. For the found out optimal condition, a new experimentation was performed and the results were arrived as follows: surface roughness: 21  $\mu\text{m}$  and MRR: 12  $\text{cm}^3/\text{min}$ . The results of ANOVA show that the process parameter spindle speed has the most influence on



**Fig. 4** Main effect plot for the grey-fuzzy reasoning grade values



obtaining best surface finish for the CNC turned SS303 (37.91%). The influence of other parameters was noted to be 36.44% (depth of cut) and 20.60% (Feed rate) [20].

## 5 Conclusions

The optimal combination of independent parameter setting for turning the SS 330 material with PVD coated insert tools using the generated grey-fuzzy model has been investigated in the present study. The best performance characteristics were obtained with an optimal setting of **A3-B1-C2** (200 m/min cutting speed—0.1 mm/rev feed rate—0.2 mm depth of cut). ANOVA results revealed that spindle speed (37.91%) and depth of cut (20.60%) are the predominant factors which affect the SR and MRR on turning SS303.

## References

- Asiltürk, I., Neseli, S.: Multi response optimization of CNC turning parameters via Taguchi method-based response surface analysis. *Measurement* **45**(4), 785–794 (2012)
- Korkut, I., Kasap, M., Çiftci, I., Seker, U.: Determination of optimum cutting parameters during machining of AISI 304 austenitic stainless steel. *Mater. Des.* **25**(4), 303–305 (2004)
- Trent, E.M., Wright, P.: *Metal cutting*, 4th edn. Butterworths Press, Woburn (2000)
- Xavior, A.M., Adithan, M.: Determining the influence of cutting fluids on tool wear and surface roughness during turning of AISI 304 austenitic stainless steel. *J. Mater. Process. Technol.* **209**(2), 900–909 (2009)
- Nalbant, M., Gokkya, H., Sur, G.: Application of Taguchi method in the optimization of cutting parameters for surface roughness in turning. *Mater. Des.* **28**(4), 1379–1385 (2007)
- Gaitonde, V.N., Karnik, S.R., Davim, J.P.: Multiperformance Optimization in Turning of Free-Machining Steel Using Taguchi Method and Utility Concept. *J. Mater. Eng. Perform.* **18**, 231–236 (2009)

7. Lin, C.L., Lin, J.L., Ko, T.C.: Optimisation of the EDM process based on orthogonal array with Fuzzy Logic and Grey relational analysis method. *Int. J. Adv. Manufacturing Tech.* **19**, 271–277 (2002)
8. Laxane, R.B., Bhide, R.S., Patil, A.S., Sane, S.G.: Characterisation of chromium nitride physical vapour deposition coating on diesel engine pistons. *Surf. Eng.* **22**(1), 78–80 (2006)
9. Bharathi, S.R.S., Ravindran, D., Moshi, A.A.M.: Multi response optimization of CNC turning parameters on Austenitic stainless steel 303 using Taguchi based Grey Relational Analysis. *Trans. Can. Soc. Mech. Eng.* **44**(4), 592–601 (2020)
10. Rajesh, M., Moshi, A.A.M., Mathew, J., Gowthaman, K.: Hybrid optimization of turning parameters using Copras-Taguchi technique. *Int. J. Appl. Eng. Res.* **11**(3), 719–728 (2016)
11. Logesh, K., Hariharasakthisudhan, P., Moshi, A.A.M.: Optimizing the ultrasonication effect in stir-casting process of aluminum hybrid composite using desirability function approach and artificial neural network. *Proceedings of the Institution of Mechanical Engineers, Part L: J. Mat.: Design and Appl.* (2021). <https://doi.org/10.1177/14644207211025706>.
12. Bharathi, S.R.S., Ravindran, D., Moshi, A.A.M., Rajeshkumar, R., Palanikumar, R.: Multi objective optimization of CNC turning process parameters with Acrylonitrile Butadiene Styrene material. *Materials Today Proceedings* **27**(3), 2042–2047 (2020)
13. Moshi, A.A.M., Madasamy, S., Bharathi, S.R.S., Periyannayaganathan, P., Prabakaran, A.: Investigation on the mechanical properties of sisal—banana hybridized natural fiber composites with distinct weight fractions. *AIP Conference Proceedings* 2128, 020029 (2019)
14. Hariharasakthisudhan, P., Moshi, A.M.M., Bharathi, S.R.S., Logesh, K.: Regression and Grey Relational Analysis on friction and wear behavior of AA6061/Al<sub>2</sub>O<sub>3</sub>/Si<sub>3</sub>N<sub>4</sub>/graphite hybrid nanocomposites. *Materials Res. Exp.* **6**, 085017 (2019)
15. Selvan, S.A., Ravindran, D., Moshi, A.A.M.: Multi-criteria optimization of machining parameters for wirecut electrical discharge machined taper parts of inconel 825 alloy. *Sylwan* **163**, 77–93 (2019)
16. Moshi, A.A.M., Ravindran, D., Bharathi, S.R.S., Rex, F.M.T., Kumar, P.R.: TIG welding process parameter optimization for Aluminium Alloy 6061 using Grey Relational Analysis and Regression Equations. In: *Numerical Optimization in Engineering and Sciences, Part of the Advances in Intelligent Systems and Computing book series (AISC, volume 979)*, 412–425 (2020)
17. Bharathi, S.R.S., Ravindran, D., Moshi, A.A.M.: Experimental investigation of surface roughness and chip morphology during machining of austenitic stainless steel 303 with PVD coated (TiAlN) insert. *Surface Topography: Metrology and Prop.* **9**, 025022 (2021)
18. Arulselvan, S., Ravindran, D., Moshi, A.A.M., Prince, D.: Optimization of surface roughness, material removal rate and taper Error for wirecut electrical discharge machined taper parts of inconel 825 alloy. *J. Balkan Tribological Assoc.* **25**(4), 1028–1037 (2019)
19. Senthilkumar, S., Karthick, A., Madavan, R., Moshi, A.A.M., Bharathi, S.R.S., Saroja, S., Dhanalakshmi, C.S.: Optimization of transformer oil blended with natural ester oils using Taguchi-based grey relational analysis. *Fuel* **288**, 119629 (2021)
20. Selvan, S.A., Ravindran, D., Moshi, A.A.M., Kumar, D.V.: Process-parameter optimization of WEDM with inconel 825 alloy using GRA. *Mat. Tech.* **55**, 219–229 (2021)

# The Study of Kenaf/E-Glass Fibre Content on Mechanical Properties of Biopolymer Cashew Nut Shell Liquid/Epoxy Matrix Blended Composites



R. Prabhakaran, R. Venkatakrishnan, and N. Narmada Devi

## 1 Introduction

Fibre-strengthened polymer composite materials are being utilized for creating transportation vehicle body parts, building development works, marine structures and air space application structures widely [1]. In the new recent years, the utilization of composite materials has been expanded in businesses step by step. Polymer composites are progressively being utilized alternative for conventional metal materials because of their light weight, high solidness to weight proportion and higher solidarity to weight proportion [2]. Different attributes of composite materials, for example, grating obstruction, complete surface profile, improved exhaustion flexibility strength and noble cause execution caused fast expansion in the use of composite materials [3]. Regardless, to additionally broaden the use of composite materials, the presence of such structures should be perceived under particular mechanical stacking conditions going from semi-static to dynamic and effect stacking [4]. Cashew nut shell liquid (CNSL), an extraction from cashew nut shell has a wide range of functional products. Cost of raw materials is better advantage over conventional synthetic phenolic resins and gives excellent properties to meet the improving needful for quality and durability in bonding between surfaces. The CNSL resins are primarily used in the production of different kinds of end products in the various industries such as Polymer, coating paints, synthetic plastic, etc. These resins material give a higher performance to composite materials [5].

---

R. Prabhakaran (✉) · R. Venkatakrishnan · N. N. Devi  
Department of Mechanical Engineering, IFET College of Engineering (Autonomous),  
Villupuram, Tamil Nadu, India

© The Author(s), under exclusive license to Springer Nature Singapore Pte Ltd. 2022  
S. K. Natarajan et al. (eds.), *Recent Advances in Manufacturing, Automation, Design  
and Energy Technologies*, Lecture Notes in Mechanical Engineering,  
[https://doi.org/10.1007/978-981-16-4222-7\\_40](https://doi.org/10.1007/978-981-16-4222-7_40)

339

## 2 Fibre and Resin Materials of Composite

### 2.1 Sources of Materials

Kenaf/E-glass fibres are easily available resources in market. Both fibres are stretching in the way of woven mat. The orientations of fibres are perpendicular stands of fibre mats. The matrix materials of CNSL/Epoxy resin along with Hardener were bought from private manufacturing company [6].

### 2.2 Processing of Chemically Alkali Treatment of Fibres

In alkaline chemical treatment of natural fibres is dipped in Sodium hydroxide solution for a 24 h of time. The 50 g of Sodium hydroxide mixed to one litre of water; natural fibres dipped in these alkali solutions. After some given hours, the fibres are deeply washing in running water to remove NaOH in surface of the fibres. These chemical treatments promote to induce the improvement of surface roughness, obtained results in good mechanical interlocking bonds [7].

### 2.3 Methods of Preparation of Composite Materials

The Kenaf/E-glass fibre composite materials which fabricated as per prepared percentage of samples composition as shown in Table 1. Mostly matrix material which has higher percentage when compared to fibre reinforcement, because of good wettability of the composites. From these Table 1 as shown, 30% of fibre and 70% of resin were taken. Further 70% of resin can be divided as per blending ratios of 0, 20, 40, 60, 80 and 100% of CNSL/Epoxy resin [8]. The mixing ratio of resin with hardener is 10:1 ratio for curing of liquid form to solid form of resin materials. These are primary preparation of composite materials. And next preparation is

**Table 1** Characterization of preparation of samples

Samples	Fibre 30%		Resin 70% (g)	Blended polymer		
	kenaf (g)	E glass (g)		Cnsl	EPOXY	Cnsl + EPOXY
A	60	60	280	0	280	0% + 100%
B	60	60	280	56	224	20% + 80%
C	60	60	280	112	168	40% + 60%
D	60	60	280	168	112	60% + 40%
E	60	60	280	224	56	80% + 20%
F	60	60	280	280	0	100% + 0%

**Fig.1** Prepared 80% CNSL sample



mould preparation as given required size of samples. The size of mould is 300 mm of length, 300 mm of breadth and 10 mm of thickness to fabricate rectangular plate of composite materials. Before applying of resin, polyvinyl acetate or spray wax is coated in outer surface of the mould for easy removal of fabricated composite after curing. After coating of wax, initially first layer of resin was applied to wettability of fibres. These composites consist of six layers of lamina of Kenaf/E-glass woven mat fibres. Layer by layer resin and fibre are compressed by dead weight above the film sheets of mould. After curing of composite materials, it is removed from mould surface without cracking/ damages in fibres as shown in Fig. 1. Table 1 shows that different samples preparation of composite materials.

#### ***2.4 Various Testing of Composites***

The experimental testing of natural fibre composite materials involves a wide extends of testing types and test in a variety of different environments. The main objective of the mechanical testing of natural composite is the examination of mechanical parameters such as strength, stiffness and other physical properties. Elasticity, flexural bending strength and impact strength property were obtained by ASTM testing standards machines. Six specimen samples were tried for every creation, and normal outcomes were utilized. Rigidity, flexural strength and Impact strength esteems were resolved for different examples and are appeared.

### 3 Results and Conversation

#### 3.1 Longitudinal of Tensile Strength

Longitudinal of tensile strength is the amount of load or stress that can be withstood by a composite material before it stretches and cracks. The longitudinal tensile strength of composite materials is determined mostly by the strength and volume content of the fibre reinforcement. For tensile strength, specimens are prepared as per the ASTM standard of ASTM D3039. Figures 2 and 3 show that before and after testing of tensile test samples. The results were obtained after carried out specimen test, and the data are plotted in graph shown in Fig. 4. From these plotted graph data, the obtained results CNSL resin added to epoxy matrix which can be reduce brittle property of epoxy resin. From specimen (A) has higher value when compared to specimen of pure CNSL resin.

Fig.2 Tensile specimen

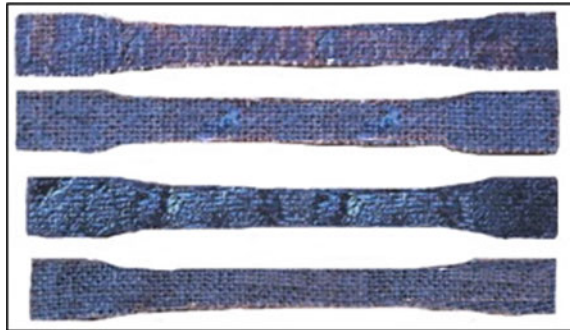


Fig.3 Tensile specimen after tensile test



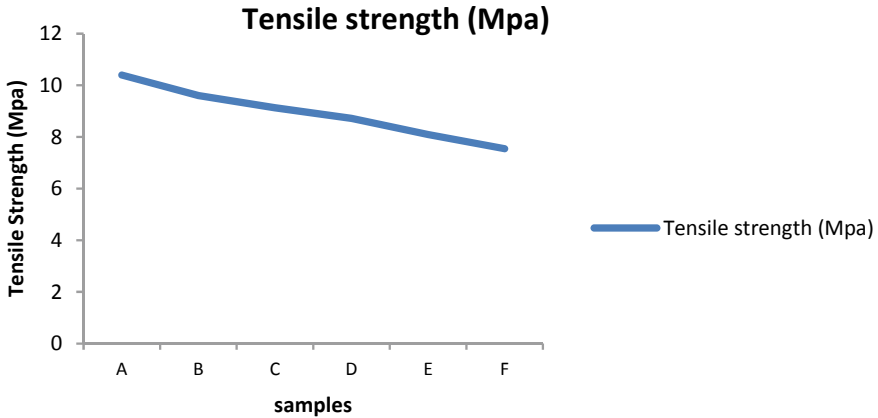


Fig.4 Different proportion of CNSL/Epoxy Composite on tensile strength

### 3.2 Flexural Test

The flexural properties of composite materials can be varied depends upon rate strain, working temperature and thickness of specimens. For flexural strength, specimens are prepared as per the ASTM standard of ASTM D7264. This experiment was carried out by three point bend test. The results were obtained after carried out flexural specimen test, and the values are plotted in graph shown in Fig. 5. From these plotted graph data, the obtained results CNSL resin added to epoxy matrix which can be reduce brittle property of epoxy resin. From specimen (A) has higher value when compared to specimen of pure CNSL resin. The epoxy resin which has higher flexural strength because of toughness of materials.

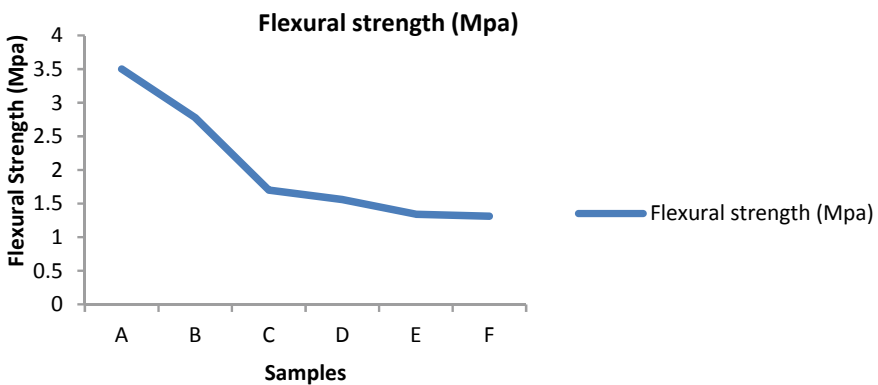
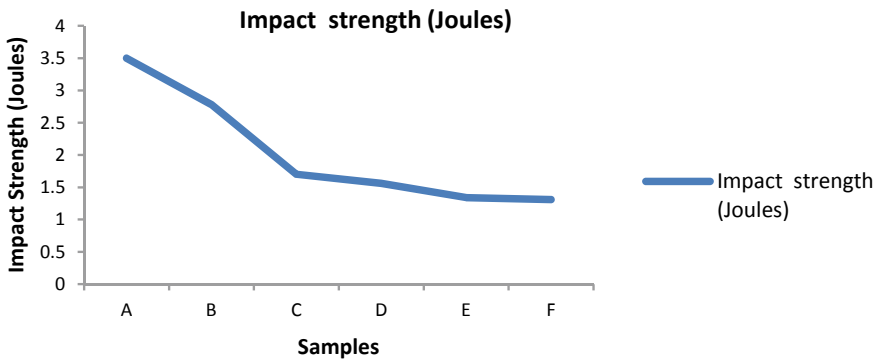
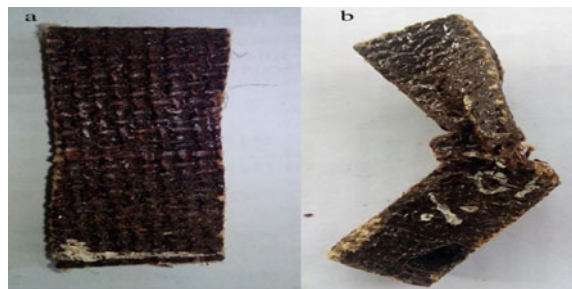


Fig.5 Different proportion of CNSL/Epoxy Composite on flexural strength

### 3.3 Drop Weight Impact Test

The impact resistance of composite materials can be performed with a swinging or a dropping known weight. For impact strength, specimens are prepared as per the ASTM standard of ASTM D7136. The results were obtained after carried out impact specimen test, and the values are plotted in graph shown in Fig. 6. From these plotted graph data, the obtained results CNSL resin added to epoxy matrix which can be reduce brittle property of epoxy resin. From specimen (A) has higher value when compared to specimen of pure CNSL resin. The epoxy resin which has higher impact strength because of toughness of materials and CNSL resin has high viscosity and ductile materials. The pure CNSL composite materials absorb impact load to restrict crack formation of specimens. Figure 7 indicates the impact strength of different proportion of CNSL/Epoxy composite which advocates this concept.

**Fig.6** Impact specimen **a** before impact test **b** after impact test



**Fig.7** Different proportion of CNSL/Epoxy composite on impact strength



## 4 Conclusion

The combination of kenaf/E glass fibre reinforcement with various blended matrix ratio of CNSL/Epoxy matrix composite has been fabricated. Testing results of various strength of tensile, flexural and impact strength of natural composite can be examined. From the results, the elongation of tensile property of pure epoxy matrix composite which higher than the 100% CNSL resin materials. CNSL resin highly resists impact load on materials due to ductile property. The biodegradable cashew nut shell liquid (CNSL) improves elasticity as extent increments because of changing fragile into malleable property in those composite materials.

## References

1. Njokua, R.E., Olib, I., Agbiogwuc, D.O., Agud, C.V.: Effect of alkali treatment and fiber content variation on the tensile properties of coir fiber reinforced CNSL composite. *Nigerian J. Tech.* **31**, 107–110 (2012)
2. Mwaikamboand, L.Y., Ansellb, M.P.: Hemp fiber reinforced cashew nut shell liquid Composites. *Composites Sci. Tech.* **63**, 1297–1305 (2003)
3. Nishino, T., Hirao, K., Kotera, M., Nakamae, K., Inagaki, H.: Kenaf reinforced biodegradable composite. *Compos Science Tech.* **63**, 1281–1286 (2003)
4. Sanadi, A.R., Prasad, S.V., Rohatgi, P.K.: SEM observations on the origin of toughness of natural fiber-polyester composites. *J. Mat. Sci. Let.* **5**, 395–396 (1986)
5. Cheung, H.Y, Mei, P.H, Lau, K.T., Hui, D.: Natural fiber-reinforced composites for bio-engineering and environmental engineering application. *Composites Part B* **40**, 655–663 (2009)
6. Venkatakrishnan, R., Senthilvelan, T., Vijayakumar, T.: Fabrication and mechanical properties of hybrid natural composite. *Appl. Mechanics Mat.* **813**, 57–61(2015)
7. Gopinath, T., Senthilvelan, T., & Venkatakrishnan, R.: Characterization of hybrid matrix natural fibre composite. *ARPN J. Eng. Appl. Sci.* **11**(12), June (2016)
8. Venkatakrishnan, R., Prabhakaran, R., Narmada Devi, N.: The effect of e-waste particle on mechanical behavior of particulate reinforced epoxy matrix composite. *IOP Conf. Ser.: Earth Environ. Sci.* **573**, 012013

# Study on Mechanical Behaviours of Newly Formulated Aluminium Alloy (6082) Reinforced with Boron Carbide and Rice Husk Ash



V. Thirumaran, M. Ganesh, K. Ganesha Balamurugan, and M. Sutharsan

## 1 Introduction

Aluminium-based matrix composites are famous for their extraordinary combination of mechanical and tribological properties which are hardly achievable due to excess usage of metals. Metal matrix composites based on aluminium are useful in the design of modules in, and many more, marine structures, boats, automotive and equipment, combat assemblies, leisure and recreation. Low strength and low melting point are still a concern. Metal matrix composites (MMCs) have improved greatly properties, including high specific strength, specific module, damping ability and strong wear resistance compared to unreinforced alloys. Composites containing low density and low cost reinforcements seem to be of growing interest. Rice husk ash (RHA) [1–3] is a tremendous environmental hazardous material and harms the land and the surrounding area in which it is deserted. The atmosphere is thus safe from such waste. Its excellent combination of properties such as good wear, low thermal expansion coefficient, high specific strength, rigidity, corrosion and high temperature resistance, among others, is due to the well-recognized good performance in operation and consequent high demand for aluminium metal matrix composites (AMCs). The density [4–6] of B<sub>4</sub>C (2.52 g/cm<sup>3</sup>) is lower than that of aluminium, and its total density is decreased by adding B<sub>4</sub>C to RHA (1.63 g/cm<sup>3</sup>) based al6082-based metal matrix composite [7–10] and the other characteristics will be further strengthened.

---

V. Thirumaran (✉) · M. Ganesh · K. Ganesha Balamurugan · M. Sutharsan  
IFET College of Engineering, Villupuram, Tamilnadu 605108, India

© The Author(s), under exclusive license to Springer Nature Singapore Pte Ltd. 2022  
S. K. Natarajan et al. (eds.), *Recent Advances in Manufacturing, Automation, Design and Energy Technologies*, Lecture Notes in Mechanical Engineering,  
[https://doi.org/10.1007/978-981-16-4222-7\\_41](https://doi.org/10.1007/978-981-16-4222-7_41)

347

## 2 Materials and Methods

### 2.1 Matrix Materials

The 6082 aluminium alloy is a moderate alloy with outstanding strength and corrosion resistance. With Al 0.8 Mg 0.9 Si 0.8 Mn is its main composition. The higher strength aluminium alloy (Al) 6082 has substituted the aluminium alloy (AA) 6061 in different applications as a comparatively recent alloy. An addition of large amounts of manganese makes the alloy stronger. It is indeed usually heat treated to generate tempers with a higher strength but lower ductility, but it cannot be work hardened. Al 6082 is most widely used in military-based application, ship building structures, towers and motorboats due to high corrosion resistances.

### 2.2 Reinforcements

**Boron carbide (B<sub>4</sub>C).** Boron carbide's tendency to withstand neutrons without producing long-lived radio nuclides makes it desirable in nuclear plants as an absorbent for neutron bombardment. The covering, control rod and close down pellets are nuclear applications of boron carbide. Boron carbide is also powdered inside control rods, in order to increase its surface area. One of the toughest materials known is boron carbide, ranked third below diamonds and spherical beryllium nitride. The density of B<sub>4</sub>C is 2.52 g/cm<sup>3</sup>. Due to reduction in density the mechanical properties of newly formulating alloy come reduced its density and increase its strength-to-weight ratio.

**Rice husk ash (RHA).** In recent days investigation found that the rice husk ash contains more amorphous silica (80–95%) in their ash particles. It makes the silica to convert and acts like a cristobalite in the forming cluster and increase the bonding capacity of a particles. The density of an RHA is much lesser with compared to Al6082, which shows reduction in density and increases in bonding and clusters to its formulation of a metal matrix composites. RHA is most widely preferred to reduce the agro waste and eco-friendly to environment (Table 1).

**Table 1** Chemical composition of the RHA compound/element wt%

Component	Percentage (%)
Silica (SiO <sub>2</sub> )	90.23
Carbon (C)	4.4
Calcium-oxide (CaO)	2.53
Potassium oxide (K <sub>2</sub> O)	1.40
Haematite (Fe <sub>2</sub> O <sub>3</sub> )	1.44



**Fig. 1** Blending of B<sub>4</sub>C & RHA with Al6082

The RHA is rinsed well and dried for around three days, and it is burned with a charcoal burner after dried for long days and maintained around 300 °C. The roasted RHA is ground with a mixer, and powdered particles are made small in microstructure particles. And after that it is preheated around 600 °C for 7 h before the preparation of blending of powder components. The silica is more in ash, and thus, it will act as a fine filler to that reinforcement materials and forms a fine blending reduces its fine porosity at different compositions. Figure 1 shows the blended particles with aluminium.

### 2.3 Samples Preparation

From the previous investigation, we tabulated various compositions of adding reinforcement with the based matrix material. And it is tabulated in Table 2. The total percentage of variation in reinforcement varies from 0 to 20 wt% of overall weight calculation of newly formulated alloy.

**Table 2** Composition of newly formulated Al6082-B<sub>4</sub>C-RHA

Sample No	Al6082 (%wt)	RHA (%wt)	B <sub>4</sub> C (%wt)
1	80	2.5	17.5
2	80	5	15
3	80	7.5	12.5
4	80	10	10
5	80	12.5	7.5
6	80	15	5
7	80	17.5	2.5
8	80	20	0
9	80	0	20



**Fig. 2** Compaction press, crucible, die and ejected specimen

**Development of composites.** In this work we had taken Al6082 as a matrix material, and B<sub>4</sub>C and RHA were selected as reinforcement material to fabricate composite by using powder metallurgy technique. The blend is prepared for different compositions of each powder material weighted individually for the required composition using a digital weighing scale. The measured blend is taken in a ceramic beaker and stirred well with the help of a stirrer made by ceramic. The stirring has to be done for ten minutes properly to get the homogenous mixture. The prepared blend is poured into the die and filled to the desired level. Using filler the blend is filled thoroughly into the die for better compaction. The die is placed safely into the MCTM machine. The load is then applied gradually to the die for compaction. Figure 2 shows the schematic diagram of powder metallurgy route.

#### **2.4 Theoretical Calculation of Density and Porosity**

The density of formulated matrix is used to measure the bonding strength and compactness of the reinforcement particle in the substance. The experimental density is calculated by Archimede's principle. The theoretical density ( $\rho$ ) of Al6082-B<sub>4</sub>C-RHA is calculated by

$$\begin{aligned} \rho(\text{Al6082} + \text{B}_4\text{C} + \text{RHA}) &= \text{Vol. Al6082} \times \rho_{\text{Al6082}} \\ &+ \text{Vol. B}_4\text{C} \times \rho_{\text{B}_4\text{C}} \\ &+ \text{Vol. RHA} \times \rho_{\text{RHA}} \end{aligned} \quad (1)$$

##### **Calculation for 1 composition: Al-80%, B<sub>4</sub>C-17.5%, RHA-2.5%**

$$\text{Al} = 3.927 \times 0.80 = 3.142 \text{ g.}$$

$$\text{B}_4\text{C} = 3.927 \times 0.175 = 0.687 \text{ g.}$$

$$\text{RHA} = 3.927 \times 0.025 = 0.098 \text{ g.}$$

Porosity is the formation of bubbles inside of the casting after cooling the hybrid metal matrix composite. Porosity takes place since a large volume of dissolved gas

can be absorbed by most liquid materials, but the rigid structure of the same material cannot, so the gas forms bubbles within the composite material as it cools. In surface the gas porosity might be trapped on some surface to the presence of oxygen, hydrogen and other components. Porosity (P) of Al6082 metal matrix composites compared with the newly formulated composites was calculated by.

$$(P) = 1 - \frac{\rho_{\text{Experimental}}}{\rho_{\text{Theoretical}}} \quad (2)$$

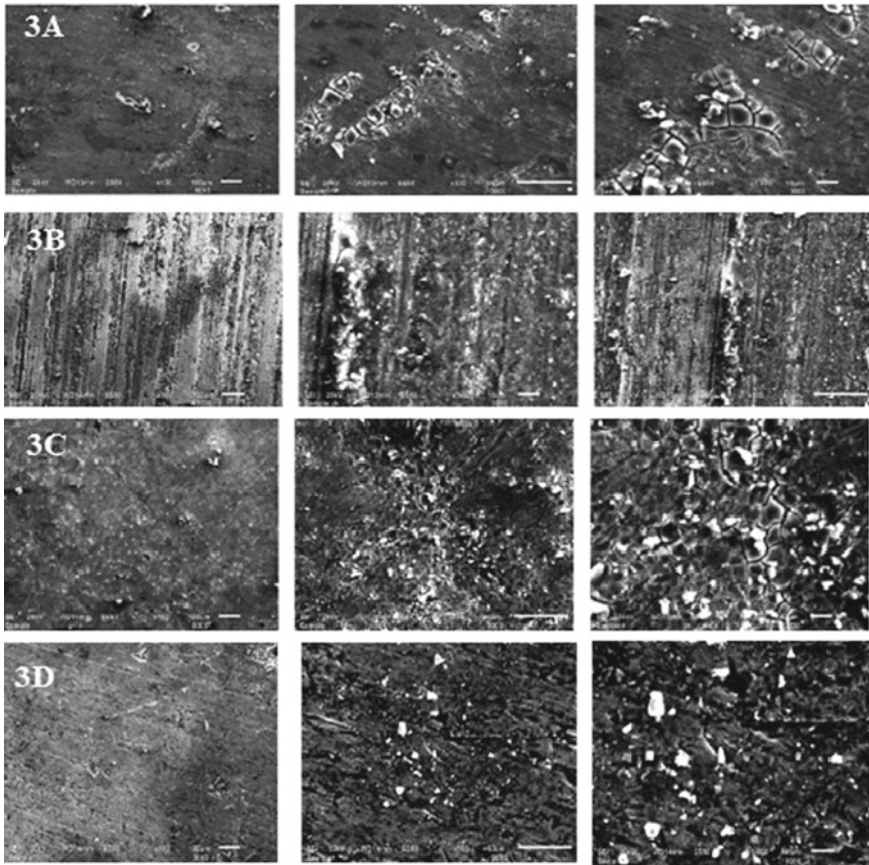
### 3 Results and Discussion

#### 3.1 Microstructure Analysis of Newly Formulated Composite

In this investigation we have micro scoped the fabricated specimens in to 1000X, 1500X, 2000X using scanning electron microscopy after heat treatment, Fig. 3 shows the microstructure of the alloyed specimens with rice husk ash particle and boron carbide particle. The boron carbide phase is fined in dark phase with the metal phase white, and some clusters are formed in interlocking of phase materials as shown in Fig. 3A. Some agglomeration is formed at the bonding with reinforcement in Fig. 3B. Finally, we have observed that in Fig. 3C Sample 6, the particles are equally distributed and alloyed with matrix phase, there is no agglomeration and clusters are formed in the alloying element and give better continuity of phase distribution. This shows the fine surface texture and clear phase distribution of an alloying element. In Fig. 3D the particle of reinforcement increased and it has been found that cracks on the surface and phase distribution is also not clear and porosity is much increased and the fragile nature is out bounded in the surface. From this we have observed that the particle distribution of RHA and B<sub>4</sub>C is cleared up to the phase of figure shown in 3C.

#### 3.2 Evaluation of Mechanical Properties

**Tensile strength.** Tensile strength of newly fabricated composite with different weight ratios of reinforcement (B<sub>4</sub>C & RHA) in shown in Fig. 4. From this we have observed that increase in weight percentage of RHA decreases the tensile strength of the matrix materials and same time the increase in B<sub>4</sub>C the tensile strength increases versatile up to 15%wt and 5%wt RHA. After addition of boron carbide with a weight of 15% tends to reduced the tensile strength of the fabricated element. The maximum tensile strength of 167.5 Mpa is observed at sample 6. From the result we concluded that the maximum strength is achieved up to 15wt% of boron carbide, and



**Fig. 3** Microstructure of AA6082/B<sub>4</sub>C/RHA of different Samples **A** 10% of B<sub>4</sub>C and 10% of RHA is added with aluminium 6082 powder. **B**. 12.5% of B<sub>4</sub>C and 7.5% of RHA is added with aluminium 6082 powder. **C**. 15% of B<sub>4</sub>C and 5% of RHA is added with aluminium 6082 powder. **D**. 17.5% B<sub>4</sub>C and 2.5%RHA is added with aluminium 6082 powder

the secondary reinforcement particles RHA possesses higher strength by offering more resistance. Henceforth after heat treatment 17% of increase in tensile strength is observed on the same sample.

**Ductility.** The influence of the reinforcement ratio add-on RHA and B<sub>4</sub>C on the ductility of the composite is shown in Fig. 5. We have observed that increase in wt% of RHA increases the ductility of and composite. This is due to the presence of cluster particle in boron carbide (Fig. 3B). This is due to the increase in hardness of B<sub>4</sub>C cluster. Sample of Al6082- 12.5 wt% RHA and 7.5 wt% B<sub>4</sub>C shows the maximum ductile. The experimental value is compared with theoretical value after heat treatment, and we have observed that 16.7% increase in ductility is obtained and it is shown in Fig. 5.



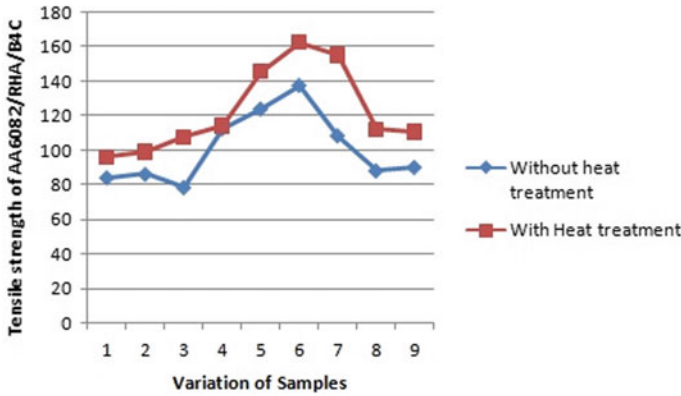


Fig. 4 Tensile strength of Al6082-RHA-B<sub>4</sub>C

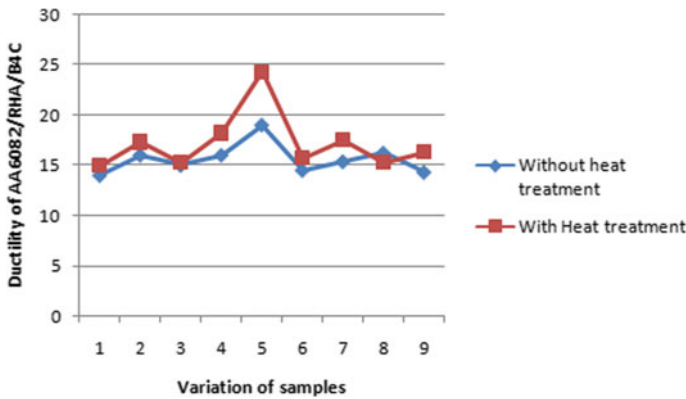
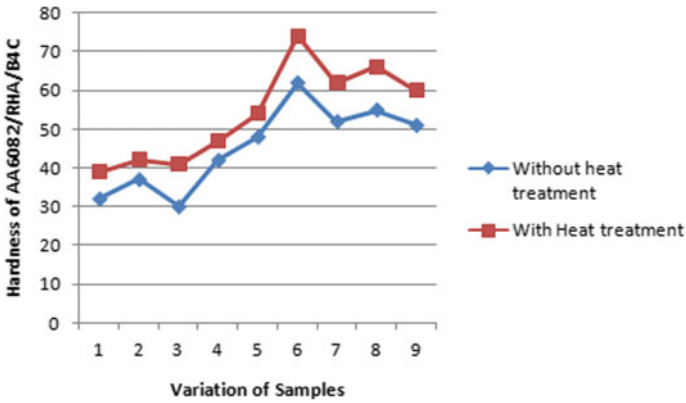


Fig. 5 Ductility of AA6082/RHA/B<sub>4</sub>C

Hardness. Figure 6 shows the hardness of various compositions of reinforcement before heat treatment and after heat treatment. From this we have observed that sample 6 (Al 6082 of 15wt% B<sub>4</sub>C and 5wt% RHA) shows maximum hardness of 62BHN before heat treatment and after heat treatment the hardness is further improved to 74BHN and surface textures are very clear and clean. The particle distribution and cluster formation in the phase show better results, almost 15.3% increase in hardness is observed after heat treatment.

**Specific strength.** In Table 3 the experiment and theoretical density are compared and specific strength after heat treatment is compared. We observed density of 15% wt B<sub>4</sub>C and 5% wt RHA (sample 6) with Al6082 matrix being 2.74 g/cm<sup>3</sup>. The theoretical density of this composition is calculated, and it was found to be 2.70 g/cm<sup>3</sup>. The composition Al6082 with 7.5wt% of B<sub>4</sub>C and 2.5% RHA shows better mechanical properties. The theoretical density is compared with the fabricated hybrid aluminium





**Fig.6** Hardness of AA6082/RHA/B<sub>4</sub>C

**Table 3** Experimental evaluation of porosity and specific strength

Sample. No	Theoretical density value (g/cm <sup>3</sup> )	Experimental density value (g/cm <sup>3</sup> )	Porosity (%)	Tensile strength as cast	Specific strength (kN-m/kg)
1	2.43	2.72	1.49	87	21.58
2	2.65	2.72	2.64	91	16.76
3	2.63	2.70	2.66	100	17.48
4	2.60	2.71	4.23	110	22.34
5	2.71	2.72	0.36	125	15.73
6	2.70	2.74	1.48	167.5	47.35
7	2.69	2.63	1.85	153.4	43.94
8	2.69	2.51	2.23	102.3	20.14
9	2.67	2.72	1.87	104.3	19.83

matrix 6082, and it shows the maximum increase in the sample 6 and gives higher strength-to-weight ratio among the newly fabricated materials.

### 4 Conclusion

A newly formulated Al6082-RHA-B<sub>4</sub>C composite with different weight ratios of reinforcement is fabricated by using powder metallurgy routing process. By studying the microstructure and properties of composites, the following conclusions can be drawn:

- A newly formulated hybrid metal matrix composite Al6082-RHA-B<sub>4</sub>C has been fabricated by using the powder metallurgy routing method.

- In microstructure analysis we have found that phase changes and particle distribution of reinforcements with different weight ratios. And sample 6 (15wt% of B<sub>4</sub>C and 5wt% of RHA) shows a clear bonding texture and even particle distribution after heat treatment.
- The maximum tensile strength of 167.5Mpa is observed at sample 6, with a weight ratio of reinforcement 15wt% of B<sub>4</sub>C and 5wt% of RHA shows maximum value on both heat treatment processes.
- Sample No. 6 (Al6082 of 15wt% B<sub>4</sub>C and 5wt% RHA) shows maximum hardness of 62BHN before heat treatment and after heat treatment the hardness is further improved to 74BHN and surface textures are very clear and clean.
- Maximum ductility is observed on (Al6082 with 15wt% B<sub>4</sub>C and 5wt% RHA).
- Specific strength of Al6082 and 15%B<sub>4</sub>C and 5% RHA composites shows maximum of 47.35kN-m/kg, its shows much higher when compared with base matrix material.

## References

1. Ilandjezian, R., Gopalakannan, S.: Mechanical and micro-structural behavior of lignite coal based fly-ash and microsphere reinforced Al 6061 metal matrix composite. *Appl. Mech. Mater.* **85**(2), 123–129 (2016)
2. Ravindran, P., Manisekar, K., Narayanasamy, P.: Application of factorial techniques to study the wear of Al hybrid composites with graphite addition. *Mater. Des.* **39**, 42–54 (2016)
3. VenkatPrasat, S., Subramanian, R.: Tribological properties of AlSi10Mg/ fly ash/graphite hybrid metal matrix composites. *Industrial Lubrication and Tribology*. **65**(6), 399–408 (2013)
4. Shalaby, E., Churyumov, A.Y., Solonin, A.N.: Preparation and characterization of hybrid A359/(SiC+Si<sub>3</sub>N<sub>4</sub>) composites synthesized by stir/squeeze casting techniques. *Mater. Sci. Eng.* **674**, 18–24 (2017)
5. Baradeswaran, A., Perumal, A.E.: Influence of B<sub>4</sub>C on the tribological and mechanical properties of Al 7075–B<sub>4</sub>C composites. *Compos. B Eng.* **54**, 146–152 (2013)
6. Surappa, M.K.: Aluminium matrix composites challenges and opportunities. *Sadhana* **28**(1), 319–334 (2018)
7. Danasegaran, S.K., Britto, E.C., Xavier, S.C.: Exploration of trigonal patch antenna characteristics with the impact of 2D photonic crystal of various air hole shapes. *J. Elec. Mater.* **50**, 5365–5374 (2021). <https://doi.org/10.1007/s11664-021-09071-8>
8. Britto, E.C., Danasegaran, S.K., Johnson, W.: Design of slotted patch antenna based on photonic crystal for wireless communication. *Int J Commun Syst.* **34**, e4662 (2021). <https://doi.org/10.1002/dac.4662>
9. Danasegaran, S.K., Britto, E.C., Johnson, W.: Investigation of the influence of fluctuation in air hole radii and lattice constant on photonic crystal substrate for terahertz applications. *Opt. Eng.* **59**(8), 087102 (13 August 2020). <https://doi.org/10.1117/1.OE.59.8.087102>
10. Karthikeyan, A., Nallusamy, S.: Experimental analysis on sliding wear behaviour of aluminium–6063 with SiC particulate composites. *Int. J. Eng. Res. Afr.* **31**, 36–43 (2017)

# Automation

# Attractor Plot as an Emerging Tool in ECG Signal Processing for Improved Health Informatics



Varun Gupta, Yatender Chaturvedi, Parvin Kumar, Abhas Kanungo, and Pankaj Kumar

## 1 Introduction

Nowadays healthcare demands qualitative as well as quantitative analysis to face the current situation with high detection accuracy [1]. For scrutinizing the cardiac status of the patient, heart conduction system is analyzed. Heart comprises of four chambers in which two upper chambers belong to atria and two lower chambers belong to ventricles which results in contraction (atria muscles) and pumping of the blood (ventricles) [2, 3]. All these activities are seized in terms of three waves: P-wave, QRS-wave, and T-wave, known as electrocardiogram (ECG) signal [4–6]. It is mostly incorporated in the healthcare systems for presenting electrical conduction of the heart and underlying arrhythmia in computational medicine [7–14]. There are various factors on which arrhythmia depends, viz. high blood pressure, heart muscle damage, coronary artery disease, etc. [2]. The main necessary conditions which ensure the arrhythmia condition are abnormal heart rate or rhythm, abnormal conduction pathway, etc. [3].

ECG helps to analyze breathing pattern with heart diseases [15–18]. In the literature, numerous authors have proposed multifold techniques based on great efforts. These computer-aided diagnosis (CAD) techniques were not completely succeeded due to large number of detection/classification error (false negatives-FNs, false positives-FPs) [19–23]. In this article, chaos-based features are extracted and used with support vector machine (SVM) technique for classification, respectively, to assist current health scenario around the world. The motivation behind utilization of SVM is due to its several strengths, viz. memory efficient, effective for

---

V. Gupta (✉) · Y. Chaturvedi · P. Kumar · A. Kanungo  
KIET Group of Institutions, Delhi-NCR, Ghaziabad, India

P. Kumar  
SCRIET, CCS University, Meerut, India

high-dimensional feature space, and small chances of overfitting. For performance assessment, mean-squared error (MSE) and detection error (DE) are used.

The next section is devoted to materials and methods which is proposed in this paper for analyzing different ECG datasets.

## 2 Materials and Methods

In this paper, different recorded ECG datasets are used which were prepared in the presence of experts at NIT, Jalandhar, Punjab, India, by selecting sampling rate of 360 Hz. These records are nonstationary in nature which are mixed with power line interference (PLI) and baseline wander (BLW) and sometimes other biomedical signals are overlapped with it [24–26]. Therefore, Savitzky–Golay digital filtering is utilized for pre-processing the ECG signal as described below. Figure 1 shows proposed methodology in which attractor plots are used to pore over different cardiac conditions at different time delays. After feature extraction step, classification step is performed using support vector machine (SVM) in different iterations for covering different pathological datasets.

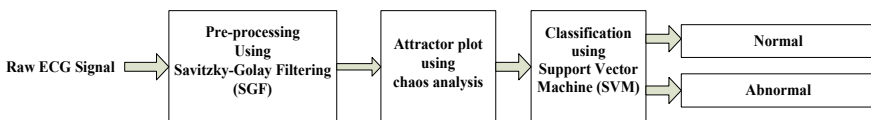
### 2.1 Savitzky-Golay Filtering (SGF)

The operation of pre-processing using SGF has the essential pathological attributes which are generally lost during normal filtering step [27]. Mathematically, it is given by [20, 28, 29]

$$[g]_{dn} = \sum_{k=0}^D [[W]^{-1}]_{dk} t_n^k \tag{1}$$

$$\alpha = [g]x \tag{2}$$

where  $\alpha$  denotes filtering coefficients, and  $x$  denotes input signal.



**Fig.1** Proposed methodology

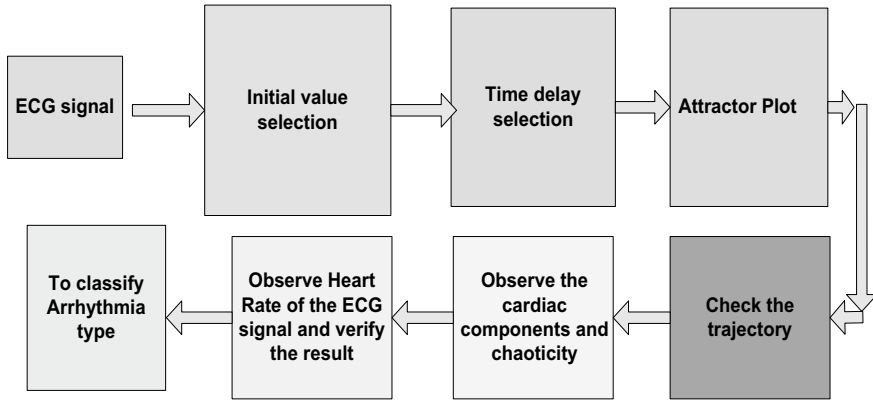


Fig.2 Procedure to apply chaos theory on ECG dataset

### 2.2 Theory of Chaos Analysis

In chaos analysis, time series of ECG datasets are analyzed using attractor plots [30]. The mathematical expression for attractor plot is presented in terms of correlation coefficient function which is given by

$$R_{pq}(r) \propto \mu r^\delta \tag{3}$$

where  $\mu, \delta, r$  are the constant, correlation coefficient, and radius, respectively, of the correlation coefficient function [30]. Further, correlation coefficient is presented as

$$\delta = \lim_{r \rightarrow 0} \frac{\log R_{pq}(r)}{\log r} \tag{4}$$

Figure 2 shows general procedure to apply chaos theory on ECG dataset. In first block, initial value is selected, in second block time delay is selected, and in third block attractor plot is presented. Next trajectory plots are investigated with associated cardiac components and chaoticity. Finally, heart rate (H.R.) of the ECG signal is observed and the result on the basis of obtained trajectory plot is verified.

### 2.3 Support Vector Machine (SVM)

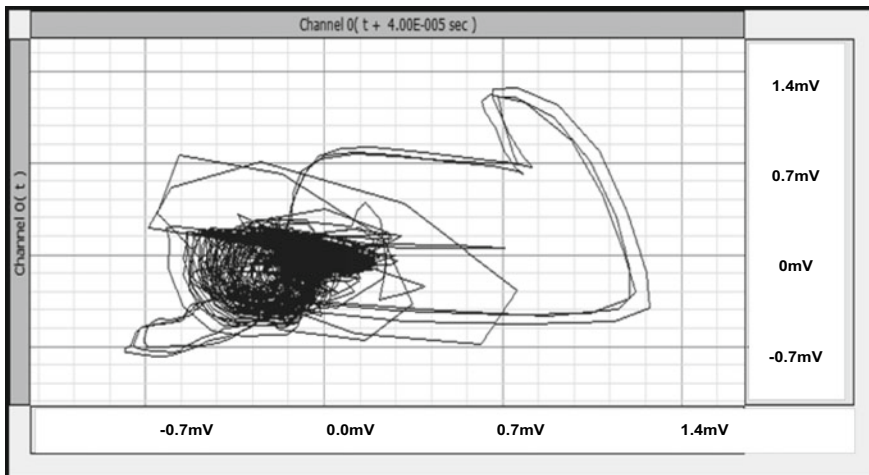
SVM is a supervised learning to obtain the optimal separating hyperplane from the training data. It helps to classify the normal and abnormal ECG signal classes during different situations by increasing the margin width between vectors. For classification using SVM, 77/23 ratio is used for training and testing, where 77% was devoted for

training set and remaining 23% was devoted for test data. It classifies data using vectors known as support vectors. In this paper, two feature samples ( $x_1$  and  $x_2$ ) are used to build the margin width (hyperplane). These two feature samples belong to normal and abnormal conditions. It effectively handles the nonlinear segments of ECG signals in the high-dimensional feature space [31–33].

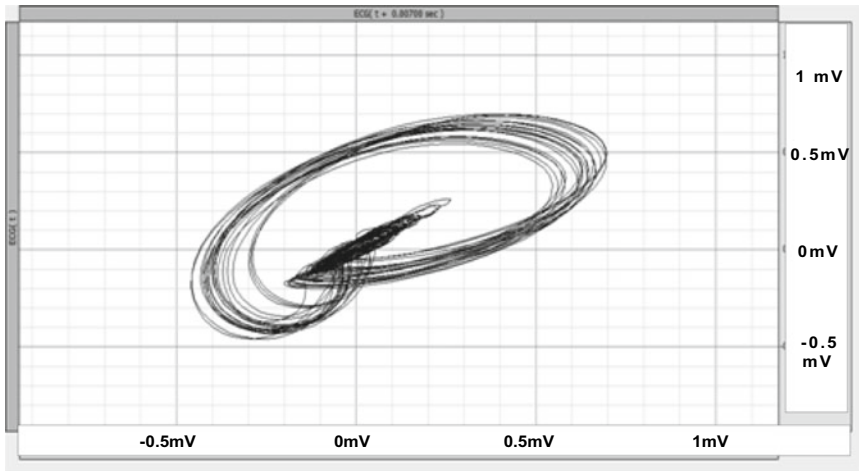
### 3 Results and Discussion

The obtained H.R. for a healthy heart is observed in the range of 60–100 beats a minute. During any abnormality in the heart rhythm, chances of blood clots may increase. It may propagate from heart to brain by which blood flow may interrupted causing a heart stroke. In chaos theory, attractor plots are used to identify different types of heart diseases in the computer graphics window. Figure 3 ensures that chaos analysis is also powerful combination in clinical (pathological) databases for effectively identifying the underlying arrhythmia. For clinical ambulatory subject recording, measured H.R. was between 60 beats per minute to 100 beats per minute (varying R-R interval).

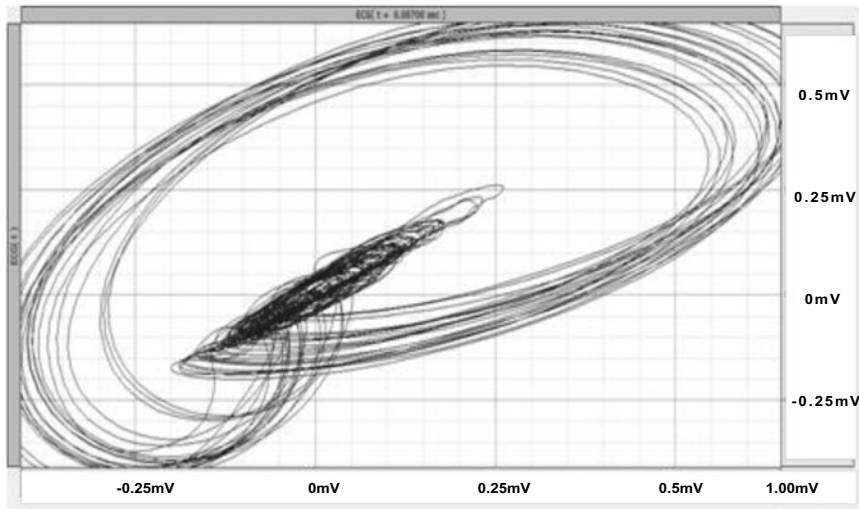
Figure 4a shows chaos analysis of atrial fibrillation (AFi) patient ECG in full view. During AFi, ECG signals gets irregularity in their shape and H.R. goes high which may come in the range of 100–175 beats per minute. In AFi, conduction of blood supply is disturbed which presents chaotic electrical activity in the ECG signal. In this paper for AFi, the measured H.R. is 167 beats per minute. Figure 4b shows wider view of AFi patient ECG with coordinates (0.13527, -0.80024).



**Fig.3** Chaos analysis of clinical ambulatory subject (patient) ECG dataset at time-delay dimension of 4 sample interval with co-ordinate value (147.57806, -956.41176)



(a)

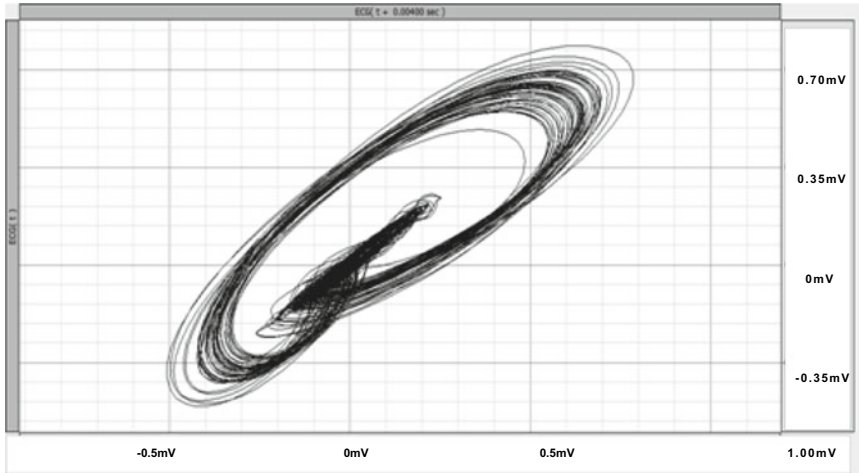


(b)

**Fig.4** Chaos analysis of atrial fibrillation patient ECG **a** full view and **b** wider view with coordinates (0.13527, -0.80024)

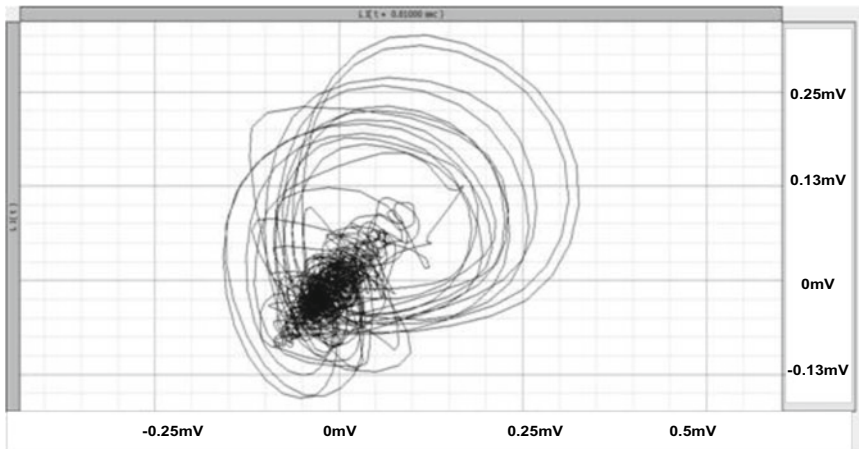
Figure 5 shows chaos analysis of ventricular tachycardia (VT) patient ECG at optimal time delay dimension of 4 with coordinates (-0.18231, 0.15583). During VT, abnormal activity is shown in the lower chambers of the heart in which H.R. comes in the range of 60–100 beats per minute at rest. In this case measured H.R. is 87 beats per minute.



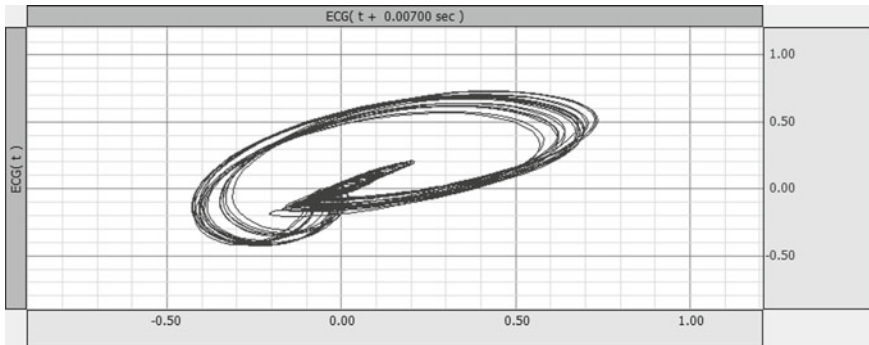


**Fig.5** Chaos analysis of ventricular tachycardia patient ECG at optimal time delay dimension of 4 with coordinates  $(-0.18231, 0.15583)$

Figure 6 shows chaos analysis of ventricular fibrillation (VF) patient ECG at optimal time delay dimension of 7 with coordinates  $(0.21408, -0.80161)$ . During VF, blood supply is interrupted in ventricles which adds abnormality in the ECG signal waveform. This condition of VT may lead to cardiac arrest which generates due to inappropriate blood supply in the heart muscle, heart muscle damage or injury, body function irregularities, etc.



**Fig.6** Chaos analysis of ventricular fibrillation (VF) patient ECG at optimal time delay dimension of 5 with coordinates  $(-0.12269, 0.09233)$



**Fig.7** Chaos analysis of atrial flutter patient ECG at optimal time delay dimension of 7 with coordinates (0.21408, -0.80161)

**Table 1** Performance comparison of the proposed and existing research works

Ref	MSE (%)	DE (%)
Proposed	0.023	0.077
[13]	–	0.097
[14]	–	0.387
[16]	–	0.227
[28]	0.813	–

Figure 7 shows chaos analysis of atrial flutter (AF) patient ECG at optimal time delay dimension of 7 with coordinates (0.21408, -0.80161). During AF, upper chambers, i.e., atria of heart, beat very fast. In this case, the measured H.R. is 400 beats per minute, i.e., atria beats very rapidly. It is very dangerous and may lead to stroke. In AF, the heart beats are more rhythmic and constant [34].

Table 1 shows performance comparison of the proposed and existing research works on the basis of %MSE and %DE. The existing research work reported %DE of 0.097, 0.387, 0.227 in [13, 14, 16], respectively, and %MSE of 0.813 in [28]. The proposed technique outperforms the existing research work and presented %MSE of 0.023 and %DE of 0.077.

## 4 Conclusion

A chaos theory-based feature extraction has been established by sketching different trajectories, and different cases of heart diseases are successfully analyzed in this paper. Using SVM, heart diseases are classified with MSE of 0.023% and DE of 0.077%. The proposed method observed the H.R. and extracted the correct pathological condition of a patient. In future, the proposed method may establish as a strong candidate in the processing of ECG signals.

## References

1. Gupta, V., Mittal, M.: Arrhythmia detection in ECG signal using fractional wavelet transform with principal component analysis". *J. Inst. Eng. India Ser. B.* **101**(5), 451–461 (2020)
2. Heart arrhythmia. <https://www.mayoclinic.org/diseases-conditions/heart-arrhythmia/symptoms-causes/syc-20350668>. Last accessed 21 October 2020
3. Cardiac Arrhythmias. [https://www.health.harvard.edu/a\\_to\\_z/cardiac-arrhythmias-a-to-z](https://www.health.harvard.edu/a_to_z/cardiac-arrhythmias-a-to-z). Last accessed 21 October 2020
4. Rao, K.D.: DWT based detection of R-peaks and data compression of ECG signals. *IETE J. Res.* **43**, 345–349 (2015)
5. Kaya, Y., Pehlivan, H.: Comparison of classification algorithms in classification of ECG beats by time series. In: *Proc IEEE Conference on Signal Processing and Communications Applications (SIU)*, May 16–19, Malatya, Turkey (2015)
6. Kaya, Y., Pehlivan, H., Tenekeci, M.E.: Effective ECG beat classification using higher order statistic features and genetic feature selection. *J. Bio. Res.* **28**(17), 7594–7603 (2017)
7. Gupta, V., Mittal, M., Mittal, V.: R-peak detection based chaos analysis of ECG signal. *Analog Integr. Circ. Sig. Process* **102**, 479–490 (2019)
8. Gupta, V., Mittal, M.: R-peak detection in ECG signal using Yule–Walker and principal component Analysis. *IETE J. Res.* (2019). <https://doi.org/10.1080/03772063.2019.1575292>
9. Patro, K.K., Prakash, A.J., Rao, M.J., Kumar, P.R.: An Efficient optimized feature selection with machine learning approach for ECG biometric recognition. *IETE J. Res.* <https://doi.org/10.1080/03772063.2020.1725663> (2020)
10. Gupta, V., Mittal, M., Mittal, V.: Chaos theory: An emerging tool for Arrhythmia detection. *Sensing and Imaging.* **21**(10), 1–22 (2020)
11. Gupta, V., Mittal, M.: Efficient R-peak detection in electrocardiogram signal based on features extracted using Hilbert transform and Burg method. *J. Inst. Eng. India Ser. B.* **101**, 23–34 (2020)
12. Acharya, R., Krishnan, S.M., Spaan, J.A. Suri, J.S.: *Advances in cardiac signal processing.* Springer (2007).
13. Gupta, V., Mittal, M.: QRS complex detection using STFT, Chaos analysis, and PCA in standard and real-time ECG databases. *J. Inst. Eng. India Ser. B.* **100**(5), 489–497 (2019)
14. Gupta, V., Mittal, M., Mittal, V.: R-peak detection using chaos analysis in standard and real time ECG databases. *IRBM* **40**(6), 341–354 (2019)
15. Kaur, I., Rajni, R., Marwaha, A.: ECG signal analysis and Arrhythmia detection using wavelet transform. *J Inst Eng India Ser B.* **97**(4), 499–507 (2016)
16. Gupta, V., Mittal, M.: A novel method of cardiac arrhythmia detection in electrocardiogram signal. *Int. J. Medical Engineering and Informatics* **12**(5), 489–499 (2020)
17. Gupta, V. and Mittal, M.: Respiratory Signal Analysis using PCA, FFT and ARTFA. In *Proc IEEE 2016 International Conference on Electrical Power and Energy Systems (ICEPES-16)*, Dec. 14–16, pp. 221–225, MANIT Bhopal, India (2016)
18. Kaur, H., Rajni, R.: On the detection of Cardiac Arrhythmia with principal component analysis. *J. Wireless Pers. Commun.* **97**(4), 5495–5509 (2017)
19. Gupta, V., Kanungo, A., Kumar, P., Sharma, A.K., Gupta, A.: Auto-regressive Time Frequency Analysis (ARTFA) of Electrocardiogram (ECG) signal. *Int. J. of Appl. Eng. Res.* **13**(6), 133–138 (2018)
20. Gupta, V., Mittal, M.: ECG Signals Interpretation using Chaos Theory. *J. Adv. Res. Dyna. & Cont. Syst.* **9**, 2392–2397 (2018)
21. Kora, P., Annavarapu, A., Yadlapalli, P., Krishna, K.S.R., Somalaraju, V.: ECG based atrial fibrillation detection using Sequency ordered complex Hadamard transform and hybrid firefly algorithm. *J of Eng Sci and Tech.* **20**(3), 1084–1091 (2017)
22. Singh, G., Gupta, V., Sekharmantri, A.K., Gupta, A., Kumar, P.: Real-time online monitoring of electrocardiogram (ECG) using very low cost for developing countries. In *Proc 2010 AIP Conference*, pp. 251–254, Chandigarh, India (2010)

23. Mehta, S.S., Shete, D.A., Lingayat, N.S., Chouhan, V.S.: K-means algorithm for the detection and delineation of QRS-complexes in Electrocardiogram. *IRBM* **31**(1), 48–54 (2010)
24. Sud, S.K., Gupta, S.C., Kamal, A.K.: Correlation technique for ECG interpretation. *IETE J. Res.* **18**(9), 421–424 (2015)
25. Ari, S., Das, M.K., Chacko, A.: ECG signal enhancement using S-Transform. *Comp. Biol. Med.* **43**(6), 649–660 (2013)
26. Kaya, Y., Pehlivan, H.: Feature selection using genetic algorithms for premature ventricular contraction classification. In: *Proc IEEE 9th International Conf on Electrical and Electronics Engineering*, November 26–28, 2015, pp. 1229–1232, Turkey (2015)
27. Kranjec, J.: Non-contact heart rate and heart rate variability measurements: A review. *J. Biom Sig Process and Cont.* **13**, 102–112 (2014)
28. Gupta, V., Mittal, M.: ECG Signals Interpretation using Chaos Theory. *J. Adv. Res. Dyna. & Cont. Syst.* **9**, 2392–2397 (2018)
29. Gupta, V., Mittal, M.: R-peak detection for improved analysis in health informatics. *Inter. J Medical Eng. Infor.* **13**(3), 213 (2021)
30. Gupta, V., Mittal, M.: An efficient AR modeling based Electrocardiogram signal analysis for Health Informatics,” *Inter. J Medical Eng. Infor. (IJMEI)* (in press)
31. Akgul, A., Calgan, H., Koyuncu, I., Pehlivan, I., Istanbulu, A.: Chaos-based engineering applications with a 3D chaotic system without equilibrium points. *Nonlinear Dyn.* (2015). <https://doi.org/10.1007/s11071-015-2501-7>
32. Mehta, S.S., Lingayat, N.S.: Development of SVM based ECG Pattern recognition technique. *IETE J. Res.* **54**(1), 5–11 (2008)
33. Mehta, S.S., Lingayat, N.S.: Development of SVM based classification techniques for the delineation of wave components in 12-lead electrocardiogram. *Biom. Sig. Proc. Cont.* **3**(4), 341–349 (2008)
34. Support Vector Machine—Classification (SVM), [https://www.saedsayad.com/support\\_vector\\_machine.htm](https://www.saedsayad.com/support_vector_machine.htm). Last accessed October 22, 2020
35. Everything you want to know about arrhythmia. <https://www.healthline.com/health/arrhythmia>. Last accessed 21 October 2020



## 1 Introduction

Quanser QUBE twinning means making the two devices work the same way. One Qube is made as a master and another as a slave, which follows the master. If any changes occurred in the master, then the slave detects and follows the master. The master and slave communicate through NI-PSP. NI-PSP is National Instruments' exclusive publish–subscribe protocol (PSP). NI-PSP is made out of a worker considered the shared variable engine that hosts values, timestamps, and other data. NI-PSP is used in the situation where numerous devices must access or update the most recent information data between each other. Utilizing the NI-PSP, you can sent to and receive from shared variables nodes in the LabVIEW over an Ethernet organization.

Quanser was established in 1989 reacting to the requirement for work area equipment stages streamlined for instructing and examination in designing training. Quanser created QFLEX 2 processing interface technology, and QUBE-Servo 2 offers instructors greater adaptability in laboratory arrangements, utilizing a PC, or microcontrollers, for example, NI myRIO, Arduino, Raspberry Pi, and IoT appliances.

The total Internet of things in 2010 had exceeded the population of total human [1]. For instance, the review by Atzori et al. [2] explains the wired and wireless communication advances, wired and remote and architecture of wireless sensor networks (WSNs). In [3], the reviewer explains the IoT engineering and difficulties in deploying IoT appliances. An incorporated cloud vision of IoT applications is introduced in [4]. The creators in [5] give a review of clinical wireless devices for mHealth and eHealth applications. The current IETF norms and difficulties review for the IoT had been introduced in [6]. Once the IoT technologies are popular, the

---

B. Phanindra (✉) · P. Srinivas · K. V. Lakshmi  
Velagapudi Ramakrishna Siddhartha Engineering College, Vijayawada, India

usage of Quanser QUBEs is drastically increased in industries because of remote control flexibility.

The controller can likewise be deployed in an embedded processor that gave us the ability to make an IoT application [7] running on the embedded target and the additional capacity (running the control calculations and any rationale). Likewise note that the gadgets would now be able to talk through NI-PSP. In such a manner, each QUBE-Servo turns into a “digital physical” gadget fit for doing, detecting, thinking, and chatting.

## 2 Block Diagram of Quanser QUBE Twinning

The Quanser QUBE-Servo is connected to myRIO using MXP cable. The Quanser control board is connected to NI Elvis III. Elvis III and myRIO are connected to host computer via USB cable. The data among the two real-time targets are transmitted through a wireless network using network-published shared variables.

The detailed block diagram of the Quanser QUBE twinning is shown in Fig. 1

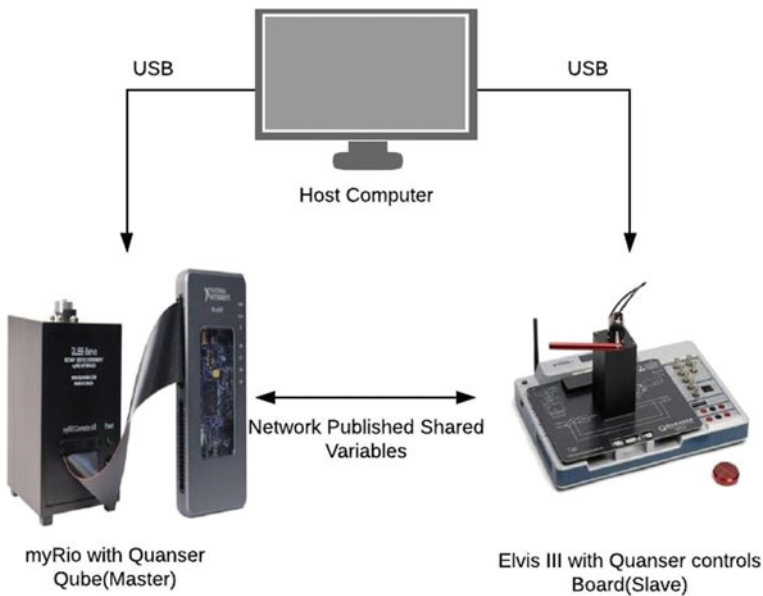


Fig. 1 Block diagram of Quanser QUBE twinning

## 2.1 Hardware

**Introduction.** A detailed explanation about hardware components used in the Quanser QUBE twinning paper is discussed in later sections. They are.

- Quanser QUBE-Servo
- NI Elvis III and Quanser Control Board
- myRIO

**Quanser QUBE-Servo.** The hardware components of QUBE-Servo are shown in Fig. 2. The QUBE-Servo myRIO interface incorporates an MXP connector [8].

The collaboration among the different components on the QUBE-Servo is outlined in Fig. 3. In the data acquiring (DAQ) device, pendulum and motor encoders are associated with encoder input channels 1 and 0. DAQ is connected to the PC through USB port in the QUBE-Servo with USB interface [9].

The QUBE-Servo components for an USB, NI myRIO, and direct I/O interfaces are given in Table 1. Since only the myRIO module is used, the table contains parts respective to myRIO module only.

The top view and front view of QUBE-Servo are shown in Fig. 4

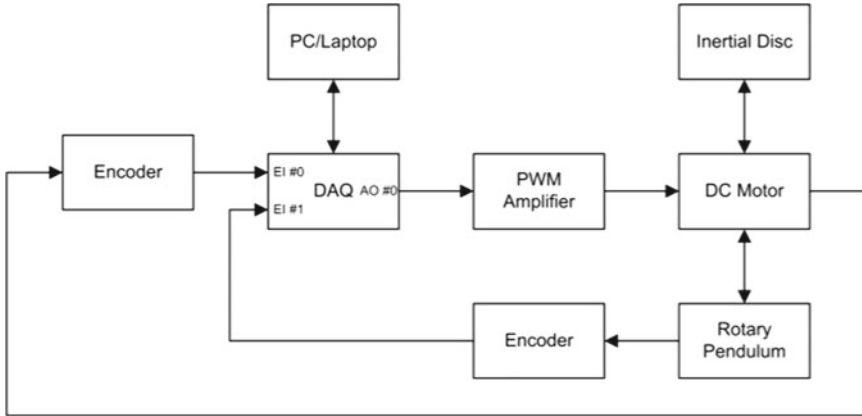
*System setup.* The system setup of QUBE-Servo requires its components and USB interface hardware. The details of QUBE-Servo and USB interface are discussed in detail in further subsections.

*Components required for QUBE-Servo setup.* The following components are required to set up a QUBE-Servo, which are given and shown in Fig. 5.

- QUBE-Servo (direct I/O, NI myRIO, or USB version)
- Inertial disk module

**Fig. 2** Quanser QUBE-Servo





**Fig. 3** Interaction between QUBE-Servo parts

**Table 1** QUBE-Servo components

Id	Components	Id	Components
1	Aluminum body	8	Rotating disk
2	Connector for module	9	Rotating pendulum
3	Module connector magnets	10	Pendulum connection
4	USB DAQ connector	11	Pendulum encoder
5	Pendulum link	12	Rotary pendulum magnets
6	Power connector	13	Encoder 0 connector
7	Power LED	20	NI myRIO MXP connector



**Fig. 4** QUBE-Servo top and interior view





Fig. 5 QUBE-Servo components

- Rotary pendulum (ROTPEN) module
- 15 V 2A power supply
- Cable for power input
- USB cable, an RCA and 2 5-pin-DIN cables, or myRIO MXP cable are provided depending on QUBE-Servo version.

**NI ELVIS III and Quanser Control Board.** The Quanser control board pictured in Fig. 6 is a finished stage for examining practically all parts of the present-day control hypothesis from system modeling and PID control to steadiness and advanced control design. The framework comprises a deterministic DC motor with a high-resolution encoder, just as a pendulum connection for balance control [10].

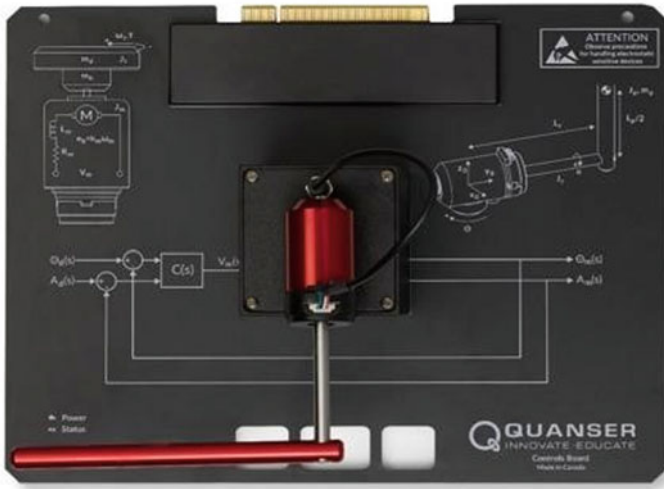


Fig. 6 Quanser control board

### 3 System Software

#### 3.1 Introduction

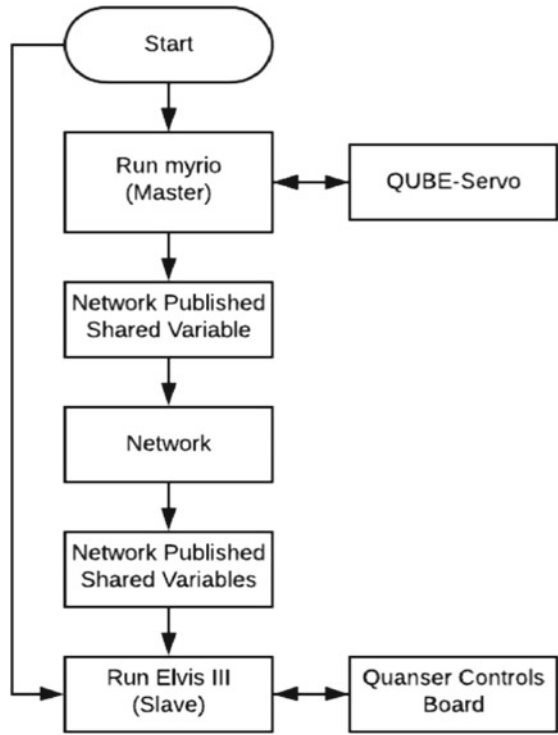
The software used is LabVIEW, and the information from one Qube to another Qube is shared using NI network-published shared variables. The logic flow is shown in Fig. 7.

#### 3.2 Network-Published Shared Variables

A shared variable is an improved programming technology for sharing information presented in LabVIEW [11]. Utilizing the network-published shared variable, anybody can undoubtedly send information inside a framework and among frameworks. The pictorial portrayal of the network-published shared variables appears in Fig. 8 [12]. When a variable was made utilizing the network-published degree, entire information kept in touch with the variable is accessible to every framework's coordinate with the main PC. Shared variables are designed with dialogs available in the project explorer window. Information like administrations to shared variables can be added, for example, logging, alarm, by dialogs utilizing the data logging and a module called supervisory control [12].

The shared variable system deals with the utilization, availability, execution of all shared variables and control frameworks by utilizing the NI-PSP.

Fig. 7 Software flowchart



### 4 Results and Discussion

The twinning of the inverted pendulums is completed by using the network-published shared variables in the LabVIEW. The resulting graphs of both the pendulums that show the position of the rotary arm of the pendulum are shown in Figs. 9 and 10. At the time 22.5 s, when the master direction changes at the same time the slave also changes its direction.

### 5 Conclusion and Future Scope

The communication between the master and slave is achieved using network-shared variables rather than using IBM Watson cloud. This is mainly because of the delay occurred while publishing the variable, which greatly affects the balancing control. Thus, this paper helps to implement IoT to the cyber physical system “The Quanser Servo,” which can be applied to all other similar systems and has various applications in different fields. This can be extended for a single master and many numbers of slaves at various remote places. These are achieved by implementing the same using

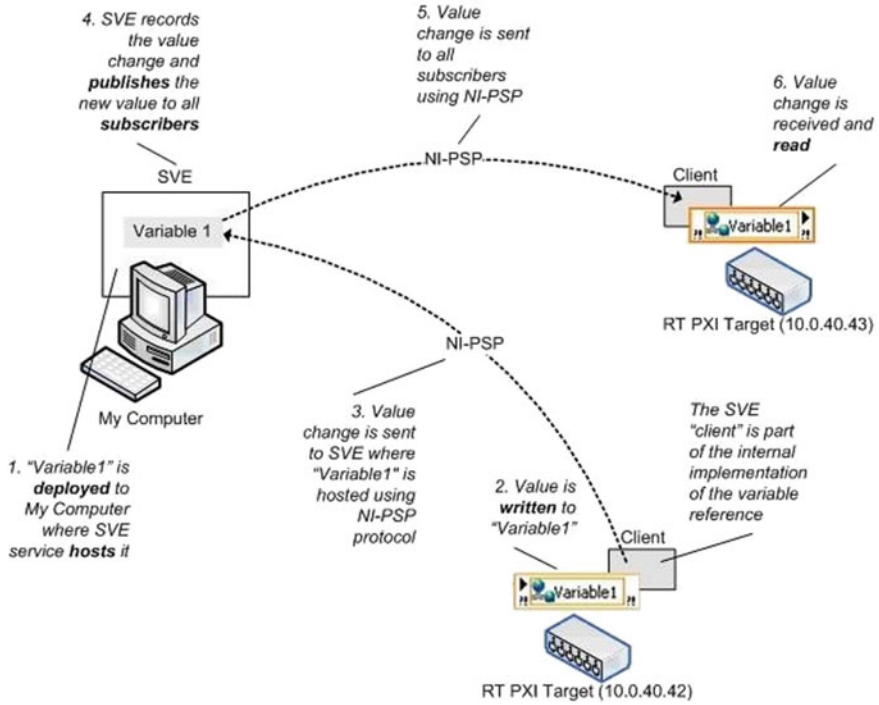
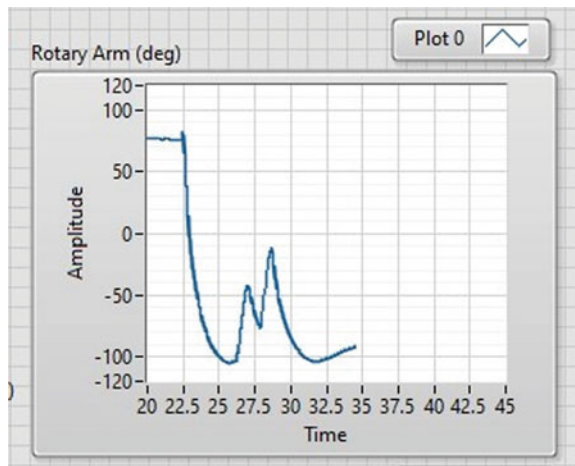
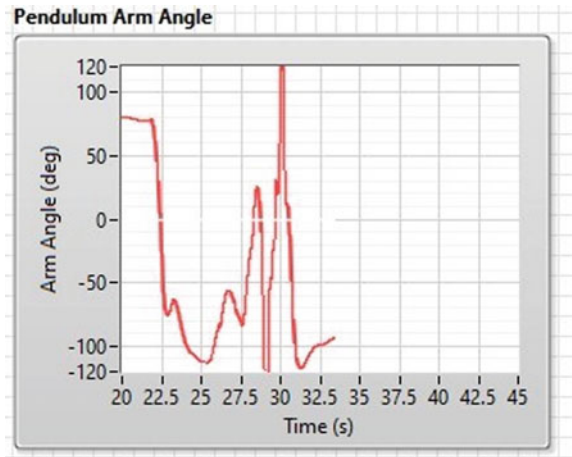


Fig. 8 Network-published shared variables [12]

Fig. 9 Rotary arm angle of master



**Fig. 10** Rotary arm angle of slave



appropriate cloud services for many real-time remote applications. The wide range of applications is to develop machine learning and reinforcement learning applications and to develop autonomous vehicles and IoT implementations in robotics, control systems, aerospace, mechatronics, etc.

## References

1. Evans, D.: The Internet of things: How the next evolution of the Internet is changing everything (2011)
2. Atzori, L., Iera, A., Morabito, G.: The Internet of Things: A survey. *Comput. Netw.* **54**(15), 2787–2805 (2010)
3. Khan R, Khan SU, Zaheer R, Khan S (2012) Future internet: the internet of things architecture possible applications and key challenges. *Proc. 10th Int. Conf. FIT*, 257–260 (2012)
4. Gubbi, J., Buyya, R., Marusic, S., Palaniswami, M.: Internet of Things (IoT): A vision architectural elements and future directions. *Future Gener. Comput. Syst.* **29**(7), 1645–1660 (2013)
5. Lopez, P., Fernandez, D, Jara A.J., Skarmeta, A.F.: Survey of Internet of Things technologies for clinical environments. *Proc. 27th Int. Conf. WAINA*, 1349–1354 (2013)
6. Sheng, Z., et al.: A survey on the IETF protocol suite for the Internet of Things: Standards challenges and opportunities. *IEEE Wireless Commun.* **20**(6), 91–98 (2013)
7. Al-Fuqaha, A., Guizani, M., Mohammadi, M., Aledhari, M., Ayyash, M.: Internet of Things: A survey on enabling technologies, protocols, and applications. *IEEE Comm. Surveys & Tutorials* **17**(4), 2347–2376 (2015)
8. Wang, C., Yin, G., Liu, C., Fu, W.: Design and simulation of inverted pendulum system based on the fractional PID controller. In: *IEEE 11th Conference on Industrial Electronics and Applications (ICIEA)*, Hefei, pp. 1760–1764 (2016)
9. Levis, M.: Quanser’s perspectives on Internet of Things for academic applications (2018)

10. Lévis M.: The Quanser platform for control systems research validation (2018)
11. Chen, W., Su, J.: Comparison of several communication methods between host computer and compact RIO. In: Proceedings of the 10th World Congress on Intelligent Control and Automation, Beijing, pp. 3962–3965 (2012)
12. Network published shared variables. <https://www.ni.com/en-in/support/documentation/supplemental/06/using-the-labview-shared-variable.html>

# Finite Element Analysis of Lightweight Robot Fingers Actuated by Pneumatic Pressure



M. Appadurai  and E. Fantin Irudaya Raj 

## 1 Introduction

In recent years, an increase in automation in various industries enhances the usage of robots in the modern production process. The lightweight robot end effectors play a vital role to perform multiple functions in the automated process. The contemporary robot fingers fitted on robots could be used on different tasks of the work environment. The robot fingers should be lightweight and have accurate displacement and quick response, which lead to higher productivity, superior quality, reduced process cycle time, eliminating human intervention and zero defects.

Nagarajan et al. [1] analysed the multi-sectioned arm, which looks like an elephant trunk. The manipulator is modelled in ADAMS, and the multi-body dynamic numerical simulation is done in ANSYS. The kinematic analysis of the arm is made with user-specified variables, and the robot manipulator orientation is identified for any model and end load using this software package. Li et al. [2] evaluated the behaviour of a robotic tool changer in multi-body simulation. The robotic tool changer is the flexible one, and the 3D model is made using design explorer. The robot tool changer structure is analysed in dynamic simulation through ADAMS and ANSYS software package. The effect of the load on the flexible robot end effectors is identified by monitoring the stress and strain rate. The final results gave the optimisation dimensions of the robotic tool changer.

Oh et al. [3] designed and fabricated the end effectors using honeycomb sandwich structure by carbon fibre epoxy materials. The composite materials have larger

---

M. Appadurai (✉)

Department of Mechanical Engineering, Dr. Sivanthi Aditanar College of Engineering, Tiruchendur, India

E. Fantin Irudaya Raj

Department of Electrical and Electronics Engineering, Dr. Sivanthi Aditanar College of Engineering, Tiruchendur, India

stiffness and higher damping than many other isotropic materials corresponding to the various loads. Finite element analysis is made to optimise the design under different loading conditions. The composite material end effectors had 50% less weight compared to the existing aluminium end effectors. Mroz et al. [4] simulated the wire-actuated robot with central linkage due to its unique features such as low weight, cost and power consumption. The analysis is done with the help of Nastran and ANSYS. Usually, these kinds of robot arm could have large displacements and be in unstable condition while applying force on end effectors. The identical prototype of the wire-actuated robots is made with two different 4 degrees of freedom. The steadiness of two designs is investigated through finite element simulation.

Sakthimurugan et al. [5] fabricated C-type gripper bracket for forming process having two gripper plates, and each gripper had six electromagnets. These electromagnets hold the clutch cover plates. The clearance is made between the cover plates and took to avoid fracture and plastic deformation during the forming process. The numerical analysis is done on the gripper plates to identify the deformation under various loading conditions.

Mahanta et al. [6] produced a conceptual design of three-jaw robotic gripper having flexural hinges. This robotic gripper design fitted with soft materials can be used to handle small delicate objects. The conceptual design is modelled in CATIA, and the numerical analysis was done in ANSYS.

Tawk et al. [7] proposed a soft robotic finger controlled by pneumatic chambers. The soft robotic fingers were used for their own specific advantages. The touch and position sensors were used to get the feedback signal from the fingers for attaining the real-time control. Mayyas et al. [8] fabricated the micro-grippers for grasping micro-size items. The numerical analysis is done to evaluate the behaviour of micro-grippers under different loading conditions.

## 2 Robot Fingers

The artificial hand for the robots is designed and fabricated [6] to attain the exact manipulation and standard grasping during product handling. The specifications of the robot end effectors fingers are taken from the existing work [9] shown in Fig. 1. The joint axis of the robot finger is properly tested when contact with the thumb during materials handling. The index and middle fingertip motion coupled with a thumb is essential for powered and precision grasping. This paper aims to study the behaviour of the middle fingertip motion, which is actuated by pneumatic power through numerical analysis. The optimum dimensions are taken from the experimental study of the robotic fingertip joints of different dimensions.



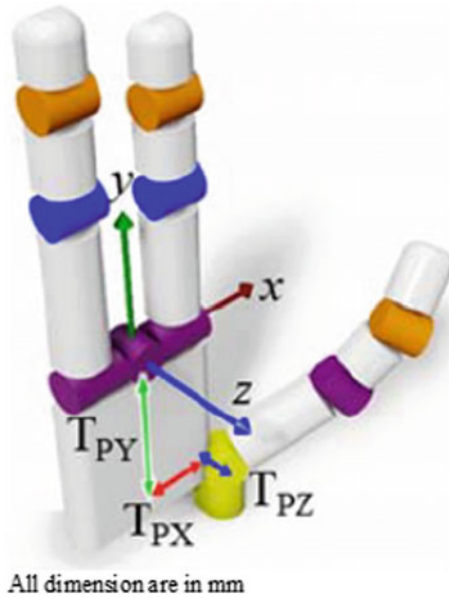


Fig. 1 Dimensions of the robot hand

### 3 Numerical Analysis of Robot Fingers

The 3D model of the robot finger is modelled in ANSYS workbench (Fig. 2), and its dimensions are 80 mm × 15 mm × 10 mm. The seven slots are made on the robot finger for applying the required pneumatic pressure, and the slot chamber volume is 1182.5 mm<sup>3</sup>. The input material is isotropic having Young’s modulus  $2 \times 10^6$  N/m<sup>2</sup> and Poisson ratio 0.48 is the material properties of the geometry.

The model is discretised by triangular nodes in meshing software (Fig. 2). During discretisation, mesh quality is carefully noted for the predicted accurate results of the given problem. The discretisation study is made on the model, and the model containing the 62,345 nodes is identified as the proper meshing.

The robotic pneumatic finger is a simply supported beam which has load at its free end. The boundary conditions such as fixed support on one end (Fig. 3), frictionless

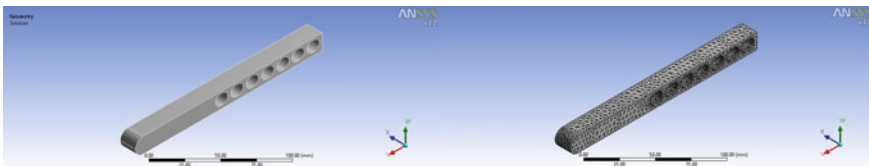


Fig. 2. 3D model and meshing of robot finger

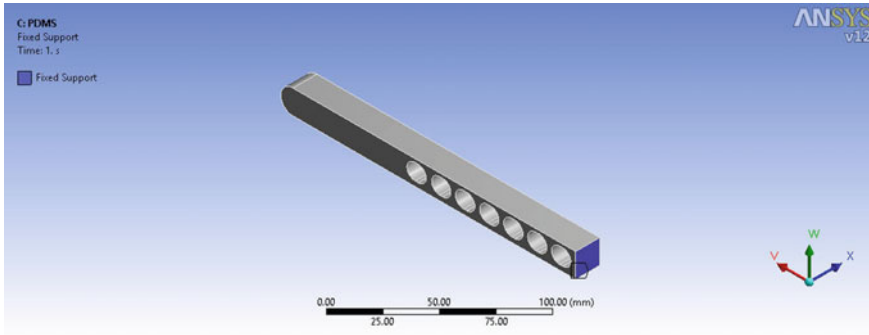


Fig. 3 Boundary conditions

support on the front face and pressure on the chamber are applied. The finite element model is solved in the ANSYS solver, and the results are shown.

### 4 Results and Discussion

From the result, we have identified that the pneumatic fingers have a lot of benefits while handling the micro-size objects. The deformation of the robot finger under 0.1 MPa is shown in Fig. 4. The maximum principal stress occurred on the slots of the robot finger is visualised in Fig. 5. Larger acceleration is feasible in pick and place applications, which is superior to conventional methods. The gripper actuation is simple and required less actuation force. The numerical results obtained from the ANSYS solver for the various values of pressure are represented in Figs. 6 and 7. As the pressure increased, the deflection of the robot finger increased and also the maximum principal stress of the robot finger increased. Intermediate positions are

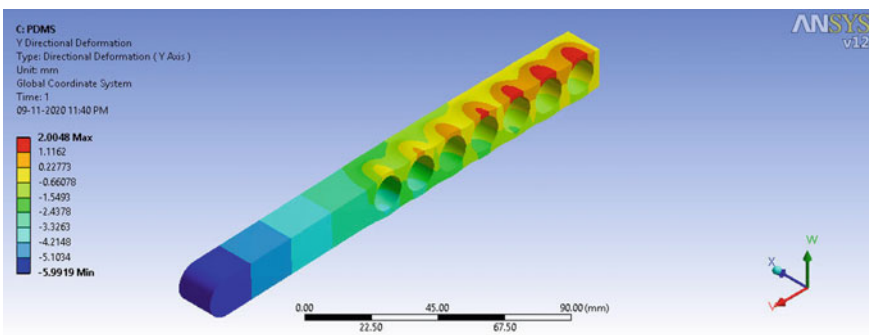


Fig. 4 Deformation of the robot finger under pneumatic pressure

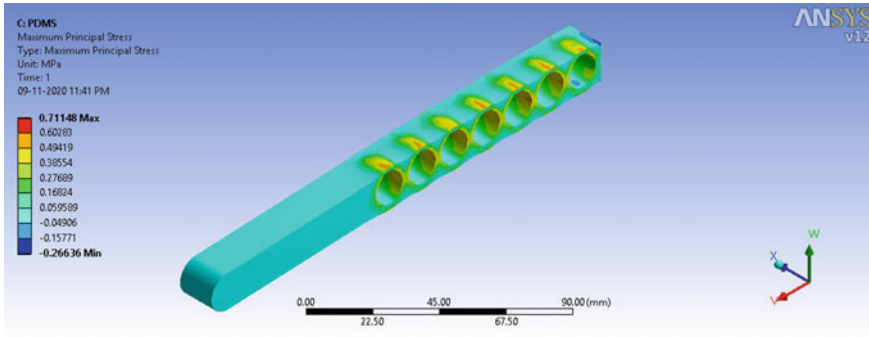


Fig. 5 Maximum principal stress on the robot finger under pneumatic pressure

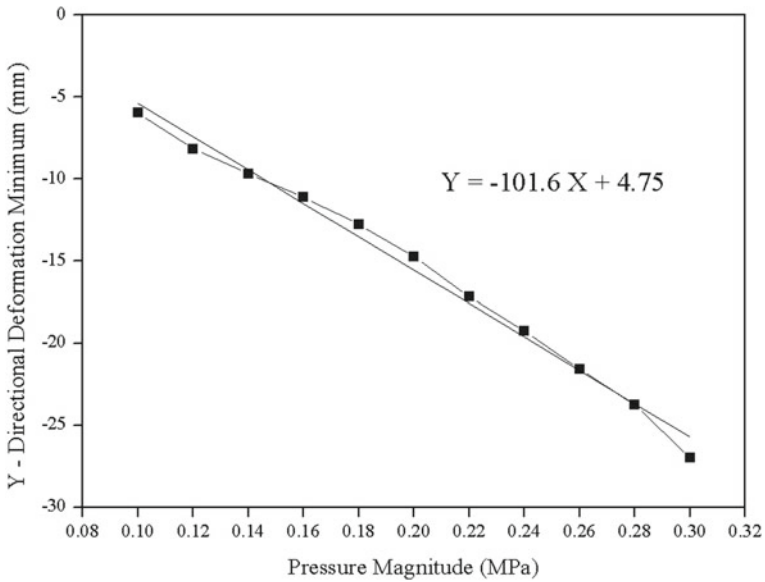
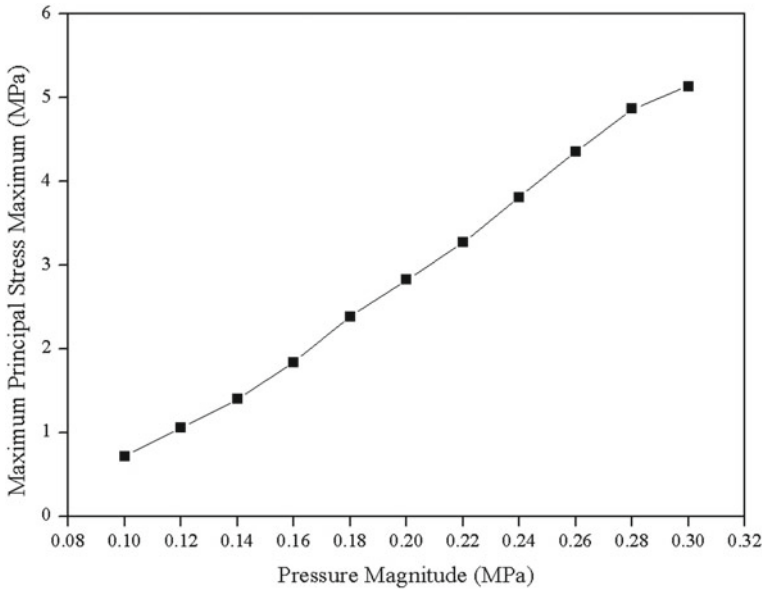


Fig. 6 Deflection of the free end under various pneumatic pressures

attained easily for highly precise applications. The pneumatic finger is very cheap and precise in handling the weak and thin objects. The wear damage and impingement of gripper on workpiece are negligible in this gripper while comparing the metal gripper usage. The components of the gripper are readily available and required less maintenance cost.



**Fig. 7** Maximum principal stress occurred under various pneumatic pressures

The simple linear regression analysis is done for the deformation under input pressure, and the equation is found to be

$$y = -101.6x + 4.75 \quad (1)$$

where  $y$  is the deformation with respect to the input pressure  $x$ .

## 5 Conclusion

The numerical analysis is done on the optimal size of the robot finger from the research work. The pneumatic grippers are very sensitive to applied force and control of gripper position is very simple while handling fragile objects without damage due to gripping force. The maximum deformation is 26.9 mm under the 0.3 MPa pressure at the free end of the robot finger. The maximum principal stress is 5.13 MPa on the chamber top end under the 0.3 MPa pressure. The regression analysis is made for obtained values from the numerical analysis.

## References

1. Nagarajan, A., Kanna, S. R. Kumar, V. M.: Multi-body dynamic simulation of a hyper redundant robotic manipulator using ADAMS Ansys interaction. In: 2017 International Conference on Algorithms, Methodology, Models and Applications in Emerging Technologies (ICAMMAET), pp. 1–6, February (2017)
2. Li, N., Yang, Z., Huang, H., Zhang, G.: The dynamic simulation of robotic tool changer based on adams and ansys. In: 2016 International Conference on Cybernetics, Robotics and Control (CRC), pp. 13–17, August (2016)
3. Oh, J.H., Kim, H.S.: Composite robot end effector for manipulating large LCD glass panels. *Compos. Struct.* **47**(1–4), 497–506 (1999)
4. Mroz, G., Notash, L.: Design and prototype of parallel, wire-actuated robots with a constraining linkage. *J. Robot. Syst.* **21**(12), 677–687 (2004)
5. Sakthimurugan, D., Raj, L.A.M., Raj, V.A.A., Balaji, R., Thavasilingam, K., Bharath, N.: Static analysis of a C-channel robot gripper arm using finite element analysis. In: *Innovative Design, Analysis and Development Practices in Aerospace and Automotive Engineering*, pp. 231–237. Springer, Singapore (2020)
6. Mahanta, G.B., Rout, A., Deepak, B.B.V.L., Biswal, B.B.: Conceptual design and analysis of three jaw robotic gripper with flexural joints. In: *Innovative Product Design and Intelligent Manufacturing Systems*, pp. 1035–1042. Springer, Singapore (2020)
7. Tawk, C., Zhou, H., Sariyildiz, E., Panhuis, M.I.H., Spinks, G., Alici, G.: Design, modeling and control of a 3D printed monolithic soft robotic finger with embedded pneumatic sensing chambers. *IEEE/ASME Transactions on Mechatronics*
8. Mayyas, M., Mamidala, I.: Prosthetic finger based on fully compliant mechanism for multi-scale grasping. *Microsyst. Technol.* **27**, 1–15.
9. Dalli, D., Saliba, M.A: Towards the development of a minimal anthropomorphic robot hand. In: 2014 IEEE-RAS International Conference on Humanoid Robots, pp. 413–418, November (2014)

# Design and Development of Home Automation System



R. Boopathi Rani, N. Bavithran, and S. Prasannakumar

## 1 Introduction

IoT means the Internet of Things. It is about linking computers, processors, micro-controllers and various electronic devices to the internet. The tools and devices that we use daily are the forefront of IoT. Such devices and things are linked through a network using ZigBee [1] or Wi-Fi with Raspberry PI or Arduino, etc., to provide bidirectional communication links with a reasonable longer range and lower power and meet data rate requirement to collect information from several connected devices [2]. Home automation or smart homes can be defined as an integrating technology within the home environment to provide its occupants with convenience, comfort, protection and energy efficiency. But all these technologies are available as components or specific appliance only. We need to depend on manufacturing companies for other compact appliances, if we want to develop an automation system for an entire house. A very few foreign companies provide these kinds of services but at a higher cost. For Indian market conditions, these products may take decades to be commercialized. Motivation of this work is to design a system which takes care of many home appliances that can usually be difficult for people with physical disabilities and the aged persons. Our main objective is to develop a low-cost, efficient and secured home automation system, customized and reasonably priced by meeting the purchaser needs.

---

R. B. Rani (✉) · N. Bavithran · S. Prasannakumar  
National Institute of Technology Puducherry, Puducherry, India  
e-mail: [rbrani@nitpy.ac.in](mailto:rbrani@nitpy.ac.in)

© The Author(s), under exclusive license to Springer Nature Singapore Pte Ltd. 2022  
S. K. Natarajan et al. (eds.), *Recent Advances in Manufacturing, Automation, Design and Energy Technologies*, Lecture Notes in Mechanical Engineering,  
[https://doi.org/10.1007/978-981-16-4222-7\\_45](https://doi.org/10.1007/978-981-16-4222-7_45)

387

## 2 Literature Review

The home automation system based on SMS (Short Message Service) through GSM (Global System for Mobile Communications) phone was proposed by Teymourzadeh et al. In this, the user has an option to switch ON or OFF the home appliance via SMS [3]. Multiple home or industry automation using a centralized server was proposed by Dey et al. [4]. In this, the smart phone, computer and control system were used. The system was able to sense and control the appliances. There was no smart control. Home automation using Arduino and IoT was proposed by Mahalakshmi et al. [4]. In this, Wi-Fi-based home automation was proposed as well as GSM was used when Wi-Fi was not available. This system was proposed only for ON or OFF. Smart decisions were not taken. Another home and office automation was proposed by Ali et al. using GPRS (General Packet Radio Service) on mobile phones. Using a PC (Personal Computer) and a micro-Java application, the user interacts with the home through the use of a client/server architecture implemented at residence [5].

A GPRS-based home automation system was proposed by Danaher et al. They suggested a home security framework [6]. They have used a camera to display video and home images via GPRS to the owner's mobile. This system requires high bandwidth, and it is much expensive.

A device controller controls the home devices, which is linked to the parallel port of the PC. This architecture allows users to remotely control and query the status of devices connected to the device controller. Jin et al. have proposed a WSN (Wireless Sensor Network) and GPRS for smart automation. It allows users to control equipment at home and collect data about the status and climatic conditions of a device in apartment [7]. Again, this method lacks a smart mode execution by the system itself and required human control signals to operate.

Hence, there are number of home automation systems proposed by the researchers. Most of them are working based on the input command from the user, i.e., either to switch ON or OFF. But there are necessities for the system to have knowledge about the usage of appliances and make automatic decisions. Considering the smart decision process and tailoring the need of user, the home automation system is proposed in this paper. The subsequent sections brief various modules in the proposed system and the reason for selecting the particular component, how they are integrated, the logical implementation of the system and the smart decision-making process.

## 3 Hardware Selection

Many microcontrollers are available for the automation purposes. Arduino serves as a worthy microcontroller in automation world. But it is mainly preferred only for small-scale projects. Raspberry Pi, on the other hand, is a mini-computer with its own Linux-based operating system (Rasbian OS). One of the disadvantages of Arduino is that it can only perform one task at a time, due to memory constraints. But Raspberry

Pi is capable of multitasking and is 40 times faster than Arduino. Hence, we choose Raspberry Pi microcontroller with inbuilt Wi-Fi to interface mobile application. Moreover, the Raspberry Pi has an inbuilt voice recognition system which can be used to perform voice control over the appliances in home automation. This can be achieved by installing a PiAUISuite. The voice control features can be installed as per the customer requirements during installation.

### 4 Implementation Technique

Our goal is to control home appliances with mobile application. Hence, we need to develop a hardware that can interface with a mobile android application. We achieve this through hosting a compact webserver in our Raspberry Pi system and checking for http requests from the mobile application. These requests are then processed into actions using an Application Program Interface (API). The API will act as a bridge between the input from the user and response from the machine. The 240 V AC home power supply is interfaced with the Raspberry Pi controller using a four-channel 230 V relay. It gives an option to have a control over a 230 V system using 5 V control signals from the microcontroller. The overall working is shown in Fig. 1. The block diagram of the system is shown in Fig. 2.

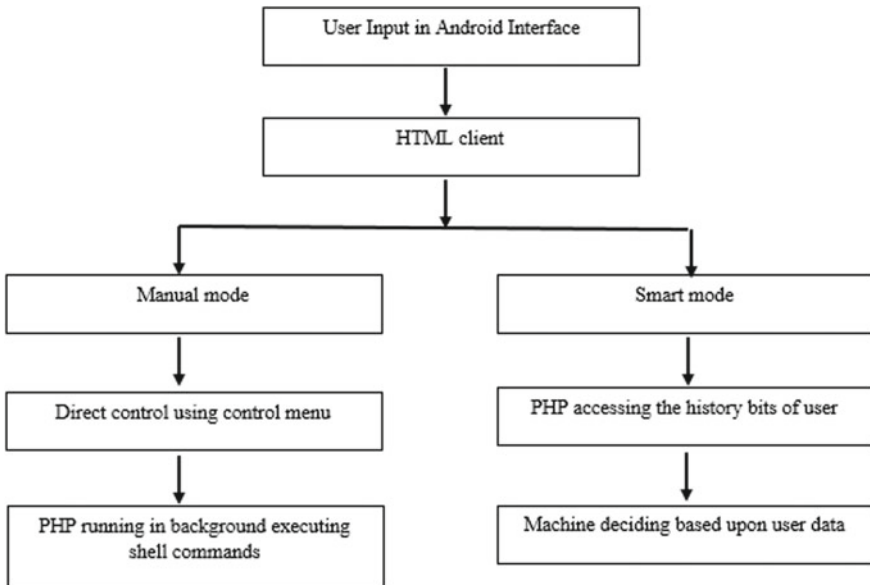


Fig. 1 Block diagram of the home automation system



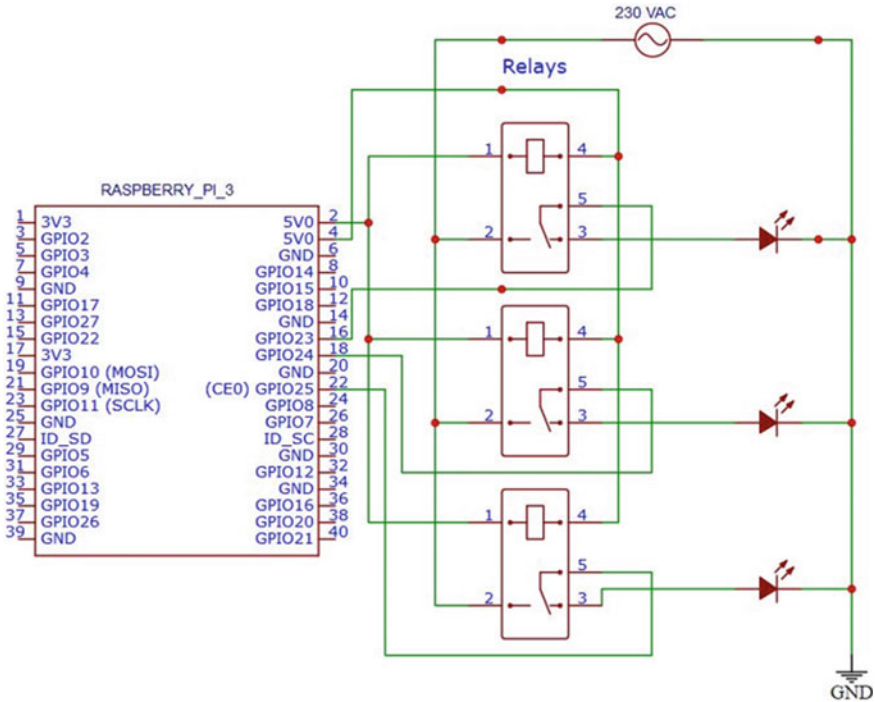


Fig. 2 Block diagram of the home automation system

## 5 Software Installations

### 5.1 MobaXterm X Server

MobaXterm is an ultimate remote-computer toolbox. It uses the secure shell (SSH) method to connect to Raspberry Pi. We use this software to interface the Raspberry Pi microcontroller with personal computer.

### 5.2 Apache2 Webserver

Since the proposed mobile application is a client, we need a server to complete the network. This can be achieved by Apache2 webserver which is a free open-source software and is widely used with the Raspbian OS. The simple architecture of the program enables us to edit the root files and modify the webserver according to our requirements. Due to this flexibility, we choose Apache2 webserver over the number of other servers available.

### **5.3 PHP 7.4**

The API acts as a bridge between the html server and mobile client which is developed on PHP. The PHP script runs on Apache2 webserver. The commands which modify the system settings are called as shell commands which are normally excluded from the html access. We can access the shell commands only through the PHP script in the background.

### **5.4 HTML Design**

A customer-accessible webpage interface is developed in html platform for the user to access the automation system using their laptops or other devices apart from android platform. This gives the user to go with number of control platforms to access their home devices. The first html page gives the menu of manual and smart control option. The second webpage will be hyperlinked to manual button which directs us to manual control menu. The smart option will be directly linked to the PHP API in the background and make the system to automatically switch to the smart mode. The manual menu has the options turn ON and OFF. The users can switch between the manual and smart controls according to their wish. A Python program runs in the background for executing the smart mode.

## **6 Data Acquisition and Working**

A Python program continuously runs in the background to record the status of each I/O (input/output) pins and store them in a data file. The data file is nothing but a Python pickle file which we already created and saved in an accessible location. The pickle file is a form of list which stores the data of about 20 days into a 5-min time-frame structure.

### **6.1 Python Structure**

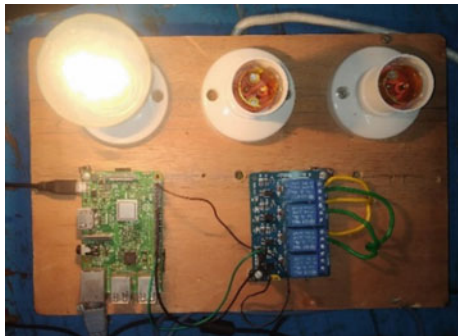
We use the inbuilt Python option of storing the data in a list structure in order to save our user data and use it for later computations. In this way, we can avoid use of database systems in the Raspberry Pi microcontroller which makes it fast and smooth for doing calculations and executing commands. In order to create the data set, we need to divide a day into several time frames of each 5 min. It gives us 288 data sets per day, and for 20 days we would get 5760 data entries. The data are shown in Fig. 3.





Fig. 4 Output of the smart mode in terminal

Fig. 5 Hardware implementation



the conditions given in Sect. 6.2 for smart mode operation. From 21st day onwards, the system continues to store the appliance state for every 5 min and retains past 20-day data. A test data set is created and demonstrated to show smart mode. The implemented hardware is shown in the Fig. 5.

### 7 Results

The manual and smart modes were implemented successfully in the Raspberry Pi microcontroller. The current market products like Mangalam InfoTech and AEI Automations offer the automation systems at INR 25,000. DYFO automations provide service at INR 15,000–20,000. The overall cost of our project is below ₹5000 which met the primary objective of being cost-effective. The pickling method instead of RDBMS (Relational Database Management System) made the process faster by reducing time required to load the database. It also eliminates the cost of being dependent on a database server of foreign companies which charges on monthly basis.. Currently, it is developed to automate three lights in the home. To add the appliances, we just need to add a data entry in the Python pickle list. The lights can be directly controlled over the manual mode by the user as well as used in smart mode. This approach can be applied to any other appliance in the home.

In smart mode previous user data are interpreted and decision is taken. Accuracy depends on the amount of user data available. The initial user data are required for the operation of the smart mode. If previous 20 days of data are available to the system, then the program performs accurately. The initialization of the program was coded to the boot folder of the Raspbian OS, which ensures to load the automation system once the system receives power. This ensures that the system does not fail. Voice control can also be established, if requested by the customer during installation. The code analysis of the program will be done in the testing platforms (like Sonarcube) once we add some more features to the system.

### 7.1 Android Interface

The mobile application is developed on Kotlin platform. We have to connect our mobile to the hotspot of the Raspberry Pi. The hotspot can be created by turning the microcontroller into an access point. This can be achieved in different boards by different methods which can be found on developer forums. Another method is to connect the mobile and microcontroller in the same network. Either of the above methods can be used to send the http requests from the mobile application to the Apache server hosted by the microcontroller. The mobile application interface is shown in the Fig. 6.

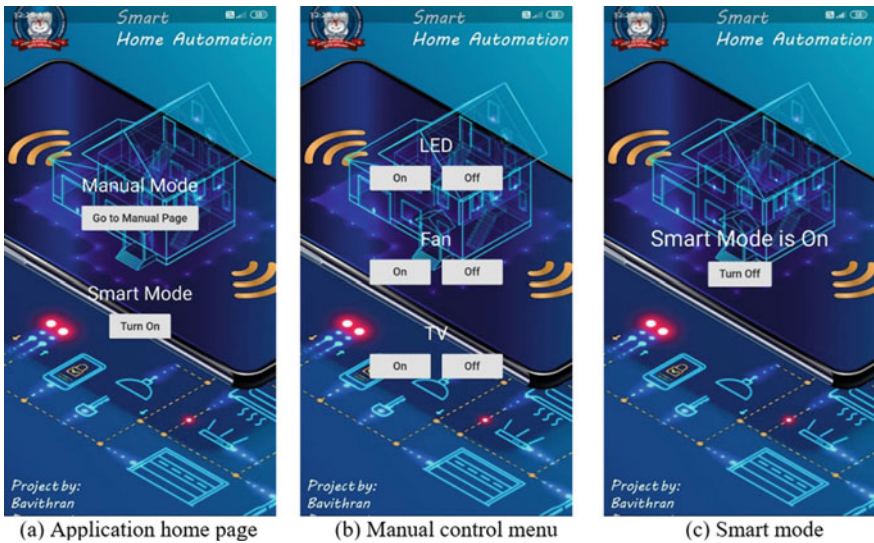


Fig. 6 Mobile application interface

## 8 Conclusion

The home automation system with both manual and smart modes was designed and implemented. It comes under the cost of ₹5000/- which meets the demands of the Indian Market. The system is also customizable according to end user's requirement. The customized mobile application gives the user comfortable experience and makes the product more efficient. We hope to bring this product into market as soon as possible and to give a new experience on smart home to the users. The project can be further improved by introducing smart control over individual appliances instead of overall control option. A voice module can be interfaced and voice automation can be carried over the same system if requested by the user. The camera surveillance can be implemented by using a Raspi-Cam module available in the market

## References

1. Karlof, C., Wagner, D.: Secure routing in wireless sensor networks: attacks and countermeasures. *Ad Hoc Net.* **1**(2–3), 293–315 (2003)
2. Wang, W., Siau, K.: Artificial intelligence, machine learning, automation, robotics, future of work and future of humanity: A review and research agenda. *J. Database Manag.* **30**(1), 61–79 (2019)
3. Teymourzadeh, R., Ahmed, S.A., Chan, K.W., Hoong, M.V.: Smart GSM based home automation system. In: *IEEE Conference on Systems, Process & Control*, pp. 306–309 (2013)
4. Dey, S., Roy, A., Das, S.: Home automation using Internet of Thing. In: *IEEE 7th Annual Ubiquitous Computing, Electronics & Mobile Communication Conference*, pp. 1–6 (2016); Mahalakshmi, G., Vigneshwaran, M.: IOT based home automation using Arduino. *Int. J. Engineering Adv. Res. Tech.* **3**(8), 7–11 (2017)
5. Ali, U., Nawaz, S.J., Jawad, N.: A real-time control system for home/Office appliances automation, from mobile device through GPRS network. In: *13th IEEE International Conference on Electronics, Circuits and Systems*, pp. 854–857 (2006)
6. Danaher, M., Nguyen, D.: Mobile home security with GPRS. In: *8th International Symposium for Information Science*, pp. 377–380 (2002)
7. Ali, U., Nawaz, S.J., Jawad, N.: A real-time control system for home/office appliances automation, from the mobile device through GPRS network. In: *13th IEEE International Conference on Electronics, Circuits, and Systems*, pp. 854–857 (2006)

# Design and Development of Automatic System to Protect Crop from Animals and Birds



R. Boopathi Rani, A. Preetha, and S. Gnanavalli

## 1 Introduction

As need and greediness of the human increases, human move into the forest to satisfy their livelihood, for land and agricultural practices and rapid industrialization, which causes spreading of urban ground. Due to this, animals enter into the nearby villages for water during summer due to dried water bodies. Animals such as elephant or boar tramp the vegetation in farmland in the need of nutritious food. Need of the animal or human puts the others in danger. When the animals enter the field, they destroy the irrigation canals, consume the crop, and they destroy the vegetation, which leads to the economic loss for the farmer. In the case of birds, due to the abundant availability of food, they attack the farm. If the crop is at sprouting stage at the time of birds' invasion, the damage will be so severe that, the farmer has to resow his field. Hence, we have attempted to take care of this important issue by designing an automatic system using Raspberry Pi. This paper explains the design and implementation of the proposed system.

## 2 Literature Review

A brief review about the literature related to the proposed concept is discussed in this section. Srinivasan et al. proposed a Complex Animal Movement Capture and Live Transmission (CAMCALT) system. CAMCALT is a device specifically tailored for the need of the forest surveillance and monitoring system. It integrates the IoT with the forest trap cameras for the live feed from any part of the world. It was

---

R. Boopathi Rani (✉) · A. Preetha · S. Gnanavalli  
National Institute of Technology Puducherry, Thiruvettakudy, India  
e-mail: [rbrani@nitpy.ac.in](mailto:rbrani@nitpy.ac.in)

designed with the help of user-friendly interface which is connected with Raspberry Pi-3B [1]. This system was also focused on detection of animal and monitoring its movement. Alippi et al. had presented a Lightweight and Energy-efficient Internet-of-Birds Tracking System. This is an engineering framework for following animal movements particularly birds, and it is only a tracking system [2].

Jeevitha et al. presented a review on existing intrusion detection systems. Mostly, the existing systems were able to detect the entry, but countermeasures were not proposed to drive them away [3]. Ashwini et al. presented a comparative study and analysis of approaches toward agricultural supervision [4]. The idea was to give data about existing methodologies and give a superior answer for defeating the current issues. Techniques, such as, image processing, radar system, voice recognition, and motion sensors are utilized for identification. In this study, there were more than 80% of researches focused on identification and monitoring. An IoT-based automatic crop protection system was proposed by Dev et al. [5]. In that, ultrasonic sound was used depending on the intruding animal. The response time and complexity of the system proposed by Dev et al. were high. There was no complete system to drive away the intruding birds and animals. Hence, it is important to develop a system to protect crops from animals and birds which take preventive action as well as alert the farmer.

### 3 Proposed System

Initially, the field study was conducted by the project team to know the nature of the field, and the animals and birds often enter the field and how they might be driven away. It was found that the greater part of the creatures' can be threatened by sound, and feathered creatures can be driven away by showering water. Then, the system is proposed to be designed using Raspberry Pi [6]. The functions of the system include detection of animal or bird using PIR motion sensor, taking appropriate action to drive them away and send information to the farmer. To recognize the movement, PIR sensor is used. Two PIR sensors are kept at two different heights to identify whether the entered creature is animal or bird. It was assumed that if the top sensor detects, it will be bird, and if bottom sensor detects, it will be animal. It was found in the survey that birds can be driven away by sprinkling water, and animal can be driven away using blaze light. Accordingly, the proposed system is designed to take appropriate actions and inform farmer as well. The PIR sensors are kept on head of a stepper motor for monitoring the field throughout 360°. More frequent messages will annoy the farmer. Hence, the program is written in a way that the PIR sensor distinguishes any movement at the 10th, 30th, 50th, etc., step instead of each step of the stepper motor to avoid superfluous collection of information. With these ideas, the system is designed and implemented.



### 4 System Overview

Figure 1 describes the architecture of the proposed system. This section briefs the selection of hardware component and its integration in the system. The complete details of specific hardware components can be referred from [6–11]. A sensor is needed to detect the movement of species that enters. In this system, the PIR sensor is used for detecting the animal or bird movement [7]. A field may be vulnerable to both animals and birds. So, we need to detect both. Hence, the minimum number of PIR sensors needed is two. As they cover 90–110°, the two PIR sensors are kept at a distance on pile. So that, the covering angles does not interfere. A field may be larger. So, we cannot make that pile stand stationary at the edge. For a surveillance of 360°, the PIR sensors pile has to be rotating around 360°, covering an area of nearly 314.2 m<sup>2</sup>. Hence, it is kept on stepper motor.

The hybrid stepper motor consists of the features of both the permanent and variable reluctance stepper motors. As they are cheap, highly reliable, provide high torque at low speed, easy, and rugged construction made it to work in almost all the environment [8], we chose it and kept the PIR sensors pile on it. We have programmed the system to detect the motion at 10th, 30th and 50th, etc., step of rotation instead of every rotation to avoid unnecessary flooding of data in the event of detection. The program is written in python using MobaXterm software.

Here, we use the Raspberry Pi (R-Pi) microcomputer to implement the system which interfaces the software with the PIR sensors and the stepper motor. With the help of R-Pi's 40 General Purpose Input Output (GPIO) pins, we connect the PIR

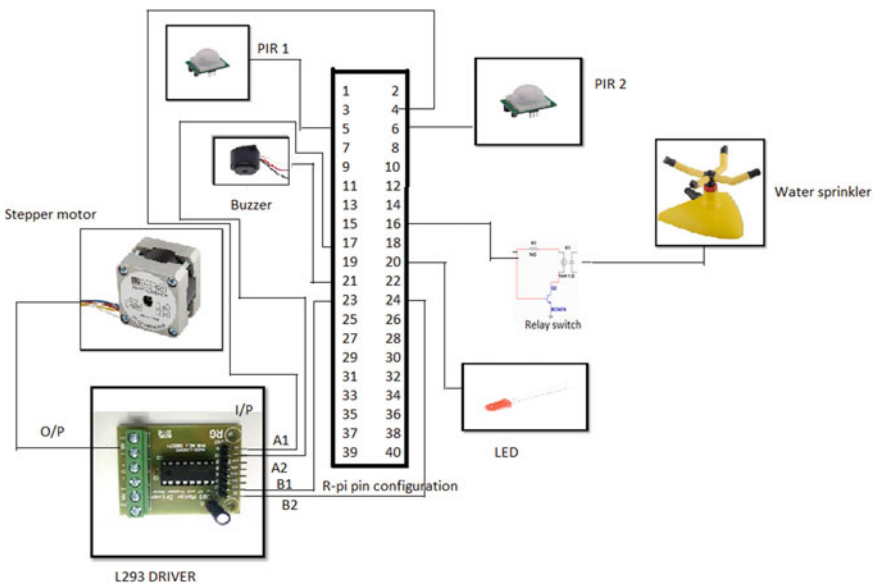


Fig. 1 System architecture

sensors. As stepper motor works with 230 V and the output of R-Pi GPIO pins is 5 V [6], we need a H-bridge circuit. So, we use the L293 driver for driving the bidirectional motor. This Integrated Circuit (IC) allows DC stepper motor to drive in both the directions. It can control two DC motors simultaneously in any direction due to the presence of two H-bridge circuit inside the driver [9]. Once movement is detected and then comes the preventive measures.

If the animal enters the field, the PIR sensor at the bottom will detect. From our study, we found that most of the animals are afraid of light and sound. So, we can connect the flash light and alarm. For the prototype, we have used led and buzzer. Both are connected with the GPIO pins of R-Pi. If there are a flock of birds entering the field, we can sprinkle water to drive them away as we found it in our study. To sprinkle water, water sprinkler is used. To connect the water sprinkler with R-Pi, we use relay. It controls an electrical circuit by the energization of open or close contacts through coils [10]. The solenoid valve is used to have a controlled water flow. Once the motion is detected, the relay permits the current to flow through the solenoid valve. The current triggers the plunger, and there will be flow of water and is sprinkled with the help of water sprinkler [11]. If there is a bigger animal, then both the sensors detect. Then light and buzzer will be ON, and the water sprinkler will sprinkle water.

## 5 Software Used

**Mobaxterm:** It is an enhanced terminal for windows, which brings all essential UNIX (an operating system) commands to windows desktop. It is the tool box for remote computing and is compatible with Raspberry Pi. Here the codes were written in Python script. Once interfaced, the model can be controlled with the help of programmed codes.

**Communication Network:** TWILIO is the communication platform used in this experiment. It is the developer platform for communications. TWILIO API (Application Performing Interface) is used for the applications like voice, video, and messaging.

## 6 Flowchart

Figure 2 explains the working model. When the sensor 1 (at the bottom) detects any movement, LED and buzzer will be ON, and at the same time, message will be sent to the farmer about the detection. Similarly, when the sensor 2 (at the top) detects any movement, the relay will be ON, and it will make the water sprinkler to sprinkle the water, and at the same time, message will be sent to the farmer about the detection. When both the sensor detects motion, the LED and buzzer will turn ON, and water

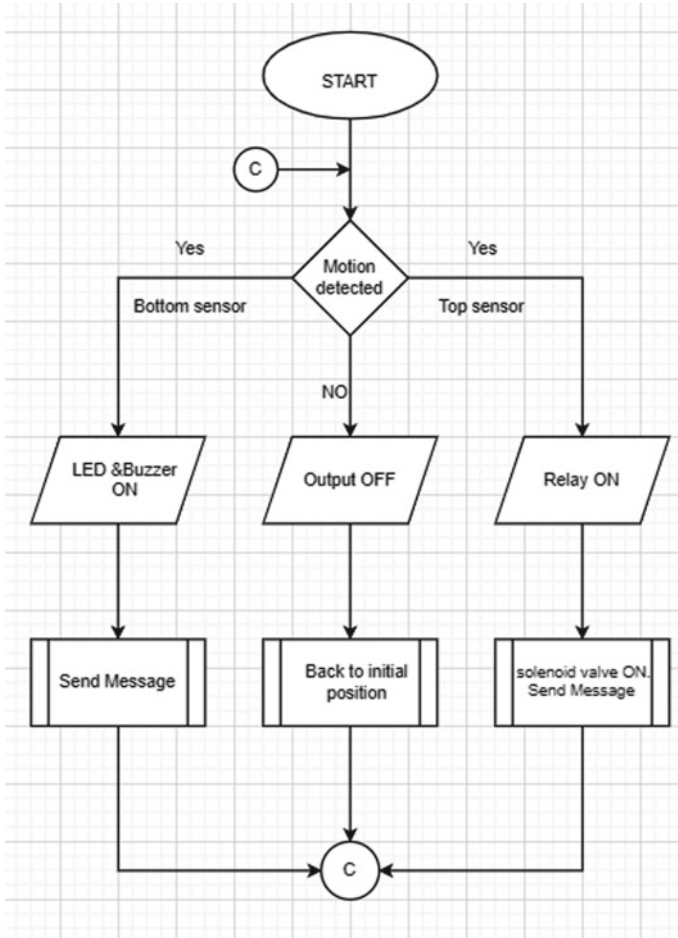
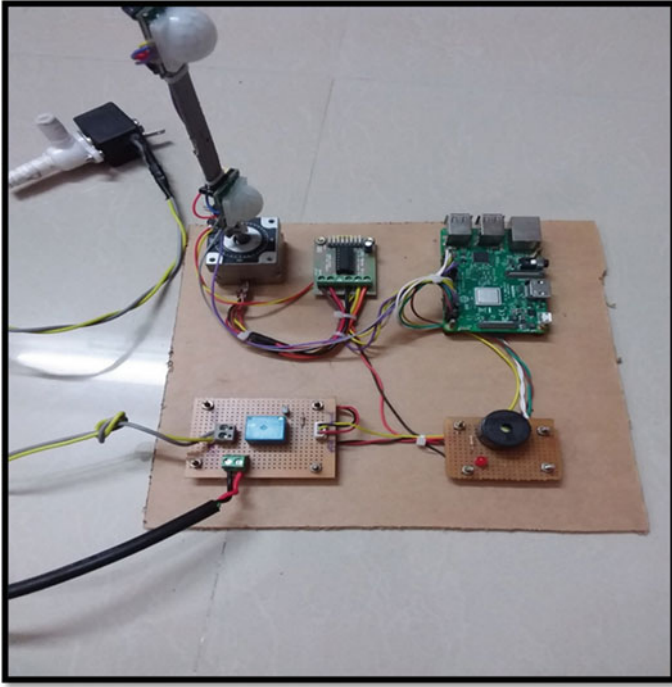


Fig. 2 Flowchart of the proposed system

will be sprinkled. As in all other cases, message will be sent to the farmer about the detection. But, when no detection takes place, LED, buzzer, and relay will be off, and therefore, no operation takes place.

## 7 Experimentation and Results

Figure 3 shows the experimental setup of the proposed system. The two PIR sensors are kept at a distance on a pile and are connected to the R-Pi in such a way that, it can sense movement at two different heights. The PIR sensor pile is kept on the stepper motor. It is connected to the R-Pi with the help of L293 driver. L293 driver consists



**Fig. 3** Experimental setup

of H-bridge circuit which helps in controlling the DC motor. Inputs are given from the GPIO pins of R-Pi to the driver. The PIR sensor detects the motion at 10th, 30th, 50th step, and so on of the stepper motor instead of every step to avoid unnecessary accumulation of data.

When the PIR sensor at the bottom senses any motion, the LED and the buzzer which are connected to the R-Pi will turn ON. When the sensor at the top senses any motion, the relay will get tripped. It gives power to the solenoid valve, and the water will sprinkle with the help of water sprinkler. When both sensors detect the motion, then the LED and the buzzer will turn ON, and the water sprinkler sprinkles the water. This condition is shown in Fig. 4

Once the motion is detected, the message about the detection is sent to the farmer with the help of an API interface TWILIO. A message will be sent from a TWILIO account to the mobile of the farmer. The message is shown in Fig. 5

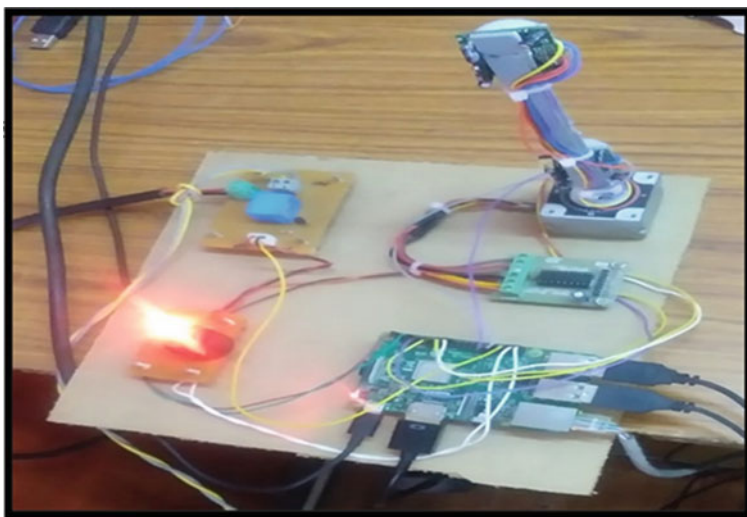
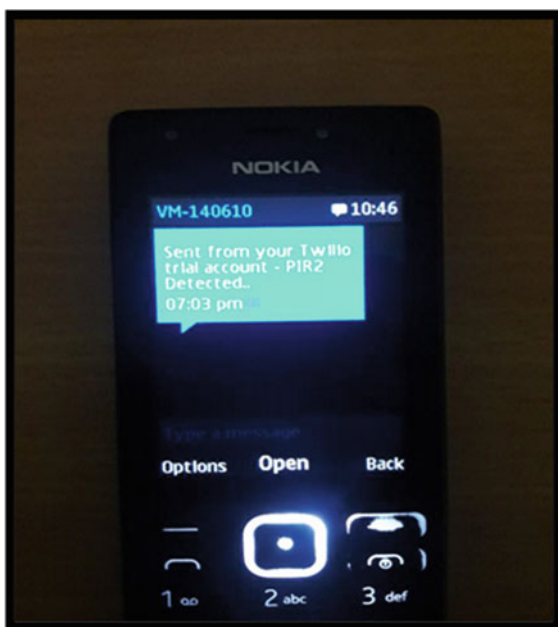


Fig. 4 Working condition

Fig. 5 Message from Twilio



## 8 Limitations and Future Work

PIR sensor can be easily interfered by any heat source. To avoid confusion, image processing techniques can be introduced to detect the source of heat. Currently, PIR sensor is connected with the help of wire, and it can be made wireless.

## 9 Conclusion

The agricultural field is destroyed by the unwanted entry of animal and bird. As a protective measure, the animals were usually threatened or exposed to electric fencing which may harm the animal. Hence, the farms must be monitored continuously to prevent the destruction and drive away the animals and birds. In this regard, a prototype is designed and implemented for detecting the intrusion of animal or bird with the help of PIR sensor, drive away them by suitable counter actions and informing the farmer about the detection. The experiment and the observation validate the proposed system, and it will be a better solution for the animal intrusion problem in the farming fields.

## References

1. Srinivasan, S.R., Sridhar, S., Balasubramanian, G., Vasu, K.: Complex animal movement capture and live transmission (CAMCALT). In: IEEE Region 10 Conference TENCON, pp. 0978–0981 (2018)
2. Alippi, C., Ambrosini, R., Longoni, V., Cogliati, D., Roveri, M.: A lightweight and energy-efficient internet-of-birds tracking system. In: IEEE International Conference on Pervasive Computing and Communications, pp. 160–169 (2017)
3. Jeevitha, S., Kumar, V.: A review of animal intrusion detection system. *Int. J. Eng. Res. Technol.* **9**(5), 1219–1221 (2020)
4. Akula, A., Deshmane, P., Thorat, S., Bagbande, A., Pawar, M.A.: A comparative study and analysis of approaches towards agricultural supervision. In: IEEE International Conference on Global Trends in Signal Processing, Information Computing and Communication, pp. 510–515 (2016)
5. Gogul Dev, N.S., Sreenesh, K.S., Binu, P.K.: IoT based automated crop protection system. In: 2nd International Conference on Intelligent Computing, Instrumentation and Control Technologies, vol. 1, pp. 1333–1337 (2019)
6. Information about Raspberry pi. Website: <https://www.raspberrypi.org/>
7. Information about PIR sensor. Website: <https://learn.adafruit.com/pir-passive-infrared-proximity-motion-sensor/overview>
8. Athani, V.V.: Stepper motors: fundamentals, applications and design. New Age Int. (1997)
9. Information about Motor Driver. Website: [https://embetronicx.com/tutorials/tech\\_devices/1293d-motor-driver-working/](https://embetronicx.com/tutorials/tech_devices/1293d-motor-driver-working/)

10. Information about Relays. Website: <https://www.galco.com/comp/prod/relay.htm>
11. Information about Solenoid valve. Website: <https://www.Brighthubengineering.com/manufacturing-technology/56397-parts-of-the-solenoid-valve-how-solenoid-valve-works/>

# Spectrogram as an Emerging Tool in ECG Signal Processing



Varun Gupta, Monika Mittal, Vikas Mittal, and Nitin Kumar Saxena

## 1 Introduction

Heart comprises of four chambers—the right & left atrium and the right & left ventricle. The automatic pacemaker in the heart is known as the sinoatrial (SA) node which is located in the right atrium [1]. It presents its activity in the form of electrical signal known as Electrocardiogram (ECG) signal. ECG is a non-invasive process of heart diagnosing during which action potentials are generated and combined in the form of three waves known as P-QRS-T waves [2, 3]. ECG is mostly used for diagnosing arrhythmias, coronary heart disease, heart attacks and cardiomyopathy [4, 5].

Over the last two decades, cardiac arrhythmia seeks huge attention in health care due to availability of ECG diagnostic tool which has great reproducibility [6]. During cardiac arrhythmias, heart's blood supply is blocked or interrupted during coronary heart disease and is completely blocked suddenly [7, 8]. And heart walls get thickened or enlarged during cardiomyopathy.

Other important ECG features are estimation of optimal trajectory of P-QRS-T wave in case of normal and highly noisy environment, spectral components estimation, etc. [9, 10]. In past literature, various techniques have already been incorporated in ECG signal analysis such as maximum mean minimum (MaMeMi) filter [11], autoregressive time-frequency analysis (ARTFA) [12, 13], chaos analysis [14–16], fractional Fourier transform (FrFT) [17], wavelet-based techniques [18–20], signal entropy [21], K-means algorithm [22], support vector machine (SVM) [23], principal component analysis (PCA) [24, 25], savitzky golay digital filtering (SGDF) [26], autoregressive (AR) modelling [27] and Stockwell transform (S-transform)

---

V. Gupta (✉) · N. K. Saxena  
KIET Group of Institutions, Delhi-NCR, Ghaziabad 201206, Uttar Pradesh, India

M. Mittal · V. Mittal  
National Institute of Technology, Kurukshetra 136119, Haryana, India



[28]. Unfortunately, these proposed techniques have not universally accepted due to its operating limitations. Moreover, these techniques were resulted into large FNs and FPs. These issues are motivated to propose an emerging tool in biomedical digital signal processing (BDSP). In this paper, a spectrogram-based feature extraction is proposed which is squared magnitude of the short-time Fourier transform (STFT) presenting a signal in joint time-frequency domain [29–31].

## 2 Related Work

Every new research work is initiated in the context of shortcomings of the previous methodologies. Therefore, this section contains the diverse literature survey on ECG signal analysis [32–39].

In [32], M. Mortezaee et al. proposed a singular spectrum analysis (SSA)-based denoising the ECG signals. They used the following steps—(i) embedding, (ii) singular value decomposition, (iii) grouping and (iv) diagonal averaging. But the execution of these steps is not easy even requires special attention. In [33], S. Chandra et al. used cosine modulated filter bank for data compression of ECG datasets. It requires the involvement of interpolated finite impulse response prototype filter, linear iteration technique, thresholding and run length encoding for its smooth conduction. In [34], S. S. Mehta and N. S. Lingayat proposed the detection of QRS complexes using support vector machine (SVM). They used two techniques for pre-processing of raw ECG datasets—(i) digital filtering and (ii) entropy criterion and presented detection rate (DR) of 99.79%. In [35], P. Marwaha and R. K. Sunkaria proposed sample entropy for investigation of ECG datasets. They used physiologic and pathologic time series with multiscale entropy for classifying different types of cardiac arrhythmias.

## 3 Materials and Methods

Electrical signals are recorded using electrodes from the surface of the body. Electrodes convert the ionic current energy into electrical current energy. In this paper, 23 real-time datasets are used obtained by BIOPAC machinery MP35 at 360 Hz sampling rate. Figure 1 shows proposed methodology.

### 3.1 Pre-processing Using DBPF

Digital band pass filtering (DBPF) is obtained by cascading of high pass and low pass filtering sections [40]. To get the smooth conduction of DBPF, proper selection of cut-off frequencies of high pass and low pass sections is so important.

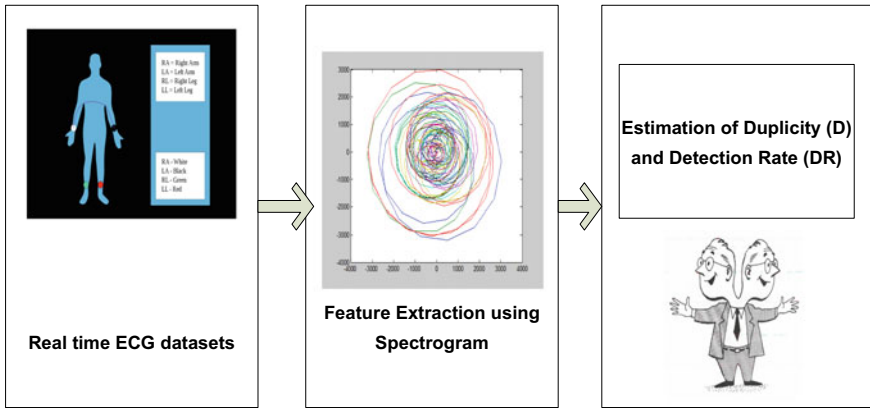


Fig. 1 Proposed methodology

### 3.2 Spectrogram

In spectrogram, sequences of spectra are shown [41–43] in which one axis is dedicated to time, and second axis is dedicated to frequency. And brightness or colour shows strength of a frequency component at each time frame [42]. It is given as [44–46]

$$X_f(t, f; s) = \int_{-\infty}^{+\infty} f(\alpha) \cdot s^*(\alpha - t) \cdot e^{-j2\pi f\alpha} \cdot d\alpha \tag{1}$$

where  $s$ ,  $t$  and  $f$  are the window function, time variable and frequency variable, respectively.

### 3.3 K-Nearest Neighbour (KNN) Classifier

KNN is used in classification problem due to three main reasons such as easy to interpret output, accuracy and predictive power. These are the main motivations to apply KNN in this paper. For achieving it, the distance between test data and each row of training data is estimated [47–49].

### 3.4 Figures-of-Merit (FoM)

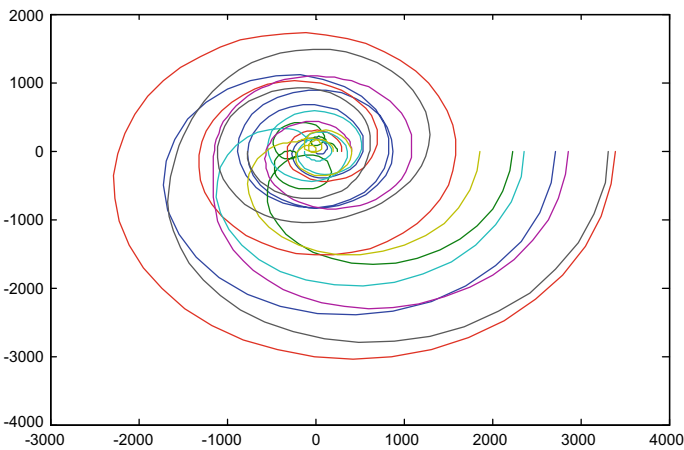
In this paper, two figures-of-merit (FoM) are considered which are duplicity ( $D$ ) and detection rate (DR) [49, 50].

$$\text{Duplicity}(D) = \frac{\text{No. of (TP + FP + FN)} - \text{Actual beats}}{\text{Actual beats}} \times 100\% \quad (2)$$

$$\text{Detection Rate (DR)} = \frac{\text{Total True Positive (TP)}}{\text{Total actual beats}} \times 100\% \quad (3)$$

## 4 Results and Discussion

Baseline wander (BLW) and power line noises (PLNs) are very annoying problem in ECG signal which makes its interpretation/classification problem very tedious [51]. After digital band pass filtering, these are effectively removed, and feature extraction step starts. It is achieved by selecting different window functions which is selected according to the condition of ECG datasets/minimum spectral leakage effect [12]. Figure 2 shows spectrogram plot in which wave components of ECG dataset is not making any loop which indicates the presence of cardiac and non-cardiac components. For verification of frequency components, contour plot is shown in Fig. 3. In Fig. 3, it is clearly revealed that noise components are shown by red colour. Here it is not clearly mentioned the noise components according the P-Q-R-S-T wave components (cardiac components shown by sky blue, blue, green, orange, light green colour) of the ECG signal.



**Fig. 2** Spectrogram of recorded ECG dataset

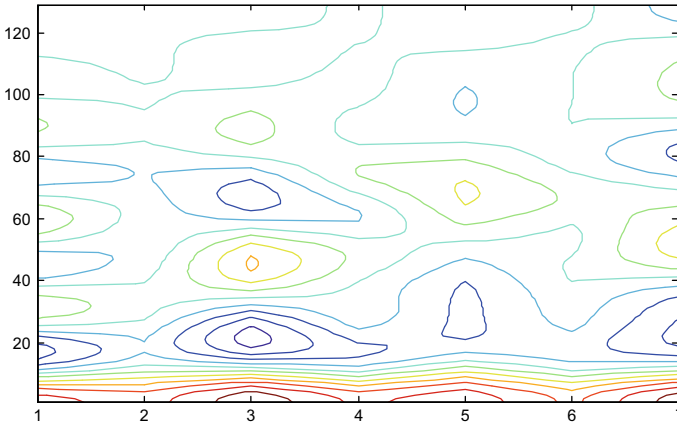


Fig. 3 Contour plot of recorded ECG dataset

Figure 4 shows spectrogram plot in which ECG dataset of the patient is making loop which indicates the removal of non-cardiac components (BLW, PLNs, etc.). Figure 5 shows cardiac components shown by sky blue, blue, green, orange and light green colour with corresponding noise components (shown by small red circles).

It has been observed that the proposed work achieves DR of 99.48%, whereas Mehta and Lingayat [34] achieved DR of 99.79%. In this paper, KNN classifier is used which can handle new data seamlessly; whereas in Mehta and Lingayat [34], SVM classifier was used which is not suitable for large datasets.

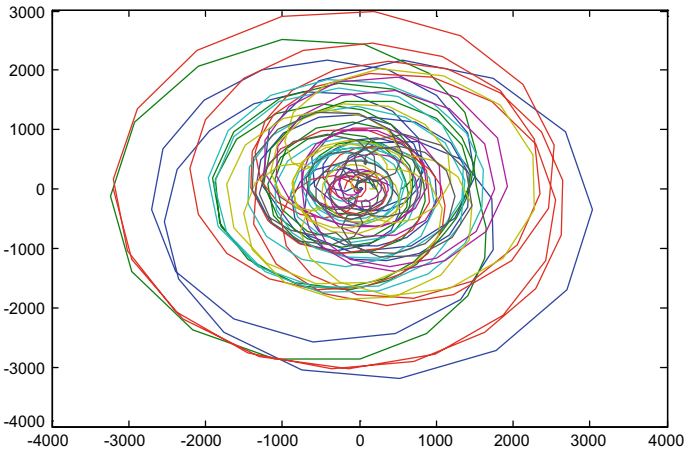
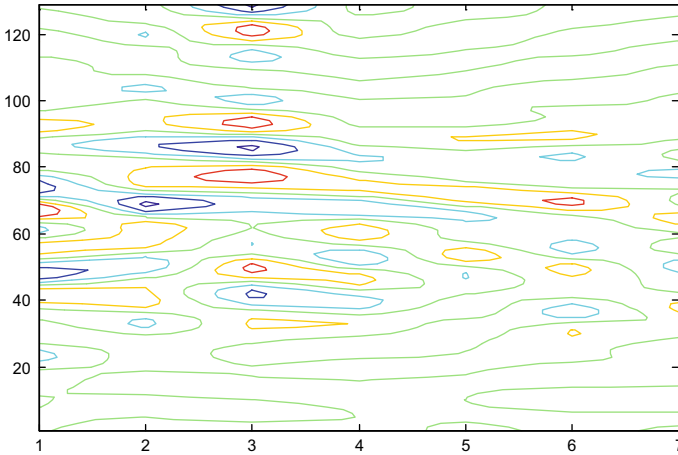


Fig. 4 Spectrogram of filtered ECG dataset using hamming window



**Fig. 5** Contour plot of filtered ECG dataset using hamming window

## 5 Conclusion

This paper sketches the landscape of the raw and filtered ECG datasets and verifies using contour plot. Spectrogram effectively showcases the time-frequency-intensity spectrum using contour and trajectory plot with hamming window. It may cover various important applications and features related to computational medicine of ECG signal. The proposed technique has been tested on 23 real-time datasets and obtained D of 0.4% and DR of 99.48%.

As STFT relies on window length for better time and frequency resolution. In future, this technique may be replaced by—(i) Fractional S-transform and (ii) short-time fractional Fourier transform (STFrFT).

## References

1. Heart structure. <https://www.online-sciences.com/tag/heart-structure/>. Last accessed 09 Sept 2020
2. Singh, R.S., Saini, B.S., Sunkaria, R.K.: Times varying spectral coherence investigation of cardiovascular signals based on energy concentration in healthy young and elderly subjects by the adaptive continuous Morlet wavelet transform. *IRBM* **39**(1), 54–68 (2018)
3. Singh, D., Saini, B.S., Kumar, V.: Heart rate variability—a bibliographical survey. *IETE J. Res.* **54**(3), 209–216 (2008)
4. Zidelmal, Z.: QRS detection based on wavelet coefficients. *Comp. Met. Prog. Biomed.* **107**(3), 490–496 (2012)
5. Luz, E.J.S., Schwartz, W.R., Chávez, G.C., Menotti, D.: ECG-based heartbeat classification for arrhythmia detection: a survey. *J. Com. Met. Prog. Biom.* **127**, 144–164 (2016)

6. Singh, R.S., Saini, B.S., Sunkaria, R.K.: Arrhythmia detection based on time–frequency features of heart rate variability and back-propagation neural network. *Iran J. Comput. Sci.* (2019). <https://doi.org/10.1007/s42044-019-00042-1>
7. Chakraborty, M., Ghosh, D.: Quantitative assessment of arrhythmia using non-linear approach: a non-invasive prognostic tool. *J. Inst. Eng. India Ser. B.* (2017). <https://doi.org/10.1007/s4031-017-0307-3>
8. Jung, W.H., Lee, S.G.: An arrhythmia classification method in utilizing the weighted KNN and the fitness rule. *IRBM* (2017). <https://doi.org/10.1016/j.irbm.2017.04.002>
9. Rai, H.M., Trivedi, A., Chatterjee, K., Shukla, S.: R-peak detection using Daubechies wavelet and ECG signal classification using radial basis function neural network. *J. Inst. Eng. India Ser. B.* **95**(1), 63–71 (2014)
10. Halder, B., Mitra, S., Mitra, M.: Classification of complete myocardial infarction using rule-based rough set method and rough set explorer system. *IETE J. Res.* (2019). <https://doi.org/10.1080/03772063.2019.1588175>
11. Sheetal, A., Singh, H., Kaur, A.: QRS detection of ECG signal using hybrid derivative and MaMeMi filter by effectively eliminating the baseline wander. *Analog Integr. Circ. Sig. Process.* **98**(1), 1–9 (2019)
12. Gupta, V., Mittal, M.: Respiratory signal analysis using PCA, FFT and ARTFA. In: *Proceeding of the 2016 International Conference on Electrical Power and Energy Systems (ICEPES)*, December 14–16, pp. 221–225. India (2016)
13. Gupta, V., Kanungo, A., Kumar, P., Sharma, A.K., Gupta, A.: Auto-regressive time frequency analysis (ARTFA) of electrocardiogram (ECG) signal. *Int. J. Appl. Eng. Res.* **13**(6), 133–138 (2018)
14. Gupta, V., Mittal, M., Mittal, V.: R-peak detection based chaos analysis of ECG signal. *Analog Integr. Circ. Sig. Process.* (2019). <https://doi.org/10.1007/s10470-019-01556-1>
15. Nguomkam, A., Kengne, J.: A minimal three-term chaotic flow with coexisting routes to chaos, multiple solutions, and its analog circuit realization. *Analog Integr. Circ. Sig. Process.* (2019). <https://doi.org/10.1007/s10470-019-01436-8>
16. Gupta, V., Mittal, M.: Electrocardiogram signals interpretation using Chaos theory. *J. Adv. Res. Dyn. Con. Sys.* **9**, 2392–2397 (2018)
17. Gupta, V., Mittal, M.: A comparison of ECG signal pre-processing using FrFT, FrWT and IPCA for improved analysis. *IRBM* **40**(3), 145–156 (2019)
18. Kora, P., Krishna, K.S.R.: ECG based heart arrhythmia detection using wavelet coherence and bat algorithm. *Sens. Imag.* **17**, 1–16 (2016)
19. Xingyuan, W., Juan, M.: Wavelet-based hybrid ECG compression technique. *Analog Integr. Circ. Sig. Process.* **59**(3), 301–308 (2009)
20. Rajankar, S.O., Talbar, S.N.: An electrocardiogram signal compression techniques: a comprehensive review. *Analog Integr. Circ. Sig. Process.* **98**(1), 59–74 (2019)
21. Mehta, S.S., Lingayat, N.S.: SVM based QRS detection in electrocardiogram using signal entropy. *IETE J. Res.* **54**(3), 231–240 (2008)
22. Mehta, S.S., Shete, D.A., Lingayat, N.S., Chouhan, V.S.: K-means algorithm for the detection and delineation of QRS-complexes in electrocardiogram. *IRBM* **31**, 48–54 (2010)
23. Mehta, S.S., Lingayat, N.S.: SVM-based algorithm for recognition of QRS complexes in electrocardiogram. *IRBM* **29**, 310–317 (2008)
24. Gupta, V., Mittal, M.: Arrhythmia detection in ECG signal using fractional wavelet transform with principal component analysis. *J. Inst. Eng. (India): Ser. B* (2020). <https://doi.org/10.1007/s40031-020-00488-z>
25. Gupta, V., Mittal, M.: QRS complex detection using STFT, Chaos analysis, and PCA in standard and real-time ECG databases. *J. Inst. Eng. India Ser. B* **100**(5), 489–497 (2019)
26. Gupta, V., Mittal, M.: A novel method of cardiac arrhythmia detection in electrocardiogram signal. *Int. J. Med. Eng. Inf.* **12**(5), 489–499 (2019)
27. Gupta, V., Mittal, M., Mittal, V.: An efficient AR modeling based electrocardiogram signal analysis for health informatics. *Int. J. Med. Eng. Inf. (IJMEI)*. In press (2022)

28. Das, M., Ari, S.: Analysis of ECG signal denoising method based on S-transform. *IRBM* **34**(6), 362–370 (2013)
29. Emresoy, M.K., Jaroudi, A.E.: *Sig. Process.* **64**, 157–165 (1998)
30. Sallo, Z.G.: Efficient ECG signal parameters extraction using multiresolution analysis. In: *Proceedings of the International Conference on Advancements of Medicine and Health Care Through Technology, Romania* (2009)
31. Gupta, V., et al.: ECG signal analysis using CWT, spectrogram and autoregressive technique. *Iran J. Comput. Sci.* In press (2021)
32. Mortezaee, M., Mortezaie, Z., Abolghasemi, V.: An improved SSA-based technique for EMG removal from ECG. *IRBM* **40**, 62–68 (2019)
33. Chandra, S., Sharma, A., Singh, G.K.: Computationally efficient cosine modulated filter bank design for ECG signal compression. *IRBM* (2019). <https://doi.org/10.1016/j.irbm.2019.06.002>
34. Mehta, S.S., Lingayat, N.S.: Development of SVM based ECG pattern recognition technique. *IETE J. Res.* **54**(1), 5–11 (2008)
35. Marwaha, P., Sunkaria, R.K.: Cardiac variability time-series analysis by sample entropy and multiscale entropy. *Int. J. Med. Eng. Inf.* **7**(1), 1–14 (2015)
36. Amar, D., Abboud, S.: P-wave morphology in focal atrial tachycardia using a 3D numerical model of the heart. *Int. J. Med. Eng. Inf.* **8**(3), 263–274 (2016)
37. Salman, M.N., Rao, P.T., Rahman, M.Z.U.: Cardiac signal enhancement using normalised variable step algorithm for remote healthcare monitoring systems. *Int. J. Med. Eng. Inf.* **9**(2), 145–161 (2017)
38. Murthy, H.S.N., Meenakshi, M.: Novel and efficient algorithms for early detection of myocardial ischemia. *Int. J. Med. Eng. Inf.* **9**(4), 351–372 (2017)
39. Rawal, K., Saini, B.S., Saini, I.: Effect of age and postural related changes on cardiac autonomic function in the pre-menopausal and post-menopausal women. *Int. J. Med. Eng. Inf.* **9**(4), 299–315 (2017)
40. Gupta, V., et al.: Performance evaluation of various pre-processing techniques for R-peak detection in ECG signal. *IETE J. Res.* (2020). <https://doi.org/10.1080/03772063.2020.1756473>
41. Gramatikov, B., Georgiev, I.: Wavelets as alternative to short-time Fourier transform in signal-averaged electrocardiography. *Med. Biolo. Eng. Comput.* **33**(3), 482–487 (1995)
42. Wyse, L.: Audio spectrogram representations for processing with convolutional neural networks. In: *Proceeding of the First International Workshop on Deep Learning and Music Joint with IJCNN*, vol. 1(1), pp. 37–41. Anchorage, US (2017)
43. Rohini, R., et al.: A new paradigm for plotting spectrogram. *J. Inf. Syst. Commun.* **3**, 158–161 (2012)
44. Ranjan, R., Jindal, N., Singh, A.K.: Fractional S-transform and its properties: a comprehensive survey. *Wirel. Pers. Commun.* **113**, 2519–2541 (2020)
45. Speaker Control-Time Frequency Analysis (TFA). <https://www.klippel.de/products/rd-system/modules/tfa-time-frequency-analysis.html>. Last accessed 09 Sept 2020
46. Sejdic, E., Djurovic, I., Jiang, J., Stankovic, L.J.: *Time–frequency based feature extraction and classification: considering energy concentration as a feature using Stockwell transform and related approaches*, vol.1, 1st ed. VDM Verlag Publishing, Germany (2009)
47. Gupta, V., Mittal, M.: ECG signal analysis: past, present and future. In: *Proceeding of the 8th IEEE Power India International Conference (PIICON)*, December 10–12, 1–6. NIT Kurukshetra, Haryana, India (2018)
48. Gupta, V., Mittal, M.: KNN and PCA classifier with autoregressive modelling during different ECG signal interpretation. *Procedia Comput. Sci.* **125**, 18–24 (2018)
49. Gupta, V., Mittal, M.: Efficient R-peak detection in electrocardiogram signal based on features extracted using Hilbert transform and Burg method. *J. Inst. Eng. India Ser. B.* (2020). <https://doi.org/10.1007/s40031-020-00423-2>
50. Kaur, I., Rajni, R., Marwaha, A.: ECG signal analysis and arrhythmia detection using wavelet transform. *J. Inst. Eng. India Ser. B.* **97**(4), 499–507 (2016)
51. Rahman, A., et al.: A statistical designing approach to MATLAB based functions for the ECG signal pre-processing. *Iran J. Comput. Sci.* (2019). <https://doi.org/10.1007/s42044-019-00035-0>

# Automation to Find Adulteration in Downstream Petroleum Monitoring Using Machine Learning: An Overview



S. Hemachandiran, G. Aghila, and R. Siddharth

## 1 Introduction

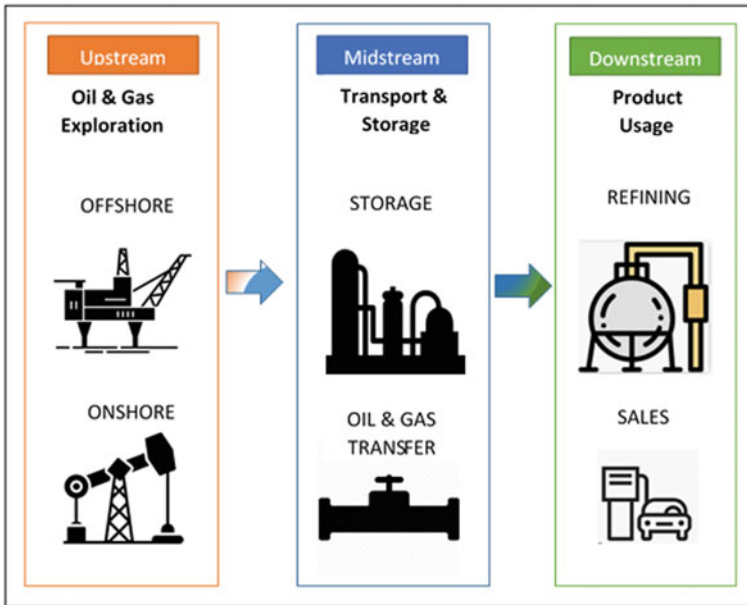
In terms of dollar value, the petroleum industry is considered the world's largest market. The petroleum industry is a global superpower that uses hundreds of thousands of employees worldwide and produces hundreds of billions of dollars annually and contributes a large amount to domestic GDP worldwide. The petroleum industry is the source of various fuels: petrol, diesel, butane, propane, liquefied petroleum gas (LPG), liquefied natural gas (LNG), and kerosene [1]. The largest volumes of the petroleum industry are petrol and diesel. The operation of the petroleum industry is generally classified into three sectors: upstream, midstream, and downstream. Figure 1 visually represents the operation of each sector.

1. **Upstream:** The key processes in this sector are exploring, drilling, and extraction. In exploration phase, the search for potential underground or under water fields and reserves of petroleum sources is searched and explored. The explored places are drilled in the second phase. At last, the hydrocarbons are extracted and produced the crude oil or natural gas to the surface.
2. **Midstream:** The major role of this sector is to transport the crude oil or refined petroleum products. Various medium like trains, ships, pipelines, and tanks are used for transportation. The transportation is between the source to refinery or refinery to downstream distributors.
3. **Downstream:** This sector involves filtering of the petroleum crude oil and processing the raw natural gas. The fuel products such as petrol, diesel, kerosene, etc., are extracted and delivered to the consumers [2].

---

S. Hemachandiran (✉) · G. Aghila · R. Siddharth  
Department of CSE, National Institute of Technology Puducherry, Karaikal, India





**Fig. 1** Three important sectors in petroleum industry and its functionality

The main aim of this article is to

- provide an overview about various adulteration issues in the downstream sector of petroleum monitoring.
- introduce the various machine learning (ML) and artificial intelligence-based solutions to the issues.
- identify the open-research challenges in automation of this less explored petroleum sector.

The next section enlists the various issues in the downstream sector of petroleum monitoring.

## 2 Issues in Downstream Monitoring

There are several critical challenges in all the three sectors listed above. The upstream and midstream involve larger scale of infrastructure and business which attracts various researchers working toward in that area to provide functions like detecting leakage in pipeline transportation, monitoring the surroundings, pressure and ensuring safety, etc. In contrast, the small scale of business and infrastructure there are very limited research available in the downstream sector. But the various kind of adulteration issues in the downstream sector directly affects the end consumer

and also spoil the reputation of the retailer [3]. Adulterated petroleum products damaged the consumers' benefits as well as it also threatened their safety. Therefore, to guarantee and promote products quality, the identification of the qualified and adulterated petroleum products is quite essential. This article aims to identify and enlists the various adulteration issues in the downstream sector which will enhance and provide in-depth knowledge to the reader about the importance of downstream sector. Adulteration is defined as the illegal or unauthorized introduction of foreign substance into the quality petroleum products [2]. This results that the product does not meet the requirements and also deteriorates the quality of the product. Foreign substances like kerosene or lubricants are called adulterants which alter and degrade the quality of the qualified product. The adulteration may happen in in the following ways:

1. **Intentional adulteration:** In this type, the person who may be a transportation driver, worker in retail outlet intentionally mix adulterants with petrol/diesel for gaining higher profit or spoil the reputation of the outlet or refinery.
2. **Unintentional adulteration:** This is the most common problem faced by the consumer and retail outlet owners where the ignorance or negligence of any individual leads to this unintentional mix up.

The next subsection clearly explains the various scenarios where the adulteration can happen.

## ***2.1 Scenarios in Adulteration***

The intentional addition of other petroleum solvents in the petrol/diesel is very common, and this adulteration weakens the quality of the petroleum product along with that it also increases the pollution. This adulteration may lead to engine malfunction and also hazardous to the environment. It is driven by the great economic benefit and greed by varying tax and evasion, since industrial solvents and fuels have different taxation. It is very much important to monitor the fuel quality in the fight against such irregularities which directly aimed at consumer protection. The two scenarios where the intentional and unintentional adulteration in the downstream section may happen are:

**Scenario 1: Transportation from refineries to retailers:** As the first step in the downstream, petroleum refineries transport the purified petroleum products to the retail outlet. In this transportation, there is a chance of mixing other solvents in the quality product. In intentional adulteration, the main motto of the greedy is to hide the theft of the quality petroleum product. Whereas in unintentional adulteration, the worker in retail outlet or transportation driver unintentionally filled the wrong products in the retailer's storage. These kind of adulteration can be verified by analyzing the density value using density hydrometer or filter paper test. Both these techniques are manual and widely adopted method across retailers. There is

**Table 1** Latest Bharat stage-VI petrol specification (India)

Characteristics	Unit	BS-VI specification
Density at 15 °C	kg/m <sup>3</sup>	720–775
Research Octane number (RON)	min	91/95 <sup>+</sup>
Anti Knock Index (AKI) or Motor Octane Number (MON)	min	81/85 <sup>+</sup>
Sulfur, Max	ppm	10
Lead, Max	g/L	0.005
Benzene, Max	% volume	1.0
Aromatics, Max	% volume	35
Olefin, Max	% volume	21/18 <sup>+</sup>
Oxygen Content, Max	% mass	2.7
Reid Vapor Pressure (RVP)@37.8 °C, Max	kPa	60

<sup>+</sup>Fuel quality specification for regular/premium gasoline

a scope of automation in this scenario to reduce the manual operation in the retail outlets.

**Scenario 2: Transportation from retailers to consumers:** In this scenario, the adulteration is done at the retail outlet where the end consumer is the victim. The intentional adulteration may spoil the reputation of the retail outlet; hence, there is a less chance of intentional adulteration happen in this scenario. Most of the cases in this scenario are unintentional due to the carelessness of the individual (either consumer or retail worker).

The periodical manual quality audit by the refineries and retail outlet helps to solve the intentional adulteration. There are no preventive methods emphasized against the unintentional adulteration. The major consequences of the adulteration are explained in the next subsection.

## 2.2 Consequences of Fuel Adulteration

In India, the Bureau of Indian Standards (BIS) provides guidelines to the specifications for petrol and diesel. Blending/mixing of adulterants into the base transport fuels leads to the change in the specification as per the guidelines. The latest Bharat stage-VI fuel specification of petrol is given in Table 1, and diesel is represented in Table 2.<sup>1</sup> The various types of fuel adulteration are mixing kerosene to petrol/diesel, blending used lubricants to the diesel, etc. The major consequences of fuel adulteration are:

- Malfunctioning/seizure of the engine, failure of vehicle components, and safety hazards.

<sup>1</sup> <https://www.transportpolicy.net/standard/india-fuels-diesel-and-gasoline/>.

**Table 2** Latest Bharat stage-VI diesel specification (India)

Characteristics	Unit	BS-VI specification
Ash, Max	% mass	0.01
Carbon residue (Ramsbottom) on 10% residue, Max	% mass	0.3
Centane number (CN), Min	–	51
Centane index (CI), Min	–	46
Distillation 95% vol. recovery at °C, Max	°C	370
Flash point Abel, Min	°C	35
Kinematic viscosity @ 40 °C	cst	2–4.5
Density @ 15 °C	kg/m <sup>3</sup>	820–860
Total sulfur, Max	mg/kg	10
Water content, Max	mg/kg	200
Cold filter plugging point (CFPP)	(a) °C	(a) 18
(a) Summer, Max	(b) °C	(b) 6
(b) Winter, Max		
Oxidation stability, Max	g/mg <sup>3</sup>	25
Polycyclic aromatic hydrocarbon (PAH), Max	% mass	11
Lubricity, corrected wear scar diameter (wsd1.4)@60 °C, Max	µm (microns)	460
Copper strip corrosion for 3 h@50 °C	Rating	Class I

- Increased emission of greenhouse gases like carbon monoxide and other toxic substances.
- Financial losses to national GDP where the lower taxed kerosene is mixed with higher taxed petrol/diesel.

The success of ML algorithm can be utilized to prevent this intentional and unintentional adulteration. The next section list out various ML approaches for handling some of the key research challenges faced by each sector in the petroleum industry.

### 3 Overview of ML Based Research in Petroleum Industry

#### 3.1 Introduction to Machine Learning

Machine learning, which is a subset of artificial intelligence, plays an important role in training computer systems to become experts that can then be used to make predictions and decisions. Before ML, AI programs only used to automate simpler tasks based on simple rule-based classification. The ML algorithm makes the automation system to evolve over each iteration by learning from the data. ML systems can generally improve their performance on certain tasks as experience increases. The

*training* and *testing* are the two important steps in ML. In training, the input data is fed to the ML algorithm, and it will find the pattern or relationship between the data. In testing, the test data is fed to the trained model, and it will give the pattern of the test data based on the information gathered during training. ML algorithms are broadly classified into two types:

- **Supervised:** This ML model is generated based on the labeled input data, and the supervised algorithm tries to find the matching class label of the test data. Some example algorithms: k-nearest neighbor (k-NN), support vector machine (SVM).
- **Unsupervised:** In real world, we cannot able to get the labeled data all the time. This ML model finds the pattern in the unlabeled data. Some example algorithm: k-means clustering.

In this article, an extensive overview is provided of how ML techniques have been used for various applications in the three sectors of petroleum production and monitoring. The purpose of this study is not to deliver an in-depth analysis of each ML approach, but rather to show the overall application of ML in petroleum industry. On the other hand, we want to make the researchers aware of such use cases. The overview of the solution is represented based on the sectors.

### ***3.2 Use-Cases in Upstream***

Qiao et al. [4] proposed a production forecasting model for petroleum products, and the model is created using particle swarm optimization (PSO) with least squares support vector machine (LS-SVM) classifier. The existing data of the petroleum industry is simulated and analyzed the factors impacting the production. The deep learning algorithm (which is a subset of ML algorithm) is also used for identifying patterns and information for profit making in petroleum industry [5]. On the other hand, genetic algorithms (GA) are also used for scheduling the production, characterization of oil reservoirs, etc. Another important application of ML in upstream sector is to predict failures or anomaly detection [6]. Jin et al. [7] proposed a ML model for leakage detection using SVM classifier for various levels of leakage from normal to large level. The economy of the countries strongly relies on petroleum industry. Prediction of oil prices is also one of the important ML application in upstream sector. Kristjanpoller et al. [8] use artificial neural network (ANN) with generalized auto-regressive conditional heteroscedasticity (GARCH) to anticipate the unpredictability of fuel prices.

### 3.3 *Use-Cases in Midstream*

Supply chain management is one of the key research areas in midstream. The dynamic demand nature of the petroleum industry makes the supply chain management more complex and challenging. Sinha et al. [9] use the multi-agent system along with particle swarm optimization to manage the supply chain. The results showed that multi-agent system favored the maintenance of optimum quantity of petroleum products in the inventories. Julka et al. [10] introduced a new simulator petroleum refinery integrated supply chain modeler and simulator (PRISMS) for decision support system. The PRISMS simulates the refinery division such as logistic, storage, procurement, and sales. During the setup, certain functions in the refinery are simulated for a prescribed number of days. The effectiveness of the PRISMS for supply chain has been illustrated by considering changes in the policy and external factors [11].

### 3.4 *Use-Cases in Downstream*

Moreira et al. [12] have discussed about the quality analysis of the petroleum products using gas chromatography technique. In gas chromatography technique, a noted quantity of fuel sample is injected; then it is carried by inert gases like helium or nitrogen. Finally, a detector measures the concentration of fuel by calculating the peak retention time. The author also proposed to use the mass spectrometry analysis to improve the detection of adulterated gasoline. The results in the article showed that the type of organic solvent can also be detected along with adulterated samples by comparing the chromatographic profiles. However, the analysis finds the contaminated gasoline and declines the adulterated samples approved as a good quality. Kanyathare et al. [13] identify the fuel adulteration in real time using optical fiber sensor and controller. The author presented a model and validated to identify the percentage of adulteration in petrol/diesel by kerosene as an adulterant. The handheld device is very simple to use, and there is no need of sophisticated chemometric analytical method; however, this method results are dependent on the surface of the fuel (roughened glass) which is not feasible in real-time automation.

Ranhotra et al. [14] introduced the image processing-based identification of adulteration in petroleum industry. The author utilized texture-based image classification to identify the fuel adulteration. Likewise, Han et al. [15] investigated the qualified and unadulterated petrol using quantized histogram matrix and independent component analysis-based hyper-spectral image analysis. Chen et al. [16] use semi-supervised ML algorithm to identify petrol and diesel using onboard diagnostic data. Frederick et al. [17] use ML-based approach to analyze the sound of the engine to identify whether it is petrol or diesel. Similarly, there are various possible applications which are not explored in-depth, and some of the important open challenges are described in the next subsection.

### 3.5 Open Research Challenges

From the in-depth analysis of the literature, it is observed that there are many research gaps in all the three sectors in the petroleum industry. It is also noted that one single ML algorithm cannot provide all solutions to the problems. From the observation, it is clearly visible that there are very few literature available in the downstream and almost all the articles focused on sensor-based data analysis. There are various open-research challenges in the downstream adulteration monitoring application. Some of the key research areas are

- The powerful computer vision techniques in the ML algorithms are still an open-research problem where it could be utilized for automation in petroleum monitoring and finding adulteration.
- The role of fog computing and edge computing in the petroleum industry is less explored, and it also have potential significance in downstream application where consumer devices can be used as edge device for performing real-time analysis.
- The blockchain technology is still in the early stage and identifying the widespread application of blockchain in the downstream sector is also a crucial research area.

## 4 Conclusion

The objective of this article is to highlight the importance of machine learning in the various sectors of the petroleum industry. This article mainly focused on the automation to find adulteration in the downstream sector and also introduced the various types of adulteration and its consequences. The existing application of ML in the petroleum industry is studied, and some of the open-research challenges are discussed. This article aims to create a timely awareness for new interdisciplinary/multidisciplinary researchers to work on this research area where a sea of automation process is available.

## References

1. Ejofodomi, O., Ofualagba, G.: Automated volume measurement, adulteration detection, and tracking of petroleum products, p. 12. Society of Petroleum Engineers, Virtual, sPE (2020)
2. Dilip Kumar, S., Sivasubramonia Pillai, T.: Estimating fuel adulteration in automobiles using robust optical fiber sensors. *Microprocess. Microsyst.* **79**, 103289 (2020)
3. Babu, V., Krishna, R., Mani, N.: Review on the detection of adulteration in fuels through computational techniques. In: *Materials Today: Proceedings 4(2, Part A)*, pp. 1723–1729 (2017), 5th International Conference of Materials Processing and Characterization (ICMPC 2016)
4. Qiao, Y., Peng, J., Ge, L., Wang, H.: Application of PSO IS-SVM forecasting model in oil and gas production forecast. In: *2017 IEEE 16th International Conference on Cognitive Informatics Cognitive Computing (ICCI\*CC)*, pp. 470–474 (2017)

5. Li, H., Misra, S.: Long short-term memory and variational autoencoder with convolutional neural networks for generating NMR T2 distributions. *IEEE Geosci. Remote Sens. Lett.* **16**(2), 192–195 (2019)
6. Velez-Langs, O.: Genetic algorithms in oil industry: an overview. *J. Petrol. Sci. Eng.* **47**(1), 15–22 (2005), *Intelligent Computing in Petroleum Engineering*
7. Jin, H., Zhang, L., Liang, W., Ding, Q.: Integrated leakage detection and localization model for gas pipelines based on the acoustic wave method. *J. Loss Prev. Process Ind.* **27**, 74–88 (2014)
8. Kristjanpoller, W., Minutolo, M.C.: Forecasting volatility of oil price using an artificial neural network-GARCH model. *Expert Syst. Appl.* **65**, 233–241 (2016)
9. Sinha, A.K., Aditya, H.K., Tiwari, M.K., Chan, F.T.S.: Multi-agent based petroleum supply chain coordination: a co-evolutionary particle swarm optimization approach. In: 2009 World Congress on Nature Biologically Inspired Computing (NaBIC), pp. 1349–1354 (2009)
10. Julka, N., Karimi, I., Srinivasan, R.: Agent-based supply chain management—2: a refinery application. *Comput. Chem. Eng.* **26**(12), 1771–1781 (2002)
11. Hanga, K.M., Kovalchuk, Y.: Machine learning and multi-agent systems in oil and gas industry applications: a survey. *Comput. Sci. Rev.* **34**, 100191 (2019)
12. Moreira, L.S., d’Avila, L.A., Azevedo, D.A.: Automotive gasoline quality analysis by gas chromatography: study of adulteration. *Chromatographia* **58**(7), 501–505 (2003)
13. Kanyathare, B., Kuivalainen, K., Rätty, J., Silfsten, P., Bawuah, P., Peiponen, K.E.: A prototype of an optical sensor for the identification of diesel oil adulterated by kerosene. *J. Eur. Opt. Soc. Rapid Publ.* **14**(1), 3 (2018)
14. Ranhotra, S.S.: Checking automobile fuel adulteration using image processing techniques. In: 2013 IEEE Second International Conference on Image Information Processing (ICIIP-2013), pp. 592–596 (2013)
15. Han, Z., Wan, J., Deng, L., Liu, K.: Oil adulteration identification by hyperspectral imaging using QHM and ICA. *PLoS ONE* **11**(1), 1–13 (2016)
16. Chen, S., Lin, C.R., Liu, W., Tsai, J.: The semi-supervised classification of petrol and diesel passenger cars based on OBD and support vector machine algorithm. In: 2017 International Conference on Orange Technologies (ICOT), pp. 164–167 (2017)
17. Frederick, H., Winda, A., Iwan Solihin, M.: Automatic petrol and diesel engine sound identification based on machine learning approaches. *E3S Web Conf.* **130**, 01011 (2019)



# Smart Dispensing of Ingredients Using VL53LOX and Piezoelectric Polymer Sensor



K. R. Prakash, V. Guruprasad, and K. S. Nithin

## 1 Introduction

The food materials are preliminarily categorized based on daily requirements for a house of 4–6 members. This includes rice, dal, and food grains such as rava, broken wheat and seeds, etc., are considered as high-volume consumables. Other items such as mustard seeds, chili powder, salt and sugar, etc., are considered as low-volume requirement. Figure 1 explains the working of smart inventory. A set of standard containers are designed to meet the high- and low-volume requirements, keeping in mind, the volumes of containers are so designed using standard regular shape such as circular, square and rectangular of different dimensions to store raw material at their respective position [1]. The container will be provided with a cap, and a bottom plate on which it sits exactly. VL53LOX sensor is mounted on the cap. VL53LOX sensor is very small in size and can be fitted very easily to any size of the cap. At the bottom, a plate with piezoelectric polymer sensor along with circuit consisting Arduino nano board will log the values from both the sensors and push those values to cloud. An AI engine with a web application will display the physical container in a virtual platform showing filling status.

---

K. R. Prakash · V. Guruprasad (✉)

Department of Mechanical Engineering, The National Institute of Engineering, Mysuru, Karnataka, India

K. S. Nithin

Department of Chemistry, The National Institute of Engineering, Mysuru, Karnataka, India



**Fig. 1** Working diagram of smart inventory

### ***1.1 Objectives***

1. The first and foremost objective of this project is to raise the level of the automation that is currently employed in the existing system.
2. Integration of sensors data for accurate analysis.
3. A system for automatically maintaining inventory status of dry/liquid items with self-calibration/correction ability.
4. This project designed to provide self-learning techniques AI for smart containers.

### ***1.2 Scope of the Project***

The smart container will have combination of sensors mainly VL53LOX nano sensors with robust electronics, which is mounted on the cap side and piezoelectric polymer gasket which acts as sensor to indicate resistance change when the volume is dispensed and is embedded to bottom of container. However, in this project, implementing smart container concept for few numbers of the containers for a particular dispensing application has been achieved mainly for an automatic cooking machine where the ingredients are dispensed according a set program. These kinds of smart containers are developed and integrated with a display device and a mobile application where user can monitor live updates on inventory, quantity dispensed, minimum level, and maximum level.

### 1.3 Design of Machine and Container

The project aimed at selecting regular shape container as it is easy to predict the exact volume changes during the dispensing of the ingredients. To suit the machine, cylindrical jars were preferred in the project. However, it is possible with any standard regular shape containers and even non regular containers can be used by initially calibrating it. Based on the geometry of the container, a program calculates the volume.

$$A = \pi * r^2 \quad (1)$$

$$V_1 = \pi * r^2 * h_1 \quad (2)$$

$$V_2 = A * (h_1 - h_2) \quad (3)$$

- 'r' is radius of the container.
- 'A' is area of the container.
- 'V<sub>1</sub>' inside full volume of empty container.
- 'V<sub>2</sub>' is the volume occupied by the material inside.
- 'h<sub>1</sub>' inside height of empty container.
- 'h<sub>2</sub>' is the depth of remaining material from top edge (Data from the sensor).

Similarly, by giving basic dimensions to the software allows direct display of the volume and weight. However, during the trials, it is observed that there is an error in measurement mainly when solid ingredients are used in the container and dispensed. As our machine needed accurate dispensing with minimum error, the containers were modified and fitted with a sensor made by piezoelectric polymer material as a base which gives resistance change with respect to volume stored in the container. By clubbing these two data, dispensing errors were minimized. The author has already published paper [1], and recently, the machine was modified and built in different layers with circular profile to house different components used for cooking ingredients in smart cooking machine which comprises of four layers. Layer 1 contains machine base, heating element, vessel and vessel clamping device. Layer 2 contains layer split, exhaust assembly, thadka assembly and cube vegetables dispenser assembly. Layer 3 contains ingredients transfer system. Layer 4 has ingredients container, spices container and liquid dispensing containers. Different types of containers were used based on the application with the provision for mounting sensor and routing wire for example as shown in Figs. 2 and 3. Provision for mounting sensors on to the containers is made during the design stage in the container cap. 1. Machine chassis, 2. Controlled heating device, 3. Tadka heating vessel, 4. Stirrer assembly, 5. Exhort, 6. Veggies containers, 7. Ingredients transfer line, 8. Spicy box, 9. Main ingredients containers, 10. Layer height adjustment, 11. Cooking vessel, 12. Cooking vessel position lock, 13. Layer spilt, 14. Base heating element mount.

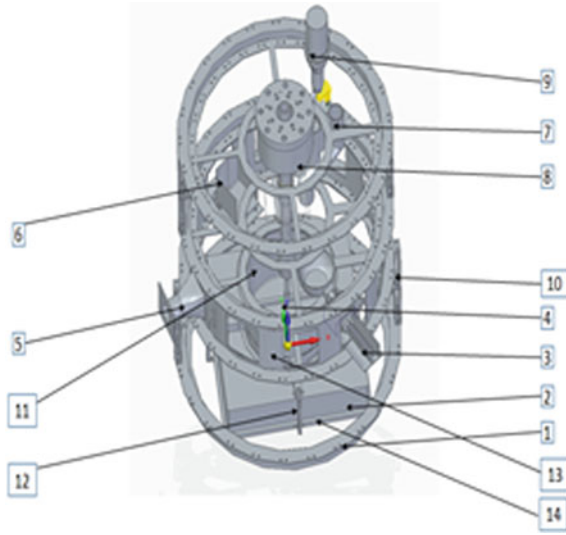


Fig. 2 Components of cooking machine

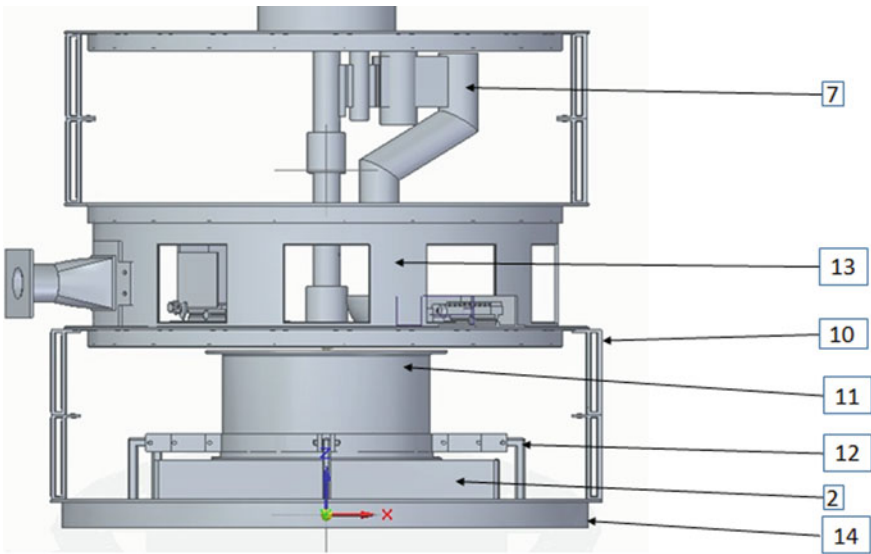
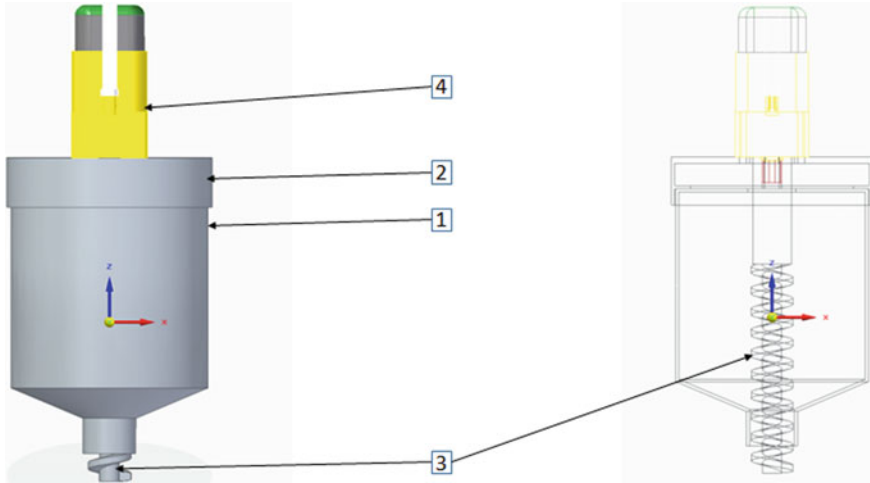


Fig. 3 Different layers of smart cooking machine



**Fig. 4** Container

Design of the container is shown in Fig. 4. 1. Containers 2. Motor holders 3. Screw rod mechanism 4. Geared DC motor.

Screw rod mechanism used will remain in the machine, whereas the containers can be separated and stored elsewhere without disturbing the ingredient contents inside (can be refrigerated and dish-washable). Spice container assembly will get opened only when positioned in respective location of the machine with proper locking mechanism which includes a Poke-Yoke system.

### **1.4 VL53LOX Sensor**

Due to compactness required, VL53LOX sensor was finally used which gives the distance in millimetre. Figure 5 shows the schematic representation of VL53LOX sensor. This VL53LOX sensor is very small in size and provides longer-ranging distance measurement [3]. It has higher immunity to ambient light and better robustness, and uses the flight sense technology for the precise measurement. The pulses of IR laser light are emitted from the emitter and reaches the nearest object then it reflects back to the detector, so it can be considered as a tiny, self-contained lidar system. The TOF (time of flight) measurement enables to accurately determine the absolute distance from the target without the object's reflectance greatly influencing the measurement.

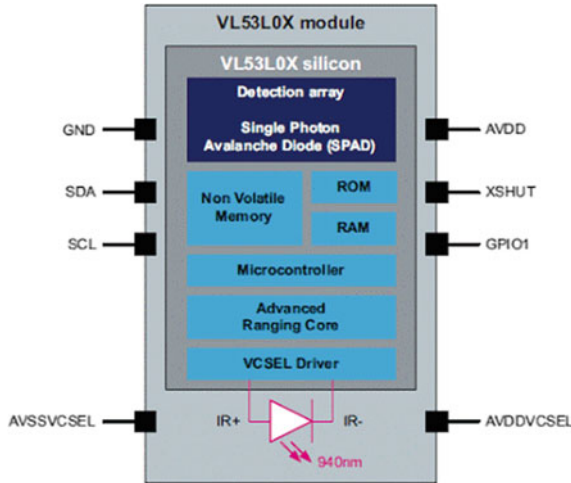


Fig. 5 Schematic diagram of VL53LOX sensor

### 1.5 Piezoelectric Polymer Sensor

The piezoelectric polymer sensor in our experiment is sensitive to the change in volume or change in the weight. This change is interpreted as resistance change by the piezoelectric polymer sensor. The sensor is a thin layer made up of piezoelectric polymer material. The advantages of using polymers in sensors are their high surface to volume ratio, response time, cost-effective and sensitivity [4, 5]. The sensor is placed on the bottom of the container further this sensor is placed on the fixture as shown in Fig. 6. Copper terminal embedded to the piezoelectric polymer is connected to the controller to acquire continuous data. When the level of the ingredients is varied the corresponding height change is given by the VL53LOX sensor and the corresponding volume change is given by piezoelectric polymer sensor. Both these sensors act as closed loop system to dispense the required quantity of ingredients.

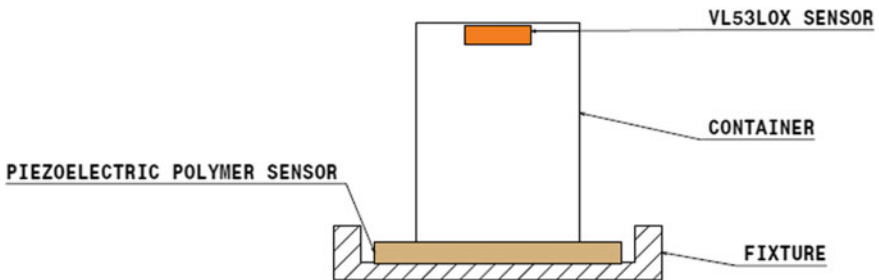


Fig. 6 Setup of the container with sensors

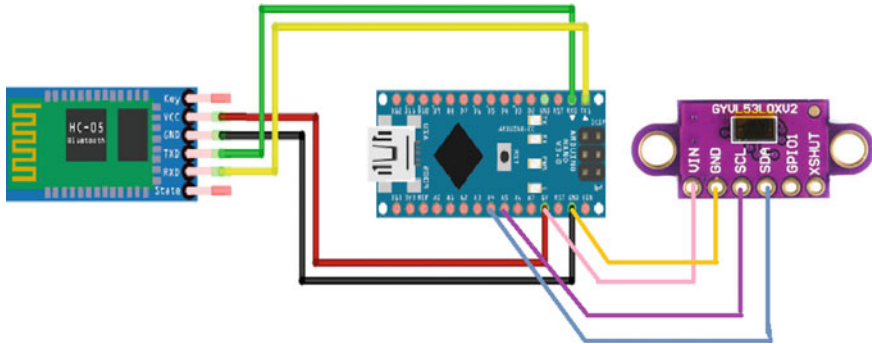


Fig. 7 Circuit diagram of VL53LOX model

### 1.6 Arduino Nano Module

Arduino nano is small, compatible and flexible. It is based on ATmega328p/ATmega168. The operating voltage of nano is 5 V, and the input voltage is 7–12 V. There are 14 digital pins, 8 analog pins, 2 reset pins and 6 power pins. Since the size of the microcontroller is smaller, it can be used in the applications where the size of the electronic components is of great concern.

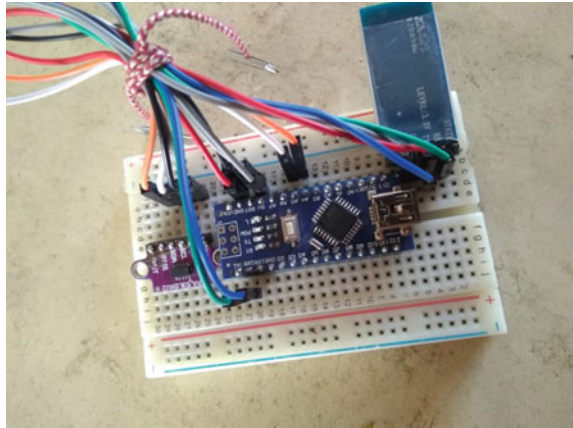
### 1.7 Arduino Bluetooth Module

The Arduino Bluetooth module is used to send the data from microcontroller to the android device. Here, we are using HC-05 Bluetooth module. It is a serial Bluetooth module for Arduino and other microcontrollers. The range is less than 100 m. This module can either work as master or slave. And also, it can be easily interfaced with laptops and smart phones. Figures 7 and 8 show circuit connection of VL53LOX to microcontroller and Bluetooth module.

## 2 Result and Discussion

Table 1 shows the reading of sensors with respect to the weight of ingredients in the container. The container is filled with item and cap is closed and is placed on the auto cook machine, piezo sensor will start showing the resistance value corresponding to the weight of ingredient stored, also the current level inside the container is detected using VL53LOX sensor using time of flight concept. The data fetching is done by Bluetooth modules, and it calculates the distance process the information to arrive at weight of ingredient. Now, the dispenser will start dispensing material using screw

**Fig. 8** Connecting VL53LOX to microcontroller and Bluetooth module



**Table 1** Sensor readings

VL53LOX sensor reading (mm)	Weight of ingredient in container (kg)	Piezoelectric polymer sensor reading (kΩ)
205–210	0.892	11.4
220–224	1.206	9.6
225–230	1.300	8.8
192–197	1.508	6.6
180–185	1.553	6.5
170–175	1.613	6.1
173–175	1.708	5.6
160–165	1.909	4.3
155–160	2.127	4.1
145–150	2.338	3.6
135–140	2.451	3.2
70–75	2.6615	2.1

type feeder mechanism as per the program resulting in change of the height values and resistance values. Taking the new values of both sensor data, AI module will display the net amount of material dispensed from the container. In that way, it can also take commands for serves based on number of persons to whom the food is to be prepared. As the machine is under patenting process and one of the major innovations is on dispensing technology, the paper focuses on only on the basic methodology. In the trails , some amount of ingredients has been dispensed randomly from the



container. For particular quantity of ingredients dispensed, the remaining weight is calculated. Simultaneously, the height of ingredient level from top of the cap is given by VL53LOX sensor, and the value of resistance for current weight of ingredient is taken from piezoelectric polymer sensor. However, the accuracy level is proved at 97%.

### 3 Scope for Improvement

The smart inventory proposed will have containers with artificial intelligence elements built in it to indicate the levels of the necessary stock and can communicate between the server/user by graphical interface or to a mobile phone. However, in this project, implementing smart container concept for few numbers of containers for a particular dispensing application has been done. In future, item storage can be replaced with smart containers with integration to display devices to deploy it in a mobile application where monitoring and live updates on inventory is possible. The project uses Bluetooth module HC-05 for the simplicity. Further, Wi-Fi module or RF master-slave device can be used for long range. The concept can be extended to warehouses, hotels, restaurants and other areas where monitoring may help to avoid the wastage of materials. Also, this can be a tool for kitchen inventory management.

### 4 Conclusion

The auto cooking machine with smart containers integrated with VL53LOX sensor and a polymer sensor for individual containers proved to be a good system to dispense the ingredients to the process as the two sensors data are fused the system will be a reliable and accurate and is suitable for small capacity machines used, the same may be used in medium scale industries, groceries shop and also in kitchen inventory. Because of its miniature size, it can be integrated in very less space. The containers periodically “wake up” and communicate to a base station regarding their inventory status and dispensed quantities, and the fill status is automatically updated using the same sensor [2]. By implementing AI, the container will be smart and self-learning over a period of time.

**Acknowledgements** This project was supported by KCTU Government of Karnataka. A part of the patent project—6018/CHE/2014.

## References

1. Shivraj, C.S., Madan, G., Prakash, K.R., Neha, M.R.: Design and development of smart containers using smart sensors to maintain inventory. *Int. Res. J. Eng. Technol. (IRJET)* **06**(06) (2019)
2. Voyles, R.M., Bae, J.: Smart Tupperware I: an example of Bluetooth wireless sensor networks for human assistive mechatronic systems.
3. Joseph, J., Manju, K.M., Sajith, M.R., Nair, S., Viay, V.P., Krishnan, S.: Water management system using IoT. *Int. Res. J. Eng. Technol. (IRJET)* **05**(04) (2018)
4. hoon Kim T., Arias, A.C. (Ed.): Characterization and applications of piezoelectric polymers. Technical Report No. UCB/EECS-2015-253, Electrical Engineering and Computer Sciences, University of California at Berkeley, December 18, 2015
5. Bauer, S., Bauer, F.: Piezoelectric polymers and their applications. *Series in Materials Science*, vol. 114, pp. 157–177. Springer

# Implementation of Industrial IoT Laboratory for Sensors



K. R. Prakash, Pratiksha Narake, and M. V. Ramya

## 1 Introduction

Machining tools are conventionally categorized into two groups: Forming and chip-making machines. In forming processes such as forging, pressing, bending and shearing, a desired shape is obtained by deformation. When it comes to chip-making type machining processes, material is removed from a work piece in the form of chips. The main types of these machining processes are drilling, milling, boring, grinding and turning. Defects and errors in the final product may result from various factors starting from human errors, machinery and material characteristics/wear and tear, temperature and pressure and environmental conditions, etc. In order to achieve zero defects, minimum down time and setting time, an IoT based intelligent control and monitoring system are needed at the industry where process data acquired from sensor network is transmitted to controllers [1, 2].

Data captured from manufacturing lines can be logged to a cloud storage housed in a data center through an indexing server. Controllers should give the right response based on the current sensor inputs as well as from the analytics of historical data from cloud [3]. However, these are possible only through proper knowledge of sensors, and use of the sensors data in various analysis techniques to provide skills in these areas. It is essential to develop proper laboratories in the institute and generate data for the purpose of analysis. One such laboratory setup is visualized by the development and implementation of PLC, industrial PC (IPC) and hydraulic laboratories. The

---

K. R. Prakash · P. Narake (✉)

Department of Mechanical Engineering, The National Institute of Engineering, Mysuru, Karnataka, India

M. V. Ramya

Department of Electronics and Communication, JSSSTU (Formerly SJCE), Mysuru, Karnataka, India

experiments connected in each of the laboratories can be accessed with the IoT controller/data logger by the remote user from different locations at any time [4].

In this paper, an attempt has been made to develop industry Internet of Things-based laboratory in the institute and bring the concept of practical learning in the areas of sensors and IoT.

### ***1.1 Architectural Framework***

Monitoring the parameters such as temperature, pressure, position, etc., need integration of sensors or detecting devices to be put on the machine or on the object and ensure that they are maintained at required set levels throughout the production time/process time. In this paper, application of IoT to capture data, and use of analytics to understand the cause of variations is discussed. This approach can be a big game changer for precision manufacturing industries in terms of quality production and realization of six sigma level. Figure 1 gives architectural framework of such system.

### ***1.2 Field-Devices Network***

Manufacturing industries employ huge number of devices, equipment, machineries which perform machining operations on workpieces using tools and support equipment. Devices could be I/O blocks, systems, readers, process instruments and drives, etc. All these machine-level operational and monitoring components could be made smarter by incorporating AI technique and smart control whose operations are triggered by control signals from remote terminal units (RTU's) or I/O modules. Thus, data from various sensors, i.e., analog/digital signals are communicated to control system through these RTU's transmit control signals from controller to actuators. These remote terminal units are basically channeling for data transmission to and from field equipment with embedded controllers. They control device management functions with device level protocols like foundation fieldbus, highway addressable remote transducer (HART), PROFIBUS-PA, and most of them have 4–20 mA analog current or 0–10 V.

### ***1.3 Connectivity Network***

Operational data to/from RTU's across the plant should communicate with master controller. Master controller being the center of control, intelligence and coordination across the complete system should process these input data signals from

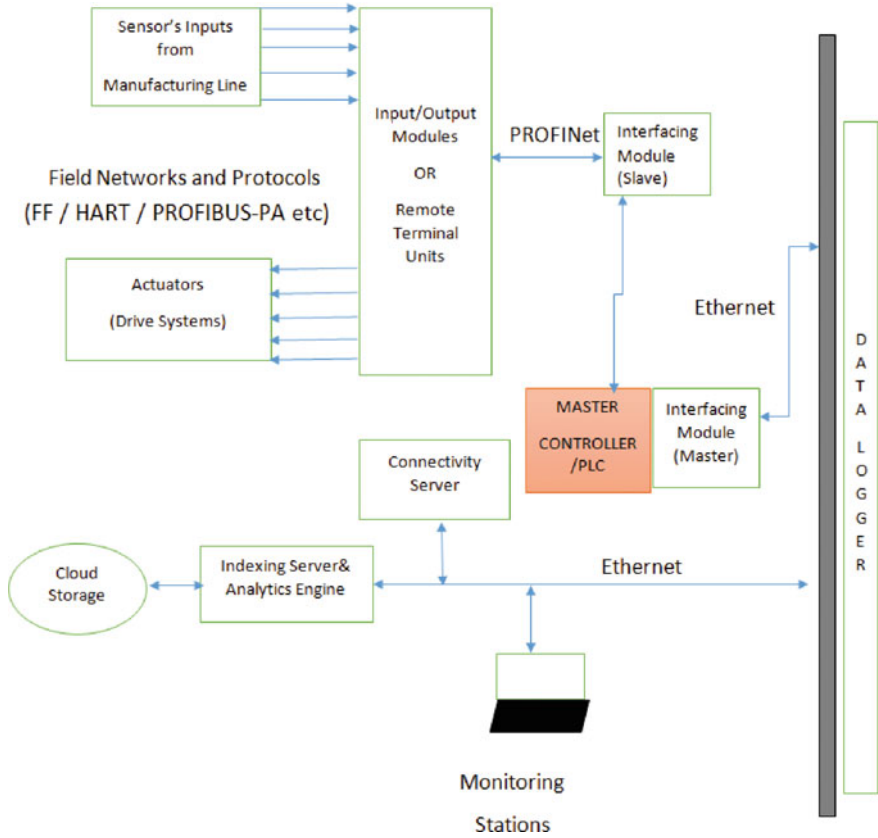
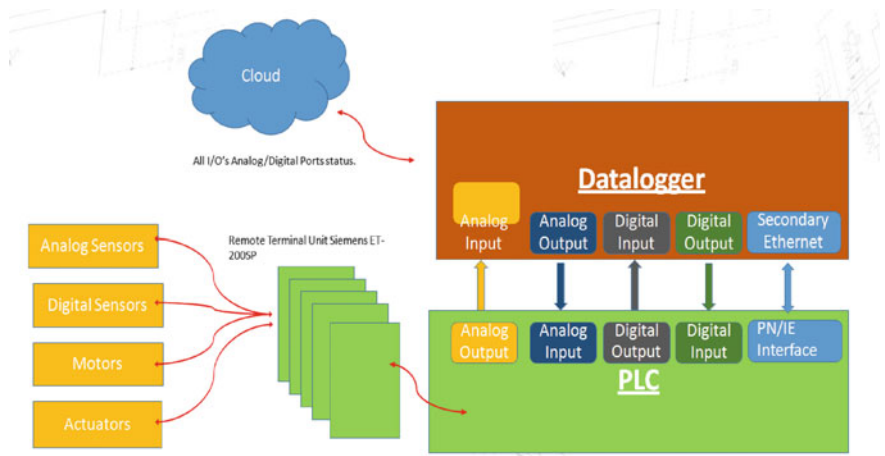


Fig. 1 Architectural framework

sensors and give out responsive control signals on real time basis. Every set of operational data processed by controller is logged to cloud infrastructure. Hence, response given by controller for any input signal should also consider analytics of data logged previously, ensuring self-learning and improvisation.

Data transfer from RTU's to ethernet network switch would require interfacing modules, as communication from RTU's, all through the plant should be using protocols which are rugged and match industrial standards. PROFINET is an ethernet-based industrial communication protocol, which utilizes physical interface RJ-45 ethernet jack. PROFINET cables contain robust shielding and are designed to function well in harsh environments with less than 1 ms, making it ideal for high-speed applications. In order to provide similar kind of experimentation at laboratory setup in the institution, different types of sensors and actuators were connected to Siemens ET-200SP which intern links to PLC with single cable. These kinds of arrangement create a flexible link between the sensors, actuators and PLC. Student can program PLC and realize the input/output operations of sensors/actuators as per requirement.



**Fig. 2** Connectivity network between sensors, clouds, data logger, RTU and PLC

PLC in turn connects to a data logger and communicates the outputs to a cloud server using message queue telemetry transport (MQTT) protocol, JAB Hibernate is used to communicate with database and http-based protocol for data transfer from server to web application and http REST APIS protocol for data transfer from server to mobile applications. Figure 2 shows connectivity network between RTU, PLC, cloud, data logger and sensors.

## 2 Cloud Infrastructure, Configuration and Monitoring Network

In order to configure, program and monitor the control activities of the system, servers and client machines are configured with software tools, which can support building, debugging, configuring and downloading the logic to controller.

This software should ensure proper and distinct access for operator functions (Switch ON/OFF on HMI), engineering functions (Building Topologies, Designs, I/O Tags and Logics) [5], monitoring functions (SCADA Tools, etc.) and analytic functions (where ML based algorithms are developed, debugged, triggered and monitored), etc. These server/client workstations should link to ethernet switch, while connecting to cloud infrastructure at another end. Also, a connectivity server system is required, which runs few critical services depending on operating system of server/client nodes.

### 3 IoT Sensors for Industrial Applications

#### 3.1 Experiment on Digital Sensor Using PLC and Data Logger

Sensor applications and few characteristic experiments can be conducted using the developed laboratory. In this section, digital sensors such as inductive, capacitive, etc., are considered and one of them is operated using a PLC to demonstrate an application of an industry. In this example, an inductive sensor is connected to the PLC and to the data logger to detect the conductive materials, and result is pushed to the cloud as 0 or 1 in value column no.-5 through ethernet. Table 1 gives the port name and corresponding digital outputs. Figure 3 shows connection of data logger to PLC.

**Table 1** Process parameters when data logger connected to PLC

Time and date	Port	Port no.	Sensor name	Value	Type (V)
2020/10/27, 16:17:35	Digital Input	DIO	Q1	1	0–24
2020/10/27, 16:17:30	Digital Input	DIO	Q1	1	0–24
2020/10/27, 16:17:25	Digital Input	DIO	Q1	0	0–24
2020/10/27, 16:17:20	Digital Input	DIO	Q1	1	0–24
2020/10/27, 16:17:15	Digital Input	DIO	Q1	1	0–24



**Fig. 3** PLC connected to data logger

### 3.2 Experiment on Analog Sensor

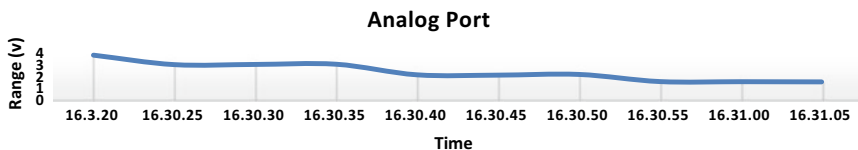
Balluff position sensor is used to measure the linear distance. As the sensor is moved from 0 to 500 mm, the values of voltage change are recorded through the data logger. The same is shown in Table 2. Column 5 shows the voltage values varying from minimum value of 1.54 V to maximum value of 3.83 V. Figure 4 shows the sensor connected to the data logger for conduction of the experiment manually by moving the sensor actuator rod. The output is shown as graph in Fig. 5 (Fig. 6).

**Table 2** Process parameters when Balluff sensor connected to data logger

Time and date	Port	Port no.	Sensor name	Value
2020/10/19, 16:30:20	Analog	AIO3	Position sensor	3.83608
2020/10/19, 16:30:30	Analog	AIO3	Position sensor	3.0428
2020/10/19, 16:30:40	Analog	AIO3	Position sensor	2.15304
2020/10/19,16:30:50	Analog	AIO3	Position sensor	2.1852
2020/10/19, 16:31:00	Analog	AIO3	Position sensor	1.56344
2020/10/19, 16:31:05	Analog	AIO3	Position sensor	1.54736



**Fig. 4** Balluff sensor connected to Data Logger



**Fig. 5** Graph shows the voltage reading of position sensor over time



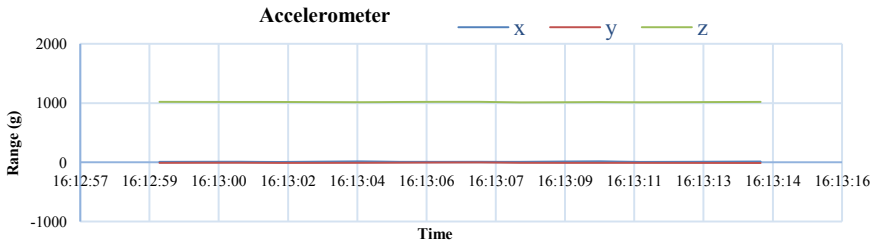


Fig. 6 Graph shows the accelerometer reading (g) in x, y and z direction over time

### 3.3 Experiment on XDK Sensor Without Data Logger

It is an IoT sensor used to measure multiple parameters with a single device. This is used to log various parameters such as ambient temperature, atmospheric pressure, light intensity, acceleration of the body in three directions, humidity, angular velocity, strength and direction of magnetic field and rotation of the body in degrees. Based on the industrial application requirement, any of these parameters can be monitored, and data is logged as shown in Table 3. Based on the data obtained, process is controlled.

**Accelerometer**—It measures the acceleration of the body in three different axes, i.e., x, y and z. Column 2 of Table 3 shows the values for x, y and z directions.

**Gyroscope**—Gyroscope is used for measuring angular velocity. It is measured in terms of (rad/s). Column 3 of Table 3 shows the values for x, y and z directions (Fig. 7).

Table 3 Process parameters of XDK sensor

Time and date	Accelerometer	Gyroscope	Temp	Pressure	Humidity
2020/10/28, 16:13:14	13, -12, 1019	610, 1220, -448	33	1	34.23
2020/10/28, 16:13:11	6, -10, 1013	-3417, -4638, -4150	29	1	34.59
2020/10/28, 16:13:10	16, -10, 1016	3906, 2685, 1953	29	1	34.58
2020/10/28, 16:13:08	7, -9, 1011	-366, 2075, 2075	29	1	34.59
2020/10/28, 16:13:07	8, -3, 1020	3540, 7934, 5371	29	1	34.58
2020/10/28, 16:13:05	7, -7, 1018	-1220, -1831, 1708	29	1	34.58
2020/10/28, 16:13:04	15, -9, 1014	-4150, -1220, 1708	29	1	34.6
2020/10/28, 16:13:02	5, -11, 1018	1098, 3295, -3051	29	1	34.59
2020/10/28, 16:13:01	9, -8, 1018	-1708, -2319, 3906	29	1	34.59
2020/10/28, 16:12:59	7, -10, 1020	-1708, 1708, 5493	29	1	34.6

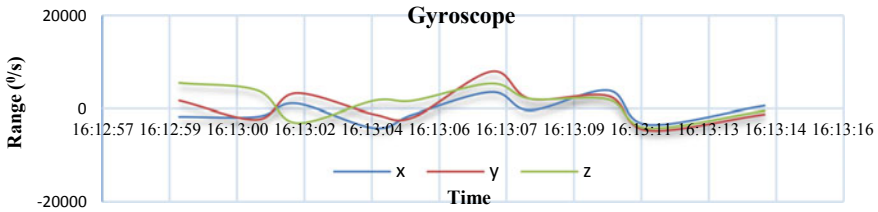


Fig. 7 Graph shows the gyroscope reading ( $^{\circ}/s$ ) in x, y and z direction over time

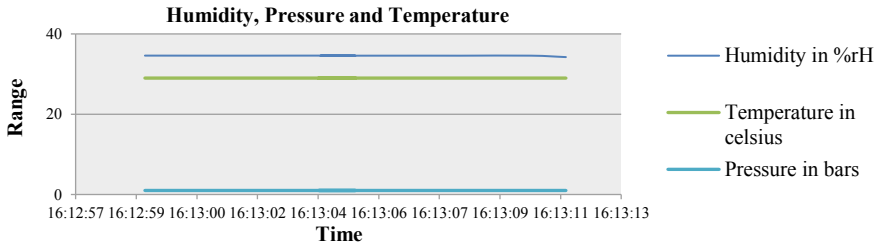


Fig. 8 Graph shows humidity, temperature and pressure readings over time

Columns 4, 5 and 6 of Table 3 indicate the values of room temperature, atmospheric pressure and humidity obtained at the time of conduction of the experiment. Also, other parameters such as magnetometer reading, rotation and light intensity may be recorded (Fig. 8).

### 4 Conclusion

In the project, IoT laboratory with suitable data logger from Hydac India was used along with Siemens and Delta PLC to conduct various experiments related to sensors. This has enabled the institute to have a separate lab of 2 credits on IoT applications related to sensor which is designed and conducted. The system so developed to enable the student login from anywhere through the internet and conduct the experiments as per the data logger availability. However, on every experiment completion, data logger is to be released by a lab supervisor to enable the same data logger to the others.

To avoid this, a program is proposed such that auto release is done after the completion of the experiment. All the experiment conducted is satisfactory and recorded either in table or graphical form as per the laboratory requirement along with student registration details for proper validation process.

## References

1. Banagar, A.N., Khattar, R.: IoT based smart laboratory system. *IJERT* **9**(01) (2020)
2. Abraham, S., Miguel, A.: Creation of an Internet of Things (IoT)-based innovation lab. *American Society for Engineering Education* (2017)
3. Poongothai, M., Muthu Subramanian, P., Rajeswari, A.: Design and implementation of IoT based smart laboratory. In: *5th International Conference on Industrial Engineering and Application* (2018)
4. Prakash, K.R., Purushothama, G.K., Ramya, M.V.: An approach to convert conventional laboratories into an IoT enabled laboratories. *Int. J. Web-Based Learn. Teach. Technol.* (2020)
5. Mader, A.: A classification of PLC models and applications. In: *Proceeding of the Springer International Series in Engineering and Computer Science (SECS)*, vol. 569

# A Mechatronic System to Distribute Tennis Balls Using Pneumatics



Pradnya Avinash Patil

## 1 Introduction

The main objective of this report is to design a mechatronic system capable of uniformly distribute tennis balls from a hopper onto a production line using pneumatics. This system shall be composed of a electrical, mechanical and software sub-systems in order to practice such skills. To accomplish this objective, a system composed basically by one pneumatic actuator, a motor, two ultrasonic sensor and the mechanical system that integrates the hopper to the production line was designed. A pneumatic cylinder is used to push the tennis ball that comes from the hopper and is unable to enter the production line because of a gate, into a rail that leads to a conveyor with a line of tennis ball's packages. The first ultrasonic sensor is set to detect any object that is below 6 cm of distance and sends a signal to the solenoid valve that activates the cylinder, and this step is required to verify if there are any balls coming from the surveyor. After the ball goes through the rail, it ends up on the package and a second ultrasonic sensor, set to detect object at a distance below 20 cm, senses if the package is full and send a signal to the motor that pushes another package one step forward completing the cycle. This report begins explaining why the use of pneumatics in conjunction with other systems, such is electrical actuation, is widely used. Then, the actuation used on the model is discussed as well as the electronics and sensors. The simulation tools used are then explained and also how they interact with each other. Finally, the outcome of this project is discussed and the conclusions exposed.

---

P. A. Patil (✉)

Dr. J. J. Magdum College of Engineering, Jaysingpur, Maharashtra, India

## 2 Methodology

At this section of the report, for each aspect of the project, a small discussion and the necessary explanations that will support the decisions made around pneumatics, actuation, electronic control and simulation will be rendered. The intention is to, first, give a general view of the parts of the subject that will have an impact in what was used on the project. Second to explain why this was done. For example, on pneumatics, compressors and reservoirs are discussed and why they are not on simulations. Also, the tools and software used to achieve the results and how these results were achieved. Finally, the relation of each part with the objectives of the report is exposed. Figures and listings will illustrate the explanation wherever necessary.

(A) **Pneumatics** In a pneumatic system normally, air is drawn from the atmosphere via an air filter and raised to the system required pressure by an air compressor, which is normally driven by a AC motor [1]. Because the air contains a significant amount of water vapor, the air must be cooled and treated before being used. Pressurized air is then stored in a reservoir and can be released to the cylinder, without the reservoir the valve action could be slow, if the pressure was to be raised every time the valve was to be used. The pneumatic systems may look complex and for small applications such as this demonstration project it is no feasible, although many factories produce compressed gas at a central and distribute it on a air ring main to all places on the site, in a similar fashion as electricity or water. The development of a pneumatic system will make possible, by studying small systems like this project to have a better idea on large scale plants and how they integrate their systems. For a matter of convenience, the pressure reservoir and compressor will be excluded of the simulations included in this report.

(B) **Actuation** The actuation systems are responsible for transforming the control system output into an action that will control the system [2], and on this project, solenoid valves are used to control the flow of air which will start the pneumatic cylinder. The pneumatic cylinder is an example of a linear actuator, and it consists of a cylindrical tube along which a piston can slide. The cylinder is used on the project.

To control the motor which will control the conveyor belt, a relay is used, it is represented by the LED at the electronic simulation, and it works as a mechanical switch acting as the motor actuator. Relays are widely used on control systems in conjunction with a transistor to switch on the current through the solenoid to switch on the much larger current needed to switch on or off a final correction element such as a motor [2]. These are some of the various kinds of actuation systems, to know how to integrate them on pneumatic systems is crucial for modern operations.

(C) **Electronic System** The electronic system is composed by two ultrasonic sensors, a liquid crystal display (LCD) display, and a microcontroller. The LCD monitor displays the actual distance between the ultrasonic sensors and the subjects of measurement, and there will be displayed UT cm: for the first

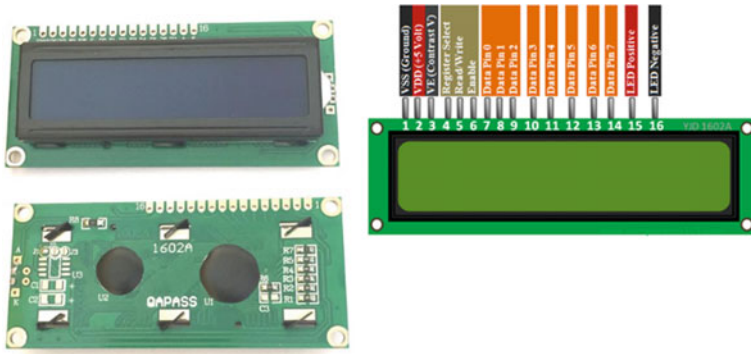


Fig. 1. 16 × 2 LCD module and 16 × 2 LCD module Pinout

measurement and  $UT \text{ cm}^2$ : for the second. This is necessary so the correct functioning of the system can be judged.

1. *LCD display* The LCD module used was a 16 × 2 display as seen in Fig. 1 very commonly used in embedded projects, because it is cheap, available and easy to program. They are very common on calculators. It has 16 Columns and 2 Rows. So, it will have 32 characters in total and each character will be made of 5 × 8 Pixel Dots [4].
2. *Ultrasonic sensors* An ultrasonic transducer transforms mechanical sound waves in electricity via a piezoelectric crystal. This crystal if cut on the  $x$ -axis has the property of changing size and shape when energy is applied, making the crystal vibrate and producing sound waves. The same occurs at the reception of a sound wave, where the crystal receive the impact and produces energy. Figure 2 illustrates how this can be done [6]. This ultrasonic sensor can be used in quantity by the same microcontroller, as can be seen in Fig. 3, in this project only two were used.

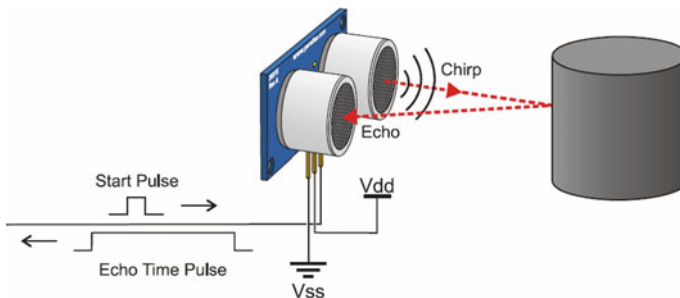
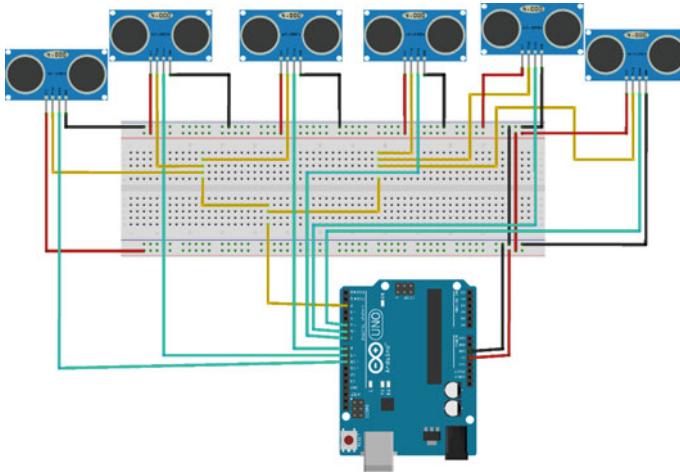


Fig. 2 Ultrasonic sensor



**Fig. 3** Multiple sensors

(D) **Microcontrollers** A microcontroller is basically a whole computer as a miniature. Different from the microprocessor that is the part of the system that process data, the microcontroller has memory, CPU, Digital pins for I/O (Input/Output). The microcontrollers used in this project is the ATmega328P mounted on an Arduino Uno board. This microcontroller weighs only 25 g and have 1 KB of EEPROM, 2 KB of SRAM and 32 KB of flash memory [5].

1. **Control Methodology** The control methodology consists, first, in verify if the there is a tennis ball in place, in front of the first ultrasonic sensor, if affirmative the cylinder will push the ball down the rails and into the package, it will wait for one second and will verify again. In the case of no balls in front of the first ultrasonic sensor, the system stops. Then, as a second verification, using the second ultrasonic sensor, the distance between the sensor and the inside of the package containing the balls is measured and if the distance is less than 20 cm, which means that there are three balls inside the package, a signal is sent to the motor they will roll the belt and place another empty package on the place. The motor works for 1 s, time necessary to put another pack in place and time enough for another ball to come if the hopper is not empty yet.

### 3 Design Process

The design process consisted of three main phases, first an ideation process and research. In this phase, a research around previous projects, interview with other students, literature review was first conducted as well as discussions with the professors to understand the problem. Also, in this phase, an ideation process was conducted to realize what would the project be in a high level and what kind of tools would be the best for the purpose. After the first phase was decided that a system with two ultrasonic sensors, a cylinder and a conveyor belt with a motor would be designed. A second phase consisted in making the electrical simulation of the control system using potentiometers to mock the ultrasonic response for the distance and to analyze the control system timing. The great advantage of these phase is to avoid errors when buying the real parts and making sure the system is working prior to irreversible decisions. This phase is possible even to further the capabilities of the project, add features and improve the concept of the project. Once satisfied with the electronic design and control system, a CAD model was developed to study the dynamics of the interactions between the parts of the mechanical design and well as to have the measurements for the implementation of the project in future. The disadvantage is that theoretical components are much closer to ideal situations than to the reality and some adjustments may be necessary in the case of implementation in the real world, specially involving motors and pressurized systems as in the case of this project. The use of more robust software and real specifications from vendors as well as environment modifications on the simulation can mitigate some of these problems but never at a level of total confidence. Although, for the present work, the tools used were more than suitable.

(A) **Electronic simulation** Virtual Prototyping enables system testing before fabrication and electronic devices such as sensors and microcontrollers can be simulated in specialized software such as Proteus, which has over 15 million parts designed and can accelerate the design process.

1. **Proteus** The Proteus Design Suite is used across various industry sectors as a solution for professional PCB design and as a rapid prototyping tool for R&D [3]. This tool was chosen due to the ease of use and simulating capacity, as well as per the amount of parts available, including the ones used on the project. With Proteus, there is the possibility of importing the programming to the part and simulate accurately the results. In order to simulate the ultrasonic sensors, input, a potentiometer, is connected to the ultrasonic sensor test, and a DC generator is connected in one side and ground on the other side. The first ultrasonic sensor, connected on pins 8 and 9, receives a DC generator of 50 mV in order to simulate a distance below 6 cm stipulated. If a distance below 6 cm is detected then it means that there is a tennis ball waiting to be pushed through the gate to the conveyor and the cylinder is activated, as shown in Fig. 4. The second sensor receives a DC generator of 500 mV and simulates a 20 cm



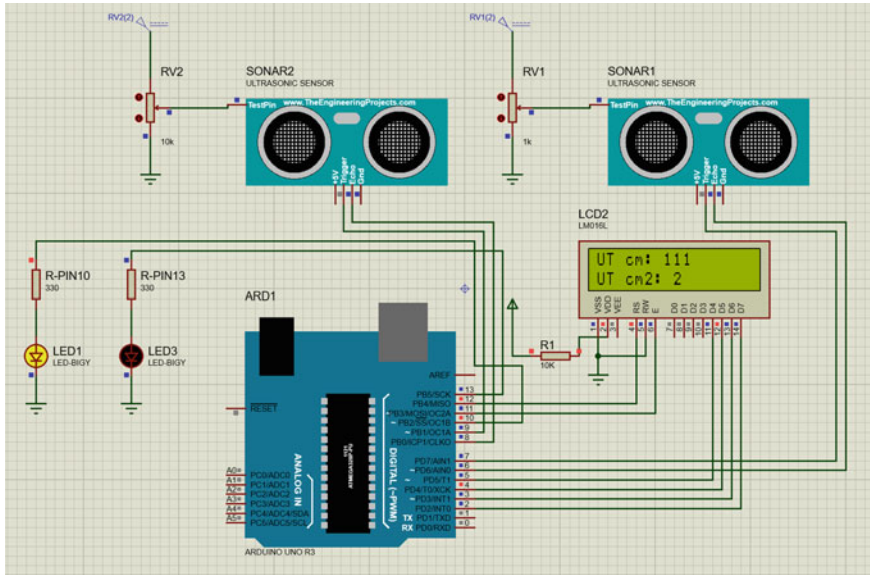


Fig. 4 Simulation in proteus—sensor 2 below 6 cm

distance. It is located on top of the packing station and when there are three balls inside the pack it activates a motor that makes the conveyor belt roll a distance of one pack, and the full pack is projected forward, while another one empty takes its place. Figure 5 shows the system simulating a full pack being detected.

- (B) **Mechanical simulation** The mechanical design was made using Solidworks. There are many reasons to use this tool, its popularity results in a huge community of developers, amateurs and professionals that exchange experiences and solve problems.

Solidworks have various modules that enable one to make physical simulations, animations and much more. An overall view of the system is shown in Figs. 9 and 10. Figures 6 and 7 are possible to see the position of the ultrasonic sensors.

A view of the cylinder in Fig. 8 shows a tennis ball being pushed by the gate and going at the production line’s direction (Figs. 9 and 10).

### 4 Results

The results of the simulation are not ideal due to the many factors that have to be considered on a real project. The physical interaction of all the components has to be taken into consideration. All these factors can be seen on a real model and that’s

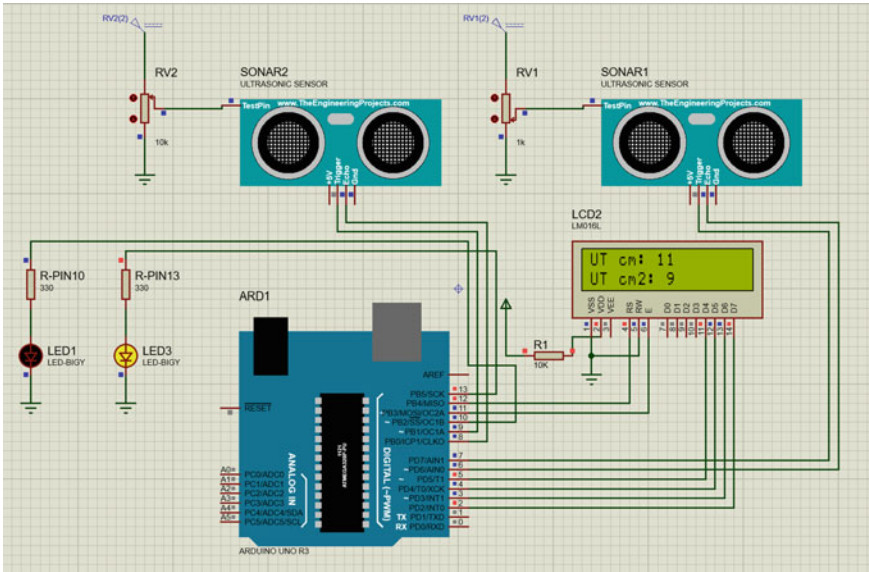


Fig. 5 Simulation in proteus—sensor 1 below 20 cm

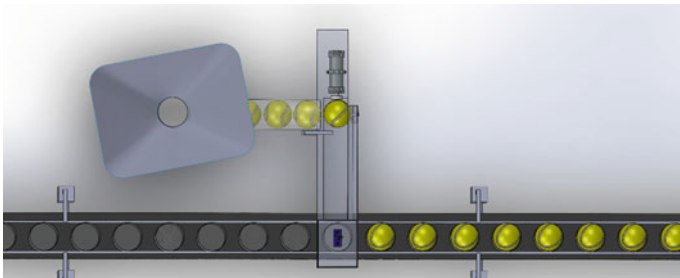


Fig. 6 Sensor 2

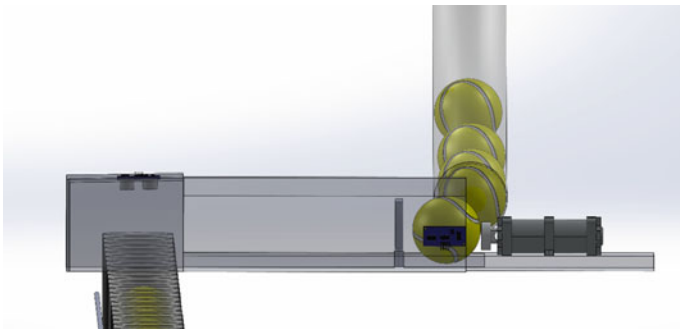
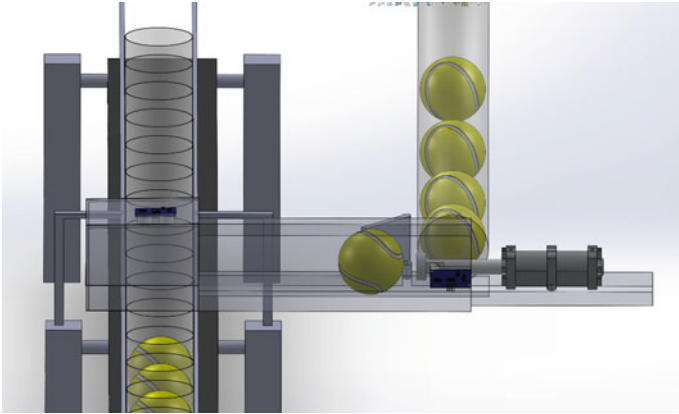
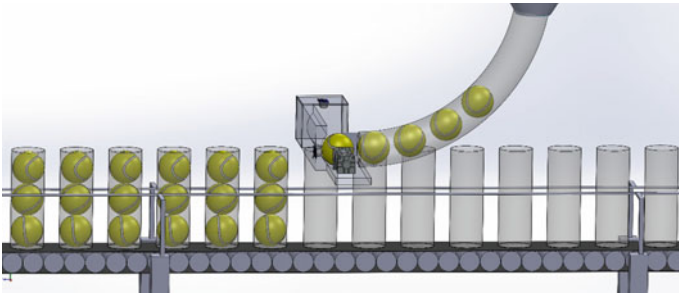


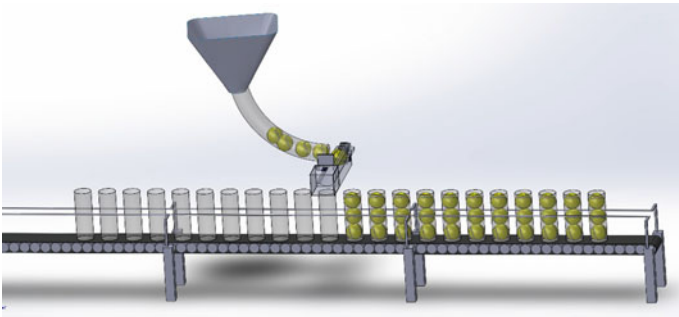
Fig. 7 Sensor 1



**Fig. 8** View of the cylinder



**Fig. 9** Overall system—perspective



**Fig. 10** Overall system

the idea behind a design process like this, where we round the intrinsic factors that are of minor importance in favor of having the big picture revealed and then measure and adjust the real product at the end. Although since the aim of the project was to practice the design process, it was fully achieved since an electrical, mechanical and software; therefore, mechatronic system was fully developed and integrated.

## 5 Discussion and Conclusions

In this project, an electrical, mechanical and software system were developed and integrated, fulfilling the aims of the project. The performance of the project can only be measured but assessing the simulations, unfortunately the real implementation of the project is not possible at this moment. Although the knowledge of how to integrate the systems was of great value. Improvements and recommendations for the project in future developments include the following, to name a few:

1. If the project were to be implemented, the first idea measures the real-world performance and compare with the simulations.
2. The system can be improved by changing the LED's for a real motor and the solenoid valve on the electronic simulation.
3. Use real parts Datasheets and a more robust simulator like Eagle.
4. Another use of counters to specify the amount of packs delivered and also a check system to count the amount of balls inside the package is of easy implementation using computer vision and tools like OpenCV.

## References

1. Parr, A.: *Hydraulics and Pneumatics—A Technician's and Engineer's Guide*, 2nd edn. Butterworth-Heinemann, Oxford, UK (1998)
2. Bolton, W.: *Mechatronics—Electronic Control Systems in Mechanical and Electrical Engineering*. Pearson Education Limited, United Kingdom (2019)
3. (Proteus Website Online Help) Labcenter (2020). Available <https://www.labcenter.com/>
4. (16 × 2 LCD Module) Datasheet (2020). Available <https://components101.com/16x2-lcd-pin-out-datasheet>.
5. (Arduino Store) (2020). Available <https://store.arduino.cc/usa/arduino-uno-rev3>
6. (Ultrasonic Sensors: Applications in the Internet of Things) (2020). Available <https://blog.seebo.com/iot-ultrasonic-sensors/>. Hasan, H.M., Sanyal, F., Chaki, D., Ali, M.: An empirical study of important keyword extraction techniques from documents (2017). <https://doi.org/10.1109/ICI-SIM.2017.8122154>.

# Weld Microstructural Image Segmentation for Detection of Intermetallic Compounds Using Support Vector Machine Classification



Nalajam Pavan Kumar, Ramesh Varadarajan, K. N. Mohandas,  
and Muni Kumar Gundu

## 1 Introduction

The weld microstructural is an important task in determining the presence of intermetallic compounds (IMCs), IMC layer thickness and the presence of defects such as gas pores, voids and cracks. The microstructural examination heavily relies on human experts to draw conclusions on the weld quality, which is time-consuming and tends to result in uncertain conclusions. The rise of computing power and machine learning techniques helps in determining the weld quality with high accuracy in less time. The microstructural images can be evaluated using image segmentation. Image segmentation is a well-known tool that separates desired parts or objects from the whole picture, and it can be subsequently analyzed with greater accuracy. Image segmentation has an extensive application range in medical image processing quantitative analysis. Numerous image segmentation algorithms have been reported in the literature in the recent years. Image segmentation algorithms are broadly categorized as edge detection [1–3], template matching [4, 5], thresholding [6, 7], clustering [8–10] and the region growing [11–13]. However, none of these algorithms have generic applicability to all the images.

The applications of aluminum alloys are growing in manufacturing industries because of their low weight and high strength characteristics. The major drawback of aluminum alloys is difficulty in welding, and it still remains a challenge for many

---

N. P. Kumar · R. Varadarajan (✉)  
Vellore Institute of Technology, Vellore 632014, India  
e-mail: [vramesh@vit.ac.in](mailto:vramesh@vit.ac.in)

K. N. Mohandas  
Ramaiah Institute of Technology, Bangalore 560054, India

M. K. Gundu  
Invesco (India) Private Limited, Hyderabad 500032, India

researchers. The common problems associated with the resulted poor welds are feedability, porosity, cracking and intermetallic compounds. In recent years, many of these limitations were addressed by industrialists and the researchers. However, the formation of intermetallic compounds still needs to be addressed. Cold metal transfer (CMT) welding is a sophisticated version of metal inert gas/metal active gas welding process with many automated features incorporated in it, particularly low heat input feature which allows the welding of aluminum alloys with higher efficacy [14]. Evolution of machine learning and artificial intelligence propels the fully automated systems in manufacturing industries for welding processes, and significant research was carried out in this field. Most of the research was performed on the weld defect detection from the images obtained from nondestructive testing methods such as radiography testing, acoustic emission testing, ultrasonic testing, eddy current testing. Online monitoring of weld quality system has been developed to control the process parameters. Automated weld system containing seam tracking, weld inspection and positing from the vision-based measurements has been developed [15].

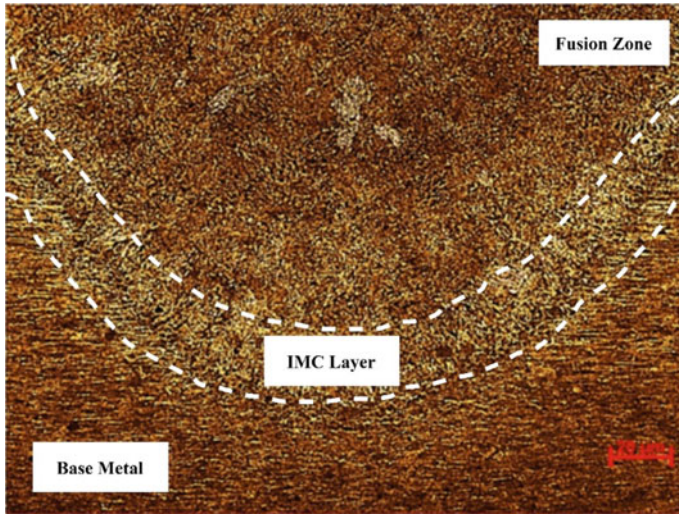
In this study we propose a microstructural image segmentation for determination of intermetallic compounds and its associated layer using pixel-level support vector machine classification. The image segmentation was carried out to detect the intermetallic layer in the weld region of cold metal transfer welded AA6061 sheets. The SVM classifier model is trained with pixelwise color and texture features. The model is trained using pixel features extracted from fuzzy c-means (FCM) clustering algorithm. The obtained model results are in good agreement with the manual inspected results.

## 2 Experimentation and Data Acquisition

Aluminum alloy 6061 (AA6061) thin sheet with thickness of 2 mm is employed to carry out the experiments. Elemental composition of the AA6061 is given in Table 1. In this study, a suitable filler wire, AA4043, is utilized with thickness of 1.6 mm. Prior to welding, samples are cleansed with acetone for eliminating foreign elements such as dirt, oxides, oil residues and moisture. Argon as a shielding gas is applied with a steady flow rate (18 L/min) during fusion welding to remove unwanted impurities in the weldment. In the linear direction, seam welding (Fronius advanced CMT 7000 VR machine) for AA6061 sheet is carried out using the robotic machine

**Table 1** Chemical composition of AA6061 used in this study

Component	Al	Mg	Si	Fe	Cu	Zn	Ti	Mn	Cr	Others
Amount (wt%)	Bal.	0.8–0.12	0.4–0.8	0.7	0.15–0.40	0.25	0.15	0.15	0.04–0.35	0.05



**Fig. 1** Microstructural image of AA6061 weldment (welding current—50 A and welding speed—10 mm/s)

(Yaskawa Motoman robot) with six degrees of freedom. Post welding, slags are removed through stainless steel wire brush.

The important process parameters chosen in this process are welding current and speed. Robotic machine with six axes provided the desired speed variations and welding path. Other process parameters such as arc length and gas flow rate used in this study are kept constant which can be controlled using remote control unit (RCU) of CMT system.

Samples are extracted from the weldments in the transverse direction (perpendicular to weld direction) for capturing microstructures. Sample preparation was made as per ASTM metallographic standards. After polishing the samples, etching is done with keller's etchant to extract the clear microstructures. Olympus optical microstructure (OM) device is used to obtain the microstructures. Figure 1 shows the sample microstructure of CMT welded AA6061, base metal used in this study.

### 3 Support Vector Machine

Image segmentation allows to analyze the information that is contained in different regions on an image. The process mainly depends on the intensity of each pixel which is somewhat different from another pixel. With the help of pixel feature, image can be segmented with the similar characteristic. Classification can be done into several regions based on the input pixel feature of any available classification



models. One of the prominent classification techniques is SVM which is a widely used and well-known method for its accuracy.

Support vector machine is a supervised machine learning technique and is mainly used for classification and regression where the boundary is chosen as at the center of the farthest difference between pairs of datasets. The basic idea of this approach is to map input variables space to a high-dimensional space through a kernel and then classification formally defined by the hyperplane maximizing the distance between classes.

The available vectors are divided into two sets in the simple decision problem, and to divide these vectors, the optimal decision limit has to be found. The distance from the limit to the data is maximized by this optimal choice. A line is the decision limit in a two-dimensional case, and a hyperplane is the decision limit in a multi-dimensional case. The decision function has another form.

$$f(x) = \sum_{i=1}^l \alpha_i y_i (X_i \cdot X) + b \quad (1)$$

The  $y$  values in the above expression would always be  $-1$  for negative training vectors and  $+1$  for positive training vectors. The vector that has to be classified and each training input are taken to execute the inner product. Thus, to figure out the classification function, we would be required to gather a set of training data  $(x, y)$ . The minimization process provides the Lagrange multiplier values, and  $l$  value is the number of vectors contributed in the training process to form the decision limit. Those vectors that contributed to form decision limit have a value not equal to zero and are called support vectors.

This scheme is not allowed to use directly, if these data are not linearly separable. SVMs will map a high-dimensional feature space with the input data to avoid such issues. An optimal hyperplane is constructed by the SVMs in a high-dimensional space, and this hyperplane is transformed into a nonlinear decision limit before returning to the original space. The classification function has a nonlinear expression as given in (2), where the nonlinear mapping is performed by the kernel  $K$ .

$$f(x) = \sum_{i=1}^l \alpha_i y_i K(X_i \cdot X) + b \quad (2)$$

The performance of the SVMs is determined by the choice of kernel or this nonlinear mapping function. The radial basis function is used as a kernel in author's work. The expression of the function is given in (3).

$$K(x, y) = \exp(-\gamma(x - y^2)) \quad (3)$$

To find the application of generalization degree to the data used, we need to select the parameter  $\gamma$ . Normalization task will be executed by this parameter, if the normalization is not applied to the input data. A penalty term ( $C$ ) is included in the



minimization by the SVMs if it is not possible to separate the data into sets, where the importance of misclassification is considered. If the value of this parameter is great, misclassification error is more important for the minimization procedure.

## 4 Results and Discussion

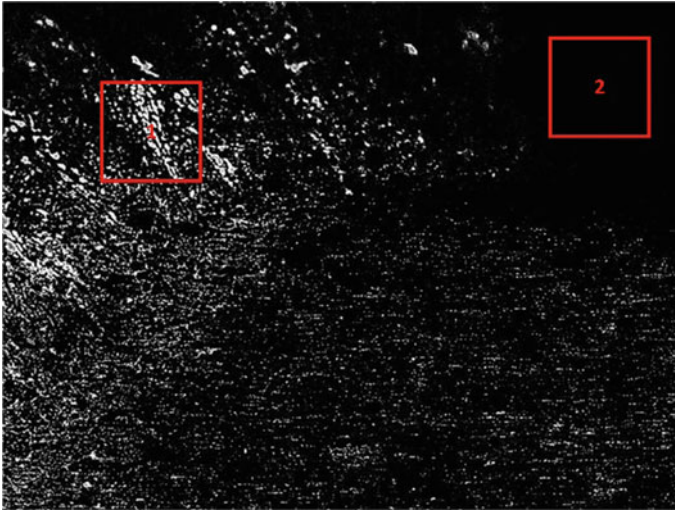
### 4.1 Image Segmentation

This section provides the details of the implementation of SVM for finding intermetallic compounds in the weld microstructures. The first step is extraction of pixel-level texture and color features of an image that is carried out by using local homogeneity model and Gabor filter techniques. The pixel feature extracted from the image is given as an input vector  $x$  to the SVM classifier model. Each color image of microstructures contains information of RGB and stored in three components. To perform the binary classification, all the color images are converted to YCbCr color space, where  $Y$  is the luminance and  $Cb$  and  $Cr$  are the chrominance components, respectively. The Gabor filter with 4 orientations is applied to the luminance component of images. The  $y$  values of the SVM model are set to  $+1$  for the desired values and set to  $-1$  for the other values.

### 4.2 Training Procedure

After constructing the local image window, we distinguished the color zone for assigning  $+1$  and  $-1$ . From the fuzzy c-means clustering, it is clearly observed that the regions with intermetallic compounds are brighter when compared to the microstructures of the base metal. The brighter regions are assigned with  $+1$ . Figure 2 shows the example of assigning labels  $+1$  and  $-1$ .

All the labeled pixels in these regions are used as an input vector for training of SVM classification model. MATLAB 2018b software is used for SVM classification model. The training process depends on the selection of kernel function. Each kernel function tends to give different degrees of accuracy. The best SVM classifier model is obtained by adjusting the parameters with minimal support vectors, as the support vectors are directly related to the computational speed.



**Fig. 2** Data extraction for training—Region 1 is assigned +1 and Region 2 is -1

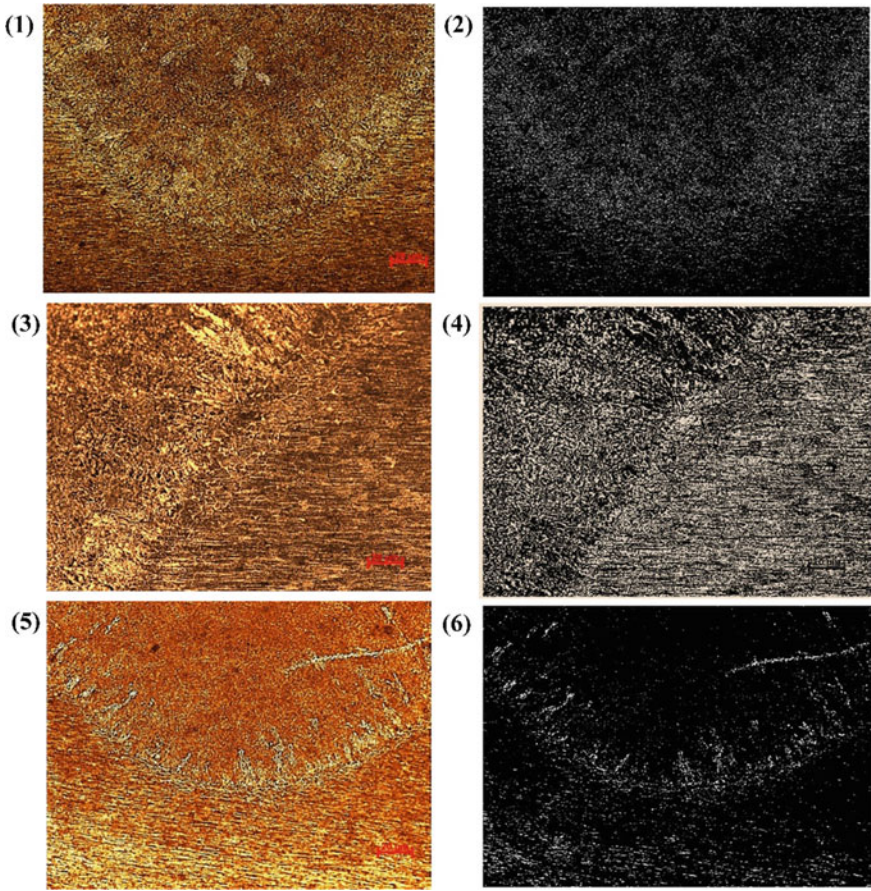
### ***4.3 Pixel-Based Microstructural Image Segmentation Using FCM and SVM***

The classification of intermetallic compounds from the base metal was carried out using FCM and SVM. Figure 3 provides the FCM thresholded images of the microstructures. Images with high resolution tend to perform poorly in SVM classifier model. In Fig. 3, Images 1 and 5 have higher noise when compared to the image 3. The intermetallic layer and its compounds are clearly distinguished in images 1 and 5.

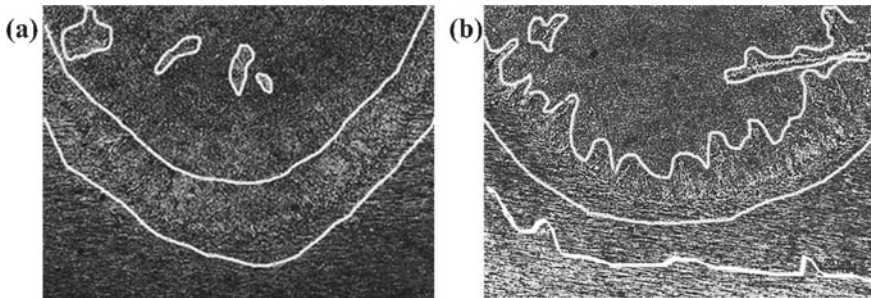
### ***4.4 Performance Evaluation***

The results obtained from the testing set have better segmented regions of intermetallic compounds. The presence of intermetallic compounds of fusion welded joints cannot be inhibited due to the solidification phases of different eutectic temperatures. Images that have higher magnification show higher noise and the associated classification results are poor. As the magnification increased, brighter is the visibility of compounds present in the base metal. This makes difficult for FCM algorithm to segregate the regions of intermetallic compounds from the base metal region.

Figure 4a and b, shows the SVM classifier output images of low- and high-magnification microstructural images. There is large deviation of the classifier image to determine the intermetallic compound layer and its thickness. However, the image with lower magnification resulted in the good segmentation by the classifier model.



**Fig. 3** Original microstructures (left side) and threshold microstructural images (right side) used for input space of SVM classifier model



**Fig. 4** SVM classifier output: **a** low-magnification image—20  $\mu\text{m}$ , **b** high-magnification image—300  $\mu\text{m}$

## 5 Conclusions

An attempt was made an attempt to determine the regions of intermetallic compounds and layer thickness from the microstructural images. In this study, image segmentation was carried out using FCM and SVM algorithms. The major conclusions that can be drawn from this research are the following:

- The SVM classifier model is trained with pixel-level color and texture features. The feature extraction is performed by using local homogeneity model and Gabor filters.
- The FCM algorithm clearly distinguishes the brighter regions which correspond to the intermetallic compounds and the darker regions that are related to the base metal microstructures.
- Images that have higher magnification show higher noise and the associated classification results are poor. A conclusion obtained from the classifier model is that it can be applied to the lower-magnification microstructural images with good accuracy.

## References

1. Bao, P., Zhang, L., Wu, X.: Canny edge detection enhancement by scale multiplication. *IEEE Trans. Pattern Anal. Mach. Intell.* **27**(9), 1485–1490 (2005)
2. Christoudias, C., Georgescu, B., Meer, P.: Synergism in low-level vision. In: *Proceedings of the 16th International Conference on Pattern Recognition*, vol. IV, Quebec City, Canada, August 2002, pp. 150–155
3. Chung, K.-L., Yang, W.-J., Yan, W.-M.: Efficient edge-preserving algorithm for color contrast enhancement with application to color image. *J. Vis. Commun. Image Represent.* **19**(5), 299–310 (2008)
4. Zeng, X.Y., Chen, Y.W., Nakao, Z., Lu, H.Q.: Texture representation based on pattern map. *Sig. Process.* **84**(3), 589–599 (2004)
5. Chen, G.-Y., Chen, Y.-C., et al.: Template-based automatic segmentation of drosophila mushroom bodies. *J. Inf. Sci. Eng.* **24**(1), 99–113 (2008)
6. Madhubanti, M., Amitava, C.: A hybrid cooperative-comprehensive learning based PSO algorithm for image segmentation using multilevel thresholding. *Expert Syst. Appl.* **34**(2), 1341–1350 (2008)
7. Yuksel, M.E., Borlu, M.: Accurate segmentation of dermoscopic images by image thresholding based on type-2 fuzzy logic. *IEEE Trans. Fuzzy Syst.* **17**(4), 976–982 (2009)
8. Wang, X., Sun, Y.: A color-and texture-based image segmentation algorithm. *Mach. Graph. Vis.* **19**(1), 3–18 (2010)
9. He, R., Datta, S., Sajja, B.R.: Generalized fuzzy clustering for segmentation of multi-spectral magnetic resonance images. *Comput. Med. Imaging Graph.* **32**(5), 353–366 (2008)
10. Shi, J., Malik, J.: Normalized cuts and image segmentation. *IEEE Trans. Pattern Anal. Mach. Intell.* **22**(8), 888–905 (2000)
11. Ugarriza, O.G., Saber, L., Vantaram, E., et al.: Automatic image segmentation by dynamic region growth and multi resolution merging. *IEEE Trans. Image Process.* **18**(10), 2275–2288 (2009)

12. Petera, Z., Boussone, V., Bergote, C., Peyrina, F.: A constrained region growing approach based on water shed for the segmentation of low contrast structures in bone micro-CT images. *Pattern Recogn.* **41**, 2358–2368 (2008)
13. Krinidis, M., Pita, I.: Color texture segmentation based on the modal energy of deformable surfaces. *IEEE Trans. Image Process.* **18**(7), 1613–1622 (2009)
14. Kumar, N.P., Vendan, S.A., Shanmugam, N.S.: Investigations on the parametric effects of cold metal transfer process on the microstructural aspects in AA6061. *J. Alloy Compd.* **658**, 255–264 (2016)
15. Nacereddine, N., Tridi, M., Hamami, L., Ziou, D.: Statistical tools for weld defect evaluation in radiographic testing. In: *Proceedings of 12th European Conference on Non-destructive Testing—ECNDT* (2006)

# Navigation of Mobile Robot Through Mapping Using Orbbec Astra Camera and ROS in an Indoor Environment



M. Basavanna, M. Shivakumar, and K. R. Prakash

## 1 Introduction

An autonomous mobile robot (AMR) is a robot that can navigate in an indoor/outdoor environment without being supervised directly by an operator. This autonomous functionality is achieved through a series of on-board sensors and maps which allow the autonomous mobile robots to understand interpret and react to the surrounding environment. The autonomous mobile robot has been extensively used in many sectors such as material handling in light and heavy industries, household tasks, underwater and outer space applications.

The robot environment mapping is the process of generating 2D or 3D model of the real working environment of the robot using specific environmental data obtained from the sophisticated sensors [1]. The environment mapping is one of the important necessary features in mobile robotics when dealing with localization, positioning, and autonomous navigation of mobile robot without collision [2]. Most of the mobile robots have equipped with Inertial Measurement Unit (IMU), gyroscope, accelerometers and magnetometer to measure the orientation, angular velocity and acceleration of the robot which are used for localization of the robot. The mobile robot localization by using above-mentioned inertial navigation systems results in navigation errors as

---

M. Basavanna (✉)

Department of ECE, GSSSIETW, Mysuru, India

e-mail: [basavannam@gsss.edu.in](mailto:basavannam@gsss.edu.in)

M. Shivakumar

Department of E&IE, GSSSIETW, Mysuru, India

e-mail: [drshivakumarm@gsss.edu.in](mailto:drshivakumarm@gsss.edu.in)

K. R. Prakash

Department of ME, NIE, Mysuru, India

e-mail: [krp@nie.ac.in](mailto:krp@nie.ac.in)



they suffer from integration drift; small errors in the measurement of acceleration and angular velocity result in position error during localization of robot [3].

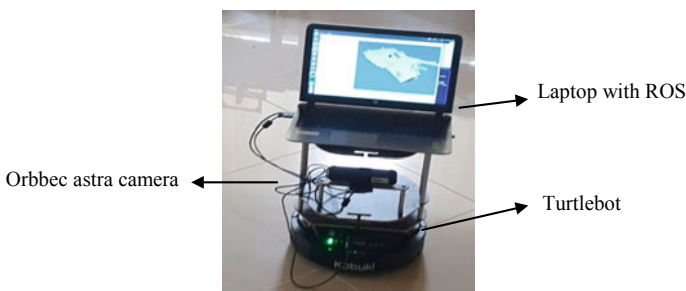
In early days, LIDAR sensor was widely used for mobile robot mapping and navigation [4, 5]. The Lidar sensor scans and detects the objects which are above floor level using only a single horizontal scanning line [4]. There is some kind of structures such as holes or staircases which can't be detected by Lidar. This limitation of mapping using Lidar can be overcome by using Kinect Camera. The Kinect camera can detect the objects which are above and below axis of scanning line. Objective of current research work is to scan an unknown indoor environment using Orbbec Astra camera which is a kind of Kinect camera and ROS in order to generate the map of environment and navigate the mobile robot from starting location to target locations without colliding with obstacles. Experimental results show that the generated map of the indoor environment looks more close to real environment than mapping using Lidar, and mobile robot is navigated to reach target from start location without collision with obstacles.

## 2 System Overview and Implementation

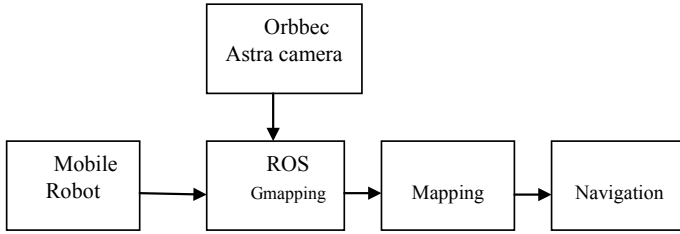
### 2.1 Mobile Robot Setup and Block Diagram

The Turtlebot2 mobile robot which is having Kobuki base with maximum speed of 0.65 m/s is interfaced with laptop having Orbbec Astra camera and Robotic Operating System (ROS). Orbbec Astar (Kinect) camera was mounted on mobile robot for obstacle detection and mapping. The experimental setup consisting of Turtlebot mobile robot, Astra camera and Laptop with ROS is as shown in Fig. 1.

The Orbbec Astra camera is mounted on the Turtlebot2 mobile robot which is teleoperated to move around the environment to be mapped. The camera which is mounted on the mobile robot will detect the objects around the robot in the environment and send the information about obstacles to the ROS. Minimal SLAM



**Fig. 1** Mobile robot and Astra camera setup for mapping and navigation



**Fig. 2** Block diagram of unknown indoor mapping using Orbbec Astra camera



**Fig. 3** Orbbec Astra camera. Astra Series – Orbbec (orbbec3d.com)

Gmapping technique is used to map the environment and map can be visualized using Rviz tool in ROS. The generated map is used to navigate the mobile robot from start point to goal point without any collision with obstacles. The Fig. 2 shows the block diagram of methodology used in mapping and navigation of mobile robot.

**2.1.1 Orbbec Astra Camera**

An Orbbec Astra camera is a 3D depth camera with VGA color and superior long-range depth tracking up to 8 m [4]. This device contains an IR sensor, RGB sensor, microphones, advanced eye protector and a coded pattern projector. It is widely used for mapping and navigation applications in mobile robots using ROS (Robot Operating System) (Fig. 3).

**2.1.2 Robot Operating System**

The Robotic Operating System (ROS) is an open-source robotic middleware for the development of robotic systems. The main function of the ROS is to provide communication between the user, robot and equipment external to the computer such as sensors and cameras. A ROS system is comprised of a number of small and independent programs that can run concurrently called ROS nodes and each of which communicates with the other nodes by sending or receiving messages. The messages can consist of data, or commands, or other information necessary for the application . Some nodes provide information for other nodes through ROS topic.



The ROS master is responsible for establishing communication between the nodes and provides naming and registration services to the nodes in the ROS system. It also tracks publishers and subscribers nodes to the topics [5, 6].

### 2.1.3 Gmapping Technique

In the present work, Gmapping technique is used for mapping of environment. The Gmapping is a localization technique that runs on unknown environment to perform simultaneous localization and mapping. It uses the Rao-Blackwellized Particle Filter (RBPF) and receives data from both sensor and robots pose to generate a 2D grid map of the environment without IMU information [7]. In Gmapping, the robot constantly updates the pose on each processed particle by estimating odometry. During execution of mapping as the first scan is received, it is directly registered in the map. Afterward, registration occurs only if the linear distance or angular distance traversed by the robot exceeds specific thresholds. Once scan match is received, correction of the estimation of pose in the map of each particle is performed for each laser scan to generate the map of environment [8, 9].

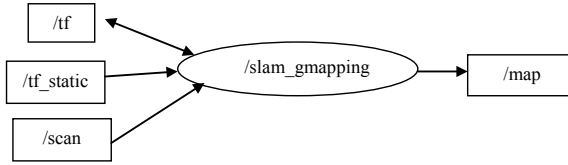
### 2.1.4 RViz Tool

The RViz is a visualization tool for ROS applications. It captures the information from the laser scanners and replays captured data in the form of visual. In current work, RViz is used to display the generated map of environment.

## 3 Flow Chart

### 3.1 Mapping Process

The Orbbec Astra camera mounted on mobile robot will detect the obstacles in the environment and give information regarding obstacles to the ROS. The obstacle information along with odometry information of mobile robot is used generate map of environment using SLAM Gmapping technique. The mapping process is as follows: initially running the ROScore and Gmapping node in the ROS terminal. The ROS core establishes the connection between Gmapping node, Astra camera and mobile robot [9, 10]. The Gmapping node receives obstacle information from Astra camera in the form messages through '/scan' topic and odometry position information from the mobile robot in order to create the 2D grid map as shown in Fig. 4. The mobile robot is teleoperated using keyboard in the indoor environment to be mapped and run the RViz in another terminal in order to visualize the mapping process.



**Fig. 4** Gmapping

The accuracy of the map is determined when the mobile robot completes the mapping process.

$$\text{Accuracy}\% = (a/b) \times 100 \tag{1}$$

Equation (1) is used to find the accuracy of the map generated based on the dimension of the actual layout of indoor environment to be mapped. The ‘a’ indicates the total length of the map generated by the robot where ‘b’ indicates the total length of the actual real map. If the accuracy of the generated map is high or more than 80%, then it will be saved using map saver command, and if accuracy is less than 80%, then the robot will be moved again in the environment to be mapped to map the unmapped regions of the map. The detailed flow chart of mapping process is shown in Fig. 5.

### 3.2 Navigation Process

The generated map is used to navigate the mobile robot from start to target location without collision with obstacles. The generated map and robot position array topics are loaded in to global planner. Locate the robot position on the map using 2D pos estimate button and target location to be reached by the robot is indicated using 2D Nav Goal button on the generated map. Then, global path planner estimates the path from start location to target location without collision with obstacles. The detailed flow chart of navigation process is shown in Fig. 6.

## 4 Experimental Results and Discussion

The mapping of the indoor environment is performed using Orbbec Astra camera mounted on a Turtlebot2 mobile robot and ROS. The scanning and detection of obstacles in the environment are carried using Orbbec Astra camera to collect obstacle information present in the indoor environment. Initially, the mobile robot with Astra camera and ROS is teleoperated using keyboard ‘ssh’ commands manually in the environment to be mapped. While mobile robot is moving around, the Orbbec Astra

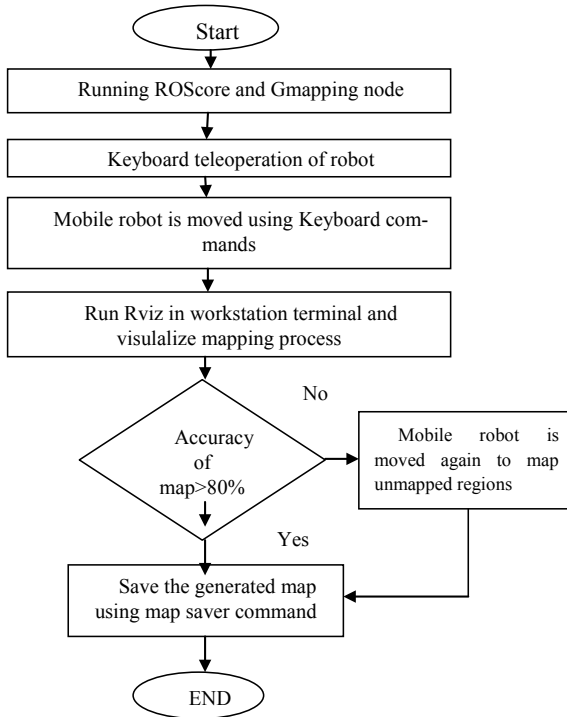


Fig. 5 Flow chart of mapping process

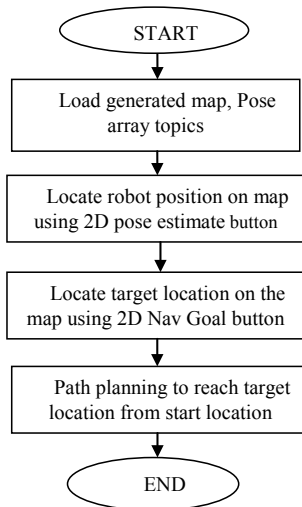


Fig. 6 Flow chart of navigation process

camera collects information of obstacles present in the environment and which is sent to gmapping node through ROS topic called '/scan'. The gmapping node in ROS will combine obstacle information received from Astra camera with mobile robot odometry and generate the map of indoor environment using Gmapping technique. The map generation process can be visualized using RViz tool in ROS as shown in Fig. 8. The generated map of the indoor environment generated using Orbbec Astra camera shown in Fig. 8 matches with real indoor environment shown in Fig. 7.

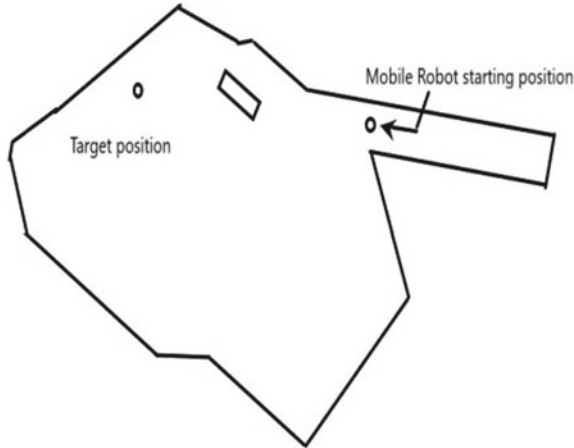


Fig. 7 Actual layout of environment

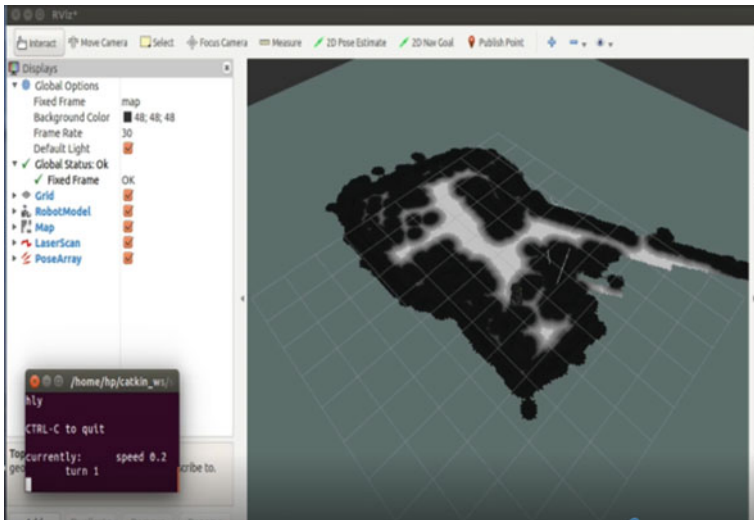


Fig. 8 Map generation visualized using RViz

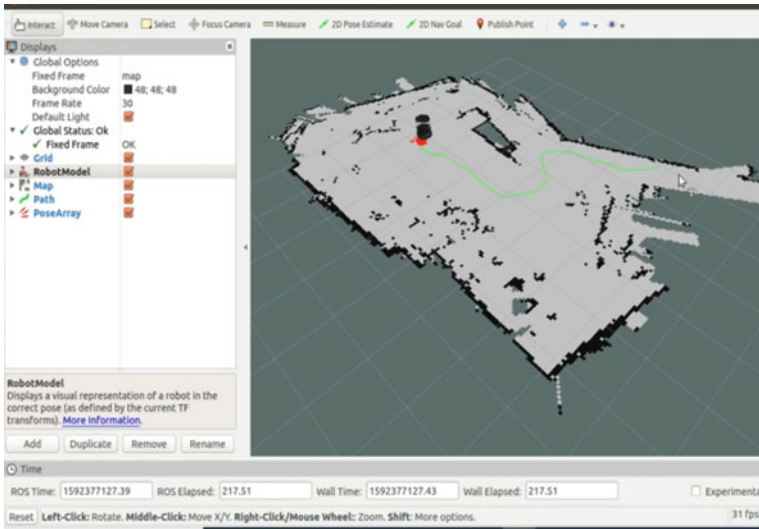


Fig. 9 Navigation of mobile robot seen in RViz

The generated map of the environment is used to safely navigate the mobile robot from start to target location without any collision with obstacles. The starting position of the robot is located on the generated map using 2D Pos estimate button, and target is located using 2D nav Goal button on the map. The mobile robot plans the route from start to target using path planning algorithm and navigates without any collision with obstacles. The green color in Fig. 9 indicates the navigation path of mobile robot from start to target location and is also tested experimentally by navigating Turtlebot mobile as shown in Fig. 10.

## 5 Conclusion

The navigation of mobile robot in unknown indoor environment is difficult without knowing structure of environment. In order to support the collision free navigation of mobile robot in an unknown indoor environment, the environment should be mapped first to know the information of obstacles present in the indoor environment. In this work, the Orbbec Astra 3D depth camera is used is for mapping of indoor environment by detecting the objects which are below and above axis of scanning line where the obstacles below the axis of scanning line are missing in normal laser scan using Lidar. The mapping using Orbbec Astra camera gives better accuracy than

**Fig. 10** Navigation of Turtlebot robot



mapping using Lidar as Orbbec Astra camera performs scanning of objects which are even below axis of placement of sensor which is missing in the Lidar. The generated map of environment using Orbbec Astra camera and ROS has been used to navigate the mobile robot successfully from start to target location without colliding with obstacles.


## References

1. Park, S.Y., Lee, G.H.: Mapping and localization of cooperative robots by ROS and SLAM in unknown working area. In: Proceedings of the SICE Annual Conference 2017, September 19–22, 2017
2. Rubinstein, A., Erez, T.: Autonomous robot for tunnel mapping. In: International Conference on the Science of Electrical Engineering (2016)
3. Zaman, S., Slany, W., Steinbauer, G.: ROS-based mapping, localization and autonomous navigation using a Pioneer 3-DX robot and their relevant issues. In: 2011 Saudi International Electronics, Communications and Photonics Conference, Riyadh, pp. 1–5 (2011)
4. Ghani, M.F.A., Sahari, K.S.M.: Detecting negative obstacle using Kinect sensor. *Int. J. Adv. Robot. Syst.* (2017)
5. Basavanna, M., Shivakumar, M.: Mapping of unknown indoor environment using Lidar and ROS. *Int. J. Adv. Sci. Technol.* **5**(12) (2020)
6. Voisan, I., Precup, B.P., Dragan, F.: ROS-based robot navigation and human interaction in indoor environment. In: 10th Jubilee IEEE International Symposium on Applied Computational Intelligence and Informatics, May 21–23, 2015
7. Grisetti, G., Stachniss, C., Burgard, W.: Improved techniques for grid mapping with Rao-Blackwellized particle filters. *IEEE Trans. Robot.* **23**(1), 34–46 (2007)
8. Norzam, W.A.S., Hawari, H.F., Kamarudin, K.: Analysis of mobile robot indoor mapping using GMapping based SLAM with different parameter. *IOP Conf. Ser. Mater. Sci. Eng.* (2019)

9. Santos, J.M., Portugal, D., Rocha, R.P.: An evaluation of 2D SLAM techniques available in robot operating system. In: 2013 IEEE International Symposium on Safety, Security, and Rescue Robotics (SSRR), Linkoping, pp. 1–6 (2013)
10. Ochiai, Y., Takemura, K., Ikeda, A., Takamatsu, J., Ogasawara, T.: Remote control system for multiple mobile robots using touch panel interface and autonomous mobility. In: 2014 IEEE/RSJ International Conference on Intelligent Robots and Systems, Chicago, IL, pp. 3272–3277 (2014)

# Automation in Retail ‘Follow-Me-Auto Shopping Cart’: A Self-propelled Computer Vision-Based Shopper Following Cart with Auto-billing Feature Using IIoT



Ayaskanta Mishra , Aditya Mohan, Abhranil Mandal, Anamika Mohanty, and Akashdeep Chowdhury

## 1 Introduction

Major technological advancements gravitate towards automation of systems and processes that would need minimum to no human intervention. Automation in retail can be achieved through smart shopping trolley whose aim is mechanization of user shopping experience by CV using Internet of Things and cloud-based web technologies. Rupanagudi et al. [1] have developed a cost-effective smart trolley prototype using RFID, Wi-Fi, Zigbee. The smart trolley developed is enabled with a web camera along with video processing capability. Sainath et al. [2] have proposed an automated Shopping Trolley which integrates a Raspberry Pie Embedded Chip with two Bar code Scanners and a Battery kit to allow users for self-checkouts at Super Markets. Wankhede et al. [3] have proposed an Electronic Shopping Trolley for getting products scanned using a barcode scanner. Lekhaa et al. [4] have designed an intelligent shopping cart using IoT consisting of barcode scanner, Liquid Crystal Display (LCD) display, Bolt ESP8266. Sutagundar et al. [5] have designed IoT-based smart shopping mall system that uses ESP8266 Wi-Fi module along with web application that enables customer login and data entry to the cloud for automatic payment. Lestari et al. [6] have proposed a method for automatic trolley control that follows a user based on the clothes color; coordinate locations, speed of movement, and size of the object captured by the camera. The proposed system uses Python application Camshift algorithm to develop the model. Athauda et al. [7] have proposed a low-cost, robust, passive Ultra High Frequency (UHF) RFID-based shopping trolley that allows tracing and processing shopping data in real time. Sarala et al. [8] have developed a prototype using an Arduino ATmega2560, Infrared (IR) sensor, barcode

---

A. Mishra (✉) · A. Mohan · A. Mandal · A. Mohanty · A. Chowdhury  
School of Electronics Engineering, Kalinga Institute of Industrial Technology, Deemed to be University, Bhubaneswar 751024, India



acceptance button, power supply, LCD display, Global System for Mobile communications (GSM) modem for automatic identification of shopping items. Viswanadha et al. [9] have proposed a smart shopping cart is with barcode scanner and touch-screen display to scan the products and display the product information, cost and total bill. Awati et al. [10] have designed an AtmelAT89V51 microcontroller-based Trolley by using optical sensor, barcode scanner, RF Transmitter-Receiver to design a smart trolley for malls. Sanap et al. [11] have developed a prototype of Smart Mobile Autonomous Robotic Trolley (SMART) using ATmega 16 microcontroller interfaced with EM18 RFID reader module, buzzer and Light Emitting Diode (LED) indicator. Data transfer between the trolley billing system and billing station system is done via an XBee ZigBee. Dhianeswar et al. [12] have proposed a Smart Shopping Trolley to follow the customer automatically using a Kinect Sensor.

## 2 Proposed System

In the era of Industry 4.0 and Industrial Internet of Things (IIoT), modern sensors and actuator control have enhanced the conventional machines to smart machines. In this paper, we are proposing a smart mechanized shopping cart using embedded system and motor drive control circuitry based on computer vision algorithm-based real-time shopper tracking. Figure 1 shows proposed Smart automated shopping cart for automation in retail using Computer Vision (CV) and IIoT in the era of industry 4.0.

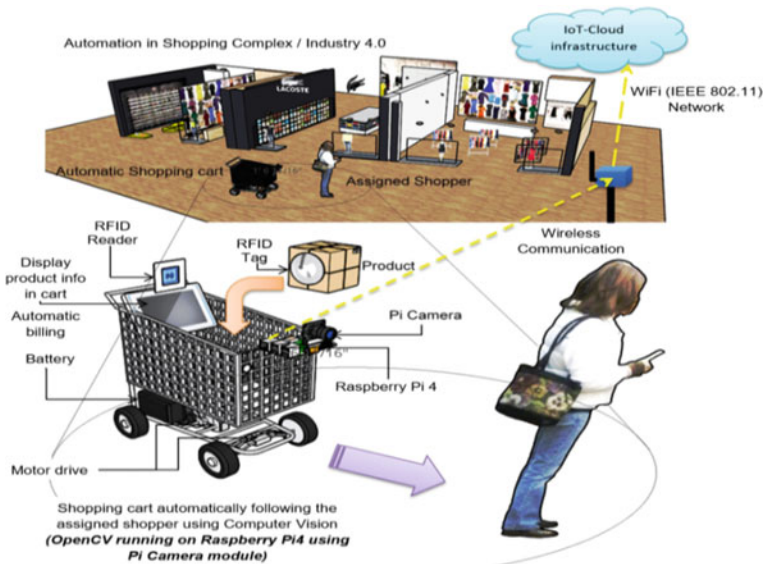


Fig. 1 Proposed smart automated shopping cart for automation in retail using CV & IIoT

The system comprises of many functional blocks: (1) Pi Camera and OpenCV based object tracking for making the shopping cart track the movement of the registered shopper and follow automatically. (2) Raspberry Pi4 as the embedded edge computation platform. (3) Mechanical and drive sub-system comprises of a L298N motor drive, which controls two motors (left and right) using a novel Finite State Machine (FSM) based software sub-routine. (4) Battery and power supply sub-system. (5) MFRC522 module for RFID-based product sensing for automatic billing. (6) Touch screen display unit for providing user interface/experience (UI/UX). The objective of this proposed system is to get a complete automation in retail sector using fully automatic shopping cart. The cart would automatically follow the registered shopper and the shopper can buy products by simply dropping them on to the cart and the RFID module of the cart can sense the passive RFID tags (attached with all the products) hence having a list and database of all the products inside the cart. Finally at the time of check out the total products and the price can be computed and a bill can be generated automatically and processed for online payment using integrated payment gateway solutions. This proposed system would provide a complete end to end solution for automation in retail sector with the vision of industry 4.0 using computer vision, embedded system control of mechanical system using Industrial IoT technology. Figure 2 shows the block diagram of our proposed smart automated shopping cart system. The Pi Camera is interfaced with Raspberry Pi4 for acquisition of real-time video feed of the registered shopper. The computer vision algorithm implemented on the raspberry pi using OpenCV python-library to track the movement of the registered shopper. Subsequently the OpenCV would give a tracking output as movement of the target as five distinct states left movement, right movement, forward movement, backward movement or stop- no movement.

These five tracking states are feed to the FSM to create software sub-routine to control the motor drive L298N which subsequently controls the direction of Battery

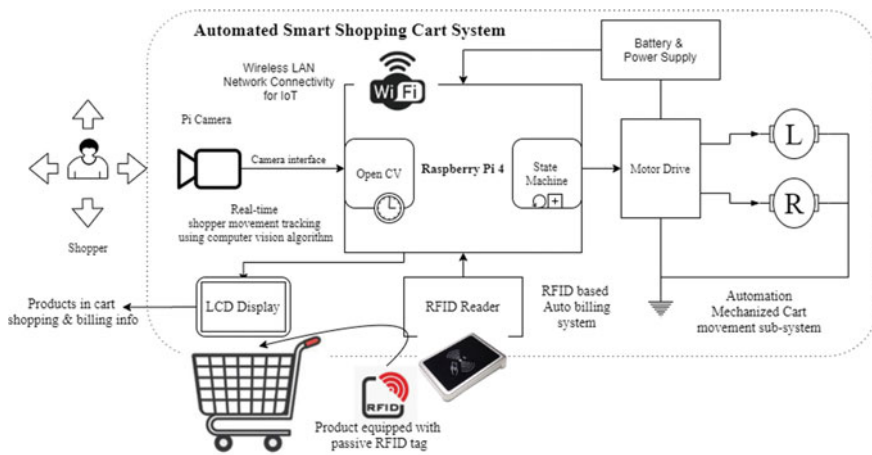


Fig. 2 Block diagram of proposed smart automated shopping cart

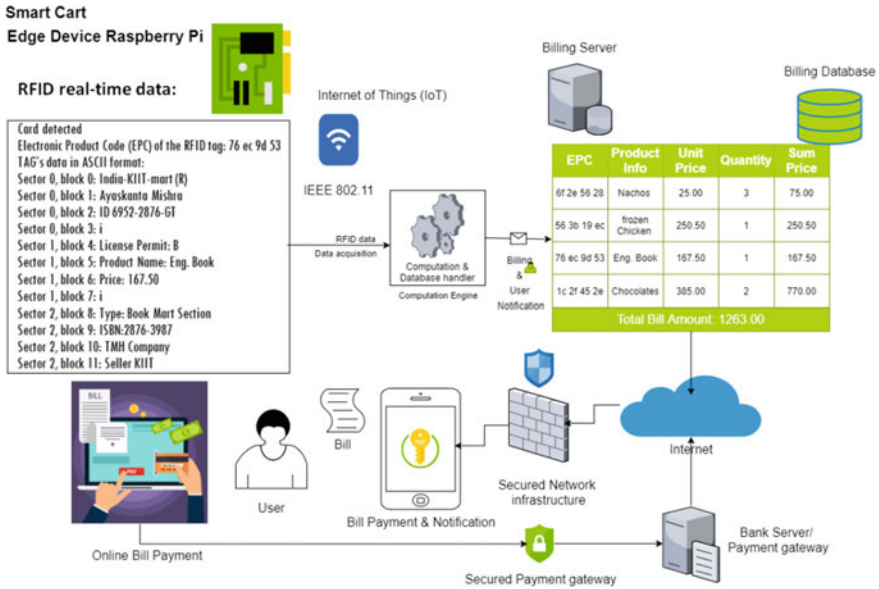


Fig. 3 RFID based automatic billing system for smart shopping cart

Operated (BO) DC motors. Two motors are equipped in the cart for direction and movement control in the mechanical sub-system. Figure 3 shows the automatic billing sub-system. The registered shopper would put products inside the cart. The cart is equipped with a RFID reader which would send Electronic Product code (EPC), Product info, unit price, quantity and sum price to the billing server using IEEE 802.11 (Wi-Fi) of Raspberry Pi. The data is going through a computation process and database handler to send all product purchase information to the billing server. The billing server is integrated with internet to provide the billing information and payment option to the shopper. Subsequently the shopper may pay the bills using secured online payment gateways to finish the shopping transaction.

### 3 System Implementation

The proposed system is implemented using Raspberry Pi 4 and other required axillary hardware and software (1) Pi Camera, (2) Power supply unit (DC-DC buck converter) and battery and voltage regulator and charger circuit. (3) Motor drive and Motor as mechanical control and drive sub-system. (4) MFRC522 RFID reader module, (5) Touch screen display unit for UI/UX. Figure 4 shows the flow chart of the software running on the raspberry pi to perform all the required actions. For functional modularity we have used two distinct python processes one for the object tracking and mechanical drive sub-system control and other one for RFID based auto-billing. The

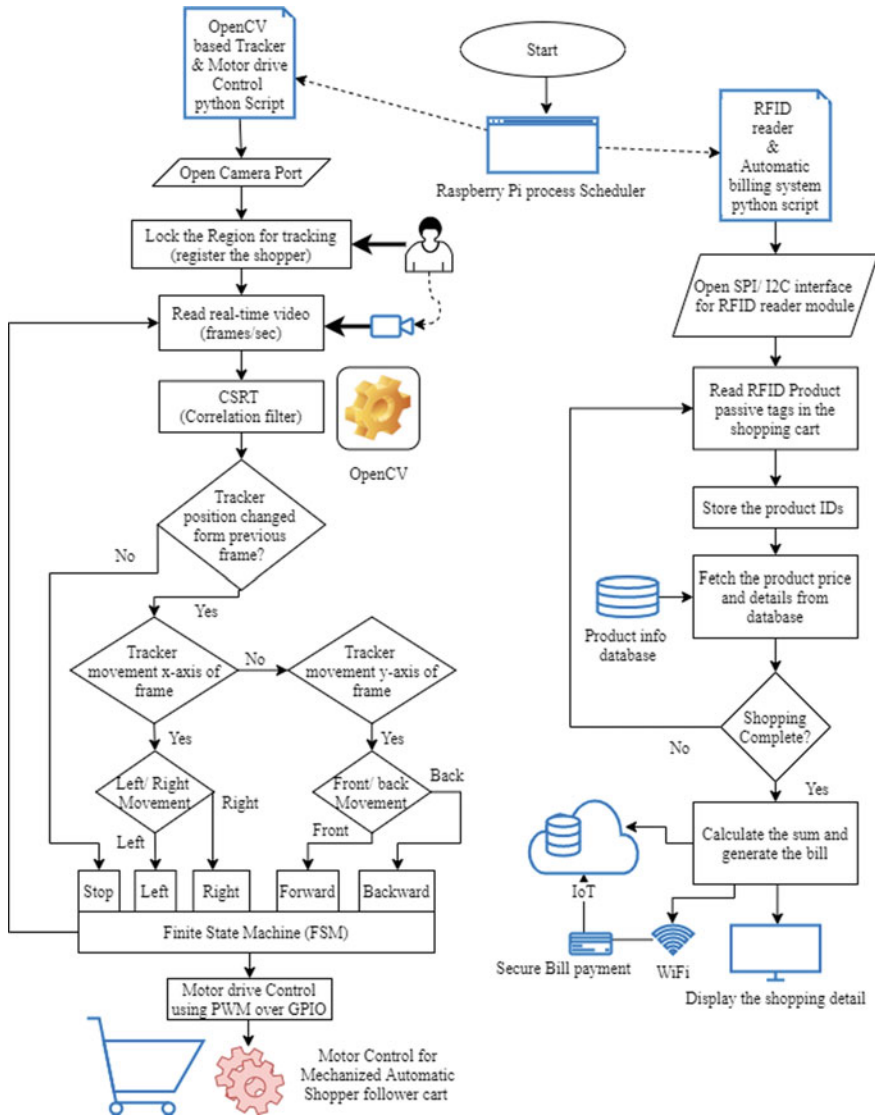


Fig. 4 Smart automated shopping cart system flowchart

two processes are running through two independent terminal programs using raspberry pi OS program scheduler. First process starts with switching on the Pi camera and acquiring real-time video feed. First the target shopper image is registered and locked. We are using Channel Spatial Reliability Tracking (CSRT) correlation-based filer for tracking the target object. The output of OpenCV-based correlation filter is obtained as left, right, forward, backward or stop as tracked movement and the same is

fed to our proposed novel FSM. FSM would send control signals to the L298N motor driver module. The motor driver module then controls the direction of two motors to maneuver the automated cart system. Second process is for a RFID-based purchased product tracking and auto billing. The MFRC522 RFID reader is interfaced with raspberry pi using I2C (Inter-integrated Circuit)/Serial Peripheral Interface (SPI) protocol for sending passive RFID tag information for computation and communication. The program would read the passive RFID tag and first stored the EPC of a particular tag (attached with the product). MFRC522 would next fetch the data sector and block wise from the tag and this process would provide all the basic information of the purchased product like product ID, name, unit price. This process would be repeated for the entire set of products put into the cart for purchasing. All these data would be computed and communicated to the billing server using IEEE 802.11 (Wi-Fi) data network using IoT. At the checkout all purchased product and their billing information would be displayed on the UI/UX using the display unit and also on the android app on shopper/s mobile device. Then the shopper would complete the online payment using relevant payment gateways and finish the shopping process.

Figure 5 shows the complete system implementation comprising of all the sub-systems discussed above. We have using Firtzing software tool to model the prototype of electronic and embedded sub-system. The mechanical and motor drive sub-system is controlled using FSM driven by computer vision (OpenCV) algorithms implemented through software sub-routines and stand-alone processes (python programming).

We have studied different techniques of real-time tracking of object and by the study we have found CSRT technique is promising for our application and hence we have used the same in our proposed system.

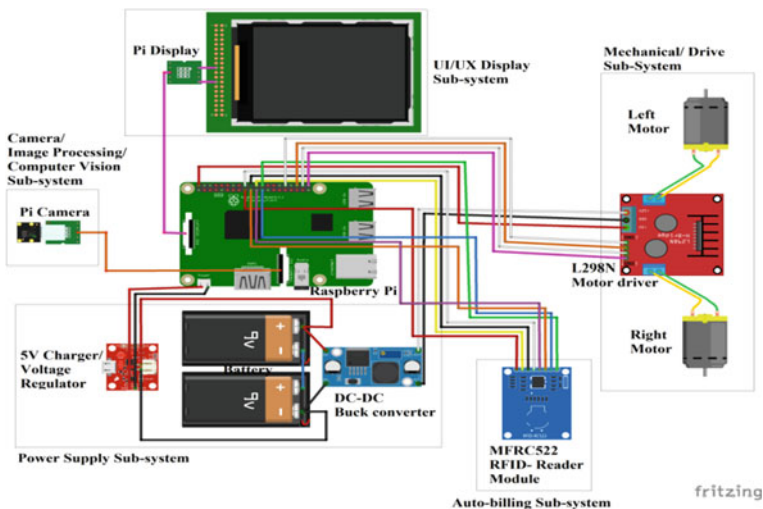


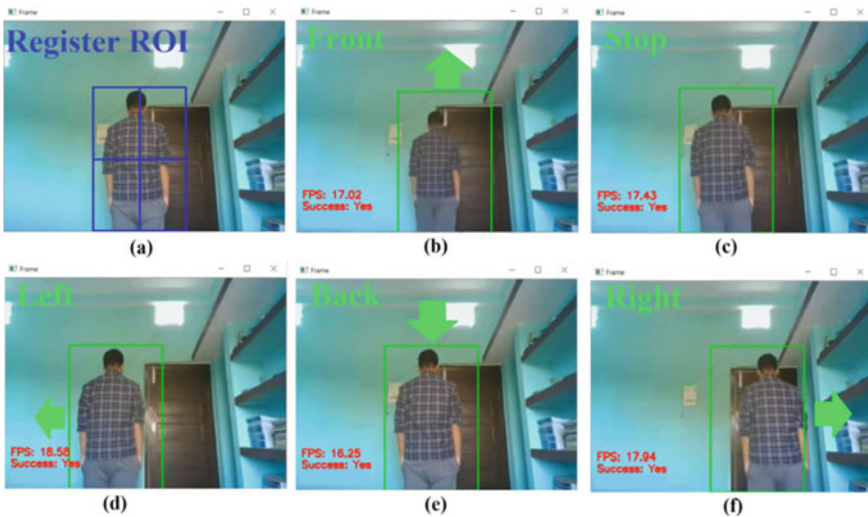
Fig. 5 System implementation

## 4 Results and Discussion

In this section, we are presenting our results after applying the CSRT algorithm for real-time object tracking. Figure 6 shows the output of CSRT algorithm for real-time of the target object in this case our registered shopper.

Based on the real-time tracking of the target object CSRT algorithm would provide five distinct states (1) forward (F), (2) stop (S), (3) backward (B), (4) left (L) and (5) right. Figure 7 shows the proposed novel FSM to send control signals to the L298N motor drive module. The state-machine is designed taking into consideration all the excitations possible in each of the states.

Figure 8a shows the FSM-based signaling timing diagram for L298N Motor drive control. S1(forward), S2(left), S3(right), S4(backward) & S5(stop). The signaling timing-diagram shows (IN-input) IN1 & IN2 pins of L298N motor driver for Motor 1 (Left Motor) control and IN3 & IN4 pins for Motor 2 (Right Motor) control. This system would give a complete navigation to the automation in mechanized drivability of the cart system by controlling the direction of motors hence ensuring a practical maneuverability based on real-time tracking of shopper (object) based on computer vision algorithm. Figure 8b shows the photograph as results of automatic billing screen of android app for the smart cart system. The screen shows the EPC of all purchased items and total price computer at the checkout using IoT and RFID technologies.



**Fig. 6** Computer vision based CSRT algorithm for real-time target tracking implemented in our proposed shopper follower automatic mechanized shopping cart **a** Register Region of Interest (ROI), **b** Tracking front movement of target object **c** Tracking stop **d** Tracking left movement **e** Tracking back movement **f** Tracking right movement



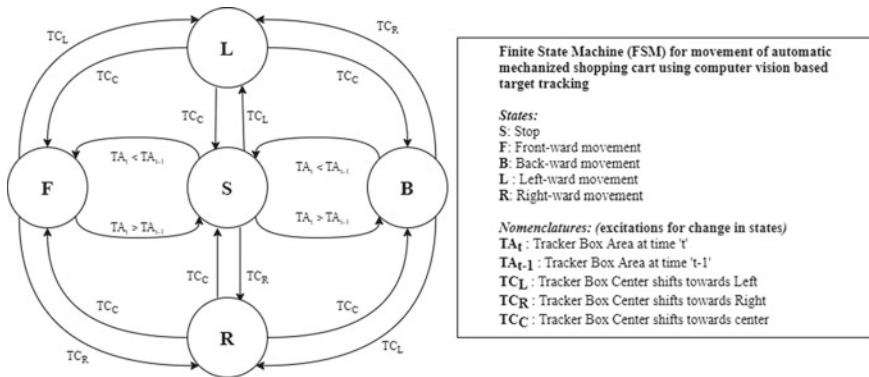


Fig. 7 Finite State Machine (FSM) for smart automated shopping cart movement

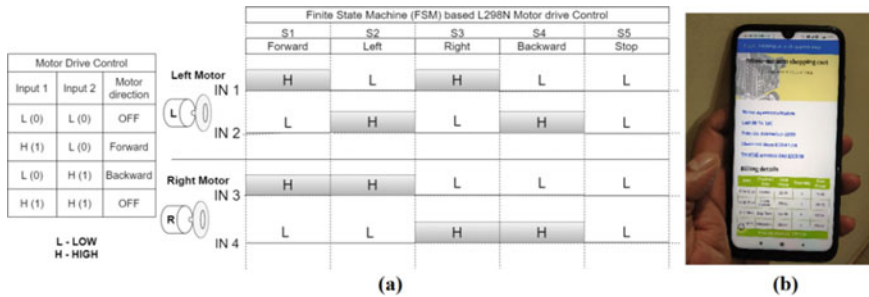


Fig. 8 a FSM based signaling timing diagram for L298N Motor drive control using real-time tracking of target shopper for automatic mechanized shopper follower cart b Smart shopping cart automatic billing Android app: RFID based product tracking and bill payment feature

## 5 Conclusion

In this paper, we have proposed a complete automation process of shopping cart by real-time object tracking using computer vision and RFID-based auto-billing feature. This proposed work would be instrumental in automation in retail section in the vision of industry 4.0 and industrial IoT and allied technologies. CSRT algorithm locks the target and track it real-time based on the Region of Interest (ROI), hence other object coming on the frame is not going to create hindrance in tracking. This feature would enable the cart to track and follow the registered shopper even in an overwhelming scenario of Indian shopping complex. Further enhancement in CV algorithm for better tracking mechanism in Indian scenario may be a research motivation for future work. This is a CV-based tracking and shopper following cart hence does not required any specific global location awareness rather the localization is achieved by the frame of reference of the registered shopper.

## References

1. Rupanagudi, S.R., et al.: A novel video processing based cost effective smart trolley system for supermarkets using FPGA. In: International Conference on Communication, Information & Computing Technology (ICCICT), pp. 1–6. IEEE, Mumbai, India (2015)
2. Arvind, V., Sainath, S., Surender, K., et al.: Automated shopping trolley for super market billing system. In: IJCA International Conference on Communication, Computing and Information Technology (ICCCMIT), pp. 7–9. IJCA, Chennai, India (2015)
3. Wankhede, S.S., Nikose, A., Radke, D.P., et al.: Electronic shopping trolley for shopping mall using android application. In: 2018 3rd International Conference on Communication and Electronics Systems (ICCES), pp. 948–953. IEEE, Coimbatore, India (2018)
4. Lekhaa, T.R., Rajeshwari, S., Sequeira, J.A., et al.: Intelligent shopping cart using Bolt Esp8266 based on internet of things. In: 2019 5th International Conference on Advanced Computing & Communication Systems (ICACCS), pp. 758–761. IEEE, Coimbatore, India (2019)
5. Sutagundar, A., Ettinamani, M., Attar, A.: IoT based smart shopping mall. In: 2018 Second International Conference on Green Computing and Internet of Things (ICGCIoT), pp. 355–360. IEEE, Bangalore, India (2018)
6. Lestari, D., Sendari, S., Sanjaya, S.D., et al.: Locking object position using Camshift algorithm for automatic trolley. In: 2019 International Conference on Electrical, Electronics and Information Engineering (ICEEIE), pp. 90–95. IEEE, Denpasar, Bali, Indonesia (2019)
7. Athauda, T., Marin, J.C.L., Lee, J., et al.: Robust low-cost passive UHF RFID based smart shopping trolley. *IEEE J. Radio Freq. Ident.* **2**(3), 134–143 (2018)
8. Sarala, T., Sudha, Y.A., Sindhu, K.V., et al.: Smart electronic trolley for shopping mall. In: 2018 3rd IEEE International Conference on Recent Trends in Electronics, Information & Communication Technology (RTEICT), pp. 2422–2427. IEEE, Bangalore, India (2018)
9. Viswanadha, V., Kumar, P.P., Reddy, C.S.: Smart shopping cart. In: 2018 International Conference on Circuits and Systems in Digital Enterprise Technology (ICCSDET), pp. 1–4. IEEE, Kottayam, India (2018)
10. Awati, J.S., Awati, S.B.: Smart trolley in mega mall. *Int. J. Emerg. Technol. Adv. Eng.* **2**(3), 474–477 (2012)
11. Sanap, M., Chimurkar, P., Bhagat, N.: SMART-smart mobile autonomous robotic trolley. In: 2020 4th International Conference on Intelligent Computing and Control Systems (ICICCS), pp. 430–437. IEEE, Madurai, India (2020)
12. Dhianeswar, R., Gowtham, M., Sumathi, S.: Smart trolley with automatic master follower and billing system. In: Pandian, A., Senjyu, T., Islam, S., Wang, H. (eds.) *Proceeding of the International Conference on Computer Networks, Big Data and IoT (ICCBI—2018)*. LNDECT, vol. 31, pp. 778–791. Springer, Cham (2020)



# An Intelligent and Robust Fault Diagnostics for an Electromechanical System Using Vibration and Current Signals



Purushottam Gangsar, Zeeshan Ali, Manoj Chouksey, and Anand Parey

## 1 Introduction

One of the goal of Industry 4.0 is to increase the automation and decision-making capabilities by incorporating various information from different sensors for condition monitoring of various machines. The introduction of artificial intelligence (AI) and machine learning (ML) to Industry 4.0 is found to be very critical for a sustained plant operation, unpredicted breakdown, reducing monetary losses, improving human machine collaboration and improving personnel safety [1]. The motor–rotor–bearing systems are the backbone of the industries, as they play an important role in the manufacturing, power generation, automobile, transportation, robotics and other industries [2]. The condition monitoring of such electromechanical systems based on AI and ML has now attracted many researchers from industry as well as academicians. By detecting faults in advance, the catastrophic failure can be avoided which reduces unexpected production losses and sometimes major human injuries [3, 4].

The main focus of the present work is to consider various mechanical and electrical faults occurred in a combined motor–rotor–bearing system. The faults occurred in motor may be mechanical or electrical [1]. The mechanical faults in motor may be bearing fault and rotor faults. The electrical faults in motor may be stator winding fault (SWF), phase unbalance, broken rotor bar (BRB), etc. The faults in the rotor systems may be the misaligned rotor (MR), unbalanced rotor (UR) and bent rotor (BR) [3]. The bearing fault (BF) may be outer race, inner race, ball element and cage faults [5]. Various traditional methods are used to detect the faults in motor–rotor–bearing systems. In recent years, researchers have moved their focus toward

---

P. Gangsar (✉) · Z. Ali · M. Chouksey  
Shri G. S. Institute of Technology and Science, Indore, Madhya Pradesh, India

A. Parey  
Indian Institute of Technology Indore, Indore, Madhya Pradesh, India

artificial Intelligence technique like fuzzy logic, ANN, SVM, DNN, etc., in condition monitoring as the AI has so many advantages over traditional methods [6–8]. These AI-based diagnostics systems have been successfully developing for various machines like motor, bearings, gears, centrifugal pumps, etc., [5, 8–10]. The fuzzy logic-based classifier has been developed and successfully used for detecting faults in individual machines like bearing, motors, etc. [11, 12]. Various researchers have been working to develop a robust diagnostics based on various ANN [13]. In the last two decades, the application of SVM has been gaining recognition in machine condition monitoring and diagnosis field [14–16]. Various authors have compared the performance of SVM with other AI techniques like ANN, fuzzy logic and neuro-fuzzy methods, and found that SVM-based diagnostics show better performance in terms of accuracy and computational time even with less no. of samples [15]. The SVM and ANN have been also explored for limited data cases and effective results are found [16, 17]. Moreover, many people have been exploring DNN in this field and found better results [9, 18].

After doing extensive literature review, it is found that various AI-based techniques have been developing for fault monitoring of machine. Most of the researchers have used individual faults in machines; however, very few researchers have considered the study of multiple or combined faults. In addition, hardly any researcher has worked on the multiple faults in a combined systems like an electromechanical system. The development of an intelligent and robust diagnostics system for detecting multiple faults in a combined system is the need of hour. In this work, the combined fault study has been done in an electromechanical system comprised of motor–rotor–bearing system using a MSVM. Ten combined fault situations comprised of electrical and mechanical faults are studied here. In order to detect these faults, vibration as well as current signals are utilized. The experimental data are generated in the laboratory using machine fault simulator (MFS). This experimental data are used to develop an intelligent and robust diagnostics based on MSVM. The results from the study are discussed in the result and discussion section.

## 2 SVM Methodology

The SVM is developed by Vapnik in 1994 [19]. The SVM has been used in various fields like handwriting recognition, speech recognition, etc. From last two decades, this has been used by many researchers in the field of condition monitoring and fault diagnosis for pattern recognition and regression analysis. The basic SVM is used to solve a binary class problem [19]. The binary class SVM classifies the data of two classes, for example, positive (+) class and negative (–) class (as shown in Fig. 1). In order to classify these classes, SVM constructs a hyperplane or set of it. The aim of SVM is to select the optimal hyperplane by maximizing the margin between nearest data points of two classes. The nearest data points of two classes are called support vectors. After separating the two classes as wide as possible, new data or example is

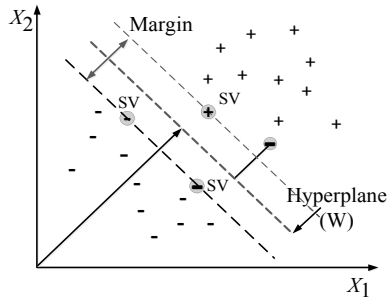


Fig. 1 Binary class SVM

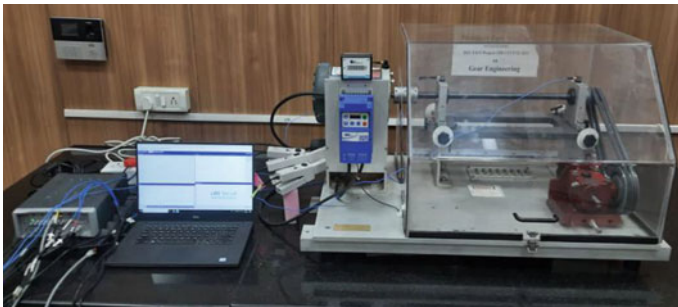


Fig. 2 Experimental setup for electromechanical system fault diagnosis

mapped into the same space. Now SVM tries to classify the new data in the respective class, i.e., either positive class or negative class [19].

In order to classify more than two class data, multiclass support vector machine (MSVM) methods have been developed. These MSVM methods are one-against-one method, one-against-all method and direct-acyclic graph SVM method [20]. In a study, Hsu and Lin [20] have done the study to check to performance of these methods on real data and found that the one-against-one method is more effective. In the present work, one-against-one method is used to develop MSVM for diagnosing multiple fault classes. In order to solve  $N$  class problem, one-against-one multiclass SVM constructs  $N(N - 1)/2$  number of binary class SVMs. Each binary class SVM considers one pair of classes. The multiclass SVM problem solves by combining the output of all binary class SVMs. The voting approach is used to select the class with maximum votes.

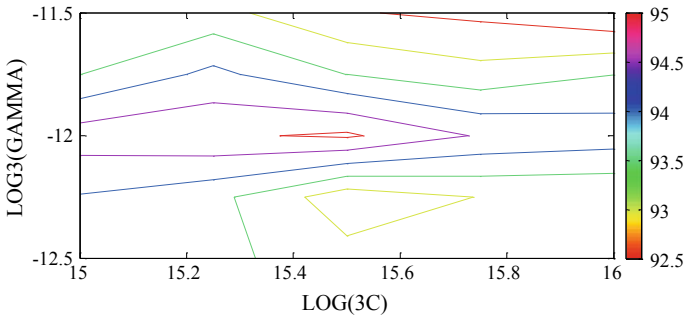
### 3 Experimental Setup and Data Generation

The experiment is performed on an experimental setup as shown in Fig. 2. The experimental setup consists of a machine fault simulator (MFS). In MFS, a three-phase induction motor (IM) is coupled with an external rotor using a flexible coupling. This rotor is installed with a disk at the center of the rotor. This disk is used to create an unbalance in the rotor. The rotor is installed on two external bearings on the end. The rotor is coupled with pulley belt drive at the other end which is further attached to the gear box. This gear box is attached to a magnetic clutch or brake. This brake is used for loading the IM. A variable frequency drive (VFD) system in MFS is used to change the motor speed. In this work, ten combined fault situations are considered such as healthy motor with healthy external rotor (HM-HR), healthy motor with external bearing faults (HM-BF), healthy motor with external unbalanced rotor (HM-UR), bearing fault in motor with healthy external rotor (MBF-HR), bearing fault in motor with external bearing fault (MBF-BF), bearing fault in motor with external unbalanced rotor (MBF-UR), stator winding fault with healthy external rotor (SWF-HR), stator winding fault with external unbalanced rotor (SWF-UR), stator winding fault with external bearing fault (SWF-BF) and bearing fault in motor with external bearing fault and unbalanced rotor (MBF-BF-UR). These fault situations are simulated in the MFS one by one by doing the suitable arrangement.

In order to study these combined faults, vibration and current signals are acquired here. The vibrations in triaxial directions ( $x$ -axial,  $y$ -transverse,  $z$ -transverse) are acquired from three different locations, i.e., one from the top of the motor, one from the left bearing of the rotor and one from right bearing of the rotor (as shown in Fig. 2). The current is acquired in all the three phases by AC current probes (as shown in Fig. 2). The acquisition of vibration and current signals was done with a sampling rate of 20,480 Hz with 20,480 number of samples. In total, 327,680 data points were acquired in 16 s. These total data points are collected into 80 datasets with each dataset containing 4096 sample points. The signals were acquired from all ten fault situations tested under two loads (no load and full load) and four speeds (10, 20, 30 and 40 Hz). The total data were stored in the system for post-signal processing. After generating the datasets, the data are further processed for extracting critical features. In this study, three features (standard deviation, skewness and kurtosis) are extracted using the 80 datasets of raw time domain vibration and current signals [8, 10, 16]. These features are collected for all the fault conditions and the different operating speeds and loads of the motor. The 80 feature datasets are further used in building MSVM model for diagnosing purpose.

### 4 Result and Discussion

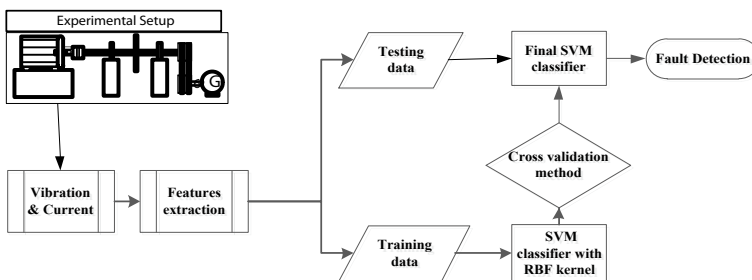
The suitable features obtained from raw signals are now divided into training and testing datasets. The training and testing data are divided in 80% and 20% of whole



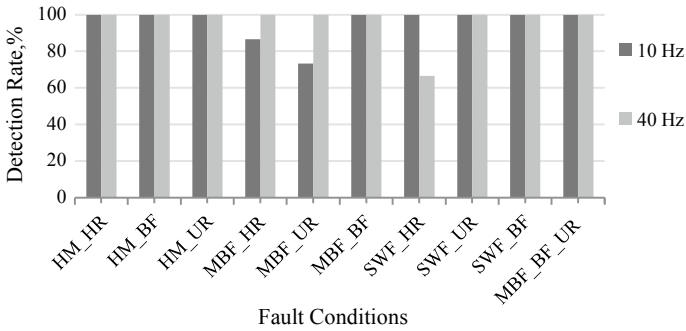
**Fig. 3** Training accuracy plot by cross-validation method at 10 Hz speed

datasets, respectively. Now the MSVM model is developed and trained with the 80% datasets. In order to develop best MSVM model, radial basis kernel (RBF) is used here which one of the best kernels especially for nonlinear data. Finally, the optimal model of MSVM is built by selecting optimal parameters, i.e., MSVM penalty parameter ‘C’ and RBF kernel parameter ‘Gamma’ by using ten cross-fold validation method. Figure 3 shows the training accuracy plot for different values of the two parameters. The best MSVM model selected from here is used for final testing on unseen datasets, i.e., 20% testing data (as shown in Fig. 4). The results obtained from the testing are added in Fig. 5.

Figure 5 shows the performance of MSVM in the form of detection rate for ten fault situations. Here, two speeds at no load condition are considered for the fault diagnosis, i.e., 10 and 40 Hz. From Fig. 5, it can be seen that at 40 Hz speed all fault situations except SWF-HR are classified with 100% detection rate, while at 10 Hz speed all fault situations except MBF-HR and MBF-UR are classified with 100% detection rate. The overall detection rate at 40 Hz and 10 Hz is found to be 99.7% and 95%, respectively. All the fault situations are classified successfully based on selected features (standard deviation, skewness and kurtosis) of time domain vibration and current signals. It can say that all the fault situations generate very distinct features in vibration and current signals, and therefore, these features of ten faults situations



**Fig. 4** Flow diagram of proposed methodology



**Fig. 5** Detection rate at 10 and 40 Hz speeds

are easily classified by MSVM. From here, it can say that the developed MSVM diagnostics is able to detect all the combined fault situations very well. However, the detection rate is very effective at higher speeds, i.e., at 40 Hz.

In order to check the misclassification of the data for different fault situations, confusion matrices have been obtained. The confusion matrices are added in Tables 1 and 2 for 10 Hz and 40 Hz speeds, respectively. Table 1 shows that the 100% data are successfully classified for all the fault classes except MBF-HR and MBF-UR classes. It is noted that the 13.33% data of MBF-HR are misclassified in MBF-UR class and 26.67% data of MBF-UR are classified in MBF-HR class. Table 2 shows that the 100% data are successfully classified for all the fault classes except SWF-HR class. It is noted that the 33.33% data of SWF-HR are misclassified in the SWF-UR class. It is noted that at both the speeds, some data of UR and HR are misclassified in each other. The reason may be that the unbalance created in the external rotor is very small, so it may generate similar features as HR. However, results may be checked after creating some large unbalance in the rotor.

## 5 Conclusions

An intelligent and robust intelligent fault diagnostic system is developed based on MSVM for detecting combined fault situations in an electromechanical system. For this, vibration and current signals are utilized for detecting different combined faults (electrical and mechanical) in motor-rotor-bearing system. Total ten combined or multiple fault situations are considered here for diagnosis. Results show that the proposed MSVM-based diagnostics is found to be very effective in diagnosing combination of electrical and mechanical faults of the electromechanical system. Moreover, the proposed methodology is successfully able to diagnose the multiple faults at different operating speeds. This work obviously is a good step in developing







an automated diagnostics for diagnosing faults at a very early stage for an electromechanical system where individual or combined fault situations may be occurred in one or two machines, simultaneously.

**Acknowledgements** Authors would like to thank NPIU/AICTE for providing financial support through Collaborative Research Scheme (CRS). We are also thankful to IIT Indore for providing experimental facilities for this collaborative work.

## References

1. Henao, H., Capolino, G.A., Fernandez-Cabanas, M., Filippetti, F., Bruzzese, C., Strangas, E., Hedayati-Kia, S.: Trends in fault diagnosis for electrical machines: a review of diagnostic techniques. *Ind. Electron. Mag. IEEE* **8**(2), 31–42 (2014)
2. Saxena, A., Chouksey, M., Parey, A.: Measurement of FRFs of coupled geared rotor system and the development of an accurate finite element model. *Mech. Mach. Theory* **123**, 66–75 (2018)
3. Tiwari, R.: *Rotor Systems: Analysis and Identification*. CRC Press, Boca Raton, FL (2017)
4. Saxena, A., Parey, A., Chouksey, M.: Study of modal characteristics of a geared rotor system. *Procedia Technol.* **23**, 225–231 (2016)
5. Gangsar, P., Tiwari, R.: Multiclass fault taxonomy in rolling bearings at interpolated and extrapolated speeds based on time domain vibration data by SVM algorithms. *J. Fail. Anal. Prev.* **14**(6), 826–837 (2014)
6. Gangsar, P., Tiwari, R.: Signal based condition monitoring techniques for fault detection and diagnosis of induction motors: a state-of-the-art review. *Mech. Syst. Sig. Process.* **144**, 106908 (2020)
7. Liu, R., Yang, B., Zio, E., Chen, X.: Artificial intelligence for fault diagnosis of rotating machinery: a review. *Mech. Syst. Sig. Process.* **108**, 33–47 (2018)
8. Gangsar, P., Tiwari, R.: Taxonomy of induction-motor mechanical-fault based on time-domain vibration signals by multiclass SVM classifiers. *Intell. Ind. Syst.* **2**(3), 269–281 (2016)
9. Tiwari, R., Bordoloi, D.J., Dewangan, A.: Blockage and cavitation detection in centrifugal pumps from dynamic pressure signal using deep learning algorithm. *Measurement*, 108676 (2020)
10. Bordoloi, D.J., Tiwari, R.: Support vector machine based optimization of multi-fault classification of gears with evolutionary algorithms from time–frequency vibration data. *Measurement* **55**, 1–14 (2014)
11. Tran, V.T., Yang, B.S., Oh, M.S., Tan, A.C.C.: Fault diagnosis of induction motor based on decision trees and adaptive neuro-fuzzy inference. *Expert Syst. Appl.* **36**(2), 1840–1849 (2009)
12. Yang, B.S., Oh, M.S., Tan, A.C.C.: Fault diagnosis of induction motor based on decision trees and adaptive neuro-fuzzy inference. *Expert Syst. Appl.* **36**(2), 1840–1849 (2009)
13. Ye, Z., Wu, B., Sadeghian, A.R.: Induction motor mechanical fault online diagnosis with the application of artificial neural network. In: 16th Annual IEEE Applied Power Electronics Conference and Exposition (APEC 2001), Anaheim, CA, March 4–8, pp. 1015–1021 (2001)
14. Zhang, X., Chen, W., Wang, B., Chen, X.: Intelligent fault diagnosis of rotating machinery using support vector machine with ant colony algorithm for synchronous feature selection and parameter optimization. *Neurocomputing* **167**, 260–279 (2015)
15. Kandukuri, S.T., Senanyaka, J.S.L., Robbersmyr, K.G.: A two-stage fault detection and classification scheme for electrical pitch drives in offshore wind farms using support vector machine. *IEEE Trans. Ind. Appl.* **55**(5), 5109–5118 (2019)
16. Zhao, Y.P., Wang, J.J., Li, X.Y., Peng, G.J., Yang, Z.: Extended least squares support vector machine with applications to fault diagnosis of aircraft engine. *ISA Trans.* **97**, 189–201 (2020)

17. Chouhan, A., Gangsar, P., Porwal, R., Mechefske, C.K.: Artificial neural network based fault diagnostics for three phase induction motors under similar operating conditions. *Vibroeng. PROEDIA* **30**, 55–60 (2020)
18. Chen, S., Meng, Y., Tang, H., Tian, Y., He, N., Shao, C.: Robust deep learning-based diagnosis of mixed faults in rotating machinery. *IEEE/ASME Trans. Mechatron.* **25**(5), 2167–2176 (2020)
19. Vapnik, V., Levin, E., Le, C.Y.: Measuring the VC-dimension of a learning machine. *Neural Comput.* **6**(5), 851–876 (1994)
20. Hsu, C.W., Lin, C.J.: A comparison of methods for multiclass support vector machines. *IEEE Trans. Neural Netw.* **13**(2), 415–425 (2002)

# Analysis of Cache Memory Architecture Design Using Low-Power Reduction Techniques for Microprocessors



Reeya Agrawal

## 1 Introduction

Wireless sensor network production has revolutionized our lifestyles. Sensor networks may be used for different purposes, such as military surveillance, monitoring of the environment, medical diagnosis, etc. A wireless sensor network used for medical diagnosis is defined as the body area network (Istepanian et al. 2004; Gyselinckx et al. 2005). To provide real-time input, body region networks have to do continuous health monitoring. Continuous monitoring of physiological parameters is enabled by body area networks. Compared to the physiological parameters obtained from short-term monitoring, for example, hospital stays, this continuous monitoring for long periods in the natural environment produces better results (Park et al. 2003). Miniature wireless sensor nodes with an extended operating life are needed to further expand the capabilities of the body area network. For the realization of ubiquitous sensing, the sensor nodes must have a very small form factor (Gyselinckx et al. 2005) without interfering with the object being monitored. This miniaturization results in a decrease in the energy capacity of the sensor since the battery size used to store the energy is limited. The intrusive procedure necessity (Malan et al. 2004) complicates the replacement of the embedded medical wireless sensor nodes by the battery [1, 2].

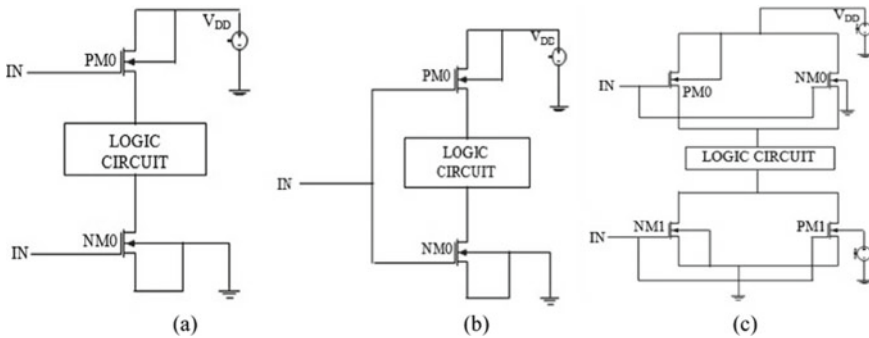
### 1.1 Power Reduction Techniques

Power reduction techniques are applied over circuits to reduce the power consumption of circuits with no effect on performance, speed, and other parameters.

---

R. Agrawal (✉)

Department of Electronics and Communication, GLA University, Mathura, India



**Fig. 1** **a** Sleep transistor technique; **b** forced stack technique; **c** dual sleep technique

### 1.1.1 Sleep Transistor Technique

The state-destructive technique disrupts both  $P_{MOS}$  and  $N_{MOS}$  transistors from sleep transistors to supply voltage or ground. These methods are called  $V_{DD}$  and gated-GND. These are technological varieties. When the logic circuits are in standby mode, the sleep transistor is disabled. By uninflecting sleep transistor operation from the logical networks, the technique of sleep semiconductor significantly reduces sleep power as shown in Fig. 1a [3].

### 1.1.2 Forced Stack Technique

Figure 1b demonstrates a forced stack technique. This second technique decreases the power by stacking transistors. When two or more transistors are uniformly switched OFF, the effect of stacking the semiconductor device reduces the sub-threshold leakage current [4].

### 1.1.3 Dual Sleep Technique

Both types of transistors are used in this technique: two PMOS ( $PM0$  and  $PM1$ ) and two NMOS ( $NM0$  and  $NM1$ ). Both PMOS and NMOS transistors are used in the header and footer. One transistor is ON in active mode, and another transistor is switched ON in OFF state mode. PMOS and NMOS are both used in standby mode to reduce power, as shown in Fig. 1c [5].

These circuits became known as high-density circuits because of their numerous transistors used and also because of the high leakage rate concerning technological developments. The input power supply was then reduced by attempting to reduce the energy consumption rate [6–8]. As compared with SRAM memories, they have higher percentages of portable devices with static memory because more power is

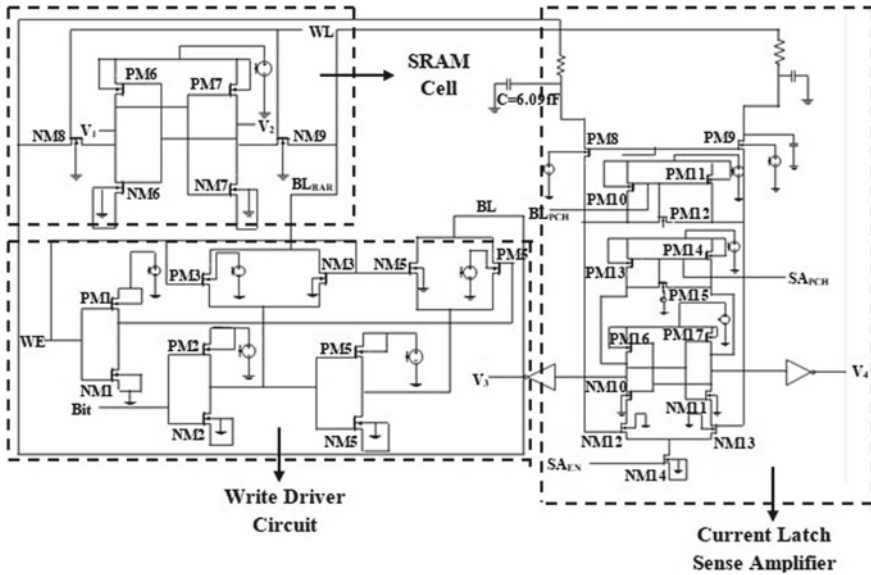


Fig. 2 Schematic of single-bit cache memory architecture

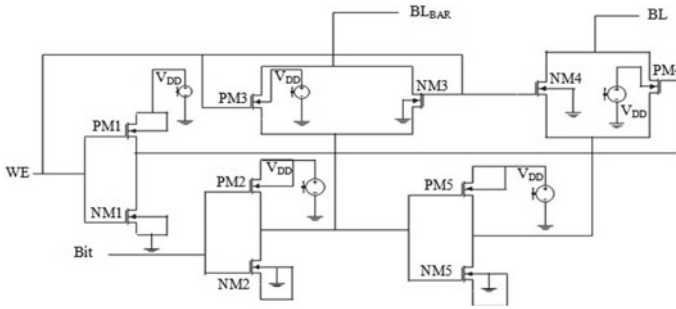
spent on data stability in DRAM memory. In both static and dynamic memories, the access time is approximately the same [9–11].

## 2 Single-Bit Memory Architecture

WDC, SRAMC, and CLSA as shown in Fig. 2 [12, 13] are the single-bit cache memory architectural blocks. The description is divided into three different parts: (a) the WDC with two input pins (word enable (WE) and Bit) and two output pins (BL and BL<sub>BAR</sub>), (b) the SRAMC, which is attached to the WDC via bit lines (i.e., BL and BL<sub>BAR</sub>), and an input pin [word line (WL)] and two output pins (V<sub>1</sub> and V<sub>2</sub>) and connected through bit lines having capacitance and resistance as a connector between them, (c) CLSA which has 4 input pins (Y<sub>sel</sub>, BL<sub>PCH</sub>, SA<sub>PCH</sub>, and SA<sub>EN</sub>) and two output pins (V<sub>3</sub> and V<sub>4</sub>).

## 3 Write Driver Circuit

Figure 3 shows the write driver schematic developed in this work. The bit line is discharged from its high pre-load level to below the SRAMC writing margin by the WDC. The voltage required to enter the desired value in the bit line is determined



**Fig. 3** Write driver circuit schematic

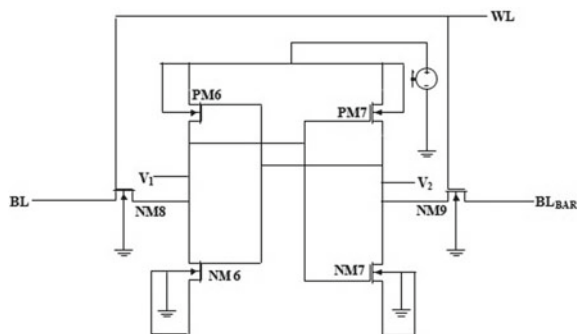
by the WDC. When “WE = 1” (write enable pulled high), data from the data input pin are entered in bit lines and transferred to the corresponding memory cell through the access transistors.

To obtain the glitch-free bit lines, the buffer circuit has been positioned before the output of the WDC. It has to enter a certain value in the bit cell up to the WDC. The circuit has the purpose of charging and discharging the bit lines in the memory cell to the desired bit being written [14].

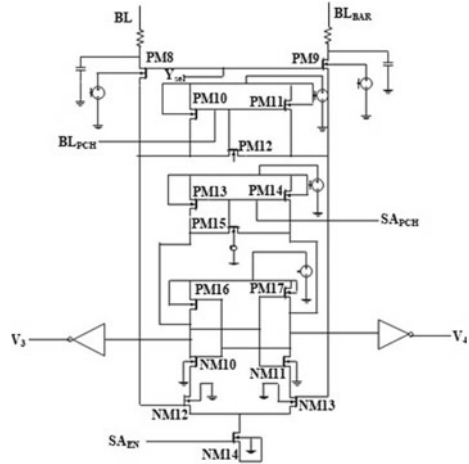
### 3.1 Conventional SRAM

The 6T SRAMC circuit diagram is shown in Fig. 4. SRAMC is called a static ram cell because the data could be held for a long time until the power is being provided forever. Six transistors are used in SRAMC; PM6, PM7, NM6, and NM7 are composed of the two cross-coupled CMOS inverters plus two NMOS transistors (NM8 and NM9) known as access transistors. It is known as the 6T cell. Each bit is a transistor-compatible SRAMC, which forms two cross-coupled inverters. This cell has two stable states either 0 or 1 [15, 16].

**Fig. 4** SRAM cell schematic



**Fig. 5** Current latch sense amplifier schematic



### 3.2 Current Latch Sense Amplifier

The sense amplifier is a circuit of great importance in cache memory architecture. One of the bit line releases during reading operation while the other bit line remains at supply voltage. Due to the capacity of the large bit line, the slow discharge is small and the bit cells access the transistor. To accomplish this, a minor difference between the values of the bit line voltages [17, 18] is amplified by the SA at digital levels. Figure 5 indicates the current latch sense amplifier schematic.

The circuit operation is as follows [19, 20]. On bit lines, the differential voltage is transferred to SA<sub>3</sub> and SA<sub>4</sub> CLSA inputs. If both SA<sub>1</sub> and SA<sub>2</sub> start discharge at high outputs SA<sub>EN</sub> is pulled high. These results in a higher power by NM12 compared to NM13 because of its higher V<sub>gs</sub>. This allows the output V<sub>3</sub> to be discharged faster than V<sub>4</sub>.

## 4 Analysis of Result

Figure 6 describes the output waveform of WDC, for cases arise: (a) when Bit = 0 V and WE = 0 V BL = V<sub>DD</sub> and BL<sub>BAR</sub> = V<sub>DD</sub>, (b) Bit = 0 V WE = V<sub>DD</sub> so, BL = 0 V and BL<sub>BAR</sub> = V<sub>DD</sub>/2, (c) Bit = V<sub>DD</sub> WE = 0 V so, BL = 0 V and BL<sub>BAR</sub> = V<sub>DD</sub>/2 and (d) Bit = V<sub>DD</sub> WE = V<sub>DD</sub> so, BL = V<sub>DD</sub> and BL<sub>BAR</sub> = 0 V.

Figure 7 describes the both write operation and hold operation of the SRAM cell. There is a pull-up network (PM6 and PM7), pull-down network (NM6 and NM7), and access transistor (NM8 and NM9) which allows data to store and sense amplifier to read the data. Figure 8 describes the read operation of CLSA when both SA<sub>EN</sub> and

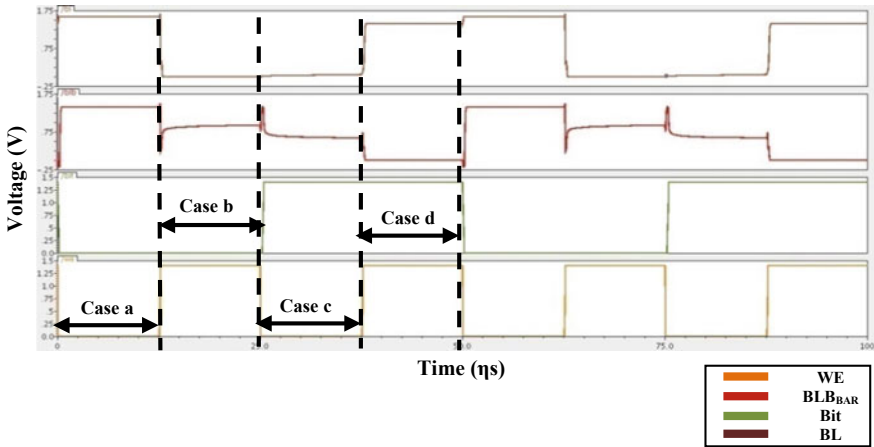


Fig. 6 Output waveform of WDC

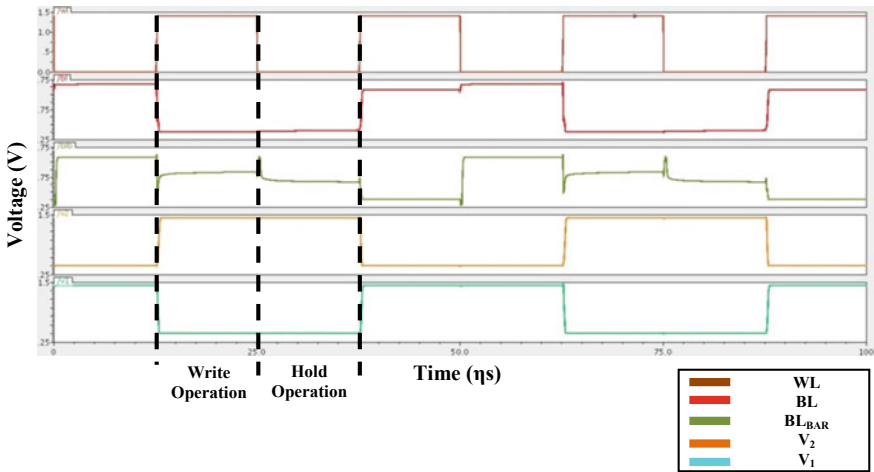


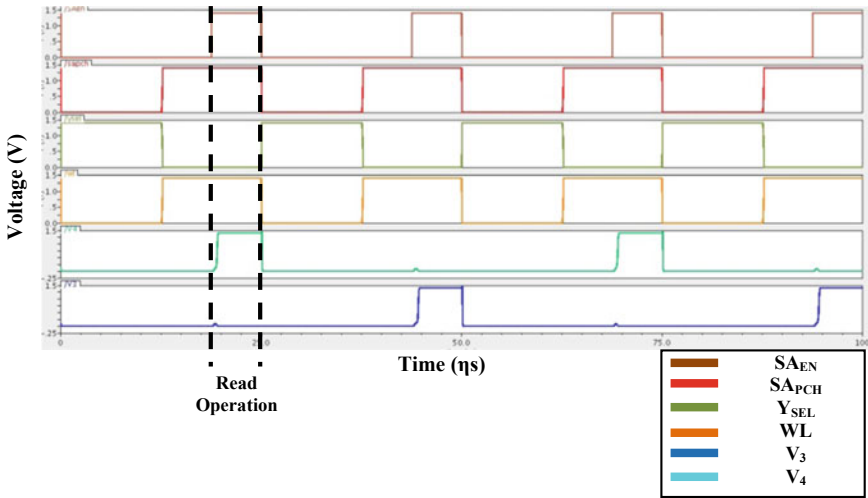
Fig. 7 Output waveform of SRAM cell

WL are pulled high, during that time only the sense amplifier senses the data from the SRAM cell at bit lines and gives output at  $V_3$  and  $V_4$ .

Table 1 describes that as increasing in value of resistance power consumption decreases as because resistance is a path stopper for current in a circuit and no effect on the area, performance, and speed whereas Table 2: describes the power reduction techniques applied over CLSA.

Table 3: describes the power consumption of single-bit cache memory architecture on applying power reduction techniques over SRAM cell and CLSA consume less power 111.58  $\mu$ W up to 56%. All the table's results depicted that single-bit





**Fig. 8** Output waveform of CLSA

**Table 1** Different parameter of single-bit cache memory architecture

S. No.	Parameters	Power consumption ( $\mu W$ )	No. of transistors	Sensing delay ( $\eta s$ )
1	$R = 42.3 \Omega$	73.92	35	18.75
2	$R = 42.3 K\Omega$	26.78	35	18.75

**Table 2** Single-bit cache memory architecture analysis of different parameters with power reduction techniques applied over CLSA

S. No.	Techniques	Power consumption ( $\mu W$ )	Sensing delay ( $\eta s$ )	No. of transistors
1	Sleep transistor technique	25.89	18.81	37
2	Forced stack technique	13.4	19.37	37
3	Dual sleep technique	25.9	18.68	39

**Table 3** Single-bit cache memory architecture analysis of different parameters with power reduction techniques applied over SRAM cell and CLSA

S. No.	Techniques	Power consumption ( $\mu W$ )	Sensing delay ( $\eta s$ )	No. of transistor
1	Sleep transistor technique	24.62	18.88	39
2	Forced stack technique	11.58	19.59	39
3	Dual sleep technique	24.64	19.12	43

cache memory architecture with forced stack technique over SRAM cell and CLSA consume the lowest power  $11.58 \mu\text{W}$  with an increase in the number of the transistor from 35 to 39. There is always a trade-off between power consumption and area.

## 5 Conclusion

In the proposed work, single-bit cache memory architecture has been implemented and it is comprised of WDC, SRAM cell, and a current latch sense amplifier. Apart from its different parameters of single-bit cache memory architecture has been analyzed at different values of resistance ( $R$ ). Furthermore, power reduction techniques such as sleep transistor technique, forced stack technique, and dual seep technique are applied over SRAM cell and CLSA. Results depicted that on the increasing value of  $R$  power consumption reduce at  $R = 42.3 \text{ k}\Omega$  consume  $26.78 \mu\text{W}$  power and a single-bit cache memory architecture having SRAM cell and CLSA with forced stack technique consume  $11.58 \mu\text{W}$ . In future scope, this work can be done in form of an array.

## References

1. He, Y., Zhang, J., Wu, X., Si, X., Zhen, S., Zhang, B.: A half-select disturb-free 11T SRAM cell with built-in write/read-assist scheme for ultralow-voltage operations. *IEEE Trans. Very Large Scale Integr. (VLSI) Syst.* **27**(10), 2344–2353 (2019). <https://doi.org/10.1109/TVLSI.2019.2919104>
2. Fragasse, R., et al.: Analysis of SRAM enhancements through sense amplifier capacitive offset correction and replica self-timing. *IEEE Trans. Circ. Syst. I Regul. Pap.* **66**(6), 2037–2050 (2019). <https://doi.org/10.1109/TCSI.2019.2902102>
3. Tripti, T., Chauhan, D.S., Singh, S.K., Singh, S.V.: Implementation of low-power 6T SRAM cell using MTCMOS technique. In: *Advances in Computer and Computational Sciences*. Springer, Singapore (2017)
4. Geetha Priya, M., Baskaran, K., Krishnaveni, D.: Leakage power reduction techniques in deep submicron technologies for VLSI applications. In: *International Conference on Communication Technology and System Design*. Elsevier (2011)
5. Sridhara, K., Biradar, G.S., Yanamshetti, R.: Subthreshold leakage power reduction in VLSI circuits: a survey. In: *2016 International Conference on Communication and Signal Processing (ICCSP)*, pp. 1120–1124 (2016)
6. Gupta, S., Gupta, K., Calhoun, B.H., Pandey, N.: Low-power near-threshold 10T SRAM bit cells with enhanced data-independent read port leakage for array augmentation in 32-nm CMOS. *IEEE Trans. Circ. Syst. I Regul. Pap.* **66**(3), 978–988 (2019). <https://doi.org/10.1109/TCSI.2018.2876785>
7. Dounavi, H., Sfikas, Y., Tsiatouhas, Y.: Periodic aging monitoring in SRAM sense amplifiers. In: *2018 IEEE 24th International Symposium on On-line Testing and Robust System Design (IOLTS)*, Platja d’Aro, pp. 12–16 (2018). <https://doi.org/10.1109/IOLTS.2018.8474169>
8. Ahmad, S., Iqbal, B., Alam, N., Hasan, M.: Low leakage fully half-select-free robust SRAM cells with BTI reliability analysis. *IEEE Trans. Device Mater. Reliab.* **18**(3), 337–349 (2018). <https://doi.org/10.1109/TDMR.2018.2839612>

9. Reddy, B.N.K., Sarangam, K., Veeraiah, T., Cheruku, R.: SRAM cell with better read and write stability with minimum area. In: TENCON 2019—2019 IEEE Region 10 Conference (TENCON), Kochi, India, pp. 2164–2167. <https://doi.org/10.1109/TENCON.2019.8929593>
10. Surkar, A., Agarwal, V.: Delay and power analysis of current and voltage sense amplifiers for SRAM at 180 nm technology. In: 2019 3rd International Conference on Electronics, Communication, and Aerospace Technology (ICECA), Coimbatore, India, pp. 1371–1376 (2019). <https://doi.org/10.1109/ICECA.2019.8822122>
11. Gomes Iuri, A.C., Cristina, M., Butzen Paulo, F.: Design of 16 nm SRAM architecture. In: South Symposium on Microelectronics (2012)
12. Kaushik, C.S.H., Vanjarlapati, R.R., Krishna, V.M., Gautam, T., Elamaram, V.: VLSI design of low power SRAM architectures for FPGAs. In: 2014 International Conference on Green Computing Communication and Electrical Engineering (ICGCCCE), pp. 1–4 (2014)
13. Choudhary, R., Padhy, S., Rout, N.K.: Enhanced robust architecture of single bit SRAM cell using drowsy cache and super cut-off CMOS concept. *Int. J. Ind. Electron. Electr. Eng.* **3**, 63–68 (2011)
14. Gajjar, J.P., Zala, A.S., Aggarwal, S.K.: Design and analysis of 32 bit SRAM architecture in 90 nm CMOS technology. *Int. Res. J. Eng. Technol. (IRJET)* **03**(04), 2729–2733 (2016)
15. Agrawal, R., Tomar, V.K.: Analysis of cache (SRAM) memory for Core I<sup>TM</sup> 7 processor. In: 9th International Conference on Computing, Communication and Networking Technologies (ICCCNT), p. 402 (2018)
16. Vanama, K., Gunnuthula, R., Prasad, G.: Design of low power stable SRAM cell. In: 2014 International Conference on Circuit Power and Computing Technologies (ICCPCT), pp. 1263–1267 (2014)
17. Chandankhede, R.D., Acharya, D.P., Patra, P.K.: Design of high-speed sense amplifier for SRAM. In: IEEE International Conference on Advanced Communication Control and Computing Technologies, pp. 340–343
18. Wei, Z., Peng, X., Wang, J., Yin, H., Gong, N.: Novel CMOS SRAM Voltage Latched Sense Amplifiers Design Based on 65 nm Technology, pp. 3281–3282
19. Mohammad, B., Dadabhoy, P., Lin, K., Bassett, P.: Comparative study of current mode and voltage mode sense amplifier used for 28 nm SRAM. In: 24th International Conference on Microelectronic (2013)
20. Sinha, M., Hsu, S., Alvandpour, A., Burleson, W., Krishnamurthy, R., Borhr, S.: High-performance and low-voltage sense-amplifier techniques for sub-90 nm SRAM. In: IEEE International [Systems-on-Chip] SOC Conference (2003)

# Low-Power SRAM Memory Architecture for IoT Systems



Reeya Agrawal

## 1 Introduction

As shown in Fig. 1, a typical internet of Things (IoT) sensor includes four main devices: a sensor, a microcontroller (MCU), a wireless computer (Bluetooth, WiFi, LoRa), and a static random access memory cell (SRAMC). These devices communicate with each other over a serial bus, such as the Serial Peripheral Interface (SPI) or Inter IC Communication (I2C) protocol, since sensor nodes operate at low data rates and low power. To negotiate all transactions between devices, the MCU serves as the master controller for the IoT node. The wireless system must send sensor data to the nearest gateway and also receive control instructions from the gateway. The sensor tests environmental parameters (temperature/humidity/etc.) and transmits the data digitally through the serial communication bus of the SPI/I2C. When a gateway is not available for communication, the SRAM is used to store local data. The innovation of this project is to generate and monitor all the signals needed for the SRAM without using internal clocks, instead of deriving all control signals from the SPI signals themselves, making it a simple and scalable circuit that can be made with slower access time to consume very little power [1, 2].

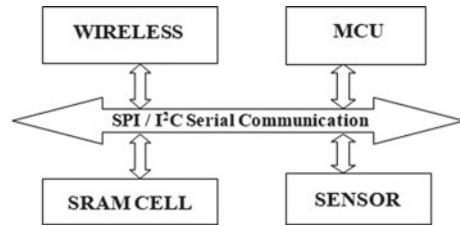
Embedded memories are popular when implementing the complex systems currently known as a system on chips (SOCs). The international technology roadmap for semiconductors (ITRS) predicts that 90% of the SOCs area will consist of memory, specifically static random access memories (SRAMCs). Memory is a key part of system design based on computers and microprocessors. This is used as a binary number (0 or 1) for storing data or information. Data used in the program are saved in the memory as well as for the execution of the program. Therefore, the storage of data in a digital system is required both temporarily and permanently [3–5].

---

R. Agrawal (✉)

Department of Electronics and Communication, GLA University, Mathura, India

**Fig. 1** Block diagram of typical IoT sensor node



Today, there have been a lot more attention than ever before to the growing use of mobile electronic equipment, such as wireless communication systems, mobile multimedia devices, and/or sensitive medical equipment with low-power circuits. This led to so many attempts to build low power circuits whereby manufacturers compress more memories and logical circuits into one chip. Scientists feel that there is a new chip industry model in which new combinations of memories and logical circuits are established and which ultimately leads to new processors with different and new memory architectures being produced extensively. As the main block in SOC circuits, static memory has also received great attention [6–8]. These circuits became known as high-density circuits because of their numerous transistors used and also because of the high leakage rate concerning technological developments. The input power supply was then reduced by attempting to reduce the energy consumption rate. However, due to the reduction, data stability will be decreased. As compared with SRAM memories, they have higher percentages of portable devices with static memory because more power is spent on data stability in DRAM memory. In both static and dynamic memories the access time is approximately the same [9–11]. The goal of this paper is to design low power SBVMA in customary gpdk 45 nm technology using Cadence Tool.

## 2 Single-Bit Memory Architecture

WDC, SRAMC, and VMSA as shown in Fig. 2 [12, 13] are the single-bit cache memory architectural blocks. The description is divided into three different parts: (a) the WDC with two input pins (word enable (WE) and Bit) and two output pins (BL and BL<sub>BAR</sub>), (b) the SRAMC, which is attached to the WDC via bit lines (i.e., BL and BL<sub>BAR</sub>), and an input pin [word line (WL)] and two output pins ( $V_1$  and  $V_2$ ) and connected through bit lines having capacitance and resistance as a connector between them, (c) VMSA which has five input pins ( $Y_{sel}$ , BL, BL<sub>BAR</sub>, PCH, and SA<sub>EN</sub>) and two output pins ( $V_3$  and  $V_4$ ).

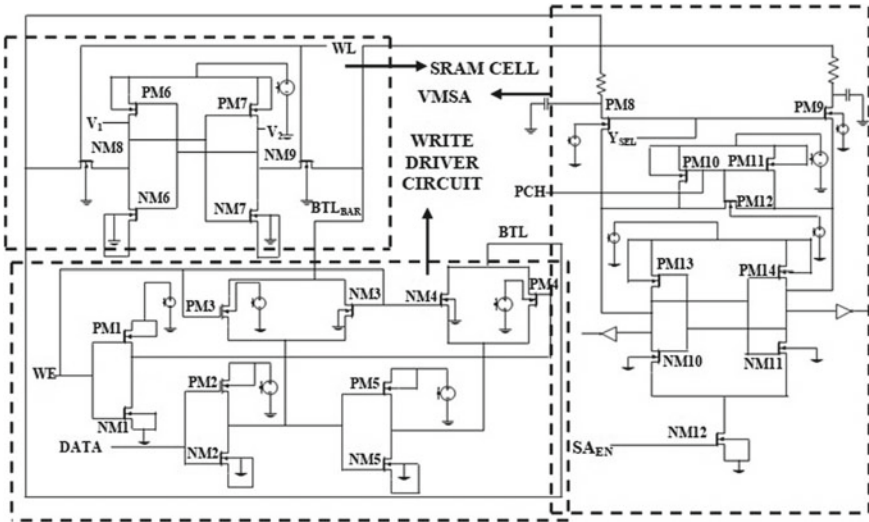


Fig. 2 Schematic of single-bit cache memory architecture having VMSA

### 2.1 Write Driver Circuit

Figure 3 shows the write driver schematic developed in this work. The bit line is discharged from its high pre-load level to below the SRAMC writing margin by the WDC. The voltage required to enter the desired value in the bit line is determined by the WDC. When “WE = 1” (write enable pulled high), data from the data input pin are entered in bit lines and transferred to the corresponding memory cell through the access transistors. To obtain the glitch-free bit lines, the buffer circuit has been positioned before the output of the WDC. It has to enter a certain value in the bit cell

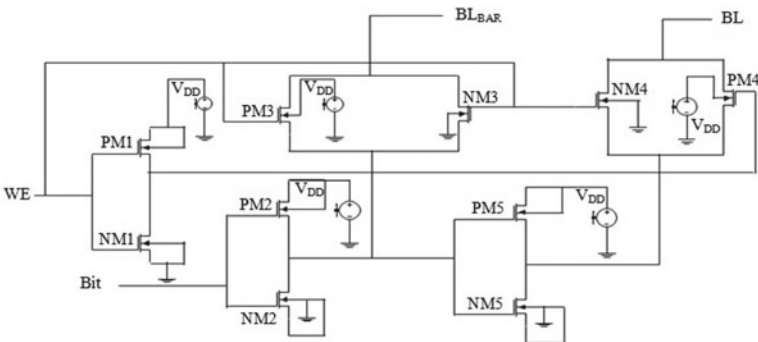
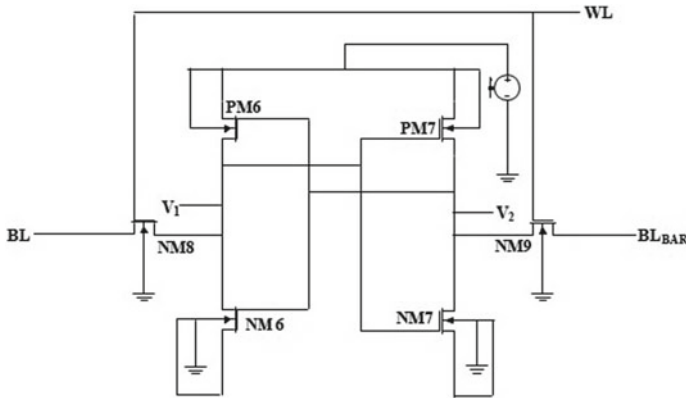


Fig. 3 Write driver circuit schematic



**Fig. 4** SRAM cell schematic

up to the WDC. The circuit has the purpose of charging and discharging the bit lines in the memory cell to the desired bit being written [14].

## 2.2 Conventional SRAM

The 6T SRAMC circuit diagram is shown in Fig. 4. SRAMC is called a static ram cell because the data could be held for a long time until the power is being provided forever. Six transistors are used in SRAMC; PM6, PM7, NM6, and NM7 are composed of the two cross-coupled CMOS inverters plus two  $N_{MOS}$  transistors (NM8 and NM9) known as access transistors. It is known as the 6T cell. Each bit is a transistor-compatible SRAMC, which forms two cross-coupled inverters. This cell has two stable states either 0 or 1 [15, 16].

## 2.3 Voltage-Mode Sense Amplifier

The basic MOS differential voltage sense amplifier circuit contains all elements required for differential sensing. A differential amplifier takes small-signal single-ended output. The effectiveness of a differential amplifier is characterized by its ability to reject common noise amplify the true difference between the signals [17, 18].

Because of the rather slow operational speed provided at considerable power dissipation and inherently high offset, a basic differential voltage amplifier is not applied in memories [19, 20]. The basic differential voltage-mode sense amplifier is shown in Fig. 5, it contains seven  $P_{MOS}$  transistors (PM8 to PM14) and three  $N_{MOS}$

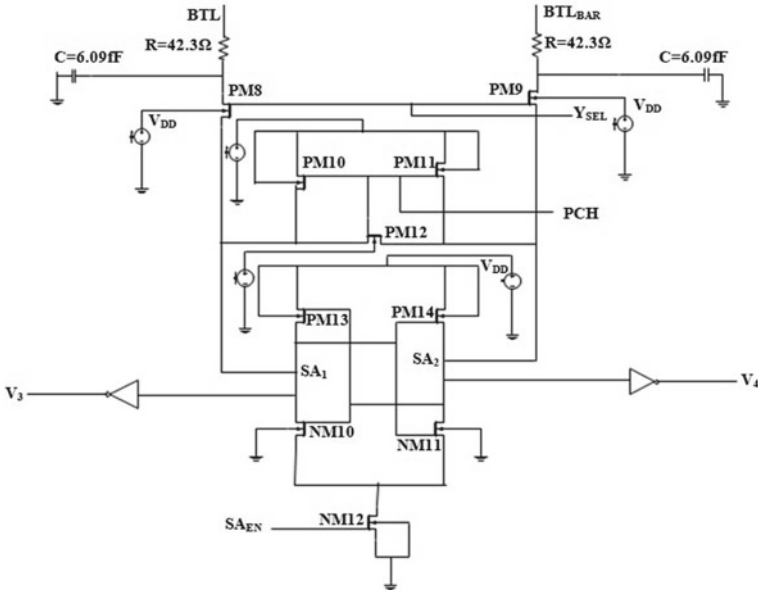


Fig. 5 Schematic of voltage-mode sense amplifiers

transistors (NM10–NM12). This circuit amplifies the small difference at bit lines to full swing at output nodes.

### 3 Analysis of Result

In this section, output of all the circuits has been shown and described.

Figure 6 describe the output waveform of WDC, for cases arise: (a) when Bit = 0 V and WE = 0 V BL = V<sub>DD</sub> and BL<sub>BAR</sub> = V<sub>DD</sub>, (b) Bit = 0 V WE = V<sub>DD</sub> so, BL = 0 V and BL<sub>BAR</sub> = V<sub>DD</sub>/2, (c) Bit = V<sub>DD</sub> WE = 0 V so, BL = 0 V and BL<sub>BAR</sub> = V<sub>DD</sub>/2 and (d) Bit = V<sub>DD</sub> WE = V<sub>DD</sub> so, BL = V<sub>DD</sub> and BL<sub>BAR</sub> = 0 V.

Figure 7 describes the both write operation and hold operation of the SRAM cell. There is a pull of the network (PM6 and PM7), pull-down network (NM6 and NM7), and access transistor (NM8 and NM9) which allows data to store and sense amplifier to read the data.

Figure 8 describes the read operation of VMSA, when both SA<sub>EN</sub> and WL are pulled high, during that time only the sense amplifier senses the data from the SRAM cell at bit lines and gives output at V<sub>3</sub> and V<sub>4</sub>.

Table 1 describes that as increasing in value of resistance power consumption decreases as because resistance is a path stopper for current in a circuit and no effect on the area, performance, and speed.



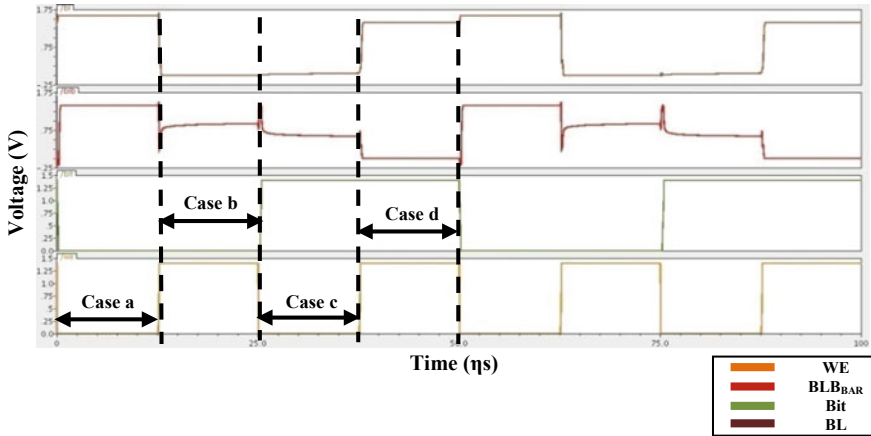


Fig. 6 Output waveform of WDC

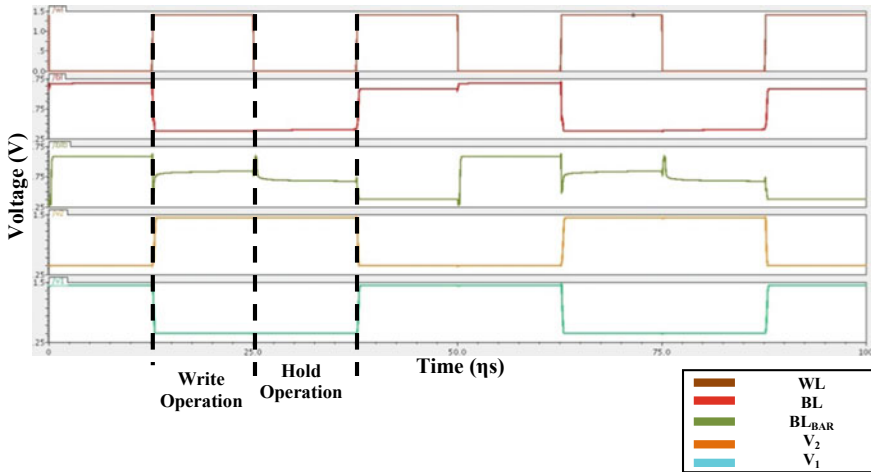


Fig. 7 Output waveform of SRAM Cell

## 4 Conclusion

In this paper, single-bit cache memory with different sense amplifiers such as voltage differential sense amplifier has been implemented, and compared on different values of resistance ( $R$ ) with different parameters such as power consumption, sensing delay, and several transistors. Results depicted that the single-bit cache memory architecture having voltage-mode differential sense amplifier consumes the lowest power ( $11.16 \mu W$ ). In future scope, this work can be done in form of an array.

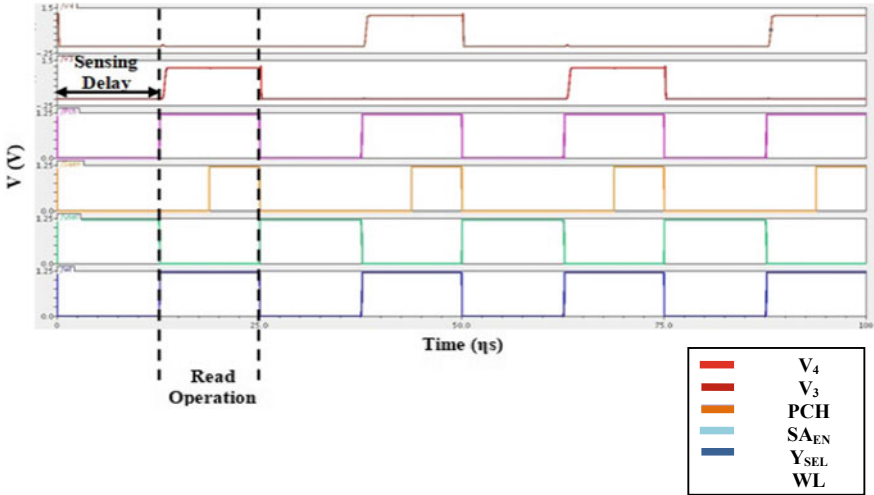


Fig. 8 Output waveform of VMSEA

Table 1 Different parameter of SBSVMA

S. No.	Parameters	Power consumption ( $\mu W$ )	No. of transistors	Sensing delay ( $\eta s$ )
1	$R = 42.3 \Omega$	13.16	30	13.51
2	$R = 42.3 k\Omega$	11.16	30	13.51

## References

1. Eslami, N., Ebrahimi, B., Shakouri, E., et al.: A single-ended low leakage and low voltage 10T SRAM cell with high yield. *Analog Integr. Circ. Sig. Process* (2020)
2. Bazzi, H., Harb, A., Aziza, H., et al.: RRAM-based non-volatile SRAM cell architectures for ultra-low-power applications. *Analog Integr. Circ. Sig. Process* (2020)
3. Pal, S., Bose, S., Islam, A.: Design of SRAM cell for low power portable healthcare applications. *Microsyst. Technol.* (2020)
4. Shah, A.P., Vishvakarma, S.K., Hübner, M.: Soft error hardened asymmetric 10T SRAM cell for aerospace applications. *J. Electron. Test* **36**, 255–269 (2020)
5. Singh, S., Mishra, V.: Enhanced static noise margin and increased stability SRAM cell with emerging device memristor at 45-nm technology. *Radioelectron. Commun. Syst.* **61**, 200–206 (2018)
6. Wang, W., Guin, U., Singh, A.: Aging-resilient SRAM-based true random number generator for lightweight devices. *J. Electron. Test* **36**, 301–311 (2020)
7. He, Y., Zhang, J., Wu, X., Si, X., Zhen, S., Zhang, B.: A half-select disturb-free 11T SRAM cell with built-in write/read-assist scheme for ultralow-voltage operations. In: *IEEE Transactions on Very Large Scale Integration (VLSI) Systems*, vol. 27, no. 10, pp. 2344–2353 (2019)
8. Fragasse, R., et al.: Analysis of SRAM enhancements through sense amplifier capacitive offset correction and replica self-timing. *IEEE Trans. Circ. Syst. I Regul. Pap.* **66**(6), 2037–2050 (2019)

9. Gupta, S., Gupta, K., Calhoun, B.H., Pandey, N.: Low-power near-threshold 10T SRAM bit cells with enhanced data-independent read port leakage for array augmentation in 32-nm CMOS. *IEEE Trans. Circ. Syst. I Regul. Pap.* **66**(3), 978–988 (2019)
10. Dounavi, H., Sfikas, Y., Tsiatouhas, Y.: Periodic aging monitoring in SRAM sense amplifiers. In: 2018 IEEE 24th International Symposium on On-Line Testing And Robust System Design (IOLTS), Platja d’Aro, pp. 12–16 (2018)
11. Pathak, A., Sachan, D., Peta, H., Goswami, M.: A modified SRAM based low power memory design. In: 2016 29th International Conference on VLSI Design and 2016 15th International Conference on Embedded Systems (VLSID), Kolkata, pp. 122–127 (2018)
12. Kaushik, C.S.H., Vanjarlapati, R.R., Krishna, V.M., Gautam, T., Elamaram, V.: VLSI design of low power SRAM architectures for FPGAs. In: 2014 International Conference on Green Computing Communication and Electrical Engineering (ICGCCEE), pp. 1–4 (2014)
13. Choudhary, R., Padhy, S., Rout, N.K.: Enhanced robust architecture of single bit SRAM cell using Drowsy cache and super cut-off CMOS concept. *Int. J. Ind. Electron. Electr. Eng.* **3**, pp. 63–68 (2011)
14. Gajjar, J.P., Zala, A.S., Aggarwal, S.K.: Design and analysis of 32 bit SRAM architecture in 90 nm CMOS technology, vol. 03(04), pp. 2729–2733 (2016)
15. Agrawal, R., Tomar, V.K.: Analysis of cache (SRAM) memory for core I<sup>TM</sup> 7 processor. In: 9th International Conference on Computing, Communication and Networking Technologies (ICCCNT) (2018)
16. Vanama, K., Gunnuthula, R., Prasad, G.: Design of low power stable SRAM cell. In: 2014 International Conference on Circuit Power and Computing Technologies (ICCPCT), pp. 1263–1267 (2014)
17. Chandankhede, R.D., Acharya, D.P., Patra, P.K.: Design of high-speed sense amplifier for SRAM. In: IEEE International Conference on Advanced Communication Control and Computing Technologies, pp. 340–343 (2012)
18. Tao, Y.-p., Hu, W.-p.: Design of sense amplifier in the high-speed SRAM. In: International Conference on Cyber-Enabled Distributed Computing and Knowledge Discovery, pp. 384–387 (2015)
19. Tao, Y., Hu, W.: Design of sense amplifier in the high-speed SRAM. In: International Conference on Cyber-Enabled Distributed Computing and Knowledge Discovery, Xi’an, 2015, pp. 384–387 (2015). <https://doi.org/10.1109/CyberC.2015.32>
20. Sinha, M., Hsu, S., Alvandpour, A., Burleson, W., Krishnamurthy, R., Borhr, S.: High-performance and low-voltage sense-amplifier techniques for sub-90 nm SRAM. In: IEEE International SOC Conference, 2003 [Systems-on-Chip] (2012)

# Design

# Design and Structural Analysis of Nano-satellite



R. Balaji, Estheru Rani Talasila, L. Oblisamy, V. S. Ajith,  
and A. Basithrahman

## 1 Introduction

Artificial Satellites have brought a revolution in the field of Astronomy. These play a critical role in today's space study and research. Satellites have many operations such as Star mapping, Mapping of planetary surfaces. Apart from research, these are also used for Earth observation, Communication and Navigation Purposes. As the technology is advancing very rapidly, we have witnessed a significant growth in the satellites. In the recent years, it is seen that the focus has been shifted to smaller and miniature satellite to compensate weight and cost of satellites. This has caught the eye of many researchers; as a result, we have seen a phenomenal increase in the launch percentage of Cube Sat among Nano-satellite industry, thus a final conclusion was drawn to take the CubeSat form factor for the structure and thermal design with their respective finite model analysis. A CubeSat is a kind of miniature spacecraft satellite consisting of multiples of 10 cm to 10 cm = 11.35 cm (~four to 4 in ~4 in ~4 to 4 in) cubic units. A CubeSat (Satellite-U-class Spacecraft). A standard CubeSat 3 Device Deployer may also be supplied in 1U, 2U, 3U from the ISIS CubeSat Store, depending on the number of CubeSats that it can contain. For making a structure that can resist space condition materials selection is the major aspect. da Silva Carneiro [1] has done a comparative study on three different Aluminum Alloys (AA6061 T6, AA5056 honeycomb, AA5051 T6). As per the study, AA5051 T6 produces a reduction in mass

---

R. Balaji (✉) · V. S. Ajith  
Department of Aeronautical Engineering, Jawaharlal College of Engineering and Technology,  
Palakkad, Kerala, India

E. R. Talasila  
School of Mechanical Engineering, Lovely Professional University, Phagwara, Punjab, India

L. Oblisamy · A. Basithrahman  
Department of Aeronautical Engineering, Nehru College of Engineering and Technology,  
Coimbatore, India

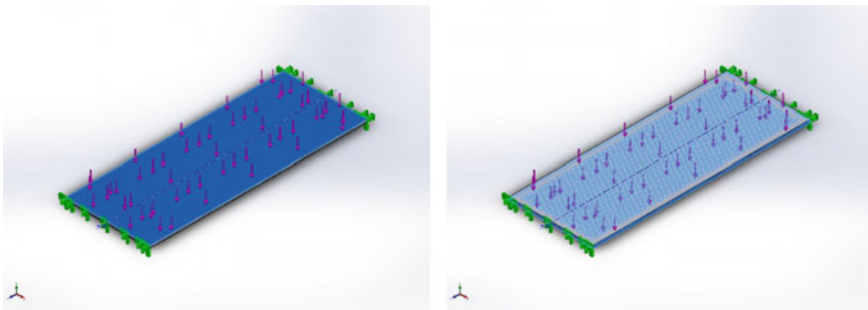
density and that will produce better results. Considering the mechanical, thermal, electrical and optical behavior. Ashby [2] suggested that composite materials will be one of the best options for space conditions as per the requirement. When the satellite reaches outer space material of the structure needs to be monitored continually as the sudden change in atmospheric property in space cause a sensitivity effect. As per the clear research Kassner [3] shows that 6061 T6 results will be most suitable for space conditions for sensitivity problems. Apart from the sensitivity affect the material going experience cyclic loading, as the orbit changes. To get the more life span of the satellite, the fatigue needs to be within the allowable limit. Various methods were available to monitor the fatigue of the satellite structure [4]. For the above-mentioned properties, aircraft materials will be one of the best options as they experiencing the same condition while flying. But the properties need to improve. To achieve that GLARE composite's core proposition needs to be reinforced [5]. We can choose Al 7075 T6 as another option for materials as the thermal behavior much better than Al5051 and Al6061 T6. Furthermore, reinforcement is advisable to achieve better results. Configuration of MMOD double sandwich structure [5] is a better method to monitor the new structural configuration. Honeycomb alloy and setoff structure configurations were created by filling the foam in the frequencies that have been improved [7].

## 2 Material Selection

See Fig. 1 and Table 1.

### (A) Mesh information

Element size is 6.5613 mm, Tolerance limit is 0.328065 m, Total Nodes 107304, Total Elements 68917 and Maximum Aspect Ratio 51.95 (Tables 2 and 3 and Fig. 2).

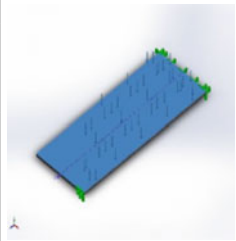


**Fig. 1** Hexagonal panel honeycomb core and sandwich panel

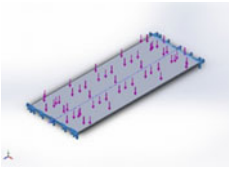
**Table 1** Properties of al 6061-T6 and 7075-T6

Properties		
Name	7075-T6 (SN)	6061-T6 (SS)
Model type	Linear elastic isotropic	Linear elastic isotropic
Default failure criterion	Max von Mises stress	Max von Mises stress
Yield strength	$5.05e + 08 \text{ N/m}^2$	$2.75e + 08 \text{ N/m}^2$
Tensile strength	$5.7e + 08 \text{ N/m}^2$	$3.1e + 08 \text{ N/m}^2$
Elastic modulus	$7.2e + 10 \text{ N/m}^2$	$6.9e + 10 \text{ N/m}^2$
Poisson's ratio	0.33	0.33
Mass density	$2810 \text{ kg/m}^3$	$2700 \text{ kg/m}^3$
Shear modulus	$2.69e + 10 \text{ N/m}^2$	$2.6e + 10 \text{ N/m}^2$
Thermal expansion coefficient	$2.36e-05 /\text{K}$	$2.4e-05 /\text{K}$

**Table 2** Load and fixtures for sandwich panel

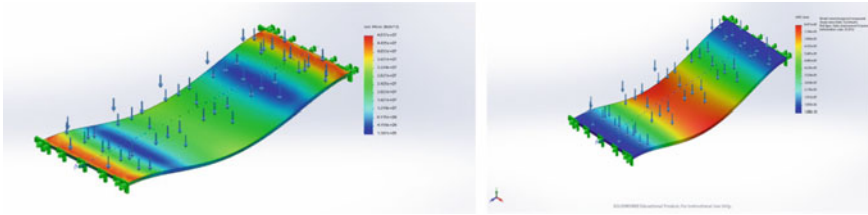
Load name	Load image	Load details	
Force-1		Entities	1 face(s)
		Type	Apply normal force
		Value	40 kgf

**Table 3** Load and fixtures for hexagonal panel honeycomb core

Fixture name	Fixture image	Fixture details	
Fixed-1		Entities	6 face(s)
		Type	Fixed geometry

*Resultant forces*

Components	X	Y	Z	Resultant
Reaction force (N)	0.052 4864	392.19 6	0.116711	392.196



**Fig. 2** Volumetric stress and total deformation of hexagonal sandwiched structure with middle honeycomb panel

### (B) Design of specialized wall configurations of the satellite structure

The main two design aspects that were taken in to account for designing specialized walls of the satellite structure are:

- To Increase the Strength to Weight ratio of structure
- To decrease the overall weight of the satellite bus
- Decrease the stress generation for different types of loadings on satellite structure.

In the first design iteration, combination of Equilateral Triangles and Hexagonal shapes was taken into consideration for material cut outs from the satellite walls. It was seen that the value of fos was 43.64.

In the second iteration, combination of Equilateral Triangles and variable diametrical circular shapes was taken into consideration for material cut outs from the satellite walls. It was seen that the value of fos was 58.32.

In the third iteration, combination of Equilateral Triangles shapes was taken into consideration for material cut outs from the satellite walls. It was seen that the value of fos was 85.16.

From the above results, it was clearly seen that combination of Equilateral Triangles gave us the best results as you can see for the same amount of forces, we have received double the value of fos that was observed in first iteration. So, it is safe to conclude by saying that it is much safer to build a satellite with Equilateral triangular cut out sections thereby meeting all our requirements (Fig. 3 and Table 4).

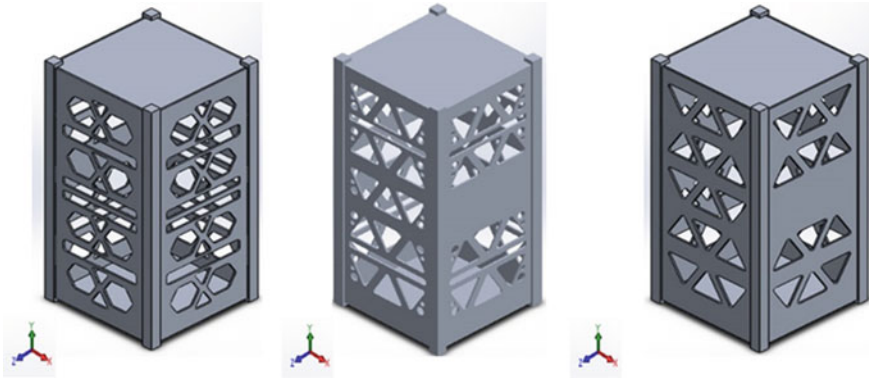
### (C) Static structural analysis

See Figs. 4, 5 and 6.

## 3 Conclusion

As per the literature review, analysis has been carried out with consideration of three different nano-satellite structures with the same materials (aluminum 6061, 7075 heat treated in T6 condition). With the analysis output, we can conclude that as the

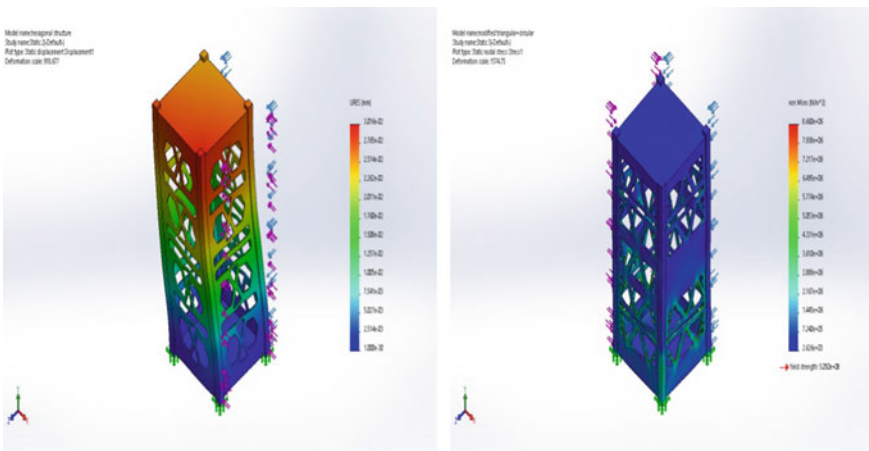




**Fig. 3** Nano-satellites with different cross-sectional design

**Table 4** Mesh properties of models

Properties	Model A	Model B	Model C
Element size	4.10171 mm	4.16597 mm	4.25037 mm
Tolerance	0.205086 mm	0.208299 mm	0.212518 mm
Total nodes	78,276	81,123	76,813
Total elements	38,564	38,725	38,411
Maximum aspect ratio	16.456	18.848	20.367



**Fig. 4** Static structural analysis model A and B

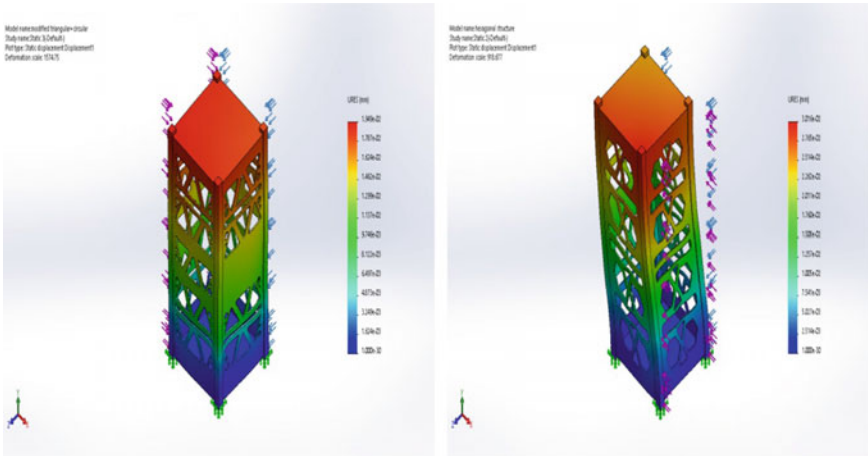


Fig. 5 Total deformation of model A and B

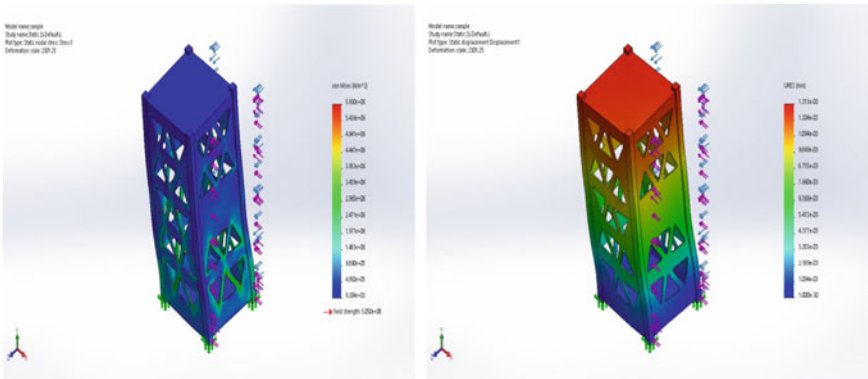


Fig. 6 Total deformation and static structural analysis of model C

weight and stiffness basis the sandwiched having high factor of safety. The Al 7075 is a good radioactive material, so the hexagonal sandwiched structure with middle honeycomb panel will be a prepared one for nano-satellite to increase the lifespan and withstand the atmospheric condition. Further, the impact test and vibration test need to be taken count for the thermal analysis.

## References

1. da Silva Carneiro, S.H.: Modal analysis of a satellite with different materials in XXXVII. Iberian Latin-American Congress on Computational Methods in Engineering
2. Ashby, M.F.: Designing hybrid materials in Acta Materialia Inc. Published by Elsevier Ltd. Materials and process for spacecraft and high reliability application by Dunn BD in Springer
3. Kassner, M.E.: A Study of the Quench Sensitivity of 6061-T6 and 6069-T6 Aluminum Alloys
4. Mohseni, E.: A Study on Surface Modification of Al7075-T6 Alloy Against Fretting Fatigue Phenomenon
5. Steven, H.: Requirements and design structure for Surya Satellite-1. IOP Conf. Ser. Earth Environ. Sci.
6. Shetty, B.P.: Finite Element Analysis for a 3U CubeSat Structure. IJSER **9** (2018)
7. Adde, K.A.: Finite element analysis of 3U CubeSat structure. Int. J. Sci. Eng. Res.
8. Ryan, S.: Honeycomb vs. Foam: Evaluating Potential Upgrades to ISS Module Shielding. Elsevier (2010)

# Unbalance Identification and Balancing Using Model Sensitivity-Based Approach



Dinesh Kumar Pasi, Manoj Chouksey, and Ashesh Tiwari

## 1 Introduction

Machinery vibration was not serious concern until the age of slow moving water wheels and wind mills [1]. However, with the advancement of the rotating machines in the nineteenth century, the subject of rotor dynamics has been developed over the years. Design of rotating machines involves rotor dynamic considerations so that the vibration levels are within acceptable limits during run-up and at the operating spin speed of the machine. Unbalance is the primary fault in rotating machines, which causes occurrence of vibrations in the machine. Balanced condition gets deteriorated during the operation due to various reasons like dust, dirt corrosion, erosion and dynamic loading conditions [2]. This requires the balancing of the rotating components; if it is not attended, the vibrations levels may increase beyond limits.

There are several methods of balancing developed over the period of time. In the conventional balancing approach, an experimental process, multiple trial runs are taken to record rotor response and phase angles for estimating the balancing masses to be added in chosen planes. Static balance requires adding balancing mass in one plane, whereas dynamic balancing is a two-plane balancing process [3]. Model-based approach is gaining popularity for identification of various rotor faults including unbalance. In model-based fault diagnosis, analytical models/finite element models of the system as well as faults and various optimization methods are employed for the fault identification. Markert et al. [3] proposed model-based method for fault identification with least square fitting algorithm [4]. Furtado et al. [5] suggested model-based approach for diagnosis and unbalance identification using artificial

---

D. K. Pasi (✉)

Department of Mechanical Engineering, Shri G. S. Institute of Technology and Science, Indore, India

M. Chouksey · A. Tiwari

Mechanical Engineering Department, IET-Devi Ahilya University, Indore, India

neural network. Jalan et al. [6] proposed a model-based approach using residual vibrations on the rotor, which is further used in computation of residual forces due to the fault. The mathematical model/finite element model, employed in the model based approach, should be proper and reliable. To make sure that the developed model is correct and results are reliable, it is required to validate the results from model and physical system. If the results are not comparable, it will require to update the model or its selected parameters in the light of experimental data. The finite element model updating methods may be based on experimental frequency response functions (FRF's) or the modal data (i.e. eigenvalues and/or eigenvectors). Unlike non-spinning structures, rotor systems are non-self-adjoint systems. Therefore model updating methods for rotor systems differ from those for non-spinning structures. The work as given in Refs. [7–9] may be referred to explore the model updating method for rotor systems. Chouksey et al. [8] employed an updated finite element model of a single-disc rotor system to identify disc unbalance and balancing mass. However, their work involved many iterations in the estimation of balancing mass.

Many times single-plane balancing proves sufficient for balancing rotating machinery e.g. in case of fans, impellers, etc. In the single-plane balancing, an estimated counter (balancing) weight is placed at an appropriate location in the plane. There are various experimental methods developed for finding out the balancing weight and the corresponding phase angle. Influence coefficient method of single-plane balancing involves three runs for balancing, namely (i) initial run, (ii) trial run, and (iii) final run. Keyphasor signal is generally used to measure the response phase angle to locate the heavy spot. Carlson [10] proposed the four-run balancing method which reduces the requirement of keyphasor signal for calculating balancing mass and its heavy spot (phase angle). However, the number of runs by this method increases by one when compared with the three-run influence coefficient method. More number of runs make the balancing process more lengthy, and hence researchers have attempted their work to reduce the number of trial runs [11]. The finite element model-based balancing method proposed in this work takes two runs, first for the rotor response and other for the phase angle, to estimate the balancing mass and its location.

This work proposes a novel model-based approach for unbalance identification using unbalance response sensitivities. The method has been used to balance a single-disc rotor system using simulated studies. It involves two runs for balancing the single-disc rotor system (initial run and final run) instead of three runs of the conventional method of balancing. Initial run is required to measure the initial response and to locate the heavy spot. The trial run, which takes maximum time in a balancing process, is eliminated. It is proposed to calculate the influence coefficient using the updated finite element model of the rotor system; hence, the necessity of the trial run on the actual rotor system is reduced in the present approach.

## 2 Unbalance Identification Using Unbalance Response Sensitivity

The sensitivity-based approach for unbalance identification in the generalized form has been discussed in this section. The method employs the measured unbalance response at selected locations and the model-based unbalance response sensitivity in the computation of the rotor unbalance. The finite element model of the rotor system is used to compute the unbalance response sensitivities and the sensitivity matrix.

The unbalance response sensitivity  $s_{ij}$ , as computed using the finite element model, is defined as the unbalance response at point  $i$  ( $i = 1, 2, 3, 4 \dots m$ ) in a particular direction due to unit rotating unbalance force at point  $j$  ( $j = 1, 2, 3, 4 \dots n$ ), where  $m$  and  $n$  represent the number of measurement points and the unbalance locations, respectively, on the rotor system.

Hence, the sensitivity matrix in the generalized form may be written as

$$S = \begin{bmatrix} s_{11} & s_{12} & s_{13} & \dots & s_{1n} \\ s_{21} & s_{22} & s_{23} & \dots & s_{2n} \\ s_{31} & s_{31} & s_{33} & \dots & s_{3n} \\ \dots & \dots & \dots & \dots & \dots \\ s_{m1} & s_{m2} & s_{m3} & \dots & s_{mn} \end{bmatrix} \tag{1}$$

This work proposes use of the measured unbalance response at selected locations in the process of unbalance identification. However, this work uses model unbalance response as the reference data to simulate the measured unbalance responses. The measured vector of the unbalance response may be expressed as per Eq. (2). If ‘ $n$ ’ number of unbalance locations are considered, then the unbalance force vector ‘ $f$ ’ is given by Eq. (3).

$$Y = \begin{Bmatrix} y_1 \\ y_2 \\ y_3 \\ \dots \\ y_m \end{Bmatrix} \tag{2}$$

$$f = \begin{Bmatrix} f_1 \\ f_2 \\ f_3 \\ \dots \\ f_n \end{Bmatrix} \tag{3}$$

Once the sensitivity matrix is computed and the vector of measured unbalance responses formed, the unbalance in the rotor system can be identified. This work demonstrates unbalance identification and balancing of a single-disc rotor system with centrally located disc as well as offset disc positions.

Unbalance ( $f_j$ ) for the disc position at any point (say  $j$ ) on the rotor-shaft can be computed by measuring the unbalance response ( $y_i$ ) at any point (say point  $i$ ) on the rotor-shaft. For this, it will be required to compute/consider the unbalance response sensitivity ' $s_{ij}$ '. The following equation may be used for the estimation of magnitude of the unbalance:

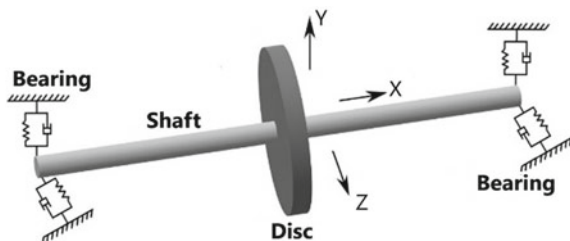
$$f_j = \frac{y_i}{s_{ij}} \quad (4)$$

### 3 Illustrative Example

Figure 1 shows the single-disc rotor system supported on rolling element bearings as considered for illustration in this work. The bearings have been modelled using support direct stiffnesses in the horizontal and vertical directions. The steel rotor-shaft is 430 mm long and 13 mm in diameter. The steel rotor-disc is 126 mm in diameter, 15.3 mm thick, and its weight is 1.484 kg. Density, Young's modulus and Poisson's ratio for the shaft and disc material are considered as  $7800 \text{ kg/m}^3$ , 210 GPa and 0.3, respectively determined from 3D modeling and direct measurement are  $7850 \text{ kg/m}^3$ , 210 GPa and 0.3 respectively. Inertial properties obtained from 3D modeling of disc from direct measurement are polar moment of inertia  $I_{xx} = 2799.879 \text{ kg mm}^2$ , moment of inertia about diameter  $I_{yy} = I_{zz} = 1444.337 \text{ kg mm}^2$ . The supports are considered isotropic with radial stiffness value of  $6 \times 10^5 \text{ N/m}$ .

Figure 2 shows the meshed finite element model of the rotor-shaft system along with marked sensitivity measurement points. Study has been conducted for two cases namely **case 1** for centrally located (i.e. at point 5) and **case 2** for offset (i.e. at point 6) positions of the rotor-disc along the rotor-shaft.

**Fig. 1** Single-disc rotor system considered



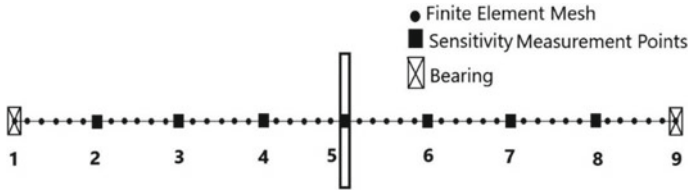


Fig. 2 Meshed model of the rotor system

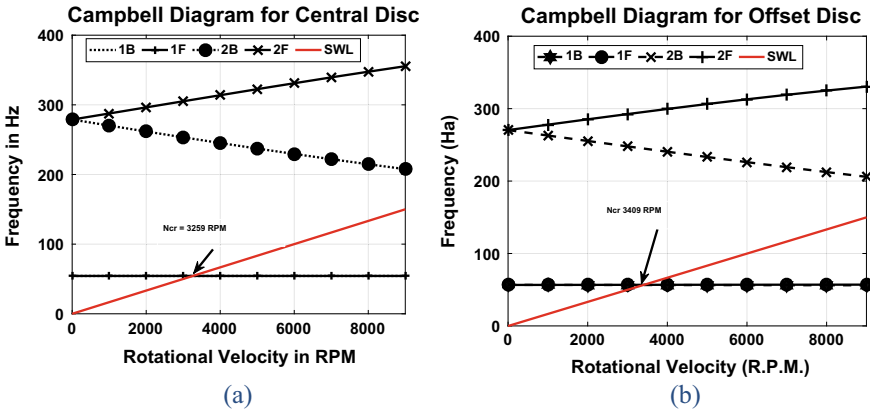


Fig. 3 Campbell diagram for a case 1, b case 2

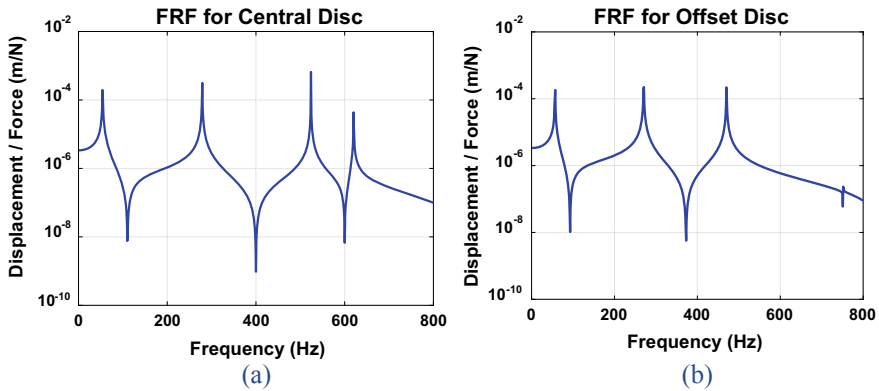
### 3.1 Critical Speed Determination

Campbell diagram or whirl speed map is a plot of natural frequencies against rotor spin speed. Figure 3a and b shows the Campbell diagrams for the case 1 (centrally located disc position) and case 2 (offset disc position), respectively. The intersection of the natural frequency line in first forward mode with the synchronous whirl line (corresponding to unbalance excitation) is marked as the first critical speed in both cases. It may be seen that the split in 1st forward and 2nd backward modes is very small due to the lesser gyroscopic effect in these modes. However, this effect is clearly visible in the split in the 2nd forward and 2nd backward modes. The critical speed is marked as 3259 RPM and 3409 RPM in the case 1 and case 2 respectively.

### 3.2 Frequency Response Plots

This work demonstrates the unbalance response identification in rotor system using simulated study. However, actual application will involve studies of frequency response functions and their use in model updating. Frequency response functions





**Fig. 4** Frequency response functions **a** Central disc in case 1 and **b** offset disc in case 2

are measured in the process of modal testing. Frequency response function ‘ $H_{ij}$ ’ is defined as the response at point  $i$  due to unit harmonic force at point  $j$ . These functions are used to estimate modal natural frequencies and mode shapes as required in the finite element model updating process.

Figure 4a and b shows the FRFs ‘ $H_{23}$ ’ and ‘ $H_{33}$ ’ under case 1 and case 2, respectively. The natural frequencies in various modes can be read from these functions as the corresponding peak positions.

### 4 Sensitivity Analysis

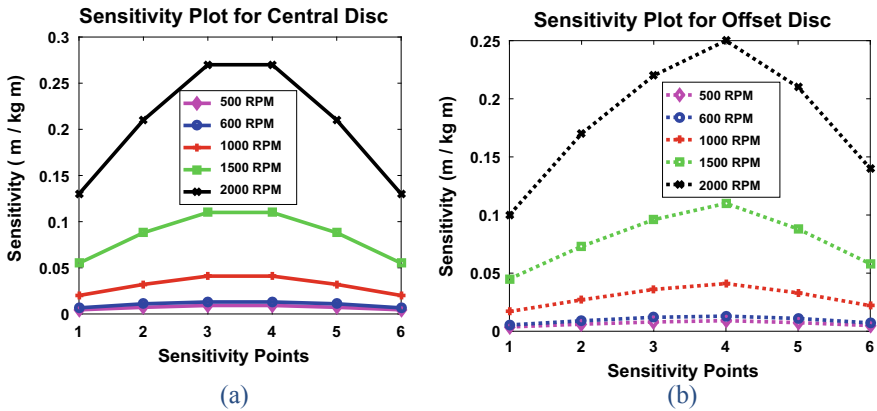
Tables 1 and 2 show the unbalance response sensitivities of the rotor system under case 1 and case 2, respectively. Different spin speeds have been considered to study

**Table 1** Sensitivities (m/kg m) under case 1 (central disc)

Sensitivity/speed (RPM)	$s_{25}$	$s_{35}$	$s_{45}$	$s_{65}$	$s_{75}$	$s_{85}$
500	$4.64 \times 10^{-03}$	$7.44 \times 10^{-03}$	$9.53 \times 10^{-03}$	$9.53 \times 10^{-03}$	$7.44 \times 10^{-03}$	$4.64 \times 10^{-03}$
600	$6.74 \times 10^{-03}$	$1.08 \times 10^{-02}$	$1.39 \times 10^{-02}$	$1.39 \times 10^{-02}$	$1.08 \times 10^{-02}$	$6.74 \times 10^{-03}$
1000	$2.04 \times 10^{-02}$	$3.28 \times 10^{-02}$	$4.19 \times 10^{-02}$	$4.19 \times 10^{-02}$	$3.28 \times 10^{-02}$	$2.04 \times 10^{-02}$
1500	$5.56 \times 10^{-02}$	$8.91 \times 10^{-02}$	$1.14 \times 10^{-01}$	$1.14 \times 10^{-01}$	$8.91 \times 10^{-02}$	$5.56 \times 10^{-02}$
2000	$1.35 \times 10^{-01}$	$2.15 \times 10^{-01}$	$2.75 \times 10^{-01}$	$2.75 \times 10^{-01}$	$2.15 \times 10^{-01}$	$1.35 \times 10^{-01}$

**Table 2** Sensitivity (m/kg m) under case 2 (offset disc)

Sensitivity/speed (RPM)	$s_{26}$	$s_{36}$	$s_{46}$	$s_{56}$	$s_{76}$	$s_{86}$
500	$3.81 \times 10^{-03}$	$6.32 \times 10^{-03}$	$8.36 \times 10^{-03}$	$9.52 \times 10^{-03}$	$7.72 \times 10^{-03}$	$5.06 \times 10^{-03}$
600	$5.54 \times 10^{-03}$	$9.19 \times 10^{-03}$	$1.21 \times 10^{-02}$	$1.38 \times 10^{-02}$	$1.12 \times 10^{-02}$	$7.35 \times 10^{-03}$
1000	$1.68 \times 10^{-02}$	$2.78 \times 10^{-02}$	$3.67 \times 10^{-02}$	$4.17 \times 10^{-02}$	$3.38 \times 10^{-02}$	$2.21 \times 10^{-02}$
1500	$4.53 \times 10^{-02}$	$7.49 \times 10^{-02}$	$9.87 \times 10^{-02}$	$1.12 \times 10^{-01}$	$9.09 \times 10^{-02}$	$5.92 \times 10^{-02}$
2000	$1.07 \times 10^{-01}$	$1.77 \times 10^{-01}$	$2.33 \times 10^{-01}$	$2.64 \times 10^{-01}$	$2.12 \times 10^{-01}$	$1.39 \times 10^{-01}$



**Fig. 5** Sensitivity plot over the rotor-shaft under **a** case 1 and **b** case 2

the effect of spin speeds on the unbalance identification. Figure 5a and b shows the variation of these sensitivities along the rotor-shaft at different spin speeds.

As discussed above, three speeds 600, 1000 and 1500 RPM are chosen to determine sensitivity. Figure 5 is self-explanatory that with the increase in speed the sensitivity increases, and position maximum value of sensitivity along the shaft changes with changing the position of the disc.

## 5 Unbalance Response

In the case of the balancing requirement, initial response should be measured. The response thus recorded needs to be balanced. Unbalance identification as proposed in this work uses this measured unbalance response for computing the balancing mass.

**Table 3** Unbalance response at different speeds under case 1 (central disc position)

Response(m)/speed RPM	y <sub>2</sub>	y <sub>3</sub>	y <sub>4</sub>	y <sub>6</sub>	y <sub>7</sub>	y <sub>8</sub>
500	$2.93 \times 10^{-06}$	$4.69 \times 10^{-06}$	$6.01 \times 10^{-06}$	$6.01 \times 10^{-06}$	$4.69 \times 10^{-06}$	$2.93 \times 10^{-06}$
600	$4.25 \times 10^{-06}$	$6.82 \times 10^{-06}$	$8.74 \times 10^{-06}$	$8.74 \times 10^{-06}$	$6.82 \times 10^{-06}$	$4.25 \times 10^{-06}$
1000	$1.29 \times 10^{-05}$	$2.07 \times 10^{-05}$	$2.65 \times 10^{-05}$	$2.65 \times 10^{-05}$	$2.07 \times 10^{-05}$	$1.29 \times 10^{-05}$
1500	$3.51 \times 10^{-05}$	$5.62 \times 10^{-05}$	$7.19 \times 10^{-05}$	$7.19 \times 10^{-05}$	$5.62 \times 10^{-05}$	$3.51 \times 10^{-05}$
2000	$8.50 \times 10^{-05}$	$1.36 \times 10^{-04}$	$1.74 \times 10^{-04}$	$1.74 \times 10^{-04}$	$1.36 \times 10^{-04}$	$8.50 \times 10^{-05}$

**Table 4** Unbalance response at different speeds under case 2 (for offset disc position)

Response (m)/speed RPM	y <sub>2</sub>	y <sub>3</sub>	y <sub>4</sub>	y <sub>5</sub>	y <sub>7</sub>	y <sub>8</sub>
500	$2.40 \times 10^{-06}$	$3.99 \times 10^{-06}$	$5.28 \times 10^{-06}$	$6.01 \times 10^{-06}$	$4.87 \times 10^{-06}$	$3.20 \times 10^{-06}$
600	$3.50 \times 10^{-06}$	$5.80 \times 10^{-06}$	$7.67 \times 10^{-06}$	$8.72 \times 10^{-06}$	$7.08 \times 10^{-06}$	$4.64 \times 10^{-06}$
1000	$1.06 \times 10^{-05}$	$1.75 \times 10^{-05}$	$2.32 \times 10^{-05}$	$2.63 \times 10^{-05}$	$2.13 \times 10^{-05}$	$1.40 \times 10^{-05}$
1500	$2.86 \times 10^{-05}$	$4.73 \times 10^{-05}$	$6.23 \times 10^{-05}$	$7.07 \times 10^{-05}$	$5.70 \times 10^{-05}$	$3.74 \times 10^{-05}$
2000	$6.78 \times 10^{-05}$	$11.2 \times 10^{-05}$	$14.7 \times 10^{-05}$	$16.6 \times 10^{-05}$	$13.4 \times 10^{-05}$	$8.75 \times 10^{-05}$

As the utility of the method has been demonstrated using simulated studies, a known magnitude of unbalance is applied on the disc at different speeds. Response which simulates the measured (initial) unbalance response due to the unbalance induced is listed in Tables 3 and 4 for case 1 and case 2, respectively. However, the developed method has been tested for unbalance identification after including  $\pm 5\%$  random noise into the simulated response.

## 6 Unbalance Identification

This section demonstrates the unbalance ( $f_j$ ) identification, as per Eq. (14), at any disc position ( $j = 5$  for case 1,  $j = 6$  for case 2) along the rotor-shaft using the proposed methodology. An unbalance of  $6.31 \times 10^{-4}$  kg m has been induced in the

**Table 5** Comparison of identified unbalance at different rotor spin speeds for case 1

Speed (RPM)	500	600	1000	1500	2000
Actual UB (kg m)	$6.31 \times 10^{-04}$	$6.31 \times 10^{-04}$	$6.31 \times 10^{-04}$	$6.31 \times 10^{-04}$	$6.31 \times 10^{-04}$
Identified UB (kg m)	$6.23 \times 10^{-04}$	$6.41 \times 10^{-04}$	$6.16 \times 10^{-04}$	$6.54 \times 10^{-04}$	$6.07 \times 10^{-04}$
Error (%)	1.23	1.61	2.26	3.66	3.80

**Table 6** Comparison of identified unbalance at different rotor spin speeds for case 2

Speed (RPM)	500	600	1000	1500	2000
Actual UB (kg m)	$6.31 \times 10^{-04}$	$6.31 \times 10^{-04}$	$6.31 \times 10^{-04}$	$6.31 \times 10^{-04}$	$6.31 \times 10^{-04}$
Identified UB (kg m)	$6.43 \times 10^{-04}$	$6.16 \times 10^{-04}$	$6.13 \times 10^{-04}$	$6.51 \times 10^{-04}$	$6.55 \times 10^{-04}$
Error (%)	1.98	2.29	2.80	3.21	3.95

simulated work at the disc positions in the two cases. Unbalance response sensitivity at the point  $i$  due to unit unbalance at point  $j$ , i.e.  $s_{ij}$ , is taken from Table 1 (for case 1) and Table 2 (for case 2), whereas simulated measured unbalance response at the point  $i$ , i.e.  $y_i$ , is considered as per Table 3 (for case 1) and Table 4 (for case 2).

Table 5 shows the comparison of identified value of unbalance with the actual unbalance for case 1 (central disc position) along with the percentage error at different speeds as obtained from the method present in this work. It can be noted from the results that the unbalance has been identified quite accurately with less than 4 % error even under the presence of measurement noise. It is also to be noted that the initial run data should be used to locate the heavy spot for putting the balancing weight in actual rotor systems.

Similar study of unbalance identification has been conducted for offset disc position. Table 6 shows the identified values of the unbalance at different speeds along with the corresponding percentage errors. In Case 2 also the error in identified value of unbalances is less than 4 %.

## 7 Conclusion

Finite element model-based generalized method has been presented for balancing of rotor systems. The method has been used to balance a single-disc rotor system using simulated studies. It has been shown that the proposed method is capable of balancing the single-disc rotor system using two runs only, i.e. initial run and the final run instead of three runs as are required in conventional method of balancing. Initial run data provide the unbalance response, that is to be balanced, and the heavy spot location. The method utilizes the finite element model of the rotor system to calculate the unbalance response sensitivity (influence coefficient). It is concluded that the proposed method identifies the unbalances effectively and hence can be extended to balance the actual single-disc rotor systems. The influence of increasing

spin speeds has also been investigated on the identified unbalances. It is seen that the percentage error is lesser at smaller spin speeds. The method has potential of application to balance single-disc industrial rotors. It is expected that it will reduce time and effort to balance the industrial rotors as it eliminates the time-consuming step of trial run. However, experimental studies will be conducted in future to find out the effectiveness of the proposed method to balance industrial rotors.

**Acknowledgements** The research grant provided in the research promotion scheme of AICTE, New Delhi, for the work titled “A noble method for unbalance response prediction and balancing of rotor systems” (File No. 8-66/RIFD/RPS/POLICY-1/2016-17), is gratefully acknowledged.

## References

1. Rao, J.S.: History of Rotating Machinery Dynamics. Springer, Netherlands (2011)
2. Rao, J.S.: A note on Jeffcott warped rotor. *Mech. Mach. Theory* **36**, 563–575 (2001)
3. Norfield, D.: Practical Balancing of Rotating Machinery, 1st edn. Elsevier (2006)
4. Markert, R., Platz, R., Seidler, M.: Model based fault identification in rotor systems by least squares fitting. *Int. J. Rotating Mach.* **7**(5), 311–321 (2001)
5. Furtado, R.M., Dedini, K.L.C., Pennacchi, P., Lopes, V. Jr.: Fault identification in rotor system using model based methods, experimental data and artificial neural network. In: 18th International Congress of Mechanical Engineering, Ouro Preto, MG (2005)
6. Jalan, A.K., Mohanty, A.R.: Model based fault diagnosis of a rotor-bearing system for misalignment and unbalance under steady-state condition. *J. Sound Vibr.* **327**(3–5), 604–622 (2009). <https://doi.org/10.1016/j.jsv.2009.07.014>
7. Chouksey, M.: Studies in modal analysis, frequency response characteristics and finite element model updating of rotor systems. Ph.D., Mechanical Engineering, Indian Institute of Technology, Delhi, New Delhi, TH-4224 (2012)
8. Chouksey, M., Dutt, J.K., Modak, S.V.: Model updating of rotors supported on ball bearings and its application in response prediction and balancing. *Measurement* **46**(10), 4261–4273 (2013)
9. Chouksey, M., Dutt, J.K., Modak, S.V.: Model updating of rotors supported on journal bearings. *Mech. Mach. Theory* **71**, 52–63 (2014)
10. Carlson, P.O.L.: Four run balancing without phase. In: Proceedings, Machinery Vibration Monitoring and Analysis Seminar and Meeting, New Orleans, LA (1979)
11. Delgado, E.P., Bannister, R.H.: Balancing of an experimental rotor without trial runs. *Int. J. Rotating Mach.* **8**, 99–108 (2002)

# 8-Bit Electromechanical Processor Design for Education in Digital Computation



Shashwath Sundar and Vijay Kumar Tayal

## 1 Introduction

Almost all modern electrical and electronic devices use digital processors in one form or the other. They may be used as simple microcontrollers, as in small devices such as remote controllers and microwave ovens or as microprocessors, as in personal computers, smart mobile phones, etc. Regardless of where they are used, the fundamentals of digital computation remain the same in all instances. Since digital processors have become ubiquitous, it has become essential for students, irrespective of their field of study, to know how digital processors work. To do so, an educational tool needs to be designed and implemented that does the following:

1. Acts as a fully functional digital processor.
2. Acts as a teaching aid for demonstrating the various concepts related to digital technologies.
3. Provides hands-on experience at assembly language and machine language programming to its users.
4. Provides visual aid for teaching basic computer architecture.
5. Acts as an illustrative tool to develop a detailed understanding among students about execution of computer programs.

When it comes to educating students in the field of digital processors and computer architectures, there have been significant studies in the teaching methods using virtual machines [1], hardware implementations using FPGAs [2, 14] and using animation and computer simulations [3]. While there has been much research on the tools for education in digital computation, the tools, however, are only applicable for students

---

S. Sundar (✉) · V. K. Tayal  
Amity University, Noida, Uttar Pradesh 201313, India

V. K. Tayal  
e-mail: [vktayal@amity.edu](mailto:vktayal@amity.edu)

at undergraduate level or beyond [10]. While students are exposed to using computers at high school level, the concepts of digital processors are introduced to students only at the undergraduate level [13]. This is mainly because understanding of these machines requires the student to have prerequisite knowledge about semiconductor technologies as in the case of using FPGAs [4–6, 9, 11] or logic chips and counters. On the other hand, use of simulations and animations may not allow the students to understand hardware implementations [15] of the processor limiting the students' understanding to a theoretical level. Hence, there is a need for educational tools that allow students to learn about digital computation [7, 12] with an understanding of its hardware implementation without the need for learning about semiconductor technologies [8]. The goal of this paper is to describe the electromechanical processor and its learning environment for teaching the fundamentals of digital computation. This paper is organized as follows: Sect. 2 describes the overview of the architecture, Sect. 3 describes the software emulator, and the conclusion is mentioned in Sect. 4.

## 2 Processor Overview

To make concepts easy to grasp the processor, architecture has been simplified and has a minimalistic instruction set, while ensuring that the machine is Turing complete. Digital logic elements and memory elements have been implemented using monostable electromechanical relays and silicon diodes. Table 1 shows the processor characteristics.

### 2.1 Instruction Set Architecture (ISA)

The instruction set comprises of 18 instructions that have been grouped into 6 classes/categories (Table 2). All instructions either occupy a single byte or 2 bytes of program memory. The first byte is the operation code, and the second byte is the data or address (depending on the instruction). Since there are only 18 instructions in the instruction set, the instruction register only needs to be 5 bits wide. To encode the instructions, the most significant 3 bits (B7-B5) are used for encoding the instruction class, the next 2 bits are for encoding the operation and the lowest three bits are don't cares (B2-B0).

**Table 1** Processor characteristics

ALU width	8 bits
DATA bus width	8 bits
Address bus width	8 bits
Signed number encoding	2's complement
General-purpose register width	8 bits

**Table 2** Instruction set

Instruction class		Instruction		OPCODE	
0 (#000)	CTRL OP	0 (#00)	NOP	#000 00 000	0 × 00
		1 (#01)	HLT	#000 01 000	0 × 08
1 (#001)	MOV OP	0 (#00)	MOV A2B	#001 00 000	0 × 20
		1 (#01)	MOV B2A	#001 01 000	0 × 28
2 (#010)	A OP	0 (#00)	ADD	#010 00 000	0 × 40
		1 (#01)	INC	#010 01 000	0 × 48
3 (#011)	L OP	0 (#00)	AND	#011 00 000	0 × 60
		1 (#01)	OR	#011 01 000	0 × 68
		2 (#10)	NOT	#011 10 000	0 × 70
		3 (#11)	XOR	#011 11 000	0 × 78
4 (#100)	JMP OP	0 (#00)	JMP <Address>	#100 00 000	0 × 80
		1 (#01)	JZ <Address>	#100 01 000	0 × 88
		2 (#10)	JC <Address>	#100 10 000	0 × 90
		3 (#11)	JS <Address>	#100 11 000	0 × 98
5 (#101)	MEM OP	0 (#00)	LDA <Address>	#101 00 000	0xa0
		1 (#01)	STA <Address>	#101 01 000	0xa8
		2 (#10)	LDI A <Data>	#101 10 000	0xb0
		3 (#11)	LDI B <Data>	#101 11 000	0xb8

## 2.2 Arithmetic Logic Unit (ALU)

The arithmetic and logic unit of the processor is based on the A register which is the accumulator of the processor. The ALU has been designed in a way such that operations requiring a single operand are always done on the data in the A register and operations requiring 2 operands are done on the data in A and B registers.

The program counter (PC) is incremented in the ALU itself during the fetch cycle of the processor, eliminating the need for a standalone incremter circuit. This is achieved by multiplexing the A register and PC (Fig. 1). The output of the ALU is directly connected to the temporary register. This allows processes to run in parallel with arithmetic and logical operations since the ALU does not utilize the internal data bus. The ALU circuit has been designed using 7 relays (Fig. 2) for computing each bit and has been designed to do 2 Arithmetic and 4 logical operations (Table 3).

## 2.3 Memory Registers

The electromechanical processor has 7 memory registers out of which 3 registers are programmer visible, namely PC (program counter), A register (accumulator)



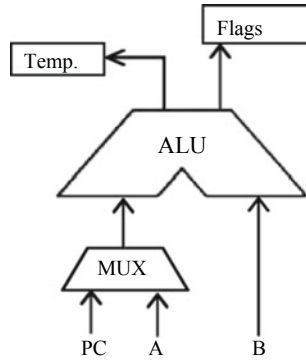


Fig. 1 ALU organization

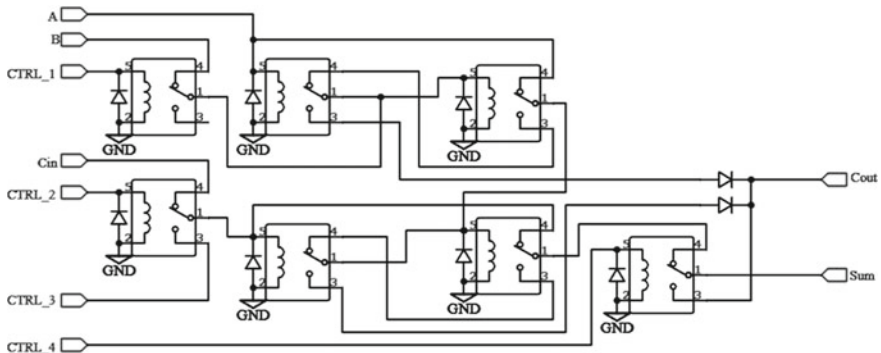


Fig. 2. 1-bit ALU circuit

Table 3 ALU operations

Arithmetic operations	Addition
Logical operations	Increment
	Bit-wise AND
	Bit-wise OR
	Bit-wise NOT
	Bit-wise XOR

and B register. The remaining four registers are the MA (memory address) register, instruction register, temporary register and the status flag. The status flag is connected to the flag output of the ALU. All the remaining registers are connected to each other via a common 8-bit bus (Fig. 3).

Each register has two control lines, namely enable line and reset line (Fig. 4). The enable line connects the register to the data bus, and the reset clears the data. The latches in the register have been designed such that a logic high on the latch input can

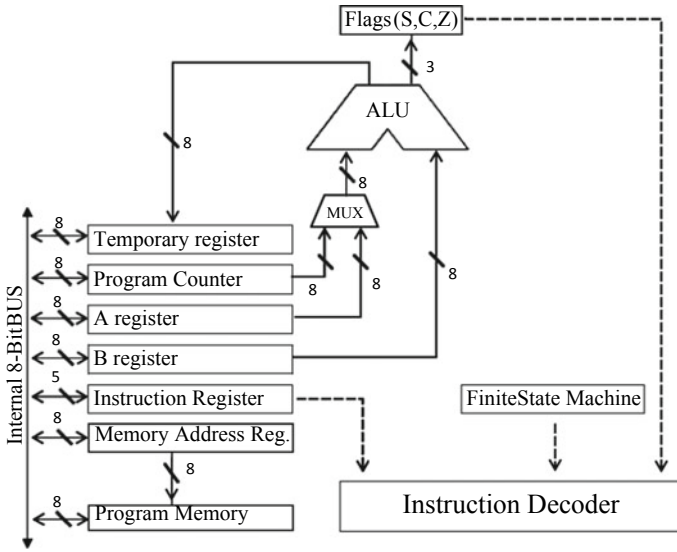


Fig. 3 Processor data path

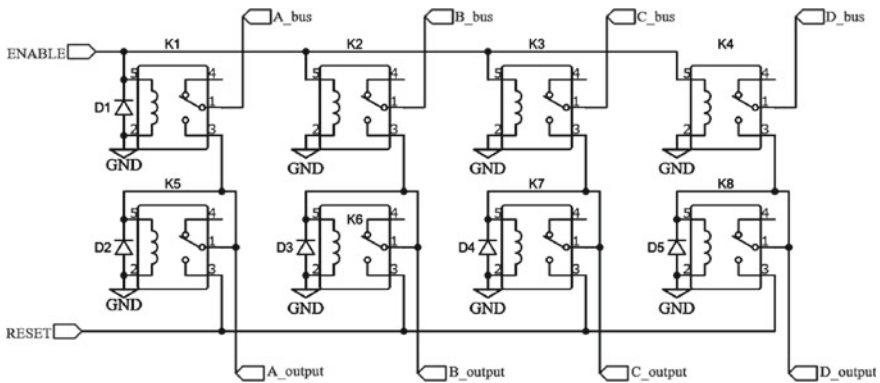


Fig. 4 4-bit memory register

set the latch, but a logic low on the latch cannot reset the latch. Hence, to read data from the register the enable line needs to be held high, but to rewrite the data on the register we first need to reset the register to clear its contents and then pull the enable line high to load new data from the bus. This method of loading new data, however, takes two clock cycles, but reduces the number of relays that are being used to make the register.

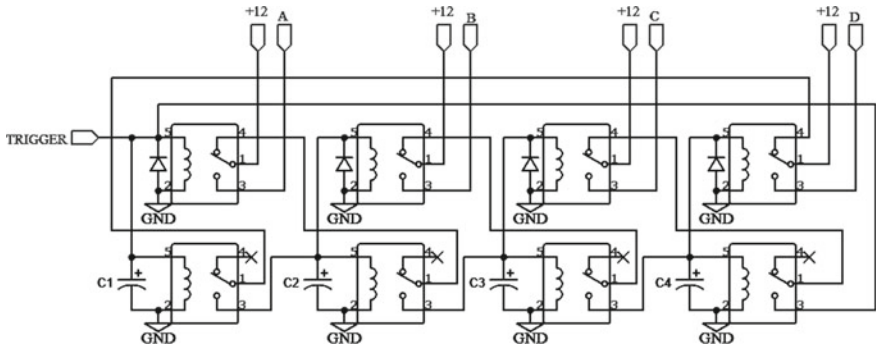


Fig. 5. 4-stage ring counter

### 2.4 The Finite State Machine (FSM)

The finite state machine for the processor is unique. It does not use an external clock. The FSM is a self-propagating ring counter made out of relays, and the timing is controlled using RC time constant of resistance of relay coils and capacitors (Fig. 5). On power up, the FSM does not start running automatically and needs to be triggered. To halt the state machine, the feedback line running from the last state to the first state needs to be disconnected. The FSM can be set in 2 different modes of operation, namely continuous running mode and instruction-wise stepping mode. In the continuous running mode, the FSM runs indefinitely till it is either stopped by a HLT instruction or a manual halt button on the control panel. In instruction-wise stepping mode, the processor needs to be manually triggered for executing each instruction.

The longest instructions in the ISA require 13 states for complete execution. Hence, the finite state machine needs to have a maximum of 13 states. On the other hand, the majority of instructions require 9 states. The FSM has been designed with 13 states with an abort line after 9 states to optimize the time usage for each instruction.

### 2.5 Program Memory

The processor has 256 bytes of program memory/RAM. The program memory has been implemented using the Arduino Nano development board that is based around the ATMEGA328P microcontroller. The Arduino Nano has been programmed to have 2 modes of operation-programming mode and RAM mode. In programming mode, the programs for the electromechanical processor can be uploaded from the software emulator to the Arduino Nano. In the RAM mode, the digital I/O lines of the Arduino Nano are configured as pins of a parallel RAM chip with 8 address lines, 8 data lines, read line and write line.

### 3 Software Emulator

Apart from the hardware, a software model of the processor has also been developed for analyzing the behavior of the processor. The emulator can run on any personal computer and has been developed for easy programming and debugging of the programs. The software has been written such that its operations are as visual and illustrative as the hardware processor itself. For example, the contents of the various memory units have been represented as black and white tiles to represent bits where black tiles represent '1' and white tiles represent a '0.'

The emulator has been written in JAVA programming language and is clock cycle accurate. Since the processor has been designed for teaching, the emulator has an interactive and easy to use Graphic User Interface (GUI) (Fig. 6).

Programs written for the processor can be written in the emulator as well in hexadecimal encoding in the emulator's program memory matrix or in assembly language in the instruction set window of the emulator. Like the hardware version, the emulator also has a virtual control panel that can be used to manually control the control line of the various elements of the processor. So, students can manually toggle the control lines and understand microinstruction execution in greater depth. After running and debugging the programs in the emulator, the same programs can also be uploaded to the program memory of the electromechanical processor via USB using a serial port at a standard 9600 baud rate.

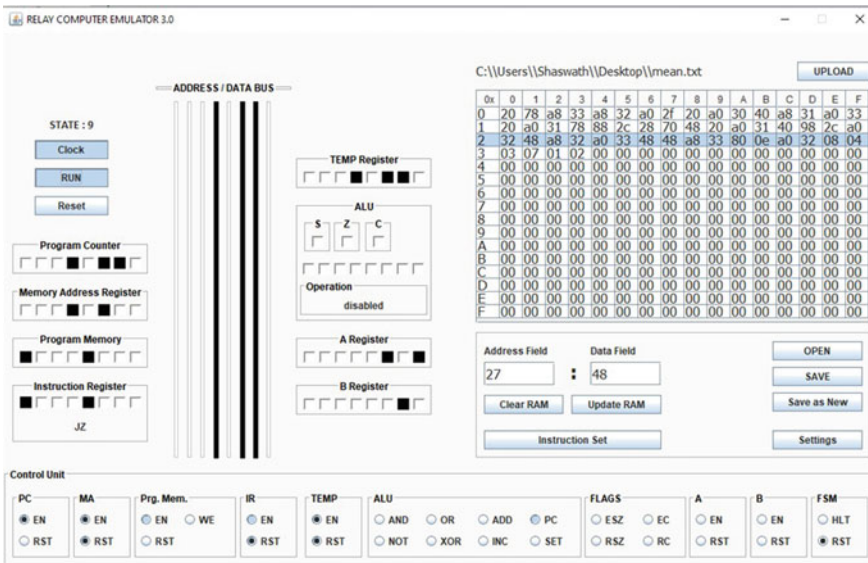


Fig. 6 Emulator GUI

## 4 Conclusion

The electromechanical processor presents itself as a tool for developing fundamental understanding of computer organization and machine-level programming. While it can be used for training at undergraduate level, its implementation using electromechanical relays widens its scope to school students. The students can learn and write programs in machine code and can see the programs running in real time because of the highly visual and illustrative hardware implementation of the processor. The students can also use the clock cycle accurate software emulator of the processor to thoroughly understand its functionality and can come up with creative programs to test on the processor.

An electromechanical processor exposes the student to the hardware aspects of a computer processor such as instruction decoding, fetch and execute cycles and propagation delays and familiarizes with the general concept of computation. On the other hand, virtual machines provide exposure in advanced computation techniques, software development and testing. In comparison with FPGAs, the electromechanical processor offers a visual and auditory feedback to the user. Further, for studying the electromechanical processor, the students are required to have a basic knowledge of electricity, binary number system and logic gates, whereas with FPGAs knowledge of the fundamentals of semiconductors, digital electronics and hardware description languages such as VHDL and Verilog is needed.

The electromechanical processor facilitates to understand the computation techniques. The proposed processor may act as a supplementary educational tool to easily understand the fundamentals of computer processors.

## References

1. Agren, O.: Virtual machines as an aid in teaching computer concepts. In: *Computer Architecture Newsletter IEEE Computer Society*, pp. 72–76 (2000)
2. Becvar, M., Pluhacek, A., Danecek, J.: DOP—A CPU core for teaching basics of computer architecture. In: *Proceedings of the Workshop on Computer Architecture Education*, pp 14–21 (2003)
3. Brorson, M.: MipsIT—A simulator and development environment using animation for computer architecture education. In: *Proceeding of Workshop of Computer Architecture Education*, Anchorage, USA (2002)
4. Anjana, R., Gandhi, K.: VHDL implementation of a MIPS RISC processor. *Int. J. Adv. Res. Comput. Sci. Softw. Eng.* **2**(8), 83–88 (2012)
5. Maxfield, C.: *The Design Warrior's Guide to FPGAs: Devices Tools and Flows*. Elsevier, USA (2004)
6. Anthony, I.E.: VHDL implementation of pipelined DLX microprocessor. M. Sc. Thesis, University Technology Malaysia (UTM), Malaysia (2008)
7. Hennessy, J.L., Patterson, D.A.: *Computer Architecture: A Quantitative Approach*. Morgan Kaufmann, San Francisco, USA (2007)
8. Reaz, M.B.I., Jalil, J., Rahman, L.F.: Single core hardware modeling of 32-bit MIPS RISC processor with a single clock. *Res. J. Appl. Sci. Eng. Technol.* **4**(7), 825–832 (2012)

9. Kishore Kumar, M., Shabeena Begum, M.D.: FPGA based implementation of 32 bit RISC processor. *Int. J. Eng. Res. Appl.* **1**(3), 1148–1151 (2011)
10. Arias, J.R., Garcia, D.F.: Introducing computer architecture education in the first course of computer science career. *Computer Architecture Newsletter*, IEEE Computer Society, pp. 37–39 (1999)
11. Gray, J.: Hands-on computer architecture teaching processor and integrated systems design with FPGAs. *Computer Architecture Newsletter*, IEEE Computer Society, pp. 90–97 (2000)
12. Pastor, E., Sanchez, F., del Corral, A.M.: A rudimentary machine. Experiences in the design of a pedagogic computer. *Computer Architecture Newsletter*, IEEE Computer Society, pp. 51–53 (1999)
13. Stanley, T.D., Wang, M.: An emulated computer with assembler for teaching undergraduate computer architecture. In: *Proceedings of the Workshop on Computer Architecture Education*, pp. 38–45 (2005)
14. Sugawara, Y., Hiraki, K.: A computer architecture education curriculum through the design and implementation of original processors using FPGAs. In: *Proceedings of the Workshop on Computer Architecture Education*, pp. 3–7 (2004)
15. Patterson, D.A., Hennessy, J.L.: *Computer Organization and Design: The Hardware/Software Interface*, 2nd edn. Morgan Kaufmann Publishers (1997)

# Effect of Nonlinearly Varying Loads and Position of Stiffener on Buckling Behaviour of Stiffened Composite Panels



K. S. Subash Chandra , T. Rajanna , and K. Venkata Rao 

## 1 Introduction

Laminated plates are an unavoidable member in several complex structure networks operated in marine, aerospace, civil and mechanical engineering. The upswing in composite material used in the modern era is primarily due to its high strength/stiffness-to-weight ratio. These are modified by the variety of fibre orientation and stacking sequence to obtain a valuable configuration. The thin-walled composite plates are strengthened by stiffeners to improve further the specific strength/stiffness, especially the buckling behaviour [1]. Buckling is a significant characteristic in these thin-walled configurations due to the in-plane load appearing from the surrounding portions in a complicated structure.

As the in-plane loads are appearing from the adjacent members, they seldom remain uniform in essence [2]. For instance, the load exerted on the aircraft wings, or the stiffened plate in the ship configurations or on the slabs of a multi-storey building by the adjacent structures is usually non-uniform. For the comprehensive application of composite stiffened plates in many industries, most of the works have been done on stiffened isotropic panels' buckling behaviour. Panda and Barik [3] have analysed the flexural stability of stiffened plates for different boundary conditions. Guo et al. studied stiffened laminate behaviour using a layer-wise (zig-zag) finite element method under uniform loading conditions [4]. Numerous researchers have studied stiffened panels under non-uniform loading conditions. Hamedani and Ranji

---

K. S. Subash Chandra (✉)  
BMS College of Engineering, Bengaluru 560019, India  
e-mail: [subashks.17pm@bmsce.ac.in](mailto:subashks.17pm@bmsce.ac.in)

T. Rajanna  
Department of Civil Engineering, BMS College of Engineering, Bengaluru 560019, India

K. Venkata Rao  
Department of Mechanical Engineering, BMSE College of Engineering, Bengaluru 560019, India

[5] analysed the effect of buckling loads subjected to bidirectional varying loads in the case of isotropic panels with two orthogonal stiffeners. The buckling response of laminated stiffened composite panels under partial in-plane loading is made by Rajanna et al. [6] and Patel and Sheik [7]. Rajanna et al. [8] investigated the effect of buckling response under linearly varying load for composite panels with a circular stiffener around the circular cutouts.

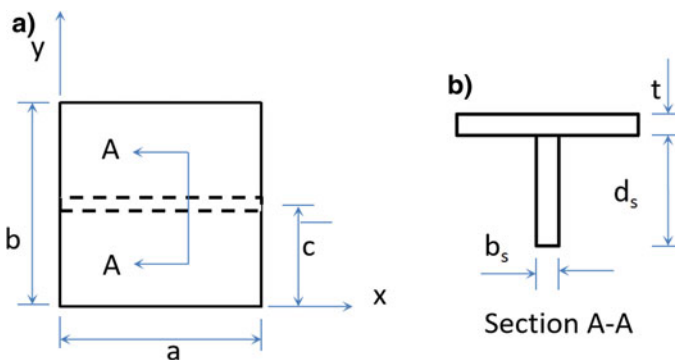
The previous works show that the effect of nonlinearly varying loads is not studied for composite panels with stiffeners. Hence, the present investigation is intended to focus on the stability response assuming nonlinearly varying loads. A considerable improvement in the overall stiffness of laminate can be achieved by establishing an appropriate stiffener dimension. In this work, buckling analysis of a composite panel with eccentrically placed x-oriented stiffener is analysed and compared to that of the unstiffened panel under various nonlinearly varying configuration of loads using commercial software—ABAQUS.

## 2 Physical Description and FE Formulation

The laminated square panel considered has dimension ‘ $a$ ’ in x-direction and ‘ $b$ ’ in y-direction with plate thickness ‘ $t$ ’ having centrally placed stiffener parallel to x-direction which is shown in Fig. 1a. The stiffener is eccentrically placed with height and width denoted by ‘ $d_s$ ’ and ‘ $b_s$ ’, respectively, Fig. 1b.

### 2.1 Governing Equation

The equilibrium equation for a plate under in-plane edge load is governed by



**Fig. 1** a) Centrally placed eccentric stiffener b) Cross-section of stiffened plate



$$[M]\{\ddot{q}\} + [[K] - P_0[K_g]]\{q\} = 0 \tag{1}$$

For buckling analysis, Eq. (1) reduces to static, when  $\{\ddot{q}\}$  becomes zero

$$[K]\{q\} - P_{cr}[K_g]\{q\} = 0 \tag{2}$$

The Eigen-value in Eq. (2) gives the buckling load for modes. The buckling load with the least value is the critical or fundamental load [8].

### 2.2 Panel Modelling Using Finite Element

The finite element software is used in the present investigation to find out the buckling load. The nonlinearly varying load force  $N_x^0$  can be expressed in Eq. (3), in which,  $N_0$  is the intensity of compressive force at the edge.  $\eta = y/b$  is the loading edge distance, and  $\gamma, \lambda$  and  $\kappa$  determines these nonlinear variation of quadratic loading, as shown in Fig. 2, along the edge  $x = 0$ . For example, the plate under nonlinearly varying uniaxial edge load in case of  $\beta = 1$  (see Fig. 3a) is when  $\gamma = 1, \lambda = 1$  and  $\kappa = -2$ . Simply supported boundary condition is represented with mesh in Fig. 3b.

$$N_x^0 = -N_0(\gamma - \lambda\eta - \kappa\eta^2) \tag{3}$$

The material properties for present study for both plate and stiffener [8] is given:  $E_{11}/E_{22} = 25.0, G_{12}/E_{22} = G_{13}/E_{22} = 0.5, G_{23}/E_{22} = 0.2$  and  $\nu_{12} = 0.25$ .

Non-dimensional buckling load parameter ( $\gamma_{cr}$ ) is given by

$$P_{cr}b^2/E_{22}t^3 \tag{4}$$

where  $P_{cr}$  is the absolute critical load and  $E_{22}$  is laminate stiffness in lateral direction.

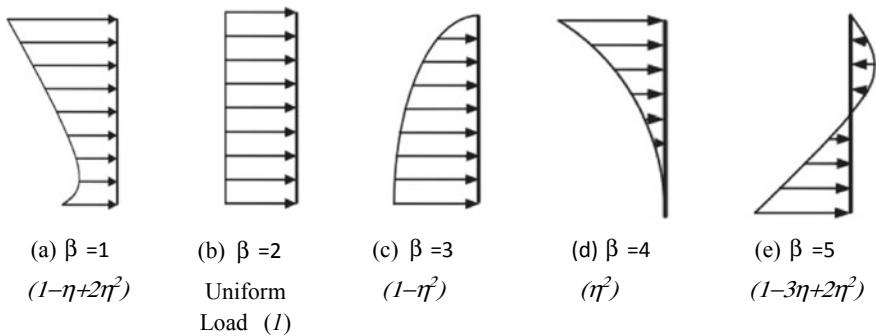
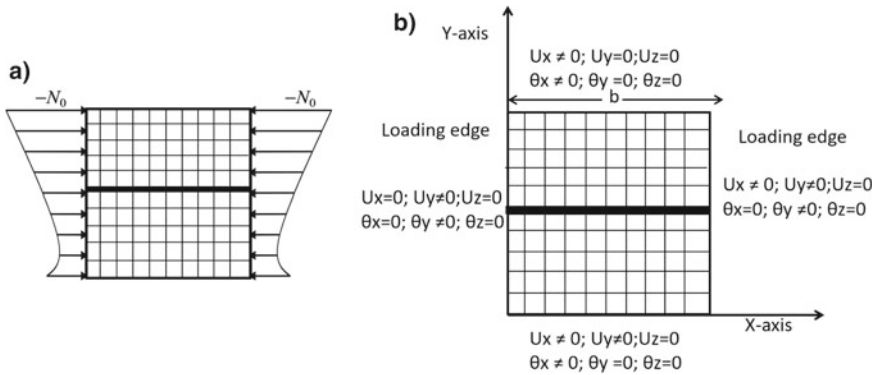


Fig. 2 Types of in-plane edge loading under present study, along the edge  $x = 0$



**Fig. 3** a Uniaxial quadratic loading ( $\beta = 1$ ) with centrally placed eccentric stiffener. b Selected meshing pattern and simply supported boundary condition with loading edges

**Table 1** Non-dimensional buckling load for isotropic plate with two orthogonal stiffeners under compressive loads relevant to previous literature mentioned below

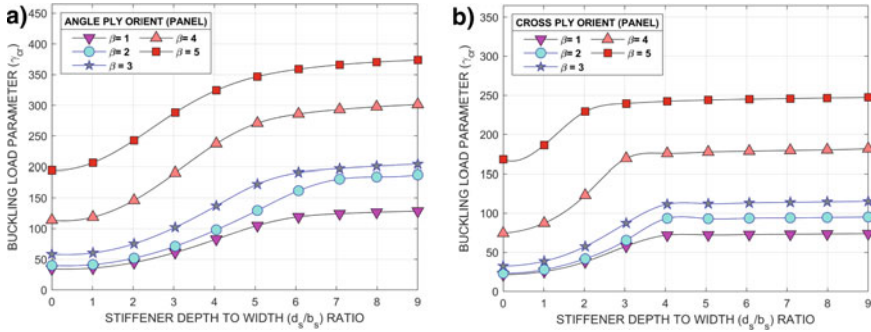
Load types	(Present) $10 \times 10$	[5]
Biaxial uniform	11.59	11.68
Biaxial parabolic	17.86	17.92

### 3 Comparative Studies

The assessment of present work with previous studies is essential to evaluate the accuracy and effectiveness of the buckling analysis. The results obtained for isotropic panel with two orthogonal stiffeners under biaxial compressive load types are validated with the results obtained by Hamedani and Ranji [5]. The present results obtained using the S8R5 element for plate and three-node quadratic B32 beam element for stiffener in ABAQUS [9] are found in good agreement with the literature (Table 1).

### 4 Results and Discussion

The buckling behaviour of a square composite panel of eight-layered symmetric laminate with thickness ratio  $t/b = 0.01$  and x-oriented stiffener placed at mid-position of 'y' axis is studied under various nonlinearly varying load patterns. The plate considered is analysed for different ply-orientations, while in the case of the stiffener, the fibre orientation considered remains parallel to the stiffener's axis.



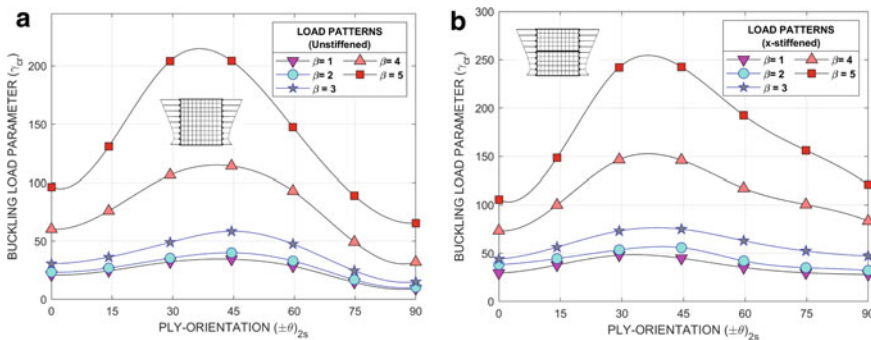
**Fig. 4** Variation in buckling load parameter with stiffener depth-to-width ( $d_s/b_s$ ) ratios for **a)** angle-ply  $(45/-45)_{2s}$  **b)** cross-ply  $(0/90)_{2s}$  configurations, under nonlinearly varying loads

### 4.1 Effect of Stiffener Depth-to-Width ( $d_s/b_s$ ) Ratio

The depth-to-width ratio of the stiffener ( $d_s/b_s$ ) is increased from 0 to 9 for angle-ply  $(45/-45)_{2s}$  and cross-ply  $(0/90)_{2s}$  configuration of ply sequence as shown in Fig. 4. It is seen that the buckling load increases with an increase in  $d_s/b_s$  ratio up to a certain extent, and after that, further increase in  $d_s/b_s$  ratio has no effect or minimal effect in the increase of buckling load. It is also observed here, and there is a change in the mode shape after a particular  $d_s/b_s$  ratio.

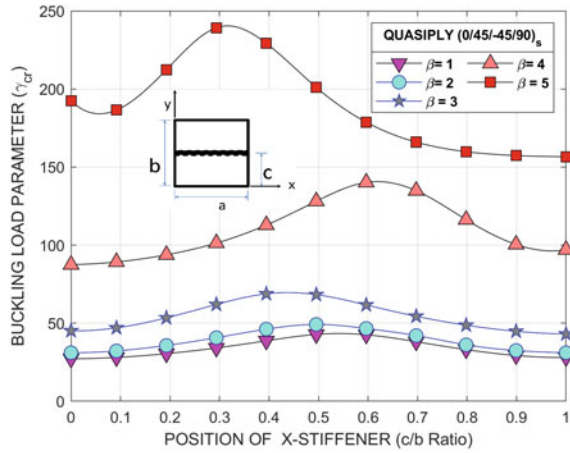
### 4.2 Effect of Ply-Orientation

Figure 5 shows that the effect of ply-orientation  $(\pm\theta)_{2s}$  is analysed without and with x-stiffener having  $d_s/b_s = 2$ , subjected to various non-uniform loads. It is observed



**Fig. 5** Variation in non-dimensional buckling load with different ply-orientations  $(\pm\theta)_{2s}$  for **a)** unstiffened panels **b)** x-stiffened panels with  $d_s/b_s = 2$ , under nonlinearly varying loads

**Fig. 6** Variation in buckling load parameter in different positions of x-stiffener along 'y' direction, under nonlinearly varying loads



that stiffened panels have higher buckling resistance when compared to an unstiffened plate due to improve in the stiffness of the stiffened panel. It is also seen that the ply-orientation angle for maximum buckling resistance is different for each of the nonlinearly varying loads.

### 4.3 Effect of Position of x-stiffener

The effect of the x-stiffener at different positions along 'y' direction is observed with  $d_s/b_s = 2$ , under nonlinearly varying loads for quasi-ply (0/45/-45/90)<sub>s</sub> configuration which is depicted in Fig. 6. The ratio of distance of x-stiffener from x-axis to width of the plate (c/b) is plotted against buckling load parameter. It is shown that the non-uniform loading pattern will seriously affect the maximum buckling load. There exist an optimal distance that gives maximum buckling load. For uniformly distributed load conditions, maximum buckling load occurs at mid-position of the y-axis, while for other cases, the position of maximum buckling load differs and is maximum where the loads are most concentrating.

### 4.4 Effect of Panel Thickness with Constant Stiffener $d_s/b_s$ Ratio

The effect of an increase in the panel thickness-to-width of plate (t/b) ratio is compared for unstiffened panel with that of x-oriented stiffened panel having  $d_s/b_s$  ratio = 2, placed horizontally at mid-position, for quasi-ply configuration. The buckling load increases with an increase in the panel thickness (t/b) ratio and is observed

that the stiffener effect is nullified for a higher panel thickness ratio (see Table 2). The difference ceases to exist for the panels with and without stiffener in the case of thick plates.

#### ***4.5 Effect of Increasing the Number of Stiffener***

The effect of adding the stiffeners to the angle-ply composite panel is analysed for buckling behaviour under various nonlinearly varying in-plane edge loads in Fig. 7. Panels without stiffener and with x-oriented, x- and y-oriented, equally spaced 3 x- and 3y-oriented stiffeners having  $d_s/b$  ratio = 2 are compared under various non-uniform loads. It is shown that adding stiffeners helps to better the buckling resistance of panel, irrespective of loading.

### **5 Conclusion**

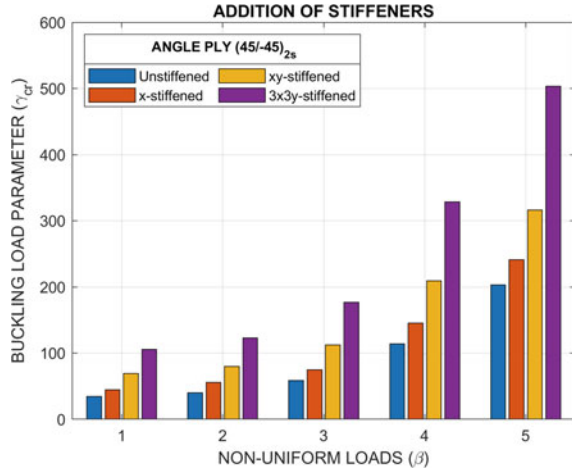
A comparison of buckling loads obtained under non-uniform loading conditions matches well with previous studies. The outcomes of the present analysis are:

- The increase in depth-to-width ratio shall improve the buckling load only up to a certain level, and after that, there is no significant difference.
- The sequence of ply-orientation of the panel has a significant effect on the stiffened panel's buckling behaviour.
- The position of stiffener for maximum buckling load differs under non-uniform loading conditions.
- Stiffened thick panels have no significant effect when compared with unstiffened thick panels.
- The plate in which maximum load concentrating toward the edges shows the highest buckling resistance.

**Table 2** Buckling load parameter for different  $t/b$  ratios of the panel with and without stiffener

$d_s/b_s = 2$	$t/b = 0.01$			$t/b = 0.015$			$t/b = 0.02$		
	Unstiffened	Stiffened	% age diff	Unstiffened	Stiffened	% age diff	Unstiffened	Stiffened	% age diff
$\beta = 1$	26.86	42.9	59.7	26.62	31.72	19.2	28.39	28.39	0
$\beta = 2$	30.35	49.18	62.0	30.09	35.96	19.5	32.11	32.11	0
$\beta = 3$	42.99	68.07	58.3	42.61	50.39	18.3	45.34	45.34	0
$\beta = 4$	88.03	128.83	46.3	87.17	101.38	16.3	92.06	92.06	0
$\beta = 5$	158.04	199.81	26.4	156.28	172.58	10.4	161.25	161.25	0

**Fig. 7** Variation in buckling load parameter with addition of stiffeners, subjected to nonlinearly varying loads



## References

1. Timoshenko, S.P., Gere. J.M.: Theory of elastic stability. New York, McGraw-Hill (1961)
2. Subash Chandra, K.S., Rajanna, T., Venkata Rao, K.: A parametric study on the effect of elliptical cutouts for buckling behavior of composite plates under non-uniform edge loads. *Latin Am. J. Solids Struct.* **17**(8), (2020)
3. Panda, S., Barik, M.: Flexural stability analysis of stiffened plates using the finite element method. *Comput. Assisted Methods Eng. Sci.* **24**(3), 181–198 (2018)
4. Guo, M.W., Harik, I.E., Ren, W.X.: Buckling behavior of stiffened laminated plates. *Int. J. Solids Struct.* **39**(11), 3039–3055 (2002)
5. Hamedani, S.J., Ranji, A.R.: Buckling analysis of stiffened plates subjected to non-uniform biaxial compressive loads using conventional and super finite elements. *Thin-Walled Struct.* **64**, 41–49 (2013)
6. Rajanna, T., Banerjee, S., Desai, Y.M., Prabhakara, D.L.: Effects of partial edge loading and fibre configuration on vibration and buckling characteristics of stiffened composite plates. *Latin Am. J. Solids Struct.* **13**(5), 854–879 (2016)
7. Patel, S.N., Sheikh, A.H.: Buckling response of laminated composite stiffened plates subjected to partial in-plane edge loading. *Int. J. Comput. Methods Eng. Sci. Mech.* **17**(5–6), 322–338 (2016)
8. Rajanna, T., Banerjee, S., Desai, Y.M., Prabhakara, D.L.: Effect of reinforced cutouts and ply-orientations on buckling behavior of composite panels subjected to non-uniform edge loads. *Int. J. Struct. Stab. Dyn.* **18**(04), 1850058 (2018). <https://doi.org/10.1142/S021945541850058X>
9. Dassault Systems Simulia Corp., Abaqus Analysis User’s Manual, Version 6.4, Providence, RI, USA (2009)

# Determination of Exact Optimal Tuning of Dynamic Vibration Absorbers to Control Vibration Due to Rotating Mass Unbalance



Anant J. Sheth and Utkarsh A. Patel

## Abbreviations

$m_0$	Primary system mass
$K_0$	Primary system stiffness
$c_0$	Primary system damping coefficient
$m$	DVA system mass
$k$	DVA system stiffness
$c$	DVA damping coefficient
$\mu$	DVA to primary system mass ratio
$Z_p$ or	Primary system damping factor
$\zeta_d$	DVA system damping factor
$\Omega$	Unbalance mass angular frequency
$\omega_0$	Primary system angular frequency
$\omega_d$	DVA system angular frequency
$f$	Frequency ratio
$g$	Forcing frequency ratio

## 1 Introduction

For the healthy functioning of any rotating primary system, it is necessary that the vibration caused must be within the proposed ISO limits. Through the condition

---

A. J. Sheth (✉)  
Gujarat Technological University, Gujarat, India

U. A. Patel  
Mechanical Engineering Department, L D College of Engineering, Ahmedabad, Gujarat, India



monitoring, we come to know about the root cause of the problem. For the unbalance problem, most of the industries would prefer offline balancing. In that case, dismantling rotor from the machine becomes mandatory. The industry would also be facing a problem of production loss. The other alternate way for vibration attenuation is attaching properly tuned dynamic vibration absorber. There are three types of DVA: (1) passive DVA, (2) active DVA and (3) partial active DVA. The basic idea of DVA is attaching a secondary lumped mass properly tuned DVA with the primary system. As it is properly tuned, it will absorb vibration from the primary system. The efforts for the determination of the optimal parameters for vibration control of undamped primary structure were carried out by attaching undamped DVA [1]. The natural frequency ratio, an optimal tuning parameter equation, was determined. The frequency control range was very small [1, 2]. The “fixed point theory” is the theory where all responses also called FRF curves pass through two points irrespective of damping factor. Brock had also derived an analytical solution for the optimum tuning for the damped DVA [3]. The optimal DVA parameters in the form of graphical representations were also presented [7]. Numerical optimization techniques such as a hybrid-coded genetic algorithm (HCGA) are used to optimize placement and properties of DVA. In contrast to the steepest descent approach for the determination of the optimal DVA parameters, a numerical technique ant colony optimization with parabolic technique was used [8]. Optimal parameters were also determined using a numerical search technique, and particle swarm optimization was also used [9]. For undamped DVA, optimization process was also carried out by the steepest descent mini–max method. The design constraints were used which include rattle space concept to limit the system motion [5]. The optimal tuning parameters were also derived by using Newton’s method [6]. The fixed point theory is revisited by considering the natural frequency ratio value one and other than one. The optimum damping ratio obtained from both the definitions is found different, but the tuning ratio obtained is same. For understanding the effect of the damping ratio, a numerical simulation of kinetic energy component of a simply supported beam with an optimum TVA was done and proved that the concept of fixed point may be used to obtain flat response for the continuous structure. With the help of equivalent linearization method, the complexity of analytical solution was vanished [14]. Here, the damping element was replaced by the equivalent stiffness. Thus, optimal parameter determination becomes simple [16] and the required refinement of the optimal parameters for DVA was carried out [2]. More accurate optimal equations were available. By using the Taguchi method, the optimal tuning parameters were determined and compared with the Anh method [17]. It is found that for reducing vibration in a narrow band of the frequency resonating, the method performs well relative to the solution proposed [13]. A geometrically modified DVA where damping agency of DVA is connected to ground directly was emerged. The optimal parameters were determined by using two numerical approaches; the first approach solves a set of nonlinear equations suggested by the Chebyshev’s equioscillation theorem. And, the other one minimizes a compound objective. Both the methods were applied to a undamped classical system which has no damping agency, and the outcome was compared with those that were obtained analytically. The modified Chebyshev’s

equioscillation theorem method was applied to determine the optimum damping factors for the damped DVAs attached with the damped system [11]. The solution techniques of  $H_\infty$  and  $H_2$  optimization problems for a geometrically modified dynamic vibration absorber (DVA) applied to damp vibration in beam structures are derived analytically. The reduction in maximum amplitude motion response of a beam using the DVA is compared with the proposed DVA. Numerical results show that the geometrically modified DVA with the optimum tuning has better vibration suppression of beam structures than the traditional design of DVA. Comparing the  $H_\infty$  and  $H_2$  optimization techniques for a beam under random force excitation shows that the DVA performs well with  $H_2$  optimum parameters compared to the  $H_\infty$  solution [12]. With the damping element, it is very difficult to determine exact solution for optimal damping factor. Using perturbation, the approximate solution is determined by considering lower-order terms. Here, the primary system damping is neglected [14]. Thus, by using perturbation method and L'Hospital rule with higher orders, the optimal damping factor as a function of mass ratio power series could be found for the rotating mass unbalance system. The optimal damping factor is determined using  $H_\infty$  as well as  $H_2$  optimization. The obtained results from analytical comparison with the approximate result were carried out [15]. The optimal damping parameter was obtained by using L'Hospital rule. The equation contains two parameters. One is mass ratio, and the other is negative stiffness constant. By putting value zero for the negative stiffness constant, the equation will become as same as that obtained by using fixed point theory, i.e., approximate optimal damping parameter equation [18].

## 2 Determination of Optimal Damping Factor of DVA for the Rotating Mass Unbalance System

The unbalanced system shown in Fig. 1 is excited by centrifugal force caused due to unbalance mass. The equation of motion is determined by using some dimensionless parameters.

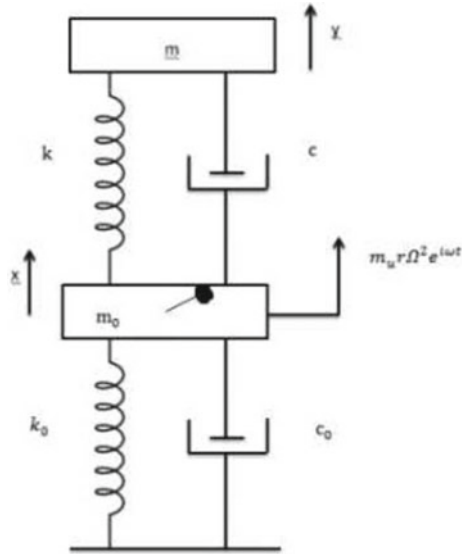
$$\mu = \frac{m}{m_0}, \omega_0^2 = \frac{k_0}{m_0}, \omega_d^2 = \frac{k}{m}, \zeta = \frac{c_0}{2\sqrt{k_0 m_0}},$$

$$\zeta_d = \frac{c}{2\sqrt{km}}, f = \frac{\omega_d}{\omega_0}, g = \frac{\Omega}{\omega_0}$$

$$(1 + \mu)\ddot{x} + \mu\ddot{y} + 2\zeta\omega\dot{x} + \omega_0^2 x = \frac{m_u}{m_0} r \Omega^2 e^{i\omega t} \tag{1}$$

$$\mu\ddot{x} + \mu\ddot{y} + 2\zeta_d \omega_d \mu \dot{y} + \omega_d^2 \mu y = 0 \tag{2}$$

**Fig. 1** Rotating mass unbalance damped system with damped DVA



The exact optimal damping factor of DVA is determined by using the perturbation method with higher orders of  $\delta$ .

$$\begin{aligned} \lim_{\delta \rightarrow 0} \zeta_d^2 &= \lim_{\delta \rightarrow 0} \frac{P_0 + P_1\delta + P_2\delta^2 + P_3\delta^3 + \dots}{Q_0 + Q_1\delta + Q_2\delta^2 + Q_3\delta^3 + \dots} \\ &= \lim_{\delta^2 \rightarrow 0} \frac{P_0 + P_1\sqrt{\delta^2} + P_2\delta^2 + P_3(\delta^2)^{3/2}}{Q_0 + Q_1(\delta^2)^{1/2} + Q_2\delta^2 + Q_3(\delta^2)^{3/2}} \\ \zeta_d^2 &= \frac{[g^2(f^2 - g^2)]^2 - [g^4 - (1 + f^2 f_{opt}^{-2})g^2]^2 \frac{2}{\mu(1+\mu)}}{4 \left[ \{fg(1 - g^2 f_{opt}^{-2})\}^2 - \left(\frac{2}{\mu(1+\mu)}\right)^2 - (fg^3)^2 \right]} \end{aligned}$$

By doing further rigorous mathematical operations with the L'Hospital rule, the following exact optimal damping factor equation for the DVA agency could be obtained.

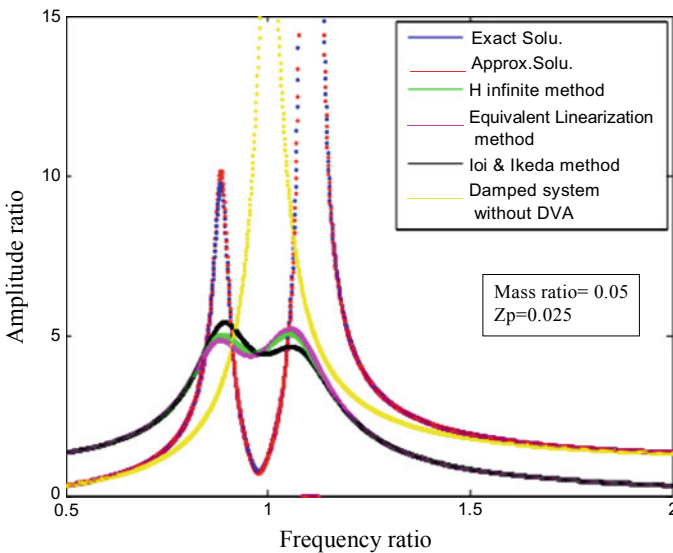
$$\zeta_{d(opt)} = \sqrt{\frac{4\mu^{10} + 12\mu^9 - 52\mu^8 - 188\mu^7 - 181\mu^6 - 52\mu^5 - 192\mu^4 - 129\mu^3 - 60\mu^2}{128\mu^6 + 128\mu^4 + 384\mu^2 + 1024\mu - 512}} \tag{3}$$

### 3 Comparison of Vibration Response of the Primary Unbalanced System and DVA with Exact Optimal Solution

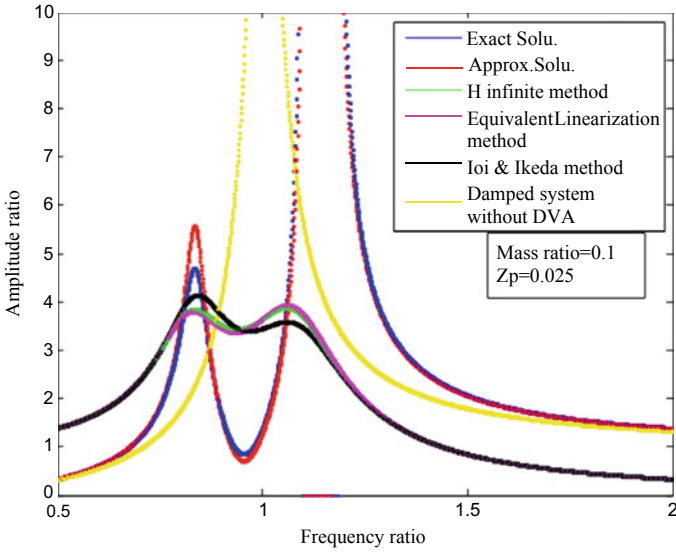
The aim behind finding the optimal mass ratio is to design DVA for the optimal response. For the mass ratio 0.1, the primary system amplitude pick is almost 5.5, while with the exact solution, it is 4.5 as seen in Fig. 3. Also, the results obtained with the equivalent linearization solution and the  $H_\infty$  solution are found to be performing well. In Fig. 2, responses for mass ratio 0.05 are compared with the above said listed methods.

The challenge here is to determine optimal mass ratio for the main system damping 0.025. In Fig. 4 as well as Table 1, we can see for the said primary system damping factor, the optimal mass ratio found was 0.128. Here, the numerical result shows that vibration reduction with the attached DVA was performing well with the exact solutions compared to the approximate solution,  $H_\infty$  method, equivalent linearization method and also the method proposed by Ioi and Ikeda.

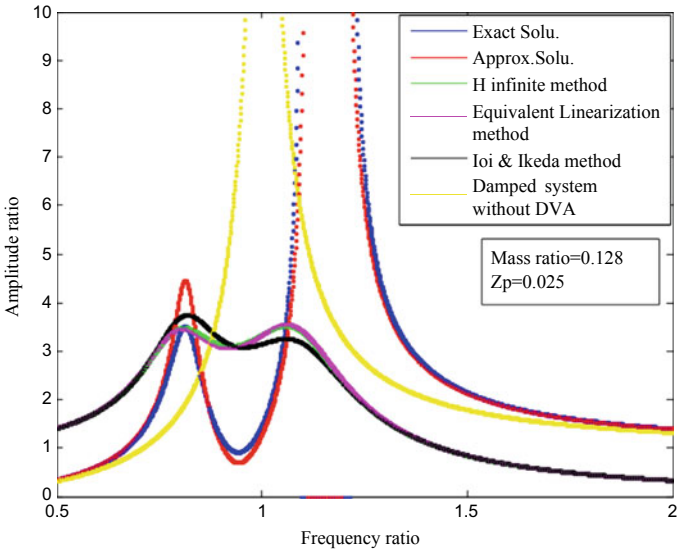
Going with the exact solution, the requirement of optimal damping factor value for 0–30% mass ratio is considerably less compared to the approximate solution. Up to 6% mass ratio, the optimal damping factor required for the classical system and approximate solution is almost equal, and after that, as in Fig. 5, the requirement differs. For mass ratio range 0.05 to 0.125, the required optimal damping factor with exact solution found to be reduced in the range of 85–75%.



**Fig. 2** Comparison of exact DVA solution to other solutions for the rotating mass unbalance system attached with DVA mass ratio 0.05



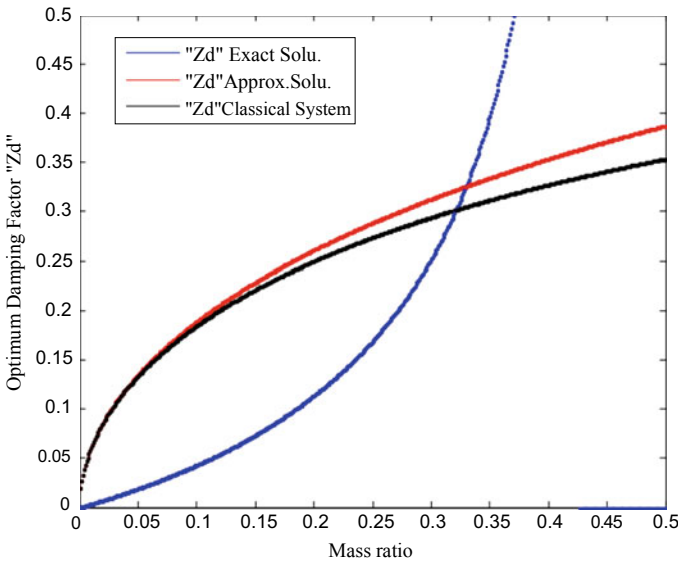
**Fig. 3** Comparison of exact DVA solution to other solutions for the rotating mass unbalance system with DVA mass ratio 0.1



**Fig.4** Comparison of exact DVA solution to other solutions for the rotating mass unbalance system with DVA mass ratio 0.128

**Table 1** Effect of mass ratio on the frequency response

Sr	Mass ratio	Remarks on frequency response amplitude
1	0.05	Exact solution and approximate solution responses are almost same
2	0.1	Exact solution and approximate solution responses differ by value 1 The frequency response is poor compared to other methods in comparison
3	0.128	Response with exact solution is appreciable compared to approximate solution. The frequency response is equal to other methods



**Fig. 5** Comparison of exact DVA optimal damping factor to other solutions for the rotating mass unbalance system with DVA

Referring Fig. 5, the percentage reduction in the  $\xi_d$  is almost 75% with exact solution in comparison with approximate solution for the optimal mass ratio 0.128. Thus, for designing passive linear DVA for the primary system having damping factor 0.025, one should use 12.8 % mass ratio for the optimal reduction in the frequency reduction curve.

### 4 Conclusion

The exact solution for the optimal tuning damping factor of a DVA coupled to a primary unbalanced system has been presented. The developed analytical solution is found to be investigated numerically by using MATLAB® with the conventional approximate solution, H∞ method, equivalent linearization method, solution

proposed by Ioi and Ikeda and system without DVA. With the numerical optimal mass ratio 0.128 and primary damping factor 0.025, appreciable primary system amplitude reductions are observed. Compared to the approximate solution results, the percentage reduction of optimal DVA damping factor with exact solution ranges 85% to 75% for the mass ratio range 0.05 to 0.125, respectively.

## References

1. Frahm, H.: Device for damping vibrations of bodies. U.S Patent No: 989, 958 (1911)
2. Den Hartog, J.P., Ormondroyd, J.: The theory of the dynamic vibration absorber. *Trans. Am. Soc. Mech. Eng.* **49**, A9-22 (1928)
3. Brock, J.E.: A note on the damped vibration absorber. *J. Appl. Mech.* **68**(A), 284 (1946)
4. Snowdon, J.C.: Dynamic vibration absorbers that have increased effectiveness. *Am. Soc. Mech. Eng.* (1974). <https://doi.org/10.1115/1.3438465>
5. Arora, J.S., Haug, E.J., Kwak, B.M.: Optimum design of damped vibration absorbers over a finite frequency range. *Am. Inst. Aeronaut. Astronaut. J.* **13**, 540–542 (1975)
6. Ikeda, K., Ioi, T.: On the dynamic vibration damped absorber of the vibration system. *Bull. Jpn. Soc. Mech. Eng.* **21**, 64–71 (1978)
7. Halsted, D.M., Randall, S.E., Taylor, D.L.: Optimum vibration absorbers for linear damped system. *J. Mech. Des. Am. Soc. Mech. Eng.* **103**, 908–913 (1981)
8. Ktinda, G.J., Rade, D.A., Steffen, V., Jr., Viana, F.A.C.: Tuned DVA by using Ant colony optimization. *Comput. Struct.* **86**, 1539–1549 (2008)
9. Leung, Z.H.: Particle swam optimization of tuned mass dampers. *Eng. Struct.* **31**, 715–728 (2009)
10. Dayou, J.: The fixed point theory revisited with new applications. *Archive Proc. Inst. Mech. Eng. Part C J. Mech. Eng. Sci.* **224**(C8), 1627–1634 (2009)
11. Coppola, G., Liu, K.: Optimal design of damped dynamic vibration absorber for damped primary systems. *Can. Soc. Mech. Eng.* **34**, 119–135 (2010)
12. Farshidianfar, A., Noori, B.: Optimum design of dynamic vibration absorbers for a beam based on  $H_{\infty}$  and  $H_2$  Optimization. *Arch. Appl. Mech.* **83**(12), 1773–1787 (2013)
13. Anh, N.D., Nguyen, N.X.: Design of non-traditional dynamic vibration absorber for damped linear structures. *Proc. Inst. Mech. Eng. C J. Mech. Eng. Sci.* (2014). <https://doi.org/10.1177/0954406213481422>
14. Argentini, T., Belloli, M., Borghesani, P.: A closed-form optimal tuning of mass dampers for one degree-of-freedom systems under rotating unbalance forcing. *J. Vib. Acoustics. Am. Soc. Mech. Eng.* **137**(034501), 1–6 (2015)
15. Shen, Y., Peng, H., Wen, S., Yang, S., Xing, H.: Analytically optimal parameters of fractional-order dynamic vibration absorber. *J. Vibroengineering* **18**(5), 2714–2734 (2016)
16. Awrejcewicz, J., Puzyrov, V.: On the optimum absorber parameters: revising the classical results. *J. Theoretical Appl. Mech.* 1081–1089 (2017)
17. Duong, D.T., Khang, N.V., Huong, N.T.V., Phuc, V.D.: A procedure for optimal design of a dynamic vibration absorber installed in the damped primary system based on taguchi's method. *Vietnam J. Sci. Technol.* **56**(5), 649–666 (2018)
18. Zhou, S, Jean-Mistral, C., Chesne, S.: Closed-form solutions to optimal parameters of dynamic vibration absorbers with negative stiffness under harmonic and transient excitation. *Int. J. Mech. Sci. Elsevier* (2019)

# Finite Element Analysis for Material Optimization of a Spur Gear by Radial Holes



Sanjay Sutar, G. C. Mohan Kumar, and Mrityunjay R. Doddamani

## 1 Introduction

Gears are the most preferred for motion and power transmission among all the mechanical components. The need for better gears design; advancement in gear technology continuously focuses on both the strength and weight of gear. By removing material or creating stress relief features in the stressed zone having circular, aero-fin and elliptical shape, researchers studied the stresses. Removing the material from gear makes gear lighter in weight. Creating holes of particular depth radially removes the material from gear and makes it lighter in weight. These holes can be utilized as an oil port for effectively improving the lubrication of the mating gears. G. C. Mohan Kumar et al. [1] studied the stresses and their distribution in gears upon optimization of gear tooth material weight. They created holes at different locations and dimensions parallel to the gear axis to optimize material volume inside the tooth, to reducing the gear weight. Few articles discussed on gear stress reduction and spur gear tooth stresses [2, 3] while the effect of material removal on bending stress and also optimization of spur gear [4]. Rajaprabakaran and M. Ashokraj [5] discussed the effect of different shaped holes in the gears to reduce stress concentration. They considered finite element model of spur gear with a three teeth segment having stress concentration reducing holes of various sizes and different locations. After studying the stress flow direction, they concluded that aero-fin-shaped holes give better results. M. Pramod Reddy and M. Santhosh [6] developed finite element

---

S. Sutar · G. C. Mohan Kumar (✉)

Polymer Composites Laboratory, Department of Mechanical Engineering, National Institute of Technology Karnataka, Surathkal, Mangalore 575025, India  
e-mail: [mkumargc@nitk.edu.in](mailto:mikumargc@nitk.edu.in)

M. R. Doddamani

Lightweight Materials Laboratory, Department of Mechanical Engineering, National Institute of Technology Karnataka, Surathkal, Mangalore 575025, India



model and studied the effect of hole size and hole location on tooth root stress. And, they summarized possibility to reduce the tooth root tensile stress without producing stresses in the holes greater than on an actual gear. And, similar studies for stress relieving using discontinuous geometries were discussed [7, 8]. Jakub Korta and R. Ramadani discussed optimization methods for design of lightweight gears [9, 10]. Umit Atila, Murat Dorterler, S Panda, Edmund S and Zhong Wan studied different methods for spur gear optimization [11, 12]. The present research work focuses on removing material from the gear tooth for developing lightweight gears. Circular holes are introduced radially through the gear tooth, and results obtained from the finite element method are discussed.

## 2 Design of Gear Pair

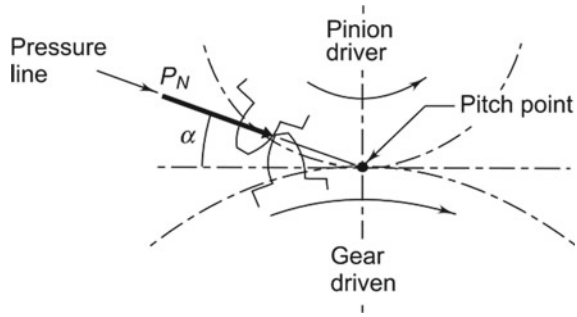
A spur gear pair of 20° full-depth involute systems with a fixed center of 100 mm and pinion rotating with speed of 360 rpm is considered. The involute gears and non-involute gears have distinguished advantages over each other. For an involute profile, the line of action between two curved surfaces is along the common normal to the two curves at the tangential point of contact. Table 1 shows specifications of the gear and pinion used for FEA analysis. The driving pinion tooth applies force  $P_N$  on the driven gear tooth. (Fig. 1). The force  $P_N$  combines the effect of tangential force  $P_t$  and radial force  $P_r$ . Torque transmitted by the gear for 0.5 kW power transmission is given as,

$$M_t = \frac{60 \times 10^6 (kW)}{2\pi N} \tag{1}$$

**Table 1** Specifications of gear pair

Parameters	Gear	Pinion
Pressure angle (degree)	20	20
Module(m)	5	5
Pitch circle diameter (mm)	100	100
Gear ratio	1	
Teeth count	20	20
Pitch circle radius (mm)	50	50
Addendum (1 m)(mm)	5	5
Dedendum (1.25 m)	6.25	6.25
Addendum circle radius(mm)	55	55
Dedendum circle radius(mm)	43.75	43.75
Base circle radius (mm)	46.98	46.98
Fillet radius (0.4 m)(mm)	2	2

**Fig. 1** Forces in meshed gear



**Table 2** Applied torque and forces for pinion

Applied torque and forces for pinion	Value
Applied torque(N-mm)	13,262.9
Tangential force $P_t$ (N)	530.52
Radial force $P_r$ (N)	193.09
Normal force $P_N$ (N)	564.56

The tangential force  $P_t$  acting on the gear for a given pitch circle diameter ( $d$ ) is calculated using torque transmitted by gear  $M_t$  (N-mm), power transmitted between gears kW (kilo watt) and speed of rotation  $N$  (rpm) by following equation,

$$P_t = \frac{2 \times M_t}{d} \tag{2}$$

Radial force  $P_r$  and normal force  $P_N$  are calculated as,

$$P_r = P_t \tan \alpha; \quad P_N = \frac{P_t}{\cos \alpha} \tag{3}$$

Table 2 shows different parameter values for pinion used for FEA analysis. Assuming tooth of gear as cantilever beam, the equation which considers bending stresses of gear and tangential component of force on gear is given as,

$$P_t = m \times b \times \sigma_b \times Y \tag{4}$$

Gear tooth of 20 teeth,  $20^\circ$  pressure angle, Lewis form factor of 0.320 and having 10 mm thickness with permissible bending stress  $16.57 \text{ N/mm}^2$  are considered for FEA analysis.

### 3 Gear Assembly in CREO Parametric

The gear assembly is modeled in CREO software. For generation of involute profile, CREO software uses parametric equations. Standard involute curve of a gear tooth can be generated by spinning straight line around the base circle of a gear. By spinning segment S around the base circle, endpoint A of a segment S gives involute profile (Fig. 2).

In CREO modeling, variable (t) varies from 0 to 1. Coordinates of involute (x, y) are generated by referring to point (x<sub>1</sub>, y<sub>1</sub>) which lies on involute curve. The coordinates (x, y, z) of an involute curve are given by the equation,

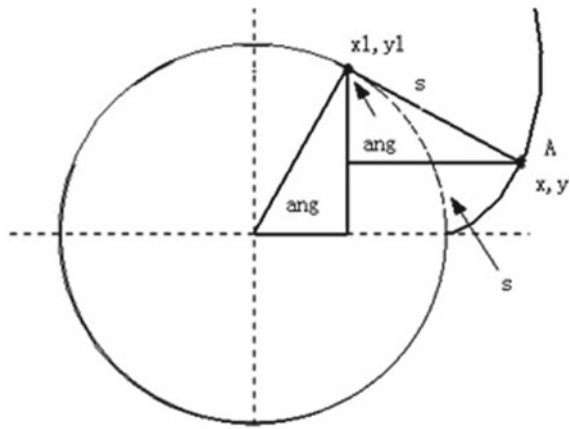
$$x = \text{base circle radius} \times \cos(t \times 90) + \text{base circle radius} \times \sin(t \times 90) \times t \times \pi/2 \tag{5}$$

$$y = \text{base circle radius} \times \sin(t \times 90) - \text{base circle radius} \times \cos(t \times 90) \times t \times \pi/2 \tag{6}$$

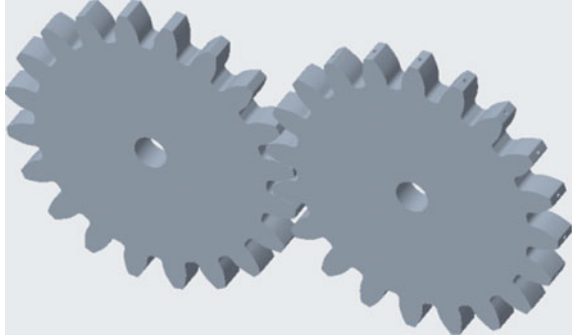
$$z = 0 \tag{7}$$

Inserting the above Eqs. (5), (6) and (7) in CREO software generates the involute curve. Figure 3 shows parametric spur pinion and spur gear assembly considered for FEA analysis.

**Fig. 2** Involute profile in Cartesian coordinate system



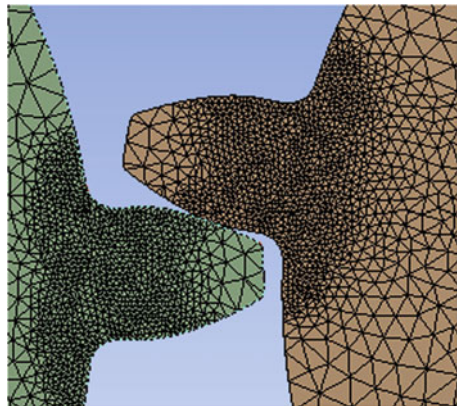
**Fig. 3** Parametric spur pinion and spur gear assembly



## 4 FEM Analysis

The CAD file (20 teeth gear and 20 teeth pinion gear assembly) from CREO is imported for analysis which has been carried out in Ansys Workbench 17.2. From the surface of the top land of pinion, holes were created with varying depths from 5 mm to 20 mm. The created holes of certain depth remove material from the pinion and make pinion lighter in weight. In FEA, studied the various stresses like equivalent stresses, top root stresses, bottom root stresses for both the pinion and gear. Finer mesh is provided near the root region for both pinion and gear. The depth of holes varying from 5 to 20 mm removes material which will reduce the cross-sectional area near the root region and affects variation in stresses values near the root region. Figure 4 shows element quality provided for pinion and gear assembly. The FEA analysis is carried out for boundary condition (Fig. 5) where rotation of gear is fixed and pinion given torque of 13262 N-mm.

**Fig. 4** Finite element model of gear pair



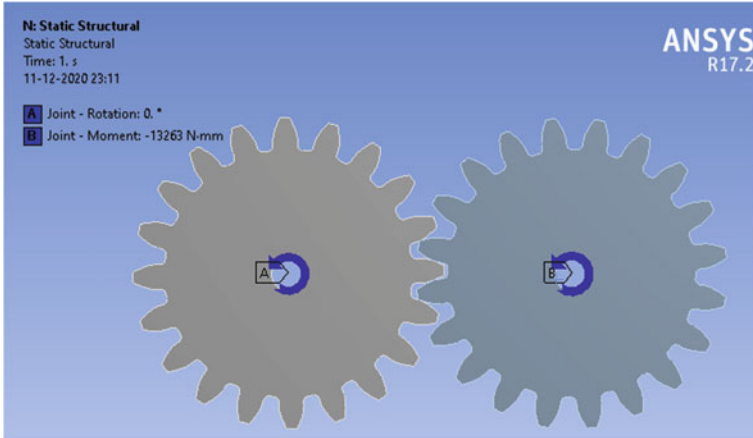


Fig. 5 Rotation of gear fixed and pinion torque of 13,262.91192 N-mm

### 5 Results and Discussion

For pinion and gear assembly for a radial hole of 5–20 mm depth, equivalent stress values at the top root stress and bottom root stress are shown in Figs. 6, 7, 8, 9,

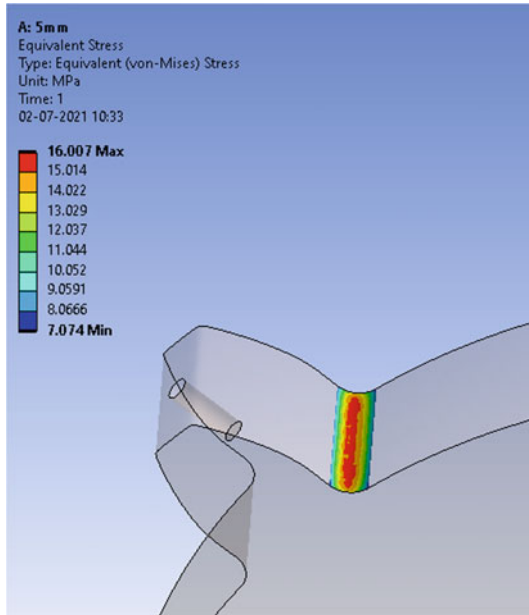
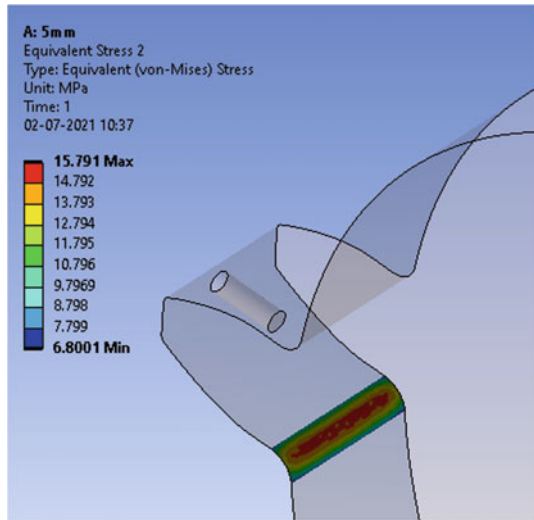
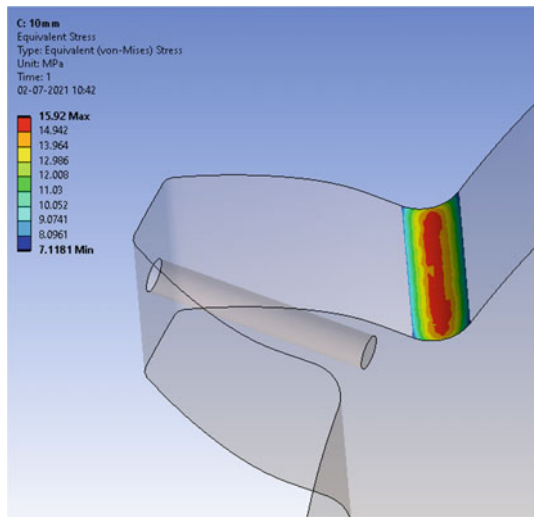


Fig. 6 5 mm radial hole pinion top root stress

**Fig. 7** 5 mm radial hole pinion bottom root stress

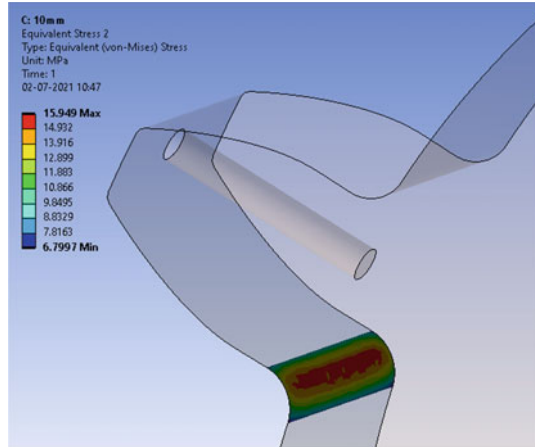


**Fig. 8** 10 mm radial hole pinion top root stress

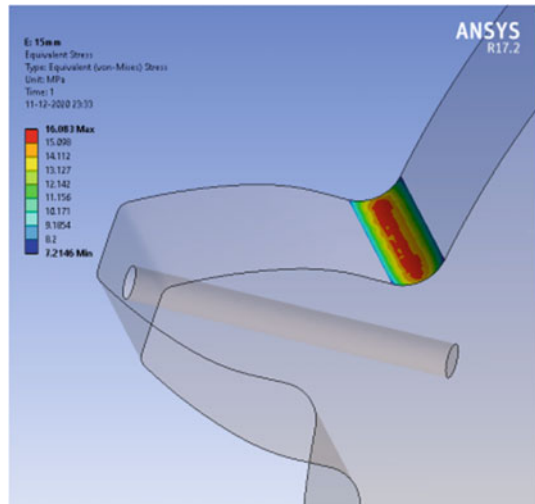


10, 11, 12 and 13. Top root stress values increase from 16.007 MPa to 16.083 MPa for a radial hole of 5–15 mm. The bottom root stress values increase from 15.791 to 16.024 MPa for a radial hole of 5–15 mm. For the gear which has fixed involute joint, equivalent stress values for top and bottom root stresses are 19.463 and 22.835 MPa, respectively. The equivalent alternating stress values for fatigue life evaluation for a radial hole of 5–mm depth are increasing from 37.817 to 38.09 MPa. (Figs. 14 and 15). Comparison of stress values with hole and without hole for pinion summarized in the graph is shown in Fig. 16.

**Fig. 9** 10 mm radial hole pinion bottom root stress



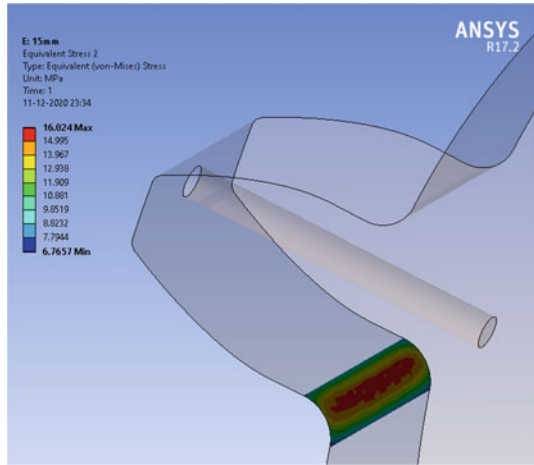
**Fig. 10** 15 mm radial hole pinion top root stress



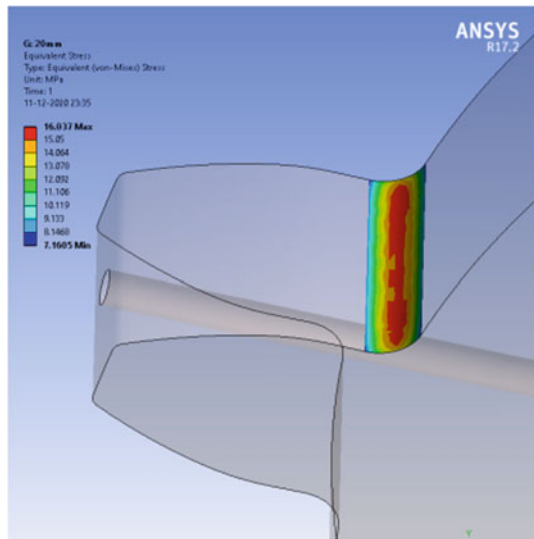
## 6 Conclusion

For a circular hole of 1.5 mm diameter for radial hole of 5 mm to 20 mm, minimum of 2.49% to a maximum of 12.451% volume reduction is achieved comparing with gear tooth having no radial hole; for which an increase in equivalent stress values at top root stress and bottom root stress for both pinion and gear is observed. As the depth of hole comes nearer to the root area for pinion, variation in equivalent stress values for the whole pinion body as well as root stress values for top and bottom region of the pinion is observed. Increasing the amount of volume reduction makes

**Fig. 11** 15 mm radial hole pinion bottom root stress



**Fig. 12** 20 mm radial hole pinion bottom root stress

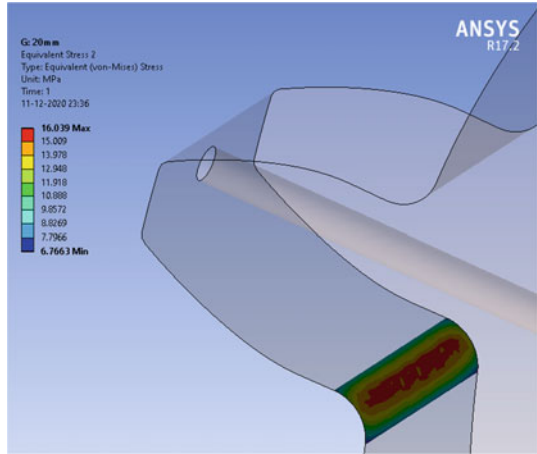


pinion lighter in weight at the expense of increased stress values which makes pinion weaker in strength. Regarding the stress distribution, the following can be stated,

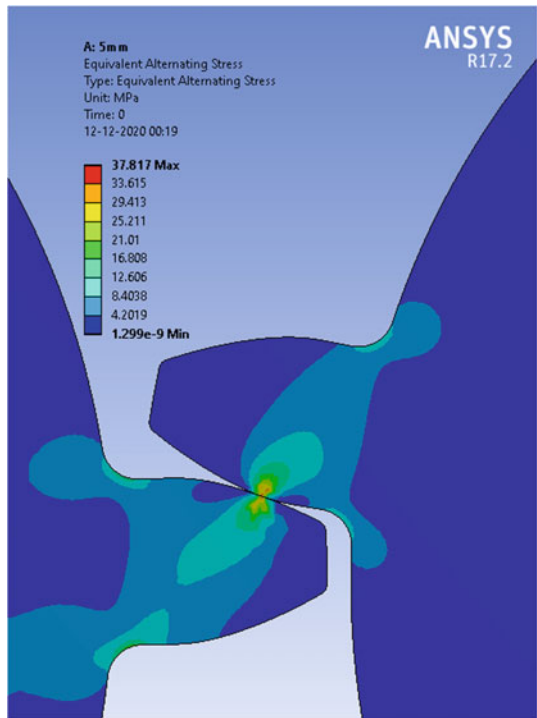
- (1) As per the basic theory, it is confirmed that for a smaller elemental area at the loading point, more stress concentration is observed.
- (2) For both pinions with hole and without hole type, higher stresses are observed at tooth bottom root as compared to the tooth top root.
- (3) It is better to have the depth of hole less than 20 mm so that up to 9.961% volume reduction can be achieved keeping the equivalent stress values well below the permissible limit of the material.



**Fig. 13** 20 mm radial hole pinion bottom root stress



**Fig. 14** Equivalent alternating stress for 5 mm radial hole



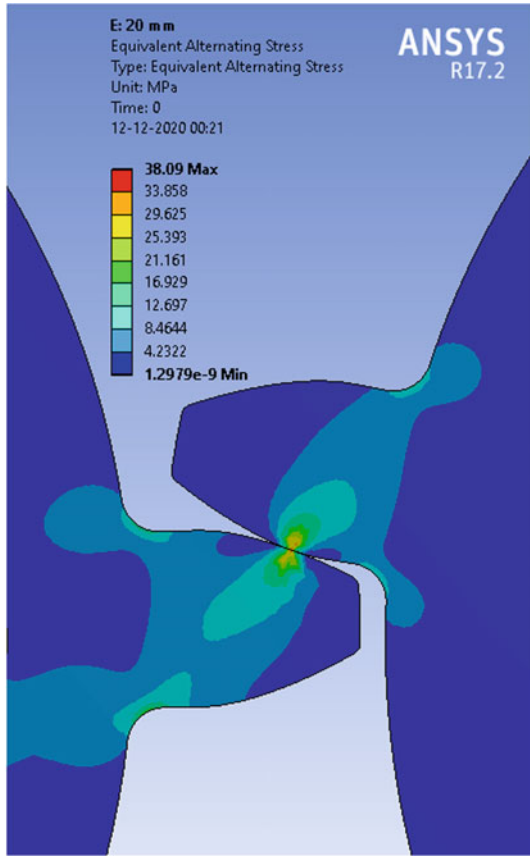


Fig. 15 Equivalent alternating stress for 20 mm radial hole

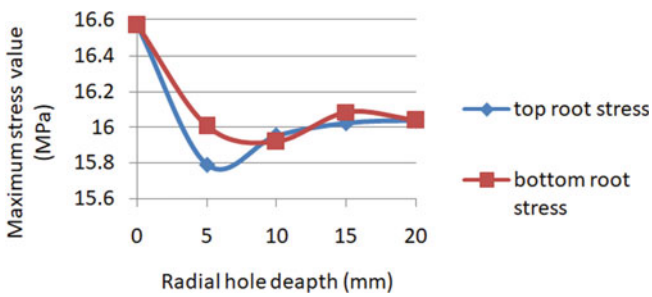


Fig. 16 Comparison of stress values with hole and without hole

## References

1. Mohan Kumar, G.C., Basheer, B., Sutar, S., Doddamani, M.: Material optimization of spur gear tooth, AIP Conference Proceedings **2247**, 020020 (2020). <https://doi.org/10.1063/5.0003865>
2. Ramachandra, R.: Analysis of stress reduction and spur gear tooth stress. *Int. J. Sci. Res. Sci. Technol.* **3**(1), 608–616 (2017)
3. Fredette, L., Brown, M.: Gear stress reduction using internal stress relief features. *J. Mech. Des.* **119**(4), 518–521 (1997). <https://doi.org/10.1115/1.2826398>
4. Pramod Reddy, M., Santhosh, M.: Spur gear tooth stress analysis and stress reduction using stress-reducing geometrical features. *Int. J. Mech. Eng. Technol.* **6**(9), 17–29 (2015)
5. Rathore, R.K., Tiwari, A.: Bending stress analysis and optimization of spur gear. *Int. J. Eng. Res. Technol.* **3**(5) (2014)
6. Rajaprabakaran, V., Ashokraj, R.: Spur gear tooth stress analysis and stress reduction. *IOSR J. Mech. Civ. Eng.* 38–48 (2014)
7. Muminovic, A.J., Muminovic, A., Mesic, E., Saric, I., Pervan, N.: Spur gear tooth topology optimization finding optimal shell thickness for spur gear tooth produced using additive manufacturing. *TEM J.* **8**(3), 788–794 (2019)
8. Badithe, M., Srikanth, S., Bodapalli, J.: Stress and reduction analysis of a spur gear tooth. *Int. J. Emerg. Technol. Adv. Eng.* **4**(3) (2014)
9. Korta, J., Mundo, D., Ambrogio, G., Folino, B., Shweiki, S., Filice, L.: Topology optimization and analysis of static transmission error in lightweight gears. *Adv. Italian Mech. Sci. Mech. Mach. Sci.* [https://doi.org/10.1007/978-3-319-48375-7\\_21](https://doi.org/10.1007/978-3-319-48375-7_21)
10. Ramadani, R., Belsak, A., Kegl, M., Predan, J., Prehan, S.: Topology optimization based design of lightweight and low vibration gear bodies. *Int. J. Simul. Model* **17**, 92–104 (2018). [https://doi.org/10.2507/IJSIMM17\(1\)419](https://doi.org/10.2507/IJSIMM17(1)419)
11. Atila, U., Dorterler, M., Durgut, R., Sahin, I.: A comprehensive investigation into the performance of optimization methods in spur gear design. *Eng. Optim.* <https://doi.org/10.1080/0305215X.2019.1634702>.
12. Dorterler, M., Sahin, I., Gokçe, H.: A grey wolf optimizer approach for optimal weight design problem of the spur gear. *Eng. Optim.* **51**(6), 1013–1027 (2019). <https://doi.org/10.1080/0305215X.2018.1509963>

# Inhibiting COVID-19 Transmission in India Through Design of Automated Contactless Face Mask Vending Cum Disposal Machine with Self-Sterilization Unit



Aniruddha Ghosh, Rajendran Dinesh Kumar, and Varthini Rajagopal

## 1 Introduction

SARS-CoV-2 is a deadly viral pandemic disease of the twenty-first century which inhibited human mobility across the globe. Though its mortality rate is less compared to other pandemics (Black Death in fourteenth century and plague in nineteenth century), COVID-19 has a higher transmission rate and is predicted to affect almost 70 percentage of the Indian population at the end of 2021. [1, 2] Few countries across the globe are in the process of developing vaccine against COVID-19. However, the vaccine will be available to the public after clearing the clinical trials and obtaining regulatory permissions which would roughly include a year period. Ninety percentage research on SARS-CoV-2 reports COVID-19 as an aerosol disease, and the transmission occurs through nucleic acid in saliva and nasal fluid. As a precautionary measure from the possible infection, many countries have mandated the use of face mask. Various kinds of face masks provide users with varying levels of safety. Reusable models comprise half/complete facepiece respirators with attached filtration systems and fabric/cloth masks, whereas disposable models consist of surgical (3/4 ply) masks, N95 and KN95. Indian people prefer using surgical and fabric masks because of their cost-effectiveness. [3] Studies have shown that fabric masks generally made with cotton and synthetic fabric have far greater pore size as compared to that of SARS-CoV-2 (i.e., 60–140 nm) and do not effectively filter the virus. [3, 4] The surgical face masks are made with polymers like polypropylene, polyurethane, polyacrylonitrile, polystyrene, polycarbonate, polyethylene or polyester. A 3-ply surgical

---

A. Ghosh

Cooch Behar Government Engineering College, Cooch Behar, West Bengal 736170, India

R. D. Kumar (✉)

National Institute of Technology Srinagar, Indian Institute of Technology, Guwahati, India

V. Rajagopal

Government Engineering College Srirangam, Tiruchirapalli, Tamil Nadu 620012, India

facemask is made of three layers: an inner hydrophilic layer made of soft fibers that absorbs moisture and sweat; a middle layer of melt-blown filter developed by traditional micro- and nano-fiber processing where melted polymer is extruded through small nozzles with high-speed blowing gas; and an outer layer made of water-resistant non-woven fibers that repels virus-laden respiratory droplets and fluid spills. A 4-ply surgical face mask has an additional active carbon filter fiber layer in comparison with 3-ply masks. [4] Because of their higher virus-filtration efficiency as compared to cloth masks and cost-effectiveness as compared to N95 and KN95 masks, surgical face masks are gaining a huge demand among Indians. However, the extensive utilization of surgical face masks has led to their inappropriate disposal in public areas resulting in community transmission since SARS-CoV-2 virus can sustain at any temperature less than 50 degrees for more than 18–24 h. This creates a need for design of automatic face mask vending cum disposal unit with self-sterilization system as suggested by WHO. [5, 6] Though many researchers have designed automated vending and disposal unit for applications ranging from recycled papers to sanitary pads [7–9], no work has been reported on the design of integrated vending and disposal of surgical face masks. Hence, our work has attempted to address this research gap by designing an integrated face mask vending cum disposal machine with self-sterilization unit to support our country during this pandemic and inhibit the COVID-19 spread through disposed face masks.

## 2 Design of Automated Face Mask Vending Cum Disposal Machine

The proposed prototype consists of three modular units: (1) face mask vending unit, (2) face mask disposal unit and (3) sterilization unit.

### 2.1 Face Mask Vending Unit

The face mask vending unit is an air-controlled chamber consisting of a chassis (see Fig. 1) and a rotating glass door of dimension  $1166.40 \times 1060.00 \times 35$  mm (see Fig. 1). The chassis is made of a 20 mm thick sheet metal and consists of (i) 7 separators or trays (each of 10 mm thickness and separated by a gap of 125.64 mm) which holds the masks, and (ii) five helical springs in each tray placed perpendicular to tray axis and positioned against the face mask and (iii) a mask-collecting unit made of 50 mm thick sheet placed below the trays and (iv) a conveyor unit (see Fig. 1) at the bottom end of chassis. Each helical spring is connected to an electric motor [7, 10]. The helical spring (see Fig. 2) designed with helix feature of a circle diameter 48 mm, height 550 mm, pitch 40 mm and start angle 0 degree in anticlockwise direction. Then, using the sweep feature of a circular profile and with diameter of 5 mm, the

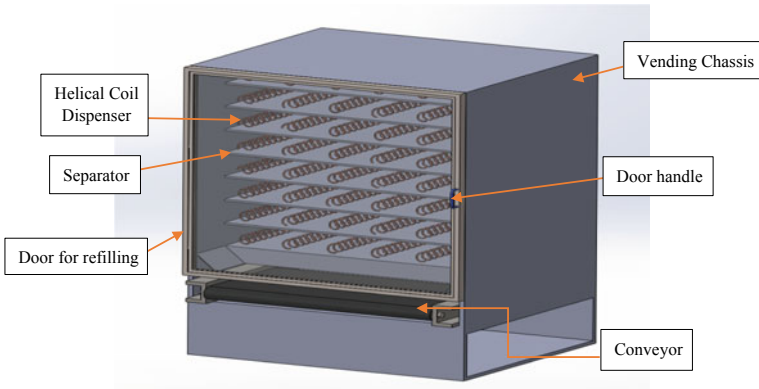


Fig. 1 Assembled vending unit (3D view)

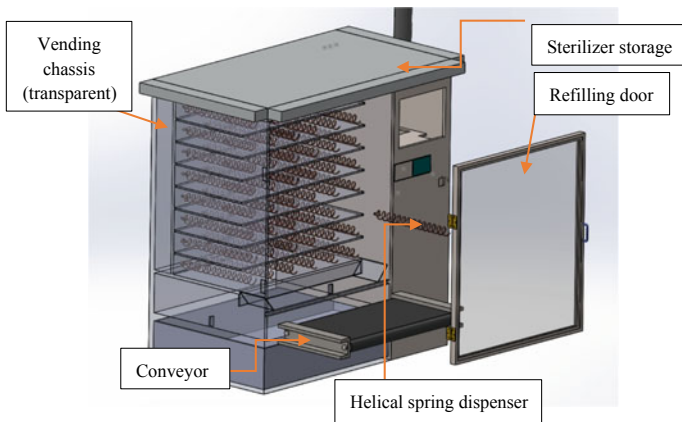


Fig. 2 Exploded vending unit

thickness of the spring is designed. To align the designed helical spring with the electric motor's hollow shaft axis, an extended portion has been added to the helical spring with same thickness at one end (see Fig. 2). The shaft is 40 mm long and 15 mm outside diameter and 5 mm inner diameter. The keys are made with reference English standard keyway and key sizes. A collar of 2 mm thickness and 20 mm diameter is added to constraint the linear motion of the shaft. The conveyor has two rollers (see Fig. 2) of length 900 mm and diameter 60 mm and constrained between two clamps. At the ends of each roller, a shaft of 30 mm diameter and 30 mm length is provided for power transmission. One of the extended shafts is powered by an electric motor rotating at 80 rpm.

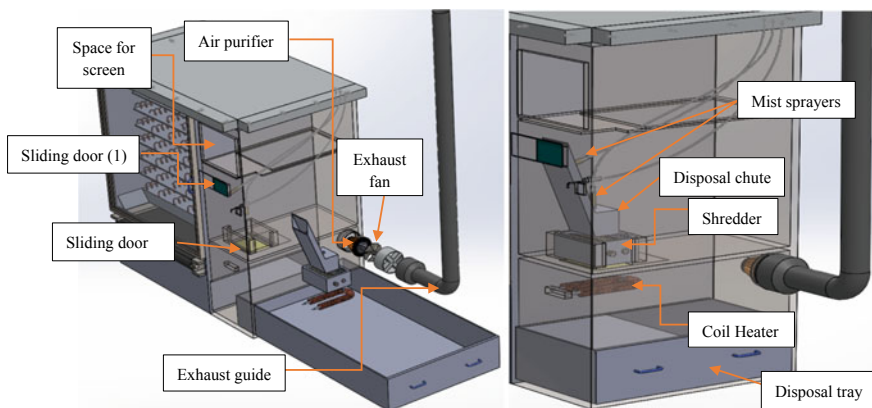
When a user selects the vending option button in the automated machine, the electric motor aligned with the helical spring rotates at 30 rpm and the helical spring exerts a pushing force onto the mask packet located in the tray, and the mask is

released from the tray and drops into the mask-collecting unit within 2 s. The roller conveyor then moves the mask from the mask-collecting unit to the user, thereby achieving a contactless transaction. The capacity of vending unit will be 450 mask units after which the vending unit can be restocked by opening the vendor sliding door. The 3D view of the assembled vending unit is given in Fig. 1.

## 2.2 Face Mask Disposal Unit

The disposal unit consists of (i) disposal chassis, (ii) shredder unit, (iii) firing unit, (iv) glass insulators, (v) exhaust unit and (vii) sanitizer unit. The disposal chassis (see Fig. 3) has three compartments separated by two horizontal plates each with 20 mm thickness. The soiled masks are fed through a chute in the intermediate compartment. The soiled face mask in the chute (see Fig. 4) is sterilized using two alcohol mist sprayers (see Fig. 4). The sanitizer supply to the mist sprayers is provided by a sanitizer/sterilizer storage unit (see Fig. 4) located in the top compartment. The outside of the intermediate compartment also holds a sensor-activated sprayer/tap (see Fig. 5) which enables the user to sanitize his hands before and after vending and/or disposing the face mask. After sterilization of the soiled masks, the chute drops them into the shredding unit located in the intermediate compartment. The bottom compartment houses a disposal tray (see Fig. 3) consisting of the firing and exhaust units. The exploded and assembled views of the disposal unit are given in Fig. 3.

The soiled masks after sterilization are first cut by the shredding unit (see Fig. 3) in the intermediate compartment. The shredding unit consists of two columnar series of shredder blades. Each shredder blade is of diameter 90 mm, thickness 10 mm and circumference  $\sim 283$  mm with a rotational speed of 100 rpm. With this specification,



**Fig. 3** Exploded view [left] and assembled view [right] of disposal unit with transparent chassis (3D view)

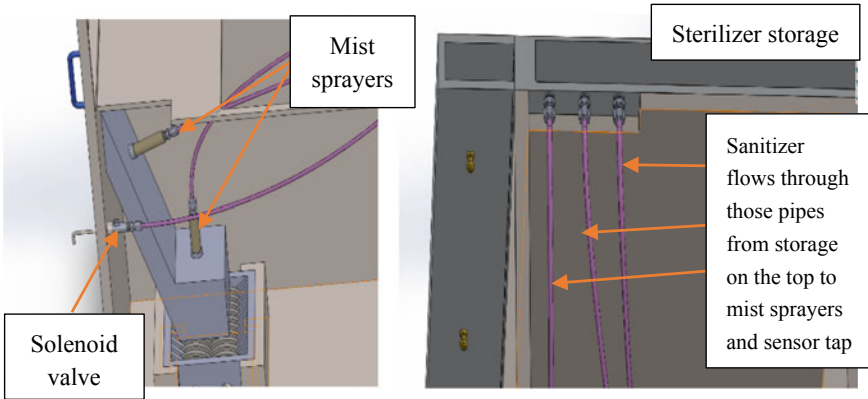


Fig. 4 Intermediate compartment of disposal unit

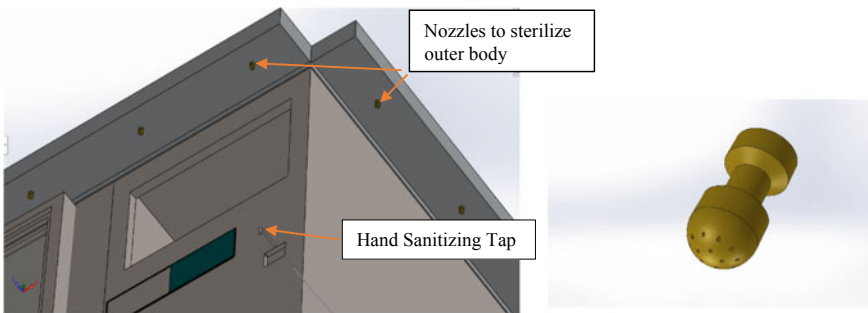


Fig. 5 Self-sterilization unit [left] and nozzles [right] (3D view)

the soiled masks are shredded within 3–5 s. The shredded pieces are then dropped into the firing unit located in the disposal tray (see Fig. 3). The firing unit consists of a heating coil (see Fig. 3) of 1000 W power and can heat up to a temperature of 400 degree Celsius at which the shredded mask completely burns into ash. The soiled masks are burned as the mask might contain contagious COVID-19 viruses, and reusing of the soiled mask after treatment is not recommended since the presence of even a 0.001% error in the treatment process would drastically enhance the virus transmission [11, 12].

The exhaust unit in the bottom compartment consists of air purifier, exhaust fan, exhaust holder and guide. The exploded view of the exhaust unit is shown in Fig. 3. The fumes generated during the firing process will be treated using an air purifier (see Fig. 3) before releasing into the atmosphere through an exhaust guide. The purified fumes are captured by an exhaust fan (see Fig. 3) and released through an exhaust guide (see Fig. 3). Two sliding doors are provided at the disposal unit. The sliding door (1) (see Fig. 3) is opened to accept used mask in disposal unit, and the sliding door (2) at the bottom of shredder floor (see Fig. 3) is opened after action of shredder



and acts as an insulator and protects the other components of disposal unit from the heat and fire generated from the heating coil, because the previous chamber has higher percentage of rich alcohol sanitizer mist. Whole inner side of disposal unit has glass wool coating to insulate heat from outer environment.

There is a blank square space/hole at the front of the top compartment of disposal unit to fit a voice-recognized/button-accessed screen or monitor and necessary electronics to take commands from user and to deliver information to user (see Fig. 3).

### ***2.3 The Sterilization Unit***

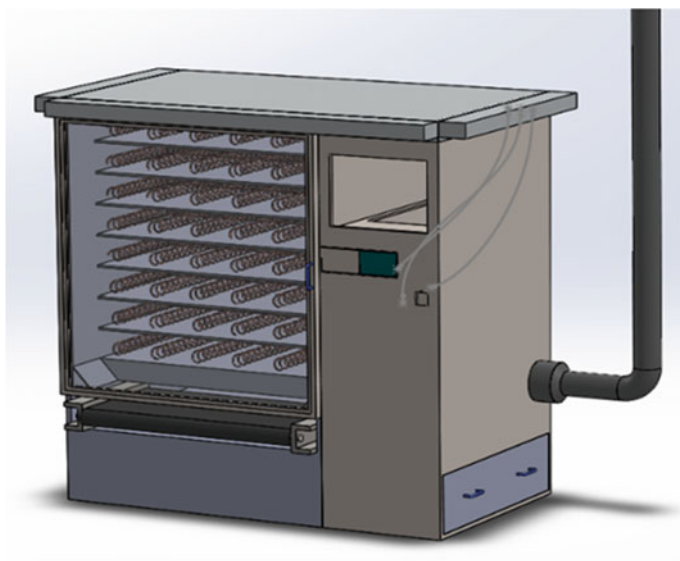
The sterilization units are installed across three sections: Sterilization unit 1, housed in the front face of the intermediate compartment of the disposal chassis, enables the user to sanitize his/her hands before and after using the machine (see Fig. 4) and is operated by a sensor and solenoid valve [13, 14]; the second unit is installed across the chute in the disposal unit to sterilize the chute and shredder units (see Fig. 4); and the third unit (named as the self-sterilization unit) functions to sanitize the automated machine completely once in two hours making the machine viral-free for the users. The self-sterilization unit consists of three flanges placed at the side and front faces of the machine. Each flange is provided with four nozzles (see Fig. 5) facing downward. These nozzles spray the sanitizing alcohol which is fed from the sanitizing storage unit situated on the top of machine chassis. The proposed automated face mask vending cum disposal machine with self-sterilization unit is shown in Fig. 6.

## **3 Conclusion**

This automated vending cum disposal unit of 3/4 ply mask offers a superior solution to prevent the spread of COVID-19 due to usage of disposable face masks in bus stand, railway station, airport, hospitals, mall, temples and other public places.

## **4 Future Work**

Structural analysis of the designed prototype can be performed. The fabrication of the vending cum disposal unit can also be carried out to determine the cost-effectiveness of the prototype.



**Fig. 6** Automated mask vending cum disposal machine

## References

1. Author, F.: Article title. Journal **2**(5), 99–110 (2016) Kasilingam, D., Prabhakaran, S.P.S., Dinesh Kumar, R., et al.: Exploring the growth of COVID-19 cases using exponential modelling across 42 countries and predicting signs of early containment using machine learning. *Transbound Emerg Dis* (2020). <https://doi.org/10.1111/tbed.13764>
2. Rajendran, D.K., Rajagopal, V., Alagumanian, S., et al.: Systematic literature review on novel corona virus SARS-CoV-2: a threat to human era. *VirusDisease* **31**, 161–173 (2020). <https://doi.org/10.1007/s13337-020-00604-z>
3. Sudhir, P., Delma, D.: Comparison of body image perception and the actual BMI and correlation with self-esteem and mental health: A cross-sectional study among adolescents Sudhir. *Int. J. Heal. Allied. Sci.* **7**, 145–150 (2018). <https://doi.org/10.4103/ijhas.IJHAS>
4. Chua, M.H., Cheng, W., Goh, S.S., et al.: Review article face masks in the new COVID-19 normal : materials, testing, and perspectives. *Research* **2020**, 40 (2020)
5. WHO: Water , sanitation , hygiene and waste management for the COVID-19 virus (2020)
6. Methods SD (2020) COVID-19 | Coronavirus Report : 2020–03–09 COVID-19 | Coronavirus Report : 2020–03–09
7. Olutoye, M. a: Design of a manually operated paper-recycling machine. *Leonardo Electron J Pract Technol* 49–54 (2005)
8. Torque, C.: Calculating torque, shear force and diameter of the shaft (2011)
9. WHO: Cleaning and Disinfection of Environmental Surfaces in the context of COVID-19 (2020)
10. Raut, M.A.B.: Design and fabrication of paper shredder machine. *Int. J. Res. Appl. Sci. Eng. Technol.* **6**, 485–492 (2018). <https://doi.org/10.22214/ijraset.2018.4084>.
11. Jain, P., Gupta, C.: Textile Recycling Practices in India: a Review. *Int. J. Text Fash. Technol.* **6**, 21–36 (2016)
12. Ryan, S.W.: SANTARY NAPKIN WITH BRAID. *Syst. Method Program. a Weigh. Scale Usinga Key Signal To Enter a Program. Mode 1:14* (2009)

13. Oluwole, O.I., Samuel, T.A., Adeolu, A.A., et al.: Design and fabrication of waste paper recycling machine for laboratory and medium scale operation. *J. Prod. Eng.* **22**, 19–24 (2019). <https://doi.org/10.24867/jpe-2019-01-019>.
14. Lander, C.W.: Disposal bag and system for disposing of sanitary product. 1 (2007)

# Investigation on Mechanical Behaviour of Kenaf Fabric/Bio-Epoxy/Egg-Shell Powder Reinforced Composites for Medical Applications



M. Nalla Mohamed and G. VR. Sakthivel

## 1 Introduction

A human bone is a rigid frame for the body tissues and also saves internal organs from impact forces [1]. The thigh bone known as femur in the leg is used for walking or jumping. When load applied on the bone exceeding its strength, fracture occurs [2]. A break in the continuity of bone, either on a macroscopic or microscopic level is termed as fracture. Orthopaedic surgeons have been using metallic plate in the fracture site to promote bone structure stabilization, if a bone fracture occurs [3]. These metallic plates are usually made of titanium alloys and stainless steel which cause problems like corrosion and delay in fracture healing, metal incompatibility [4–6]. The difference in stiffness of bone and metallic fixator gives rise to misalignment or loosening between the implant and bones [7]. Thus, alternative materials with similar stiffness of bone have been under research for the past few decades. Since natural fibre reinforcements are in abundance, hence, the increase in utilization of the biodegradable natural fibres can be seen in the past few years [8]. Unlike metal fixators, Kenaf fibre reinforced composites can be made with mechanical stiffness closer to that of bone properties [9, 10]. The performance of composite materials is scientifically predicted through their mechanical properties. The mechanical strength of composites depends on interfacial bonding as well as the constituents strength, and the stiffness of the composite depends on weight fractions of the constituents. During formation of composites, the interfacial bonding is more important than the fibre failure because the composite structure exists only when its interfacial bonding between the matrix and reinforcements is maintained. Therefore, natural fibres are treated with alkaline solution to increase the surface adhesion property and, finally,

---

M. N. Mohamed (✉) · G. VR. Sakthivel

Department of Mechanical Engineering, Sri Sivasubramaniya Nadar College of Engineering, Kalavakkam, Kancheepuram District, Tamilnadu, India  
e-mail: [nallamohamedm@ssn.edu.in](mailto:nallamohamedm@ssn.edu.in)

to exhibit better interfacial bonding with the matrix. Though many researchers have conducted study of alkali treated unidirectional natural fibres and their effect [10, 11], but still related to woven fabric is very rare. The mechanical properties of natural fibre reinforced composites can be further enhanced by filler inclusions [12–15, 17] such as egg-shell powder, fly ash, etc. However, the study of combined effect of fillers and alkali treated fibres on properties of reinforced composites is very limited. Moreover, there is no work so far to identify the feasibility of alkaline-treated Kenaf fabrics / biodegradable epoxy resin composite with and without fillers alternative to metallic bone plate by evaluating the tensile properties as per ASTM standards. Hence, the objectives of the presents research work are, (i) to produce the kenaf-based bio-composite with different compositions of fly ash / egg-shell powder. (ii) to study tensile properties of kenaf-based bio-composites (iii) to compare results of tensile properties of different compositions of kenaf-based composites with orthopaedic femur bone to suggest suitable bio-materials for orthopaedic implant plate.

## 2 Materials and Methods

### 2.1 Material

The kenaf fabric was plain woven by weavers of Anakaputhur, India, having mass of 300 GSM. The chemical composition of kenaf fabric is 20.1% lignin, 44.4% cellulose and 4.6% ash. Tensile modulus (GPa) and tensile strength of the kenaf fabric are 53 GPa and 400–900 MPa, respectively. Bio-epoxy resin Grade 3554-A and hardener 3554-B were used as matrix for the present analysis since these resins are commercially available in the market. There are abundance amounts of fly ashes as by-product in Thermal Power Plant, from where it is obtained and sieved to fine particles of size 500  $\mu\text{m}$ . Similarly the egg-shells collected from poultry form were washed in water and dried in atmosphere. Then they were well ground into smaller fragments using grinding machine and later carbonized. Both uncarbonized and carbonized egg-shell power were used in this study. The egg-shell particles too were sieved to fine particles of 500  $\mu\text{m}$ . Then these sieved fillers were introduced into matrix medium.

### 2.2 Methods

The cell wall of kenaf fibres contains complex compounds such as lignin, hemicellulose and other strains of oil wax, etc. These complex compounds can be removed by drenching the fibres thoroughly in solution of 6 wt. % NaOH for 3 h and allowed to dry at room temperature (27 °C) in dust free atmosphere for nearly 24 h. After treating with NaOH, the fibres thoroughly rinsed by distilled clear water and again allowed

to dry for 12 h and finally kept in hot oven which was to be maintained around 60 °C. The hot dry air removes the trapped moisture content underneath the fibre tangles. Non-treated kenaf fabric-based composites were also used for comparison purpose.

### 2.3 Preparation of Composite Specimen

In this study, hand layup process was utilized to fabricate all composite specimens. Wooden mould of size 500 × 500 × 5 mm was prepared for making composite laminates. Bio-epoxy with fly ash particles / egg-shell particles at various weight percentages (5, 10, 15, 20 and 25%) was prepared by stirring for 5–10 min. Four kenaf fabric were laid one over the others in the prepared homogeneous mixture. The air bubbles are usually formed while curing which create cavities, hence during curing, pressure force of dead weight was gradually applied upto 25kgf on the top of the mould, and the curing of laminates takes place for 24 h at room temperature free from moisture. The weight percentage of matrix medium, reinforcements and along with filler constituents is shown in Table 1. The overall density of composite plates was determined both experimentally as per ASTM: D792 standard as well as theoretically by Eq. (2) taking void into the account by Eq. (1).

$$V_c = \frac{\rho_{ct} - \rho_{ce}}{\rho_{ct}} * 100 \quad (1)$$

$$\rho_{ct} = \frac{1}{\left( \frac{W_f}{\rho_f} + \frac{W_r}{\rho_r} + \frac{W_{fi}}{\rho_{fi}} \right)} \quad (2)$$

### 2.4 Tensile Test

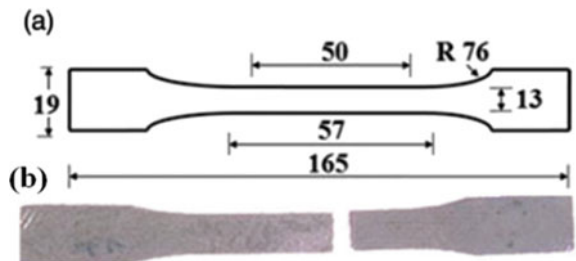
The tensile tests specimen, as shown in Fig. 1, was machined from the composite specimen according to the ASTM D: 638 test standards. The tensile strength of the specimens was determined using data acquisition UTM, having 60 tonnes capacity. Cross-head displacement was maintained at the rate of 5 mm/min, displaced till the specimen got ruptured. The tests were conducted on all the specimens. In order to ensure the repeatability of the results, minimum of three samples are tested at each sample type.

**Table 1** Prepared composite laminated samples

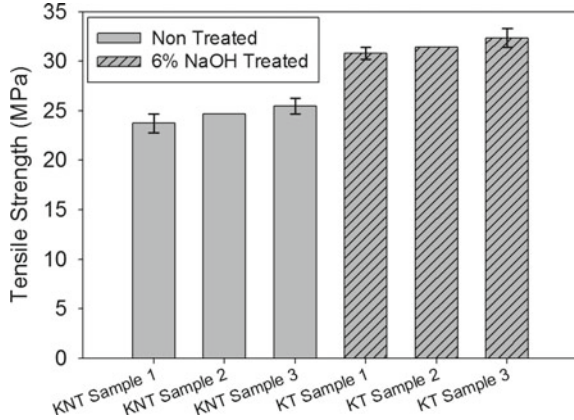
Sl.No	Designation	Weight fraction (%)			Theoretical density	Experimental density	Void content	Thickness of composite
		Fibre	Resin	Filler	(g/cc)	(g/cc)	(%)	(mm)
1	KNT/E	25	75	0	1.21	1.175	2.89	4.4
2	KT/E	25	75	0	1.21	1.15	2.64	4.5
3	KT5/E/F	25	70	5	1.225	1.205	1.6	4.5
4	KT10/E/F	25	65	10	1.235	1.21	2.0	4.6
5	KT15/E/F	25	60	15	1.265	1.225	2.7	4.7
6	KT20/E/F	25	55	20	1.265	1.228	2.7	4.7
7	KT25/E/F	25	50	25	1.265	1.227	2.7	4.7
8	KT5/E/H/UC	25	70	5	1.51	1.49	1.3	5.1
9	KT10/E/H/UC	25	65	10	1.66	1.63	1.8	5.2
10	KT15/E/H/UC	25	60	15	1.78	1.74	2.24	5.1
11	KT20/E/H/UC	25	55	20	1.89	1.85	2.1	5.3
12	KT20/E/H/UC	25	50	25	1.98	1.92	3.03	5.4
13	KT5/E/H/C	25	70	5	1.51	1.46	3.31	4.9
14	KT10/E/H/C	25	65	10	1.66	1.58	4.8	5.1
15	KT15/E/H/C	25	60	15	1.78	1.70	4.4	5.1
16	KT20/E/H/C	25	55	20	1.89	1.80	4.7	5.0
17	KT25/E/H/C	25	50	25	1.98	1.90	4.04	5.1

Note KNT—Kenaf fabric non-treated 5,10,15,20, 25—Wt. % of filler particles  
 KT—alkaline-treated kenaf fabric UC—Uncarbonized  
 F—Fly ash powder C—Carbonized  
 H—Hen egg-shell powder

**Fig. 1** Tensile test samples.  
**a** Specimen's dimension  
**b** Ruptured sample after test



**Fig. 2** Influence of alkaline treatment on tensile properties of KNT and KT composites



### 3 Results and Discussion

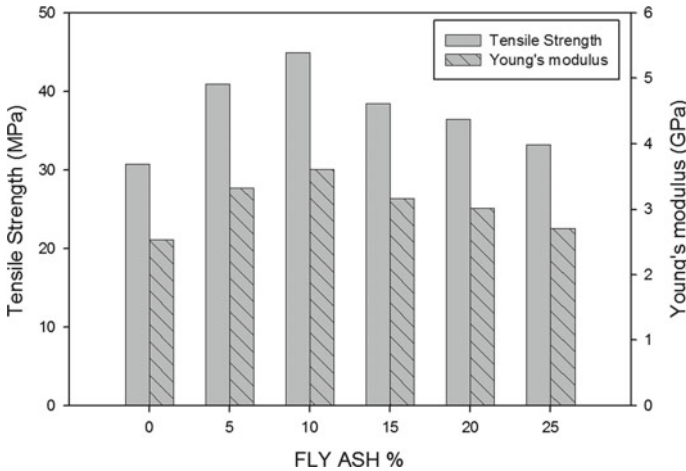
#### 3.1 Influence of Alkaline Treatment on Tensile Properties

Figure 2 displays the effect of NaOH treatment on the tensile strength of KT and KNT composites. From Fig. 2, the treated fibre composites exhibit higher tensile strength, and this is because of good physical interlocking between surface treated fibre and matrix. The surface treatment enhances the interfacial bonding by improving the adhesion properties of Kenaf fibres.

#### 3.2 Influence of Fly Ash Particles on Tensile Properties

The fly ash particles were incorporated by varying weight percentage (5, 10 15, 20 and 25 wt. %) into kenaf fibre composite medium, and their influence in tensile properties was studied. The results of the tensile test are shown in Fig. 3. It is witnessed from Fig. 3 that kenaf composite with 10 wt. % fly ash reinforcement had higher tensile strength compared to other composite. However, beyond the range of 10 wt. % of fly ash, there is a slight reduction in tensile strength. This may be due to increase in higher volume fraction of fly ash particles which reduces the chance of developing interface between fibre and matrix medium, and ultimately, the lack of bonding strength reflects in tensile strength of the fibre composite. Hence, the optimum weight percentage of fly ash inclusion supposed to be incorporated is 10 wt.% to get better material strength of kenaf fibre composites.

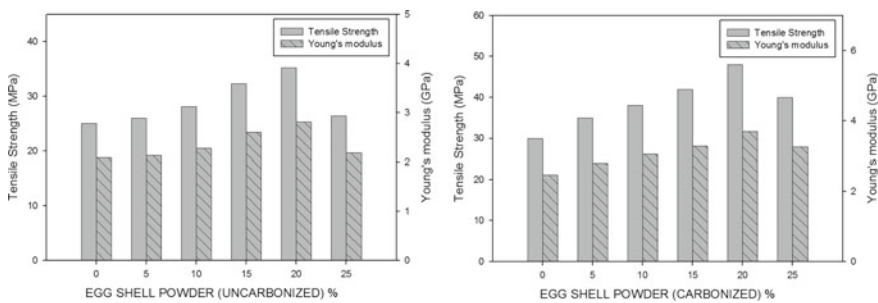




**Fig. 3** Comparison of tensile strength and tensile modulus of kenaf composites with various wt. % of fly ash reinforcements

### 3.3 Effect of Egg-Shell Powder on Tensile Properties

Figure 4 represents the egg-shell inclusion's effects on the tensile strength of kenaf fibre composites. The ultimate tensile strength of the uncarbonized egg-shell powder reinforced composite increases as the wt.% egg-shell powder addition increases. The tensile strength is increased from 25 to 35 MPa by adding uncarbonized egg-shell inclusions of about 0–20 wt %, whereas carbonized egg-shell inclusions could be able to achieve maximum tensile strength of 48 MPa at 20 wt %. It is evident that the carbonized egg-shell inclusion is more effective than the uncarbonized egg-shell inclusion at all mass fractions. This is mainly due to carbonized egg-shell particles; effective surface area is more than that of uncarbonized inclusions, thereby increasing the interface between matrix medium and fillers for better mechanical interlocking.



**Fig. 4** Variation of UTS and tensile modulus of egg-shell composites with wt% egg-shell powder addition

**Table 2** Mechanical properties for human cortical femur bone of male and female [19]

Mechanical test	Male	Female	P value
Tensile strength MPa	39.74 ± 4.80	30.08 ± 7.96	< 0.001

**Table 3** Mechanical properties for human cortical femur bone with respect to ages [19]

Mechanical test	30 ≤ Years	31–50 Years	51–70 Years	71 ≤ Years
Tensile strength MPa	43.44 ± 3.62	39.82 ± 4.29	33.16 ± 6.43	30.16 ± 7.09

### 3.4 General Findings, Practical Implications

The conventional metal fixators such as cobalt chrome alloy (Young's modulus = 210 GPa) titanium (Young's modulus = 110 GPa), stainless steel (Young's modulus = 200 GPa), etc., exhibit high axial stiffness cause osteopenia after removal of the implant which leads to lowering bone density. Hence, a fixation plate must exhibit similar longitudinal stiffness of fractured bone and to be designed to bear a considerable clinical load as well as to reduce the relative motion in the fractured zone. [18].

According to experimental results, the UTS of the 10% fly ash composite and 20% of the carbonized composite is 45 MPa and 48 MPa, respectively. From Tables 2 and 3 obtained from literature [19], it was observed that the tensile strength of femur bone is 43 ± 3.62 MPa. Therefore, kenaf fibre reinforced filler composites offer better strength and enough stability in terms of stiffness near fractured zone preventing from dislocations of fractured bones. However, tensile modulus ranging from 2–3 GPa of the developed 10% fly ash composite or 20% carbonized egg-shell composite is greater than the tensile modulus of the femur bone [16]. Hence, the proposed composite material can minimize stress shielding compared to conventional titanium and stainless steel.

## 4 Conclusion

The following conclusions were drawn based on the observation made from tensile test results carried out on prepared kenaf fabric reinforced bio-composites.

- The results showed that surface modification techniques improve the fibre matrix adhesion which resulted improvement in the tensile properties. The tensile strength of the composite increased 30% due to the surface modification techniques (i.e. alkaline treatment).
- The incorporation of fillers into resin matrix increases the tensile strength. According to experimental results, the UTS of the 10wt.% fly ash composite and 20wt.% of the carbonized composite is 45 and 48 MPa, respectively.

Finally, it is concluded that this developed composite is more axially flexible and limits to desirable stiffness compared to conventional metallic fixations. The developed composite exhibits considerable material strength to withstand enough clinical load during routine human activities. Therefore, in this aspect, bone plate made up of Kenaf fabric-based composite with 10wt.% fly ash fillers or 20wt.% carbonized egg-shell powder may be recommended as bone fixation plate for treatment of long bone fractures.

## References

1. Tacvorian, E.: Evaluation of Canine Fracture Fixation Bone Plates, **11** (2012)
2. Maharaj, P.S.R.S., Maheswaran, R., Vasanthanathan, A.: Numerical analysis of fractured femur bone with prosthetic bone plates, **I 64**, 1242–1251 (2013)
3. Das, S., Sarangi, S.K., Finite element analysis of femur fracture fixation plates, **II**, 1–5 (2014)
4. Farsh, J.W., Craig, R.G., Meroueh, K.A., Oral Rehab **J. 16**, 603 (1989)
5. Ramakrishna, S., Mayer, J., Winter Mantel, E., Leong, K.W., Biomedical applications of polymer-composite materials: a review. *Comp. Sci. Tech* **61**, 1189–224 (2001)
6. Yildiz: Composite Hip Prosthesis Design, Ph. D. Thesis, Stanford University (1993)
7. Baixauli, et al.: Carbon fiber composite bone plates for fixation of forearm fractures. *J. Bone Joint Surg. [Br]*, **77-B(2)**, 227 (1995)
8. Bledzk, A.K., Gassan, J.: Composites reinforced with cellulose-based fibres. *Prog. Polym. Sci.* **24**, 211–274 (1999)
9. Chand, N., Rohatgi, P.K.: Natural fibers and their composites. New Delhi, India: Periodical Experts Book Agency (1994)
10. Nishino, T., Hirao, K., Kotera, M., et al.: Kenaf reinforced biodegradable composite. *Compos Sci Technol* **63**, 1281–1286 (2003)
11. Yousif, B.F., Shalwan, A., Chin, C.W., et al.: Flexural properties of treated and untreated kenaf/epoxy composites. *Mater Des* **40**, 378–385 (2012)
12. Fiore, V., Di Bella, G., Valenza, A.: The effect of alkaline treatment on mechanical properties of kenaf fibers and their epoxy composites. *Compos Part B* **68**, 14–21 (2015)
13. Jena, H., Pandit, M.K., Pradhan, A.K.: Effect of cenosphere on mechanical properties of bamboo–epoxy composites. *J. Reinf. Plast. Compos.* **32**, 794–801 (2013)
14. Dalbehera, S., Acharya, S.K.: Effect of cenosphere addition on the mechanical properties of jute-glass fiber hybrid epoxy composites. *J. Ind. Text* **46**, 177–188 (2016)
15. P. Toro, R. Quijad, M. Yazdani-Pedram, J.L. Arias.: Eggshell, a new bio-filler for polypropylene composites. *Mater. Lett.* **61(22)**, 4347–4350 (2007)
16. Edeerozey, A.M.M.: Chemical modification of kenaf fibers. *Mater Lett* **61**, 2023–2025 (2007)
17. Nalla Mohamed, et.al.: A comparative analysis on tensile strength of dry and moisture absorbed hybrid kenaf/glass polymer composites, **47(8)**, 2050–2073 (2018)
18. Bartel, D.L., Davy, D.T., Keaveny, T.M.: Orthopaedic Biomechanics: Mechanics and Design in Musculoskeletal Systems, New Jersey (2006)
19. Havaladar, R., Pilli, S.C., Putti, B.B.: Insights into the effects of tensile and compressive loadings on human femur bone. *Adv. Biomed. Res.* **3**, 101 (2014)

# Effect of Wall Thickness Variation on the Energy Absorption Efficiency of Cylindrical Tubes Under Axial Loading



M. Nalla Mohamed

## 1 Introduction

Making lightweight vehicle is an important issue in the automotive industry to meet the urgent environmental problems. In this connection, the reduction in the mass of the vehicle improves fuel economy and carbon oxides emission [1]. At the same time, lighter vehicles are more vulnerable than heavy duty vehicles during frontal impact collision [2]. In this regard, design of efficient crash energy absorbers is very much required during the vehicular crash event. Thin-walled tubular structures are commonly used as crash energy absorbers in transportation sector for safety applications due to cost-efficient, lightweight and crashworthy [3–10]. Extensive researches have been done over the past decades to analyse the crushing performance characteristics of thin-walled tubular structures with various regular periphery profiles especially circular cross section [11]. It is known that these cylindrical tubes are having constant thickness formed by extrusion process. This uniform thickness leads to high initial peak crushing force which is undesirable for occupants' safety [12]. Also, the straight tubes with constant wall thickness are not a good design in terms of initial peak crushing force as well as specific energy absorption [13]. On the other hand, the thickness variation of wall acts as trigger mechanism causing progressive local buckling; thus, the initial peak crushing force is reduced, and also specific energy absorption capacity is increased [14–18]. Therefore, it is important to develop cylindrical tubes with varying thickness for maximising energy absorption with reduced material utilisation. In order to understand the effectiveness of variable thickness tubes (VT), a comparison with uniform thickness tubes (UT) based on crushing

---

M. Nalla Mohamed (✉)

Department of Mechanical Engineering, Sri Sivasubramaniya Nadar College of Engineering(SSN), Kalavakkam, Kancheepuram District, Tamilnadu, India  
e-mail: [nallamohamedm@ssn.edu.in](mailto:nallamohamedm@ssn.edu.in)

performance is hence required. However, there are only very limited scientific analyses on crushing performance characteristics of circular tubes with varying thickness (VT) which have been performed to date. Hence, this experimental study compares the circular tubes with five different thickness ratio. The crushing energy absorption (EA) and the initial peak crushing force (IPF) of the VT tubes are subsequently compared with UT tubes to map the similarities and dissimilarities. Finally, suggestions are given for the deployment of VT tubular structures in place of conventional extruded tubes effectively.

## 2 Experimental Procedure

### 2.1 Materials

The specimens used in the present study are of uniform thickness (UT) cylindrical tube and five varying thickness thin-walled cylindrical tubes in axial direction. In this study, an aluminium alloy AA6061-O was used to fabricate all the tube specimens due to its ductile nature. The geometry of the fabricated tubes is shown in Fig. 1. The length of the specimens is 150 mm, and their cross-sectional base diameter is 50 mm. In case of VT tubes, their shell thickness, from the base to the top end is linearly reduced along axis. To get the material property of the specimens, the samples were cut from the tubes as per ASTM E8 standards as shown in Fig. 2, and the representative engineering stress–strain response obtained from a tensile test is also shown in Fig. 2.

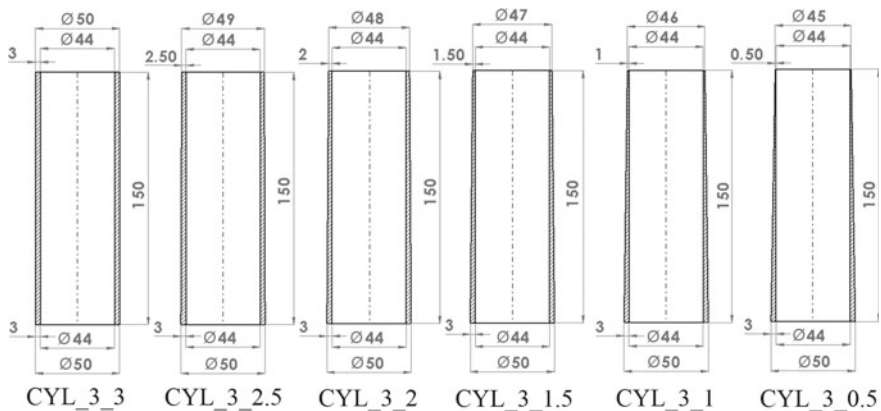


Fig. 1 Geometric details of the thin-walled cylindrical tubes with varying thickness

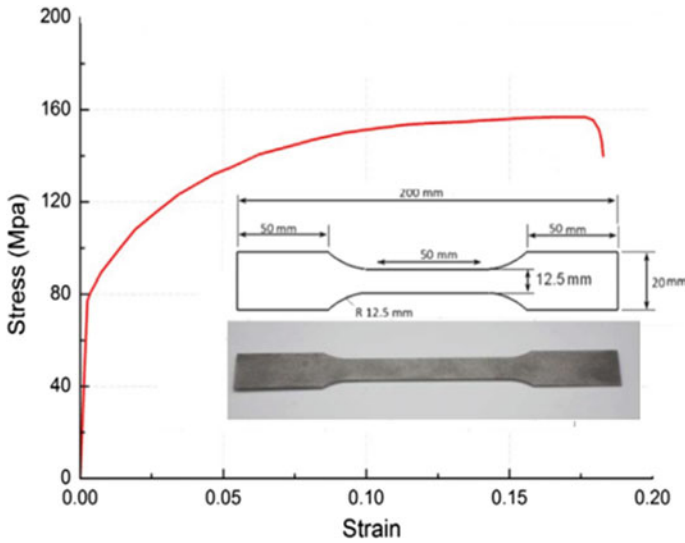


Fig. 2 Tensile specimen and the engineering stress–strain curve of AA 6061-O thickness

### 2.2 Methods

The axial quasi-static crushing experiments were carried out on the data acquisition UTM as shown in Fig. 4, having 60 tonnes capacity to investigate the crushing performance of the varying thickness cylindrical tubes as shown in Fig. 3. These tubes were manufactured by turning process in the lathe. Quasi-static axial compressions of 100 mm cross head displacement at the rate of 2 mm/min were conducted on all the specimens. The data acquisition system records both cross head displacement as well as crushing force reaction at the bottom end of tubes. The displacement precision is about 1 mm, and corresponding crushing load curves were recorded.

### 3 Results and Discussion

The specimen tubes were subjected to experimental quasi-static axial compression, in order to analyse their crushing performance characteristics. Moreover, the quasi-static test is preliminary to dynamic test as well as cost-effective test to determine the crushing performance of thin-walled structures.



Fig. 3 Machined aluminium tubes

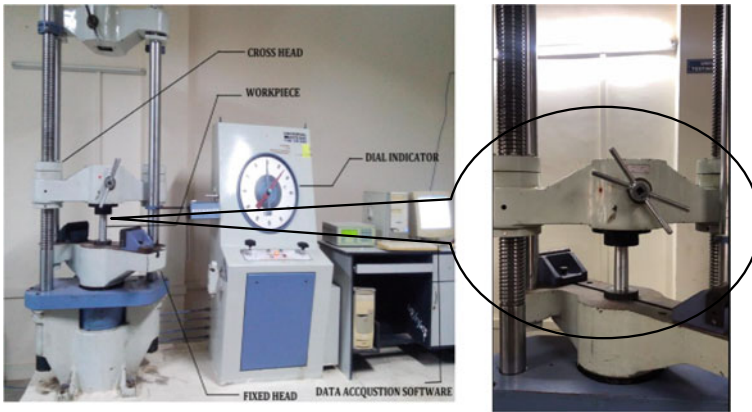


Fig. 4 UTM machine, zoomed view of the tube

### 3.1 *Quasi-Static Test on Uniform Thickness Cylindrical Tubes (UT)*

The testing was initiated with the cylindrical tube with uniform thickness  $t = 3$  mm to obtain the required of force–displacement response for comparison purpose. Figure 5 presents captured images of the progressive deformation mechanism of UT tubes



Fig. 5 Sequence of deformation of UT tubes obtained through experiments

under quasi-static axial compression. The progressive deformation mechanism starts from bottom end initially and then followed by series of consecutive folds accumulating one over the other. As the crushing load increases, the deformation continues its series of local buckling folds, up to the prescribed deformation of 120 mm. The final deformation lobes of the UT tubes which were subjected to quasi-static compression, are presented in Fig. 6a.

Figure 6b displays the force–displacement curve for uniform thickness (UT) circular tube. The initial peak crushing force (IPF) for the UT tube was 100 kN. Tremendous initial peak force produces jerks and causes serious injuries to the passengers, and this problem arises exclusively in high impact energy absorbers. Therefore, the initial peak crush force is one of the major criteria to be considered during designing of impact energy absorbers. Since it is related to occupant safety, hence, IPF is one of the most important bio-mechanical factors which must be under consideration while designing of crash energy absorber. For this main reason, more number of folds are being introduced to decrease the initial peak crushing.

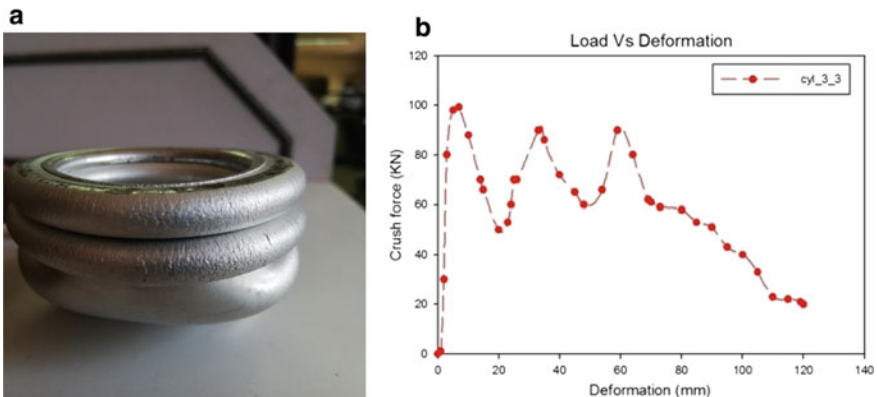


Fig. 6 a Final deformed shape of the UT tube b force–displacement curves for UT tube



### 3.2 *Quasi-Static Test on Varying Thickness Cylindrical Tubes (VT)*

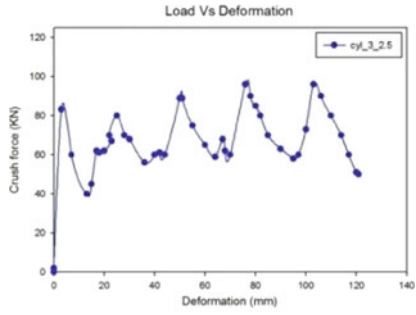
In this connection, variable thickness tubes were introduced for minimising the initial peak crushing force occurred in the UT tubes, and their deformation behaviours were investigated. The final deformation lobes of the VT tubes under quasi-static loading are presented in Fig. 7. There are few fractures on the lobes which were formed during the hinge formation while undergoing the crushing process. When we compare the number of lobes, i.e. folding hinges in case of VT and UT tubes, it is noted that UT tubes have three regular lobes, while the VT tubes generates more than three lobes. It means that the crushing energy absorption capacity of VT tube is more than that of the UT tube. Figure 7 displays force–displacement curves for VT tubes with corresponding deformed pattern of the VT tubes obtained through experiments. Initially, all VT tubes experienced peak force which is lesser than the UT's peak force mainly because of linear variation in shell thickness of VT tubes. It was found that the initial peak crushing force of the VT tubes is lower than UT tubes by 20–50%. Figures 8 and 9 show the comparison of the energy absorption capacity of the VT tubes. It is clearly understood that the VT tubes (CYL\_3\_2.5) absorb more energy than the UT tubes (CYL\_3\_3). Thus, a VT tubes can lower the initial peak crushing force and can enhance their specific energy adsorption capacity, thereby the overall weight and material usage is reduced. The energy absorption capacities (EA) of specimens were computed from the area enclosed by force–displacement curve using trapezoidal rule up to crushing distance of 120 mm.

## 4 Conclusion

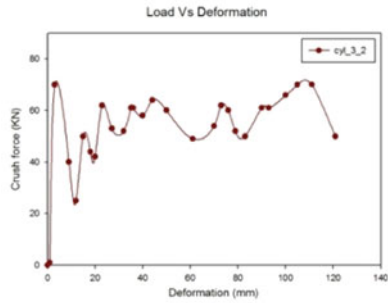
This paper has proposed varying thickness in thin-walled cylindrical tubes. The crushing characteristics of the VT tubes were analysed experimentally in this paper. The outcome of the research provides base line comparison and effectiveness of VT tubes over UT tubes. The initial peak crush force of VT tubes is remarkably lower than that of UT tubes. Also, the specific energy absorption capacity of VT tubes can be witnessed higher than that of UT tubes significantly, and hence, these variable thickness (VT) tubular structures can be suggested for better alternative in place of conventional types (UT) crushing energy absorbers which are exhibiting higher initial peak force. The obtained experimental results showed the advantages of utilising variable thickness (VT) tubular structures in the transport sector to design a vehicular crash safety system during vehicular crash events.



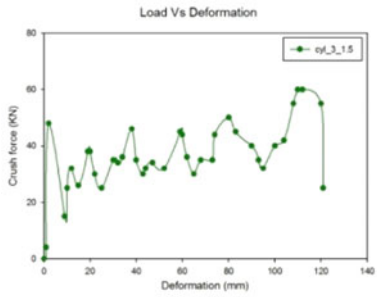
CYL 3\_2.5



CYL 3\_2



CYL 3\_1.5



CYL 3\_1

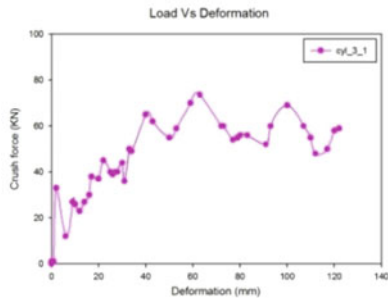


Fig. 7 Crushing force–displacement curves for VT tubes



CYL 3\_0.5

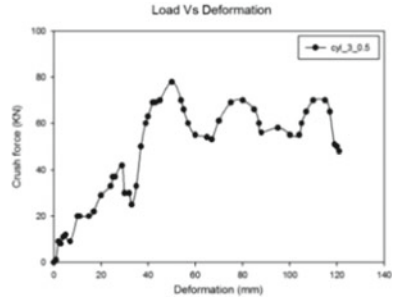


Fig. 7 (continued)

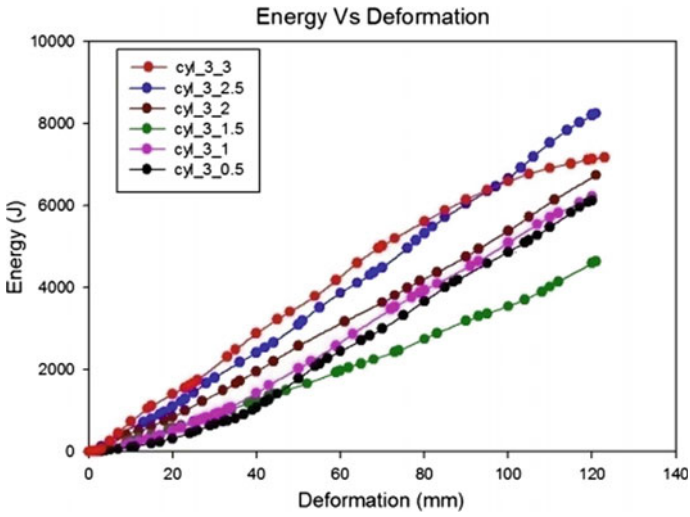
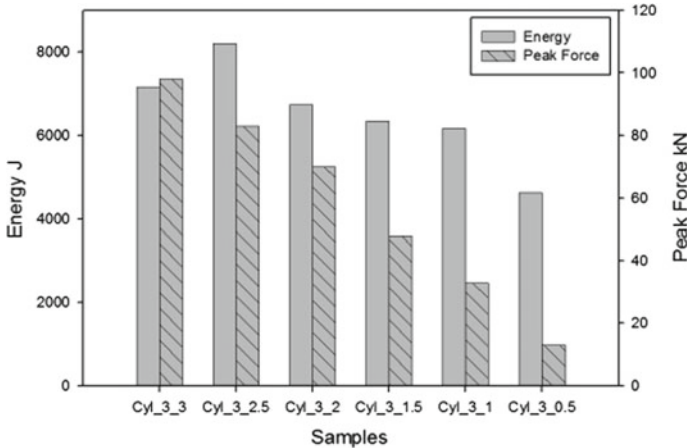


Fig. 8 Comparison of energy absorption capacity of VT tubes



**Fig. 9** Comparison of energy absorption capacity and peak crushing force of VT tubes

## References

1. Fukuo, K., Fujimura, A., Saito, M., Tsunoda, K., Takiguchi, S.: Development of the ultra-low-fuel-consumption hybrid car—INSIGHT. *JSAE Rev.* **22**, 95–103 (2001)
2. Evans, L.: Causal influence of car mass and size on driver fatality risk. *Am. J. Public Health* **91**, 10761081 (2001)
3. Shen, W., Gu, X., Jiang, P., Hu, J., Lv, X., Qian, L.: Crushing analysis and multiobjective optimization design for rectangular unequal triple-cell tubes subjected to axial loading. *Thin-Walled Struct.* **117**, 190–198 (2017)
4. Abramowicz, W., Jones, N.: Dynamic progressive buckling of circular and square tubes. *Int. J. Impact Eng.* **4**, 243–270 (1986)
5. Alghamdi, A.A.A.: Collapsible impact energy absorbers, an overview. *Thin-Wall. Struct.* **39**, 189–213 (2001)
6. Alavi, N.A.J., Hamedani, H.: Comparative analysis of energy absorption and deformations of thin walled tubes with various section geometries. *Thin-Wall. Struct.* **48**, 946–954 (2010)
7. Nalla Mohamed, M., Yuvarajan, P., Umasankar, M.: Energy enhancement of long cylindrical tubes with grooves subjected to axial impact. *App. Mech. Mater.* **787**, 345–349 (2015)
8. Nalla Mohamed, M. et al.: New insight to energy absorption characteristics of long circular tubes with stiffeners as controllable energy-dissipating devices. *Proc. Eng.* **173**, 1300–1406 (2017)
9. Nalla Mohamed, et al.: Axial crash performance of press-formed open and end-capped cylindrical tubes—a comparative analysis. *Thin-Walled Struct.* **124**, 468–488 (2018)
10. Mohamed, N., et al.: Crush performance analysis of combined geometry tubes under axial compressive loading. *Proc. Eng.* **173**, 1415–1422 (2017)
11. Baroutaji, A., Sajjia, M., Olabi, A.G.: On the crashworthiness performance of thin walled energy absorbers: recent advances and future developments. *Thin-Walled Struct.* **118**, 137–163 (2017)
12. Guillow, S., Lu, G., Grzebieta, R.: Quasi-static axial compression of thin-walled circular aluminum tubes. *Int. J. Mech. Sci.* **43**, 2103–2123 (2001)
13. Sun, G., Pang, T., Zheng, G., Song, J., Li, Q.: On energy absorption of functionally graded tubes under transverse loading. *Int. J. Mech. Sci.* **115**, 465–480 (2016)
14. Zhang, X., Zhang, H.: Relative merits of conical tubes with graded thickness subjected to oblique impact loads. *Int. J. Mech. Sci.* **98**, 111–125 (2015)

15. Zhao, L., Chen, W.Q.: Symplectic analysis of plane problems of functionally graded piezoelectric materials. *Mech. Mater.* **41**, 1330–1339 (2009)
16. Fang, J., Gao, Y., Sun, G., Zheng, G., Li, Q.: Dynamic crashing behavior of newextrudable multi-cell tubes with a functionally graded thickness. *Int. J. Mech. Sci.* **103**, 63–73 (2015)
17. Xu, F.: Enhancing material efficiency of energy absorbers through graded thickness structures. *Thin-Walled Struct* **97**, 250–265 (2015)
18. Zhang, Y., Lu, M., Sun, G., Li, G., Li, Q.: On functionally graded composite structures for crashworthiness. *Compos. Struct.* **132**, 393–405 (2015)

# Low – Cost Portable Smart Ventilator



Sourabh Dogra, Lokendra Singh, and Arpan Gupta

## 1 Introduction

Oxygen is the most important constituent for running human's biological cycle, which is being fulfilled by the lungs. Lungs perform the most important task, i.e., gas exchange [1]. It mixes the oxygen in the blood and removes the carbon dioxide. Lungs are constantly exposed to particles, chemicals, and infectious organisms in ambient air. Any minute trouble in the lungs causes severe health damage or even death [2–4]. According to the World Health Organization (WHO) report [5], about 65 million people suffer from the chronic obstructive pulmonary disease (COPD), and 3 million dies from it. Asthma, the most common childhood disease affects 14% of children globally. Almost 334 million people in the world have asthma. Pneumonia is the leading cause of the death of children under five years old. Tuberculosis (TB) is a common fatal infection nowadays and kills 1.4 million annually out of 10 million. Globally, two billion people exposed to household chemical like sanitizers, home cleansing agents, dust particles, etc., whereas one billion inhale the tobacco smoke and one billion outdoor smoke, but ongoing COVID-19 epidemic has made the condition vulnerable [6]. The ventilator is an artificial life support system used to handle lungs diseases explained above. Ventilators are capable of exchanging oxygen and carbon dioxide mechanically with the help of various sensors [7]. These machines are available in the most expensive area of the hospital, intensive care unit (ICU) [8]. The average cost of ICU is 10,364 INR per day with ventilator in India [9]. For developing countries like India, where the per capita income is not more 12,000 INR per month, it becomes impossible for the people to afford such kind of treatments [10]. According to a report from The Center Disease Dynamics Economics and

---

S. Dogra (✉) · L. Singh · A. Gupta  
Acoustics and Vibration Laboratory, School of Engineering, Indian Institute of Technology,  
Mandi, Himachal Pradesh 175005, India  
e-mail: [s19001@students.iitmandi.ac.in](mailto:s19001@students.iitmandi.ac.in)

© The Author(s), under exclusive license to Springer Nature Singapore Pte Ltd. 2022  
S. K. Natarajan et al. (eds.), *Recent Advances in Manufacturing, Automation, Design  
and Energy Technologies*, Lecture Notes in Mechanical Engineering,  
[https://doi.org/10.1007/978-981-16-4222-7\\_67](https://doi.org/10.1007/978-981-16-4222-7_67)

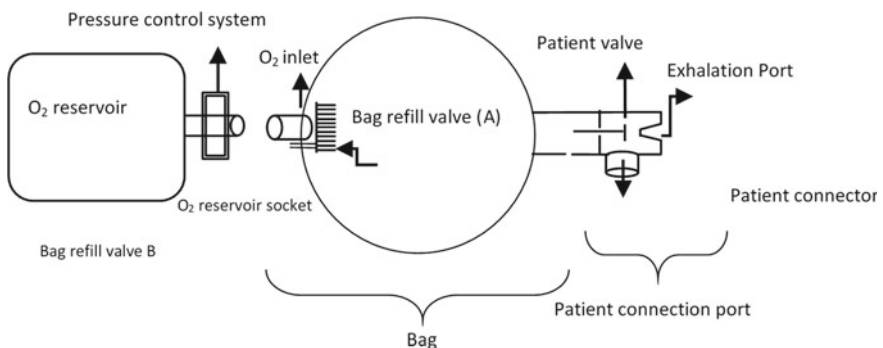
599

Policy (CDDEP), there are total 47,481 public and private ventilators in India [11]. Different ventilator companies like VORTAN, CAR Event are available. Electric ventilators can operate anywhere. The COVID-19 made these medical conditions more vulnerable. We have come up with low-cost mechanical ventilators design with breath per minute (BPM) and tidal volume control. The ventilators can work both remotely and as well manually. The developed design ensures the safety of both patients as well as doctors.

## 2 Device Design

### 2.1 Air Delivery System

Air delivery system ensures the correct amount of mixture of oxygen and air to be delivered to the human body. To fulfill these needs, bag valve mask (BVM), known as Ambu bag, is used. Ambu bag is compressed mechanically and delivers air to the patient. A constant pressure source can be used to deliver the air from time to time, but it involves large cost associated with pneumatic components. Also, additional power is required to drive the motor of the compressor. Ambu bag is the hand-held device and is used to supply oxygen to a patient suffering from the respiratory problems. An Ambu bag consists of an air chamber which is connected to the unidirectional valve. This valve is further extended to connect mask or endotracheal tube. When the air chamber compresses, the required amount of the air is delivered to the patient. An oxygen reservoir is also connected at the back of the bag to supply sufficient oxygen to the patient (Fig. 1).



**Fig. 1** Bag valve mask [12]

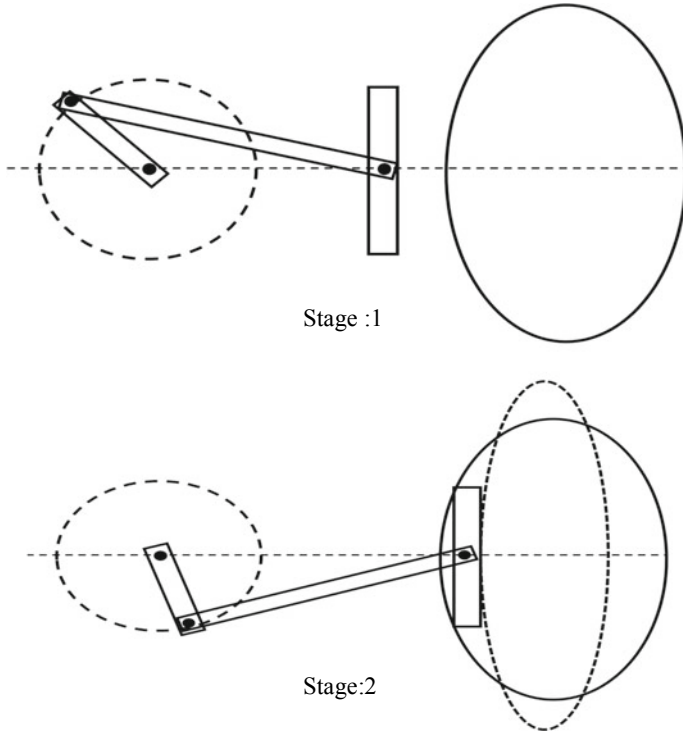


Fig. 2 Two stages of slider-crank mechanism in compression

### 2.2 Mechanism

Ambu bag is generally compressed with hands, but this can be replaced by a mechanism which can actuate linearly to and fro. We come across two mechanisms slider-crank mechanism and cam mechanism. Both are effective and can be able to perform the same task effectively, but we use only slider crack mechanism because the cam is difficult to design and involves very precise manufacturing. Slider-crank mechanism is easy to design and involve very small capital (Fig. 2).

### 2.3 Control System

The control system for the device has been designed in the three phases:

- For manual control mode
- Remote control mode
- Emergency alarm



In the first phase, a potentiometer, NPN transistor, and a 220-ohm resistor have been used to control the speed of DC motor. A rotating knob has been provided to the potentiometer, by which the speed of the motor can be controlled as per desired conditions.

In the second phase to control the system remotely via Wi-Fi, a Lolin ESP-8266 microprocessor has been used which works on Arduino code. ESP-8266 itself consists of Wi-Fi module which is connected to L298-N motor driver to drive the motor. The microprocessor has been assigned an IP address which can be connected by using the designed application software name 'IIT MANDI VENTILATOR' for the android smartphones. The application consists of speed variation control, shift to manual mode, and also indicates the amount of breath per minute with certain speed mode (Fig. 3).

During the final phase, an emergency alarm has been added to the system which consists of a relay module, buzzer, LED, and emergency push button. Relay module has been used to cut the supply and at the same time to ring the buzzer. To cut the voltage supply to the motor via the relay module, the emergency push button is connected to the microprocessor to process signal. As someone presses the push button, it stops the system, turns on the LED and emergency alarm rings (Fig. 4).

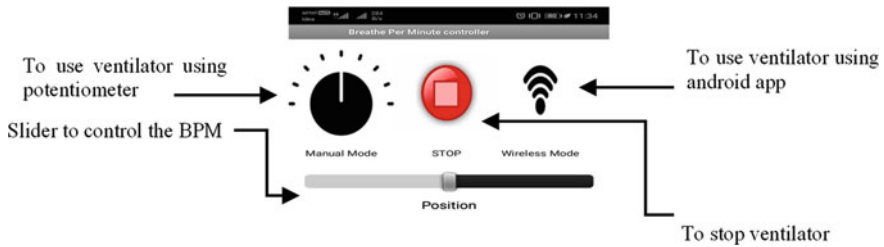


Fig. 3 IIT MANDI VENTILATOR android app user interface with various options

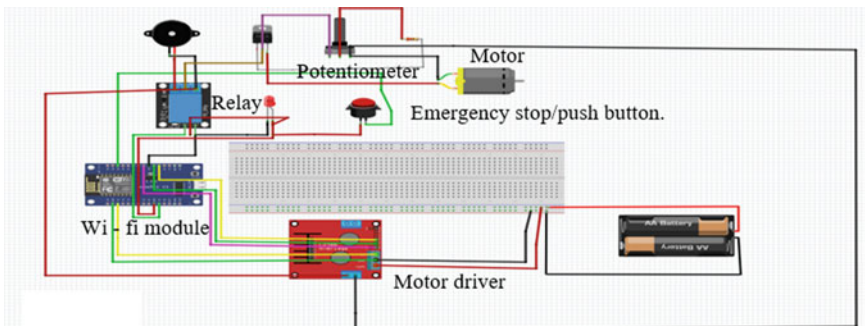


Fig. 4 Circuit diagram

### 3 Prototype Design

The slider-crank mechanism is chosen for the automation compression of the Ambu bag. A 60 × 60 cm acrylic sheet of 5 mm thickness is used for the base design. 10 mm thickness clear acrylic is used for the assembling the motor over the base. All the parts are bolted to base through screws.

#### 3.1 Slider-Crank Mechanism Design

Slider-crank mechanism involves three revolute pair and one sliding pair. Revolute pair is designed by using the two bearings where one is directly connected to the motor. A drawer slider is used as a sliding pair. Crank and connecting rod are made of acrylic sheet. One end of the connecting rod is connected to the crank through bolt and bearing, whereas other is connected to the slider. On the crank, a slot is provided to vary the crank radius. At the one end of the slider, a piston is welded to compress the Ambu bag (Figs. 5 and 6).

Fig. 5 Slider-crank mechanism

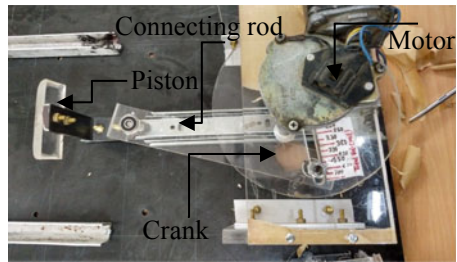
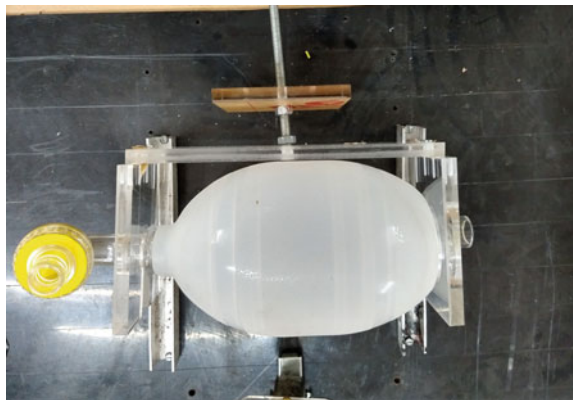


Fig. 6 Ambu bag base





**Fig. 7** Prototype

### ***3.2 Ambu Bag Base Design***

The Ambu bag is fixed over the two acrylic sheets ( $11 \times 11$  cm) with central holes to support the Ambu bag. The Ambu bag is backed by rigid support ( $22 \times 6$  cm) of acrylic to compress against the piston. This whole assembly is placed over U-shaped aluminum channel. This U-shaped aluminum channel enables the Ambu bag to have forward and backward movements through the lead screw provided at the back of the Ambu bag.

### ***3.3 Remote Control***

An Arduino-based Wi-Fi module is used to control the rotation per minute (RPM) of the motor. To control RPM remotely, an android application is designed using the MIT app inventor. This app connects with ventilator over Wi-Fi. The user interface of the app is shown in Fig. 3. There are ten basic modes of speed, ranges from 10 to 45 RPM. Manual control button enables the user to control the RPM manually with a potentiometer (Fig. 7).

### ***3.4 Features***

This low-cost smart ventilator can control two basic features, i.e., tidal volume and breath per minute.

### ***3.5 Tidal Volume Control***

Tidal volume is defined as the amount of air required by the lungs. Air quantity to lungs should be optimum. Lesser air supply leads to collapsing of lungs which can cause death. On the crank, a slot is provided in which connecting length is fixed the nut and bolt. The position of nut and bolt can vary according to the required tidal volume. The range of the air that can be supplied to the patient is 300–750 mL. Also, tidal volume can be varied with help lead screw provide at the back of the Ambu bag base. The Ambu bag moves over the U-shaped aluminum lengths by rotating the lead screw. This movement can be automated with the help of a motor.

### ***3.6 Breath Per Minute Control***

Breath per minute is also short-termed as BPM. It is the rate of supply of oxygen to the lung of the patient through the device. It may vary according to the age of the patient. The device's BPM varies minimum 12 to maximum 45. BPM supplied by the device varies according to the speed of the motor, which is controlled using the potentiometer knob in manual mode and using the mobile application in remote control mode. In smartphone app, amount of BPM has been shown on the screen at a particular speed which is well calibrated using tachometer.

### ***3.7 Cost-Effectiveness***

Different types of ventilators are available in market with best facilities, but the low cost and easy to use features are missing in these ventilators. This low-cost proposed ventilators works on the cheap Arduino available in market. The basic slider-crank mechanism is used to compress the Ambu bag. Simple operating mechanism and cheap control system reduce its cost to very large extent. Ventilator can be effective for the non-critical patients suffering from breathing problems or patients which are in the initial stages of corona. Rather using the full-fledged ventilator which costs around 10,000 INR per day, this can be helpful for non-critical patients. This can be helpful for non-critical patients.

## **4 Conclusion and Scope**

This ventilator is designed to meet the rapid requirement of ventilators on a large scale to handle the COVID-19 pandemic. The size of the ventilator is very small such that it can be easily mounted over the walls. The ventilator weighs not more than 7 kg and

is readily transportable in remote locations. This ventilator assures the safety of both patient and doctor through its remote control feature. In its initial version ventilator can control both tidal volume and breath per minute. The volume of air deliverable through ventilator ranges from 250 to 750 mL with breath per minute varies from 10 to 45 BPM for a different kind of patient according to their age group. Cost-effectiveness of the ventilator is one more feature. The whole setup costs 4000INR, excluding the labor cost. The ventilator of such cost is a prime need of the countries like India in this pandemic scenario. The additional features like continues positive airways pressure (CPAP) and positive end-expiratory pressure (PEEP) can also be added in future to ensure more safety to the patient.

## References

1. Melén, E., Guerra, S.: "Recent advances in understanding lung function development," *F1000 Res.*, **6**(May), 1–11 (2017)
2. Ryu, J.H., Colby, T.V., Hartman, T.E., Vassallo, R.: Smoking-related interstitial lung diseases: a concise review. *Eur. Respir. J.* **17**(1), 122–132 (2001)
3. De Lauretis, A., Veeraraghavan, S., Renzoni, E.: Connective tissue disease-associated interstitial lung disease: how does it differ from ipf? how should the clinical approach differ? *Chron. Respir. Dis.* **8**(1), 53–82 (2011)
4. El-Zammar, O.A., Katzenstein, A.L.A.: Pathological diagnosis of granulomatous lung disease: a review. *Histopathology* **50**(3), 289–310 (2007)
5. Forum of International Respiratory Societies. *The Global Impact of Respiratory Disease- 2<sup>nd</sup> Ed* (2017)
6. World Health Organization, 2020, "Weekly Epidemiological Update on COVID-19," (3 November), p. 1;4
7. Pettenuzzo, T., Fan, E.: 2016 year in review: mechanical ventilation. *Respir. Care* **62**(5), 629–635 (2017)
8. Rani, U., Naveen Kumar, P., Naha, A.: Cost analysis and utilization of mechanical ventilators in intensive care units of South India. *Pakistan J. Med. Heal. Sci.* **12**(2), 950–951 (2018)
9. Shweta, K., Kumar, S., Gupta, A.K., Jindal, S.K., Kumar, A.: Economic analysis of costs associated with a respiratory intensive care unit in a tertiary care teaching hospital in Northern India. *Indian J. Crit. Care Med.* **17**(2), 76–81 (2013)
10. Bhawan, S.P., Marg, S.: "Government of India Ministry of Statistics and Programme Implementation." (2016)
11. Kapoor, G., Sriram, A., Joshi, J., Nandi, A., Laxminarayan, R.: "COVID-19 in India : state-wise estimates of current hospital beds, intensive care unit (ICU) beds and ventilators," (April), p. 12 (2020)
12. De Godoy, A.C.F., Vieira, R.J.: Comparison of the FiO<sub>2</sub> delivered by seven models of the self-inflating bag-mask system. *Rev. Bras. Anesthesiol.* **59**(1), 21–27 (2009)

# Investigation on the Effect of Patterned Holes on Energy Absorption Characteristics of Aluminium Square Tubes



M. Nalla Mohamed and R. Sivaprasad

## 1 Introduction

Crash energy absorbers are boon to the vehicular safety management during accidental crash events. Thin-walled tubular structures are one such energy absorbing systems to reduce the shock loads that transmit to the people and goods during the crash event by deforming progressively [1]. In this connection, research interests turned focus on thin-walled tubular structures having regular profiles like square, elliptical, hexagonal and circular [2–5]. Among regular profiles, square shaped aluminium tubes have grabbed the researcher’s attention in the recent decades because of their ease of manufacturing, strength to weight ratio, and moreover, the square profiles are easily constrained and mounted on the ends [6, 7]. Despite the superior impact performance of the square tube, the high initial peak force is the major problem which has potential to cause heavy damage to the occupants and the vehicle. Generally high IPF leads to jerk and causing potential damage to occupants inside the vehicle. A good crash energy absorbing device needs to be designed in such a manner that it should exhibit enough crushing energy absorption (EA) with lower initial peak [8]. Hence, numerous scientific experiments have been carried out on regular profiled thin-walled structures by implementing progressive triggers such as indentations, grooves, notches, corrugation, holes and buckling starter, etc., in order to decrease the IPF without compromising energy absorption performance during vehicular collisions [9–11]. Among these methods, placing holes on the lateral sides of tubular structures is found to be both cost effective as well as exhibiting enhancement of crushing performance [12, 13]. From the review of the reported literature, it is revealed that studies related to effect of patterned holes on crashworthiness of square

---

M. Nalla Mohamed (✉) · R. Sivaprasad  
Department of Mechanical Engineering, Sri Sivasubramaniya Nadar College of Engineering,  
Kalavakkam, Kancheepuram District, Tamilnadu, India  
e-mail: [nallamohamedm@ssn.edu.in](mailto:nallamohamedm@ssn.edu.in)

© The Author(s), under exclusive license to Springer Nature Singapore Pte Ltd. 2022  
S. K. Natarajan et al. (eds.), *Recent Advances in Manufacturing, Automation, Design and Energy Technologies*, Lecture Notes in Mechanical Engineering,  
[https://doi.org/10.1007/978-981-16-4222-7\\_68](https://doi.org/10.1007/978-981-16-4222-7_68)

607

tube structures are scanty. In this regard, commercially available aluminium alloy grad extruded square tubes were selected for the crushing performance study. Strategies were undertaken to analyse the factors affecting the crushing performance of the extruded plain square tubes by introducing of a variety of perforations of different dimensions and shapes on the lateral sides in patterned manner followed by axial quasi-static compression experiment. The following sections include preparation of test specimens, required experimental setup, evaluation of crushing performance and deformation mechanisms related to pattern perforated extruded square tubes.

## 2 Experimentation

### 2.1 Geometry Description

For the quasi-static axial compression test, commercially available extruded square tubes with 6 m long were purchased, and the tubes were cut to the required dimensions. All the tubes considered in this study are having 50 mm width, 150 mm length and 3 mm wall thickness.

A sample of these tubes is presented in Fig. 2. Quantometry material grade test was conducted to ensure the chemical constituents of alloy grade as shown in Table 1. Based on the Table 1 and Reference [14], the material used for this study is confirmed as aluminium alloy grade AA6061-O.

Material strength test for AA6061-O was carried out in accordance with ASTM E8M-04 as shown in Fig. 1. For this purpose, samples of specimens were cut from the square tube by means of wire-cutting process based on ASTM E8/E8M-09 test standard [15]. Later, the samples were subjected to tensile tests at the rate of 2 mm/min in (UTM) universal testing machine. The stress–strain curve for AA6061-O is shown in Fig. 1.

Patterned holes were created in the square tube using wire-cut. Three holes were made in the vertical centre line of the wall of the front and back side, and the remaining two sides are left without holes. The position of the centre hole is kept at a constant, while the positions of remaining two holes are varying. It is designated as R\_1\_T, R\_2\_T, R\_3\_T and R\_4\_T. The details of designation are as follows: R-Round hole square, 1, 2, 3 and 4 tube specimen numbers and T-Through holes. The fabricated specimens are shown in Fig. 2.

**Table 1** Chemical constituents of AA6061-O grade

Elements	Al	Mg	Fe	Cu	Cr	Si	Ti	Zn	Mn
Weight (%)	98.05	0.41	0.62	0.15	0.032	0.54	0.009	0.12	0.065

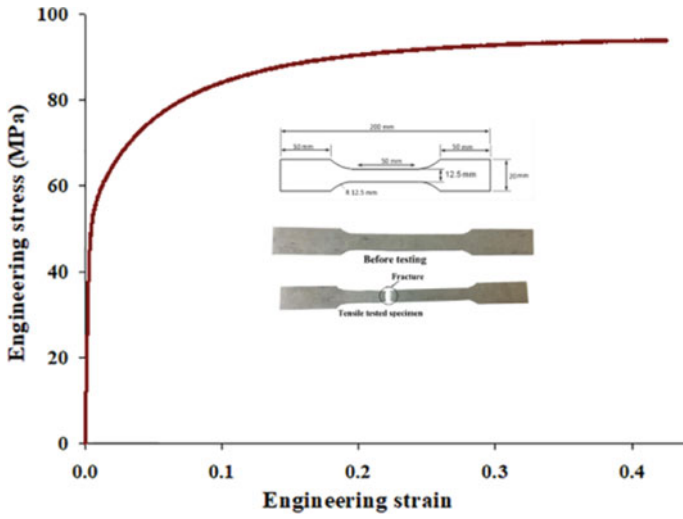


Fig. 1 Stress-strain curves of AA6061-O

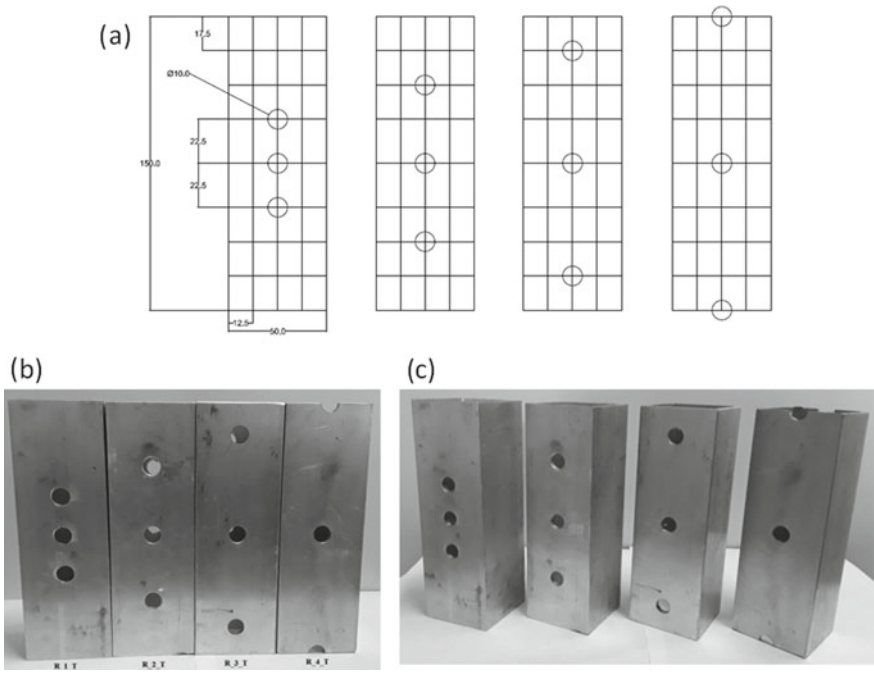
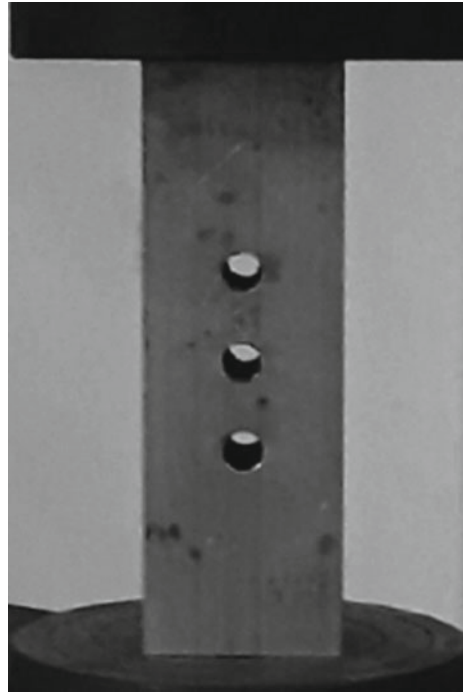


Fig. 2 Fabricated specimens



**Fig. 3** Tube in between two plates of UTM machine

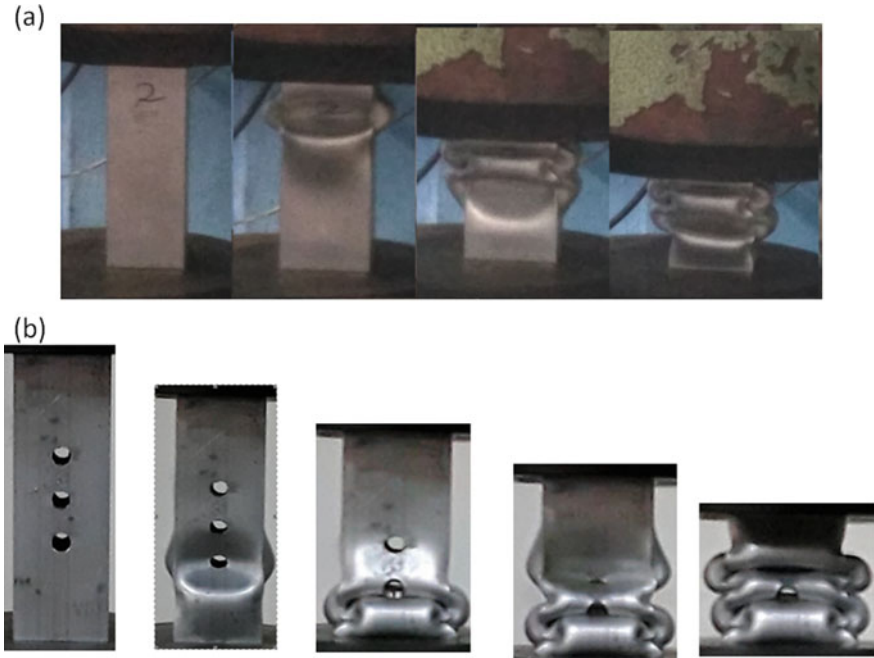


## **2.2 Testing Methods**

To compare the energy absorption, quasi-static compression on plain extruded square tubes and square tube with patterned circular perforations (shown in Fig. 3) was carried out by data acquisition UTM, having 60 tonnes capacity. Quasi-static axial compressions of 100 mm cross head displacement at the rate of 5 mm/min were conducted on all the specimens. The data acquisition system records both cross head displacement as well as crushing force reaction at the bottom end of tubes. The displacement precision is about 1 mm, corresponding crushing load curves were recorded. In order to ensure the repeatability of the results, minimum of three samples are tested at each sample type. Initial crushing peak force (IPF) from the force displacement curves and crushing energy absorption capacity (EA) from area under the force displacement curves were obtained.

## **3 Results and Discussion**

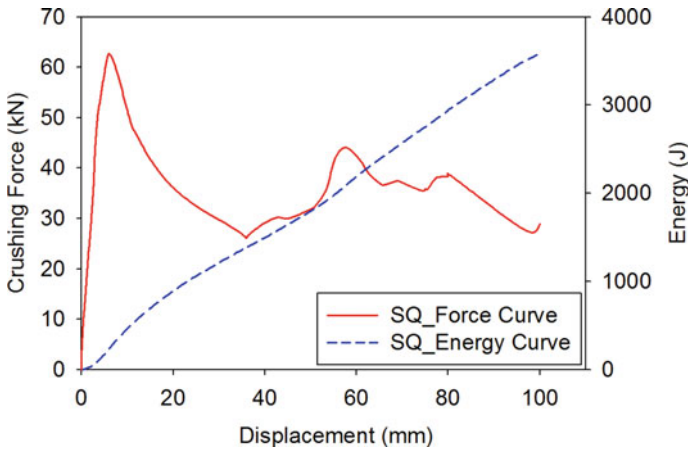
In the axial crushing quasi-static process, maximum crushing force, energy absorbing capacity (area enclosed by force–displacement curve) and specific energy absorption are the important performance characteristics of thin-walled structures. The initial



**Fig. 4** Deformation history of **a** square tube **b** square tube with patterned hole

peak crushing force (IPF) is to be reduced as possible to minimize the damage to occupants. Hence, the lower IPF is, the better in energy absorber's design. The axial compression tests on the bare tube and tube with patterned perforations were performed, and results were compared. Figure 4 presented the step-by-step crushing behaviour of both bare square tube and holed square tubes under axial loading. As it can be seen, after applying pressure in the plain square tube, the stress distribution is evenly throughout the surface, and then gradually with increasing in crosshead compression, the initial plastic hinge takes place. The progressive deformation was initiated by forming folding from bottom end and continuation of series of progressive folds takes place until the cross head reaches 100 mm displacement (compression). In case of patterned holed tubes, the moment the load is applied, plastic hinge is initiated in one of the holes under a same displacement and followed by progressive series of local buckling or hinges. It is noted that the IPF of patterned holed tubes is less than that of plain square tube. A similar observation was observed by Trong Nhan Tran [3] while crushing square tubes.

For a clarified comparison, the quasi-static compression of bare tubes and patterned perforation tubes resulted the force–displacement curves and crash energy–displacement curves which are presented in Figs. 5 and 6, respectively. It is seen from this figure that the maximum crushing force for the square tube is relatively higher than that of tubes with holes. The initial peak force (IPF) and the total energy absorption for the extruded square tube were found to be 63 kN and 3000 J, respectively.



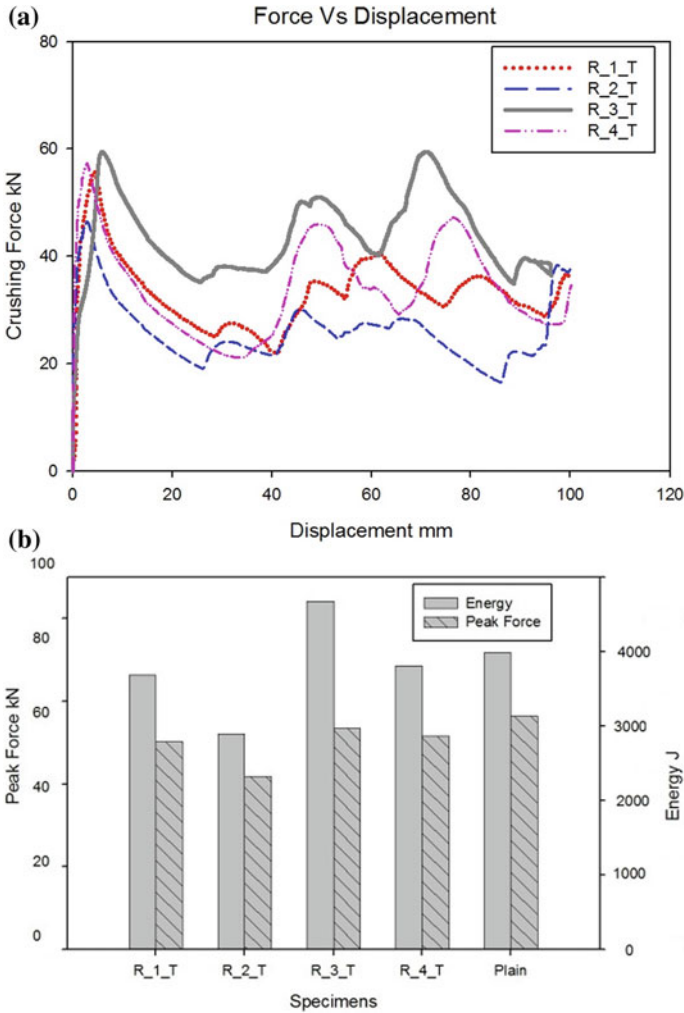
**Fig. 5** Crushing Force—displacement and Energy—displacement curves of the square tube

In this connection, patterned holes were introduced in tubes for the crushing performance enhancement. From Fig. 6a, the predicted initial peak force (IPF) and the total energy absorption capacity for the holed square tube (R\_3\_T) were 58 kN and 4000 J, respectively. Among holed tubes, R\_3\_T specimen has largest EA. The energy absorption capacities (EA) of specimens were computed from the area enclosed by force displacement curve using trapezoidal rule up to crushing distance of 100 mm.

## 4 Conclusion

In this experimental study, comparison between plain extruded tubes and patterned perforated tubes based on axial crushing response was carried out. The following conclusions can be drawn:

- Under quasi-static axial comparison, triggering mechanism like placing perforated holes can significantly increase mean crushing force of energy absorbers, since mean crushing force depends on the placement of holes. This method is not only effective in cost, but also the initial peak force was witnessed to be decreased due to influence of patterned holes, but it increases with the use of the bare square tube.
- The initial peak crush force was decreased in the range of 5–25%, and total energy absorption was increased up to 17% due to the introduction of the patterned holes.
- Thus, the results of the conducted experiment have shown the effectiveness of placing perforated holes on the lateral sides of the square tubes to improve the crushing performance.



**Fig. 6** a Force–displacement curve of the tubes with holes b Peak crushing force and energy comparison of the tubes with holes vs square tubes

## References

1. Sani, M.S.M., A review on crashworthiness studies of crash box structure, Thin-Walled Structures **153**, 106795 (2020)
2. Qvale, K.et.al, An experimental study on pre-stretched double-chamber 6000-series aluminium profiles subjected to quasi-static and dynamic axial crushing, Thin-Walled Structures **158** 107160 (2021)
3. Tran, T.N.: Study on the crashworthiness of windowed multi-cell square tubes under axial and oblique impact. Thin-Walled Struct. **155**, 106907 (2020)

4. Zhang a, H., Zhang, X.: Axial crushing of self-lock multi-cell tubes with foam filler and tube envelope, *Thin-Walled Structures* **155**, 106847 (2020)
5. Mamalis, A.G, Manolakos, D.E., Baldoukas, A.K., Viegelah, G.L.: Deformation characteristics of crashworthy thin-walled steel tubes subjected to bending. *Proc. Inst. Mech. Eng. Part C: J. Mech. Eng. Sci.* **203**, 411–417 (1989)
6. Song, J.: Numerical simulation on windowed tubes subjected to oblique impact loading and a new method for the design of obliquely loaded tubes. *Int. J. Impact Eng.* **54**, 192–205 (2013)
7. Tarigopula, V., Langseth, M., Hopperstad, O.S., Clausen, A.H.: Axial crushing of thin-walled high-strength steel sections. *Int. J. Impact Eng.* **32**, 847–882 (2006)
8. Abramowicz, W., Jones, N.: Dynamic axial crushing of square tubes. *Int. J. Impact Eng.* **2**, 179–208 (1984)
9. Abramowicz, W., Jones, N.: Dynamic progressive buckling of circular and square tubes. *Int. J. Impact Eng* **4**, 243–270 (1986)
10. Nalla Mohamed, M., Yuvarajan, P., Umasankar, M.: Energy enhancement of long cylindrical tubes with grooves subjected to axial impact. *Appl. Mech. Mater.* **787** Trans Tech Publications, pp. 345–349 (2015)
11. El-Hage, H., Mallick, P.K., Zamani, N.: A numerical study on the quasi-static axial crush characteristics of square aluminum tubes with chamfering and other triggering mechanisms. *Int. J. Crashworthiness* **10**(2), 183–196 (2005)
12. Chiu, Y.-S., Jenq, S.-T.: Crushing behavior of metallic thin-wall tubes with triggering mechanisms due to quasi-static axial compression. *J. Chin. Inst. Eng.* **37**(4), 469–478 (2014)
13. Shengyin, Wu., Li, G., Sun, G., Xin, Wu., Li, Q.: Crashworthiness analysis and optimization of sinusoidal corrugation tube. *Thin-Walled Struct.* **105**, 121–134 (2016)
14. ASTM E1251: Standard test method for analysis of aluminum and aluminum alloys by spark atomic emission spectrometry, American Society for Testing and Materials (2011)
15. ASTM International, ASTM E8/E8M—09 Standard Test Methods for Tension Testing of Metallic Materials, ASTM, (2009)

# Ansys Fluent Analysis of a Thermo-Hydrodynamically Lubricated Journal Bearing



N. Vaithianathan and S. Annamalai

## 1 Introduction

The present modern production industries necessitate machines which should be spinning at great speediness as well as it would transfer heavyweight loads. Hydro dynamically lubricated journal bearings are extensively applied in such machines as they meet this requirement. While a journal rotating at great speediness, it uninterruptedly deliveries energy to a film of lubricating oil. This leads toward the increase in the high temperature of the lubricating oil film owing to friction between the fluid layers of lubricant and shearing of lubricant layer. A great shearing level in the lubricating oil film heavily drops the viscosity of the lubricating oil. So thermo-hydrodynamic investigation is to be performed in objective to obtain the representative performance properties of the any journal bearing.

## 2 Literature Review

Gertzos et al. [1] worked on CFD investigation of Bingham lubricant on journal bearing under the hydrodynamic lubrication condition. They observed that a Bingham solid's load carrying capacity, film pressure, and frictional force are greater than those of Newtonian lubricants. M. Shau et al. [2] investigated the thermo-hydrodynamic analysis of three-dimensional energy equations using CFD technique for the accurate prediction of performance characteristics of a plain journal bearing. From their observation, the thermal effect on the lubricant property can be obtained by considering only the actual value of performance parameters obtained. Wang et al. [3]

---

N. Vaithianathan (✉) · S. Annamalai

Department of Mechanical Engineering, IFET College of Engineering, Gangarampalaiyam, TN 605108, India

made a thermo-hydrodynamic analysis of the partial texture of the journal bearing that is built on the journal surface. Based on the computational fluid dynamics system, a three-dimensional thermo-hydrodynamic analysis model has been developed. Performance parameter of textured and un-textured high-speed journal bearings is contrasted with different external loads under different eccentricity ratios. They say that the load carrying capacity of the textured bearing is greater than that of the un-textured bearing. Kim and Seireg [4] have developed mathematical model for thermo-hydrodynamic analysis incorporating Bingham rheological model. The dimensionless equations are solved using finite difference method. They conclude that results obtained are matched with the experimental values based on non-Newtonian fluid. Various boundary conditions and fluid flow conditions are implemented to journal bearing for simulation to get the actual value of pressure developed are illustrated in [5–11].

## 2.1 Theory

Computational fluid dynamics (CFD) is a fluid dynamics division that uses computational techniques and algorithms to resolve and analyze fluid flow problems. The Finite volume method (FVM) is the discretization technique mainly employed in computational fluid dynamics Fluent solvers. A domain is discretized into the finite range of control volumes (or cells). On this set of control volumes, general conservation (transport) equations for mass, momentum, energy, etc., are resolved. The fundamental governing equations for a viscous, heat-conducting fluid are the Navier–Stokes equations. It is a vector equation that is generated by applying the Law of Motion of Newton to a fluid variable, which is often referred to as the equation of momentum. The useful form of Navier–Stokes equations used in finite volume method is described below.

$$\rho \frac{\partial u}{\partial t} = -\frac{\partial p}{\partial x} + \text{div}(\mu \text{ grad } u) + S_{Mx} \quad (1)$$

$$\rho \frac{\partial v}{\partial t} = -\frac{\partial p}{\partial y} + \text{div}(\mu \text{ grad } v) + S_{My} \quad (2)$$

$$\rho \frac{\partial w}{\partial t} = -\frac{\partial p}{\partial z} + \text{div}(\mu \text{ grad } w) + S_{Mz} \quad (3)$$

where  $\mu$  is viscosity;  $S_M$  is momentum source.

The energy equation for incompressible and steady-state flow in three dimensional is given as below.

$$\frac{\partial}{\partial t}(\rho C_p T) + \nabla(\rho u C_p T) = \nabla(K \cdot \nabla T) + Q_v \quad (4)$$

where  $Q_V$  denotes volumetric heat source;  $C_p$  and  $K$  symbolize the specific heat of lubricating oil and thermal conductivity of the lubricating oil, respectively.

The viscosity of the lubricant is expected to vary with the temperature, which is given by the Barus equation as

$$\mu(T) = \mu_0 e^{-\beta(T-T_0)} \tag{5}$$

where  $\mu_0$  is the viscosity of oil at  $T_0$  and  $\beta$  Temperature viscosity coefficient of lubricating oil.

Temperature viscosity coefficient ( $\beta$ ) = 0.034 °C<sup>-1</sup>.

## 2.2 Computational Results

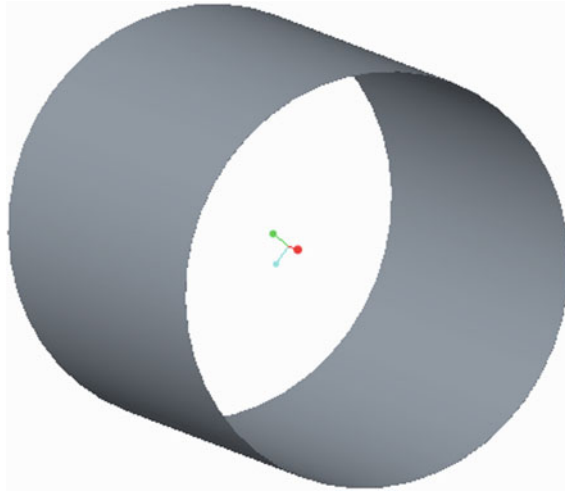
The CFD analysis was made on the hydro dynamically lubricated journal bearing to study the performance parameters such as pressure distribution using ANSYS® FLUENT 18.1. The results obtained in the present work on the journal bearing were obtained by varying the L/D as 0.5 to 2 and with different speed range of shaft from 1500 to 3000 rpm. The various input parameter for design as well simulation of journal bearing is given in Table 1. In this simulation, the fluid film is only considered to evaluate the pressure developed in process. The solid modeling technique is used to create the fluid film which is shown in Fig. 1.

If the viscosity of oil remains constant, then the pressure found is entitled as isothermal pressure, while the pressure obtained is called thermal pressure when the temperature dependent viscosity of lubricant is taken into account. In this simulation, flow of fluid has been considerate as laminar flow; because for initially, all the fluids are considered as regular flow with Newtonian behavior. And coming to the operating boundary condition of bearing for the rotation of lubricant in journal bearing are one side of fluid layer (inlet) is assumed as working at atmospheric condition (atmospheric pressure). Reaming parameters like temperature and pressure are computed by the speed of the bearing operated.

**Table 1** Input parameters

SL.NO	Parameter	Value
1	Journal diameter (mm)	100
2	Radial clearance (mm)	0.1
3	L/D ratio	0.5,1,1.5,2
4	Eccentricity ratio	0.5
5	Lubricant viscosity (Pas)	0.04986 and 0.057

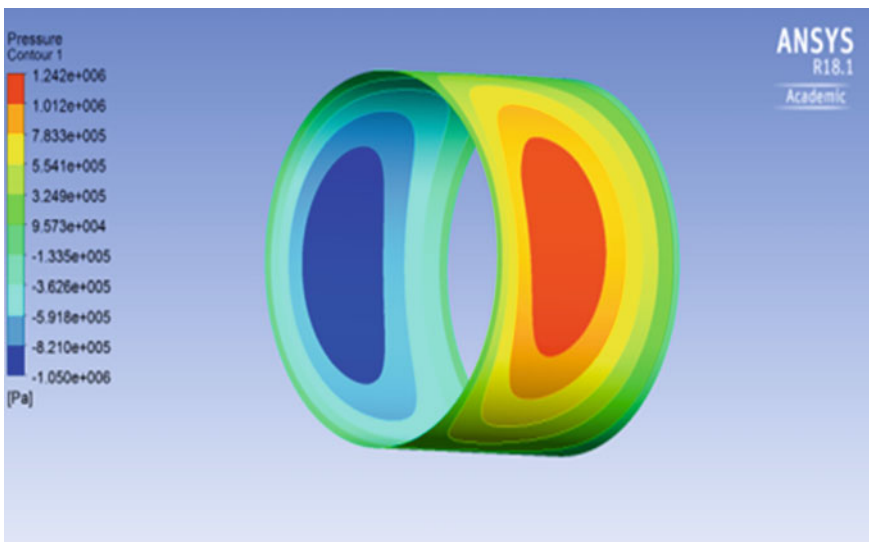




**Fig. 1** Typical solid model of fluid domain

### 3 Results and Discussion

By simulating the fluid layer with corresponding values, the pressure developed in the system is shown in Fig. 2. From the figure, it is clearly identified that pressure



**Fig. 2** Thermal pressure contour for Full-Sommerfeld's boundary conditions at viscosity 0.04986 Pas and 2500 rpm for  $L/D = 1$

developed in the journal bearing has produced both maximum positive pressure as well as negative pressure in the equal amount. This type of bearings is generally known as Full-Sommerfeld's boundary conditions operated journal bearing. As the input operating parameters of journal bearing varies, the pressure developed is also differs for corresponding input value which are shown by Fig. 3 and Fig. 4.

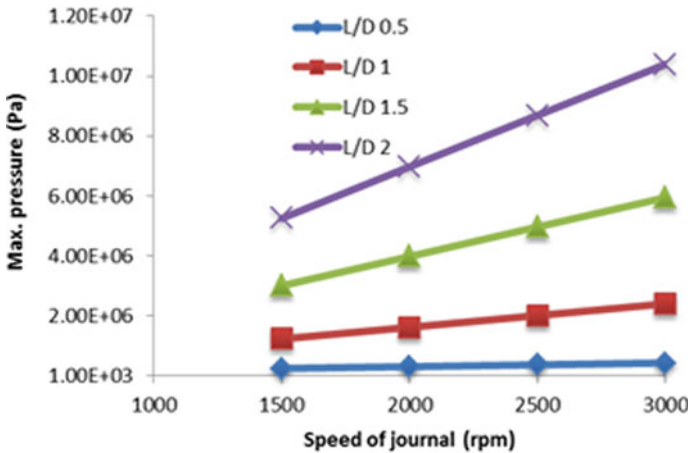


Fig. 3 Maximum pressure for various speed for  $\mu = 0.049$  Pas

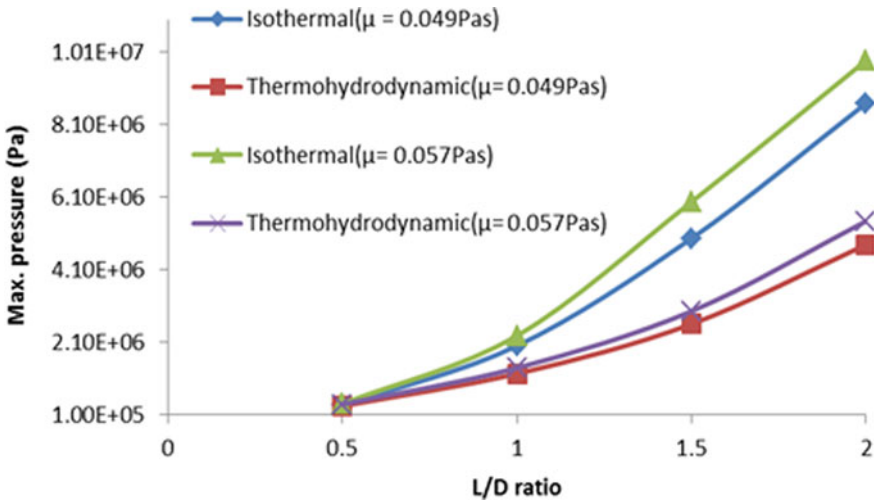


Fig. 4 Maximum pressure developed for different L/D ratio for fluid with two viscosities at 2500 rpm

## 4 Conclusion

A numerical calculation generally gives only pure theoretical values instead of that if the simulation is performed, the end value may approach the realistic one. For fluid computational, fluid dynamic is one of the tools to get the realistic fluid behavior. CFD analyses have been performed for a journal bearing using fluent with some conditions such as the pressures developed has been affected by increasing the temperature in fluid due to change in fluid behavior on operation. From the results presented, it is inferred that.

- When the input parameters such as viscosity, operating speed of bearing, and L/D ratio increase, the performance parameter of journal bearing such as pressure developed increases.
- By considering the temperature effect on the viscosity of the lubricant, the pressure developed decreases when compared to simulation of simple hydrodynamic lubricated journal bearing.

## References

1. Gertzos, K.P., Nikolakopoulos, P.G., Papadopoulos, C.A.: “CFD analysis of journal bearing hydrodynamic lubrication by bingham lubricant”. *Tribol. Int.* 1190–1204 (2008)
2. Sahu, M., Giri, A.K., Das, A.: “Thermohydrodynamic analysis of a journal bearing using CFD as a tool”. *Int. J. Sci. Res. Publ.* 1–7 (2012)
3. Wang, L., Han, Z., Chen, G., Su, H.: “Thermo-hydrodynamic analysis of large-eccentricity hydrodynamic bearings with texture on journal surface”. *J. Mech. Eng. Sci.* 1–6 (2017)
4. Kim, J.H., Seireng, A.A.: “Thermohydrodynamic lubrication analysis incorporating bingham rheological model. *ASME J. Tribol.* 137–46 (2000)
5. Wada, S., Hayashi, H., Haga, K.: “Behavior of a bingham solid in hydrodynamic lubrication (part 3, application to journal bearing)”. *JSME*, 1182–1191 (1974)
6. S.T.N. Swamy, B.S. Prabhu, B.V.A. Rao, “Steady State and Stability Characteristics of a Hydrodynamic Journal Bearing with a Non-Newtonian Lubricant”, *Wear*, 1977, p. 229–244
7. Tiwari, P., Kumar, V.: “Analysis of hydrodynamic journal bearing using CFD and FSI technique”. *IJERT*, 1210–1215 (2014)
8. Singla, A., Singh, P., Kumar, A., Chauhan, A., Bala, S.: “Thermo-hydrodynamic analysis on temperature profile of circular journal bearing using computational fluid dynamics”. *IEEE*, 1–6 (2014)
9. Michaud, P., Souchet, D., Bonneau, D.: “Thermohydrodynamic lubrication analysis for a dynamically loaded journal bearing”. *J. Eng. Tribol.* 49–61 (2007)
10. Bagul, K.H., Patil, P.N., Patil, R.Y.: “Thermal analysis of journal bearing using CFD software for performance enhancement”. *IJARIT*, 287–293 (2017)
11. Yoo, J.G., Kim, K.W.: “Numerical analysis of grease thermal elastohydrodynamic lubrication problems using the herschel-bulkley model”. *Tribol. Int.*, 401–408 (1997)

# Investigation on Deflection Characteristics of Auxetic Beam Structures Using FEM



Hrishikesh G. Menon , Shammo Dutta , M. P. Hariprasad ,  
and Balakrishnan Shankar 

## 1 Introduction

It is a well-known fact that when an ordinary object/structure is stretched in one direction, it contracts in the lateral direction, and conversely, when compressed in one direction, it elongates laterally. A certain class of structures, on the other hand, do not behave in this prescribed manner; an elongation longitudinally results in an elongation laterally, and the same goes for compression. Such structures are termed as auxetic or Negative Poisson's Ratio (to be abbreviated as NPR throughout the rest of the manuscript) structures.

A re-entrant hexagonal honeycomb and its parent, the conventional hexagonal honeycomb, are studied by [1, 2]; early studies carried out by these authors on the mechanics of such structures reveal the fact that such a response of the auxetic material is largely attributed to its geometry and not to its material prospects. The re-entrant honeycomb, structures like the RCA, has been investigated in detail by Alomarah et al. [3, 4].

A comprehensive research on the performance of honeycomb was presented by Masters et al. [5]. A follow up study has been conducted by Lan et al. [6] in the same context. In addition investigation regarding the crushing stress of the honeycomb has been carried out by [7].

Najafi et al. [8] explored the energy absorbing capacities of various types of auxetic structures. A subsequent study by Zhichao Dong et al. [9] on the deformation modes of thick walled and thin walled re-entrant honeycombs proves to be vital in assessing the structures' overall behaviour. Vibrational isolation capacity of the re-entrant honeycomb has been investigated by Zhang et al. [10]. [11, 12] carried out works in fabricating auxetic gradient cellular cored sandwich panels to test its load-bearing capacities.

---

H. G. Menon · S. Dutta · M. P. Hariprasad (✉) · B. Shankar  
Department of Mechanical Engineering, Amrita Vishwa Vidyapeetham, Amritapuri, India

The influence of residual stresses and Poisson's ratio on the stress intensity factors as well a detailed study in determining the tensile properties of pressure vessels through automated ball indentation was carried out by [13–15].

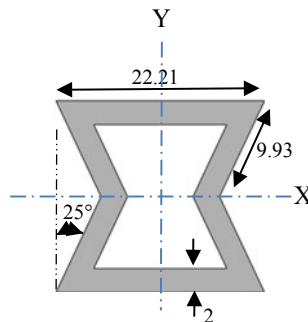
In this work, different variations of 2D re-entrant structured beams are designed by arranging clusters of re-entrant unit cells with a bounded frame and are tested using numerical simulations. Deformations characteristics of the designed auxetic beams are analysed, and the deflection characteristics are investigated. Based on the analysis of the deflection characteristics of conventional auxetic beams, improved designs with the filler materials are developed for the structural enhancement of conventional beams. In order to understand the effect of filler materials on the deflection characteristics of auxetic beams, multiple foreign filler materials are introduced in the design.

## 2 Modelling and FE Analysis

Finite element analysis is adopted to study the behaviour of re-entrant structured beams. The single cell structure of re-entrant honeycomb, as shown in Fig. 1, is designed with its cell angle and rib thickness to be  $25^\circ$  and 2 mm, respectively. The slant and horizontal length of the cells are 9.93 mm and 22.21 mm. Multiple cells of this kind are repeated in a two-dimensional periodic manner to form a cluster of auxetic cells.

The required final structure is designed by placing this cluster of re-entrant cells in a bounded frame with a specified thickness. The frame dimensions, 408 mm x 108 mm, running 4 mm thick, are kept constant throughout the study.

The FE models are developed in ABAQUS 6.14. All the models are made with Aluminium having a density of 2.7 kg/m<sup>3</sup>, and a Young's Modulus and Poisson's ratio value of 68,000 MPa and 0.36, respectively. The FE model is meshed with an



**Fig. 1** Dimensions of the re-entrant honeycomb unit cell

element size value of a quarter of the rib thickness with CPS4R, a 4 node plain stress element. All the beams are subjected to four—point loading with 1000 N, and the deflection characteristics are analysed.

### 2.1 Conventional Auxetic Beams

In the conventional auxetic beam structures, the auxetic re-entrant structures are arranged as shown in Fig. 2. Figure 2a shows a re-entrant beam with auxetic clusters aligned along Y axis (indicated in Fig. 1), and Fig. 2b shows the beam with clusters aligned along X axis (indicated in Fig. 1). The type of beams shown in Fig. 2a is referred as re-entrant structured Beam 1, and the one shown in Fig. 2b is referred as re-entrant structured Beam 2. In both the cases, the designs (Fig. 2a and b) are abbreviated as RS Beam 1 and RS Beam 2, respectively.

Poor performance of these beams may have been the potential reason for lesser amount of research into these aspects [12]. In order to understand the deflection characteristics of top and bottom regions, the deflection values along the lines AB and CD (in Fig. 2a) are plotted and are shown in Fig. 3a and b, respectively.

On close observation of Fig. 3a and b, one can notice that the deflection characteristics of RS Beam 2 at the compressive and tensile side (bottom-most and top-most

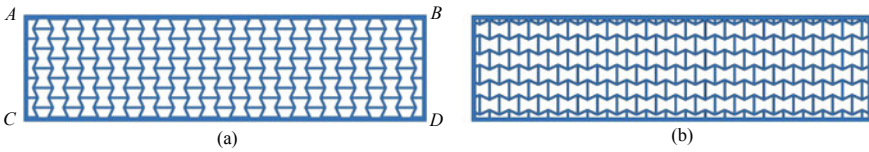


Fig. 2 Conventional re-entrant beams

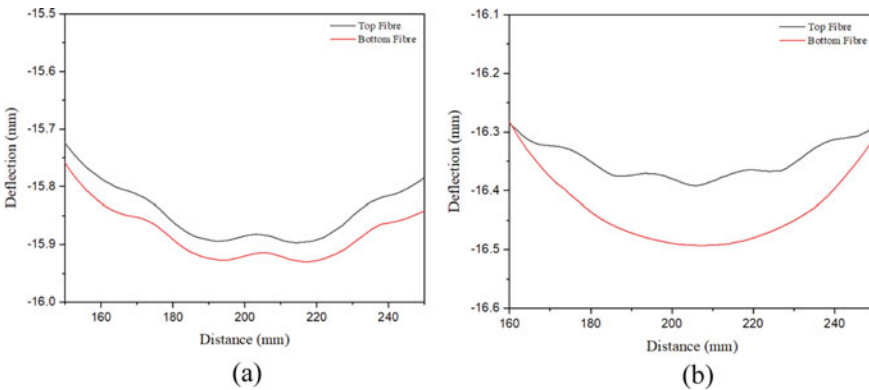


Fig. 3 Deflection of top and bottom fibre for a RS Beam 1 b RS Beam 2

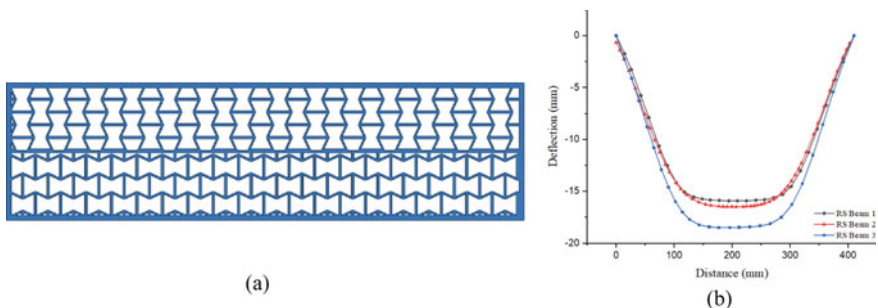
horizontal fibre of the frame) are varying in magnitude as well as characteristics. This irregularity (of the top-most fibre curve) is verified to be not only concentrated at the loading point but to be spread throughout the beam's length, while, on the other hand, the RS Beam 1 shows expected behaviour at both sides. It can be inferred from this that cells placed at different locations in the beam and their types influence the behaviour of the beam to a significant amount, or in other words, the position of packing of the unit cells plays a vital role in understanding the beam characteristics.

In this paper, an attempt is made to address this point by designing a novel structure that combines both RS Beam 1 and RS Beam 2 into one single structure. Following sections highlight an effort in this direction.

## 2.2 Combination of RS Beam 1 and RS Beam 2

The cluster of cells is now arranged in two different manners into a single frame. A portion of the RS Beam 1 is placed above a dimensionally similar portion of the RS Beam 2 with a merger link in between. The resultant structure is placed in a frame with the same specified dimensions to maintain uniformity in design and analysis. The merger link is a design requirement to impart a satisfactory linkage between both the clusters. The link is designed to be 4 mm thick. The resultant is as shown in Fig. 4a. This combined structure will be addressed to as RS Beam 3 henceforth. This re-entrant structured beam is then tested via simulations, and the results for displacement characteristics are recorded as measured long the line *CD*. The trends are as shown in Fig. 4b.

One can notice from Fig. 4b that the deflection characteristics of RS Beam 3 have not seen a significant improvement from that of RS Beam 1 and RS Beam 2. The range of maximum deflection is in the order of 17 mm. Improvement in structural performance requires an integration of design as well as material aspects. Instead of changing the material of the structure, one can incorporate a foreign filler material.



**Fig. 4** a RS Beam 3 b Deflection characteristics of RS Beam 3 against RS Beam 1 and 2

### 2.3 Filler Material Embedded Structures

The deflection characteristics of re-entrant beams with structural modifications were explored in the previous sections. However, the capabilities of structural performance of the beams by introducing filler materials-in the cellular voids were not explored. Relatively lower density of the filler materials is judiciously selected so as to retain the overall mass of the structure in comparison with the non-filler design. However, a choice for higher values of Young's modulus for the filler material provides better load-bearing capacities by which the deflections characteristics can be improved for such structures.

Fillers are introduced in all the three RS Beams. Numerical analysis is carried out on the designed models, and the trends in deflection characteristics for each of the RS Beam with each individual fillers are shown in Fig. 5, which provides a systematic display of the deflection characteristics for each of the filled beams and provides a visual comparison of what fillers assist in producing superior results. Deflection, being in the 'Y' direction, is represented by  $\delta_y$  (in mm), and the horizontal length of the beam is represented by 's' (in mm). Filler materials are seen to have a positive influence on the response of the beams. From Fig. 5, one can note that lower range in deflections are shown by beams when filled with materials like PMMA, as pointed out visually by the adopted biasing method among the graphs.

## 3 Results and Discussion

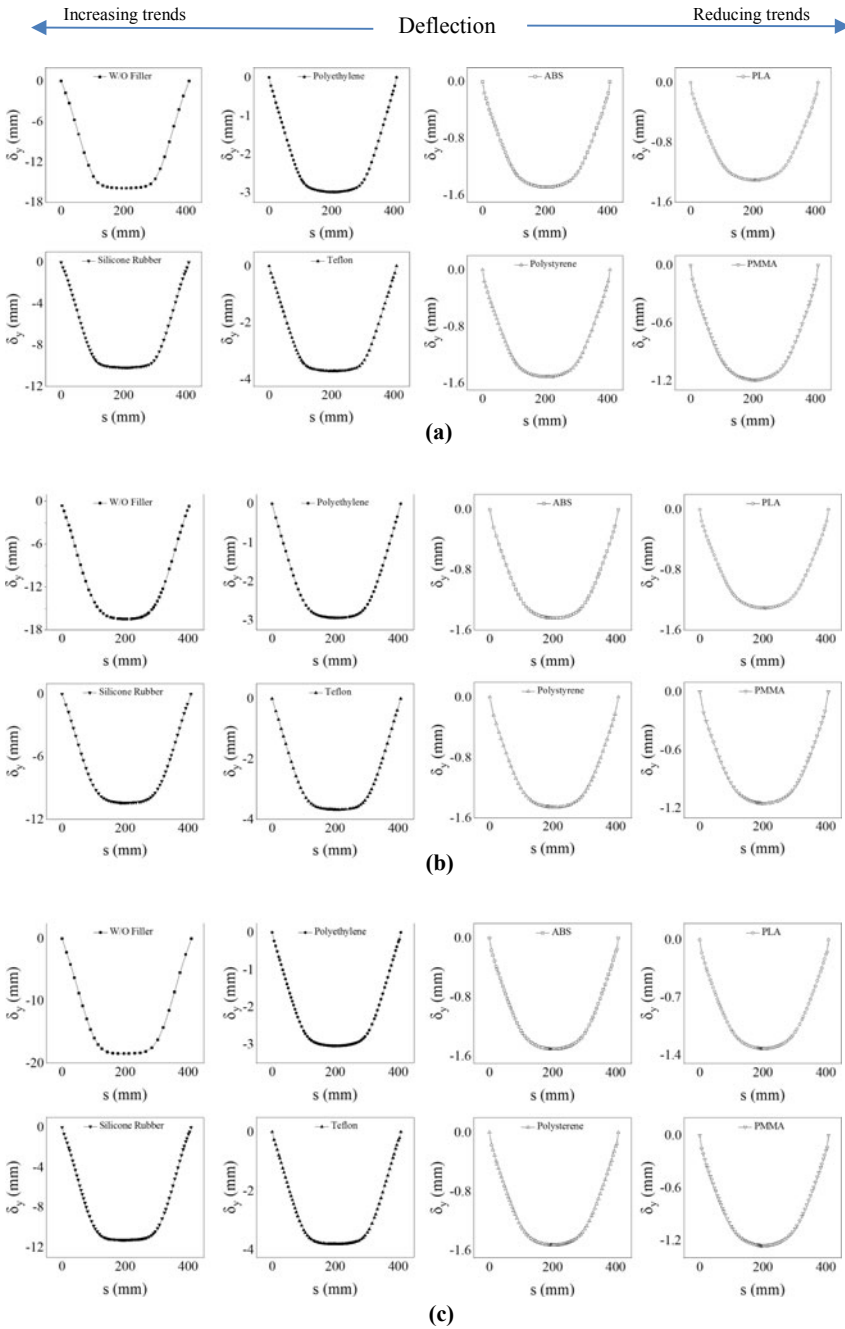
Optimization of auxetic beams is discussed mainly in two methods here: firstly by exploiting the factor of placement of cells and secondly by introducing appropriate fillers.

From Fig. 3, it is evident that the placement of cells at different locations of the beam influences the deflection characteristics of the beam to a significant amount, or in other words, the position of packing of the unit cells plays a vital role in understanding the beam characteristics.

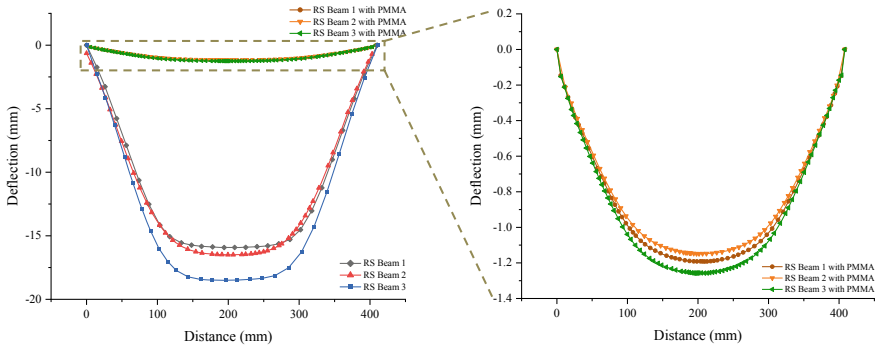
A preliminary understanding of the measure of how efficient a filler material would be, in terms of its ability to assist a structures' load-bearing capacity, is arrived at by estimating a ratio of the filler's Young's modulus to that of the material used in the structure.

Results from the FE analysis are finally clubbed together to obtain a holistic understanding of the behaviour of the RS Beams and the influence of filler elements. Observing Fig. 5, one can infer that introduction of PMMA has proven to be the most beneficial of all the fillers. Figure 6 presents deflections characteristics of the RS Beams with and without PMMA. The deflection behaviour of PMMA filled beams is shown in the sub-graph which is highlighted through the blue box. Although the three RS Beams displayed poor mechanical properties (as observed from Fig. 4b), one can notice from Fig. 6 that the same beams show a significant amount of improvement





**Fig. 5** Deflection characteristics of RS Beams with filler material **a** RS Beam 1 **b** RS Beam 2 **c** RS Beam 3



**Fig. 6** Deflection characteristics of RS Beams with PMMA filler

when embedded with PMMA. The final deflection of the RS Beams with PMMA, as observed from Fig. 6, is in the range of 1.1–1.3 mm.

## 4 Conclusion

In this paper, re-entrant structured beams are designed and tested numerically. Effects of introducing a filler material are discussed, and its positive responses are recorded and shown. Out of the family of fillers used in this paper, it is observed that PMMA filled beams responds relatively better to the applied loads, when placed in comparison with the same beam without any filler. Profitable designs are provided, and the results show enhancement in mechanical properties. Digital Image Correlation, Digital Photoelasticity and other whole field optical experimental techniques would be of interest in observing the stress and displacement fields of such auxetic structures, considering the fact that most of the fillers used here are birefringent materials [16–19]. This paper calls for methods to optimize the existent designs of auxetics as well as to explore the possible ways to implement such efficient designs in practical scenarios.

## References

1. Abd El-Sayed, F., Jones, R., Burgess, I.: A theoretical approach to the deformation of honeycomb based composite materials. *Composites* **10**(4), 209–214 (1979). [https://doi.org/10.1016/0010-4361\(79\)90021-1](https://doi.org/10.1016/0010-4361(79)90021-1)
2. Gibson, L.J., Ashby, M.F.: *Cellular solids: structure and properties*. Cambridge University Press (1999)

3. Alomarah, A., Ruan, D., Masood, S.: Tensile properties of an auxetic structure with re-entrant and chiral features—a finite element study. *The International Journal of Advanced Manufacturing Technology* **99**(9–12), 2425–2440 (2018). <https://doi.org/10.1007/s00170-018-2637-y>
4. Alomarah, A., Ruan, D., Masood, S., Sbarski, I., Faisal, B.: An investigation of in-plane tensile properties of re-entrant chiral auxetic structure. *The International Journal of Advanced Manufacturing Technology* **96**(5–8), 2013–2029 (2018). <https://doi.org/10.1007/s00170-018-1605-x>
5. Masters, I., Evans, K.: Models for the elastic deformation of honeycombs. *Compos. Struct.* **35**(4), 403–422 (1996). [https://doi.org/10.1016/s0263-8223\(96\)00054-2](https://doi.org/10.1016/s0263-8223(96)00054-2)
6. Lan, L., Fu, M.: Nonlinear constitutive relations of cellular materials. *AIAA J.* **47**(1), 264–270 (2009). <https://doi.org/10.2514/1.39531>
7. Yin, H., Wen, G.: Theoretical prediction and numerical simulation of honeycomb structures with various cell specifications under axial loading. *Int. J. Mech. Mater. Des.* **7**(4), 253–263 (2011). <https://doi.org/10.1007/s10999-011-9163-5>
8. Najafi, M., Ahmadi, H., Liaghat, G.: Experimental investigation on energy absorption of auxetic structures. *Materials Today: Proceedings* (2020). <https://doi.org/10.1016/j.matpr.2020.06.075>
9. Dong, Z., Li, Y., Zhao, T., Wu, W., Xiao, D., Liang, J.: Experimental and numerical studies on the compressive mechanical properties of the metallic auxetic reentrant honeycomb. *Mater. Des.* **182**, 108036 (2019). <https://doi.org/10.1016/j.matdes.2019.108036>
10. Zhang, X., Yang, D.: Numerical and experimental studies of a light-weight auxetic cellular vibration isolation base. *Shock Vibration*, 1–16, (2016). <https://doi.org/10.1155/2016/4017534>
11. Hou, Y., Tai, Y., Lira, C., Scarpa, F., Yates, J., Gu, B.: The bending and failure of sandwich structures with auxetic gradient cellular cores. *Compos. A Appl. Sci. Manuf.* **49**, 119–131 (2013). <https://doi.org/10.1016/j.compositesa.2013.02.007>
12. Shammo, D., Hrishikesh, G., Menon, M.P., Krishnan, H.A., Shankar, B.: Study of auxetic beams under bending: a finite element approach. *Mate. Today: Proceed.* ISSN 2214–7853, (2020). <https://doi.org/10.1016/j.matpr.2020.10.479>
13. Ravi Kiran, B., Arunkumar, S., Manoj Reddy, G.: Influence of residual stress and poisson's ratio on the stress intensity factor of standard specimens. *Int. J. Mech. Eng. Technol.* **9**(10), 219–227, (2018). <http://www.iaeme.com/IJMET/issues.asp?JType=IJMET&VType=9&IType=10>
14. Arunkumar, S., Prakash, R. V.: Estimation of Tensile Properties of Pressure Vessel Steel Through Automated Ball Indentation and Small Punch Test. *Trans Indian Inst Met* **69**, 1245–1256 (2016). <https://doi.org/10.1007/s12666-015-0680-z>
15. Babu, J.S., Mondal, C., Sengupta, S., Karmakar, S.: Excess vibrational density of states and the brittle to ductile transition in crystalline and amorphous solids. *Soft Matter* **12**(4), 1210–1218 (2016). <https://doi.org/10.1039/c5sm02200b>
16. Hariprasad, M.P., Ramesh, K.: Evaluation of Hertzian contact parameters from whole field displacement data. *J. Strain Anal. Eng. Design* **52**(7), 403–409, (2017). <https://doi.org/10.1177/0309324717723274>
17. Hariprasad, M.P., Ramesh, K., Prabhune, B.C.: Evaluation of Conformal and Non-Conformal Contact Parameters Using Digital Photoelasticity. *Exp Mech* **58**, 1249–1263 (2018). <https://doi.org/10.1007/s11340-018-0411-6>
18. Hariprasad, M.P., Ramesh, K.: Analysis of contact zones from whole field isochromatics using reflection photoelasticity. *Optic. Laser. Eng.* **105**, 86–92, ISSN 0143–8166 (2018). <https://doi.org/10.1016/j.optlaseng.2018.01.005>
19. Kumar, P., Hariprasad, M.P., Menon, A., Ramesh, K.: Experimental study of dry stone masonry walls using digital reflection Photoelasticity. *Strain* **56**, e12372 (2020). <https://doi.org/10.1111/str.12372>

# Interdependence of Eccentric Force and Torque on Joint Angle and Angular Velocity During Human Multi-joint Leg Extension



Rajesh Kumar Bhushan and Ashutosh Swain

## 1 Introduction

Muscle force made throughout isometric contractions could be a function of the muscle length (the length-tension relation). Throughout the movement in vivo, the length-tension relation of muscles is usually understood in terms of the joint angle-torque relation [1] that is outlined by the lever system or joint configuration additionally to the length-tension relation of the muscle itself. For human muscles, maximum voluntary force can be expressed as a mathematical function dependent on both joint angle ( $T-\theta-r$ ) and angular speed ( $T-\omega-r$ ). Though the contribution of every part of the ensuing force is troublesome to discriminate, the  $T-\theta$  and  $T-\omega$  relationships are necessary properties required to characterize the in vivo human muscle operation. It is still wide assumed that joint angle and angular speed are thought-about as independent regulators of torque-output that scale according to the acceptable level of activation. Therefore, the bulk of those studies have centered solely on joint angle or angular speed effects singly. There is experimental proof suggesting interdependency [2, 3].

Data on the interdependency of force, joint angle, and angular speed throughout eccentric muscle action is distributed. Eccentric torque is varied from 0.9–1.18 of the isometric references counting on muscle length and speed [4]. These interactions were neither analyzed systematically nor statistically. In 2011 and 2013, Forrester and Pain analyzed that no increased torques and no systematic interdependency of calculated fiber forces, muscle lengths, and continuation velocities were found. However, maximum voluntary eccentric joint force is diminished with increasing stretching speed [5, 6].

For joints apart from the knee, knowledge on the interdependency of joint angles and angular speed as well as eccentric muscle action is very rare. Yeadon and King [7] developed a mathematical function to suit and extrapolate measured knowledge

---

R. K. Bhushan · A. Swain (✉)

Department of Mechanical Engineering, NIT Manipur, Imphal, India

of the ankle joint, knee, hip, and shoulder to specific joint force as a function of joint angle and joint angular speed. Therefore, the purpose of this study is to visualize the interdependency of force/ torque, joint angles, and angular speed throughout multi-joint leg extension, that tries to copy the muscle action conditions in real-life movement of humans [8, 9]. For eccentric muscle action, Hanh et al. [10] hypothesized that force and torque don't exceed the isometric references and reduce with increasing angular speed a minimum of on the far side an exact purpose.

The analysis of variance takes a look at the initial step in analyzing factors that have an effect on a given knowledge set. Once the analysis is finished, the analyst performs more testing based on the factors that contribute to the dataset's inconsistency. The ANOVA takes a look at results which are used in an f-test to get extra knowledge that aligns with the planned regression models. The analysis of variance takes a look at comparison of over two teams at an equivalent time to work out whether or not a relationship exists between them. The results of the analysis of variance formula, the F data point (also referred to as the F-ratio), permit for the analysis of multiple teams of information to work out the variability between samples and inside samples.

## 2 Research Methodology

Data from Hahn et al. [10] was used for the analysis of the interdependence of force, torque, joint angle, and angular velocity. The data is gathered in normalized form. For simplification, the mean normalized values were taken into consideration. This data is then used for the analysis in two different software, namely MATLAB and DX design expert software. A MATLAB code was written to find the linear regression analysis of the dependence of force and torque on the joint angles and angular velocity and also to find the graphical analysis. In the design expert software, the data was analyzed using response surface methodology (RSM). ANOVA was used to carry out the statistical significance tests. The test data from Hahn et al. [10] is in the following Table 1.

## 3 Results and Discussion

The regression equations are as follows:

$$\begin{aligned} \text{Force} = & 0.72804 + 5.58257E - 003 * \text{Angle} \\ & - 1.78106E - 003 * \text{Velocity} + 3.80630E \\ & - 005 * \text{Angle} * \text{Velocity} \end{aligned} \quad (1)$$

**Table 1** Influence of joint angle and angular velocity on eccentric forces and torques normalized to their corresponding isometric values

Normalized force or torque at (velocity)	Knee joint flexion Angle(°)					
	40	50	60	70	80	90
F(-30 s <sup>-1</sup> )	0.94	1.03	1.09	1.13	1.13	1.1
F(-60 s <sup>-1</sup> )	0.97	0.95	1.01	1.1	1.14	1.15
F(-90 s <sup>-1</sup> )	1.03	1.02	0.89	0.88	1.05	1.13
F(-120 s <sup>-1</sup> )	1.04	1.05	0.96	0.85	0.9	1.02
M(-30 s <sup>-1</sup> )	1.01	1.09	1.24	1.26	1.25	1.23
M(-60 s <sup>-1</sup> )	1.06	0.98	1.12	1.22	1.26	1.27
M(-90 s <sup>-1</sup> )	1.09	1.03	0.97	0.99	1.2	1.3
M(-120 s <sup>-1</sup> )	1.09	1.04	1.01	0.93	0.98	1.14

ANOVA model for the above equation is as follows:

The model F-value of 7.28 implies that the model is significant. There is only a 0.17% chance that a “Model F-Value” this large could occur due to noise.

$$\begin{aligned} \text{Torque} = & 0.76954 + 6.78935E - 003 * \text{Angle} - 1.08604E \\ & - 003 * \text{Velocity} + 3.18321E - 005 * \text{Angle} * \text{Velocity} \end{aligned} \quad (2)$$

ANOVA model for the above equation is as follows:

The model F-value of 11.07 implies that the model is significant. There is only a 0.02% chance that a “Model F-Value” this large could occur due to noise.

The plots of the data are as follows:

While angular velocity had little to no impact on force/torque for joint angles less than or equal to its specific  $\theta$  at same velocity, eccentric force/torque varied consistently with angular speed for joint angles larger than its velocity-specific  $\theta$  (Figs. 1 and 2). From Figs. 3 and 4, for the eccentric contractions, there was heavy angle dependence of the velocity relation for each, force F and torque M.

From Table 1, we can see that at 60° knee flexion angle, force peaked at 1.09 F0 for  $\omega = -30 \text{ s}^{-1}$ , dropped to 1.01 F0 for  $\omega = -60 \text{ s}^{-1}$  and maintained the trend. Similarly, at a 60° knee flexion angle, force peaked at 1.24 M0 for  $\omega = -30 \text{ s}^{-1}$ , dropped to 1.12 M0 for  $\omega = -60 \text{ s}^{-1}$  and failed to show torques beyond it for the remaining angular velocities. But in 90° knee flexion, there was a major increase in force for all angular velocities that is analogous to as reported in Hanh et al. [10]. Brown et al. [11] and Scott et al. [3] found results which are in agreement. These results may have been caused by muscle inhibition to safeguard the quadriceps femoris cluster against extreme tension [10]; however, more analysis on this finding is needed.

From these results, we are able to see that in agreement with literature for eccentric contractions, these are the findings:

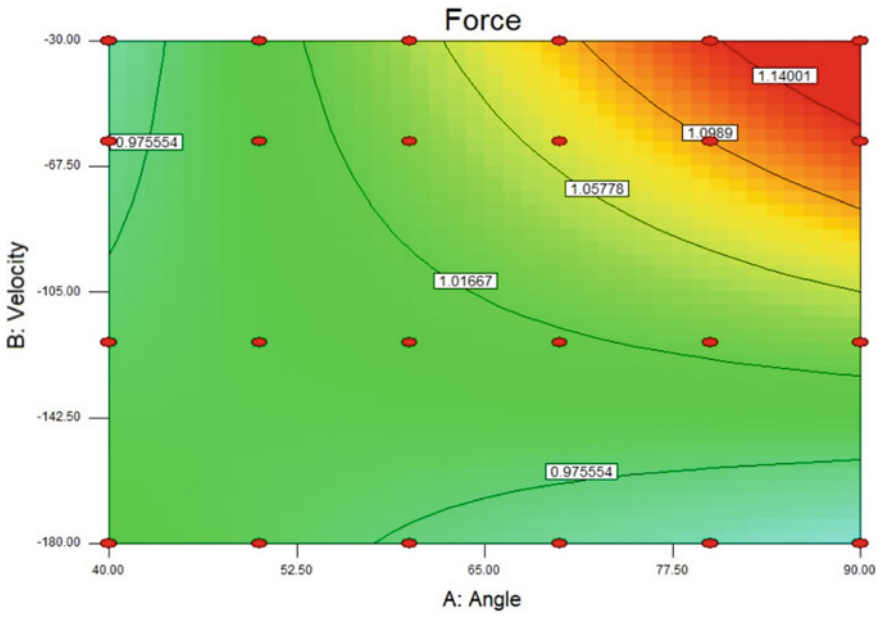


Fig. 1 Interaction plot of force with joint angle and angular velocity

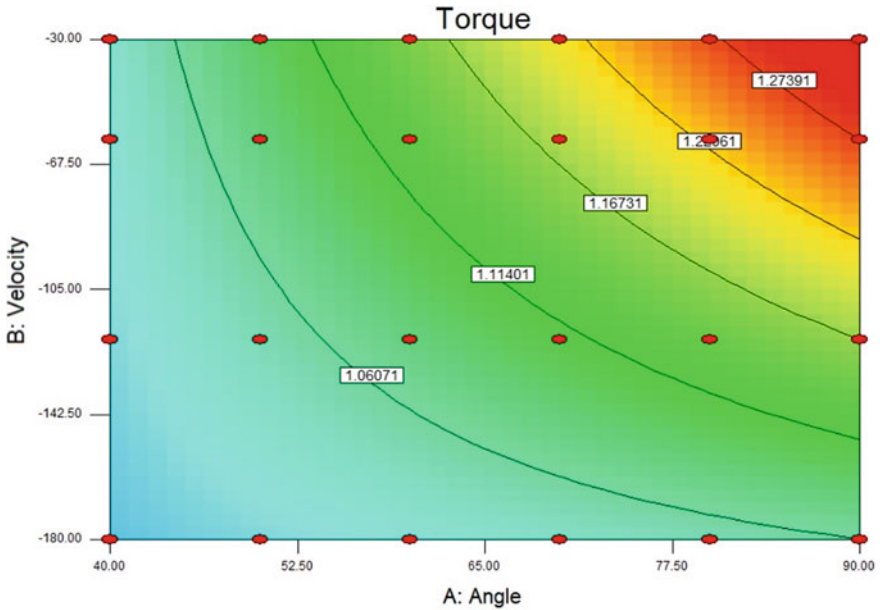


Fig. 2 Interaction plot of torque with joint angle and angular velocity

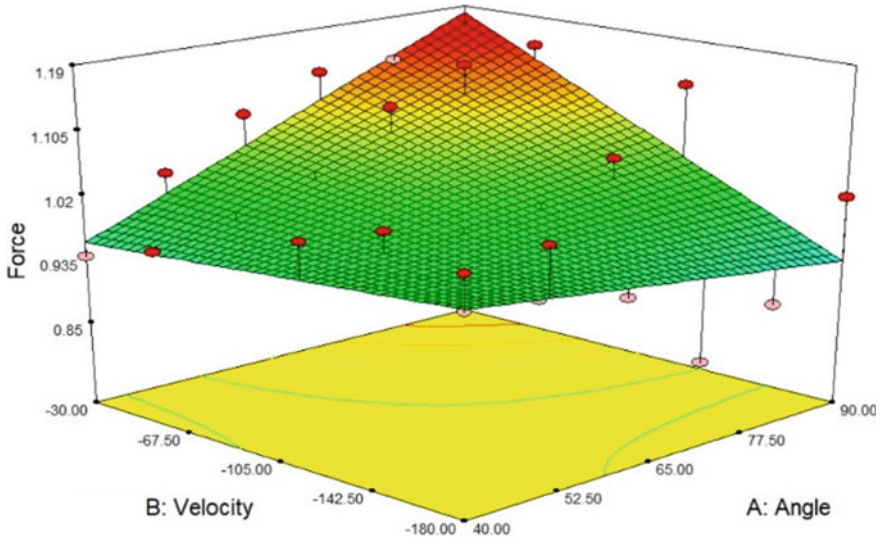


Fig. 3 Three-dimensional force–angle–angular velocity plot of normalized knee joint force (y-axis), joint angle (z-axis), and angular velocity (x-axis)

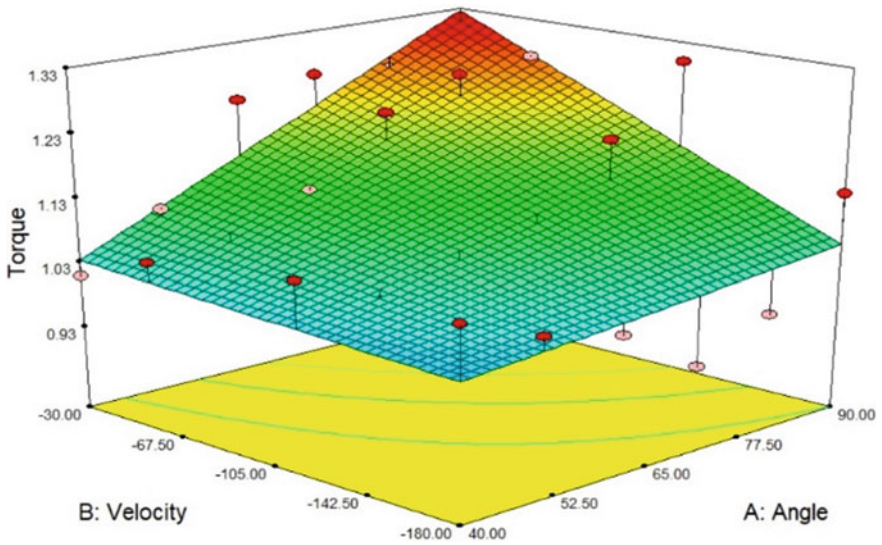


Fig. 4 Three-dimensional torque–angle–angular velocity plot of normalized knee joint torque (y-axis), joint angle (z-axis), and angular velocity (x-axis)



1. Normalized eccentric force F and force M enlarged with knee flexion.
2. Dependence of eccentric force/torque on angular speed was discovered for knee flexion angles.
3. Once joint angles exceeded 60° knee flexion, a major increase in force/torque was discovered.

## 4 Conclusion

Data was taken from Hanh et al. [10]. The data was then analyzed using programming in MATLAB. The regression equations were formed using MATLAB, and the graphical models were created. The analysis was cross checked by comparing with ANOVA analysis.

From Figs. 1 and 2, it was found that the force and torque felt during multi-joint leg extension heavily depends on the combination of both joint angle and angular velocity. Force and torque show a marked steep increase after knee flexion angle goes over 60°. Tables 2 and 3 validate the regression equations.

**Table 2** ANOVA model of force

Source	Sum of Squares	df	Mean Square	F Value	p-value Prob > F
Model	0.096	3	0.032	7.28	0.0017
A-Angle	0.017	1	0.017	3.92	0.0616
B-Velocity	0.038	1	0.038	8.66	0.0080
AB	0.034	1	0.034	7.62	0.0121
Residual	0.088	20	4.415E-003		
Cor Total	0.18	23			

**Table 3** ANOVA model of torque

Source	Sum of Squares	df	Mean Square	F Value	p-value Prob > F
Model	0.20	3	0.065	11.07	0.0002
A-Angle	0.082	1	0.082	13.89	0.0013
B-Velocity	0.077	1	0.077	13.07	0.0017
AB	0.024	1	0.024	4.00	0.0594
Residual	0.12	20	5.890E-003		
Cor Total	0.31	23			

## References

1. Gordon, A.M., Huxley, A.F., Julian, F.J.: The variation in isometric tension with sarcomere length in vertebrate muscle fibres. *J. Physiol.* **184**, 170–192 (1966)
2. Krylow, A.M.: Sandercock TG Dynamic force responses of muscle involving eccentric contraction. *J. Biomech.* **30**(1), 27–33 (1997)
3. Scott, S.H., Brown, I.E., Loeb, G.E.: Mechanics of feline soleus. I. effect of fascicle length and velocity on force output. *J. Muscle Res. Cell Motil.* **17**(2), 207–219 (1996)
4. Westing, S.H., Seger, J.Y., Karlson, E.: Ekblom B Eccentric and concentric torque–velocity characteristics of the quadriceps femoris in man. *Eur. J. Appl. Physiol. Occup. Physiol.* **58**(1–2), 100–104 (1988)
5. Forrester, S.E.: Pain MT A combined muscle model and wavelet approach to interpreting the surface EMG signals from maximal dynamic knee extensions. *J. Appl. Biomech.* **26**(1), 62–72 (2010)
6. Forrester, S.E., Yeadon, M.R., King, M.A.: Pain MT Comparing different approaches for determining joint torque parameters from isovelocity dynamometer measurements. *J. Biomech.* **44**(5), 955–961 (2011)
7. Yeadon, M.R.: King MA Evaluation of a torque-driven simulation model of tumbling. *J. Appl. Biomech.* **18**, 195–206 (2002)
8. Mondal, S., Ghosh, R.A.: Numerical study on stress distribution across the ankle joint: effects of material distribution of bone, muscle force and ligaments 0972–978X(17)30101–0 (2017)
9. Amirudin, A.N., Parasuraman, S., Kadirvel, A., Khan, M.K.A., Vazuthi, I.E.: L Biomechanics of Hip, Knee and Ankle joint loading during ascent and descent walking. *Procedia Comput. Sci.* **42**, 336–344 (2014)
10. Hahn, D., Herzog, W., Schwirtz, A.: Interdependence of torque, joint angle, angular velocity and muscle action during human multi-joint leg extension. *Eur. J. Appl. Physiol.* **114**, 1691–1702 (2014)
11. Brown, I.E., Scott, S.H., Loeb, G.E.: Mechanics of feline soleus. II. design and validation of a mathematical model. *J. Muscle Res. Cell Motil.* **17**(2), 221–233 (1996)

# Design and Analysis of 3D Printable Prosthetic Foot



T. Prakash, N. Jayakumar, V. Monish Kumar, P. Karthick, A. Mutharasu, and A. Naveen Kumar

## 1 Introduction

Prosthetic foot can be fabricated from wood, rubber, titanium, carbon fibre, polyethylene and composite material. Many of the people use plastic, wood, fibres, etc., which are commercially popular in the medical field. This foot is produced by weight and weightless products, which are convenient for the patient's comfort. A number of technologies are there but additive manufacturing technology with energy storage and return (ESAR) through which, it can produce weightless products and with maximum strength. FEA conducted for the foot prosthesis design in every one of the three support phases of the walking cycle (controlled dorsiflexion, controlled plantarflexion, push-off phase or powered plantarflexion) [1]. Use of Polylactic acid (PLA) material is used to the design and analyses of the prosthetic foot using 3D printing technique deals motion prosthetic foot [2]. To mimic the real foot, the optional component permits the reproduced prosthetic foot to adjust the lower leg joint for the physiological lower leg during various exercises and in various periods of the gait cycle [3]. The design of a new prosthetic foot, fatigue foot analyzer according to ISO 10328, estimating the ground response force by force plate and gait properties by testometric machine [4]. The prosthesis' capacity to be altered and delivered nearby, on demand might actually rethink the chances accessible to prosthetists for obliging changing stride designs [5]. For optimizing the size and shape, the prosthetic foot is developed with the nylon 6/6 material on minimum LLTE using Bezier curve to describe the geometry [6].

Fusion deposition modelling (FDM) processes commonly use filaments like Polylactic acid (PLA), Acrylonitrile Butadiene Styrene (ABS), nylon, polycarbonate (PC)

---

T. Prakash (✉) · N. Jayakumar · V. M. Kumar · P. Karthick · A. Mutharasu · A. N. Kumar  
Department of Mechanical Engineering, Bannari Amman Institute of Technology, Erode 638401,  
India  
e-mail: [prakasht.me19@bitsathy.ac.in](mailto:prakasht.me19@bitsathy.ac.in)

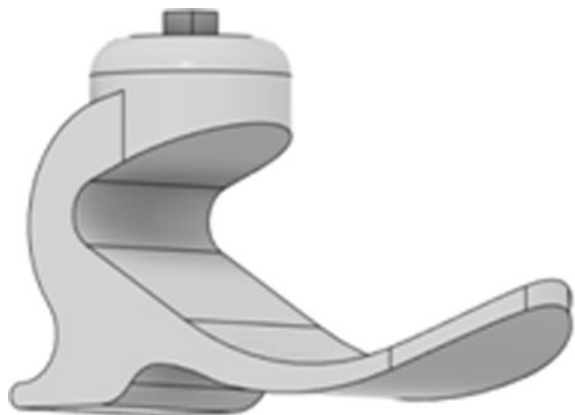
and polyphenylsulfone (PPS). Considering the strength and durability, nylon 66 is selected as the material for analysing the foot. It is also less brittle than ABS and PLA. In this paper, a 3D printable foot is developed using nylon 66 materials. Compared to other materials, nylon is lightweight, flexible, and it can withstand much load. The model is designed by using Fusion 360 CAD software and imported into ANSYS workbench to analyse the model and generate accurate results. The additive manufacturing technology makes it possible to have all the properties of commercially passive feet. Fused deposition modelling (FDM) can be used for printing purposes. This 3D printable foot is beneficial for the poor people who cannot buy other commercially available passive feet that are often costlier than this foot.

## 2 Materials and Methods

### 2.1 CAD Design

Many numbers of foot patterns have been designed, and alterations were done according to FEA to ensure its strength. The heel and forefoot provide 2-point support. The forefoot and heel supports were set like the manlike foot. Figure 1 shows the CAD model of the prosthetic foot with the dimensions of 145-mm height, 248.5-mm long and 80-mm width. It ensures a human foot so that the amputees feel it as a natural foot.

**Fig. 1** CAD model of the prosthetic foot



**Table 1** Properties of Nylon 66

Sl.No	Description	Value
1	Density	1.14e-06 kg/mm <sup>3</sup>
2	Young's modulus	1.480 Mpa
3	Poisson's ratio	0.41
4	Bulk modulus	2740.7 Mpa
5	Shear modulus	524.82 Mpa
6	Tensile ultimate strength	64.7 Mpa
7	Tensile yield strength	57.1 Mpa
8	Isotropic secant coefficient of thermal expansion	s0.128°C

## 2.2 Material

The flexibility and durability of nylon help the 3D printing with thin walls. Its low coefficient of friction with high-melting point makes it exceptionally resistant to abrasion. It has better stiffness, tensile modulus and flexural modulus. Nylon 66 showed the best attributes for a promptly accessible, simple to machine material, with a strain energy density of 1.77 kJ/kg and a yield strain of 0.034. The reason for selecting the nylon as a material is a low-cost prosthetic foot. The high proportion of yield strength to elastic modulus permits it to get a high-strain energy density, and subsequently high deformations prior to yielding. The properties of Nylon 66 material are shown in Table 1.

## 2.3 Finite Element Analysis (FEA)

FEA plays a significant role in product designing. This helps the Engineers to reduce the physical prototype and run the simulation to optimize the designs.

The FEA is done in two positions (when the person is standing, and the other is the walking phase). The human body mass was assumed as 60 kg for finite element analysis (FEA). A vertical load of 1000 N that is 1.66 times the person's weight was applied to the model. Nylon 66 is used to analyse the foot, and practical constraints are given to the model and analyzed. The results are generated according to the load applied, material and conditions.

## 2.4 Topology Optimization

Topology optimization is a recently developed technique, and it plays a vital role nowadays. This technique is adopted in this model which reduces the material, which



**Fig. 2** Prosthetic foot after topology optimization

also reduces cost and mass and ensures maximum stiffness. Suitable materials, loads, constraints, mesh and the area to be preserved are given according to the work to optimize the model. Figure 2 shows the topology optimized CAD model.

### 2.5 3D Printing Processes

The finite element analysis was done in a prepared CAD model. Nylon 66 filament with a diameter of 1.75 mm was used for printing. The prototype was printed with a grid infill pattern with 3-mm shell thickness, and the infill density was set to 50% to improve its strength is as shown in Table 2. The prototype was decreased to 563.22 g from 574 g because of the topology optimized model. Figure 3 shows the infill pattern of the prototype. The prototype was printed in Wol 3D printer, and the estimated printing time is about 21 h.

**Table 2** Infill

S.No	Description	Value
1	Shell thickness	3 mm
2	Top or bottom thickness	2.25 mm
3	Infill overlap	75%
4	Infill density	50%
5	Layer	0.2 mm

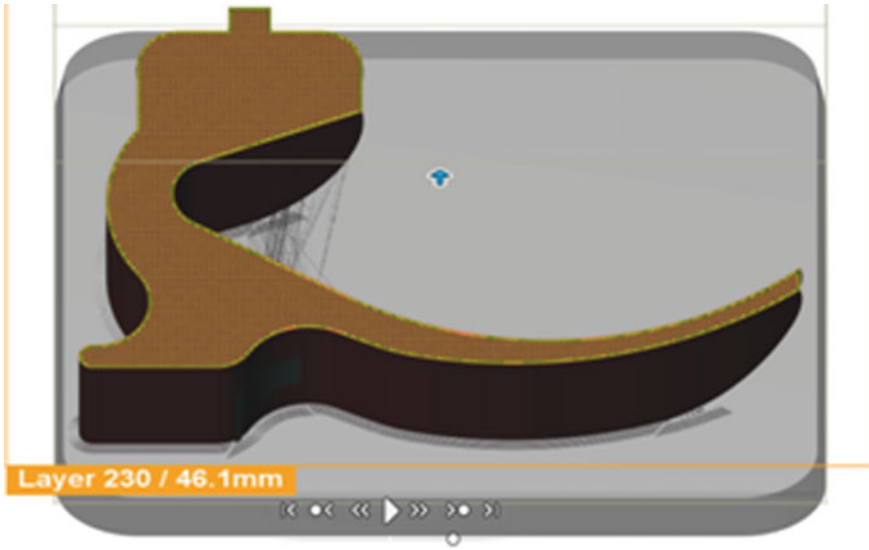


Fig. 3 Infill pattern

### 3 Results and Discussion

#### 3.1 Equivalent Stress Results

Figure 4 graph indicates the change in the values of equivalent stress in the standing and walking phases with different loads.

In the first case, it is assumed as the person is in standing phase, keeping the heel and the forefoot point as fixed support 600 N, 800 N and 1000 N loads are applied at the top of the cylindrical surface. The maximum stress was calculated at the ankle's inner side as 2.6134 Mpa, 3.4846 Mpa, and 4.3557 Mpa as shown in Figs. 5, 6 and 7.

In the second case, it is assumed as the person is in walking phase, keeping the heel and the forefoot point as fixed support 600 N, 800 N and 1000 N loads are applied at the top of the cylindrical surface. The maximum stresses are calculated at the top surface of the sole as 9.0021 Mpa, 12.003 Mpa and 15.003 Mpa as shown in Figs. 8, 9 and 10.

#### 3.2 Total Deformation Results

Figure 11 graph indicates the change in deformation values in the standing and walking phases with different loads.

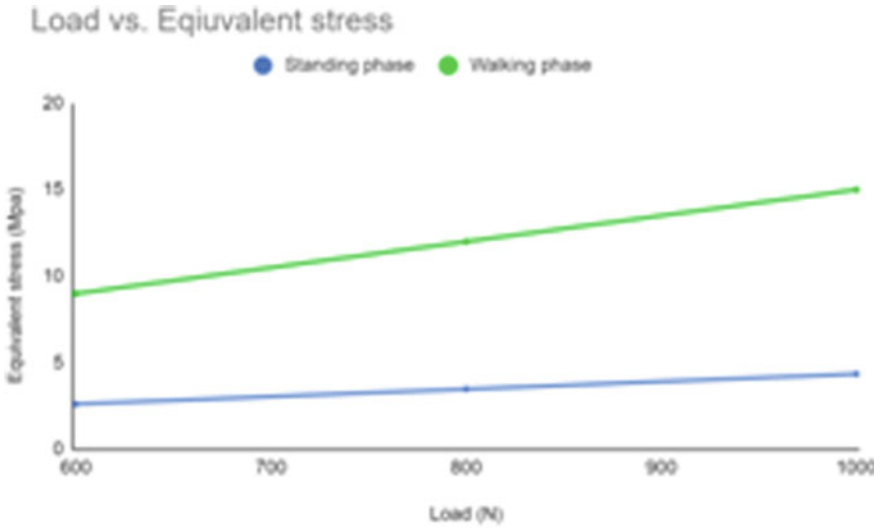


Fig. 4 Load vs Equivalent Stress for Standing and Walking Phase

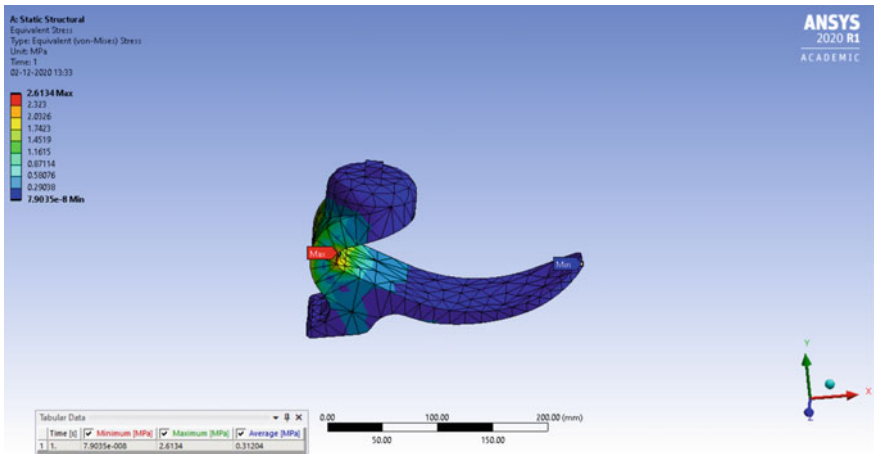


Fig. 5 600 N

In the first case, it is assumed as the person is in the standing phase; the loads are applied on the top surface of the cylindrical region. The heel and the forefoot are given fixed constraints. In Figs. 12, 13 and 14, the analysis is taken for different loads 600 N, 800 N and 1000 N, and the results are generated as 0.0051863 mm, 0.006915 mm and 0.0086438 mm, respectively.

In the second case, it is assumed as the person is in the walking phase; the loads are applied on the top surface of the cylindrical region. The forefoot is given frictionless



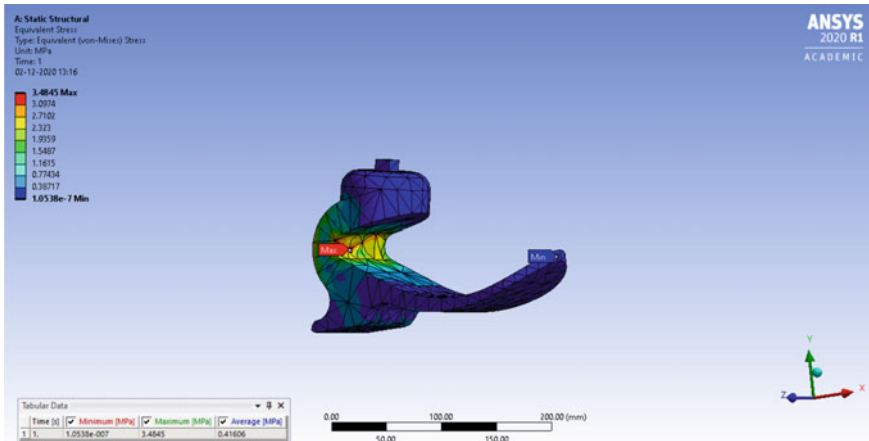


Fig. 6 800 N

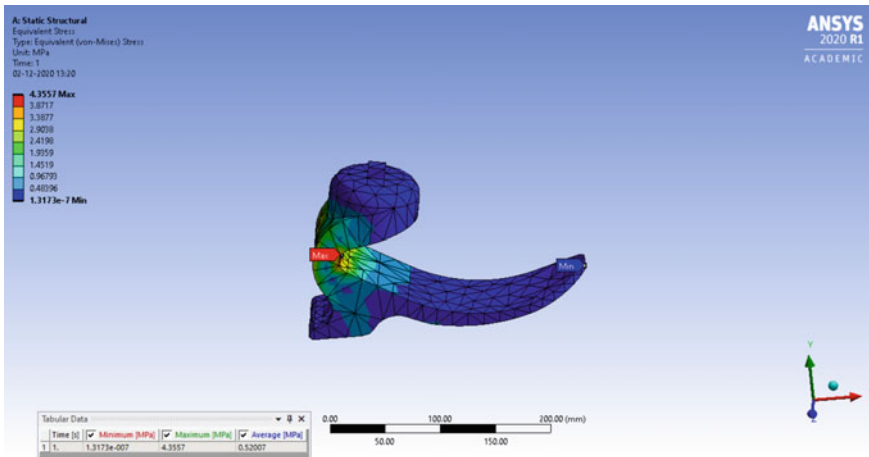


Fig. 7 1000 N

and pin constraints. In Figs. 15, 16 and 17, the analysis is taken for different loads 600 N, 800 N and 1000 N, and the results are generated as 3.5008 mm, 4.6677 mm and 5.8346 mm, respectively.

### 3.3 Directional Deformation Along X-axis

In the first case, it is assumed as the person is in the standing phase; the loads are applied on the top surface of the cylindrical region. The heel and the forefoot are

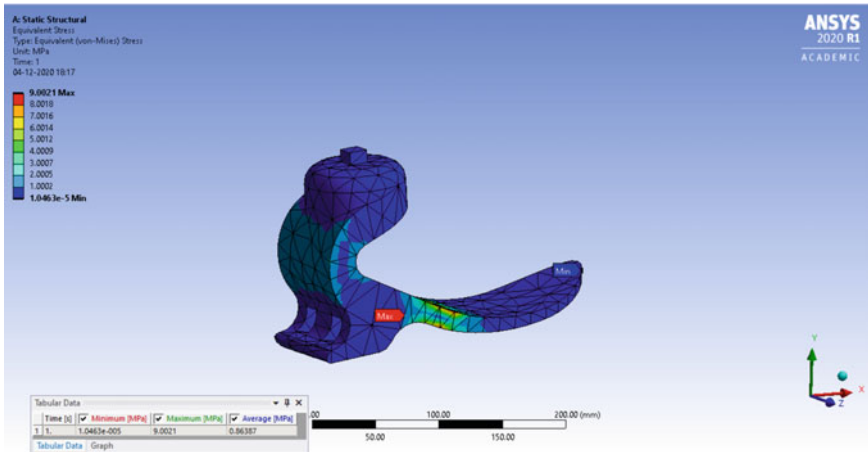


Fig. 8 600 N

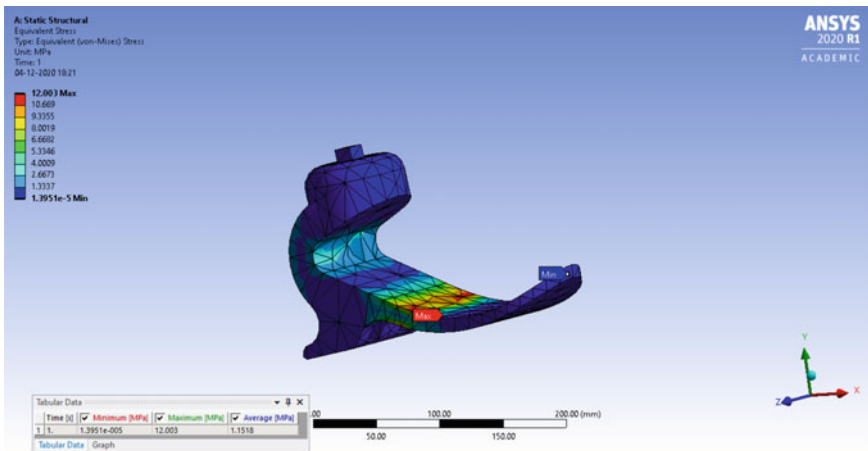


Fig. 9 800 N

given fixed constraints. In Figs. 18, 19 and 20, the analysis is taken for different loads 600 N, 800 N and 1000 N, and the results are generated as 0.0043358 mm, 0.0057811 mm and 0.0072264 mm, respectively.

In the second case, it is assumed as the person is in the walking phase; the loads are applied on the top surface of the cylindrical region. The forefoot is given frictionless and pin constraints. In Figs. 21, 22 and 23, the analysis is taken for different loads 600 N, 800 N and 1000 N, and the results are generated as 0.42495 mm, 0.5666 mm and 0.70825 mm.

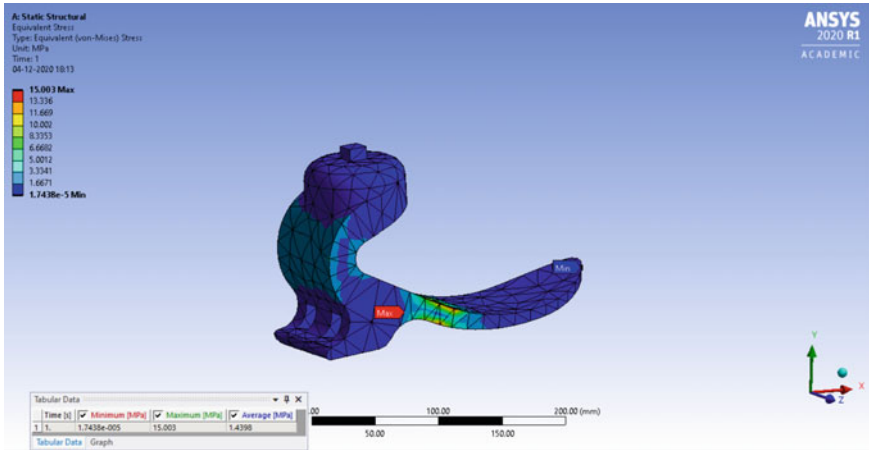


Fig. 10 1000 N

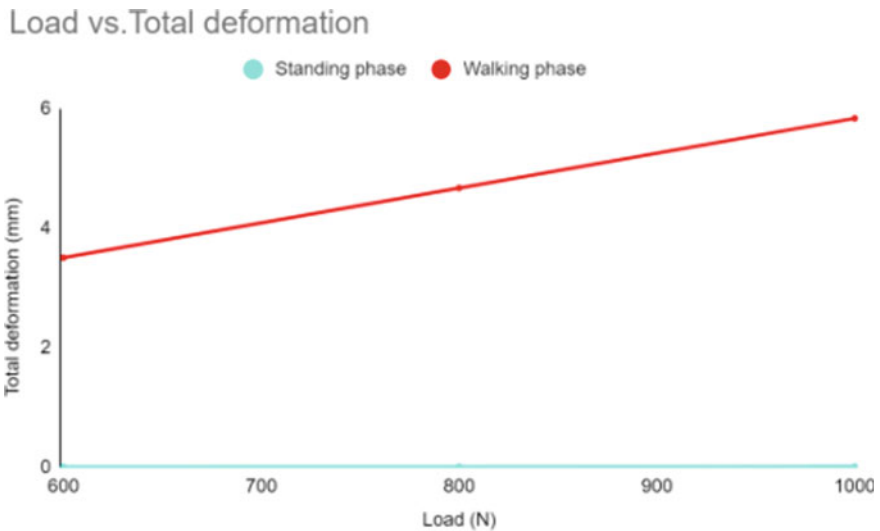


Fig. 11 Load vs Total Deformation for Standing and walking phase

### 3.4 Directional Deformation Along Y-axis

In the first case, it is assumed as the person is in the standing phase; the loads are applied on the top surface of the cylindrical region. The heel and the forefoot are given fixed constraints. In Figs. 24, 25 and 26, the analysis is taken for different loads 600 N, 800 N and 1000 N, and the results are generated 0.00045603 mm, 0.00060804 mm and 0.00076006 mm.

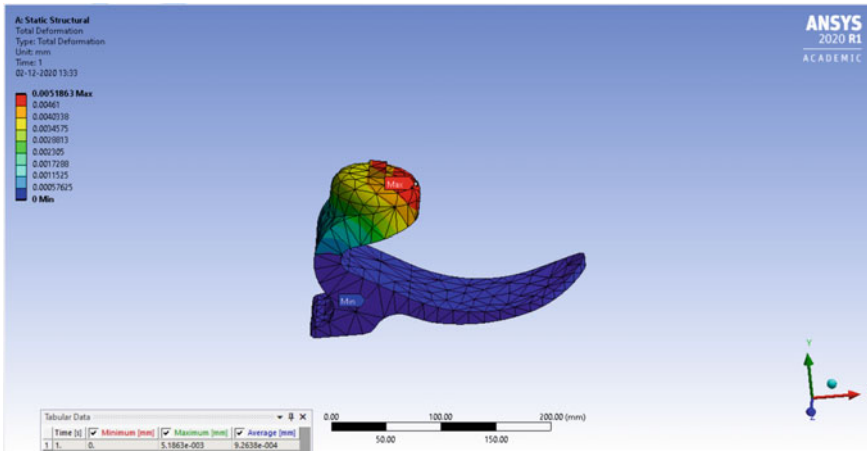


Fig. 12 600 N

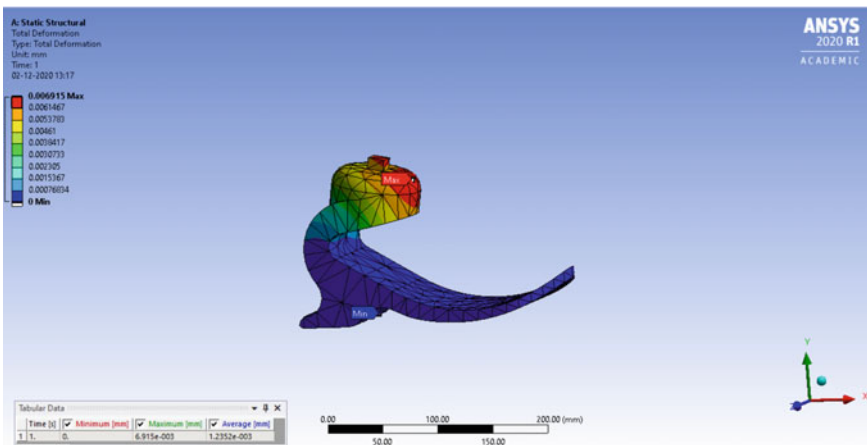


Fig. 13 800 N

In the second case, it is assumed as the person is in the walking phase; the loads are applied on the top surface of the cylindrical region. The forefoot is given frictionless and pin constraints. In Figs. 27, 28 and 29, the analysis is taken for different loads 600 N, 800 N and 1000 N, and the results are generated as 0.013563 mm, 0.018084 mm and 0.022605 mm, respectively.

1.66 times of body weight are assumed for analysing on the prototype using FEA. For providing a more natural feeling for the user, human foot weight is considered a couple of times higher than the prototype; it is desirable to increase its mass to improve its strength. The success or failure of the prototype depends upon the safety factor taken from the analysis. If the safety factor is less than one than the design is a

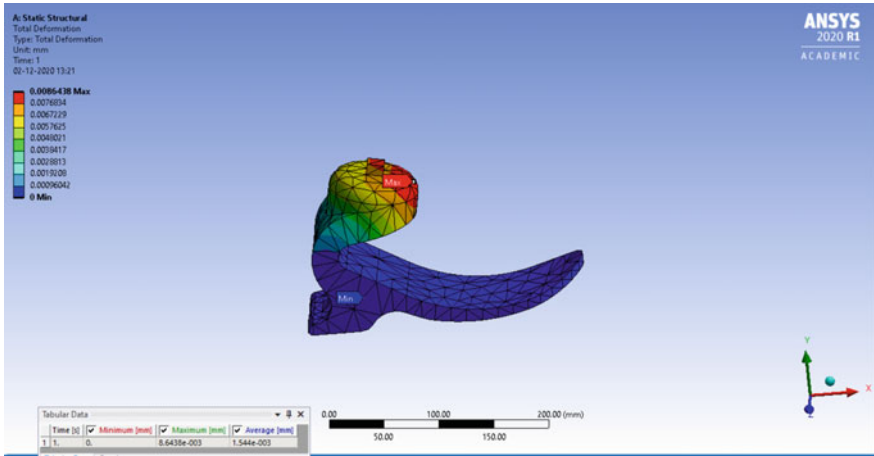


Fig. 14 1000 N

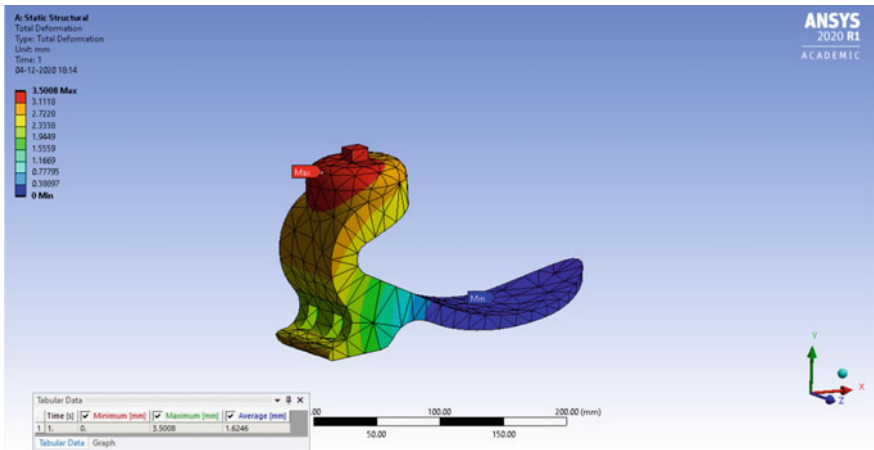


Fig. 15 600 N

failure, and if the safety factor is greater than one, then it means that the design does not fail for the applied load conditions. The overall results show that the prototype does not bend or break as the minimum and maximum value of the safety factor for the three different loads applied. The FEA results confirm that the prototype is successful in all aspects. The FEA pointed out that the top cylinder surface area and foot do not bear much stress compared to the basic lower leg region. It may be considered as future work.

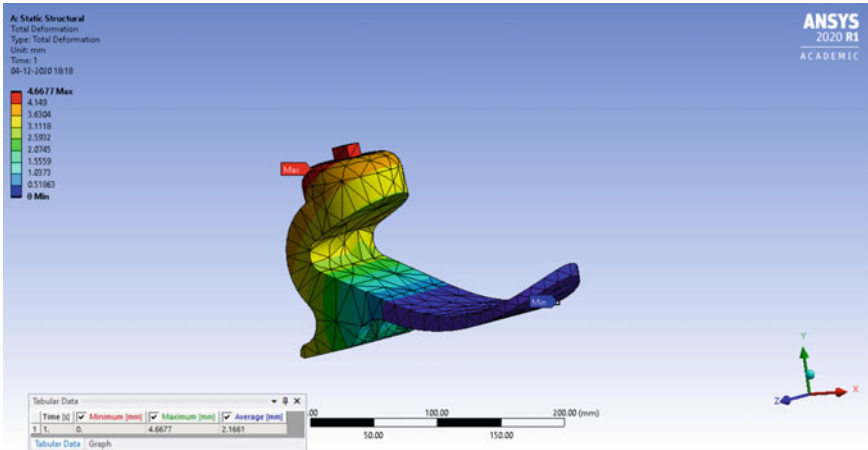


Fig. 16 800 N

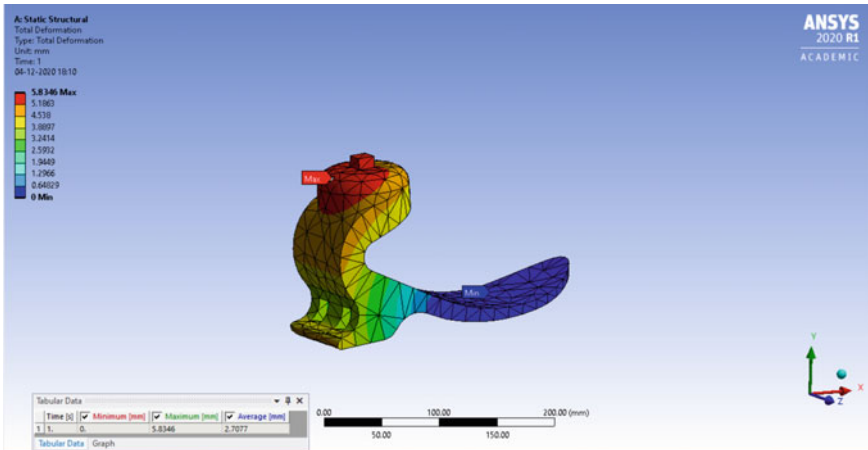


Fig. 17 1000 N

## 4 Conclusions

In this study, a prosthetic foot is designed and analyzed by following the standards. The use of nylon 66 ensures that the prosthesis can be used for long term use. Prosthetic foot's shape has been developed at good strength and optimized at less weight by using topology optimization. The prototype has been reduced to 563.22 g from 574 g due to the topology optimized model. Based on the simplified model, it can be manufactured using a 3D printer. The finite element analysis is done to find

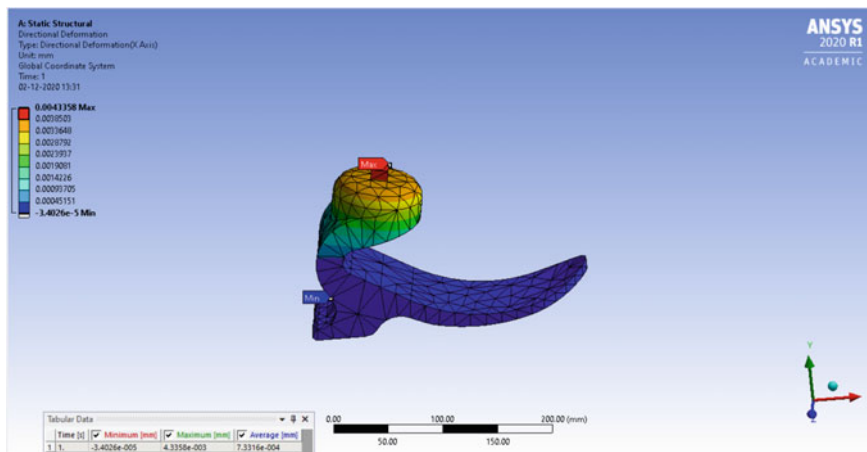


Fig. 18 600 N

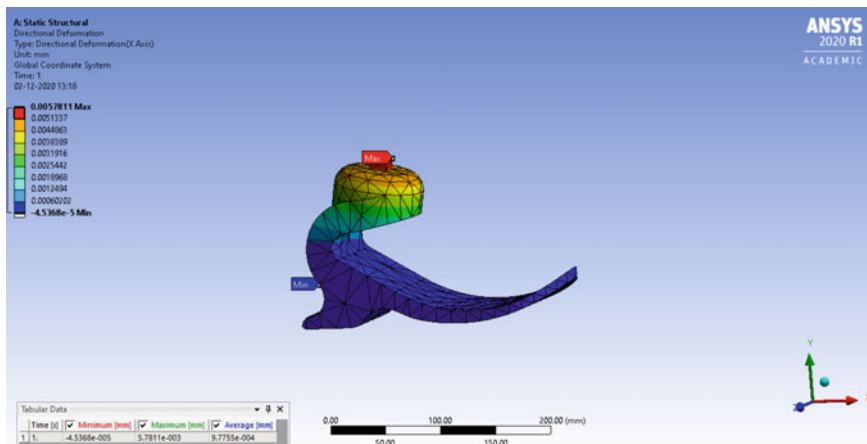


Fig. 19 800 N

the structure validation. When it is manufactured in bulk production, the cost of the foot will be reasonable.

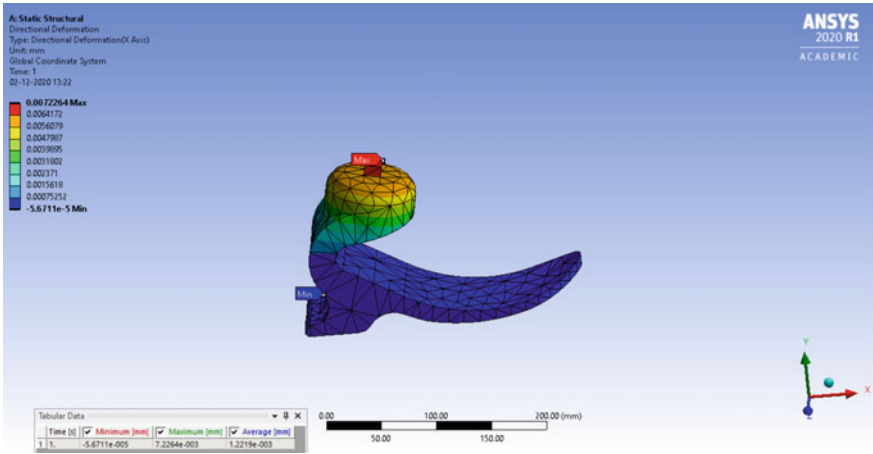


Fig. 20 1000 N

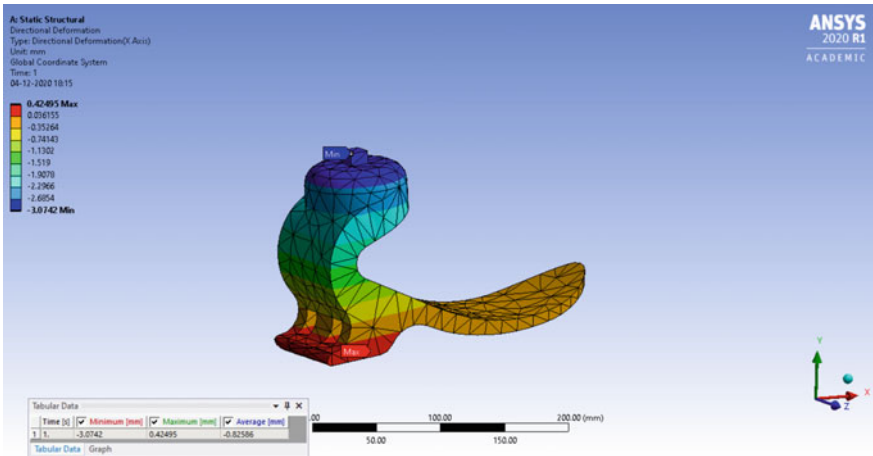


Fig. 21 600 N



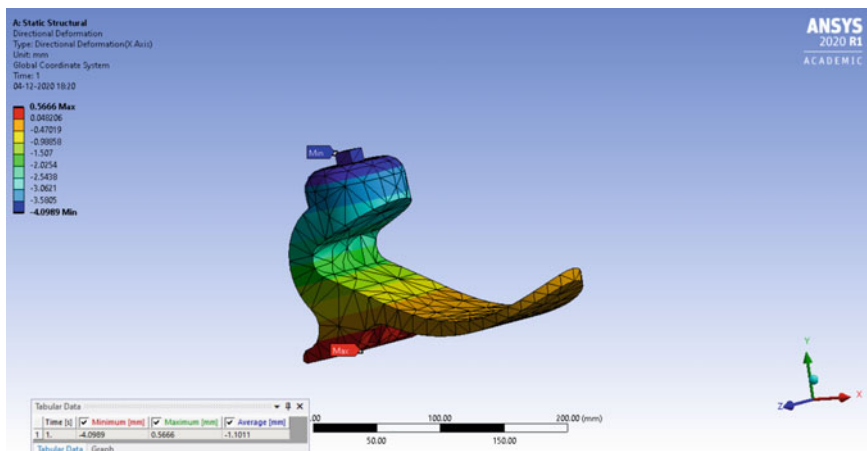


Fig. 22 800 N

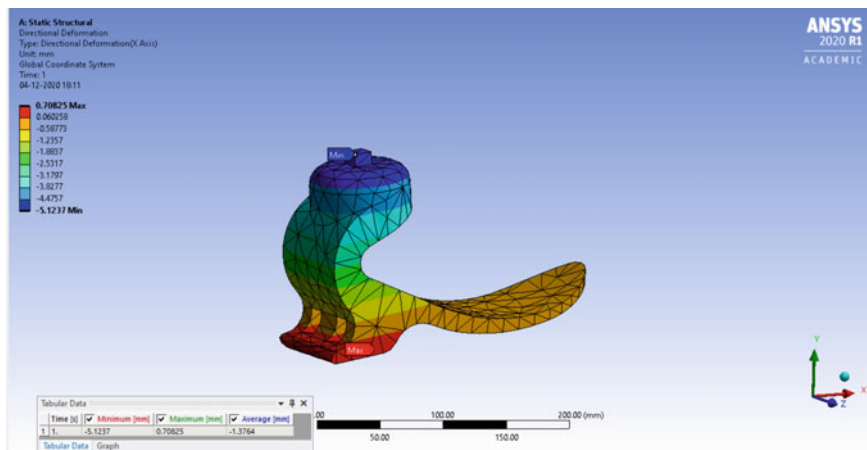


Fig. 23 1000 N

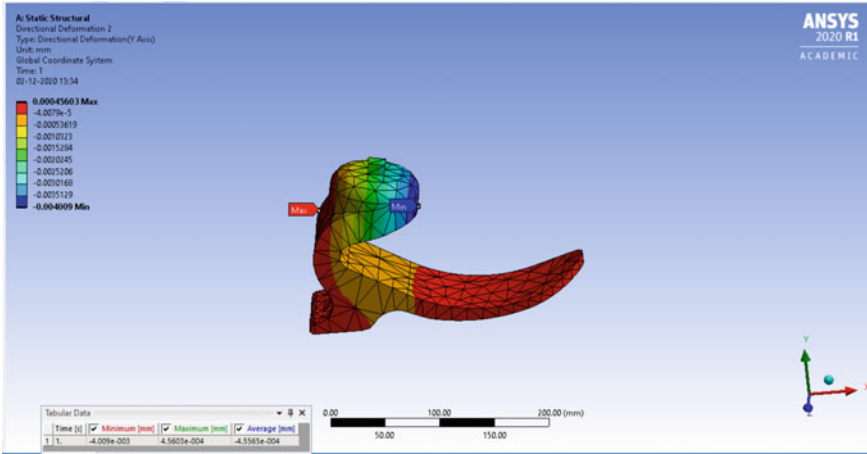


Fig. 24 600 N

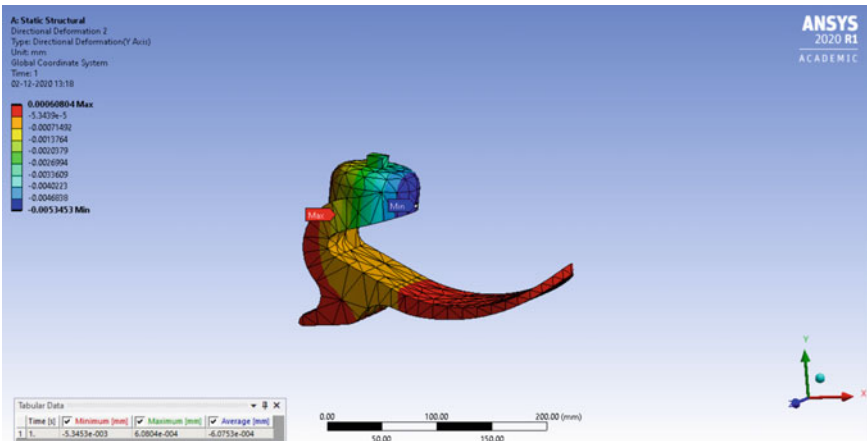


Fig. 25 800 N

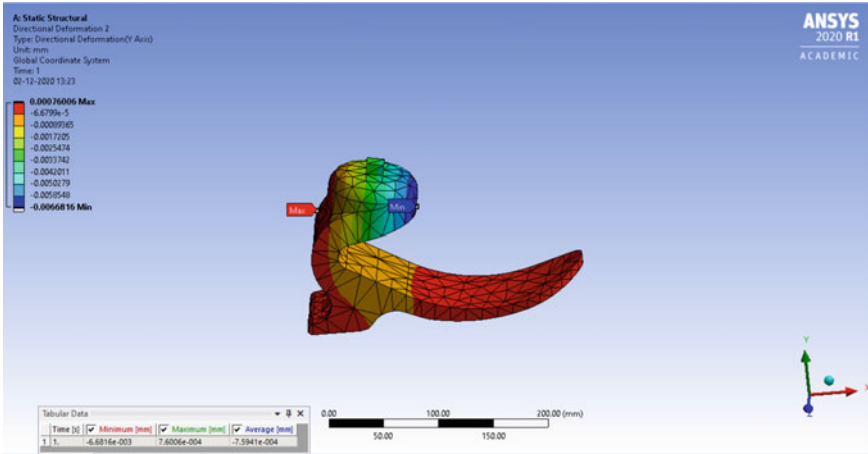


Fig. 26 1000 N

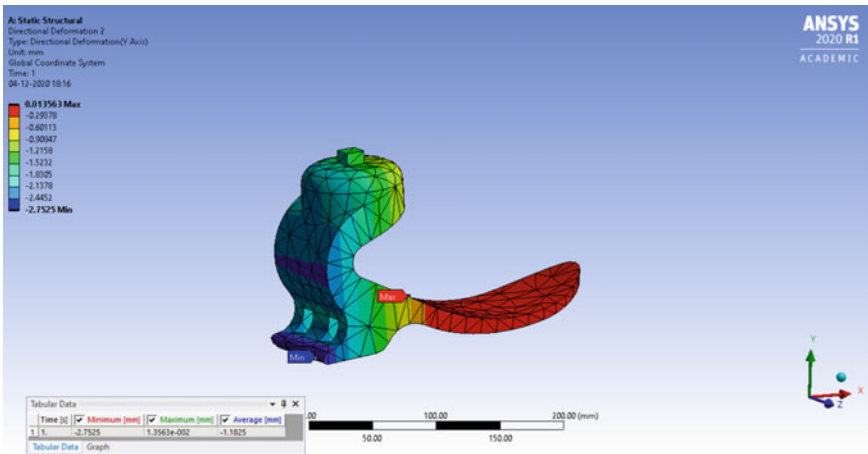


Fig. 27 600 N

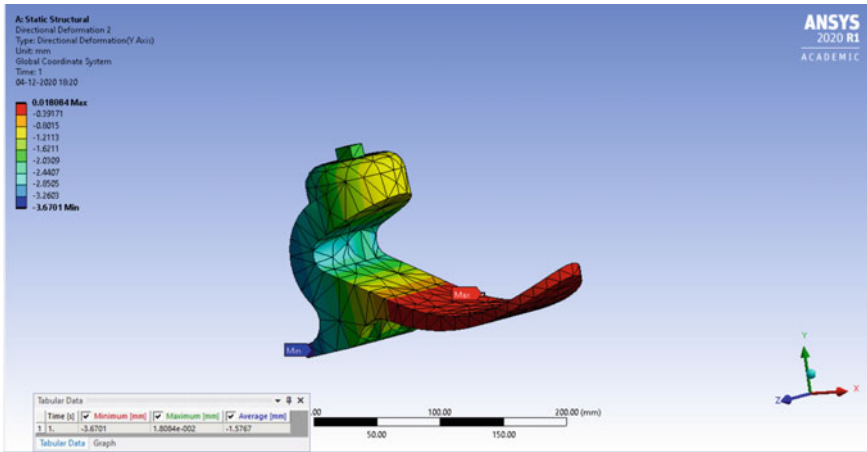


Fig. 28 800 N

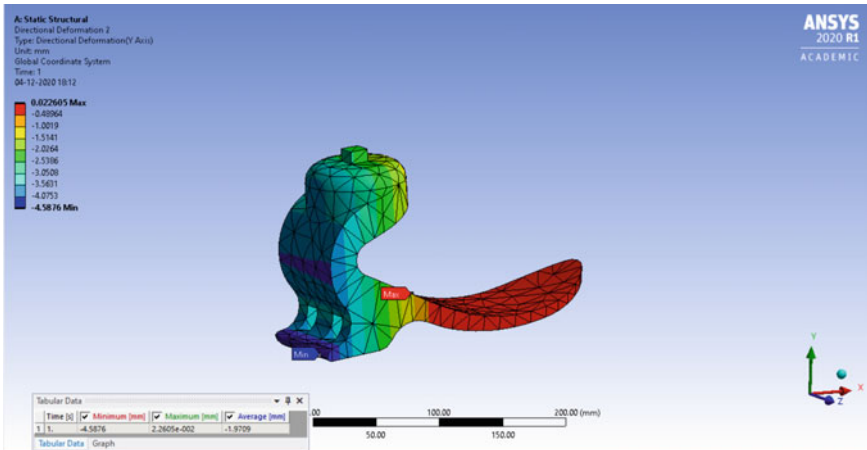


Fig. 29 1000 N

## References

1. Rochlitz, B., Pammer, D.: Design and analysis of 3D printable foot prosthesis. *Period. Polytech. Mech. Eng.* **61**, 282–287 (2017)
2. Vijayan, V., Arun Kumar, S., Gautham, S., Mohamed Masthan, M., Piraichudan, N.: Design and analysis of prosthetic foot using additive manufacturing technique. *Mater. Today Proc.* (2020). <https://doi.org/10.1016/j.matpr.2020.07.195>
3. Tryggvason H, Starker F, Lecompte C, Jónsdóttir F. Modeling and simulation in the design process of a prosthetic foot. *Proc 58th Conf Simul Model (SIMS 58) Reykjavik, Iceland*, **138**, 398–405 (2017). <https://doi.org/10.3384/ecp17138398>
4. Gweeg MJ. Design and analysis of a new prosthetic foot

5. Yap J. Low-cost 3D-printable prosthetic foot (2015)
6. Olesnavage, K.M., Prost, V., Johnson, W.B., Amos Winter, V.G.: Passive prosthetic foot shape and size optimization using lower leg trajectory error. *J. Mech. Des. Trans. ASME* **140**, 1–11 (2018)

# Experimental Investigation on Adhesive Bonded Fold Tubes Under Quasi-Static Loading



M. Nalla Mohamed and R. Sivaprasad

## 1 Introduction

Aluminium square profile tubes are continuously employed as thin-walled structures in the transportation sector to save weight, reduction of CO<sub>2</sub> emissions and for high-energy absorption during the crash event [1]. Hence, the crush resistance of conventional plain square tubes has got attentions during the past few decades [2–4]. But these square tubes are generally metal formed through the process of extrusion, [5] and special metal forming dies are required based on the dimension or shape of the profile. Not only traditional square tubes have significant impact resistance, but also exhibits high-initial peak crushing force which causes vulnerable jerks and injury to the occupants [6]. Unlike existing extruded square tubes, sheet metal working is beneficial in terms of both cost-effective as well as ease of fabrication. The effective thickness of the net folds depends on the number of folding sheets. Thus, its flexible nature has attracted the researcher.

On the other hand, global buckling arises along with irregular deformation when these folded tubes are subjected to direct axial crush and ultimately affects energy absorption capacity [7]. By employing few constraints along the folded walls, the deformation mechanism retains its progressive nature similar to that of convectional plain extruded tubes [8]. These constraints are in form of adhesive bonding between walls of lateral ends of folded tubes. This inexpensive joint process is very affordable in the sheet metal working technology. From the literature review, it is understood that sufficient information relating to extruded plain square tubes subjected to quasi-static is readily available, whereas the availability of experimental study related to folded tubes is very limited. For occupant safety in the automotive vehicle, a detailed

---

M. N. Mohamed (✉) · R. Sivaprasad

Department of Mechanical Engineering, Sri Sivasubramaniya Nadar College of Engineering, Kalavakkam, Kancheepuram District, Tamilnadu, India

e-mail: [nallamohamedm@ssn.edu.in](mailto:nallamohamedm@ssn.edu.in)

**Table 1** Chemical constituents of AA6061-O alloy

Constituents	Al	Cr	Fe	Cu	Mg	Si	Mn	Ti	Zn
Mass (%)	98.05	0.032	0.62	0.15	0.41	0.54	0.065	0.009	0.12

study relating to crushing performance characteristics of folded tubular structures is needed. Though some researchers [9, 10] reported the influences of the joining techniques on the crashing characteristics of simple geometry like hat section, similar kind of work has not been available for folded tubes with bonded joints.

Hence, this study initially compares the energy absorption characteristics of folded tubes and folded tubes bonded with adhesives under axial crushing experimentally. The crushing energy absorption (EA) and the initial peak crushing force (IPF) of the folded tubes are subsequently compared with conventional extruded plain square tubes to map the similarities and dissimilarities. Finally, suggestions are given for the deployment of folded tubular structures in place of conventional extruded tubes effectively.

## 2 Experimental Methodology

### 2.1 Material Characterization

In the study, aluminium alloy sheets (Grade -AA6061-O) of thickness  $t = 1$  mm are chosen for the fabrication of folded tubes. Grade -AA6061-O exhibits higher elongation, hence it is preferable for crash energy safety management in transport sector [11]. A chemical constituents test was carried out in accordance with ASTM-E1251 standard. The chemical constituents of the specimen grade are shown in Table 1.

To obtain material property, the test samples were cut out from the same sheets which were later used to fabricate the folded tubes as per ASTM E8 standards as shown in Fig. 1a and b. The tensile strength tests were carried out on those specimens shown in Fig. 1c. Very consistent material stress/strain behaviour was observed in all the three repeated trails which is shown in Fig. 2.

### 2.2 Tube Fabrications

The folded tubes were formed by sheet metal working of aluminium alloy AA6061-O sheets as shown in Fig. 3. P1, P2, P3 and P4 are 4 different plain folded sections varying by increase in folds. The length of the specimens is 200 mm and their cross-sectional square side width is 30 mm. With the help of the prismatic die, the aluminium sheets were bent with fillet corners. The fillet corners of radius 2 mm

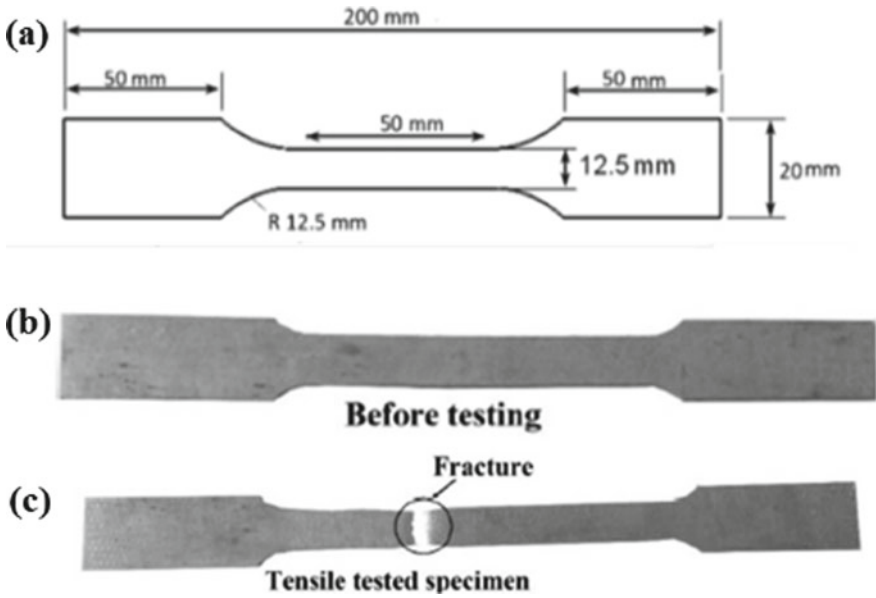


Fig. 1 Dimensions of tensile test specimen

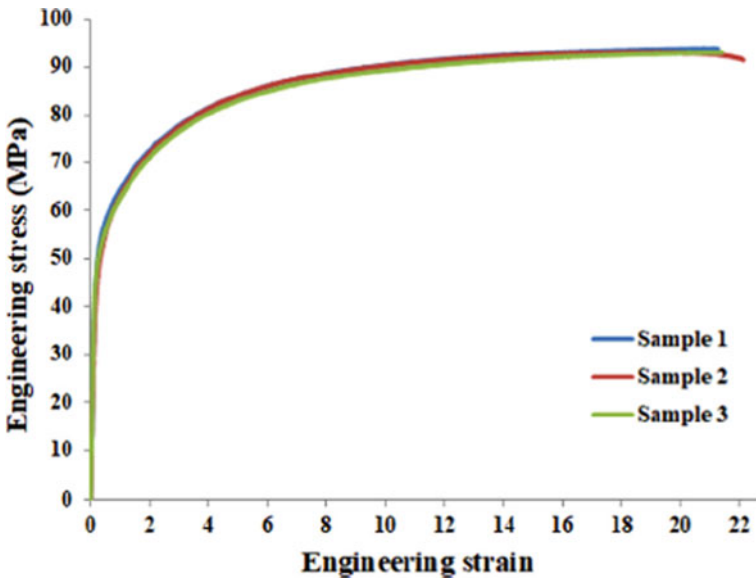


Fig. 2 Stress-strain curves of AA6061-O



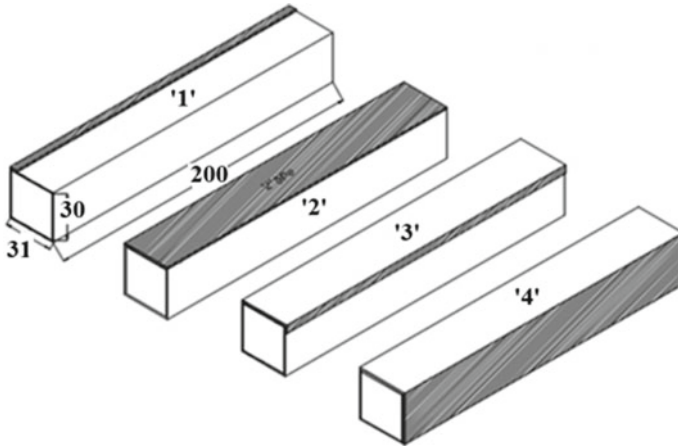


Fig. 3 Dimensions of the specimens

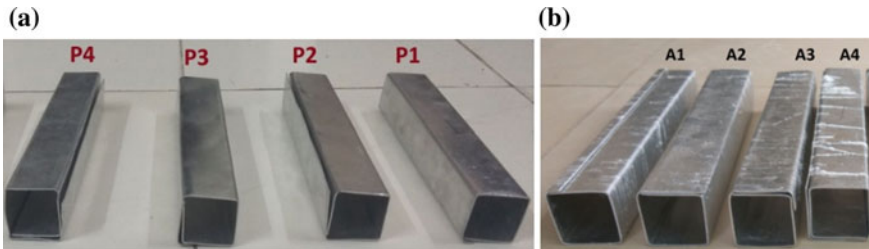


Fig. 4 a Representative plain folded tubes, b representative adhesive bonded folded tubes

reduce the stress concentration during axial crush. Four representative specimens are shown in Fig. 4a with three repetitions in each type. Spring back and artificial errors are the challenges during sheet metal working, hence secondary operations were required to achieve a perfect structural accuracy. In case of adhesive bonding, there are various methods of curing, amongst them, room temperature cure and external heat cure are mostly followed. The former one is generally followed for automotive components and best practice to remove moisture content. Conveniently, the room temperature curing type adhesive was used to constrain the bonded folding tubes in this study. Folded tubes were fabricated by applying epoxy adhesive in between the contact portion of the folded layers. The adhesive layer's film thickness was maintained around 0.3 mm. No other surface treatment was done on bonding surface except degreasing. To ensure proper bonding, ropes were tied around the tubes for 24 h. The representative of the adhesive bonded tubes is shown in Fig. 4b.

### 2.3 Testing Methods

The axial quasi-static crushing experiments were conducted on the data acquisition UTM, having 60 tonnes capacity, shown in Fig. 5. Quasi-static axial compressions of 100 mm cross head displacement at the rate of 5 mm/min were conducted on all the specimens. The data acquisition system records both cross head displacement as well as crushing force reaction at the bottom end of tubes. The displacement precision is about 1 mm, and corresponding crushing load curves were recorded. Each configuration specimen consists of three samples were to be tested to determine the deviation in observation. The acceptable deviation in mean crush force (MCF) of three samples of same specimen is about 4%. Initial crushing peak force (IPF) from the force displacement curves and crushing energy absorption capacity (EA) from area under the force displacement curves for each specimen are listed in Table 2.

### 3 Results and Discussions

Axial crush test was carried in UTM to understand the deformation behaviour of the extruded square tube, plain folded (P-type), adhesive bonded (A-type) tubes. The energy absorption capacities (EA) of specimens were computed from the area enclosed by force displacement curve using trapezoidal rule up to crushing distance of 100 mm. The crushing performance indices of all the specimens are listed in Table 2.

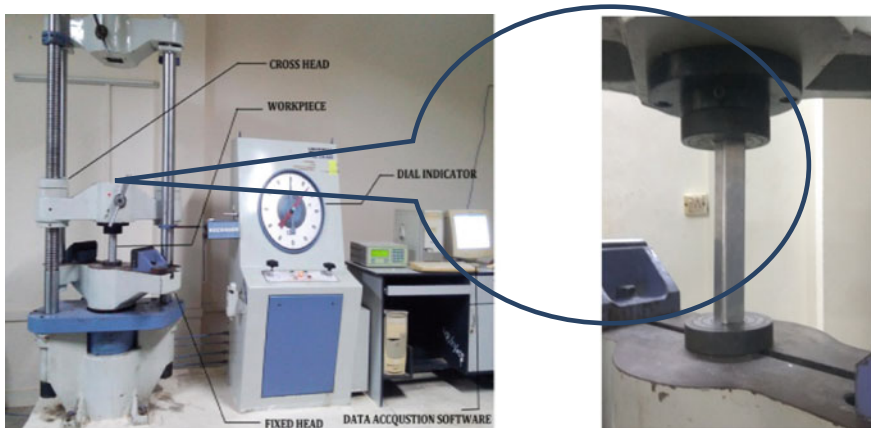
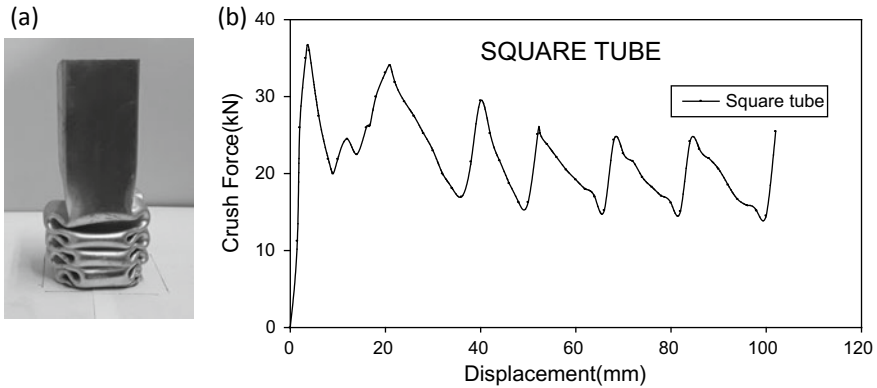


Fig. 5 UTM machine, Zoomed view of the tube

**Table 2** Performance indices for plain folded and adhesive bonded tubular structures

Specimen	P <sub>max</sub> (kN)	Average P <sub>max</sub>	Energy (J)	Average Energy(J)	Specimen	P <sub>max</sub> (kN)	Average P <sub>max</sub>	Energy (J)	Average Energy(J)
P <sub>1</sub>	1	8.43	126.25	124.89	A <sub>1</sub>	1	18.01	775.65	
	2	8.51	121.55			2	18.06	773.21	772.98
	3	8.38	126.89			3	18.05	770.09	
P <sub>2</sub>	1	9.41	245.35	241.92	A <sub>2</sub>	1	19.06	910.23	
	2	9.42	239.21			2	19.08	906.45	908.29
	3	9.37	241.22			3	19.11	908.21	
P <sub>3</sub>	1	10.52	315.65	320.52	A <sub>3</sub>	1	19.88	810.02	
	2	10.63	326.42			2	19.87	809.24	810.27
	3	10.55	319.51			3	19.91	811.56	
P <sub>4</sub>	1	16.26	462.12	463.89	A <sub>4</sub>	1	24.87	876.54	
	2	16.29	458.34			2	24.92	871.21	874.40
	3	16.21	471.21			3	24.98	875.45	



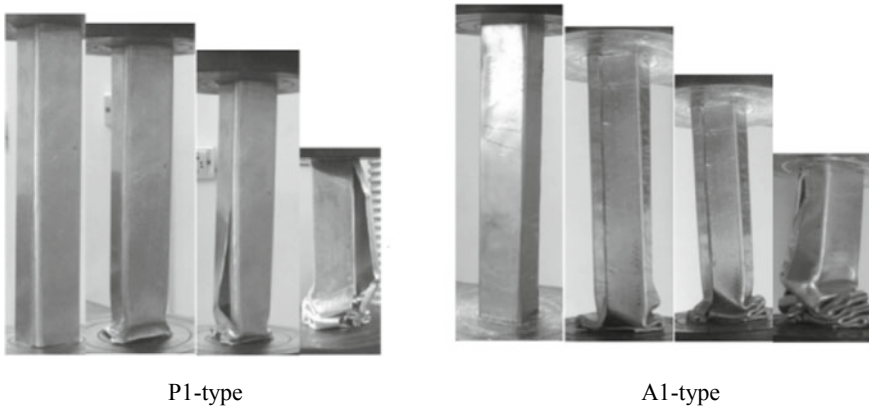
**Fig. 6** **a** Final deformation pattern of extruded square tube, **b** Force–displacement curves square tubes

### 3.1 Quasi-Static Test Square Tubes

The testing was initiated with the traditional square tube, due to the requirement of force–displacement response for comparison purpose. The deformation of the extruded square tube experimentally shown in Fig. 6a. The progressive deformation mechanism starts from bottom end in the first stage then, followed by successive folds stacking over initial fold. As the crushing load increases, the deformation continues its series of local buckling folds up to the prescribed deformation of 100 mm. Figure 6b shows the crushing force–displacement curves of the square tubes. The initial crushing peak force (IPF) for the extruded tube was found to be 36 kN. Tremendous initial peak force produces jerks and cause serious injuries to the passengers, and this problem arises exclusively in high-impact energy absorbers. Therefore, the initial peak crush force is one of the major criteria to be considered during designing of impact energy absorbers. Since it is related to occupant safety, hence IPF is one of the most important bio-mechanical factors. For this main reason, many folded tubes are being introduced to decrease the initial peak crushing.

### 3.2 Quasi-Static Compression Test on Plain Folded and Adhesive Bonded Square Tubular Structures

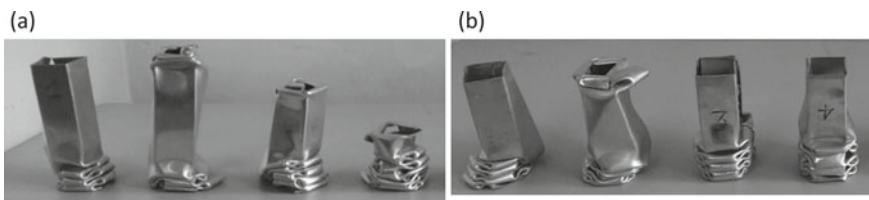
Since adhesive bonding influences in energy absorption capacity by creating constraints, thus the plain folded tubes and adhesive bonding folded tubes were compared under axial quasi-static experiment. The comparison on the deformation mechanism of the folded tube (P1- type specimen) and folded tube bonded with adhesives (A1 type) under axial compression is shown in Fig. 7.



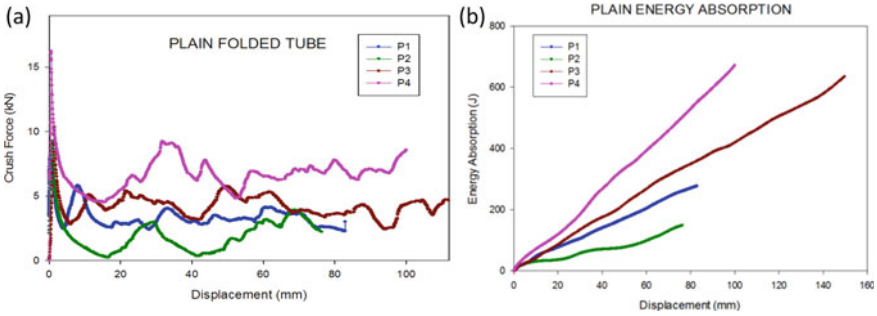
**Fig. 7** Comparison of the deformation mechanism of P1 & A1 type specimen

It is observed that in ‘P1’ type, the periphery wall fold of the tube gets separated during axial compression, followed by progressive local buckling becomes unstable and ultimately we can witness the rise of global buckling as shown in Fig. 7. The moment it reaches global buckling, and the crush force drops down to near zero. It is observed that for P1-type, the specimens underwent lateral deformation. However, in remaining groups, the specimens underwent progressive deformation mode. In contrast, the A1-type deformed progressively and showed a larger plastic deformation area, and thus absorbed more energy. In other words, the adhesive bonding alters the modes of deformation of the folded tubes and resulted in increase in crushing energy absorption capacity. The final mode of deformations of plain folded tubes and folded specimen bonded with adhesives comparison are compared and shown in Fig. 8.

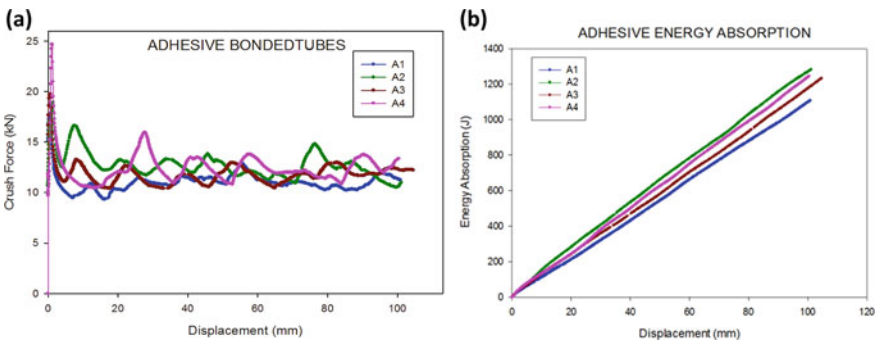
The crushing force displacement curves and energy curves obtained from the axial quasi-static experiment for plain folded (P-types) and the adhesive bonded (A-types) are depicted in Fig. 9 and 10, respectively. It is observed that there was progressive deformation in adhesive bonded tubes compared to the plain folded tubes. From the results, we can observe initial peak crushing force was decreased from 36 kN (in case of extruded square tubes) to 18.04 kN (in case of adhesive bonded tubes) without affecting the crushing energy absorption capacity. The plain folded tubes exhibit



**Fig. 8** Comparison of the deformation mode of **a** folded tubes and **b** folded specimen bonded with adhesives



**Fig. 9** a Comparison of peak force of folded tubes b Comparison of energy absorption of folded tubes



**Fig. 10** a Comparison of peak force of adhesive bonded folded tubes b Comparison of energy absorption of adhesive bonded folded tubes

unstable fluctuation in mean crush force, whereas the adhesive bonded tubes exhibit gradual mean crushing force and thus absorbed greater energy.

## 4 Conclusion

Quasi-static compression on plain folded and adhesives bonding folded tubes were experimentally analysed. The remarkable outcomes are briefed as follows:

- The plain folded tubes failed irregularly and loses progressiveness and ultimately lead to global buckling. Because of global buckling, these structural specimens are lacking in crushing resistance and stability. Thus, adhesive bonding was implemented, making constraints to enhance the stability.
- The initial peak crush force of adhesive bonded tubular structural members is 15 to 30% remarkably lower than that of extruded plain square tube, and hence these

adhesive bonded tubular structures can be suggested for better alternative in place of conventional types crushing energy.

- The crushing energy absorption efficiency of bonded tubes approaches nearer to that of the traditional square tube with increasing in number of overlapping sheets. The remarkable outcomes related to adhesive bonded tubes showed the advantages of utilizing adhesive bonded tubes in vehicular crash safety system during vehicular crash events.

## References

1. Lu, G., Yu, T.: *Energy Absorption of Structures and Materials*. CRC Press, Woodhead, Boca Raton, Cambridge (2003)
2. Abramowicz, W., Wierzbicki, T.: Axial crushing of multi-corner sheet metal columns. *J. Appl. Mech. Trans. ASME* **56**, 113–120 (1989)
3. Tang, Z., Liu, S., Zhang, Z.: Energy absorption properties of non-convex multi-corner thin-walled columns. *Thin Wall Struct.* **51**, 112–120 (2012)
4. Liu, S., et al.: Bionic design modification of non-convex multi-corner thin-walled columns for improving energy absorption through adding bulkheads. *Thin Wall Struct.* **88**, 70–81 (2015)
5. Kohar, C.P., Zhumagulov, A., Brahme, A., Worswick, M.J., Mishra, R.K., Inal, K.: Development of high crush efficient, extrudable aluminium front rails for vehicle light weighting. *Int. J. Impact Eng.* **95**, 17–34 (2016)
6. Sun, G., Zhang, H., Lu, G., Guo, J., Cui, J., Li, Q.: An experimental and numerical study on quasi-static and dynamic crushing behaviours for tailor rolled blank (TRB) structures. *Mater. Des.* **118**, 175–197 (2017)
7. Kotelko, M., Mania, R.J.: Quasi-static and dynamic axial crushing of TWCF open section members. *Thin Wall Struct.* **61**, 115–120 (2012)
8. Zhang, X., et al.: Bending collapse of folded tubes. *Int. J. Mech. Sci.* **117**, 67–78 (2016)
9. Carlberger, T., Stigh, U.: Dynamic testing and simulation of hybrid joined bi-material beam. *Thin-Walled Struct.* **48**(8), 609–619 (2010)
10. Barnes, T.A., Pashby, I.R.: Joining techniques for aluminium space frames used in automobiles PartII—adhesive bonding and mechanical fasteners. *J. Mater. Process. Technol.* **99**(1–3), 72–79 (2000)
11. Sun, G., Pang, T., Fang, J., Li, G., Li, Q.: Parameterization of criss-cross configurations for multiobjective crashworthiness optimization. *Int. J. Mech. Sci.* **124**, 145–157 (2017)

# Numerical Crashworthiness Investigation of Multi-Section Tubes



M. Nalla Mohamed and R. Sivaprasad

## 1 Introduction

Thin-walled structures have vital role during the crash event as they can absorb a significant amount of energy and decrease the impact on the occupant. Along with advancement in technology, stringent safety regulations are needed to deal with enormous impetus around us. Widely used periphery cross sections are either square or circular cross sections due to their ease of manufacturing. Amongst them, most preferred cross section profile is square tubes since they can be easily assembled and constrained at the ends [1–3]. Particularly, square tubes made of aluminium are preferred due to its lightness and progressive deformation behaviour during the crash for occupant safety, and its properties are unchanged even after recycling [4–7]. In recent years, many investigative studies were carried out on different cross-sectional profiles including multi-walled sections in order to obtain better crashworthiness. Amongst plain extruded thin-walled tubes consisting of regular shapes, regular hexagon profile exhibits better energy absorbing capacity as well as manufacturable with reasonable cost [8]. The idea of bi-tubular tubes combining two profiles and assembled with common axis, witnessed the combination consists of the square profile enclosed by regular hexagon showed better crashworthiness in terms of specific energy absorption [9]. The challenge arises in bi-tubular tubes due to non-similar profiles having different deforming mechanisms, to overcome this, constraining ribs can be provided onto lateral sides of each other [10]. Adding multi-cell internal sections of regular profiles is one of the essential ways of enhancing the energy absorption significantly [11].

---

M. Nalla Mohamed (✉) · R. Sivaprasad  
Department of Mechanical Engineering, Sri SivasubramaniyaNadar College of Engineering,  
Kalavakkam, Kancheepuram District, Tamilnadu, India  
e-mail: [nallamohamedm@ssn.edu.in](mailto:nallamohamedm@ssn.edu.in)



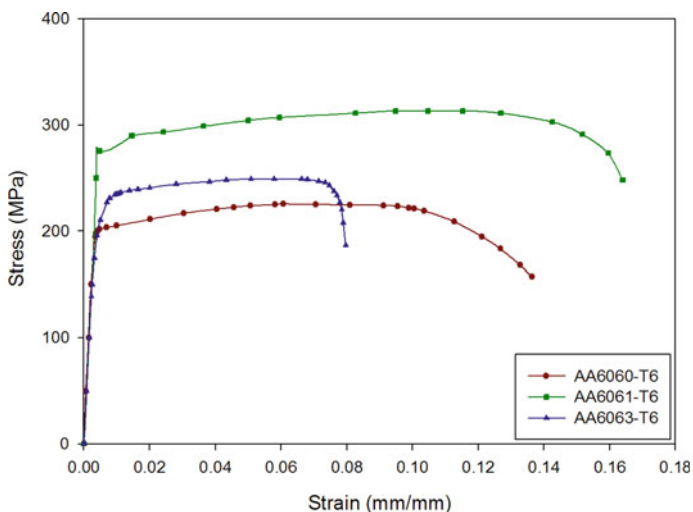
The above-mentioned literature review shows that there has been considerable studies on the combinations of profiles through assemblage but blending of two profiles (MTSC) is scanty literature data. Hence, the present research work deals with the thin-walled structure comprises of two profiles (square on one end and circular on other end). The transition takes place in smooth manner such that the tube exhibits infinite multi-sections during the transition between two profiles. Three different aluminium alloys namely AA6060-T6, AA6061-T6 and AA6063-T6 tubes have been chosen for initial investigation, an attempt have been made to study the energy absorption characteristics and initial peak force of the above materials numerically. Furthermore, 9 different (MTSC) profiles have been evaluated to find out which profile exhibits performance indices numerically and compared with USS-USC tubes using a finite element analysis. Since numerical simulation helps to understand the deformation mechanism as well as reduces the cost of expensive prototypes. Even though superior impact performance in terms of energy absorbing capacity exists, still then high-initial peak force is the major problem which has the potential hazard to the occupant, hence the specimen exhibiting minimum IPF and considerable SEA is far better.

## 2 Design Methodology and Material Properties

The present study consists of three phases. In the first phase, thin-walled circular tubes (USC) of three different aluminium grades AA6060-T6, AA6061-T6 and AA6063-T6 are modelled with same dimensions ( $\varnothing$ 71-mm diameter, 2-mm thickness and 150-mm length) to select the suitable material. The engineering stress-strain curves of different grades were derived from literatures [12–14] as shown in Fig. 1. The effective stress-strain data points are used in numerical simulations. The second phase deals with the 9 sets of MTSC are modelled with varying dimensions. In order to investigate the geometry that exhibits better crashworthiness, the study conducted on MTSC tubes with the chosen material from the first phase. The dimensions of proposed tubes are shown in Table 1. The final phase includes comparison of performance parameters of MTSC tubes against their counterparts.

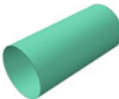
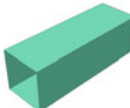
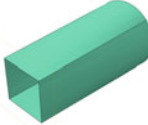
## 3 FE Model and Simulation Procedures

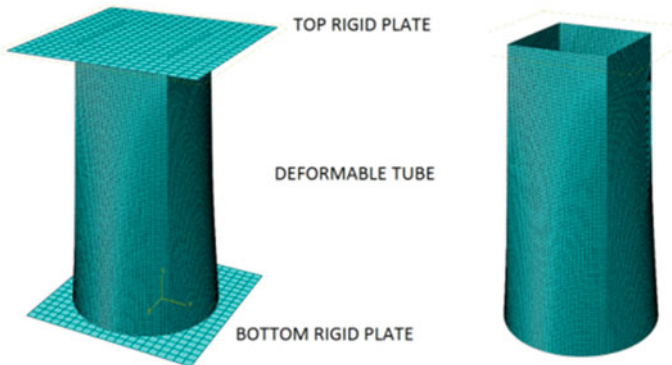
The finite element (FE) models of USS, USC and MTSC tubes along with flat rigid plates are developed using nonlinear ABAQUS explicit code® to understand the crushing behaviour under quasi static loading conditions. In this study, S4RR3D4 elements are chosen for the deformable tubes and flat rigid plates, respectively. The top rigid plate is allowed to translate freely along the axis of the deformable tubes to apply axial quasi static compression loading on the tubes, whereas the bottom rigid plate is fully fixed. The contact interaction between the top plate and



**Fig. 1** True stress–strain curves of aluminium alloy AA6060-T6, AA6061-T6, AA6063-T6 [11–13]

**Table 1** Geometry and dimensions of tubes used for study

Profile	Specimen ID	Dimension (mm)	Length (mm)	Thickness (mm)	Geometry
Circular	USC	Ø71	150	2	
Square	USS	50	150	2	
Multi-section	MTSC_1	Ø71, 40	150	2	
	MTSC_2	Ø71, 42.5	150	2	
	MTSC_3	Ø71, 45	150	2	
	MTSC_4	Ø71, 47.5	150	2	
	MTSC_5	Ø71, 50	150	2	
	MTSC_6	Ø73.5, 50	150	2	
	MTSC_7	Ø76, 50	150	2	
	MTSC_8	Ø78.5, 50	150	2	
	MTSC_9	Ø81, 50	150	2	



**Fig.2** FE model of MTSC tube

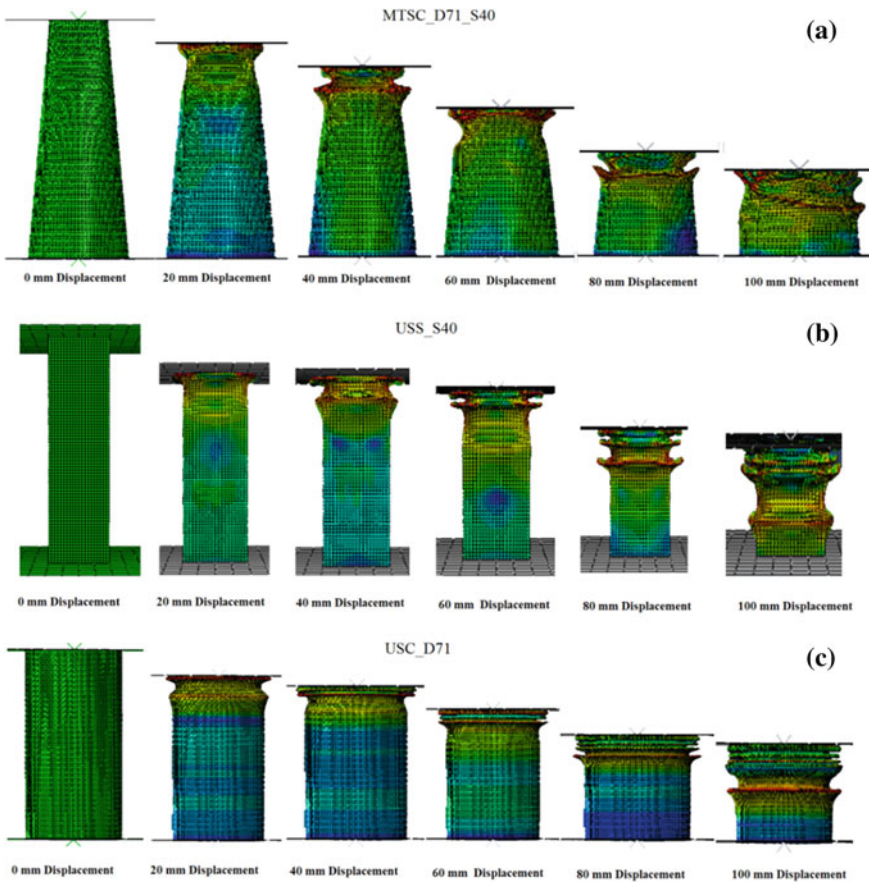
the deformable tube is surface-to-surface contact, and tie constraint is placed between the deformable tube and bottom rigid plate. The assembly of the FE model is shown in Fig. 2. The quasi-static axial compression is applied through top plate which displaces downwards at a rate of 2 mm/min and covers up to 100 mm displacement of axial compression. The mesh convergence study was also performed to determine the mesh size that gives more accurate results for the given FEA model. This is performed by running the simulations with the USC FE model by discretizing with elements ranging from 0.8 mm to 2 mm. The finely meshed FE model of size between 1 mm and 0.8 mm exhibits good results. In order to carry out the simulations with minimum computation time, mesh size 1 mm is considered as optimum size without compromising the accuracy.

## 4 Results and Discussion

The comparison of performance indicator for USC tubes with different material grades is presented in Table 2. From Table 2, it is evidenced that the IPF of AA6063 T6 is considerably less when compared to the other two materials, i.e. AA6061 T6 and AA6060 T6. Therefore, AA6063 T6 material has been chosen for further analysis and evaluations, since it exhibits favourable properties. The deformation history of MTSC, USS and USC is shown in Fig. 3. Typical force–displacement curves of

**Table 2** Crashworthiness parameters of aluminium alloys

Material	IPF (kN)	MCF (kN)	SEA(kJ/kg)	Energy absorption (KJ)
AA6060-T6	65.73	47.09	26.02	4.71
AA6061-T6	62.25	48.66	26.89	4.87
AA6063-T6	60.02	48.60	26.55	4.81



**Fig. 3** Deformation history of **a** MTSC\_D71\_S40, **b** USS\_S40, **c** USC\_D71

MTSC, USS and USC are presented in Fig. 4. The area under the curve gives the energy absorption capacity of the deformed tube.

The comparison of performance indicators such as initial peak force and specific energy absorption for MTSC tubes are shown in Fig. 5. From graph shown in Fig. 5, it is evidenced that Profile Number MTSC\_1 (MTSC\_D71\_S40) has least IPF and highest SEA. Therefore, this particular profile has been chosen for comparison with its uniform section counter parts.

Comparison of performance parameter for MTSC\_D71\_S40, USS\_S40 and USC\_D71 is presented in Table 3. It is inferred that USC\_D71 has higher IPF, which is undesirable for the passengers. On the other hand, MTSC\_D71\_S40 has proved to exhibit lower IPF with higher SEA when compared to square and cylindrical tubes with uniform thickness tubes.

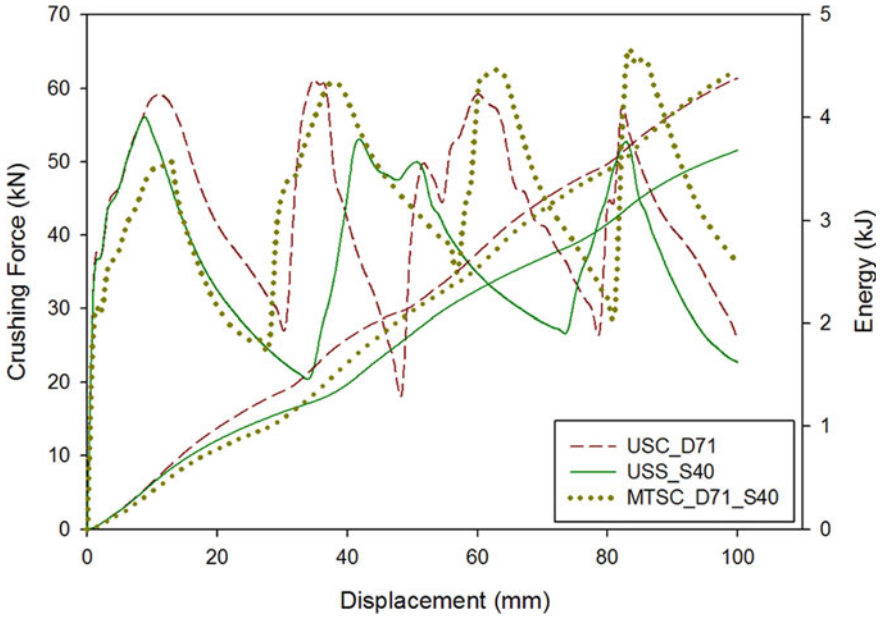


Fig. 4 Force–displacement and energy-displacement curves of MTSC\_D71\_S40, USS\_S40, USC\_D71, respectively

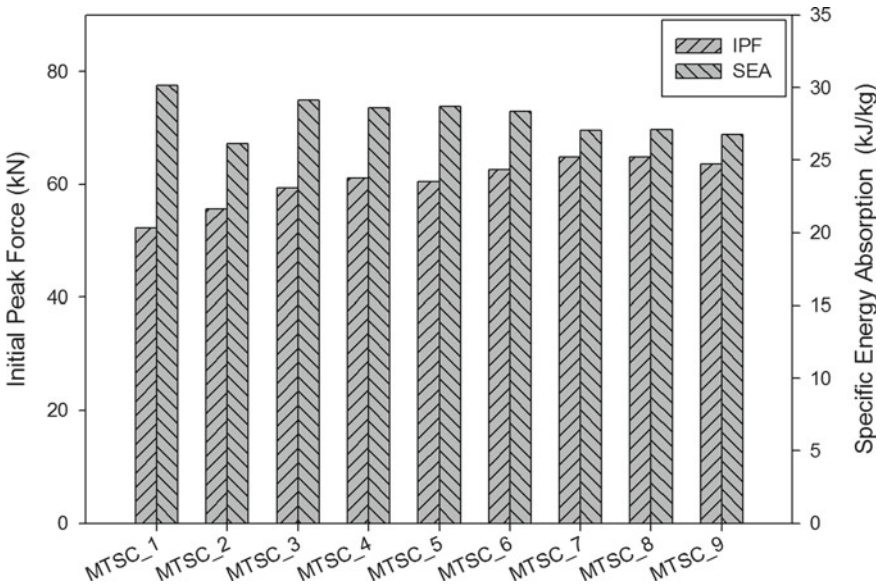


Fig. 5 Initial peak force and specific energy absorption of MTSC tubes

**Table 3** Comparison of performance parameter for MTSC\_D71\_S40, USS\_S40 and USC\_D71

Profile parameters	IPF (kN)	MCF (kN)	SEA (kJ/kg)	Energy absorption (KJ)
MTSC_D71_S40	49.83	45.26	30.17	4.526
USS_S40	56.01	37	28.45	3.7
USC_D71	60.02	44.26	24.45	4.426

## 5 Conclusion

Thin-walled tubes have widely been used as energy absorbers in automobiles in the event of a crash to ensure safety to the passengers in the cabin. This study was carried out with the scope of increasing the crashworthy performance of crash boxes by introducing thin-walled multi-sectional tubes with square geometry at one end and circle at the other end. The two main parameters are initial peak force (IPF) and specific energy absorbed (SEA) were taken in to account. From the results of numerical analysis, the following conclusions were made.

1. From the initial material analysis of AA6061-T6, AA6060-T6 and AA6063-T6, it has been inferred that AA6063 T6 was found to exhibit the least IPF and almost equal SEA when compared to the other two alloys.
2. When MTSC profiles of different dimensions were subjected to axial compression tests, MTSC\_D71\_S40 was found to exhibit least IPF and high SEA when compared to other MTSC profiles.
3. MTSC\_D71\_S40 which geometrically combines both USC\_D71 and USS\_S40 has proved to exhibit an IPF significantly lower than both USC\_D71 and USS\_S40. It also has the highest SEA when compared to the other two regular profiles.
4. Therefore, it is concluded that the crashworthiness behaviour of multi-sectional tubes with square cross section at one end and circle at the other end is better than that of regular cylindrical and square tubes with uniform section.


## References

1. Chen, S., Haiyan, Yu., Fang, J.: A novel multi-cell tubal structure with circular corners for crashworthiness. *Thin-Walled Struct.* **122**, 329–343 (2018)
2. Qi, C., Yang, S., Dong, F.L.: Crushing analysis and multi objective crashworthiness optimization of tapered square tubes under oblique impact loading. *Thin-Walled Struct.* **59**, 103–119 (2012)
3. Zhou, Y., Lan, F.C., Chen, J.: Crashworthiness research on S-shaped front rails made of steel aluminum hybrid materials. *Thin-Walled Struct.* **49**, 291–297 (2011)
4. Zhang, X., Zhang, H., Ren, W.: Axial crushing of tubes fabricated by metal sheet bending. *Thin-Walled Struct.* **122**, 252–263 (2018)

5. Simhachalam, B., Srinivas, K., Rao, C.L.: Energy absorption characteristics of aluminium alloy AA7XXX and AA6061 tubes subjected to static and dynamic axial load. *Int. J. Crashworthiness* **19**(2), 139–152 (2014)
6. Institute for Energy and Environmental Research, Improving Sustainability in the Transport Sector through Weight, Reduction and the Application of Aluminium, Transport and Aluminium, International Aluminium Institute, London (2008)
7. Nalla Mohamed, M., Yuvarajan, P., Umasankar, M.: Energy enhancement of long cylindrical tubes with grooves subjected to axial impact. *Appl. Mech. Mater.* **787** Trans Tech Publications, pp. 345–349 (2015)
8. Tarlochan, F., Samer, F., Hamouda, A.M.S., Ramesh, S., Khalid, K.: Design of thin wall structures for energy absorption applications: enhancement of crashworthiness due to axial and oblique impact forces. *Thin-Walled Struct.* **71**, 7–17 (2013)
9. Manaf, E.H.A., Rahman, M.T.A., Rahman, A., Rahman, A.S.A., Mat, F., Basaruddin, K.S.: Crashworthiness analysis of bi-tubular aluminium tubes with varying shapes in LS-Dyna'. *Materials Science and Engineering*, Vol. 429, International Conference on Advanced Manufacturing and Industry Applications, pp. 15–17.
10. Pirmohammad, S., EsmailiMarzdashti, S.: Crushing behavior of new designed multi-cell members subjected to axial and oblique quasi-static loads. *Thin-Walled Struct.* **108**, 291–304 (2016)
11. Alavi Nia, A., Parsapour, M.: Comparative analysis of energy absorption capacity of simple and multi-cell thin-walled tubes with triangular, square, hexagonal and octagonal sections. *Thin-Walled Struct.* **74**, 155–165 (2014)
12. Jin, S.Y., Altenh, W.: Control of load/displacement responses of AA6061-T6 and T4 circular extrusions under axial compressive loads. *Int. J. Impact Eng.* **38**, 1–12 (2011)
13. Sun, G., Guo, X., Li, S., Ruan, D., Li, Q.: Comparative study on aluminum/GFRP/CFRP tubes for oblique lateral crushing. *Thin-Walled Struct.* **152**, 106420 (2020)
14. Mróz, A., Mania, R.J.: The complex influence of aluminium aging on the dynamic response of the thin-walled AL-6060 alloy profile. *Thin-Walled Struct.* **79**, 147–153 (2014)

# Design of Tabletop Automated Plane Polariscopes for Digital Photoelastic Measurements



M. Gagan Keerthi, Ananthesh D. Shenoy, B. Devanarayanan, V. S. Sharath, and M. P. Hariprasad 

## 1 Introduction

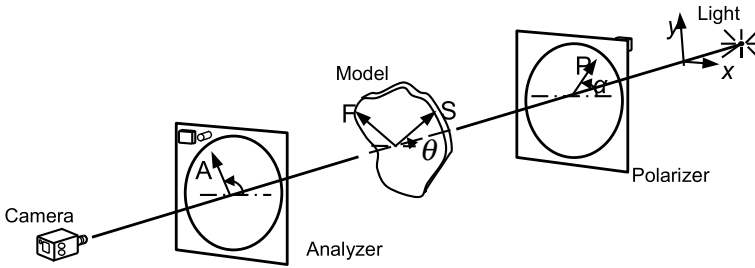
The broad spectrum of solid mechanics mainly focuses on the behaviour of solid bodies, including displacement and deformations when subjected to various conditions such as external loads, temperature changes and phase changes. Stress analysis is that branch of engineering that uses various methods for the estimation of the stresses and strains induced in a material or a structure when it is subjected to an externally applied load. Photoelasticity is an optical technique which can be used for stress and strain analysis. It is a non-contact technique. With advancements in digital photoelasticity [1–4], this technique emerged as the first choice for many researchers for the evaluation of stress/strain analysis and is the most widely used method under whole field stress analysis. Digital photoelasticity has found its place in the broad engineering fields including civil [5, 6], mechanical [7, 8], aerospace, biomedical [9, 10] involving structural design, analysis and maintenance. Recent developments in the field of applied mechanics and materials demand whole field appreciation of the stress/strain analysis. Photoelasticity could be an ideal choice for the stress analysis in many of the emerging areas of applied mechanics [11–15].

Photoelasticity deals with changes in the optical properties of a material which is subjected to mechanical deformation and thereby provides us the principal stress difference and directions at a point of interest on the domain. It depends on the principle of stress induced birefringence. Photoelastic experimental test facility includes a polariscopes, appropriate loading mechanisms and data acquisition systems. Polariscopes are the building blocks of any photoelastic experiments. Conventional photoelastic experiments utilises the basic configurations such as plane or circular polariscopes. In the plane polariscopes, linearly polarized light falls on the mode and

---

M. G. Keerthi · A. D. Shenoy · B. Devanarayanan · V. S. Sharath · M. P. Hariprasad (✉)  
Department of Mechanical Engineering, Amrita Vishwa Vidyapeetham, Amritapuri, India





**Fig. 1** Schematic arrangement of a plane polariscope

the optical elements such as analyser and polarizer are kept in a crossed positions. A generalised figure of a plane polariscope is given in Fig. 1.

In digital photoelasticity, one utilises the intensity processing of various configurations of the polariscope and the methods are broadly classified into single acquisition and multi-acquisition methods. Phase shifting technique (PST) algorithms serves the purpose of evaluating the isochromatic and isoclinic data with more accuracy [16–19]. Among various PST algorithms, ten-step PST [20] is found to be effective in providing the isochromatic and isoclinic information with enhanced accuracies. Optical element configurations of a ten-step phase-shifting algorithm are shown in Table 1.

In conventional digital photoelastic measurements, phase shifting is attained on manual rotation of the optical modules. The idea of automation of polariscopes came into existence in various forms. In 1959, the primary initiative to develop a polariscope to automatically evaluate the parameters pertaining to isoclinic and isochromatic fringe order at a point was conducted by Zandman [21] with the introduction of a babinet compensator which would be driven by a servo motor. In 1961, Sapaly

**Table 1** 10 Step PST table

$\alpha$	$\xi$	$\eta$	$\beta$	Intensity equation
$\pi/2$	–	–	0	$I_1 = I_b + I_a \sin^2 \frac{\delta}{2} \sin^2 2\theta$
$5\pi/8$	–	–	$\pi/8$	$I_2 = I_b + \frac{I_a}{2} \sin^2 \frac{\delta}{2} (1 - \sin 4\theta)$
$3\pi/4$	–	–	$\pi/4$	$I_3 = I_b + I_a \sin^2 \frac{\delta}{2} \cos^2 2\theta$
$7\pi/8$	–	–	$3\pi/8$	$I_4 = I_b + \frac{I_a}{2} \sin^2 \frac{\delta}{2} (1 + \sin 4\theta)$
$\pi/2$	$3\pi/4$	$\pi/4$	$\pi/2$	$I_5 = I_b + \frac{I_a}{2} (1 + \cos \delta)$
$\pi/2$	$3\pi/4$	$\pi/4$	0	$I_6 = I_b + \frac{I_a}{2} (1 - \cos \delta)$
$\pi/2$	$3\pi/4$	0	0	$I_7 = I_b + \frac{I_a}{2} (1 - \sin 2\theta \sin \delta)$
$\pi/2$	$3\pi/4$	$\pi/4$	$\pi/4$	$I_8 = I_b + \frac{I_a}{2} (1 + \cos 2\theta \sin \delta)$
$\pi/2$	$\pi/4$	0	0	$I_9 = I_b + \frac{I_a}{2} (1 + \sin 2\theta \sin \delta)$
$\pi/2$	$\pi/4$	$3\pi/4$	$\pi/2$	$I_{10} = I_b + \frac{I_a}{2} (1 - \cos 2\theta \sin \delta)$

[22] came up with a new innovative idea to identify the fractional fringe orders, with an analyser that spins continuously. Owing to the limitations of the manual operations of polariscopes configurations, this work aims to design a customisable tabletop automated plane polariscopes for whole field stress analysis measurements for digital photoelasticity.

## 2 Automating the Optical Elements of Plane Polariscopes

The optical elements analyser and polarizers are similar in its construction, and the polariser close to the light source makes the light linearly polarized. The same element when kept at the analysing end is called as an analyser. The rotation of optical elements is to be automated by using stepper motors. The design is proposed to have a flexibility in configuring the optical element as required. The plane polariscopes phase shifting algorithms will be automated by using appropriate motors which would be controlled by a coding platform, and the entire system could be implemented in a short time period.

Selection of appropriate motor: A motor which would rotate with high precision levels and produce high torque at low operating speeds was the main requirement. The stepper motor was found to be the best suiting these requirements due to its various features. It has precise movement making it the ideal choice for applications requiring precise positioning such as in the case of 3D printers and CNC's. Due to the precise increment in its movement, it is the most favoured choice for applying in process automation and robotics. It achieves maximum value of torque at low speeds making it ideal for applications requiring high precision at low running speed.

Appropriate coding platform is identified for the control of the stepper motor and all the operations are controlled by the programmable logic controller (PLC). The main requirement was that the entire experimental procedure must be simple to implement, and the user specific-values of the orientation can be communicated to the motor such that a person without much programming background would not find it much of an issue while conducting the experiment.

## 3 Design of Optical Plate for Polariser and Analyser

Lack of availability of automated polariscopes made the initial design very challenging and this work brought out an innovative design idea. Initially, rotating unit comprised of a belt drive with a timer pulley was designed. This, however, increased the size of the setup as additional holding platforms had to be built for the motors and this was not ideal for a tabletop assembly. This leads to the need for designing an entirely new polariscopes setup such that the modules must move horizontally and its optical elements rotated individually. The light needed to pass through all four modules and reach the camera at the opposite end. Four pinion gears mounted at each corner of

the module. The optical box and gear dimensions were calculated and accordingly designed. The modules were made flexible enabling easy mounting and dismantling from the rails on which the optical modules would be mounted and could have lateral movement.

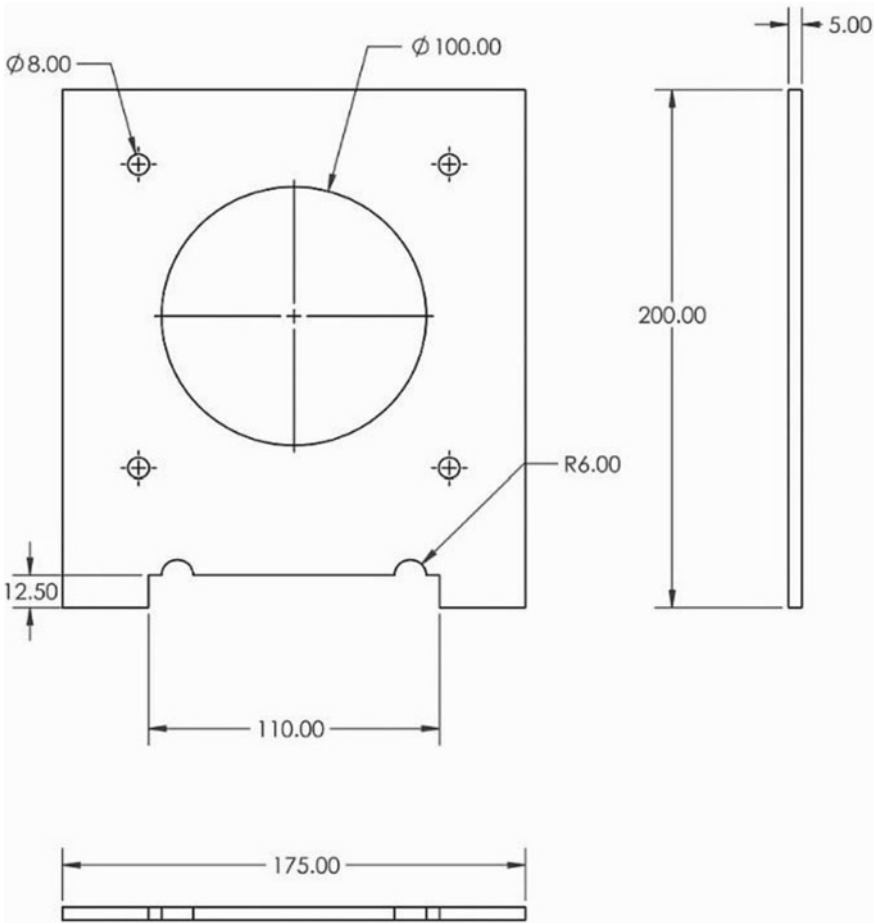
### ***3.1 Part Design and Data***

In order to facilitate the customisation of polariscope for various experiments, the individual optical modules are designed to move independently along the light path direction. Further, optical elements can be rotated individually as per the user-specific inputs. The light needed to pass through all the four optical modules and reach the image grabbing module at the opposite end. The rotary component is designed based on four pinion gear system mounted at each corner of the optical module. The optical box and gear dimensions were based on the tabletop arrangement requirement. The modules were made flexible enabling easy mounting and dismantling from the rails, which facilitate an easy lateral movement for the modules. Dassault Solidworks was chosen as the design software for the entire part design aspect due to the user-friendly interface it provides.

The individual part design for the single optical element is discussed next:

1. **Optical box plate:** The optical box plate shown in Fig. 2 is having a length of 200 mm height of 175 mm and a width of 5 mm, and there is a central circular space of 100 mm diameter to accompany the optical element. Holes for accompanying the pinion gears have a 10 mm diameter. Figure 2 depicts a schematic of the optical box plate.
2. **Optical box beadings:** The top beading is sandwiched in between the two plates and having dimensions, 175 mm in length, 20 mm in height and 10 mm width. It is made up of aluminium. A side beading is also used to cover all these gears from both sides. Dimensions of the side beading is fixed as 20 mm in thickness, 165 mm length and 10 mm in width.
3. **Gears:** The optical element inside the module should be freely rotatable and easily replaceable by the operator, and no obstructions should rise within the spaces between the optical elements. Gear with a module of 2, inner diameter of 95 mm, outer diameter of 139 mm and 68 teeth was developed. As the gear is placed between the two box plates, it has a thickness of 19 mm. To hold the optical element in the gear, a groove is made with diameter of 100 mm through 2 mm thickness and next to it another groove of diameter 105 mm is made through another 2 mm thickness to insert the rubber O ring.

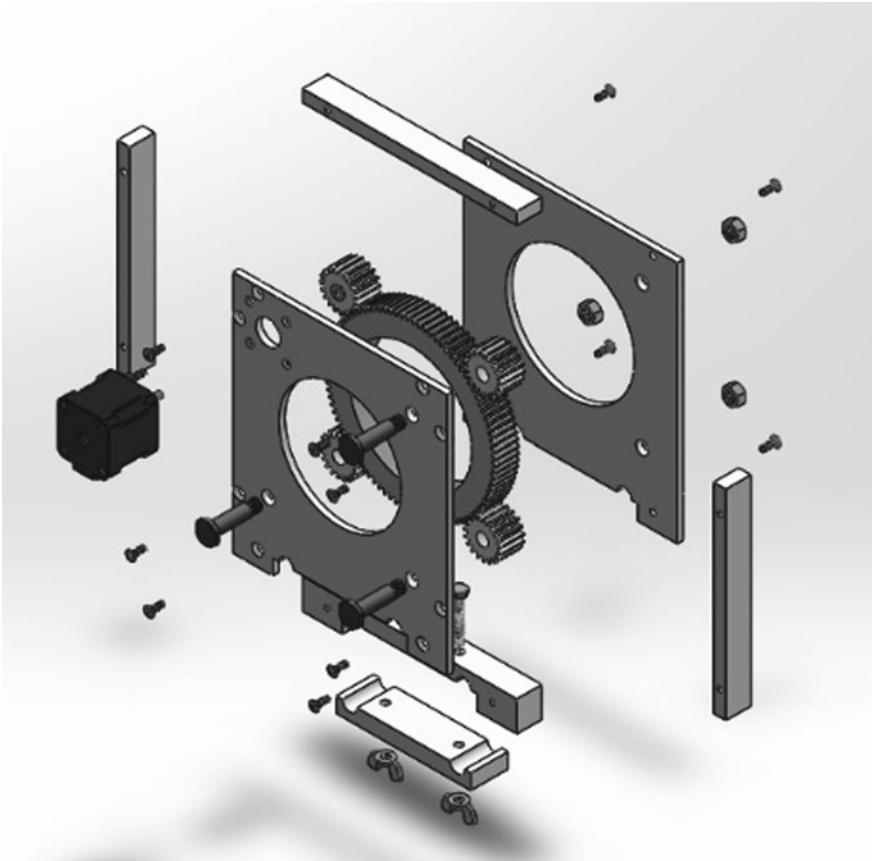
The four pinion gears are mounted to the four corners of the optical box base plate. Three pinion gears are attached using the pinion shaft. The optic element is inserted to the main gear into the 100 mm groove. The four modules are aligned together by connecting them on two horizontal rails. The rails are inserted into the two slotted provisions on the box plates. The position of the optical plates can be



**Fig. 2** Schematics of optical box plate

varied depending on the user’s wish and also the configuration of polariscopes is required. Exploded view of the assembled single optical plate is shown in Fig. 3.

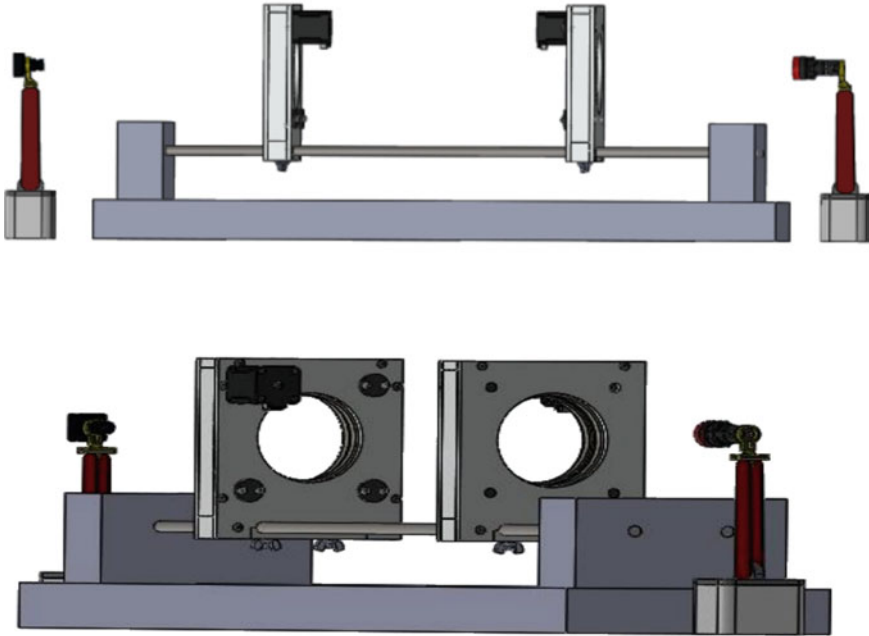
Rails are used so that the modules can easily slide on them and easy removal was also possible. Another feature was that all the modules would be aligned in a straight manner and no errors would arise for the alignment. The assembled plane polariscopes is depicted in Fig. 4. The optical plates in order from the light source are polarizer and analyser. The position of the optical plates can be varied depending on the user’s wish and also the configuration of polariscopes is required. The experimental specimen would be kept in a specimen holder which would be located between the analyser and polariser.



**Fig. 3** Exploded view of a single optical plate

## 4 Conclusion

Photoelasticity is widely used in 2D and 3D studies, impact testing, residual stress analysis, glass inspection, flaw detection, assembly stress analysis and FEA model inspection. In photoelasticity, one make use of polarized light. In conventional digital photoelastic measurements, phase shifting is achieved by manual rotation of the optical elements of the polariscope. The design envisaged for automating the plane polariscope enables one to overcome the long-term faced problem of increased rate of errors due to manual rotation of the optical elements in the plane polariscopes. Due to the development of this unique system of automation, one could explore the plane polariscope-based phase shifting algorithms for achieving greater accuracy for the stress/birefringence measurements. The polariscope can be conveniently used in any small-scale lab facilities, and it can be used as a tabletop apparatus.



**Fig. 4** Assembled view of automated plane polariscopes

## References

1. Ramesh, K.: *Digital Photoelasticity: Advanced Techniques and Applications*. Springer Verlag, Berlin (2000)
2. Patterson, E.A.: *Digital Photoelasticity: principles, practices and potential*. *Strain* **38**(1), 27–39 (2002)
3. Ramesh, K.: *Photoelasticity*. In Sharpe, W.N. (eds.), *Springer Handbook of Experimental Solid Mechanics*, Springer NY, pp. 701–742 (2008)
4. Ramesh, Sasikumar, S.: “Digital photoelasticity: recent developments and diverse applications”. *Optics Lasers Eng.* (2020)
5. Kumar, P., Hariprasad, M.P., Menon, A., Ramesh, K.: *Experimental study of dry stone masonry walls using digital reflection photoelasticity*. *Strain*, **56**, e12372 (2020) <https://doi.org/10.1111/str.12372>.
6. Baig, I., Ramesh, K., Hariprasad, M.P.: “Analysis of stress distribution in dry masonry walls using three fringe photoelasticity”. In *Proc. SPIE 9302, International Conference on Experimental Mechanics 2014*, 93022P (2014)
7. Hariprasad, M.P., Ramesh, K.: *Analysis of contact zones from whole field isochromatics using reflection photoelasticity*. *Optics Lasers Eng.* **105**, 86–92 (2018)
8. Hariprasad, M.P., Ramesh, K., Bhagyashree, C.: Prabhune, “Evaluation of Conformal and Non-Conformal Contact parameters Using Digital Photoelasticity.” *Exp. Mech.* **58**(8), 1249–1263 (2018)
9. Ramesh, K., Hariprasad, M.P., Bhuvaneshwari, S.: “Digital photoelastic analysis applied to implant dentistry. *Digit. Optical Imaging Methods Struct. Mech.* **87**, 204–213 (2016)

10. Harpirasad, M.P., Ramesh, K.: "Contact zone evaluation of dental implants using digital photoelasticity", In *Mechanics of Biological Systems and Materials*, Vol. 6, Proceedings of the Society for Experimental Mechanics Series (2017)
11. Hariprasad, M.P., Ramesh, K., Prabhune, B.C.: Evaluation of conformal and non-conformal contact parameters using digital photoelasticity. *Exp Mech* **58**, 1249–1263 (2018). <https://doi.org/10.1007/s11340-018-0411-6>
12. Dutta, S., Menon, H.G., Hariprasad, M.P., Krishnan, A., Shankar, B.: Study of auxetic beams under bending: a finite element approach. *Materials Today: Proceedings*, ISSN 2214–7853 (2020). <https://doi.org/10.1016/j.matpr.2020.10.479>
13. Ravi Kiran, B., Arunkumar, S., Reddy, G. M.: Influence of residual stress and poisson's ratio on the stress intensity factor of standard specimens. *Int. J. Mech. Eng. Technol.* **9**(10), 219–227 (2018). <http://www.iaeme.com/IJMET/issues.asp?JType=IJMET&VType=9&IType=10>
14. Arunkumar, S., Prakash, R.V.: Estimation of tensile properties of pressure vessel steel through automated ball indentation and small punch test. *Trans Indian Inst. Met.* **69**, 1245–1256 (2016). <https://doi.org/10.1007/s12666-015-0680-z>
15. Rohith, K.P., Sajay Rajan, E., Harilal, H., Jose, K., Shankar, K.V.: Study and comparison of A356-WC composite and A356 alloy for an off-road vehicle chassis. *Mater. Today: Proc.* **5**(11), Part 3 (2018). <https://doi.org/10.1016/j.matpr.2018.11.006>
16. Patterson, E.A., Wang, Z.F.: "Towards full field automated photoelastic analysis of complex components". *Strain* **27**(2), 49–56 (1991)
17. Brown, G.M., Sullivan, J.L.: The computer-aided holophotoelastic method. *Exp. Mech.* **30**, 135–144 (1990)
18. F.W. Hecker and B. Morche. "Computer-aided measurement of relative retardations in plane photoelasticity", *experimental Stress Analysis*, page 535–543, (1986).
19. Ajovalasit, A., Barone, S., Petrucci, G.: A review of automated methods for the collection and analysis of photoelastic data. *J. Strain Anal.* **33**(2), 75–91 (1998)
20. Ramji, M., Rameh, K.: Whole Field evaluation of stress components in digital photoelasticity—Issues, implementation and application. *Opt. Lasers Eng.* **46**, 257–271 (2008)
21. Zandman, F.: "Photostress analysis". *Product Eng. March* (1959)
22. Sapaly, J.: "Contribution a l'étude de la photoextensometrie statique et dynamique", *Th. Sc. Phys.*, series A3761, (4612), Paris (1961)

# Structural and Vibration Analysis of Barge Ship Hull



S. Ramana Babu and Baswani Harikrishna Raju

## 1 Introduction

A barge ship is flat-shaped on its foot, rather like a flatboat. The most reason for this specific shape is to guarantee that the cargo-carrying capacity is improved and more bulk can be shipped and transported. A sort of vessel that is essentially utilized for transporting cargo is named as a ‘barge’ [1]. Barge ships are not something like free vessels or ships but are engineers coasting vessels generally towed or pulled beside other vessels [2]. For centuries, the wood is the main material for shipbuilding, but later on, the shipbuilders realized that the steel material is stronger and lighter compared to wood [3]. In any case, the foremost critical portion almost barge ships is the reality that they are not free boats or vessels, and they need to be pulled or towed alongside other naval vessels within the water [4]. Barge ships are utilized for the most part in smaller water parts like rivers, lakes, or canals; however, they are presently utilized broadly at seaports [5]. Barges are not modern to utilize, but the world had seen marine barge ships even before the industrial revolution. Before the industrial transformation in Europe, marine barges were utilized as the main strategy of transportation to ship cargo across places connected by water bodies [6].

## 2 Design of Ship Hull

This work deals with the structural analysis of barge ship hull configuration for structural rigidity, estimation of machinery, and mechanical equipment [7]. All design

---

S. Ramana Babu · B. H. Raju (✉)  
Department of Mechanical Engineering, Sanketika Vidya Parishad Engineering College,  
Visakhapatnam 530041, India

© The Author(s), under exclusive license to Springer Nature Singapore Pte Ltd. 2022  
S. K. Natarajan et al. (eds.), *Recent Advances in Manufacturing, Automation, Design  
and Energy Technologies*, Lecture Notes in Mechanical Engineering,  
[https://doi.org/10.1007/978-981-16-4222-7\\_76](https://doi.org/10.1007/978-981-16-4222-7_76)

683



**Table 1** Design calculations

Name	Formula
Deck plating	$t = (6.5 + 0.02L)C\sqrt{\frac{ks_1}{S_b}}$
Double-bottom plate	$d_{DB} = 32B + 190\sqrt{d}$
Side plate	$t = (6.5 + 0.02L)C\sqrt{\frac{ks_1}{S_b}}$
Bulkheads	$t = 0.004Sf\sqrt{h_4K}$
Stress	$S = \text{force (load)/unit area}$

selections, estimation, and calculation on board the work barge were done by Lloyd's rules and regulations.

## 2.1 Design Calculation

Table 1 represents the design calculations which are used in constructing the barge ship hull with pre-assumed values. The calculation is done by using Lloyd's rules and regulations [8].

## 2.2 Design and Assembling

The DELFTship software specializes in the development of high-end marine software. It is a free-version software where it can be learned by any individual without any training just by following their help manual. The ship hull surface structure is generated using DELFTship software. All dimensions of the outer surface are used to generate the ship hull. The barge ship hull model is selected in this work.

Figure 1 shows the barge ship hull after selecting the type of hull, length, width, and draft dimensions. According to the dimensions, the barge hull model is created in this software. It also shows the different views of the barge ship hull, and by selecting the angle view of the ship, we can see the front, top, and back views of the barge ship. The model which is created in DELFTship software is further modified into a DXF file. In AutoCAD software, we are using the DXF file which is generated. In DELFTship software, we create the outlook of barge hull and further modified into IGES file. Before using the sketch, select the plane of CATIA display and then got to sketch so that the generating face can be done in CATIA software. In this, the drawing which is an accurate dimension is then converted to three-dimensional solid (3D).

Figure 2 represents the 3D model of barge ship hull which is created in CATIA software. The surface is initially created, stiffness is provided according to calculated values, and the file is further modified into UGES file.

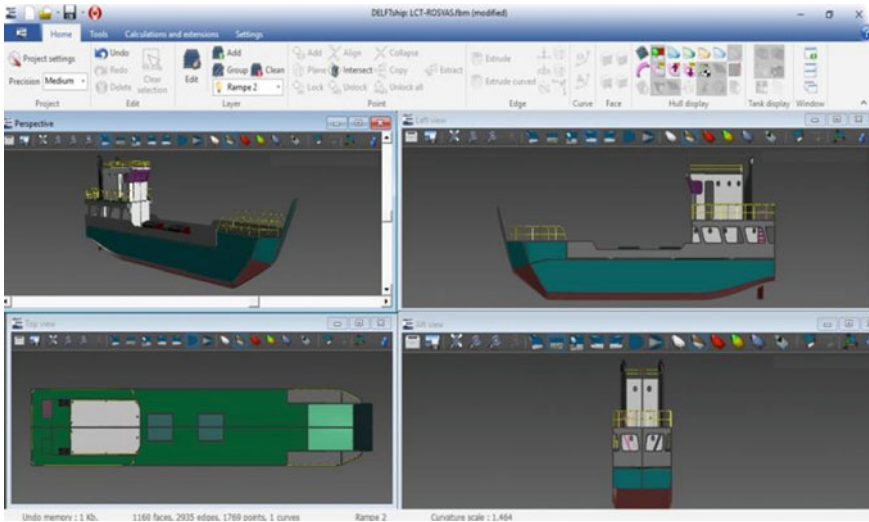


Fig. 1 Barge ship hull in DELFTship software

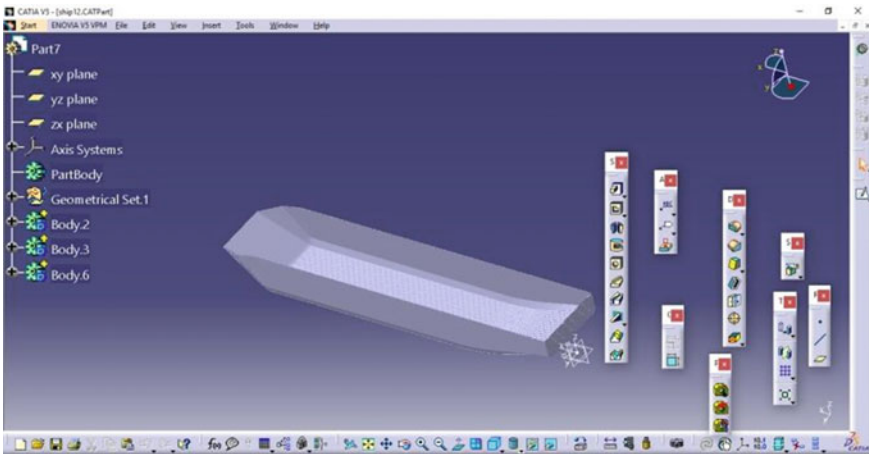


Fig. 2. 3D model of barge ship hull

Hypermesh is a popular multi-disciplinary pre- and post8-processor, which manages the generation of large and complex models. In this work, the geometry model is imported from CATIA as a UGES file. And, steel, aluminium, wood, and fibreglass materials are considered in this work.

Table 2 which is shown below represents the material components such as Young’s modulus and Poisson’s ratio for different materials.

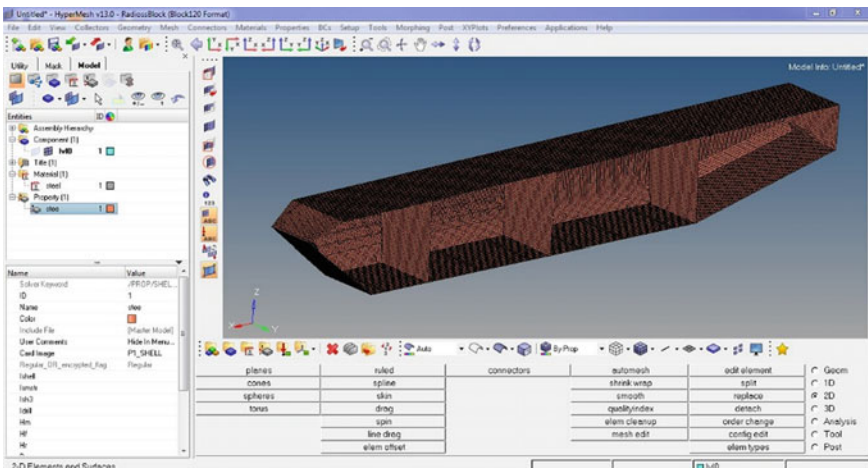
**Table 2** Material components

Material	Young’s modulus (GPa)	Poisson’s ratio	Density (kg/m <sup>3</sup> )
Steel	210	0.3	7850
Aluminium	69	0.33	2500
Wood	9.5	0.3	600
Fibreglass	72	0.21	2400

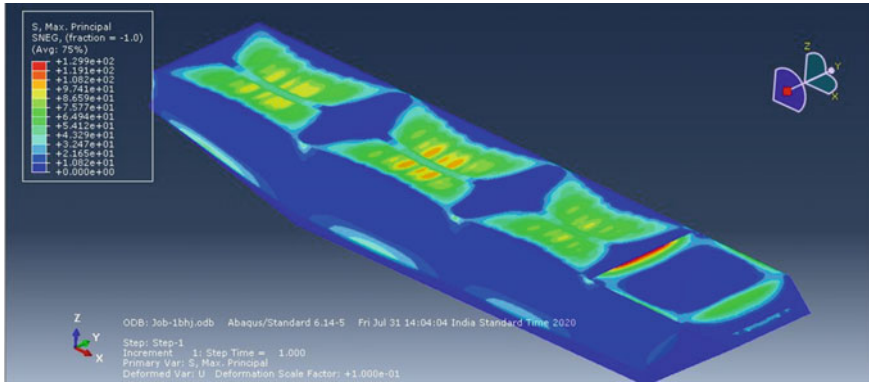
Generally, a 2D mesh element is available in the Hypermesh. These elements are used to solve in the shell and solid element. When there are several elements present, we can get exact results. At the same time, quadrilateral meshing gives the best results. Using this software, we can get the required types of machines.

Figure 3 shows the finite element model in Hypermesh. The 3D shell at quadratic element is prepared for steel plates as well as a link element is selected for steel channels for completing the finite element model; the geometry has 201,951 quadric shell elements and 251,231 nodes, as well as the number of links are observed as 255,484. After assigning the material properties, the element, and sections, the model is transferred to the Abaqus file.

In this present work, initially, we took different geometric parameters using the detailing drawings we created in CATIA software and saved as IGS file in a particular location of the computer. In Abaqus, static structure and modal analysis are performed. A 2D shell element is used to divide the geometric body into small strips (finite elements). The entire hull component is divided into 21,830 shell elements and 21,884 nodes.



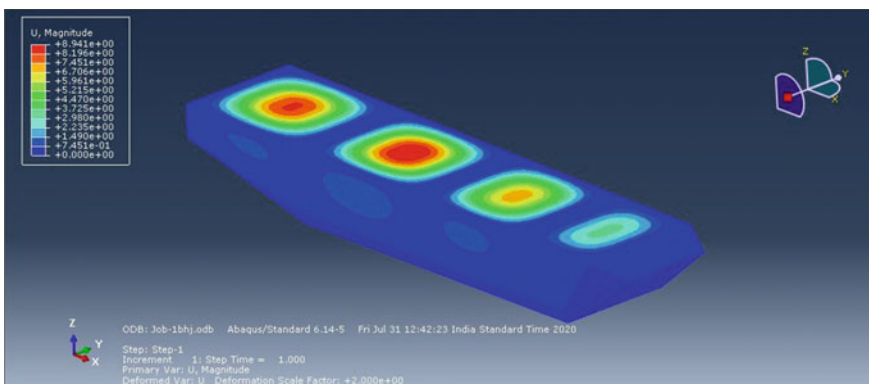
**Fig. 3** Finite element model in Hypermesh



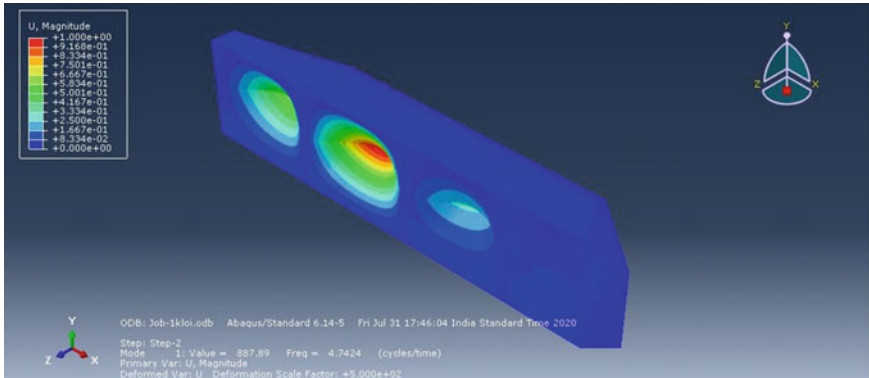
**Fig. 4** Stress of steel ship hull

Figure 4 shows the stress of steel ship hull symmetric model after 500-T force applied on the top supported plate, the red indicates maximum stress, and blue indicates minimum stress. All together maximum stress is 129 MPa. The stress is much of considerable stress. Similarly, this analysis was done for remaining materials; for aluminium, the maximum stress is 130.1 MPa; for wood, the maximum stress is 129.2 MPa; and for fibreglass, the maximum stress is 128.7 MPa.

Figure 5 shows the total deformation of the steel ship hull symmetric model after 500-T force applied on top supported plate, the red indicates the maximum deformation, and blue indicates minimum deformation. All together maximum deformation is 8.9 mm. This deformation is much of considerable deformation. Similarly, this analysis was done for remaining materials; for aluminium, the maximum deformation is 26.4 mm; for wood, the maximum deformation is 185 mm; and for fibreglass, the maximum deformation is 27.1 mm.



**Fig. 5** Deformation of steel ship hull



**Fig. 6** Mode of barge ship hull for steel sheet

### 3 Modal Analysis

Modal analysis is used to determine the natural frequencies and mode shapes of a structure. The natural frequencies and mode shapes are important parameters in the design of a structure for dynamic loading conditions. All models are created in CATIA (Computer Aided Three-dimensional Interactive Application) software. And, model structural analysis is performed in the Abaqus version.

Figure 6 shows the mode shape of a barge ship hull for steel sheet that can be determined by the eigenvalue of vibration equation like single or two degrees of freedom system. Here, mode shape at first frequency is expanding towards the top face of the hull and 1st natural frequency of 4.74 Hz. Similarly, this process is done for the remaining materials; for aluminium sheet, 1st natural frequency of 5.31 Hz; for wood sheet, 1st natural frequency of 11.54 Hz; and for fibreglass sheet, 1st natural frequency of 5.04 Hz.

### 4 Frequency Response Analysis

Harmonic analyses are used to determine the steady-state response of a linear structure to loads that vary sinusoidally (harmonically) with time, thus enabling you to verify whether or not your designs will successfully overcome resonance, fatigue, and other harmful effects of forced vibrations. The transient vibrations, which occur at the beginning of the excitation, are not accounted for in a harmonic analysis.

Figure 7 shows the natural frequencies in various modes for different materials. The orange line indicates steel, the red line indicates aluminium, the violet line indicates wood, and the blue line indicates fibreglass. The frequencies are measured in Hz. In the above graph, the wood materials have high natural frequencies, and others tend to be in the limit. For aluminium, till mode 2, the frequencies are straight, and



Fig. 7 Graph of natural frequencies for different materials

after mode 2, there is a slight change in frequencies and gradually increases. Whereas in the fibreglass and steel, it is constant frequencies till mode 3, and after mode 3, the frequencies will be slightly raised.

### 5 Results and Discussion

Initially, the geometry model dimension is pre-assumed and taken from the real-time ship article. All dimension of the barge hull is calculated theoretically, and the allowable steel stress is 125 M Pa. According to the dimension ship, the 3D model is prepared in DELFTship software, and CATIA software is used to find the 3D model and saved as an IGES file. It was imported into Hypermesh, and the geometry is divided into a finite element model with different materials.

Finally, Table 3 represents the structural analysis results which are done using Abaqus software. The results are as follows:

Therefore, Table 4 represents the natural frequencies for different materials which are done in the modal analysis and frequency response analysis for finding out the mode shapes and natural frequencies. The results are as follows:

Table 3 Structural analysis results

Material	Deformation (mm)	Stress (MPa)
Steel	8.91	129
Aluminium	26.4	130.1
Wood	185	129.2
Fibreglass	27.1	128.7

**Table 4** Natural frequency for different materials

Material	Mode 1	Mode 2	Mode 3	Mode 4	Mode 5
Steel	4.742	5.221	5.7907	8.89	9.95
Aluminium	5.1	5.89	9.06	10.13	11.1
Wood	11.5	12.71	14.09	21.65	24.23
Fibreglass	5.04	5.53	6.3	9.39	10.52

Based on the results achieved from the theoretical results and the numerical simulation results, we conclude that the barge ship hull with different materials performed in both theory and analysis has given good results and proven which is better among the materials, and given has the best outcome that which materials give less cost and better output and better maintenance cost for ship hull, and from the vibration analysis, it is shown that the data are accurate and stiffness of the ship hull is well based on the results, and finally, from this paper, we have achieved a comprised results, and the error in stress between the theoretical and numerical simulation results is almost less than 8% which means it is safe to build the barge ship hull using these parameters.

## 6 Conclusion

The 3D modelling of ship hull design and analysis are very important factors for design engineers who work in shipping industries. The selection of the size of the ship and its materials is a complex task for the engineers. In this work, a pre-assumed load-charring barge ship hull is designed from real-time ship article according to Lloyd's rules and regulations. The required number of thicknesses, cross-section size of the channel, and the number of channels are calculated using this regulation.

In this work, the 3D ship model was prepared using DELFTship software and modified into the DXF file; the outlook of the barge ship hull is prepared in AutoCAD, then the model is further modified into the IGES file, and the 3D model is created using CATIA software. To get quadratic elements as well as accurate results, Hyper-mesh software is preferred, and analysis is done using Abaqus. Four types of materials are applied to the ship model with 500-T loading and found that steel has minimum deformation but has heavyweight compared to other materials. Wood has high deformation and less corrosion material because compared to other materials, the wood is having low elastic properties and less Young's modulus. Aluminium and fibreglass have almost the same deformation and less weight when compared to steel material. Stresses of each material have almost value because stresses depend on area and load, but in this work, we are not changing the load (or) any area, and model analysis was done for four materials. If the natural frequency is high, automatically the stiffness of the structure will improve. Wood, aluminium, and fibreglass materials have high natural frequencies when compared to steel. The structure, number of channels,

and its sizes are designed based on allowable steel stress 125 MPa. Theoretical and analytical results have a good agreement. Finally, aluminium or fibreglass materials are preferred to improve life and reduce weight because the fibreglass material of reducing weight can reduce the required engine power as well as increase the payload.

**Acknowledgements** This is to certify the teaching and non-teaching staffs of department of Mechanical Engineering, Sanketika Vidya Parishad Engineering College, P. M. Palem, Visakhapatnam, Andhra Pradesh, for their valuable support and encouragement.

## References

1. Samson, N., Ogbonnaya, E.: Calculation for hull strength construction in offshore structures. *West Afr. J. Indus. Acad. Res.*, 3–12 (2013)
2. Parunov, J., Uroda, T., Senjanovic, I.: Structural Analysis of a General Cargo Ship. Brodogradnja, 28–33 (2010)
3. Tawfik, B.E., Leheta, H., Elhewy, A., Elsayed, T.: Weight reduction and strengthening of marine hatch covers by using composite materials. *Int. J. Naval Archit. Ocean Eng.*, 1–14 (2016)
4. Um, T.-S., II Roh, M.: Optimal dimension design of a hatch cover for lightening a bulk carrier. *Int. J. Naval Archit. Ocean Eng.*, 270–287 (2015)
5. Samson, N.: Stress and resistance analysis for the design of a work barge. *Int. J. Sci. Eng. Res.*, 878–894 (2015)
6. Ostapenko, A.: Strength of Ship Hull Girders under Moment, shear and Torque. The society of naval architects and marine engineers, 149–166 (1981)
7. Mathai, A., George John, P., Jacob, J.: Direct strength analysis of container ships. *Int. J. Eng. Res. Dev.*, 98–106 (2013)
8. Lloyd's Register.: Rules and Regulations for the Classification of Ships (2016)



# Investigation of Failure in L-shaped Woven Carbon Fiber-reinforced Polymer Composite Under Pull-out and 4-Point Bending



Bipin Kumar Chaurasia, Deepak Kumar, and Vasvani Ashish Maheshbhai

## 1 Introduction

Nowadays for development of aircrafts, medical equipment, and advance technologies, lightweight and high-strength material is in demand. These material characteristics can be achieved by an innovative composite materials. Generally, the composite materials have lightweight, high strength to weight ratio, good thermal and electrical resistances, and long life in comparison to the conventional materials [1–3]. Curved laminates are regularly used in aerospace, machine parts, automobile industries, marine industries, and medical equipment industries. Three applied loads are acted in the middle part of the L-shaped laminates: (i) axial load (parallel to arm), (ii) shear load (perpendicular to arm), and (iii) moment load, due to variation in applied-force direction. These applied loads generate inter-laminar normal stress and inter-laminar shear stress at the interface of the L-shaped laminate. As applied force is varying in the curved laminates, in result, force exerts at higher stress concentration region in the curved part and leads to the failure of laminates in terms of matrix cracking and delamination [4]. Moreover, various researchers [5–7] studied different types of curved laminates such as corrugated laminates, L-shaped, goggles or T-shaped. One of the important conclusions they made is that curvature in T-shaped and L-shaped has higher stress concentration compared to others, due to sudden change in the axis direction.

When the quasi-static load is applied, L-shaped laminate starts deforming. Observed deformation leads to tension in the bottom surface of the curved regions, whereas compression in the top part of the surface. Because of compression and tension in the top and bottom laminas, separation and delamination failures occur

---

B. K. Chaurasia · D. Kumar (✉) · V. A. Maheshbhai  
Department of Mechanical Engineering, National Institute of Technology Jamshedpur,  
Jamshedpur 831014, India  
e-mail: [deepak.me@nitjsr.ac.in](mailto:deepak.me@nitjsr.ac.in)

in the laminates. These failures reduce the strength near the curved region, and finally, L-shaped laminates fail [8, 9]. Inter-laminar tensile strengths are very important properties of composite laminates, and finding of these properties is the most difficult task. Generally, ASTM D-6415 is used to determine the inter-laminar properties of carbon fibre-reinforced polymer [10]. Here, they found a large scatter of data in tensile strength values during the experiment. Further, their research suggests that scattering in tensile values is found due to fabrication of curved laminates with uniform thickness and radius. Makeev et al. [11] developed an accurate and efficient method to determine the inter-laminar tensile strength. In their analysis, they concluded that short-beam and modified curved-beam methods provide the better approach to determine inter-laminar tensile strength. Fiber direction and laminates stacking sequence affect the strength and stiffness of curve-shaped laminates along with its mechanical properties [12]. Stacking sequence effects on the mechanical properties are extensively studied by Pan et al. [13]. They investigated the initial fracture modes of the L-shaped laminates. Many researchers [14, 15] found from the experiments that failures in the L-shaped composite laminate occur in the curved region because of higher stress concentration. Uyar et al. [16] conducted experiment and evaluated stress concentration value in the L-shaped composite laminates. It is found that dynamic delamination occurs in L-shaped laminates under quasi-static shear loading. Inter-laminar normal stresses (ILNS) will be induced together with inter-laminar shear stresses (ILSS) in the curved laminates at the interfaces. Various failures such as delamination, matrix cracking, and their interaction are still not clear. To incorporate these failures in the numerical model, Cao et al. [17] proposed a computational approach to explicitly model inter-laminar delamination and intra-laminar matrix cracking in L-shaped composite laminate. These failures are incorporated in the finite element model by inserting zero-thickness cohesive elements at the interfaces and using mixed-mode traction-separation law.

In this paper, L-shaped composite laminates are fabricated with a stacking sequence  $[0^\circ/45^\circ/90^\circ/-45^\circ]_{3s}$  for the pull-out test and 4-point bend test. The quasi-static load is applied, and specimens were tested under both loading conditions in UTM for their failure strength and failure interactions. Most of the published research articles are focused on strength and delamination failures. However, in this paper, failure strengths are evaluated for each test along with interaction of failure mechanisms investigated. Furthermore, microstructure of L-shaped laminates is recorded by using optical microscope before experiment and after the experiment. Finally, it is concluded that matrix cracking started initially and that leads to the separation/delamination failure in the L-shaped laminates.

## 2 Specimens and Test

CFRP laminates are fabricated by UD carbon fiber fabric, LY 556 epoxy resin (bisphenol-A-diglycidyl-ether) and HY 951 hardener [18]. Mold is polished by the wax to remove minor surface imperfections such as scratches, spotting, and oxidation.

Carbon fiber fabric is cut in such a manner that different orientations of the required stacking sequence can be achieved. After that, PVA is applied on the mold to release the laminates easily without any defects such as impurity and voids. Epoxy resin and hardener are mixed in the ratio 10:1. After mixing, prepared solution is applied on the mold with the help of brush. Carbon fiber fabric (CFF) are placed according to stacking sequence, and prepared solution is applied on each layers of fibers. Here, ratio of CFF and resin solution must be maintained as 1:1. Carbon fibers are arranged in stacking sequence  $[0/45/90/-45]_{3s}$ . After applying prepared resin solution on each lamina, excess resin is removed with the help of roller. Fabricated laminate is kept for minimum 24 h at room temperature for curing. After curing, fabricated laminates are removed from the mold (see Fig. 1).

Average thickness of the fabricated laminate is measured as 7.17 mm. Further, laminates are cut into ten specimens based on ASTM standards for pull-out test and 4-point bending test (see Fig. 2). The test was desired largely to initiate the delamination failure mode in the curved region. Therefore, we chosen the pull-out and 4-point bending tests for our fabricated specimens. The test was modified from ASTM to fit the facilities available in the laboratory. Five specimens are fabricated and tested, denoted as to F1 to F5 for pull-out test and H1 to H5 for 4-point bend test (see Fig. 3a, b). These tests are conducted on Blue Star, 20 kN, universal testing machine (UTM) of Jinan testing corporation [19]. The whole testing procedure is recorded by Nikon DSLR D7000 camera. A side face of each curved composite

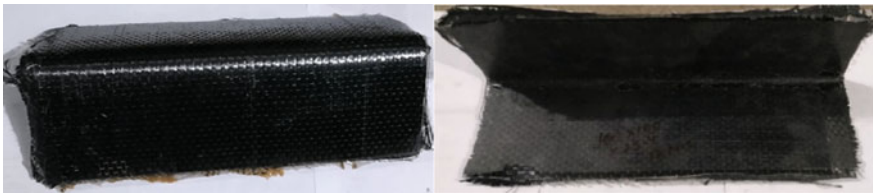
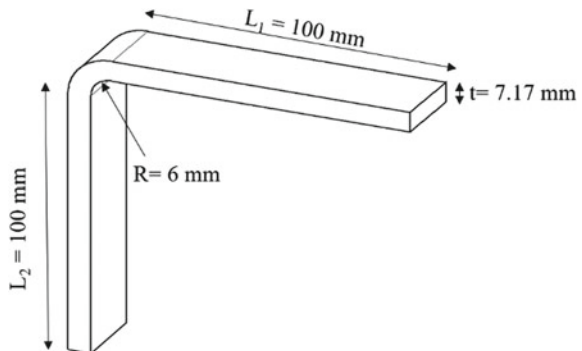
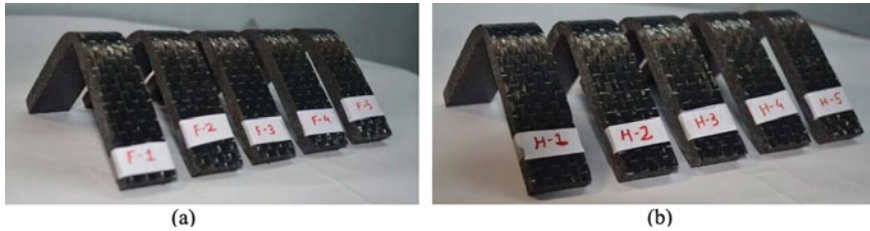


Fig. 1 Fabricated CFRP laminates

Fig. 2 Schematic of L-shaped specimen





**Fig. 3** Specimen for **a** pull-out test (F1–F5) **b** Four-point bend test (H1–H5)

specimen was painted white by using chalk dust to see delamination failure clearly after the test.

## 2.1 Pull-out Test

Pull-out test is conducted based on modified ASTM D-6415 standard [11] for the specimen F1 to F5. To conduct pull-out test, 10 mm diameter hole is created in each specimen (leg part). Fixture for gripping the specimen is designed, and it consists of M10 bolt and MS plates. Further, 30 mm length of arm (L-shaped) is kept fixed, and load is applied on the other arm through the fixture. Displacement rate of 2 mm/min is applied during the test (Fig. 4).

Load and displacement recorded during the tests are shown in Fig. 5. From Fig. 5, it is clear that the load is increasing nonlinearly with the displacement. Here, load has increased to the maximum value for all the five specimens, and six drops in the load were noted in one specimen (F2 specimen). In almost four specimens with several cracks, a large crack was initiated at the first peak, subsequently followed by crack propagation. Second peak is noted after the first peak after some seconds of nonstop loading. Afterward, the specimens failed with extra-large cracks or several cracks. Therefore, the first drop of loading initiates the first crack at the interface, near to the top lamina of the specimen. Successively, the second drop occurs after a large crack on the failure surface. As the load is applied on the specimens, failures such as delamination and matrix cracking can be predicted from the load–displacement curve (Fig. 5). Crack initiates at the applied load 0.9 kN, and finally, failure takes place at 1.7 kN in each specimen. Here, multiple (at least 6) delaminations have been reported.

## 2.2 Four-Point Bend Test

On the similar note, 4-point bend test is conducted on 20 kN universal testing machine (UTM). To achieve this, two rollers in both upper and lower supports have been

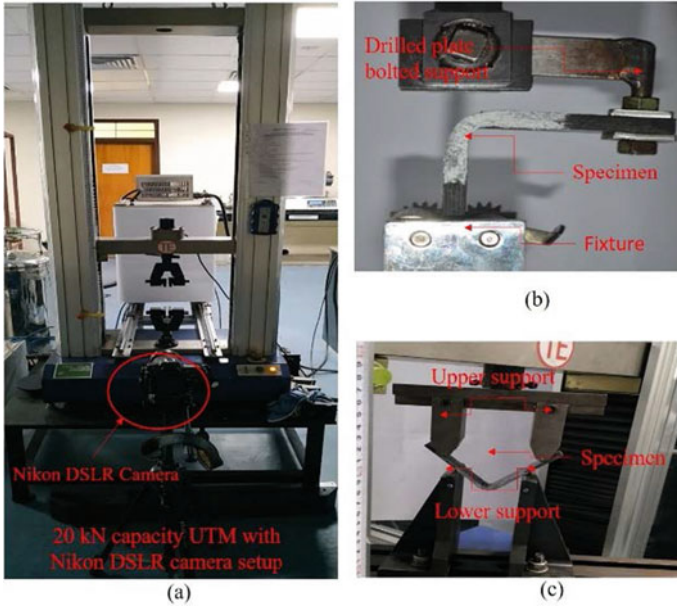


Fig. 4 Experiment a UTM setup b Pull-out arrangement c Four-point bend arrangement

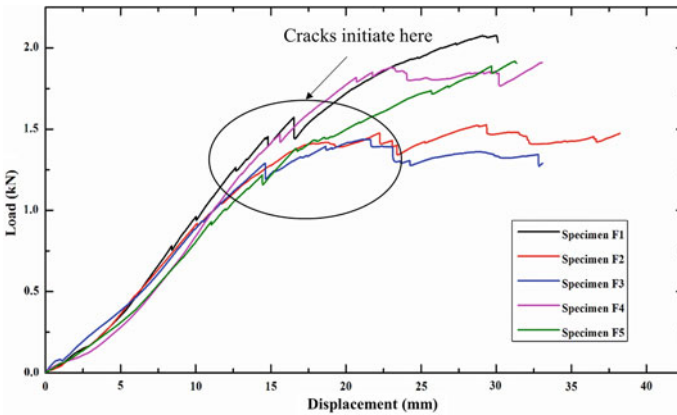


Fig. 5 Load-displacement curve under pull-out loading

provided. Distance between bottom two rollers is 75 mm, and the distance between the top two rollers is 100 mm. The test was aimed to create an area with a dominant bending moment between the two upper pins. The feed rate of 2 mm/min is applied from top support (see Fig. 4). Consequently, the delamination was expected to be the only failure mode in this area. Six specimens, denoted as H1 to H5, were fabricated and tested. The load and displacement curve is recorded.

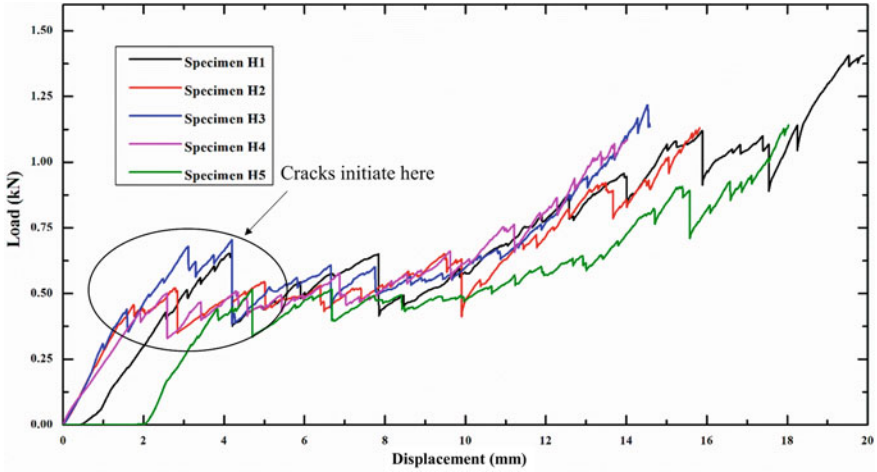


Fig. 6 Load–displacement curve under 4-point bending

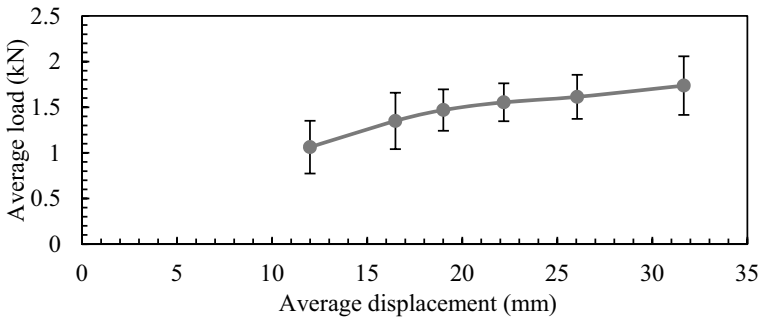


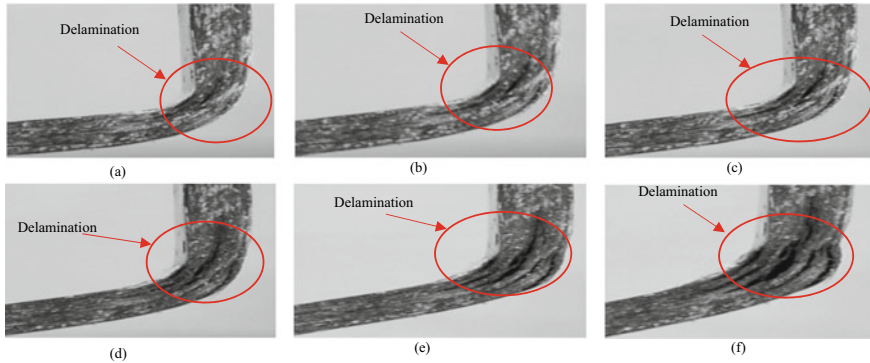
Fig. 7 Standard deviation in load during each delamination failure (pull-out test)

Unfolding load is applied by two roller supports. Load versus displacement curve is plotted (see Fig. 6). Average peak load of specimen “H” is found as 1.1 kN. From Fig. 6, it is clear that the first crack initiates at around applied load of 0.4 kN. Further, delamination failure has been observed in all the specimens.

### 3 Results and Discussion

#### 3.1 Failure Investigation in Laminates Under Pull-out Test

In Fig. 7, peak load for delamination is shown for each specimen (F1–F5). It shows that deviation in load for third and fourth delaminations are similar for each specimen,



**Fig. 8** **a** First delamination (0.91 kN) **b** Third delamination (1.24 kN) **c** Fourth delamination (1.45 kN) **d** Fifth delamination (1.52 kN) **e** Multiple delaminations (1.43 kN) **f** Delamination at ultimate failure

but the first and sixth delaminations show the variation of deviation in load values. Also, overall strength of the laminates reduces with the delamination failure; i.e., load drops with delamination initiation and increases with propagation. Specimen “F2” is shown in Fig. 8 to represent delamination initiation and propagation in order.

In specimen “F2,” the first and second delaminations start at 0.916 kN and 1.414 kN, respectively. Also, location of the first delamination is found at the interface of 11th interface ( $90^\circ/-45^\circ$ ), and second delamination is observed at sixth interface ( $45^\circ/90^\circ$ ) as shown in Fig. 8a, b. Third and fourth delaminations initiate at 2nd interface ( $45^\circ/90^\circ$ ) and 22nd interface ( $90^\circ/45^\circ$ ), respectively. Further, fifth delamination started at the 15th interface ( $45^\circ/0^\circ$ ) as shown in Fig. 8d. Finally, at the applied load 1.7 kN, multiple delaminations can be observed as shown in Fig. 8f. Also, optical microscope is used to check the specimen “F2” before and after the test as shown in Fig. 9. It is clear from the image that fiber splitting occurred in 1st, 2nd, 4th, 8th, 12th, and 20th plies, mainly in  $-45^\circ$  layers because of shear force, and at some extent in  $0^\circ$  layers. All the six delaminations are clearly visible from top to bottom. Also, a specific crack pattern is observed between seventh and eighth laminas. This clearly reveals that delamination was initiated after matrix cracking [6].

### 3.2 Failure Observed in Laminates Under 4-point Bending

For specimen “H4,” the first three delaminations were observed for applied load 0.5 kN. These delaminations were found at the interface  $90^\circ/-45^\circ$  (7th lamina),  $90^\circ/-45^\circ$  (11th lamina), and  $90^\circ/45^\circ$  (18th lamina). After the application of 0.483 kN, 6th delamination initiated at the interface  $-45^\circ/-45^\circ$  (12th lamina). Seventh delamination is observed a peak load of 0.576 kN at interface  $90^\circ/45^\circ$  (22nd lamina). The eighth delamination is initiated at interface  $90^\circ/-45^\circ$  (seventh ply). Delaminations



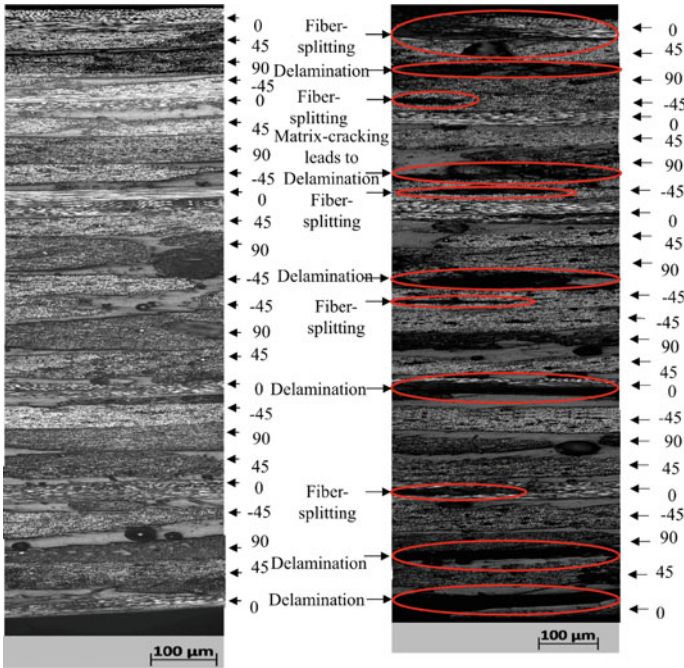


Fig. 9 Microstructure of specimen F2 before and after the test (curved region)

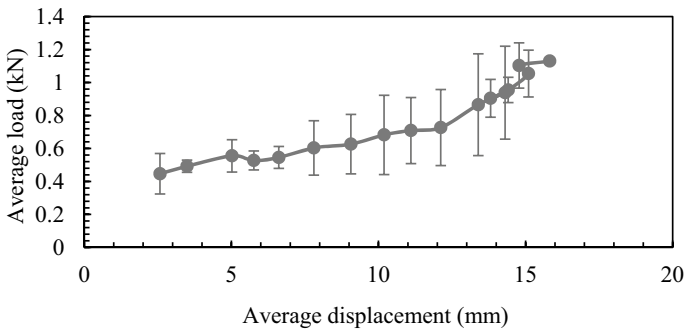
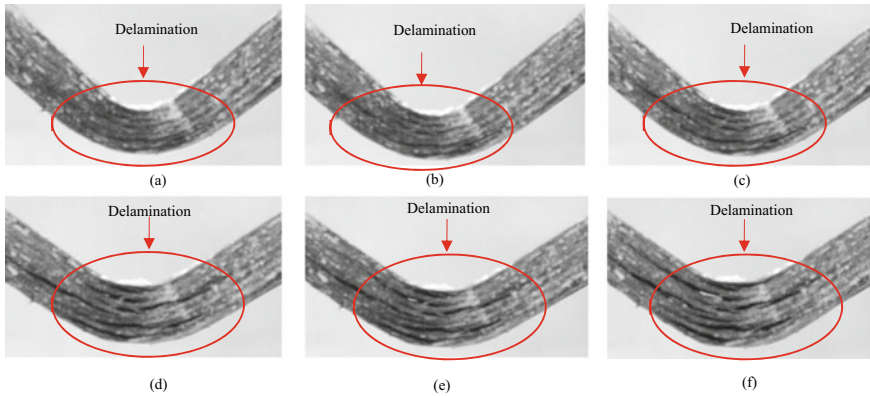


Fig. 10 Standard deviation in load during each delamination failure (4-point bending)

are observed in the specimen with a peak load of 1.083 kN. Furthermore, standard deviation in peak load is plotted between load and displacement as shown in Fig. 10. Minimum deviation in load is observed in 2nd, 4th, and 5th delaminations, whereas maximum deviation in load is found for 8th, 10th, 11th, and 12th delaminations. As the number of delamination increases in the specimen, it is impossible to predict the failure and peak load. The sequence of delamination initiation and propagation for specimen “H4” are shown in Fig. 11. From Fig. 6, it is clear that load increases





**Fig. 11** a First three delaminations (0.46 kN) b Sixth delamination (0.48 kN) c Seventh delamination (0.58 kN) d Eighth delamination (0.661 kN) e Multiple delaminations (1.08 kN) f Delamination at ultimate load

nonlinearly with the displacement. Here, the load has been increased to the largest value, and drop in loading is noted in all five specimens, while more than twelve drops in load were noted in the four other cases (H2–H5 specimens). In all the specimens with several cracks, a large crack was initiated at the first peak, subsequently followed by crack propagation. In all the specimens with multiple peaks, a large crack was generated at the first peak, and this was followed by crack propagation. Second peak is noted after the first peak after some seconds of nonstop loading. Afterward, the specimens failed with extra-large cracks or several cracks. Therefore, the first drop of loading initiates the first crack at the interface, near to the top lamina of the specimen. In the case of the specimen with only twelve drops, several cracks appear on the failure surfaces. Therefore, delamination dominated the failure modes. Delamination failure occurred from the inner radius to around two-third of the thickness of the specimen.

Figure 12 shows the microscopic image of the specimen before and after the test. Fiber splitting occurred in 2nd, 3rd, 8th, and 20th plies. It is observed that these types of failures mainly occur in 45° laminas because of unfolding load applied on the laminates. This results in tension as well as shear actions in 45° and 90° layers at some extent. Three delaminations are clearly visible from top to bottom (Fig. 12). Also, matrix cracking is observed between fifth and sixth laminas. In this, a specific crack pattern is found between 15th, 16th, and 17th laminas, which is in-line to the crack pattern observed in the pull-out test. These crack patterns clearly reveal that matrix cracking led to the multiple delamination failures.

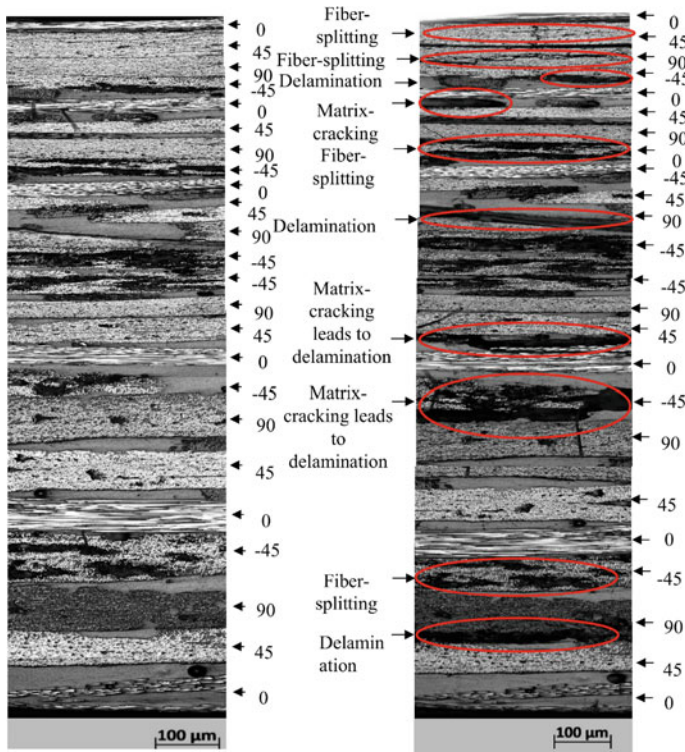


Fig. 12 Microstructures of specimen H4 before and after the test (curved region)

### 4 Conclusion

L-shaped composite has lower strength than flat composite because of the curved section. When load is applied in L-shaped composite, then body starts deforming. Deformation leads to tension in the lower surface of curved part, whereas compression on the top surface. Compression and tension on the top and bottom laminas cause matrix or fiber cracking in the laminates. Due to the separation in layers, delamination occurs in the laminates. These failures reduce the strength of curved region of laminates and leading to overall failure of the laminates. Pull-out and 4-point bend tests were conducted, and failure behavior have been studied. Average load carrying capacity is evaluated as 1.7646 kN for pull-out test, while in the case of 4-point bend test, average load capacity is found as 1.1 kN for the same laminates. From optical microscope, delamination and matrix cracking have been observed in both types of tests. Further, it is observed that fiber splitting mainly occurred in 45° layers and in 45° and 90° layers at some extent. More matrix cracking is observed between fifth and sixth plies of laminates under 4-point bending. This is due to bigger volume

under stress compared to pull-out test. One important conclusion has been made that matrix cracking leads to delamination failure in both the tests.

**Acknowledgements** This research work is funded by TEQIP -III of MHRD, Government of India, and sanctioned to NIT Jamshedpur, Jamshedpur (India).

## References

1. Herakovich, C.T.: Mechanics of composites: a historical review. *Mech. Res. Commun.* **41**, 1–20 (2012)
2. Shalwan, A., Yousif, B.F.: In state of art: mechanical and tribological behavior of polymeric composites based on natural fibres. *Mater. Des* **48**, 14–24 (2013)
3. Herwig, A.: Short time tensile behavior of unidirectional glass and carbon fiber reinforced polymer laminates with curved shapes. *Compos. Part B Eng.* **47**, 344–347 (2013)
4. Geleta, T.N., Woo, K., Lee, B.: Delamination behavior of L-shaped laminated composites. *Int. J. Aeronaut. Sp. Sci.* **19**(2), 363–374 (2018)
5. Thurnherr, C., Groh, R.M.J., Ermanni, P., Weaver, P.M.: Investigation of failure initiation in curved composite laminates using a higher-order beam model. *Compos. Struct.* **168**, 143–152 (2017)
6. González-Cantero, J.M., Graciani, E., López, B., París, F.: Competing mechanisms in the unfolding failure in composite laminates. *Compos. Sci. Technol.* **156**, 223–230 (2018)
7. Arca, M.A., Coker, D.: Experimental investigation of CNT effect on curved beam strength and interlaminar fracture toughness of CFRP laminates. *J. Phys. Conf. Ser.* **524**(1) (2014)
8. Gozluklu, B., Uyar, I., Coker, D.: Intersonic delamination in curved thick composite laminates under quasi-static loading. *Mech. Mater.* **80**(PB), 163–182 (2015)
9. Gözlüklü, B., Coker, D.: Modeling of the dynamic delamination of L-shaped unidirectional laminated composites. *Compos. Struct.* **94**(4), 1430–1442 (2012)
10. ASTM, D.: 6415. Standard test method for measuring the curved beam strength of a fiber reinforced polymer-matrix composite (2001)
11. Makeev, A., Seon, G., Nikishkov, Y., Lee, E.: Methods for assessment of interlaminar tensile strength of composite materials. *J. Compos. Mater.* **49**(7), 783–794 (2015)
12. Hitchen, S.A., Kemp, R.M.J.: The effect of stacking sequence on impact damage in a carbon fibre/epoxy composite. *Composites* **26**(3), 207–214 (1995)
13. Pan, Z.Y., Duan, Q.F., Zhong, Y.C., Li, S.X., Cao, D.F.: Stacking sequence effect on the fracture behavior of narrow L-shaped cross-ply laminates: experimental study. *Strength Mater.* **50**(1), 203–210 (2018)
14. Fraternali, F., Bilotti, G.: Nonlinear elastic stress analysis in curved composite beams. *Comput. Struct.* **62**(5), 837–859 (1997)
15. Lauke, B.: Stress concentration along curved interfaces as basis for adhesion tests. *Compos. Interfaces* **14**(4), 307–320 (2007)
16. Uyar, I., Gozluklu, B., Coker, D.: Dynamic delamination in curved composite laminates under quasi-static loading. *J. Phys. Conf. Ser.*, **524**(1) (2014)
17. Cao, D., Duan, Q., Hu, H., Zhong, Y., Li, S.: Computational investigation of both intra-laminar matrix cracking and inter-laminar delamination of curved composite components with cohesive elements. *Compos. Struct.* **192**, 300–309 (2018)
18. Epoxy Resin Exporter, Epoxy Hardener Supplier. <http://www.singhalchemical.com/>
19. Electromechanical Universal Testing Machine—Jinan Testing Equipment, Yinfeng Group. [http://www.testingequipmentie.com/products/Superior\\_Electromechanical\\_Universal\\_Testing\\_Machine\\_66111.html](http://www.testingequipmentie.com/products/Superior_Electromechanical_Universal_Testing_Machine_66111.html).

# Vibrations Characteristics Analysis of Rotor-Bearings System Due to Surface Defects Based in CNC Machines



R. G. Desavale, Jitendra Kumar Katiyar, and T. Jagadeesha

## 1 Introduction

Rolling contact bearings are most commonly used bearings in machine tools. During machining, various cutting forces such as tangential, radial, and axial load comes on the spindle of CNC machines. There are various statistical methods in use to find out the defect in the bearing systems. Many known statistical techniques using the chaos, probability theory, and random theory are used to find out the defects in the bearing and various statistical parameters are used to compare the distribution between healthy and unhealthy bearings used in both process and manufacturing industries [1–5]. Sophisticated control theory has been also explored using envelop analysis to find the easy and earlier defects in the bearing systems. Signal control theory is well established using signal demodulations principle for condition monitoring of the bearing systems [6, 7]. Noise analysis is also extensively used to find the patterns of the healthy and unhealthy bearings of the rotor shaft systems commonly used in rotary machines [8, 9]. Wavelet theory is becoming a popular tool in analyzing defective bearings. Both physics and mathematics of the failure behavior can be established [10–12]

---

R. G. Desavale

Department of Mechanical Engineering, Rajarambapu Institute of Technology, Sakharale Sangli, Urun Islampur, Maharashtra 415414, India

Shivaji University, Kolhapur, Maharashtra, India

J. K. Katiyar

Department of Mechanical Engineering, SRM Institute of Science and Technology, Kattankulathur, Chengalpattu District, Tamil Nadu 603203, India

T. Jagadeesha (✉)

Department of Mechanical Engineering, National Institute of Technology Calicut, Calicut, Kerala 673601, India

e-mail: [jagdishsg@nitc.ac.in](mailto:jagdishsg@nitc.ac.in)

**Table 1** Dimensionless  $\pi$ -products

Variables	Pi terms	Designations
$D, N_s, W$ and $A$	$\pi_1$	$\frac{A}{D}$
$D, N_s, W$ and $D_{in}$	$\pi_2$	$\frac{D_{in}}{D}$
$D, N_s, W$ and $D_{out}$	$\pi_3$	$\frac{D_{out}}{D}$
$D, N_s, W$ and $D_r$	$\pi_4$	$\frac{D_r}{D}$
$D, N_s, W$ and $R_r$	$\pi_5$	$\frac{R_r}{D}$
$D, N_s, W$ and $L_r$	$\pi_6$	$\frac{L_r}{D}$
$D, N_s, W$ and $D_p$	$\pi_7$	$\frac{D_p}{D}$
$D, N_s, W$ and $B$	$\pi_8$	$\frac{B}{D}$
$D, N_s, W$ and $C_d$	$\pi_9$	$\frac{C_d}{D}$
$D, N_s, W$ and $Z_r$	$\pi_{10}$	$\frac{Z_r}{D}$

## 2 Analysis of the Bearing Defects

The various parameter of the bearings is taken and dimensionless parameters are obtained. Few dimensionless parameters are given in Table 1 and reduced dimensionless parameters are given in Table 2.

After the detailed analysis following expression is obtained.

$$\frac{A}{D} = f\left(\gamma \times \left(\frac{HTS}{K_d E}\right)^a \times \left(\frac{B \Delta T_f}{C_d C_v K_c}\right)^b \times \left(\frac{K U_b W}{q C N_s}\right)^c \times \left(\frac{V f_{rd} \rho D^2}{\delta W}\right)^d \times \left(\frac{d_p n_d \alpha_t}{D Z}\right)^e\right) \quad (1)$$

Equation 1 can be used to predict the vibration behavior of the bearings.

## 3 Experimentation and Instrumentation

The experimental setup has been developed in house and is shown in Fig. 1. Rotor and shaft are machined precisely and coupled using the love joy coupling. Direct electric motor is used to run the rotor shaft system. To change the speed of the shaft a variable frequency controller is used which can change the rotation of shaft in the range of 400–1200 RPM. Additionally, a tachometer is also used to measure the rotational speed of the shaft. Faults in the bearing are created in house using electro discharge machines. Fault details are given in Table 3. Artificially generated defect on outer race, inner race, and roller are shown in Fig. 2. Accelerometer is mounted on the unhealthy bearing to find out its characteristic behavior in terms of amplitude and frequency. Fast Fourier analysis is done using data obtained.

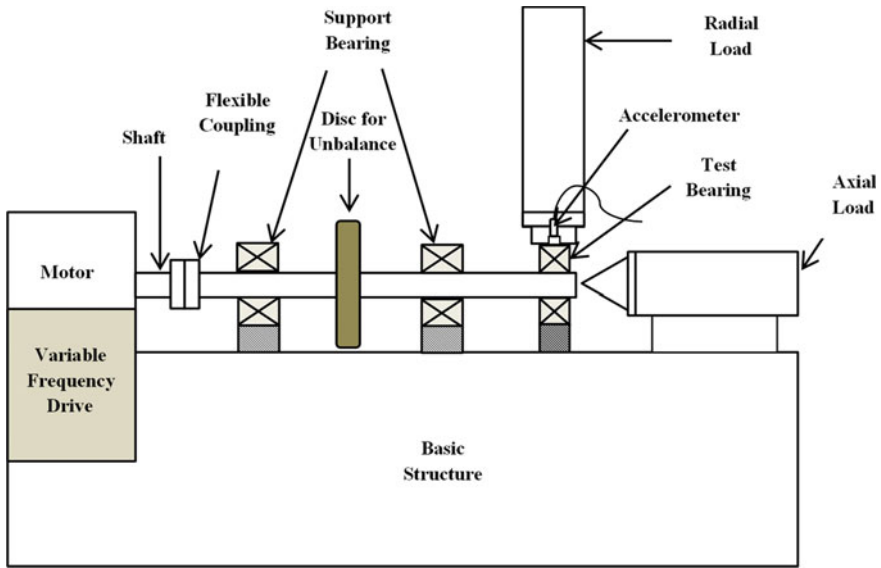
**Table 2** Reduced dimensionless  $\pi$ -products

Dimensionless parameter	Ratio of the parameters	Ratios in terms of variables
$\pi_a$	$\frac{\pi_2}{\pi_3}$	$\frac{D_{in}}{D_{out}}$
$\pi_b$	$\frac{\pi_4}{\pi_5}$	$\frac{D_r}{R_r}$
$\pi_c$	$\frac{\pi_6}{\pi_7}$	$\frac{L_r}{D_p}$
$\pi_d$	$\frac{\pi_8}{\pi_9}$	$\frac{B}{C_d}$
$\pi_e$	$\frac{\pi_{30}}{\pi_{48}}$	$\frac{F_a}{FH}$
$\pi_f$	$\frac{\pi_{35}}{\pi_{36}}$	$\frac{m_r}{m_i}$
$\pi_g$	$\frac{\pi_{37}}{\pi_{38}}$	$\frac{m_0}{m_{ro}}$
$\pi_h$	$\frac{\pi_{41}}{\pi_{42}}$	$\frac{f_c}{f_r}$
$\pi_i$	$\frac{\pi_{46}}{\pi_{47}}$	$\frac{f_{tff}}{f_{vcf}}$
$\pi_j$	$\frac{\pi_{43}}{\pi_{44}}$	$\frac{f_{id}}{f_{od}}$
$\pi_k$	$\frac{\pi_{16}}{\pi_{50}}$	$\frac{VD}{I}$
$\pi_l$	$\frac{\pi_{33}}{\pi_{50}}$	$\frac{H D^2}{I N_s}$
$\pi_m$	$\frac{\pi_{40}}{\pi_{50}}$	$\frac{\delta D^3}{I}$
$\pi_n$	$\frac{\pi_{26}}{\pi_{50}}$	$\frac{\Delta D^3}{I N_s^3}$
$\pi_0$	$\frac{\pi_{28}}{\pi_{29}}$	$\frac{C_v D^2}{I N_s^2}$
$\pi_p$	$\frac{\pi_{26}}{\pi_{50}}$	$\frac{K_d D^2}{I N_s}$
$\pi_q$	$\frac{\pi_{42}}{\pi_{50}}$	$\frac{f_{rd} D^4}{I N_s}$
$\pi_r$	$\frac{\pi_{20}}{\pi_{50}}$	$\frac{W}{\rho I N_s^2}$
$\pi_s$	$\frac{\pi_{31}}{\pi_{20}}$	$\frac{K}{\rho D^3 N_s^2}$
$\pi_t$	$\frac{\pi_{32}}{\pi_{20}}$	$\frac{C}{\rho D^3 N_s}$

## 4 Results

Using the experimental setup shown in Fig. 1 and for the various defects as shown in the Table 3. The various experiments are run at 900, 1800, and 2700 RPMs and outer race frequency, inner race defect frequency, and rolling element defect frequency are noted for each of these RPMs. Both theoretical and experimental results are given in Table 4

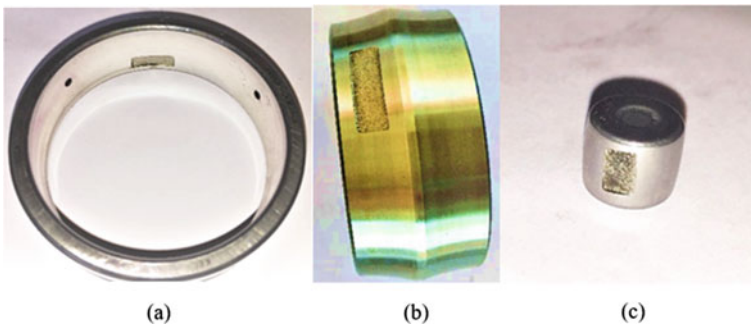
It is clear from the Table 4 that outer race defect frequency depends on the rotational speed of the rotor shaft system. When the shaft is running at 900 rpm, the defect frequency is 94.22 Hz. When the speed is doubled the frequency is also almost doubled. It is found that inner race defect frequency at 900 rpm occurs at a



**Fig. 1** Schematics of an experimental setup

**Table 3** Classification of bearing defects and values

Type of defect created	Size in mm
Defect pattern 1	05 × 02 × 0.1
Defect pattern 2	07 × 03 × 0.2
Defect pattern 3	12 × 05 × 0.4



**Fig. 2** Artificially generated defect pattern on **a** outer race, **b** inner race, **c** roller

higher value when compared to outer race defect frequency at the same rpm. It can be observed that frequency caused by the defects in rolling element shows a similar pattern compared to frequency caused by the defects in the outer race of the bearings.

**Table 4** Characteristic defect frequencies

Defect frequency	Theoretical			Experimental		
	900 rpm	1800 rpm	2700 rpm	900 rpm	1800 rpm	2700 rpm
Defect frequency (Outer race)	94.22	188.44	282.66	83.21	187.99	272.36
Defect frequency (Inner race)	130.77	261.55	392.33	131.84	245.36	401.30
Defect frequency (Rolling element)	92.43	184.87	277.31	95.21	168.46	256.32

## 5 Conclusions

In roller contact bearings, it is important to identify the cause root of the defect in early stages to reduce the preventive and corrective maintenance costs. There are various techniques that are used in industry to monitor the life of the bearing. In this study defective bearings are studied under various process conditions. The vibration analysis of the bearing can detect the defective bearings. Different types of defects produce a unique vibration signature. The frequency and amplitude of the vibration depend on the type of the defect, location of the defect, and other controlling parameters such as speed, load, unbalance, clearance, etc. At a given speed, vibration signature of both healthy and unhealthy bearings is captured and compared with the theoretical equations developed using dimensional analysis theorem. The speed has a predominant effect on the vibration characteristics of the defects in the bearings. As speed increases the defect frequency also increases and there is a specific signature for each defect in the various elements of the bearings.

## References

1. Tandon, N., Nakra, B.C.: Detection of defects in rolling element bearings by vibration monitoring. *J. Inst. Eng. (India) Mech. Eng. Div.* **73**, 271–282 (2003)
2. Tandan, N., Choudhury, A.: A review of the vibration and acoustic measurement methods for detection of defects in rolling element bearings. *Tribol. Int.* **32**(8), 469–480 (1999)
3. Choy, F.K., Zhou, J., Braun, M.J.: Vibration monitoring and damage quantification of faulty ball bearings. *Trans. ASME J. Tribol.* **127**, 776–783 (2005)
4. Sebastian, V., Mario P.: Rolling Bearing Condition Monitoring Based on Frequency Response Analysis. *IEEE*, pp. 29–35 (2007)
5. Tandon, N., Choudhury, A.: A theoretical model to predict the vibration response of rolling-element bearing in a rotor-bearing system to distributed defects under radial load. *J. Tribol.* **122**, 609–615 (2000)
6. McFadden, P.D., Smith, J.D.: Vibration monitoring of roller element bearings by the high-frequency resonance technique—a review. *Tribol. Int.* **17**, 3–10 (1984)
7. Sheen, Y.T.: An analysis method for the vibration signal with amplitude modulation in a bearing system. *J. Sound Vib.* **303**(3–5), 538–552 (2007)
8. Dalpiaz, G., Rivola, A., Rubini, R.: Effectiveness, and sensitivity of vibration processing techniques for local fault detection in gears. *Mech. Syst. Signal Process.* **14**(3), 387–412 (2000)



9. Yesilyurt, I.: Gear Fault Detection and Severity Assessment Using Vibration Analysis. Ph.D. Thesis, The University of Manchester, Manchester (1997)
10. Mori, K., Kasashima, N., Yoshioka, T., Ueno, Y.: Prediction of spalling on a ball bearing by applying the discrete wavelet transform to vibration signals. *Wear* **195**, 162–168 (1996)
11. Prabhakar, S., Mohanty, A.R., Sekhar, A.S.: Application of discrete wavelet transform for detection of ball bearing race faults. *Tribol. Int.* **35**, 793–800 (2002)
12. Purushothama, V., Narayanana. S., Suryanarayana. A., Prasad,N.: Multi-fault diagnosis of rolling bearing elements using wavelet analysis and Hidden Markov model-based fault recognition. *NDT & E Int.* **38**, 654–664 (2005)

# The Diagnostic Analysis of the Rolling Element Bearings for the Machine Tool Applications Using Dimension Theory



R. G. Desavale, Jitendra Kumar Katiyar, and T. Jagadeesha

## 1 Introduction

Antifriction bearings or roller contact bearings are commonly used types of bearing in most rotating machines. It is used to provide support and carry the radial and axial load. The failure of these types of bearings can cause shut down of the machines and expensive maintenance [1, 2].

There are various methods of monitoring the failures in industry. The temperature analysis, wear debris analysis, lubricating oil analysis, noise analysis, and vibration analysis. The vibration online monitoring is gaining importance in industry due to its robustness and simplicity. The available electronics in the industry also made it more user-friendly and adaptable. They are accurate and data can be extracted in real time. Healthy and unhealthy bearings give different amplitude and frequency patterns which can be measured and recorded easily [3]. Sunnersjo [4] has carried out experimental studies on bearings by varying stiffness of the system. They considered mass and damping force and taken bearing accuracy and quality is taken as independent parameters. It is shown that clearance has a predominant role to play in bearing system and by adjusting the clearance of the bearing, system behavior such

---

R. G. Desavale

Department of Mechanical Engineering, Rajarambapu Institute of Technology, Sakharale Sangli, Uran Islampur 415414, India

Shivaji University, Kolhapur, Maharashtra, India

J. K. Katiyar

Department of Mechanical Engineering, SRM Institute of Science and Technology, Kattankulathur, Chengalpattu District, Tamil Nadu 603203, India

T. Jagadeesha (✉)

Department of Mechanical Engineering, National Institute of Technology Calicut, Calicut, Kerala 673601, India

e-mail: [jagdishsg@nitc.ac.in](mailto:jagdishsg@nitc.ac.in)

as compliance or stiffness can be changed considerably. Yamauchi [5], Saito [6] experimented on non-linear bearing systems and suggested new balance techniques and novel algorithm which uses Fast Fourier Transformation. They stated that in non-linear bearing systems certain harmonics are important for a specific rotation of the rotor systems. They observed that through proper control strategies, unwanted harmonics can be reduced or eliminated. Ehrich [7–9] studied behavior of rotor shaft system at very high rotational frequency and they observed irregular chaotic behavior of the systems. In addition, they also noted specific harmonic responses for these high-speed rotor shaft systems.

## 2 Mathematical Formulation

To mathematically model the system the various parameters are to be chosen. Dimensionless groups obtained from the analysis is as follows

$$\pi_a = \frac{\pi_2}{\pi_3} = \frac{D}{R_c} \times \frac{R_c}{d_b} = \frac{D}{d_b} \quad (1)$$

$$\pi_b = \frac{\pi_4}{\pi_5} = \frac{d_i}{R_c} \times \frac{R_c}{d_o} = \frac{d_i}{d_o} \quad (2)$$

$$\pi_c = \frac{\pi_6}{\pi_7} = \frac{d_m}{R_c} \times \frac{R_c}{B} = \frac{d_m}{B} \quad (3)$$

$$\pi_d = \frac{\pi_7}{\pi_8} = \frac{B}{R_c} \times \frac{R_c}{L} = \frac{B}{L} \quad (4)$$

$$\pi_e = \frac{\pi_9}{\pi_{10}} = \frac{\rho R_c^5}{W_u} \times \frac{W_u N_r^2}{E_S R_c} = \frac{\rho R_c^4 N_r^2}{E_S} \quad (5)$$

$$\pi_f = \frac{\pi_{10}}{\pi_{11}} = \frac{E_S R_c}{W_u N_r^2} \times \frac{W_u N_r^2}{E_R R_c} = \frac{E_S}{E_R} \quad (6)$$

$$\pi_g = \frac{\pi_{12}}{\pi_{13}} = \frac{W_s}{W_u} \times \frac{W_u}{W_r} = \frac{W_s}{W_r} \quad (7)$$

$$\pi_h = \frac{\pi_{14}}{\pi_{15}} = \frac{I_s R_c}{W_u N_r^2} \times \frac{W_u N_r^2}{I_r R_c} = \frac{I_s}{I_r} \quad (8)$$

$$\pi_j = \frac{\pi_{10}}{\pi_{17}} = \frac{E_S R_c}{W_u N_r^2} \times \frac{W_u N_r}{C} = \frac{E_S R_c}{C N_r} \quad (9)$$

$$\pi_k = \frac{\pi_{10}}{\pi_{18}} = \frac{E_S R_c}{W_u N_r^2} \times \frac{W_u N_r^2 R_c^2}{T} = \frac{R_c^3 E_S}{T} \quad (10)$$

$$\pi_l = \frac{\pi_2}{\pi_{19}} = \frac{D}{R_c} \times \frac{R_c}{\Delta} = \frac{D}{\Delta} \quad (11)$$

$$\pi_m = \frac{\pi_2}{\pi_{16}} = \frac{D}{R_c} \times \frac{R_c}{\delta} = \frac{D}{\delta} \quad (12)$$

$$\Psi = (\pi_a \times \pi_b \times \pi_c \times \pi_d \times \pi_f \times \pi_g \times \pi_h \times \pi_l \times \pi_m) \quad (13)$$

$$\pi_1 = f(\Psi, \pi_e, \pi_j, \pi_k, \pi_{20}) \quad (14)$$

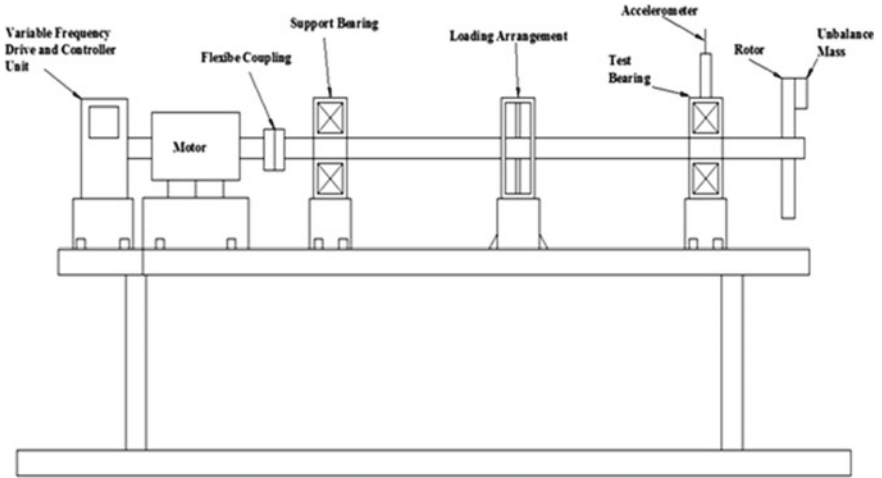
$$\frac{V}{R_c N_r^2} = f\left(\Psi \times \frac{\rho R_c^4 N_r^2}{E_S} \times \frac{E_S R_c}{C N_r} \times \frac{R_c^3 E_S}{T} \times \frac{f_s}{N_r}\right) \quad (14)$$

$$\frac{f_s}{N_r^2} = f\left(\Psi \times \frac{\rho R_c^4 N_r^2}{E_S} \times \frac{E_S R_c}{C N_r} \times \frac{R_c^3 E_S}{T} \times \frac{\delta}{R_c} \times \frac{V}{R_c N_r^2}\right) \quad (16)$$

After obtaining vibration amplitude and fault frequency of rotor bearing systems for clearance and unbalance using experimentation, the same can be evaluated with the new DA method and RSM techniques. The computation follows a closed loop linking the variations of the speed, load, clearance, and unbalance. This loop is repeated until the difference of the amplitudes of vibration and defect frequency between two adjacent iterations is less than the prescribed tolerance error. Once the convergence is reached, one can increase the load, speed, clearance, and unbalance and start the next step.

### 3 Experimental Study

The schematics of inhouse experimental setup developed is shown in Fig. 1. Speed of the direct current motor is varied using variable frequency controller unit. Accelerometer is placed on bearing housing for fault detection. Vibration frequency and amplitudes are captured using FFT analyzer. Experiments are conducted for various process parameters. Between Shaft and Sleeve, a clearance of 0.04 is created artificially and measurement is done using the Feeler gage as shown in Fig. 2. Between Sleeve and Inner Race, a clearance of 0.04 is created artificially and measurement is done using the Feeler gage as shown in Fig. 3.



**Fig. 1** Schematics of an experimental setup

**Fig. 2** Shaft and sleeve clearance of 0.04 mm



**Fig. 3** Sleeve and inner race clearance of 0.04 mm



## 4 Results and Discussions

To investigate the effect of unbalance on vibration amplitude the nine experiments were carried out with maximum speed of 12,000 rpm to investigate the unbalancing effects. Few results are given in Fig. 4.

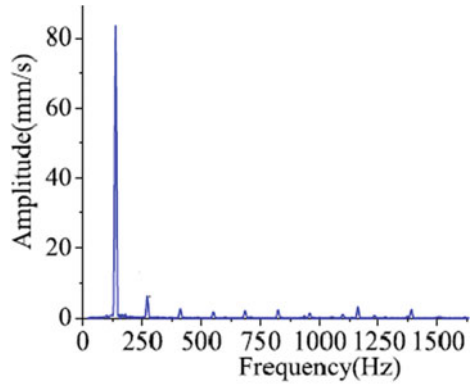
Figure 4 depicts the vibration spectrum of effect of unbalance on vibration amplitude of rotor bearing system. From Fig. 4b, c it is clear that if increase of unbalance from 0.30 to 0.80 g mm two peaks are observed at 1160 and 1385 Hz, and the amplitude of vibration are increased with unbalance weight. Additional nine experiments were performed and the significant effects of unbalance weight on vibration amplitude were noticed. Figure 5 shows the response of vibration amplitude due to unbalance weight and is obtained by using Eq. (16). Similarly, Fig. 6 shows the experimental results of vibration amplitude with unbalance effect. Some fluctuations in the vibration amplitude are observed because of unbalanced weights.

Additional five experiments were performed to observe the effects of clearance with unbalance. The past literature indicates that radial clearance is the main cause of significant effect on vibration characteristics of bearing systems. Figure 7 shows the comparison of effect of clearance on vibration amplitude. It is observed that with the increase of clearance from 0.00 to 0.16 mm the vibration amplitude increases and then unchanged and afterward shows decreasing fashion. In addition, it shows that small clearance is good to reduce the effect of unbalance on vibration amplitude.

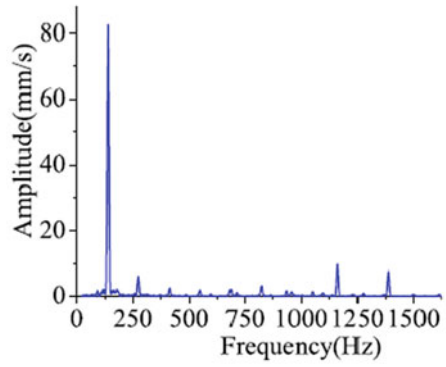
## 5 Conclusions

The condition monitoring of the bearing is very important in the process industry. Early detection of the faults saves energy time and cost. In this work, the fault diagnosis of the faulty bearings is done. Various defects are created artificially and the vibration amplitude and frequencies are measured. It is found that unbalance on the rotor system completely changes the vibration amplitude and frequency and it can be detected and analyzed easily. Various values of unbalances are studied and different patterns are obtained for different unbalance and precise unbalance can be easily detected and can be predicted using the developed model. Clearance also has an important effect on the performance of the bearing and as clearance increases the vibration pattern changes. Changes in the vibration patterns decide the amount of clearance present in the bearing.

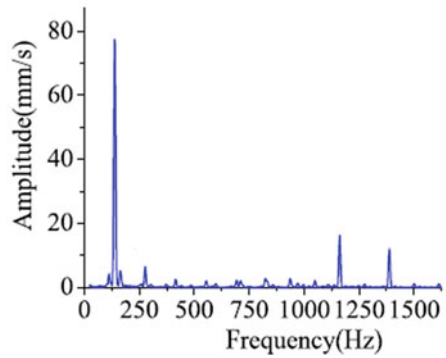
**Fig. 4** Vibration spectra of effect of unbalance on amplitude of vibration



(a) 0.30 g.mm

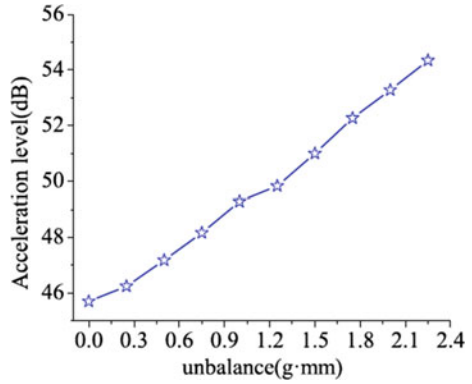


(b) 0.80 g.mm

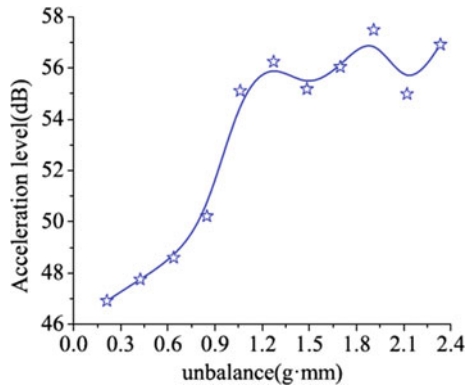


(c) 1.35 g.mm

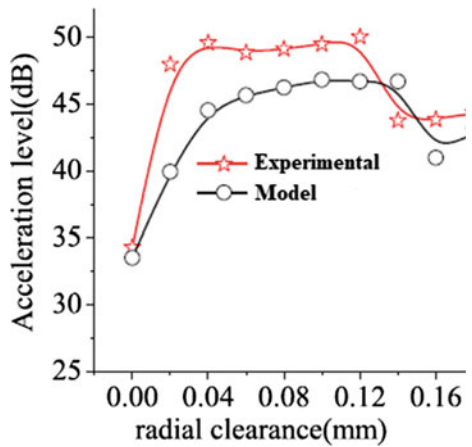
**Fig. 5** Prediction of unbalance effect on acceleration level using model



**Fig. 6** Experimental values of unbalance on acceleration level



**Fig. 7** Comparison of effect radial clearance on vibration amplitude





## References

1. Childs, M.D.: *Turbomachinery Rotordynamics*. Wiley, Chichester (1993)
2. Ehrich, F.F.: *Handbook of Rotordynamics*. McGraw-Hill, New York (1992)
3. Yamamoto, T.: On the vibration of a shaft supported by bearings having radial clearances. *Trans. JSME* **21**, 182–192 (1955)
4. Sunnersjo, C.S.: Varying compliance vibrations of rolling bearings. *J. Sound Vibr.* **58**, 363–373 (1978)
5. Yamauchi, S.: The non-linear vibration of flexible rotors. *Trans. Jpn. Soc. Mech. Eng.* **446**(49), 1862–1868 (1983)
6. Saito, S.: Calculation of non-linear unbalance response of horizontal Jeffcott rotors supported by ball bearings with radial clearances. *J. Vibr. Acoust. Stress Reliab. Des.* **107**, 416–420 (1985)
7. Ehrich, F.F.: Subharmonic vibration of rotors in bearing clearance. *J. Eng. Power* **88**, 56–65 (1966)
8. Ehrich, F.F.: Higher order sub harmonic response of high-speed rotors in bearing clearance. *J. Vibr. Acoust. Stress Reliab. Des.* **110**, 9–16 (1988)
9. Ehrich, F.F.: Observation of sub-critical super-harmonic and chaotic response in rotor dynamic. *J. Vibr. Acoust. Stress Reliab. Des.* **114**, 93–99 (1991)

# Topology Optimization of Bench Problems—Stress and Deformation Perspective



Dara Ashok, M. V. A. Raju Bahubalendruni, and Johnney Mertens

## 1 Introduction

Industrial components demand complex topologies in order to fulfill the design, manufacturing, and space constraints. In most instances, these topologies are not optimal with regard to stiffness and compliance. Often there is great possibility to reduce the weight further for the detailed external loads. These kinds of topological changes to optimize the functional requirements are perceptible in stem, root, leaf venation, the insect exoskeleton of wings, and cardio-vascular system of animals and humans [1]. This directed to the development of structures for optimization with adequate compliance and stiffness. The Structural topology optimization methods become useful for industries applications since the prominent work by Bendsoe and Kikuchi [2]. After the pioneering work on homogenization of structural members with voids and solid cells and rotation as design variables, several researchers developed many methods in structural topology optimization. Traditional structural optimization algorithms are constructed through Karush—Kuhn—Tucker conditions but are ineffectual to meet the actual optimal structure due to singularity uncertainties. To control the mesh independence and checkerboard problem, density filters are applied to avoid the uncertainties in density-based topology optimization [3, 4]. The power law policy or SIMP introduced to convergence improvement of the complexity of hominization method [5–7], this gives better relation between density variables and material property. For relaxation of global optimality, discrete approach is used such as structural optimization method generated from Hard kill strategies which eliminate the elements having lower strain energy, bi-directional structural optimization scheme [7]. These are limited to solve problems that deal with only discrete density constraints. The level-set method derived by Osher and Sethian to get proven to be

---

D. Ashok (✉) · M. V. A. Raju Bahubalendruni · J. Mertens  
National Institute of Technology Puducherry, Karaikal 609609, India

© The Author(s), under exclusive license to Springer Nature Singapore Pte Ltd. 2022  
S. K. Natarajan et al. (eds.), *Recent Advances in Manufacturing, Automation, Design and Energy Technologies*, Lecture Notes in Mechanical Engineering,  
[https://doi.org/10.1007/978-981-16-4222-7\\_80](https://doi.org/10.1007/978-981-16-4222-7_80)

719

stable with free boundaries is numerically efficient without the complexity of sensitivity filter for continuously morphing and multi materials phase problems [8, 9]. The reliability as design variable concept is considered to study the effect of stress uncertainties corresponding to the material properties and externally applied loads [10]. By the perspicuity of stress role and importance in structural optimization, we need to extend the solution for uncertainties by stresses in structural optimization.

## 2 Stress-Based Topology Optimization Problem Formulation

### 2.1 Generalized Formulation

In stress constrain topology optimization, the model should be consisting adequate stiffness and strength. The domain is divided into finite number of unit cell as FE domain grid and each cell act as isotropic material with void representation as shown in Fig. 1. The objective is to find the optimum value of design variable for each unit cell.

The finite element with relative density  $\rho_e$  which are related to the design variables are represent 0 for void and 1 for solid of domain. The stress minimization concept is just as mimic of density-based topology optimization problems subjected to stiffness and displacement as constrained. The stress constrained problem for the figure shown in Fig. 2 can be formulated as given in Eq. (1).

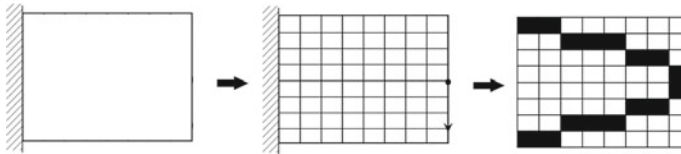
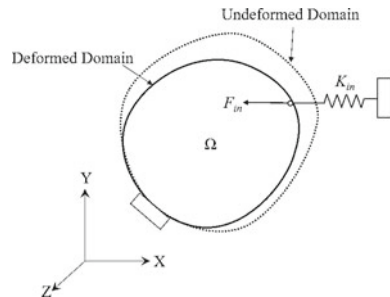


Fig. 1 The transformation of topology optimization problem from fixed domain

Fig. 2 Representation of stress-based topology optimization problem



$$\text{minimize } V = \sum_{e=1}^N v_e \rho_e \tag{1}$$

$$\text{subject to : } Ku = f$$

$$(\sigma_e)_{VM} \leq \rho_e^p \text{ if } p > 0,$$

$$0 < \rho_{\min} \leq \rho_e \leq 1,$$

$$e = 1, 2, \dots, N.$$

where

$(\sigma_e)_{VM}$  = the higher von-Mises stress in the structure,

$\rho_e$  = the virtual density,

$v_e$  = Design variable (Stress),

$N$  = the total finite elements in the mesh,

$\rho_{\min}$  = the minimum virtual elemental density (take  $10^{-4}$ ),

$P$  = Penalty Function (Varies 1–3) and

### 3 Stress Singularity Constraints and Density Filter

The stress values converge with refined mesh for an element the element level stresses are influenced by its neighboring elements. This will continuously be controlled by the adjected existing circles centers distance and tangency to form like closed packing like show in the Fig. 3. This will give on to stress singularities and uncertainties in final results [11]. The material removal in such a way that the mean stress at the interior point ( $i$ ) surrounded points ( $j$ ) within reference of circle ( $r_{\min}$ ) whose weights are compared between the elements which are connected with the points [12–15]. Mathematically, the mean von-mises stress is given in Eq. (4),

$$\bar{\sigma}_i^{vm} = \frac{\sum_{j=1}^N w_j \sigma_j^{vm}}{\sum_{j=1}^N w_j} \tag{2}$$

where  $\bar{\sigma}_i^{vm}$  = Mean von-Mises stress at the interior center point of circle  $i$ ,

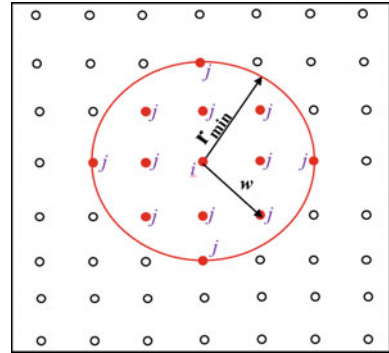
$\sigma_j^{vm}$  = The von-Mises stress for  $j$  points in the radius  $R$ .

$N$  = The total  $j$  points within the radius  $R$ ,

$w_j$  = The reciprocal of the distance from  $i$  points to  $j$  points (Fig. 3).

$$= \frac{1}{\sqrt{(x_j - x_i)^2 + (y_j - y_i)^2}}$$

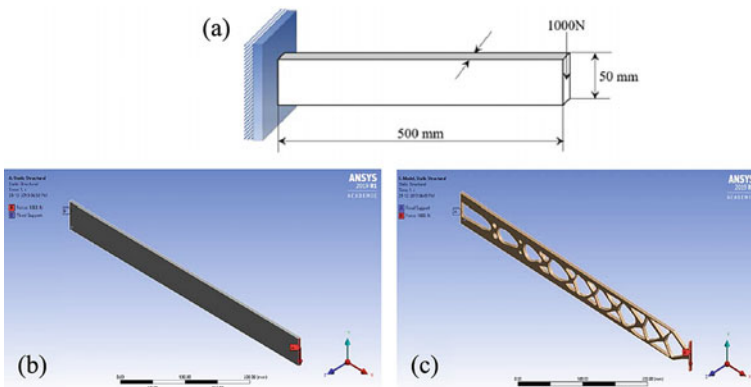
**Fig. 3** Weight function for finding the mean stress for filter



### 4 Model Results

The traditional Mitchel cantilever (MC), MBB Beam and L-bracket Problems are considered as Benchmark problems with corresponding mesh size and assuming material is steel which is isotropy and homogeneous subjected to static loading of 1000 N. Initially, static structural analysis is performed in ANSYS software by varying mesh size starting from 1 to 10 mm with unit increment and Young's modulus of  $2.1 \times 10^6$  N/mm<sup>2</sup>, Poisson's ratio of 0.3, applied load 1000 N, and filter radius  $r_{min} = 1$  mm.

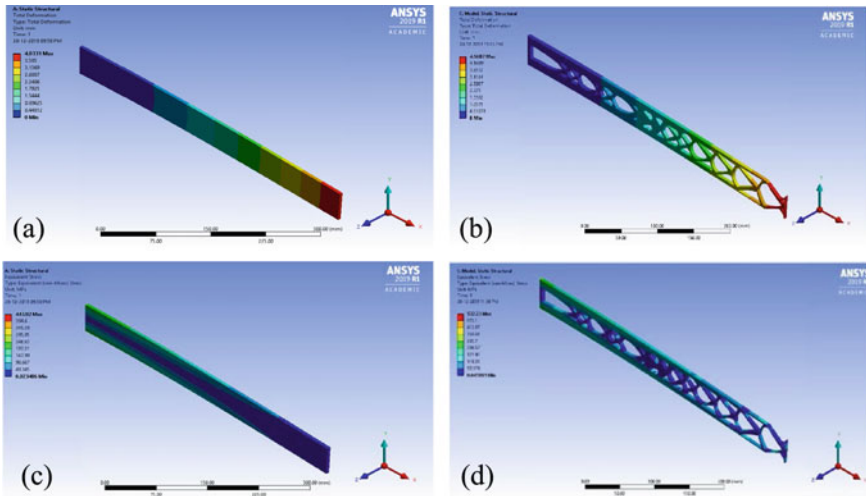
The MC beam is shown in Fig. 4a, The input data for the MC is: length 500 mm, width 50 mm, thickness of 5 mm, the total No. of elements are 11,493 and No. of iteration are 409. For the analysis in ANSYS, SOLID186 element is taken to find the Stress and displacement with variation mesh size given below. The boundary conditions, displacement, and Stresses for MC beam and Topology optimized MC



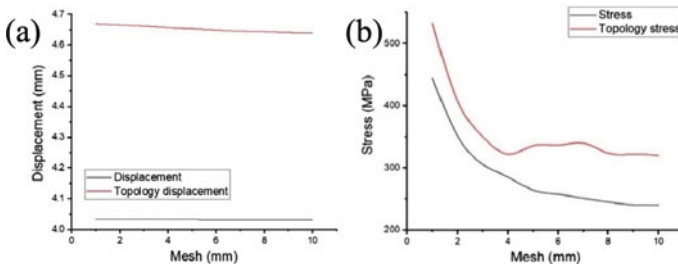
**Fig. 4** a Schematic diagram for Mitchel cantilever, b boundary conditions of Mitchel cantilever beam, c boundary conditions of topology optimized Mitchel cantilever beam

beam shown are in Figs. 4b, c and 5a–d respectively. The variation of displacements and stresses are showing in Fig. 6a, b and Table 1.

The geometry for MBB Beam shown in Fig. 7a, The input data for the Mitchel cantilever is: length 1000 mm, width 50 mm, thickness of 5 mm, the total No. of elements are 99,918, No. of iteration are 335. The MBB beam and topology optimized MBB beams boundary conditions are shown in Fig. 7b, c, displacement and stresses are showing Fig. 8a–d respectively the variation of displacements and stresses are showing in Fig. 9a, b and Table 2. Similarly, The L-Bracket and topology optimized L-Bracket, boundary conditions are shown in Fig. 10b, c, displacement and stresses are showing Fig. 11a–d respectively the variation of mesh vs deformation and stresses of L-Bracket are shown in Fig. 12a, b and Table 3.



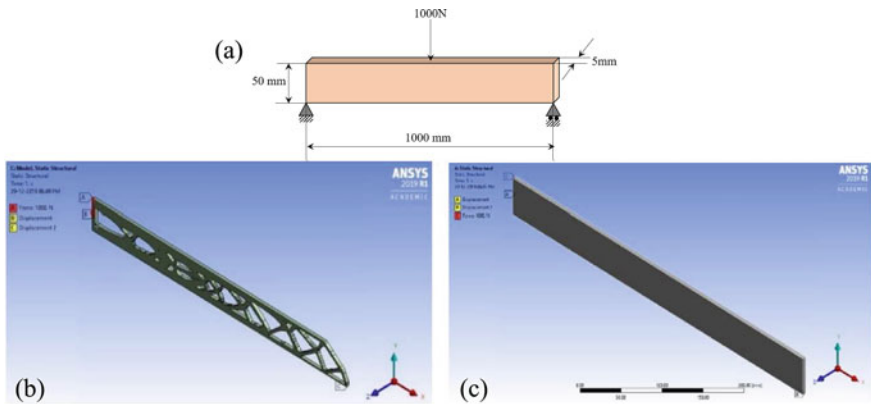
**Fig. 5** a Total displacement of MC beam and b topology optimized MC beam, c stress distribution of MC beam and d stress distribution of topology optimized MC beam



**Fig. 6** a Mesh size versus total displacement and b mesh size versus stresses in Mitchel cantilever beam including topology optimized member

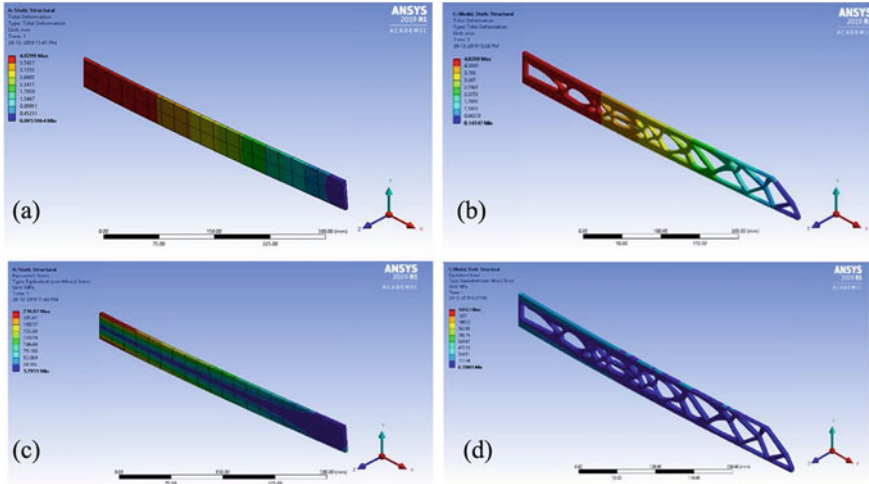
**Table 1** Stress and displacement variations with mesh refinement of MC including topology optimization model

S. No.	Mesh element size in mm	Mitchel Cantilever beam		Topology optimized Mitchel Cantilever	
		Total deformation (Max) in mm	Maximum stress (Max) in MPa	Total deformation (Max) in mm	Maximum stress (Max) in MPa
1.	1	4.0331	443.92	4.6687	532.23
2.	2	4.0328	351.55	4.665	407.72
3.	3	4.0325	305.69	4.6613	350.24
4.	4	4.0324	285.35	4.6566	322.05
5.	5	4.0321	264.33	4.6527	335.61
6.	6	4.0319	257.5	4.6486	336.43
7.	7	4.0318	251.16	4.645	339.82
8.	8	4.0316	245.18	4.6429	323.64
9.	9	4.0314	240.41	4.64	321.88
10.	10	4.0311	240.4	4.6687	319.87

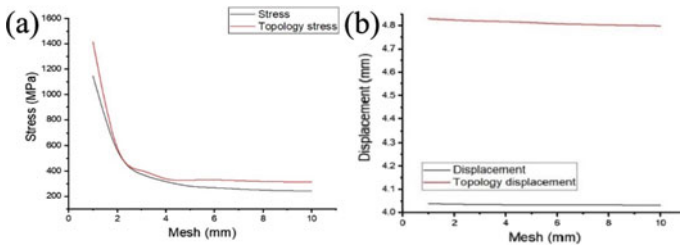


**Fig. 7** **a** Schematic diagram of MBB beam, **b** boundary condition of MBB beam, **c** boundary condition of topology optimized MBB beam

From analysis, we can observe at the range of 2–1 mm mesh size, the stresses are increasing above 160% with reference to 10 mm meshes in Mitchel cantilever, closed to 400% in MBB Beam, and 180% in the L-Bracket. For accuracy and precision, need to take the element with small size but it is coincidental to get stress singularities.



**Fig. 8** **a** Total displacement of MBB beam and **b** topology optimized MBB beam, **c** stress distribution of MBB beam and **d** topology optimized MBB Beam



**Fig. 9** **a** Mesh size versus total displacement and **b** mesh size versus stresses in MBB Beam including topology optimized member

## 5 Conclusion

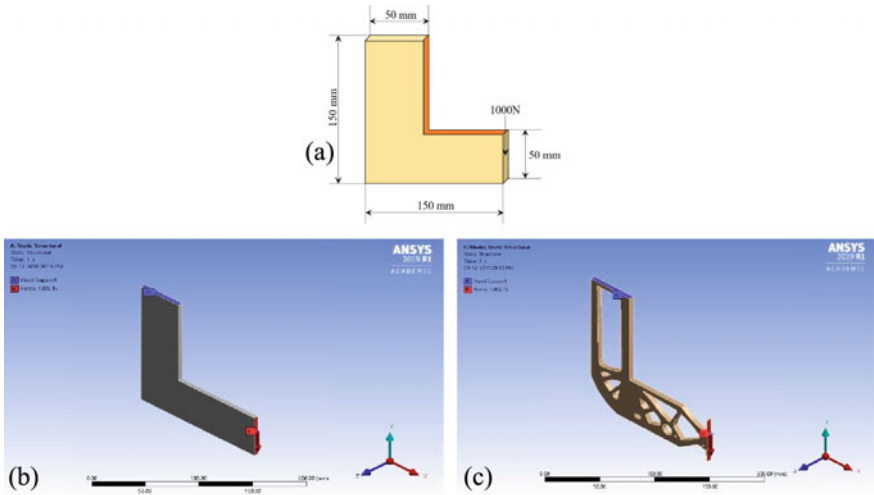
In topology optimization, the elements are formed in voxel distribution with unit geometry and finite element analysis is conducted. It is observed from the simulation, the higher stresses are obtained with reducing mesh size and converging without problems with Derived quantities such as stresses and strains converge as the mesh is refined, but not as fast or smooth displacements. In some cases, derived quantities will not converge as the mesh is refined at artificially high stresses.

In present work, the Mitchel cantilever, MBB Beam, and L-Bracket members are analyzed to study the significance of derived stress distribution by varying the mesh size while in process of topology optimization. If proper mesh size is not converging then it leads to stress singularity and error in solution at Fixed supports and other constraints which avoid Poisson’s effect with the artificially high stress area will keep



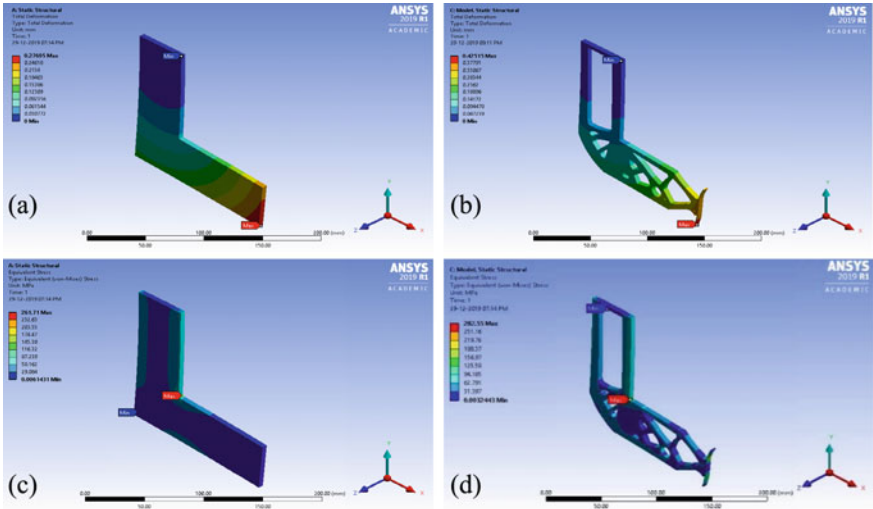
**Table 2** Stress and displacement variations with mesh refinement of MBB including topology optimization model

S. No.	Mesh element size in mm	MBB beam		Topology optimized MBB beam	
		Total deformation (Max) in mm	Maximum stress (Max) in MPa	Total deformation (Max) in mm	Maximum stress (Max) in MPa
1.	1	4.039	1146.6	4.8298	1414.1
2.	2	4.0367	564.35	4.8245	585.16
3.	3	4.0353	375.14	4.8202	403.35
4.	4	4.0345	317.47	4.817	338.36
5.	5	4.0337	280.58	4.8126	327.74
6.	6	4.0334	267.98	4.8077	329.91
7.	7	4.0332	257.84	4.8048	323.91
8.	8	4.0329	249.52	4.8022	317.6
9.	9	4.0326	244.31	4.8003	314.79
10.	10	4.0323	242.69	4.798	313.67

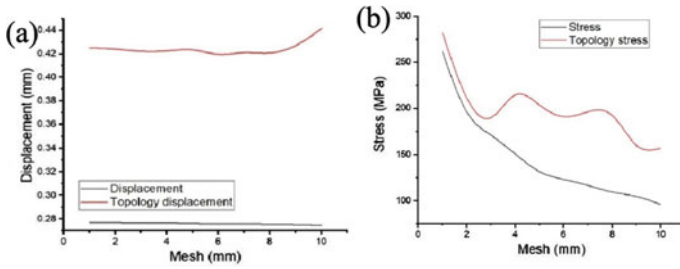


**Fig. 10** a Schematic diagram of L-bracket, b boundary condition of L-bracket and c topology optimized L-bracket

increasing the stresses. Clearly, further study of the better practical design tool for topology optimization issues is still required.



**Fig. 11** a Total displacement of L-bracket and b topology optimized L-bracket, c stress distribution of L-bracket and d topology optimized L-bracket



**Fig. 12** Mesh size versus total displacement and stress of a L-bracket and b topology optimized L-bracket

**Table 3** Stress and displacement variations with mesh refinement of L-Bracket including topology optimization model

S. No.	Mesh element size in mm	L-bracket		Topology optimized L-bracket	
		Total deformation (Max) in mm	Maximum stress (Max) in MPa	Total deformation (Max) in mm	Maximum stress (Max) in MPa
1.	1	0.27695	261.71	0.42515	282.55
2.	2	0.27672	196.68	0.42407	211.84
3.	3	0.27649	170.96	0.42225	189.69
4.	4	0.27629	151.22	0.42255	214.43
5.	5	0.276	131.86	0.42341	203.72
6.	6	0.27587	123.4	0.41972	190.93
7.	7	0.2757	116.81	0.42105	196.09
8.	8	0.27548	109.62	0.42087	192.38
9.	9	0.27517	104.77	0.42708	160.44
10.	10	0.27474	96.119	0.44152	157.15

## References

1. Kobayashi, M.H.: On a biologically inspired topology optimization method. *Commun. Nonlinear Sci. Numer. Simul.* **15**(3), 787–802 (2010)
2. Bendsoe, M.P., Kikuchi, N.: Generating optimal topologies in structural design using a homogenization method. *Comput. Methods Appl. Mech. Eng.* **71**(2), 197–224 (1988)
3. Sigmund, O., Petersson, J.: Numerical instabilities in topology optimization: a survey on procedures dealing with checkerboards, mesh-dependencies and local minima. *Struct. Optim.* **16**(1), 68–75 (1998)
4. Bendsoe, M.P., Sigmund, O.: Material interpolation schemes in topology optimization. *Arch. Appl. Mech.* **69**(9–10), 635–654 (1999)
5. Bendsoe, M.P., Sigmund, O.: *Topology Optimization: Theory, Methods, and Applications*. Springer, Berlin (2003)
6. Sigmund, O.: A 99 line topology optimization code written in Matlab. *Struct. Multidiscip. Optim.* **21**(2), 120–127 (2001)
7. Mattheck, C., Burkhardt, S.: A new method of structural shape optimization based on biological growth. *Int. J. Fatigue* **12**(3), 185–190 (1990)
8. Xie, Y.M., Steven, G.P.: A simple evolutionary procedure for structural optimization. *Comput. Struct.* **49**(5), 885–896 (1993)
9. Young, V., Querin, O.M., Steven, G.P., Xie, Y.M.: 3D and multiple load case bi-directional evolutionary structural optimization (BESO). *Struct. Optim.* **18**(2–3), 183–192 (1999)
10. Allaire, G., Jouve, F., Toader, A.M.: Structural optimization using sensitivity analysis and a level-set method. *J. Comput. Phys.* **194**(1), 363–393 (2004)
11. Wang, M.Y., Wang, X., Guo, D.: A level set method for structural topology optimization. *Comput. Methods Appl. Mech. Eng.* **192**(1–2), 227–246 (2003)
12. Wang, X., Wang, M.Y., Guo, D.: Structural shape and topology optimization in a level-set-based framework of region representation. *Struct. Multidiscip. Optim.* **27**(1–2), 1–19 (2004)
13. Yulin, M., Xiaoming, W.: A level set method for structural topology optimization and its applications. *Adv. Eng. Softw.* **35**(7), 415–441 (2004)

14. James, K.A., Lee, E., Martins, J.R.: Stress-based topology optimization using an isoparametric level set method. *Finite Elem. Anal. Des.* **58**, 20–30 (2012)
15. Guo, X., Zhang, W., Zhong, W.: Stress-related topology optimization of continuum structures involving multi-phase materials. *Comput. Methods Appl. Mech. Eng.* **268**, 632–655 (2014)

# Internal Logistics Optimization in the Assembly Line Using Lean Techniques



P. Jeyaraman, R. Jeeva, T. Niruban Projoth, and R. Rohith Renish

## 1 Introduction

Nowadays, manufacturing sectors [1] are faced with fierce competition in this uncertain, complex, and widespread global economy. As a result, businesses have stressed lean concepts [2, 3] and methods as a way to deal with this competition. In this regard, businesses are often too focused on enhancing only the value-added activities or processes in the manufacturing flow from a lean viewpoint [4, 5], but the internal logistics of the transport of products at factory and company level and the related knowledge flows remain largely unchanged despite their close links to production. In addition, the material handling and transport activities constitute a large portion of the overall lead time, and it is important that these activities be assisted with due consideration of the various downstream value-added activities in the supply chain. It is therefore obvious that the form of production system (either push or pull) and the internal logistics [6, 7], system are critical for improving the overall material flows, taking into account/depending on the environmental aspects of production [8], such as demand, unlevelled production, resource constraints, and product mix.

---

P. Jeyaraman · T. Niruban Projoth · R. Rohith Renish (✉)  
Department of Mechanical Engineering, Veltech Rangarajan, Dr. Sagunthala R&D Institute of Science and Technology, Chennai, India  
e-mail: [rohithrenish@veltech.edu.in](mailto:rohithrenish@veltech.edu.in)

R. Jeeva  
Department of Aeronautical Engineering, S.A Engineering College, Chennai, India

© The Author(s), under exclusive license to Springer Nature Singapore Pte Ltd. 2022  
S. K. Natarajan et al. (eds.), *Recent Advances in Manufacturing, Automation, Design and Energy Technologies*, Lecture Notes in Mechanical Engineering,  
[https://doi.org/10.1007/978-981-16-4222-7\\_81](https://doi.org/10.1007/978-981-16-4222-7_81)

731

## ***1.1 Purpose of the Project***

This study has been carried out in one of the bays in the assembly line called Drive line control which consists of four lines. They are the manufacturers of Vacuum Boosters of different variants. It is seen that there is a significant Nonstandard, non-cyclic movement of the water spider that is non-value [9] adding. Quantity of the parts delivered by supplier does not synchronize with production requirements. There is a lot of material mix up/damage and WIP Inventory is high. It is totally manually communicated and replenishment of parts is need based. Container sizes are not clearly defined. Rehandling and repacking of parts take place inside the assembly hall. This project follows a DMAIC procedure in order to solve the above stated issues.

The Aim of this project is:

- To standardize the random movement of Water Spider and the reduction of material mix up/damage and WIP Inventory using the first lean principle of Right Part at Right Time.
- To eliminate manual communication in the lines along with standardizing the container sizes using built in Quality which is the second principle of lean.
- To synchronize Quantity of the parts delivered by supplier with production requirement using the Principle of shorter lead time. Rehandling and repacking of parts are to be planned in such a way that they take place outside the assembly hall based on the same principle.

## **2 Methodology**

This chapter presents the structure of process steps that are followed in this present work. DMAIC is a systematic five-step [10] problem-solving technique that is used to complete projects through the creation and implementation of solutions designed to resolve the root cause of quality and process issues and to create best practices to ensure that solutions are permanent and can be repeated in other business operations. This chapter describes DMAIC and presents a number of resources at each stage. This interpretation is used as a working structure to carry out the work of this project.

### ***2.1 Multi Movement Analyzes (MMA)***

Current movement of the Water spider is studied using Multi Movement Analysis. Figure 1 is a work content table which is used in Multi Movement Analysis to calculate the overall number of appearances of the water spider. Two cycles are considered wherein picking, walking with and without parts, rehandling, searching, waiting, counting, and weighing are noted in the work content table. Accordingly

TOS- Work Content Analysis											Station : DLC Line	
Date of Analysis : 24/03/2019		Time (Begin /End): 3.00 p.m - 4.30 p.m			Recorded By : Jeyaraman			Cycle Time :30 Min				
Cycle No.	Type	Picking	Walking with Parts	Working	-	Re-handling	Searching	Waiting	Walking with parts	Counting & Weighing	Miscellaneous	Appearances per cycle
1	Not affe-	54	15	10	-	33	3	0	7	10	-	132
2	-	35	9	6	-	17	0	5	17	10	-	99
3												0
4												0
5												0
6												0
7												0
8												0
9												0
10												0
11												0
12												0
13												0
14												0
15												0
Overall Appearances		89	24	16	0	50	3	5	24	20	0	231
Appearances (%)		38.5	10.4	6.9	0.0	21.6	1.3	2.2	10.4	8.7	0.0	100

Fig. 1 Work content table

overall appearances and its percentage are calculated. For instance, consider picking time. Overall appearances are the total number of appearances only for the collection of the pieces, which is 89. Overall presence percentage is the percentage of time spent in the set of parts ie, 38.5%. In Fig. 2 All the activities of water spider are listed in the X axis and the Y axis represents the percentage of appearances made. In this

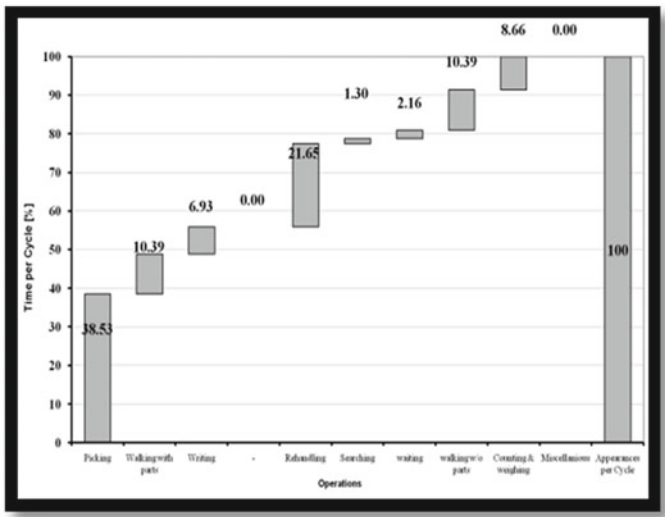


Fig. 2 Multi movement analysis graph (Current state)

**Fig. 3** Example of chute installed



case, two cycles are considered and the overall appearances are plotted in the graph according to the details provided in the work content table of MMA excel sheet.

### 2.1.1 Work Station

The table where a particular assembly process is taking place is known as a Work Station. Each and every workstation shall have its own assembly process [11, 12]. The materials used in each station are different and are constructed on the basis of the materials used, either attached to the work table or fixed closer to the work table without affecting the assembly process.

### 2.1.2 Brain Size

Every chute is designed based on the bin sizes of the particular material being used in that station. Based on the bin size, the chute's input, as well as output, is designed. For example, consider Fig. 3, it represents a chute with A-11080, B BIN25, and D-32150 towards the left side of the station and D-32150 and CBIN25 towards the right side of the station.

### 2.1.3 Details of Parts in Line 2 Station 7

Based on these details chute is designed and placed as shown in Fig. 4, Here height of the chute is based on the station which can be variable. Similarly collecting the data of all the four lines, number of stations and the parts used in every station, the ideal bin sizes of those parts accordingly these chutes are designed for all the stations in line 1, 2. Hence two bin system with 100% FIFO is implemented in all the two lines. For another example consider Line 2 Station 7 in Table 1.



**Fig. 4** Chute design in line 2 station 7



**Table 1** Details of parts in line 2 station 7

Part no	Part name	Bin size	Dimensions (mm)
100472690	Retainer	A-11080	330*110
100472670	White filter	B BIN15	370*145
100910620	Nut	B BIN15	370*145
100472680	Yellow filter	C BIN25	435*160
100460130	Fork	D-32150	590*230
100472700	Gaiter	E BIN25	680*240

**2.1.4 Material Presentation Improvements**

Figure 5 represents Operating Rod Trolley in Line 2 whereas no standard containers available for parts Used as an additional storage area with no FIFO and Pull also undefined and high inventory in covers.

Figure 6 represents Final Assembly Trolley in Line 2 whereas the lead time is reduced due to the installation of lean trolley in the line which can store all the variants of parts like operating rod, push rods, spring seats, etc. Ideal size containers



**Fig. 5** Operating rod trolleys in line 2



**Fig. 6** Final assembly trolleys in line 2

in place according to the parts. FIFO and pull followed Parts repacked in stores into the bins and can be fed from backside by the water spider.

### 3 Results and Discussion

After the implementation results are obtained based on the following analysis.

- Value-added/Non-Value-added Analysis (VA/NVA) status
- Analyzing Work Content Using Multi Moment Analysis
- Standard Work By Standard Work Combination Table.

#### 3.1 *Value-Added/Non-Value-Added Analysis (VA/NVA) Status*

After the VA/NVA from Fig. 7 it is evident that the value adding work has increased from 10 to 33%. Incidental activities have reduced from 49 to 45%, the non-value adding activities has reduced from 41 to 22%.

#### 3.2 *Analyzing Work Content Using Multi Moment Analysis*

From the following work content Fig. 8 we can analyze the movement of the water spider in the current state before implementation. We obtain the following graph through the MMA Excel sheet which gives the percentage of appearances made by the water spider per each activity.

The objective of achieving Right Part at Right Time was achieved by using the concepts Of Bin System and Selection of Ideal Containers. Built in Quality was

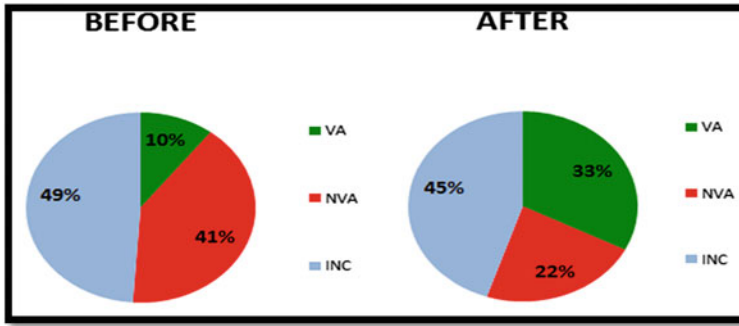


Fig. 7 Percentages of value-added/non-value-added activities

CYCLE NO	PICKING	WALKING WITH PARTS	WRITING	REHANDLING	SEARCH -ING	WAIT- ING	WALKING WITHOUT PARTS	COUNTING AND WEIGHNING	APPEARANCES PER CYCLE
1	54	15	10	33	3	0	7	10	122
2	35	9	6	17	0	5	17	10	89
OVERALL APPEARANCES	89	24	16	50	3	5	24	20	221
APPEARANCE %	38.53	10.39	6.93	21.39	1.30	2.16	10.39	8.66	100

Fig. 8 Work content table of the water spider

achieved by applying the concepts of Signaling Mechanisms (Kanban Bin System) [13, 14], Visual Management along with the concepts of Bin System and Selection of Ideal Containers. Shorter lead time is the objective that was achieved by removing eight line side material stores in the bay and installing two lean trolleys for the entire bay. Hence, the objectives of Right Part at Right Time [15], Shorter Lead Time and Built in Quality were achieved.

### 3.3 The Benefits of This Project is Tabulated in Table

From Table 2 the following interpretations are made. It is seen that 32,500\$ is saved by the company in four months by the reduction in Work-In-Process Inventory. Number of water spiders is reduced from 3 to 1. Hence remaining two water spiders can be used for other works in the assembly line. 650 s of lead time is saved which is now used by the water spider in repacking area outside the assembly line. Water spider

**Table 2** Details of parts in line 2 station 7

Category	Before	After	Benefit
WIP inventory	39,000\$	6500\$	32,500\$
No of water spiders/shift	3	1	2
Time/cycle (s)	1810	1160	650
Water spider frequency	Random (Nonstandard)	Once in four hours	Standardized route

frequency is now once in four hours thereby a highly standardized route is followed by the water spider.

## 4 Conclusion

In the DLC assembly line it was found that there was a significant Nonstandard, Non-Cyclic Movement of the Water Spider that was Non-Value Adding. Quantity of the parts delivered by suppliers did not synchronize with production requirement. There was a lot of material mix up/damage and WIP Inventory was high. Communication was totally manual and replenishment of parts has always been need based. Container sizes were not clearly defined. Rehandling and repacking of parts took place inside the assembly line. DMAIC procedure which includes the lean principle namely Right Part at Right Time, Built in Quality, Shorter Lead Time, was adopted to solve the problems stated above.

The objective of getting Right Part at Right Time was achieved by using the concepts of Bin System and Selection of Ideal Containers which has lead to the eventual reduction of material mix up/damage and WIP Inventory. The random movement of Water Spider is standardized by considering the cycle frequency as once in four hours. Built in Quality was achieved by applying the concepts of Signaling Mechanisms (Bin Kanban System), through this concept manual communication is eliminated and now the bay follows pull system. Built in quality was also achieved by the concepts of Visual Management, Bin System, and Selection of Ideal Containers.

Shorter lead time is obtained by removing eight line side material stores in the bay and installing two lean trolleys with 100% First-In-First-Out (FIFO) for the entire bay. Quantity of the parts delivered by supplier now synchronizes with production requirement after the implementation of supplier pack size optimization. Rehandling and repacking of parts were carried out in the repacking area outside the assembly line. There is a 78% reduction in NVA of the water spider and the cycle time is reduced by 39%, thereby reducing the number of water spiders from three to one after the implementation of the model. Eventually, there is a 62% fall in the WIP which in turn has also resulted in balanced stock levels with zero line stoppers.

As a result, the entire process is standardized and a Potential State Implementation Model has been developed to match other product families in the facility.

## References

1. Abdulmalek Jayant RajgopalInt, F.A.: Analyzing the benefits of lean manufacturing and value stream mapping via simulation: a process sector case study. *J. Prod. Econ.* **107**, 223–236 (2007)
2. Peter, R.S., Ward, T.: Defining and developing measures of lean production. *J. Oper. Manag.* **25**, 785–805 (2007)
3. Holweg, M.: The genealogy of lean production. *J. Oper. Manag.* **25**, 420–437 (2007)
4. Melton, T.: The benefits of lean manufacturing—what lean thinking has to offer the process industries. *Trans IChemE, Part A Chem Eng Res Des* **83**(A6), 662–673 (2005)
5. Morrison, K.R.: Transformation to lean manufacturing by an automotive component supplier. In: *19th International Conference on Computers and Industrial Engineering*, vol. 31(1), pp. 95–98. Pergamon Press, Inc. Tarrytown 2 (1996)
6. Bin Adnan, A.N.: Implementation of just in time production through Kanban system. *Int. Inst. Sci. Technol. Educ. Technical Report No 6*, 3, ISSN 2224-6096 (2013)
7. Moghimi, R., Anvari, A.: The strategic approach to exploration review on TQM and lean production. *J. Contemp. Manag.* **01**, 71–82 (2012)
8. Plenert, G.: *Reinventing Lean Introducing Lean Management into the Supply Chain*, chap. 6. Butterworth Heinemann (2006)
9. Saukkorippi, L.: *Perspectives on Non-valued Added Activities. Building Economics and Management*. Chalmers University of Technology, Sweden (2000)
10. Chen, J.C., Cheng, C.-H., Huang, P.B.: Supply chain management with lean production and RFID application: a case study. *Expert Syst. Appl.* **40**, 3389–3397 (2013)
11. Anvari, A., Mojahed, M., Zulkifli, N.: A group AHP-based tool to evaluate effective factors toward leanness in automotive industries. *J. Appl. Sci.* **17**, 3142–3151 (2011)
12. Parry, G.C., Turner, C.E.: Application of lean visual process management tools. *Prod. Plan. Control* **17**, 77–86 (2006)
13. Rahman, N.A.A., Sharif, S.M., Esa, M.M.: Lean manufacturing case study with Kanban system implementation. In: *International Conference on Economics and Business Research*, pp. 174–180. Interscience Publishers, U.K 7 (2013)
14. Laga junior, M., Godinho Filho, M.: Variations of the Kanban system: literature review and classification. *Int. Prod. Econ.* **125**, 13–21 (2010)
15. Yerian, L.M., Seestadt, J.A., Gomez, E.R., Marchant, K.K.: A Collaborative Approach to Lean Laboratory Workstation Design Reduces Wasted Technologist Travel, vol. 138, pp. 273–280. *American Society for Clinical Pathology*, 138 (2012)

# Energy

# Control Strategies for Transient Stability of Power Grid for Large Sudden Change in Electrical Load



Subash Chandra Parida, V. K. Tayal, and S. K. Sinha

## 1 Introduction

In modern day power market design is enthused by many criteria's such as global welfare, available transfer capacity (ATC) and market player and congestion management. Congestion management of transmission lines is important for power trading purposes. It is dependent on various criteria's such as line thermal limit, voltage limit, frequency limit, stability limit, protection equipment ratings and proper dispatch schedule [1]. The primary objective of multi area automatic generation control scheme is to meet the dispatch schedule and amend the correction on the schedule to avoid transmission line congestion. This can be achieved by amending the generation with respect to change in load [2]. In the other words, it is known as load frequency control. The reason behind frequency variation is dynamic load variation tracked by generation change. Interconnected power systems are basically connected through tie line arrangements & contains various sub systems to balance available power and transfer it [2]. The objective behind multi area automatic generation control unit is to monitor the deviation of present values of power and frequency with generation and load demand [1].

In multi area generation units, it is impractical to meet the equilibrium condition for generation and demand because of various reasons such as climatic conditions, change in utilization of power at various industry and process segments [3]. Area control error (ACE) is defined as the difference between present and available power within the control area of AGC [4, 5]. The inspiration of AGC is to minimize the area control error (ACE) and optimize the steady state performance. Traditional

---

S. C. Parida (✉) · V. K. Tayal · S. K. Sinha  
Amity University, Uttar Pradesh, Noida, Uttar Pradesh, India

© The Author(s), under exclusive license to Springer Nature Singapore Pte Ltd. 2022  
S. K. Natarajan et al. (eds.), *Recent Advances in Manufacturing, Automation, Design and Energy Technologies*, Lecture Notes in Mechanical Engineering,  
[https://doi.org/10.1007/978-981-16-4222-7\\_82](https://doi.org/10.1007/978-981-16-4222-7_82)

743

controllers such as PI and PID have been implemented to meet the objective because of stability issues. To enhance the controllability of AGC units, conventional PID controllers have been purposed. Conventional PID controller creates better response by diminishing non linearity and disturbances [6, 7]. It improves steady state stability, optimizes control action to sensible extent reduce non linearity and optimize the system dynamic performance.

## 2 System Modelling

The study of multi area interconnected power systems using PID controllers as in Fig. 1 has revealed considering two thermal units as area-1 & area-2 as shown in Fig. 2. The objective of control scheme is to diminish the difference in respective frequencies  $\Delta f_1$  &  $\Delta f_2$  of area-1 and area-2 respectively due to change in tie line power considering disturbances in load  $\Delta Pd_1$  and  $\Delta Pd_2$  [8].

The model equation for area control error (ACE<sub>1</sub>) taking biasing factor into consideration is given by [2, 8, 9]

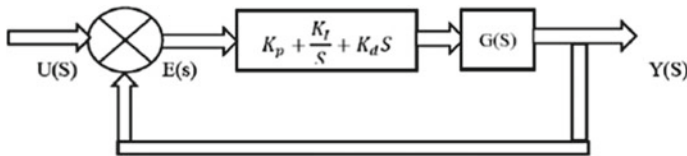


Fig. 1 PID control scheme

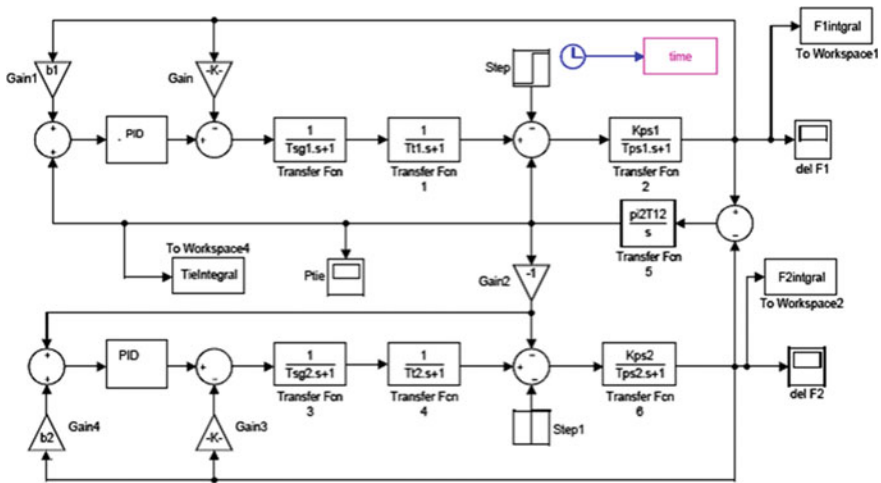


Fig. 2 Model of automatic generation control using PID control



$$ACE_1 = \Delta P_{12} + \Delta\omega B_1 \quad (1)$$

The model equation for area control error ( $ACE_2$ ) taking biasing factor into consideration is given by [2, 8, 9]

$$ACE_2 = \Delta P_{21} + \Delta\omega B_2 \quad (2)$$

where  $B_1$  &  $B_2$  are considered as biasing factor. It refers to amount collaboration involved during disturbances in the other area. The model equation for area control error ( $ACE_1$ ) is given by [9].

$$ACE_1 = \Delta P_{12} + \Delta\omega\beta_1 \quad (3)$$

The model equation for area control error ( $ACE_2$ ) is given by [9].

$$ACE_2 = \Delta P_{21} + \Delta\omega\beta_2 \quad (4)$$

The model equation for change in load for both areas is given by [9]

$$\Delta P_{12} = \frac{1}{\beta_1 + \beta_2} (-\Delta P_1\beta_2 + \Delta P_2\beta_1) \quad (5)$$

The model equation for change in frequency due to change in load for area-1 is given by [9]

$$\Delta f_1 = \frac{-\Delta P_{L1}}{\beta_1 + \beta_2} \quad (6)$$

The model equation for change in frequency due to change in load for area-2 is given by [9].

$$\Delta = \frac{-\Delta P_{L2}}{\beta_1 + \beta_2} \quad (7)$$

The change in load of both areas is given by

$$\Delta P_{m1} - \Delta P_{12} - \Delta P_{L1} = \Delta\omega D1 \quad (8)$$

$$\Delta P_{m2} - \Delta P_{12} - \Delta P_{L2} = \Delta\omega D2 \quad (9)$$

where  $D = \% \text{ Change in frequency due to percentage change in load (Frequency dependence load)}$  and  $R = \text{Frequency regulation (Change in frequency related to \% change in generation)}$ .  $\beta_1$  and  $\beta_2$  are frequency biasing factors for area-1 and area-2 of area-1 and area-2 respectively.  $\Delta P_{L1}$  and  $\Delta P_{L2}$  are increase in load of area-1 and area-2 respectively.  $\Delta P_1$  and  $\Delta P_2$  are the change in power flow from area-1 to

area-2 and vice versa.  $\Delta P_{m1}$  and  $\Delta P_{m2}$  are change in generation of area-1 & area-2 respectively. Specification of generators is of power rating: 220 MW, voltage rating: 11 kV, frequency rating: 60 Hz, Speed: 1500 RPM, model No. GE-aero-derivative, Fuel Type: Natural Gas, Manufacturer: GE.

### 3 Design of PID Controller

Traditional PID controller as shown in Fig. 1 are implemented in various industrial applications to minimize noise, improve steady state response & moderate settling time [5-7, 10, 11].

The model equation for PID controller is given by [6]

$$p(t) = K_P e(t) + K_P K_I \int e(t) dt + K_P K_D \frac{de(t)}{dt} \dots + P(0) \quad (10)$$

where  $P(0)$  is initial value of output,  $K_P$  is proportional gain constant,  $K_I$  is integral gain constant and  $K_D$  is derivative gain constants. In conventional PID controller, proportional mode works in proportion with output error, integral mode is based on history of error whereas derivative controller works on anticipatory action mode. It is because of composite control action the controller attains better steady state performance such as stability and accuracy by reducing offset error, oscillations and noise. Tuning is PID controller is carried out by using Ziegler-Nichols method [6].

PID:

The procedure for tuning of composite PID controller is as follows.

1. Put the system in closed loop.
2. Proportional gain will need to be increased up to oscillation in the output persist.
3. Peak time for each output needs to be monitored.
4. Proportional gain constant ( $K_P$ ), Integral gain constant ( $K_I$ ) & derivative gain constant ( $K_D$ ) needs to be monitored with period of oscillation. The modelling equation for calculation of gain constants are as follows.

$$\text{Fit} = \frac{K e^{-ts}}{\Delta s + 1} [0 \leq t_0/t \leq 0.5] \quad (11)$$

For proportional controller tuning,

$$K_f = \left(\frac{1}{k}\right) \left(\frac{T_o}{T}\right) - ts \quad (12)$$

For proportional- Integral (PI) controller tuning,

$$K_c = \left(\frac{0.9}{k}\right) \left(\frac{T_o}{T}\right) - 1 \quad (13)$$

For (PID) controller tuning,

$$K_{c1} = \left(\frac{1.2}{k}\right)\left(\frac{T_o}{T}\right) - 1 \tag{14}$$

where  $K$  is proportional gain,  $T$  = Effective process time constant and  $T_o$  = Effective process dead time.

### 4 Pi Controller Response

The step change in load of 0.01 pu has been applied for area-1 and area-2 with use of PI controller. The deviation of rise time, settling time, maximum peak value and no. of oscillations have been observed and interpreted in the Tables. The difference in frequency  $\Delta f_1$ ,  $\Delta f_2$  and Tie line power  $P_{Tie}$  under disturbance of 0.01 pu is depicted in the Figs. 3, 4 and 5 respectively. The actual values for quality parameters such as rise time, peak over shoot, settling time and no. of oscillations have been mentioned in the comparison Tables 1, 2 and 3.

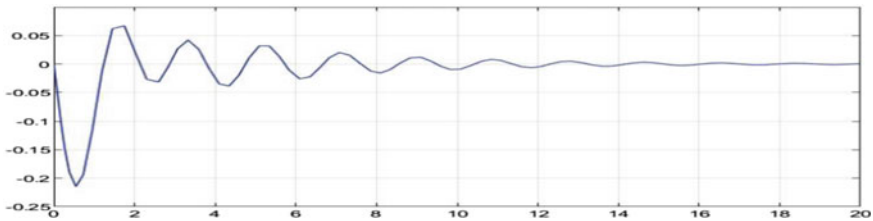


Fig. 3 Response of unit-1 (Frequency vs. time plot)

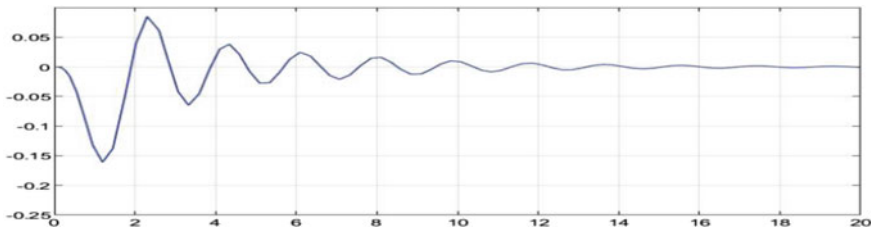
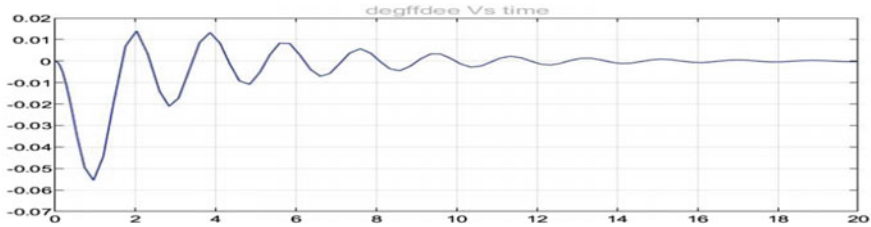


Fig. 4 Response of unit-2 (Frequency vs. time plot)



**Fig. 5** Response of tie line power (Tie line power vs. time plot)

**Table 1** Performance comparison (Figs. 3 and 6)

Parameter	PI controller	PID controller
Rise time (s)	1.75	1.6
Peak overshoot (%)	7.5	2.5
Settling time (s)	15	11
No of oscillations	8	5

**Table 2** Performance comparison (Figs. 4 and 7)

Parameter	PI controller	PID controller
Rise time (s)	2.25	1.8
Peak overshoot (%)	16	2
Settling time (s)	15	11
No of oscillations	9	6

**Table 3** Performance comparison (Figs. 5 and 8)

Parameter	PI controller	PID controller
Rise time (s)	2	2
Peak overshoot (%)	12	0.5
Settling time (s)	16	12
No of oscillations	9	6

## 5 Pid Controller Response

By Implementation of PID controller and step change in load of 0.01 pu to both area-1 and area-2, we have observed the deviations of rise time, settling time, maximum peak value and no. of oscillations and interpreted in the Tables. The frequency deviation  $\Delta f_1$ ,  $\Delta f_2$  and Tie line power  $P_{Tie}$  under disturbance of 0.01 pu is depicted in the corresponding Figs. 6, 7 and 8 respectively. Through comparison in Tables 1, 2 and 3, we have deliberated the actual values for quality parameters such as rise time, peak over shoot, settling time and no. of oscillations.

Through comparison of Tables 1, 2, 3 and 4, it has been indicated that overall performance of PID controller is better with respect to PI controller. With increment

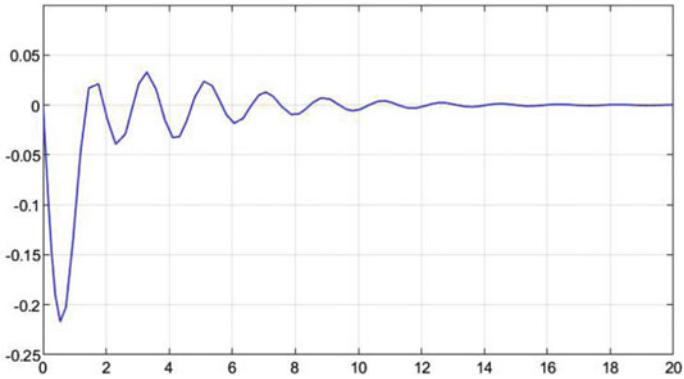


Fig. 6 Response of unit-1 (Frequency vs. time plot)

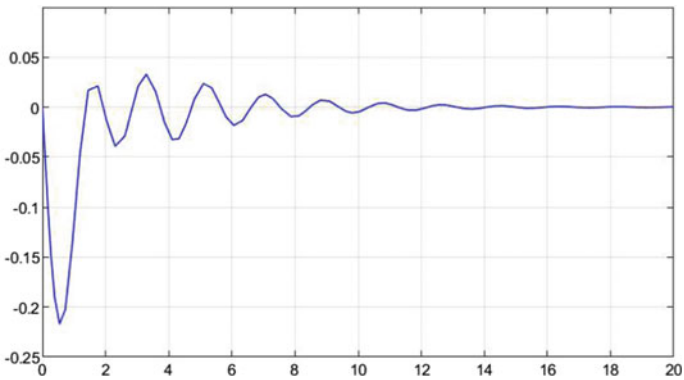


Fig. 7 Response of unit-2 (Frequency vs. time plot)

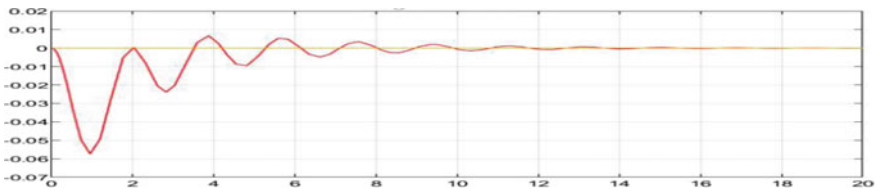


Fig. 8 Response of unit-2 (Tie line power vs. time plot)

of gain values, the response of PID controller is being enhanced whereas PI controller is going with reverse action. The setting of gain values in PID controller is a bit complex than that of PI controller.

**Table 4** Performance comparison (Figs. 3, 4, 5, 6, 7 and 8)

Criteria	PI controller	PID controller
Complexity (Operational)	Higher	Lower
Control Action	Large disturbance and noise in the response	Comparatively low disturbance and noise in the response
Speed (operational)	Slower due to transportation delay	Better than previous
Rise time	Higher	Lower
Max peak	Higher	Comparatively better
Stability time	Higher	Comparatively lower

## 6 Conclusion

In this research study, we have modelled various conventional control schemes with AGC units such as integral control, PI control and PID control through MATLAB SIMULINK. The results of PI and PID controllers have been interpreted through comparison Table as shown in Table 4. The performance of the system has been assessed through various technical parameters such as rise time, peak over shoot, oscillation level and settling time. The PID control stability aspect and speed of operation has produced better impact than PI controller. The projected PID controller has provided the better response time in control action of AGC units for step change in load. The scheme is economic and easy to implement. As the reliability of power supply depends on low frequency deviation and proper terminal voltage, this method of PID control will be able to achieve the desired objective. Hence, to maintain security and quality aspect of power system, this method will enhance the network stability aspect.

## References

1. Patel, R., Li, C., Meegahapola, L., McGrath, B., Yu, X.: Enhancing optimal automatic generation control in a multi-area power system with diverse energy resources. *IEEE Trans. Power Syst.* **34**, 0885–8950 (2019)
2. Khamari, J.D., Sahu, R.K., Gorripotu, T.S., Panda, S.: Automatic generation control of power system in deregulated environment using hybrid TLBO and pattern search technique. *Ain Shams Eng. J.* **10** 2090–4479 (2019)
3. Moghadam, M.R.V., Ma, R.T., Zhang, R.: Distributed frequency control in smart grids via randomized demand response. *IEEE Trans. Smart Grid* **5**, 2798–2809 (2014)
4. Tayal, V.K., Lather, J.S., Sharma, P., Sinha, S.K.: Power system stability enhancement using fuzzy logic based power system stabilizer. In: *Advances in Proceedings of the Third International Conference on Soft Computing for Problem Solving Intelligent Systems and Computing*, vol. 258, 55–68 (2014)
5. Sinha, S.K., Prasad, R., Patel, R.N.: PSO tuned combined optimal fuzzy controller for AGC of two area interconnected power system. In: *IEEE conference on World Congress on Nature and Biologically Inspired Computing*, 537–542 (2009)

6. Verma, R., Pal, S.: Intelligent automatic generation control of two-area hydrothermal power system using ANN and fuzzy logic. *IEEE Comput. Soc. (CSNT 2013)* **13**, 7695–4598 (2013)
7. Kaur, H., Kumar, P., Kumar, S., Vijay, S., Tayal, V.K.: Automatic generation control using PSO optimized PI and optimal fuzzy controller. In: *Annual IEEE India Conference (INDICON)*, 1–6 (2015)
8. Gupta, I., Hemant, M.: A case study on load frequency control with automatic generation control on a two area network using MiPower. *IEEE Trans. Power Syst.* **33**, 5386–6159 (2018)
9. Abass, Y.A., Al-Awami, A.T., Jamal, T.: Integrating automatic generation control and economic dispatch for microgrid real-time optimization. *IEEE Conf.* **10**, 1944–9933 (2016)
10. Saikia, L.C., Nanda, J., Mishra, S.: Performance comparison of several classical controllers in AGC for multi-area interconnected thermal system. *Int. J. Electr. Power Energy Syst.* **33**, 394–401 (2011).
11. Ulbig, A., Arnold, M., Chatzivasileiadis, S., Andersson, G.: Framework for multiple time-scale cascaded MPC application in power systems. In: *Proceedings of 18th IFAC World Congress*, 10472–10480 (2011)
12. Masrur, H., Erdoush, A., Rabbani, M.G.: Automatic generation control of two area power system with optimized gain parameters. *IEEE Trans.* **15**, 4673–6676 (2015)
13. Srinivasa Rao, C.: Design of artificial intelligent controller for automatic generation control of two area hydrothermal system. *Int. J. Electr. Comput. Eng. (IJECE)* **2**, 183–190 (2012)
14. Rahman, A., Saikia, L.C., Sinha, N.: Load frequency control of a hydrothermal system under deregulated environment using biogeography-based optimised three-degree-of-freedom integral-derivative controller. *IET Gener. Transm. Distrib.* **9**, 2284–2293 (2015)
15. Anand, B., Jeyakumar, A.E.: Load frequency control of interconnected hydro-hydro system with fuzzy logic controll. In: *International Conference on Process Automation, Control and Computing (PACC)*, 1–4 (2011)
16. Chakraborty, D.W.T., Rodgers, M: Automatic generation control using an energy storage system in a wind park. *IEEE Trans. Power Syst.* **33**, 198–205 (2018)
17. Jayawardene, I., Wei, Y., Kumar, G., Gamoorthy, V.: Optimized automatic generation control in a multi-area power system with particle swarm optimization. *IEEE Trans.* **17**, 5386–2726 (2017)
18. Sathans, S., Swarup, A.: Intelligent load frequency control of two area interconnected power system and comparative analysis. In: *IEEE Xplore, International Conference on Communication Systems and Network Technologies (CSNT 2011)*, 360–365 (2011)

# Improved Control Design for AGC of Two Area Thermal-Thermal Power System Using Hybrid Fuzzy-PID Control



Subash Chandra Parida, V. K. Tayal, and S. K. Sinha

## 1 Introduction

The power industries across the globe are experiencing a fundamental change in business and operational model where the vertical integrated utilities are being unbundled and opened up for competition with private players. Automatic generation control not only enhances the operational ability of power sector but also it provides flexibility to an independent system operator to balance the outputs of various generating stations and grids in a manner of optimal dispatch with respect to load variation without violating equipment protection limits, maintaining safety and security of power system [1]. The motto of multi area automatic generation control scheme is to encounter the area control errors in the dispatch schedule and advise the corrective action through controllers to expedite the correction factors to avoid the transmission line congestion. This can be achieved by amending the generation with respect to change in load [2]. In the other words, it is known as load frequency control. The reason behind frequency variation is dynamic load variation tracked by generation change. Interconnected power systems are basically connected through tie line arrangements and contain various sub systems to balance available power and transfer it [2]. The aim of multi area automatic generation control unit is to adequately observe the deviation encountered of present values of power and frequency with generation and load demand [1].

In multi area generation units, it is unreasonable to adopt the equilibrium condition for generation and demand because of various reasons such as climatic condition, change in utilization of power at various industry and change in demand process segments [3]. Area control error (ACE) is defined as the difference between present and available power within the control area of AGC [4, 5]. The inspiration of AGC

---

S. C. Parida (✉) · V. K. Tayal · S. K. Sinha  
Amity University, Uttar Pradesh, Noida, Uttar Pradesh, India



is to minimize the area control error (ACE) and optimize the steady state performance. Hybrid controllers Fuzzy—PID controllers have been executed to encounter the objective because of stability issues. Hybrid controllers Fuzzy—PID controller creates better response by diminishing non linearity and disturbances [6, 7]. It improves steady state stability, optimize control action to a sensible extent reduce non linearity and optimize the system dynamic performance.

## 2 System Modelling

The study of multi area interconnected power systems has revealed considering two thermal units as area-1 & area-2 as shown in Fig. 1. The objective of control scheme is to diminish the difference in respective frequencies  $\Delta f_1$  &  $\Delta f_2$  of area-1 and area-2 respectively due to change in tie line power considering disturbances in load  $\Delta P_{d1}$  and  $\Delta P_{d2}$  [8]. The model equation for area control error (ACE<sub>1</sub>) taking biasing factor into consideration is given by [2, 5, 8].

$$ACE_1 = \Delta P_{12} + \Delta \omega B_1 \tag{1}$$

The model equation for area control error (ACE<sub>2</sub>) taking biasing factor into consideration is given by [2, 5, 8]

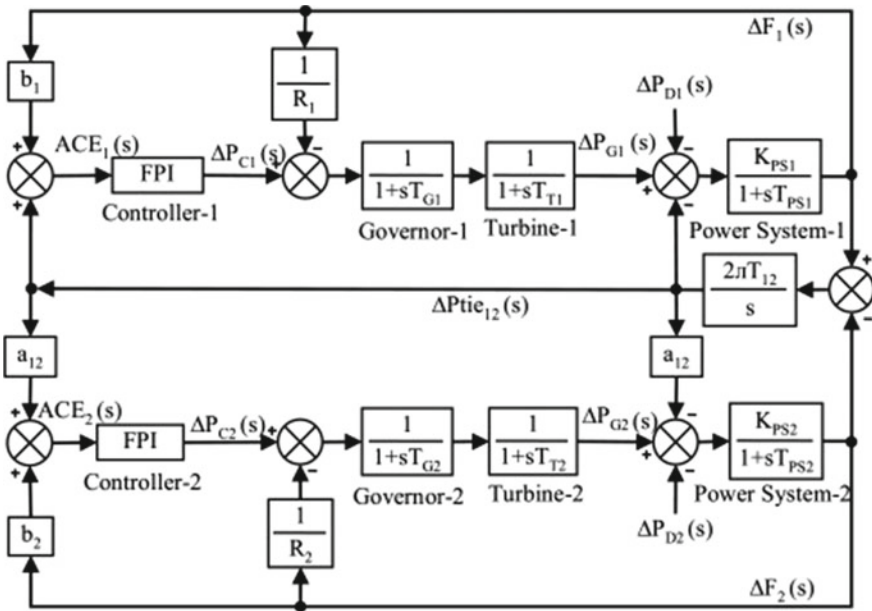


Fig. 1 Model of automatic generation control using hybrid fuzzy—PID control

$$ACE_2 = \Delta P_{21} + \Delta \omega B_2 \quad (2)$$

where  $B_1$  &  $B_2$  are considered as biasing factor. It refers to amount of collaboration involved during disturbances in the other area. The model equation for area control error ( $ACE_1$ ) is given by [5].

$$ACE_1 = \Delta P_{12} + \Delta \omega \beta_1 \quad (3)$$

The model equation for area control error ( $ACE_2$ ) is given by [5].

$$ACE_2 = \Delta P_{21} + \Delta \omega \beta_2 \quad (4)$$

The model equation for change in load for both areas is given by [5]

$$\Delta P_{12} = \frac{1}{\beta_1 + \beta_2} (-\Delta P_1 \beta_2 + \Delta P_2 \beta_1) \quad (5)$$

The model equation for change in frequency due to change in load for area-1 is given by [5]

$$\Delta f_1 = \frac{-\Delta P_{L1}}{\beta_1 + \beta_2} \quad (6)$$

The model equation for change in frequency due to change in load for area-2 is given by [5].

$$\Delta f_2 = \frac{-\Delta P_{L2}}{\beta_1 + \beta_2} \quad (7)$$

The change in load of both areas is given by

$$\Delta P_{m1} - \Delta P_{12} - \Delta P_{L1} = \Delta \omega D1 \quad (8)$$

$$\Delta P_{m2} - \Delta P_{12} - \Delta P_{L2} = \Delta \omega D2 \quad (9)$$

where  $D = \% \text{ Change in frequency due to percentage change in load (Frequency dependence load)}$  and  $R = \text{Frequency regulation (Change in frequency related to \% change in generation)}$ .  $\beta_1$  and  $\beta_2$  are frequency biasing factors for area-1 and area-2 of area-1 and area-2 respectively.  $\Delta P_{L1}$  and  $\Delta P_{L2}$  are increase in load of area-1 and area-2 respectively.  $\Delta P_1$  and  $\Delta P_2$  are the change in power flow from area-1 to area-2 and vice versa.  $\Delta P_{m1}$  and  $\Delta P_{m2}$  are change in generation of area-1 & area-2 respectively, FPI is the fuzzy-PID hybrid controller. Refer Fig. 1 for control scheme of AGC with hybrid controller.

Specification of generators is of power rating: 220 MW, voltage rating: 11 kV, frequency rating: 60 Hz, Speed: 1500 RPM, model No. GE-aero-derivative, Fuel Type: Natural Gas, Manufacturer: GE.

### 3 Design of Fuzzy—PID Hybrid Controller

Traditional PID controllers are implemented in various industrial applications to minimize noise, improve steady state response & moderate settling time [6,7,9–11]. The model equation for PID controller is given by [6]

$$p(t) = K_p e(t) + K_p K_i \int e(t) dt + K_p K_d \frac{de(t)}{dt} \dots + P(0) \tag{10}$$

where  $P(0)$  is initial value of output,  $K_p$  is proportional gain constant,  $K_i$  is integral gain constant and  $K_d$  is derivative gain constants. In conventional PID controller, proportional mode works in proportion with output error, integral mode is based on history of error whereas derivative controller works on anticipatory action mode.

The main objective of combinational control [12, 13] is to optimize the area control error thereby stabilizing the power flow between two areas and maintaining the frequency deviation of two areas in an acceptable predefined limit. The non linearity involved in fuzzy controller (Ref. Fig. 2) are diluted through PID controller by adjusting Proportional gain ( $K_p$ ), derivative gain ( $K_d$ ) and integral gain ( $K_i$ ). Fuzzy logic comprises classical two-value logic and multivalued logic systems, as well as probabilistic logic. Fuzzy logic provides a smooth transition between members and nonmembers. Function of a fuzzifier is to transform crisp value to fuzzy value. Fuzzy knowledge base retains the knowledge about fuzzy input and output relationships. It contains membership function that outlines the input variables to fuzzy rule base and output variables to regulate the plant. Fuzzy rule base stores the knowledge about operation in the process domain. It simulates human decisions by approximate reasoning. Defuzzification is a process to map the action of fuzzy control demarcated over the discourse of output into a space of crisp (Non-fuzzy) control actions.

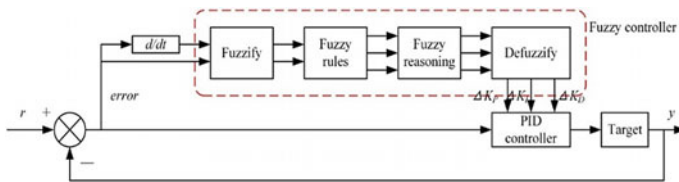


Fig. 2 Fuzzy—PID hybrid control scheme

### 4 PI Controller Response

The step change in load of 0.01 pu has been applied for area-1 and area-2 with the use of PI controller. The deviation of rise time, settling time, maximum peak value and no. of oscillations have been observed and interpreted in the Tables. The difference in frequency  $\Delta f_1$ ,  $\Delta f_2$  and Tie line power  $P_{Tie}$  under disturbance of 0.01 pu is depicted in Figs. 3, 4 and 5 respectively. The actual values for quality parameters such as rise time, peak over shoot, settling time and no. of oscillations have been mentioned in the comparison Tables 1, 2 and 3.

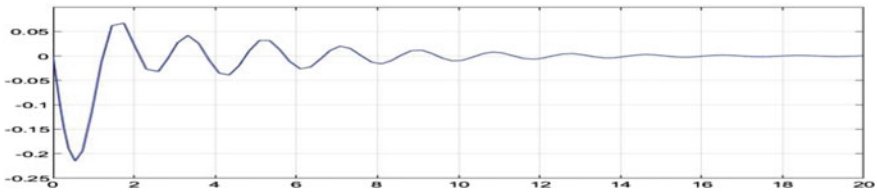


Fig. 3 Response of unit-1 (Frequency vs. time plot)

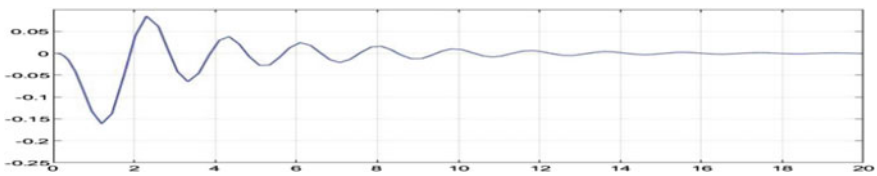


Fig. 4 Response of unit-2 (Frequency vs. time plot)

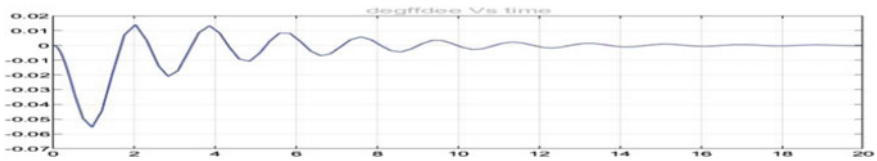


Fig. 5 Response of tie line power (Tie line power vs. time plot)

Table 1 Performance comparison of frequency (Area-1)

Parameter	PI controller	PID controller	Fuzzy-PID
Rise time (s)	1.75	1.6	0.2
Peak overshoot (%)	7.5	2.5	0.1
Settling time (s)	15	11	4
No of oscillations	8	3	3

**Table 2** Performance comparison of frequency (Area-2)

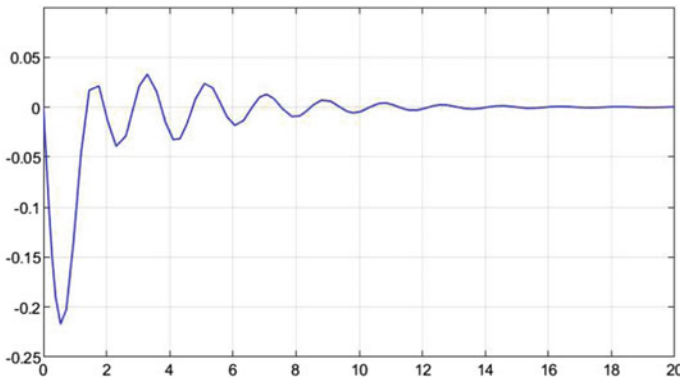
Parameter	PI controller	PID controller	Fuzzy-PID
Rise time (s)	2.25	1.8	0.2
Peak overshoot (%)	16	2	0.1
Settling time (s)	15	11	4
No of oscillations	8	6	3

**Table 3** Performance comparison for tie line power (Area-1 & 2)

Parameter	PI controller	PID controller	Fuzzy-PID
Rise time (s)	2	2	0.1
Peak overshoot (%)	12	0.5	0.1
Settling time (s)	16	12	4
No of oscillations	8	6	3

### 5 PID Controller Response

By Implementation of PID controller and step change in load of 0.01 pu to both area-1 and area-2, we have observed the deviations of rise time, settling time, maximum peak value and no. of oscillations and interpreted in the Tables. The frequency deviation  $\Delta f_1$ ,  $\Delta f_2$  and Tie line power  $P_{Tie}$  under disturbance of 0.01 pu is depicted in the corresponding Figs. 6, 7 and 8 respectively. Through comparison in Tables 1, 2 and 3, we have deliberated the actual values for quality parameters such as rise time, peak over shoot, settling time and no. of oscillations. The gain values of PID controller is as  $K_p = 50$ ,  $K_I = 100$  and  $K_D = 200$ .



**Fig. 6** Response of unit-1 (Frequency vs. time plot)

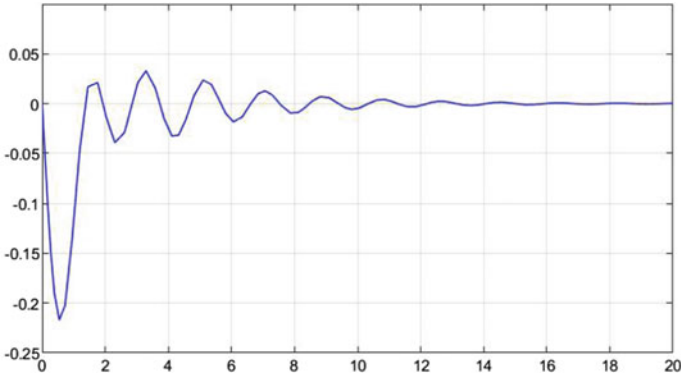


Fig. 7 Response of unit-2 (Frequency vs. time plot)

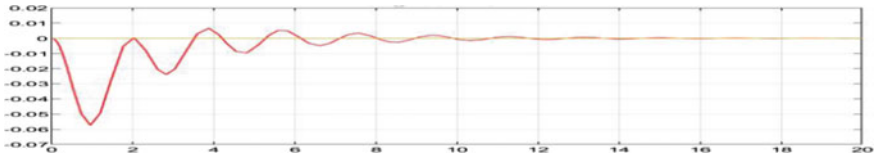


Fig. 8 Response of unit-2 (Tie line power vs. time plot)

### 6 Fuzzy—PID Hybrid Controller Response

By Implementation of fuzzy—PID controller is shown in the Fig. 2 and step change in load of 0.01 pu to both area-1 and area-2, we have observed the deviations of rise time, settling time, maximum peak value and no. of oscillations and interpreted in the Tables. The frequency deviation  $\Delta f_1$ ,  $\Delta f_2$  and Tie line power  $P_{Tie}$  under disturbance of 0.01 pu is depicted in the corresponding Figs. 9, 10 and 11 respectively. Through comparison in Tables 1, 2 and 3, we have deliberated the actual values for quality parameters such as rise time, peak over shoot, settling time and no. of oscillations. Gain Values of PID controller is  $K_D = 600$ ,  $K_I = 650$  and  $K_D = 800$ .

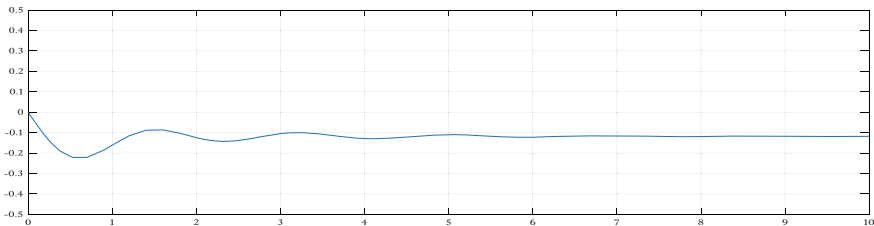
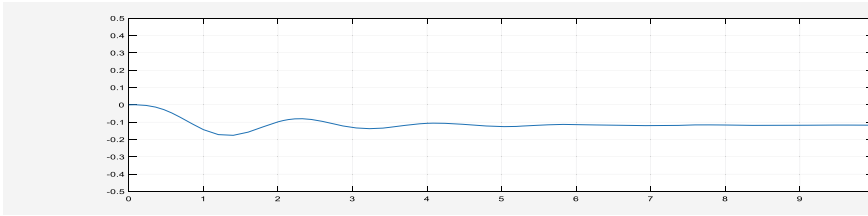
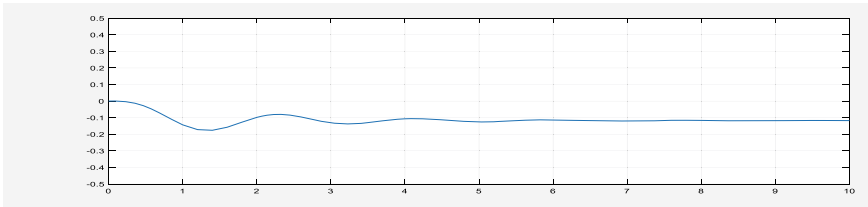


Fig. 9 Response of unit-1 (Frequency vs. time plot)



**Fig. 10** Response of unit-2 (Frequency vs. time plot)



**Fig. 11** Response of unit-2 (Tie line power vs. time plot)

Through comparison of Tables 1, 2, 3 and 4, it has been indicated that overall performance of fuzzy-PID controller is better with respect to PI controller and PID controller is superior to PID controller. With increment of gain values, the response of PID controller is being enhanced whereas PI controller is going with reverse action. The setting of gain values in PID controller is a bit complex than that of PI controller.

**Table 4** Performance comparison

Criteria	PI controller	PID controller	Fuzzy-PID
Complexity (Operational)	Higher	Lower	More than PID
Control Action	Large disturbance and noise in the response	Comparatively low disturbance and noise in the response	Comparatively low disturbance and noise
Speed (operational)	Slower due to transportation delay	Better than previous	Better than previous
Rise time	Higher	Lower	Extensively better than previous
Max peak	Higher	Comparatively better	Extensively better than previous
Stability time	Higher	Comparatively lower	Extensively better than previous
Output variation	Higher	Better	Extensively better than previous

## 7 Conclusion

In this research study, we have modelled various conventional control schemes with AGC units such as integral control, PI, PID and hybrid (fuzzy- PID) control through MATLAB SIMULINK. The significance of MATLAB simulation result of all controllers is to catch the best performance in between the available controllers by comparing and interpreting the controller performance through the quantified result obtained inside the comparison table. The enactment significance of the AGC system has been assessed through various technical parameters such as rise time, peak over shoot, oscillation level and settling time. The fuzzy—PID hybrid control stability aspect & speed of operation has produced better impact than PI and PID controller. The projected hybrid controller has provided a better response time in control action of AGC units for step change in load. The scheme is economic and easy to implement. As the reliability of power supply depends on low frequency deviation and proper terminal voltage, this method of hybrid fuzzy—PID control will be able to achieve the desired objective. Hence, to maintain security and quality aspect of power system, this method will enhance the network stability aspect.

## References

1. Patel, R., Li, C., Meegahapola, L., McGrath, B., Yu, X.: Enhancing optimal automatic generation control in a multi-area power system with diverse energy resources. *IEEE Trans. Power Syst.* **34**, 0885–8950 (2019)
2. Khamari, J.D., Sahu, R.K., Gorripotu, T.S., Panda, S.: Automatic generation control of power system in deregulated environment using hybrid TLBO and pattern search technique. *Ain Shams Eng. J.* **10**, 2090–4479 (2019)
3. Moghadam, M.R.V., Ma, R.T., Zhang, R.: Distributed frequency control in smart grids via randomized demand response. *IEEE Trans. Smart Grid* **5**, 2798–2809 (2014)
4. Masrur, H., Erdoush, A., Rabbani, M.G.: Automatic generation control of two area power system with optimized gain parameters. *IEEE Trans.* **15**, 4673–6676 (2015)
5. Abass, Y.A., Al-Awami, A.T., Jamal, T.: Integrating automatic gen. control and economic dispatch for microgrid real-time optimization. *IEEE Conf.* **10**, 1944–9933 (2016)
6. Verma, R., Pal, S.: Intelligent automatic generation control of two-area hydrothermal power system using ANN and fuzzy logic. *IEEE Comput. Soc. (CSNT 2013)* **13**, 7695–4598 (2013)
7. Ulbig, A., Arnold, M., Chatzivasileiadis, S., Andersson, G.: Framework for multiple time-scale cascaded MPC application in power systems. In: *Proceedings of 18th IFAC World Congress*, 10472–10480 (2011)
8. Gupta, I., Hemant, M.: A case study on load frequency control with automatic generation control on a two area network using MiPower. *IEEE Trans. Power Syst.* **33**, 5386–6159 (2018)
9. Srinivasa Rao, C.: Design of artificial intelligent controller for automatic generation control of two area hydrothermal system. *Intl. J. Electr. Comp. Eng. (IJECE)* **2**, 183–190 (2012)
10. Rahman, A., Saikia, L.C., Sinha, N.: Load frequency control of a hydrothermal system under deregulated environment using biogeography-based optimised three-degree-of-freedom integral-derivative controller. *IET Gener. Transmiss. Distrib.* **9**, 2284–2293 (2015)
11. Sinha, S.K., Prasad, R., Patel, R.N.: PSO tuned combined optimal fuzzy controller for AGC of two area interconnected power system. In: *IEEE Conference on World Congress on Nature and Biologically inspired Computing*, 537–542 (2009)



12. Anand, B., Jeyakumar, A.E.: Load frequency control of interconnected hydro-hydro system with fuzzy logic controlled. In: International Conference on Process Automation, Control and Computing (PACC), 1–4 (2011)
13. Tayal, V.K., Lather, J.S., Sharma, P., Sinha, S.K.: Power system stability enhancement using fuzzy logic based power system stabilizer. In: Advances in Proceedings of the Third International Conference on Soft Computer for Problem Solving Intelligent Systems and Computing, vol. 258, 55–68 (2014)
14. Saikia, L.C., Nanda, J., Mishra, S.: Performance comparison of several classical controllers in AGC for multi-area interconnected thermal system. *Int. J. Electr. Power Energy Syst.* **33**, 394–401 (2011)

# Experimental Investigation of a Line Focus Solar Collector Using Flat and Parabolic Reflector



Gunjan Kumar and Hemant Gupta

## 1 Introduction

The concentrated solar power (CSP) system is mainly used to produce process heat in many applications. This system is best suitable where the intensity of solar insolation and the number of sunny days are high [1]. CSP systems are capable to produce the steam at a temperature in the range of 400–1000 °C by using solar collectors accompanied by the number of reflecting mirrors [2]. Solar collectors are devices that absorb the solar insolation to collect the heat energy. The thermal energy thus collected is carried away by a moving fluid and used either for the operation of the process or for electricity generation. The solar collectors are mainly classified as line focus and point focus collectors [3]. Parabolic trough collector (PTC) and linear Fresnel collector (LFC) are the two main collectors which come under line focus technology. In line focus technology, sun rays are reflected into the receiver where a line focus is created and maintained [4]. PTC technology consists of a reflector in the shape of a parabolic trough and one absorber which is placed in the focal line of trough. Reflectors direct solar radiation into the receiver efficiently. This system has many advantages over LFC technology such as optical performance as their trough elements may be placed along the common focal line [5]. LFC system comprises the fixed receiver mounted separately and tracking is not provided to the receiver. Radiations are directed to the receiver by one axis tracking flat or slightly curved reflectors that are placed at a lower elevation. Receivers may be combined with a secondary concentrator to increase the heat flux [6, 7]. This system is cost-effective because of simple geometry. In this technology, direct steam generation eliminates the need for heat exchangers [8]. PTC systems are though matured technology but LFC systems have been recognized to reduce the cost of electricity [9, 10]. LFC has

---

G. Kumar (✉) · H. Gupta  
Shroff S R Rotary Institute of Chemical Technology, Ankleshwar, India  
Gujarat Technological University, Ahmedabad, India

**Table 1** Comparison of modified prototype with PTC and LFC

Parameters	PTC	LFC	Modified prototype	References
Efficiency	High	Less	Moderate	[21]
Cost effectiveness	High	Less	Moderate	[11, 12]
Receiver position	Mobile	Fixed	Fixed	[12, 13]
HTF choice	Limited	Multiple	Multiple	[12]

less capital cost because of light and simple structural support, flat geometric reflectors and fixed absorber without moving joints [11, 12]. There are certain traditional benefits of the LFC system such as small reflector size and fixed receiver position [13].

PTC systems need to focus on increasing the operating temperature. The next generation heat transfer fluids (HTFs) for CSP technology with a PTC system should be developed at a low cost without toxins. Thermal analysis of the PTC system shows that a continual improvement in thermal efficiency can be achieved by optimizing the key parameters such as absorber materials, absorber coatings and various working fluids [14, 15].

It is observed that current line focus technologies have some disadvantages such as a mobile receiver in PTC, the efficiency of LFC, the selection of HTFs in PTC, etc. In this work, an attempt has been made to meet these challenges by utilizing the combined effect of flat and parabolic reflectors. The objective of this project is to develop and examine a modified prototype for thermal performance. The expected advantages of the proposed modification over PTC and LFC are shown in Table 1.

## 2 Design of Prototype

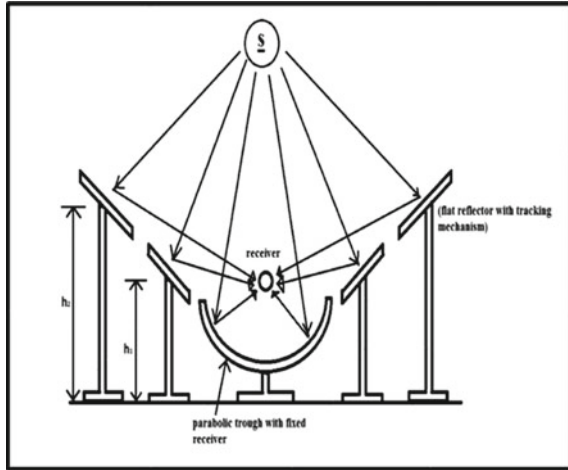
The novel modification of the work is illustrated in Fig. 1. A modified collector has a combination of a parabolic trough and four flat reflectors. The reflectors are employed to direct the radiations into a receiver located in the focal line of the parabolic trough. A single-axis tracking device powered by a solar panel is fitted with flat reflectors. Tracking is not provided to the parabolic reflector to reduce the cost.

Flat facets and parabolic trough are dedicated to direct the solar radiation into the receiver. There are four flat reflectors and one parabolic trough of equal length. A cylindrical receiver is kept in the focal line of the parabolic trough.

The tilt of flat reflector is adjusted to ensure maximum radiations reaching receiver. An appropriate gap is maintained between the reflectors to avoid the shading and blocking effect. Three parameters, namely position ( $X_n$ ), tilt ( $\theta_n$ ), and gap ( $S_n$ ) can then define each flat reflector.

The following expressions (1–4) are used to obtain these parameters using basic geometrical optics [16–18].

**Fig. 1** Schematic of the modified prototype



$$\theta_n = 0.5 \tan^{-1} \left[ \left\{ S_n + \left( \frac{b1}{2} \right) \cos \theta_{n-1} \right\} / \left\{ h - \left( \frac{b1}{2} \right) \sin \theta_{n-1} \right\} \right] \quad (1)$$

$$S_n = b1 \sin \theta_{n-1} \tan (2\theta_n + \xi_0) \quad (2)$$

$$X_n = X_{n-1} + b1 \cos \theta_{n-1} + S_n \quad (3)$$

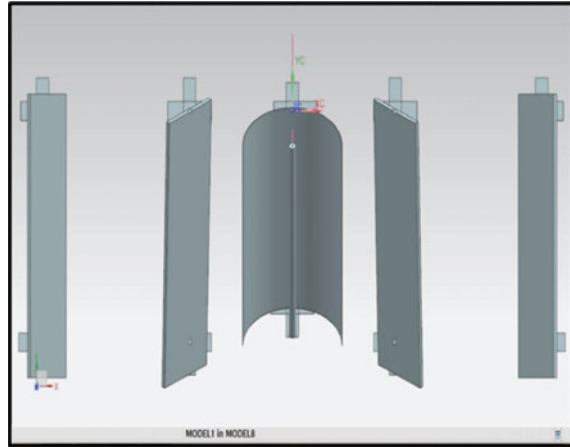
$$Q_r = (A_c) I \rho \tau \gamma \alpha \quad (4)$$

where,  $A_c$  is total area of reflector,  $I$  is global solar radiation,  $\rho$  is specular reflectance,  $\tau$  is transmittance of the glass cover,  $\gamma$  is fraction of reflected radiation and  $\alpha$  is absorbance of the receiver surface.

Assembly of the prototype is illustrated in Fig. 2 which is drafted using Solidworks software. The prototype has been designed assuming the width,  $b_1$  and length,  $L$  of the flat reflector to be 0.5 m and 1.2 m respectively [19]. The aperture of the parabolic trough has a length of 1.2 m and a width,  $b$  is 0.8 m. The concentration ratio is taken as 24. The receiver is placed on the focal line of the parabolic trough which is 0.45 m above the rim of the parabola. The aperture area of a parabolic trough is 0.96 m<sup>2</sup>. The position, tilt, and gap of flat reflectors could be determined with the help of Eqs. (1–3). Considering the different radiative absorber parameters that can be estimated using Eq. (4) [18], the available heat energy  $Q_r$  on the receiver is determined at different concentration ratios of the Fresnel concentrating collector.

The instantaneous collector thermal efficiency,  $\eta$  of the solar concentrator–receiver system is evaluated by Eq. (5) [17, 20].

$$\eta = \frac{m_f c_p (T_O - T_I)}{Q_r} \quad (5)$$

**Fig. 2** Draft of prototype

where,  $T_o$  and  $T_i$  are the corresponding water temperature of the outlet and inlet. The water mass flow rate is  $m_f$  and specific heat capacity of water is  $C_p$ .

### 3 Prototype Description and Experimental Procedure

The prototype is developed and tested for thermal performance evaluation at Ankleshwar, Gujarat, India. The prototype consists of one parabolic trough accompanied by one fixed receiver and four flat reflectors aiming to focus at the receiver. Single-axis tracking powered through the solar panel is provided to flat reflectors only. The reflectors are auto tracked in east–west direction. Solar rays are directed to the fixed receiver by reflectors and thus heat gets transmitted to the working fluid.

Tap water is used as HTF and its mass flow rate is kept as low as 0.033 kg/s. The mass flow rate is calculated by using a marked beaker and stopwatch. A regulating valve is mounted across the receiver to regulate and maintain the flow rate. The movement of every flat plate reflector is controlled by a solar tracking system working autonomously with the controller. The cylindrical absorber is enveloped into a non-evacuated glass cover. A photograph of the newly designed prototype is shown in Fig. 3. The instruments used during the experiment for measuring parameters like solar radiations, temperatures, and wind velocities are listed in Table 2.

### 4 Results and Discussion

The experimental results and thermal analysis of a newly developed prototype are recorded in this section. The setup is tested in April 2019 for the climatic condition of Ankleshwar, Gujarat, India. The measurement and assessment of performance



**Fig. 3** Photograph of developed prototype

**Table 2** Instruments used during experimentation

S. No.	Name of instruments	Properties of instruments	Parameters
01	Solar power meter	Accuracy: $\pm 10 \text{ W/m}^2$ , resolution: $0.1 \text{ W/m}^2$ , range: $2000 \text{ W/m}^2$	Solar radiation
02	RTD sensor $100 \Omega$ PLT 4 wire	Accuracy: $\pm 1 \text{ }^\circ\text{C}$ , range: $0\text{--}1200 \text{ }^\circ\text{C}$	Temperature
03	Anemometer	Accuracy: $\pm 5\%$ , range $0.4\text{--}30 \text{ m/s}$	Wind velocity

parameters are displayed in Table 3. The parameters such as water inlet temperature,  $T_i$ , exit temperature,  $T_o$ , wind velocity,  $V$  and global solar radiation,  $I$  are measured periodically through calibrated and precise instruments. With the aid of measured parameters, heat absorbed by the receiver,  $Q_r$  and water,  $Q_a$  is determined. In the same situations, experimental data is also gathered for PTC. To understand the thermal behavior of a prototype, test results are compared. The efficiency,  $\eta$  and temperature difference,  $\Delta T$  are compared and recorded in Table 4 for different durations. The modified collector has more temperature difference each time due to additional tracking flat reflectors. Due to lower ratio of temperature difference and aperture area, the efficiency of a modified collector is noted a little less.

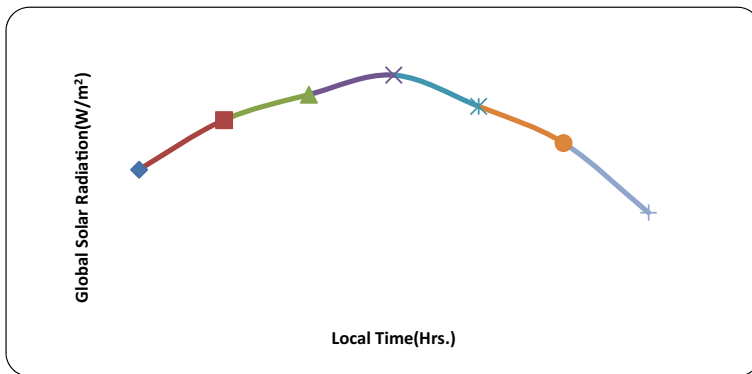
The global solar radiations at the test location are measured and Fig. 4 shows its variations. At 13:00 h, maximum solar radiation of  $1100 \text{ W/m}^2$  is observed. For the

**Table 3** Experimental results of prototype on the 16th April 2019

Local time (H.)	$T_i$ (°C)	$T_o$ (°C)	$\Delta T$ (°C)	$V$ (m/s)	$I$ (W/m <sup>2</sup> )	$Q_r$ (W)	$Q_a$ (W)
10:00	25.8	29.2	3.4	2.22	680	1942.08	473.259
11:00	26.1	33.1	7.0	2.22	900	2570.40	974.358
12:00	27.2	37.8	10.6	1.77	1013	2893.12	1475.456
13:00	29.0	41.4	12.4	1.33	1100	3141.60	1726.006
14:00	29.2	37.2	8.0	2.61	961	2744.61	1113.552
15:00	28.2	32.7	4.5	2.88	798	2279.08	626.373
16:00	28.1	30.1	2.0	2.44	489	1396.58	278.388

**Table 4** Performance comparison with PTC

Collectors	Time (H.)	10:00	11:00	12:00	13:00	14:00	15:00	16:00
Modified	$\Delta T$ (°C)	03.40	07.00	10.60	12.40	08.00	04.50	02.00
	$\eta$ (%)	24.36	37.90	50.99	54.94	40.57	27.48	19.93
Parabolic trough	$\Delta T$ (°C)	02.60	05.90	08.80	11.00	06.60	03.80	01.30
	$\eta$ (%)	25.30	38.20	52.40	56.00	41.80	28.30	20.90



**Fig. 4** Global solar radiation variations on 16th April, 2019

collectors, inlet and exit temperatures of water are monitored regularly. The variance of temperature variations for a day in both collectors is shown in Fig. 5. For an updated one, the excess temperature difference is observed each time. It is observed that the maximum difference between the collectors is 1.8 °C, while the average is 6.85 °C.

The thermal efficiency at various times is determined and shown in Fig. 6 for the same day. The performance pattern for both collectors is close, but there is little deviation between them at all times. The overall thermal efficiency at 13:00 h is 54.94%, while the minimum thermal efficiency at 16:00 h is 19.93%.

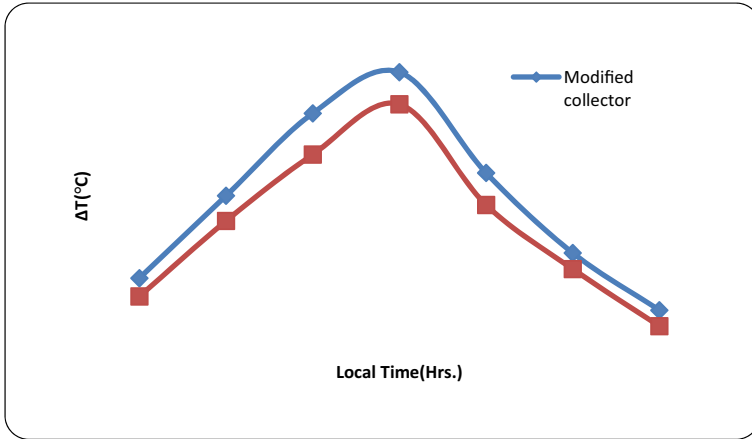


Fig. 5 Temperature difference variations on 16th April 2019

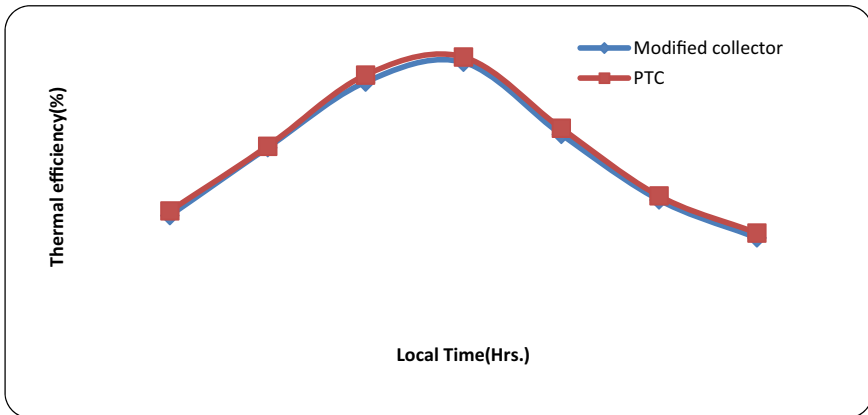


Fig. 6 Thermal efficiency plot on 16th April 2019

## 5 Conclusion

There are several benefits as well as drawbacks to current line concentration techniques. The PTC technology is known for its best optical performance, while the LFC technology features a stationary receiver and lower initial costs. Output is not considered competitive in LFC technology because of optical performance. PTC technology’s mobile receiver limits the option of HTFs and raises the cost of tracking.

In this project, novel modification is done to remove the limitations of line focus technologies. For the development of new configurations, a mixture of parabolic troughs and flat linear reflectors is used. Tracking is provided only for flat reflectors, leading to lower tracking costs. The parabolic trough adds optical performance



characteristics, while flat reflectors increase the aperture area. To hold the receiver stationary, the parabolic trough is kept in a fixed orientation.

The prototype is developed and investigated experimentally. Output parameters for the same conditions are measured and compared with the PTC. To observe and compare the patterns of parameter variations during a day, the graphs are plotted. It is noted that the average temperature difference is 6.85 °C, which is 1.14 °C higher than PTC. It has been found that up to 54.94% of the prototype collector efficiency is achieved, which is slightly less than the PTC. These findings are proof of the strong performance of the modified solar collector.

## References

1. International Energy Agency.: Technology Roadmap: Concentrating Solar Power, Paris (2010). [https://www.promes.cnrs.fr/uploads/pdfs/documentation/csp\\_roadmap%20IEA%202010.pdf](https://www.promes.cnrs.fr/uploads/pdfs/documentation/csp_roadmap%20IEA%202010.pdf)
2. Teske.: Solar Thermal Electricity Global Outlook. European Solar Thermal Electricity Association (ESTELA), Greenpeace International, and Solar PACES (2016). [http://www.solarpaces.org/new-web-nasertic/images/pdfs/GP-ESTELA-SolarPACES\\_Solar-Thermal-Electricity-Global-Outlook-2016](http://www.solarpaces.org/new-web-nasertic/images/pdfs/GP-ESTELA-SolarPACES_Solar-Thermal-Electricity-Global-Outlook-2016)
3. Siddharth, S., Khan, M.K., Pathak, M.: Performance enhancement of solar collectors—a review. *Renew. Sustain. Energy Rev.* **49**, 192–210 (2015)
4. Lovegrove, K., Stein, W.S.: Concentrating Solar Power Technology: Principles, Developments, and Applications. Woodhead Publishing, ISSN 2044-9364 (2012)
5. Tiana, Y.: A review of solar collectors and thermal energy storage in solar thermal applications. *Appl. Energy* **104**, 538–553 (2013)
6. David, R.M., Graham, L.M.: Compact linear Fresnel reflector solar thermal power plants. *Sol. Energy* **68**, 263–283 (1999)
7. Ishan, P., Pallav, P.: Techno-economic evaluation of concentrating solar power generation in India. *Energy Policy* **38**(6), 3015–3029 (2010)
8. Chu, Y.: Review and Comparison of Different Solar Energy Technologies Global Energy Network Institute (GENI), San Diego, (2015). <http://www.geni.org/globalenergy/research/review-and-comparison-of-solar-technologies/Review-and-Comparison-of-Different-Solar-Technologies.pdf>
9. Ishan, P., Pallav, P., Shekhar, S.: Evaluating the potential of concentrating solar power generation in Northwestern India. *Energy Policy* **62**, 157–175 (2013)
10. Sait, H.H., Martinez, J.M., Abbas, R., Anton, J.M.: Fresnel-based modular solar fields for performance/cost optimization in solar thermal power plants: a comparison with parabolic trough collectors. *Appl. Energy* **141**, 175–189 (2015)
11. Abbas, M., Boumeddane, B., Said, N., Chikouche, A.: Dish Stirling technology: a 100 MW solar power plant using hydrogen for Algeria. *Int. J. Hydrogen Energy* **36**(7), 4305–4314 (2011)
12. Baharoon, D.A., Rahman, H.A., Wan Omar, W.Z., Fadhl, S.O.: Historical development of concentrating solar power technologies to generate clean electricity efficiently—a review. *Renew. Sustain. Energy Rev.* **41**, 996–1027 (2015)
13. Mills, R.D., Morrison, L.G.: Compact linear Fresnel reflector solar thermal power plants. *Sol. Energy* **68**, 263–283 (1999)
14. Fuqiang, W., Ziming, C., Jianyu, T., Yuan, Y., Yong, S., Linhua, L.: Progress in concentrated solar power technology with parabolic trough collector system: a comprehensive review. *Renew. Sustain. Energy Rev.* **79**, 1314–1328 (2017)
15. Jebasingh, V.K., Joselin, G.M.: A review of solar parabolic trough collector. *Renew. Sustain. Energy Rev.* **54**, 1085–1091 (2016)

16. Mathur, S.S., Negi, B.S., Kandpal, T.C.: Geometrical designs and performance analysis of a linear Fresnel reflector solar concentrator with a flat horizontal absorber. *Int. J. Energy Res.* **14**, 107–124 (1990)
17. Singh, P.L., Ganesan, S., Yadava, G.C.: Performance of a linear Fresnel concentrating solar device. *Renew. Energy* **18**, 409–416 (1999)
18. Singh, P.L., Sarviya, R.M., Bhagoria, J.L.: Thermal performance of linear Fresnel reflecting solar concentrator with trapezoidal cavity absorbers. *Appl. Energy* **87**, 541–550 (2010)
19. Ihsan, D., Reşat, S., Arzu, S.: Experimental investigation of a linear Fresnel collector system. *Thermal Sci. Technol.* **34**, 77–83 (2014)
20. Zhai, H., Dai, Y.J., Wu, J.Y., Wang, R.Z., Zhang, L.Y.: Experimental investigation and analysis on a concentrating solar collector using linear Fresnel lens. *Energy Convers. Manage.* **51**, 48–55 (2010)
21. Guangdong, Z., Tim, W., Michael, W.J., Chuck, K.: History, current state, and future of linear Fresnel concentrating solar collectors. *Sol. Energy* **103**, 639–652 (2014)

# Design and Implementation of a 3 Level Battery Management System (BMS) for an Electric Vehicle



Bhumica Dutta, Sharestha Jaiswal, Vinay Phatarpekar, Vijay Kumar Tayal, and H. P. Singh

## 1 Introduction

EV's are gaining more popularity nowadays due to their quiet operation and pollution free emission. The designing and incorporating an efficient BMS is a tedious and important aspect [1]. Owing to its growing importance, many researchers and enthusiasts around the globe have shown their interest, and as a result, numerous research schemes have been proposed in the literature. This work aims to design a 3 level BMS and implement in EV's [2, 3]. This will help in increasing the efficiency of the battery of the vehicle by utilizing the battery in more efficient way. The maximum battery charge of the EV will be divided into three levels. As the charge will go below every level, a corresponding facility will be turned off in the vehicle. Basically, as the charge level of the battery falls below the first level, the driver will get the notification regarding it and the non-essential service like the radio (speaker) will get turned off or the driver will not be able to turn it on. Further, if the battery charge falls below the second level the AC (fan) will be turned off or the driver will be unable to turn it on and will get intimated too. Similarly, if the charge further decreases and goes below the third level, then the maximum speed range of the vehicle will decrease. The most important aspect of this prototype lies in the continuous monitoring of SOC of the battery pack, cell balancing and speed range control. This will ensure the maximum and efficient use of charge in the battery. The paper is organized as follows; Sect. 2 describes the working of the prototype. The main components of the design, i.e., SOC estimation, cell balancing and speed range control are detailed in Sect. 3. The

---

B. Dutta (✉) · S. Jaiswal · V. Phatarpekar · V. K. Tayal · H. P. Singh  
Electrical and Electronics Engineering Department, Amity University Uttar Pradesh, Noida, India

V. K. Tayal  
e-mail: [vktayal@amity.edu](mailto:vktayal@amity.edu)

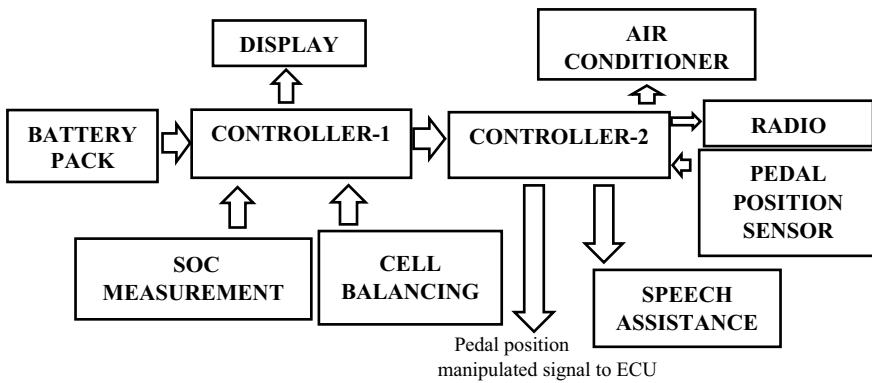
H. P. Singh  
e-mail: [hpsingh2@amity.edu](mailto:hpsingh2@amity.edu)

Simulink and proteus models and simulation results are presented and discussed in Sect. 4. The conclusion is mentioned in Sect. 5.

## 2 Working of the Prototype

The overall working of this prototype is divided into three parts and to be performed by two separate controllers that are able to communicate with each other. (i) Controller 1 (ii) Controller 2 (iii) Voltage regulation for appliances. Figure 1 depicts the working of the prototype.

The working process flow is summarized in Table 1.



**Fig. 1** Block diagram of proposed scheme

**Table 1** Working process flow

Step No	Process
1	SOC calculation is done
2	Cell monitoring is done
3	Cell balancing is done
4	SOC value is transferred to controller 2
5	Appliances are switched off when specific level is reached
6	Speed range control is done
7	Information are given to the user using speech assistance

### 3 Main Components of Design

#### 3.1 SOC (State of Charge) Estimation

SOC and its estimation play a very important role in BMS of an electric vehicle [4, 5]. The SOC is the ratio of the amount of charge left also known as the current capacity [ $Q(t)$ ] to the total or nominal capacity [ $Q(n)$ ] of the battery pack. As, working of this work depends on the current amount of charge left in the battery pack, continuous determination of SOC is needed and hence plays the key role. The SOC can be defined mathematically by Eq. (1):

$$\text{SOC}(t) = Q(t)/Q_n \quad (1)$$

There are various methods that can be employed for SOC estimation such as Coulomb counting, internal resistance, Kalman filtering, voltage, chemical methods. The basic idea about these methods is mentioned as follows:

- **Coulomb counting method**

This method uses the concept that charge is the time integral of current. As the name implies, it integrates the battery current and gives an estimation of the charge left in the battery pack [6].

- **Kalman filtering**

This method uses the electrical model of the battery pack which is used by the Kalman filter to predict the overvoltage due to the current. Coulomb counting method is used in combination with it to perform SOC estimation [7].

- **Voltage method**

This is the method that has been used in this prototype for SOC estimation primarily due to its easy and moderately reliable SOC estimation. This method basically converts the reading of the battery voltage into corresponding SOC with the help of discharge curve of the battery [8].

- **Chemical method**

This method is limited with batteries that offer access to their liquid electrolyte, such as lead acid batteries which are non-sealed. The specific gravity or pH of the electrolyte is considered for the SOC estimation [9].

The simulation circuit for the same is shown in Fig. 5. And, its results are displayed in Figs. 9 and 10. The simulation results show how the voltage across the battery pack, and hence the SOC varies, while discharging.

#### 3.2 Cell Balancing

Another important aspect which is indirectly involved but plays a key role in any BMS is the cell balancing. Without involving cell balancing, proper functioning of BMS

is impossible. Thus, cell balancing refers to a technique which involves maintaining the voltage at same level of each cell connected to form the battery pack [10]. The difference in voltage level arises from the fact that when different cells are connected to form a battery pack, and it is required that they are of the same chemistry and voltage value. However, once the pack is installed in the vehicle and is subjected to charging and discharging, the voltage values of the individual cells tend to vary. The main reasons behind cell unbalancing are temperature and internal resistance variations [11]. Role of cell balancing is very important as it protects the battery pack from the following problems: (i) Thermal Runaway (ii) Cell Degradation (iii) Incomplete charging of Pack (iv) Incomplete use of Pack energy.

There are mainly two methods [12] for achieving cell balancing each having its own pros and cons (i) Passive cell balancing (ii) Active cell balancing.

**Passive Cell Balancing:** The idea behind this cell balancing approach is that the excess charge is dissipated across a load which is a resistor also known as bleeding resistor. It is the simplest method of all, cost-effective and is best to be employed in places where size is a major issue [13].

**Active Cell Balancing:** This method is comparatively very complicated, costly but at the same time in this, the excess charge from the cell is taken and is transferred to the cell with low charge [14]. Hence, this method uses the charges of all the cells in the battery pack in the most efficient way which is the objective behind designing this prototype. Hence, we have used active method of cell balancing. There are various methods for achieving this like using capacitors, inductors (in the buck-boost converter form or flyback converter form). In this prototype, a push-pull converter is used for cell balancing. The circuit that is used mainly comprises of a transformer, MOSFET's, Schottky diodes, relays and a micro-controller. The working algorithm behind it is that first of all the cells with maximum voltage and minimum voltage are identified, and the average of all cell voltages is calculated. Then, if the difference between these cells is greater than 5 mV cell balancing among them takes place as the respective relays get switched on after getting signal from the micro-controller till it becomes nearly equal to the average. Once the selected cells are balanced, SOC of each cell is estimated and again average is calculated. Then, again the cells with highest and lowest voltages are identified and again balancing takes place the same way. This process is carried out till all cells are balanced. The algorithm of cell balancing is shown in Fig. 2.

### ***3.3 Speed Range Control***

One of the main components of this work is the speed range control or limitation. The role of speed range control is to limit the speed range of the electric vehicle when the state of charge of the car battery pack reaches or is below the third level as it is being desired in the aim of this work. The driver of the EV may not be able to increase the speed of the vehicle from a certain maximum speed that is predefined. There would be two sublevels of speed range that is from 0 to 60 for one sublevel

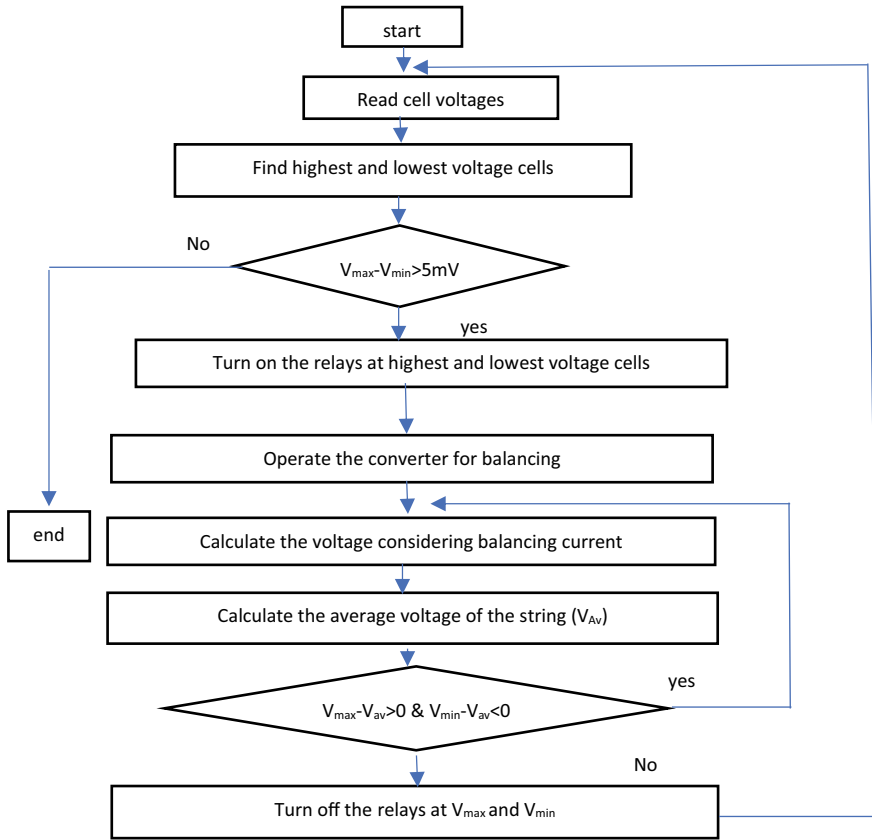


Fig. 2 Algorithm of cell balancing

and then 0–40 for another sublevel. Generally, in all the pure electric vehicles, there is a common process of desired speed attainment.

The **pedal position sensor** is the first step toward communicating with the vehicle control unit. It tells the vehicle control unit as to how much speed is requested by the driver [15]. It generally consists of two potentiometers of same voltage range and of different outputs (one of 4.7 v and other of 2.5v).

The mathematical expression shown in Eq. (2) is used to calculate the torque request provided to the vehicle control unit.

$$\tau_a = \left( \frac{p - p_{cu}}{p_m - p_{cu}} \right)^y \cdot \tau_{am} \tag{2}$$

The voltage generated from the pedal position sensor then is sent to the **vehicle control unit**, i.e., VCU. It does the further calculation of the torque as was represented in the previous section [16]. The key of the vehicle driving control methodology

are the torque figuring, which computes the required torque of the engine through the pedal position input and flow driver information and vehicle status [17]. The quickening agent pedal position MAP table is checked by the quickening agent pedal sign, and the vehicle speed sign to get an uncorrected standardized forward solicitation force [18]. At that point, the forward solicitation force was remedied by the SOC [19].

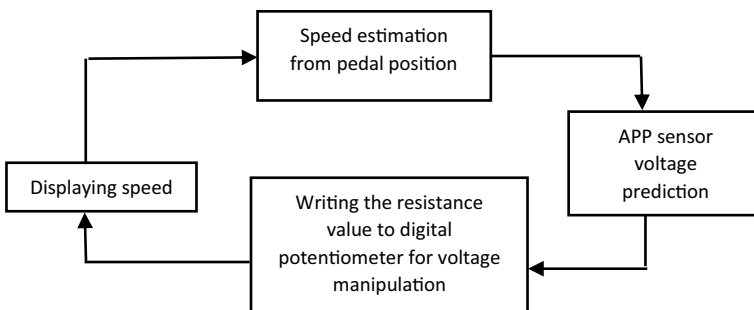
The torque request is received at the **inverter** input, and the required power request is sent to the battery pack controller to get the required power for the desired maximum speed [20].

**Methodology of Speed Range Control Used**

After the careful study of the speed attainment method as done by the VCU as shown in the above section, we have proposed an idea for speed prediction from the formulas shown above and also the speed limitation by reducing the maximum speed of the vehicle because we also need to know the speed before limiting it [21]. Before developing an electric vehicle, some calculations are done to predict the maximum speed of the vehicle by the maximum power required by the vehicle [22]. The formula given below shows the relation between the maximum power and the maximum speed. We also used this formula for the prediction of speed [23].

$$P_m = \left( \frac{MgfV_{\max}}{3600} + \frac{C_dAV_{\max}^3}{76,140} \right) \cdot \frac{1}{\eta_T} \tag{3}$$

*M* represents mass of the vehicle, *g* represents acceleration due to gravity, *f* represents rolling resistance coefficient, *V<sub>max</sub>* represents maximum speed attained, *C<sub>d</sub>* represents drag coefficient, *A* represents frontal area, and *η<sub>T</sub>* represents efficiency of power transmission system [24]. The block diagram in Fig. 3 shows the speed range control algorithm.



**Fig. 3** Speed range control algorithm



### 4 Simulation Results and Discussion

The Simulink models developed for SOC estimation and cell balancing and proteus models developed for SOC estimation and overall circuit are shown in Figs. 4, 5 and 6, respectively. The simulation result obtained in Fig. 7 shows the variation of SOC with time (upper fig.) and variation of load current with time (lower fig.). Figure 8 shows the variation of voltage of the battery pack with time. All these simulation results are obtained, while discharging of the battery pack for 200 s. Figure 9 corresponds to the simulation results of the cell balancing circuit shown in Fig. 5.

The initial SOC for each cell was kept at 96%, considering the losses due to internal resistance of the cell. As seen from Fig. 7 (upper figure), the SOC value falls to 81% from 96% after discharging for 200 s. The lower figure in Fig. 7 corresponds

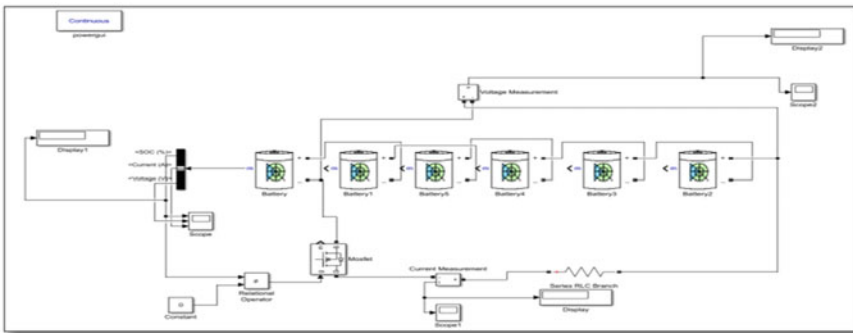


Fig. 4 Simulink SOC estimation model

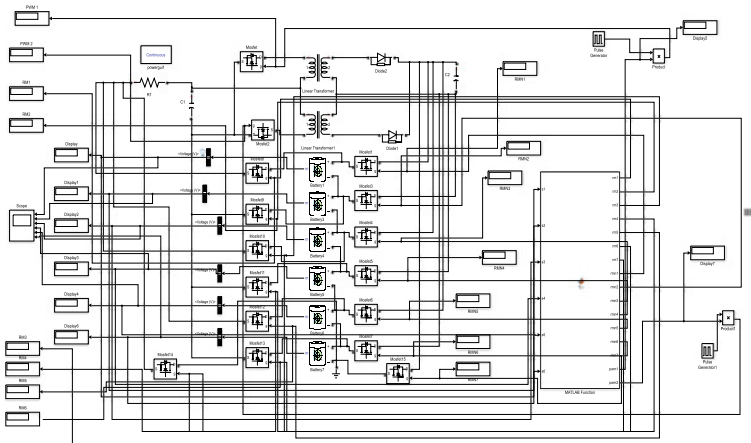


Fig. 5 Simulink cell balancing model

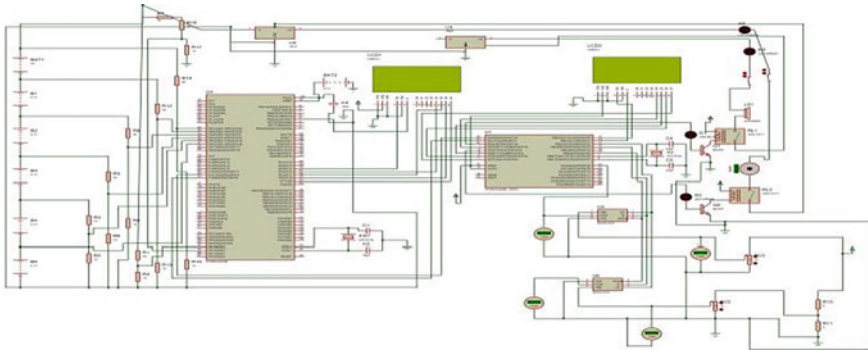


Fig. 6 Proteus total simulation model

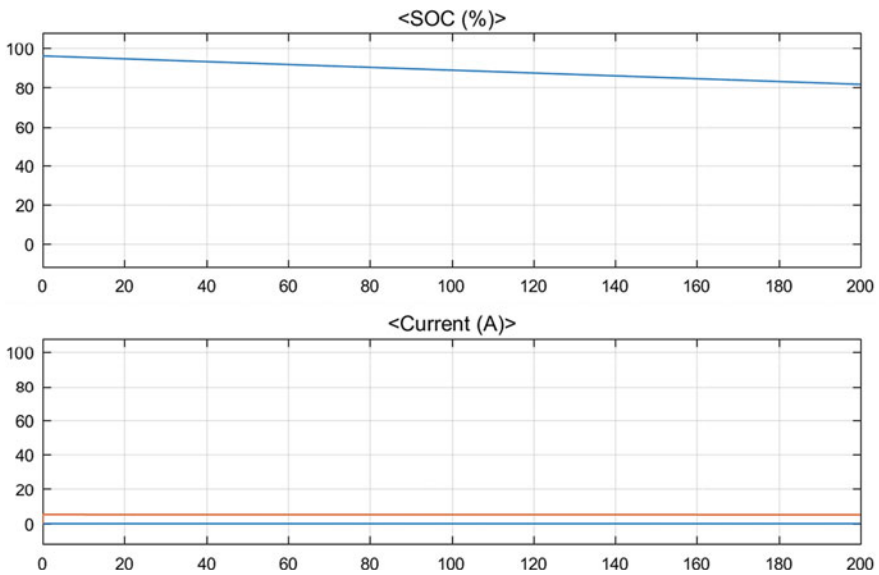
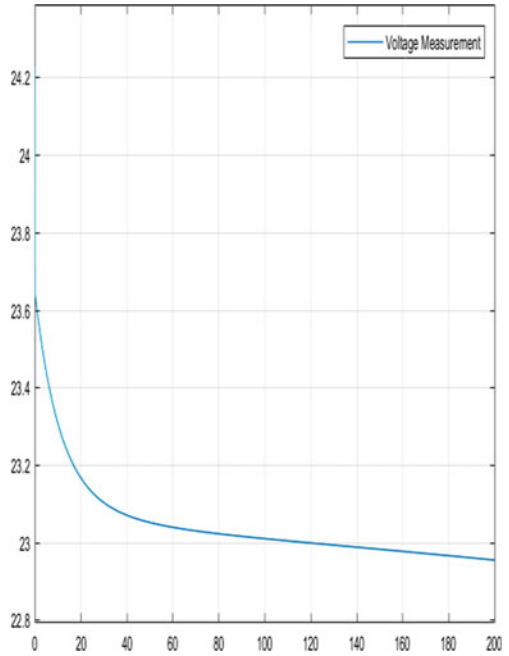


Fig. 7 Variation of SOC and load current with time

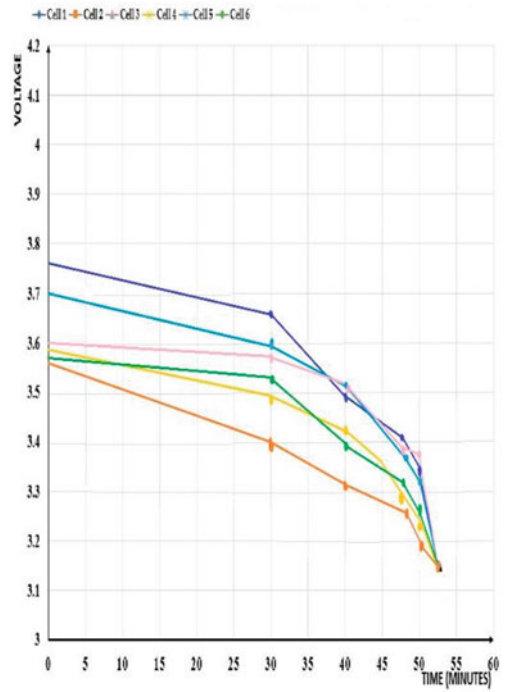
to the load current. As, load is considered to be resistive, and the result shows a constant current.

As the cells had an initial SOC of 96%, the variation of voltage is from 24.2 V. From Fig. 8, it can be seen that the value of voltage across the battery pack decreases from 24.2 to 22.9 V, while discharging. Figure 9 shows how the cell balancing process occurs across the battery pack. This takes about 55 min to achieve complete cell balancing.

**Fig. 8** Variation of battery voltage with time



**Fig. 9** Voltage versus time (Cell balancing)



## 5 Conclusion

A battery management system (BMS) being the heart of any electric vehicle is a very crucial part to be designed effectively. The battery should be able to give a proper drive to the vehicle by delivering required power to all the subsystems attached to the vehicle. The paper aims at making maximum use of the charge in the battery pack. To track the current SOC, firstly, the SOC estimation circuit for the complete battery pack has been designed. Further, designing of an appropriate cell balancing circuit and speed range control is carried out. Finally, all the subsystems designed are combined and synchronized. With successful designing of all the subsystems and validating their working, the objective of the proposed prototype is achieved. In the event of low battery, power supply to non-essential equipment such as radio and air conditioner is stopped, followed by reduction in speed range of the EV. Thus, the battery pack charge is utilized mainly by the car motor at the time of low battery.

## References

1. Chang, W.Y.: State of charge estimation for LiFePO<sub>4</sub> battery using artificial neural network. *Int. Rev. Electr. Eng.* **7**(5), 5874–5880 (2012)
2. Rao, Z., Wang, S., Zhang, G.: Simulation and experiment of thermal energy management with phase change material for ageing LiFePO<sub>4</sub> power battery. *Energy Convers. Manag.* **52**(12), 3408–3414 (2011)
3. He, H.W., Xiong, R., Guo, H.Q.: Online estimation of model parameters and state-of-charge of LiFePO<sub>4</sub> batteries in electric vehicles. *Appl. Energy* **89**(1), 413–420 (2012)
4. Cai, Z.H., Liu, G.F., Luo, J.: Research state of charge estimation tactics of nickel-hydrogen battery. In: *Proceedings of the International Symposium on Intelligence Information Processing and Trusted Computing (IPTC '10)*, pp. 184–187, Huanggang, China (2010)
5. Watrin, N., Blunier, B., Miraoui, A.: Review of adaptive systems for lithium batteries state-of-charge and state-of-health estimation. In: *Proceedings of IEEE Transportation Electrification Conference and Expo*, pp. 1–6, Dearborn, Mich, USA (2012)
6. Alzieu, J., Smimite, H., Glaize, C.: Improvement of intelligent battery controller: state-of-charge indicator and associated functions. *Power Sourc.* **67**, 157–161 (1997)
7. Besselink, I.J.M., Wang, J., Nijmeijer, H. Evaluating the TU/e Lupo EL BEV Performance, pp. 1–12, Barcelona, Spain (2013)
8. Lee, J., Nelson, D., Lohse-Busch, H.: Vehicle Inertia Impact on Fuel Consumption of Conventional and Hybrid Electric Vehicles Using Acceleration and Coast Driving Strategy. SAE Technical Paper, pp. 01–1322 (2009)
9. Rauh, J., Ammon, D.: System dynamics of electrified vehicles: some facts, thoughts, and challenges. *Vehicle System Dynamics*, pp. 1005–1020 (2011)
10. Elgammal, A.A.A., Sharaf, A.M.: Self-regulating particle swarm optimised controller for (photovoltaic-fuel cell) battery charging of hybrid electric vehicles. *IET Electr. Syst. Transp.* **2**(2), 77–89 (2012)
11. Singh, S., Rathore, P., Tayal, V.K., Sinha, S.K.: Improved design of automatic car battery charging system. In: *2nd International Conference on Power Energy, Environment and Intelligent Control (PEEIC)*, Greater Noida, India, pp. 1–5 (2019)
12. Prajapati, V., Hess, H., William, E.J., et al.: A literature review of state of-charge estimation techniques applicable to lithium poly-carbon monofluoride (Li/CF<sub>x</sub>) battery. In: *Proceedings*

- of the India International Conference on Power Electronics (IICPE '10), pp. 1–8, New Delhi, India (2011)
13. Sahu, A.R., Bose, B., Kumar, S., Kumar Tayal, V.: A review of various power management schemes in HEV. In: IEEE International Conference on Reliability, Infocom Technologies and Optimization (Trends and Future Directions) (ICRITO), pp. 1296–1300 (2020)
  14. Liu, H., Wei, Z., He, W., Zhao, J.: Thermal issues about Li-ion batteries and recent progress in battery thermal management systems: a review. *Energy Convers. Manag.* **150**, 304–330 (2017)
  15. Min, C., Rincón-Mora, G.A.: IEEE Transactions on Circuits and Systems, pp. 1180–1184 (2006)
  16. Aung, H.; Low, K.S.; Soon, J.J.: State-of-charge estimation using particle swarm optimization with inverse barrier constraint in a nanosatellite. In: Proceedings of the 2015 IEEE 10th Conference on Industrial Electronics and Applications (ICIEA), pp. 1–6. Auckland, New Zealand (2015)
  17. Won, W.J., Son, J., Park, G., et al.: Design and implementation procedure of the AUTOSAR I/O driver cluster, pp. 5618–5623. *Iccas-Sice, IEEE* (2009)
  18. Evtimov, I., Ivanov, R.: *Electric Vehicles* (Ruse: Print center of University of Ruse) ISBN 978-954-712-682-4, pp. 232 (2016)
  19. Saw, L.H., Tay, A.A.O., Zhang, L.W.: Thermal management of lithium-ion battery pack with liquidcooling. In: Proceedings of the 2015 31st Thermal Measurement, Modelling & Management Symposium (SEMI-THERM), San Jose, pp. 298–302 (2015)
  20. Guirong, Z., Henghai, Z., Houyu, L.: The driving control of pure electric vehicle. *Procedia Environ. Sci.* **10**, 433 (2011)
  21. Evtimov, I., Ivanov, R.: Comparative assessment of the efficiency of electric vehicles and conventional cars. In: Proceedings of International Scientific Conference BULTRANS-2009 (Sozopol) p. 94.1 (2009)
  22. Besselink, I.J.M., et al.: Design of an efficient, low weight battery electric vehicle based on a VW Lupo 3L, EVS25, Shenzhen China (2010)
  23. Sakai, S.-i., Hori, Y.: Advantage of electric motor for anti skid control of electric vehicle. *EPE J.* **11**(4) (2001)
  24. Mirheidari, S., Fallahi, A., Zhang, D., et al.: AUTOSAR model-based software component integration of supplier software. *SAE Int. J. Commer. Veh.* **8**(2), 544–548 (2015)

# Effect of Flow Velocity on the Performance of the Savonius Hydrokinetic Turbine



Vimal Patel  and Kushal Shah 

## 1 Introduction

### 1.1 Preface

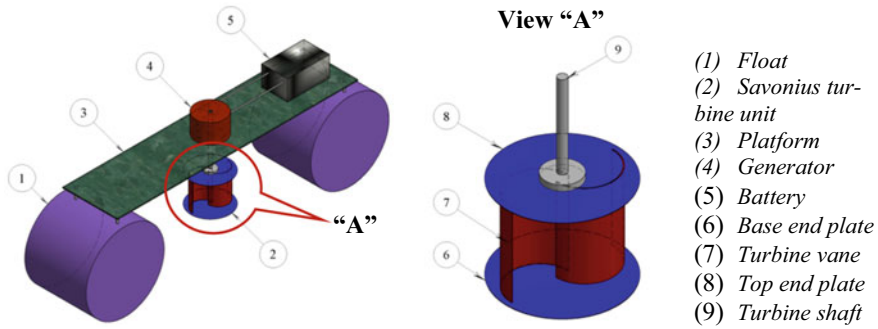
Compared to the wind power, small hydropower generation units gathered much attention due to its predictable power development and high power density. It can generate the electrical power directly by installing in the natural path of the water streams, without use of massive structure of dam. It can be used as a standalone power generation unit in the remote location where the water stream is naturally available, as shown in Fig. 1. The Savonius turbine is one of the hydrokinetic turbines, predominantly a drag force-driven type of turbines. In spite of its low power coefficient, their starting characteristic is quite good.

### 1.2 Status of Global Research and the Aim of the Present Work

River current turbines, which operate at lesser depths, are necessarily smaller, and their rated output rarely exceeds 400 kW, even in very strong currents of 4.5 m/s. [1]. The hydrokinetic turbine installed by Hydro-Québec is in the experimental and pre-commercialization stage. In September 2010, a first industrial prototype was connected to the Hydro-Québec grid. The hydro turbine was submerged in the Fleuve Saint Laurent (St. Lawrence River) near the old port of Montréal, with a planned

---

V. Patel (✉) · K. Shah  
Sardar Vallabhbhai National Institute of Technology, Surat, Gujarat, India



**Fig. 1** Standalone power generation using Savonius turbine

capacity of 100 kW. It fed electricity into the Hydro-Québec grid from 2010 to 2013 [1].

Patel et al. [2] carried out an in-depth experimental investigation to find the effect of gap between the two vanes (overlap ratio) and height of Savonius turbine (aspect ratio). They concluded that the overlap ratio nearly 0.11 provides best performance with minimum aspect ratio of 1.8. The turbine shows higher power coefficient if the experiments are carried out in narrow canal. The in-depth methodology for the performance correction is explained by Patel et al. [3] for Savonius turbine. The theoretical calculations for prediction of the performance of the Savonius turbine are given by Patel et al. [4] based on impulse-momentum principal and stagnation pressure.

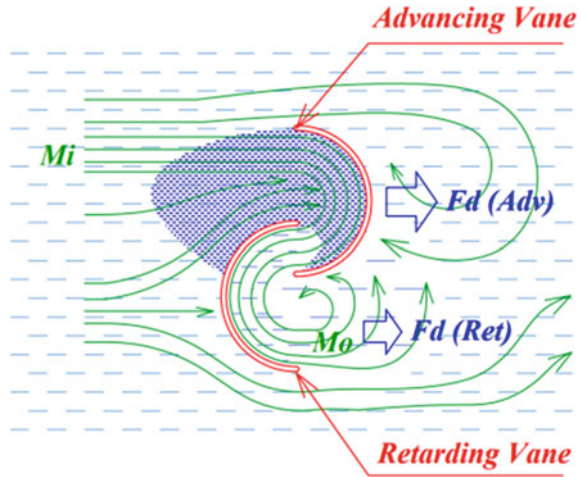
Based on the literature review, it is observed that the effect of flow velocity, vane thickness, and various vane shapes on the performance of the Savonius turbine for hydrodynamic application is still not investigated extensively. In the present investigation, it is targeted to analyze the effect of flow velocity on the performance of the Savonius turbine with CFD simulation.

## 2 Conceptual Discussion

The fundamental concept by which torque generates by water flow on the Savonius turbine runner is shown in Fig. 2. The drag force developed by the concave surface,  $F_d(Adv)$ , of advancing vane is quite high compared to the drag force,  $F_d(Ret)$ , generated by the convex surface of the retarding vane. Power development is depending on (a) momentum change of the water passing from the vane surfaces and (b) pressure difference between upstream and downstream side of the vane. Two cases can be considered at this stage, (i) high incident water flow velocity and (ii) slow incident water flow velocity.

If the incidence of water flow velocity is relatively high, the pressure difference between upstream and downstream of the vane will increase. It will enhance the

**Fig. 2** Conceptual flows over Savonius turbine vane



momentum change ( $M_o - M_i$ ) of the water passing from the gap of the vanes, as pressure condition at the downstream of the retarding vane is comparatively low. Subsequently positive torque due to momentum change of water from advancing vane increases.

If the incidence water flow velocity is relatively less, the mass flow rate of water from the vane gap reduces due to the water backflow from the downstream side of the water, toward retarding vane. Subsequently, the momentum change ( $M_o - M_i$ ) of water passing from the gap decrease, and it may adversely affect the performance of the turbine.

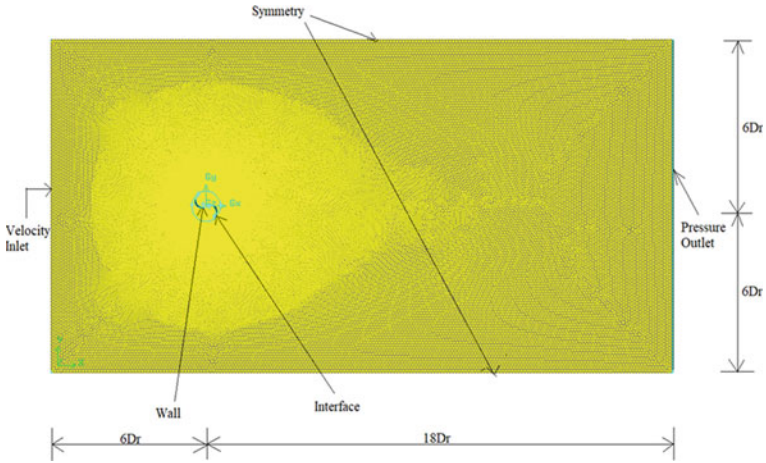
To validate the considered concept, it is decided to study the effect of water velocity on the performance of the Savonius turbine by CFD simulations. Also, the study is further extended to find the cutoff velocity to provide best performance from the turbine.

### 3 Numerical Simulation

The numerical study was carried out to check the validity of specific turbulence models in the computational fluid dynamics (CFD). In the present investigation, the pressure-based, transient, absolute, planner with viscous turbulent  $K-\omega$  SST two-equation models are selected. The boundary conditions used for the investigations are shown in Fig. 3. The mesh was prepared using triangular elements and 15 inflation layers with growth rate of 1.15. The average aspect ratio, orthogonal quality, and skewness of the used elements are 32, 0.36, and 0.76, respectively.

The grid-independent and domain optimization study are also carried out before investigation of the flow velocity effect. The conditions used for grid-independent study are inlet velocity equal to 0.85 m/s, diameter of rotor equal to 0.22 m, rotational



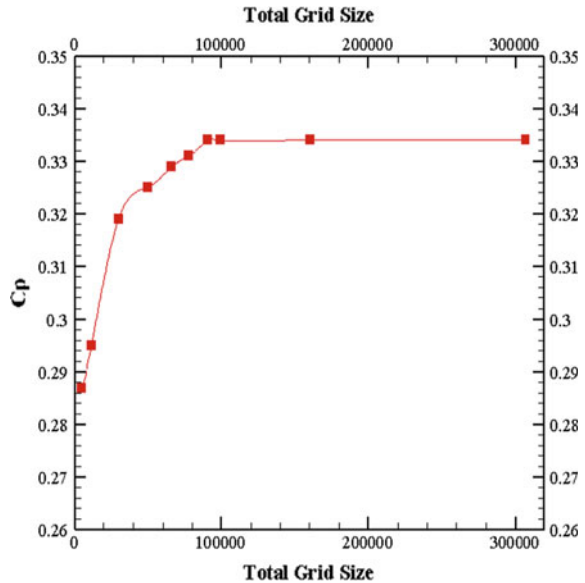


**Fig. 3** Boundary conditions and domain used in the present investigation

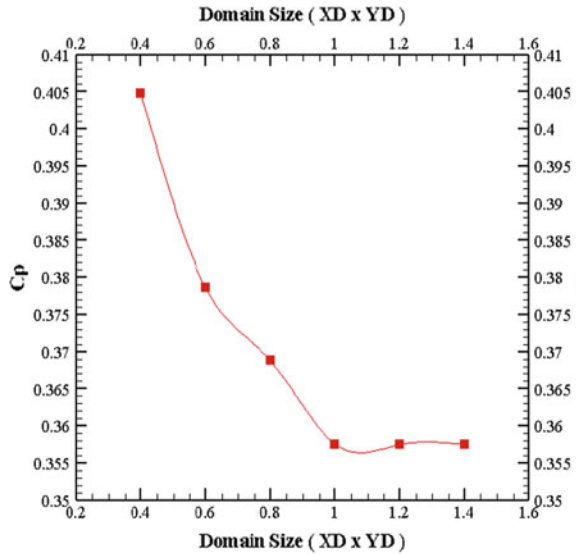
velocity equal to 9.35 m/s, TSR equal to 1.1 also constant rectangular domain  $12D \times 24D$ . Graph of  $C_p$  versus total grid size is shown in Fig. 4, which says that after total grid size as 90,962  $C_p$  value remains constant.  $C_p$  value is 0.334. All the numerical simulations are done using total grid size higher than 90,962.

The size of the study domain also affects the results obtained by the simulation. Hence, domain optimization study is carried out with free stream velocity  $V = 0.85$  m/s, diameter of rotor  $D_r = 0.2$  m, thickness of blade  $t = 5$  mm, eccentricity

**Fig. 4** Effect of the number of elements on  $C_p$

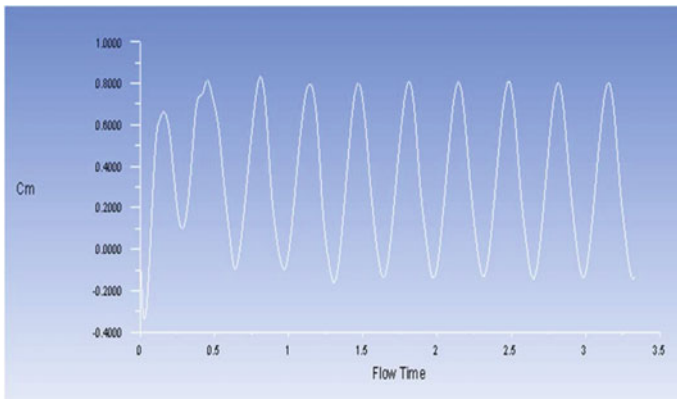


**Fig. 5** Effect of domain size on the obtained value of  $C_p$



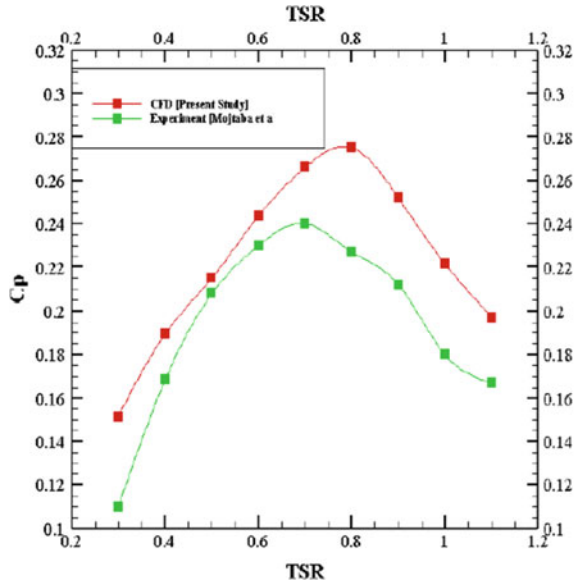
$e = 0.01$ , and  $TSR = 1.0$ . Domain study is done in the multiplication of the basic domain size  $12D \times 24D$ . From Fig. 5, the graph of the  $C_p$  versus TSR with the multiplication factor of 1 [means ( $12D \times 24D$ )] the result indicates nearly constant value of  $C_p$ . So, it can be assumed that for the higher multiplication it will remain same. Therefore, domain size can be taken as  $12D \times 24D$ .

The average value of the coefficient of moment ( $C_m$ ), after reaching steady-state variation in  $C_m$  was obtained from simulation. The variation of  $C_m$  with different flow time is shown in Fig. 6



**Fig. 6** Variation of  $C_m$  during analysis

**Fig. 7** Validation of the methodology used in the present investigation



For the validation of the considered methodology, the grid size and domain size are kept as 110,652 elements and (2.4 m × 4.8 m), respectively. Also, boundary conditions were velocity inlet at left edge with 6 m/s of wind, pressure outlet at right edge, top, and bottom was taken as symmetry. The blade radius  $r$  was 0.0585 m, the endplate diameter  $D$  was 0.23 m, and the eccentricity is 0.023 m. The results obtained from the present simulation are quite matching with the experimental results available in the published literature [5]. The close matching and same variation trend validate the adopted methodology used in the present investigation (Fig. 7).

## 4 Effect of Flow Velocity

### 4.1 Investigated Parameters

The numerical analysis is carried out for the conventional Savonius rotor. The diameter of the blade ( $D$ ) is 0.1 m, the gap between the vane is 0.01 m, diameter of rotor is 0.2 m, and thickness of the blade is 5 mm. The simulations are carried out for different values of velocity of water (0.5, 0.6, 0.7, 0.8, 1.0, 1.4, 2.0, 2.5, 3.0, 3.5 m/s) keeping the remaining parameters as constant. Here, simulations were done for tip speed ratio values 0.4–1.2. So, rotational velocity value is between 3.6 and 10.2 rad/s.

### 4.2 Results and Discussion

The pressure and velocity contour obtained with the present investigations are shown in Figs. 8 and 9, respectively.

The upstream side pressure is comparatively higher than that of downstream side of the rotor. This higher pressure is generated due to stagnation of the flow due to resistance offered by the turbine rotor.

The downstream side velocity is also quite low compared to the upstream side of the rotor. It is due to the utilization of the kinetic energy to generate mechanical power, which decreases the velocity of the flow at downstream side.

The simulations are carried out for different velocity of water in the range of 0.5–3.5 m/s. The variation of  $C_p$  for different TSR obtained from the present investigation is shown in Fig. 10. The result indicates that the  $C_p$  value increases as the velocity of flow increases. Also, the value of  $C_{p_{max}}$  appears at higher TSR as flow velocity increases.



Fig. 8 Pressure contour

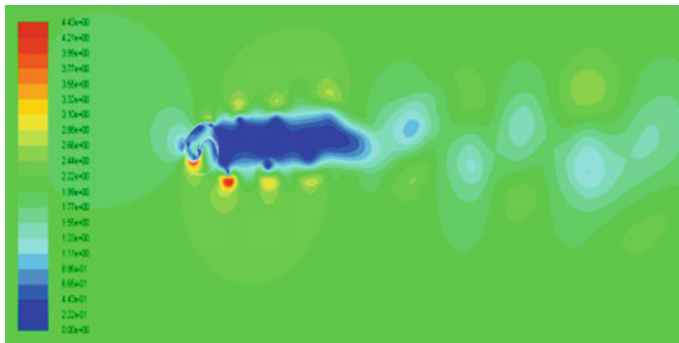
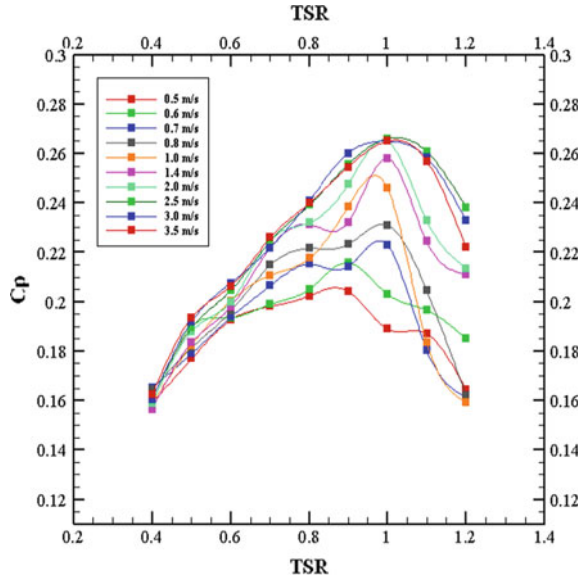


Fig. 9 Velocity contour

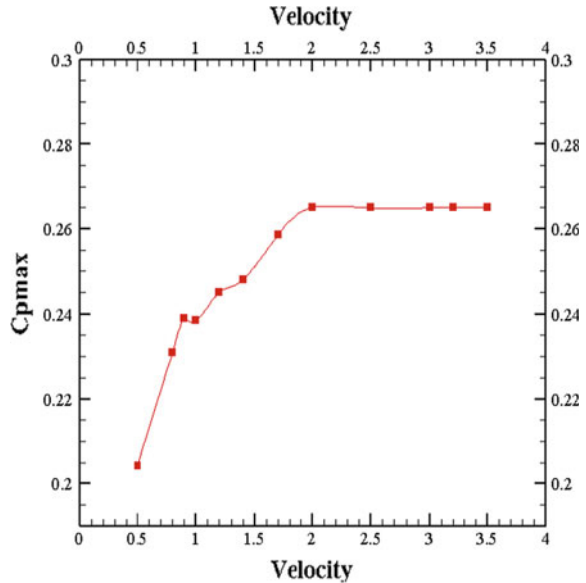
**Fig. 10** Effect of flow velocity on the performance of the turbine



### 5 Conclusion

To obtain the optimum value of the velocity of water, the graph of  $C_{pmax}$  obtained at different velocity is drawn and shown in Fig. 11. From the results, it can be concluded

**Fig. 11** Obtaining critical velocity for optimum performance of the turbine



that the coefficient of power becomes constant from velocity value 2.0 m/s. Hence, to get optimum performance from the turbine, minimum 2 m/s velocity is required for the considered design of the turbine. It is to note here, the power output will be continuing to increase flow velocity rise even beyond 2 m/s. However, the coefficient of power becomes nearly stagnant beyond flow velocity of 2 m/s.

## References

1. Hydro Quebec.: A renewable energy options—hydrokinetic power. ISBN 978-2-550-72232-8 2015G033-2 (2015)
2. Patel, V., Bhat, G., Eldho, T.I., Prabhu, S.V.: Influence of overlap ratio and aspect ratio on the performance of Savonius hydrokinetic turbine. *Int. J. Energy Res.* **41**(6), 829–844 (2017)
3. Patel, V., Eldho, T.I., Prabhu, S.V.: Velocity and performance correction methodology for hydrokinetic turbines experimented with different geometry of the channel. *Renew. Energy* **131**, 1300–1317 (2019)
4. Patel, V., Eldho, T.I., Prabhu, S.V.: Theoretical study on the prediction of the hydrodynamic performance of a Savonius turbine based on stagnation pressure and impulse momentum principle. *Energy Convers. Manage.* **168**, 545–563 (2018)
5. Tahani, M., Rabbani, A., Kasaeian, A., Mehrpooya, M., Mirhosseini, M.: Design and numerical investigation of Savonius wind turbine with discharge flow directing capability. *Energy* **130**, 327–338 (2017)

# Review on Pragmatic Refrigerants Deployed in Refrigeration and Air Conditioning System



Shaik Abdulla  and T. S. Ravikumar 

## 1 Introduction

The release of chemical gases like carbon monoxide, carbon dioxide and other such type of gases into the atmosphere which makes the sun's heat energy to be absorbed and not reflected back to earth's atmosphere, due to which earth's surface becomes warmth this process is referred as greenhouse effect [1]. The sunlight directly enters the earth's surface and gets trapped in the atmosphere the gases shield the atmosphere and prevents the heat radiation to escape the atmosphere. Greenhouse gases such as carbon dioxide, methane, water vapor are naturally available. The montreal protocol agreement states [2] the manufacturing of chlorofluorocarbons should be stopped and used for fundamental purposes only. Chlorofluorocarbons (CFCs) are being utilized for a long time in the air conditioning and refrigeration system. The chlorine atoms present in CFC's damage the ozone layer which causes ultra violet rays to reach the earth's surface due to which there will be harmful effects on human skin and the health-related issue such as skin cancer, leathery skin and leads to form of other skin diseases. The countries around the world have agreed to sign the protocol which agreed to ban the CFCs in January 1996 and gave a grace period of 10 years to use for developing countries and then to stop and look for other environmentally friendly refrigerants. Refrigerant R134a was recommended as an alternative to R12 [3] but due to the high-global warming potential of R134a, its use has to be minimized. R123 emerges as a probable refrigerant with low GWP and ODP values. The R290 which comes into the picture can be used in blend with R123 with another refrigerant. The development of refrigerants presented [4] from past to present reviews, split the entire history of refrigerants into four generations. In the first generation,

---

S. Abdulla (✉) · T. S. Ravikumar

Department of Mechanical Engineering, Hindustan Institute of Technology and Science, Chennai, India

concentration was based on natural refrigerants like carbon dioxide was considered, but its performance was low. Then, they worked on ammonia and water which required more number of centrifugal compressors for performing and in which water gave low efficiency of performance. In the second generation, safety and durability were taken into consideration, and refrigerants introduced were Chlorofluorocarbon (CFCs), and Hydro chlorofluorocarbons (HCFCs). They were popularized more and compared with CFCs in the second generation refrigerants. In the third generation, ozone protection was considered due to climate change and 'greenhouse gas effect' and all countries agreed to phase out CFCs and HCFCs which have high ODP and to find best alternative refrigerants. In the fourth generation, concentration was based on climate emergency potential decided for utilization of only small GWP hydro chlorofluorocarbon refrigerants. The present work is to analyze the best alternate refrigerant available for us from available refrigerants which have zero ODP and low GWP based on the review of the research papers. In recent times, nanoparticles were introduced in the refrigeration and air conditioning system because of its promising results shown. Nanofluids enhance the ability to conduct heat. Nanoparticles in the range of (1–100 nm) suspended in the working fluid improve the heat transfer characteristics when compared without nanoparticles in the working fluid.

## 2 Refrigerant Properties

Messineo et al. [5] Compared the refrigerant R22 with three non-chlorine fluids R417A, R407C, and R404A. Molar mass of refrigerants is as follows: R22 was 86.48, R417A was 106.75, and R407C was 86.20. The boiling temperature of R22 was  $-40.80$ , R417A was  $-39.12$ , R404A was  $-46.60$ , and R407C was  $-43.80$ . The critical temperature of R22 was 9.5% more compared to R417A, 25% more compared to R404A, and 10.5% more than R407C. Certainly, all the four refrigerants were the same [6]. Refrigerants, R410A and R507, were considered as a substitute for R22 in which the critical temperature of R410A and R507 was very close, and critical pressure of R410A was 22% more when compared with R507. The molecular weight of R410A was 26% less when compared with R507 [7]. Compared the refrigerant R407C with the blend R410A in terms of thermodynamic characteristics. It was observed that the critical temperature of R407C was  $86.05$  °C which was 15% more compared with R410A. The GWP value of R407C was less than R410A [8]. When the refrigerants selected for this study were observed that the critical temperature of water (R-718) was  $373.9$  °C which was high when compared with other refrigerants. Water as a refrigerant consumes more power to produce useful refrigeration [9]. Experimented with similar refrigerant blends instead of R404A, R447A, and R22. The climate change value was used to measure the infrared radiations which were also an important factor in selecting alternative heat absorbing fluid [10]. Made an experimental comparison between R134a and HFO 1234ze. In the domestic refrigerator, it was observed that the critical temperature of R134a was  $101.1$  °C, which was higher than HFO1234ze and, while in terms of GWP values, and



HFO1234ze was much lower than R134a. The nanoparticle-based refrigerants were highlighted, because it enhanced the thermodynamics properties [11] silicon dioxide  $\text{SiO}_2$  nanoparticles as lubricant taken for experimental investigation [12]. Conducted experiment on heat pump which shows that the COP of nanofluid-based refrigerant are low when compared with R22. The power consumption of the compressor was more for nanofluid than R22 [13]. Made a model of air conditioning system using nanofluids, and the efficiency of refrigeration system with R22, and 0.1% volume of 3 types of nanofluids namely Copper oxide, Zinc oxide,  $\text{Al}_2\text{O}_3$  were examined. Minichannel two-phase flow boiling heat transfer coefficient study was done on R32 [14],  $\text{CO}_2$ , and R290. Test information was obtained by conducting experiment in steel tubes with different ranges of mass fluxes. It was observed from the experiment that with the increase in heat flux the heat transfer coefficient has increased [15]. Investigated on the performance of R290 with R22 in a refrigeration system, the thermo-physical properties of selected refrigerant for an experiment, and it was observed that the critical temperature of R22 and R290 was very close and small variation of value in the normal boiling point of two refrigerants.

Devecioğlu and Oruç [16] Discussed on R1234yf, R444A, and R445A refrigerants. The evaporation and condenser temperature were considered between  $-5^\circ\text{C}$  to  $+5^\circ\text{C}$ ,  $30^\circ\text{C}$  and  $60^\circ\text{C}$ , respectively. It was observed that the critical temperature of R445A was higher than R444A and R1234yf. Whereas the GWP value of R1234yf was very less when compared to R444A and R445A.

Kasera and Bhaduri [17] Predicted that R407C would be a substitute to R22 refrigerant. ODP of R407C was zero, and GWP was less compared to R22 [18]. Presented refrigerant R1234yf and R1234ze as replacement to R134a, theoretical evaluation was carried out at low temperature. It was experimentally shown that R1234yf absorbs more pump power than R134a and R1234ze obtained lesser power than R134a [19]. Experimented on pure HFC refrigerants to find out which refrigerant had a higher COP. HFC refrigerants considered were R32, R134a, R143a, and R152a. Using REFPROP software, thermodynamic criterion of some pure HFC refrigerants was studied. In [20], theoretical performance investigation was carried out on HFC and HC blends as an alternative to replace the refrigerant R22. The research paper published [21] theoretical thermodynamic performance with ten binary refrigerant mixture consisting of propane and propylene. It was observed that refrigerant blend M1 critical temperature was very close to R22. GWP of R22 was 1760, whereas the remaining all refrigerants GWP was less than 3. The research involves an investigation of alternatives of R134a in the automobile air conditioning system. The refrigerants studied were R290, R600a, R407C, R410A, R404A, R152a, R1234yf and compared with R134a.

Gaurav Kumar [22] Utilized REFPROP software to check the properties of refrigerants. From the results, it was published that relative COP and energy and exergy efficiency of R290 were more when compared to other refrigerants studied. The alternative to R134a was 38% R1234ze, 22% R1234yf, 40% HFC 134a [23]. Worked with low-GWP organic refrigerants like R1233zd[E] and R1224yd[Z] and suggested as alternative for R245fa refrigerant in existing system [24]. Discussed on the screening of refrigerant substitutes to R290 and R600a. The refrigerants selected for the study

of R290, R600a, R600, R1270, R152a, R32, R1234yf, R1234ze (E), R1233zd, R744, and R134a. It was observed that the critical temperature of R-152a was higher than R600a and R290. The GWP for both R600a and R290 was 3, whereas GWP of R1234zd was 1 which was very small compared to other refrigerants [2]. Discussed on ozone depletion potential and global warming potential, the problem in halo-carbon refrigerants was, when released to atmosphere, it harms ozone layer. Due to release of greenhouse gases in the atmosphere, global warming increases. It is always necessary to select those refrigerants which is having lowest values of ODP and GWP.

### 3 Experimental Results and Discussions

REFPROP software was used in the analysis [3] for a refrigerant mixture containing 70% R123 and 30% R290 results show it was very close to R12. The results also show the same performance as the new mixture. From the experimental results shown [5], the COP of R22 was high compared to R404A, R417A, and R407C but considering ODP and GWP points of view HFC refrigerants can be considered as alternative to R22. Experimental results show that the HFC blend of R410A has a higher COP compared to R507 [6]. R507 refrigerants show 10% lower performance than R410A.

Kundu et al. [7] Conducted experiment it was observed in general cases by increasing heat flux there will be an increase in heat transfer characteristics. The heat transfer coefficient of R410A was 30–45% more than that of R407C at 10 kW/m<sup>2</sup>. Simulation results showed [8] using REFPROP software and experimental prediction that CO<sub>2</sub> show the best quality factor for the temperature range from –20 to 70 °C, whereas R1234yf will be the best for commercial water heating application when compared with other refrigerants selected for the analysis. The REFPROP software was used for calculating the thermodynamic properties of refrigerants, [9] understood that selected alternative refrigerants will have some variation in terms of performance, and they have lower greenhouse effect. It was concluded from this article that R1234yf, blend mixture of R-32/R-152a/R-1234yf/R-1234ze(E) will be the fair alternatives compared to other refrigerants taken in this study. The results presented [10] shows that in terms global warming potential, and R134a was having higher GWP value than HFO 1234ze.

From the experiment conducted, it was identified that the thermal conductivities of nano refrigerants were higher than traditional refrigerants [11]. It was observed that energy saving can be achieved using nano lubricant compared to the traditional refrigerant. The results shown in [12] that by adding nanoparticle TiO<sub>2</sub> decreases the COP than R22, whereas nanofluid can increase the COP of the heating cycle significantly due to increased power consumption of the compressor. The results presented [13] shows that COP increase with the usage of nanofluids in vapor compression system (VCS) when compared with R22. Among the three nanofluids, nano CuO was better than ZnO, and AlO<sub>3</sub>. From the experiment, [14] it was identified that with increasing heat flux, refrigerants CH<sub>2</sub>F<sub>2</sub>, (C<sub>3</sub>H<sub>8</sub>), CO<sub>2</sub> heat transfer coefficient of

refrigerants increases. The results showed that [15] lower discharge temperature was possible by using R290 which improves the compressor performance. The COP of R290 was very close to R22, a higher COP with R290 can be achieved especially by designing the system for R290. Therefore, R290 can be a better alternative to R22.

The experimental results of [16] showed that COP of R1234yf was high compared with R444A and R445A [17]. Summarized that the effect of R407C in comparison with R22 was that COP, cooling capacity, and discharge temperature of R407C were lower compared to that of R22. Energy consumption and discharge pressure were higher compared to R22 [19] compared the supply water temperature of air source heat pump with R143a. The COP of R152a > R134a > R143a > R32. As per the paper, R152a can be used as a reasonable choice for space heating. From the theoretical results, [20] it was observed that COP of refrigerant blend R134a/R1270/R290 results increase in COP higher than the R22. The results show [21] the refrigerant blend M8 (R1270/R290) composition by mass% (75/25) COP (3.566) was nearest to R22 (3.601) among all the refrigerants taken into consideration. The discharge temperature of refrigerants was in the range of 5.6 to  $-8.4$  °C when compared with R22.

The results showed that [24] a mixture of R-1234yf/R-600a and R-1270/R-600a offers an increase in COP compared with R600a. From the experimental results of [25], it was shown with passive techniques and inclusion of nanoparticles with refrigerant performance of system is increased. The TiO<sub>2</sub> based nanolubricants [26] (i.e., 0.2, 0.4, and 0.6 g/L) gave higher power per ton of refrigeration than baseline refrigerant. The addition of TiO<sub>2</sub> nanolubricant enhances the cooling rate, whereas the COP was slightly less than baseline refrigerant. From the experiment conducted [27], it was concluded that the nanoparticle-based refrigerant worked safely in a domestic refrigerator. The performance was better than R600a with TiO<sub>2</sub>-R600a nano refrigerant. At 40 g of R600a, the nano refrigerant has the highest refrigerating effect and COP than R600a. In the results published by [28], suitable heat rejection without any blockage in the condenser was observed with an evaporative cooling pad and nano refrigerant the performance is enhanced compared to without nano refrigerant. From the experiment, the results show [29] the power utilization of compressor was decreased by 25% when nanolubricant was utilized rather than ordinary POE oil.

## 4 Merit and Analysis from the Research Papers

1. It is observed that mixing different refrigerants blends will give better coefficient of performance for pure hydrocarbons.
2. Hydrofluoro-olefins (HFO) refrigerants can be drop in substitute to R134a refrigerant.
3. Adding nanoparticle to lubricants or directly mixing with refrigerant will enhance the heat transfer characteristics in refrigeration and air conditioning systems.

## 5 Conclusion

From the results published from various papers, it was concluded that in terms of performance, we can choose nano-based refrigerants which give high performance compared to other refrigerants. If the performance of the system was not the first criteria, then we can choose eco-friendly refrigerants like R-1234yf, R1234ze as their global warming potential was very small compared to other HFC and HCFC refrigerants. Nanoparticles mixing with lubricants in compressor and nanofluid refrigerants were better alternative refrigerants when compared to currently employed refrigerants. Hence, more research work has to be done on nanoparticles to enhance their performance when deploying in vapor compression refrigeration system.

## References

1. Greenhouse Gases Monitoring References National Centers for Environmental Information (NCEI). <https://www.ncdc.noaa.gov/monitoring-references/faq/greenhouse-gases.php?section=watervapor> (Accessed 04 Jun. 2020)
2. Partridge, M.R.: The Montreal protocol. What does transition to CFC free metered dose inhalers mean for the health professional now? *Revue Française d'Allergologie et d'Immunol. Clinique* **38**(7), Supplement 1, pp. S94–S96 (1998). [https://doi.org/10.1016/S0335-7457\(98\)80079-8](https://doi.org/10.1016/S0335-7457(98)80079-8)
3. Kumar, K.S., Rajagopal, K.: Computational and experimental investigation of low ODP and low GWP HCFC-123 and HC-290 refrigerant mixture alternate to CFC-12. *Energy Convers. Manage.* **48**(12), 3053–3062 (2007). <https://doi.org/10.1016/j.enconman.2007.05.021>
4. Calm, J.M.: The next generation of refrigerants—historical review, considerations, and outlook. *Int. J. Refrig.* **31**(7), 1123–1133 (2008). <https://doi.org/10.1016/j.ijrefrig.2008.01.013>
5. Messineo, A., La Rocca, V., Panno, G.: On-site experimental study of HCFC-22 substitution with HFCs refrigerants. *Energy Procedia* **14**, 32–38 (2012). <https://doi.org/10.1016/j.egypro.2011.12.893>
6. Hernandez, J.I., Roman, R., Best, R., Dorantes, R., Gonzalez, H.E.: The behavior of an ejector cooling system operating with refrigerant blends 410A and 507. *Energy Procedia* **57**, 3021–3030 (2014). <https://doi.org/10.1016/j.egypro.2014.10.338>
7. Kundu, A., Kumar, R., Gupta, A.: Performance comparison of zeotropic and azeotropic refrigerants in evaporation through inclined tubes. *Procedia Eng.* **90**, 452–458 (2014). <https://doi.org/10.1016/j.proeng.2014.11.755>
8. Abas, N., Nawaz, R., Khan, N.: Parametric quantification of low GWP refrigerant for thermosiphon driven solar water heating system. *Procedia Comput. Sci.* **52**, 804–811 (2015). <https://doi.org/10.1016/j.procs.2015.05.136>
9. Devocioğlu, A.G., Oruç, V.: Characteristics of some new generation refrigerants with low GWP. *Energy Procedia* **75**, 1452–1457 (2015). <https://doi.org/10.1016/j.egypro.2015.07.258>
10. Aprea, C., Greco, A., Maiorino, A., Masselli, C., Metallo, A.: HFO1234ze as drop-in replacement for R134a in domestic refrigerators: an environmental impact analysis. *Energy Procedia* **101**, 964–971 (2016). <https://doi.org/10.1016/j.egypro.2016.11.122>
11. Desai, N.S., Patil, P.R.: Application of SiO<sub>2</sub> Nanoparticles as Lubricant Additive in VCRS: An Experimental Investigation, vol. 4, p. 6 (2015)
12. Li, H., Yang, W., Yu, Z., Zhao, L.: The performance of a heat pump using nanofluid (R22+TiO<sub>2</sub>) as the working fluid—an experimental study. *Energy Procedia* **75**, 1838–1843 (2015). <https://doi.org/10.1016/j.egypro.2015.07.158>

13. Vandaarkuzhali, S., Elansezhian, D.R.: Performance evaluation of air conditioning system using nanofluids. *Austr. J. Basic Appl. Sci.*, 10 (2015)
14. Chien, N.B., Vu, P.Q., Choi, K.-I., Oh, J.-T.: Boiling heat transfer of R32, CO<sub>2</sub> and R290 inside horizontal minichannel. *Energy Procedia* **105**, 4822–4827 (2017). <https://doi.org/10.1016/j.egypro.2017.03.955>
15. Choudhari, C.S., Sapali, S.N.: Performance investigation of natural refrigerant R290 as a substitute to R22 in refrigeration systems. *Energy Procedia* **109**, 346–352 (2017). <https://doi.org/10.1016/j.egypro.2017.03.084>
16. Devecioğlu, A.G., Oruç, V.: An analysis on the comparison of low-GWP refrigerants to alternatively use in mobile air-conditioning systems. *Therm. Sci. Eng. Progr.* **1**, 1–5 (2017). <https://doi.org/10.1016/j.tsep.2017.02.002>
17. Kasera, S., Bhaduri, S.C.: Performance of R407C as an alternate to R22: a review. *Energy Procedia* **109**, 4–10 (2017). <https://doi.org/10.1016/j.egypro.2017.03.032>
18. Molés, F., Navarro-Esbrí, J., Peris, B., Mota-Babiloni, A., Mateu-Royo, C.: R1234yf and R1234ze as alternatives to R134a in organic rankine cycles for low temperature heat sources. *Energy Procedia* **142**, 1192–1198 (2017). <https://doi.org/10.1016/j.egypro.2017.12.380>
19. Nie, J., Li, Z., Kong, X., Li, D.: Analysis and comparison study on different HFC refrigerants for space heating air source heat pump in rural residential buildings of North China. *Procedia Eng.* **205**, 1201–1206 (2017). <https://doi.org/10.1016/j.proeng.2017.10.354>
20. Shaik, S.V., Babu, T.P.A.: Theoretical performance investigation of vapour compression refrigeration system using HFC and HC refrigerant mixtures as alternatives to replace R22. *Energy Procedia* **109**, 235–242 (2017). <https://doi.org/10.1016/j.egypro.2017.03.053>
21. Shaik, S.V., Babu, T.P.A.: Thermodynamic performance analysis of eco friendly refrigerant mixtures to replace R22 used in air conditioning applications. *Energy Procedia* **109**, 56–63 (2017). <https://doi.org/10.1016/j.egypro.2017.03.049>
22. Gaurav Kumar, R.: Computational energy and exergy analysis of R134a, R1234yf, R1234ze and their mixtures in vapour compression system. *Ain Shams Eng. J.* **9**(4), 3229–3237 (2018). <https://doi.org/10.1016/j.asej.2018.01.002>
23. Eyerer, S., Dawo, F., Kaindl, J., Wieland, C., Spliethoff, H.: Experimental investigation of modern ORC working fluids R1224yd(Z) and R1233zd(E) as replacements for R245fa. *Appl. Energy* **240**, 946–963 (2019). <https://doi.org/10.1016/j.apenergy.2019.02.086>
24. Calleja-Anta, D., Nebot-Andrés, L., Catalán-Gil, J., Sánchez, D., Cabello, R., Llopis, R.: Thermodynamic screening of alternative refrigerants for R290 and R600a. *Results Eng.* **5**, 100081 (2020). <https://doi.org/10.1016/j.rineng.2019.100081>
25. Rahman, S., Issa, S., Said, Z., El Haj Assad, M., Zadeh, R., Barani, Y.: Performance enhancement of a solar powered air conditioning system using passive techniques and SWCNT /R-407c nano refrigerant. *Case Stud. Therm. Eng.* **16**, 100565 (2019). <https://doi.org/10.1016/j.csite.2019.100565>
26. Adelekan, D.S., Ohunakin, O.S., Gill, J., Atiba, O.E., Okokpujie, I.P., Atayero, A.A.: Performance of a domestic refrigerator infused with safe charge of R600a refrigerant and various concentrations of TiO<sub>2</sub> nanolubricants. *Procedia Manuf.* **35**, 1158–1164 (2019). <https://doi.org/10.1016/j.promfg.2019.06.071>
27. Adelekan, D.S., Ohunakin, O.S., Gill, J., Atiba, O.E., Okokpujie, I.P., Atayero, A.A.: Experimental investigation of a vapour compression refrigeration system with 15nm TiO<sub>2</sub>-R600a nano-refrigerant as the working fluid. *Procedia Manuf.* **35**, 1222–1227 (2019). <https://doi.org/10.1016/j.promfg.2019.06.079>
28. Dhamneya, A.K., Rajput, S.P.S., Singh, A.: Comparative performance analysis of ice plant test rig with TiO<sub>2</sub>-R-134a nano refrigerant and evaporative cooled condenser. *Case Stud. Therm. Eng.* **11**, 55–61 (2018). <https://doi.org/10.1016/j.csite.2017.12.004>
29. Subramani, N., Prakash, M.: Experimental studies on a vapour compression system using nanorefrigerants. *Int. J. Eng. Sci. Tech* **3**(9), 95–102 (2012). <https://doi.org/10.4314/ijest.v3i9.8>

# Optimization of Nanofluid Parameters for Double Pipe Heat Exchanger



K. Manjunath

## 1 Introduction

Nanofluids usage for upgrading the performance of heat transfer equipment are increasing from last one decade. Various nanoparticles which have high value of conductivity and heat capacity are mixed in required proportions to base fluids and are used in various heat exchangers that resulted in improvements in heat transfer. At the same time, the usage of nanofluids turns to disadvantages in terms of more of fluids pressure drop due to increase of properties like viscosity and density. These aspects are not been able to easily investigate by the use of first law thermodynamic analysis. The different irreversibilities occurring because of heat transfer, imbalance between the streams, pressure drop, etc., in heat exchanger processes are able to analyze by second law analysis. The methods of second law involve entropy generation and exergy analysis [1]. Extensive reviews of heat exchangers were carried out by Manjunath et al. [2] using the method of second law analysis and constructal law.

In the last one decade, researchers are carrying out the research of second law analysis of nanofluid heat exchangers. Some of the literature which is related to this analysis are reviewed. Entropy generation analysis of applications of nanofluids in different thermal equipments is analyzed by [3–18] using numerical, experimental, and analytical methods.

From the literature review, it is found that there are very scare papers which uses entropy generation and exergetic efficiency analysis of counterflow DPHE. The best volume concentrations and diameter of nanoparticle selection are usually done by the first law thermodynamics analysis. While this resulted in improve of heat transfer and effectiveness of heat exchangers, there is no sure that the losses are reduced. These aspects can be easily found out by the use of second law thermodynamics

---

K. Manjunath (✉)

Department of Mechanical Engineering, Delhi Technological University, Bawana Road, Delhi 110042, India

procedures in which various types of irreversibilities are found out in heat exchangers. The second law efficiency considers these losses and provides optimum values of volume concentrations and diameter of nanoparticle which not only reduces losses but also increases performances. This is illustrated for a type of counterflow heat exchanger which is commonly used in process heating and cooling that is DPHE. Comparison of the performance of nanofluid with the normal fluid is carried out. The commonly used nanofluid combination, namely water-alumina (water- $\text{Al}_2\text{O}_3$ ), is used by varying its volume fractions and particle diameter. Other parameters which are considered for the analysis are hot fluid temperature drop, surface area, and length-to-diameter ratio. Improvements of second law efficiency is observed by the use of optimum values of nanoparticle parameters.

## 2 Analysis

For this analysis, the counterflow DPHE is considered as shown in Fig. 1 which consists of its geometrical parameters. In DPHE, nanofluid (cold fluid) flowing in outer tube is heated by hot water flowing in inner tube. Some of the assumptions considered for the analysis are the flow will be fully developed turbulent, and the fluids flow pressure drop is assumed to be friction in constant cross section of tube only and pressure loss due to joints are neglected. The heat transfer between cold and hot streams is excellent, and fouling resistances are neglected [19].

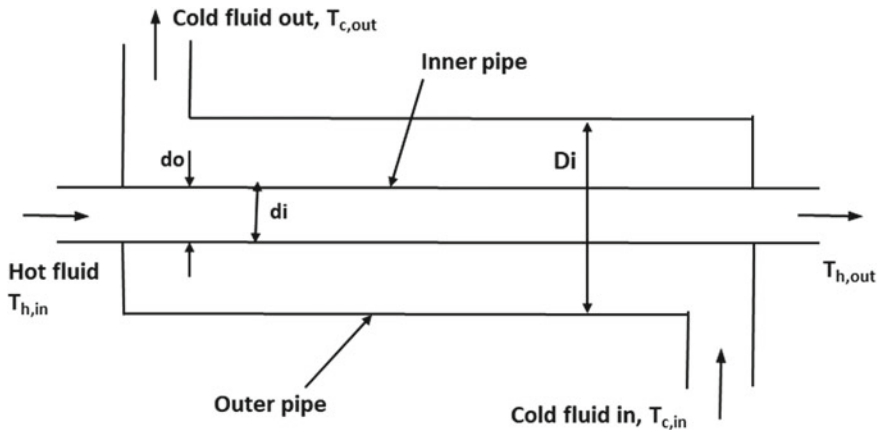


Fig. 1 Double pipe counterflow nanofluid heat exchanger nomenclature

### 2.1 Properties of Nanofluid

As provided in [6], the following thermophysical properties are used in the analysis. Density of nanofluid is given as,

$$\rho_{nf} = (1 - \varphi)\rho_{bf} + \varphi\rho_p \tag{1}$$

Nanofluid specific heat at constant pressure is found by the following relation,

$$c_{p,nf} = \frac{(1 - \varphi)\rho_{bf}c_{p,bf} + \varphi\rho_p c_{p,p}}{\rho_{nf}} \tag{2}$$

Thermal conductivity of nanofluid is found by the following relation,

$$\frac{k_{nf}}{k_{bf}} = 1 + 4.4Re_d^{0.4}Pr_{bf}^{0.66} \left(\frac{T_{nf}}{T_{fr}}\right)^{10} \left(\frac{k_p}{k_{bf}}\right)^{0.03} \varphi^{0.66} \tag{3}$$

where  $T_{fr}$  will be base fluid freezing point and  $Re_d$  will be the nanoparticles Reynolds number given as

$$Re_d = \frac{\rho_{bf}u_b d_p}{\mu_{bf}} \tag{4}$$

Here  $u_b$  is the Brownian velocity given as,

$$u_b = \frac{2k_b T_{nf}}{\pi \mu_{bf} d_p^2} \tag{5}$$

where  $k_b$  is Boltzmann’s constant given as  $1.38 \times 10^{-23}$  J/K. Nanofluid viscosity is found by the following relation,

$$\frac{\mu_{nf}}{\mu_{bf}} = \frac{1}{1 - 0.10255d_p^{-0.264}\varphi^{1.028}} \tag{6}$$

### 2.2 Exergetic Efficiency and Entropy Generation Number

The exergetic efficiency expression for heat exchanger is given as [20, 21],

$$\psi = \frac{\dot{E}_c^T}{\dot{E}_c^T + \dot{I}} \tag{7}$$



The cold stream thermal part of exergy is given by the following expression [20],

$$\dot{E}_c^T = C_c \left[ \varepsilon (T_{h,in} - T_{c,in}) - T_o \ln \left\{ 1 + \varepsilon \left( \frac{T_{h,in}}{T_{c,in}} - 1 \right) \right\} \right] \quad (8)$$

The irreversibility expression given by Gouy–Stodola formula is defined as product of reference temperature and entropy generation rate,

$$\dot{i} = T_o \dot{S}_{gen} \quad (9)$$

The  $S_{gen}$  is obtained in terms of  $N_s$  and  $C_{min}$  as,

$$\dot{i} = T_o (N_s C_{min}) \quad (10)$$

where the  $N_s$  is obtained by dividing  $S_{gen}$  with  $C_{min}$  [1] as follows.

$$N_s = \frac{\dot{S}_{gen}}{(\dot{m}c_p)_{min}} \quad (11)$$

The  $S_{gen}$  is defined as [2],

$$\begin{aligned} \dot{S}_{gen} = & (\dot{m}c_p)_c \ln \left( \frac{T_{c,out}}{T_{c,in}} \right) + (\dot{m}c_p)_h \ln \left( \frac{T_{h,out}}{T_{h,in}} \right) \\ & + \left( \frac{\dot{m}}{\rho T_{ave}} \right)_c (\Delta P)_c + \left( \frac{\dot{m}}{\rho T_{ave}} \right)_h (\Delta P)_h \end{aligned} \quad (12)$$

Equation (12) is divided into terms of  $Q$  and  $\Delta P$  as follows, respectively [1],

$$\dot{S}_{gen,T} = (\dot{m}c_p)_c \ln \left( \frac{T_{c,out}}{T_{c,in}} \right) + (\dot{m}c_p)_h \ln \left( \frac{T_{h,out}}{T_{h,in}} \right) \quad (13)$$

$$\dot{S}_{gen,P} = \frac{8\dot{m}^3 f Re}{\pi^2 \rho^2 T_{ave} D^5} \quad (14)$$

Heat capacity of heat exchanger is obtained by multiplying the specific heat and flow rate for both streams.

$$(\dot{m}c_p)_c = C_c \quad \text{and} \quad (\dot{m}c_p)_h = C_h \quad (15)$$

The ratio of heat capacity rate is given as,

$$C = \frac{C_{max}}{C_{min}} \quad (16)$$

Here in this analysis, defining  $C_{max} = C_c$  and  $C_{min} = C_h$ , [19],

$$C = \frac{C_c}{C_h} \quad (17)$$

Substituting entropy generation rate Eqs. (13) and (14) in Eq. (11), we will obtain the dimensionless  $N_s$  for unbalanced heat exchanger (including imbalance irreversibility) as,

$$N_s = \ln \left[ 1 + \varepsilon \left( \frac{T_{h,in}}{T_{c,in}} - 1 \right) \right] + C \ln \left[ 1 - \frac{1}{C} \varepsilon \left( 1 - \frac{T_{c,in}}{T_{h,in}} \right) \right] + \frac{1}{C_{\min}} \left\{ \left[ \frac{8\dot{m}^3 f \text{Re}}{\pi^2 \rho^2 T_{\text{ave}} D^5} \right]_c + \left[ \frac{8\dot{m}^3 f \text{Re}}{\pi^2 \rho^2 T_{\text{ave}} D^5} \right]_h \right\} \quad (18)$$

The number of units of heat transfer (NTU) and effectiveness expression for heat exchanger with counterflow is given as,

$$\varepsilon = \frac{1 - e^{-\text{NTU}(1-C_{\min}/C_{\max})}}{1 - (C_{\min}/C_{\max})e^{-\text{NTU}(1-C_{\min}/C_{\max})}} \quad (19)$$

Here NTU is defined as,

$$\text{NTU} = \frac{U A_s}{C_{\min}} \quad (20)$$

where  $A_s$  is the area of heat transfer surface given as,

$$A_s = \pi d_o L \quad (21)$$

where  $L$  is the length of the DPHE. The overall heat transfer coefficient which is based on the outside area of the inner tube is given as [22],

$$\frac{1}{U} = \frac{d_o}{d_i h_i} + \frac{d_o \ln(d_o/d_i)}{2k_m} + \frac{1}{h_o} \quad (22)$$

where  $h_i$  is the heat transfer coefficient of inner tube carrying hot fluid, which is found as follows,

$$h_i = \frac{\text{Nu}_h k}{d_i} \quad (23)$$

where  $\text{Nu}_h$  is the Nusselt number of inner tube fluid turbulent flow (fully developed) given as,

$$\text{Nu}_h = 0.023 \text{Re}_h^{0.8} \text{Pr}_h^{0.4} \quad (24)$$

where  $\text{Re}_h$  is the Reynolds number given as,

$$\text{Re}_h = \frac{\rho_h V_h d_i}{\mu_h} \quad (25)$$

where  $V_h$  is the velocity of inner tube fluid. The friction factor for the hot fluid is given as,

$$f_h = 0.316 \text{Re}_h^{-0.25} \quad (26)$$

The heat transfer coefficient,  $h_o$  of outer tube in which cold nanofluid flows is obtained by the following procedure.

$$h_o = \frac{\text{Nu}_c k}{D_e} \quad (27)$$

where  $D_e$  is the outer pipe equivalent diameter given as,

$$D_e = \frac{D_i^2 - d_o^2}{d_o} \quad (28)$$

The  $\text{Nu}_c$  is the Nusselt number of outer tube fluid turbulent flow (fully developed) given as [6],

$$\text{Nu}_c = 0.021 \text{Re}_c^{0.8} \text{Pr}_c^{0.5} \quad (29)$$

Here  $\text{Re}_c$  is the Reynolds number given as,

$$\text{Re}_c = \frac{\rho_c V_c D_c}{\mu_c} \quad (30)$$

where  $V_h$  is the velocity of outer tube fluid.  $D_c$  is the hydraulic diameter of outer tube given as,

$$D_c = D_i - d_o \quad (31)$$

The friction factor for the cold fluid is given as [6],

$$f_c = [0.79 \ln(\text{Re}_c) - 1.64]^{-2} \quad (32)$$

The heat transfer rate of DPHE is obtained as,

$$\dot{Q} = U A_s (T_{h,in} - T_{c,out}) \quad (33)$$

Heat exchanger pressure drop is given as,

$$\Delta P = \frac{f_c L \rho_c V_c^2}{2D_c g} + \frac{f_h L \rho_h V_h^2}{2d_i g} \quad (34)$$

### 3 Results and Discussion

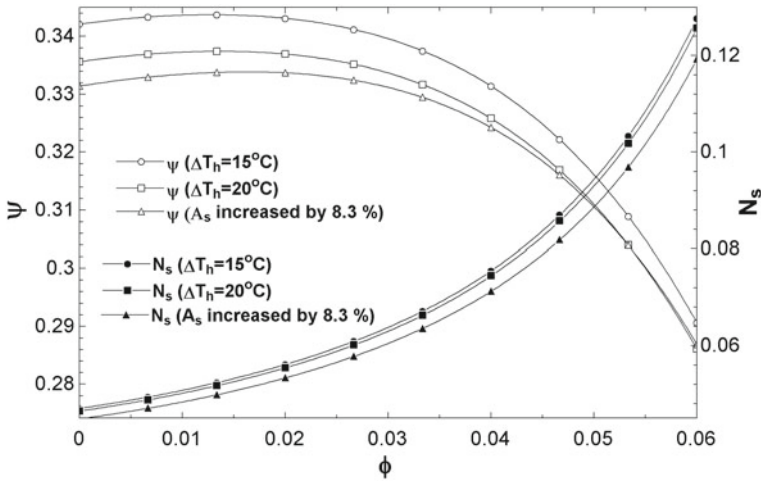
For the simulations, the parameter input values considered for the analysis with reference to [22] are as follows: The geometrical dimensions of double pipe heat exchanger (DPHE): inner pipe inside diameter ( $d_i$ ) = 0.0525 m, outside diameter ( $d_o$ ) = 0.0603 m. For the given length-to-diameter ratio ( $L/D$ ), the length will be obtained. The DPHE outer pipe inside diameter ( $D_i$ ) = 0.0779 m. The DPHE material is carbon steel having conductivity ( $k_m$ ) = 54 W/mK.

Operating parameters: The hot water is made to flow in the inner pipe at the inlet temperature ( $T_{h,in}$ ) = 140 °C, temperature drop ( $\Delta T_h$ ) = 15 °C. The cold nanofluid or only cold water is made to flow in the outer pipe, and its temperature is raised from ( $T_{c,in}$ ) = 20 °C to ( $T_{c,out}$ ) = 35 °C. The base fluid and hot water properties are referred by the average temperature of fluids.

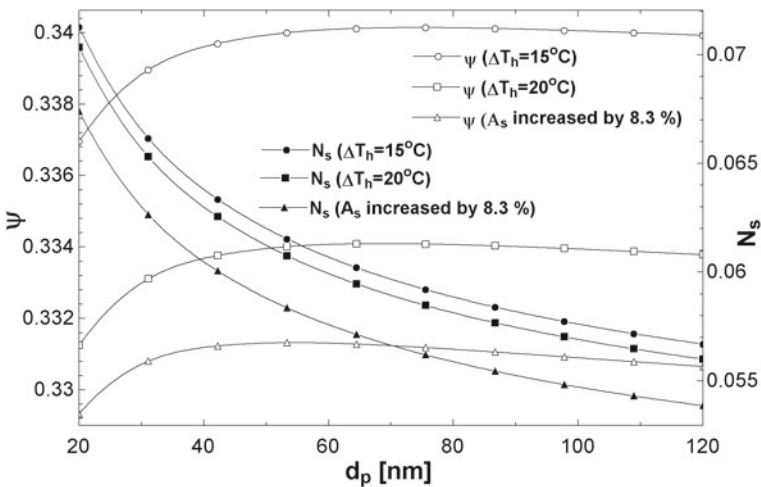
In this analysis, to compare the performance for DPHE with and without nanofluid (only base fluid) the surface area ( $A_s$ ) and temperature difference between the fluids ( $\Delta T$ ) are considered the same. The nanofluid considered is water–alumina ( $Al_2O_3$ –water) and its properties are referred from [3]. For nanoparticle (alumina): density ( $\rho_p$  = 3900 kg/m<sup>3</sup>), conductivity ( $k_p$  = 40 W/m K), specific heat ( $c_{p,p}$  = 880 J/kg K). The simulations are carried out in EES software [23], and the outputs are obtained. Reynolds number for turbulent flow (fully developed) is analyzed for  $2 \times 10^4$  [6]. The general values of nanofluid are volume concentrations ( $\varphi$  = 0.03) and particle diameter ( $d_p$  = 40 nm).

Figure 2 displays the behavior of exergetic efficiency ( $\psi$ ) and dimensionless entropy generation number ( $N_s$ ) for variations in the value of nanoparticles volume concentration ( $\varphi$ ) for different values of hot fluid temperature drop ( $\Delta T_h$ ) and increase in the surface area ( $A_s$ ), (as an example to study the increase in surface area parameter). Maxima value of  $\psi$  is obtained as the  $\varphi$  increased, while there is increasing trend of  $N_s$ . For the considered input values, optimum value of  $\varphi$  is obtained for higher value of exergetic efficiency. As the value of  $\Delta T_h$  increased,  $\psi$  decreases because of increase of irreversibility due to heat transfer as shown in the variations of  $N_s$ . For the increase of  $A_s$  value, the value of  $\psi$  decreases. This is due to decrease in the value of NTU which is also reflected in the result of  $N_s$ . The NTU equation is defined in Eq. (20) and affects Eqs. (19), (18), (10) and (7)—which affects  $\psi$ .

Figure 3 displays the variations  $\psi$  and  $N_s$  for the increase of another important parameter of nanofluid particle diameter ( $d_p$ ). Here also, maxima value of  $\psi$  is resulted by the increase of  $d_p$ , but  $N_s$  will decrease. The reason is that as  $d_p$  increases due to increase in thermal conductivity of nanoparticles, the  $Q$  increases which resulted in increase of  $\psi$ . But after some value of  $d_p$ , the viscosity of nanofluid



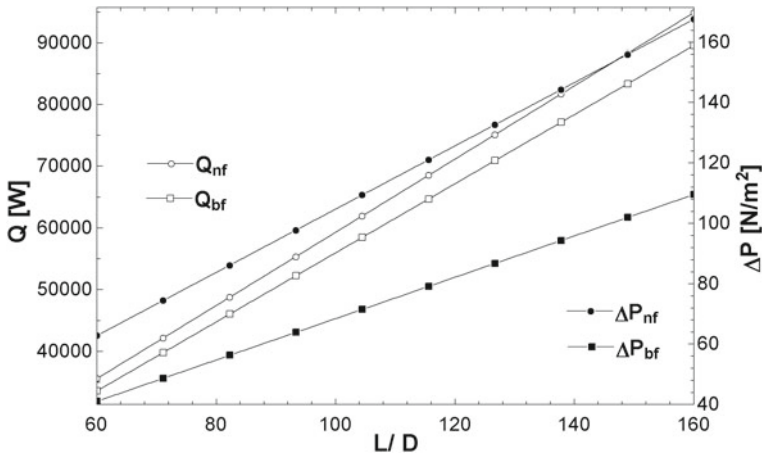
**Fig. 2** Relationship of exergetic efficiency ( $\psi$ ) and entropy generation number ( $N_s$ ) with volume concentrations ( $\phi$ )



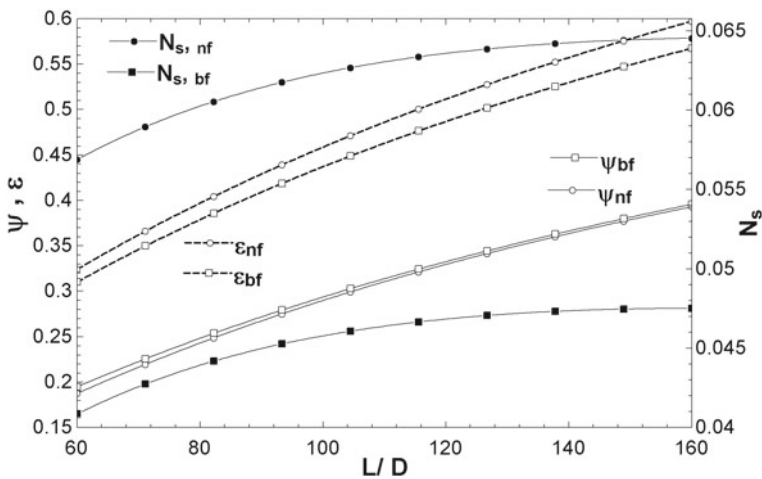
**Fig. 3** Relationship of exergetic efficiency ( $\psi$ ) and entropy generation number ( $N_s$ ) with nanoparticle diameter ( $d_p$ )

increases, which results in the increase of  $\Delta P$  which resulted in decrease of  $\psi$ . Optimum value of  $d_p$  obtained for the considered input parameters will provide higher performance based on second law method. For increase in  $\Delta T_h$  and  $A_s$ , the  $\psi$  and  $N_s$  decrease due to lower value of NTU.

Figures 4 and 5 show the variations of  $Q$ ,  $\Delta P$ ,  $\psi$ ,  $\varepsilon$ , and  $N_s$  for the variations of length-to-diameter ratio ( $L/D$ ). All these parameters, increases for increase in  $L/D$ .



**Fig. 4** Relationship of heat transfer rate ( $Q$ ) and pressure drop ( $\Delta P$ ) with length-to-diameter ratio ( $L/D$ )



**Fig. 5** Relationship of exergetic efficiency ( $\psi$ ), effectiveness ( $\epsilon$ ), and entropy generation number ( $N_s$ ) with length-to-diameter ratio ( $L/D$ )

Also, the comparison of the performance of DPHE with and without nanofluid (base fluid only) is produced in Figs. 4 and 5. For the considered conditions of same heat transfer surface area and temperature difference between fluids, there is increase in the value of rate of heat transfer for nanofluid DPHE ( $Q_{nf}$ ) compared to rate of heat transfer without nanofluid ( $Q_{bf}$ ). But there is increase of pressure drop  $\Delta P$  for nanofluid because of increase of viscosity due to added nanoparticles. The reasons for this are explained with the help of Fig. 5. For nanofluid, there will be more losses

happens in particularly in terms of higher pressure drop entropy generation ( $N_{s,nf} > N_{s,bf}$ ) as shown in Fig. 5. Because of this, the  $\psi_{nf}$  is having lower value in comparison with  $\psi_{bf}$ . From first law analysis, these aspects cannot be found out as the case of effectiveness ( $\epsilon_{nf} > \epsilon_{bf}$ ).

Table 1 gives the values of important results for the optimum values of nanoparticles volume concentration and nanofluid particle diameter based on the outputs from Figs. 2 and 3. With the use of optimum values of nanofluid properties, the  $\psi_{nf}$  has higher value in comparison with  $\psi_{bf}$ , even though in Fig. 5 there is ( $\psi_{nf} < \psi_{bf}$ ). It is observed from Table 1 that there are advantages of using nanofluid in DPHE with increase in following outputs ( $Q_{nf} > Q_{bf}$ ), ( $\epsilon_{nf} > \epsilon_{bf}$ ), ( $NTU_{nf} > NTU_{bf}$ ). But, at the same instance, there is increase in the following outputs ( $\Delta P_{nf} > \Delta P_{bf}$ ), ( $N_{s,nf} > N_{s,bf}$ ) which are disadvantages of using nanofluid in heat exchangers.

Although, from Table 1, the increase in pressure drop resulting to 11%, this does not indicate the overall performance of the DPHE. The pressure drop parameter is a part of irreversibilities of whole DPHE which also includes irreversibility due to

**Table 1** Results based on optimum values of  $\varphi$  and  $d_p$

Results with symbol	Values with units
Nanoparticles volume concentration ( $\varphi$ )	0.01288
Nanofluid particle diameter ( $d_p$ )	74.51 nm
Exergetic efficiency ( $\psi_{nf}$ )—with nanofluid	34.28%
Exergetic efficiency ( $\psi_{bf}$ )—without nanofluid	33.59%
Entropy generation number ( $N_{s,nf}$ )—with nanofluid	0.05096
Entropy generation number ( $N_{s,bf}$ )—without nanofluid	0.04716
Heat transfer rate ( $Q_{nf}$ )—with nanofluid	69,584 kW
Heat transfer rate ( $Q_{bf}$ )—without nanofluid	67,197 kW
Pressure drop ( $\Delta P_{nf}$ )—with nanofluid	92.39 N/m <sup>2</sup>
Pressure drop ( $\Delta P_{bf}$ )—without nanofluid	82.18 N/m <sup>2</sup>
Effectiveness ( $\epsilon_{nf}$ )—with nanofluid	0.3428
Effectiveness ( $\epsilon_{bf}$ )—without nanofluid	0.3359
Number of heat transfer units ( $NTU_{nf}$ )—with nanofluid	0.9009
Number of heat transfer units ( $NTU_{bf}$ )—without nanofluid	0.87

heat transfer and imbalance between the fluid streams. This can be explained with the help of  $\psi$  Eq. (7),  $N_s$  Eq. (18) (both are non-dimensional performance parameters). The increase of  $\psi$  in terms of 0.7% is resulted as a whole performance of DPHE including the other increasing and decreasing parameters. The increase in  $\psi$  is also resulted by the increase of other parameters such as  $\varepsilon$  (2% increase) and NTU (3.4% increase). This is the reason that why it is needed to analyze the thermal systems by using second law.

## 4 Conclusions

The nanofluid parametric optimization is carried out for the double pipe counter-flow heat exchanger. The second law thermodynamics performance parameters like exergetic efficiency and entropy generation number are used for parametric analysis along with effectiveness. Nanofluids are nowadays used to increase the heat transfer rate. For the considered input values for DPHE, optimum values of nanofluid volume concentrations and nanoparticle diameter are obtained for higher values of exergetic efficiency. The variations of other important parameters such as hot fluid temperature drop, surface area, and length-to-diameter ratio are investigated for the considered DPHE. Comparisons of DPHE with nanofluid and without (only use of base fluid) are carried out by considering the same heat transfer surface area and fluids temperature difference.

Although there is increase in heat transfer and effectiveness of DPHE by using nanofluid as working fluid, at the same time there is increase of fluid pressure drop. This results in increase of entropy generation of nanofluid and reduction in exergetic efficiency. So, from the adopted procedure in this paper, the DPHE needs to be operated with optimum nanofluid parameters at which the highest performance is obtained with lower irreversibilities.

By considering the obtained optimum values of nanoparticle concentrations and diameter, the exergetic efficiency of DPHE will improve and achieve higher value as compared to base fluid only.

## References

1. Bejan, A.: Entropy-Generation-Minimization. CRS Press. Boca Raton (1996)
2. Manjunath, K., Kaushik, S.C.: Second-law-thermodynamic study of heat exchangers: a review. *Renew. Sustain. Energy Rev.* **40**, 348–374 (2014)
3. Singh, P.K., Anoop, K.B., Sundararajan, T., Das, S.K.: Entropy generation due to fluid flow and heat-transfer in nanofluids. *Int. J. Heat Mass Transfer* **53**(21–22), 4757–4767 (2010)
4. Moghaddami, M., Mohammadzade, A., Esfehiani, S.A.V.: Second-law analysis of nanofluid flow. *Energy Convers. Manag.* **52**(2), 1397–1405 (2011)
5. Sohel, M.R., Saidur, R., Hassan, N.H., Elias, M.M., Khaleduzzaman, S.S., Mahbulul, I.M.: Analysis of entropy-generation using nanofluid flow through the circular micro channel and mini channel heat sink. *Int. Commun. Heat Mass Transfer* **46**, 85–91 (2013)



6. Bianco, Vincenzo, Oronzio Manca, and Sergio Nardini.: Entropy-generation analysis of turbulent convection flow of  $\text{Al}_2\text{O}_3$ -water nanofluid in circular tube subjected to constant wall heat-flux. *Energy Conversion and Management* **77**, 306–314 (2014).
7. Bianco, V., Manca, O., Nardini, S.: Performance analysis of turbulent convection heat-transfer of  $\text{Al}_2\text{O}_3$  water nanofluid in circular tubes at constant-wall temperature. *Energy* **77**, 403–413 (2014)
8. Khaleduzzaman, S.S., Soheli, M.R., Mahbubul, I.M., Saidur, R., Selvaraj, J.: Exergy and entropy-generation analysis of  $\text{TiO}_2$  water nanofluid flow through the water block as an electronics device. *Int. J. Heat Mass Transf.* **101**, 104–111 (2016)
9. Bahiraei, M., Majd, S.M.: Prediction of entropy-generation for nanofluid flow through a triangular mini channel using neural-network. *Adv. Powder Technol.* **27**(2), 673–683 (2016)
10. Sarlak, A., Ahmadpour, A., Hajmohammadi, M.R.: Thermal design improvement of a double layered micro channel heat sink by using multi walled carbon nanotube nanofluids with non Newtonian viscosity. *Appl. Therm. Eng.* **147**, 205–215 (2019)
11. Hajmohammadi, M.R., Toghrayi, I.: Optimal-design and thermal-performance improvement of a double layered micro channel heat sink by introducing  $\text{Al}_2\text{O}_3$  nano particles into the water. *Phys. A* **505**, 328–344 (2018)
12. Bhattad, A., Sarkar, J., Ghosh, P.: Energetic and exergetic performances of plate-heat exchanger using brine based hybrid nanofluid for milk chilling application. *Heat Transfer Eng.* **41**(6–7), 522–535 (2020)
13. Rashidi, M.M., Nasiri, M., Shadloo, M.S., Yang, Z.: Entropy-generation in a circular tube heat exchanger using nanofluids effects of different modeling approaches. *Heat Transfer Eng.* **38**(9), 853–866 (2017)
14. Deymi-Dashtebayaz, M., Akhoundi, M., Ebrahimi-Moghadam, A., Arabkoohsar, A., Moghadam, A.J., Farzaneh-Gord, M.: Thermo hydraulic analysis and optimization of CuO water nanofluid inside helically dimpled-heat exchangers. *J. Thermal Anal. Calorimetry* 1–16 (2020)
15. Nakhchi, M.E., Rahmati, M.T.: Entropy-generation of turbulent Cu water nanofluid flows inside thermal systems equipped with transverse cut twisted turbulators. *J. Thermal Anal. Calorimetry* 1–10 (2020)
16. Bhattad, A., Sarkar, J., Ghosh, P.: Heat-transfer characteristics of plate heat exchanger using hybrid nanofluids: effect of nanoparticle mixture-ratio. *Heat Mass Transfer* 1–16 (2020)
17. Shafee, A., Sheikholeslami, M., Jafaryar, M., Babazadeh, H.: Irreversibility of hybrid-nanoparticles within a pipe fitted with turbulator. *J. Thermal Anal. Calorimetry* 1–9 (2020)
18. Wang, Z., Han, F., Ji, Y., Li, W.: Performance and exergy-transfer analysis of heat exchangers with graphene-nanofluids in seawater source marine heat pump system. *Energies* **13**(7), 1762 (2020)
19. Manjunath, K., Kaushik, S.C.: Second-law efficiency analysis of heat-exchangers. *Heat Transfer Asian Res.* **44**, 289–108 (2015)
20. Kotas, T.-J.: *The Exergy-Method of Thermal Plant Analysis*. Elsevier (2013)
21. Manjunath, K., Kaushik, S.C.: The second-law analysis of an unbalanced-constructal heat exchanger. *Int. J. Green Energy* **11**(2), 173–192 (2014)
22. Kakac, S., Liu, H.: *Heat Exchangers Selection, Rating and Thermal Design*. CRC Press (1997)
23. Klein, S.A.: *Engineering-Equation-Solver, Version 8.158*. F-Chart Software, Middleton, WI (2008)

# CFD Analysis of a Mixed Convection Heat Transfer Square Cavity with Hybrid Nanofluids



Chinta Rajeev Durga Sai, Satish Pujari, B. Sreenivasulu, and Ajit Burra

## 1 Introduction

Combined forced and natural convections are important mechanisms for heat transfer. Nanofluids are comprehending particles with nanometer size, known as nanoparticles. Those nanofluids are colloidal suspensions of nanoparticles with convectioal fluid. Nanofluids are especially used for different applications to replace convectioal fluids with more heat transfer characteristics and their other properties include thermal diffusivity, viscosity and thermal conductivity associated with a conventional fluid. The entire evaluation is executed in phrases of dimensionless numbers consisting of Richardson number and Reynolds number by changing all of the equations used for the heat transfer evaluation in phrases of dimensionless numbers. Applications for square cavity space were sun strength collector, heat exchangers, digital gadgets touch panels, LED, smart windows (single-pane windows, double pane home windows). Hasan et al. [1]. Evaluation of flow fields and thermal in the cavity is analyzed with respect to isotherms, stream lines and heat traces for a huge variety of solid volume fraction of the nanoparticle and Richardson number. They have a look and suggests that large heat transfer fees may be finished with nanofluid than the bottom fluid for all situations. Basak et al. [2]. The heat transfer between nanofluid and bottom surface of blended convection lid driven square cavity under uniform and nonuniform heating is observed. It can be observed from the local Nusselt variety plot that heat transfers decrease from corners to center under uniform heating, whereas under non uniform heating, heat transfer rates are low at the edges

---

C. R. D. Sai (✉)

G. V. P College of Engineering, Visakhapatnam, Andhra Pradesh, India

S. Pujari

Lendi Institute of Engineering and Technology, Vizianagaram, Andhra Pradesh, India

B. Sreenivasulu · A. Burra

Gayathri Vidya Parishad College of Engineering, Visakhapatnam, Andhra Pradesh, India

of bottom wall. Labib et al. [3]. A two-phase mixture version of pressured convective heat transfer of nanofluids of extra ordinary base fluids to analyze effect of base fluids used. The computational technique has been confirmed within the case of  $\text{Al}_2\text{O}_3/\text{water}$  nanofluids. Kim and Kwon [4]. In alumina nanofluids containing three volume percentage of suspended debris, the increase in thermal conductivity is found to be 8% and convective heat transfers 20%. In other terms, improvement in properties of convective heat transfer are better than that of the properties related to thermal conductivity. Suresh et al. [5]. Heat transfer effects confirmed increase of 13.56% in Nusselt number at ( $\text{Re} = 1730$ ) while in comparison to the Nusselt number for water. The consequences additionally display that 0.1%  $\text{Al}_2\text{O}_3\text{-Cu}/\text{water}$  nanofluids high friction component whilst in comparison to 0.1%  $\text{Al}_2\text{O}_3/\text{water}$  nanofluid.

## 2 Materials and Modelling

The nanoparticles such as graphene, copper, silver and zinc are used where these are having high thermal conductivities than oxides and carbides. Graphene as the main component and the remaining three nanoparticles copper, silver and zinc are added to graphene separately to make hybrid nanoparticles. The nanoparticles are well-thought-out and varying from 10 to 50% of volume fraction and the base as water (Table 1).

The 2D cavity which is shown in Fig. 1 is a square cavity with water-based hybrid nanofluid contains (graphene-Cu, Ag, Zn) nanoparticles. The fluid is optimally diluted with the volume fraction  $\phi = 0.1$ , on this wise, it is contemplated as a Newtonian as well as incompressible fluid. The pairing of density and flow fields for varying temperatures is obtained using Boussinesq approximation neglecting viscosity in dissipation effect and considering no heat generation.

Mathematical equations describing the above approximation is given below.

### Continuity Equation

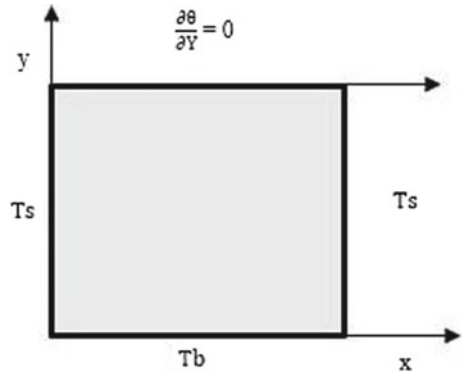
$$\frac{\partial u}{\partial X} + \frac{\partial v}{\partial Y} = 0 \quad (1)$$

### Momentum Equation

**Table 1** Thermal-physical properties of nanoparticles and base fluid at a temperature,  $T = 25^\circ\text{C}$

Properties	Graphene	Copper (Cu)	Silver (Ag)	Zinc (Zn)
$C_p$ (J/kg-k)	790	385	235	390
$K$ (W/m-K)	5000	401	429	112.2
$\rho$ ( $\text{kg}/\text{m}^3$ )	2200	8933	10,500	7100
$\beta$ ( $\text{K}^{-1}$ ) $\times 10^{-5}$	0.6	1.67	1.89	3.12

Fig. 1 Physical model



$$u \frac{\partial u}{\partial X} + v \frac{\partial u}{\partial Y} = -\frac{\partial p}{\partial X} + \frac{\mu_{\text{hnf}}}{\rho_{\text{hnf}} \nu_{\text{bf}}} \frac{1}{\text{Re}} \left( \frac{\partial^2 u}{\partial X^2} + \frac{\partial^2 u}{\partial Y^2} \right) \quad (2)$$

$$u \frac{\partial v}{\partial X} + v \frac{\partial v}{\partial Y} = -\frac{\partial p}{\partial Y} + \frac{\mu_{\text{hnf}}}{\rho_{\text{hnf}} \nu_{\text{bf}}} \frac{1}{\text{Re}} \left( \frac{\partial^2 v}{\partial X^2} + \frac{\partial^2 v}{\partial Y^2} \right) + \frac{(\rho\beta)_{\text{hnf}} \text{Ri}\theta}{\rho_{\text{hnf}} \beta_{\text{bf}}} \quad (3)$$

### Energy Equation

$$u \frac{\partial \theta}{\partial X} + v \frac{\partial \theta}{\partial Y} = \frac{\alpha_{\text{hnf}}}{\alpha_{\text{bf}}} \frac{1}{\text{RePr}} \left( \frac{\partial^2 \theta}{\partial X^2} + \frac{\partial^2 \theta}{\partial Y^2} \right) \quad (4)$$

where

$$X = \frac{x}{L}, Y = \frac{y}{L}, U = \frac{u}{U}, V = \frac{v}{U}, \theta = \frac{T - T_s}{T_b - T_s},$$

$$\text{Re} = \frac{\rho v L}{\mu}, \text{Pr} = \frac{\mu C_p}{k}, \text{Ri} = \frac{g \beta \Delta T L}{\nu^2} = \frac{\text{Gr}}{\text{Re}^2} \quad (5)$$

Density ( $\rho_{\text{hnf}}$ ), specific heat ( $C_{\text{p, hnf}}$ ), thermal expansion ( $\beta_{\text{hnf}}$ ) of hybrid nanofluids as a function of volume fraction ( $\phi$ ), properties of base fluid and nanoparticles is presented below

$$\rho_{\text{hnf}} = [(1 - \phi)\rho_{\text{bf}}] + (\phi_1 \times \rho_{\text{s1}}) + (\phi_2 \times \rho_{\text{s2}}) \quad (6)$$

$$\beta_{\text{hnf}} = [(1 - \phi)\beta_{\text{bf}}] + (\phi_1 \times \beta_{\text{s1}}) + (\phi_2 \times \beta_{\text{s2}}) \quad (7)$$

Brickmans's and Maxwell's models can be modelled as follows

$$\mu_{\text{hnf}} = \frac{\mu_{\text{bf}}}{(1 - \phi)^{2.5}} \quad (8)$$

$$k_{\text{hnf}} = k_{\text{bf}} \left[ \frac{\frac{(\phi_1 k_1 + \phi_2 k_2)}{\phi} + 2k_{\text{bf}} + 2(\phi_1 k_1 + \phi_2 k_2) - 2\phi k_{\text{bf}}}{\frac{(\phi_1 k_1 + \phi_2 k_2)}{\phi} + 2k_{\text{bf}} - (\phi_1 k_1 + \phi_2 k_2) + \phi k_{\text{bf}}} \right] \quad (9)$$

where

$\mu_{\text{hnf}}$  dynamic viscosity  
 $k_{\text{hnf}}$  effective thermal conductivity.

The Nusselt number of Square Cavity calculated from the following formulae.

$$\text{Nu} = \frac{1}{L} \int_0^L -\frac{k_{\text{hnf}}}{k_{\text{bf}}} \frac{\partial T}{\partial y} dx = \int_0^1 -\frac{k_{\text{hnf}}}{k_{\text{bf}}} \frac{\partial \theta}{\partial Y} dX \quad (10)$$

### 3 Numerical Procedure

#### 3.1 Grid Independence Test

Grid independence test is conducted within the square cavity with the copper as a nanoparticle and water as a base fluid in COMSOL MULTI PHYSICS data base by varying number of elements in a mesh (free triangular), the average Nusselt number is varied. In this analysis, geometry mesh is obtained in a free triangular form represents  $920 \times 100$  which is 21,204 elements in a square cavity is considered with approximate values of average Nusselt number with the maximum coincidence.

#### 3.2 Validation

Validation is done for Hasan et al. [1] to demonstrate the process which we followed is correct. These various validations are done with square cavity which is filled with nanofluids, whereas the bottom wall is uniformly heated and vertical walls are kept cool and top wall is an insulated constant moving wall. The obtained average Nusselt numbers are found to be similar results obtained from Hasan et al. [1], and the same have been presented graphically in Fig. 2 (Table 2).

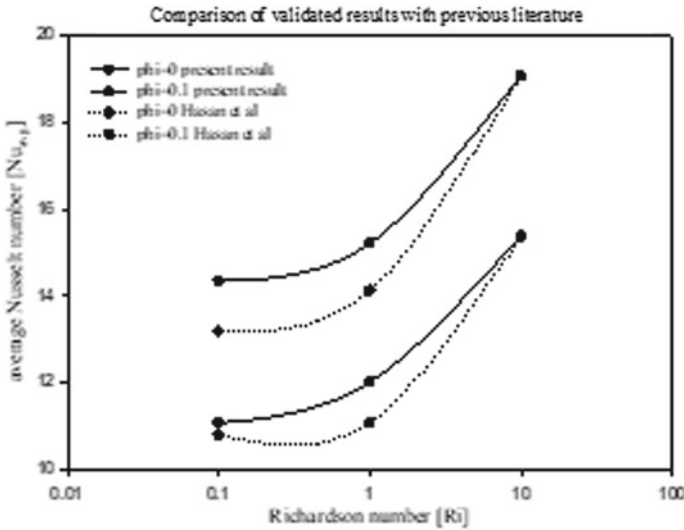


Fig. 2 Comparison of validated result with previous literature at different volume fraction and Ri

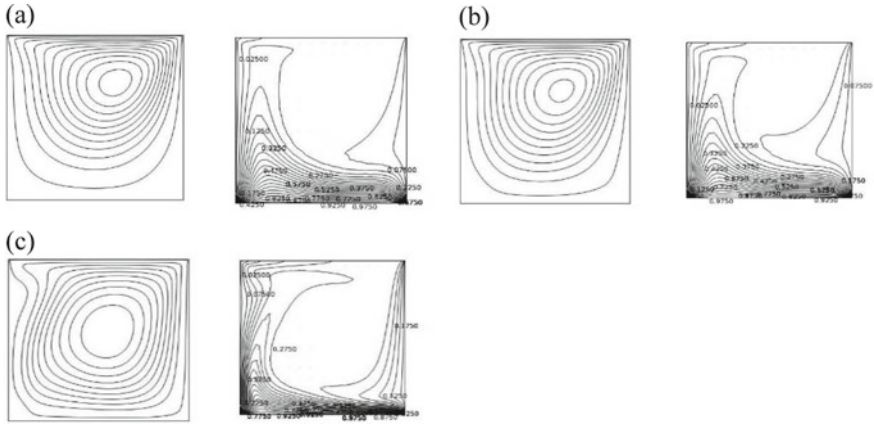
**Table 2** Comparison of  $Nu_{avg}$  for a bottom heating wall at different volume fractions and Richardson number ( $Ri = 10$ ) at  $Re = 100$ , and  $Pr = \frac{\rho_l}{\alpha_f}$  for Cu -water

Volume fraction of nanoparticles ( $\phi$ )	$(Nu_{avg})$ Cu-water Hasan et al.	$(Nu_{avg})$ Cu-water Present result
0	15.35784	15.36784
0.1	19.05899	19.05906

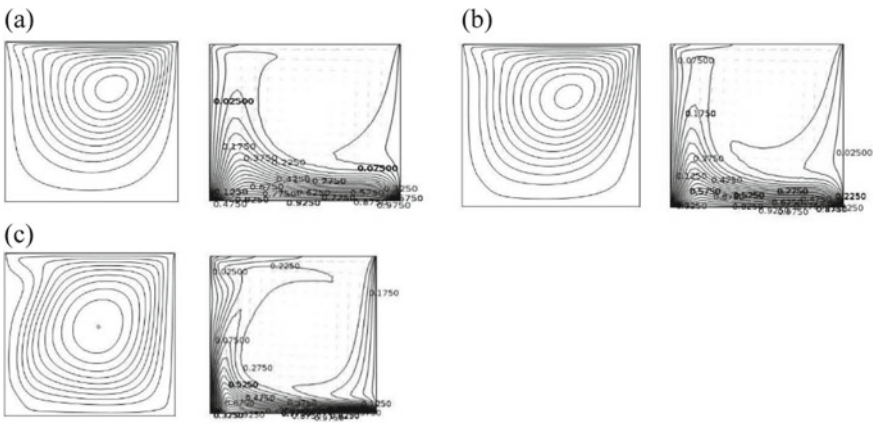
### 4 Results and Discussions

$Nu_{avg}$  is the product of the ratio of thermal conductivity of hybrid nanofluid to the base fluid ( $k_{hnf}/k_{bf}$ ) and temperature gradient with the direction and is proportional to the heat gradient of heat functions along the surfaces of the wall.

Isotherms, streamlines for water and different combination of hybrid nanofluids for a range of ( $0.001 \leq Ri \leq 10$ ) and volume fraction of nanoparticles ( $\phi = 0.1$ ). Figures 3, 4 and 5: Streamlines (right) and Isotherms (left) for  $Ri = 0.001, 1, 10$  and at different nanoparticles at specific volume fraction  $\phi = 1$ . Richardson number effects are shown in isothermal contour and velocity stream lines. The distributions of temperature are nearly undistinguishable at bottom wall. At higher Richardson numbers  $Ri = 10$ , buoyancy forces are more dominant. The viscosity increases with increase in volume fractions of hybrid nanoparticles. From results  $\phi = 0.1$ , Figs. 3, 4 and 5 at  $Ri = 1, 10$ , the fluid circulation intensity becomes stronger at the center, convective heat flow in center have high intense of base fluid and hybrid nanofluid. There are small changes in isotherms of hybrid nanofluids apart from base fluid at lower Ri values but changes significantly for higher Ri. If the Richardson

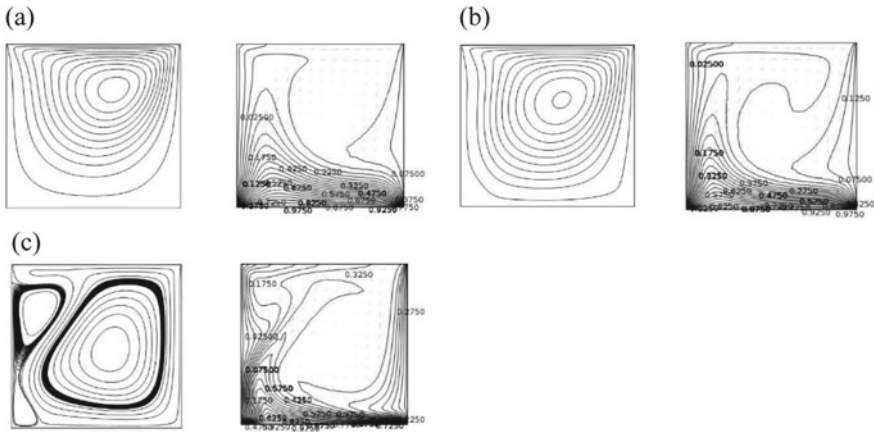


**Fig. 3** Streamlines (right) and Isotherms (left) for **a**  $Ri = 0.001$ , **b**  $Ri = 1$  and **c**  $Ri = 10$  for (graphene + copper) of proportions 10:90 hybrid nanoparticles at specific volume fraction  $\phi = 0.1$  and at  $Re = 100$  in a square cavity



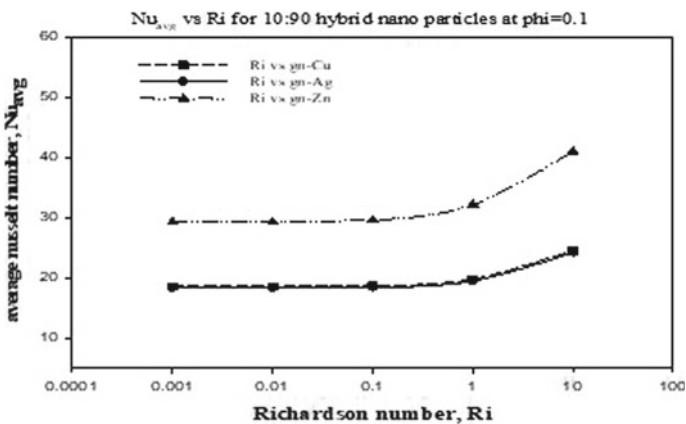
**Fig. 4** Streamlines (right) and Isotherms (left) for **a**  $Ri = 0.001$ , **b**  $Ri = 1$  and **c**  $Ri = 10$  for (graphene + silver) of proportion 10:90 hybrid nanoparticles at specific volume fraction  $\phi = 0.1$  and at  $Re = 100$  in a square cavity

number further increases, forced convection can be neglected. Heat function gradient is directly proportional to ratio of normal heat flux and thermal diffusivities. And at the greater value of Richardson number  $Ri = 10$ , the forces of buoyancy lead the forces of viscous and pressure drop is observed. The outlines of flow motion sections affected by hybrid nanofluids are observed. It is clearly observed that the flow is due to viscous influence at low  $Ri$ , and by adding nanoparticles into fluid, the fluid becomes higher in viscous effect which leads to low intense flow for nanoparticles.



**Fig. 5** Streamlines (right) and Isotherms (left) for **a**  $Ri = 0.001$ , **b**  $Ri = 1$  and **c**  $Ri = 10$  for (graphene + Zinc) of proportion 10:90 hybrid nanoparticles at specific volume fraction  $\phi = 0.1$  and at  $Re = 100$  in a square cavity

Figure 6 illustrates the comparison of different hybrid nanofluids, the average Nusselt number versus logarithmic Richardson number along the surface of heating wall are plotted. From the above graph, it is predicted that the average Nusselt number for the surface of a heating wall does not vary much up to  $Ri = 1$  with  $Re = 100$ . This is because the fluid flow of field reduces in these conditions. The average Nusselt number increases at  $Ri = 10$  with  $Re = 100$ . The proportions of hybrid nanoparticles are compared as  $Nu_{avg}$  versus  $Ri$ . The average Nusselt number increases with increase in  $Ri$  value for any proportion of hybrid nanoparticles. This is due to increased buoyancy forces at high  $Ri$  value. More significant enhancement of heat transfer



**Fig. 6** Variation and comparison of different hybrid nanofluids at different,  $Ri$



is observed in (graphene–Zinc)/water compared to (graphene–Copper)/water and (graphene–Silver)/water.

### Average Nusselt Number ( $Nu_{avg}$ )

Average Nusselt numbers of various combinations of hybrid nanofluids are plotted into a graph for at various Richardson numbers, and volume fraction of hybrid nanoparticles as  $\phi = 0.1$  with base fluids as water Fig. 6 drawn from the average Nusselt numbers of the bottom heating wall inside the square cavity are shown where the heat transfer enhancement is more in (graphene + Zinc)-water than (graphene + Copper)-water and (graphene + Silver)-water. By accumulating volume fractions of nanoparticles with water, then thermal conductivity is raised and the heat transfer rate increases. The variation in average Nusselt number is more significant for greater Richardson number.

## 5 Conclusions

- $Nu_{avg}$  increased with increase in Richardson number from 0.001 to 10 for (graphene–copper)–water, i.e., **(18.57 to 24.53)** at  $\phi = 0.1$  and  $Re = 100$  for 10:90 proportion of nanoparticles. Similarly, observed for (graphene–silver)–water is **(18.30 to 24.20)** and (graphene–zinc)–water is **(29.26 to 40.99)**.
- There is an increment of **32.11, 32.21, 40.06%** at  $\phi = 0.1$  and  $Re = 100$  for 10:90 proportion of nanoparticles of (graphene–copper)–water, (graphene–silver)–water and (graphene–zinc)–water, respectively.
- From the results of average Nusselt number at  $\phi = 0.1$  and  $Ri = 10$  for a proportion of 10:90, it is observed that graphene–zinc (**40.98**) has **67.06%** and **69.39%** increment of heat transfer rate when compared with graphene–copper (**24.53**) and graphene–silver (**24.19**), respectively.

From the combination of hybrid nanofluids and for all governing factors, it was observed that (graphene–zinc) hybrid nanofluid is showing great enhancement of heat transfer rate compared with (graphene–copper), (graphene–silver) respectively.

## References

1. Hasan, M.N., Samiuzzaman, K.: Mixed convection heat transfer inside a square cavity filled with Cu-water nano fluid. In: 6th BSME International Conference on Thermal Engineering, vol.105, pp. 438–445 (2015)
2. Basak, T., Roy, S., Sharma, P.K.: Analysis of mixed convection flows within a square cavity with uniform and non-uniform heating of bottom wall. *Int. J. Therm. Sci.* **48**, 891–912 (2009)
3. Nuim Labib, M., Nine, Md. J., Chung, H.: Numerical investigation on the effect of base fluids and hybrid nanofluid in forced convective heat transfer. *Int. J. Thermal Sci.* **71**, 163–171 (2013)
4. Kim, D., Kwon Y.: Convective heat transfer characteristics of nanofluids under laminar and turbulent flow conditions. *Curr. Appl. Phys.* **9**, 119–123 (2009)

5. Suresh, S., Venkitaraj, K.P., Chandra Sekar, M.: Effect of  $\text{Al}_2\text{O}_3$ -Cu/water hybrid nanofluid in heat transfer. *Exp. Thermal Fluid Sci.* **38**, 54–60 (2012)

# Impact of Graphene Nanoparticles Addition to Jatropha Biodiesel Blend on the Performance and Emission Characteristics of a Diesel Engine



D. Mallikarjuna Rao, Venkata SomiReddy Janga, V. Dhana Raju, and Syed Arifa

## 1 Introduction

The practice of diesel operation in transport industry expansively provoked receding of diesel scope. Numerous researchers confer diminution of hazardous emissions from the diesel engine utilizing discrete techniques, for example, fuel modifications, engine adjustments, and handling of emission gases. Fuel modification can be incorporated to employment of biodiesels and substitutes. Biodiesels came into existence because to save the continuous utilization of petroleum products for various applications. In contrast with diesel and biodiesel, recent works on the mixing of nanoparticles in biodiesels as additives complement biodiesel peculiarity. The biodiesel traits can be intensified using catalytic oxides and metals.

Nanthagopal et al. [1] investigated leverage of titanium dioxide and zinc oxide blend biodiesel on radiation peculiarities of diesel engine. The cerium oxide nanoparticle blend biodiesel execution on diesel engine and discharge gases was explored Khalife et al. [2]. Jena et al. [3] investigated ferric chloride blend biodiesel effect on a diesel engine and found the  $\text{NO}_x$  in the exhaust was extended by 15%. Kumar Patel et al. [4] and Sadhik Basha et al. [5] examined the impacts of Al-oxide nanoparticle blend biodiesel on the exhibition and performance attributes of a diesel motor. Basha and Anand [6] and Hosseini et al. [7] inspected the exhibition of a diesel motor with carbon nanotubes (CNTs) accumulated in diesel. The influence of multi-wall CNTs, cerium oxide, graphene, and silver nanoparticle-added substances on a diesel motor execution was investigated by Mirzajanzadeh et al. [8] and Tewari et al. [9]. The impact of accumulating cerium oxide nanoparticles and CNTs in ethanol, biodiesel, and diesel fuel mixes on a diesel motor execution was investigated by Arul Mozhi Selvan et al. [10]. From the experimental studies, it was evident that catalytic

---

D. Mallikarjuna Rao (✉) · V. S. Janga · V. Dhana Raju · S. Arifa  
Department of Mechanical Engineering, Lakireddy Bali Reddy College of Engineering,  
Mylavaram, Andhra Pradesh, India

nanoparticle accumulation to biodiesel blends improved BTE and reduced CO, UHC, NO<sub>x</sub>, and smoke in the emissions. Also, from the earlier studies [11–13], 20% to 30% blend of biodiesel with diesel is relatively good in the exchange of diesel fuel. In the exhaust, the proportion of CO and HC reduced and NO<sub>x</sub> proportion enriched with a boost in the ratio of biodiesel blend in the diesel.

In the present study, jatropha seed methyl ester was prepared and meld with diesel. The blends of different proportions are optimized before the addition of graphene nanoparticles. The impact of graphene nanoparticles is analysed with different proportional blends of jatropha biodiesel was investigated.

## 2 Materials and Methods

### 2.1 Preparation of Jatropha Seed Methyl Ester

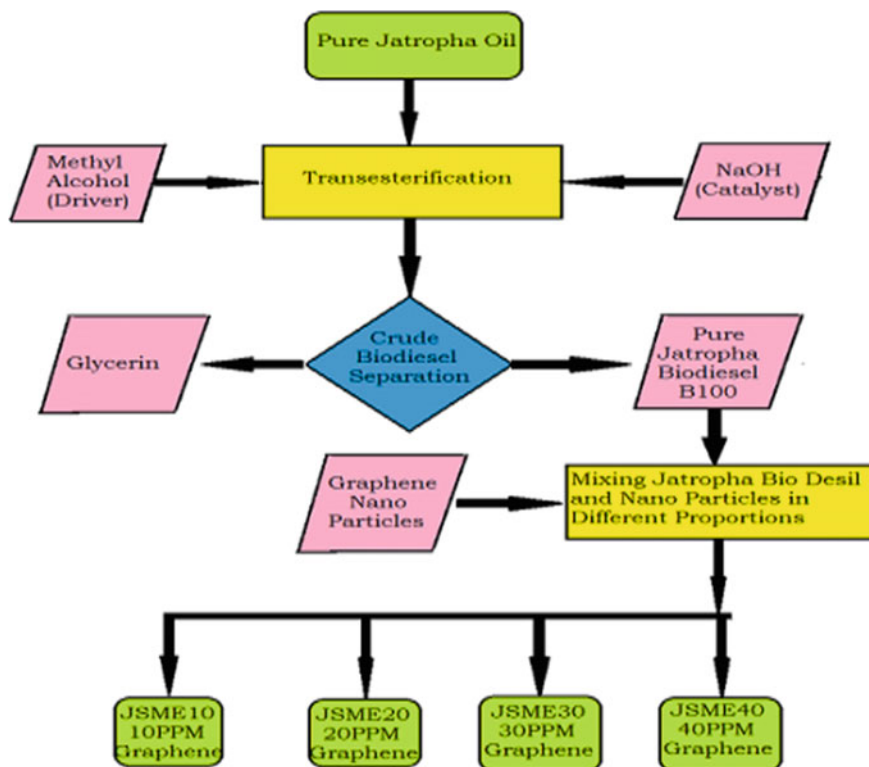
Jatropha oil has a higher viscosity and density. There are diverse approaches for viscosity decrement of vegetable oils, and transesterification is one such technique with enhanced efficiency. In this process, the oil viscosity is abated and the characteristics of biodiesel are enriched. The jatropha crude oil transesterification process is outlined in Fig. 1.

### 2.2 Blend Optimization

After the jatropha seed methyl ester extraction from jatropha seeds, various diesel blends by the proportions like 10%, 20%, 30%, and 40% by volume are processed, and named JSME10, JSME20, JSME30, and JSME40, respectively. The blends are analysed, and the optimum blend is proposed before adding the graphene nanoparticles. The properties like cetane number, kinematic viscosity, flash point, density, and calorific value are estimated. Among the blends, JMSE20 gives values similar to diesel.

### 2.3 Addition of Nanoparticles to the Best Blend

Once obtaining the best blend from the jatropha seed methyl ester blends further step is to add nanoparticles to get better performance and diminish unsafe emissions of the diesel motor. The traits of graphene nanoparticles are mentioned below in Table 1. The SEM and XRD construction of synthesized graphene nanoparticles are shown in Fig. 2. In this experiment, graphene is opted as a nanoparticle to mix with the JSME20 blend. The graphene is added in the proportions of 25, 50, 75, and 100 ppm.



**Fig.1** Jatropha methyl ester production through transesterification process

**Table 1** Properties of graphene nanoparticles

Property	Quantity
Molecular weight	12.01 g/mole
Purity	>98%
PH value	7.5
Carbon	92.95%
Oxygen	6.57%
Sulphur	0.48%
Layered thickness	~1–5 nm
Diameter	20–60 $\mu\text{m}$

Graphene nanoparticles are added by the process of ultrasonication. After mixing nanoparticles in required proportions again the blends of Nano additives are tested.

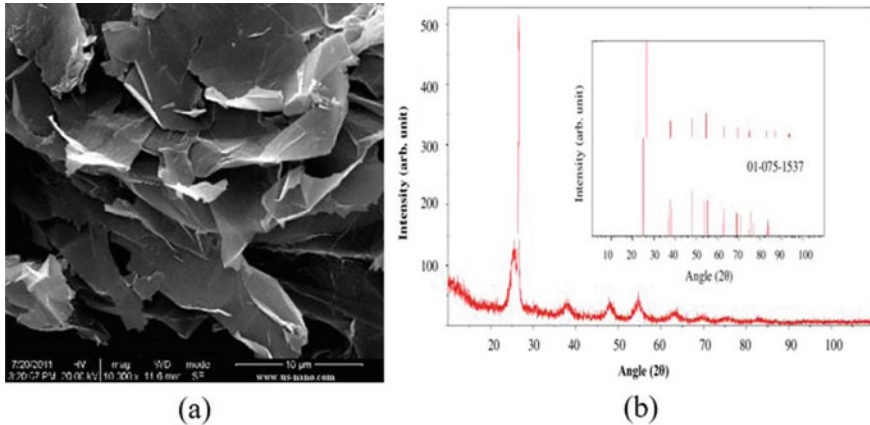


Fig. 2 a SEM and b XRD construction of graphene nanoparticles

### 3 Experimental Setup

A single-cylinder, compression ignition diesel engine was utilized in the current study. The swept volume of the engine is 661 cc, the compression ratio is 17.5:1 and the rated power is 3.5 kW. The diesel engine with a smoke metre utilized in the present study is shown in Fig. 3. Various loads settings of zero load, 25, 50, 75, and 100% were chosen for investigation with consistent speed of 1500 rpm. AVL Digas444 analyser was utilized for calculating proportion of CO, NO<sub>x</sub>, HC in emissions. AVL 437C smoke metre was used to calculate smoke opacity. The engine performance parameters such as BTE, BSFC, and attribute of emissions are noted.

### 4 Results and Discussion

The traits of diesel and JSME20 with proportions of Nano additives are presented in Table 2. In contrast with diesel, JSME20 has similar traits and therefore JSME20 was selected for adding graphene nanoparticles. The emission and performance attributes and of diesel and jatropha methyl ester blends are presented in Table 3. It was confirmed further that JSME20 is the optimum blend of nanoparticle accumulation.

Diesel has the highest BTE of 34.94% compared to other JSME blends this is because of specific gravity and diminished heating value. JSME20 + 75 ppm shows a higher BTE of 37.69% which is 4.86% more than diesel. In such conditions, the engine doesn't work effectively. Whereas JSME20 + 50 ppm have 34.03%, which is 3.46% higher than JSME20. The values are plotted on the graph as shown in Fig. 4a. The accumulated GNP's in the blends catalyses combustion and oxygen buffering ensuring outright burning of fuel mixture. GNP's presence enhances atomization and enriches air-fuel mixing which was significant in improving BTE.



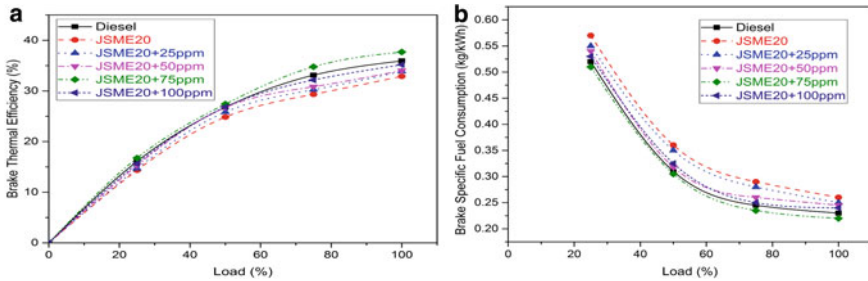
**Fig. 3** Schematic layout of engine setup

**Table 2** Attributes of diesel, JSME20, and nanoadditive blends

Attribute	DIESEL	JSME20	JSME20 + 25GNPS	JSME20 + 50GNPS	JSME20 + 75GNPS	JSME20 + 100GNPS
Calorific value (kJ/kg)	42,500	41,142	41,160	41,190	41,210	41,230
Flash point(°C)	56	88	101	113	136	148
Kinematic viscosity (cSt)	2.47	3.33	4.18	4.18	4.21	4.22
Density (kg/m <sup>3</sup> )	850	852	855	857	866	873
Cetane number	48.9	51.6	52.3	53.5	55.2	57.4

**Table 3** Performance and emission attributes of diesel and jatropha methyl ester blends

Tested fuels	Performance				Emissions			
	BTE (%)	VE (%)	BSFC (Kg/KWh)	ME (%)	CO (%)	NO <sub>x</sub> PPM	HC PPM	Smoke (%)
Diesel	35.94	81.74	0.23	71.93	0.146	1041	49	78
JSME10	31.28	81.74	0.27	60.59	0.129	1094	76	95
JSME20	32.89	79.25	0.26	65.77	0.152	1062	45	76
JSME30	30.49	81.74	0.283	56.16	0.134	1116	78	101
JSME40	29.34	80.92	0.296	62.56	0.149	1132	83	106

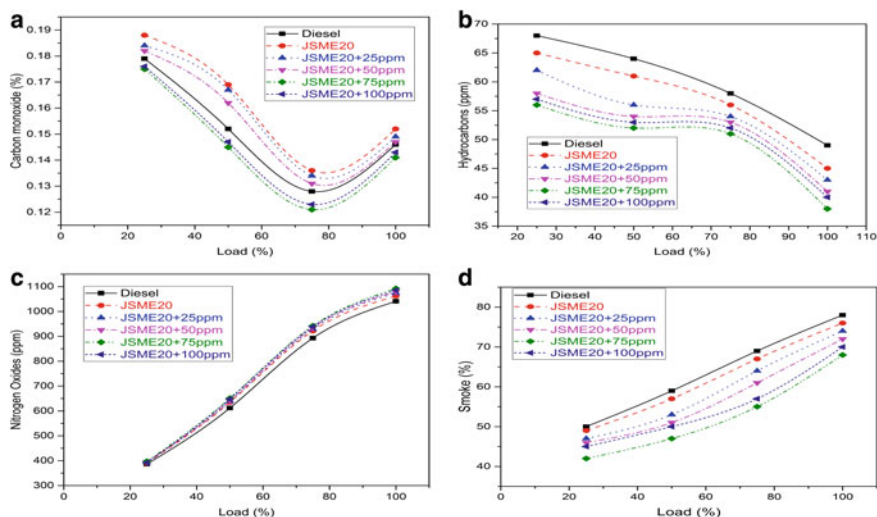


**Fig. 4** a BTE variation with engine load. b BSFC variation with engine load

In Fig. 4b, fuel consumption of JSME20, GNP’s accumulated JSME20 and diesel at proposed load settings was presented. At all load settings BSFC for the diesel found merest as the density of the blends is superior and having low content of energy. In contrast with diesel, JSME blends have poor atomization credit to higher viscosity influencing combustion. BSFC at full load setting for diesel is 0.23 kg/kW h, JSME20 is 0.26 kg/ kW h, JSME20 + 25 ppm is 0.253 kg/kW h, JSME20 + 50 ppm is 0.245 kg/kW h, JSME20 + 75 ppm is 0.22 kg/kW h and JSME20 + 100 ppm is 0.24 kg/ kW h.

Carbon monoxide emissions for diesel, JSME20, JSME20 graphene blended fuels are shown in Fig. 5a. The CO emissions for the JSME20 blend have 0.152% higher compared to diesel 0.146% due to its lower brake thermal efficiency. The CO emission for JSME20 + 100 ppm has 0.101% slightly lesser value than diesel and JSME20 due to catalysis aided better combustion attributes of GNP’s. The unburnt hydrocarbons for diesel, JSME20, JSME20 Nano additive blends are plotted on the graph as shown in Fig. 5b. The HC emission for JSME20 + 75 with 38 ppm which is mere compared to base diesel of 49 ppm due to diminished thermal efficiency. The HC emission gradually decreases with the addition of graphene nanoparticles for JSME20 due to catalytic activity and better combustion characteristics of graphene nanoparticles. The NO<sub>x</sub> emissions of diesel, JSME20, and nanoparticles additives of graphene to JSME20 blend are plotted on the graph are shown in Fig. 5c. Diesel has shown lower NO<sub>x</sub> emissions of 1041 ppm in contrast to the JSME20 blends. With GNP’s





**Fig. 5** a CO proportion variation with engine load. b HC proportion variation with engine load. c  $\text{NO}_x$  proportion variation with engine load. d Smoke opacity proportion variation with engine load

accumulation, the emission of  $\text{NO}_x$  intensified compared to the diesel and JSME20 blend. The variations in smoke emission of diesel, JSME20, and Nano additives of graphene to JSME20 blend are plotted on the graph as shown in Fig. 5d. As the load increases, emission of smoke increases in all cases. Diesel emits higher smoke of 78%, which is higher than JSME20 blend which has 76% emission. The addition of graphene nanoparticles tends to emit less smoke due to shorter ignition time. Among the JSME20 Nano additive blends JSME20 + 75 ppm emit less smoke of 68% this is because of the molecular structure of graphene nanoparticles, whereas JSME20 + 25 ppm emit 74% of smoke which is 2.7% lesser than the JSME20 blend. The performance and emission attributes of JSME20, blends of GNP's and diesel at full load settings are tabulated in Table 4.

**Table 4** Effects of JSME20 and GNP's accumulation to diesel engine attributes

Parameters	DIESEL	JSME20	JSME20 + 25	JSME20 + 50	JSME20 + 75	JSME20 + 100
BTE (%)	35.94	32.89	33.87	34.03	37.69	35.18
BSFC (Kg/kW h)	0.23	0.26	0.253	0.245	0.22	0.24
CO (%)	0.146	0.152	0.149	0.147	0.141	0.143
HC (PPM)	49	45	43	41	38	40
$\text{NO}_x$ (PPM)	1041	1062	1074	1079	1092	1085
Smoke (%)	78	76	74	72	68	70

## 5 Conclusions

JSME20 and GNP's blends of diesel were processed and their emission attributes and performance characteristics are analysed. There is a considerable increment in BTE, JSME20 + 75 ppm show a higher BTE which is 4.86% more than pure diesel. JSME20 + 75 ppm blend has lower BSFC of 0.22 kg/kW h, compared to diesel of 0.23 kg/kW h. The accumulation of nanoparticles to the JSME20 blend benefits reduction in emission values of HC, smoke, and CO in contrast with diesel. *Jatropha* seeds have more yield percentage of oil and these plants produce a greater quantity of seeds even at low rainfall. This biodiesel has the highest calorific value with the lowest moisture content. At present, the *jatropha* oil blend of only 20% in biodiesel is suggested. In future, by developing efficient techniques to improve the quality of combustion, we can increase the proportion of *jatropha* oil in biodiesel.

## References

1. Nanthagopal, K., Ashok, B., Tamilarasu, A., Johny, A., Mohan, A.: Influence on the effect of zinc oxide and titanium dioxide nanoparticles as an additive with *Calophyllum inophyllum* methyl ester in a CI engine. *Energy Convers. Manage.* **146**, 8–19 (2017). <https://doi.org/10.1016/j.enconman.2017.05.021>
2. Khalife, E., Tabatabaei, M., Najafi, B., Mirsalim, S.M., Gharehghani, A., Mohammadi, P., Aghbashlo, M., Ghaffari, A., Khounani, Z., Roodbar Shojaei, T., Mohd Salleh, M.A.: A novel emulsion fuel containing aqueous nano cerium oxide additive in diesel–biodiesel blends to improve diesel engines performance and reduce exhaust emissions: Part I—Experimental analysis. *Fuel* **207**, 741–750 (2017). <https://doi.org/10.1016/j.fuel.2017.06.033>
3. Jena, S.P., Acharya, S.K., Das, H.C., Patnaik, P.P., Bajpai, S.: Investigation of the effect of FeCl<sub>3</sub> on combustion and emission of diesel engine with thermal barrier coating. *Sustain. Environ. Res.* **28**, 72–78 (2018). <https://doi.org/10.1016/j.serj.2017.10.002>
4. Kumar Patel, H., Kumar, S.: Experimental analysis on performance of diesel engine using mixture of diesel and bio-diesel as a working fuel with aluminum oxide nanoparticle additive. *Thermal Sci. Eng. Prog.* **4**, 252–258 (2017). <https://doi.org/10.1016/j.tsep.2017.09.011>
5. Sadhik, J., Anand, R.B.: Role of nanoadditive blended biodiesel emulsion fuel on the working characteristics of a diesel engine. *J. Renew. Sustain. Energy*. **3**, 023106 (2011). <https://doi.org/10.1063/1.3575169>
6. Basha, J.S., Anand, R.B.: An experimental investigation in a diesel engine using carbon nanotubes blended water–diesel emulsion fuel: In: Proceedings of the Institution of Mechanical Engineers, Part A: Journal of Power and Energy (2011). <https://doi.org/10.1177/2041296710394247>
7. Hosseini, S.H., Taghizadeh-Alisaraei, A., Ghobadian, B., Abbaszadeh-Mayvan, A.: Performance and emission characteristics of a CI engine fuelled with carbon nanotubes and diesel–biodiesel blends. *Renew. Energy* **111**, 201–213 (2017). <https://doi.org/10.1016/j.renene.2017.04.013>
8. Mirzajanzadeh, M., Tabatabaei, M., Ardjmand, M., Rashidi, A., Ghobadian, B., Barkhi, M., Pazouki, M.: A novel soluble nano-catalysts in diesel–biodiesel fuel blends to improve diesel engines performance and reduce exhaust emissions. *Fuel* **139**, 374–382 (2015). <https://doi.org/10.1016/j.fuel.2014.09.008>
9. Tewari, P., Doijode, E., Banapurmath, N.R., Yaliwal, V.S.: Experimental investigations on a diesel engine fuelled with multiwalled carbon nanotubes blended biodiesel fuels

10. Arul , V., Anand, R.B., Udayakumar, M.: Effect of Cerium Oxide Nanoparticles and Carbon Nanotubes as fuel-borne additives in Diesterol blends on the performance, combustion and emission characteristics of a variable compression ratio engine. *Fuel* **130**, 160–167 (2014). <https://doi.org/10.1016/j.fuel.2014.04.034>
11. Godiganur, S., Suryanarayana Murthy, C.H., Reddy, R.P.: 6BTA 5.9 G2–1 Cummins engine performance and emission tests using methyl ester mahua (*Madhucaindica*) oil/diesel blends. *Renew. Energy* **34**, 2172–2177 (2009)
12. Loganathan, M., Velmurugan, A.A., A.: Emission characteristics of jatropha–dimethyl ether fuel blends on a di diesel engine. *Int. J. Sci. Technol. Res.* **1**, 28–32 (2012)
13. Vijayaraj, K., Sathiyagnanam, A.P.: Experimental investigation of methyl ester of cotton seed oil blend with diesel on CI engine (2014). <https://doi.org/10.3844/AJASSP.2014.1819.1829>

# Numerical Investigation on the Thermal Management of 18650 Battery Module Using Phase Change Material



Priya Chaudhary and Abhik Majumder

## 1 Introduction

Conventional IC engine-based vehicles are accountable for most CO<sub>2</sub> emissions, and it is high time already to think of an alternative. Electric vehicles can be a stand-in here, in the perpetuation of environment. However, it's market faces hindrances due to EV's complete reliability on electric batteries [1].

Among profusely available batteries, Lithium-ion (li-ion) seems very promising option; however, the operating temperature conditions (25–50 °C) of these batteries are very marginal and beyond this range its performance decreases drastically [2]. Therefore, it is very important to study the battery performance under various heat loading conditions to provide manufacturers useful input for effective design of cooling systems to maintain optimum temperature range, to extend the battery life and to enhance operational safety of the battery. With increase in the capacity and charging/discharging rates (C-rate),<sup>1</sup> battery security needs more attention. Various battery thermal management system (BTMS) has been advanced to fulfill demands of high power and speedy charge rates [3].

The different types of cooling strategies include - air cooling (natural/forced convection) [1], liquid cooling [4], using phase change materials (PCM) for thermal storage or combination of methods like thermo-electric cooling, solid-state cooling, cooling by using heat pipes, etc. BTMS may be divided into two groups viz: active in which a built-in source provides cooling/heating and passive where, through only

---

<sup>1</sup> C rate is the ratio of battery capacity to the numbers of hours taken for total discharge. C-rate of 1 mean for a cell capacitance of 1 Ah, 1 amperes current can drawn out, similarly C-rate to 2 would mean 2 amperes current can be drawn but for 30 min only.

---

P. Chaudhary (✉) · A. Majumder  
National Institute of Technology Agartala, Agartala, Tripura 799046, India  
e-mail: [priyame.stud@nita.ac.in](mailto:priyame.stud@nita.ac.in)

**Table 1** Different Paraffin thermal properties

Material	Latent heat (kJ/kg)	Melting point (°C)
C16–C18	152	20–22
FMC	130	20–23
RT20	172	20–22
RT25	164	24
R27 C 21	179	26–28

interaction with environment and no use of external energy source heating/cooling takes place.

Air cooling through just convection is not very adequate for battery cooling as instances of using precooled air for cooling of EVs was used in case of Honda insight and Toyota Pirus where the BTMS failed completely [5]. On the other hand, using liquid coolants which require separate closed channels and passage for the purpose of heat transfer, inevitably results in more complex design [4].

The traditional BTMS includes air/liquid cooling, making altogether system sturdy, compounded and expensive in relation of pumps, fans, pipes, etc., adding to system's weight and increases the parasitic power requirements [6]. Phase change materials, particularly non-metals, have low thermal conductivity but provides an opportunity of latent heat diffusion, therefore PCM can be a viable solution for optimum thermal management of battery [7].

Paraffins are organic compounds of long alkane chains with empirical formula  $\text{CH}_3(\text{CH}_2)_n\text{CH}_3$ . The length of chain decides its melting temperature and that is directly proportional to its chain length, thus wide range of melting points is available [8] as mentioned in Table 1.

PCM introduces less compounded battery design [9]. The material surrounds the cells of the battery system and uses latent heat storage to maintain the temperature. Phase change materials as passive cooling technique are employed in the present case for heat transfer analysis. In such systems, absorption and release of the generated heat take place through the process of melting and solidification.

Investigations are performed on heat generation and transfer of heat during cooling of the 18650 li-ion battery, while the battery cell is in the discharging mode. The study is also extended to explore the effect of PCM on the thermal characteristics of the battery cell.

## 2 Methodology

Heat generated during discharging of battery is governed by Eq. (1) below

$$\partial(\rho CT)/\partial t - \nabla \cdot (K_T \nabla T) = \dot{q} \quad (1)$$

**Table 2** Battery cell properties input to fluent

Properties	Input values
Cell capacity (Ah)	3.4 [10]
Voltage (V)	3.65 [10]
uds_0-conductivity( $\sigma_-$ ) of -ve electrode (S/m)	5.96E+7
uds_1- conductivity( $\sigma_+$ ) of +ve electrode (S/m)	3.77E+7
Density (Kg/m <sup>3</sup> )	2695
Specific heat capacity (J/KgK)	566

where  $\rho$  is density,  $C$  is the specific heat constant and  $K_t$  is the thermal conductivity of the active cell material,  $\dot{q}$  is the heat generation rate.

The heat generation in cell is calculated with the help of NTGK approach. The Multi scale multi domain (MSMD) approach in ANSYS-fluent concerns with different physics in different cell domains and is therefore best suited for the Battery analysis. In the dual potential MSMD framework, used in the paper, negative and positive current collectors, anode, and cathode are not re-solved, and the battery is considered as a homogeneous body, therefore computational mesh need not have to be adjusted to all layers of battery domain. The NTGK submodel is a electrochemical model, proposed by Kwon [10] and been used here. In this formulation, the current transfer relates to the potential field by Eq. (2)

$$\nabla \cdot (\sigma \nabla \varphi) = J \tag{2}$$

Here,  $\sigma$  is the effective electric conductivity,  $\varphi$  is phase potential of electrode and  $J$  is volumetric current density. The conductivities of electrodes are the user inputs as mentioned in Table 2.

$$J = a * Y [U - (\varphi_+ - \varphi_-)] \tag{3}$$

$$D = [V / (3600 * Q)] \int_0^t J dt \tag{4}$$

Current density and potential fields are specified uniquely based on nominal voltage inputs,  $V$  is the battery volume,  $Q$  is the battery’s electrical capacitance in Ampere hours. The voltage-current response curve from experimentation is used to curve fit data and get  $U$  and  $Y$  values needed by ANSYS fluent, which have the following formulation for the  $U$  and  $Y$  functions, as

$$Y = \left( \sum_{n=0}^5 a n(D)^n \right) \exp[-A(1/T - 1/T_r)] \tag{5}$$

$$U = \left( \sum_{n=0}^3 b n(D)^n \right) - B(T - T_r) \tag{6}$$

Here, A and B are the NTGK model constants which depend upon batteries physical parameters.

$$\dot{q} = \sigma_+ \nabla^2 \varphi_+ + \sigma - \nabla^2 \varphi_- + J[U - (\varphi_+ - \varphi_-) - T * (dU/dT)] \tag{7}$$

$q$  includes Joule, electrochemical and entropic heating. The external surface of the battery system is imposed with convective boundary condition assuming air, convective heat transfer coefficient of 5 W/m<sup>2</sup> K and free stream temperature = 26.85 °C. The enthalpy of the PCM is iterated as sum of latent heat ( $L$ ) and sensible enthalpy ( $h$ ) as  $H$  in the solver.

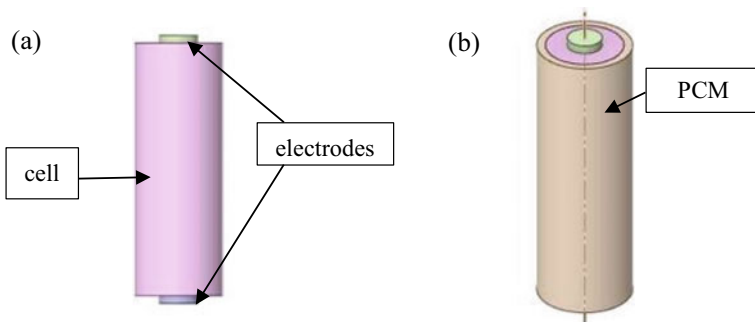
$$H = h + \Delta H T_r \tag{8}$$

$$H = \dot{h} + \int_0^t C dT \tag{9}$$

Here,  $T_r$  is reference temperature,  $\dot{h}$  is reference enthalpy and  $C$  is specific heat at constant pressure of PCM. Latent heat being generated in respect to latent heat of the material,  $L$  is  $H = X * L$ ,  $X$  being the liquid fraction of PCM. The energy equation solved in the PCM domain is:

$$\partial(\rho * H)/\partial t = \nabla.(K_t * \nabla T) + \dot{q} \tag{10}$$

where  $\rho$  is density and  $K_t$  is thermal conductivity of PCM. The source term  $\dot{q}$  is from Eq. (1)



**Fig. 1** 18650 Li-ion battery cell, model-1 (a), cell with 2 mm thick PCM jacket, model-2 (b)

**Table 3** Material properties of PCM input

Properties	RT-31	RT-35
Density (Kg/m <sup>3</sup> )	880–760	880–770
Specific heat (J/Kg K)	2100	2100
Thermal conductivity (W/mK)	0.20	0.20
Latent heat (J/Kg)	165,000	160,000
Melting range(°C)	27–33	34–35

### 2.1 Physical Model and Grid Test

Two models are considered for simulations. Figure 1a illustrates the first model for studying the heat generation in the battery at varied discharge rates and Fig. 1b, to study the influence of PCM on maximum temperature rise of cell.

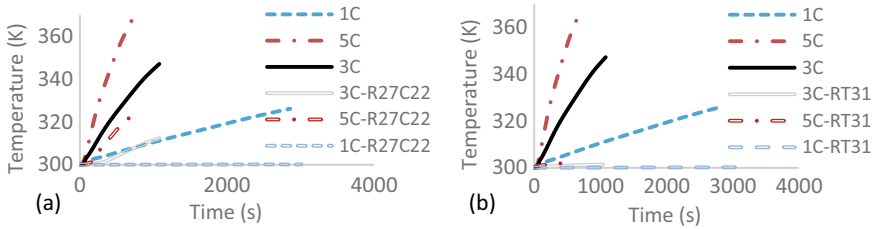
To model the li-ion battery cell, MSMD approach is considered. The details of the parameters considered are given in Table 3. The diameter of the cylindrical battery model is 18 mm and length is 65 mm. The electrodes are also cylindrical in shape with 8 mm in diameter and 2 mm in length, In model 2, an additional 2 mm uniform thickness PCM layer is applicable. Three different PCM is considered to study the effect of thermo-physical properties of heat transfer and temperature distribution. The details of the thermo-physical properties are given under Table 3. Grid independence test was studied with 520,918, 451,673 and 321,306 grids. The difference between 520,918 and 451,673 temperature profile was close to 0.001 °C. Therefore, the simulations are carried out with 451,673 grids as it gave better accuracy in temperature rise profile than 321,306 grids with lesser computational time than 520,918 grids.

## 3 Results and Discussion

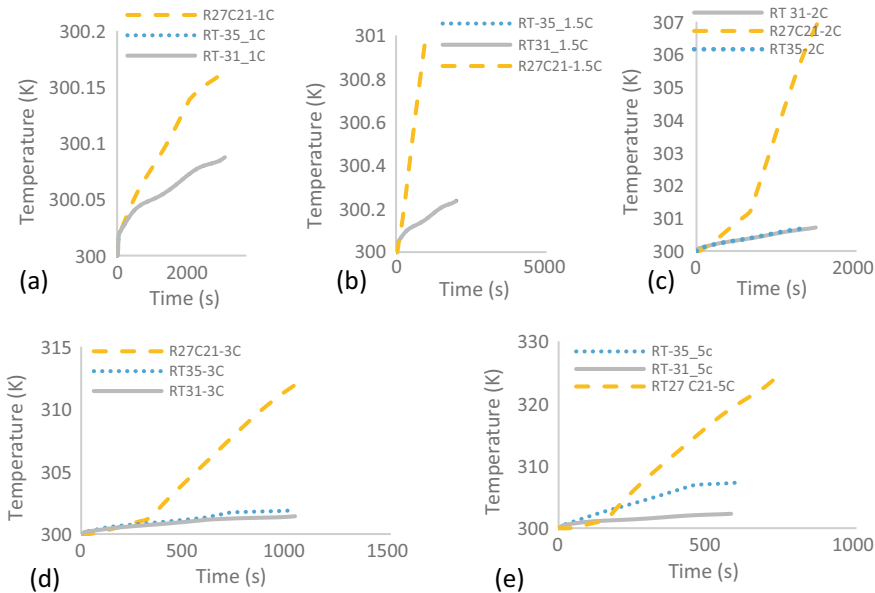
Two different models as shown in Fig. 1 are considered for the simulations at different discharge rates. Maximum temperature of battery system is important parameter for comparing the transient thermal behavior of such systems. The value of such temperature should be kept minimum for optimum operation of the battery. Figure 2 illustrates a comparative study of such maximum battery temperature at different discharge rates for these two different models. It is very much clear from the image that the application of PCM layer significantly lowers the maximum battery temperature. This observation is consistent for all the discharge rates studied in the present investigation. The transient analysis shows that heat generated from battery is absorbed by PCM.

Figure 3 shows temperature rise in battery cell under influence of three PCMs RT-31, RT-35 and R27C22 at 1C, 1.5C, 2C, 3C and 5C discharge rates, respectively. In order to obtain, the contrast between the temperature characteristics of the cell





**Fig. 2** Temperature rise in the battery at different discharge rates against discharging time with and without PCM-R27C21 (a) and PCM-RT31 (b) cooling



**Fig. 3** Temperature rise in the cell at a 1C; b 1.5C; c 2C; d 3C and e 5C rate of discharging with the presence of considered PCM

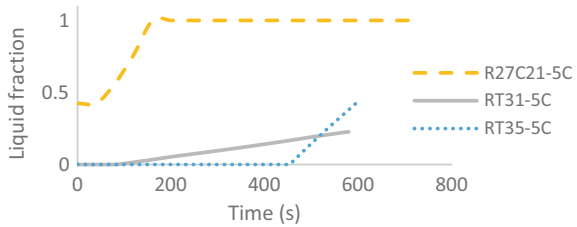
with and without PCM, the heat generated in the cell without PCM is computed as given in Table 4. The heat generated from the cell at considered discharge rates has been summarized to give a robust proof of dependency of temperature rise due to heat generation with discharge rate as observed from Eq. (4). We observe that cell discharging at 1C, 1.5C and 2C both RT-31 and RT-35 follows the same trend. This happens because the heat generated from battery isn't sufficient to start melting process in case of RT-31 and RT-35; whereas, in R27C 22 shows phase change in all the discharge rates because of its low melting temperature range.

In both the cases, heat is absorbed by the PCM material as sensible heat. It is observed that RT-31 exhibits minimum cell temperature rise in comparison with RT-35 and R27C22. This may be due to the wide melting temperature range of RT-31.

**Table 4** Thermal variants at different discharge rates

Discharge rate	Discharging time (s) (min)	Heat generation rate (W)	Heat generation source (W/m <sup>3</sup> )
1C	3600(60)	0.23	12,170
1.5C	2400(40)	0.39	21,813
2C	1800(30)	0.59	33,960
3C	1200(20)	0.83	47,642
5C	720(12)	2.08	121,714

**Fig. 4** PCM melting at 5C discharge rate under the influence of all three PCMs considered



The melting process initiates once the temperature of the battery reaches 27 °C in case of RT-31.

To compare thermal characteristics of PCMs considered, liquid fraction profile at 5C is plotted against time as shown in Fig. 4.

This illustrates that the RT-31 and RT-35 do not melt completely unlike R27C22. Although the normal discharge rate of battery is in the range of 0.6C–1C, in a typical EV, in special cases, the EV may experience higher discharge rates, for example, during acceleration, etc. Thus, a comparison of thermal characteristics of PCM at higher discharge rates is important and justifiable. The present comparison renders a complete phase transition of R27C22 within first 200 s of the operation (approximately) as shown in Fig. 4. Whereas, RT-35 exhibits initiation of phase transition at around 450 s and 100 s (approximately) in case RT-31. However, it is also evident that the liquid fraction is much smaller in case of RT-31 as compared to RT-35. This signifies that the performance of RT-31 at moderately higher discharge rate is better in comparison with the other PCM considered in the work. From Fig. 3e, for discharging at 5C, we observe temperature rise in RT-31 is less than RT-35. This happens because of differences in their latent heat capacities (*L*). RT-35 has less latent heat capacity than RT-31. This results in rapid phase change and higher liquid fraction in case of RT-35.

## 4 Conclusion

In the present work, a numerical simulation of 18650 single cell li-ion battery is considered for the investigation of thermal characteristics under different discharge rates with and without PCM layer. The numerical model is based on NTGK submodel, and MSMD approach is considered in the present work. Grid independence study is conducted to ensure accuracy of the work. The transient analysis enables to understand the effect of thermo-physical properties of three different PCM at different discharge rate. The maximum battery cell temperature is observed to obtain the comparative analysis of PCM. The comparison shows that RT-31 exhibits better performance among the group considered. In addition to that, specifically at higher discharge rates RT-31 is found to be most efficient with the lowest maximum temperature rise and minimum liquid fraction.

**Acknowledgements** The author acknowledge the financial and laboratory support received from National Institute of Technology Agartala.

## References

1. Bandhauer, T.M., Garimella, S., Fuller, T.F.: A critical review of thermal issues in lithium-ion batteries. *J. Electrochem. Soc.* **158**, 3–25 (2011)
2. Zhao, R., Zhang, S., Liu, J., Gu, J.: A review of thermal performance improving methods of lithium ion battery: electrode modification and thermal management system. *J. Power Sources* **20**, 557–577 (2015)
3. Kizilel, R., Sabbaha, R., Selmana, J.R., Halla, S.A.: An alternative cooling system to enhance the safety of Li-ion battery packs. *J. Power Sources* **194**, 1105–1112 (2009)
4. Panchal, S., Dincer, I., Agelin-Chaab, M., Fraser, R., Fowler, M.: Thermal modeling and validation of temperature distributions in a prismatic lithium-ion battery at different discharge rates and varying boundary conditions. *Appl. Therm. Eng.* **96**, 190–199 (2016)
5. Alaoui, C., Salameh, Z.: Modeling and simulation of a thermal management system for electric vehicles. In: *IECON Proceedings (Industrial Electronics Conference) 2003*, *IECON Proceedings*, vol. 1 (2003)
6. Agyenim, F., Hewitt, N., Eames, P., Smyth, M.: A review of materials, heat transfer and phase change problem formulation for latent heat thermal energy storage systems (LHTESS). *Renew. Sust. Energ. Rev.* **14**, 615–28 (2010)
7. Souayfane, F., Fardoun, P., Biwole, H.: Phase change materials (PCM) for cooling applications in buildings: a review. *Energy Build.* **129**, 396–431 (2016)
8. Zalba, B., Marín, J.M., Cabeza, L.F., Mehling, H.: Review on thermal energy storage with phase change: Materials, heat transfer analysis and applications. *Appl. Therm. Eng.* **23**(3), 251–283 (2003)
9. ANSYS-Fluent Battery Model Manual 15.0 (2013)
10. Tesla Battery Module Controller, Version 1.00 (2017)

# MPC-Based Power Quality Solution Using Energy Storage Technology for PV Based Islanded Microgrids



M. Jayachandran and G. Ravi

## 1 Introduction

PV and wind energy systems are commonly used renewable energy sources (RES) in DG to generate power regionally and satisfy the electricity demand in remote areas. DG systems are incorporated to microgrid through inverter with filter impedance. A microgrid can perform both isolated and grid connected mode to supply uninterrupted electricity to local loads [1]. Three phase three-wire system has been commonly used in the distributed power system to supply power to balanced loads effectively in past decades. However, under unbalanced load conditions, this system creates large circulating current resulting in output voltage distortion [2]. To overcome this problem, three phase four wire system has been employed in recent years to distribute power to loads. Split dc-link capacitor is used in the distributed system to form the neutral terminal. However, the major drawback of this approach is that it needs two large capacitors. To reduce capacitor size and to improve the dc-link utilization, 3-phase 4-leg inverter is the best option for microgrids [3]. The fourth leg of a power inverter is linked to neutral terminal of load. This four-leg inverter topology has fault tolerant capability and control flexibility [4]. Moreover, microgrid connected with unbalanced and nonlinear loads creates power quality issues like voltage unbalance/harmonics, and harmonic current sharing between DGs. In order to solve these issues, power quality improvement (PQI) devices have been used recently to compensate harmonics and unbalanced voltages [5]. However, installation of additional PQI devices are expensive. Meanwhile, virtual impedance based methods have been developed for harmonic current sharing, and voltage harmonics and unbalance compensation, but they require central low-bandwidth communication [6].

---

M. Jayachandran (✉) · G. Ravi  
Puducherry Technological University, Puducherry 605014, India  
e-mail: [jayachandran.escet@pec.edu](mailto:jayachandran.escet@pec.edu)

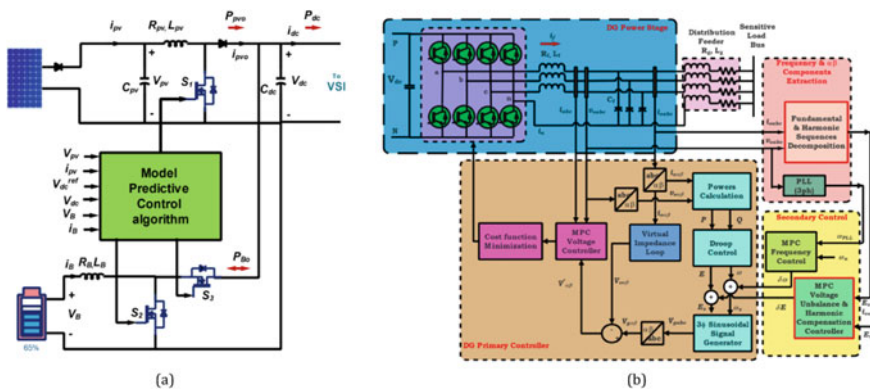
© The Author(s), under exclusive license to Springer Nature Singapore Pte Ltd. 2022  
S. K. Natarajan et al. (eds.), *Recent Advances in Manufacturing, Automation, Design and Energy Technologies*, Lecture Notes in Mechanical Engineering,  
[https://doi.org/10.1007/978-981-16-4222-7\\_92](https://doi.org/10.1007/978-981-16-4222-7_92)

Recent evidence suggests that the compensation of power quality issues can be realized through proper control of voltage source inverter (VSI) in DG units [7]. Regarding PV based microgrid system, the power generation and consumption are varied in every second due to the random fluctuation of the PV power and the variable load profile. Therefore, it is essential to use battery energy storage system (BESS) within the microgrid to facilitate the gap between electricity generation and consumption [8]. More recently, in [9] MPC based ESS control has been an increasing interest to smooth the fluctuated PV power generation. In [10], cost-function-based approach is developed for parallel inverters to deal with unbalance and harmonic compensation. Such approaches, however, have failed to address the potential impact on nonlinear load with unequal feeder impedance in an inverter interfaced DGs.

This study provides a novel approach to enhance power quality and power sharing. Especially, predictive control concepts are applied to secondary level in the hierarchical control to compensate the voltage unbalance and harmonic sequences. The objective of this research is to supply high-quality power to loads, irrespective of fluctuated PV power generation and load.

## 2 PV/Battery Hybrid Source Converter Control

PV converter system extracts maximum available solar energy and injects into dc bus. BMS has designed and operated using predictive control concept to ensure the output power is proportional to system frequency. The control objective of proposed control is to operate the voltage source inverter (VSI) within the specified limits. If the inverter power is negative, BMS operates the converter to buck mode and absorbs energy from PV system, otherwise, it delivers energy to the load as shown in Fig. 1a. In the discharge operation mode,  $SoC^{ref}$  is estimated based on the lowest SoC value



**Fig. 1** a Schematic diagram of distributed generator system. b Predictive hierarchical control scheme for an islanded microgrid

among all the batteries. Moreover, battery with higher state of charge (SoC) delivers more energy, whereas lower SoC delivers less energy. The converse is also true in charging process. Using the discrete-time model of the system, the future behavior of the PV and battery converters can be predicted as,

$$V(k+1) = [I + (A_1 + A_2S)T_s]x(k) + [B_1T_s]V(k) \quad (1)$$

$$\text{SoC}(k+1) = \text{SoC}(k) - \frac{P_{\text{battery}}(k+1) * T_s}{C_{\text{battery}}} \quad (2)$$

$$P_{\text{battery}}(k+1) = u(k+1) + P_{\text{battery}}(k) \quad (3)$$

$$g_{(\text{track})} = \sum_{j=1}^p [ |V_{\text{dc}}^{\text{ref}} - V_{\text{dc}}(k+j|k)| ] + \lambda_1 |\Delta u(k+j-1)| \quad (4)$$

where,  $A_1$ ,  $A_2$ , and  $B_1$  are state-space matrices.  $x(k)$  represents the measured variables.  $V(k)$  is the feasible voltage vectors. The battery SoC and its power can be calculated using Eq. (3). Minimizing the cost function of PV converter  $g_{(\text{track})}$  yields optimal switching sequence to track its reference output voltage. During charging and discharging process, the cost function for each prediction of battery can be obtained to select the switching states as,

$$g_{(\text{discharge})} = \sum_{j=1}^p \lambda_1 [ |V_{\text{dc}}^{\text{ref}} - V_{\text{dc}}(k+j|k)| ] + \lambda_2 [ |\text{SoC}^{\text{ref}} - \text{SoC}(k+j|k)| ] \quad (5)$$

$$g_{(\text{charge})} = \sum_{j=1}^p \lambda_1 [ |V_{\text{B}}^{\text{ref}} - V_{\text{B}}(k+j|k)| ] + \lambda_2 [ |\text{SoC}^{\text{ref}} - \text{SoC}(k+j|k)| ] \quad (6)$$

### 3 Predictive Hierarchical Control for Enhancing Power Quality

Power quality is enhanced by proper control of voltage source inverter (VSI). Taking the advantages of RHC (also known MPC) scheme that has been used in VSI, a new VUHC strategy for microgrids [1](#) at the secondary level of hierarchical control is proposed as shown in Fig. b. The control objective of proposed control is to operate the inverter within the specified limits and maintain a stable PCC voltage with regard to frequency and amplitude.

### 3.1 Frequency Regulation

To regulate the load frequency locally  $\omega_s = \omega + \delta\omega$ , the correcting signal ( $\delta\omega$ ) is obtained from SCS using receding horizon strategy by minimizing the cost function equation as,

$$J = \sum_{j=1}^p [\omega_{\text{PLL}}(k+j|k) - \omega_n]^2 + \lambda \sum_{j=1}^m [\Delta\omega_n(k+j-1)]^2 \quad (7)$$

The first and second term represent frequency tracking and control action.  $\omega_n$  is the nominal frequency, and  $\lambda$  is the weighting factor.

### 3.2 Voltage Regulation

To regulate the PCC voltage  $E_s = E + \delta E$ , the compensation voltage ( $\delta E$ ) is generated from SCS and applied to the primary controller. The state observer and predictor can be determined using Eq. (8) and (9) as,

$$\begin{aligned} \begin{bmatrix} i_f(k) \\ i_{\text{dis}}(k) \end{bmatrix} &= \Phi \begin{bmatrix} i_f(k-1) \\ i_{\text{dis}}(k-1) \end{bmatrix} + \Gamma \begin{bmatrix} E_{\text{comp}}(k-1) \\ 0 \end{bmatrix} \\ &+ \Lambda \left( \begin{bmatrix} E_{\text{out}}(k-1) \\ i_{\text{out}}(k-1) \end{bmatrix} - H \begin{bmatrix} i_f(k-1) \\ i_{\text{dis}}(k-1) \end{bmatrix} \right) \end{aligned} \quad (8)$$

$$\begin{bmatrix} E_{\text{out}}(k+1) \\ i_{\text{out}}(k+1) \end{bmatrix} = H \begin{bmatrix} i_f(k) \\ i_{\text{dis}}(k) \end{bmatrix} + w(k) \quad (9)$$

where,  $i_{\text{out}}$  and  $E_{\text{out}}$  are output current and voltage of DG system.  $i_f$  and  $i_{\text{dis}}$  are inductor current of LC filter and disturbance current. It is assumed that the future  $\Delta u = 0$ , then the  $j$ -step ahead predictor equation state-space domain can be represented as,

$$\begin{bmatrix} E_{\text{out}}(k+j|k) \\ i_{\text{out}}(k+j|k) \end{bmatrix} = H\Phi_j \begin{bmatrix} i_f(k) \\ i_{\text{dis}}(k) \end{bmatrix} + H\Phi_{j-1}\Lambda \left( \begin{bmatrix} E_{\text{out}}(k) \\ i_{\text{out}}(k) \end{bmatrix} - H \begin{bmatrix} i_f(k) \\ i_{\text{dis}}(k) \end{bmatrix} \right) \quad (10)$$

The cost function of the MPC based secondary control can be obtained for voltage regulation as,

$$J = \beta_1 \sum_{j=1}^p [Y_{\text{out}}(k+j|k) - Y_{\text{ref}}]^2 + \beta_2 \left[ \sum_{j=1}^m [\Delta u(k+j-1)]^2 \right] \quad (11)$$

By minimizing the objective function, the compensation voltage ( $\delta E$ ) is generated from SCS and applied to local controllers. The output variable  $Y_{\text{out}}(k) =$

$[E_{\text{out}}(k)i_{\text{out}}(k)]^T$  is controlled by MPC scheme. The variation of the control input vector,  $\Delta u(k) = u(k) - u(k-1)$ . In order to share the harmonic current between DGs, and minimize the unbalance/harmonic voltages, the weighting factors ( $\beta_1$  and  $\beta_2$ ) are properly tuned. The tuning parameter  $\beta_1$  is determined based on the trade-off between current sharing accuracy and DG output voltage steady state error. In order to share the output current ( $i_o$ ) of each DG unit, set  $\beta_1$  value equally and predict the output voltage ( $V_o$ ) correctly.

$$i_o = -\frac{S_{\text{DG}}}{\beta_1 V^{*2}} V_o \quad (12)$$

$$\varepsilon_{(i_o)} = -\frac{S_{\text{base}}}{\beta_1 V_{\text{base}}^2} \text{err}_{(v_o)} \quad (13)$$

$S_{\text{DG}}$  and  $V^*$  are power rating and reference voltage of each DG unit. It is observed from Eq. (13) that smaller  $\beta_1$  leads to smaller negative and harmonic sequence. However, it might be voltage estimation error and resulting in larger current sharing error as represented in Eq. 13. If  $\beta_1$  is too small, it will slow down the dynamic response of the system and if  $\beta_1$  is too large, it will make the system unstable. Moreover, tuning parameter  $\beta_2$  determines the trade-off between dynamics of current balancing and stability. Smaller  $\beta_2$  results in faster dynamic response of the system, whereas larger  $\beta_2$  results in system becoming more stable. For optimal tuning of weighting parameters to operate the MPC as fast as possible, the weighting parameters ( $\beta_1$  and  $\beta_2$ ) are recommended for power quality compensation [12].

## 4 Simulation Results

Two DG units have same capacity and connected with nonlinear/unbalanced load through VSI with unequal distribution feeders. In order to make imbalance voltage, Phase-C resistance is disconnected from three phase resistive load. Table 1 presents the simulation data on microgrid system. The unequal feeder impedances are used. The power quality analysis is carried out using %V UF and %THD parameters. When battery is not in operating condition, the intermittent nature of PV power distorts the DC bus and PCC voltages as shown in Fig. 2a. If battery storage system is operated, the charging and discharging control strategy using Eqs. (5) and (6) modulate the battery power relying on the PV power fluctuation in order to smooth the PCC voltage as shown in Fig. 2b. Thus, the BMS is employed in microgrid system to smooth the PV power generation output. The effectiveness of the proposed compensation control is validated with conventional hierarchical control under unequal feeder impedance and nonlinear plus unbalanced loads. Firstly, the rectifier load is connected to the common bus. The harmonic currents are not properly shared between inverters because of unequal feeder impedance, and DG<sub>1</sub> offers larger harmonic currents due to a lower feeder impedance. As a result, PCC voltage is distorted as shown in Fig. 2c. When



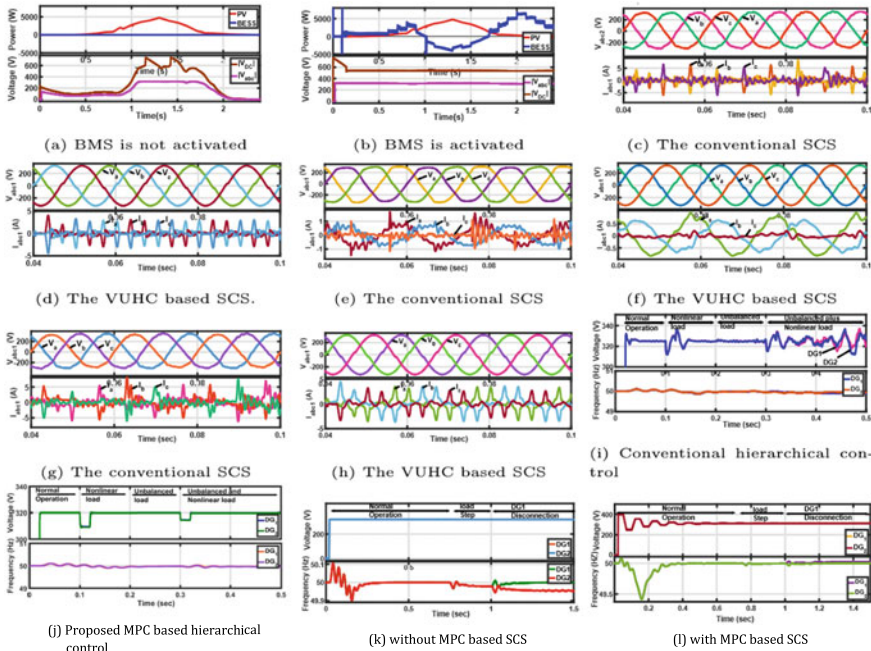
**Table 1** Parameters of microgrid

Parameters	Value
<i>Power stage</i>	5 KW
PV maximum power ( $P_{pv}$ )	
DC-link voltage ( $V_{dc}$ )	550 V
Battery nominal voltage ( $V_{battery}$ )	500 V
Battery rated capacity ( $C_{battery}$ )	100 Ah
PV converter inductance and resistance ( $L_{PV}, R_{PV}$ )	450 $\mu$ H, 0.3 $\Omega$
PV input and output capacitors ( $C_{PV}, C_{dc}$ )	1000, 1000 $\mu$ F
Battery converter inductance and resistance ( $L_B, R_B$ )	400 $\mu$ H, 0.3 $\Omega$
Filter resistance, inductance and capacitance ( $R_f, L_f, C_f$ )	0.05 $\Omega$ , 2 mH, 80 $\mu$ F
Nominal voltage ( $E_0$ )	325 V
Rated frequency ( $f_0$ )	50 Hz
Feeder resistance and reactance ( $R_{g1}, R_{g2}, L_{g1}, L_{g2}$ )	0.4060, 0.8765, 1.1885, 0.2898 $\Omega$
<i>Controller tuning parameters</i>	0.1, 0.99, 0.01
Weighting factor ( $\lambda, \lambda_1, \lambda_2$ )	
Droop coefficients ( $m_p, m_q$ )	0.0001 rad/s/W, 0.0001 V/Var
Virtual inductance and resistance ( $L_v, R_v$ )	4 mH, 0.2 $\Omega$
Control and prediction horizons ( $m, p$ )	5, 10
<i>Sampling period (<math>T_s</math>)</i>	1, 33, 0.05 $\mu$ s
Hybrid source, Primary, and Secondary controllers	
<i>Load</i>	230 $\Omega$
Unbalanced load resistance ( $R_{UL}$ )	
Resistance, inductance and capacitance of nonlinear load ( $R_{NL}, L_{NL}, C_{NL}$ )	460 $\Omega$ , 84 $\mu$ H, 235 $\mu$ F

compensation control is activated, the power sharing errors are compensated, and the harmonic currents are shared between DGs according to their power ratio by the proposed secondary control. Moreover, the voltage at PCC is less distorted as shown in Fig. 2d.

Secondly, in the case of unbalanced resistive load, the circulating harmonic current between DGs create unbalance and harmonic currents as shown in Fig. 2e. As a result, unbalanced voltage is observed. After the enabling the compensation controller, the voltage unbalances are effectively suppressed, and current harmonics are properly shared between inverters as illustrated in Fig. 2f. The harmonic and unbalance currents between DGs are appropriately shared in the presence of proposed hierarchical control as illustrated in Fig. 2h which is not observed in conventional control as shown in Fig. 2g. Moreover, the currents in each DG unit are similar.

With regard to the power sharing, the three phase rectifier load is applied between 0.1 and 0.2 s, unbalanced resistive load is connected between 0.2 and 0.3 s and unbalanced plus nonlinear load is attached between 0.3 and 0.5 s at PCC. The active,



**Fig. 2** a, b Power and voltage waveforms. c, d DG with nonlinear load. e, f DG with Unbalanced load. g, h DG with Unbalanced and Nonlinear load ( $I - l$ ) $V/f$  of microgrid at PCC

reactive, unbalance, and harmonic power sharing errors occur due to circulating current caused by nonlinear/unbalanced load.

Concerning the voltage and frequency regulation at different load conditions, the slight voltage rise and fall are observed as shown in Fig. 2i by conventional PI based SCS. The proposed SCS method quickly regulates the reference voltage of each phase within 1 ms and maintains voltage stable at PCC under steady state as depicted in Fig. 2j. Frequency stability is also attained in proposed SCS under steady state, which is not observed in conventional control. It is clear that the output (capacitor) voltages and inductor currents track their references effectively with the proposed hierarchical control strategy. Moreover, Fig. 2k, l illustrates the performance of the proposed SCS for an islanded microgrid system. Before activation of SCS, the system frequency and node voltage vary when sudden resistive load is applied at  $t = 0.75$  s. The disconnection of DG<sub>1</sub> at  $t = 1$  s results further deviation of voltage and frequency of DG<sub>2</sub>. After activation of SCS at  $t = 0.02$  s, there has been a gradual rise in  $V$  and  $f$  to reach its rated value as presented in Fig. 2k, l. Table 2 compares the results obtained from the analysis of power quality performance of the conventional and the proposed hierarchical control strategies under nonlinear/unbalanced loads. %V<sub>UF</sub>, %THD, and %V<sub>error</sub> are used to analyse the power quality in an islanded microgrid. The percentage of error voltage in all phases is lower than the traditional method and maintains fundamental voltage to its nominal value. As compared to conventional

**Table 2** Unbalance factor and harmonic distortion of microgrid with conventional and proposed hierarchical control

Load	Parameters	PR based Hierarchical control			Proposed hierarchical control		
		Phase-a	Phase-b	Phase-c	Phase-a	Phase-b	Phase-c
Unbalanced load	%error	2.00	2.61	0.05	0.25	0.09	0.09
	%THD	3.70	4.44	3.90	3.59	3.54	3.58
	%UF	<b>2.58</b>			<b>0.20</b>		
Nonlinear load	%error	0.18	0.36	0.43	0.09	0.06	0.06
	%THD	3.81	3.34	3.89	3.58	3.58	3.60
	%UF	<b>0.47</b>			<b>0.02</b>		
Nonlinear plus unbalanced load	%error	2.00	2.55	0.61	0.03	0.05	0.05
	%THD	3.74	4.59	3.94	3.57	3.54	3.62
	%UF	<b>2.57</b>			<b>0.25</b>		

control, the proposed hierarchical scheme can largely reduce the unbalance voltage error and the %V UF is maintained below 2%. Thus, the phase voltages at PCC are balanced. Moreover, %THD of DG<sub>1</sub> and DG<sub>2</sub> are maintained below 4%.

Overall, these simulation results indicate that proposed predictive SCS not only restores the  $V/f$  deviations but also enhances the power quality and load sharing. Therefore, the proposed MPC based hierarchical control offers high-quality output voltage to load, regardless of PV and load uncertainties.

## 5 Conclusion

This study has examined the concept of a decentralized MPC strategy for power quality improvement in a PV based islanded microgrids. The proposed control utilizes a prediction algorithm to smooth the PV power fluctuation. In addition to the battery management system, the VUHC method is developed in SCS to compensate for the unbalance and harmonics voltages. The load sharing among DGs are realized by regulating the system frequency to its rated value and maintains the node voltage constant using hierarchical control. Hence, the proposed controller offers high-quality power to load with balanced, symmetrical three phase sinusoidal voltages at mismatched feeder impedance under fluctuated PV power. It also ensures that the desired power sharing among DG systems with an excellent output voltage quality at PCC under steady state conditions.

## References

1. Han, H., Hou, X., Yang, J., Wu, J., Su, M., Guerrero, J.M.: Review of power sharing control strategies for islanding operation of AC microgrids. *IEEE Transactions on Smart Grid* **7**(1), 200–215 (2016)
2. Kim, G.-H., Hwang, C., Jeon, J.-H., Ahn, J.-B., Kim, E.-S.: A novel three-phase four-leg inverter based load unbalance compensator for stand-alone microgrid. *Int. J. Electr. Power Energy Syst.* **65**, 70–75 (2015)
3. Miveh, M.R., Rahmat, M.F., Ghadimi, A.A., Mustafa, M.W.: Control techniques for three-phase four-leg voltage source inverters in autonomous microgrids: a review. *Renew. Sustain. Energy Rev.* **54**, 1592–1610 (2016)
4. Bayhan, S., Abu-Rub, H.: Model predictive control of quasi-z source three-phase four-leg inverter. In: *IECON 2015—41st Annual Conference of the IEEE Industrial Electronics Society*, IEEE, pp. 362–367 (2015)
5. Naderi, Y., Hosseini, S.H., Zadeh, S.G., Mohammadi-Ivatloo, B., Vasquez, J.C., Guerrero, J.M.: An overview of power quality enhancement techniques applied to distributed generation in electrical distribution networks. *Renew. Sustain. Energy Rev.* **93**, 201–214 (2018)
6. Savaghebi, M., Vasquez, J.C., Jalilian, A., Guerrero, J.M.: Secondary control for compensation of voltage harmonics and unbalance in microgrids. In: *2012 3rd IEEE International Symposium on Power Electronics for Distributed Generation Systems (PEDG)*, pp. 46–53 (2012)
7. Han, Y., Shen, P., Zhao, X., Guerrero, J.M.: An enhanced power sharing scheme for voltage unbalance and harmonics compensation in an islanded ac microgrid. *IEEE Trans. Energy Convers.* **31**(3), 1037–1050 (2016)
8. Hu, J., Zhu, J., Guerrero, J.M.: Model predictive control of smart microgrids. In: *2014 17th International Conference on Electrical Machines and Systems (ICEMS)*, pp. 2815–2820 (2014)
9. Shan, Y., Hu, J., Li, Z., Guerrero, J.M.: A model predictive control for renewable energy based AC microgrids without any PID regulators. *IEEE Trans. Power Electron.* 1–1 (2018)
10. Liu, J., Miura, Y., Ise, T.: Cost-function-based microgrid decentralized control of unbalance and harmonics for simultaneous bus voltage compensation and current sharing, *IEEE Trans. Power Electron.* 1–1 (2018)

# Biogeography-Based Centralized PID Controller for ALFC in Presence of Wind Farms



E. Sri Lalitha, A. M. S. V. Sushma, G. Pavan Kumar, and Ch. Durga Prasad

## 1 Introduction

Frequency control of multi-source power system is more complex with renewable sources integration due to continuous power imbalance between generation and demand. In the presence of interconnected power system, generating electricity usually involves a combination of thermal, hydro, gas and wind power generations [1–3]. For large power systems with interconnected parts, increasing the automatic load control (ALFC) to minimize the system frequency disturbances is important and has the potential to connect to areas adjacent to the protected [4]. Since the system is a large and complex electrical unit, it is composed of power generation, transmission and distribution units, and these loads share the load over a large area through the entire network.

Over the last 20 years, renewable energy sources utilization for electric power generation is increased, particularly wind energy [5–12]. The control (droop and inertia control) flexibilities of turbines provides a chance for wind to suppress load perturbations [5]. Other side, new challenges arises from the penetration of wind generation into the conventional electrical power systems [6]. In this line of research, a critical survey on the ALFC of power systems has been presented in [6–12] on various aspects. Recently, modern control theory [6], neural networks and fuzzy system [7–10], is considered for improvement of LFC performance. However, these modern methods have a particular degree of complexity which successively limits their application in complex scenarios. Therefore, PID controller is not a bad choice for maintaining system frequency within limits during load changes with proper tuning algorithm. Recently, a few more works were proposed in the load frequency control area [12, 13].

---

E. Sri Lalitha (✉) · A. M. S. V. Sushma · G. Pavan Kumar · Ch. Durga Prasad  
Department of Electrical and Electronics Engineering, SRKR Engineering College, Bhimavaram,  
India

In this paper, the best parameter values of PI and PID controllers are identified by the BBO algorithm. These controllers are set up on centralized mode in secondary control loop of single area include thermal, hydro and gas plants [4]. Additionally, the system is integrated with wind farm connected by HVDC links. The droop and inertia control of the wind farm are also a part of frequency control of the aforementioned system. Investigations provided in subsequent sections show the merits of the proposed structure. All the simulations are performed in MATLAB-SIMULINK environment.

## 2 Investigated Multi Source System and Tuning Mechanism

Multi-source isolated power system is opted for biogeography-based centralized PID controller scheme application in presence of droop and inertia controlled wind farm integrated to system with HVDC link. The block diagram representation of the simulated test system shown in Fig. 1. Centralized PID control scheme is presented in secondary control loop to supervise the control actions of the conventional plants, and wind power is controlled by droop and inertia control [5]. The system specifications are available in [5].

The centralized PID controller optimal parameter gains are obtained by using BBO algorithm. Based on immigration and emigration of species between different habitats, this BBO algorithm is implemented. The mechanism of the algorithm is different from other optimization algorithms, but updating the solution towards optimal point is similar. Each habitat represents one possible solution of search space and characterized by two indices known suitability index for variables and suitability index of habitats [10–12]. The habitat with high suitability index has more species and the habitat with low suitability index has less species. The species moves towards highly

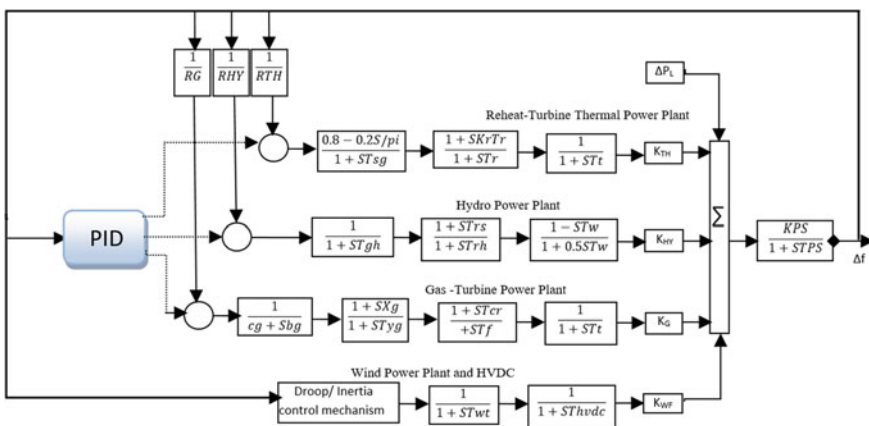


Fig. 1 Block diagram representation of simulated power system

populated habitat with the help of updating mechanism in which two probabilistic operators are used. Migration and mutation are the two probabilistic operators. Migration operation depends on immigration rate and emigration rate. The immigration ( $\lambda$ ) and emigration ( $\mu$ ) rates for  $k$ th particle are given by [10],

$$\mu = E \frac{k}{n} \tag{1}$$

$$\lambda = I \left( 1 - \frac{k}{n} \right) \tag{2}$$

In Eq. (1),  $E$  is the maximum emigration rate and ‘ $n$ ’ represents number of habitats. In Eq. (2), ‘ $I$ ’ is the maximum immigration rate. The best habitat with good suitability index is retained, and the habitat with poor index is mutated for acquiring better features. This algorithm is adopted to minimize the total frequency deviations of the system framed with integral square error (ISE) objective function given by

$$J = \int_0^t (\Delta f)^2 dt \tag{3}$$

As centralized control scheme using in this paper makes the control problem as three-dimensional and the three decision variables are the optimal gain parameters of the proportional, integral and derivative components of the PID controller with upper and lower limits are given by  $k_p, k_i, k_d \in [k_{min} k_{max}]$ . This scheme is tested in both increase and decrease demand scenarios of the test system, and results are compared with optimal PSO PID controller. Along with PID controller scheme, the inertia and droop control strategies are provided for wind farm to control its output power during load perturbations.

**Table 1** PI controller parameter gains for multi-source power system using BBO

Case	Proportional gain	Integral gain
1% change	0.6311	0.4061
5% change	0.6277	0.4077

**Table 2** PID controller parameter gains for multi-source power system using BBO

Case	Proportional gain	Integral gain	Derivative gain
1% change	1.3631	2.5042	1.2556
5% change	1.3736	2.5088	1.2507

### 3 Simulation Results

The optimal gain parameters obtained by BBO are presented in Tables 1 and 2 for both demand increase and decrease scenarios of the multi-source power system shown in Fig. 1. For comparison, BBO-tuned PI and PSO-tuned PID controller are chosen. Case-1 corresponding to 1% load change parameter gains and case-2 corresponding to 5% load case. Figure 2 shows the response of the system with PI and PID controllers when 1% load change (decrease) occurs. The response is a clear evidence for the improvements in time domain specifications with PID controller in terms of peak overshoot, settling time and steady state error. The proposed BBO centralized PID control scheme maintain system frequency as constant compared to PI controller even during generation changes and provided good performance specifications compared to PSO-PID controller. For 1% load increase case, result is provided in Fig. 3. Figure 4 shows the response of the system with PI, PSO-PID

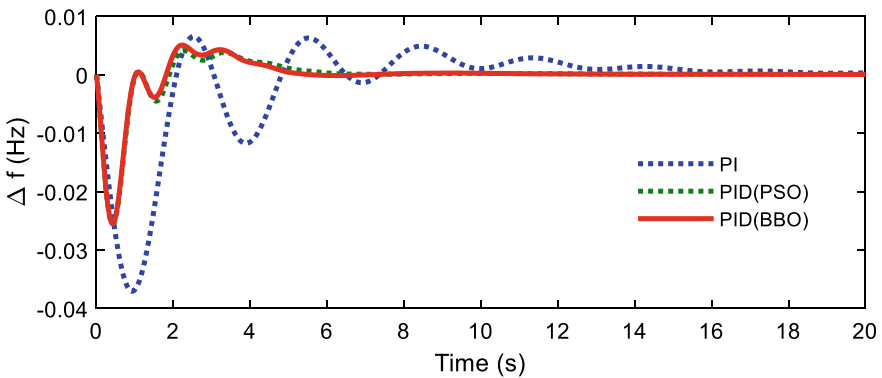


Fig. 2 Change in frequency signal during load decrease (1%)

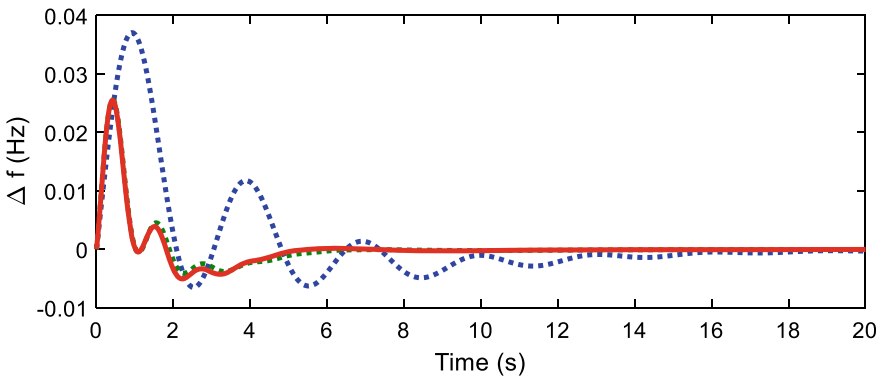
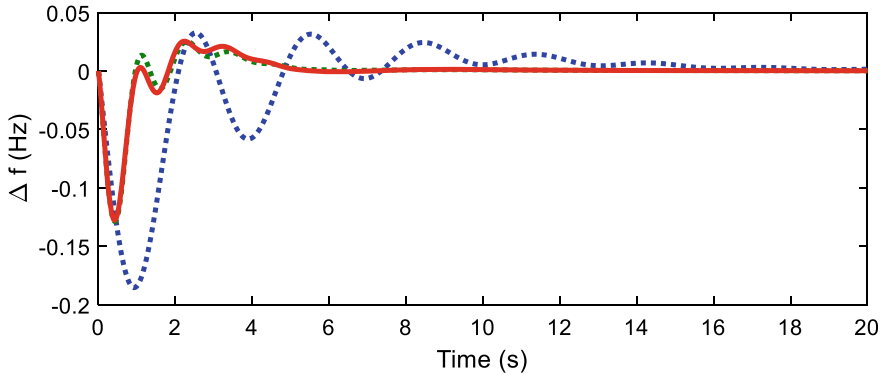


Fig. 3 Change in frequency signal during load increase (1%)





**Fig. 4** Change in frequency signal during load decrease (5%)

and BBO-PID controllers when 5% load change (decrease) occurs. PID controller able to reduce frequency oscillations in quick time with less peak overshoot and no steady-state error.

The results in conventional simulation studies (Figs. 2, 3 and 4) show the superiority of PID controller over PI in terms of dynamic and steady-state specification since the additional derivative parameter gain enhances its stability. However, better performance specifications are achieved with BBO-tuned PID than PSO tuning. During load disturbances, when the wind is suddenly disconnected from system, the PID is quite impressive over PI to supervise the system and to minimize the frequency oscillations.

## 4 Conclusions

Centralized PID controller scheme presented in this paper for conventional plants to suppress the frequency oscillation of the multi-source power system. The controller optimal parameter gains were obtained by BBO algorithm. Along with this controller, wind power with droop and inertia control mechanisms also investigated in this paper. Together, the proposed scheme had the ability to supervise the control action than other controllers.

## References

1. Hassan, B.: Robust Power System Frequency Control. Springer (2009)
2. Ekanayake, N., Jenkins, J.: Comparison of the response of doubly fed and fixed-speed induction generator wind turbines to change in network frequency. *IEEE Trans. Energy Convers.* **19**(4), 800–802 (2004)

3. Kayikci, M., Milanovic, J.V.: Dynamic contribution of DFIG-based wind plants to system frequency disturbances. *IEEE Trans. Power Syst* **24**(2), 859–867 (2009)
4. Mohanty, B., Panda, S., Hota, P.K.: Controller parameters tuning of differential evolution algorithm and its application to load frequency control of multisource power system. *Int. J. Electr. Power Energy Syst* **54**, 77–85 (2014)
5. Tavakoli, M., Pouresmaeil, E., Adabi, J., Godina, R., Catalão, J.P.: Load-frequency control in a multi-source power system connected to wind farms through multi terminal HVDC systems. *Comput. Oper. Res.* **96**, 305–315 (2018)
6. Mohamed, T.H., Morel, J., Bevrani, H., Hiyama, T.: Model predictive based load frequency control design concerning wind turbines. *Int. J. Electr. Power Energy Syst.* **43**(1), 859–867 (2012)
7. Shang-Guan, X., He, Y., Zhang, C., Jiang, L., Spencer, J.W., Wu, M.: Sampled-data based discrete and fast load frequency control for power systems with wind power. *Appl. Energy* **259**, 114202 (2020)
8. Bevrani, H., Daneshmand, P.R.: Fuzzy logic-based load-frequency control concerning high penetration of wind turbines. *IEEE Syst. J.* **6**(1), 173–180 (2011)
9. Abazari, A., Monsef, H., Wu, B.: Load frequency control by de-loaded wind farm using the optimal fuzzy-based PID droop controller. *IET Renew. Power Gener.* **13**(1), 180–190 (2018)
10. Dahiya, P., Sharma, V., Naresh, R.: Hybridized gravitational search algorithm tuned sliding mode controller design for load frequency control system with doubly fed induction generator wind turbine. *Optimal Control Appl. Methods* **38**(6), 993–1003 (2017)
11. Simon, D.: Biogeography-based optimization. *IEEE Trans. Evol. Comput.* **12**(6), 702–713 (2008)
12. Mohammadikia, R., Aliasghary, M.: A fractional order fuzzy PID for load frequency control of four-area interconnected power system using biogeography-based optimization. *Int. Trans. Electr. Energy Syst.* **29**(2), e2735 (2019)
13. Azaharahmed, M., Raja, K., Patan, M.K., Prasad, C.D., Ganeshan, P.: Invasive weed optimized area centralized 2 degree of freedom combined PID controller scheme for automatic generation control. *J. Electr. Eng. Technol.* 1–12 (2020)

# CFD Analysis of Heat Transfer Through Natural Convection Inside Square Cavity Using Various Nano Fluids



Hari Kishan Veeranki , Sreenivasulu Bondala, and Ajit Burra

## 1 Introduction

Natural convection is a heat and mass transport method, and the fluid motion happens naturally due to buoyancy. Nanofluids have nanometer sized particles called nanoparticles. These nanofluids are colloidal suspensions of convective fluid with a specific volume concentration of nanoparticles. Nanofluids have more heat transfer characteristics, and thermo-physical properties of the fluid compared to conventional fluids. Investigated natural convection inside square enclosure. The average Nusselt number for alumina-water and copper-water at  $Ra = 10^5$  is more [1]. Numerically investigated recto-trapezoidal in natural convection. The results show that heat transfer enhancement is 30% more at  $Ra = 10^6$  over  $Ra = 10^3$  [2]. Investigated in square enclosure and enclosure with convex walls in natural convection method. The outcomes determined that heat transfer in square cavity is better than concave enclosures [3]. Examined mathematically through free convection inside trapezoidal enclosure. Average Nusselt number  $Nu_{Avg}$  is increased by increasing Rayleigh number [4]. Numerically investigated on natural convection in a square enclosure, with a conductive baffle plate. Average Nusselt number improved by increasing volume fraction and relocating the baffle towards the cavity center [5]. Executed on experimentation on the natural convection process in a rectangular enclosure. Maximum heat transfer rate, increasing the width ratio to length [6]. Studied numerically on free convection inside square enclosure. The average Nusselt numbers showed complete lower rates of heat transfer for nonuniform heating case [7]. Numerically analyzed the natural convection inside a square enclosure the effects of distinct heating locations in the lowermost wall, and the local heat source on the lowermost wall were evaluated [8]. Numerically studied on natural convection inside a square enclosure detected that the enhancement of heat transfer depends on different combinations of nanofluids

---

H. K. Veeranki (✉) · S. Bondala · A. Burra  
Gayathri Vidya Parishad College of Engineering, Visakhapatnam, Andhra Pradesh, India

used [9]. Present investigation aims to analyze nanofluids flow and thermal characteristics in square cavity. Investigation of heating characteristics within square cavity carried out. Based on governing equations are mass, momentum, and energy equations as input parameters in the software to obtain the average Nusselt numbers results. Comparison of heat transfer enhancement made for nanofluids based on average Nusselt numbers.

## 2 Geometry Model and Analysis

A geometrical model of square cavity is represented in dimensional form in Fig. 1. The cavity's top wall is insulated, and the side and bottom walls are kept at constant temperatures of  $T_c$  and  $T_h$ , respectively. The cavity length is  $L$ , the height of the cavity is  $H$ .

Nanofluids filled inside the square cavity, where the nanoparticles are silver, copper, graphene, and titanium oxide, and the base fluids are water and ethylene glycol. These nanofluids are assumed to be incompressible and Newtonian with the non-dimensional variables mentioned below

$$X = \frac{x}{L}, Y = \frac{y}{L}, U = \frac{uL}{\alpha f}, V = \frac{vL}{\alpha f}, \theta = \frac{T - T_c}{T_h - T_c},$$

$$Pr = \frac{\mu C_p}{k}, Ra = \frac{g\beta(T_h - T_c)L^3 Pr}{\vartheta^2}$$

$U, V$  are the velocity components along with  $x$  and  $y$  directions, respectively.  $L$  is the characteristic length-scale of geometry (side of a square).  $\vartheta$  is kinematic viscosity, and  $\mu$  is dynamic viscosity.  $T$  is the temperature at any location in a square

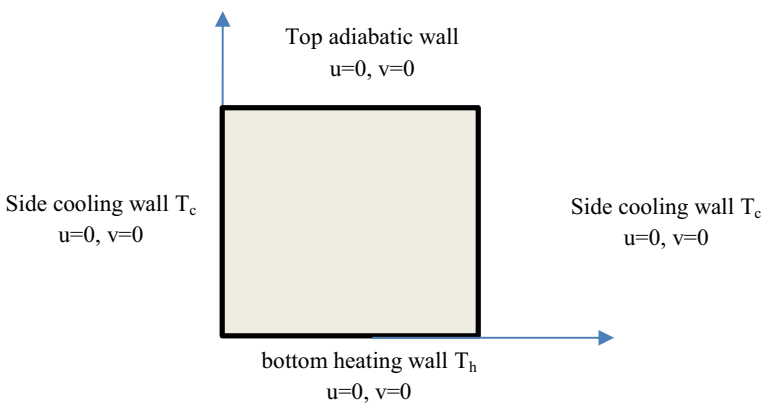


Fig. 1 Geometrical model of square cavity

cavity. Pr is Prandtl number, Ra is Rayleigh number,  $T_h$  and  $T_c$  are the temperatures of hot and cold fluids, respectively.

The dimensionless or non-dimensional governing equations are mass, momentum, and energy equations mentioned below:

- Continuity equation:

$$\frac{\partial U}{\partial X} + \frac{\partial V}{\partial Y} = 0 \tag{1}$$

- Momentum equation:

$$U \frac{\partial U}{\partial X} + V \frac{\partial U}{\partial Y} = -\frac{\partial P}{\partial X} + \frac{\mu_{nf}}{\rho_{nf}\alpha_f} \left( \frac{\partial^2 U}{\partial X^2} + \frac{\partial^2 U}{\partial Y^2} \right) \tag{2}$$

$$U \frac{\partial V}{\partial X} + V \frac{\partial V}{\partial Y} = -\frac{\partial P}{\partial Y} + \frac{\mu_{nf}}{\rho_{nf}\alpha_f} \left( \frac{\partial^2 V}{\partial X^2} + \frac{\partial^2 V}{\partial Y^2} \right) + \frac{(\rho\beta)_{nf}}{\rho_{nf}\beta_f} Ra Pr \theta \tag{3}$$

- Energy equation:

$$U \frac{\partial \theta}{\partial X} + V \frac{\partial \theta}{\partial Y} = \frac{\alpha_{nf}}{\alpha_f} \left( \frac{\partial^2 \theta}{\partial X^2} + \frac{\partial^2 \theta}{\partial Y^2} \right) \tag{4}$$

Nanofluids thermo-physical properties are density, specific heat capacity, thermal diffusivity, thermal expansion coefficient, and thermal conductivity are calculated with following equations, respectively. The effective properties of nanofluid mentioned below

$$\alpha_f = \frac{k_f}{\rho_f c_{pf}} \tag{5}$$

$$\vartheta_f = \frac{\mu_f}{\rho_f} \tag{6}$$

$$\rho_{nf} = [(1 - \phi)\rho_f] + (\phi\rho_s) \tag{7}$$

$$\rho_{nf}c_{pnf} = (1 - \phi)\rho_f c_{pf} + (\phi\rho_s c_{ps}) \tag{8}$$

$$\beta_{nf} = [(1 - \phi)\beta_f] + (\phi\beta_s) \tag{9}$$

$$\alpha_{nf} = \frac{k_{nf}}{\rho_{nf}c_{pnf}} \tag{10}$$

$$k_{nf} = k_f \left[ \frac{k_p + 2k_f - 2\phi(k_p - k_f)}{k_p + 2k_f + \phi(k_p - k_f)} \right] \tag{11}$$

$$Pr = \frac{\nu_f}{\alpha_f} \tag{12}$$

$$\rho_{nf}\beta_{nf} = (1 - \phi)\rho_f\beta_f + (\phi\rho_s\beta_s) \tag{13}$$

$$\mu_{nf} = \frac{\mu_f}{(1 - \phi)^{2.5}} \tag{14}$$

Boundary conditions:

The cavity’s top wall is insulated, vertical sidewalls are kept cold, and the bottom wall is kept hot. Hence, the boundary conditions of velocities are

$$U(X, 0) = U(X, 1) = U(0, Y) = U(1, Y) = 0,$$

$$V(X, 0) = V(X, 1) = V(0, Y) = V(1, Y) = 0.$$

The boundary conditions for temperature in various cases

$$\theta = 1 \text{ (for uniform bottom heating wall)}$$

$$\theta = 0 \text{ (for cold wall)}$$

$$\frac{\partial\theta}{\partial Y} = 0 \text{ (for adiabatic wall)}$$

### 2.1 Material Properties

The thermophysical properties of various nanoparticles like copper, silver, graphene, and titanium oxide are mentioned in Table 1.

Local Nusselt number is calculated for bottom heating wall in the square cavity from the relation mentioned below

$$Nu = -\frac{k_{nf}}{K} \frac{\partial\theta}{\partial n} \Big|_{\text{wall}} \tag{15}$$

**Table 1** Thermo-physical properties of nanoparticles at  $T = 25^\circ\text{C}$

Properties	Copper	Titanium oxide	Silver	Graphene
$C_p(\text{J/kg}\cdot\text{K})$	385	686.2	235	790
$k(\text{W/m}\cdot\text{K})$	401	8.9538	429	5000
$\rho(\text{kg/m}^3)$	8933	4250	10,500	2200
$\beta(\text{K}^{-1}) \times 10^5$	1.67	0.9	1.89	0.6

Average Nusselt number is calculated for bottom heating wall in the square cavity from the relation mentioned below

$$Nu = \frac{1}{L} \int_0^L Nu \, dX \tag{16}$$

### 3 Numerical Method

The governing differential equations (Eqs. 1–4) are solved numerically using the finite element-based solver COMSOL multiphysics. Specific boundary conditions are considered in square cavity and simulated to validate the investigation. The acquired results are validated with Basak and Chamkha results [1]. Fluid flow patterns in the natural convection mechanism and the transfer of heat inside the square cavity filled with Cu-water, Al<sub>2</sub>O<sub>3</sub>-water, and TiO<sub>2</sub>-water as nanofluids with different boundary conditions investigated. From validation, results are similar to ensure that the process we considered for the present investigation is correct to obtain accurate results. The grid independence test study is done with natural convection heat transfer in the square cavity to check the number of mesh elements to select for the present investigation. The square enclosure filled nanofluids at different volume concentrations of nanoparticles in the range of  $0 < \phi < 0.1$  and with varying numbers of Rayleigh in the field of  $10^3 < Ra < 10^5$ . We considered some different grids in free triangular mesh for the present investigation. The results presented in terms of average Nusselt numbers at the bottom heating wall are shown in Table 3.

#### 3.1 Grid Independence Test

Before analyzing results of the present work, it is important to verify correctness of numerical scheme. The accuracy of the calculated results is dependent on a careful choice of the grid size. Results are tabulated in Table 2 with different grid sizes such as  $459 \times 459$ ,  $469 \times 469$ ,  $479 \times 479$ , and  $489 \times 489$  for  $\phi = 0.1$  and  $Ra = 10^5$

**Table 2** Average Nusselt number values for the bottom heating wall at the different number of mesh elements at  $\phi = 0.1$  and  $Ra = 10^5$  for present study Cu-water

Number of elements	Average Nusselt number $Nu_{avg}$	Percentage of error = $\frac{ Nu_{new} - Nu_{old} }{Nu_{new}} \times 100$
459	13.66	–
469	13.73	0.07
479	13.79	0.06
489	13.79	0

**Table 3** Average Nusselt number values for bottom heating wall at different volume fractions ( $\phi$ ) and  $Ra = 10^5$  for different nanoparticles

Volume concentration of nanoparticles ( $\phi$ )	Average Nusselt number $Nu_{avg}$ Ref. Basak and Chamkha [1]			Average Nusselt number $Nu_{avg}$ (present results)		
	Al <sub>2</sub> O <sub>3</sub>	Cu	TiO <sub>2</sub>	Al <sub>2</sub> O <sub>3</sub>	Cu	TiO <sub>2</sub>
0	9.60	9.60	9.60	9.50	9.50	9.50
0.05	–	–	–	10.34	10.41	10.16
0.1	11.30	11.40	10.90	11.20	11.37	10.84

for Cu-water. In this work, we have chosen 479 as the number of mesh elements for generating results.

The validation of fluid flow in natural convection and heat transfer inside a square enclosure from Basak and Chamkha [1] compared with the present investigation results are revealed in Table 3. We can observe average Nusselt numbers for various nanofluids at different nanoparticles and Rayleigh number  $Ra = 10^5$ .

## 4 Results and Discussion

In present investigation work, the fluid flow results in natural convection and heat transfer analysis inside square cavity with various nanofluids are shown. This current investigation with parameters like Rayleigh number in the range of  $10^3 < Ra < 10^5$  and the volume concentrations of nanoparticles in the field of  $0 < \phi < 0.1$ . The results are shown in terms of average Nusselt numbers at different Rayleigh numbers and different volume concentrations of nanoparticles in square cavity.

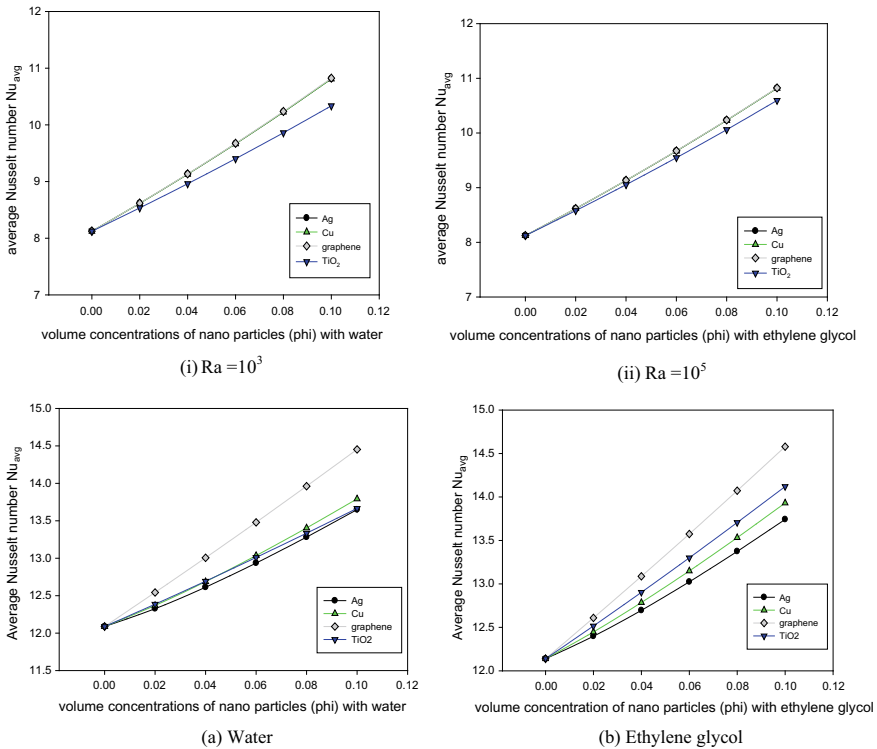
### 4.1 Average Nusselt Number

The Nusselt number (Nu) is the convective proportion to conductive heat movement at a liquid limit. Nusselt number values signify conductive heat transfer within the range of 1–10 of distinguishing laminar stream and higher Nusselt number for convection of turbulent flow in the range of 100–1000.

1.  $Ra = 10^3$
2.  $Ra = 10^5$ .

Average Nusselt numbers of various combinations of nanofluids were plotted into graph at Rayleigh number (Ra)  $10^3$  and  $10^5$  and different nanoparticles volume concentrations  $\phi = 0$ –0.1. With base fluids like water and ethylene glycol, Fig. 2 drawn from average Nusselt numbers of the bottom heating wall inside square cavity with water and ethylene glycol. From Fig. 2, it is observed that the average Nusselt





**Fig. 2** Variation of average Nusselt numbers with different volume concentrations of nanoparticles  $\phi$  at  $Ra = 10^3$  and  $Ra = 10^5$  **a** water, **b** ethylene glycol

number increases with increasing volume concentrations of nanoparticles with base fluids like water and ethylene glycol and at a higher Rayleigh number. Nanoparticles have more thermal conductivity than conventional fluids. Nanoparticles are suspended with base fluids by adding volume concentrations of nanoparticles with convective liquids; the thermal conductivity increases with volume concentrations. Then, results are shown in Nusselt number. In another case, by adding high concentrations of nanoparticles due to particles density, nanoparticles settled at the bottom of the cavity, and it loses stability inflow. Also, there will be a chance of forming layers of nanoparticles at the bottom of the hot in the square cavity, leading to reduced heat transfer between the fluid and cavity. Different nanofluids, graphene and copper combinations, have more heat transfer characteristics in both water and ethylene glycol as base fluids in a square cavity. Enhancement of heat transfer is more with ethylene glycol with nanoparticles than pure water. Heat transfer characteristics are more in graphene when compared with copper. The highest average Nusselt number in a square cavity with base fluid as water is 14.453 for graphene and 13.792 for copper with nanoparticles volume concentration is 0.1, and the Rayleigh number is  $10^5$ . Similarly, the highest average Nusselt number in a square cavity with base fluid

as ethylene glycol is 14.579 for graphene and 14.12 for titanium oxide at Rayleigh number  $10^5$  and nanoparticles volume concentration 0.1. These minor variations in Nusselt numbers between nanoparticles are due to thermophysical properties, like thermal conductivity for graphene is more than other nanoparticles. At higher Rayleigh numbers, the stream is appeared to become two-dimensional with various crest formation and development.

## 5 Conclusions

This investigation of fluid flow in natural convection and heat transfer in a square enclosure is filled inside with various combinations of nanofluids using variable properties. The effect of solid particles volume fraction ( $\phi$ ), Rayleigh number (Ra), Prandtl number (Pr) on the average Nusselt number is investigated. The average Nusselt number increases while increasing solid particles volume fraction. Based on the attained results, mentioned the conclusions.

From the results, by comparing different nanofluids with their average Nusselt numbers with varying fractions of volume, among various nanoparticles, graphene has more heat transfer enhancement in the square cavity at various volume concentrations  $\phi$  and Rayleigh number Ra. The average Nusselt number in a square cavity with graphene–water is 14.453, and graphene–ethylene glycol is 14.579, with a percentage change of 0.8574%.

At lower Rayleigh number as  $Ra = 10^3$ , heat transfer through conduction is a leading factor by increasing in Rayleigh number as  $Ra = 10^5$ , buoyancy induced heat transfer through convection leads viscous force due to changes in density and thermal expansion of the fluid. At higher volume concentration of nanoparticles  $\phi = 0.1$ , changes in thermal conductivity and thermal diffusivity of fluid occur due to nanoparticles interaction in the liquid. The fluid's viscosity is more, and fluid motion is low compared to a lower concentration of nanoparticles  $\phi = 0$ .

## References

1. Basak, T., Chamkha, A.J.: Heat line analysis on natural convection for nanofluids confined within square cavities with various thermal boundary conditions. *Int. J. Heat Mass Transfer* **55**, 5526–5543 (2012)
2. Shantan, D., Arup Kumar, B.: A numerical investigation of natural convection heat transfer of copper-water nanofluids in a recto trapezoidal enclosure heated uniformly from the bottom wall. *Int. Inf. Eng. Technol. Assoc. Math. Model. Eng. Prob.* **6**, 105–114 (2019)
3. Yahiaouia, A., Djazzara, M., Najib, H.: Simulating of heat transfer enhancement via a water-based nanofluid in enclosures with curved side walls. *Int. Commun. Heat Mass Transfer* **100**, 118–132 (2019)
4. Hemmat Esfe, Md., Ali Akbar, A., Yan, W.-M., Ehteram, H., Alireza, A., Afrand, M.: Natural convection in a trapezoidal enclosure filled with carbon nanotube–EG–water nanofluid. *Int. J. Heat Mass Transfer* **92**, 76–82 (2016)

5. Khorasanizadeh, H., Amani, J., Nikfar, M.: Numerical investigation of Cu-water nanofluid natural convection and entropy generation within a cavity with an embedded conductive baffle. *Scientia Iranica Trans. F: Nanotechnol.* **19**, 1996–2003 (2012)
6. Brusly Solomona, A., van Rooyena, J., Renckena, M., Sharifpura, M., Meyera Josua, P.: Experimental study on the influence of the aspect ratio of square cavity on natural convection heat transfer with  $\text{Al}_2\text{O}_3$ /water nanofluids. *Int. Commun. Heat Mass Transfer* **88**, 254–261 (2017)
7. Basak, T., Roy, S., Balakrishnan, A.R.: Effects of thermal boundary conditions on natural convection flows within a square cavity. *Int. J. Heat Mass Transfer* **49**, 4525–4535 (2006)
8. Noor-A-Alam Siddiki, Md.: Free convective heat transfer in a square cavity with heated from below and symmetrically cooling from the sides. *Int. J. Innov. Sci. Eng. Technol.* **2**, 1041–1045 (2015)
9. Bhuiyanaa, A.H., Shahidul Alamb, Md., Alim, M.A.: Natural convection of water-based nanofluids in a square cavity with partially heated of the bottom wall. *Procedia Eng.* **194**, 435–441 (2017)

# Working Fluids for Ejector Refrigeration Systems: A Comprehensive Review



C. Manimaran, A. Sathiamourthy, and A. Selvaraju

## 1 Introduction

The advancement in lifestyle of man in this era has made refrigeration and air conditioning as inseparable technologies that find wider applications ranging from preservation of food, medicine and perishable commodities to human comfort and improvement of productivity along with higher-level processing of materials. It is reported in the literature that the consumption of electricity for refrigeration and air conditioning is close to 40% of total energy produced across the globe [1]. Since electricity is produced from thermal sources like fossil fuels and fissile materials, the technologies that could be operated with thermal energy directly are most welcome in order to avoid dependence on electricity and to conserve available energy sources. The beginning of the last century has witnessed invention of different refrigeration technologies such as vapour compression refrigeration system (VCRS), vapour absorption refrigeration system (VA<sub>b</sub>RS), ejector refrigeration system (ERS) and other conceptual and specialized systems. On the basis of method of actuation these refrigeration systems, VA<sub>b</sub>RS and ERS are known as heat-operated systems as they utilize thermal energy by avoiding any mechanical compressor for actuating the systems. Among the heat-operated refrigeration systems, ejector refrigeration system has become popular as it can produce temperatures as low as 65 °C and thus can harness the thermal energy of low intensity as that of solar radiation falling on the earth's surface. The necessity for utilization of renewable energy sources has attracted the attention of many researchers world-wide. Theoretical and experimental studies have been carried out

---

C. Manimaran (✉) · A. Sathiamourthy · A. Selvaraju  
Department of Mechanical Engineering, Pondicherry Engineering College, Puducherry 605014, India

C. Manimaran  
Department of Mechanical Engineering, IFET College of Engineering, Villupuram, Tamilnadu 605108, India

in order to test and enhance the efficiency of ERS. The schematic diagram of a typical ERS is shown in Fig. 1, whereas Fig. 2 illustrates the geometrical features of an ejector. It is well known that refrigerants are the working fluids that play vital role in bringing down the temperature of confined space like refrigerator and living room or hall. The requirement for realizing temperatures below 0 °C has brought in the use of halocarbon compound refrigerants in refrigeration systems. Many refrigerants belonging to this group have been identified and used in different types of refrigeration systems. The selection of these refrigerants has been done on the basis of thermal, physical, chemical and other material properties that ought to match with

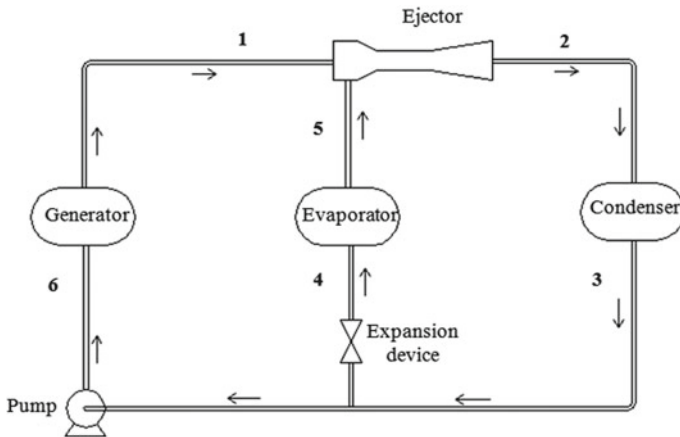


Fig. 1 Schematic diagram of a typical ERS

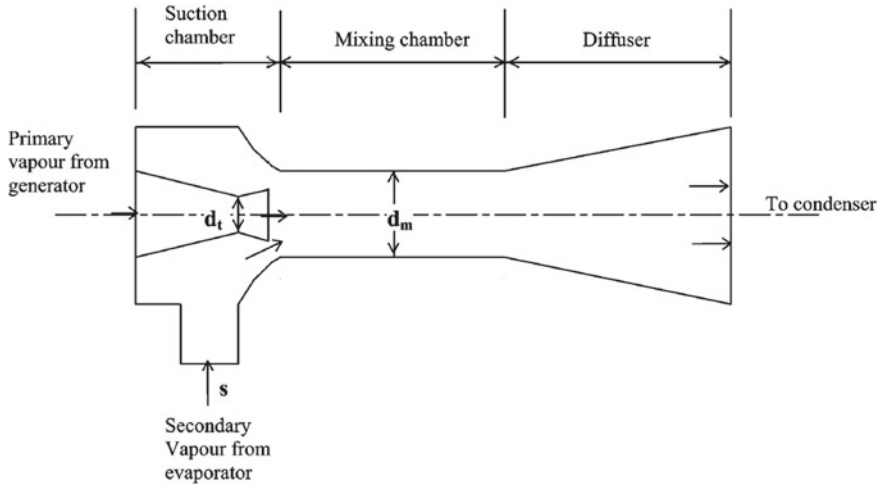


Fig. 2 Geometrical features of an ejector

the applications. This paper discusses on working fluids used in ERS along with theoretical and experimental investigations carried out by various researchers. The comprehensive outcome of research works focussed towards improving the overall performance of ejector refrigeration systems has also been reviewed.

## 2 Refrigerants and Their Utilization in ERS

The first ejector refrigeration system, popularly known as the steam jet refrigeration system, which was used to generate a cooling effect, dated back to the beginning of the twentieth century. The development of this system is generally credited to Maurice LeBlanc and Sir Charles Parsons [2]. The main drawbacks of this system are (1) necessity of a high-temperature source to power it, (2) failure to produce sub-zero temperatures and (3) demand for ejectors with large geometrical dimensions. With the advent of halocarbon compound refrigerants, much research works have been done to overcome the above drawbacks and to make the ejector refrigeration system more viable and suitable for various cooling applications. Some of the important research on ERS and halocarbon compound refrigerants considered for theoretical and experimental investigations are R11 [2–17], R12 [8, 18], R113 [3, 5, 7, 9, 10], R114 [7, 10], R21 [18], R22 [8], R123 [13, 19], R141b [12, 13], R142b [10, 18], R152a [15, 17] R245fa [3, 13–18, 20, 21], R365fa [13], R134a [14, 15, 17], R227ea [26], R245ca [14], R245fa [13, 17, 20] R236ea [14], R236fa [14], R600 [13, 14, 17], R152a [15–18], RC318 [17], R290 [16, 17], R600a [14, 16, 17], R430A [17], R436B [17], R1234ze [17] and R500 [17]. Besides, the aforesaid refrigerants R717 [13, 15, 16, 22], R718 [10, 13] and methanol have also been used for investigations. Every working fluid selected for its use in ERS should have not only suitable thermodynamic properties, but also must congregate the subsequent requirements: no flammability, low toxicity, high chemical and thermal stability, compatibility with materials. But, with the discovery of depletion of ozone layer in the atmosphere, the primary criterion adopted in selecting working fluid is changed so that it must have acceptable ecological properties. Halogenated hydrocarbon compound refrigerants, which dominated refrigeration and air-conditioning fields for more than sixty years due to their favourable thermodynamic and thermo-physical properties, are eclipsed because of their environmental unacceptability. These refrigerants known as chlorofluorocarbons (CFCs) and hydrochlorofluorocarbons (HCFCs) are considered to be the serious cause of weakening of stratospheric ozone and global warming. Hence, the Montreal and subsequent International Protocols have called for a total phasing out of these refrigerants. With the total ban on production and usage of environmentally harmful refrigerants, rigorous research and developmental activities have been taken up to identify substitutes for existing refrigerating and air-conditioning machines. Thrust has also been given to find newer refrigerants and refrigerant mixtures for the future use and to study the performance of systems with new refrigerants.

### 3 Theoretical Investigations

Theoretical investigations have been carried out by several researchers with a single refrigerant or with many refrigerants. The use of single refrigerant has been aimed at identifying and improving geometrical features of the ejector which decides the satisfactory operation and higher performance of the complete ERS. The investigations on the performance of ERS with many refrigerants have been done to identify the competency of selected refrigerants on one another within the selected range of operating conditions. Sun et al. [19] have used R123 as refrigerant and reported that the optimum performance of ERS can be achieved with a coefficient of performance (COP) ranging from 0.19 to 0.29 at evaporator temperature of 5–10 °C, temperature of condenser 30 °C and vapour generator temperature of 80 to 90 °C by varying geometry of the ejector. Huang et al. [12] have analysed the ejector performance at its critical mode at which both primary flow and secondary flow choking occur and predicted accurately the ejector coefficients such as nozzle efficiency, secondary flow efficiency and mixed flow efficiency as 0.95, 0.85 and 0.88, respectively, using one-dimensional theory with R141b as working fluid. Tyagi and Murthy [5] have explored the operation of ERS with R11 and R113 as working fluid, and it is reported that ERS is best suited for the low-intensity heat source that would be wasted and the higher efficiency of ERS could be achieved at lower condenser temperature. Selvaraju et al. [15] have conducted a theoretical study on ERS using R123, R134a, R152a and R717 as refrigerants. They have reported that the entrainment of secondary vapour in the ejector and the overall performance of ERS, that is, COP depends primarily on geometrical dimensions of the ejector and the compression ratio which is defined as the ratio of condenser pressure to evaporator pressure. Selvaraju and Mani [16] have used five refrigerants R134a, R152a, R290, R600a and R717 for their investigation of ERS. They have claimed that maximum performance is obtained when the ejector in ERS operates at its critical mode and R134a performs better as compared to other refrigerants at evaporator temperature of 5 °C when the condenser temperature varies from 25 to 35 °C and generator temperature changes from 65 to 85 °C. Shovon et al. [13] have used six refrigerants, namely R717, R718, R245fa, R123, R141b and R365fa and reported that when the ejector operates at its subcritical mode, the performance of ERS varies in direct proportionality to the generator temperature, and it reaches maximum when the operation of the ejector becomes critical. Among the selected refrigerants, R717 exhibits better performance than other refrigerants. Saleh [14] has studied theoretically the performance of ERS with R134a, R227ea, R245ca, R245fa, R236ea, R236fa, R600 and R600a. He has concluded that the ERS cycle performance is more sensitive to condenser temperature than that of driving and driven vapours. Among the selected refrigerants, R245ca is found to be a best candidate for ERS at the selected operating temperatures, viz., generator temperature ranging from 65 to 110 °C, condenser temperature from 25 to 35 °C and evaporator temperature from –5 to 15 °C. Chen et al. [17] have probed the performance of ERS with different types of working fluids classified as wet (R134a, R152a, R290 and R430A), dry (R245fa, R600, R600a and R1234ze) and isentropic (R436B). It is

reported that superheating of driving vapour always improves ejector performance for all wet, dry and isentropic refrigerants. The cycle performance of ERS is always better with all selected refrigerant when the temperature of condenser temperature is reduced, and the temperature of evaporator is increased. Sun [17] has compared the performance of 11 working fluids, steam, R11, R12, R113, R21, R123, R142b, R134a, R152a, RC318 and R500. He has observed that the performance of ERS is the lowest with steam as working fluid while that of R152a is better among the selected refrigerants.

## 4 Experimental Investigations

Experimental studies have been carried out, in order to determine the real-time efficiency of ERS. These studies have also been focussed on to identify the best geometry of the ejector that would match with the selected working fluid for yielding higher efficiency. Nahdi et al. [3] have conducted experimental analysis using R11 for different compression and motoring ratio. The compression ratio is defined as the ratio between condenser pressure to evaporator pressure, and motoring ratio is defined as the ratio between generator pressure to condenser pressure. It is reported that for compression ratio ranging from 1 to 3.5 and motoring ratio varying from 3 to 8.5 that the ejector performance is decided by geometric parameters of an ejector and ejector geometric ratio (area ratio of the constant mixing area tube to the nozzle's throat). It is observed further that the entrainment of secondary fluid becomes maximum at the optimum value of ejector geometric area ratio. Al Khalidy and Zayonia [9] have used R113 as refrigerant, and their experimental investigation has revealed that the ejector efficiency of 31% has been achieved as maximum when the heat source temperature is varied from 70 °C to 100 °C. Further, the overall performance of ERS is found to influence more by the condenser temperature than generator and evaporator temperatures. Eames et al. [20] have examined the application of R245fa in ERS, and it is concluded from the experimental COP values ranging from 0.25 to 0.7 that ERS with R245fa as working fluid can be actuated efficiently using low-grade heat for air conditioning. Sankarlal and Mani [22] have used R717 as working fluid and reported that the refrigerating capacity of the system increases from 176 to 450 W for the generator temperature range from 62 to 72 °C at a condenser temperature of 30 °C and evaporator temperature of 5 °C. They have also presented that the entrainment ratio which is defined as the ratio of mass of driven vapour to that of driving vapour and COP of ERS increase as the ejector area ratio and expansion ratio increases (ratio of generator pressure to evaporator pressure) but decrease with increase in compression ratio. Chen et al. [10] have assessed the performance of ERS using R113, R114, R142b and R718. They have claimed that R113 as dry fluid exhibits best performance with the highest COP of 0.55 while the wet fluid R142b yields the lowest COP of 0.22 among the four refrigerants. Murthy et al. [6] have probed experimentally the geometrical features of an ejector in ERS



using R11, and it is revealed from testing eight primary nozzle-mixing tube combinations of different geometrical dimensions that the ejector with larger geometric ratio provides lower evaporator temperature with the highest COP of 0.33. Hamzaoui et al. [21] have studied the effect of choking in ejectors using R245fa. It is revealed that the entrainment ratio along with COP decreases as the evaporator temperature at single choking mode increases (primary vapour only), whereas increase in entrainment ratio and COP is observed with increase in evaporator pressure at double choking mode. Paliwoda [4] has done experimental investigation using R11, and it is concluded that ERS is best suited for higher evaporating temperature such as air conditioning when sufficient availability of condenser cooling water availability and ready industrial waste heat source availability.

## 5 Concise Discussion on Investigations

It is understood from this reviews that pressure and temperature along with specific volume of a working fluids are primary properties while enthalpy at salient points becomes derived properties from the thermodynamic point of view. Range of temperature or pressure in generator is so chosen that it can be attained from available solar heat source or by utilizing industrial waste heat from any process. The ambient air whose temperature varies with season in a particular locality acts as an ultimate heat sink and thus dictates the range of temperature to be considered for both theoretical and experimental investigations. The range of pressure or temperature relating to evaporator is decided on the basis of the lowest temperature of cooling to be achieved in a particular application. Investigators have used these thermodynamic properties for assessing the performance of ejector as well as ERS. It can be noted in Fig. 2 that ejector being a main part in ERS consists of sub-components (nozzle, suction chamber mixing chamber and diffuser) of variable cross-section except mixing chamber. Thus, the geometry of ejector decides the amount of secondary vapour that could be entrained from the evaporator with the help of primary vapour issuing from the nozzle. The maximum entrainment could be achieved with an ejector with optimum geometrical dimensions. However, geometric ratio of an ejector plays a key role under critical mode of operation with triple choking, such as choking in the nozzle, suction chamber and in the mixing chamber.

## 6 Conclusions

The satisfactory operation of ERS depends on thermo-physical and thermodynamic properties of working fluids selected in accordance with the application such as freezing, cooling and air conditioning. The thermodynamic properties help to determine the performance of ERS, whereas the thermo-physical properties augment the design and development of the ejector, the heart of ERS. It is understood from this

review that the geometrical features and dimensions of an ejector are decided by the nature of selected refrigerant and its properties. Further, the critical mode of operation of an ejector becomes different when different working fluids are used.

## References

1. Jadhav, N.Y.: *Green and Smart Building—Advanced Technology Options*. Springer, Singapore (2016)
2. Gosney, W.B.: *Principles of Refrigeration*. Cambridge University Press, Cambridge (1982)
3. Nahdi, E., Champoussin, J.C., Hostache, G., Cheron, J.: Optimal geometric parameters of a cooling ejector-compressor. *Int. J. Refrig.* **16**, 67–72 (1993)
4. Paliwoda, A.: Experimental study on low grade heat and solar energy operated halocarbon vapour jet refrigeration systems. *Tropical Studies, IIR Bull* (1968)
5. Tyagi, K.P., Murty, K.N.: Ejector-compression systems for cooling: utilising low-grade waste heat. *Heat recovery systems* **5**, 545–550 (1985)
6. Srinivasa, S., Balasubramanian, R., Krishna Murthy, M.V.: Experiments on vapour jet refrigeration system suitable for solar energy applications. *Renew. Energy* **1**, 757–768 (1991)
7. Hamner, R.M.: An alternative source of cooling: the ejector-compression heat pump. *ASHRAE J.* **22**, 62–66 (1980)
8. Mizrahi, J., Solomiansky, M., Zisner, T., Resnik, W.: Ejector refrigeration from low temperature energy sources, *Bull. Res. Council. Isreal* **60**, 1–8 (1957)
9. Al Khalidy, N., Zayonia, A.: Design and experimental investigation of an ejector in an air-conditioning and refrigeration system. *ASHRAE Trans.* **101**, 383–391 (1995)
10. Chen, S.L., Yen, J.Y., Huang, M.C.: An experimental investigation of ejector performance based upon different refrigerants. *ASHRAE Trans. Res.* **4193**, 153–160 (1998)
11. Huang, B.J., Chang, J.M.: Empirical correlation for ejector design. *Int. J. Refrig.* **22**, 379–388 (1999)
12. Huang, B.J., Chang, J.M., Wang, C.P., Petrenko, V.A.: A 1-D analysis of ejector performance'. *Int. J. Refrig.* **22**, 354–364 (1999)
13. Shovon, M.K.B., Senthil, R., Suryan, A., Kim, T.H., Kim, H.D.: Performance of ejector refrigeration cycle based on solar energy working with various refrigerants. *J. Thermal Anal. Calorimetry* **141**, 301–312 (2020)
14. Saleh, B.: Performance analysis and working fluid selection for ejector refrigeration cycle. *Appl. Therm. Eng.* **107**, 114–124 (2016)
15. Selvaraju, K., Mani, A., Groll, M.: Performance comparison of vapour jet refrigeration system with environmentally friendly working fluids. *App. Thermal Eng.* **21**, 585–595 (2001)
16. Selvaraju, A., Mani, A.: Analysis of an ejector with environment friendly refrigerants. *Appl. Therm. Eng.* **24**, 827–838 (2004)
17. Chen, J., Havtun, H., Palm, B.: Screening of working fluids for the ejector refrigeration system. *Int. J. Refrig* **47**, 1–14 (2014)
18. Sun, D.-W.: Comparative study of the performance of an ejector refrigeration cycle operating with various refrigerants. *Energy Convers. Manage.* **40**, 873–884 (1999)
19. Sun, D.-W., Eames I.W.: Performance characteristics of HCFC-123 ejector refrigeration cycle'. *Int. J. Energy Res.* **20**, 871–885 (1996)
20. Eames, I.W., Ablwaifa, A.E., Petrenko, V.: Results of an experimental study of an advanced jet-pump refrigerator operating with R245fa. *Appl. Therm. Eng.* **27**, 2833–2840 (2007)
21. Hamzaoui, M., Nesreddine, H., Aidoun, Z., Balistrout, M.: Experimental study of a low grade heat driven ejector cooling system using the working fluid R245fa. *Int. J. Refrig.* **86**, 388–400 (2018)

22. Sankarlal, T., Mani, A.: Experimental investigations on ejector refrigeration system with ammonia. *Renew. Energy* **32**, 1403–1413 (2007)
23. Besagni, G.: Ejectors on the cutting edge: The past, the present and the perspective. *Energy* **170**, 998–1003 (2019)

# Experimental Study on Heat and Mass Exchanger of a Dew Point Indirect Evaporative Cooler



C. Deepak , Rudra Naik, and H. K. Prashanth 

## 1 Introduction

Standards of living are drastically increasing as human beings upgrading their life. As per energy statistics-2015 issued by the Government of India, out of total electricity consumption in the year 2013–14, the industrial sector consumed 43.83%, followed by the domestic sector with consumption of 22.46%. It is also reported that electricity consumption by the industrial and commercial sectors has increased at a higher pace with compound annual growth rate of 10.97% and 8.82%, respectively [1]. International Energy Outlook (IEO) released report on energy expenditure of various countries recently and also said that due to usage of traditional air conditioning systems the global temperature may further increase to 3–4% more annually and energy demand of earth increases to 30–40% by 2030 [2]. Major conventionally available air conditioners are vapor compression systems, and they use cryogenic or chemical refrigerants which boils at very low temperatures for producing cold surroundings. Even though these air conditioners satisfy the requirements, they consume more power and liberate very environmentally hazardous greenhouse gasses like CFC, HCFC, and HFCs.

One of the workable solution for the aforementioned problems will be evaporative cooling, which uses water to cool air. In the direct evaporative cooling (DEC), process water is atomized by absorbing the latent heat of evaporation, but the major problem with this system is that moisture content of air is increased. In Mina Valley, Saudi Arabia, nearly 48,000 DEC units were installed in public places [3]. The major applications of air conditioning systems like electronic industries, process plants, cold rooms, data centers, etc., do not need moist air for their efficient working. To overcome the moisture content problem in DEC, indirect evaporative cooling (IEC) techniques were developed, in which supply air will not come in contact with water;

---

C. Deepak (✉) · R. Naik · H. K. Prashanth  
B.M.S. College of Engineering, Bengaluru, Karnataka 560019, India

hence, moisture will not be present in it. However, the temperature at the outlet will be less than that of DEC. A theoretical model was developed by Baakeem et al. [4] on direct evaporative coolers, and they have taken relative humidity and temperature inputs on hourly average for summer weather conditions in July at Riyadh and found that wet bulb effectiveness is 0.7 to 0.8. Simulation study conducted by Singh and Das [5], using energy plus software on dedicated outdoor air system, with integrated evaporative cooling arrangement showed only 2.62% of electrical energy savings on annual basis. In a regenerative evaporative cooler study by Kim [6], numerical model of heat and moisture transfer was developed and validated with available experimental data. It was found in their study that dew point effectiveness is increased due to increase in inlet temperature. Experimental study on modified evaporative cooling (MEC) system was conducted at Ahmedabad, India, for weather conditions for the entire year. Maximum temperature drop recorded during their study is 17.85 °C. They have used aluminum and kraft paper for fabrication of evaporative cooler [7].

To achieve temperature below wet bulb, two-stage evaporative coolers are developed. They had combination of direct and indirect systems. A performance test of a two-stage evaporative cooler was conducted, using a mathematical model developed by Gilani et al. [8]. In their study, it was found that comfort conditions can be achieved easily if the outdoor conditions are 34–54 °C and 10–60% RH. It is also said that if the cooling load increases, the two-stage evaporative cooling system becomes expensive. The invention of the M-cycle evaporative cooler made by Maisotsenko [9] solves the problem of cooling air below the wet bulb. One more advantage of this cycle is that cooling is achieved without the addition of moisture to supply air.

Many researchers are continuously experimenting different designs of M-cycle HMX. Studies have been conducted for controlled water and air flow parameters and observed improved performance of this cooler up to a maximum of 114%, and wet bulb temperature effectiveness with 52.5 COP is obtained during experimental testing [10]. Under different atmospheric conditions, about 58%–84% dew point cooling effectiveness can be gained [11] which is a very good result since it can easily replace the conventional air conditioners. In experimental investigations carried so far, M-cycle IEC system gives 10–30% higher wet bulb effectiveness when compared to normal IEC [12].

For the improvement in performance of dew point evaporative cooling system, many researchers carrying out numerical and experimental studies similar to literature discussed above. To the authors knowledge, there are limited experimental studies that have been carried out for different climatic regions on dew point IEC system. Experimental study presented in this paper is on mixed-flow dew point IEC, which is carried out to overcome the short fall in experimental investigations.

## 2 Dew Point IEC Test Setup

The cooling system considered here is M-cycle IEC having a mixed-flow configuration heat mass exchanger. The schematic of a dew point evaporative cooler is shown in Fig. 1.

### 2.1 Elucidation of the Cooling System

M-cycle heat and mass exchanger is a core of cooling system; it is fabricated by using aluminum sheets for wet and dry channels. Cellulose-rich cotton fabric is used as water-absorbing material to hold water in the wet channel. In wet channel, cotton fabric layers are stacked one above the other for a thickness of 2 mm, this stacking arrangement helps in holding water for longer duration, and due to this, more time is given for water evaporation. Figure 2 shows the front view of one set of dry and wet channel.

There are 35 sets of dry and wet channel combination present in heat mass exchanger (HMX). The specifications of the system are given in Table 1. The channel gap of wet and dry channels is maintained uniform using acrylic strips, which are cut to accurate dimensions using water jet cutting machine. The channel gap for dry channel is 5 mm, and for wet channel, it is 7 mm. The bypass holes of 7 mm diameter are made on the partition plate which is separating dry and wet channels. For each set, there are five bypass holes on top and five holes on bottom, and these holes help in bypassing air from dry channel to wet channel.

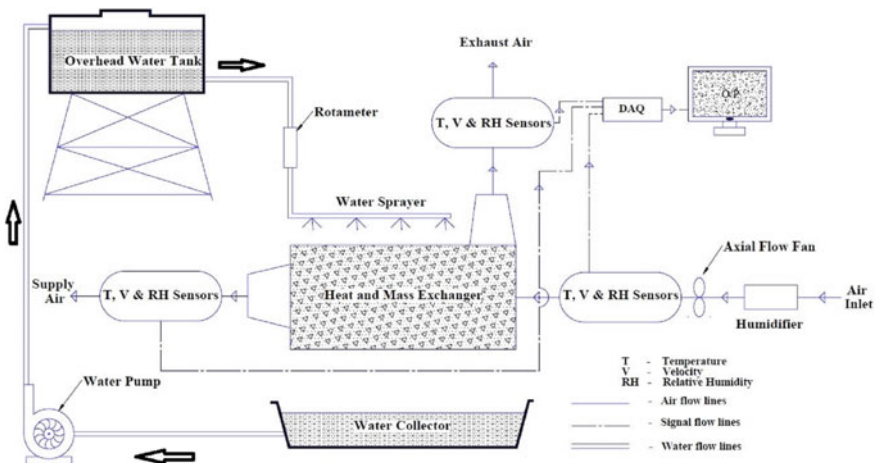
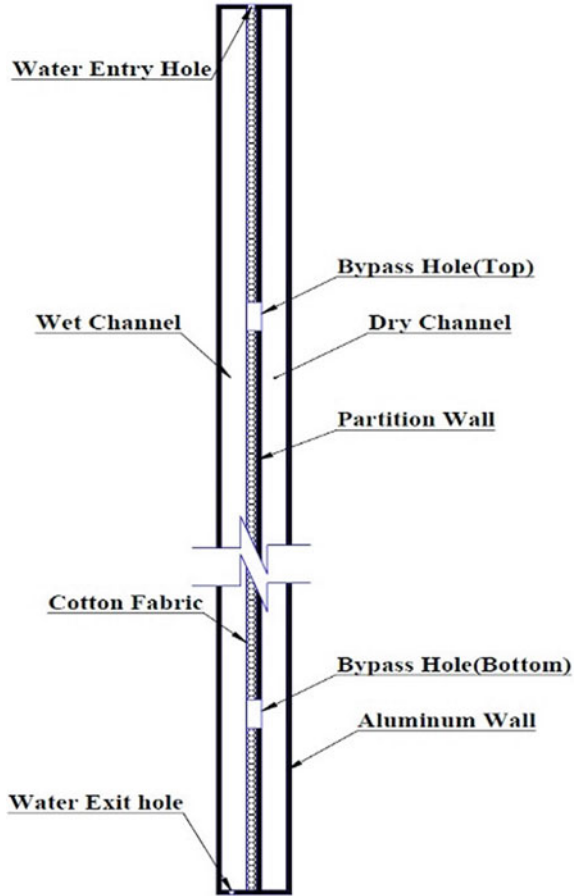


Fig. 1 Schematic of dew point evaporative cooler setup

**Fig. 2** Front view of one set of dry and wet channel



**Table 1** Specifications of the system

Parameter	Symbol	Value (in mm)
Width of dry channel	$W_d$	5.0
Width of wet channel	$W_w$	7.0
Thickness of cotton fabric layer	$t_{cotton}$	2.0
Thickness of aluminum plate	$t_{plate}$	1.0
Length of channel	$L$	800
Height of channel	$H$	400
Width of HMX	$W$	510

## 2.2 Experimental Procedure

The inlet air to heat mass exchanger of dew point IEC is taken from atmosphere using a variable-speed axial-flow ID Fan. The relative humidity of incoming air is maintained constant using a humidifier. It is operated using a set point humidity sensor and a humidity controller. Inlet air velocity is controlled manually using a regulator. Acrylic duct is placed at entry, exit, and bypass of HMX to evenly distribute air. Water flow rate is controlled using an acrylic body rotameter. Temperature, velocity, and %RH of air are measured at inlet, outlet, and bypass of HMX. The details of measuring instruments are provided in Table 2.

Air enters dry channel with a preset velocity and temperature. A portion of it enters wet channel through bypass holes. The air which is bypassed to the wet channel will enable evaporation of water, thereby latent heat of evaporation is taken from the water. Due to this, water gets cooled and the partition sheet which is in contact will also get cooled. The air flowing in dry channel comes in contact with this cold partition wall, and cooling of air is achieved. As the air in dry channel did not come in contact with water during its passage through HMX, the humidity will remain same as that of inlet.

## 3 Results and Discussions

Experimental investigation on dew point IEC has been carried out to study the effect of inlet air velocity and temperature on performance parameters such as cooling capacity, COP, and effectiveness. Study is carried out at different inlet air velocities and temperatures by maintaining constant water flow rate and percentage of relative humidity at inlet.

**Table 2** Details of measuring instruments

Physical parameter measured	Type of instrument	Range	Accuracy
DBT of air and water	K-type thermocouple	-270 to 1260 °C	±0.5 °C
Relative humidity of air	Capacitive RH sensor	0-100% RH	±1% RH
Velocity of air	Vane type anemometer	0.1-30 m/s	±1% speed range
Water flow rate	Rotameter	0-50 LPM	±1 LPM
Data acquisition	Data logger customized by MICROSENSE		



### 3.1 Performance Parameters

Performance parameters considered in this study are cooling capacity (CC), coefficient of performance (COP), wet-bulb effectiveness (WBE), and dew point effectiveness (DPE), which are defined as:

$$\text{Cooling Capacity (CC)} = m_2 \times C_p \times (T_{db1} - T_{db2}) \text{ kW} \tag{1}$$

$$\text{Total Electrical Power (P}_{ele}) = P_F + P_P \text{ kW} \tag{2}$$

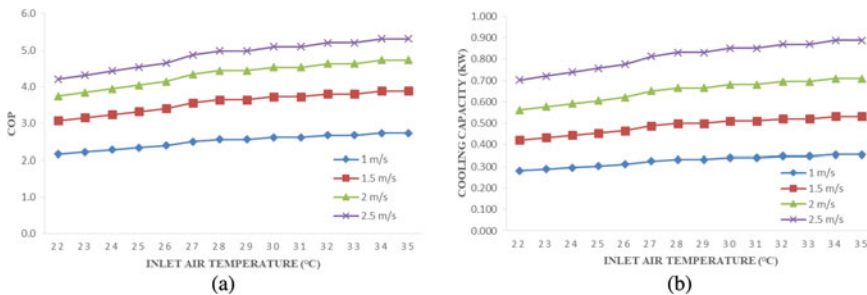
$$\text{Coefficient of Performance (COP)} = \frac{\text{Cooling Capacity}}{\text{Total Electrical Power}} = \frac{CC}{P_{ele}} \tag{3}$$

$$\text{Wet Bulb Effectiveness}(\epsilon_{wb}) = \frac{(T_{db1} - T_{db2})}{(T_{db1} - T_{wb1})} \tag{4}$$

$$\text{Dew Point Effectiveness}(\epsilon_{dp}) = \frac{(T_{db1} - T_{db2})}{(T_{db1} - T_{dp1})} \tag{5}$$

### 3.2 Effect of Inlet Air DBT on Cooling Capacity (CC)

The capability of cooling system to remove heat is described well by using term called cooling capacity (CC). Figure 3b is a graph showing effect on CC of the system with respect to inlet air DBT and its velocity. At 27 °C CC of the system is 0.325, 0.488, 0.651, and 0.813 kW for 1, 1.5, 2, and 2.5 m per second of inlet air velocities. Further at 34°C, CC varies as 0.355, 0.532, 0.710, and 0.887 kW, respectively. It is observed that higher CC of the indirect evaporative dew point cooler is obtained at 2.5 m/s and



**Fig. 3** **a** Effect of inlet air DBT and its velocity on COP, **b** effect of inlet air DBT on CC

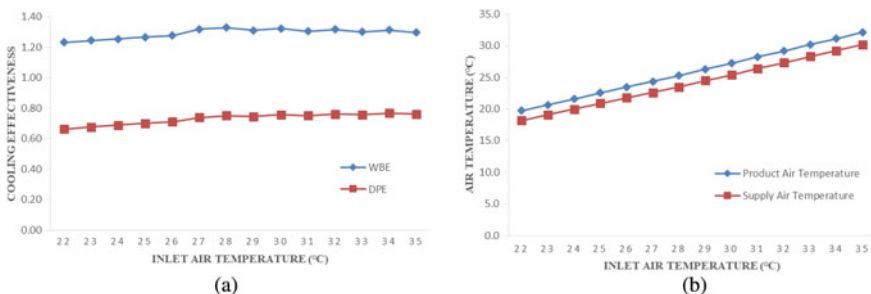
34 °C Concisely, it is clear from these values that increasing inlet air temperature and its velocity increases the CC of the system.

### 3.3 Effect of Inlet Air DBT and Its Velocity on COP

As per standard results given by various authors and researchers publications [2, 13, 14], it is shown that coefficient of performance is one of most important parameter. COP is considered in designing of any air conditioning or refrigeration system. Figure 3a shows variations in COP with respect to inlet air DBT at different velocities of 1, 1.5, 2, and 2.5 m per second. From the plot, it can be observed that, at 28°C COP is 2.6 and at 35 °C COP is 2.7 for 1 m/s air velocity. At 1.5, 2, and 2.5 m/s, COP of the system is 3.9, 4.7, and 5.3 at 35 °C, respectively. Thus, we can say as inlet air temperature increases along with incoming air velocity, the COP of dew point IEC system increases.

### 3.4 Variations in WBE and DPE with Respect to Inlet Air DBT

One of the main objective of indirect evaporative cooling system is to obtain better cooling effectiveness. Figure 4a shows variations in dew point and wet bulb effectiveness of the system against the inlet air temperature. For the temperature range of 22–35 °C, wet bulb effectiveness (WBE) is in the range of 1.22–1.36, whereas dew point effectiveness (DPE) values are 0.66–0.79 for same temperature range. It is observed that WBE and DPE both increase with increases in inlet air temperature. The WBE is more than one for all temperatures, and therefore, we can say that dew point IEC can reduce incoming air temperature below its WBT.



**Fig. 4** **a** Variations in WBE and DPE with respect to inlet air DBT, **b** variations in product air and supply air temperature with respect to inlet air DBT

### 3.5 Variations in Temperature of Product and Supply Air with Respect to Inlet Air DBT

Even though we are only concerned about supply air temperature in dew point evaporative cooler, it is very important to look at the product air temperature also, because it has effect on supply air temperature. More the heat is taken from system, then the temperature of air supplied will be less. Thus, if product air has higher temperature, then it is obvious that it also results in lower supply air temperature. Figure 4b shows the variations of product and supply air temperature with respect to inlet air DBT. For 25, 29, and 35°C product and supply air temperatures are 22.5 °C and 20.9 °C, 26.3 °C and 24.5 °C, and 32.1 °C and 30.2 °C, respectively. From these three cases, it can be concluded that increases in inlet air temperature also increases the product and supply air temperature. To obtain lower supply air temperature, inlet air temperature must be less.

## 4 Conclusions

In this study, experimental investigation on mixed-flow dew point IEC is carried out. Outcome of this study is that the WBE and DPE of the system reach to a maximum value of 1.36 and 0.79, respectively. Conclusion from this study is that the supply air temperature goes below WBT and near to DPT of inlet air without inclusion of moisture. Maximum COP achieved in this study is 5.3 for 35°C with inlet air velocity of 2.5 m per second. COP increases as incoming air velocity and DBT increases. COP and cooling capacity follow the same trend with respect to inlet air conditions. Optimization of HMX can be done by selecting proper flow configurations and appropriate material for water adsorption. Further experimental studies on dew point IEC required at different climatic zones of India.

**Acknowledgements** Financial support to carry out this work is provided by, Science and Engineering Research Board (SERB), DST's statutory body, Government of India.

## References

1. Office, C.S.: Energy Statistics. [http://mospi.nic.in/sites/default/files/publication\\_reports/Energy\\_stats\\_2015\\_26mar15.pdf](http://mospi.nic.in/sites/default/files/publication_reports/Energy_stats_2015_26mar15.pdf) (2015)
2. Sadighi Dizaji, H., Hu, E.J., Chen, L.: A comprehensive review of the Maisotsenko-cycle based air conditioning systems. *Energy* **156**, 725–749 (2018)
3. Alharbi, A., Boukhanouf, R., Habeebullah, T., Ibrahim H.: Thermal performance and environmental assessment of evaporative cooling systems: case of Mina Valley, Saudi Arabia. *Int. J. Environ. Ecol. Eng.* 546–550 (2014)

4. Baakeem, S.S., Orfi, J., Bessadok-Jemai, A.: Thermodynamic and economic analysis of the performance of a direct evaporative cooler working under extreme summer weather conditions. *J. Mech. Sci. Technol.* **32**, 1815–1825 (2018)
5. Singh, G., Das, R.: Energy saving potential of an air-conditioning system with desiccant and solar assisted ventilation. In: Biswal, B.B., Sarkar, B.K., Mahanta, P. (eds.) *Advances in Mechanical Engineering*, pp. 1351–1359. Springer, Singapore (2020)
6. Kim, N.-H.: Heat and moisture transfer in a counter flow regenerative evaporative cooler made of plastic film/paper composite. *J. Mech. Sci. Technol.* **30**, 1449–1457 (2016)
7. Lata, M., Gupta, D.K.: Experimental investigation and simulation of modified evaporative cooling system. In: Kalamkar, V.R., Monkova, K. (eds.) *Advances in Mechanical Engineering*, pp. 441–448. Springer, Singapore (2021)
8. Gilani, N., Poshtiri, A.H.: Thermal design of two-stage evaporative cooler based on thermal comfort criterion. *Heat Mass Transf.* **53**, 1355–1374 (2017)
9. United States Patent (2005)
10. Xu, P., Ma, X., Zhao, X., Fancey, K.: Experimental investigation of a super performance dew point air cooler. *Appl. Energy* **203**, 761–777 (2017)
11. Riangvilaikul, B., Kumar, S.: An experimental study of a novel dew point evaporative cooling system. *Energy Build.* **42**, 637–644 (2010)
12. Riangvilaikul, B., Kumar, S.: Numerical study of a novel dew point evaporative cooling system. *Energy Build.* **42**, 2241–2250 (2010)
13. Zhan, C., et al.: Comparative study of the performance of the M-Cycle counter-flow and cross-flow heat exchangers for indirect evaporative cooling—Paving the path toward sustainable cooling of buildings. *Energy* **36**, 6790–6805 (2011)
14. Wang, L., Zhan, C., Zhang, J., Zhao, X.: Optimization of the counter-flow heat and mass exchanger for M-cycle indirect evaporative cooling assisted with entropy analysis. *Energy* **171**, 1206–1216 (2019)

# Effect of Nozzle Inclination Angle on the Performance of Hybrid Jet Impingement Microchannel Heat Sink



Jyoti Pandey, Mohd. Zahid Ansari, and Afzal Husain

## 1 Introduction

Enormous heat dissipation occurs in high-power consuming compact electronic devices due to continuous loading of large number of small-sized components with additional features. This can enhance heat load over appliances and lead the temperature of the device above critical value. Previously, heat sink with increased surface area and liquid cooling were best known heat transfer techniques for the thermal management of the electronic devices. Based on the traditional cooling solutions, appliances are employed with fins integrated cold plates and microchannels to transfer heat from the hot surface of the device to surrounding. But, as the power density level is escalating every year and exceeded even  $100 \text{ W/cm}^2$ , conventional conduction and free or forced convection-based cooling techniques become inadequate in maintaining device temperature within limits. Perceiving the severity of the problem, several other passive and active schemes like flow obstruction, rough surface, secondary flows, fluid additives, spray cooling, external excitation, etc., were incorporated [1–5]. These techniques are capable of increasing surface area-to-volume ratio, enhancing conduction heat transfer, reducing boundary layer thickness and intensifying fluid mixing by inducing chaotic advection, local turbulence, vortices, flow recirculation, etc., that assist to reduce thermal resistance. Thus, by exploiting the benefits of various mentioned techniques wisely, heat exchange can be augmented at low power loss.

---

J. Pandey (✉) · Mohd. Z. Ansari  
PDPM-Indian Institute of Information Technology Design and Manufacturing, Airport Road,  
Jabalpur, MP 482005, India  
e-mail: [1813602@iiitdmj.ac.in](mailto:1813602@iiitdmj.ac.in)

A. Husain  
Department of Mechanical and Industrial Engineering, Sultan Qaboos University, Muscat, Oman

One of these cooling techniques is jet impingement that provides a proficient solution to enhance heat transfer rates by using even the small amount of coolant in an efficient manner [6, 7]. In impingement cooling, jet of a coolant strikes normal to the surface through nozzle and thus breaks the stagnant boundary layer developed due to the parallel laminar flow of coolant. Also, turbulence induces in the surrounding fluid near the stagnation point in the form of local vortices that assist in enhancing heat transportation. Several studies were conducted to explore the hydrothermal characteristic in case of jet impingement technique using single or multiple jet nozzles delivering coolant over a surface in a confined or unconfined space [8]. It was observed that high heat transfer coefficient as well as more uniform temperature distribution can be obtained by using jet impingement method reasonably. However, hydrothermal performance of jet impingement depends on several factors such as nozzle configuration and orientation, flow rate, nozzle to target distance, nozzle-to-nozzle distance, etc. [9]. Choo et al. [10] done experimental investigation for single slot air jet impingement obliquely ( $0^\circ < \theta < 40^\circ$ ) on the small nozzle to plate spacing ( $H/d_h \leq 1$ ) and observed that Nu increased with increasing the nozzle angle for  $H/d_h \leq 1$ .

Seyedein et al. [11] experimentally analyzed the multiple air jet impingement from the slots on an inclined confined surface. As the maximum Nusselt number decreases along the downstream direction, therefore, to minimize deviation, nozzle plate is inclined such that flow accelerates along the downstream direction. The phenomena that limiting the thermal performance of impinging jet in case of confined surface is flow entrainment where heated up fluid mixes and thus preheats the freshly coming fluid. Therefore, to manage the spent fluid in the system, concept of effusion holes evolved. Rhee et al. [12] experimentally conducted the study for array of air impinging jets with effusion hole to eject spent air. It was observed that for small gap distance, heat transfer augmented by approximately 60–20% due to decreased cross flow as well as heat transfer coefficient was distributed more uniformly.

Husain et al. [13] done numerical investigation for hybrid heat sink design to exploit the combined benefit of flow obstructing pillars, jet impingement technique, and liquid cooling microchannel heat sink. Local vortical turbulence was induced that disturbed the stagnant boundary layer and enhanced flow mixing. Pillars separate and recombine the flow to create chaos in the laminar flow layers that supports to improve the heat transfer. In the present analysis, comparative study is performed numerically for jet of deionized (DI) water as coolant striking through nozzle at different inclination angle over the bottom surface of microchannel heat sink incorporated with circular pillars. Heat transfer and flow characteristics are computed for different Reynolds number and varying nozzle configuration using computational fluid dynamics (CFD)-based commercial software ANSYS CFX.

## 2 Numerical Model

Analysis of jet impingement integrated and micropillar infused microchannel heat sink having 24 mm length is done. A channel of  $0.4 \times 0.5 \text{ mm}^2$  cross-sectional area is designed and meshed as a computational domain in the Ansys design modeler (Fig. 1) to save the computation time. The heat sink design is taken from the work of Hussain et al. [13] and analyzed for varying nozzle orientation. Hybrid heat sink consists of jet nozzles distributed at equal distance along the length, and in between every two nozzles, a pillar is mounted inside the channel.

Channels are made on the copper block while keeping substrate thickness to 0.2 mm at the bottom and 0.1 mm on the side walls. Nozzle diameter ( $D_J$ ) as well as pillar diameter ( $D_P$ ) is fixed as 0.2 mm in a 0.5 mm ( $W_c$ ) wide channel. Channel is made 0.4 mm ( $H_c$ ) deep and covered by 0.4 mm thick nozzle/cover plate at the top. Water as fluid is delivered from the nozzles to strike normally on the microchannel bottom surface at multiple points simultaneously. Coolant is directed to travel along the channel length in both the directions. Nozzles are designed on the cover plate at different inclination angle from  $30^\circ$  to  $90^\circ$  to investigate the effect of nozzle orientation on the hybrid heat sink performance. Mesh refinement test is performed to found number of mesh elements in a given range where characteristic parameters remains unvarying with element size. Characteristic parameters were observed at

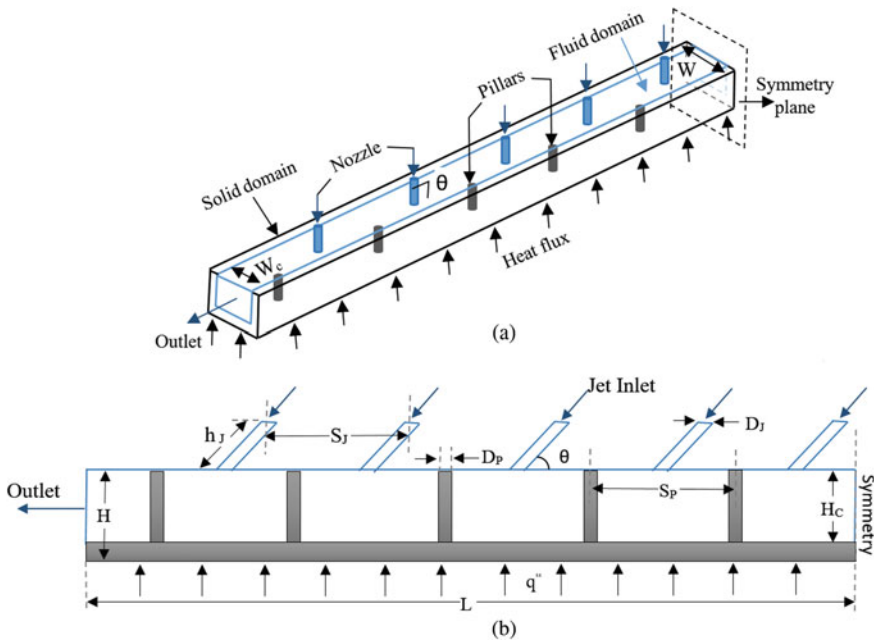


Fig. 1 Schematic of hybrid microchannel hat sink a isometric view, b side view

node sizes in between 0.1 and 1.5 million and found 1.2 million nodes as optimum for best results in comparatively less computation time.

Heat is conducted through the heat sink substrate layer in the bottom and then carried away by the fluid flowing in the microchannel. Physical model is simulated in the CFD based commercial software Ansys CFX considering several assumptions such as (1) steady and incompressible flow; (2) three-dimensional and laminar flow; (3) neglecting radiation, gravity, and viscous dissipation effect; (4) constant substrate material properties; (5) no slip condition at the wall. Fluid properties are considered to be varying with temperature to obtain more accurate results [13]. To compute the flow and thermal behavior, below-mentioned fundamental governing equations are to be solved numerically in the CFX solver.

Fluid:

Continuity equation:

$$\nabla \cdot (\rho V) = 0 \tag{1}$$

Momentum equation

$$V \cdot \nabla (\rho V) = -\nabla p + \nabla \cdot (\mu \nabla V) \tag{2}$$

Energy equation

$$V \cdot \nabla (\rho CT) = \nabla \cdot (k \nabla T) \tag{3}$$

Solid:

Energy equation

$$\nabla \cdot (k_{\text{subs}} \nabla T_{\text{subs}}) = 0 \tag{4}$$

Only half of the channel is considered for the computation to save time and cost. Atmospheric outlet condition is adopted at one end of the domain and symmetry wall condition fixed at the other end. Fluid is delivered from the nozzles at the top at constant mass flow rate and temperature. Bottom wall is supplied with constant heat flux conditions while other walls are assumed adiabatic. Thermal characteristic parameters such as heat transfer coefficient and maximum temperature rise are compared for flow and geometric variables. Heat transfer coefficient is the indicator of amount of convection heat exchange. It is defined as

$$h = \frac{q''}{T_{\text{avg,w}} - T_{\text{avg,f}}}$$

$T_{\text{avg,w}}$  and  $T_{\text{avg,f}}$  are the average temperature at the bottom surface and average temperature in the fluid domain, respectively. Thermal resistance,  $R_{\text{th}}$  is the hindrance offered by the system against heat exchange which is expressed as.



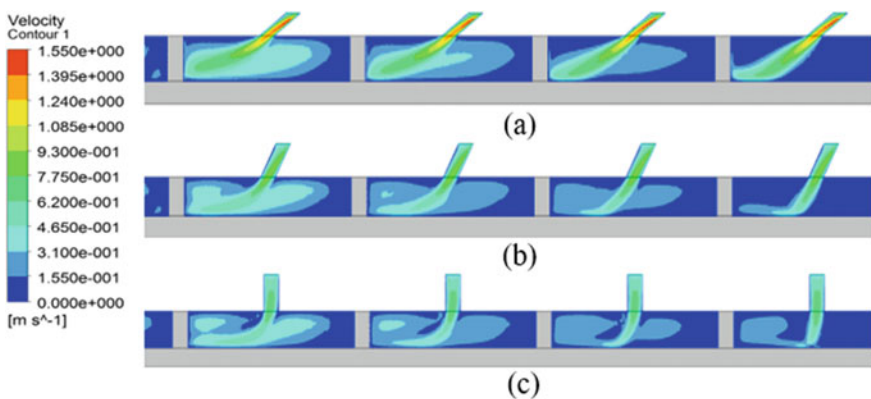
$$R_{th} = \frac{\Delta T_{max}}{q'' A}$$

Maximum temperature rise is the difference in maximum temperature obtained at the bottom surface and the temperature of the fluid at inlet ( $\Delta T_{max} = T_{w,max} - T_{in}$ ). Pressure drop along the channel is an important parameter to be analyzed to manage pumping power requirement which is defined as the difference in the pressure at the inlet and the outlet ( $\Delta P = P_{inlet} - P_{outlet}$ ).

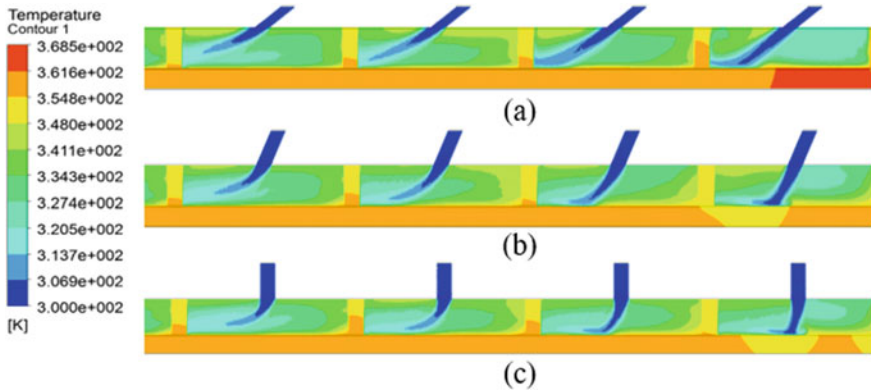
### 3 Results and Discussion

This study focused specifically on the effect of nozzle jet inclination angle, varying in between 30° and 90°, on the performance of heat sink. Hydrothermal characteristic parameters such as maximum temperature at bottom wall ( $T_{w,max}$ ), average heat transfer coefficient ( $h$ ), pressure drop ( $\Delta P$ ), and thermal resistance ( $R_{th}$ ) were observed. Numerical analysis was done considering variation in flow variable that is Reynolds number ( $Re$ ) and variation in geometric variable that is nozzle angle ( $\theta$ ).

Figure 2 showed the contour of flow velocity distribution in the mid-plane of the channel for 30°, 60°, and 90° inclined nozzle. Among different impingement angle, highest velocity is found for the 30° nozzle angle that is 1.5 m/s. A local turbulence loop can be seen around the jet that grows as the flow moves downstream. For the jet nozzles, impact of the jet impingement over the heat sink bottom surface was reduced along the flow direction. Impact of the impinging jet was also found low for small impingement angle. Similarly, Fig. 3 illustrated the temperature contour for 30°, 60°, and 90° nozzle angles at the same Reynolds number. Temperature in the channel is highest for the 30° nozzle angle near the symmetry wall that is 368.5 °C.



**Fig. 2** Contour of flow velocity at the mid-plane along the channel length for **a** 30°, **b** 60°, and **c** 90° nozzle angle

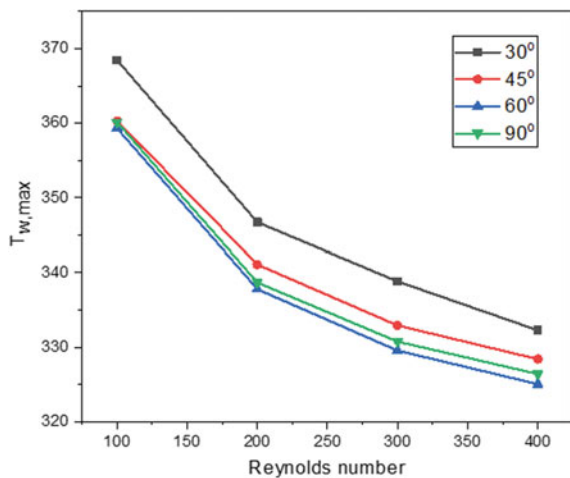


**Fig. 3** Contour of temperature at the mid-plane along the channel length for **a** 30°, **b** 60°, and **c** 90° nozzle angle

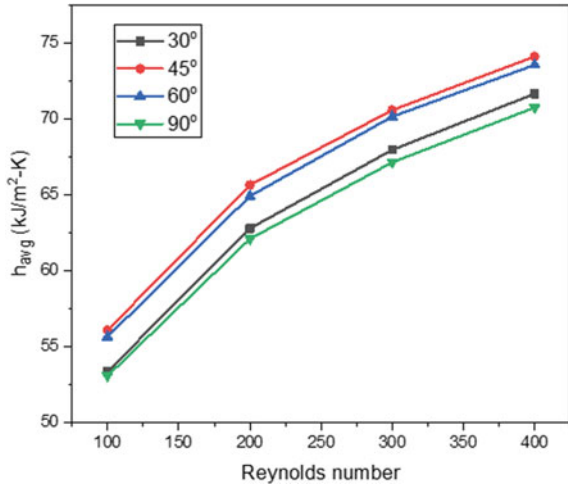
However, temperature distribution along the channel length is also most uniform for the 30° nozzle angle.

Figure 4 compared the variation of maximum wall temperature with the  $Re$  varied from 100 to 400 for different nozzle angles such as 30°, 45°, 60°, and 90°. Wall temperature is reducing as the  $Re$  increasing regardless of the nozzle configuration because of the higher mass flow rate. An approximately 10% reduction was obtained when the  $Re$  elevated from 100 to 400 for 60° nozzle angle. Lowest bottom wall temperature is obtained for 60° nozzle angle that is 52 °C, while other nozzle angles such as 30° and 45° yielded temperature value higher than the temperature obtained at 90° nozzle angle. Minimum temperature in case of 60° nozzle angle attributed to highest average heat transfer coefficient (Fig. 5) and lowest thermal resistance (Fig. 6)

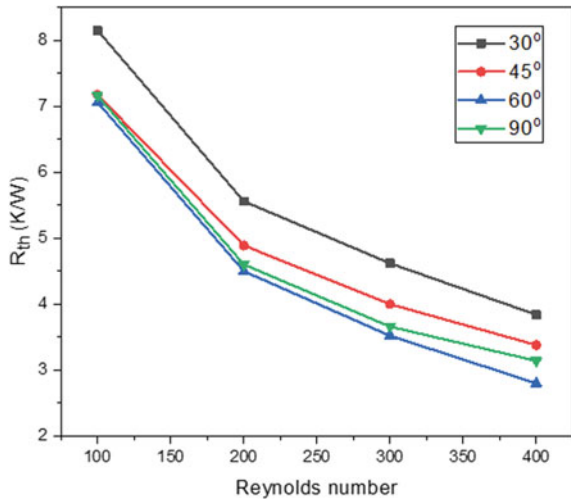
**Fig. 4** Variation of maximum wall temperature with the  $Re$



**Fig. 5** Variation of average heat transfer coefficient with the Re



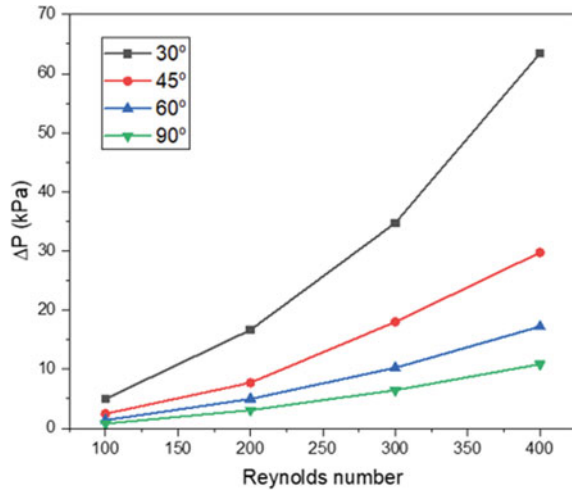
**Fig. 6** Variation of maximum thermal resistance with the Re



produced. Because of the longer path of disturbance and stronger flow penetration in case of 60° nozzle angle than 90°, stagnant laminar boundary layer is reduced more and higher turbulence occurred. For 60° nozzle angle, approximately 32% increment in the heat transfer coefficient and 60% reduction in thermal resistance is obtained when *Re* varied from 100 to 400.

That means, 60° nozzle angle offered lowest thermal resistance as well as induced highest heat transfer coefficient for same mass flow rate in comparison with other angles. This result illustrates that as the nozzle angle is decreased, path between the nozzle injection point and striking point is increased, that cause disturbance in larger fluid content. Hence, more turbulence and chaos are induced with decreasing the

**Fig. 7** Variation of pressure drop with the  $Re$



nozzle angle and thus higher heat transfer occur. But, thermal resistance in case of 45° nozzle angle is relatively more than 90°, and this must be because of the less impingement effect and the dominance of stagnant layer of fluid. This revealed that, as the value of nozzle angle decreased, though the disturbance in fluid is higher, but penetration effect against the stationary flow is reduced. Therefore, for the 45° nozzle angle, in spite of getting higher heat transfer coefficient relative to 90°, thermal resistance is more owing to higher boundary layer thickness and thus higher wall temperature is obtained. Moreover, the dominance of parallel laminar flow is so much higher in case of 30° nozzle angle that the effect of chaotic disturbance is suppressed, and thus, both thermal resistance as well as heat transfer coefficient is reduced, and hence, highest temperature is obtained at the bottom surface.

From the study, it is observed that pressure drop is increasing with the  $Re$ , and rate of increment is also increasing at higher  $Re$  as shown in Fig. 7. For 90° nozzle angle, as the  $Re$  varied from 100 to 400 pressure drop increased by almost 13 times. Due to higher disturbance in the fluid, more resistance offered, and thus, higher pressure loss occur. Lowest pressure drop found for the 90° nozzle angle as in this case flow disturbance is least, while pressure drop is highest for 30° nozzle angle due to highest disturbance in the fluid volume. At a fixed  $Re$  400, as the nozzle angle increased from 30° to 90°, pressure drop reduced by approximately six times. In this study, overall performance of the heat sink for nozzle angle in between 45° and 60° overruled other angle as higher heat transfer coefficient as well as lower bottom wall temperature and pressure loss occurred, while for heat sink with nozzle angle 90° (more than 60°), though pressure drop reduced but bottom wall temperature increased. However, heat sink with nozzle angle 30° or less than 30° is the worst as lower heat transfer coefficient is provided at largest pressure drop cost.

## 4 Conclusions

The comprehensive report presented herein determined the role of nozzle configuration in the microscale level. An understanding is developed for the behavior of micronozzle inclination on the microchannel cooling efficiency. Increasing  $Re$  condition is found favorable for enhancing heat transfer irrespective of nozzle inclination but at the cost of higher pressure loss. Likewise, increasing nozzle angle is also promising condition for better cooling of the electronic devices at relatively lower pumping power. Maximum heat transfer coefficient and lowest bottom wall temperature were obtained at  $60^\circ$  nozzle angle, whereas largest pressure drop occurred for  $30^\circ$  nozzle angle. Thermal resistance is decreased by 27% when inclination angle varied from  $30^\circ$  to  $60^\circ$ , but as the impingement angle is further increased from  $60^\circ$  to  $90^\circ$ , thermal resistance is increased by almost 11%. However, when nozzle angle increased from  $30^\circ$  to  $90^\circ$ , pressure drop is reduced by almost six times. At  $60^\circ$  nozzle angle, best overall performance was obtained as highest heat transfer occurred as well as lowest pumping power required.

## References

1. Shafeie, H., Abouali, O., Jafarpur, K., Ahmadi, G.: Numerical study of heat transfer performance of single-phase heat sinks with micro pin-fin structures. *Appl. Therm. Eng.* **58**(1–2), 68–76 (2013)
2. Chai, L., Xia, G.D., Wang, H.S.: Numerical study of laminar flow and heat transfer in microchannel heat sink with offset ribs on sidewalls. *Appl. Therm. Eng.* **92**, 32–41 (2016)
3. Zheng, L., Zhang, D., Xie, Y., Xie, G.: Thermal performance of dimpled/protruded circular and annular microchannel tube heat sink. *J. Taiwan Inst. Chem. Eng.* **60**, 342–351 (2016)
4. Ghani, I.A., Kamaruzaman, N., Sidik, N.A.C.: Heat transfer augmentation in a microchannel heat sink with sinusoidal cavities and rectangular ribs. *Int. J. Heat Mass Transf.* **108**, 1969–1981 (2017)
5. Chen, C., et al.: A study on fluid flow and heat transfer in rectangular microchannels with various longitudinal vortex generators. *Int. J. Heat Mass Transf.* **69**, 203–214 (2014)
6. Sung, M.K., Mudawar, I.: Effects of jet pattern on single-phase cooling performance of hybrid micro-channel/micro-circular-jet-impingement thermal management scheme. *Int. J. Heat Mass Transf.* **51**(19–20), 4614–4627 (2008)
7. Tran, N., Chang, Y.J., Tong Teng, J., Greif, R.: A study on five different channel shapes using a novel scheme for meshing and a structure of a multi-nozzle microchannel heat sink. *Int. J. Heat Mass Transf.* **105**, 429–442 (2017)
8. Carlomagno, G.M., Ianiro, A.: Thermo-fluid-dynamics of submerged jets impinging at short nozzle-to-plate distance: a review. *Exp. Therm. Fluid Sci.* **58**, 15–35 (2014)
9. Bolek, A., Bayraktar, S.: Heat and fluid flow analyses of an impinging jet on a cubic body. Elsevier (2018)
10. Choo, K., Kang, T.Y., Kim, S.J.: The effect of inclination on impinging jets at small nozzle-to-plate spacing. *Int. J. Heat Mass Transf.* **55**(13–14), 3327–3334 (2012)
11. Seyedein, S.H., Hasan, M., Mujumdar, A.S.: Laminar flow and heat transfer from multiple impinging slot jets with an inclined confinement surface. *Int. J. Heat Mass Transf.* **37**(13), 1867–1875 (1994)

12. Rhee, D.H., Yoon, P.H., Cho, H.H.: Local heat/mass transfer and flow characteristics of array impinging jets with effusion holes ejecting spent air. *Int. J. Heat Mass Transf.* **46**(6), 1049–1061 (2003)
13. Husain, A., Ariz, M., Al-Rawahi, N.Z.H., Al-Ansari, M.Z.: Thermal performance analysis of a hybrid micro-channel, -pillar and -jet impingement heat sink. *Appl. Therm. Eng.* **102** (2016)

# Numerical Investigation of Swirl Flow on Heat Transfer Enhancement in a Stepped Pipe



**B. Prince Abraham, F. Michael Thomas Rex, P. Samuel Ponraj, R. Jayavenkatesh, and A. Andrews**

## 1 Introduction

Effectiveness in convective heat transfer is an important factor required for a lot of applications in thermal engineering [1]. Generally, the techniques used for heat transfer enhancement include modifications in the heat transfer surface and other novel geometric modifications in the fluid flow path [2–5]. Yilmaz et al. [6] experimentally investigated the enhancement characteristics of swirl flow by considering three different types of swirl generators. Further, the experiments were made with different Reynolds number and swirl intensities. A recent numerical study by Ho et al. [7] reported that the heat transfer in a tube with laminar flow and forced convection could be increased by having a concentric inner tube. A duct with smaller outer radius and operating with relatively larger flow rate can transfer the heat effectively. Tawfik et al. [8] analyzed the influence of swirl in wall-bed heat transfer and flow behavior in a fluidized bed reactor. They concluded that the heat transfer coefficient of fluidized bed reactor was higher by introducing swirl in the lower portion of the bed and it found to be lesser at the upper portion of the bed in all radial positions.

Swirl flow got its importance in many industrial applications that include multi-phase flows which don't take account of heat transfer. A theoretical model was established by Liu et al. [9] on swirling annular flow for investigating the transition from churn flow to annular flow. They reported that the gas velocity necessary for the transition of flow from churn to annular is less if swirl is introduced. Swirlers with different geometries were considered and Polyethylene particles were made to flow in a horizontal straight acrylic pipe having diameter 80 mm [10]. Particle Image

---

B. Prince Abraham (✉) · F. Michael Thomas Rex · P. Samuel Ponraj · R. Jayavenkatesh · A. Andrews

Department of Mechanical Engineering, National Engineering College, Kovilpatti, Tamil Nadu 628503, India

Velocimetry (PIV) is used to observe the particle flow characteristics and the pressure drop involved is also compared. Xu et al. [11] studied the effect of swirl flow on coal gasifiers. A Computational Fluid Dynamic simulation of swirl flow induced by twist vanes has been done by Xiong et al. [12] and investigated the accuracy of  $k - \epsilon$  model for nuclear applications. Uddinet al. [13] performed a comparative study by impinging a jet under swirl, active and passive excitations in order to enhance the heat transfer. However, they have reported that the swirl does not give appreciable heat transfer rate.

This work mainly focuses on numerically investigating the effect of swirl on convective heat transfer and on introducing a stepped pipe as shown in Fig. 1 to make it enhanced. A step in pipe, either converging or diverging will provide a significant change in flow properties such as velocity, pressure and turbulence. Hence, it is imperative to study its effect along with induced swirl. Such a stepped pipe with swirl flow has not been considered in the existing literature.

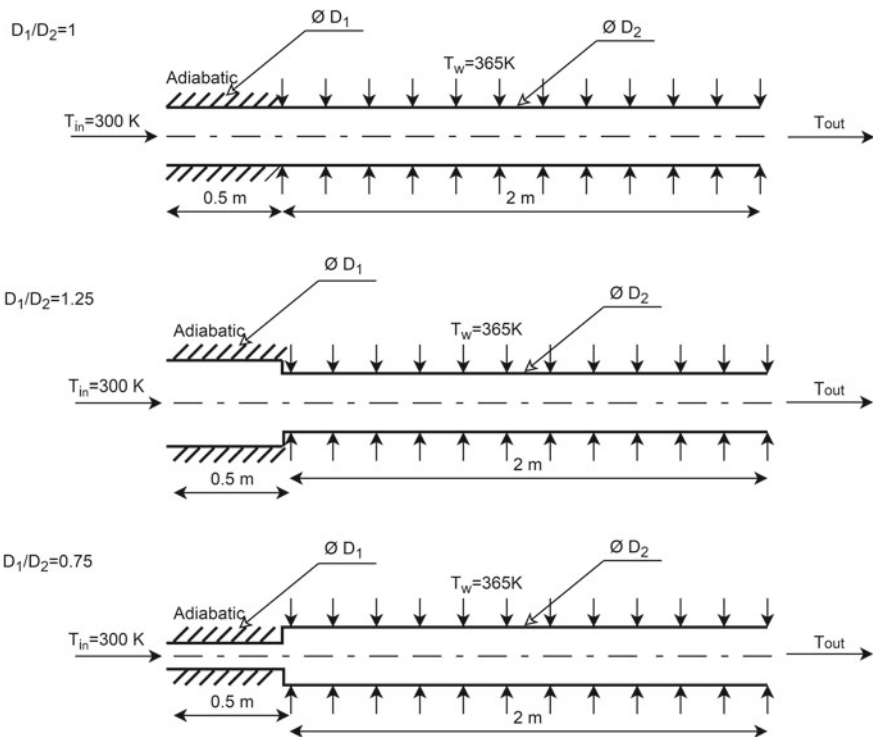


Fig. 1 Schematic diagram of the problem with various diameter ratios



## 2 Problem Definition

The physical configuration of the pipe with a constant temperature boundary is shown in Fig. 1. A pipe with a diameter of 3 cm and of length 2 m is maintained at a constant temperature of 365 K while the entrance pipe of length 0.5 m is modeled as adiabatic wall. Water flows at 300 K through the inlet of the pipe and in due course, it is heated by the wall and hence the temperature gets increased. The diameter of the heating pipe ( $D_2$ ) is kept constant but the inlet pipe diameter ( $D_1$ ) is varied as illustrated in Fig. 1. The ratio between the diameters of inlet pipe and outlet pipe is termed as diameter ratio ( $D_1/D_2$ ). Nevertheless, the mass flow rate of the water is kept constant in all the cases so as to compare the effect of the diameter ratio. Moreover, the axial velocity of the flow is maintained constant and the swirl velocity is varied for a range of values and its effect on the heat transfer with the aforesaid diameter ratios are investigated.

Reynolds number of the flow is maintained around 3300 and the same can be calculated by

$$Re = \frac{\rho v D}{\mu} \quad (1)$$

where  $\rho$  is the density of water,  $v$  is the velocity of flow in the heating pipe,  $D$  is the hydraulic diameter and  $\mu$  is the dynamic viscosity of water.

As the heating wall is defined as a constant temperature source, the heat flux ( $Q_w$ ) through the wall is computed. The convective heat transfer coefficient is computed as follows.

$$h = \frac{Q_w}{(T_w - T_\infty)} \quad (2)$$

where the  $Q_w$  is the heat flux and the  $T_w$  and  $T_\infty$  are the temperatures at the wall and the bulk fluid temperature. The convective heat transfer is defined from the Nusselt number and it is given by

$$Nu = \frac{hD}{k} \quad (3)$$

The operating conditions and the fluid flow parameters are given in Table 1.

## 3 Numerical Method

Numerical modeling of the flow has been done by assuming that the flow domain as two-dimensional and axisymmetric. The swirl velocity has been considered

**Table 1** Operating conditions and fluid properties

Variable	Quantity	Unit
Inlet temperature ( $T_{in}$ )	300	K
Wall temperature ( $T_w$ )	365	K
Outlet pressure ( $P_{out,abs}$ )	101,325	Pa
Mass flow rate ( $\dot{m}$ )	$70.5087 \times 10^{-3}$	kg/s
Density ( $\rho$ )	998.2	kg/m <sup>3</sup>
Specific heat ( $C_p$ )	4182	J/kg K
Viscosity ( $\mu$ )	0.001003	kg/m s

and predicted by assuming that swirl velocities exist in the flow and having no circumferential gradients.

The continuity equation in differential form can be expressed as

$$\frac{\partial \rho}{\partial t} + \nabla \cdot (\rho u) = 0 \tag{4}$$

where  $\rho$  is the density of water,  $t$  is the time and  $u$  is the flow velocity vector field.

The momentum conservation equation for swirl velocity in two-dimensional domain can be written as

$$\begin{aligned} \frac{\partial}{\partial t}(\rho w) + \frac{1}{r} \frac{\partial}{\partial x}(r \rho u w) + \frac{1}{r} \frac{\partial}{\partial r}(r \rho v w) &= \frac{1}{r} \frac{\partial}{\partial x} \left[ r \mu \frac{\partial w}{\partial x} \right] \\ + \frac{1}{r^2} \frac{\partial}{\partial r} \left[ r^3 \mu \frac{\partial}{\partial r} \left( \frac{w}{r} \right) \right] - \rho \frac{v w}{r} \end{aligned} \tag{5}$$

The circumferential motion in the flow creates centrifugal forces and that can be expressed by

$$\frac{\partial p}{\partial r} = \frac{\rho \omega^2}{r} \tag{6}$$

The appropriate turbulent model is chosen based on the swirl number that is the ratio between the axial flux of angular momentum and the axial flux of axial momentum that can be defined by

$$S = \frac{\int r w \vec{v} \cdot d\vec{A}}{\bar{R} \int u \vec{v} \cdot d\vec{A}} \tag{7}$$

where  $\bar{R}$  is the hydraulic radius,  $\vec{A}$  is the cross-sectional area of the pipe and  $u$  is the axial velocity of flow. Finite volume method is adopted for solving the mass conservation, momentum and turbulence equations. Maximum face size of the mesh

elements is chosen by mesh sensitivity analysis and it is identified that 1.5 mm is the optimum size. Decreasing the face size of the mesh results in a dramatic increase in the number of elements in the grid whereas the change in the Nusselt number is insignificant. Semi Implicit Method for Pressure Linked Equations algorithm is used for solving the discretized equations and all the equations are set to be second order. Convergence of the numerical solutions is confirmed by ensuring that all the scaled residuals are less than  $10^{-6}$ .

## 4 Results and Discussion

### 4.1 Effect of Swirl Velocity

In this section, the effect of swirl velocity on the Nusselt number (Nu) is described as it is the primary assessment criteria for convective heat transfer. The convective heat transfer coefficient is also plotted for various swirl velocities. The output parameters for various swirl velocities is presented in Tables 2, 3 and 4. As stated earlier, the mass flux of the water is kept constant for all the cases. In order to achieve constant mass flux in all the three different configurations, the velocity at the inlet ( $V_{in}$ ) is calculated based on the cross-sectional area of the inlet as follows.

$$V_{in} = \frac{\dot{m}}{\rho A} \tag{8}$$

Figure 2a, b clearly shows an increasing trend in Nusselt number and heat transfer coefficient with the increase in swirl velocity. But the swirl has a better influence in the stepped pipe with 1.25 diameter ratio than the parallel pipe in Fig. 2a. Further, it is evident from Fig. 2c that the maximum Nusselt number is reported in the case

**Table 2** Output variables for diameter ratio 1

Swirl velocity (m/s)	h (W/m <sup>2</sup> K)	Nu	$Q_w$	$\Delta P$ (Pa)	Pump work (W)	Heat transfer (W)
0	6041.45	9062.175	79,198.3	47.233	0.003	14,920.960
0.3	6050.72	9076.080	79,224.9	86.776	0.006	14,925.971
0.5	6063.3	9094.950	79,261.1	142.391	0.010	14,932.791
0.7	6077.99	9116.985	79,303.2	216.386	0.015	14,940.723
1	6103.09	9154.635	79,374.5	366.289	0.026	14,954.156
2	6225.78	9338.670	79,717.4	1279.774	0.090	15,018.758
3	6369.04	9553.560	80,104.9	2846.948	0.201	15,091.763
4	6511.99	9767.985	80,477.9	5060.980	0.357	15,162.036
5	6649.74	9974.610	80,825.2	7918.134	0.558	15,227.468

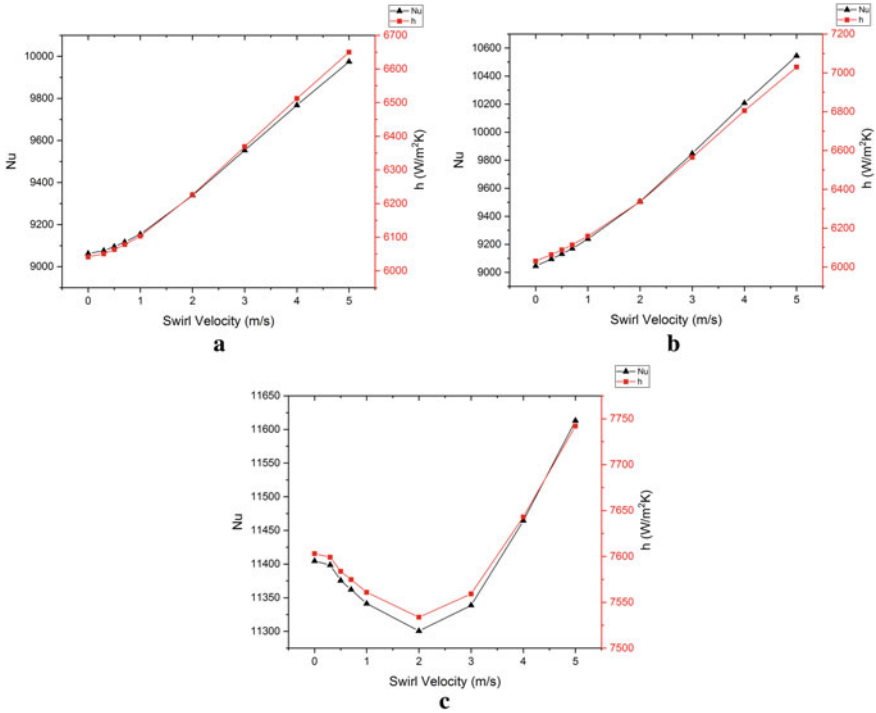
**Table 3** Output variables for diameter ratio 1.25

Swirl velocity (m/s)	h (W/m <sup>2</sup> K)	Nu	Q <sub>w</sub>	ΔP (Pa)	Pump work (W)	Heat transfer (W)
0	6030.3	9045.45	79,167.7	41.768	0.003	14,915.195
0.3	6063.47	9095.205	79,263.1	77.924	0.005	14,933.168
0.5	6087.67	9131.505	79,332.2	129.876	0.009	14,946.186
0.7	6113.52	9170.28	79,405.6	205.014	0.014	14,960.015
1	6159.21	9238.815	79,534.4	368.514	0.026	14,984.281
2	6336.62	9504.93	80,019.9	1349.456	0.095	15,075.749
3	6564.99	9847.485	80,614.1	2993.936	0.211	15,187.696
4	6805.01	10,207.52	81,204.3	5305.864	0.374	15,298.890
5	7029.66	10,544.49	81,727.3	8286.044	0.584	15,397.423

**Table 4** Output variables for diameter ratio 0.75

Swirl velocity (m/s)	h (W/m <sup>2</sup> K)	Nu	Q <sub>w</sub>	ΔP (Pa)	Pump Work (W)	Heat transfer (W)
0	7603.04	11,404.56	82,843.2	76.245	0.005	15,607.659
0.3	7599.10	11,398.65	82,835.2	96.595	0.007	15,606.152
0.5	7583.66	11,375.49	82,804.2	186.700	0.013	15,600.311
0.7	7574.73	11,362.10	82,786.2	274.637	0.019	15,596.920
1	7560.87	11,341.31	82,758.2	441.608	0.031	15,591.645
2	7533.71	11,300.57	82,702.9	1317.701	0.093	15,581.226
3	7559.17	11,338.76	82,754.6	2811.136	0.198	15,590.967
4	7642.97	11,464.46	82,922.8	4970.694	0.35	15,622.656
5	7742	11,613	83,117.6	7782.463	0.549	15,659.356

with 0.75 diameter ratio. The relation between the swirl velocity and the Nusselt number is almost linear in the cases with diameter ratios 1 and 1.25. However, the graph shows a peculiar trend in the change in Nusselt number with respect to the change in swirl velocity. Up to the swirl velocity 2 m/s, the heat transfer coefficient gets decreased and after that point, it starts to increase. This is because of the reduced size of the inlet which could not transfer the swirl effectively to the heating pipe at low swirl velocities. Further, as the inlet is smaller in diameter, the effect of swirl is insignificant than the other two cases.



**Fig. 2** Effect of swirl velocity on heat transfer coefficient and Nusselt number **a**  $D_1/D_2 = 1$  **b**  $D_1/D_2 = 1.25$  **c**  $D_1/D_2 = 0.75$

### 4.2 Heat Flux and Pressure Drop

As the flow becomes swirl, the pressure drop keeps on increases as the turbulence in the flow domain gets increased. From Fig. 3a–c, one can infer that the increase in pressure drop due to swirl in all the three cases are more or less equal.

However, significant difference in heat flux could be observed among the cases with three diameter ratios. Further, Fig. 3c reports the maximum heat flux where the diameter ratio is 0.75. Hence it shows that increase in diameter ratio leads to reduced heat transfer.

A comparison is also made between the cases with the three diameter ratios in view of heat flux and pressure drop. The pressure drop gets increased as the diameter ratio is reduced. But by considering the heat flux, pipe with a smaller diameter ratio serves better as shown in Fig. 4. However, there is no significant change in heat flux between the diameter ratios 1.25 and 1.

Figure 5 shows a consolidated view of the effect of swirl as well as the diameter ratio in the percentage of change in heat flux. The percentage of change is calculated from the heat flux in the case without swirl. From the graph, it is evident that the case with higher diameter ratio ( $D_1/D_2 = 1.25$ ) is very sensitive to the swirl component

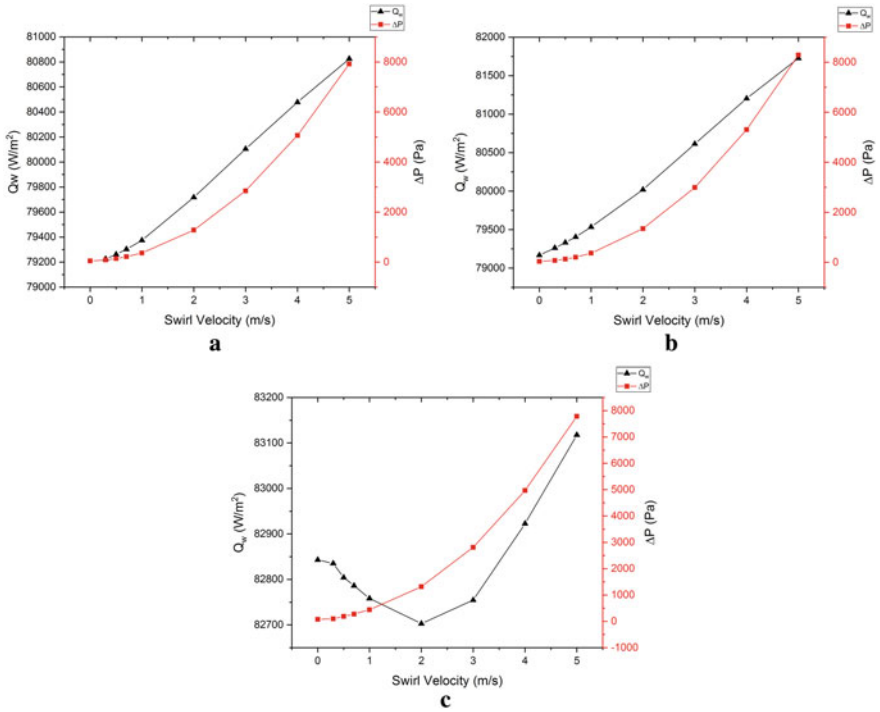


Fig. 3 Heat flux and change in pressure drop for various swirl magnitudes a  $D1/D2 = 1$  b  $D1/D2 = 1.25$  c  $D1/D2 = 0.75$

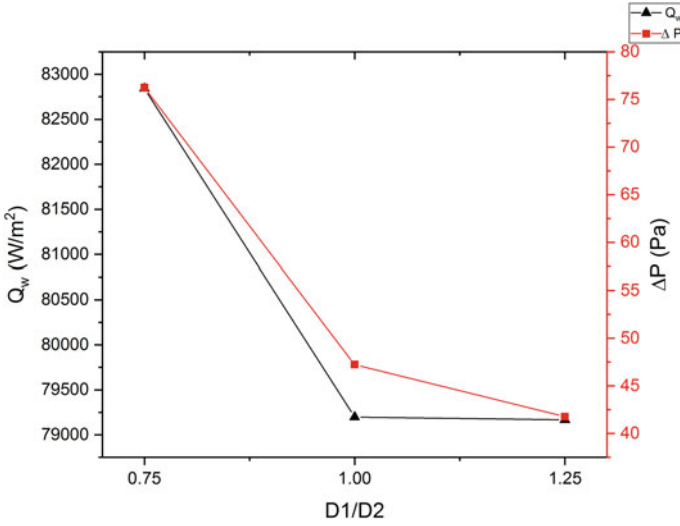
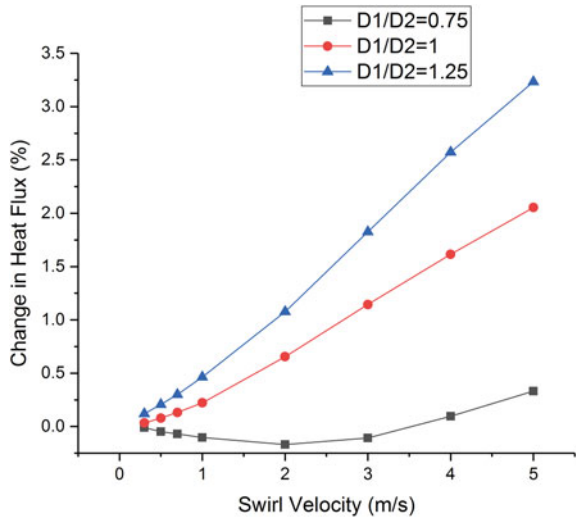


Fig. 4 Heat flux and change in pressure drop for inlet diameter ratios ( $V_s = 0$ )

**Fig. 5** Percentage of change in heat flux for various inlet diameter ratios and magnitude of swirl



of flow and the heat flux increased up to 3.23% for the case without swirl. Whereas insignificant change is observed (i.e., 0.33%) when the diameter ratio is 0.75.

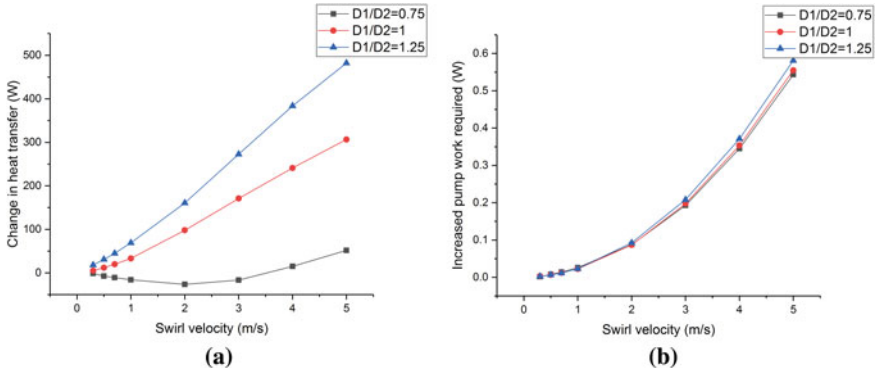
### 4.3 Pressure Drop and Increase in Pump Work Required

By way of increasing the heat transfer with the swirl component in the flow, a significant pressure drop is observed in the pipe. As the induced swirl results in an increase in heat transfer and increase in pressure drop, there should be a pay off between those two parameters. The increased pump work required to overcome the pressure drop resulted by swirl is calculated by

$$W_p = \frac{\dot{m} \Delta P}{\rho} \tag{9}$$

where  $\dot{m}$  is the mass flux through the pipe,  $\Delta P$  is the drop in pressure in addition to the case without swirl and  $\rho$  is the density of water.

It is obvious from Fig. 6a, b that the increase in heat transfer due to swirl velocity is considerably higher than the pump work required to overcome the pressure drop caused.



**Fig. 6 a** Change in heat transfer and **b** additional pump work required for pressure drop compensation

### 5 Conclusions

In this study, numerical analysis is performed by two-dimensional axisymmetric swirl model to investigate the effects of swirl flow in a stepped pipe on convective heat transfer. By the increase in swirl velocity, the increase in Nusselt number is very minimum in the case of diameter ratio 0.75 and it is around 5 times and 10 times greater in the cases with diameter ratio 1 and 1.25 respectively. Further, the relationship between the swirl velocity and the Nusselt number is almost linear in the cases with diameter ratios 1 and 1.25. Irrespective of the diameter ratio, the trend of pressure drop remains the same in all the three cases with respect to the swirl velocities. But the effective heat flux increases with reduced diameter ratio. With mere axial velocity and zero swirl velocity, it is observed that there is no significant change in heat transfer rate as well as pressure drop between the diameter ratios 1 and 1.25. But the increase in the heat transfer as well as pressure drop is significant in the case of 0.75 diameter ratio. The effect of swirl is not much influencing the case with 0.75 (i.e., 0.33% increase from the case without swirl), the maximum Nusselt number recorded in this case (11,613) is far higher than the other two configurations. Hence, the heat transfer takes place effectively when the diameter ratio is smaller. However, it is less responsive for the swirl. Conversely, the heat transfer is not as effective as the diameter ratio is higher. But it is highly sensitive for the swirl flows and the heat transfer could be enhanced by swirling flows in such cases. This work may be extended to improvise the heat transfer in specific applications such as absorber tube in solar concentrating collectors in future.



## References

1. Liu, S., Sakr, M.: A comprehensive review on passive heat transfer enhancements in pipe exchangers. *Renew. Sustain. Energy Rev.* 19:64–81 (2013)
2. Han, H.Z., Li, B.X., Yu, B.Y., He, Y.R., Li, F.C.: Numerical study of flow and heat transfer characteristics in outward convex corrugated tubes. *Int. J. Heat Mass Transf.* 55(25–26), 7782–7802 (2012)
3. Gunes, S., Ozceyhan, V., Buyukalaca, O.: Heat transfer enhancement in a tube with equilateral triangle cross sectioned coiled wire inserts. *Exp. Therm. Fluid Sci.* 34(6), 684–691 (2010)
4. Kareem, Z.S., Abdullah, S., Lazim, T.M., Mohd Jaafar, M.N., Abdul Wahid, A.F.: Heat transfer enhancement in three-start spirally corrugated tube: experimental and numerical study. *Chem. Eng. Sci.* 134, 746–757 (2015)
5. García, A., Solano, J.P., Vicente, P.G., Viedma, A.: The influence of artificial roughness shape on heat transfer enhancement: Corrugated tubes, dimpled tubes and wire coils. *Appl. Therm. Eng.* 35(1), 196–201 (2012)
6. Yılmaz, M., Yapici, S., Çmakli, Ö., Şara, O.N.: Energy correlation of heat transfer and enhancement efficiency in decaying swirl flow. *Heat Mass. Transf. und Stoffuebertragung* 38(4–5), 351–358 (2002)
7. Ho, C.J., Yen, J.Y., Kung, X.Y., Yang, T.S., Wen, C.D.: Enhancing convective heat transfer for laminar flow in a tube by inserting a concentric inner tube and controlling concurrent flows: a numerical assessment. *Int. Commun. Heat Mass Transf.* 99, 26–36 (2018)
8. Tawfik, M.H.M., Refaat Diab, M., Mohamed Abdelmotalib, H.: An experimental investigation of wall-bed heat transfer and flow characteristics in a swirling fluidized bed reactor. *Appl. Therm. Eng.* 155, 501–507 (2019)
9. Liu, W., Lv, X., Bai, B.: The effect of swirl on transition from churn flow to annular flow in an intermediate diameter pipe. *Exp. Therm. Fluid Sci.* 109861 (2019)
10. Dong, L., Rinoshika, A.: Comparison between rotation swirler and non-rotation swirler in a horizontal swirling flow pneumatic conveying. *Powder Technol.* 346, 396–402 (2019)
11. Xu, J., Liang, Q., Dai, Z., Liu, H.: The influence of swirling flows on pulverized coal gasifiers using the comprehensive gasification model. *Fuel Process. Technol.* 172:142–154 (2018)
12. Xiong, J., Cheng, R., Lu, C., Chai, X., Liu, X., Cheng, X.: CFD simulation of swirling flow induced by twist vanes in a rod bundle. *Nucl. Eng. Des.* 338, 52–62 (2018)
13. Uddin, N., Weigand, B., Younis, B.A.: Comparative study on heat transfer enhancement by turbulent impinging jet under conditions of swirl, active excitations and passive excitations. *Int. Commun. Heat Mass Transf.* 100: 35–41 (2019)

# An Integrated Approach by Using Various Approaches for a Green Supplier Selection Problem



A. V. A. R. Durga Rao, A. K. Chaitanya, T. Sessaiah, P. Bridjesh, and Sivakrishna

## 1 Introduction

At present, numerous undertakings want to fortify their item quality and innovation and should zero in on the incorporation of upstream and downstream of the whole inventory network with the goal that clients, providers, and important associations have continuously nearer collaboration. Along these lines, the nature of providers is related to the activity of the store network and furthermore incredibly impacts the achievement of endeavors. Toward this path and looks to preferably manage the physical and data streams traded between every one of the entertainer in a store network. In this way, endeavors ought to decide provider execution assessment records dependent on their own ascribes, essentials, and encounters to discover adjusting providers. Subsequently, it is needed to join a green natural insurance record into provider execution assessment lists. Green inventory network includes cost, quality, plan, material sourcing and choice, fabricating measure, delivery of the end result to the buyers.

---

A. V. A. R. D. Rao · A. K. Chaitanya  
Department of Mechanical Engineering, Potti Sriramulu Engineering College, Vijayawada, A.P,  
India

T. Sessaiah (✉)  
Department of Mechanical Engineering, QIS College of Engineering and Technology, Ongole 523  
272, India  
e-mail: [sessaiah.t@qiscet.edu.in](mailto:sessaiah.t@qiscet.edu.in)

P. Bridjesh  
Department of Mechanical Engineering, MLR Institute of Technology, Hyderabad, India

Sivakrishna  
Department of Mechanical Engineering, Vignan's Lara Institute of Technology and Science,  
Vadlamudi, A.P, India

## 2 Literature Survey

Makina, 2006 et al. [1] provider determination is a basic buying of an activity for some establishments. The present purchasers demand more affordable, great items, on-time conveyance, and superb after-deal administrations. Later work identifies with evaluating natural parts of communications with a provider. Chih-Chao. 2016 et al. [2] implement the analytic network process method based on the analytic hierarchy process method, and it is one of the greatest frequently used approaches. Few problems are not solved in hierarchy model because the interrelationships of criteria's should be considered. Eyed Hamid Hashemi et al. 2015[3] In this paper, green store network the board has gotten a lot of consideration from professionals and specialists consider measures, for example, cost, quality and conveyance to assess the provider's presentation likewise considering the ordinary standards, for example, natural issues utilize both financial and ecological rules like Resource utilization, Pollution creation and Management responsibility. Atefeh et al. 2012 [4] mainly focus on the environment and energy consumption mainly depending on those criteria/sub-criteria proposed onto an evaluation of ranking of providers. It has been also applying various approaches of supplier selection to choose suitable supplier including significant level of criterion and execution of those criterion essential based on these parameters has been applying implemented on experts view.

Refer all the above papers; up to now we did not consider the cause-and-effect relationship between criteria's. The significant distinction among analytical hierarchy (AHP) and entropy strategies are savvy examination grid is considered in AHP where as in Entropy pair shrewd correlation lattice isn't thought about it straightforwardly ascertains loads on chief evaluations framework for example for every standard as for every provider. This is primary bit of leeway of entropy strategy. So for calculating the weights again, we are not considering the same pair-wise comparison matrix; instead we are calculating weights by considering decision-makers' rating given for each supplier criteria in entropy process.

## 3 Proposed Methodology

### 3.1 DEMATEL Method

It is utilized to see multifaceted connections and build an organization connection map between models. It relies upon an idea of pair-wise examination of dynamic credits (options, standards). The qualities are in contrast with deference with relative impact of each over the other. The principal objective of DEMATEL strategy is to straightforwardly think about the connection between various factors of a convoluted framework to decide immediate and roundabout causal connections and impact levels between the factors. DEMATEL technique depends on the thought of digraphs, which can isolate the thought about rules into circumstances and logical results gatherings

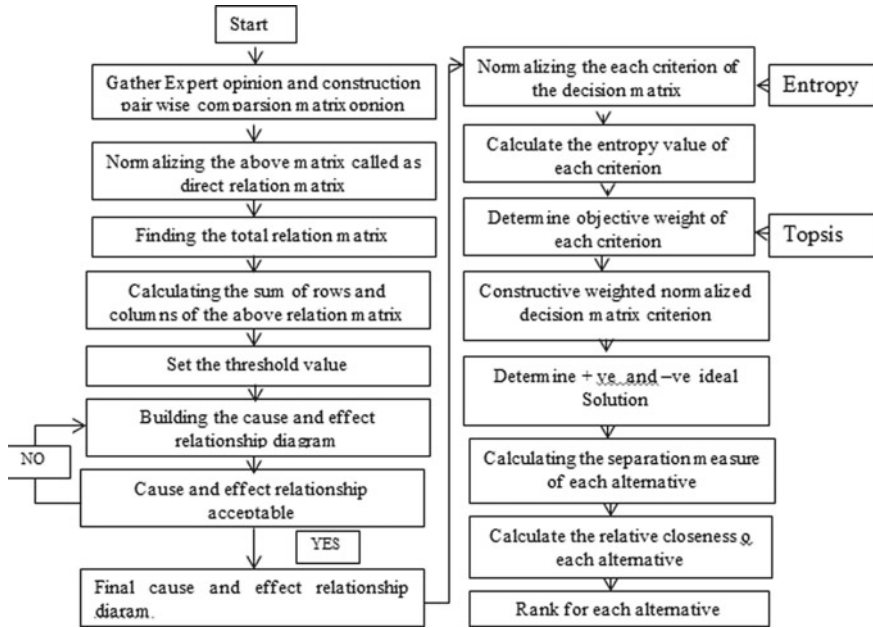


Fig. 1 Flowchart for proposed methodology (DEMATEL, ENTROPY, and TOPSIS)

to outwardly notice within an unpredictable framework/issue. It expects a framework containing a bunch of parts with pair-wise relations that can be assessed from Fig. 1.

**Step 1:** Collect and taking expert’s judgment and compute the average matrix Z.

Basically, two elements are to follow up the pair-wise comparison matrix how much the master apparent factor I consequences for factor j is meant as  $X_{ij}$ .

$$Z_{ij} = 1 / m \sum_{i=1}^m X_{ij}^k$$

**Step 2:** Compute the standardized preliminary direct-relation matrix X.

The controlled primary direct-relation matrix  $X = [X_{ij}]$ ,

where matrix value ranges between [0, 1].

$$X = \lambda * Z \quad [X_{ij}]_{n \times n} = \lambda [Z_{ij}]_{n \times n}$$

$$\lambda = \min \left[ 1 / \max_{1 \leq i \leq n} \sum_{j=1}^n Z_{ij}, 1 / \max_{1 \leq i \leq n} \sum_{i=1}^n Z_{ij} \right]$$

**Step 3:** Originate the total matrix (T).

The all-out impact lattice  $T$  is acquired in which  $I$  is a  $n \times n$  personality network. The component of  $t_{ij}$  signifies the aberrant impacts that factor  $I$  and  $j$ , and afterward the framework  $T$  mirrors the complete connection between each pair of framework factors.

$$\begin{aligned}
 T &= \lim_{m \rightarrow \infty} = X^1 + X^2 + \dots + X^m = \sum_{m=1}^{\infty} X^i \\
 \sum_{m=1}^{\infty} X^i &= X^1 + X^2 + \dots + X^m = X(I + X^1 + X^2 + \dots + X^{m-1}) \\
 &= X(I - X)^{-1}(I - X) \\
 &\quad (I + X^1 + X^2 + \dots + X^{m-1}) \\
 T &= X(I - X)^{-1}
 \end{aligned}$$

**Step 4:** Determine the rows and columns of matrix  $T$

$$r = [d_i]_{n \times n} = \sum_{j=1}^n t_{ij_{n \times 1}} C = [C_j]_{1 \times n}' = \sum_{j=1}^n t_{ij_{n \times 1}}$$

where is  $[C_j]'$  denoted as transposition matrix.

**Step 5:** Set a threshold value ( $\alpha$ ).

Where ( $\alpha$ ) was computed by the average of the elements in matrix  $T$

$$\alpha = \sum_{i=1}^n \sum_{j=1}^n t_{ij} / N$$

where  $N$  is the total number of elements in the matrix  $T$ .

**Step 6:** Construct a cause-and-effect relationship illustration.

The circumstances and logical results of graph are developed by planning all arrange sets of  $(r_i + c_i, [r]_{i-} c_{-j})$  to imagine the intricate interrelationship and give data to pass judgment.

### 3.2 Entropy Method

This entropy loads are the proportions of vulnerabilities in the data planned utilizing likelihood hypothesis and this data content of this property estimations of the other options, assessing each credits handiness in identifying contrasts in the information.

**Step 1:** Standardize individually matrix

$$r_{ij} = x_{ij} / \sqrt{\sum x_{ij}^2} (i = 1, 2, \dots, m; j = 1, 2, \dots, n)$$

$r_{ij}$  is standardized value of  $X_{ij}$ ,

$X_{ij}$  is the measurement of  $i$ th another w.r.t to  $j$ th criterion,

**Step 2:** Compute the entropy value ( $e_j$ ) of each decision criterion.

$$e_j = -k \sum_{i=1}^m (r_{ij}^* \log r_{ij})$$

where  $k = 1/(\ln m)$  is a constant that assures  $0 \leq e_j \leq 1$ .

**Step 3:** Determine the target weight of every measure.

$$w_j = 1 - e_j / \sum_{i=1}^m 1 - e_j$$

### 3.3 TOPSIS Method:

This proposed TOPSIS method is used to calculate weighted normalization matrix, and eventually rankings are calculated.

**Step 1:** Create an assessment matrix by  $m$  alternatives and  $n$  criteria given by  $x_{ij}$ .

**Step 2:** Calculate a stabilized decision matrix

$$r_{ij} = x_{ij} / \sqrt{\sum x_{ij}^2}$$

**Step 3:** Construct the weighted-controlled decision matrix by weights.

$$v_{ij} = w_{ij} * r_{ij}$$

**Step 4:** Regulate the optimistic ideal solution and negative ideal solution

$$v^+ = \{(\max v_{ij}), (\min v_{ij})\} v^- = \{(\max v_{ij}), (\min v_{ij})\}$$

**Step 5:** Compute the parting measure. The separation of each alternative from the positive ideal one is given by

$$s_i^+ = \sqrt{\sum (v_{ij} - v_j^+)^2}$$

Similarly, the parting of each alternative from the negative ideal one is given by

$$s_i^- = \sqrt{\sum (v_{ij} - v_j^-)^2}$$

**Step 6:** Find out the comparative solution of  $s_i^+$  with respect to  $s_i^-$  defined as

$$C_i^* = s_i^- / (s_i^+ + s_i^-)$$

**Step 7:** Rank the preference order.

## 4 Numerical Example

In this paper, a model of mathematical instance taking into by considering some data from local manufacturing industries and few assumptions efficiency of the methodology is evaluated.

Presumed practiced rating for suppliers.

Ten-point scales are chosen for attributes:

$C_{r1}$ —Cost;  $C_{r2}$ —Quality;  $C_{r3}$ —Technology;  $C_{r4}$ —Resource Consumption;  $C_{r5}$ —Pollution Production;  $C_{r6}$ —Management Commitment.

**Step 1:** Gather specialist’s opinion and construct pair-wise comparison matrix.

**Step 2:** Calculate the regularized initial direct-relation matrix ( $X$ ) values as shown in Table 1.

**Step 3:** Originate the total matrix ( $T$ ) values as shown in Table 2 by using the below relation, i.e.  $= X (I - X)^{-1}$

**Table 1** Regularized initial direct-relation matrix (X) values

Criteria	C <sub>r1</sub>	C <sub>r2</sub>	C <sub>r3</sub>	C <sub>r4</sub>	C <sub>r5</sub>	C <sub>r6</sub>
C <sub>r1</sub>	1	1.3333	2	1.8181	2.5	4
C <sub>r2</sub>	0.75	1	0.5714	1.6	2	3.3898
C <sub>r3</sub>	0.5	0.75	1	1.2121	8	1.8867
C <sub>r4</sub>	0.55	0.625	0.825	1	0.4324	0.7619
C <sub>r5</sub>	0.4	0.5	0.125	2.3125	1	3.4782
C <sub>r6</sub>	0.25	0.295	0.53	1.3125	0.2875	1

**Table 2** Originate the total matrix (T) values

Criteria	C <sub>r1</sub>	C <sub>r2</sub>	C <sub>r3</sub>	C <sub>r4</sub>	C <sub>r5</sub>	C <sub>r6</sub>
C <sub>r1</sub>	-0.3727	-0.3993	-0.0292	-1.0907	-0.0766	-0.2188
C <sub>r2</sub>	0.0096	-0.1135	-0.1954	-0.6615	-0.6234	0.1859
C <sub>r3</sub>	-0.3411	-0.2510	-0.8134	-0.0617	0.5502	-0.3611
C <sub>r4</sub>	0.0219	0.0116	-0.0066	-0.6539	-0.1088	-0.6085
C <sub>r5</sub>	-0.0265	-0.1516	-0.0864	0.1623	-0.8098	-0.0328
C <sub>r6</sub>	-0.0758	-0.0802	0.0291	-0.0071	-0.1362	-0.5837

**Step 4:** Work out the sums of the rows and columns of matrix (T) values as shown in Table 3.

**Step 5:** Establish a threshold value ( $\alpha$ )

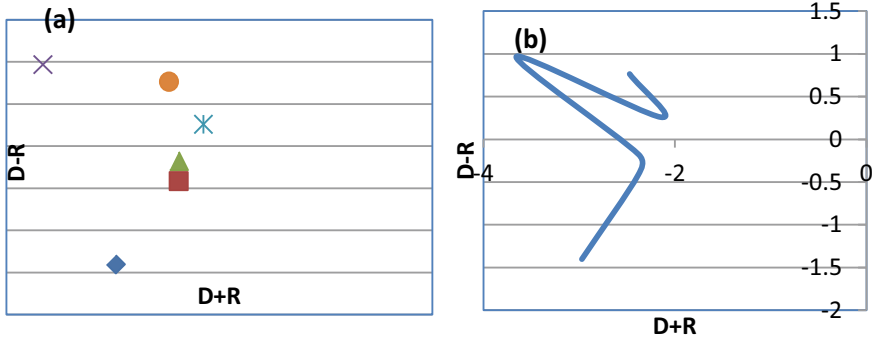
$$\alpha = \frac{\sum_{i=1}^n \sum_{j=1}^n t_{ij} / N}{6} = \frac{-0.3727 + 0.0096 - 0.3411 + 0.0219 - 0.0265 - 0.0758}{6} = -0.1307$$

**Step 6:** Build a cause-and-effect relationship diagrams as shown in Fig. 2a, b. From the Fig. 2a, b observed that the following points are to be highlighted as shown in below.

**Table 3** Work out the sums of rows and columns of matrix T

Criteria↓	D <sub>k</sub>	R <sub>k</sub>	D + R	D - R
Cost	-2.1873	-0.7846	-2.9719	-1.4027
Quality	-1.3983	-0.9840	-2.3823	-0.4143
Technology	-1.2781	-1.1019	-2.3800	-0.1762
Resource consumption	-1.3443	-2.3126	-3.6569	0.9683
Pollution production	-0.9448	-1.2046	-2.1494	0.2598
Management commitment	-0.8539	-1.6190	-2.4729	0.7651





**Fig. 2** Build a cause-and-effect relationship diagrams

- All criteria are interrelated to each other.
- $C_{r4}$ ,  $C_{r5}$ ,  $C_{r6}$  are affecting the other criteria.

**Entropy Method:** Decision matrix values as shown in Table 4.

**Step 1:** Regulate every criterion of matrix values obtained by the below relation as shown in Table 5.

**Table 4** Decision matrix values

Suppliers ↓	Criteria →					
	$C_{r1}$	$C_{r2}$	$C_{r3}$	$C_{r4}$	$C_{r5}$	$C_{r6}$
$S_1$	4	4.75	5.875	5.125	5.125	5.5
$S_2$	5.5	6.25	7	6.625	5.875	6.625
$S_3$	4.75	6.25	7.375	5.875	4	5.5
$S_4$	6.25	5.5	5.875	4	4.75	7
$S_5$	5.125	4.75	6.625	6.25	5.125	4.75

**Table 5** Criterion of matrix values

Suppliers ↓	Criteria →					
	$C_{r1}$	$C_{r2}$	$C_{r3}$	$C_{r4}$	$C_{r5}$	$C_{r6}$
$S_1$	0.3453	0.833	0.3994	0.4055	0.4572	0.4146
$S_2$	0.4748	0.5044	0.4759	0.5241	0.5242	0.4994
$S_3$	0.4101	0.5044	0.5014	0.4648	0.3569	0.4146
$S_4$	0.5396	0.4435	0.3994	0.3164	0.4238	0.5277
$S_5$	0.4425	0.3833	0.4504	0.4945	0.4572	0.3580

**Table 6** Entropy value ( $e_j$ ) of every criteria values

$e_j$	0.4800	0.4818	0.4833	0.4782	0.4816	0.4806
$1 - e_j$	0.5200	0.5182	0.5167	0.5218	0.5184	0.5194

$$r_{ij} = x_{ij} / \sqrt{\sum x_{ij}^2}$$

**Step 2:** Compute the entropy value ( $e_j$ ) of every criteria values obtained by the below relation as shown in Table 6.

$$e_j = -k \sum_{i=1}^m (r_{ij} * \log r_{ij})$$

**Step 3:** Calculate the impartial weight of every criteria values obtained by the below relation as shown in Table 7.

$$w_j = 1 - e_j / \sum_{i=1}^m 1 - e_j$$

**TOPSIS Method:**

**Step 1:** Create an assessment matrix by m alternatives and n criteria's given by  $x_{ij}$ .

**Step 2:** Calculate a regulated matrix

$$r_{ij} = x_{ij} / \sqrt{\sum x_{ij}^2}$$

**Step 3:** Construct the weighted-normalized decision matrix values obtained by the below relation as shown in Table 8.

$$v_{ij} = W_{ij} * r_{ij}$$

**Step 4:** Regulate the + ve and -ve ideal solution values obtained by the below relation as shown in Table 9  $v^+ = \{(\max v_{ij}), (\min v_{ij})\}$   $v^- = \{(\max v_{ij}), (\min v_{ij})\}$ .

**Step 5:** Calculate the separation measure from the + ve and -ve values given by as shown in Table 10.

**Table 7** Entropy value ( $e_j$ ) of every criteria values

$W_j$	0.1669	0.1663	0.1659	0.1675	0.1664	0.1667
-------	--------	--------	--------	--------	--------	--------

**Table 8** Weighted-normalized decision matrix values

Suppliers ↓	Criteria →					
	C <sub>r1</sub>	C <sub>r2</sub>	C <sub>r3</sub>	C <sub>r4</sub>	C <sub>r5</sub>	C <sub>r6</sub>
S <sub>1</sub>	0.0576	0.0637	0.0662	0.0679	0.0760	0.0691
S <sub>2</sub>	0.0792	0.0838	0.0789	0.0877	0.0872	0.0832
S <sub>3</sub>	0.0684	0.0838	0.0831	0.0778	0.0593	0.0691
S <sub>4</sub>	0.0900	0.0737	0.0662	0.0529	0.0705	0.0879
S <sub>5</sub>	0.0738	0.0637	0.0747	0.0828	0.0760	0.0596

**Table 9** The + ve and -ve ideal solution values

$v^+$	0.0576	0.0838	0.0831	0.0877	0.0872	0.0879
$v^-$	0.0900	0.0637	0.0662	0.0529	0.0593	0.0596

**Table 10** Separation measure from the + ve and -ve values

Suppliers ↓	$s_i^+ = \sqrt{\sum(v_{ij} - v_j^+)^2}$	$s_i^- = \sqrt{\sum(v_{ij} - v_j^-)^2}$
S <sub>1</sub>	0.0395	0.0405
S <sub>2</sub>	0.0225	0.0568
S <sub>3</sub>	0.0366	0.0432
S <sub>4</sub>	0.0541	0.0320
S <sub>5</sub>	0.0410	0.0388

**Table 11** Relative closeness to ideal solution and rank sort preference values

$H_i^*$	0.5062	<b>0.7162</b>	0.5413	0.3716	0.4862
Rank	3	<b>1</b>	2	5	4
Supplier	S <sub>1</sub>	<b>S<sub>2</sub></b>	S <sub>3</sub>	S <sub>4</sub>	S <sub>5</sub>

**Step 6:** Determine the relative closeness to ideal solution and rank sort preference values given by as shown in Table 11.

$$C_i^* = s_i^- / (s_i^+ + s_i^-)$$

## 5 Results and Discussions

In this paper, five providers of an assembling organization are assessed depending on the particular standards. The significant distinction among Analytical hierarchy process (AHP) and entropy techniques are pair insightful examination network is

taken into Analytical hierarchy process (AHP) while in Entropy pair astute correlation grid isn't contemplated it straightforwardly ascertains loads on chief evaluations lattice for every rule individual to every provider.

. The positioning utilized for a dynamic issue, including quite a few subjective and quantitative rules and quite a few alternatives. It measures the data content in the characteristic estimations of the other options, subsequently assessing each credits' handiness in distinguishing contrasts in the information. As per results (Table 11),  $S_2$  is the best provider among different providers.

## 6 Conclusion

In the proposed methodology, we used DEMATEL method for identifying cause-and-effect relationships between criteria using pair-wise comparison matrix, i.e., criteria to criteria, and by using Entropy method, weights are calculated. Finally, TOPSIS is used for ranking the suppliers. Among the various methods used for ranking, TOPSIS is one of the efficient methods because only in this method weighted normalization is done for decision-maker rating matrix, which is not done in any of the available ranking methods. Hence from the above evaluation process, we can conclude that the proposed methodology is much more reliable due its additional benefits which are not present in other methodologies for choosing a green supplier.

**Acknowledgements** The author expresses their sincere gratefulness to PSCMR Engineering College, Vijayawada, AP, India, for valuable support to completion of this research work.

## References

1. Sonmez, M.: A review and critique of supplier selection process and practices. Occasional Paper, Loughborough: Business School, vol. 8, no. 2, pp. 520–531 (2006)
2. Chung, C.C., Chao L.C., Lou, S.J.: The establishment of a green supplier selection and guidance mechanism with the ANP and IPA, pp. 6–9 (2016, March)
3. Hashemi, S.H., Karimi, A., Tavana, M.: An integrated green supplier selection approach with analytic network process and improved Grey relational analysis. *Int. J. Prod. Econ.* **159**, 178–191 (2015)
4. Amindoust, A., et al.: Sustainable supplier selection: a ranking model based on fuzzy inference system. *Appl. Soft Comput.* **12**, 1668–1677 (2012)

# Testing the Engine Performance with Cotton Seed Oil Biodiesel



G. Senthilkumar , S. Lakshmi Sankar, and M. Purusothaman

## 1 Introduction

Even though the present-day automobile vehicles may not run completely with bio-fuels, the research on the other side keep on moving in emerging trends [1, 2]. The inclusion of additives remarkably contributes to the emission parameters in varying scales. Biodiesel produced from CSO is considered sustainable in far with other competitive combinations [3–5]. The significant amount of CSO addition to the base fuel impacted on the engine performance in a meaningful means [6, 7].

## 2 Engine Testing Procedure

The engine utilized for research is shown in Fig. 1. The engine was operated with mechanical loading for the measurement of engine performance with the mentioned fuel samples. The readings were taken in such a manner than always steady-state conditions were ensured to minimize the unaccounted errors during the process of reading.

## 3 Result and Discussion

The engine was tested for the power developed at the crank shaft, consumption rate of the tested samples and Thermal Efficiency obtained with pure diesel, B5, B10, B15, B20 and B25 were discussed in the following sections. The BP in diesel engine

---

G. Senthilkumar (✉) · S. L. Sankar · M. Purusothaman  
Sathyabama Institute of Science and Technology, Chennai, India



Fig. 1 Test engine set up

increases with increase in compression ratio [8, 9]. Variation of brake power is given in Fig. 2.

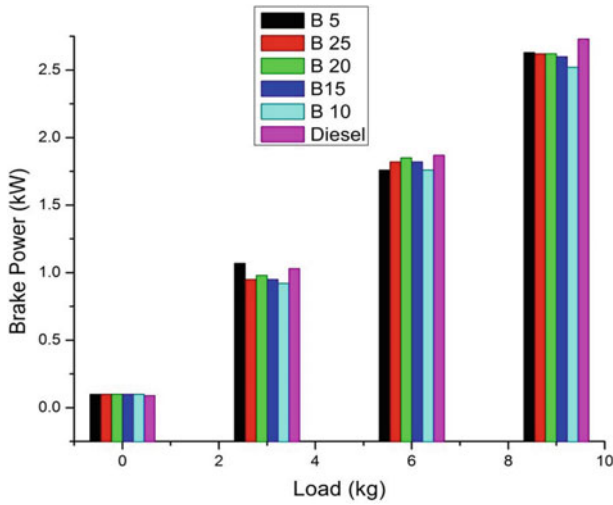


Fig. 2 Brake power with load

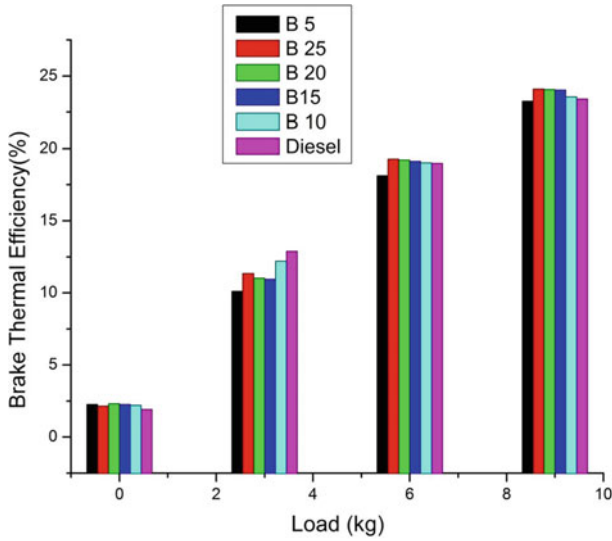


Fig. 3 BTE with load

The biodiesel has good advantages than diesel in terms of brake power. Figure 2 depicted the variation of BP with load for different biodiesel combinations in comparison with the base fuel. At lower load of 3 kg, it was reported that BP for B5 combination was increased by 3.74% due of reduced friction and increased mean effective pressure [15, 16]. At peak load of 9 kg, it was reported that BP for pure diesel was increased by 7.69% as compared to B10 due to the frictional effects [10, 11]. Variation of BTE of diesel, CSO blends (B5, B10, B15, B20, and B25) is given in Fig. 3.

From the above graph, it be evident that the BTE is in direct variation with the input load [12, 13]. The least BTE was obtained at no load conditions. There was 17.24% increase in BTE for B20 for the increase in BP at this load [14]. At 3 kg, 21.42% diminution in BTE was obtained for B10 but at 9 kg, B25 was observed with 2.86% increase in BTE than pure diesel because of increase in BP at this load.

Figure 4 shows the impact on TE by the input power. There was an exponential increase in TE with load. The variation in TE at peak load for all the fuel blends was not having any significant variations [15].

At lower compression ratio, the BSFC was higher due to incomplete combustion. The fuel consumption rate for diesel, CSO combinations is presented in Fig. 5.

The quantity of BSFC decreased drastically with inverse proportion to the input power. Except no load conditions, it was reported that the BSFC was less than 0.5 kg/kW h for all the CSO combinations and pure diesel [5]. At the beginning of combustion, the crank angle was controlled by the injection timing. The characteristics of diesel-based fuels spray mainly influenced by rate of fuel injection, nozzle design and injection pressure. For a specified injection timing, the direct injection

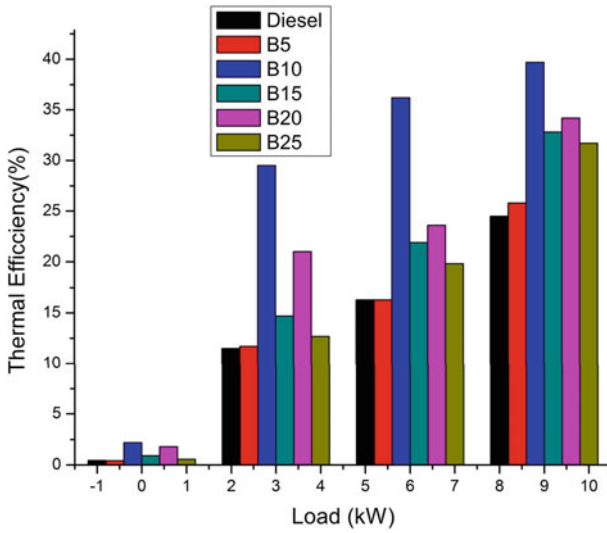


Fig. 4 TE with load

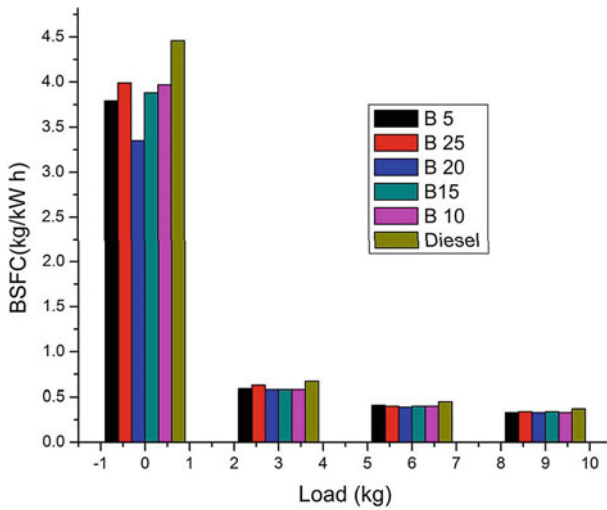


Fig. 5 BSFC with load

diesel engine showed an optimum BSFC at a specific Start of Injection (SOI) with speed and fuel supplied per cycle being fixed.



## 4 Conclusions

The CSO blends contributed significantly in the aspects of performance of engine tested and the following conclusions could be summarized as:

1. The thermal efficiency of CSO blends was increased at an average of 10–15% in comparison with raw fuel.
2. For B5 and B10 CSO blends, the fuel consumption rate was considerably less at the given load conditions.
3. The Presence of DHFA influenced the engine characteristics in a remarkable manner.

## References

1. Lin, C.Y., Chen, L.W.: Engine performance and emission characteristics of three phase diesel emulsions prepared by an ultrasonic emulsification method. *Fuel* **85**, 593–600 (2006)
2. Senthilkumar, G., Kuruvilla, A., Joy, A.: Impact of second-generation alcohols on emission characteristics of biodiesel. *Int. J. Ambient Energy* **39**(6), 547–550 (2017)
3. Senthilkumar, G., Sajin, J.B., Yuvarajan, T., Arunkumar, T.: Evaluation of emission, performance and combustion characteristics of dual fuelled research diesel engine. *Environ. Technol.* **41**(6), 711–718 (2018)
4. Nadeem, M., Rangkuti, C., Anuar, M.R.U., Haq, I., Tan, I.B., Shah, S.S.: Diesel engine performance and emission evaluation using emulsified fuels stabilized by conventional and Gemini surfactants. *Fuel* **85**, 2111–2119 (2006)
5. Selim, M.Y.E., Elfeky, S.M.S.: Effects of diesel/water emulsion on heat flow and thermal loading in a precombustion chamber diesel engine. *Appl. Therm. Eng.* **21**, 1565–1582 (2001)
6. Gobinath, S., Senthilkumar, G., Beemkumar, N.: Air nanobubble-enhanced combustion study using mustard biodiesel in a common rail direct injection engine. *Energy Sources Part A Recovery Utilization Environ. Effects* **41**(15), 180–1816 (2018)
7. Kadota, T., Yamasaki, H.: Recent advances in the combustion of water fuel emulsion. *Prog. Energy Combust. Sci.* **28**, 385–404 (2002)
8. Rameshbabu, A., Senthilkumar, G.: Emission and performance investigation on the effect of nano-additive on neat biodiesel. *Energy Sources, Part A Recovery Utilization Environ. Effects* (2019)
9. Rameshbabu, A., Senthilkumar, G.: Experimental investigation of variable compression ratio (VCR) diesel engine performance and characteristics of emission rate of cotton seed oil biodiesel With  $\text{TiO}_2$  as a biodiesel blend. *Int. J. Mechan. Production Eng. Res. Dev. (IJMPERD)* **10**(2), 1217–1226 (2019)
10. Gaikwad, P.U., Gnanamani, S., Purusothaman, M., Lakshmi Sankar, S., Jeya Jeevahan, J.: Performance evaluation of variable compression ratio engine fueled with bio diesel from waste cooking oil. *Indian J. Environ. Prot.* **40**(1), 110–112 (2020).
11. Gaikwad, P.U., SenthilKumar, G., Bobade, S.N: Performance and emission analysis of waste cooking oil biodiesel added with  $\text{Al}_2\text{O}_3$  nanoadditive using VCR engine. *Int. J. Adv. Sci. Technol.* **28**(20), 122–132 (2019)
12. Gaikwad, P.U., Senthilkumar, G., Bobade, S.: Experimental investigation and performance parameter analysis of biodiesel blend-methyl ester on single cylinder diesel engine. *Springer Lecture Series*, pp. 315–333 (2019)
13. Bobade, S., Gaikwad, P., Senthilkumar, G., Kumbhar, R.: To study the impact of emissions of methyl esters blends in diesel engine. *Springer Lecture Series*, pp. 433–449 (2019)

14. Rameshbabu, G., Senthilkumar, A.P.: Emission study of palm biodiesel and octanol blends in a direct injection diesel engine. *Int. J. Ambient Energy* (2020). <https://doi.org/10.1080/01430750.2020.1852111>
15. Gaikwad, P.U., Senthilkumar, G., Bobade, S.: Experimental and characterization analysis of hybrid biodiesel blends on compression ignition engine. *Int. J. Mechan. Production Eng. Res. Dev. (IJMPERD)* **10**(3), 6477–6488 (2020)

# A Study on the Combustion Characteristics of Dieseline Blend in HCCI Engines



P. S. Srivathsan, Praveen Ramanujam, K. Prasanth,  
and S. Soma Sundaram 

## 1 Introduction

Diesel engines are known for performance and high overall efficiency among the various internal combustion (IC) engines available in the world, for the commercial use. In diesel engines, liquid fuel is injected into the highly compressed air. The injected liquid fuel undergoes atomization, vaporization and finally mixes with air at the molecular level. The mixture then undergoes combustion at spots where the local equivalence ratio falls into the combustible limit. The combustion process takes place until the end of the expansion stroke. The process of mixing controls the engine, so the diesel engines are called as purely mixing controlled [1]. The heterogeneous mixture of the diesel engine leads to the formation of NO<sub>x</sub> as well as soot. The formation of NO<sub>x</sub> is highly inclined to the high-temperature combustion process. The sole way of reducing the NO<sub>x</sub> emissions is to reduce the in-cylinder combustion temperature and increasing the injection pressure [2] without compensating on the performance standards of the engine. The characteristic emission of the diesel engines is the soot emissions caused by lack of mixing of fuel with air molecules. The fuel molecule undergoes gas-phase reactions to form a single ring-like structure (benzene). The benzene undergoes hydrogen abstraction carbon addition (HACA) mechanism to form a highly ringed structure called polycyclic aromatic hydrocarbon

---

P. S. Srivathsan

Department of Chemical Engineering, University of Melbourne, Melbourne, Australia

P. Ramanujam

Department of Mechanical Engineering, Eindhoven University of Technology, Eindhoven, The Netherlands

K. Prasanth

Design Engineer, Hivec Rhino Tech. Pvt. Ltd., Mevalurkuppam, India

S. Soma Sundaram (✉)

Assistant Professor, Department of Mechanical Engineering, NIT Puducherry, Karaikal, India

(PAH) [3, 4] containing around 20–25 carbon atoms. The formed PAH undergoes nucleation, coagulation, condensation and the surface reactions to form a soot particle of 10–100 nm size. The NO<sub>x</sub> and particulate emissions have to be controlled simultaneously. High level of mixing and low combustion temperature can bring down the characteristic emissions of these engines.

Weaver et al. [5] reviewed natural gas/diesel technology and determined potential advantages of high efficiency, lower NO<sub>x</sub> and particulate emissions. The high-energy ignition provided by the diesel fuel rendered a reliable ignition source for the natural gas charge. Most of the fuel was combusted under lean premixed mode, and there was comparatively low flame temperature, probably lower NO<sub>x</sub> emissions in comparison with the diesel. As the combustion took place in premixed mode, soot production was reported to be significantly lower than the diesel engines. The emissions were in lower side using natural gas/diesel, and this technology provided to be an attractive alternative for the pure diesel.

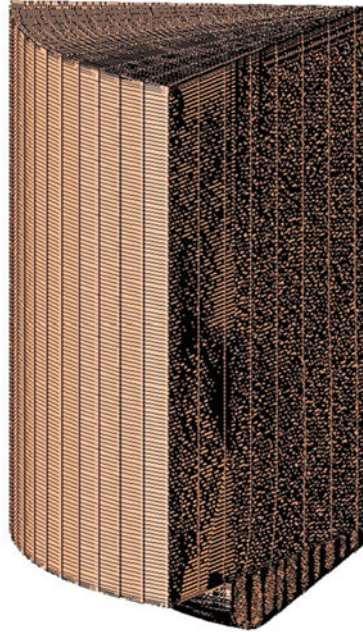
Epping et al. [6] reviewed HCCI engines and their potential benefits on high efficiency and low emissions. In HCCI, the charge was mixed thoroughly leading to low particulate emissions. As in diesel engines, the charge was compression ignited leading to higher efficiency. The concept of using multiple fuels to achieve higher efficiency and lower emissions has been carried out by others too [7, 8]. Generally, the high-reactant fuel would initiate the ignition, which would ignite the homogeneous mixture of the low-reactant fuel. The homogeneous mixing of the low-reactant fuel would result in the lower concentration of soot, while the segmentation of the combustion leads to the reduced combustion temperature and thus reduced NO<sub>x</sub> concentrations.

The main objective of this work is to carry out numerical simulation on the combustion and emission characteristics of a particular fuel blend—gasoline and diesel—as these fuels are commercially available. The gasoline and diesel blends are chosen as the low-reactivity and a high-reactivity fuel, respectively, for the simulation work. The specifications of the engine considered for the simulation are obtained from literature [9]. The results predicted from the simulation of the HCCI engine running under pure diesel fuel have been validated against the experimental results available from literature [9]. In the forthcoming section, CFD results generated from the simulation of gasoline and diesel blends have been portrayed for various gasoline compositions and various air–fuel ratios.

## 2 Simulation Details

A diesel engine operating in HCCI mode possessing a Mexican hat-type combustion chamber has been modelled using Pro/ENGINEER tool. Since the combustion phenomena need to be modelled, a sector mesh has been generated using a tool called STAR-CD. The models have been incorporated in order to capture the in-cylinder physics of the combustion process. The mesh of the sector used for the simulation is portrayed in Fig. 1. The entire cell count for the sector mesh is 0.22 million cells.

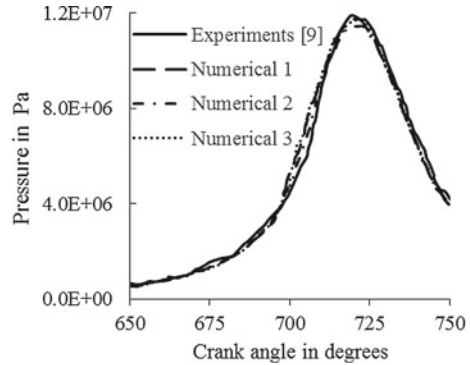
**Fig. 1** Mesh of the computational domain considered for the simulation



The mass, momentum and energy conservation equations [10] are being solved. In addition to the above models, species conservation equations are being modelled to capture the in-cylinder combustion process [11]. The detailed chemistry has been incorporated by the progress variable library model multi-fuel (PVM-MF) to capture the physics of the in-cylinder combustion process [12]. To determine the progress of the combustion process, the combustion progress variable equation is also solved. The output from the PVM library file consists of the derivative of the combustion progress variable which is the source term of solving the transport equation of the progress variable. The turbulence has been modelled using RNG k-epsilon model.

The temporal domain is discretized with varying time-step size. Since the experiments [9] carried out had set the power stroke from  $720^\circ$  to  $900^\circ$  crank angle, simulations have been carried out for a time period between  $650^\circ$  and  $900^\circ$  crank angle. The time period between  $650^\circ$  and  $700^\circ$  crank angle and between  $750^\circ$  and  $900^\circ$  crank angle has been discretized with  $0.05^\circ$ . However, for the time period between crank angles  $700^\circ$  and  $750^\circ$ , where combustion occurs and gradients are steeper, discretization has been done with a  $0.025^\circ$ . To validate the simulation methodology, a simulation, with diesel as the fuel, has been carried out. The variation of the cylinder pressure with respect to the crank angle is plotted in Fig. 2. The results predicted from this study are found to be comparable with the experimentally measured values of Bing Hu [9] with a deviation of 1%. It can be seen that the solution obtained for three different mesh conditions, 0.1, 0.22 and 0.66 million is almost similar. Albeit, there is not much deviation in the results, and the mesh with 0.22 million has been selected for further calculations.

**Fig. 2** Variation of in-cylinder pressure for various crank angle positions



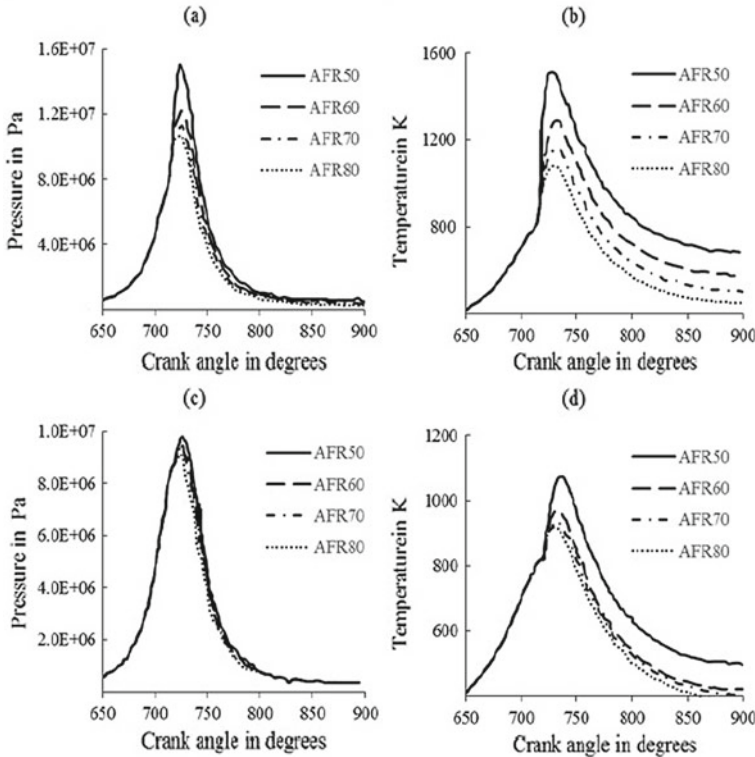
### 3 Results and Discussion

The numerical simulations on the engine have been carried out by varying the percentage of the gasoline in the gasoline–diesel blend from 50% of gasoline to 80% of gasoline. Additionally, the air–fuel ratio of the mixture has also been varied from a value of 50 to 80. The results from the numerical simulation are discussed in detail in this section.

Figure 3 portrays in-cylinder average pressure and temperature for various air–fuel ratios in the order of 50, 60, 70 and 80. From these figures, it can be seen that the average in cylinder pressure and temperature is high for lower air–fuel ratio. In the case of 50% gasoline, as the air–fuel ratio keeps on increasing, the mixture gets leaner and peak temperature and pressure decrease. At lower air–fuel ratio, the diesel fuel takes up the heat reducing the ignition delay. The diesel fuel evaporates and mixes with air forming a combustible mixture, and in turn, the mixture ignites the gasoline air charge. At higher air–fuel ratios, the amount of diesel fuel is very low, and it fails to ignite the gasoline air charge, which results in lower temperature and pressure.

Similar trend is seen when the concentration of the gasoline is increased in the diesel–gasoline blend. In case of 80% gasoline, since the amount of diesel is less, the heat release in the initial combustion process will be low, and this heat will fail to ignite the gasoline mixture. However, in low air–fuel ratio conditions, the overall fuel content is high and combustion occurs. Still, the peak pressure and peak temperature achieved in the 80% gasoline content are less than that of 50% gasoline content. Thus, there is a reduction in the peak pressure and peak temperature as the concentration of the gasoline is increased in the gasoline–diesel blend.

To look into the phenomenon of combustion, the contours of temperature are plotted in a plane for various crank angles in Fig. 4. To get the gasoline air charge ignited, it requires an ignitable mixture. In the case of 50% gasoline, the diesel fuel occupying 50% of the total fuel starts to ignite by taking up the heat and starts to evaporate and mixes with the air molecules and forms an ignitable mixture. Once the diesel mixture gets ignited (Fig. 4a), the flame gets spread into the main combustion



**Fig. 3** Variation of pressure and temperature for various crank angles with gasoline content 50% a–b and 80% c–d at different air–fuel ratios

chamber where the gasoline charge is ready for the combustion process. From Fig. 4a, it can be perceived that the high temperature occurs after 5°–10° after top dead centre, indicating the gasoline mixture has started to combust. The case tends to be similar for other air–fuel ratios.

In this case of 80% gasoline (Fig. 4b), the gasoline content is higher than the previous case. More heat source is required to burn the gasoline charge, but the diesel fuel is low to completely ignite the mixture. The temperature rise by the ignition of this diesel is comparatively lower to that of the previous case. From Fig. 4, it can be further seen that not only the maximum temperature of the 50% gasoline is higher but also the spread of this higher temperature is in larger area. At a crank angle of 20° after the top dead centre, for the case of 50% gasoline, the high temperature is spread throughout the combustion chamber, while in the case of 80% gasoline, it is not so. This would lead to poor combustion characteristics for the blend of 80% gasoline.

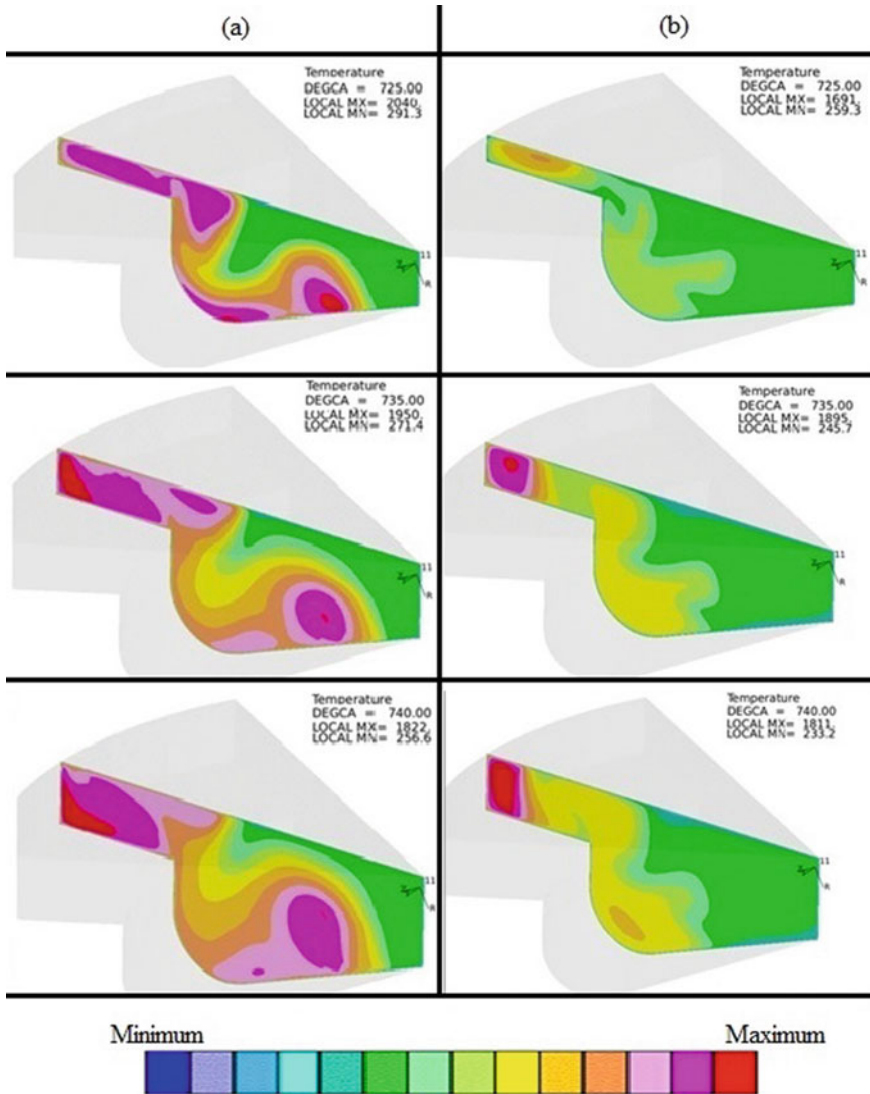


Fig. 4 Contours of temperature in a plane at various crank angles for an air–fuel ratio of 50 with a 50% gasoline and b 80% gasoline

### 4 Conclusion

CFD simulation on gasoline and diesel blend has been performed under HCCI conditions with varying air–fuel ratio and gasoline compositions. Four different air–fuel ratios (50, 60, 70 and 80) were tested for varying gasoline compositions (50%, 60%, 70% and 80%).



On the analysis of the predicted simulation results, the air–fuel ratio and the gasoline content are found to be inversely proportional to each other. Under high gasoline content, in turn, the air–fuel ratio must be low, so that the small amount of diesel content provides the required heat source of the gasoline charge to be combusted. At very low gasoline content, the engine can be operated under lean mixture conditions similar to the normal diesel operating conditions.

In the present work, the effect of swirl on the process of combustion has not been analysed. The inclusion of swirl is bound to enhance better mixing of the diesel and air; at the same time, it can also create localized high-temperature regions. Hence, studies carrying out the effect of swirl in this combustion phenomenon have been considered for future.

## References

1. Heywood, J.B.: *Internal Combustion Engine Fundamentals*. McGraw-Hill Education (1998)
2. Patterson, M. A., Kong, S.-C., Hampson, G. J., Rolf D. Reitz: Modeling the effects of fuel injection characteristics on diesel engine soot and NO<sub>x</sub> emissions, SAE Tech. Paper, 940523 (1994). <https://doi.org/10.4271/940523>
3. Frenklach, M.: Reaction mechanism of soot formation in flames. *Phys. Chem. Chem. Phys.* **4**, 2028–2037 (2002). <https://doi.org/10.1039/b110045a>
4. Frenklach, M., Wang, H.: Detailed modeling of soot particle nucleation and growth. In: *Twenty-Third Symposium (International) on Combustion*, vol 23, pp. 1559–1556 (1991). [https://doi.org/10.1016/S0082-0784\(06\)80426-1](https://doi.org/10.1016/S0082-0784(06)80426-1)
5. Weaver, C.S., Turner, S.H.: Dual fuel natural gas/diesel engines: technology, performance, and emissions. SAE Tech. Paper, 940548 (1994). <https://doi.org/10.4271/940548>
6. Epping, K., Aceves, S., Bechtold R., Dec, J.: The potential of HCCI combustion for high efficiency and low emissions, SAE Tech. Paper 2002–01–1923 (2002). <https://doi.org/10.4271/2002-01-1923>
7. Li, Y., Jia, M., Liu, Y., Xie, M.: Numerical study on the combustion and emission characteristics of a methanol/diesel reactivity controlled compression ignition (RCCI) engine. *App. Energy* **106**, 184–197 (2013). <https://doi.org/10.1016/j.apenergy.2013.01.058>
8. Teoh, Y.H., Masjuki, H.H., Kalam, M.A., How, H.G.: Comparative assessment of performance, emissions and combustion characteristics of gasoline/diesel and gasoline/biodiesel in a dual-fuel engine. *RSC Adv.* **5**, 71608–71619 (2015). <https://doi.org/10.1039/C5RA14624K>
9. Hu, B.: Development of a general diesel combustion model in the context of large eddy simulation, Ph.D. Thesis (1974)
10. Warsi, Z.V.A.: Conservation form of the Navier-Stokes equations in general non steady coordinates. *AIAA J.* **19**, 240–242 (1981). <https://doi.org/10.2514/3.7763>
11. Jayashankara, B., Ganesan, V.: Effect of fuel injection timing and intake pressure on the performance of a DI diesel engine—a parametric study using CFD. *Energy Cons. Manag.* **51**, 1835–1848 (2010). <https://doi.org/10.1016/j.enconman.2009.11.006>
12. Bo, T., Rawat, R., Johns, R., Mauss, F.: Multi-fuel and Mixed-mode IC engine combustion simulation with a detailed chemistry based progress variable library approach. In: *8th International Conference on Modelling and Diagnostics for Advanced Engine Systems*, Paper OS3-6 (2012)

# Comparative Analysis of Transformer Less Bi-directional DC–DC Converter and Conventional Converter for Battery Charging-Discharging Applications



Radhika Swarnkar and R. HariKrishnan

## 1 Introduction

With the development of modern society, fuel and environmental crisis has becoming increasingly important for research. To match the growing demand of electrical power around the world, there is a need to increase electrical power generation. Mainly, grid supply is AC in nature, but nowadays most of the electrical loads like computers, mobile, LEDs consume DC power, so DC microgrid is in main focus due to less losses. Series-parallel batteries combination fulfil the requirement of high gain output voltage. If any imbalance occurs in battery management system that would result in high battery stress, low reliability and battery life becomes short. Earlier, battery size was huge so occupy more space, expensive, heavy weight costly. Therefore, replacement of such batteries combination is necessary. A single battery equipped with new modern design of converter topology is required.

There are many ways for designing a bi-directional dc-dc converter (BDC) which is contend in various literatures [1]. BDC helps in maintaining uninterrupted power supply. Two input and two output BDC converter with six switches for electric vehicle application is discussed in [2]. Voltage stress, losses and complexity are very high due to too many switches used in this topology. H-bridge BDC with feed forward control loop is discussed in [3]. Two back-to-back boost converters with four switches are used for symmetric gain is discussed in [4]. Isolated unidirectional dc converter for fuel cell vehicle [5] allows power flow in only one direction. Isolated converter topology having line frequency transformer when connected with utility grid creates frequency mismatch so, this transformer is replaced by high frequency transformer (HFT). HFT has good properties like galvanic isolation which creates safety, reduced high frequency switching loss and compact size. Isolated BDCs

---

R. Swarnkar · R. HariKrishnan (✉)  
Symbiosis Institute of Technology (SIT), Symbiosis International Deemed University (SIDU),  
Pune 412115, India

of different topologies are compared for aircraft applications in [6]. Transformer less converters are lightweight and cheaper compared to isolated BDC [7]. Non-isolated BDC with inductor capacitor reduces inductor current [8] as compared to conventional switched capacitor and switched inductor. The transformer less BDC restricts the use of high power transfer application equipments because there is no protection between the two high power conversion circuits. In this paper, transformer less BDC with three MOSFET switches [9] is simulated in MATLAB and compared with conventional buck-boost converter. The paper is organised in nine sections as follows. Section 2–4 describes modelling of DC Microgrid and renewable sources of energy. Section 5 and 6 describes different converter topology and its working with battery. In Sect. 7, simulation results are shown. In Sect. 8, comparison of both converters via simulation is shown. In Sect. 9, conclusion of the work is mentioned.

## 2 DC Microgrid

Isolated DC Microgrid has no connection with utility grid and renewable energy sources (RES). Isolated Microgrid output with RES power depends on weather condition and load demand requirement. So, it is necessary to integrate battery with BDC for a stable DC microgrid operation as well as for uninterrupted power supply [10] which is illustrated with connection diagram is depicted in Fig. 1.

## 3 PV Cell Modelling

Photoelectric Effect is the key principle operation of PV cell. In this effect, sun rays of certain wavelength fall on panel which causes current to flow in a metal plate that is connected on top and bottom of the panel. This current and potential difference on PV cell produces required power. PV panel output mainly depends on two factors, i.e. solar irradiance and temperature which is explained by Eq. (1).

$$I_{PH} = I_{SC} + K_t(T_C - T_{ref}) \frac{\lambda}{1000} \quad (1)$$

where,  $I_{PH}$  = photovoltaic current,  $I_{SC}$  = short circuit current,  $T_C$  = ambient temp.,  $T_{ref}$  = reference temp.,  $K_t$  = constant,  $\lambda$  = wavelength.

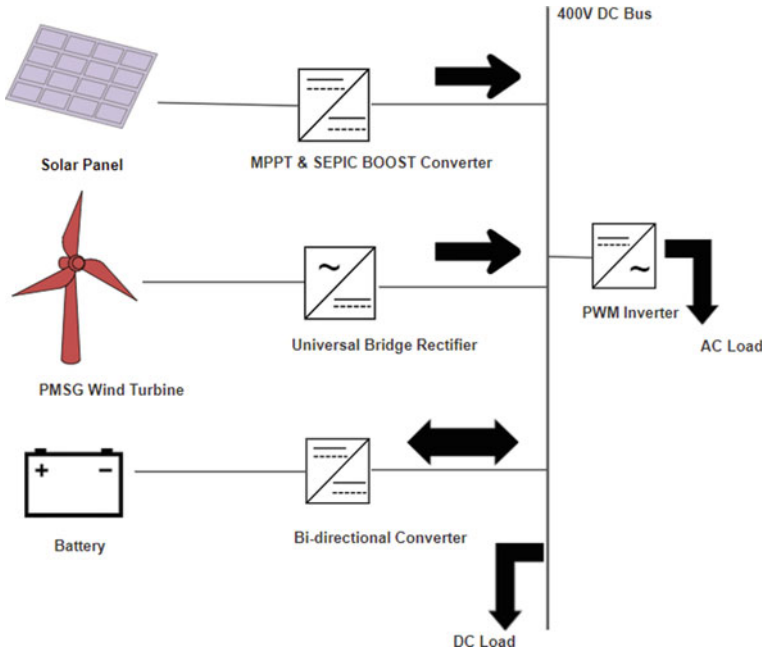


Fig. 1 Connection diagram of DC Microgrid system

### 4 Wind Turbine

Wind is another renewable source of energy through which we can generate electricity with the help of wind turbines. In general, wind passes over the blades generates lift and exerts a turning force. Gearbox helps in maintaining the speed of the generator and converts the kinetic energy into electrical energy. Then, the electrical output power goes to a transformer, which transforms into the appropriate voltage for the power collection system. Equation (2) shows wind power is given by K.E. of flowing air per unit mass.

$$\text{Captured power from wind, } P = \frac{1}{2} \rho A V^3 C_p(\lambda, \beta) \tag{2}$$

where,  $\rho$  = density of air,  $V$  = wind speed,  $A$  = blade area,  $C_p$  = coeff. of power,  $\lambda$  = ratio between speed of blade-tip and speed of wind,  $\beta$  = pitch angle.

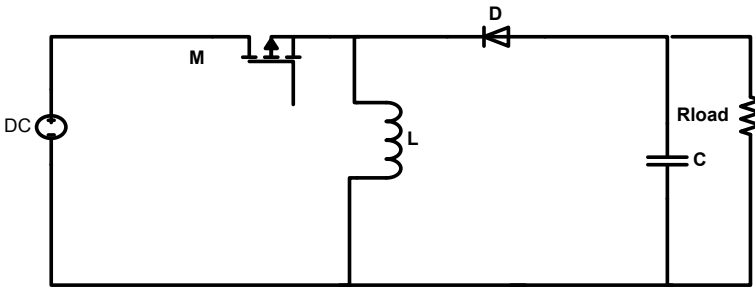


Fig. 2 Conventional buck-boost converter design

### 5 Conventional Buck-Boost Converter

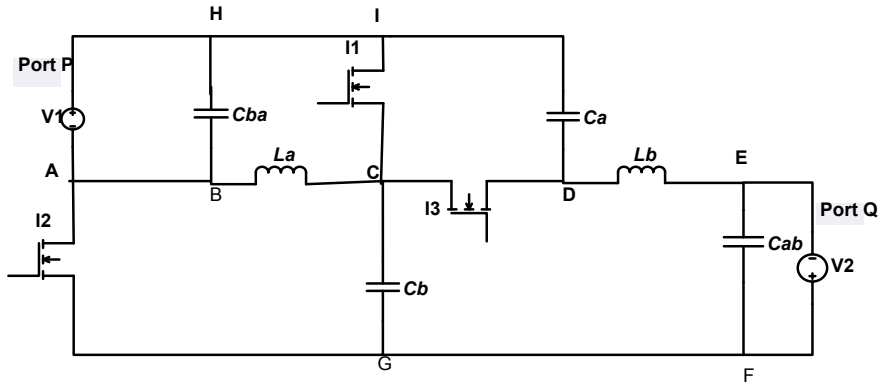
Traditional step-up (boost) and step-down (buck) converter design consists of single MOSFET switch, one inductor and one capacitor and load as shown in Fig. 2. This converter operates as charging mode with duty cycle less than 0.5 and as discharging mode with duty cycle greater than 0.5. Here, 32% pulse width for buck (charging) operation and 80% pulse width for boost (discharging) operation are considered. And inductor value of 1 mH and capacitor value of 50  $\mu$ F are considered. Conventional buck-boost converter is connected with battery for charging and discharging and acts as bi-directional converter. In mode 1, switch is ON current flows through inductor L and stores energy and capacitor discharges its energy to load. In mode 1, circuit behaves as buck converter. In mode 2, when switch is OFF inductor L discharges its stored energy to load and capacitor C. In mode 2, circuit behaves as boost converter.

### 6 Battery Associated with Transformer Less BDC

Connection and operation of transformer less buck-boost converter between battery and load is discussed below. For battery charging application, high step-up/down BDC is used [9].

#### 6.1 Connection Circuit of Transformer Less Converter

The circuit connection diagram of transformer less BDC with battery [9] is shown in Fig. 3. In this circuit, there are three power electronic switches ( $I_1, I_2, I_3$ ), four capacitors ( $C_a, C_b, C_{ab}, C_{ba}$ ), two inductors ( $L_a, L_b$ ) and batteries at port-P and Q. The gate pulse ( $G_1, G_2, G_3$ ) are given to power electronic switches ( $I_1, I_2, I_3$ ), respectively. The converter gate drive circuit decides in which direction power to



**Fig. 3** Circuit connection diagram of Transformer less BDC with battery

flow. Gate pulses  $G_2$  and  $G_3$  are operated simultaneously, whereas  $G_1$  pulse is given alternative to  $G_2$  and  $G_3$  pulses.

### 6.2 Power Flow in P to Q Port

In the boost or discharging mode of operation, P port as battery and Q port as load are considered, and load has a resistance of  $R_1$ . This converter has to be operated always at Zero Voltage Switching (ZVS), otherwise switching loss and sparking may occur across high frequency switches. Two operating states that is State 0 and State 1.

**In State 0:** In this state, Switch  $I_1$  is in ON position, whereas  $I_2$  and  $I_3$  are in OFF position. Current flow from AICBA and IGFEI (see Fig. 3). Equations are derived from this state as shown below:

$$\begin{cases} V_{La} = V_1 \\ V_{Lb} = V_{Ca} - V_2 + V_{Cb} \end{cases} \quad (3)$$

$$\begin{cases} i_{Ca} = i_{Cb} = -I_{Lb} \\ i_{Cab} = I_{Lb} - \frac{V_2}{R_1} \end{cases} \quad (4)$$

**In State 1:** In this state, switch  $I_1$  is in OFF position, whereas switches  $I_2$  and  $I_3$  are in ON position. Current flow in state 1 is from AIDCBA and AGFEDCBA (see Fig. 3), and the following equations are derived as below:

$$\begin{cases} V_{La} = -V_{Cb} = V_1 - V_{Ca} \\ V_{Lb} = -V_2 + V_{Cb} \end{cases} \quad (5)$$

$$\begin{cases} i_{Ca} = i_{Cb} = \frac{I_{La}-I_{Lb}}{2} \\ i_{Cab} = I_{Lb} - \frac{V_2}{R_1} \end{cases} \tag{6}$$

Gain  $G_{PQ}$  is expressed in Eq. (7):

$$G_{PQ} = \frac{V_2}{V_1} = \frac{2D_1}{1 - D_1} \tag{7}$$

### 6.3 Power Flow in Q to P Port

When load demand decreases then automatically voltage across load becomes higher than the source. In this situation, power flow direction is from port-Q to port-P and load acts as source and source acts as load. Switches  $I_2$  and  $I_3$  act as main switch, whereas switch  $I_1$  act as sub switch.

**State 0:** Current flows in state 0 from FGCIDEF and CIHBC (see Fig. 3). Switch  $I_1$  is in ON position, whereas  $I_2$  and  $I_3$  is in OFF position.

**State 1:** Switches  $I_2$  and  $I_3$  are in ON position, whereas  $I_1$  is in OFF position. Current flows from FGABHIDEF and FGCDEF (see Fig. 3). Gain  $G_{QP}$  is shown in Eq. (8).

$$\text{Gain at } Q \text{ to } P \text{ is given by, } G_{QP} = \frac{V_1}{V_2} = \frac{D_2}{2(1 - D_2)} \tag{8}$$

## 7 Simulation Results of BDC Converters

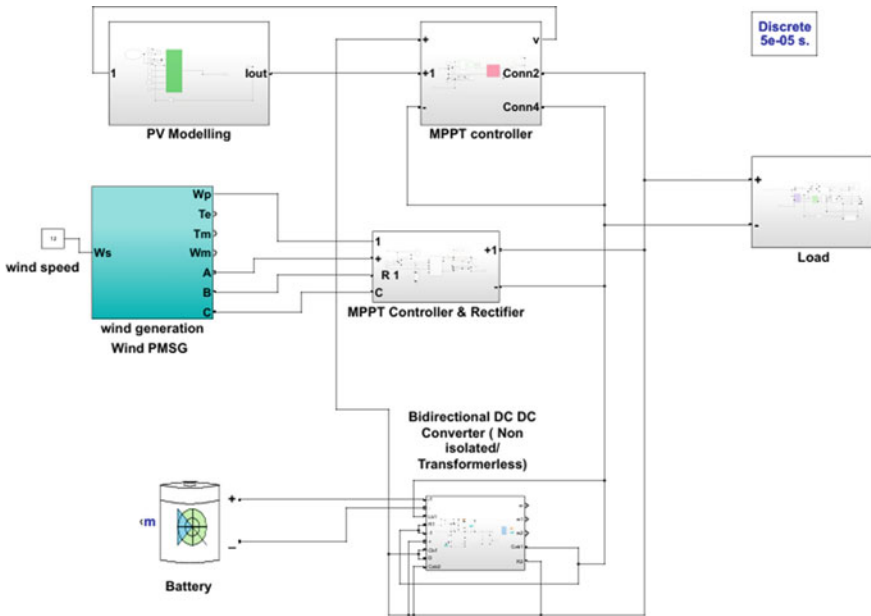
The operation of BDC converter and conventional single switch buck-boost converter is simulated and validated using MATLAB/SIMULINK. The parameters taken for the simulation of the transformer less converter is listed in Table 1.

DC Microgrid integration with battery and BDC is depicted in Fig. 4. Gate pulse for  $I_1$ , ( $I_2$  and  $I_3$ ) for P-Q operation is depicted in Fig. 5. Duty cycle for this P-Q operation is 0.7.

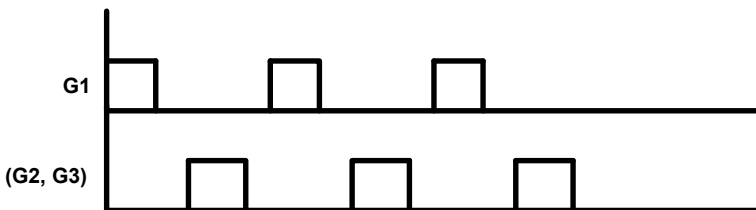
Duty cycle for this Q-P operation is 0.6 is depicted in Fig. 6.

**Table 1** Parameter specifications in proposed converter

S. No	Parameter specification	Value
1	Battery nominal voltage	85 V
2	Inductors $L_1, L_2$	300 $\mu$ H
3	Capacitor $C_1$	2 * 20 $\mu$ F
4	Capacitors $C_2, C_4$	2 * 20 $\mu$ H
5	Capacitor $C_3$	3 * 20 $\mu$ H
6	Switching Freq., $F_s$	100 kHz
7	Resistance $R_1$	100 $\Omega$
8	Resistance $R_2$	0.3 $\Omega$
9	Battery internal resistance	0.0018462 $\Omega$



**Fig. 4** Simulink circuit diagram of DC Microgrid with battery and BDC



**Fig. 5** Gate pulse  $G_1$ ; ( $G_2, G_3$ ) for switches  $I_1, (I_2$  and  $I_3)$  in  $P$  to  $Q$  operation



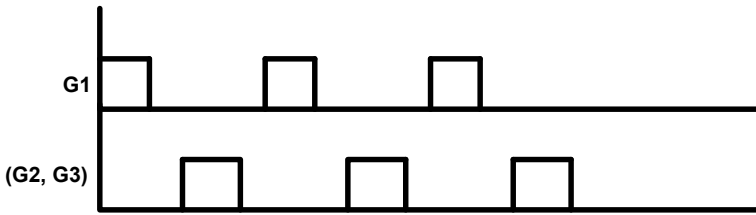


Fig. 6 Gate pulse  $G_1$ ;  $(G_2, G_3)$  for switches  $I_1$ ,  $(I_2$  and  $I_3)$  in  $Q$  to  $P$  operation

### 8 Comparison Between Transformer Less BDC and Conventional Converter

In Fig. 7, transformer less dc-dc converter has output voltage of 550 V in boost mode in comparison with conventional converter which has 450 V. This shows transformer less converter has better response in boost mode. In Fig. 8, transformer less converter has output voltage of 68 V in buck mode in comparison with conventional converter which has 65 V. This shows transformer less converter has little bit poor response in buck mode. The voltage gain of 3 switches dc-dc converter has better result than conventional one, and this is depicted in Figs. 9 and 10. Voltage stress of conventional converter is more in comparison with transformer less BDC during operation.

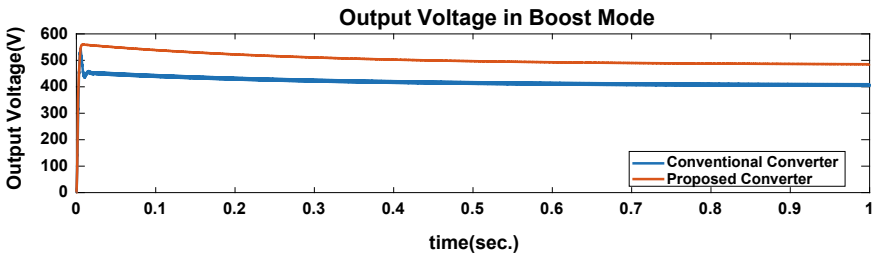


Fig. 7 Output Voltage waveform during P-Q operation (Boost mode or discharging mode)

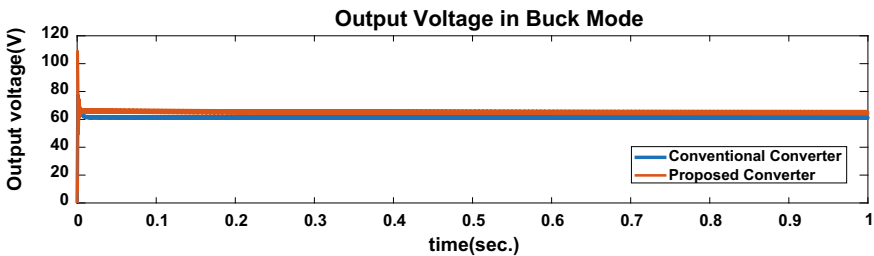


Fig. 8 Output Voltage waveform during Q-P operation (Buck mode or charging mode)

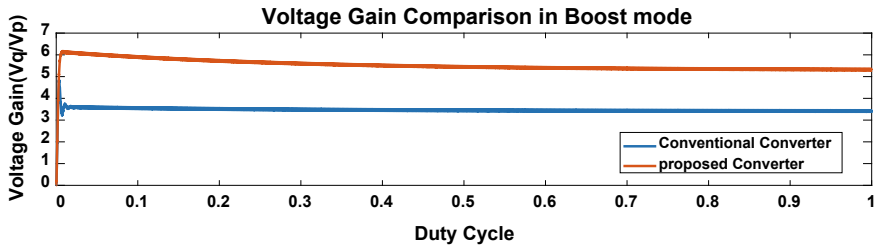


Fig. 9 Voltage gain comparison during boost operation

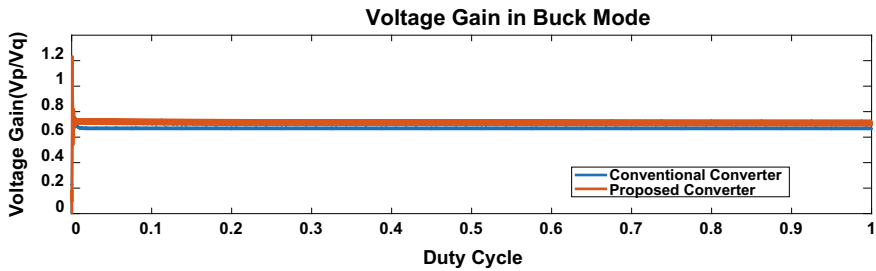


Fig. 10 Voltage gain comparison during buck operation

## 9 Conclusion

Transformer less BDC converter works more smoothly as compared to conventional converter with less voltage stress on switches and high voltage gain in boost mode and buck mode. Both converters are used for isolated DC microgrid application in the present work. Simulation is done on MATLAB and results are extracted from scope. Transformer less BDC can also be used in Electric Vehicle application during regenerative braking power is fed from motor to battery for saving energy. As a future scope, hardware designing and analysis can be done for real time results. Also, different topologies of dc-dc converters for different applications can be considered for future work.

## References

1. Tytelmaier, K.: A review of non-isolated bidirectional DC-DC converters for energy storage systems. In: 2016 II International Young Scientists Forum on Applied Physics and Engineering (YSF), pp. 22–28 (2016)
2. Yahyazadeh, S., Khaleghi M.: A new structure of bidirectional DC-DC converter for electric vehicle applications. In: 2020, 11th power electronics, drive systems, and technologies conference, pp. 1–6 (2020)

3. Han, J.: Dynamic improvement with a feedforward control strategy of bidirectional DC-DC converter for battery charging and discharging. *Electronics* **9**, 1738 (2020)
4. Keshavarzi, M.D.: A novel bidirectional DC-DC converter for dynamic performance enhancement of hybrid AC/DC Microgrid. *Electronics* **9**, 1653 (2020)
5. Farhani, S., Barhoumi, E. M., Bacha, F.: Design and hardware investigation of a new configuration of an isolated DC-DC converter for fuel cell vehicle. *Ain Shams Eng. J.* **12**(1), 591–598 (2021)
6. Rodriguez, A.O.: A survey on bidirectional DC/DC power converter topologies for the future hybrid and all electric aircrafts. *Energies* **13**, 4883 (2020)
7. Chandrasekar, B.: Non-isolated high-gain triple port DC–DC buck-boost converter with positive output voltage for photovoltaic applications. *IEEE Access* **8**, 113,649–113,666 (2020)
8. Shin, S.U.: An analysis of non-isolated DC-DC converter topologies with energy transfer media. *Energies*, **12**, 1468 (2019)
9. Elsayad, N.: Design and implementation of a new transformerless bidirectional DC–DC converter with wide conversion ratios. *IEEE Trans. Ind. Electron.* **66**, 7067–7077 (2018)
10. Kaye, R., Kalam, A.: Non-isolated DC/DC buck/boost converters for off-grid hybrid renewable system. In: 2019, 29th Australasian universities power engineering conference (2019)

# Comparative Enviro-Economic Analysis of Transparent Water Heating Systems and Conventional Systems



Kirti Tewari and Rahul Dev

## Abbreviations

Abp	Area of black paint ( $m^2$ )
As	Area of south wall of storage tank ( $m^2$ )
Atop	Area of top wall of storage tank ( $m^2$ )
AE	Area of east wall of storage tank ( $m^2$ )
Aw	Area of west wall of storage tank ( $m^2$ )
It(t)	Intensity of solar radiation on collector ( $W/m^2$ )
Is(t)	Intensity of solar radiation on south wall of tank ( $W/m^2$ )
IE(t)	Intensity of solar radiation on east wall of tank ( $W/m^2$ )
Iw(t)	Intensity of solar radiation on west wall of tank ( $W/m^2$ )
Itop(t)	Intensity of solar radiation on top wall of tank ( $W/m^2$ )
M	Mass flow rate of water (kg/s)
Mtw	Total mass of water in all collector tube (kg)
MTW	Water mass in tank (kg)
$n$	Life of MDSWH
Nt	No of collector tubes
Rii	Inner radius of inner tube (m)
Rio	Outer radius of inner tube (m)
Roi	Inner radius of outer tube (m)
Roo	Outer radius of outer tube (m)

---

K. Tewari (✉)

Department of Mechanical Engineering, NIT Sikkim, Ravangla, South Sikkim 737139, India  
e-mail: [kirti@nitsikkim.ac.in](mailto:kirti@nitsikkim.ac.in)

R. Dev

Department of Mechanical Engineering, MNNIT Allahabad, Prayagraj, Uttar Pradesh 211004, India  
e-mail: [rahuldsurya@mnnit.ac.in](mailto:rahuldsurya@mnnit.ac.in)

T <sub>cw</sub>	Water temperature in tank (°C)
T <sub>hw</sub>	Water temperature in tube (°C)
T <sub>hwo</sub>	Initial water temperature in tubes of collector (°C)
T <sub>cwo</sub>	Initial water temperature in storage tank (°C)
T <sub>a</sub>	Ambient temperature (°C)
C/C <sub>w</sub>	Specific heat of water (J/kg K)
E <sub>out-En</sub>	Solar energy output per annum (kWh)
E <sub>out-Ex</sub>	Solar exergy output per annum (kWh)
E <sub>solar</sub>	Solar energy retrieved by the system per annum (kWh)

## 1 Introduction

According to the annual report of Government of India-Ministry of New and Renewable Energy (2015–2016), there is withal a gap of 7006 MW between availability and requirement of power which can be fulfilled by the renewable energy resources. The solar energy can serve as a divine source of meeting energy demands as the world energy demand for power is 15 TW, and the 120,000 TW power can be captured from solar energy only (estimates from DOE report “Solar Energy Utilization”) which is far more than the energy requirement of the world [1].

Solar water heating is one of the solar technologies attaining explicit attention as it has the potential to provide 70% of the commercial as well as residential sanitary hot water demand [2]. The present study aims at grabbing the maximum possible amount of solar radiation falling on the solar water collector and utilizes it to heat the water using an insulating transparent material. Insulating transparent materials offer heat flow resistance and alleviate the light transmission and have very low thermal conductivity [3]. Kaushik and Sumathy [4], Plazer [5], Berardi [6] and Hollands et al. [7] carried out detailed study on the optical properties of these materials. Some of the transparent insulating materials are mineral wool, glass fiber, calcium silicate and alumina silicate having the thermal conductivity of 0.0325, 0.035, 0.0407 and 0.057, respectively [8]. From literature survey, it is equally evident that the use of transparent insulating materials tank improves the efficiency of water heating systems. These material plays a vital role in increasing the daylight performance and solar gain [9]. However, economic performance and environmental benefits of these material need further investigation. Recently, Tewari and Dev [10] presented a novel type of solar water heater named as modified domestic solar water heater (MDSWH) made of transparent insulating materials (acrylic, FRP and thermocol) integrated with the glass-to glass PV module, having a flat absorbing area as FPC and evacuated tubes and tank (as ETC). Trapezoidal-shaped storage tank instead of cylindrical shape increases the surface area-to-volume ratio. In present study, glass-to-glass PV module has been removed from the system to make it even more price-friendly and environment-friendly for the domestic uses and to provide even more

elevated water temperature. The water heater is named as thermocol-FRP-insulated domestic solar water heating system (TDSWHS).

## 2 Thermocol-FRP-Insulated Solar Water Heating System

As discussed in previous section, TDSWHS is a combination of the transparent storage tank and a modified solar collector (shown in Fig. 1), installed at the rooftop of the solar energy laboratory of the MED, MNNIT Allahabad, Allahabad, UP, India, facing due south. The design of TDSWHS is similar to the MDSWHS with PV module, only the solar module is removed and hence the mechanism involved in the heating of water is same (can be referred from Tewari and Dev [10]). Installation of PV module results in the reduced solar fraction by an average of 58.19% from top surface and 25.41% from the storage tank as shown in Fig. (2a–b).

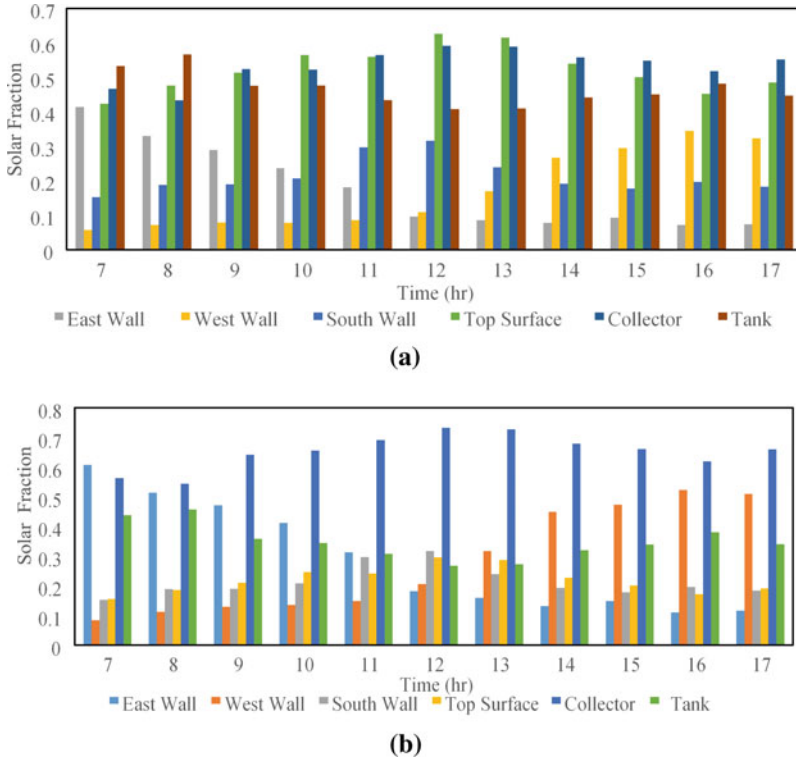
Tewari and Dev [10] carried out detailed mathematical modeling to carry out the theoretical performance analysis. Following this method, equations for the water temperature in TDSWHS have been calculated as.

**Temperature of water in storage tank:**

$$T_{tw} = \frac{1}{\beta^+ - \beta^-} \left[ \frac{1}{g_1(t)} \left\{ \frac{(1 - e^{-c^+t})}{c^+} - \frac{(1 - e^{-c^-t})}{c^-} \right\} + \frac{1}{g_2(t)} \left\{ \frac{\beta^+(1 - e^{-c^+t})}{c^+} - \frac{\beta^-(1 - e^{-c^-t})}{c^-} \right\} \right]$$



**Fig. 1** Photograph of TDSWHS installed at MNNIT Allahabad



**Fig. 2 a** Hourly variation of solar fractions at different walls of tank and collector for TDSWHS. **b** Hourly variation of solar fractions at different walls of tank and collector for MDSWHS with PV module

$$+ Tcwo(e^{-c^+t} - e^{-c^-t}) + Ttwo(\beta^+e^{-c^+t} - \beta^-e^{-c^-t}) \tag{1}$$

**Temperature of water in collector tube:**

$$T_{cw} = \frac{1}{\beta^+ - \beta^-} \left[ \frac{1}{g_1(t)} \left\{ \frac{\beta^+(1 - e^{-c^-t})}{c^-} - \frac{\beta^-(1 - e^{-c^+t})}{c^+} \right\} + \beta^+ \beta^- \frac{1}{g_2(t)} \left\{ \frac{(1 - e^{-c^-t})}{c^-} - \frac{(1 - e^{-c^+t})}{c^+} \right\} + Tcwo(\beta^+e^{-c^-t} - \beta^-e^{-c^+t}) + \beta^+ \beta^- Ttwo(e^{-c^-t} - e^{-c^+t}) \right] \tag{2}$$

Various intermediate expressions for thermal modeling of TDSWHS can be referred from Tewari and Dev [10].

### 2.1 Instantaneous thermal efficiency of TDSWHS

$$\eta_{th} = \frac{Q_{thermal}}{\sum (AI)} = \frac{mC_W(T_{tw} - T_{two})}{A_{bp}I_t(t) + A_S I_S(t) + A_{Top} I_{Top}(t) + A_E I_E(t) + A_W I_W(t)} \tag{3}$$

The formulation of output thermal energy is calculated as shown in Eq. (4)

$$Q_{thermal} = mC(T_{tw} - T_{two}) \tag{4}$$

### 2.2 Exergy Analysis

Exergy balance of TDSWHS can be written as follows:

$$\begin{aligned} & \text{Exergy inflow} \left( \sum \text{Ex}_{in} \right) - \text{Exergy outflow} \left( \sum \text{Ex}_{out} \right) \\ & = \text{Exergy destroyed} \left( \sum \text{Ex}_d \right) \end{aligned}$$

The solar radiant exergy equation derived by Petela [11] has been used to calculate the input solar radiation:

$$\text{Ex}_{in} = AI \left[ 1 - \frac{4}{3} \left( \frac{T_a}{T_s} \right) + \frac{1}{3} \left( \frac{T_a}{T_s} \right)^4 \right] \tag{5}$$

$$\text{Ex}_{out} = Q_{thermal} \left( 1 - \frac{T_a + 273}{T_o + 273} \right) \tag{6}$$

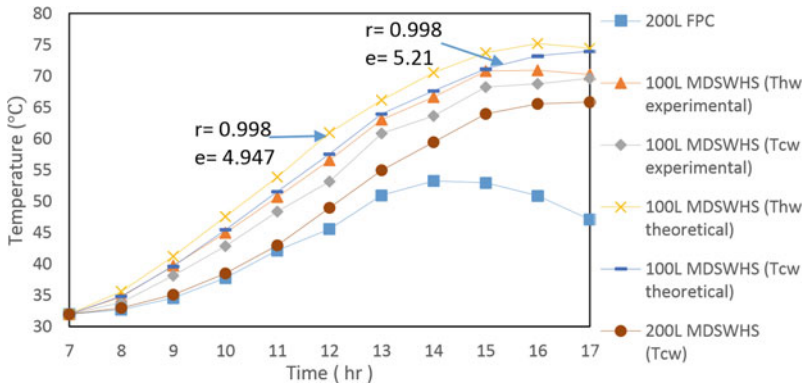
where  $T_s$  denotes the sun temperature (K), and second law efficiency has been evaluated by:

$$\eta_{ex} = 1 - (\text{Ex}_d) / (\text{Ex}_{in}) \tag{7}$$

## 3 Comparison of TDSWHS with Conventional System (FPC)

Figure 3 validates the theoretical results obtained from the mathematical modeling with the experimental results for a particular day of May 2017. Maximum temperatures of 75.3, 74, 70.9 and 68.8 °C have been obtained for the theoretical hot water temperature of the tube, theoretical storage tank water temperature, the experimental





**Fig. 3** Comparison of water temperatures in the tubes and the storage tank of TDSWHS of 100L and 200L with the conventional system of 200L for a particular day of May 2017 on hourly basis

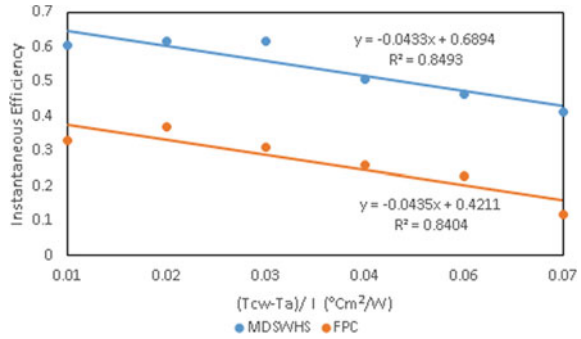
hot water temperature of the tube and experimental storage tank water temperature, respectively. The figure also compares the performance of TDSWHS with the 200L conventional FPC (Model No TEZE02008—TATA BP SOLAR INDIA LIMITED) installed there. The temperature of water in the storage tank of TDSWHS of 200L has been inferred from the experimental results obtained for 100L TDSWHS, and the figure suggests that the heat collection period of FPC is smaller than TDSWHS. The heating continued till 17:00 h in TDSWHS it, while in FPC, heating get suspended after 14:00 h. The floor covered area for the same capacity of FPC and TDSWHS is 2.16 and 1.22 m<sup>2</sup>, which indicates that covered floor area has been saved by 43.5% in TDSWHS. Moreover, the overall heat collection area has been increased by making use of transparent storage tank and collector for heating of water. In this manner, it can be concluded that heat collection area (collector and storage tank), as well as heat collection time, has been increased in TDSWHS, and the heat losses (inherent in conventional designs) have been minimized to a greater extent as the temperature is maintained at more elevated temperature than FPC all day long. For obtaining the same temperature of water, FPC lags behind the TDSWHS by approximately 1:30 h–2:00 h for the same capacity of water.

The maximum temperature of 52.5 °C has been obtained experimentally at 16:00 h. Theoretical and experimental thermal energy gain and efficiency has also been compared for summer as well as winter months and listed in Table 1. Results have been found to be satisfactory with the error in the range of 3.9–7.2% for thermal energy gain and efficiency. The linear characteristic curve for TDSWHS and the

**Table 1** Thermal energy gain and efficiency of TDSWHS

Date	Parameters of TDSWHS	Experimental	Theoretical	Error %
05/05/17	Thermal energy gain (kWh), $\eta$ (%)	4.72, 79.81	5.06, 83.71	7.2, 4.8
10/12/17	Thermal energy gain (kWh), $\eta$ (%)	3.92, 60.52	4.20, 62.86	7.1, 3.9

**Fig. 4** Comparison of instantaneous efficiency of TDSWHS with the conventional system



conventional solar water heater have been plotted in Fig. 4, and equation for their correlation has been developed. The slope is negative depicting the heat loss rate of the collector [12].

TDSWHS has been compared with FRP, and former is obtained to have better results. Now, the TDSWHS is being compared with MDSWH with PV module [10] as shown in Table 2. It can be concluded from the table that with same water carrying capacity and floor area requirement, TDSWHS producing water 5.7 and 5.0 °C hotter in collector tubes and storage tank, respectively, than MDSWH with PV module with 27.1% lower cost of the setup. The embodied energy of TDSWHS is also 500 kWh lower than MDSWH with PV module which clearly indicates that TDSWHS consumes lower energy and considering the degrading condition of atmosphere due to the emission of carbon and other pollutants, the importance of embodied energy cannot be dismissed. The thermal efficiency of TDSWHS is also higher. Thus, it can be considered as most environment friendly setup which is providing hotter water, higher thermal efficiency and lower cost.

**Table 2** Comparative study of MDSWH with PV module and TDSWHS

Parameters	MDSWH	TDSWHS
Capacity of tank	100L	100L
Tube radius	0.01 m	0.01 m
Volume of water in one tube	0.000314m <sup>3</sup>	0.000314m <sup>3</sup>
Collector area	0.61 m <sup>2</sup>	0.61m <sup>2</sup>
Maximum water temperature in tubes	75.7 °C	81.4 °C
Maximum water temperature in tank	74.7 °C	79.7 °C
Thermal energy gain ( <i>Q</i> <sub>thermal</sub> )	821.1 kWh	836.83 kWh
Thermal exergy ( <i>Ex</i> ) <sub>sssss</sub>	109.56 kWh	100.3 kWh
Cost	Rs. 22,130	Rs. 17,130
Embodied energy	1213.04 kWh	713.04 kWh
Carbon emission per year	1.854 tCO <sub>2</sub> e	1.707 tCO <sub>2</sub> e

### 4 Enviro-economic (Environmental Cost) Analysis

For 1 kWh electricity production from coal, 0.982 kg of CO<sub>2</sub> emits into the environment [13]. However, considering the losses occurring due to transmission and distribution and poor domestic appliances losses to be 40% and 20% respectively, the CO<sub>2</sub> emission becomes 2.04 kg and on annual basis of energy, CO<sub>2</sub> mitigation can be stated as:

$$\varphi_{CO_2} = \frac{\psi_{CO_2} \times Q_{thermal}}{1000} = \frac{2.04 \times 836.83}{1000} = 1.707 \text{ tCO}_2\text{e} \tag{8}$$

And in terms of exergy,

$$\varphi_{CO_2} = \frac{\psi_{CO_2} \times Ex}{1000} = \frac{2.04 \times 100.3}{1000} = 0.205 \text{ tCO}_2\text{e} \tag{9}$$

$$J_{CO_2} = \varphi_{CO_2} \times j_{CO_2} \tag{10}$$

where  $\psi_{CO_2}$  is CO<sub>2</sub> equivalent intensity for generation of electricity and  $J_{CO_2}$  is Carbon credit earned.

While  $j_{CO_2}$  is the price of one tone of CO<sub>2</sub>, i.e., 14.5 US \$ [14]. Annual energy production cost in the terms of energy and exergy for TDSWHS has been found to be Rs. 4184.15 and Rs. 419.15, respectively. CO<sub>2</sub> emission reductions in tons per years are 1.707 and 0.205 as shown in Table 3. Environmental cost for 15 years of life span has been calculated in two different ways (i) As per Elzen Den et al. [15], the international carbon price varies from 13 \$/tCO<sub>2</sub> to 16 \$/tCO<sub>2</sub> for the low subscription and high subscription scenario. Thus, following Hakan et al. [16], the intermediate value of 14.5 \$/tCO<sub>2</sub> has been taken. As per the current carbon price, i.e., 13.50 euro per ton on 11/05/2018. The cost has been calculated as Rs. 24,964.36 (371.27 US \$) and Rs.27, 753 (412.55 US \$) for case (i) and (ii) respectively in the terms of energy and Rs. 2998.06 (44.58 US \$) and Rs. 3333.04 (41.51 US \$) in the terms of exergy.

**Table 3** Enviro-economic analysis of TDSWHS on the exergy and energy basis

		Thermal energy	Thermal exergy
Annual energy production cost		Rs. 4184.15	Rs. 419.15
CO <sub>2</sub> mitigation (tones/year)		1.707	0.205
Environmental cost (carbon credit) for 15 years of lifespan	$j_{CO_2} j_{CO_2} = 14.5 \text{ US\$} = 13.50 \text{ euro}$	Rs.24,964.36 (371.27 US\$)	Rs.2998.06 (44.58 US\$)
	On 11/5/2018	Rs.27,753 (412.55 US\$)	Rs.3,333.04 (41.51 US\$)

## 5 Conclusions

1. TDSWHS performs better than MDSWHS with PV module as well as FPC,
  - (a) Under same weather conditions, TDSWHS provides 12.9 and 5 °C higher-temperature water than FPC and MDSWHS with PV module, respectively.
  - (b) TDSWHS is observed to have higher solar fraction (34.1%), water temperature than MDSWHS.
  - (c) TDSWHS abates the carbon emission into the environment by 0.147 tCO<sub>2</sub> e per year than MDSWH with PV module. CO<sub>2</sub> mitigation in the terms of energy and exergy has been found to be 1.707 and 0.205 tons per years respectively.
  - (d) The setup cost and embodied energy of TDSWHS are 27.1% and 41.2% lower than MDSWHS with PV.
2. TDSWHS provides maximum water temperature of 68.8 and 70.9 °C in the storage tank and collector tubes, respectively, for 100L capacity.
3. Net energy and exergy gain of 836.83 kWh and 100.3 kWh, respectively, have been obtained for the year 2017.

## References

1. Ummadisisingua, A., Soni, M.S.: Concentrating solar power—technology, potential and policy in India. *Renew. Sustain. Energy Rev.* **15**, 5169–5175 (2011)
2. Zhang, X., You, S., Xu, W., Wang, M., He, T., Zheng, X.: Experimental investigation of the higher coefficient of thermal performance for water-in-glass evacuated tube solar water heaters in China. *Energy Convers. Manag.* **78**, 386–392 (2014)
3. Shukla, R., Sumathy, K., Erickson, P., Gong, J.: Recent advances in the solar water heating systems: a review. *Renew. Sust. Energy. Rev.* **19**, 173–190 (2013)
4. Kaushika, N.D., Sumathy, K.: Solar transparent insulation materials: a review. *Renew. Sustain. Energy Rev.* **7**, 317–351 (2003)
5. Plazer, W.J.: Solar transmittance of transparent insulation materials. *Sol. Energy Mater.* **16**, 176–186 (1987)
6. Berardi, U.: The development of a monolithic aerogel glazed window for an energy retrofitting project. *Appl. Energy* **154**, 603–615 (2015)
7. Hollands, K.G.T., Marshal, K.N., Wedel, R.K.: An approximate equation for predicting the solar transmittance of transparent honeycombs. *Sol. Energy* **21**, 231–236 (1978)
8. Chaurasia, P.B.L., Twidell, J.: Collector cum storage solar water heating systems with and without transparent insulation material. *Int. J. Solar Energy* **70**(5), 403–416 (2001)
9. Tewari, K., Dev, R.: Performance analysis of modified solar water heating system for climatic condition of Allahabad, India. *Int. J. Electr. Comput. Energetic Electron. Commun. Eng. Paris. Open Environ Sci J.* **10**, 73 (2016)
10. Tewari, K., Dev, R.: Exergy, environmental and economic analysis of modified domestic solar water heater with glass-to-glass PV module. *Energy* **170**, 1130–1150 (2019)
11. Petela, R.: Exergy of undiluted thermal radiation. *Sol Energy* **74**, 469–488 (2003)
12. Tiwari, S., Tiwari, G.N.: Thermal analysis of photovoltaic-thermal (PVT) single slope roof integrated greenhouse solar dryer. *Sol Energy* **138**, 128–136 (2016)

13. Caliskan, H., Dincer, I., Hepbasli, A.: Exergoeconomic, enviroeconomic and sustainability analyses of a novel air cooler. *Energy Build.* **55**, 747–756 (2012)
14. Agrawal, S., Tiwari, G.N.: Enviroeconomic analysis and energy matrices of glazed hybrid photovoltaic thermal module air collector. *Sol. Energy* **92**, 139–146 (2013)
15. Elzen, M.G.J.D., Hof, A.D., Beltran, A.M., Grassi, G., Roelfsema, M., Ruijven, B.V.: The Copenhagen accord: abatement costs and carbon prices resulting from the submissions. *Environ Sci Policy* **14**, 28–39 (2011)
16. Hakan, C., Ibrahim, D., Arif, H.: Exergoeconomic, enviroeconomic and sustainability analyses of a novel air cooler. *Energy Build.* **55**, 747–756 (2012)

# Harvesting Electric Energy from Waste Vibrations of an Electric Motor Using the Piezoelectric Principle



Nitin Yadav and Rajesh Kumar 

## 1 Introduction

The conventional sources of energy are decreasing continuously, and the world's energy requirements are increasing exponentially because of population, higher comfort level requirements, and the human race in automation and technology. The continuous increase in these requirements of power prompted the development of systems that can generate energy from waste. Efforts are continuously made to decrease the wastage or reuse the waste energy (if hard to stop wastage) for some useful purpose.

Every dynamic machine and even static structure have some vibration at its structure and base [1]. This vibration is absorbed by the dampers or directly passed to the foundation. These vibrations are not desired in many cases. In condition monitoring, the level of vibration represents the condition of the system [2–4]. These vibration studies include the sensors which convert vibrations into an electric signal. Some of these sensors use a piezoelectric element for sensing the vibrations [5–8]. Piezoelectric elements are the special type of materials that produce an electric potential when they get deformed because of mechanical force or vibrations [9–11]. So, piezoelectric elements are used at many places (e.g., human body [12–16], fluid flow [17–21], and vehicles [22–27]) for energy harvesting. If used appropriately, the piezoelectric elements can be used in harvesting a significant amount of electricity from the vibration of machines.

In the present work, the harvesting of electric energy from a vibrating motor has been demonstrated using the piezoelectric element. The piezoelectric element is mounted at the base of the electric motor under the idle running and loaded conditions

---

N. Yadav (✉) · R. Kumar

Precision Metrology Laboratory, Department of Mechanical Engineering, Sant Longowal Institute of Engineering and Technology, Longowal 148106, India

e-mail: [nitin\\_pme1803@sliet.ac.in](mailto:nitin_pme1803@sliet.ac.in)

of a motor by attaching a grain-grinding machine and a chaff cutter. The power output from a single piezoelectric element is small. So, two piezoelectric elements are used to generate more electric output. Further, a study has been conducted in a laboratory environment to analyze the effect of single piezoelectric and two piezoelectric elements on total power output.

## 2 Experimental Setup

For generating electric energy from motor vibrations, a diaphragm-type piezoelectric element lead zirconate titanate (PZT) with nickel alloy electrode of diameter 27 mm (shown in Fig. 1) is placed between the electric motor base and its foundation. The output from the piezoelectric element is alternating current (A.C.) which is converted into direct current (D.C.) using a full-bridge rectifier circuit. The output of the full-bridge rectifier is measured using a multimeter. Figure 2 shows the schematic diagram of a complete system under field conditions whose pictorial view is shown in Fig. 3.

An experimental setup as shown in Fig. 4 was designed to conduct experiments in laboratory conditions. A specially designed fixed structure holds the piezoelectric element. The piezoelectric element is excited (vibrated) with the help of a mini shaker (model K2004E01, make: TMS). The mini shaker has a striker which will

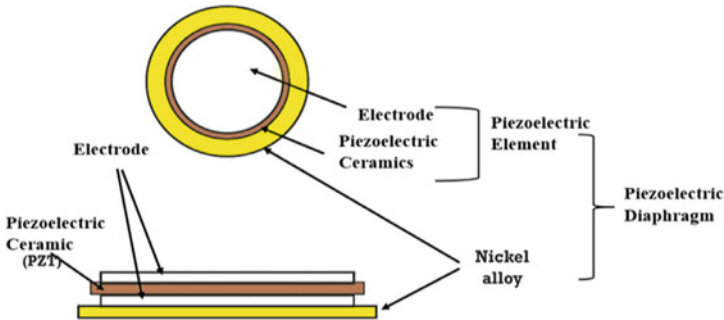
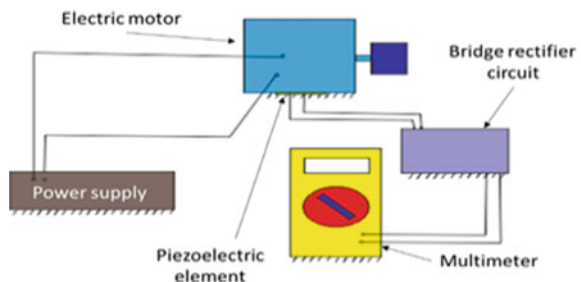
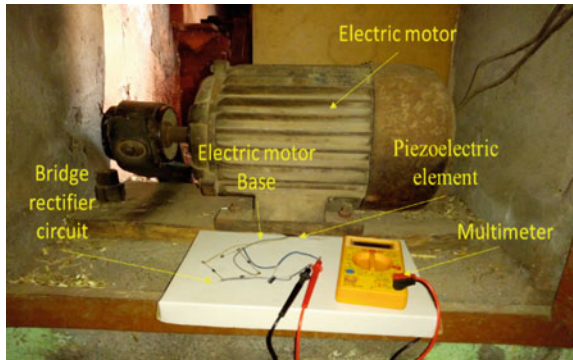


Fig. 1 Schematic of the piezoelectric diaphragm

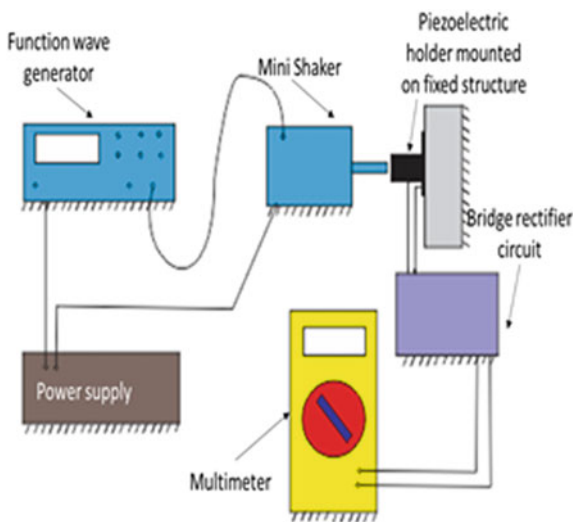
Fig. 2 Schematic diagram of the piezoelectric energy harvesting from a vibrating motor



**Fig. 3** Actual picture of piezoelectric energy-harvesting system for motor



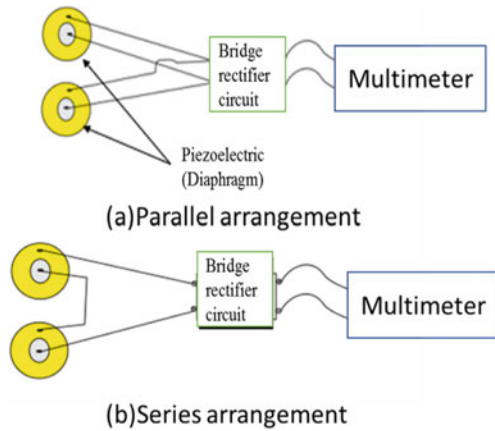
**Fig. 4** Schematic diagram of the piezoelectric energy-harvesting system for series and parallel study in the laboratory



strike the piezoelectric element at different frequency and amplitude. The amplitude and frequency of mini shaker vibration depend on the signal supplied by the function generator. This function generator (model no. 33220A, make: Agilent) is capable of generating sinusoidal, step, and different noise waves. The sinusoidal wave with a frequency range of 1–20 Hz and amplitude range of 10–150mVpp is supplied to the mini shaker in the present work. The classic bridge rectifier and the multimeter are connected to read the output. Schematics of different combinations (series and parallel connections) of two piezoelectric elements are shown in Fig. 5.



**Fig. 5** Systematic diagram of series and parallel arrangements of piezoelectric elements



### 3 Results, Output and Discussion

Results are obtained from vibrating electric motor by placing piezoelectric element(s) between base and foundation under three conditions (a) idle running motor, (b) motor under a load of a grain-grinding machine, and (c) motor under a load of a chaff cutter machine. The output from the piezoelectric element is measured with the help of a multimeter in terms of current and voltage. The result shows that the output voltage continuously increased in the beginning. So, the output voltage and current are measured after stabilizing the readings. The output from the different conditions is measured and reported in Table 1.

Table 1 shows that the output voltage from both loading conditions, i.e., when motor operating grain-grinding machine and when motor operating chaff cutter machine is 26.8% and 83.5% greater than when motor running in idle condition, respectively. Similarly, compared to the motor running in an idle condition, the output current is increased by 50% when the motor was connected to the grain-grinding

**Table 1** Output of single piezoelectric under different operating conditions of motor

Output	Motor operating condition				
	Motor running under idle condition	Motor operating grain-grinding machine		Motor operating chaff cutter machine	
		Actual output	Increase in output as compared to idle running condition (%)	Actual output	Increase in output as compared to idle running condition (%)
Voltage (volt)	0.97	1.23	26.8	1.78	83.5
Current ( $\mu$ A)	10	15	50	27	170
Power ( $\mu$ W)	9.7	18.45	90	48.06	395

machine, and an increase of 170% in the same was observed when the motor was operating the chaff cutter machine. The reason for high output in loading conditions is that vibrations from other appliances powered by the motor get summed up with the vibrations of the electric motor which yields high-level vibration at the base of the motor. Maximum power (48.06  $\mu$ W) is generated when the electric motor is connected to the chaff cutter because a sudden high-amplitude vibration is produced during the cutting operation. Further, to increase the power output, the two piezoelectric elements are connected in parallel and series, and finally, output is recorded under all the three loading conditions. The output from the different conditions is shown in Table 2.

Table 2 reveals that the output in double piezoelectric is significantly higher than the single piezoelectric element. The output given in Table 2 suggested that the output voltage in series connection is more than a parallel connection because charge generated in both the piezoelectric elements are added in the circuit and generate a larger potential difference as an output. The results given in Table 2 also indicate that the output current in parallel connection is more than in the series connection because of charge generated in both the piezoelectric elements are added in both circuits and generate more charge particles at output nodes. The maximum power generated from the motor is 151.81  $\mu$ W when it operates the chaff cutter machine, and the piezoelectric elements are arranged in parallel connection. The output power obtained from the single piezoelectric element is compared with the power output obtained from two piezoelectric elements in all three said conditions and given in Table 3.

Further, data have also been recorded under laboratory conditions for a single piezoelectric element as well as for two piezoelectric elements when connected in both series and parallel combinations. The mini shaker is used to generate vibrations that excite the piezoelectric elements. The amplitude and frequency of the generated vibrations can be varied in the mini shaker itself with the help of a function generator (model no. 33220A, make: Agilent). In a specific set of experiments, the frequency is varied from 1 to 20 Hz keeping amplitude constant at 90mVpp. During the other set of

**Table 2** Output of double piezoelectric elements under different loading conditions of motor

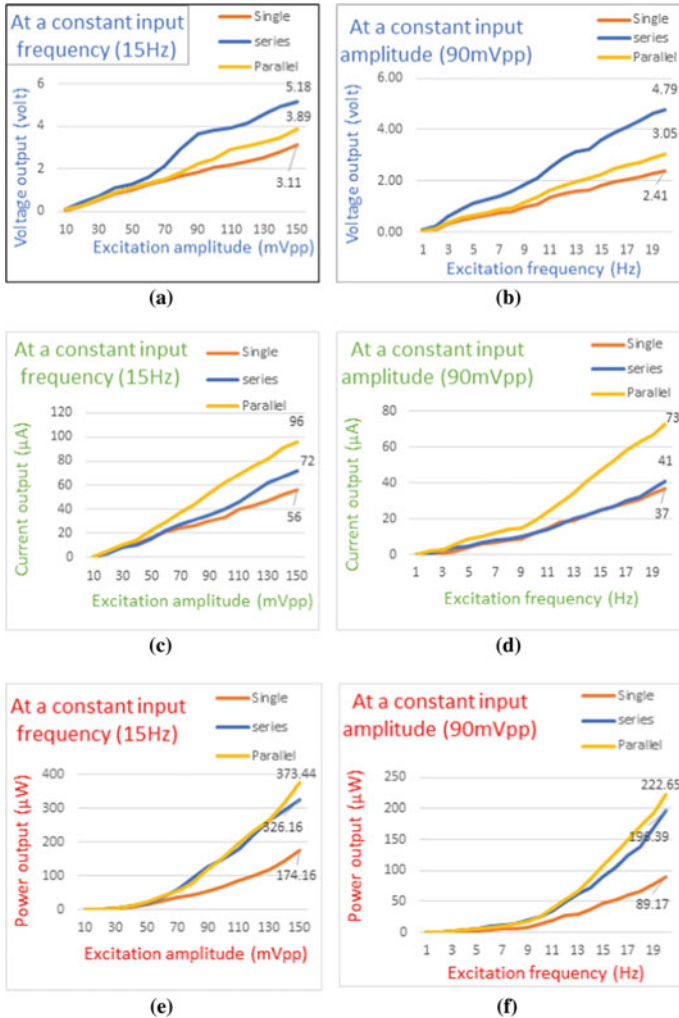
Output	Motor operating condition				
	Motor running under idle condition	Motor operating grain-grinding machine		Motor operating chaff cutter machine	
		Actual output	Increase in output as compared to idle running condition	Actual output	Increase in output as compared to idle running condition
Voltage (volt)	0.97	1.23	26.8%	1.78	83.5%
Current ( $\mu$ A)	10	15	50%	27	170%
Power ( $\mu$ W)	9.7	18.45	90%	48.06	395%

**Table 3** Comparison in power output of single piezoelectric element compared to double piezoelectric elements under different loading conditions (all the values are in  $\mu\text{W}$ )

Output power		Motor operating condition			
			Motor running under idle condition	Motor operating grain-grinding machine	Motor operating chaff cutter machine
Single piezoelectric element			9.7	18.45	48.06
Double piezoelectric elements	Series	Actual	15.62	48.32	102.96
		% more than single piezoelectric	61%	161%	114%
	Parallel	Actual	22.04	63.84	151.81
		% more than single piezoelectric	127%	246%	215%

experiments, the amplitude is varied from 10 to 150mVpp keeping frequency constant at 15 Hz. The output voltage and current from piezoelectric elements are rectified using the classic bridge rectifier and recorded with the help of a multimeter. Figure 6 shows the output from the piezoelectric element under different input excitation conditions.

Figure 6a shows the effect of excitation amplitude on output voltage when the frequency is constant. The graph shows that output voltage, while piezoelectric elements connected in series and parallel are more than the output from a single piezoelectric element. Further, the output voltage in the case of a series connection is more than in a parallel connection. The maximum voltage output from a single piezoelectric and two piezoelectrics in series and two piezoelectrics in parallel is 3.11 V, 3.89 V, and 5.18 V, respectively. Graphs shown in Fig. 6c show the output current under the same conditions. The current output graph shows that a maximum current of 96  $\mu\text{A}$  is generated when two piezoelectric elements are connected in a parallel combination. The current output from single piezoelectric and two piezoelectric elements in the series is 56  $\mu\text{A}$  and 72  $\mu\text{A}$ , respectively. Similarly, Fig. 6e shows a plot of power output and excitation amplitude at a constant frequency 15 Hz. The graph shows that power generated from the two piezoelectric elements is almost twice than the single piezoelectric element. The maximum power generated is 373.44  $\mu\text{W}$ , when two piezoelectric elements are connected in parallel combination. The power generated in the case of single piezoelectric and two piezoelectric elements in series connection is 174.16  $\mu\text{W}$  and 326.16  $\mu\text{W}$ , respectively. Graphs shown in Fig. 6b, d, f, show output voltage, output current, and output power when the piezoelectric element is excited at a constant amplitude of 90mVpp, and frequency is varied from 1 to 20 Hz. The output voltage graph (Fig. 6b) shows the maximum output of 4.79 V from the series connection, and the current graph (Fig. 6d) shows the



**Fig. 6** Plots of output entities corresponding to different vibration inputs **a** Output voltage versus excitation amplitude at constant frequency **b** Output voltage versus excitation frequency at constant amplitude **c** Output current versus excitation amplitude at constant frequency **d** Output current versus excitation frequency at constant amplitude **e** Power output versus excitation amplitude at constant frequency **f** Power output versus excitation frequency at constant amplitude

maximum output of  $73 \mu\text{A}$  from the parallel connection. The power output graph (Fig. 6f) also shows that the output from both series and parallel connections is almost twice that of the single piezoelectric element when excitation amplitude is constant, and frequency is varied. The maximum power generated from a single piezoelectric element, series connection, and the parallel connection is  $89.17 \mu\text{W}$ ,  $196.39 \mu\text{W}$ , and  $222.65 \mu\text{W}$ , respectively. Hence, the results show that the parallel connection

improves the total current output, the series connection enhances voltage output, and the parallel connection results in maximum power output.

The output in experiments is more than actual conditions because of variation in boundary conditions, vibration conditions (variation in amplitude and frequency of vibration), and additional noise vibration in actual conditions (but excitation is uniform in laboratory conditions). The results conclude that the use of piezoelectric elements under electric motor and other similar machines shows favorable technology in the field of energy harvesting which will absorb waste vibrations and produce electricity as output.

## 4 Conclusion

Piezoelectric elements play a significant role in harvesting energy from vibrations of dynamic machines. In the present work, the piezoelectric element is mounted on the motor base, and output is recorded in the form of voltage, current, and power. The output from the electric motor is recorded under three different conditions of a motor such as (a) idle running, (b) loaded with a grain grinding machine, and (c) loaded with a chaff cutter machine. The power output from the piezoelectric element (PZT diaphragm) when the motor was connected to the grain-grinding machine and chaff cutting machine is  $18.45 \mu\text{W}$  and  $48.06 \mu\text{W}$ , respectively, which is higher than the power obtained under condition when the motor was running idle. Further, to increase power output, two piezoelectric elements are arranged in different ways. The power outputs from the two piezoelectric elements when the motor was connected to the chaff cutting machine were  $102.96 \mu\text{W}$  and  $151.81 \mu\text{W}$  in series and parallel connections, respectively, which is much higher when the motor was running in idle condition and operating a grain-grinding machine. Laboratory and field experiments reveal that with an increase in force, the output parameters including power increase continuously. The results also show that the voltage output is maximum in a series combination, on the other hand, current and power output are maximum in the parallel combination. The power generated from the piezoelectric elements can operate small electronic gadgets may be of use to the farmers. It is also useful in industries having big electric motors and similar machines that generate vibrations.s

## References

1. Roundy, S., Wright, P.K., Rabaey, J.: A study of low level vibrations as a power source for wireless sensor nodes. *Comput. Commun.* **26**, 1131–1144 (2003)
2. Mirza, S., Singh, P., Kumar, R., Vyas, A.L., Shakher, C.: Measurement of transverse vibrations/visualization of mode shapes in square plate by using digital speckle pattern interferometry and wavelet transform. *Opt. Lasers Eng.* **44**, 41–55 (2006)
3. Ji, S.H., Yun, J.S.: Optimization of a flexible piezoelectric module structure based on a lead-free piezoceramic embedded in nanofiber composites. *Mech. Syst. Sig. Process.* **136**, 106447 (2020)

4. Jirungnimitsakul, S., Somwan, S., Limpichaipanit, A., Chaipanich, A., Ngamjarurojana, A.: Electrical Signal of Piezoelectric Buzzer by Impact Testing. *Integr. Ferroelectr.* **195**, 178–186 (2019)
5. Nestorović, T., Trajkov, M., Garmabi, S.: Optimal placement of piezoelectric actuators and sensors on a smart beam and a smart plate using multi-objective genetic algorithm. *Smart Struct. Syst.* **15**, 1041–1062 (2015)
6. Li, H., Liu, D., Wang, J., Shang, X., Hajj, M.R.: Broadband bimorph piezoelectric energy harvesting by exploiting bending-torsion of L-shaped structure. *Energy Convers. Manag.* **206**, 112503 (2020)
7. Hamdi, O., Mighri, F., Rodrigue, D.: Piezoelectric property improvement of polyethylene ferroelectrets using postprocessing thermal-pressure treatment. *Polym. Adv. Technol.* **30**, 153–161 (2019)
8. Zhang, Y., Song, X.-J., Zhang, Z.-X., Fu, D.-W., Xiong, R.-G.: Piezoelectric energy harvesting based on multiaxial ferroelectrics by precise molecular design. *Matter* **2**, 697–710 (2020)
9. Cho, J.Y., et al.: A multifunctional road-compatible piezoelectric energy harvester for autonomous driver-assist LED indicators with a self-monitoring system. *Appl. Energy* **242**, 294–301 (2019)
10. Song, Y., et al.: Road energy harvester designed as a macro-power source using the piezoelectric effect. *Int. J. Hydrogen Energy* **41**, 12563–12568 (2016)
11. Wang, C., et al.: Fabrication and performance of a power generation device based on stacked piezoelectric energy-harvesting units for pavements. *Energy Convers. Manag.* **163**, 196–207 (2018)
12. Pozzi, M., Zhu, M.: Characterization of a rotary piezoelectric energy harvester based on plucking excitation for knee-joint wearable applications. *Smart Mater. Struct.* **21**, 055004 (9pp) (2012)
13. Liang, R., Wang, Q.M.: High sensitivity piezoelectric sensors using flexible PZT thick-film for shock tube pressure testing. *Sensors Actuators A Phys.* **235**, 317–327 (2015)
14. Deterre, M., et al.: Energy harvesting system for cardiac implant applications. In: *Symposium on Design, Test, Integration and Packaging of MEMS/MOEMS (DTIP)*, 387–391 (2011)
15. Zhang, Z., Chen, Y., Guo, J.: ZnO nanorods patterned-textile using a novel hydrothermal method for sandwich structured-piezoelectric nanogenerator for human energy harvesting. *Phys. E Low-Dimensional Syst. Nanostruct.* **105**, 212–218 (2019)
16. Izadgoshasb, I., et al.: Optimizing orientation of piezoelectric cantilever beam for harvesting energy from human walking. *Energy Convers. Manag.* **161**, 66–73 (2018)
17. Song, R., Shan, X., Lv, F., Xie, T.: A study of vortex-induced energy harvesting from water using PZT piezoelectric cantilever with cylindrical extension. *Ceram. Inter.* **41**, S768–S773 (2015)
18. Cha, Y., et al.: Energy harvesting from a piezoelectric biomimetic fish tail. *Renew. Energy* **86**, 449–458 (2016)
19. Yadav, N., Chhabra, D.: Design and analysis of closed flow system with varying various parameters of hydrodynamics for PEH. *J. Control Instrum.* **8**, 30–37 (2018)
20. Shan, X., et al.: Enhancing the performance of an underwater piezoelectric energy harvester based on flow-induced vibration. *Energy* **172**, 134–140 (2019)
21. Hamlehdar, M., Kasaeian, A., Safaei, M.R.: Energy harvesting from fluid flow using piezoelectrics: A critical review. *Renewable Energy* **143**, 1826–1838 (2019)
22. Arivalagan, M., Lavanya, M., Deepa, S. & Suganya, B.: Piezotransducer generator energy harvesting bike vibrations. *Int. J. Emerg. Technol. Innov. Eng.* **1**, 146–149 (2015)
23. Minazara, E., Vasic, D., Costa, F.: Piezoelectric generator harvesting bike vibrations energy to supply portable devices. *Renew. Energy Power Qual. J.* **1**, 508–513 (2017)
24. Khameneifar, F., Arzanpour, S.: Energy harvesting from pneumatic tires using piezoelectric transducers. In: *Proceedings of the ASME Conference on Smart Materials, Adaptive Structures and Intelligent Systems, SMASIS2008*, vol. 1, pp. 331–337 (2008)
25. Erturk, A., Renno, J.M., Inman, D.J.: Modeling of piezoelectric energy harvesting from an L-shaped beam-mass structure with an application to UAVs. *J. Intell. Mater. Syst. Struct.* **20**, 529–544 (2009)

26. Zhang, X., et al.: A new self-powered sensor using the radial field piezoelectric diaphragm in d33 mode for detecting underwater disturbances. *Sensors* **19**, 962 (2019)
27. Zhao, X., Xiang, H., Shi, Z.: Piezoelectric energy harvesting from vehicles induced bending deformation in pavements considering the arrangement of harvesters. *Appl. Math. Model.* **77**, 327–340 (2020)

# Thermal Decomposition Kinetics of Medical Non-woven Fabrics Wastes: Model-Fitting Method



Uthayakumar Azhagu and Anand Ramanathan

## 1 Introduction

Living standard improvement causes large waste generation, which is unavoidable for developing and developed countries [1]. The medical field waste generation has increased daily because of hygiene healthcare and COVID-19 like pandemic situations [2]. Healthcare service persons need to wear protective kits such as gloves, gowns, masks, and drapes when in contact with patients to prevent infection spread [3]. Generally, textiles employed in the medical and healthcare field categorize as disposable and reusable cloths [4]. Based on COVID-19 pandemic situation observation, disposable single-use fabric usage doubled because of biological and infectious virus hazards. In the medical field, reusable woven cloth usage is drastically reduced because reusable cloths need to be sterilized and appropriately laundered to remove the pathogenic and harmful virus effects [4]. The textiles for medical purpose selection are based on the following aspects: government guidelines, protection, the comfort of usage, economic concern, and psychological tastes. The repetitive washing of reusable cloths may require massive energy consumption and vast wastewater to the environment. While disposable non-woven textiles have defending advantages over woven materials, it must be disposed of immediately because of bio-hazards. Instead of reusable cloths, many healthcare and surgical hospitals are moving toward single-use disposable non-woven fabrics [5].

Non-woven fabrics raw materials are polypropylene, polyethylene, polyester, and blends. Disposable non-woven fabrics are cost-effective, but safe disposal is difficult. Conventionally medical wastes are incinerated directly, which solves only safe discard and landfill reduction [6]. Direct incineration of hospital waste emits various

---

U. Azhagu · A. Ramanathan (✉)

Department of Mechanical Engineering, National Institute of Technology, Tiruchirappalli, India  
e-mail: [anandachu@nitt.edu](mailto:anandachu@nitt.edu)



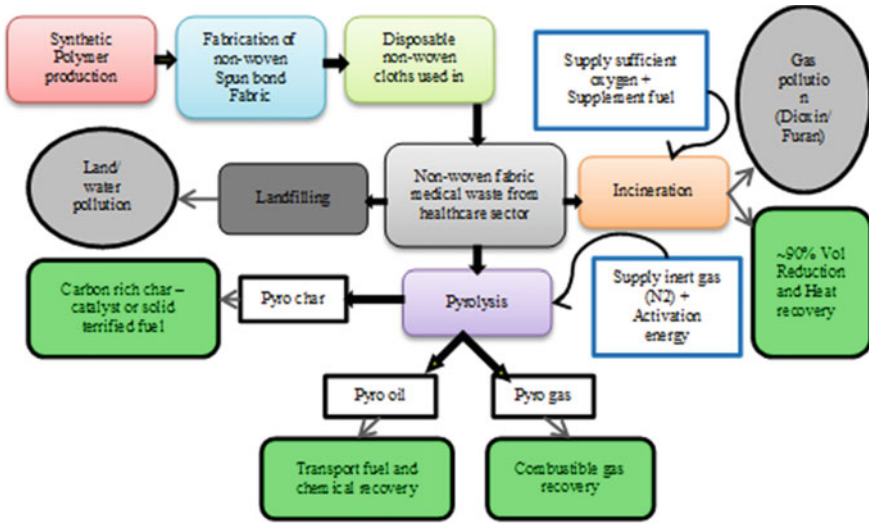


Fig. 1 Life span of medical disposable non-woven fabric

air pollutants such as hydrochloric acid, Polychlorinated dibenzo-para-dioxin, Polychlorinated dibenzofuran, and toxic metals (lead, cadmium, and mercury) [7]. Environmental and energy recovery options are not concentrated in incineration [8].

Non-woven fabric has good energy content because derived from fossil oil (non-renewable resources). The best solution to resolve conventional incineration demerits is pyrolysis [9]. Pyrolysis is a thermochemical recycling technique in which thermal degradation converts waste into fuel and chemicals in an inert atmosphere. Thermal degradation depends on the heating rate, operating temperature, and feed waste chemical composition. As a result of pyrolysis, oil, combustible gas, and char are obtained. Life span of medical disposable non-woven fabrics are shown in (Fig. 1).

Thermal degradation kinetics of medical waste carried out by thermogravimetric analysis (TGA) data. TGA data gives an idea of chemical decomposition (concentration change) based on temperature change [10]. The model fitting method is level headedly well for polymer pyrolysis reaction kinetic study and gives an acceptable kinetic result with the experimental. During polymers thermal degradation, thermal decomposition kinetics results probably show that temperature affects the pyrolysis reaction mechanism [11]. In this paper, the Arrhenius equation parameters are calculated by the model-fitting method with various reaction models. The kinetic analysis results could identify the optimum operating conditions and exact activation energy requirement for medical non-woven fabric waste pyrolysis reaction.

## 2 Materials and Methods

Medical waste is waste generated from healthcare centers and hospitals [12]. World Health Organization (WHO) guides us to categorize medical waste as general, infectious, hazardous, and radioactive waste. This work concentrated on infectious non-woven fabric waste from healthcare centers.

### 2.1 Medical Waste—Non-woven Fabric Waste

Non-woven fabrics are used in medical productive equipment: medical gowns, napkins, tissue paper, diapers, sanitary wipes, bed covers, pillow covers, and other disposable products [13]. Non-woven fabrics cut waste collected from the personal productive equipment (PPE) kits from medical. Blue color non-woven fabrics waste shredded into less than 1 mm size pieces and sample preparation for TGA analysis.

### 2.2 Thermogravimetric Analysis

The medical non-woven sample thermal decomposition was carried on a thermogravimetric analyzer (Perkin Elmer TGA 4000) at the heating rate of 10 °C/min with a 0.020 L/min nitrogen supply. Samples were prepared for TGA by shredding non-woven fabric medical waste from multiple locations. In this study, 10 mg of the finely shredded sample was uniformly spread in an aluminum crucible. Thermal degradation analysis is done between 30 and 700 °C. From TGA results shows the mass change for the concern temperature change.

### 2.3 Kinetic Study

The rate of reaction can be generally described by rate law as [14]

$$r = K(T)f(x) = \frac{dx}{dt} \quad (1)$$

$$x = \frac{(W_0 - W)}{(W_0 - W_\infty)} \quad (2)$$

The pyrolysis reaction rate depends on the operating temperature and heating rate. Hence, the Arrhenius equation is used to determine the rate constant [11].

$$K(T) = Ae^{\frac{-E_a}{RT}} \quad (3)$$

Apply Eq. (3) in Eq. (1)

$$\frac{dx}{dt} = Ae^{\frac{-E_a}{RT}} f(x) \quad (4)$$

where

- $W_0, W_\infty$  Initial and final mass of the reactant (mg).
- $W$  Reactant mass at a particular time (mg).
- $f(x)$  Reaction model.
- $E_a$  Activation energy.
- $A$  Pre-exponential factor or frequency factor.
- $A$  and  $E_a$  are commonly known as the Arrhenius parameters.
- $R$  Gas constant (kJ/kmol k).
- $T$  Operating temperature (K).

Heating rate  $\beta = \frac{dT}{dt}$  (K min<sup>-1</sup>).

Hence,  $\beta \frac{dx}{dT} = Ae^{\frac{-E_a}{RT}} f(x)$ .

Rearrange the above equation it becomes

$$\frac{dx}{f(x)} = \frac{A}{\beta} e^{\frac{-E_a}{RT}} dT \quad (5)$$

Above thermal degradation, kinetics expression can apply to the pyrolysis process [15]. Arrhenius parameters need to calculate by using the thermogravimetric analysis result.

**Model-fitting method.** Coats–Redfern (CR) approach expression: Take integration of Eq. (5) and rearrange [16].

$$\ln \frac{g(x)}{T^2} = \ln \frac{AR}{\beta Ea} - \frac{Ea}{RT} \quad (6)$$

Integral reaction model  $g(x) = \int_0^x \frac{dx}{f(x)}$ .

**Reaction model.** Different thermochemical reaction models are listed in Table 1.

### 3 Results and Discussion

Sending non-woven fabrics waste to landfills exacerbates environmental problems and energy loss due to the high energy content of non-woven fabric wastes. Pyrolysis is a process that can effectively convert polymer waste into fuel and chemicals.

**Table 1** Different reaction models  $f(x)$  with their integral function  $g(x)$ [17]

Notations	Reaction model	$f(x)$	$g(x) = \int_0^x \frac{dx}{f(x)}$
<i>Reaction order</i>			
$F_n$	Order of reaction ( $n \neq 1$ )	$(1-x)^n$	$\frac{-(1-x)^{(1-n)}}{(1-n)} + \frac{1}{(1-n)}$
$F_1$	First-order reaction	$(1-x)$	$-\ln(1-x)$
$F_2$	Second-order reaction	$(1-x)^2$	$(1-x)^{-1} - 1$
$F_3$	Third-order reaction	$(1-x)^3$	$0.5(1-x)^{-2} - 0.5$
<i>Diffusion models</i>			
$D_1$	One-dimensional diffusion	$0.5x^{-1}$	$x^2$
$D_2$	Two-dimensional diffusion	$(-\ln(1-x))^{-1}$	$-(1-x)\ln(1-x) + x$
$D_3$	Three-dimensional diffusion	$\frac{3}{2}(1-x)^{\frac{2}{3}}(1-(1-x)^{\frac{1}{3}})^{-1}$	$(1-(1-x)^{\frac{1}{3}})^2$
<i>Nucleation models</i>			
$P_{2/3}$	Power law 2/3	$\frac{2}{3}x^{-\frac{1}{2}}$	$x^{\frac{3}{2}}$
<i>Geometrical contraction models</i>			
$R_3$	Contracting volume	$3(1-x)^{\frac{2}{3}}$	$1-(1-x)^{\frac{1}{3}}$
$R_2$	Contracting area	$2(1-x)^{\frac{1}{2}}$	$1-(1-x)^{\frac{1}{2}}$

### 3.1 Thermogravimetric Analysis

The thermal decomposition of non-woven fabrics has three devolatilization stages [16]. Devolatilization is the removal of volatile substances from a solid. Three steps of thermal degradation are visualized in the TGA curve as shown in Fig. 2. The first stage is a drying stage in which moisture and physically absorbed water evaporated in the temperature range of 100–120 °C.

The second stage (150–38 °C) is the pre-pyrolysis stage, in which light and low carbon hydrocarbons are vaporized. The third stage is the main pyrolysis stage here; heavy hydrocarbons and volatile elements are wholly evaporated. Hence, the third stage gives a healthy peak in the TGA curve. Finally, after 450 °C a small quantity of non-volatile residues present in the crucible is known as fixed carbon and ash.

From the proximate analysis of the given sample, materials have a 98.5 weight percentage of volatile matters. The remaining was fixed carbon. There is no predictable moisture and ash content. The above TGA curve shows that moisture and ash content is not up to measurable. The calorific value of medical non-woven fabrics waste was 35.86 MJ/kg measured by bomb calorimeter.

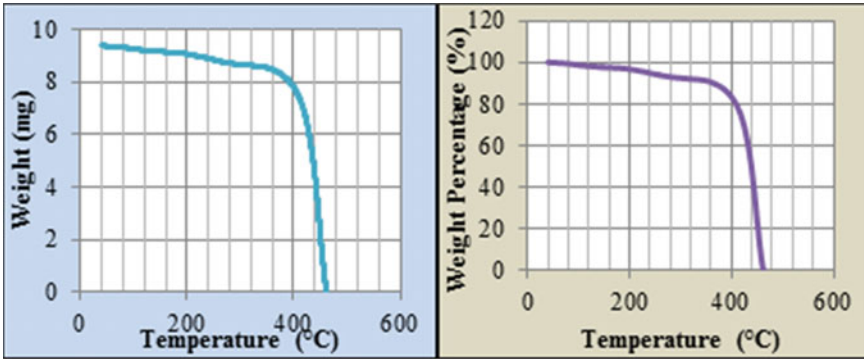


Fig. 2 Non-woven fabric TGA result (heating rate = 10 °C/min, N<sub>2</sub> flow rate = 0.020 L/min)

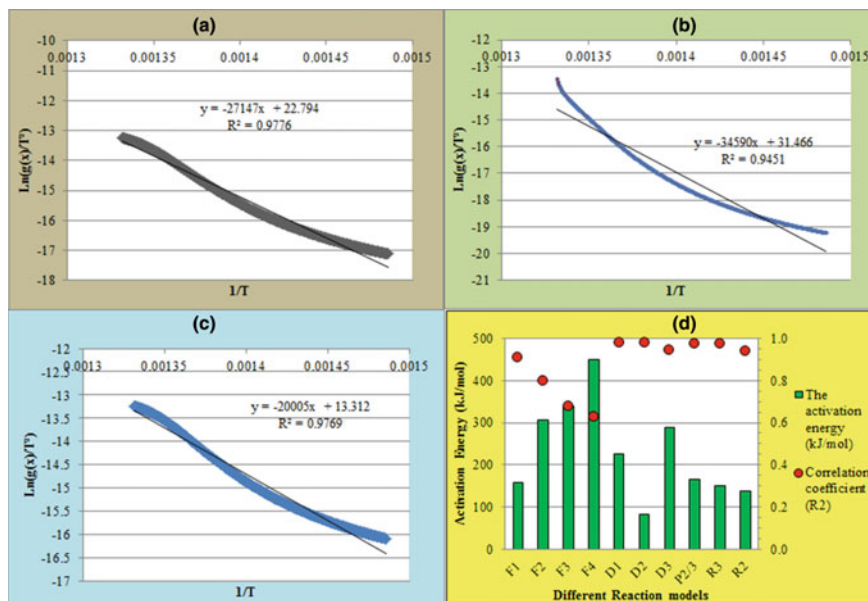
### 3.2 Kinetic Parameters

In the model fitting approach (CR method), curve drawn between  $1/T$  and  $\ln \frac{g(x)}{T^2}$ . The curve is then fitted by the line equation ( $Y = mX + C$ ) to calculate the Arrhenius parameters [18]. The line slope could calculate the activation energy, and then the pre-exponential factor was calculated by simple substitution. Correlation coefficient calculated to identify the fit quality is shown in (Fig. 3a, b & c).

The best reaction models are obtained based on the highest correlation coefficient ( $R^2$ ) [11] value of the linear regression fit. Figure 3d show the excellent fitting models for non-woven fabric wastes. Kinetic parameters of various reaction models obtained by CR model fitting method is listed in (Table 2).

## 4 Conclusion

Non-woven fabric raw materials are derived from fossil oil; hence, it has good heating value and volatility. Mostly direct incineration process is applied to destroy medical, hazardous waste. Energy recovery by the incineration process is shallow as compared to pyrolysis and generates toxic gases like dioxin/furans. The most acceptable solution for the above energy and environmental difficulties is pyrolysis. The model fitting approach with various reaction models of non-woven fabrics wastes pyrolysis gives activation energy in the range of 82.5–449.1 kJ/mol. Based on the highest  $R^2$  value and plot, the optimal reaction model for non-woven fabrics pyrolysis reaction is a one-dimensional diffusion model, a three-dimensional diffusion model, and a power law (2/3) model.



**Fig. 3** Coats–Redfern approach: **a** one-dimensional diffusion–reaction model, **b** two-dimensional diffusion–reaction model, **c** 2/3 power law reaction model, **d** comparison of Kinetic parameters for various reaction models

**Table 2** Model-fitting method (CR method) kinetic parameter for various reaction models

Notation	Reaction model	Activation energy (kJ/mol)	Pre-exponential factor	Correlation coefficient ( $R^2$ )
$F_1$	First-order reaction	158.0	$6.8E + 10$	0.91
$F_2$	Second-order reaction	305.2	$1E + 22$	0.80
$F_3$	Third-order reaction	338.4	$6.7E + 24$	0.68
$F_4$	Fourth-order reaction	449.1	$2.1E + 33$	0.63
$D_1$	One-dimensional diffusion	225.7	$2.2E + 15$	0.98
$D_2$	Two-dimensional diffusion	82.5	125,341	0.98
$D_3$	Three-dimensional diffusion	287.6	$1.6E + 19$	0.95
$P_{2/3}$	Power law	166.3	$1.2E + 11$	0.98
$R_3$	Contracting sphere	151.0	$7.6E + 09$	0.97
$R_2$	Contracting cylinder	137.9	$5.8E + 08$	0.94

## References

1. Bhatnagar, M.P.: Dealing with medical plastic waste: an aftermath of COVID—1. *Polym. Communiqué Mag* (2020). <https://www.researchgate.net/publication/342314509>
2. Ding, Z., Chen, H., Liu, J., Cai, H., Evrendilek, F., Buyukada, M.: Pyrolysis dynamics of two medical plastic wastes: Drivers, behaviors, evolved gases, reaction mechanisms, and pathways. *J. Hazard. Mater.* **402**, 123472 (2021). <https://doi.org/10.1016/j.jhazmat.2020.123472>
3. Patrício Silva, A.L., Prata, J.C., Walker, T.R., Campos, D., Duarte, A.C., Soares, A.M.V.M., Barcelò, D., Rocha-Santos, T.: Rethinking and optimising plastic waste management under COVID-19 pandemic: Policy solutions based on redesign and reduction of single-use plastics and personal protective equipment. *Sci. Total Environ.* **742**, 140565 (2020). <https://doi.org/10.1016/j.scitotenv.2020.140565>
4. Sun, G.: Disposable and reusable medical textiles. *Text. Hyg. Infect. Control.* 125–135 (2011). <https://doi.org/10.1533/9780857093707.2.125>
5. Syed, U., Parte, S., Sayed, U.: Recycling of Non Woven Waste. *Int. J. Adv. Sci. Eng.* **1**, 67–71 (2015)
6. Pandey, S., Divekar, R., Singh, A., Sainath, S.: Bio-medical waste management processes and practices adopted by select hospitals in Pune. *Oper. Supply Chain Manag.* **13**, 31–47 (2020). <https://doi.org/10.31387/OSCM0400251>
7. Zhang, L.H., Gong, Q.C., Duan, F., Chyang, C.S., Huang, C.Y.: Emissions of gaseous pollutants, polychlorinated dibenzo-p-dioxins, and polychlorinated dibenzo-furans from medical waste combustion in a batch fluidized-bed incinerator. *J. Energy Inst.* **93**, 1428–1438 (2020). <https://doi.org/10.1016/j.joei.2020.01.005>
8. Zroychikov, N.A., Fadeev, S.A., Bezruky, P.P.: Development of an environmentally safe process for medical waste disposal based on pyrolysis. *Therm. Eng.* **65**, 833–840 (2018). <https://doi.org/10.1134/S0040601518110101>
9. Anuar Sharuddin, S.D., Abnisa, F., Wan Daud, W.M.A., Aroua, M.K.: A review on pyrolysis of plastic wastes. *Energy Convers. Manag.* **115**, 308–326 (2016). <https://doi.org/10.1016/j.enconman.2016.02.037>
10. Deng, N., Zhang, Y. feng, Wang, Y.: Thermogravimetric analysis and kinetic study on pyrolysis of representative medical waste composition. *Waste Manag.* **28**, 1572–1580 (2008). <https://doi.org/10.1016/j.wasman.2007.05.024>
11. Almazrouei, M., Janajreh, I.: Model-fitting approach to kinetic analysis of non-isothermal pyrolysis of pure and crude glycerol. *Renew. Energy.* **145**, 1693–1708 (2020). <https://doi.org/10.1016/j.renene.2019.07.095>
12. Biomedical waste management in India: Priya Datta, Gursimran Kaur Mohi, J.C. Critical appraisal. *J. Lab. Physicians.* **5**, 85–88 (2018). [https://doi.org/10.4103/JLP.JLP\\_89\\_17](https://doi.org/10.4103/JLP.JLP_89_17)
13. Dash, A., Kumar, S., Singh, R.K.: Thermolysis of medical waste (Waste syringe) to liquid fuel using semi batch reactor. *Waste and Biomass Valorization.* **6**, 507–514 (2015). <https://doi.org/10.1007/s12649-015-9382-3>
14. Vasilopoulos, Y., Skořepová, E., Šoóš, M.: Comf: Comprehensive model-fitting method for simulating isothermal and single-step solid-state reactions. *Crystals.* **10**, (2020). <https://doi.org/10.3390/cryst10020139>
15. Wang, Z., Xie, T., Ning, X., Liu, Y., Wang, J.: Thermal degradation kinetics study of polyvinyl chloride (PVC) sheath for new and aged cables. *Waste Manag.* **99**, 146–153 (2019). <https://doi.org/10.1016/j.wasman.2019.08.042>
16. Liu, H., Wang, C., Zhang, J., Zhao, W., Fan, M.: Pyrolysis Kinetics and Thermodynamics of Typical Plastic Waste. *Energy Fuels* **34**, 2385–2390 (2020). <https://doi.org/10.1021/acs.energyfuels.9b04152>
17. Aboulkas, A., El harfi, K., El Bouadili, A.: Thermal degradation behaviors of polyethylene and polypropylene. Part I: Pyrolysis kinetics and mechanisms. *Energy Convers. Manag.* **51**, 1363–1369 (2010). <https://doi.org/10.1016/j.enconman.2009.12.017>

18. Xu, F., Wang, B., Yang, D., Hao, J., Qiao, Y., Tian, Y.: Thermal degradation of typical plastics under high heating rate conditions by TG-FTIR: Pyrolysis behaviors and kinetic analysis. *Energy Convers. Manag.* **171**, 1106–1115 (2018). <https://doi.org/10.1016/j.enconman.2018.06.047>



# Exergy Analysis of R1234yf and R1234ze as an Alternative to R134a in a Domestic Refrigeration System



Guna Muthuvairavan, S. Soma Sundaram, and P. K. Palani

## 1 Introduction

During the second half of the twentieth century, our day-to-day utilization of modern technological products increased. It is essential to enhance the amount of productivity and improvement in energy-related fields to cater the demand of the growing society with the ceaseless energy [1]. Toward this, researchers developed various ways of energy cycles in the past three decades to enhance energy sectors' efficiency. They illustrated two methods for the improvement of the thermodynamic system. Earlier, energy analysis was a basic method used for investigation of any process. It allowed us to compare the efficiency and process parameters by unveiling energy utilization efficiency, in selective components of the process and/or cycle with the currently attainable condition. A large quantity of heat is discharged by the thermodynamic process associated with the vapor compression refrigeration system. At a finite temperature difference, heat transfer takes place between the system and surroundings, which is the primary origin of the irreversibility of the cycle. The system performance is degraded due to the irreversibility. However, first law of thermodynamics does not present the data on, how and where the system performance getting degraded.

The second method practiced by many researchers in recent years is exergy analysis. Exergy analysis is based on the second law of thermodynamics and it is considered to be a powerful tool for design, performance evaluation, and optimization of energy system by determining the exergy destruction localities and finding out the maximum achievable performance of the system. By doing so, one can get a deep insight into each process in a realistic way, as well as further unforeseen approaches

---

G. Muthuvairavan (✉) · S. Soma Sundaram  
National Institute of Technology Puducherry, Karaikal, India

P. K. Palani  
Government College of Technology, Coimbatore, India

for improvements in the system. The exergy method usually analyzes each component of any complex system separately, which will identify the principal sites of unavailable energy, so that potential advancement can be carried out in those sites [2].

Global warming and ozone depletion are major concerns associated with heating ventilation and air conditioning (HVAC) equipment worldwide. This commenced to drop the harmful refrigerants and make a way for new suitable refrigerants as per international conventions Montreal (1987) and Kyoto protocol (1997) from time to time. Montreal protocol phases out substances including chlorofluorocarbons (CFCs), hydrochlorofluorocarbons (HCFCs), hydrofluorocarbons (HFCs), and halons which deplete the ozone layer. First, they phased out the CFCs and then halons; now the stepwise reduction of HCFCs and HFCs consumption is being carried out. HCFCs and HFCs release greenhouse gas emission which causes global warming. These substances have been ruled out as per the Kyoto protocol treaty. With this regard, even though the ozone depletion potential (ODP) value of 1,1,1,2-tetrafluoroethane (R134a) is zero, it is having 1400 global warming potential (GWP) value which is still lower than the already phased-out CFCs. The consumption of HFCs is growing in developing countries like India. Subsequently, the parties of Montreal protocol agreed on the phasedown for HFCs like R134a in 2016, which then came into force in 2019. Before that, many researches began to propose hydrocarbons (HCs) such as R600a (isobutene) and R290 (propane) which had very little GWP and zero value ODP [3, 4]. Another set of refrigerants such as R1234yf (2,3,3,3-tetrafluoro-1-propene) and R1234ze (trans-1,3,3,3-tetrafluoro-1-propene) hydrofluoroolefins (HFOs) become a sustainable solution in the near future [5–8]. The objective of the present study lies at evaluating the performance of these alternate refrigerants and analyzing their operating conditions in residential applications for better performance than conventional one [9].

## 2 Mathematical Formulation

Thermodynamic performance differs for different refrigerants since their different properties. The amount of exergy losses arises in each part of the system which is not alike [2]. To measure the exergy destruction or losses in the system, energy and exergy analysis is to be performed. The following presumptions are made in the present calculations.

1. Potential and kinetic energy changes are neglected.
2. Friction loss and other minor losses in the fluid flow domain are not counted.
3. Steady-state condition prevails in all the components of the system.
4. Condenser and evaporator pressure losses are neglected.

The input conditions used in the Engineering Equation Solver are shown in Table 1. Coefficient of performance (COP) is measure of VCR system performance based on first law of thermodynamics; it can be expressed as

**Table 1** Input conditions for EES simulation

Mass flow rate of refrigerant	$m_r$	1 kg/min
Effectiveness of liquid vapor heat exchanger	$\varepsilon$	1
Evaporator temperature	$T_{\text{evap}}$	263 K
Condenser temperature	$T_{\text{cond}}$	323 K
Ambient state temperature	$T_0$	298 K
Ambient pressure	$P_0$	100 kPa

$$\text{C.O.P} = Q_E/W_C$$

$$\text{C.O.P} = (h_1 - h_4)/(h_2 - h_1) \quad (1)$$

To get the deep insight of the component which undergoes severe destruction of available energy, exergy destruction of each element of the system can be expressed as [3]

Exergy destruction in evaporator ( $E_{\text{de}}$ ):

$$E_{\text{de}} = E_{x4} + Q_e(1 - T_0/T_r) - E_{x1}$$

$$E_{\text{de}} = m_r(h_4 - T_0s_4) + Q_e(1 - T_0/T_e) - m_r(h_1 - T_0s_1) \quad (2)$$

Exergy destruction in compressor ( $E_{\text{dcomp}}$ ):

$$E_{\text{dcomp}} = E_{x1} + W - E_{x2}$$

$$E_{\text{dcomp}} = m_r(T_0(s_2 - s_1)) \quad (3)$$

Exergy destruction in condenser ( $E_{\text{dcond}}$ )

$$E_{\text{dcond}} = E_{x2} - E_{x3}$$

$$E_{\text{dcond}} = m_r(h_2 - T_0s_2) - Q_c(1 - T_0/T_c) - m_r(h_3 - T_0s_3) \quad (4)$$

Exergy destruction in throttle valve ( $E_{\text{dthrottle}}$ ):

$$E_{\text{dthrottle}} = E_{x3} - E_{x4}$$

$$E_{\text{dthrottle}} = m_r(h_3 - T_0s_3) - m_r(h_4 - T_0s_4) \quad (5)$$

Total exergy destruction ( $\sum E_d$ ):

$$\sum E_d = E_{de} + E_{dcomp} + E_{dcond} + E_{dthrottle}$$

Exergetic efficiency ( $\eta_{exergy}$ ):

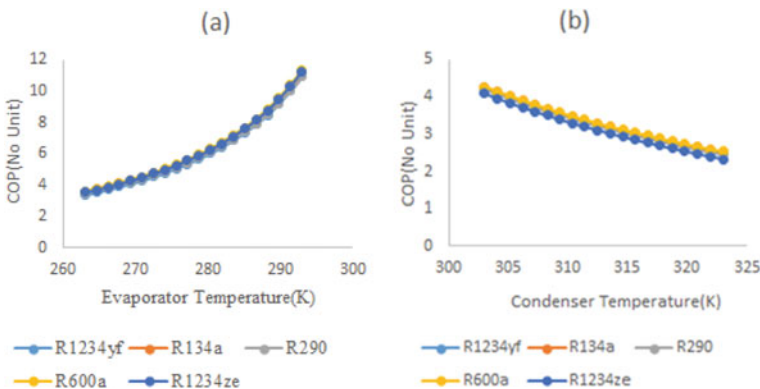
$$\eta_{exergy} = Q_e / W_c (1 - T_0 / T_r) \tag{6}$$

### 3 Results and Discussion

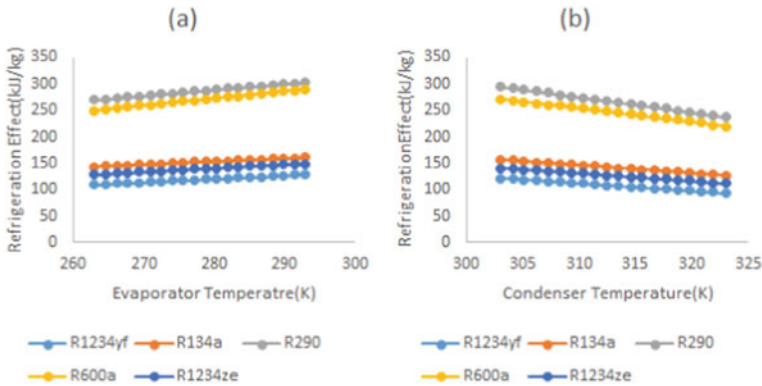
#### 3.1 Coefficient of Performance

While increasing the evaporator temperature from 263 to 293 K, for a condenser temperature of 313 K, the COP is increasing as shown in Fig. 1a, irrespective of refrigerant used, as discussed in various literatures [2–4, 7]. Pressure ratio in the compressor decreases with increase in evaporator temperature and causes the decrease in work input and increase in volumetric efficiency of the compressor, and due to increase in enthalpy of vaporization at higher evaporator temperature, cooling capacity of the system increases. Hence, both the effects of these two factors result in the COP value to increase as shown in Eq. (1). For the given range of evaporator temperature, R600a and R1234ze refrigerant offers a relatively higher COP than conventional R134a refrigerant, as they have high latent heat of vaporization [10]. However, R290 and R1234yf have slightly lower COP value than R134a.

In contrast to the evaporator temperature effect, the COP value for all the refrigerant decreases [2] as shown in Fig. 1b with rise in condenser temperature for a fixed evaporator temperature of 263 K. Figure 1b clearly implies that for the given range of condenser temperature, R600a refrigerant records relatively higher COP than other



**Fig. 1** Effect of **a** evaporator temperature and **b** condenser temperature on coefficient of performance (COP)



**Fig. 2** Effect of **a** evaporator temperature and **b** condenser temperature on refrigeration effect

refrigerants such as R290, R1234yf, and R1234ze. The performance of R600a is at par with that of R134a for the VCR system. However, R1234yf refrigerant has comparatively lower COP value than conventional R134a.

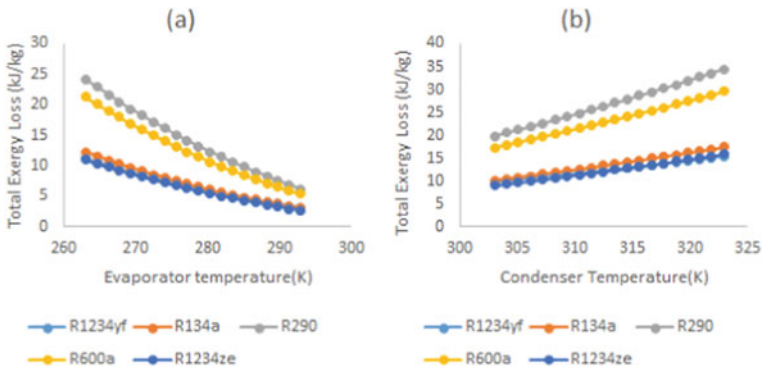
### 3.2 Refrigeration Effect

While increasing the evaporator temperature, the refrigeration effect of the system increases for all the refrigerants. From Fig. 2a, it is perceived that R290 is showing better refrigeration effect followed by R600a, R134a, R1234ze, and R1234yf for a fixed condenser temperature and given evaporator temperature range since enthalpy of vaporization at the particular operating condition is more for R290 [6].

By increasing condenser temperature, the refrigeration effect of the system decreases for all the refrigerants. From Fig. 2b, it can be found that R290 displays a higher refrigeration effect for chosen condenser temperature range (303–323 K) followed by R600a, R134a, R1234ze, and R1234yf for fixed evaporator temperature of 263 K [6].

### 3.3 Total Exergy Loss of the System

At higher evaporator temperature, the temperature difference between the evaporator and the surrounding refrigerated space is lowered which reduces the chance of irreversibility that occurs in the system which is very much essential in designing a VCR system based on the second law of thermodynamics [2–4].



**Fig. 3** Effect of **a** evaporator temperature and **b** condenser temperature on total exergy loss of the system

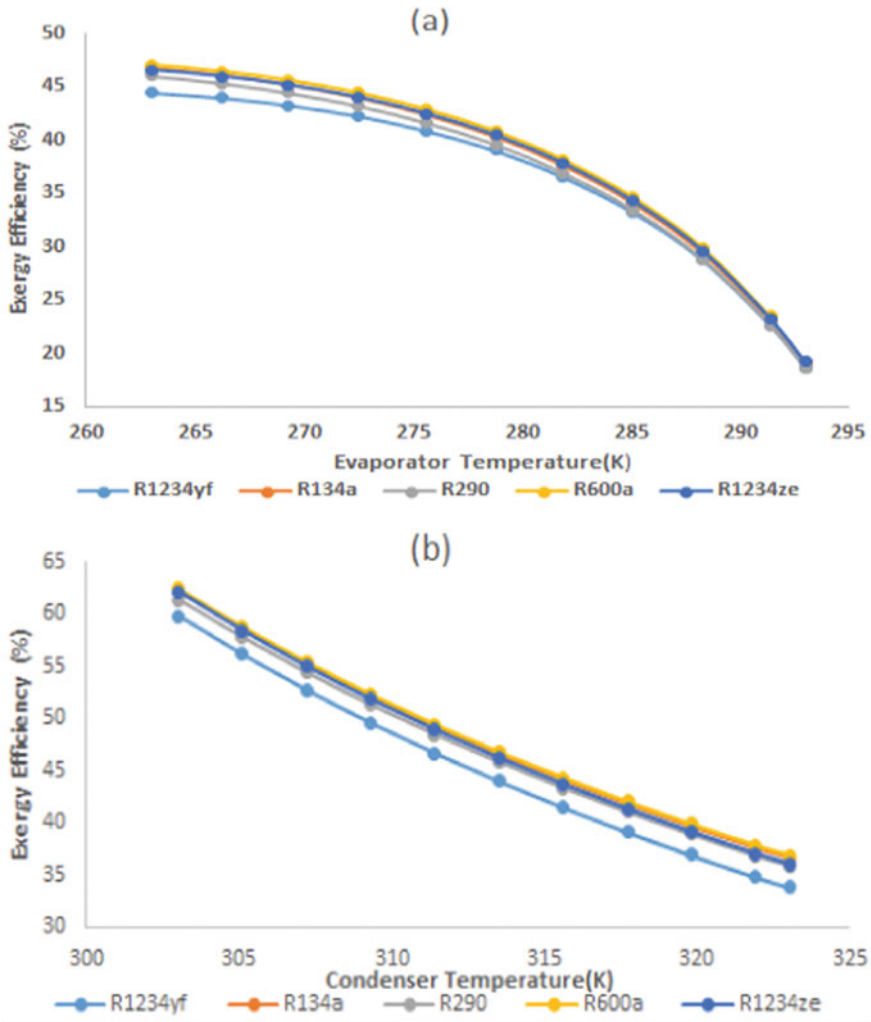
Among the selected refrigerants, R1234ze and R1234yf exhibit relatively lower total exergy loss than the traditional R134a refrigerant as well as its contemporary replacement refrigerants such as R290 and R600a refrigerants to a great extent as shown in Fig. 3a. When condenser temperature increases, the total exergy loss also increases as shown in Fig. 3b, which is not desirable one. Because at higher condenser temperature, the difference in temperature between system working fluid and surrounding air is increasing that causes the higher chance of irreversibility. Again here, R1234yf and R1234ze refrigerants show better results than other refrigerants [11].

### 3.4 Exergy Efficiency

Among the selected refrigerants chosen for this analysis, the refrigeration system with R600a refrigerant showing higher exergy efficiency and R1234ze is behaving very close with conventional R134a refrigerant as shown in Fig. 4a. Even though R1234ze is having lower exergy efficiency than R600a, it is performing very close with traditional R134a refrigerant as shown in Fig. 4b. For both condenser and evaporator temperature ranges, R1234yf is having lowest exergy efficiency [7].

## 4 Conclusion

A computational model based on the exergy destruction using EES is developed to analyze coefficient of performance, refrigeration effect, the total exergy loss, and exergy efficiency of the refrigerant R134a and its alternatives: R600a, R290, R1234yf, and R1234ze for the various ranges of evaporating and condensing temperatures are



**Fig. 4** a Effect of evaporator temperature on exergy efficiency. b Effect of evaporator temperature on exergy efficiency

evaluated. The results conclude that R600a, R290, R1234yf, and R1234ze refrigerants in comparison with R134a perform well for domestic residential applications within evaporator temperature (263–293 K) and condenser temperature (303–323 K). The following conclusions have been made:

It is suggested to operate the refrigeration system with higher evaporator temperature and lower condenser temperature as much as possible since both these conditions result in increase in coefficient of performance and cooling effect and decrease in total exergy losses.

For the given range of evaporator temperature, R600a and R1234ze refrigerant shows relatively higher COP than conventional R134a refrigerant for the VCR system. For the given range of condenser temperature, R600a refrigerant dispenses comparatively higher COP than other refrigerants. R290 is conferring a better refrigeration effect for a given evaporator temperature as well as the condenser temperature range. Even though, the refrigeration system with R600a refrigerant shows higher exergy efficiency than HFOs (R1234ze and R1234yf), however, HFOs (R1234ze and R1234yf) exhibit lower total exergy loss than the contemporary refrigerants such as R290 and R600a as well as the conventional R134a refrigerant to a great extent for the lower capacity refrigeration system of 0.4 to 0.7 ton of refrigeration (TR).

Although the performance parameters for R1234yf and R1234ze fall short than that of R134a as per the first law of thermodynamics, its eco-friendly properties and low exergy loss for lower capacity refrigeration system such as domestic refrigeration system offset the gap and make it a suitable alternative for R134a.

## References

1. Brown, S.: Single-site and industrial-scale schemes. *Appl. Energy* **53**(1–2), 149–155 (1996)
2. Yumrutaş, R., Kunduz, M., Kanoğlu, M.: Exergy analysis of vapor compression refrigeration systems. *Exergy An Int. J.* (2002)
3. Ahamed, J.U., Rahman, S., Masjuki, H.H.: Thermodynamic performance analysis of R-600 and R-600a as refrigerant. *Eng. e-Trans.* **5**(1), 11–18 (2010)
4. Ahamed, J.U., Saidur, R., Masjuki, H.H.: Prospect of hydrocarbon uses based on exergy analysis in the vapor compression refrigeration system. In: 2011 IEEE 1st Conference on Clean Energy Technology. CET 2011, pp. 300–304 (2011)
5. Sánchez, D., Cabello, R., Llopis, R., Catalán-Gil, J., Nebot-Andrés, L.: Energy assessment and environmental impact analysis of an R134a/R744 cascade refrigeration plant upgraded with the low-GWP refrigerants R152a, R1234ze(E), propane (R290) and propylene (R1270). *Int. J. Refrig.* **104**, 321–334 (2019)
6. Gaurav, Kumar, R.: Computational energy and exergy analysis of R134a, R1234yf, R1234ze and their mixtures in vapour compression system. *Ain Shams Eng. J.* **9**(4), 3229–3237 (2018)
7. de Paula, C.H., Duarte, W.M., Rocha, T.T.M., de Oliveira, R.N., Maia, A.A.T.: Optimal design and environmental, energy and exergy analysis of a vapor compression refrigeration system using R290, R1234yf, and R744 as alternatives to replace R134a. *Int. J. Refrig.* **113**, 10–20 (2020)
8. Rangel-Hernández, V.H., Belman-Flores, J.M., Rodríguez-Valderrama, D.A., Pardo-Cely, D., Rodríguez-Muñoz, A.P., Ramírez-Minguela, J.J.: Exergoeconomic performance comparison of R1234yf as a drop-in replacement for R134a in a domestic refrigerator. *Int. J. Refrig.* **100**, 113–123 (2019)
9. Yataganbaba, A., Kilicarslan, A., Kurtbas, I.: Irreversibility analysis of a two-evaporator vapour compression refrigeration system. *Int. J. Exergy* **18**(3), 340–355 (2015)
10. Kabul, A., Kizilkan, O., Yakut, A.K.: Performance and exergetic analysis of vapor compression refrigeration system with an internal heat exchanger using a hydrocarbon, isobutane (R600a). *Int. J. Energy Res.* **32**, 824–836 (2007)
11. Özgür, A.E., Kabul, A., Kizilkan, Ö.: Exergy analysis of refrigeration systems using an alternative refrigerant (HFO-1234yF) to R-134a. *Int. J. Low-Carbon Technol.* **9**(1), 56–62 (2014)



# Enhancement of Natural Convection Heat Transfer in Cylindrical Enclosure with Internal Heat Source



Sarthak Gautam, Mohd Juned Khan, Areeb Khan, Vivek Sharma, Fahad Farid, and Anil Kumar Sharma

## 1 Introduction

Natural convection heat transfer is also known as free convection or passive heat transfer mode. This mode of heat transfer has been a subject of research during the past decades due to its wide applications, such as in cooling of electronic equipment, nuclear reactors, aircraft cabin, heating and ventilation in building, etc. In case of nuclear industries, natural convection heat transfer plays a significant role. Heat removal by natural convection and its intensification increases significantly the safety of a reactor. Nowadays, the main heat transfer in nuclear reactor is being proposed by natural convection mode. After reactor shutdown, there is enough heat generation in the nuclear fuel due to radioactive decay called as decay heat that may lead to further melting of the fuel if this heat is not removed. In case of fast reactors, this decay heat is removed by natural convection to retain the core intact. In case of hypothetical core meltdown accident, the nuclear reactor core may melt away due to mismatch of heat generation and heat removal. The arrangements have been made to settle down core debris on a plate within the main vessel of the reactor. These collecting trays are called core catcher. Main function of core catcher is to retain, support, and cool the heat generating core debris via natural convection. For effective cooling of these core debris, central cylindrical chimney is placed in these trays that help in an efficient cooling of core debris. Jasmin Sudha et al. [1] studied multi-layer core catcher concept for future fast reactors to enhance the safety of the reactor by maintaining the main vessel integrity even for the severe

---

S. Gautam · M. J. Khan · A. Khan · V. Sharma · F. Farid  
Department of Mechanical Engineering, Jamia Millia Islamia, New Delhi 110025, India

A. K. Sharma (✉)  
Department of Mechanical Engineering, Faculty of Engineering and Technology, Jamia Millia Islamia, New Delhi 110025, India  
e-mail: [asharmal@jmi.ac.in](mailto:asharmal@jmi.ac.in)

© The Author(s), under exclusive license to Springer Nature Singapore Pte Ltd. 2022  
S. K. Natarajan et al. (eds.), *Recent Advances in Manufacturing, Automation, Design and Energy Technologies*, Lecture Notes in Mechanical Engineering,  
[https://doi.org/10.1007/978-981-16-4222-7\\_107](https://doi.org/10.1007/978-981-16-4222-7_107)

983

accident scenario. David et al. [2] reported simulations of passive heat removal after severe reactor accident in FBR. In their simulation, they found that the natural convection in the debris bed sets in, and decay heat is removed by the side wall of the enclosure. An investigation of the turbulent natural convection with multiple internal heat sources placed in liquid sodium was carried out by Sharma et al. [3]. The heat source was distributed uniformly on three plates with constant heat generation rate, and they came to the conclusion that entire core can be safely retained within the vessel. Post-accident heat removal was numerically and experimentally analysed by Das et al. [4] and focussed on molten fuel coolant interaction and grid plate melt followed by relocation of fragmented fuel. CFD simulations of heat transfer enhancement using multi-tray were carried out by Sharma et al. [5]. This study was focussed on the cooling capability of the design concept of core collection trays with multiple cylindrical chimneys. Sharma et al. [6] studied influences of cylindrical and annular central openings through the core catcher assembly to assess their relative heat transfer performances. A numerical study of natural convection from a localised heat source was carried out by Anil Kumar Sharma and Balaji [7]. Vidhyasagar and Sharma [8] analysed cooling of core debris using multiple passive jets in a liquid metal pool. They studied the influence of different orientations and angles of passive cooling pipes. The central chimney was found to have profound influence in the heat removal from heat source. Vidhyasagar et al. [9] proposed a modified core catcher plate by providing circular cooling pipes in the top collection plate. Anil Kumar Sharma et al. [10] studied natural convection of low Prandtl fluid in an enclosure with locally distributed heat source. Their study was focussed on assessing the heat distribution capacity of single and multi-trays in respecting the thermal limits on the collection trays. It is clear from the literature review that significant work has been carried out in recent past for enhancement of natural convection heat transfer from degraded core in nuclear power plants with different design options and cylindrical central chimney configuration. In the present study, the influence of four different configurations of openings/chimney is considered for effective heat removal along with cylindrical chimney. Best configuration among all feasible options is suggested for further analysis for actual plant conditions.

## 2 Computational Model

The source plate at the bottom of the cylindrical enclosure is circular in configuration. The computational axisymmetric models of the different configuration used in the present study are shown in Fig. 1. The top and bottom walls of the enclosure are considered as adiabatic, and side lateral wall is considered as sink at isothermal wall. The source plate is considered as hot isothermal wall placed in two different fluids viz air and liquid sodium.

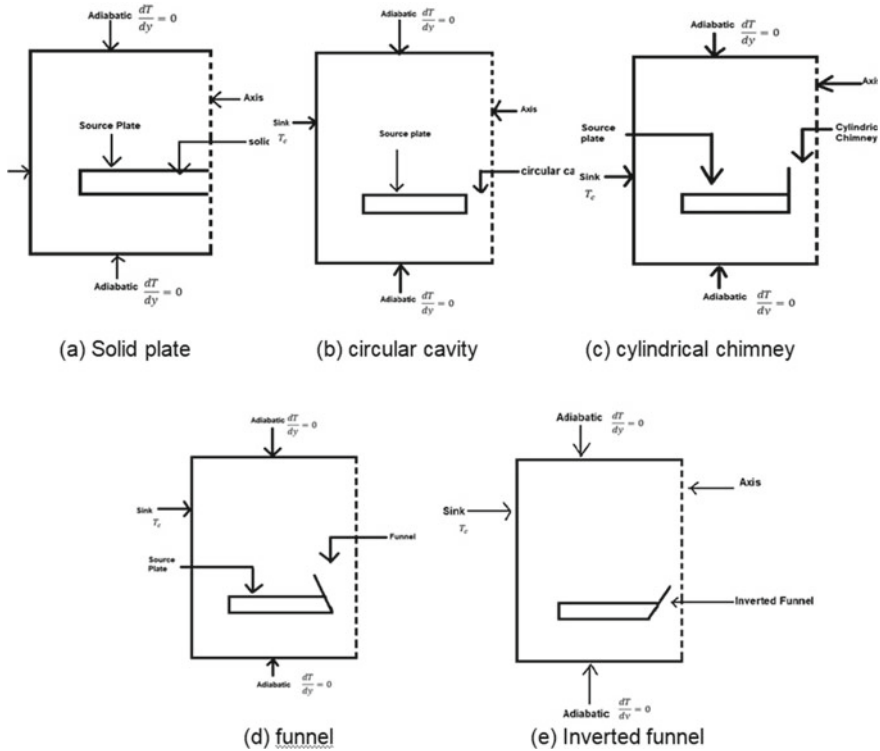


Fig. 1 Computational models

### 3 Governing Equations and Solution Methodology

The geometry under consideration is two-dimensional and axis symmetry as depicted in Fig. 1. The fluid is assumed to be incompressible, and the flow is laminar. The Boussinesq approximation is assumed to hold good, and all other thermo physical properties outside of density are assumed to be constant with respect to pressure and temperature.

The governing equations of fluid flow and heat transfer are as follows.

**Table 1** Comparison of Nusselt number for different grid sizes

Mesh size	Nusselt number	Percentage deviation
40 × 40	10.43	–
60 × 60	10.51	0.785%
80 × 80	10.55	1.150%

(a) Continuity:

$$\nabla \cdot \vec{v} = 0 \tag{1}$$

(b) Momentum:

$$\rho[\vec{v} \cdot \nabla \vec{v}] = \rho \vec{g} - \nabla p + \mu \nabla^2 \vec{v} \tag{2}$$

(c) Energy:

$$\rho c_p(\vec{v} \cdot \nabla T) = k \cdot \nabla^2 T \tag{3}$$

### 3.1 Solution Methodology

A commercial CFD solver ‘FLUENT’ is used to solve the discretized equations. This uses control volume method approach to discretize the equations. The second order upwind scheme is used for convective terms and energy equation. PISO algorithm is used for pressure–velocity coupling.

## 4 Grid Sensitivity Analysis

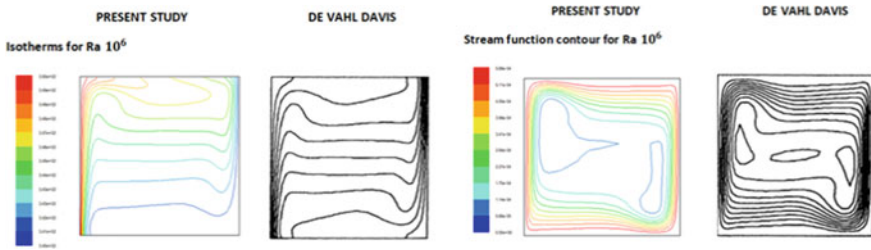
The comparison of the Nusselt number for different grid sizes is given in Table 1. It can be noted from the table that the on change in grid does not give significant variation in the Nusselt number. Thus, the obtained results are grid independent. Therefore, the further analysis is carried out by considering grid size of 60 × 60 for this case. Similar exercise is repeated for all the cases studied.

## 5 Validation Studies

In this section, the fluid flow and heat transfer characteristics given in benchmark solution of De Vahl Davis [11] inside a square cavity are repeated. Nusselt numbers were calculated by considering the heat transfer rate at hot plate and compared with

**Table 2** Variation of present results with benchmark solution

Rayleigh number	Nusselt number De Vahl Davis [11]	Nusselt number present study	Percentage deviation (%)
$10^3$	1.118	1.124	0.715
$10^4$	2.243	2.270	1.2
$10^5$	4.519	4.486	1.4
$10^6$	8.800	8.76	0.45



**Fig. 2** Isotherms and stream function for  $Ra = 10^6$  of present study with Davis [11]

benchmark solution as given in Table 2. It is found that percentage deviations of the results are not large enough to consider. All the variations are less than 1.4%.

Also the contours of isotherms and streamlines are shown in Fig. 2 for  $Ra = 10^6$ . On comparing the contours of De Vahl Davis [11] benchmark solution, it can be observed that the contours of isotherms and stream functions do not differ significantly and show similar behaviour. These results give confidence to analysis and interpretation of data and confidence in model developed to predict natural convection in the cavities.

## 6 Result and Discussion

### 6.1 Case Study with Air

In this section, the results obtained by taking air as the fluid flowing inside the cylindrical enclosure are highlighted. Heat transfer characteristics and fluid flow in the enclosure are brought out for all the cases of openings considered. Table 3 below shows the heat transfer rates obtained.

**Table 3** Heat transfer rate for different configurations with air as a fluid

Solid core plate	Circular cavity	Cylindrical	Funnel	Inverted funnel
0.955 W	6. W	6.868 W	6.832 W	6.816 W

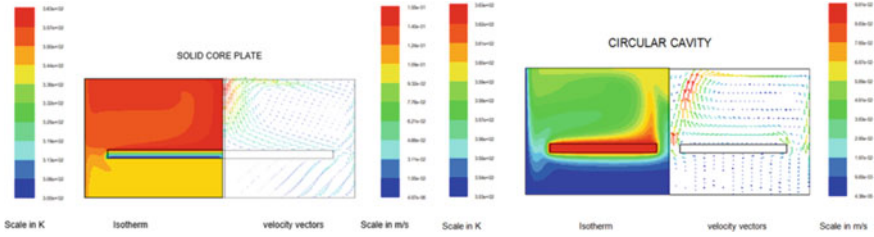


Fig. 3 Isotherm and velocity vector for solid and circular opening in source plate

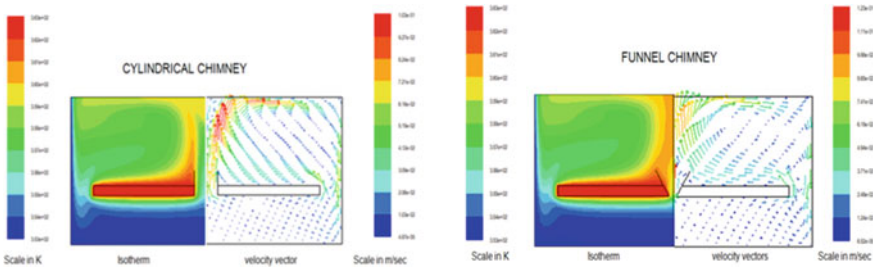


Fig. 4 Isotherm and velocity vectors for cylindrical chimney and funnel shaped chimney

From the isotherm for a case of solid source plate without any chimney, it is observed that the highest temperature prevails on the top pool of the source Fig. 3. The contour shows the temperature variation near the source plate. The temperature below the source plate is seen to be low as compared to upper part of the enclosure.

Figure 3 also gives the velocity vector on the right side along with isotherms. It is clear from it that the maximum velocity of 0.155 m/s is obtained close to the top of the enclosure in case of solid source plate. The velocity vectors emerge from the source plate and move upwards towards the top. As the top wall is assumed to be adiabatic, the velocity vectors change its direction and move towards the side walls of the enclosure. The velocity is very low below the source plate, and there is no motion of fluid is seen.

In the case of circular chimney, it can be observed from its isotherm that the bottom of the source plate, which earlier had no considerable change in temperature, shows temperature variation there as well. Heat rejected near the circular cavity flows towards the bottom of source plate through the circular cavity, which leads to change in temperature at the bottom. In velocity vector contour for circular opening, it is observed that velocity vectors emerging from the source plate go towards the top, but some of it passes through the cavity and moves towards the bottom, changing the stagnant behaviour of fluid at that place. Maximum velocity of magnitude  $9.8 \times 10^{-2}$  m/s is observed near the top of the enclosure and also in the circular cavity, and the velocity is quite high.

For a case of cylindrical chimney, the isotherm, as depicted in Fig. 4, indicates that the temperature inside the chimney is low which means that the fluid above and below the chimney is inter-mixed and shows similar behaviour. Hence, the stratification of temperature is removed considerably. Highest temperature is noted at the source plate.

Velocity vector contour, as shown in Fig. 4, clearly indicates that the fluid enters the cylindrical chimney and moves upward. Above the source plate, the fluid goes and then taking a turn near the top due to adiabatic wall. Maximum velocity is noted near the top of the enclosure of magnitude  $1.04 \times 10^{-1}$  m/s.

For case of funnel shaped chimney, the isotherm, as depicted in Fig. 4, on right hand side indicates that there is a mixing of fluid inside the chimney, but it is lower as compared to the cylindrical one. The bottom area of funnel is less due to which there is not enough movement of fluid below the source plate towards the upper side of the cylindrical enclosure. In velocity vector contour as shown in Fig. 4 for funnel shaped configuration, it clearly indicates the enhanced movement of the fluid on the source plate and fluid moves towards the bottom; but as the area of the chimney at the bottom is not large enough, there is a rise of velocity magnitude near the bottom. It can be seen from the contour that the maximum velocity is observed at that position of the chimney, and its magnitude is  $1.23 \times 10^{-1}$  m/s.

For case of inverted funnel chimney, the isotherm is depicted in Fig. 5, and we can observe that the fluid entering the chimney from the source plate loses its heat as it reaches the bottom of the chimney due to large area of bottom of chimney and significant mixing with the bottom fluid.

In velocity vector contour as shown in Fig. 5, it can be seen that most of the fluid goes up towards the top, and maximum velocity is observed there with magnitude of  $1.53 \times 10^{-1}$  m/s. The fluid entering the chimney from top has comparatively lower magnitude than the fluid at the top.

From the above table and contours, it can be easily observed that all the configurations of chimney including the circular cavity give approximately same heat transfer

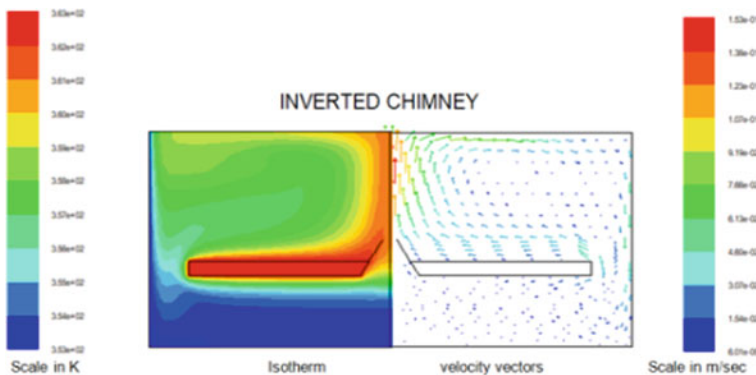


Fig. 5 Isotherm and velocity vector contours for inverted funnel chimney

**Table 4** Heat transfer rate for different configurations with liquid sodium as a fluid

Solid core plate	Circular cavity	Cylindrical	Funnel	Inverted funnel
6677.413 W	7550.637 W	7567.725 W	7670.643 W	7618.367 W

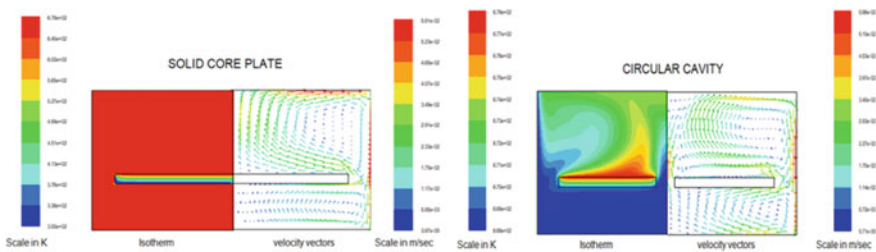
rate. On the basis on above table, it can be said that use any of the above configurations leads to effective heat removal from the plate. The source plate must have an opening on it through which the mixing of fluid takes place in the bottom region of the cylindrical enclosure as well. The opening eliminates the temperature stratification and gives motion to the bottom stagnant fluid.

### 6.2 Case Study with Liquid Sodium

In this section, the results obtained by taking low Prandtl fluid inside the enclosure are highlighted. The low Prandtl fluid used in present study is liquid sodium, which is generally used as coolant in fast reactors due to its excellent heat transfer characteristics. The results of heat transfer from the source are shown in the Table 4. It is clear from this that the heat transfer is excellent as compared to air.

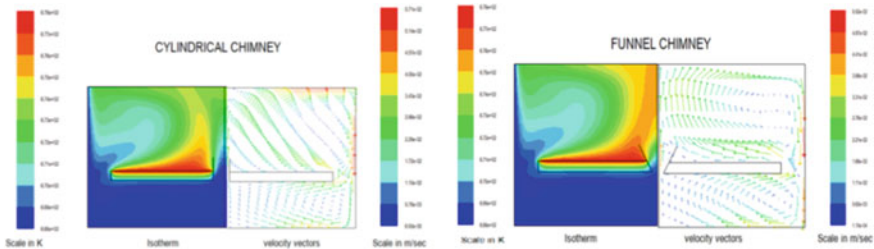
The following figures display the contours obtained for different configurations of chimney with liquid sodium. Isotherms and velocity vectors for solid plate and with circular opening in the source plate are depicted in Fig. 6. From isotherms, for a solid plate indicates that the whole fluid has almost same temperature. From its velocity vector contour, it can see that the fluid near the top wall moving towards side wall and near the side wall moving towards bottom has highest velocity of magnitude  $5.81 \times 10^{-2}$  m/s. It is evident from velocity vector that fluid near the top wall, which is adiabatic, takes a turn towards side wall which is final sink.

For a case of circular cavity, the isotherm indicates that the source plate close to the cavity has higher temperature as compared to outer side of plate. The fluid near the chimney has higher temperature and moves upwards. The fluid at the bottom side of the core is mixing with the fluid of high temperature, thus decreasing the temperature effectively.



**Fig. 6** Isotherm and velocity vector for solid and with circular opening in source plate





**Fig. 7** Isotherm and velocity vector contours for cylindrical and funnel shaped chimney

For a case of circular opening, the fluid in the enclosure has highest velocity of magnitude  $5.66 \times 10^{-2}$  m/s and moves upward (Fig. 6). The fluid takes a turn near the top wall and transfers the heat to the side lateral wall of the enclosure. The fluid just below the chimney gets heated up and starts moving upward, thus increasing the motion of fluid in the below the source plate.

For a case of cylindrical chimney, the isotherm as depicted in Fig. 7 on right hand side indicates that fluid at the bottom is getting sufficient space to move up which decreases the temperature of fluid effectively. Also, the bottom fluid is playing significant role in decreasing the temperature of fluid near the side walls.

The maximum velocity of fluid is found to be  $5.71 \times 10^{-2}$  m/s at the lateral walls of the enclosure. The fluid is moving up through the chimney and takes a turn towards the lateral walls to remove heat through it. The proper mixing of fluid is displayed near the side walls which decreases the overall temperature near the source effectively.

For a case of funnel chimney, the isotherm indicates that the top centre area of the reactor has lower temperature as compared to the other configurations. Different patterns of temperature are observed in the chimney. Also, the bottom low temperature fluid also helps in decreasing the high heated fluid near the lateral walls. From its velocity vector contours as shown in Fig. 7, it can be observed that the maximum fluid velocity of magnitude  $5.51 \times 10^{-2}$  m/s is at the bottom of the chimney, due to the less area. The upper side of the chimney spreads the fluid to a larger area therefore, decreasing the surrounding temperature. Due to this motion of fluid at the bottom of chimney, the rest of the bottom fluid gains significant velocity and starts interacting with the high-temperature fluid near the corners.

In case of the inverted funnel chimney, the fluid at the bottom is participating actively to enhance mixing of the fluid. The colder fluid at the bottom of chimney moves up and improves coolability. However, it is observed that the funnel shaped chimney increases the heat removal from to the sink to a much higher extent than any other configuration. Hence, a funnel chimney is suggested to maximise heat removal.

## 7 Conclusion

Present study focussed on the detailed analysis on the different chimney configurations by selecting two different fluids, air and liquid sodium. The elaborate validation and verification of the computational model used in the study are carried out. The detailed heat transfer and flow characteristics are investigated in five different chimney configurations. It is found that the use of chimney enhances the rate of heat transfer from the source irrespective of the fluid used. For air, any plate which has at least one opening in it can be selected to maximise the heat removal from the plate. However, for liquid sodium, the funnel chimney configuration gives the best results to maximise heat transfer rate.

## References

1. Jasmin Sudha, A., Velusamy, K., Chellapandi, P.: Amulti layer core catcher concept for future sodium cooled fast reactors. *Ann. Nucl. Energy* **65**, 253–261 (2014)
2. David, D.K., Nashine, B.K., Selvaraj, P., Chellapandi, P.: Numerical simulation of passive heat removal under severe core meltdown scenario in a sodium cooled fast reactor. *Nucl. Eng. Des.* **291**, 188–203 (2015)
3. Sharma, A.K., Velusamy, K., Balaji, C.: Conjugate transient natural convection in a cylindrical enclosure with internal volumetric heat generation. *Ann. Nucl. Energy* **35**(8), 1502–1514 (2008)
4. Das, S.K., Sharma, A.K., Hemanth Rao, E., Anandan, J., Avinash, C.H.S.S., Kondala Rao, R., Murthy, S.S., Malarvizhi, B., Lydia, G., Kumaresan, M., Ponraju, D., Nashine, B.K., Chellapandi, P.: Post-accident heat removal: Numerical and experimental simulation. *Nucl. Eng. Des.* **265**, 1246–1254 (2013)
5. Sharma, A.K., Velusamy, K., Rakhi.: Integrated CFD investigation of heat transfer enhancement using multi-tray core catcher in SFR. *Ann. Nucl. Energy* **104**, 256–266 (2017)
6. Sharma, A.K., Das, S.K., Harvey, J.: Experimental and numerical analysis of natural convection in geometrically modelled core catcher of the liquid-metal-cooled fast reactor. *Nucl. Technol.* **165**(1), 43–52 (2009)
7. Sharma, A.K., Balaji, C.: A numerical study of natural convection from a localized heat source in the lower plenum of a fast breeder reactor under failed conditions. *Heat Mass Transf.* **40**(11), 853–858 (2003)
8. Jhade, V., Sharma, A.K.: Cooling of heat generating core debris using multiple passive jets in a liquid metal pool of LMFBR. *Prog. Nucl. Energy* **116**, 137–147 (2019)
9. Jhade, V., Sharma, A.K., Ponraju, D., Nashine, B. K., Selvaraj, P.: Natural convection heat transfer enhancement using cooling pipes in the heat generating debris bed. *Adv. Fluid Thermal Eng.* 33–42 (2019)
10. Sharma, A.K., Velusamy, K., Balaji, C.: Turbulent natural convection of sodium in a cylindrical enclosure with multiple internal heat sources: a conjugate heat transfer study. *Int. J. Heat Mass Transf.* **52**(11–12), 2858–2870 (2009)
11. De Vahl Davis, G.: Natural convection of air in a square cavity: a benchmark numerical solution. *Int. J. Numer. Meth. Fluids* **3**(3), 249–264 (1983)